Project No. 14-7829

Integrated Approach to Fluoride High Temperature Reactor Technology and Licensing Challenges (FHR-IRP)

Integrated Research Project

Farzad Rahnema
Georgia Institute of Technology

Collaborators
Texas A&M University
University of Michigan
Virginia Polytechnic Institute and State University

Tom O'Connor, Federal POC
David Holcomb, Technical POC

NEUP Nuclear Energy University Programs
U.S. Department of Energy

Integrated Approach to Fluoride High Temperature Reactor Technology and Licensing Challenges (FHR-IRP)

Final Report

Prepared by:
FHR-IRP Project Team (please see inner cover page)

Submitted by:
Farzad Rahnema (farzad@gatech.edu)
Project PI
Nuclear and Radiological Engineering
Georgia Institute of Technology
770 State Street, Atlanta, Ga 30338-0745

Performed Under:
Project Number IRP-14-7829
Under DoE Contract Number DE-NE0008306
(GT Project 2506Q45)

Technical Contact: David Holcomb
Federal Manager: Diana Li

FOR PUBLIC DISTRIBUTION

FHR-IRP Project Team

Lead Organization:
Georgia Institute of Technology, Atlanta, Georgia
Farzad Rahnema (PI)
Bojan Petrovic (Co-PI)
Dingkang Zhang
Srinivas Garimella
Preet Singh

Partnering Organizations:

Academia:
University of Michigan
Xiaodong Sun (Co-Pi)

Virginia Tech
Jinsuo Zhang (Co-Pi)

Texas A&M University, College Station, Texas
Pavel Tsvetkov (Co-Pi)

Texas A&M University, Kingsville, Texas
Yousri Elkassabgi (Co-PI)

Industry:
AREVA Federal Services LLC, Lynchburg, Virginia
Kim Stein (Co-PI)

Southern Company Services; Research and Environmental Affairs, Research and Technology Management, Birmingham, Alabama
Nicholas Smith

National Laboratory Collaboration:
Oak Ridge National Laboratory (ORNL), Oak Ridge, Tennessee
Grady Yoder (Co-PI)

International Research Collaboration:
Politecnico di Milano, Milano, Italy
Antonio Cammi (Co-PI)
Lelio Luzzi (Co-PI)
Marco Ricotti (Co-PI)

University of Zagreb, Zagreb, Croatia
Davor Grgic (Co-PI)
Nikola Cavlina (Co-PI)
Dubravko Pevec (Co-PI)

Shanghai Institute of Applied Physics, Chinese Academy of Sciences, Shanghai, China

Kun Chen (Co-PI)

Project/Report Contributors

Research Faculty/Scientists/Engineers, Post-Docs

Gwyn Rosaire (Texas A&M University)
Dingkang Zhang (Georgia Tech)

Graduate Students (MS and PhD)

Paul Burke (Georgia Tech)
Kristina E Reed (Georgia Tech)
Pietro Avigni (Georgia Tech)
Kevin Chan (Georgia Tech)
Stefano Terlizzi (Georgia Tech)
Andrew Johnson (Georgia Tech)
L. Michael Huang (Georgia Tech)
Giovanni Maronati (Georgia Tech)
Kyle Ramey (Georgia Tech)
Jason Hearne (Texas A&M University)
Charles Stratton (Texas A&M University)
Hanniel Honang (MS, Texas A&M University)
Grace Marcantel (Texas A&M University)
Hsun-Chia Lin (University of Michigan)
Sheng Zhang (University of Michigan)
Ryan Chesser (Virginia Tech)
Qiufeng Yang (Virginia Tech)
Yafei Wang (Virginia Tech)

Undergraduate Students

Joseph Farleo (Georgia Tech)
Hemin Noorani (Georgia Tech)
Rebecca Ambrecht (Georgia Tech)
Stephen DelSordo (Georgia Tech)
Vincent Hughes (Georgia Tech)
Robert Kiblinger (Georgia Tech)
Julie Luong (Georgia Tech)
Ryan Brownfield (BS, Texas A&M University)
Wei Lockhart (BS, Texas A&M University)

Table of Contents

List of Figures xvi
List of Tables xxxvii
List of Abbreviations xlii
1. Executive Summary 1
2. Project Tasks 6
3. Tritium Source Generation Model 7
3.1. Objectives of Subtask 3.1: Determining Radiation Environment for Tritium Management 7
3.2. Tritium Source Generation Methodology, Model and Analyses 7
3.2.1. Overview of the performed work 7
3.2.2. Previous work 8
3.2.3. Pathways of Tritium Production 8
3.2.4. Reference FHR Model 10
3.2.5. Methodology 11
3.2.5.1. MCNP6.1 12
3.2.5.2. SCALE6.2: CSAS-MG 13
3.2.5.3. SCALE6.2: COUPLE 13
3.2.5.4. SCALE6.2: ORIGEN-S 14
3.2.6. Results 14
3.2.6.1. Reference Case (Full-core at 9% enrichment) 14
3.2.6.2. Deviation of COUPLE Reaction Rates from those generated directly in MCNP Tallies 15
3.2.6.3. Impacts from Modeling and Design Parameters 16
3.2.6.4. Impact of Assumed Fuel Isotopics 19
3.2.6.5. MCNP6.1: full-core tallies 21
3.2.6.6. SCALE6.2.2: COUPLE 1-group library generation 22
3.2.6.7. SCALE6.2.2: ORIGEN tritium production calculations 23
3.2.7. Time-Evolution of Tritium Production Parameters 23
3.3. Conclusions 24
3.4. References 25
4. Liquid Salt Impurity Removal, Redox and Corrosion Control 26
4.1. Introduction 26

4.1.1. Tritium 26
4.1.2. Noble Gases 27
4.1.3. Halogens 28
4.1.4. Alkaline Metals 29
4.1.5. Rare Earths 29
4.1.6. Noble Metals and Semi-Noble Metals 30
4.1.7. Tellurium and Antimony 31
4.1.8. Actinides 32
4.1.9. Corrosion Products 32
4.1.10. Oxygen, Oxides, Hydroxides and Moisture 33
4.1.11. References 34
4.2. Primary Salt Purification Methods 37
4.2.1. Liquid/Liquid Separation 37
4.2.1.1. Equilibrium Model 37
4.2.1.2. Multistage Extraction model 40
4.2.1.3. Summary 46
4.2.2. Electrochemical Separation 47
4.2.3. Reference 50
4.3. Redox Control for the Mitigation of Material Corrosion in Molten Fluorides 52
4.3.1. Theory of Redox Control 52
4.3.2. Dissolved Salt Control Using Eu(III)/Eu(II) 53
4.3.2.1. Experimental methods 53
4.3.2.2. Results and discussion 55
4.3.2.2.1. Dynamic reference electrode 55
4.3.2.2.2. Determining of concentration ratio of Eu^{3+}/Eu^{2+} by CV 57
4.3.2.2.3. Formal standard potential of Eu^{3+}/Eu^{2+} 64
4.3.2.2.4. Thermodynamic calculation 65
4.3.3. Kinetic Modeling of Molten Salt Corrosion and Redox Control 68
4.3.3.1. Kinetic model for corrosion in molten fluoride salts 68
4.3.3.2. Kinetic consideration of redox control effects 73
4.3.4. Electrochemical Sensor 74
4.3.4.1. Sensor Design 74
4.3.4.2. Reference Electrode discussion 78
4.3.5. Summary 80

4.3.6. References 80
4.4. Properties of Fission Products in the FLiNaK Melt 83
4.4.1. Experimental Setup 83
4.4.2. Cyclic Voltammetric Studies of Dy and La in FLiNaK Melt 84
4.4.3. Chronopotentiometric and Potentiometric Polarization Studies of La in FLiNaK Melt 89
4.4.4. Summary 98
4.4.5. References 99
4.5. Properties of Corrosion Products in the FLiNaK Melt 100
4.5.1. Cyclic Voltammetric and Chronopotentiometric Studies of Cr in the FLiNaK100
4.5.2. Potentiometic Polarization Studies of Cr and Fe in the FLiNaK 110
4.5.2.1. Experimental methods 110
4.5.2.2. Determining of the exchange current density 112
4.5.2.3. Exchange current density of Cr dissolution 113
4.5.2.4. Exchange current density of Fe dissolution 115
4.5.2.5. Activation energies for Cr and Fe dissolution in FLiNaK melt 117
4.5.3. Preliminary Investigation of Corrosion in FLiNaK 117
4.5.4. Summary 122
4.5.5. References 122
4.6. Separation and Properties of La_2O_3 in Molten FLiNaK Salt 123
4.6.1. Solubility Study of La_2O_3 in Molten FLiNaK Salt 123
4.6.1.1. Introduction 123
4.6.1.2. Experiment Set up 123
4.6.1.3. Results and Analysis 124
4.6.1.4. Conclusions and Future work 132
4.6.2. Electrochemcial Separation Study of La_2O_3 in Molten FLiNaK Salt 133
4.6.2.1. Introduction 133
4.6.2.2. Experimental Setup 133
4.6.2.3. Results and Analysis 135
4.6.2.3.1. 1st Experiment with Tungsten as Working, Counter and Reference Electrode 135
4.6.2.3.2. 2nd Experiment with Tungsten as Working, Reference Electrode and graphite as counter electrode 140
4.6.2.3.3. 3rd Experiment with Graphite as Working Electrode, Tungsten as Counter Electrode and Reference Electrode 144

4.6.2.3.4. 4th Experiment with Graphite as Working Electrode and Counter Electrode, Tungsten as Reference Electrode 150
4.6.2.4. Conclusions and Future work 156
4.6.3. First Principle Molecular Dynamics Study of Molten FLiNaK and FLiNaK-La_2O_3 Salt 157
4.6.3.1. Introduction 157
4.6.3.2. Computational Methods 157
4.6.3.2.1. First Principle Molecular Dynamics Method 157
4.6.3.2.2. Radial Distribution Function 158
4.6.3.2.3. Enthalpy of Formation $\Delta \boldsymbol{Hmix}$ 159
4.6.3.3. Results and Analysis 162
4.6.3.3.1. Structure Information of FLiNaK 162
4.6.3.3.2. Structure Information of FLiNaK-La_2O_3 168
4.6.3.3.3. Enthalpy of formation $\Delta \boldsymbol{Hmix}$ 170
4.6.3.4. Conclusions and Future work 171
4.6.4. Appendix 172
4.6.5. References 177
4.7. Electrochemical Investigation on Lanthanide Separation 179
4.7.1. Lanthanum Separation in Molten Fluoride salts by Electrochemical Methods 179
4.7.1.1. Experimental methods 179
4.7.1.2. Electrochemical Separation Study of LaF_3 in Molten FLiNaK Salt Melt 180
4.7.1.3. Electrochemical Extraction of Lanthanum in Molten Fluoride Salts Assisted by KF or NaF 186
4.7.2. Electrochemical Investigation of CeF_3 in Molten FLiNaK Salt on W, Cu, and Ni Electrodes 194
4.7.2.1. Experimental methods 195
4.7.2.2. Electrochemical Behavior of CeF_3 in FLiNaK Melt on Tungsten Electrode 196
4.7.2.3. Electrochemical Behavior of CeF_3 in FLiNaK Melt on Reactive Electrodes 200
4.7.3. Summary 209
4.7.4. References 210
4.8. Separation of Iodine from the Salt 211
4.8.1. Available data Review 211
4.8.2. Electrochemical Analysis 212

4.8.3. Tungsten as a working electrode 212
4.8.4. Graphite as a working electrode 217
4.9. Summary 228
4.10. References 229
4.11. Properties of fission products in Liquid Bi 230
4.11.1. Available Data Review 230
4.11.2. Thermodynamic Properties of Fission Products in Liquid Bismuth by Thermodynamic Assessment 230
4.11.2.1. Thermodynamic models 231
4.11.2.2. Available input information 231
4.11.2.3. Results and discussion 233
4.11.2.3.1. Phase diagram development 233
4.11.2.3.2. Thermodynamic study 239
4.11.3. Concentration-dependent Activity Coefficients of Lanthanides in Liquid Bismuth 249
4.11.4. Summary 259
4.11.5. Reference 259
4.12. Activity and activity coefficient investigation of K and Li in liquid Bi determined by EMF measurements 262
4.12.1. Experimental methods 263
4.12.2. Results and Discussions 264
4.12.2.1. The Bi-K system 265
4.12.2.2. The Bi-Li system 270
4.12.3. Summary 275
4.12.4. References 275
5. Identification and Prioritization of V&V Needs via PIRT Panel 278
5.1. Neutronics PIRT 278
5.1.1. Introduction 278
5.1.1.1. Background 278
5.1.1.2. PIRT Panel Membership 278
5.1.1.3. PIRT Overview 279
5.1.2. PIRT Preliminaries 282
5.1.3. FHR Neutronics Core Physics PIRTs 282
5.1.3.1. Category Descriptions 282
5.1.3.2. Structure of the PIRT Tables 283

5.1.3.3. Phenomena Identified for Further Consideration 283
5.2. Thermal Hydraulics PIRT-like Panel 288
5.2.1. PIRT Methodology 288
5.2.2. AHTR PIRT for Event of Station Blackout 292
5.2.3. Proposed FOMs for Event of Station Blackout 292
5.2.4. TH-PIRT for Event of Station Blackout 294
5.2.5. AHTR PIRT for the Event of Simultaneous Withdrawal of All Control Rods 300
5.2.6. Proposed FOMs for the Event of Simultaneous Withdrawal of All Control Rods 300
5.2.7. TH-PIRT for the Event of Simultaneous Withdrawal of All Control Rods 300
5.2.8. Modeling the Two Events and Path Forward 307
5.2.9. Summary 312
5.3. Phenomena Identification and Ranking Table (PIRT) Study for Metallic Structural Materials for Advanced High-Temperature Reactor (AHTR) 314
5.3.1. Introduction 314
5.3.2. PIRT Process 316
5.3.3. PIRT Results and Conclusions 319
5.4. Phenomena Identification and Categorization by the Required Level of Multiphysics Coupling in FHR Modeling and Simulation 319
5.4.1. Introduction 319
5.4.2. Phenomena Coupling Categorization Process 321
5.4.3. Overview of System Components and Operation Scenarios 322
5.4.4. Station Blackout 323
5.4.4.1. Rod Withdrawal 323
5.4.4.2. Normal Operation 323
5.4.4.3. Others 323
5.4.5. Phenomena Requiring Tight Coupling 323
5.4.6. Phenomena Requiring Loose Coupling 325
5.4.7. Others 343
5.4.8. Summary 345
5.5. Conclusion 347
6. Instrumentation 348
6.1. Visual Instrumentation and Fiberoptics as Synergistic Options 348
6.2. Research Reactors as Generation IV Environment Emulators 349
6.3. ORNL FHR Design 350

6.4. Validation Approach Using the VHTR Configuration 353
6.5. Instrumentation Options for FHRs 356
6.5.1. Neutron Flux Monitoring 356
6.5.2. Temperature Measurements 357
6.5.3. Liquid Level Monitoring 357
6.5.4. Corrosion and Vessel Thickness Monitoring 358
6.5.5. Pressure Measurements 358
6.5.6. Flow Measurements 358
6.5.7. Omni-Directional, Light-Pipe Visual Inspection Periscope 358
6.5.8. Fiber Optic Material Analysis 359
6.6. Modeling Approach 360
6.7. Radiation Field Analysis, Reconstruction, and Feature Characterization 363
6.7.1. Modeling and Visualization of Mixed Radiation Fields 363
6.7.2. Cherenkov Radiation and Its Characterization Potential 365
6.7.3. In-Core 3D Reconstruction Using 2D Data Sets 367
6.7.4. Feature Characterization Using 3D Reconstructed Mixed Field Data 371
6.8. Cherenkov Radiation Physics, Modeling and Analysis 372
6.8.1. Cherenkov Radiation Modeling in MCNP 6.1.1 372
6.8.2. Cherenkov Radiation Attenuation, Noise and Blurring Effects 373
6.8.3. Spectral Analysis of Cherenkov Radiation 375
6.8.4. Uncertainty Reduction Options in Cherenkov Radiation Simulations 380
6.9. MCNP TRIGA Model and Reference Radiation Field Analysis 382
6.9.1. TRIGA Core Topology and its Representation in Field Simulations 382
6.9.2. Fidelity of Radiation Filed Simulations 385
6.9.3. Radiation Field Simulations for the Reference TRIGA Core Configuration 386
6.10. Analysis of Select TRIGA Operation Cases for Feature Identification 392
6.11. Fiberoptics Probe Tests 414
6.12. Experimental Optical In-Core Data Capture from the Core Side Observational Position 420
6.13. In-Core Data Capture from the Core Top Observational Position 433
6.14. FHR vs. TRIGA Analysis 441
6.15. Conclusions 450
6.16. References 451
7. Qualification of Alloys for Structural Applications 454

7.1. Corrosion Resistance of Alloys in Molten FLiBe and FLiNaK 454
7.1.1. Experimental Procedures 454
7.1.1.1. Materials Tested 454
7.1.1.2. FLiNaK Salt Preparation 455
7.1.1.2.1. FLiNaK moisture content control and measurement 455
7.1.1.2.2. Atmosphere control 456
7.1.1.3. Static Corrosion Tests 458
7.1.2. Results - Corrosion Resistance of Alloys in Molten FLiNaK 459
7.1.2.1. Static Exposure Test of Alloys in FLiNaK in Glovebox using High Purity Salts 459
7.1.2.2. The role of carbon content in corrosion of type 316 stainless steel (316L vs 316H) 468
7.1.2.3. Exposure Tests of Pure Alloying Elements in FLiNaK 471
7.1.2.4. Static Exposure Tests of Alumina Forming Austenitic Stainless Steels in FLiNaK 472
7.2. Corrosion Tests in FLiNaK – Liquid Salt Test Loop (LSTL) 476
7.3. Effect of Molten Salt Impurities and Redox Conditions on Corrosion Alloys 478
7.3.1.1. Effect of Impurities 478
7.3.1.1.1. Effect of Salt Volume 478
7.3.1.1.2. Effect of Moisture 479
7.3.1.1.3. Effect of Metal Fluoride Addition 483
7.3.1.1.4. Evaluation of Salt Purification by H_2 Gas Sparge 484
7.3.1.2. Static Exposure Tests of Pre-Oxidized Alloys in FLiNaK 485
7.3.1.3. Effect of Test Time 486
7.3.2. Reference Electrode for Electrochemical Measurements in Molten Fluoride Salts 491
7.3.2.1. Ni/Ni^{2+} Reference Electrode 491
7.3.2.2. Dynamic Reference Electrode in FLiNaK 494
7.3.2.2.1. Cyclic Polarization of Hastelloy N in FLiNaK 495
7.3.2.3. Effect of Carbon on Corrosion of Alloys in FLiNaK 496
7.3.2.3.1. Effect of Carburization on Corrosion Resistance of Pure Chromium 496
7.3.2.3.2. Effect of Carburization on Corrosion Resistance of Haynes 230 500
7.3.2.3.3. Effect of Carburization on Corrosion Resistance of Ni Alloys 504
7.3.3. In-situ Carburization of Alloys in Molten Salts 510
7.3.3.1. Pure metals exposed to molten FLiNaK with added carbonate 510

7.4. References 520
8. Heat Exchangers 524
8.1. A Coupled Heat and Mass Transfer Model 526
8.1.1. Heat Transfer Model 526
8.1.2. Mass Transfer Model 529
8.1.3. Model Benchmark 531
8.2. A DWHX with Various Tube Surface Configurations and Annular Fluids 536
8.2.1. Tube Surface Configuration 536
8.2.2. Annular Fluid Species 538
8.3. AHTR P-IHX Design 540
8.3.1. Objectives for P-IHX Design Optimization 543
8.3.2. Optimum Design 545
8.4. AHTR I-PHX Design 546
8.5. AHTR DRACS Design 548
8.5.1. Single-wall DRACS Design 550
8.5.2. Double-wall DRACS Design 556
8.6. High Temperature Fluoride Salt Test Facility 558
8.6.1. Key Components 560
8.6.2. Corrosion Tests 562
8.6.3. Salt Preparation 564
8.7. Summary 567
9. Verification and Validation of Neutronics Codes, Tools, and Methodologies in Support of Licensing 571
9.1. Gaps in codes/methodologies needed to support licensing 571
9.1.1. Overview of existing codes 571
9.1.1.1. SCALE 571
9.1.1.2. MCNP 572
9.1.1.3. NEAMS Toolkit 573
9.1.1.4. ARGONNE REACTOR CODES 574
9.1.1.5. COMET 574
9.1.1.6. SERPENT 575
9.1.2. Neutronics and Multiphysics PIRTs 575
9.1.2.1. PIRT – Neutronics 575
9.1.2.1.1. Fundamental Cross Section Data 575

9.1.2.1.2. Material Composition....576
9.1.2.1.3. Computational Methodology....576
9.1.2.1.4. General Depletion....577
9.1.2.2. PIRT – Multiphysics....577
9.1.2.2.1. Normal Operation....577
9.1.2.2.2. Station Blackout....577
9.1.2.2.3. Simultaneous Withdrawal of All Control Rods....577
9.1.2.2.4. Other....578
9.2. Identification and Evaluation of Experimental Data for Benchmark Problem Development....578
9.2.1. Background Information....579
9.2.1.1. MSRE Core Description....579
9.2.1.2. Experiment Description....579
9.2.2. Model Overview....580
9.2.2.1. Model Features....580
9.2.2.2. Model Gaps/Simplifications....583
9.2.3. Preliminary Results....583
9.3. Benchmark Problem Development....584
9.3.1. Core specification....584
9.3.2. Radial and axial layout....585
9.3.3. Core configuration....586
9.3.4. AHTR fuel assembly specification....587
9.3.5. Specification of reflectors and support plates....590
9.3.5.1. Reflectors....590
9.3.5.2. Upper/Lower Support plates....592
9.4. Solution to full core benchmark problems....593
9.4.1. COMET model....593
9.4.2. Solutions to the full core benchmark problems....594
9.4.3. Summary....599
9.5. Sensitivity Analyses Using Pseudo-2D Fuel Assembly Model....601
9.5.1. Base Model....602
9.5.2. Flux Distributions....603
9.5.3. Problem Symmetry and Boundary Conditions Treatment....604
9.5.4. Particle-Wise Power Distribution....605

9.5.5. Material-Wise Spectra 606
9.5.6. Error Propagation in Assembly Depletion Simulations 608
9.5.7. Thermal Scattering Library Usage for Carbonaceous Materials 610
9.5.8. Graphite Density 611
9.5.9. Initial Assessment of SERPENT Parallel Efficiency 612
9.5.10. Assessment of SERPENT Parallel Efficiency on a Larger Parallel Cluster 613
9.5.11. Summary of Observations Related to Modeling Assumptions 614
9.5.12. References 615
9.6. Cross-Verification of SCALE, SERPENT and MCNP 616
9.6.1. Consistent Assembly-level Models 616
9.6.2. Cross-Comparison results 620
9.6.2.1. Multiplication and Fission Distribution 621
9.6.2.2. Neutron Spectrum 623
9.6.2.3. Neutron Flux and Distribution 624
9.6.3. Summary of Codes Cross-Verification 627
9.6.4. References 627
9.7. Assessing Feasibility and Practicality of FHR Monte Carlo Full Core Simulations 628
9.7.1. Impact of Tallies on Simulation Runtime 628
9.7.2. Estimate of Runtime for a Prototypic Analysis 629
9.8. Conclusions 630
10. Verification and Validation of Thermal Hydraulics Codes, Tools, and Methodologies in Support of Licensing 638
10.1. Address phenomena identified by a PIRT panel for a reference FHR design 639
10.2. Identify requirements on codes/methodologies to support licensing 640
10.3. Review the Issues with Existing Codes and Methodologies 642
10.3.1. Review of System Analysis Codes 642
10.3.2. Review of CFD Codes 648
10.4. Code Validation and Identification of Issues for Code Improvement 652
10.4.1. RELAP5/SCDAPSIM/MOD 4.0 code benchmark of startup and pump trip scenarios 653
10.4.1.1. Startup Scenarios in LTDF 655
10.4.1.2. Pump Trip Scenarios in LTDF 658
10.4.2. Benchmark study on a natural circulation loop using SAM 661
10.4.3. Code-to-code Comparison between RELAP5 and SAM 667

10.4.4. LTDF SAM model 668
10.5. AHTR System Analysis using RELAP5 678
10.5.1. Implementation molten salt properties into RELAP5/SCDAPSIM/MOD 4.0 678
10.5.2. RELAP5 AHTR Model 680
10.5.3. Steady-State of Reactor Normal Operation Results with Air Chimneys Closed 685
10.5.4. Loss of Forced Circulation (LOFC) 686
10.5.5. Simulation of Loss of Two DRACS Loops 690
10.5.6. Heat Transfer from Reactor vessel to Silo Wall 696
11. Highlighting Contributions from National Laboratory Partner 707
12. Conclusion 713

List of Figures

Figure 3-1. Microscopic cross sections for important tritium-producing reactions in FLiBe as extracted from the ENDF/B-VII.1 library provided in SCALE6.2 [8][9]. 8
Figure 3-2. Pathways of tritium production in FLiBe with effective 1-group cross sections generated by the reference case FHR. 9
Figure 3-3. AHTR preconceptual design fuel assembly and radial core layout taken from the ORNL preconceptual design [1]. 11
Figure 3-4. Schematic of the methodology. 12
Figure 3-5. The subdivision of tallies for the full-core model used in MCNP6.1. 13
Figure 3-6. Comparisons of the flux spectrum tallied in FLiBE by MCNP6.1 for each case as compared against the reference core design. 18
Figure 3-7. Tritium production rates for each case over a 100-year operating lifetime of the reactor. 19
Figure 3-8. Isotopic evolution of important actinides generated from a 2D assembly-level SERPENT model. 19
Figure 3-9. Comparison of normalized flux spectra in FLiBe for different burnups. 21
Figure 3-10. Comparison of flux spectra in FLiBe for different burnups normalized to 1MeV neutrons to demonstrate differences in thermalization. 22
Figure 3-11. Tritium production rates calcluated in SCALE from full-core MCNP tallies using diferent burnt fuel isotopics. 23
Figure 3-12. Time-Evolution of Tritium Production Parameters: Instantaneous tritium production rate (left), total produced tritium (center), and accumulated tritium (right). 24
Figure 4-1: Flowchart Diagram of Multistage Extraction System 40
Figure 4-2: Percent Removal of Actinides and Rare Earths across Extraction Cascade at 700 ^{0}C 41
Figure 4-3: Percent Removal across Cascade at 700 ^{0}C and .0025 initial mole fraction of Li in Bi phase 42
Figure 4-4: % Removal across Cascade at 700 ^{0}C and .005 initial mole fraction of Li in Bi phase 43
Figure 4-5: % Removal across Cascade at 700 ^{0}C with stage dependent initial mole fraction of Li in Bi phase 44
Figure 4-6: % Removal of Uranium across Cascade at 700 ^{0}C with varying flow rate ratios ... 45
Figure 4-7: % Removal of Cerium across Cascade at 700 ^{0}C with varying flow rate ratios 45
Figure 4-8: Effect of Temperature on Percent Removal across Extraction Cascade 46
Figure 4-9: Schematics of the electrochemical processes for contaminant removal 49
Figure 4-10: Chronopotentiograms giving the potential evolution of the tungsten electrode against Pt wire over time following current pulses at (a) 650°C, (b) 700°C and (c) 750°C. 57
Figure 4-11: Cyclic voltammograms obtained in FLiNaK melt with and without addition of 1 wt% EuF_3 at 700°C, sweep rate of 200 mV/s. 58
Figure 4-12: Cyclic voltammograms (5th cycle) of the Eu^{3+}/ Eu^{2+} couple in FLiNaK-EuF_3-EuF_2 melt at (a) 650°C, (b) 700°C and (c) 750°C. Potential scans from A to B then back to A. 59
Figure 4-13: Cyclic voltammograms (5th cycle) of FLiNaK melt without EuF_3 addition at various scan rates at 700°C. 60

Figure 4-14: Plots of peak current density versus square root of scan rate in FLiNaK-EuF_3-EuF_2 melt. 61
Figure 4-15: XPS spectra of Eu $3d_{5/2}$ of FLiNaK-EuF_3-EuF_2 melt at various temperatures. 62
Figure 4-16: Redox potential versus temperature for various redox couples in FLiNaK and FLiBe salts. Solid line: metal dissolution at limit activity of 10^{-6}; Dotted line: reduction of oxidants. HF/H_2=0.1: a mole ratio of HF/H_2=0.1 at 1 atm total pressure. Double solid line: redox potential calculated based on the measured formal potentials. 68
Figure 4-17: Schematic polarization curves for alloy corrosion in molten fluoride salts at 700°C (a) 71Fe-17Cr-12Ni alloy, (b) 73Ni-17Cr-10Fe alloy, (c) 71Ni-16Mo-7Cr-5Fe alloy, (d) 71Ni-16Mo-7Cr-5Fe alloy after 1 year of Cr selective dissolution. 71
Figure 4-18: Schematic polarization curves for chromium corrosion in the presence of a redox buffer with (a) low $\boldsymbol{i}\mathbf{0}$ *and (b) high* $\boldsymbol{i}\mathbf{0}$*, respectively.* 74
Figure 4-19: Electrochemical sensor housing dimensioned drawing 75
Figure 4-20: Drawing of the complete sensor assembly. 76
Figure 4-21: Exploded view of the sensor assembly and flanged connection. 77
Figure 4-22: Schematic of the experimental setup. 83
Figure 4-23: Cyclic Voltammetry results (left) used to characterize the redox potential of K^+/K in Flinak. Apparent potentials (right) are calculated from the CV results and consider the concentration of K^+ in the mixture as well as the soluble-insoluble nature of the redox reaction. 84
Figure 4-24: Comparison of the Flinak-Dy system with pure Flinak reveals negligible contribution from the molten Flinak media to the experimental CV curve. Disregarding the contribution from Flinak remains a source of error, but much less significant than other sources of error. 85
Figure 4-25: The CV curves are generated for Dy in Flinak with scan rates 50-400 mV/s at 700°C. Slight deviation in peak potential is observed with scan rates of 200 mV/s and higher. WE: tungsten [0.0094 cm^2]. 86
Figure 4-26: Left, peak current density plotted against square root of the scan rate, to confirm reversibility in the diffusion-controlled region (linear). Right, peak potential vs. log(scan rate) to confirm kinetic reversibility (horizontal). Significant deviation is observed in peak potential for scan rates of 200 mV/s and higher while not observed in the current density. 87
Figure 4-27: Diffusion coefficient results and temperature dependence fit to the Arrhenius Equation for dysprosium (top) and lanthanum (bottom) From the linear slope of the ln(D) vs. 1/T relationship, the activation energy is extrapolated. 88
Figure 4-28: Temperature trend of apparent standard reduction potential, E^{o*}, with reference to K^+/K in Flinak. Large error reported at 823 K is the result of a significant shift in potential with scan rate. Given the same time scale (scan rate), lower temperature systems with slower diffusion will eventually exhibit irreversible kinetics and peak potential shift. 89
Figure 4-29: Chronopotentiograms of LaF_3 in FLiNaK molten salt at the temperatures of (a) 923 K, (b) 973K, and (c) 1023 K. LaF_3=1.05×10^{-4} mol/cm^3; electrode area=0.296 cm^2. 91
Figure 4-30: Linear relationship of I versus $\tau^{-1/2}$ for the CP test of LaF_3 in FLiNaK molten salt with the concentration of (A) LaF_3=1.05×10^{-4} mol/cm^3 and (B) LaF_3=2.25×10^{-4} mol/cm^3. 92
Figure 4-31: Arrhenius plot of diffusion coefficient as a function of temperature. 93
Figure 4-32: Potentiodynamic polarization curves measured at different scan rates for LaF_3 in FLiNaK molten salt. LaF_3=1.58×10^{-4} mol/cm^3; T=923K. 94

Figure 4-33: Potentiodynamic polarization curves at different concentrations for the temperatures of (a) 923 K, (b) 973 K, and (c) 1023K. Scan rate: 5 mV/s. 95
Figure 4-34: Potentiodynamic polarization curves at the scan rate of 5 mV/s for LaF_3 in FLiNaK molten salt at the temperatures of 923, 973, and 1023 K. (a) LaF_3=6.31×10^{-5} mol/cm^3; (b) LaF_3=1.58×10^{-4} mol/cm^3; (c) LaF_3=2.59×10^{-4} mol/cm^3. 97
Figure 4-35: The plot of $i0$ from Table 4-8 versus LaF_3 concentration. 98
Figure 4-36: Cyclic voltammogram of CrF_2 in FLiNaK molten salt at the temperature of 923 K and scan rate of 100 mV/s. Working electrode: tungsten (s=0.6481 cm^2), reference electrode: platinum, counter electrode: graphite. 100
Figure 4-37: OCP evolution of the tungsten working electrode against platinum reference electrode over time by chronopotentiometry test at the temperature of 1023 K. 101
Figure 4-38: Cyclic voltammograms of redox reaction Cr (III)/Cr (II) couple in FLiNaK molten salt at (a) 923 K, (b) 973K, and (C) 1023K. Working electrode: tungsten (s=0.6481 cm^2), reference electrode: platinum, counter electrode: graphite. 102
Figure 4-39: Linear relationship of ip, c versus $v0.5$ for the cyclic voltammogram given in Figure 4-38. 105
Figure 4-40: Typical chronopotentiograms for reaction of $Cr^{3+}+e^- \leftrightarrow Cr^{2+}$ at 923 K for molten FLiNaK with addition of CrF_2. 106
Figure 4-41: Typical chronopotentiograms obtained at 923 K for molten FLiNaK with addition of CrF_2 when applying higher currents. 106
Figure 4-42: Linear relationship of I versus $\tau^{-1/2}$ for the chronopotentiometry test of redox couple Cr (III)/ Cr (II) at different temperatures. 107
Figure 4-43: Linear relationship of I versus $\tau^{-1/2}$ for the chronopotentiometry overall reaction of Cr (III) to Cr at different temperatures. 109
Figure 4-44: Schematic illustration of the electrochemical cell. Dashed circles represent glove ports. 111
Figure 4-45: Polarization curves of Cr electrode in FLiNaK melt containing 0.4 wt% CrF_2, (a) plot of $\boldsymbol{lgi-\eta}$, (b) plot of $\boldsymbol{i-\eta}$ in $\boldsymbol{\eta}$ < 40 mV. Scan rate: 1 mV/s. 114
Figure 4-46: Polarization curves of Fe electrode in FLiNaK eutectic containing 0.4 wt% FeF_2 (a) plot of $\boldsymbol{lgi-\eta}$, (b) plot of $\boldsymbol{i-\eta}$ in $\boldsymbol{\eta}$ < 40 mV. Scan rate: 1 mV/s. 116
Figure 4-47: Plots of $\boldsymbol{ln(i0)}$ versus 1/T for the dissolution of chromium and iron in molten FLiNaK melt. 117
Figure 4-48: Polarization curves of alloys in molten FLiNaK salt at 700 °C 119
Figure 4-49: EIS of alloys in molten FLiNaK salt at 700 °C at different exposure time. 120
Figure 4-50: SEM photographs and alloying element distributions of different alloys after immersion experiments for 24 hours. (a) SS316L, (b) Incoloy-800, (c) Hastelloy-N, (d) Ni-201. 121
Figure 4-51 Insoluble material on the bottom 125
Figure 4-52 XRD of the insoluble materials on the bottom 126
Figure 4-53 XRD of melting salt during heating 127
Figure 4-54 La concentration distribution at 600°C, 650°C and 700°C 129
Figure 4-55 La concentration distribution at 750°C 130
Figure 4-56 Evaporation Phenomenon at different temperatures, from left to right, A: 600°C, B: 650°C, C: 700°C, D: 750°C 130
Figure 4-57 XRD of evaporated salt on the surface of the crucible 131

Figure 4-58 linear relationship between natural logarithm of solubility and reciprocal of temperature in Kelvin 132
Figure 4-59 La concentration distribution at 700°C 132
Figure 4-60 Electrochemical experimental setup sketch 135
Figure 4-61 cyclic voltammetry, scan rate: 100 mv/s, working electrode: tungsten, counter electrode: tungsten, reference electrode: tungsten 137
Figure 4-62 cyclic voltammetry, scan rate: 100 mv/s, working electrode: tungsten, counter electrode: tungsten, reference electrode: tungsten 138
Figure 4-63 cyclic voltammetry, scan rate: 100 mv/s, working electrode: tungsten, counter electrode: tungsten, reference electrode: tungsten 139
Figure 4-64 cyclic voltammetry, scan rate: 100 mv/s, working electrode: tungsten, counter electrode: tungsten, reference electrode: tungsten 140
Figure 4-65 cyclic voltammetry, scan rate: 100 mv/s, working electrode: tungsten, counter electrode: tungsten, reference electrode: tungsten 142
Figure 4-66 cyclic voltammetry, scan rate: 100 mv/s, working electrode: tungsten, counter electrode: tungsten (W1, W2, W3) and graphite (C1, C2, C3), reference electrode: tungsten. Surface area of tungsten: 80.43mm2, surface area of graphite: 50.27mm2 143
Figure 4-67 cyclic voltammetry, scan rate: 100 mv/s, working electrode: tungsten, counter electrode: graphite (C) and tungsten (W), reference electrode: tungsten 144
Figure 4-68 cyclic voltammetry, working electrode: graphite, counter electrode: tungsten, reference electrode: tungsten 146
Figure 4-69 cyclic voltammetry, working electrode: graphite, counter electrode: tungsten, reference electrode: tungsten, red curve is FLiNaK without La_2O_3, green and red curve are FLiNaK with La2O3. Electrode surface area in pure FLiNaK: 89.54mm2, electrode surface area in FLiNaK-La_2O_3 is 87.65mm2. 147
Figure 4-70 Open circuit potential at different time in the electrochemical experiment with working electrode: graphite, counter electrode: tungsten, reference electrode: tungsten 148
Figure 4-71 cyclic voltammetry, scan rate: 200 mv/s, working electrode: graphite, counter electrode: tungsten, reference electrode: tungsten 149
Figure 4-72 cyclic voltammetry, scan rate: 1000 mv/s, working electrode: graphite, counter electrode: tungsten, reference electrode: tungsten 150
Figure 4-73 cyclic voltammetry, working electrode: graphite, counter electrode: graphite, reference electrode: tungsten 151
Figure 4-74 cyclic voltammetry, working electrode: graphite, counter electrode: graphite, reference electrode: tungsten. Electrode surface area in pure FLiNaK is 94.25mm2, electrode surface area in FLiNaK-La_2O_3 is 44.88mm2 152
Figure 4-75 Open circuit potential at different time in the electrochemical experiment with working electrode: graphite, counter electrode: graphite, reference electrode: tungsten . 153
Figure 4-76 chronopotentiometry, working electrode: graphite, counter electrode: graphite, reference electrode: tungsten 153
Figure 4-77 X-ray powder diffraction analysis on the graphite surface after deposition ... 154
Figure 4-78 cyclic voltammetry, scan rate: 200mv/s, working electrode: graphite, counter electrode: graphite, reference electrode: tungsten 155
Figure 4-79 cyclic voltammetry, working electrode: graphite, counter electrode: graphite, reference electrode: tungsten 156

Figure 4-80 Snapshot of the local ionic structure in FLiNaK molten salt at 700°C, grey balls are fluorine ions, green balls are lithium ions, yellow balls are sodium ions, pink balls are potassium balls. 163
Figure 4-81 Radial distribution function (RDF) of Li-F in FLiNaK at 700°C 164
Figure 4-82 Radial distribution function (RDF) of Na-F in FLiNaK at 700°C 165
Figure 4-83 Radial distribution function (RDF) of K-F in FLiNaK at 700°C 166
Figure 4-84 Radial distribution function (RDF) of F-F in FLiNaK at 700°C 167
Figure 4-85 Snapshot of the local ionic structure in FLiNaK-La_2O_3 molten salt at 700°C, grey balls are fluorine ions, light green balls are lithium ions, yellow balls are sodium ions, purple balls are potassium ions, deep green balls are lanthanum ions, red balls are oxygen ions. 169
Figure 4-86 Radial distribution function (RDF) of Li-F in FLiNaK-La_2O_3 at 700°C 172
Figure 4-87 Radial distribution function (RDF) of Na-F in FLiNaK-La_2O_3 at 700°C 173
Figure 4-88 Radial distribution function (RDF) of K-F in FLiNaK-La_2O_3 at 700°C 173
Figure 4-89 Radial distribution function (RDF) of F-F in FLiNaK-La_2O_3 at 700°C 174
Figure 4-90 Radial distribution function (RDF) of La-F in FLiNaK-La_2O_3 at 700°C 174
Figure 4-91 Radial distribution function (RDF) of Li-O in FLiNaK-La_2O_3 at 700°C 175
Figure 4-92 Radial distribution function (RDF) of Na-O in FLiNaK-La_2O_3 at 700°C 175
Figure 4-93 Radial distribution function (RDF) of K-O in FLiNaK-La_2O_3 at 700°C 176
Figure 4-94 Radial distribution function (RDF) of F-O in FLiNaK-La_2O_3 at 700°C 176
Figure 4-95 Radial distribution function (RDF) of La-O in FLiNaK-La_2O_3 at 700°C 177
Figure 4-96.(a) Typical cyclic voltammograms obtained in FLiNaK-LaF_3 (working electrode area=0.673 cm^2) and pure FLiNaK molten salts at the scan rate of 100 mV/s. (b) Typical chronopotentiogram obtained in FLiNaK-LaF_3 molten salt with the applied current of -4 mA for 15s (working electrode area=0.673 cm^2). Working electrode: tungsten; counter electrode: tungsten; LaF_3=1.02 wt%; T=923 K. 181
Figure 4-97. Open circuit potential evolution with time when a stable reduction current of 2 mA was applied on the tungsten electrode in FLiNaK-LaF_3 molten salt for 3500s. Working electrode: tungsten (electrode area=1.186 cm^2); counter electrode: graphite; T=973 K; LaF_3=1.68 wt%. 182
Figure 4-98. (a) Backscattered electrons (BSE) image of the cross section of polished tungsten rod electrode after electrolysis in FLiNaK-LaF_3 molten salt; (b) EDS point scan results of point 1 and point 2 in Figure 4-98a; (c)-(f) EDS mapping results of Figure 4-98a. 183
Figure 4-99. (a) Typical cyclic voltammograms obtained in FLiNaK-LaF_3 (working electrode area=1.273 cm^2) and pure FLiNaK molten salts at the scan rate of 200 mV/s. (b) Typical chronopotentiogram obtained in FLiNaK-LaF_3 molten salt with the applied current of -20 mA for 4s (working electrode area=1.273 cm^2). Working electrode: molybdenum; counter electrode: graphite; LaF_3=3.64 wt%; T=973 K. 184
Figure 4-100. Open circuit potential evolution with time when a stable reduction current of 6 mA was applied on the molybdenum electrode in FLiNaK-LaF_3 molten salt for 1800s. Working electrode: tungsten (electrode area=1.174 cm^2); counter electrode: graphite; T=973 K; LaF_3=3.45 wt%. 185
Figure 4-101. Picture of the molybdenum working electrode after chronopotentiometry electrolysis. 185

Figure 4-102. (a) Backscattered electrons (BSE) image of the cross section of polished molybdenum rod electrode after electrolysis in FLiNaK-LaF_3 molten salt; (b) EDS point scan results of the point in Figure 4-98a; (c)-(f) EDS mapping results of Figure 4-98a. 186
Figure 4-103. Standard reduction potentials of LaF_3/La, LiF/Li, NaF/Na, KF/K. 188
Figure 4-104. Cyclic voltammograms obtained in LiF-LaF_3 (working electrode area=0.385 cm^2) and pure LiF molten salts. Scan rate: 100 mV/s; working electrode: Mo; counter electrode: graphite; LaF_3=3.33 wt%; T=1173 K. 189
Figure 4-105. (a) Cyclic voltammograms obtained in LiF-KF eutectic molten salt with LaF_3 dissolved in (working electrode area=2.24 cm^2) and pure LiF-KF eutectic molten salt at the scan rate of 200 mV/s. (b) Chronopotentiogram of the system of LiF-KF-LaF_3 with the applied current of -50 mA (working electrode area=2.24 cm^2). Working electrode: Mo; counter electrode: graphite; LaF_3=2.73 wt%; T=973 K. 190
Figure 4-106. (a) Backscattered electrons (BSE) image of the cross section of polished Mo rod electrode after electrolysis in LiF-KF-LaF_3 molten salt; (b) EDS point scan results of point 1 and point 2 in Figure 4-106a; (c)-(f) EDS mapping results of Figure 4-106a. 192
Figure 4-107. (a) Cyclic voltammograms obtained in LiF-NaF eutectic molten salt with LaF_3 dissolved in (working electrode area=0.577 cm^2) and pure LiF-NaF eutectic molten salt at the scan rate of 200 mV/s. (b) Chronopotentiogram of the system of LiF-NaF-LaF_3 with the applied current of -20 mA (working electrode area=0.577 cm^2). Working electrode: Mo; counter electrode: graphite; LaF_3=3.02 wt%; T=1023 K. 193
Figure 4-108. (a) Backscattered electrons (BSE) image of the cross section of polished Mo rod electrode after electrolysis in LiF-NaF-LaF_3 molten salt; (b) EDS point scan results of point 1 and point 2 in Figure 4-98a; (c)-(f) EDS mapping results of Figure 4-98a. 194
Figure 4-109. Standard reduction potentials of the alkali elements and Ce vs. F_2/F^- in fluoride salt melt at the temperature of 973 K. 195
Figure 4-110. (a) Cyclic voltammograms obtained in FLiNaK-CeF_3 (working electrode area=0.698cm^2) and pure FLiNaK salt melt at the scan rate of 100 mV/s. (b) Chronopotentiogram of the system FLiNaK-CeF3 with the applied current of -10 mA (working electrode area=0.698cm^2). Working electrode: W. counter electrode: graphite. CeF_3=2.47×10^{-4} mol/cm^3; T=973K. 197
Figure 4-111. (a) XRD analysis result of the quenched FLiNaK-CeF_3 salt. (b) XRD analysis result of the potentiostatic electrolysis products of FLiNaK-CeF_3 melt on the tungsten foil electrode. 198
Figure 4-112. (a) Backscattered electrons (BSE) image of the cross section of polished tungsten rod electrode after electrolysis; (b) EDS point scan results of point 1 and point 2 in Figure 4-112a; (c)-(f) EDS mapping results of Figure 4-112a. 199
Figure 4-113. Cyclic voltammogram of CeF_3 in FLiNaK molten salt recorded on Cu working electrode (area=1.389 cm^2). Counter electrode: graphite. CeF_3=1.4×10^{-4} mol/cm^3; T=973K; Scan rate: 100 mV/s. 201
Figure 4-114. XRD analysis result of the potentiostatic electrolysis products of FLiNaK-CeF_3 melt on Cu electrode. 202
Figure 4-115. (a) Backscattered electrons (BSE) image of the cross section of polished copper rod electrode after electrolysis; (b) EDS point scan results of point 1 and point 2 in Figure 4-106a; (c)-(f) EDS mapping results of Figure 4-106a. 203

Figure 4-116. Cyclic voltammogram of CeF_3 in FLiNaK molten salt recorded on Ni working electrode (area=1.085 cm^2). Counter electrode: graphite. CeF_3=1.95×10^{-4} mol/cm^3; T=973K; Scan rate: 100 mV/s. 204
Figure 4-117. Cyclic voltammograms of CeF_3 in FLiNaK molten salt at various reverse potentials on Ni working electrode (area=1.085 cm^2). Counter electrode: graphite. CeF_3=1.95×10^{-4} mol/cm^3; T=973K; Scan rate: 100 mV/s. 205
Figure 4-118. OCP evolution of the Ni working electrode (area=0.698cm^2) against Pt reference electrode over time by chronopotentiometry test at the temperature of 973 K through applying a reduction current of 100 mA for 4s and an oxidation current of 40 mA for another 4s. 206
Figure 4-119. XRD analysis result of the chronopotentiometry electrolysis products of FLiNaK-CeF_3 melt on Ni electrode. 207
Figure 4-120. (a) Backscattered electrons (BSE) image of the cross section of polished nickel rod electrode with attached CeF_2 salts after electrolysis; (b) EDS point scan results of point 1 in Figure 4-120a; (c)-(f) EDS mapping results of Figure 4-120a. 208
Figure 4-121. (a) Backscattered electrons (BSE) image of the deposited $CeNi_5$ intermetallic compound at nickel rod electrode; (b) EDS point scan results of point 1, point 2 and point 3 in Figure 4-121a; (c)-(f) EDS mapping results of Figure 4-121a. 209
Figure 4-122 Redox potential (E vs. $E_{Na+/Na}$) at different temperatures for various redox couples in molten FLiNaK-NaI salt with a tungsten electrode. 214
Figure 4-123 First cycle of CVs recorded from a tungsten WE (area: 0.5 cm^2) in both FLiNaK and FLiNaK-NaI (1.5 wt%) melts at 600 ℃ under argon atmosphere. Scan rate: 100 mV/s. CE and RE: Graphite and Pt. 214
Figure 4-124 (a) First cycle and Second cycle of CVs recorded from a tungsten WE (area: 0.5 cm^2) in FLiNaK-NaI (1.5 wt%) melts at 600 ℃; (b) CVs recorded under different anodic potential limits. 215
Figure 4-125 Chronopotentiograms at different currents for 10 s. Time interval: 1 ms. 216
Figure 4-126 CVs recorded in FLiNaK-1.5 wt% NaI mixture at 600 ℃ and different scan rates before (a) and after (b) IR drop corrected. 217
Figure 4-127 CVs recorded from a tungsten WE (area: 0.5 cm^2) in both FLiNaK (black line) and FLiNaK-NaI (1.5 wt%, red line) melts at 650 (a) and 700 ℃ (b) under argon atmosphere. Scan rate: 100 mV/s. CE and RE: Graphite and Pt 217
Figure 4-128 Redox potentials (E vs. $E_{K+/K}$) at different temperatures for various redox couples in molten FLiNaK-NaI salt with a graphite electrode. 218
Figure 4-129 (a) CV curve recorded from a graphite WE (area: 0.21 cm^2) in FLiNaK melt at 700 °C under argon atmosphere; (b) the enlargement of the curve in Figure 4a. Scan rate: 500 mV/s. CE and RE: Graphite and Pt (the potential of Pt reference electrode is converted to the redox K^+/K couple for easier comparison with thermodynamic calculation). 219
Figure 4-130 (a) CV result with graphite electrode in molten FLiNaK at 700 °C. Scan rate: 100 mV/s; (b) Chronopotentiograms recorded in FLiNaK at 700 °C at different potentials (vs. Ref. Pt). Electrolysis time interval: 150s. OCP interval: 300 s. OCP curves are not shown here. 220
Figure 4-131 CVs recorded from a graphite WE in FLiNaK-0.2 wt% NaI (0.0267 mol/L) at 700 °C. (a) The typical CV test results in the FLiNaK and FLiNaK-0.2 wt%NaI. Scan rate: 1 V/s; (b) Three consecutive CV cycles in FLiNaK-0.2 wt% NaI; (c) CV tests at different scan

rates (from 0.2 V/s to 20 V/s); (d) The current peaks obtained at different scan rates (from (c)); CE and RE: Graphite and Pt. 221
Figure 4-132 Chronopotentiograms recorded in FLiNaK-0.2 wt% NaI at 700 °C and different potentials (vs. Ref. Pt). Electrolysis time interval: 300 s. OCP interval: 300 s. OCP curves are not shown here. 223
Figure 4-133 (a) CV result with graphite electrode in molten FLiNaK-0.5 wt% NaI at 700 °C. Scan rate: 500 mV/s; (b) Chronopotentiograms recorded in FLiNaK-0.5 wt% NaI at 700 °C at different potentials (vs. Ref. Pt). Electrolysis time interval: 300 s. OCP interval: 300 s. OCP curves are not shown here. 223
Figure 4-134 XRD result of the green powder inside the crucible after CA tests in FLiNaK-0.5wt% NaI salt; Insert graph: the digital photo of the crucible after experiment. 224
Figure 4-135 (a) Second electron (SE) image of the green powder; (b) EDS point scan results of point 1 and point 2 in Figure 10a; (c)-(f) EDS mapping results of Figure 10a. 225
Figure 4-136 (a) Chronopotentiograms recorded in FLiNaK-1.5 wt% NaI at 700 °C at different potentials (vs. Ref. Pt). Electrolysis time interval: 1000s. OCP interval: 300 s. OCP curves are not shown here. (b) CV results in molten FLiNaK-1.5wt% NaI before and after consecutive CA tests. Scan rate: 100 mV/s. 226
Figure 4-137 (a) CV tested recorded at different concentrations of NaI at 700 °C; Scan rates: 500 mV/s; (b) Subsequent cycles of the CV test recorded in the FLiNaK-5 wt% NaI melt; Scan rate: 500 mV/s; (c) CV tests at different scan rates (from 0.1 V/s to 2.0 V/s); (d) The CA results in FLiNaK-5.0 wt% NaI salt at 700 °C; Electrolysis time interval: 500s. OCP interval: 1000 s. OCP curves are not shown in figure. 227
Figure 4-138 (a) the photo of the crucible containing FLiNaK-5 wt% NaI held at 700 °C for 8 h without any tests; black spot: the graphite rod that immersed into the salt; (b) The typical photo of the crucible after the CA tests in the salt containing either 1.5 wt% or 5 wt% NaI; (c) The photo of the upper part of the graphite electrode after the CA tests in the FLiNaK-1.5 wt% NaI; (d) The photo of the clamp fixing the working electrode after the CA tests in the FLiNaK-5wt% NaI; (e) The XRD result of the powders on the clamp. 228
Figure 4-139.Calculated Bi-Pr phase diagram compared with literature data [20,23,24]. 234
Figure 4-140. Calculated Bi-Ce phase diagram compared with literature data [21,28,29,30]. 236
Figure 4-141. Calculated Bi-Er phase diagram compared with literature data [32]. 238
Figure 4-142. The calculated enthalpy of mixing of the liquid phase in Bi-Pr system compared with literature data [25,]. 242
Figure 4-143. The calculated enthalpy of mixing of the liquid phase in Bi-Ce system compared with literature data [25,38,]. 242
Figure 4-144. The calculated enthalpy of mixing of the liquid phase in Bi-Er system compared with literature data [25,38]. 243
Figure 4-145. Activity coefficient of Pr in liquid Bi at different concentrations under three temperatures: 873, 923, and 973 K. 244
Figure 4-146. Activity Coefficients of Ce in liquid Bi at different concentrations under three temperatures: 873, 923, and 973 K. 245
Figure 4-147. Activity Coefficients of Er in liquid Bi at different concentrations under three temperatures: 873, 923, and 973 K. 246

Figure 4-148. Activity of Pr, Ce, and Er in liquid bismuth at the temperature of 973 K. Solid line is the activity at different concentration while the dashed line is the linear relationship of the activity with concentration at dilution. 248
Figure 4-149. Calculated solubility of Pr, Ce, and Er in liquid bismuth with the fitting curve. 249
Figure 4-150.Relationship between logarithms of activity coefficient and mole fraction of lanthanides in liquid bismuth at the temperatures of 973 K (a), 923 K (b), and 873 K (c). 251
Figure 4-151. The activities of lanthanides in liquid bismuth at the temperature of 973 K. Solid line is the activity at different concentration while the dashed line is the linear relationship of the activity with concentration at dilution. 257
Figure 4-152. Schematic diagram of the designed Bi-K liquid reference electrode....264
Figure 4-153. Potential evolution of the tungsten working electrode against K-Bi reference electrode over time in FLiNaK molten salt when a 5-s pulse current was applied at (a) 973 K and (b) 1023 K. 266
Figure 4-154. Coulometric titration of K into liquid Bi working electrode in FLiNaK electrolyte at (a) 973 K and (b) 1023K.....269
Figure 4-155. Equilibrium electrode potential as a function of K mole fraction upon K deposition at 973 K and 1023K. 269
Figure 4-156. Activity and Activity coefficient of K in liquid Bi at different concentrations for the temperatures of 973 K and 1023 K.....270
Figure 4-157. Potential evolution of the tungsten working electrode against Li-Bi reference electrode over time in LiF-LiCl molten salt when a 5-s pulse current was applied at (a) 973 K and (b) 1023 K. 272
Figure 4-158. Coulometric titration of Li into liquid Bi working electrode in LiF-LiCl electrolyte at (a) 973 K and (b) 1023K.....273
Figure 4-159. Equilibrium electrode potential as a function of Li mole fraction upon Li deposition at 973 K and 1023K. 274
Figure 4-160. Activity and Activity coefficient of Li in liquid Bi at different concentrations for the temperatures of 973 K and 1023 K.....275
Figure 6-1 Details of the FHR core layout rendered using MCNP VISED editor.....351
Figure 6-2 MCNP (left) and Serpent (right) models of the FHR active core features.....352
Figure 6-3 Full core model of the FHR core for use with Serpent.....353
Figure 6-4 Details of the VHTR core layout rendered using MCNP VISED editor.....354
Figure 6-5 Cherenkov axial power profile detector.....357
Figure 6-6 TRIGA reactor model, core-level view. 361
Figure 6-7 Differences in the photon fluxes for a critical system following the regulating rod movement from its fully removed position and to its fully inserted position.....362
Figure 6-8 Photon flux into fiber optic probe vs position at the core's axial centerline. 362
Figure 6-9 Projection of electron flux tallies to the top of the reactor core.....368
Figure 6-10 Projection of the electron flux to the side of the reactor core....368
Figure 6-11 Projection of the electron flux through the front of the reactor core. 369
Figure 6-12 Reconstructed total electron flux for the reference TRIGA core. 369
Figure 6-13 Reconstructed total neutron flux for the reference TRIGA core.....370
Figure 6-14 Reconstructed total photon flux for the reference TRIGA core. 371
Figure 6-15 Range of electrons in water vs electron energy.....374

Figure 6-16 Photon flux vs photon energy leaving a 5 cm sphere of water produced by source electrons of various energies. 376
Figure 6-17 Normalized photon fluxes vs photon energy for various initial electron energies. 377
Figure 6-18 Photon flux vs photon energy for 700 keV electrons using the Cauchy (RefC) and Sellmeier (RefS) coefficients for the index of refraction in the water. 379
Figure 6-19 Photon flux vs photon energy for 4 MeV electrons in a 1mm radius sphere using the Cauchy (refC) and Sellmeier (refS) coefficients for the index of refraction in the water. 379
Figure 6-20 Axial cross section of the core. The top is the +y direction, corresponding to East in the real world. North is on the left side of this plot. 383
Figure 6-21 The TRIGA core map corresponding to the XY picture, showing various features and directions. 383
Figure 6-22 Vertical XZ cross sections of row 4 (left) and row 6 (middle) and row 2 (right) displaying fuel pins, safety shims, the transient control rod, and the regulating rod North is to the left of this plot, South is to the right. 384
Figure 6-23 XZ and XY cross sections of TRIGA showing the region covered by the mesh tallies. 387
Figure 6-24 Neutron flux per unit lethargy (arbitrary units) averaged over the entire in-core domain of the efference TRIGA core. 388
Figure 6-25 Average energy spectra of neutron, gamma, and electrons in the coolant within the reactor core domain of the reference TRIGA configuration. 389
Figure 6-26 Energy spectrum of photons crossing the Cherenkov tallying plane of 8 cm from the face of the reference TRIGA core with directions within a 0.8-cone. 390
Figure 6-27 Photon flux (arbitrary units) energy spectrum at 4 cm from the center of the +y face of the reference TRIGA core configuration. 393
Figure 6-28 Photon flux vs x-position at the core's axial centerline level as an overlay presentation illustrating the core geometry relation. 394
Figure 6-29 Photon at 10 cm above core centerline level as an overlay presentation illustrating the core geometry relation. 394
Figure 6-30 Photon flux at axial positions above the centerline facing the +y side. 395
Figure 6-31 High fidelity photon flux at axial positions above the centerline facing the +y side. 395
Figure 6-32 Reactor core cross section with tallying surfaces explicitly displayed (right) with a closeup of the effective view field (left). 396
Figure 6-33 Photon fluxes with the composition of the pin 1,4 altered. 397
Figure 6-34 Photon fluxes vs x for two critical configurations of the core with the regulating rod fully inserted and removed. 398
Figure 6-35 Difference in the photon fluxes for a critical system with the regulating rod fully removed and inserted. 398
Figure 6-36 Square of the difference in the measured photon fluxes with the regulating rod fully removed and inserted. 399
Figure 6-37 Photon fluxes with alterations to the degree of transient rod insertion. 399
Figure 6-38 Neutron fluxes with alterations to the degree of transient rod insertion. 400
Figure 6-39 Difference in the photon fluxes with the transient rod removed and fully inserted. 401

Figure 6-40 Difference in the neutron fluxes with the transient rod removed and fully inserted. 401
Figure 6-41 XY plane neutron mesh tally results with the reactor in the reference state (top left), with the transient rod inserted (top right), the absolute difference of the perturbed case minus the reference case (bottom left) and the relative difference divided by the value of the reference case at each mesh point (bottom right). 402
Figure 6-42 XY plane gamma mesh tally results with the reactor in the reference state (top left), with the transient rod inserted (top right), the absolute difference of the perturbed case minus the reference case (bottom left) and the relative difference divided by the value of the reference case at each mesh point (bottom right). 403
Figure 6-43 XY plane electron mesh tally results with the reactor in the reference state (top left), with the transient rod inserted (top right), the absolute difference of the perturbed case minus the reference case (bottom left) and the relative difference divided by the value of the reference case at each mesh point (bottom right). 403
Figure 6-44 Gamma (left) and electron (right) fluxes in an XZ mesh east of the core. 404
Figure 6-45 XZ plane electron mesh tally results with the reactor in the reference state (top left), with the regulating rod fully inserted and shims adjusted to maintain a critical configuration (top right), the absolute difference of the perturbed case minus the reference case (bottom left) and the relative difference (bottom right). 405
Figure 6-46 Cherenkov radiation 8 cm east of the core for the reference case (top left) the critical case with the regulating rod fully in (top right) the absolute difference in the flux (bottom left) and the relative difference in the flux when compared to the reference case (bottom right). 406
Figure 6-47 XZ plot of the neutron flux with the cladding of a peripheral pin removed compared to the reference (normal) reactor state. 406
Figure 6-48 XY plot of the neutron flux with the cladding of a peripheral pin removed compared to the reference (normal) reactor state. 407
Figure 6-49 XY plot of the electron flux with the cladding of a peripheral pin removed compared to the reference (normal) reactor state. 407
Figure 6-50 XY plot of the gamma flux with the cladding of a peripheral pin removed compared to the reference (normal) reactor state. 408
Figure 6-51 XY plot of the neutron flux with 1/10 of the cladding of a peripheral pin as B_4C compared to the reference (normal) state. 409
Figure 6-52 XY plot of the electron flux with 1/10 of the cladding of a peripheral pin as B_4C compared to the reference (normal) state. 409
Figure 6-53 XY plot of the neutron flux with 1/10 of the cladding of a central pin as B_4C compared to the reference (normal) state. 410
Figure 6-54 XY plot of the electron flux with 1/10 of the cladding of a central pin as B4C compared to the reference (normal) state. 410
Figure 6-55 Comparison of the Cherenkov flux with the regulating rod at 10 cm (top left) and 30 cm (top right). 411
Figure 6-56 Number of combined sigmas of difference between the cases with the regulating rod at 10 and 30 cm. 412
Figure 6-57 Comparison of the Cherenkov flux with the regulating rod at fully inserted (top left) and fully withdrawn (top right). 412

Figure 6-58 Number of sigmas of difference when the regulating rod is fully inserted and fully withdrawn. 413
Figure 6-59 Response to radiation in TRIGA experiments. 414
Figure 6-60 Comparison of the irradiated region to the entire fiber length. 415
Figure 6-61 Fiberoptics benchtop testing configuration. 416
Figure 6-62 Coiled fiber optic test rig. 416
Figure 6-63 Cobalt-60 pool source irradiation. 417
Figure 6-64 Color comparison for test rig dose ranges. 417
Figure 6-65 Sample scan of a gamma-irradiated fiber. 418
Figure 6-66 University of Cincinnati irradiation results. 418
Figure 6-67 Approximate setup of the camera and the reactor (left) and location of the reactor in the pool (right) during the video experiment. 420
Figure 6-68 Snapshot of the TRIGA reactor core taken from the experiment video. 421
Figure 6-69 XY neutron flux mesh plot comparing video states 2 and 5 with the regulating rod moved, showing state 2 (top left) state 5 (top right) the absolute difference (bottom left) and the relative difference (bottom right). 423
Figure 6-70 XY gamma flux mesh plot comparing video states 2 and 5 with the regulating rod moved, showing state 2 (top left) state 5 (top right) the absolute difference (bottom left) and the relative difference (bottom right). 423
Figure 6-71 XY electron flux mesh plot comparing video states 2 and 5 with the regulating rod moved, showing state 2 (top left) state 5 (top right) the absolute difference (bottom left) and the relative difference (bottom right). 424
Figure 6-72 Cherenkov flux plots comparing video states 2 and 5 with no scaling, showing state 2 (top left) state 5 (top right) the absolute difference (bottom left) and the relative difference (bottom right) 424
Figure 6-73 Sigmas of difference comparing video states 2 and 5 with no scaling. 425
Figure 6-74 Cherenkov flux plots comparing video states 2 and 5 with scaling, showing state 2 (top left) state 5 (top right) the absolute difference (bottom left) and the relative difference (bottom right). 425
Figure 6-75 Sigmas of difference comparing video states 2 and 5 with the scaling factor. 426
Figure 6-76 Comparison between the Cherenkov fluxes with the regulating rod at 70% and with the regulating rod at 30% with the power increased to 110%. 427
Figure 6-77 Sigmas of difference for the comparison between the Cherenkov fluxes with the regulating rod at 70% and with the regulating rod at 30% with the power increased to 110%. 427
Figure 6-78 Comparison between the Cherenkov fluxes with the regulating rod at 70% and with the regulating rod at 30% with the power increased to 120%. The absolute difference plot (left) and relative difference plot (right) are shown. 428
Figure 6-79 Sigmas of difference for the comparison between the Cherenkov fluxes with the regulating rod at 70% and with the regulating rod at 30% with the power increased to 120%.Figure 6-78 428
Figure 6-80 Comparison between the Cherenkov fluxes with the regulating rod at 70% and with the regulating rod at 30% with the power decreased to 90%. The absolute difference plot (left) and relative difference plot (right) are shown. 429

Figure 6-81 Sigmas of difference for the comparison between the Cherenkov fluxes with the regulating rod at 70% and with the regulating rod at 30% with the power decreased to 90%. 429
Figure 6-82 False color image (MatLab 'Hot') of the Cherenkov radiation profile from the TAMU NSC 1MW TRIGA reactor. Power is transitioning from 520kW to 368kW due to the regulating rod moving from the 70% position to the 50% position. 430
Figure 6-83 False color image (MatLab 'Bone') of the Cherenkov radiation profile from the TAMU NSC 1MW TRIGA reactor. Power is transitioning from 520kW to 368kW due to the regulating rod moving from the 70% position to the 50% position. 431
Figure 6-84 False color image (MatLab 'Bone') of the Cherenkov radiation profile from the TAMU NSC 1MW TRIGA reactor. Power is transitioning from 520kW to 235kW due to the regulating rod moving from the 70% position to the 30% position. 431
Figure 6-85 Tallying plane coinciding with the tips of aluminum rod caps (left) and approximate diagram showing circular area of one segment in the tally in the main fueled region. 433
Figure 6-86 Top down Cherenkov detection array shown through a cross section of the center of the core. The 11x9 array of segment tallies (shown in red) are "viewing" each internal coolant channel. 434
Figure 6-87 Comparison between the XY plots of Cherenkov flux leaving the top of the reactor with the reactor in the reference (normal) state (top left) and with the regulating rod fully removed and the shims adjusted for criticality (top right). The absolute (bottom left) and relative (bottom right) difference plots are also shown. 435
Figure 6-88 Sigmas of difference for the XY Cherenkov mesh above the core comparing the reactor in the reference (normal) state with the regulating rod fully removed. 436
Figure 6-89 Comparison between the XY plots of Cherenkov flux leaving the top of the reactor with the reactor in the reference (normal) state (top left) and with the safety shim at 4,4 fully inserted (top right). The absolute (bottom left) and relative (bottom right) difference plots are also shown. 436
Figure 6-90 Sigmas of difference for the XY Cherenkov mesh above the core comparing the reactor in the reference (normal) state with the safety shim at 4,4 (the near the left side of the plot) fully inserted. 437
Figure 6-91 Top view geometrical constraints for the in-core 3D feature reconstruction. 439
Figure 6-92 Coolant channel approximation for 3D power distribution evaluations. 440
Figure 6-93 Energy spectra in FHR and TRIGA. 442
Figure 6-94 Representative energy spectra in FHR and VHTR and in TRIGA. 443
Figure 6-95 XY neutron mesh plot of the FHR core averaged over entire height of core. 443
Figure 6-96 XY gamma mesh plot of the FHR core averaged over entire height of core. 444
Figure 6-97 Details of the TRIGA core layout rendered using MCNP VISED editor. 445
Figure 6-98 Top-down view of TRIGA reactor showing tally locations #2 and #3. 448
Figure 6-99 Various tally locations and temperatures in TRIGA compared to FHR. Best-comparison and physically realizable comparisons in TRIGA compared to FHR. 448
Figure 6-100 : Physically realizable similarity factors for FHR vs. TRIGA. 449
Figure 7-1 Figure 8-2 DSC and TGA of FLiNaK. Maximum heat flow was measured at 465.9^{o}C. 456
Figure 7-2Vacuum Atmospheres Company HE-43-2 glovebox with catalyst bed and gas analyzer. 457

Figure 7-3 SS 304 capsule for static exposure tests. 457
Figure 7-4 SS 304 box with inlet for argon cover gas. 458
Figure 7-5 Experimental setup for exposure tests inside an Ar atmosphere glovebox. 459
Figure 7-6 Cross sectional SEM image of Hastelloy N exposed to FLiNaK at 700°C. 460
Figure 7-7 EDS map of Hastelloy N cross section for Fe, Cr, Mo, and Ni. 460
Figure 7-8 Cross sectional SEM image of Haynes 244 exposed to FLiNaK at 700°C. 461
Figure 7-9 EDS map of Haynes 244 cross section for Mo, Cr, W, and Ni. 462
Figure 7-10 Cross sectional SEM image of Haynes 230 exposed to FLiNaK at 700°C. 463
Figure 7-11 EDS map of Haynes 230 cross section for Mo, Cr, W, Si, and Ni. 463
Figure 7-12 Cross sectional SEM image of SS 316L exposed to FLiNaK at 700°C. 464
Figure 7-13 EDS map of SS 316L cross section for Fe, Cr, and Ni. 464
Figure 7-14 Cross sectional SEM image of SS 304L exposed to FLiNaK at 700°C. 465
Figure 7-15 EDS map of SS 304L cross section for Fe, Cr, and Ni. 465
Figure 7-16 Cross sectional SEM image of SS 321 exposed to FLiNaK at 700°C. 466
Figure 7-17 EDS map of SS 321 cross section for Fe, Cr, Mo, and Ti. 467
Figure 7-18 Cross sectional SEM image of SS 347 exposed to FLiNaK at 700°C. 467
Figure 7-19 EDS map of SS 347 cross section for Fe, Cr, Mn, and Nb 468
Figure 7-20 Time-temperature-sensitization diagram of SS 316L heat containing 0.023% C. [2] 469
Figure 7-21 Mass loss of 316L and 316H samples exposed to FLiNaK for 100 hours at 700°C. 470
Figure 7-22 Glancing Angle XRD of 316L control sample after FLiNaK exposure. Ω = 5° 471
Figure 7-23 Corrosion rates of pure alloying elements exposed to FLiNaK at 700°C. 472
Figure 7-24 Mass loss of AFA stainless steels, Ni based alloys, and conventional stainless steels exposed to FLiNaK at 700°C for 100h. 473
Figure 7-25 Penetration depth of AFA stainless steels, Ni based alloys, and conventional stainless steels exposed to FLiNaK at 700°C for 100h. Depths were measured at multiple locations in the cross section of one sample for each alloy. 474
Figure 7-26 Plan view of OC-T after 100h FLiNaK exposure. 475
Figure 7-27 Plan view of OC-5 after 100h FLiNaK exposure. 475
Figure 7-28 Plan view of OC-8 after 100h FLiNaK exposure. 476
Figure 7-29 Sample shape and sample holder for dynamic corrosion tests in the LSTL at ORNL 477
Figure 7-30 Modifications made to flange of a 2" sump tank port. 477
Figure 7-31 Assembled sample holder with samples during and after installation into the LSTL sump tank. 478
Figure 7-32 Mass loss results of Hastelloy N exposure at 700°C in varying amounts of FLiNaK. Data for higher purity (orange triangles) and lower purity (blue circles) are shown. 479
Figure 7-33 Mass loss per surface area and attack depth for varying amounts of added water. 481
Figure 7-34 SEM/EDS analysis of Hastelloy N sample exposed to FLiNaK with 0.6 wt% moisture addition showing extent of carbon ingress. 481
Figure 7-35 SEM/EDS analysis of Hastelloy N sample exposed to FLiNaK with 0.6 wt% moisture addition showing internal oxidation layer. 482
Figure 7-36 SEM/EDS analysis of Hastelloy N sample exposed to FLiNaK with 0.6 wt% moisture addition showing layer containing Mo rich phases. 482

Figure 7-37 Mass loss data for 100h Hastelloy N exposure test in FLiNaK with NiF2 impurity addition. 483
Figure 7-38 Cross sectional SEM of Hastelloy N sample exposed to FLiNaK with 1.0 wt% NiF2 impurity. 484
Figure 7-39 Mass loss of alloys tested in H2 sparged FLiNaK. 485
Figure 7-40 Cross sectional micrographs of (a) surface-sanded and (b) pre-oxidized SS 316L after 100 hour exposure in static FLiNaK at 700°C. 486
Figure 7-41 Mass loss of alloys exposed to FLiNaK for 25, 100, and 500 hours. 487
Figure 7-42 Mass loss of alloys exposed to FLiNaK for 25, 100, and 500 hours. Horizontal axis is shown as the square root of exposure duration. 488
Figure 7-43 Mass loss of alloys exposed to FLiNaK at 700°C for 500 hours. Error bar indicates multiple samples. 489
Figure 7-44 Plan view of pre-oxidized 316L sample after 500 hour FLiNaK exposure. 489
Figure 7-45 Plan view of pre-oxidized 316L sample after 25 hour FLiNaK exposure in an area with visible oxides. 490
Figure 7-46 Mass change results for austenitic stainless steels which were pre-oxidized for varying durations at 700°C. 491
Figure 7-47 Schematic of Ni/Ni2+ reference electrode. 492
Figure 7-48 Completed Ni/Ni2+ reference electrode. 492
Figure 7-49 CAD drawing of graphite membrane for Ni/Ni2+ reference electrode. 493
Figure 7-50 Open circuit voltage of Ni/Ni2+ reference electrode vs 0.1mol% Ni2+ reference point. 494
Figure 7-51 Chronopotentiogram of Ni crucible potential against dynamic reference electrode. 495
Figure 7-52 Cyclic polarization curve of Hastelloy N in FLiNaK at 500°C. 496
Figure 7-53 Characterization of 200-hour carburized chromium sample before corrosion test: (a) SEM image of sample surface (b) SEM/EDS of FIB cross section (c) Raman spectra of sample surface (d) GAXRD analysis. 498
Figure 7-54 Characterization of 200 hour carburized chromium sample after 100 hour exposure to FLiNaK at 700° C: (a) SEM image of sample surface (b) SEM/EDS of FIB cross section (c) Raman spectra of sample surface (d) GAXRD analysis. 499
Figure 7-55 Mass loss of carburized pure chromium samples exposed to FLiNaK for 100 hours. 500
Figure 7-56 GAXRD patterns of Haynes 230 after exposure to FLiNaK at 700C for 100 hours for (a) Ω = 5° and (b) Ω = 20°. 502
Figure 7-57 SEM and EDS analysis of FIB cross section of pre-carburized Haynes 230 after exposure to FLiNaK at 700C for 100 hours. 503
Figure 7-58 Cross sections of (a) pre-carburized and (b) not pre-carburized Haynes 230 after exposure to FLiNaK at 700C for 100 hours. 503
Figure 7-59 GAXRD patterns of pre-carburized nickel based alloys a) Hastelloy N (5°), b) Haynes 244 (5°), c) Inconel 800H (20°), and d) Haynes 230 (20°) after exposure to FLiNaK at 700C for 100 hours. 505
Figure 7-60 Mass loss of alloys exposed to FLiNaK at 700C for 100h in graphite crucibles. 506
Figure 7-61 Cross sections of carburized Ni based alloys. OM image, 50x magnification. 507
Figure 7-62 Cross sections of carburized Ni based alloys. OM image, 500x magnification. 507

Figure 7-63 Cross sections of pre-carburized Ni based alloys samples after exposure to molten FLiNaK at 700°C for 100 hours. 508
Figure 7-64 Cross sections of Ni based alloy samples after exposure to molten FLiNaK at 700°C for 100 hours. 509
Figure 7-65 Exposure test configuration in Ni 205 crucible. 511
Figure 7-66 GAXRD pattern of Ni samples. 512
Figure 7-67 GAXRD pattern of Fe samples. 512
Figure 7-68 GAXRD pattern of Cr samples. 513
Figure 7-69 GAXRD pattern of Mo samples. 513
Figure 7-70 GAXRD pattern of W samples. 514
Figure 7-71 Raman spectrum of Ni sample exposed to FLiNaK with added carbonate. 515
Figure 7-72 Raman spectrum of Fe sample exposed to FLiNaK with added carbonate. 515
Figure 7-73 Raman spectrum of Cr sample exposed to FLiNaK. 515
Figure 7-74 Raman spectrum of Cr sample exposed to FLiNaK with added carbonate. 516
Figure 7-75 Raman of Mo sample exposed to FLiNaK. 516
Figure 7-76 Raman of Mo sample exposed to FLiNaK with added carbonate. 516
Figure 7-77 Raman of W sample exposed to FLiNaK. 517
Figure 7-78 Raman of W sample exposed to FLiNaK with added carbonate. 517
Figure 7-79 SEM images of sample surfaces after 100 hour exposure to FLiNaK with added carbonate. 518
Figure 7-80 Mass loss of pure element samples after 100 hour exposure to FLiNaK with added carbonate. 519
Figure 7-81 Vickers hardness measurements of Cr sample exposed to FLiNaK with added carbonate. 519
Figure 8-1 A schematic of AHTR 524
Figure 8-2 A three-fluid design concept for a double-wall heat exchanger 525
Figure 8-3 A double-wall configuration for (from left to right): (a) one unit and (b) seven units with a triangular arrangement 526
Figure 8-4 Heat transfer model for a double-wall unit 527
Figure 8-5 Flow directions of three fluids [2.9] 532
Figure 8-6 Comparisons of the fluid temperatures among the model calculations, experimental data, and Fluent simulation results for a counter-current flow pattern 533
Figure 8-7 A schematic of the experimental setup by Wang, et al. [8.17] 534
Figure 8-8 Comparisons of the hydrogen permeation rates under different temperatures and sweep gas flow rates 535
Figure 8-9 Four possible double-wall designs (from left to right): IPOP, IPOF, IFOP, and IFOF 536
Figure 8-10 Effect of the salt Reynolds number on the heat transfer rate 537
Figure 8-11 Effect of the salt Reynolds number on the tritium mass transfer rate 538
Figure 8-12 Comparison of the heat transfer rates using different annular fluids 539
Figure 8-13 Comparison of the mass transfer rates using different annular fluids 540
Figure 8-14 Overall schematic of the AHTR reactor building [8.1] 541
Figure 8-15 Layout of a double-wall P-IHX unit: (a) one tube-side pass and (b) two tube-side passes 543
Figure 8-16 NSGA optimization method 545
Figure 8-17Helical coil heat exchanger [8.29] 547

Figure 8-18 Helical-coiled fluted-tube I-PHX 547
Figure 8-19 Conceptual design of a passively-open tritium-control chimney: (a) normally closed and (b) accidentally open conditions 549
Figure 8-20 Comparison of experimental data and STAR CCM+ predictions 551
Figure 8-21 Layout of DRACS 552
Figure 8-22 Flowchart of DRACS design 553
Figure 8-23 A schematic of HT-FSTF at UM 558
Figure 8-24 Three-dimensional layout of HT-FSTF 559
Figure 8-25 Photo of HT-FSTF 559
Figure 8-26 Control panels for HT-FSTF 560
Figure 8-27 Vertical cantilever dry pit pump 560
Figure 8-28 Lab-scale DHX (left) and NDHX (right) 562
Figure 8-29 A schematic of the corrosion test system 562
Figure 8-30 Corrosion test system before and after installation of thermal insulation 563
Figure 8-31 Glove box and binary salts, LiF, NaF, and KF 565
Figure 8-32 Weight change of LiF 565
Figure 8-33 Weight change of NaF 566
Figure 8-34 Weight change of KF 566
Figure 9-1. MSRE Core Cutaway (ORNL-TM-0728) 579
Figure 9-2. MCNP Model XZ Cross Section (y = 2 in.) 580
Figure 9-3. XY Cross Section in Graphite Stringer Section 581
Figure 9-4. XY Cross Section in Horizontal Graphite Section 582
Figure 9-5. XY Cross Section, Control Rods Detail 583
Figure 9-6. The radial configuration of the stylized FHR benchmark problem 585
Figure 9-7. The axial configuration of the stylized FHR benchmark problem 586
Figure 9-8. Geometrical configuration of AHTR fuel assembly 587
Figure 9-9. Dimension of the AHTR fuel plate 589
Figure 9-10. TRISO particle geometry configuration, taken from (Varma V. K., et al., 2012) 590
Figure 9-11. Geometric configuration of reflectors 591
Figure 9-12. Geometric configuration of support plates 592
Figure 9-13. The radially-integrated fission density distributions computed by COMET and MCNP for the FC-ABO benchmark problem 595
Figure 9-14. The radially-integrated fission density distributions computed by COMET and MCNP for the FC-ABI benchmark problem 595
Figure 9-15. The radially-integrated fission density distributions computed by COMET and MCNP for the FC-CRT benchmark problem 596
Figure 9-16. Stripe-wise fission density distributions computed by COMET for the FC-ABO benchmark problem in axial level 10 597
Figure 9-17. Stripe-wise FDs computed by COMET for the FC-ABI benchmark problem in axial level 10 597
Figure 9-18. Stripe-wise fission density distributions computed by COMET for the FC-CTR benchmark problem in axial level 10 598
Figure 9-19. The deviation of MCNP assembly fission density distribution from the symmetry in axial level 9 (z=337.41 – 372.09 cm) in the FC-CRT benchmark problem 599
Figure 9-20. SERPENT 2D assembly model. 602

Figure 9-21. Normalized 3-group flux distributions. 604
Figure 9-22. Difference in normalized 3-group flux distribution due to reflective BC. (Periodic BC taken as reference.) 605
Figure 9-23. Individual TRISO particle normalized power distribution. 606
Figure 9-24. Material-wise flux spectra. 607
Figure 9-25. Material-wise flux spectra differences. 608
Figure 9-26. Eigenvalue change of fresh assembly with burnup. 609
Figure 9-27. Extrema of relative isotope concentration differences. Solid lines are the min/max differences for the standard (10^7 histories) vs reference (10^8 histories) simulation, and the dashed lines are the min/max differences for the preliminary (10^6 histories) vs reference (10^8 histories) simulation. 610
Figure 9-28. Parallel speedup (left) and parallel efficiency (right) for SERPENT fuel assembly simulations on several configurations with up to 32 CPUs. 613
Figure 9-29. Parallel speedup (left) and parallel efficiency (right) for SERPENT fuel assembly simulations on several configurations with up to 192 CPUs. 613
Figure 9-30. FHR fuel element geometry. 617
Figure 9-31. Comparison of fuel element geometries. 619
Figure 9-32. Comparison of fuel element geometries in Monte Carlo codes. 619
Figure 9-33. Fuel-stripe, spacer-grid, and C-C-box placement within geometry. 620
Figure 9-34. Full-stripe fission density distribution for each simulation. 622
Figure 9-35. Fifth-stripe fission density distributions for each simulation. 623
Figure 9-36. Total flux per lethargy for each model using an uncontrolled 2D assembly model. 623
Figure 9-37. Total flux per lethargy for each model using a poisoned 2D assembly model. 624
Figure 9-38. Normalized total flux per unit lethargy for MCNP cases showing the effect of using burnable poisons vs. an uncontrolled model. 624
Figure 9-39. Normalized fast (E>0.1MeV) neutron flux distribution. 625
Figure 9-40. Normalized epithermal (0.1MeV>E>3eV) neutron flux distribution. 626
Figure 9-41. Normalized thermal (E<3eV) neutron flux distribution. 626
Figure 10-1 Comparison of experimental and RELAP5-3D natural circulation mass flow rates with different heat inputs [10.7]. 643
Figure 10-2 Plant model in RELAP5-3D [10.8]. 643
Figure 10-3 TARCE model of AHTR [10.10]. 644
Figure 10-4 Experiment data compared with RELAP5 simulation results: (a) Temperature comparison; (b) Mass flow rate comparison [10.12]. 645
Figure 10-5 (a) LTDF model and (b) HTDF model in RELAP5 [10.12]. 646
Figure 10-6 SAM simulation results of of an SFR [10.13]. 647
Figure 10-7 Path lines colored by static pressure for FLiBe salt for a static pressure drop of 426 kPa: (a) Reverse flow direction; (b) Forward flow direction [10.20]. 649
Figure 10-8 Fuel assembly geometry: (a) 1/3 of an fuel assembly; (b) An full fuel assembly 649
Figure 10-9 Simulation results: (a) Velocity profile in coolant channels at top of fueled region; (b) Temperature profile in coolant channels at top of fuled region [10.22] 650
Figure 10-10 Upper regions of the AHTR fuel assembly [10.22]. 650

Figure 10-11 COMSOL results: (a) Cross-sectional temperature in an average fuel block; (b) Temperature profile in the fuel and graphite [10.23]. 651
Figure 10-12 Simulation of the annular PB-AHTR core: (a) Geometric configuration; (b) Bulk coolant temperature profile; (c) Fuel temperature profile (average kernel temperature in fuel pebble) [10.23]. 651
Figure 10-13 Schematic of (a) LTDF (b) HTDF 654
Figure 10-14. LTDF benchmark results of the DHX shell-side (primary loop) water inlet and outlet temperatures during DRACS startup transient. 656
Figure 10-15. LTDF benchmark results of the DHX tube-side (DRACS loop) water inlet and outlet temperatures during DRACS startup transient. 656
Figure 10-16. LTDF benchmark results of the air inlet and outlet temperatures during DRACS startup transient. 657
Figure 10-17. LTDF benchmark results of the fluid mass flow rates in the three loops during DRACS startup transient. 658
Figure 10-18. LTDF benchmark results of the mass flow rates of (a) pump side branch and DHX side branch of the primary loop (b) the three loops during the primary pump trip scenario. 659
Figure 10-19. LTDF benchmark results of the DHX shell-side (primary loop) water inlet and outlet temperatures during the primary pump trip scenario. 660
Figure 10-20. LTDF benchmark results of the DHX tube-side (DRACS loop) water inlet and outlet temperatures during the primary pump trip scenario. 660
Figure 10-21. LTDF benchmark results of the air inlet and outlet temperatures during the primary pump trip scenario. 661
Figure 10-22 Schematic of the experimental natural circulation loop [10.28] 662
Figure 10-23 Nodalization of the natural circulation loop in SAM 663
Figure 10-24 Time integration scheme comparison of backward Euler and BDF2 664
Figure 10-25 Spatial integration schemes comparison of trapezoidal rule and Gaussian quadrature rule 664
Figure 10-26 Benchmark results of the source tube inlet and outlet temperature of counter flow case (startup scenario) 666
Figure 10-27 Simulation results of the mass flow rate in the natural circulation loop of counter flow case (startup scenario) 666
Figure 10-28 Comparisons of the friction factors in SAM and RELAP5 in (a) linear scale (b) logarithm scale 667
Figure 10-29 Simple loop model in SAM 668
Figure 10-30 Comparison of the primary mass flow rates calculated from SAM and RELAP5 668
Figure 10-31 Schematic of LTDF SAM model 669
Figure 10-32 LTDF model in Paraview 669
Figure 10-33 Schematic of LTDF 671
Figure 10-34 Comaparison of the SAM simulation results and experimental data for the DHX shell-side inlet and outlet temperatures 674
Figure 10-35 Comaparison the SAM simulation results and experimental data for the DHX tube-side inlet and outlet temperatures 674
Figure 10-36 Comaparison of the SAM simulation results and experimental data for the NDHX air-side inlet and outlet temperature 675

Figure 10-37 Comaparison of the SAM simulation results and experimental data for mass flow rates in the three loops 675
Figure 10-38 Water and air temperature distributions in LTDF at (a) 0 s, (b) 10,000 s and (c) 20,000 s after pump trip initiation 676
Figure 10-39 Velocity of primary loop at (a) 0s and (b) 10,000 s after pump trip initiation 677
Figure 10-40. Schematic of the AHTR RELAP5 model 681
Figure 10-41. Comparison of the decay power, heat removal rate by three primary loops, DRACS heat removal rate of three DRACS loops during LOFC. 687
Figure 10-42. Core inlet and core outlet temperature during LOFC 688
Figure 10-43. DHX inlet and outlet temperatures in bypass channel side during LOFC 688
Figure 10-44. Mass flow rates in each bypass channel during LOFC 689
Figure 10-45. DRACS hot-leg and cold-leg temperatures during LOFC 689
Figure 10-46. Mass flow rates of each DRACS and air loop during LOFC 690
Figure 10-47. Comparison of heat removal rates by DRACS and primary loops, and decay power during loss of two DRACS loops 691
Figure 10-48 Heat removal rates by three DRACS loops and open DRACS loop during loss of two DRACS loops 691
Figure 10-49 Core inlet and core outlet temperature during loss of two DRACS loop during loss of two DRACS loops 692
Figure 10-50 DHX inlet and outlet temperatures in bypass channel side during loss of two DRACS loop 693
Figure 10-51 Mass flow rates in each bypass during loss of two DRACS loops 693
Figure 10-52 DRACS hot-leg and cold-leg temperatures during the first hour of the loss of two DRACS loop scenario 694
Figure 10-53 DRACS hot-leg and cold-leg temperatures during loss of two DRACS loops 694
Figure 10-54 Mass flow rates of the DRACS loops during loss of two DRACS loops 695
Figure 10-55 Air inlet and outlet temperatures during loss of two DRACS loops 695
Figure 10-56 Mass flow rates of the air loops during loss of two DRACS loops 696
Figure 10-57 Schematic of LS-VHTR [10.40] 697
Figure 10-58 RELAP5-3D model of LS-VHTR [10.40] 697
Figure 10-59 Comparison of RVACS heat removal rate and core decay heat generation rate during LOFC for LS-VHTR [10.40] 699
Figure 10-60 Thermal performance following a LOFC [10.40] 699
Figure 10-61. Response of AHTR to LOFC accident with: (a) high emissivity and (b) low emissivity of thermal shields [10.37] 700
Figure 10-62. Schematic of the heat transfer path from the primary salt to the surrounding soil 701
Figure 10-63. The temperature distribution from the vessel wall to the soil surrounding during reactor normal operation with a 150-mm thermal insulation to the reactor vessel 703
Figure 11-1 Finished new laboratory work space for FLiBe purification and testing inside building 4505-R26 at ORNL. 708
Figure 11-2 First FLiBe purification batch completed (1.6 L). 709
Figure 11-3 Various materials tested using the produced FLiBe salt a) Summary of samples tested during first stage of program b) Capsules after 500 hrs test. 710
Figure 11-4 Sample holder for dynamic testing being inserted into ORNL's FLiNaK loop 711

Figure 11-5 ORNL Liquid Salt Test Loop (LSTL) used for molten salt/corrosion dynamic testing 712
Figure 11-6 TRACE code simulation of a pump coast down in the LSTL facility 712

List of Tables

Table 3-1. Design parameters for the AHTR concept from ORNL. 10
Table 3-2. Initial tritium production rate by axial region throughout an FHR design. 14
Table 3-3. Contributions to reaction rates from different broad energy groups to the ^{6}Li (n, t) ^{4}He reaction and discrepancies between effective 1-group microscopic cross sections calculated in SCALE6.2 and MCNP6.1. 15
Table 3-4. Contributions to reaction rates from different broad energy groups to the ^{9}Be (n, α) $^{6}He \rightarrow {}^{6}Li$ reaction and discrepancies between effective 1-group microscopic cross sections calculated in SCALE6.2 and MCNP6.1. 16
Table 3.5. Isotopics for tritium production studies from a 2D assembly-level SERPENT model. 20
Table 3.6. 1-group transition probablities produced by COUPLE using MCNP6.1 tallies generated from using 4 cases of spent-fuel isotopics. 22
Table 4-1: The measured and calculated solubilities of Xe and Kr in LiF-BeF_2 at different temperatures. The unit of the solubility is 10^{-8} moles/(cm^3-melt atm). 27
Table 4-2: Experimentally Determined Apparent Potentials of Rare Earths and Actinides in LiF-BeF_2 Molten Salt 39
Table 4-3: Experimentally Determined Activity Coefficients of Rare Earths and Actinides in Liquid Bismuth Metal 39
Table 4-4: Summary of potassium reduction potential in FLiNaK from three replicates at each temperature. 57
Table 4-5: Predicted coordinates of cyclic voltammetric peaks and the calculated concentration ratio. 63
Table 4-6: Summary of formal standard potential from this work and references [2] and [5]. 65
Table 4-7: Diffusion coefficients of lanthanum ion in FLiNaK molten salt determined using equation (4-69). 92
Table 4-8: Optimized parameters determined by non-simplified electrode kinetic equation. . 98
Table 4-9: The obtained values of K0 at different temperatures using equation (4-75). 98
Table 4-10: Current peak potential difference determined in cyclic voltammetry at different temperatures and scan rates. 104
Table 4-11: The predicted coordinates of cyclic voltammetry current peaks at the selected bulk concentration ratios for the cyclic voltammetry results shown in Figure 4-38. 104
Table 4-12: diffusion coefficients of Cr (III) and Cr (II) obtained at different temperatures by CV and CP methods 110
Table 4-13: The exchange current densities for Cr^{2+}/Cr^{0} couple in FLiNaK eutectic containing 0.4 wt% CrF_2. 115
Table 4-14: The exchange current densities of Fe^{2+}/Fe^{0} couple in FLiNaK eutectic containing 0.4 wt% FeF_2. 116
Table 4-15: Chemical composition of the materials (in weight percent). 118
Table 4-16: Test matrix for series C100 and test status 118
Table 4-17: Electrochemical parameters of potentiodynamic polarization tests. 119
Table 4-18 Solubility Experiment information 124
Table 4-19 La concentration and La2O3 solubility at 600°C, 650°C, 700°C, 750°C 130

Table 4-20 Electrodes implied in the electrochemical experiments 134
Table 4-21 Comparison of the first peak radius for ion pairs in FLiNaK with literature data and experiment data. FPMD simulations for FLiNaK were performed at 700°C 167
Table 4-22 Comparison of first shell coordination numbers for ion pairs in FLiNaK with literature data and experiment data. FPMD simulations for FLiNaK were performed at 700°C.....168
Table 4-23 comparison of first peak radius and first shell coordination numbers for ions pairs in FLiNaK and FLiNaK- La_2O_3. FPMD simulations for FLiNaK were performed at 700°C 170
Table 4-24 Comparison of enthalpy of formation in FLiNaK and FLiNaK-La_2O_3 170
Table 4-25 Gibbs free energy of LaOF and La_2O_3 at 1200℃ 171
Table 4-26.Invariant reactions in Bi-Pr binary system......234
Table 4-27. Thermodynamic parameters of the Bi-Pr system obtained by CALPHAD method. 235
Table 4-28. Invariant reactions in Bi-Ce binary system......236
Table 4-29. Thermodynamic parameters of the Bi-Ce system obtained by CALPHAD method 237
Table 4-30. Invariant reactions in Bi-Er binary system......238
Table 4-31. Thermodynamic parameters of the Bi-Er system obtained by CALPHAD method. 239
Table 4-32. Enthalpies of formation of the intermetallic compounds in Bi-Pr system......240
Table 4-33. Enthalpies of formation of the intermetallic compounds in Bi-Ce system 240
Table 4-34. Enthalpies of formation of the intermetallic compounds in Bi-Er system......240
Table 4-35. Entropies of formation of intermetallic compounds for Bi-Pr, Bi-Ce, and Bi-Er systems......241
Table 4-36. Comparison between the calculated activity coefficients and literature values for Bi-Ce system. 245
Table 4-37. Comparison between the calculated activity coefficients and literature values for Bi-Er system. 246
Table 4-38. Solubility of Pr, Ce, and Er in liquid bismuth. 249
Table 4-39. Correlations for the activity coefficients of lanthanides in liquid bismuth. 250
Table 4-40. Solubility limit of lanthanides in liquid bismuth at the temperatures of 873 K, 923 K, and 973 K. 252
Table 4-41. Activity coefficients of lanthanides in liquid bismuth at 873 K......253
Table 4-42. Activity coefficients of lanthanides in liquid bismuth at 923 K......254
Table 4-43. Activity coefficients of lanthanides in liquid bismuth at 973 K......255
Table 4-44. Activity and activity coefficient of K in reference electrode at the temperatures of 973 K and 1023 K.....267
Table 4-45. Activity and activity coefficient of Li in reference electrode at the temperatures of 973 K and 1023 K.....272
Table 5-1: Neutronics PIRT panelists and organization......278
Table 5-2: List of Presentation on the PIRT Panel. 280
Table 5-3 Phenomena importance rankings and descriptions.....281
Table 5-4 Knowledge level ranking and descriptions.....281
Table 5-5: Knowledge level and importance ranking combinations for further consideration. 283

Table 5-6: Phenomena Requiring Further Consideration. 284
Table 5-7. Phenomena importance rankings 291
Table 5-8. Knowledge level ranking definitions 291
Table 5-9. Determination of phenomena for further consideration 292
Table 5-10. TH-PIRT chart for SBO (Core/fuel) 294
Table 5-11. TH-PIRT chart for SBO (Core/primary coolant flow) 295
Table 5-12. TH-PIRT chart for SBO (Reactor vessel) 296
Table 5-13. TH-PIRT chart for SBO (Cavity) 297
Table 5-14. TH-PIRT chart for SBO (Primary loop) 297
Table 5-15. TH-PIRT chart for SBO (Intermediate loop) 298
Table 5-16. TH-PIRT chart for SBO (Power cycle) 298
Table 5-17. TH-PIRT chart for SBO (DRACS) 299
Table 5-18. TH-PIRT chart for simultaneous withdrawal of all control rods (Core/fuel) 300
Table 5-19. TH-PIRT chart for simultaneous withdrawal of all control rods (Core/primary coolant flow) 301
Table 5-20. TH-PIRT chart for simultaneous withdrawal of all control rods (Reactor vessel) 303
Table 5-21. TH-PIRT chart for simultaneous withdrawal of all control rods (Cavity) 304
Table 5-22. TH-PIRT chart for simultaneous withdrawal of all control rods (Primary loop) 304
Table 5-23. TH-PIRT chart for simultaneous withdrawal of all control rods (Intermediate loop) 305
Table 5-24. TH-PIRT chart for simultaneous withdrawal of all control rods (Power cycle) ..305
Table 5-25. TH-PIRT chart for simultaneous withdrawal of all control rods (DRACS) 306
Table 5-26. Commentary and path forward for key phenomena identified for both events ...307
Table 5-27 List of panelists for the FHR Materials PIRT panel held at the Georgia Institute of Technology, Atlanta, GA on November 28 to 30, 2016. 315
Table 5-28: Description of degradation mechanism FoM ranking designations. 318
Table 5-29: Description of knowledge level ranking designations. 318
Table 5-30: Multi-physics PIRT Members 322
Table 5-31: Phenomena requiring tight coupling 323
Table 5-32: Phenomena Requiring Loose Coupling 326
Table 6-1 Representative characteristics of the considered FHR design 352
Table 6-2 Representative characteristics of the considered VHTR design 355
Table 6-3 Emulation of a multi-modal sensor network via simulated mesh plots 387
Table 6-4 Representative characteristics of the TRIGA reactor 446
*Table 7-1 Nominal compositions of Ni based alloys and stainless steels and other materials tested in this study * indicates XRF measurement* 454
Table 7-2 Maximum depth of attack of pre-carburized Ni based alloys after exposure to molten FLiNaK. 'NM' indicates attack was not measurable using OM images. 509
Table 8-1 Diffusivities and solubilities of potential annular fluids 538
Table 8-2 Key design parameters of AHTR [8.1] 541
Table 8-3 Inputs for a double-wall fluted-tube P-IHX design optimization 545
Table 8-4 Comparison of the optimum results of a double-wall fluted-tube P-IHX using helium and FLiBe as the annular fluid 546
Table 8-5 Optimum double-wall P-IHX design 546
Table 8-6 Inputs for I-PHX design optimization 548

Table 8-7 Optimum I-PHX design 548
Table 8-8 Unit price for the AHTR chimney and DRACS salt 553
Table 8-9 Inputs for the DRACS design optimization (single-wall design) 554
Table 8-10 Key parameters of an optimum DHX design 555
Table 8-11 Key parameters of an optimum NDHX design 555
Table 8-12 Inputs for a double-wall NDHX design optimization 556
Table 8-13 Comparison of the optimum results of a double-wall fluted-tube NDHX using helium and FLiBe as the annular fluid 557
Table 8-14 Optimum double-wall NDHX design 557
Table 8-15 Key design parameters of HT-FSTF 559
Table 9-1. AHTR core parameters 584
Table 9-2. Total number and dimension of fuel assemblies and replaceable and permanent reflectors 586
Table 9-3. Height of each axial segment 586
Table 9-4. Total number and dimension of fuel assemblies, replaceable and permanent reflectors 588
Table 9-5. Material density for AHTR fuel assembly 588
Table 9-6. Parameters for burnable poison 589
Table 9-7. Parameters of TRISO fuel lattice 590
Table 9-8. Dimension of replaceable reflector 591
Table 9-9. Material density for support plates 592
Table 9-10. Properties and dimensions of unique AHTR coarse meshes. 593
Table 9-11. Comparison of the eigenvalue and computation time for full core problems 594
Table 9-12. Comparison of the assembly-averaged fission density distribution computed by *COMET and MCNP* 596
Table 9-13. 2D SERPENT assembly dimensions. 603
Table 9-14. 2D SERPENT assembly material properties. 603
Table 9-15. Runtime statistics of various depletion simulations. 609
Table 9-16. Results of simulations with different S(α,β) treatments. 611
Table 9-17. Relative eigenvalue differences* (in pcm) for cases C-F (with respect to case C). 611
Table 9-18. Material-wise graphite density sensitivity. 612
Table 9-19. Bottom-left spacer-grid placements. 618
Table 9-20. Bottom-left fuel-stripe placements. 618
Table 9-21. MC parameters and run times for each case. 621
Table 9-22. Multiplication and peaking factors calculated by MCNP, SCALE and SERPENT. 621
Table 9-23. SERPENT runtime for different tally types. 629
Table 9-24. Estimated full core single cycle simulation runtime using SERPENT. 630
Table 10-1 Dimensions of tube bundles and the natural circulation loop [10.28] 662
Table 10-2 Boundary conditions of parallel flow and counter flow in source tube [10.28] 665
Table 10-3 DHX inputs in SAM 670
Table 10-4 NDHX inputs in SAM 670
Table 10-5 Measurement uncertainties of LTDF instruments 671
Table 10-6 Comparison of SAM simulation results and experimental data at steady state before pump trip 673

Table 10-7 Specific heat of FLiNaK and KF-ZrF_4 679
Table 10-8 Triple point temperature $T0$ *, triple point pressure* $P0$*, critical temperature* $Tcrit$ *and critical pressure* $Pcrit$ *of FLiNaK and KF-*ZrF_4 680
Table 10-9. Coolant flow areas and the power of four core rings 682
Table 10-10. P-IHX input data of AHTR RELAP5 model 683
Table 10-11. Specification of single-wall fluted tube DHX 684
Table 10-12. Specification of single-wall fluted tube NDHX 684
Table 10-13. The geometry parameters of fluted tubes in DHX and NDHX 685
Table 10-14. AHTR design value and RELAP5 simulation results in a steady state of reactor normal operation [10.37] 686
Table 10-15 Geometry information of RVACS in LS-VHTR [10.40] 698
Table 10-16 LS-VHTR nominal design parameters [10.40] 698
Table 10-17. Thermal properties of heat structures 702
Table 10-18. Steady-state simulation results with different thermal insulation thickness values 702

List of Abbreviations

BDBA	Beyond Design Basis Accidents
DBA	Design Basis Accidents
DHRS	Decay Heat Removal System
dpa	Displacement Per Atom
DRACS	Direct Reactor Auxiliary Cooling System
FHR	Fluoride High Temperature Reactor
GT	Georgia Institute of Technology
HM	Heavy Metal
HX	Heat Exchanger
IRP	Integrated Research Project
NEUP	Nuclear Energy University Programs
NGNP	Next Generation Nuclear Plant
NPP	Nuclear Power Plant
ORNL	Oak Ridge National Laboratory
OSP	Office of Sponsored Programs
OSU	Ohio State University
PIRT	Phenomena Identification and Ranking Table
PRA	Probabilistic Risk Assessment
REM	Rare Earth Metal
SINAP	Shanghai Institute of Applied Physics
TAMU	Texas A&M University
TAMU-K	Texas A&M University, Kingston
TRISO	Tristructural-Isotropic
VHTR	Very High Temperature Reactor

1. Executive Summary

This document constitutes progress made on this project by the Georgia Tech led Integrated Approach to Fluoride High Temperature Reactor Technology and Licensing Challenges (FHR-IRP). This is the first draft of the project final report.

Chapter 3 is focused on Tritium management. Tritium management in Fluoride-salt High-temperature Reactors (FHRs) presents a major operational concern and a significant challenge. Tritium is generated via multiple pathways including various interactions in fuel and structural materials, as well as coolant (primarily interaction with lithium and beryllium), leading to a complex evolution and spatial distribution of tritium generation rate. FHR generates orders of magnitude more tritium than in LWRs, and has potential for a significant release, via permeation through structural materials (due to high temperature), and through heat exchanger(s). Therefore, accurate estimate is necessary. For that purpose relevant tritium production pathways were identified. A methodology to obtain space-time dependent tritium generation rate was developed and implemented, employing SCALE and MCNP codes. Detailed models of the reference Advanced High Temperature Reactor (AHTR) design were developed. A multi-parametric metrics was introduced to capture relevant tritium production indicators, including the instantaneous tritium production rate, total tritium production (neglecting subsequent decay), and accumulated tritium production (accounting for the decay). The obtained results will inform tritium management, including the sizing of the components, and to gain insight on the impact of the core design parameters on tritium generation rates.

Research effort on Liquid Salt Impurity Removal, Redox and Corrosion Control is discussed in Chapter 4. Section 4.1 is an introduction chapter. Based on the current available knowledge and operation experience on previous MSRs and other types of nuclear reactors, the report identifies the major impurities that are related to either material compatibility, salt properties or radioactive source terms, and the potential contamination sources of these impurities, their transport in the primary coolant loop and available cleanup methodologies for a particular group of impurity. In section 4.2, the available purification methods were discussed, including the liquid/liquid extraction using liquid Bi-Li which has been applied in MSBR and electrochemical purification which is developed based on Pyroprocessing. In this section, the new multi-stage and multi-salt-component was developed and discussed. Section 4.3 discussed the redox potential control for salt chemistry and corrosion mitigation, including the control theory and the soluble/soluble buffer control method. The section also developed method on how to analyze soluble/soluble redox reaction in a molten salt system and designed an electrochemical sensor for redox potential control. Corrosion models were also reported in this section. Section 4.4 focused on how to measure the fundamental properties in a molten salt. As an example, the section focused on La fluoride in the molten salt. The section developed methods on how analyze electrochemical measurement data to obtain the fundamental properties including the redox potential, diffusion coefficient and exchange current density. All these fundamental information is important for salt purification system development. Section 4.5 focused on measurements of corrosion products in the salts. Because of the

different behaviors between Cr and La in the salt, new analysis method for Cr fluorides in the salt was developed. Some results for Fe fluoride in the salt and corrosion measurements were also reported. Section 4.6 demonstrated the separation of oxide from the salt. This section also measured the solubility of La2O3 in the salt as function of temperature. Section 4.7 focused on the separation of La and Ce from the molten salt. These two elements were selected because La was found to be separated by using inert electrode, while for separation of Ce, reactive electrode must be selected. Section 4.8 demonstrated the separation iodine ions from the molten salt. Two kinds of working electrode materials (metal W and graphite) were investigated. Section 4.9 focused on the fundamental data of fission products and actinides in liquid Bi. The chapter reviewed the available data, then based a CALPHAD model, the available data were broadened to the concentration-dependent cases.

Chapter 5 summarizes the results from four Phenomena Identification and Ranking Table (PIRT) panels to identify and prioritize verification and validation (V&V) needs in the areas of neutronics, thermal hydraulics, material, and multiphysics. This chapter also documents the overall PIRT process, ranking methods, voting procedures, rationale for all rankings, discussion of the next steps for phenomena that require further consideration, and a record of the comments and suggested path forward from the panelists.

Chapter 6 is focused on development, demonstration and evaluations of novel FHR instrumentation options and visual/optical reactor performance characterization capabilities taking advantage of the TRIGA reactor configuration as a prototypic optically (visually) accessible reactor environment. The actual reactor operation data have been compiled and used to support sensitivity studies as well as model validation efforts. Performed simulations indicate significant noise levels that potentially may complicate reconstructions of localized values of in-core parameters in FHRs. The project accomplishments include developing two 3D reconstruction methods, assessment of emulation options for scaling experimental results from TRIGA to FHR conditions, and design of the multiphysics sensor probe concept realizing optical and mixed-field sensing capabilities within a single integrated probe configuration. One of the developed 3D reconstruction methods assumes exclusive fiberoptics-based technology options. The 2nd method is based on the integration of multi-field distributed sensing approaches using fiberoptics-based and optical (image-based) technology options.

Research work in the area of FHR structure material is summarized in Chapter 7. Results from the corrosion tests showed that the chromium content of alloys had an indirect correlation with the alloys' performance. Results have shown that the impurities in molten salts have a significant effect on the corrosion behavior of alloys. Results indicated that an addition of moisture in tested range had a relatively smaller effect on the corrosion behavior of alloys. Whereas, an addition of metal fluorides, like NiF2, had a significant effect on the intergranular degradation of Hastelloy N and other alloys. As there is a finite amount of impurities in the limited amount of salts used for static corrosion tests, the effect of salt volume on the corrosion rate was evaluated. The overall corrosion increased with an increase in the salt volume, which indicates that the impurities are consumed in the corrosion reaction over time, and the salt volumes used in a test can have an effect on the

measured degradation rate. Results also indicated that the corrosion rate decreases over time due to the consumption of a limited amount of impurities in the salt. A thermodynamically stable reference electrode based on the prior work done at Oak Ridge National Laboratory (ORNL) was developed and tested. This design uses the Ni/Ni2+ redox couple in order to sustain a constant reference potential. This electrode construction was successful and allowed us to measure stable potential values in molten salt. In most FHR designs a significant amount of graphite will be used, which will come in touch with the molten salt and may even come in touch with other structural alloys. To see the effect of the presence of graphite on structural alloys, initial set of tests were carried out with pure elements in graphite crucible. It was found that chromium and tungsten readily formed carbides at the surface during these tests. The surface carbide layer was found to significantly increase the corrosion resistance of chromium in a molten FLiNaK environment. Results from this work has indicated that the carbonates in the molten salt could be a probable mechanism for the carbon transportation in molten fluoride salts. This provides a mechanism to slow down corrosion of alloys in molten fluoride salts.

Research in the area of Design, fabrication, testing, demonstration, and modeling of novel heat exchangers for FHRs is discussed in Chapter 8. For the heat exchanger task, a coupled heat and mass transfer model was first developed and benchmarked against the experimental data available in the literature to provide a DWHX design tool, which was then applied to four potential DWHX configurations, i.e., inner plain tube with outer plain tube (IPOP), inner plain tube with outer fluted tube (IPOF), inner fluted tube with outer plain tube (IFOP), and inner fluted tube with outer fluted tube (IFOF), and four potential annular fluids, i.e., helium, FLiBe, FLiNaK, and KF-ZrF4.

In addition, an optimization method, non-dominated sorting in generic algorithms (NSGA), was applied for the HX design optimization. As case studies, designs of four AHTR HXs, i.e., double-wall primary-to-intermediate heat exchanger (P-IHX), single-wall intermediate-to-power cycle heat exchanger (I-PHX), single-wall DRACS in-vessel heat exchanger (DHX), and single-/double-wall natural draft DRACS heat exchanger (NDHX), were optimized to provide baseline designs for AHTR and summarized in this report.

A high-temperature fluoride salt test facility (HT-FSTF) was designed and constructed primarily for testing HXs and some thermal-hydraulics phenomena related to FHRs, such as forced and natural circulation flows. Lab-scale fluted-tube DHX and NDHX were fabricated and are planned to be tested in HT-FSTF. Experimental data from the HX tests will be used to further validate the HX design model, while experimental data from the natural circulation experiment will be used for the benchmark of system analysis codes, such as RELAP5 and SAM.

Chapter 9 discusses research performed in the area of V&V of neutronics tools /methodologies to support licensing. A set of benchmark problems typical of FHRs has been developed. The problem was derived from the AHTR concept by simplifying the geometry and material specification of the original conceptual design while retaining the multiple heterogeneities and major physical characteristics of the core that are important from the neutronics point of view. The fuel assembly and core benchmark problems can be

used with the desired complexity in "2D" and 3D configurations including single or multi-assembly to whole core problems. The continuous energy COMET method/code was used to solve these benchmark problems. The eigenvalue and fission density distributions predicted by COMET agree very well with those computed by MCNP. The benchmark calculations against Monte Carlo have also indicated that the continuous energy COMET can serve as an excellent method for obtaining high fidelity solutions (e.g., the stripe-wise fission density distribution) to FHR full core problems because of COMET's high fidelity and high computational efficiency. As a result, the stripe-wise fission density distributions generated by the continuous energy COMET can be taken as a reference solution to the stylized FHR benchmark problems.

Accurate neutronics analysis of Fluoride-salt High-temperature Reactors (FHRs) is challenged by the complex reactor core geometry combined with the double heterogeneity of TRISO fuel. Validation is not possible or at best is very limited due to the lack of prototypic experimental data, and therefore extended verification and cross-comparison of results obtained by different codes is necessary. Investigations and analyses were performed to address: (a) Impact of modeling approaches and sensitivity to nuclear data; (b) Verification of code performance through cross-verification of results; and, (c) Feasibility of detailed Monte Carlo simulations.

In addition, three Monte Carlo codes were employed including SCALE, SERPENT and MCNP. A reduced-size core model consisting of a finite-height slice of a single fuel element was used. Sensitivity to modelling assumptions, as well as the impact of perturbation in dimensions, temperatures and cross sections were examined. Verification through cross-comparison of the results of the three Monte Carlo codes was performed. Detailed comparisons have demonstrated that the codes produce consistent results when applied to carefully developed consistent models. Regarding the computational resources required, extrapolating requirements to full core simulations shows that a single or a very limited number of benchmark simulations is feasible, but it is still far from being practical, and development of improved and novel methodologies is needed.

Chapter 10 summaries research in the area of V&V of thermal hydraulics tools /methodologies to support licensing. Two system-level codes, namely RELAP5 SCDAPSIM/MOD 4.0 and System Analysis Module (SAM), are selected for benchmark study due to their potential thermal hydraulics modeling and capabilities for AHTR. Experimental data from a single-phase natural circulation loop is used as one of the code validation studies. In addition, experimental data from a low-temperature DRACS test facility (LTDF) is also utilized for RELAP5 and SAM code validation. An extensive test matrix was developed for the LTDF tests including DRACS startup and pump trip scenario. The code simulation results of RELAP5 and SAM show good agreement with the experimental data. A high-temperature fluoride salt test facility (HT-FSTF) has been designed and constructed for testing heat exchangers and performing transient natural circulation tests. The experimental data of these experiments will be used for the further code validation once they become available. In addition, an AHTR reactor model has been developed in RELAP5 with the fluted tube DRACS heat exchanger (DHX) and natural draft DRACS heat exchanger (NDHX) designs proposed in a parallel study of this integrated research project (IRP).

Reactor steady-state normal operation and two transient scenarios, namely, loss of forced circulation (LOFC) and loss of multiple DRACS loops are analyzed using the RELAP5 AHTR model. During the transients, the decay heat is removed by the ambient air, fully relying on passive natural circulation/convection.

In Chapter 11, contributions from National Laboratory partner to support experimental efforts are described. ORNL provided consulting for all members of this collaboration team in the fields of thermal-hydraulics, materials, corrosion and neutronics. A new laboratory to handle fluoride salts with Beryllium content was completed and successfully produced a first batch of high quality purified FLiBe salt. Corrosion testing and analysis for various metallic and graphite samples in contact with FLiBe salt was performed for this IRP effort. Dynamic corrosion testing in fluoride salts (FLiNaK) using the ORNL's liquid salt test loop facility was designed and tested.

2. Project Tasks

Based on the tasks identified in the initial IRP proposal, the following tasks were addressed in this project.

- Task 3.1: Radiation Environment for Tritium Management
- Task 3.2: Liquid Salt Impurity Removal, Redox and Corrosion Control
- Task 3.3: Identification and Prioritization of V&V Needs via PIRT Panels
- Task 3.4: Instrumentation: development and demonstration of instrumentation systems taking advantage of optical and visual sensing in high temperature liquid salt environment
- Task 3.5: Qualification of Alloys for Structural Applications
- Task 3.6: Design, fabrication, testing, demonstration, and modeling of novel heat exchangers for FHRs
- Task 3.7: V&V of neutronics and thermal hydraulics tools/methodologies to support licensing
- Subtask 3.8: Contributions from National Laboratory partner to support experimental efforts

3. Tritium Source Generation Model

3.1. Objectives of Subtask 3.1: Determining Radiation Environment for Tritium Management

Tritium management in FHRs presents a major operational concern and a significant challenge. Tritium is generated via various interactions in fuel and structural materials, as well as coolant, leading to a complex spatial distribution of tritium generation rate. Tritium generated by ternary fission, the main source in other reactor types, will remain contained in FHRs as long as the fuel does not fail. However, the interaction of neutrons with lithium and beryllium in the primary coolant is specific to FHRs, generates orders of magnitude more tritium than in LWRs, and has potential for a significant release, via permeation through structural materials (due to high temperature), and through heat exchanger(s).

Tritium management is a complex topic that in addition to estimating tritium generation also requires evaluating its mass transport through the primary loop, potential for its release, and methods for its capture and management. However, the Subtask 3.1, which is documented in this topical report, focuses only on the first step, tritium generation. The objective of this task is to develop a methodology and detailed models to enable obtaining estimate of the tritium generation, with improved accuracy, including its time evolution over the reactor lifetime, and dependence on the reactor design parameters. These results are intended to inform the tritium management program, e.g., provide input to mass transfer analyses and to sizing and determining the required performance parameters of the tritium management components. They can also inform the design choices to minimize tritium production.

3.2. Tritium Source Generation Methodology, Model and Analyses

3.2.1. Overview of the performed work

The activities associated with tritium source evaluation started (as scheduled) in Year 2 and provided the following results:

- Identification of multiple pathways for tritium generation
- Selection of analytic tools and approaches for core physics modeling of FHR
- Establishing initial models and cross-verification between available tools
- Assessment of reaction/transition probabilities involved in tritium generation
- Evaluation of equilibrium concentration of isotopes relevant for tritium generation
- Examination of relevant nuclear data, generation of neutron spectra and 1-group effective cross sections

The task activities continued and were successfully completed in project Year 3:

- Models and methodology were established.
- Studies were performed to evaluate impact of various modeling assumptions.
- Sensitivity to fuel design (in particular enrichment) was examined.
- Finally, tritium generation parameters over the FHR plant lifetime were obtained, including the instantaneous tritium production rate, total tritium production

(neglecting subsequent decay), and accumulated tritium production (accounting for the decay).

- These results may be used to inform the design requirements for the tritium management system.

Details of this work and results are presented in the following sections.

3.2.2. Previous work

Fluoride-salt-cooled High-temperature Reactor (FHR) designs [1][2][3] use FLiBe salt as a coolant, and thus generate significant amount of tritium, which becomes an operational challenge. Previous studies have shown that simplified models may significantly underestimate tritium production. Therefore, detailed and accurate models have been developed under this task.

3.2.3. Pathways of Tritium Production

The primary pathway of tritium production is in the FLiBe coolant and specifically through trace amounts of ^{6}Li, which has a very large cross section for absorbing thermal neutrons (*Figure 3-1*) resulting in the reaction shown in Equation (1).

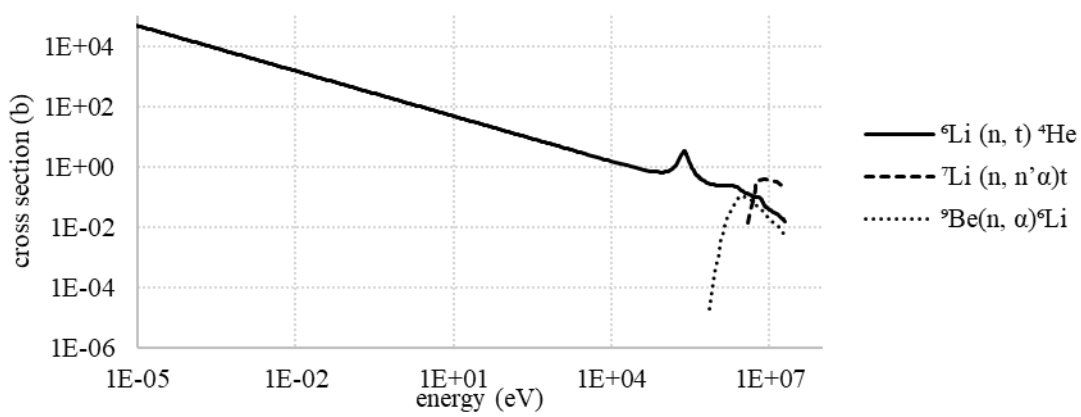

Figure 3-1. Microscopic cross sections for important tritium-producing reactions in FLiBe as extracted from the ENDF/B-VII.1 library provided in SCALE6.2 [8][9].

Reaction	*Effective XS*	*Eq.*
${}^{6}_{3}Li + {}^{1}_{0}n \rightarrow {}^{4}_{2}He + {}^{3}_{1}H$	σ=1.69E+02 (b)	(1)
${}^{7}_{3}Li + {}^{1}_{0}n \rightarrow {}^{4}_{2}He + {}^{1}_{0}n + {}^{3}_{1}H$	σ=2.52E-03 (b)	(2)
${}^{9}_{4}Be + {}^{1}_{0}n \rightarrow {}^{7}_{3}Li + {}^{3}_{1}H$	σ=1.28E-07 (b)	(3)
${}^{19}_{9}F + {}^{1}_{0}n \rightarrow {}^{17}_{8}O + {}^{3}_{1}H$	σ=4.73E-07 (b)	(4)
${}^{9}_{4}Be + {}^{1}_{0}n \rightarrow {}^{4}_{2}He + {}^{6}_{2}He$ ${}^{6}_{2}He \xrightarrow{t_{1/2}=0.81s} {}^{6}_{3}Li + e^{+} + \nu$	σ=1.89E-03 (b)	(5)

${}^{7}_{3}Li + {}^{1}_{0}n \rightarrow {}^{6}_{3}Li + 2{}^{1}_{0}n$	σ=1.11E-06 (b)	(6)

Also shown in Equations (1)-(6) are the microscopic cross-sections for important reactions in FLiBe leading to tritium production as calculated by MCNP6.1. The chemical composition of FLiBe is 2LiF-BeF_2 and average operating conditions will be at a density of 1.9506 g/cm^3 at 950K. Natural lithium is roughly 7 wt% ^{6}Li (a strong neutron absorber) and 93 wt% ^{7}Li (a weak neutron absorber). From a neutronics perspective, it is necessary to minimize ^{6}Li levels to lessen its reactivity penalty. For this reason, the lithium used in the primary salt is proposed to be enriched to 99.995 wt% ^{7}Li. While there are challenges to achieve this enrichment level in large quantities at acceptable costs, it is believed that acceptable solutions exist or will be developed [4]. Enriching the lithium in primary salt also lessens the initial tritium production rates. Other direct pathways to produce tritium from the remaining isotopes in the FLiBe are fast threshold reactions with lower cross sections and are shown in Equations (2)-(4). Additionally, ^{6}Li is continuously produced and destroyed through other isotopes as shown in Equations (5) and (6). Asymptotically (over time), an equilibrium ratio of lithium isotopes will be established. Initial ^{6}Li isotope burns away flowing through the core and in doing so produces tritium in the FLiBe coolant as shown in *Figure 3-2*. Since ^{9}Be transmutes to ^{6}Li through neutron capture, an equilibrium concentration of ^{6}Li will be reached even if starting with a completely pure ^{7}Li FLiBe [5].

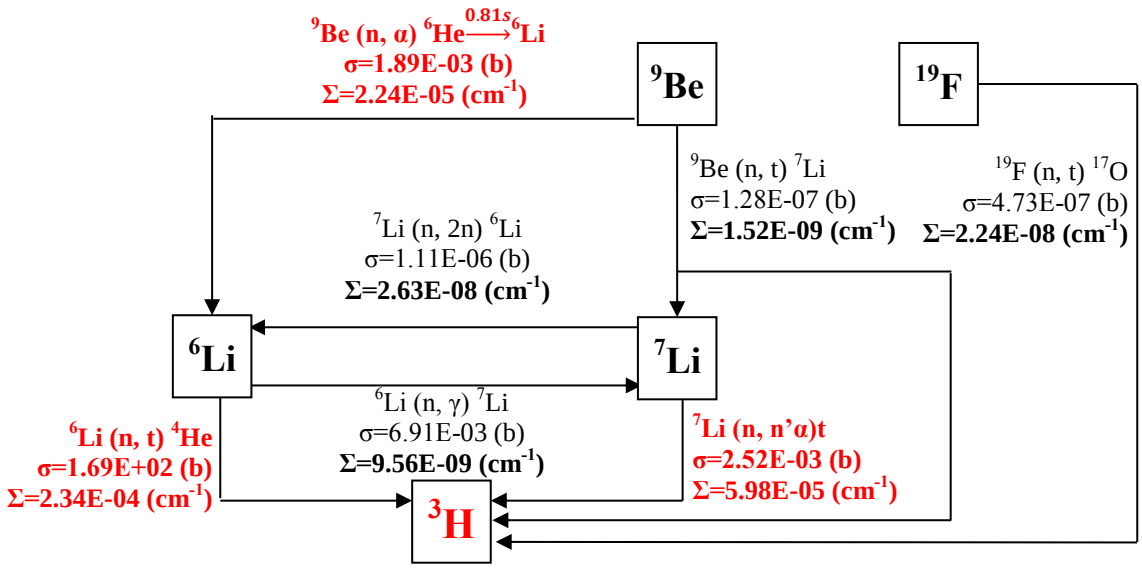

Figure 3-2. Pathways of tritium production in FLiBe with effective 1-group cross sections generated by the reference case FHR.

Tritium production in the fuel is assumed to only occur from ternary fission which is a function of the reactor thermal power and assumed to be produced at a rate of 1(10^{-4}) tritons/fission [6] with the overall production rate shown in Equation 7.

$$3400MWt \cdot \frac{\frac{MJ}{s}}{MW} \cdot \frac{MeV}{1.6021(10^{-19})MJ} \cdot \frac{fission}{200MeV} \cdot \frac{1.00(10^{-4})\ {}^{3}H}{fission} = 1.06(10^{16})\frac{{}^{3}H}{s}. \quad (7)$$

The production rates in graphite are assumed to be from lithium and boron impurities. Boron impurities were assumed to be at the threshold for ASTM nuclear-grade graphite [7] at a level 2ppm. However, lithium impurities are not specified in the standard. Previous work assumed 0.007 ppm in graphite which is also used in this study.

3.2.4. Reference FHR Model

Previous work has shown that simplifying neutronics models into fewer spatial dimensions and coarser neutron spectra can lead to underestimates of production rates [10]. Therefore, detailed models have been developed and accurate simulations used in this study. The reference FHR model being used was developed from the Advanced High Temperature Reactor (AHTR) concept designed at ORNL [1] with the overall design parameters summarized in *Table 3-1*. Tristructural-Isotropic (TRISO) particles enriched to 9% ^{235}U are embedded in graphite matrix forming thin fuel stripes in fuel plates. Eighteen fuel plates are placed into each fuel assembly delineated with a hexagonal graphite (or CC) box as shown in *Figure 3-3*, which also shows (in blue) the FLiBe coolant channels. The core consists of 252 fuel assemblies which are surrounded by replaceable reflector element and permanent reflector. The FLiBe salt coolant is heated from an inlet temperature of 650°C to an outlet average temperature of 700°C. The reactor vessel is only slightly pressurized since the primary loop operates at near-atmospheric pressure.

Table 3-1. Design parameters for the AHTR concept from ORNL.

Parameter	**Value**
Thermal Power	3400MW
Thermal Efficiency	45%
Fuel Type	Uranium (UCO)
Uranium Enrichment	9% U-235
Fuel Form	TRISO particles
# of Assemblies	252
Moderator / Reflector	Graphite
Primary Coolant	FLiBe Salt ($2LiF\text{-}BeF_2$)
Lithium Enrichment	99.995% ^{7}Li
Inlet Temperature	650 °C
Outlet Temperature	700 °C

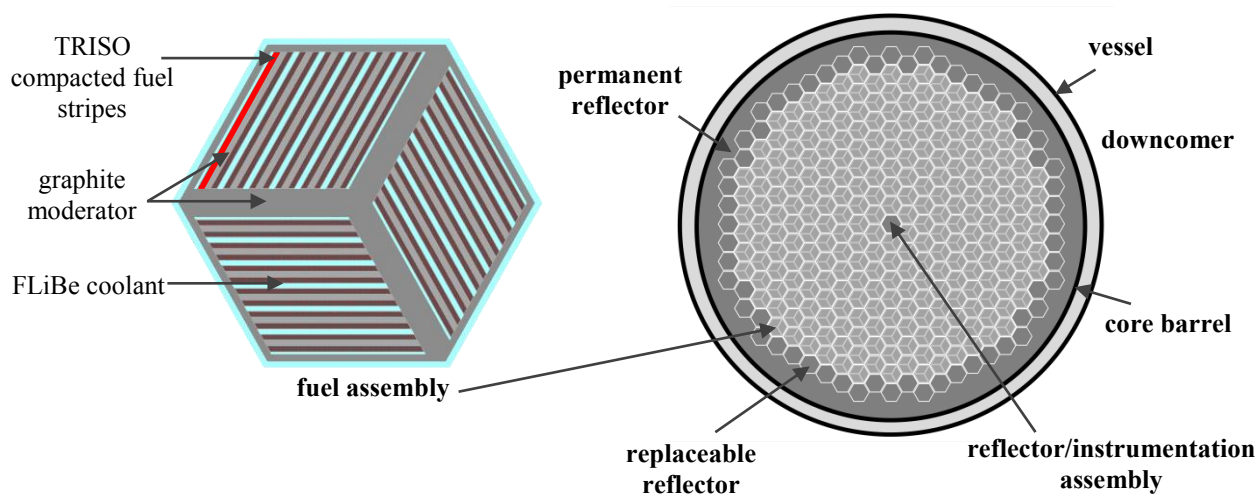

Figure 3-3. AHTR preconceptual design fuel assembly and radial core layout taken from the ORNL preconceptual design [1].

3.2.5. Methodology

For this study, it was decided to investigate tritium production rates over a 100-year lifetime, to cover all possible cases. Additionally, we have examined the impacts of modelling decisions and varying design parameters against a reference core design. Ideally, for these calculations full-core time-dependent continuous-energy calculations would be performed over the lifetime of the reactor, which is computationally unattainable. Instead, comparable accuracy could be achieved if effective, accurate, problem-dependent reaction cross sections are used in the depletion/activation sequence, as illustrated in *Figure 3-4*.

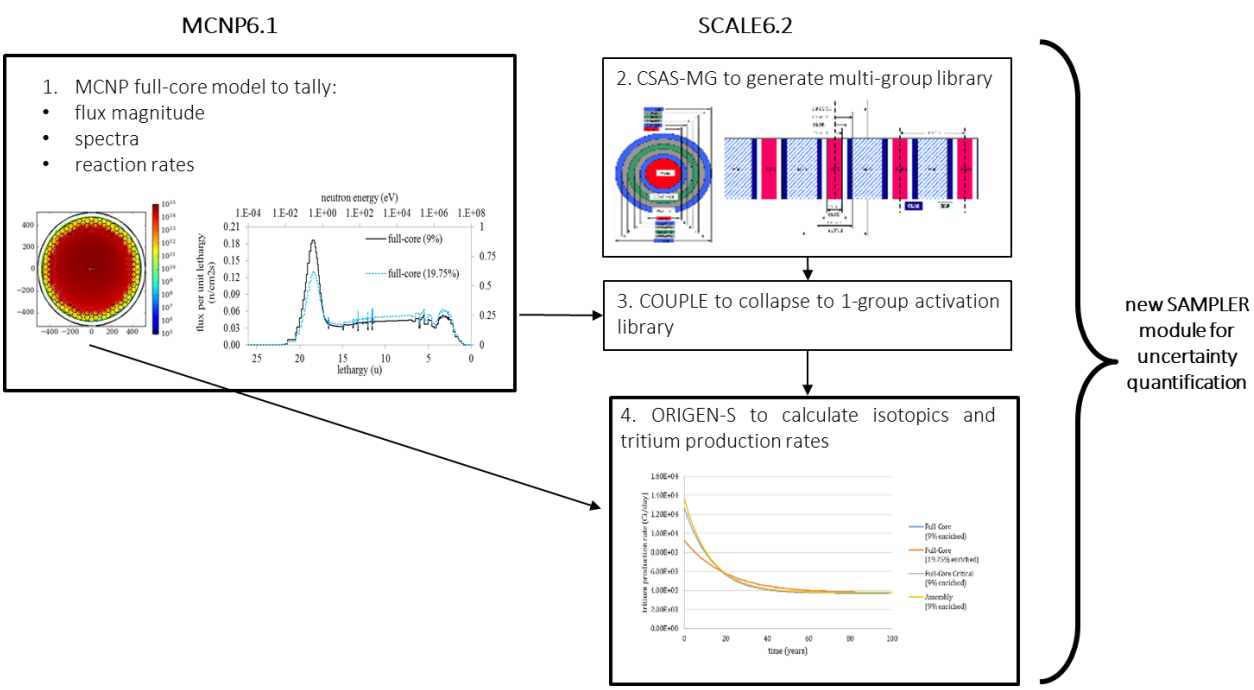

Figure 3-4. Schematic of the methodology.

The dev eloped 4-step methodology starts with MCNP 3D models and simulations to generate region-dependent neutron flux spectra and magnitude. These spectra are used to generate effective reaction/transition cross sections, which are then used in ORIGEN-S to calculate isotopics and tritium production over the reactor lifetime. Details are provided in the following sub-sections.

3.2.5.1. MCNP6.1

The first step necessary to obtain accurate lifetime tritium production rates throughout FHR is to obtain flux magnitudes and spectra in all important regions of the problem space. The MCNP6.1 3D simulations are used for that purpose. The model being used is derived from the input file generated by Stefano Terlizzi, which has been updated and extended with tallies specific to this study [13]. For these calculations, the ENDF/B-VII.0 library is used for all cross sections. It is understood that FLiBe will be the largest producer, however the graphite reflector and fuel plates will also produce a significant amount which is mainly retained locally, and needs to be considered. Since FLiBe coolant flows through the core, the MCNP6.1 tallies for tritium generation in the FLiBe must be modified to consider the total mass of FLiBe inventory within the entire primary loop.

A separate tally is used for each of the 3 main materials producing tritium in the model (FLiBe, graphite/carbon and fuel). Each tally is then subdivided into regions of the model by the lower plenum, bottom reflector, active core region, top reflector, upper plenum, radial reflector and downcomer region as shown in *Figure 3-5*. Furthermore, each tally is binned into a multi-group spectrum to match the SCALE6.2 252-group energy library structure which is eventually used to generate 1-group activation libraries. Also, the important reaction rates in FLiBe are tallied by MCNP6.1 which will be used later in the methodology to improve estimates of tritium generation rates. Each case was ran on a parallel cluster with 32CPUs for 20 inactive cycles and 50 active cycles with 100,000 particles per cycle taking roughly 4.5 hours. Additionally, a starting converged source term from previous simulations was used by inputting “srctp” files. Since most tallies were taken over large regions of the problem space this was considered sufficient to attain acceptably converged results for this study.

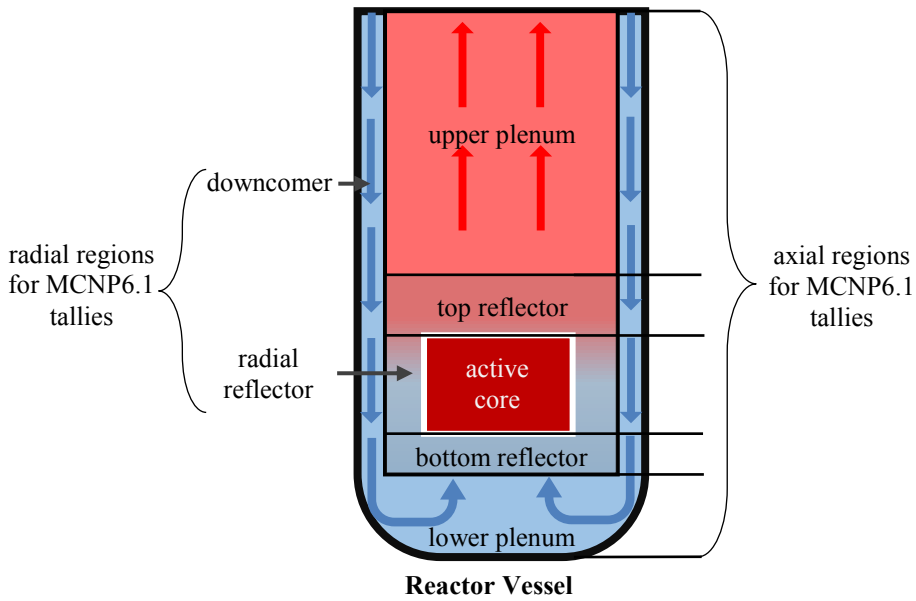

Figure 3-5. The subdivision of tallies for the full-core model used in MCNP6.1.

3.2.5.2. SCALE6.2: CSAS-MG

Next, the CSAS-MG sequence of SCALE6.2 code package is used to generate a 252-group library (ENDF/B-VII.1) that can be collapsed into a 1-group activation library. It is important to note that these cross-sections are not self-shielded which leads to a loss in accuracy from the continuous-energy MCNP6.1 calculations. Unfortunately, due to the complex geometry of the FHR fuel assembly combined with issues of double-heterogeneity there is no simple way to obtain a correctly self-shielded library. The impact of these inaccuracies will be shown later in this study. Future studies may seek to use tools available within the SCALE6.2 code package to generate more accurate multi-group libraries that are self-shielded through a more accurate representation of the FHR model.

3.2.5.3. SCALE6.2: COUPLE

Using the multigroup library generated by the CSAS-MG sequence, the COUPLE sequence of the SCALE6.2 code package is invoked to generate a 1-group activation library that is compatible with the ORIGEN-S sequence. Here, the MCNP6.1 tallies for flux spectrum in the different regions are used to collapse the 252-group cross sections into 1-group transition probabilities between isotopes. Additionally, COUPLE adds decay modes and constants from the JEFF-3.0/A library [14]. As mentioned above, the multigroup library from CSAS-MG is generated with no self-shielding. In the results section, the discrepancy due to using the unshielded cross sections will be investigated. Here, it should be noted that during this study large numerical instabilities were found in the transition probabilities produced by the COUPLE sequence when inputting a user-supplied spectrum. It was determined that the MCNP6.1 tallies should be multiplied by a factor of at least 1(10^6) to avoid erroneous 1-group transition probabilities which may lead to largely erroneous results in ORIGEN-S. The multiplication factor, as long as it is large enough, has no effect on transition probabilities since COUPLE normalizes to a single neutron.

3.2.5.4. SCALE6.2: ORIGEN-S

Finally using the 1-group activation library generated from COUPLE, the time-dependent isotopics of different elements within the FHR model can be calculated over the lifetime of the reactor using the ORIGEN-S sequence. Here, it should be noted that the same 1-group cross sections are used over all time steps for activation results which was an assumption made *in lieu* of full-core time-dependent depletion simulations in MCNP6.1. ORIGEN-S accepts a wide range of inputs and for this work it was chosen to use the isotopics in terms of atomic density (a/b•cm) and neutron flux (n/cm^{2}s). The total neutron flux is taken from MCNP6.1 tallies and scaled to the operating thermal power of the reactor. For the FLiBe calculation the flux is averaged over the total FLiBe volume within the primary loop. From the ORIGEN-S output, time-dependent, tritium-production rates can be calculated using the 1-group reaction rates outputted in either COUPLE or ORIGEN-S.

3.2.6. Results

3.2.6.1. Reference Case (Full-core at 9% enrichment)

Results from the reference case based on the AHTR design are presented first to understand the impact of tritium production rates in different regions of the model, followed by comparisons with different modelling choices and design parameters.

Table 3-2 shows the initial tritium production rates by material in all regions of the model. FLiBe is the dominant pathway responsible for 97.4% of the total tritium produced, but there is still a non-negligible amount produced in the graphite. Specifically, 94.9% of the initial tritium production occurs in FLiBe in the active core region, another 2.5% in FLiBe in other regions, and 2.1% in graphite in the active region. Ternary fission in fuel contributes 0.4%, with less than 0.1% due to other sources. However, the FLiBe production rates will slowly decline as equilibrium concentrations of isotopes, in particular ^{6}Li, are reached over decades of operation. Within the design the tritium in the FLiBe will be continuously removed through control mechanisms, while the tritium in the graphite and fuel will primarily be retained locally and accumulate, and needs to be kept in mind. The production in fuel assemblies from graphite impurities will restart fresh at each core load. Also, since the tritium production in the fuel is driven by fission it is assumed to remain constant over the lifetime of the reactor as a function of the reactor power.

Table 3-2. Initial tritium production rate by axial region throughout an FHR design.

	tritium production (Ci/day)			% contributions by material and overall		
Axial Region	FLiBe	Graphite	Fuel	FLiBe	Graphite	Fuel
Upper Plenum	9.75E+01 ± 1.7%	3.52E+00 ± 2.7%	-	0.9%	0.03%	-
Top Reflector	7.68E+01 ± 0.8%	1.89E+00 ± 1.8%	-	0.7%	0.02%	-
Active Region	1.06E+04 ± 0.03%	2.37E+02 ± 0.0%	4.43E+01 (*)	94.9%	2.1%	0.4%
Bottom	6.81E+01 ±	1.76E+00 ±	-	0.6%	0.02%	-

Reflector	0.8%	2.3%				
Lower Plenum	3.37E+01 ± 1.2%	1.13E+00 ± 4.9%	-	0.3%	0.01%	-
TOTAL	1.09E+04 ± 0.03%	2.45E+02 ± 0.6%	4.43E+01 (*)	97.4%	2.2%	0.4%

*production rate in fuel is calculated by Eq. (7).

3.2.6.2. Deviation of COUPLE Reaction Rates from those generated directly in MCNP Tallies

It is important to understand the errors due to collapsing unshielded multigroup cross sections to generate time-dependent tritium production rates. The multigroup library is collapsed using continuous energy calculations, but there will be some error when compared to the same reaction rates as calculated directly by a continuous energy simulation using MCNP6.1. The total cross sections produced within the COUPLE sequence of SCALE6.2 and the errors compared to those tallied by MCNP6.1 are given in *Table 3-3* for the ^{6}Li (n, t) ^{4}He reaction and in *Table 3-4* for the ^{9}Be (n, α) ^{6}He reaction. Also shown in the tables are the MCNP6.1 tallies presented in broad energy groups to help understand the impact of different parts of the energy spectrum where the groups are defined as follows: fast (E > 0.1MeV), epithermal (3eV < E < 0.1MeV) thermal (E < 3eV). Again, the SCALE6.2 transition probabilities are generated by collapsing unshielded 252-group libraries using spectrum tallies generated in MCNP6.1. As can be seen in *Table 3-3*, the primary tritium production reaction in ^{6}Li is affected by at most 2% using the unshielded approximation.

However, the (n, α) reaction in ^{9}Be, leading to ^{6}Li and eventually tritium, shown in *Table 3-4*, which determines the final equilibrium tritium production rates, is affected by as much as 13%. Well converged results in the core that contribute the most to the tritium production rates have an error of 12%. Uncertainties for the fast flux are notably higher in the upper and lower plenums, leading to uncertainties in the 1-group cross sections in the 6-8% range; however, the differences to SCALE6.2 obtained unshielded cross sections are within that uncertainty.

Future work may more thoroughly investigate the impact on final results. Alternatively, the COUPLE sequence allows for specific reaction rates to be overridden by the MCNP6.1 tallies which would help improve estimates of tritium production. However, overriding only single reactions for a specific isotope may be inaccurate by causing mass conservation imbalances in the rate equations without calculating all important reaction rates for that isotope.

Table 3-3. Contributions to reaction rates from different broad energy groups to the ^{6}Li (n, t) ^{4}He reaction and discrepancies between effective 1-group microscopic cross sections calculated in SCALE6.2 and MCNP6.1.

	MCNP6.1				SCALE6.2	
	fast (E > 0.1MeV)	epithermal (3eV<E<0.1MeV)	thermal (E < 3eV)	**σ (b)**	**σ (b)**	**difference**

Upper Plenum	0.001% ± 2.50%	0.57% ± 0.67%	99.42% ± 0.35%	**3.96E+02 ± 2.62%**	**4.02E+02**	**2%**
Top Reflector	0.01% ± 0.74%	1.50% ± 0.36%	98.49% ± 0.27%	**2.97E+02 ± 0.86%**	**3.01E+02**	**1%**
Active Region	0.06% ± 0.03%	4.02% ± 0.02%	95.92% ± 0.02%	**1.59E+02 ± 0.04%**	**1.61E+02**	**1%**
Bottom Reflector	0.01% ± 0.79%	1.43% ± 0.39%	98.55% ± 0.29%	**3.03E+02 ± 0.92%**	**3.07E+02**	**2%**
Lower Plenum	0.001% ± 3.12%	0.29% ± 1.12%	99.71% ± 0.56%	**4.31E+02 ± 3.36%**	**4.38E+02**	**2%**
Flux-Averaged	0.06% ± 0.03%	3.87% ± 0.02%	96.07% ± 0.02%	**1.64E+02 ± 0.04%**	**1.66E+02**	**1%**

Table 3-4. Contributions to reaction rates from different broad energy groups to the ^{9}Be (n, α) $^{6}He \rightarrow ^{6}Li$ reaction and discrepancies between effective 1-group microscopic cross sections calculated in SCALE6.2 and MCNP6.1.

	MCNP6.1				SCALE6.2	
	fast (E > 0.1MeV)	epithermal (3eV<E<0.1MeV)	thermal (E < 3eV)	**σ (b)**	**σ (b)**	**difference**
Upper Plenum	100%	-	-	**6.13E-05 ± 5.96%**	**5.81E-05**	**5%**
Top Reflector	100%	-	-	**6.31E-04 ± 1.56%**	**5.62E-04**	**11%**
Active Region	100%	-	-	**2.23E-03 ± 0.06%**	**1.95E-03**	**12%**
Bottom Reflector	100%	-	-	**6.22E-04 ± 1.65%**	**5.44E-04**	**13%**
Lower Plenum	100%	-	-	**3.08E-05 ± 7.50%**	**2.97E-05**	**4%**
Flux-Averaged	100%	-	-	**2.19E-03 ± 0.06%**	**1.92E-03**	**12%**

*this is a fast threshold reaction, so there is no contribution in the thermal or epithermal ranges.

3.2.6.3. Impacts from Modeling and Design Parameters

Three additional cases were simulated to investigate impacts of modelling approach (full core or assembly; use of the critical or as calculated spectrum) and varying design parameters (enrichment) on tritium production rates. The results are shown in Figure 3-6(comparison of spectra) and in *Figure 3-7*(tritium production rates over the lifetime). First, the enrichment of the fuel was changed to 19.75% to demonstrate the impact to tritium production results when using a higher enriched model of a super-critical system without using any control mechanisms. A comparison of the flux spectrum against the reference case is shown in Figure 3-6(a). With the higher enrichment, less thermalization

occurs in the core since neutrons are more likely to be absorbed in fuel while slowing down, so the spectrum is harder. Furthermore, this leads to lower production rates at the beginning of the reactor lifetime as shown in *Figure 3-7*. Despite much lower initial production rates, the tritium production at FLiBe equilibrium is roughly the same. However, over the lifetime of the reactor due to much lower initial production rates, the higher enriched core leads to a total of 14.5 MCi of accumulated tritium versus 21.5 MCi in the reference case or 32.4% less. Note, the use of "accumulated" refers to the fact that the decay of tritium ($t_{1/2}$ = 12.32 yr) is taken into account for the final amount so this is not the total integrated production.

Next, the spectrum of the full-core reference case is compared in Figure 3-6(b) against a reflected assembly-level calculation using the same core design parameters. The spectrum in the FLiBe coolant is only slightly affected, but the overall flux magnitude leads to an underestimate of the initial production rate by 0.5%. The production rates at FLiBe equilibrium converge to roughly the same rate and the overall 100-year accumulated tritium is 1% higher at 21.7 MCi versus 21.5 MCi for the reference case.

Lastly, a simulation was performed forcing the spectrum in MCNP6.1 to reach a k-eff of ~1.0 versus the reference case that has a k-eff of 1.07. The critical spectrum was approximated through iterations by adding boron to the coolant, whereas control rods would be used in operation to absorb thermal neutrons. Figure 3-6(c) shows a comparison of the flux spectra. Similar to the assembly-level calculation, the critical spectrum is close to that of the uncontrolled core, which is not surprising since the k-eff only changes by 0.07. However, applying the critical spectrum does have a larger impact on the overall initial production rate lowering it to 12,705 Ci/day versus 13,679 Ci/day for the reference case (a difference of 7.9%). Overall lifetime accumulated tritium increased by 1.5% from 21.7 MCi to 21.8 MCi.

While the equilibrium values reached after 60 or 70 years are very similar for all cases, it may be more relevant to consider the first 40 years where the difference in fuel design (in particular enrichment in ^{235}U) and FLiBe (^{7}Li enrichment) lead to significant difference in tritium production.

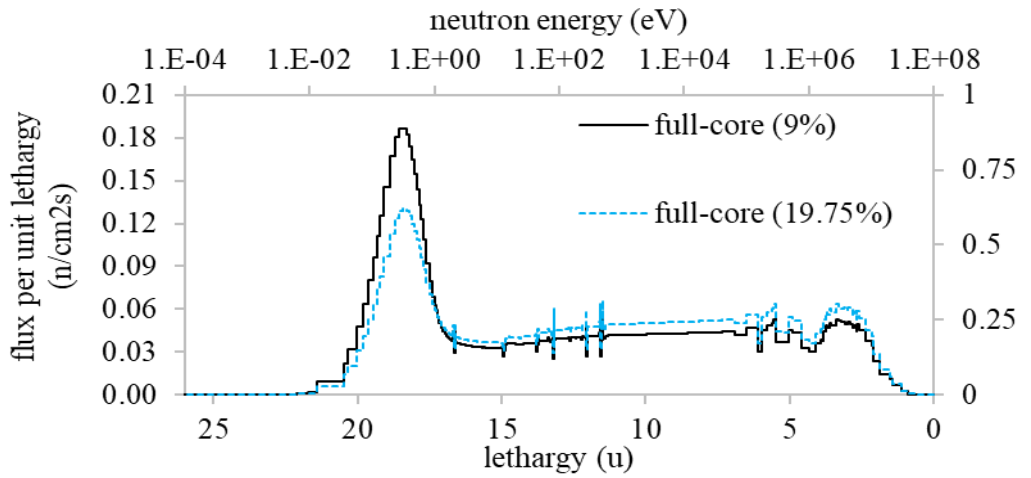

(a) Varying enrichment (9% vs 19.75%)

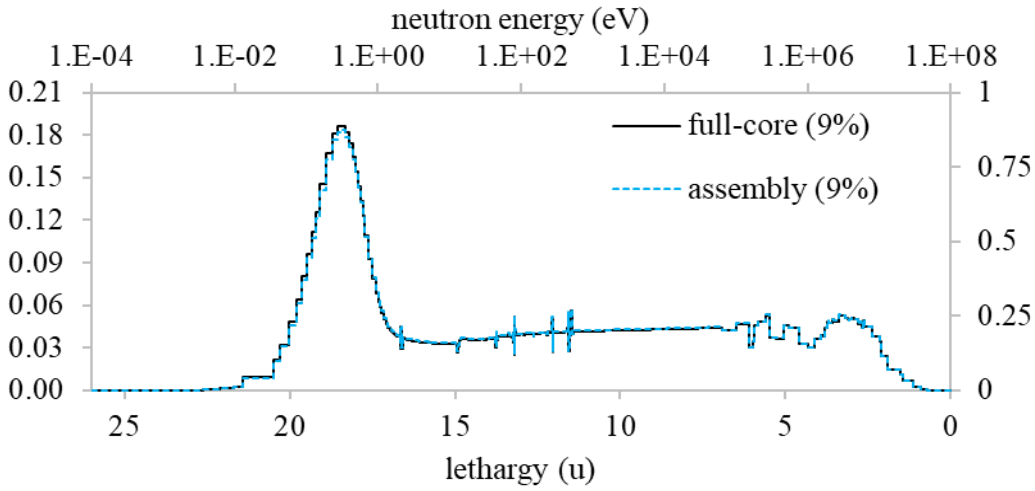

(b) Full-Core vs. Assembly-Level

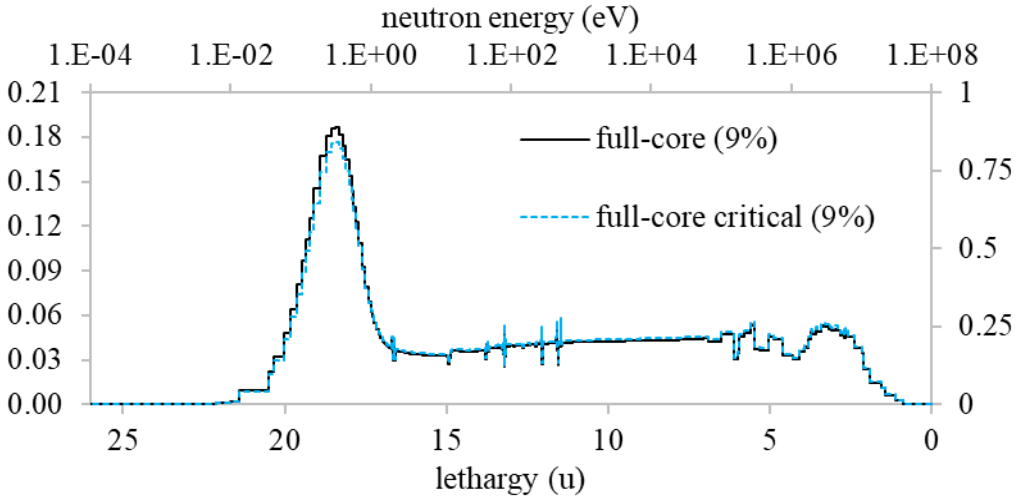

(c) Using a Critical Spectrum

Figure 3-6. Comparisons of the flux spectrum tallied in FLiBE by MCNP6.1 for each case as compared against the reference core design.

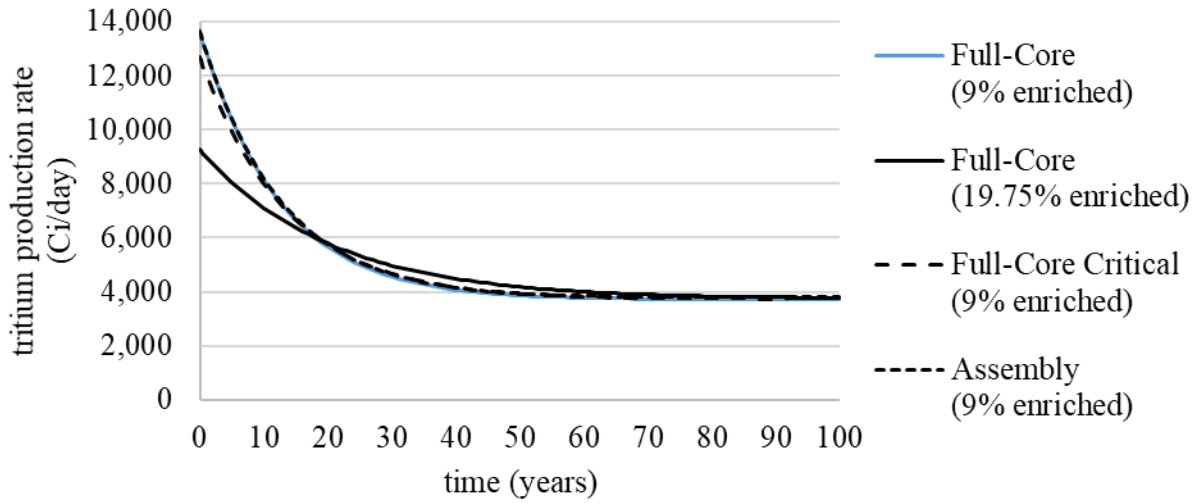

Figure 3-7. Tritium production rates for each case over a 100-year operating lifetime of the reactor.

3.2.6.4. Impact of Assumed Fuel Isotopics

We also investigated the impact of assuming all fresh fuel or accounting for the fact that some fuel will be partially depleted and have different isotopics, within full-core MCNP simulations, to obtain spectra needed for tritium production. The isotopics was generated from a 2D assembly-level SERPENT model being developed within the Task 3.7.1 for neutronics V&V. The baseline AHTR design assumes a two-batch shuffling pattern where half the assemblies are replaced during each outage. The average discharge burnup for a fuel assembly is assumed to be 72 MWd/MTU. The 2D assembly-level SERPENT model was depleted to 100 MWd/MTU. Isotopic evolution for the main actinides is shown in *Figure 3-8*.

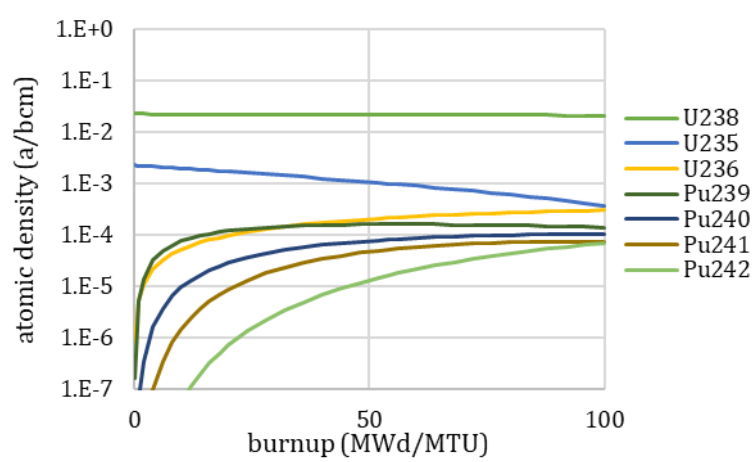

Figure 3-8. Isotopic evolution of important actinides generated from a 2D assembly-level SERPENT model.

In order to study the impact of partly depleted fuel on spectrum, and consequently on tritium production in the FLiBe coolant, 4 separate burnup cases were used with the isotopics for 9% enriched fuel:

1. Fresh fuel at 0 MWd/MTU, representing the first cycle.
2. Beginning-of-Cycle (BOC) burnup of 18 MWd/MTU which represents the average of once-burnt (36 MWd/MTU) and fresh fuel assemblies (0 MWd/MTU).
3. End-of-Cycle (EOC) burnup of 54 MWd/MTU which represents the average of once-burnt (36 MWd/MTU) and twice-burnt fuel assemblies (72 MWd/MTU),
4. Burnup of 72 MWd/MTU assuming each assembly was at the discharge burnup.

For the 4 cases, all isotopes more abundant than Pu-242 are shown in *Table 3.5*. These isotopics were then placed in each assembly across the core to approximate a full-core depleted reactor. Cases 2 and 3 should represent the variability over a representative cycles, while Cases 1 and 4 provide an extended envelope.

Table 3.5. Isotopics for tritium production studies from a 2D assembly-level SERPENT model.

Burnup [MWd/MTU]:	fresh	18 MWd/MTU	54 MWd/MTU	72 MWd/MTU
O16	3.559480E-02	3.559470E-02	3.559460E-02	3.559460E-02
U238	2.246810E-02	2.226010E-02	2.177765E-02	2.150250E-02
U235	2.250540E-03	1.748910E-03	9.990355E-04	7.138850E-04
U236	-	8.906600E-05	2.149980E-04	2.577960E-04
Pu239	-	1.126530E-04	1.605130E-04	1.569270E-04
Mo100	-	2.964260E-05	8.921730E-05	1.189710E-04
Cs137	-	2.901830E-05	8.701375E-05	1.159020E-04
La139	-	2.942650E-05	8.617235E-05	1.137350E-04
Cs133	-	2.773020E-05	8.458545E-05	1.102010E-04
Zr96	-	2.879260E-05	8.281195E-05	1.084460E-04
Zr94	-	2.905090E-05	8.218280E-05	1.068670E-04
Mo98	-	2.691810E-05	8.022630E-05	1.065620E-04
Ce142	-	2.694750E-05	7.886245E-05	1.039860E-04
Tc99	-	2.675550E-05	7.911235E-05	1.030550E-04
Zr93	-	2.798300E-05	7.825025E-05	1.010530E-04
Ru101	-	2.450440E-05	7.395165E-05	9.856100E-05
Pu240	-	2.440030E-05	8.136485E-05	9.571700E-05
Ru102	-	2.118420E-05	6.821125E-05	9.368890E-05
Pr141	-	1.510600E-05	6.486440E-05	8.951770E-05
Mo97	-	2.034280E-05	5.989400E-05	7.896590E-05
Nd143	-	1.972090E-05	5.902285E-05	7.238100E-05
Zr91	-	1.005470E-05	4.979090E-05	6.969740E-05
Mo95	-	4.757270E-06	4.396285E-05	6.807760E-05
Pu241	-	6.779300E-06	5.179510E-05	6.738370E-05
Nd145	-	1.745590E-05	4.833010E-05	6.185740E-05
Ru104	-	1.113370E-05	4.230450E-05	6.115420E-05
Ce144	-	2.207800E-05	5.063470E-05	5.968860E-05
Nd146	-	1.403220E-05	4.312910E-05	5.859550E-05
Nd144	-	3.819320E-06	3.247090E-05	5.580260E-05
Rh103	-	7.604290E-06	3.570790E-05	4.870100E-05
Xe131	-	1.155120E-05	3.492395E-05	4.431590E-05
Pu242	-	4.949810E-07	1.619925E-05	3.379210E-05

3.2.6.5. MCNP6.1: full-core tallies

For each case, a separate full-core MCNP6 model was simulated with 50 skipped cycles, 100 active cycles, and 1(10^6) particles per cycle. This may not provide sufficient particles or cycles to generate a tightly converged fission source for full-core detailed simulations, but since the primary tally is taken over all FLiBe in the reactor to obtain spectrum, it was considered sufficient for the purpose of this sensitivity studies. Each simulation took roughly 4 days on a 32 CPU cluster due to the large number of tallies. In all different regions in FLiBe the neutron spectra and reaction rates important to tritium production were separately tallied by axial and radial region. (Although the results for graphite are not presented here, the same tallying was performed over all graphite regions.) A comparison of the volume-integrated spectra over all FLiBe regions for different burnups is shown in *Figure 3-9*.

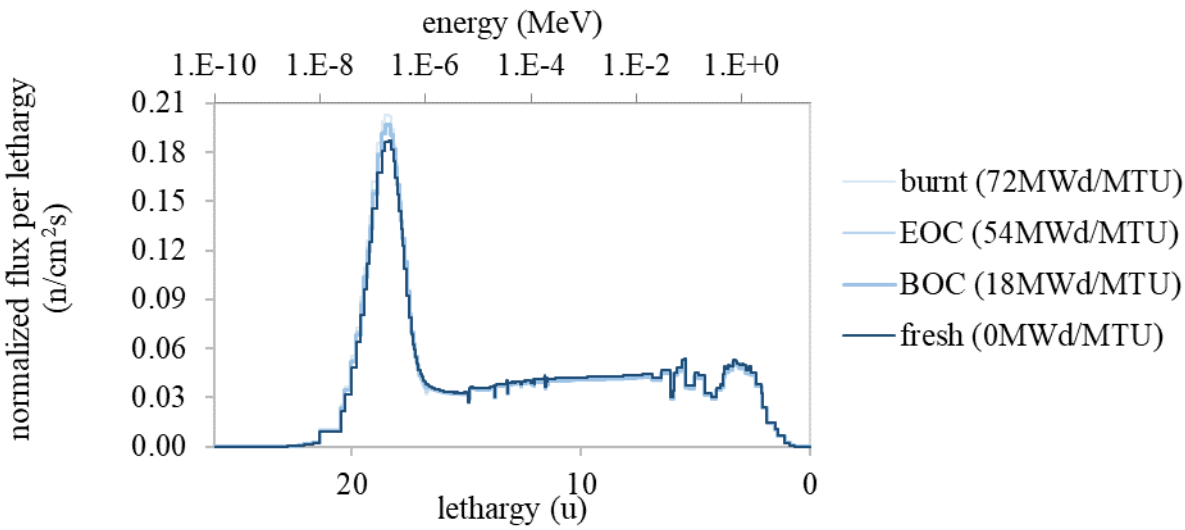

Figure 3-9. Comparison of normalized flux spectra in FLiBe for different burnups.

From *Figure 3-9Figure 3-8*, it can be seen that as the fuel assemblies are burnt through the cycle the spectrum in FLiBe becomes more thermal. With burnt fuel, less neutrons are absorbed by fission and need to be thermalized more by the graphite moderator before inducing fission. However, the production rates are also dependent upon the flux magnitude and the reaction rates. Perhaps it is more useful to look at the spectrum normalized to fission neutrons at 1MeV which helps to highlight the thermal spectrum as shown in *Figure 3-10*.

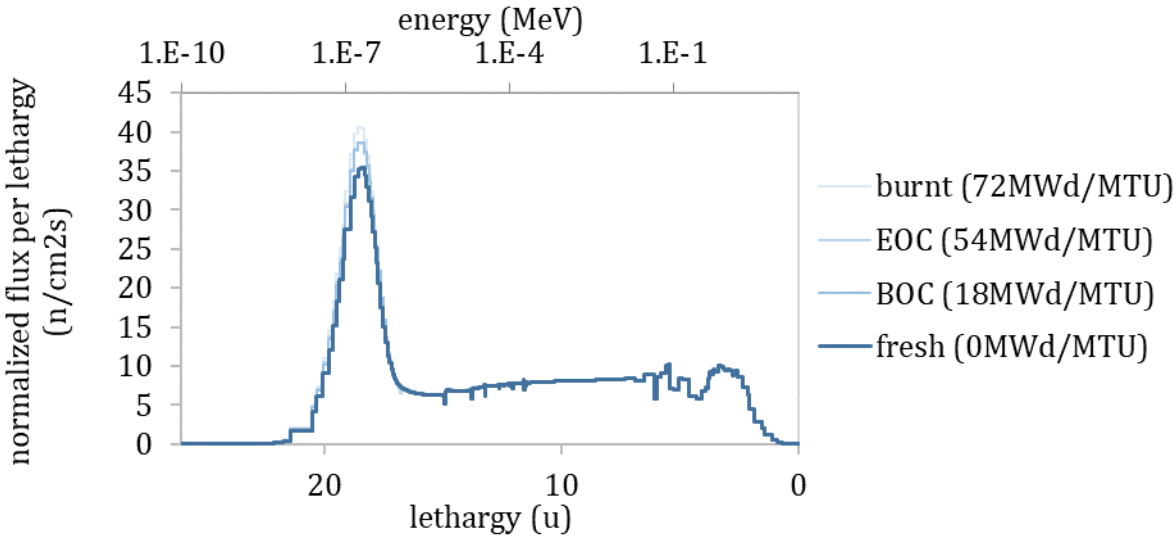

Figure 3-10. Comparison of flux spectra in FLiBe for different burnups normalized to 1MeV neutrons to demonstrate differences in thermalization.

3.2.6.6. SCALE6.2.2: COUPLE 1-group library generation

Tallies taken from MCNP6.1 full-core calculations are used to collapse multigroup cross-section libraries to 1-group activation libraries that contain 1-group transition probabilities. The 1-group libraries are then used in the ORIGEN sequence to calculate isotopics of the FLiBe coolant over the 100-year lifetime of the reactor. From COUPLE, 1-group transition probabilities between isotopes in FLiBe can be extracted for each case. Examining these probabilities helps to understand the impact that using time-dependent spent-fuel isotopics in MCNP6.1 simulations has on changing tritium generation rates. Table 3.6 presents the 1-group transition probabilities generated by COUPLE for pathways important to tritium production in FLiBe. Probability of the most critical reaction of ^{6}Li (n, t) ^{4}He increases with fuel burnup as the spectrum becomes more thermal. The other reactions are fast-threshold reactions which decrease as the spectrum becomes softer with burnup. For the realistic envelope (representative BOC and EOC), the transition probabilities stay within 1%. For the extended envelope, all results are still within +/-5%.

Table 3.6. 1-group transition probablities produced by COUPLE using MCNP6.1 tallies generated from using 4 cases of spent-fuel isotopics.

Case	fresh 0 MWd/MTU	BOC 18 MWd/MTU	EOC 54 MWd/MTU	burnt 72 MWd/MTU
^{6}Li (n, t) ^{4}He	1.67E+2 (ref.)	1.77E+2 (105%)	1.78E+2 (105%)	1.83E+2 (109%)
^{7}Li (n, n'α) t	9.68E-4 (ref.)	9.68E-4 (100%)	1.00E-3 (100%)	9.94E-4 (103%)
^{9}Be (n, α) ^{6}He → ^{6}Li	2.02E-3 (ref.)	1.97E-3 (98%)	1.99E-3 (99%)	1.95E-3 (97%)

* All fresh fuel takes as the reference for convenience, but more realistic reference would be the average of BOC and EOC (corresponding to MOC)

3.2.6.7. SCALE6.2.2: ORIGEN tritium production calculations

Lastly, the 1-group activation libraries generated by COUPLE are used in the ORIGEN sequence to calculate time-dependent isotopics in FLiBe. From the ORIGEN output containing time-dependent isotopics and the COUPLE output containing 1-group transition probabilities, tritium generation rates can be calculated. Tritium production rates for the 4 cases mentioned previously are shown in *Figure 3-11*.

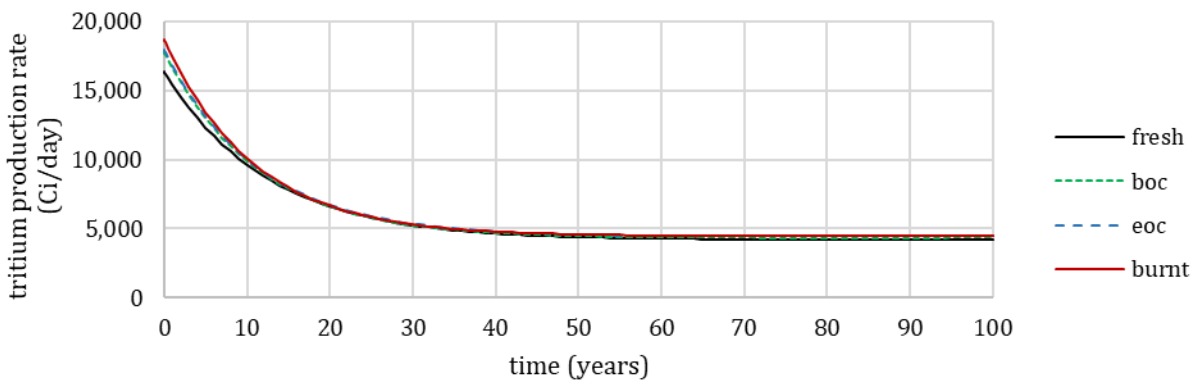

Figure 3-11. Tritium production rates calcluated in SCALE from full-core MCNP tallies using diferent burnt fuel isotopics.

With higher burnup fuel, tritium production rates increase following the trend of the ^{6}Li (n, t) ^{4}He reaction rate. Additionally, the total flux in the FLiBe increases with burnup leading to the increase. Initial generation rates using the most-burnt fuel show an increase in initial generation rates of 14.5% and equilibrium generation rates show an increase of 6.4% when compared to fresh fuel. However, both of these bounding cases are unrealistic since in normal operation there would be a mix of burnups. The 2 cases representing BOC and EOC should provide more realistic estimates for enveloping tritium production rates. For these 2 cases, the initial generation rates only differ by less than 0.9% and equilibrium generation rates differ by 2.4%.Thus, the tritium generation model can use steady-state full-core calculations to extrapolate to lifetime production rates with small error, but average burnup should be used to conservatively estimate production rates.

3.2.7. Time-Evolution of Tritium Production Parameters

Finally, it is important to understand that there are several parameters that may (and should) be used in the tritium production metrics, each serving a different purpose.

(a) Instantaneous tritium production rate. It is relevant to understand the actual time-dependent tritium production rate and when considering the required tritium

removal rate capability from FLiBe, if the management strategy is to quickly remove most of the produced tritium.

(b) Total produced tritium. This is the integral of the previous parameter. It shows how much tritium we would have to process overall, essentially all released tritium without decay, e.g., if we are quickly removing the produced tritium and capturing it in some getter material.

(c) Accumulated tritium, with decay. This represents the amount if all produced tritium is kept in a storage (or in a getter material) to decay.

Illustrative corresponding results are shown in *Figure 3-12*.

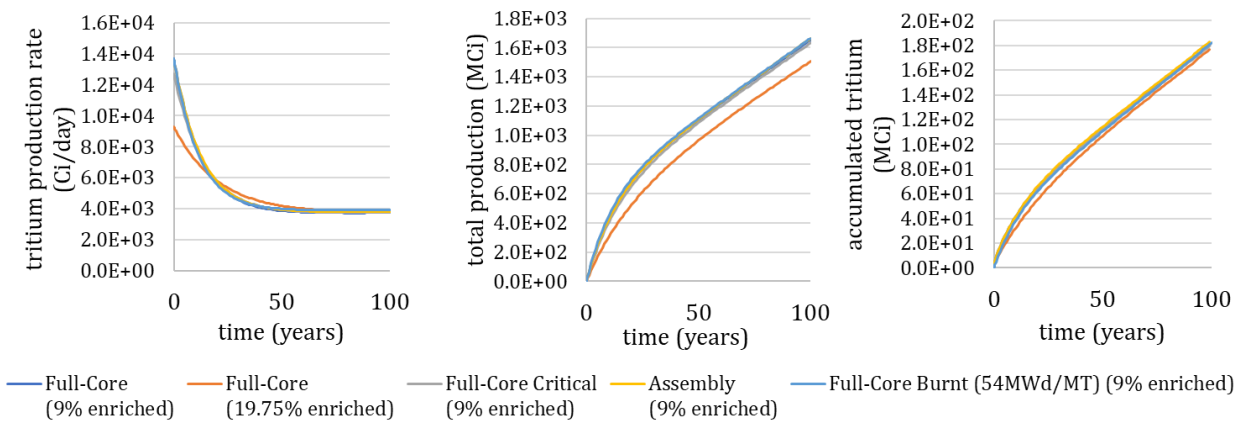

Figure 3-12. Time-Evolution of Tritium Production Parameters: Instantaneous tritium production rate (left), total produced tritium (center), and accumulated tritium (right).

3.3. Conclusions

FHR designs inherently produce orders of magnitude more tritium due to the use of FLiBe coolant. A methodology for calculating tritium production rates over the lifetime of a reference AHTR design was developed and implemented. First, a detailed full-core MCNP6.1 calculation is used to generate flux magnitudes and spectra within critical materials (FLiBe, graphite, and fuel) and regions (lower plenum, bottom reflector, active core, top reflector, upper plenum, radial reflector and downcomer). The methodology requires attention to detail when processing output from MCNP6.1 tallies into the COUPLE and ORIGEN-S sequences of the SCALE6.2 code package for time-dependent generation rates. Additionally, it is important to consider the total FLiBe inventory since this drives the equilibrium production rates over the lifetime of the reactor.

Additional analysis was performed to assess impact of a higher fuel enrichment (19.75% vs 9%) which demonstrated a lower initial production rate that eventually converges to a similar rate at equilibrium. Modelling decisions were evaluated to examine the impact of using assembly-level vs full-core calculation, the impact of using a critical spectrum on tritium production rates, and the impact of accounting for depleted fuel isotopics. For the

reference case, 21.5 MCi of accumulated tritium remain at the end of the 100-year lifetime. Initial production rates are the highest due to ^{6}Li in FLiBe at a rate of 13,700 Ci/day. Equilibrium production rates for all cases converge to roughly 3,700 Ci/day.

3.4. References

[1] Varma, V. K., Holcomb, D. E., Peretz, F. J., Bradley, E. C., Ilas, D. Q., Zaharia, N. M., "AHTR Mechanical, Structural, and Neutronic Preconceptual Design," *ORNL/TM-2012/320,* Oak Ridge, TN, Oak Ridge National Laboratory, 2012

[2] Forsberg, C., Peterson, P. F., Pickard, P. S., "Molten-Salt-Cooled Advanced High-Temperature Reactor for Production of Hydrogen and Electricity." Nuclear Technology 144(3), pp. 289–302 (2003).

[3] Xu H., "Thorium Energy and Molten Salt Reactor R&D in China," In: Revol JP., Bourquin M., Kadi Y., Lillestol E., de Mestral JC., Samec K. (eds) Thorium Energy for the World. Springer, Cham. (2016).

[4] David E. Holcomb, George F. Flanagan, Gary T. Mays, W. David Pointer, Kevin R. Robb, Graydon L. Yoder, Jr., "Fluoride Salt-Cooled High-Temperature Reactor Technology Development and Demonstration Roadmap, Report ORNL/TM-2013/401, September 2013.

[5] Jacobs, D.G., "Sources of Tritium and its Behavior upon Release to the Environment", ORNL/NSIC-37, 1968

[6] Albenesius, E.L., "Tritium as a Product of Fission," Physics Review Letter, Vol. 3, 1959, pp. 274–275

[7] ASTM D7301-11: Standard Specification for Nuclear Graphite Suitable for Components Subjected to Low Neutron Irradiation Dose, ASTM International, West Conshohocken, PA, 2015, www.astm.org, doi: 10.1520/D7301-11R15

[8] M. B. Chadwick et al., "ENDF/B-VII.1 Nuclear Data for Science and Technology: Cross Sections, Covariances, Fission Product Yields, and Decay Data," Nucl. Data Sheets 112(12), pp. 2887–2996 (2011).

[9] "SCALE 6.2.1: A Comprehensive Modeling and Simulation Suite for Nuclear Safety Analysis and Design; Includes ORIGEN and AMPX," ORNL/TM-2005/39, Version 6.2.1, Oak Ridge National Laboratory, Oak Ridge, Tennessee, 2016

[10] Flaspoehler, T., Petrovic, B., "Assessing Pathways to Tritium Production and its Detailed Spatial Distribution Throughout the VHTR," ISRD15 – International Symposium on Reactor Dosimetry, EPJ Web of Conferences, Vol. 106, 2016, doi:10.1051/epjconf/201610603005

[11] M. J. Bell, "ORIGEN B—The ORNL Isotope Generation and Depletion Code," ORNL-4628 (CCC-217), Union Carbide Corporation (Nuclear Division), Oak Ridge National Laboratory, May 1973.

[12] "MCNP—A General Monte Carlo N-Particle Transport Code," Version 6.1, LA-UR-03-1987, Los Alamos National Laboratory, Los Alamos, N.M., 2013.

[13] Terlizzi, S (personal communication 2017)

[14] Sublet, J-Ch., Koning, A. J., Forrest, R. A., Kopecky, J., "The JEFF-3.0/A Neutron Activation File—EAF-2003 into ENDF-6 Format," Commissariat à l'Énergie Atomique, France, JEFDOC-982, November 2003.

4. Liquid Salt Impurity Removal, Redox and Corrosion Control

4.1. Introduction

Similar to other types of advanced reactors such as the sodium-cooled fast reactor (SFR) [1], the impurities in the primary coolant LiF-BeF_2 of FHR can be categorized into five groups: corrosion products from structural materials, fission products and actinides from leakage of the fuels; nuclear reaction products including transmutation products and element decay products; impurities from operation environments such as water and oxygen by ingression of air; and the impurities of the coolant itself such as HF.

4.1.1. Tritium

<u>*Sources and transport:*</u> Tritium is directly generated by neutron reaction with Li and Be in the primary coolant, mainly from the reaction of ^{6}Li [2]. Tritium will either exist in the salt as tritium fluoride (TF), a dissolved ion (T^+), or as tritium gas (HT or T_2). However, the tritium gas has a very low solubility in the salt, and the equilibrium partial pressure of tritium gas over FLiBe with 1ppm T_2 is 10^5 Pa [3]. During transportation in the primary loop, the generated tritium can be trapped by the carbonaceous materials in the primary loop, escape through the primary coolant surface into the cover gas, permeate through the reactor vessel or piping, or permeate through the heat exchanger tubing.

<u>*Impact:*</u> Tritium is the one of the major radioactive source terms. In addition, when it exists in the form of TF or tritium ions, it will influence the redox potential of the salt, therefore, it will affect material corrosion[4]. Furthermore, tritium may diffusion into structural materials, which can lead to hydrogen-induced embrittlement [5].

<u>*Available removal method:*</u> Several stripping technologies have been developed to removal tririum from the primary salts. These technologies include helium-hydrogen sparging [6], ultrasonic degassing [7], spray-droplet based disengagement [8], and cathodic stripping [9]. The efficiency of all these technologies strongly relies on the mass transfer of tritium in the salt.

Another technology for stripping tritium is using a membrane reactor into an inert sweep gas from which it can be readily extracted and captured [10]. Both palladium and silver are a chemically compatible with FLiBe under the redox conditions and they have very high affinity for disassociating molecular tritium into the atomic state (enabling fast absorption and desorption), absorbs large amounts of tritium while maintaining its physical properties [11] and have high tritium diffusion rates. One of the concerns of using membrane is the mechanical stability of the thin membrane. Mechanical membrane support can be provided by affixing the membrane to a backing plate. Sintered metal porous structures (often 316 stainless steel) are commonly employed to provide membrane backing. However, inter-metallic diffusion between the SS316 substrate and the Pd-Ag alloy at high temperatures is

known to degrade permeation of hydrogen through palladium alloys [12]. For preventing the inter-metallic diffusion between the membrane and support, a sol-gel derived mesoporous yttria stabilized zirconia (YSZ) layer between the support and the palladium membrane can be applied to inhibit intermetallic diffusion, thereby preserving the membrane permeance at high temperatures, as well as providing a suitably smooth substrate for subsequent electroless deposition of defect-free palladium alloy membranes [13].

Over the past few decades, double-walled heat exchangers, which are expressly designed to prevent contact between the primary and secondary fluids, have become more common. The large surface area and thin tubing walls combined with the turbulent mixing within the heat exchanger makes tritium escape through the heat exchanger tubes a significant tritium escape mechanism in the primary side. Providing a chemical trap (i.e., a getter such as some rare earth metals which form stable hydride with hydrogen) within the central section of a double-walled heat exchanger appears to be an effective tritium removal mechanism [1].

4.1.2. Noble Gases

Source and transport: Nobel gases are fission products and they are dissolved or entrained as small bubbles in the primary coolant from leakage of failed fuel particles. Krypton and Xenon are the most important fission gases to be considered in the reactor off gas system [14]. Because of the low solubility of Kr and Xe in the primary salt, most of the gases will eventually emerge into the gas plenum above the salt pool, and some of the gas can also diffuse into the structural materials, for example, graphite [15].

The solubility of Xe in primary salt was measured [16] and the data are given in Table 4-1. There is no measured solubility data of Kr in the salt, but it was estimated [17] by a method originally proposed by Blander et al [18], and the data were also given in Table 4-1 as well as the estimated data by the same method for Xe. The comparisons between the measured data and estimated data for Xe indicated the two series of data agree well at 873K and 973K, but the difference becomes large when the temperature is reduced to 773K or increased to 1073K. Therefore, measured solubility data of Kr are needed.

Table 4-1: The measured and calculated solubilities of Xe and Kr in $LiF\text{-}BeF_2$ at different temperatures. The unit of the solubility is 10^{-8} moles/(cm^3-melt atm).

Temperature	Xe (Measured)	Xe (Calculated)	Kr (Calculated)
773	0.233	0.03	0.13
873	0.333	0.17	0.55
973	0.505	0.67	1.7
1073	0.863	2.0	4.4

Impact: Same to other types of nuclear reactor, fission products, Kr and Xe, are radioactive source terms. Another concern of noble gases is precursors of both salt seeking and noble metal elements. The high mobility of noble gas fission products will thus result in widely distributed contamination by daughter products. For example, the migration of Kr and Xe into structural materials leads to accumulation of elements with longer half-lives and stronger neutron poison in structural materials such as graphite. All these elements accumulated in the structural materials are difficult to be removed during operation.

Kr and Xe do not form compounds in molten salt reactor conditions and are only sparingly soluble. However, the graphite moderator used in the MSRE core was found to be permeable to these gases and thus their radioactive daughters must be expected in graphite samples [19]. Deposition of fission products (and daughters) on graphite is undesirable due to the neutron poison nature of the fission products. The formation of rubidium by beta decay of ^{85}Kr might cause several problems including corrosion and changes of primary coolant properties. Rb is a very reactive element and very salt seeking material by formation RbF. On the other hand, Rb metal is very corrosive, which may lead to local structural material corrosion. It is necessary to point out that Rb metal has a low boiling temperature, therefore, Rb may not exist as liquid metal in the primary loop.

Available Removal Method: The primary removal method for both of these elements is spurging with inert gas such as helium or argon in the primary loop, followed by adsorption onto a charcoal filter [20][21]. During the MSRE, a helium purge gas was used to strip these fission gases from the salt and transport them to charcoal traps in the off-gas system. This process allows the reactor to operate at lower fission product concentrations than theoretical calculations [19]. Although the gas purging method has been found to be an effective method, there are some parameters that are still not well known, for example, the salt-to-gas mass transfer kinetics and the dissolved gas diffusion coefficient. In FHR, most of the gases will eventually emerge into the gas plenum above the salt pool. Under normal operations, the upper plenum is cooled with an inert sweep gas [1].

4.1.3. Halogens

Source and transport: Iodine is the major halogen, and it is a fission product coming from the fuel or decay of its precursors, for example, Te. Iodine will form some iodides with other fission products (e.g. CsI) [22] which can dissolve into the primary salt. Therefore, nearly all iodine isotopes remain in the salt in the form of I^- instead of volitalization [23][24]. Isotope ^{131}I and ^{133}I were found in MSRE exit gas which came as a results of volatilization of Te precursors.

Impact: Since element iodine is a vaporized material, it is one of the major radioactive source term concerns for other types of reactor such as sodium-cooled reactor. However, iodine is in the form iodides that can remain in the salt for MSRs, therefore, the salt has a high retention capability of iodine. The iodides in the salt may have some impacts on the salt properties including physical and thermochemical properties. However, such data are very scarce and their impacts on the salt properties are not well understood. The iodide in the salt may also lead to corrosion. However, available experimental results show that the effects of CsI on the salt corrosion of Hastelloy-N are negligible [24].

Available Removal method: The primary method of removal of iodine in the MSBR processing plant was through HF-H_2 sparging followed by accumulation in KOH solution in gas recycle stream. This is the same method used for removal of the other halogen, bromine. In principle, the purification reaction is [23]:

$$I^-_{(d)} + HF_g \rightarrow F^-_d + HI_g \qquad (4\text{-}1)$$

where the subscript d represents the dissolved species and g represents gas species. Except the concern of the reaction of the effluent gases with metal surface in the gas exit lines [23], the experience in the method shows that the method is commercially feasible [25]. However, adding an additional source of hydrogen to the salt would dilute the dissolved tritium, which makes it more difficult to separate tritium.

4.1.4. Alkaline Metals

Source and transport: The main alkaline metals that were found in the molten salt in MSRE are Rb, Sr, Cs and Ba. All of them are fission products or decay products from their precursors. They all are very reactive materials, and can form stable fluorides or iodides. These elements were found to deposit on the surface of MSRE Graphite with a xenon/krypton precursor [23], but appear almost entirely in the molten salt, except for what is lost through volatilization of precursors.

Impact: All the alkaline metals can be radioactive source terms. For sodium-cooled fast reactor (SFR), release of alkaline metals during severe accident is a major concern because of the high vapor pressure of alkaline (especially Cs) in liquid sodium. However, for MSRs, the concern should be much less than SFRs because of the stable fluorides of the alkaline metals in the primary salt. Experimental results on the release of CsI during severe accident indicated that the amount of release for an MSR should be much less than that of an LWR [26]. The stable fluorides and other halides such as CsI and RbI may affect the primary physical, thermodynamic and chemical properties. No data are available on the potential influence. Liquid Cs and Rb are very corrosive to structural materials. Although it is impossible for Cs and Rb existing in their liquid form in the primary salt, their precursors (Kr and Xe) can migrate into the structural materials, therefore, it is possible that Cs and Rb exist in their liquid form in the structural materials and lead to localized corrosion. No such data is available, however, Cs was found in graphite in MSRE [19].

Available removal method: During the MSBR program, the primary removal operation was reductive extraction into Bi-Li alloy followed by accumulation in LiCl (e.g. [20]). Electrochemical separation can also be used to separate Cs from fluoride salt by using a reactive electrode or a liquid metal electrode such as liquid Bi [27]. However, more thermodynamic data of alkaline metal halides (e.g. fluorides, iodides) in the primary salt and of alkaline metals in the liquid electrode are needed.

4.1.5. Rare Earths

Source and transport: Rare earths are major fission products and they enter into salt from leakage of fuel particles. Some of them (for example, La, Ce, Pr, etc) can form stable trivalent fluoride, while others (for example, Eu, Sm) can form both stable trivalent and

divalent fluorides [19]. The rare earth fluorides are very stable, some of them are even more stable than the primary salt, therefore, depositing of rare metals on structural surfaces through displacement reactions is impossible. However, the rare earths may deposit out of the primary salt in form of compounds such as LaOF when oxygen is presented in the primary salt [28].

Impact: Considering the very stable rare earth fluorides, the impacts on the material corrosion and radioactive risk should be very small. However, the stable fluorides may influence the primary salt properties including some very important physical properties such as density and melting temperature. With aging, the accumulation of rare earth fluorides may lead to their compound formation, which may result in blockage of the flow path as well as a local higher temperature due to the decay heat. On the other hand, most of rare earths have a large thermal neutron cross-section and affect the neutronic property of the primary salt.

Available removal method: During the MSBR experiment, the trivalent rare earths were primarily removed in the same process of the reductive extraction into Bi-Li alloy as the divalent rare earths (Sm, Eu) [20]. Over time the liquid bismuth will contain progressively more contamination. In order to minimize the volume of radioactive waste generated, the radionuclides will be transferred from the bismuth to lithium chloride which has a high solubility for nearly all of the fission products as well as the structural material corrosion products. Reduced-scale demonstrations of the reductive extraction process were performed during the 1970s [29]. Mass transfer coefficients for the process were also measured for the MSBR program [30]. Process thermodynamics were also studied both experimentally and theoretically [31][32]. The kinetics of reductive extraction from fluoride salts continued to be studied in Japan until the 1990s [33].

Same to alkaline metals, rare earths can also be removed from molten fluoride by electrochemical separation. This method was not applied in MSRE program, but experimental measurements have demonstrated the method [34]. Another removal method can be a "cold trap". If the primary salt is saturated with a rare earth fluoride, the rare earth fluoride will precipitate out when the primary salt is cooled down slowly. If the primary salt contains two or more rare earth fluorides, the precipitate is a nearly ideal solid solution [23]. Therefore, dissolving an excess amount of another trifluoride before cooling, such as CeF_3 or LaF_3, will promote removal of the rare earth fission products.

4.1.6. Noble Metals and Semi-Noble Metals

Source and transport: Different from MSR for which the noble metal fission products are produced in the primary salt, for FHR, the noble metals are produced in the solid fuel. It is very hard for the noble metal fission products to enter into the primary salt even some fuel particles fail because the noble metal fluorides are much less stable than the primary salt. There are maybe some suspending noble metal particles in the primary salt for FHR, but the concentration should be much lower than that of MSR. Based on MSRE experience, the suspending particles can deposit on structural material surface or are transported by bubbles and accumulate in the cover gas system [35]. If the noble metal in the fuel is in its

oxide form, the oxide may dissolve into the primary salt, however, the concentration of noble metal fission products should be very low.

Impact: Noble metal fluorides in the primary salt can be an oxidizer for structural metals such as Cr, which will result in structural material corrosion. Deposition of noble metal particles on structural material surface may lead to a local higher temperature due to the decay heat. Accumulation of the suspending particle in the cover gas can lead to release to environment during a sever accident.

Available removal methods: For noble metal fluorides, liquid-liquid extraction using Li-Bi liquid metal can be applied. For the metal particles that were suspending in the salt and the cover gas sweep system, filters are needed to trap these particles. Another method to remove noble metal fission products is to deposit them on a metal surface. The MSR program predicted a clearance time of 2.4 hours for noble metal fission products due to attachment to metal surfaces [36]. Some of the noble metal fission products adhered tightly to the metal surfaces and could not be removed with flush salt [37] while others re-suspended as finely divided metal particles [38] for reasons that are not well understood.

The noble metal fluorides in the primary salt have more positive redox potentials than the salt components (LiF and BeF_2), therefore, electrochemical separation can also be applied to remove the noble metal fluorides from the primary salt.

4.1.7. Tellurium and Antimony

Source and transport: Both Te and Sb are fission products, and if there is any Te and Sb in the primary salt of FHR, they should be from the leakage of the failed fuel or decay of their precursors such as ^{132}I. Te and Sb have similar chemical properties, and their fluorides are unstable in the primary salts with respect to their elements. However, Te can exist in the salt in the form of tellurides [39]. On the other hand, Te has a high vapor pressure at the operation temperature of FHR and MSR, and can dissolve into the salt as a dissolved gas [40]. According to MSRE, Te and Sb can heavily deposit on metal surface, which provides a method for separating Te and Sb from the salt. However, the detail behaviors of Te are not well understood [35].

Impact: Both Sb and Te can form stable but brittle compounds with steel components such as Ni, Fe and Cr, therefore lead to structural material degradation, especially, the inter-granular cracking (IGC) of nickel-base alloy by the preferential diffusion of Te along the grain boundary and subsequent formations of the compounds [41]. If the primary salt is kept sufficiently reducing, Te can be in the form of tellurides in the salt, and the Te-induced IGC may be mitigated [42] [43]. Because of the high vapor pressure of Te at the FHR operation temperature, release of Te into the environment is a source term concern, particularly, ^{132}Te is of most importance because it decays to ^{132}I which is a strong gamma emitter.

Available removal methods: Same to other noble metals, Te and Sb elements were separated by plating out on surface in reaction vessel and heat exchangers in MSRE [36]. However, platting Te and Sb on structural material surface will lead to material degradation. If Te and Sb are in the form of tellurides and antimonides in the salt, electrochemical deposition is

expected a method to separate Te and Sb because of their more negative redox potential than that F in the salt. Unfortunately, there is no data on the electrochemical behaviors of Te and Sb in the FHR primary salt.

4.1.8. Actinides

Source and transport: Actinides in the FHR primary salts are from the leakage of the failed fuels. Current experience indicates that metal actinides have very low solubilities in the salt, but actinides can exist in the salt in stable fluorides. Uranium has two stable ions U^{3+} and U^{4+}, while Pu has one stable ion Pu^{3+}. Electrochemical properties such as the apparent potential of U and Pu ions in the primary salt have been studied [44][45].

Impact: The dissolved actinide fluorides will affect the primary salt properties such as the melting point of the salt [32]. The actinide fluorides also affect the redox potential of the salt, and therefore, affect the material corrosion [45]. Actinide fluorides may interact with other fluorides or oxides and lead to formation of some compounds that do not dissolve into the salt.

Available Removal Method: In MSBR, U was first removed by volatilization in the primary fluorinator through converting the dissolved U ions into UF_6 which is gas at the reactor operation condition, and then the remaining U was extracted by contacting liquid Bi-Li [46]. This method can also be applied to removal Pu because PuF_6 is gas also at the condition. Considering that the concentration of actinides in FHR primary salt is much lower than that in the MSBR, direct extraction of actinides using Bi-Li liquid/liquid extraction can be the way to remove them from FHR primary salt. A model recently developed for liquid/liquid extraction has shown the efficiency of the method [47]. Based on the success of actinide separation from molten salt in pyroporcessing, the actinides should be able to be removed by electrochemical separation [48].

4.1.9. Corrosion Products

Source and transport: The FHR primary salt is not corrosive to the Ni-base alloys such as Alloy N, however, the impurities (e.g. HF, Oxygen, some fission products) in the salt can increase the redox potential to a value at which the alloy components (e.g. Cr, Fe, Ni) can dissolve into the salt in their fluorides [4]. Although there are no solubility data of fluorides of Cr, Fe and Ni in the salt, it is believed based on MSR experience that the fluorides are stable in the salt and should have a high solubility. Different from the transport of fission products that are from the leakage of a failed fuels, corrosion products dissolve into the salt at one location (the location is not necessary at the highest temperature) and precipitate out of the salt at other locations (the location is not necessary at the lowest temperature) because of the non-isothermal nature of the primary loop [49]. Corrosion experiments in non-isothermal molten salt loops have identified such phenomenon [50].

Impact: Some corrosion product can be oxidizer of other metals, for example, the corrosion product NiF_2 is the oxidizer of Cr through a reaction:

$$Cr + NiF_{2(d)} \rightarrow CrF_{2(d)} + Ni \qquad (4\text{-}2)$$

and therefore, it leads to Cr corrosion [51]. The precipitation of corrosion products may lead to fouling at the heat exchanger and affect the heat transfer performance of the heat exchanger. On the other hand, continuous corrosion will lead to structural material degradation. When corrosion products pass through the reactor core, some radioactive nuclides such as ^{51}Cr and ^{59}Fe are produced and these nuclides can be radioactive source terms.

Available Removal Method: Cr, Ni and Fe all are soluble in liquid bismuth and will also be removed from the primary coolant salt via liquid-liquid contacting. Keeping the redox potential of the salt at a value below Cr^{2+}/Cr redox potential will also remove the corrosion products and reduce the concentration of the corrosion product fluorides. Both maintaining a slightly reducing chemical environment to minimize overall corrosion and maintaining corrosion product concentration below their solubility limits at the lowest temperature in the system are important to avoid depositing activated corrosion products in the primary loop piping. Considering that the redox potentials of Cr, Fe, and Ni fluorides are all more positive than these of the primary salt components (LiF and BeF_2), electrochemical technologies, such as electrolysis, can also be applied to remove the corrosion products from the salt.

4.1.10. Oxygen, Oxides, Hydroxides and Moisture

Source: All of the metallic surfaces of the primary coolant boundary will initially have a thin oxide coating. Metal oxides are not stable in the primary salt, and they will dissolve into the salt in operation. The primary coolant cover gas will contain small amounts of moisture and oxygen. There will be an equilibrium between the cover gas and the primary salt, therefore, the content of moisture and oxygen in the salt depends on their partial pressures in the cover gas. The reactor vessel lid will be sealed using gaskets. The containment atmosphere will likely be at slightly higher pressure than the vessel upper plenum. Improper sealing of the vessel lid would result in leakage of the containment atmosphere into the vessel upper plenum. Maintenance activities such as inspection and replacement will also present opportunities for oxygen and moisture to ingress into the primary system. Another oxide source is leakage of the fuel. FHR will use TRISO fuel with oxide fuel pellet. Some fission product oxides such as La_2O_3 will be formed during fission and these oxides have solubility in the primary salt[28], therefore, the dissolution of fission product oxides will introduce oxygen ions into the primary salt. Fluorine has a fast neutron cross-section for transmutation into ^{16}N, which decays into stable oxygen. Fluorine also has a somewhat smaller cross-section for fast neutron transmutation into ^{19}O.

Impact: The oxides, hydroxides, oxygen and moisture in the primary salt will shift redox potential to more positive and significantly enhance the corrosion rate. The presence of oxygen element or ions in the primary salt may also lead to formation of non-soluble compounds [28], of compounds that increase the salt melting temperature or of both compounds.

Available Removal Method: By using a sacrificial carbon anode, the oxygen impurity in the primary molten salt can be removed by directly electrochemically reducing oxides [52] to form carbon dioxide. The sacrificial carbon anode technology for oxygen removal was successfully demonstrated in the MSBR program [1]. However, the use of a sacrificial carbon anode has not been well tested. One of the major concerns with the sacrificial carbon anode is the formation of carbides due to the reduction of carbonates [53]. The other issue is that this type of impurity removal has not previously been implemented and detailed performance requirements for the sacrificial electrode have yet to be determined.

4.1.11. References

1. H Feuerstern, A. J. Hooper, F. A. Johnson, Mechanism of release of radioactive products into liquid-metal coolents, their transport within the circuits and removal from LMFBRS, Atomic Energy Review 173 (1979), 697-761.
2. C. W. Forsberg, et al., Nuclear Technology, 197(2017): 119-139.
3. Satoshi Fukada, Flibe-Tritium Research for Fission or Fusion Reactors at Kyushu University, J. Plasma Fusion Res., 10 (2013), 22-26.
4. J. Zhang, et al., Redox potential control in molten salt system for corrosion mitigation, Corrosion Science, 144 (2018), 44-53.
5. P. Cotterill, The hydrogen embrittlement of metals, Progress in Material Science, 9(1961): 205-250.
6. [M. D. Shapiro and C. M. Reed, Removal of Tritium from the Molten Salt Breeder Reactor Fuel, ORNL-MIT-117, Oak Ridge, TN, Nov. 1970
7. G. I. Eskin, Cavitation Mechanism of Ultrasonic Melt Degassing, Ultrasonics Sonochemistry, 2(1995): S137–S141.
8. Jan. B. Talbot, A Study of Tritium Removal from Fusion Reactor Blankets of Molten Salt and Lithium-Aluminum, ORNL/TM-5104, March 1976.
9. W. F. Calaway, "Electrochemical Extraction of Hydrogen from Molten LiF-LiCl-LiBr and its Application to Liquid-Lithium Fusion Reactor Blanket Processing," Nuclear Technology, 39(1978):63–74.
10. David E. Holcomb and Dane F. Wilson, Apparatus and Method for Stripping Tritium from Molten Salt, US Patent Application 14333627, filed July 17th, 2014
11. E. L. Compere, S. S. Kirslis, E. G. Bohlmann, F. F. Blankenship, and W. R. Grimes, Fission Product Behavior in the Molten Salt Reactor Experiment, ORNL-4865, Oak Ridge National Laboratory, Oak Ridge, TN, October 1975.
12. Peter P. Mardilovich, Ying She, Yi Hua Ma, and Min-Hon Rei, Defect-Free Palladium Membranes on Porous Stainless Steel Support, AIChE Journal, 44(1998): 310-322.
13. Ke Zhang, Huiyuan Gao, Zebao Rui, Peng Liu, Yongdan Li, and Y. S. Lin, High-Temperature Stability of Palladium Membranes on Porous Metal Supports with Different Intermediate Layers, Industrial & Engineering Chemistry Research, 48 (2009): 1880–1886.

14. Browning, W.E., Adams, R.E., Ackley, R.D., "Removal of Fission Product Gases from Reactor Off-Gas Streams by Adsorption," ORNL 59-6-47, Oak Ridge, Tennessee, June 11, 1959
15. D. Scott, W. P. Eatherly, Graphite and xenon behavior and their influence on molten salt reactor design. Nuclea Applications and Technology, 8(1970): 179-189.
16. G.M. Watson, R. B. Evans III, W. R. Grimes, N. V. Smith, Solubility of noble gases in molten fluorides, Journal of Chemical Engineering Data, 7(1962): 285-287.
17. S. Cantor, Physical properties of molten salt reactor fuel, coolant, and flush salts, ORNL-TM-2316, 1968
18. M. Blander, et al., Solubility of Boble gases in molten fluorides. II in the LiF-NaF-Kf eutectic mixture, J. Phys. Chem. 63(1959): 1164-1167.
19. Grimes, W.R., "Molten-Salt Reactor Chemistry," Nuclear Applications & Technology, vol. 8(1970): 137-155.
20. Engel, J.R., et. Al., "Molten-Salt Reactors for Efficient Nuclear Fuel Utilization Without Plutonium Separation," Oak Ridge National Laboratory, August 1978.
21. Browning, W.E., Adams, R.E., Ackley, R.D., "Removal of Fission Product Gases from Reactor Off-Gas Streams by Adsorption," ORNL 59-6-47, Oak Ridge, Tennessee, June 11, 1959.
22. D. Grabaskas, et al., Regulatory technology development plan sodium fast reactor, Report of Argonne National Laboratory, ANL-ART-3, 2015.
23. Grimes, W.R., "Chemical Research and Development for Molten-Salt Breeder Reactors," Oak Ridge National Laboratory, 1967
24. M. Yamawaki, et al., Evaluation study of source term for severe accident analysis of molten salt reactors, J. Plasma Fusion Res. Series, 11(2015): 113-119.
25. C. F. Baes, Jr. The chemistry and thermodynamics of molten salt reactor fluoride solutions. ORNL-P-1428, 1965.
26. M. Taira, Y. Arita, M. Yamawaki, The evaporation behavior of volatile fission products in FliNaK salt, the Open Access Journal of Science and technology, 5, 101315, 2017
27. M. Matsumiya, R. Takagi R. Fujita, Recovery of caesium using liquid metallic cathodes in molten fluoride system, Journal of nuclear Science and Technology, 35(1998): 137-147.
28. M. Ambrova, et al., On the solubility of lanthanum oxide in molten alkali fluorides, Journal of Thermal Analysis and calorimetry, 91(2008): 596-573.
29. H. C. Savage, and J. R. Hightower, Jr. Engineering Tests of the Metal Transfer Process for Extraction of Rare-Earth Fission Products from a Molten-Salt Breeder Reactor Fuel Salt, ORNL-5176, Oak Ridge, TN, February 1977
30. C. H. Brown, Jr., J. R. Hightower, Jr., and J. A. Klein, Measurement Of Mass Transfer Coefficients In A Mechanically Agitated, Nondispersing Contactor Operating With A Molten Mixture Of LiF–BeF2–ThF4 And Molten Bismuth, ORNL-5143, November 1976
31. L. M. Ferris, Some Aspects of the Thermodynamics of the Extraction of Uranium, Thorium, and Rare Earths form Molten LiF-BeF2 into Liquid Li-Bi Solutions, ORNL-TM-2486, Oak Ridge, TN, March 1969
32. C. F. Baes, Jr., The Chemistry and Thermodynamics of Molten Salt Reactor Fuels, Journal of Nuclear Materials, 51(1974): 149-162.
33. Hirotake Moriyama, Masafumi Miyazaki, Yoshiyuki Asaoka, Kimikazu Moritani, and Jun Oishi, Kinetics Of Reductive Extraction Of Actinide And Lanthanide Elements From Molten Fluoride Into Liquid Bismuth, Journal of Nuclear Materials, 182(1991): 113-117.

34. P. Chamelot, et al., Lanthanides extraction processes in molten fluoride media, in Molten Salt Chemistry, 2013, 521-540.
35. R. J. Kedl, The migration of a class of fission products (noble metals) in the molten salt actor experiments, ORNL-TM-3884. 1972.
36. M. W. Rosenthal, R. B. Briggs, P. N. Haubenreich, Molten-Salt Reactor Program Semiannual Progress Report for Period Ending August 31, 1971, ORNL-4728, Oak Ridge, TN, February 1972, p. 181
37. M. W. Rosenthal, et al, Molten-Salt Reactor Program Semiannual Progress Report for Period Ending February 28, 1970, ORNL-4548, Oak Ridge, TN, August 1970, p.39
38. E. L. Compere, S. S. Kirslis, E. G. Bohlmann, F. F. Blankenship, and W. R. Grimes, Fission Product Behavior in the Molten Salt Reactor Experiment, ORNL-4865, p136. Oak Ridge, TN, October 1975
39. L. M. Toth and G. E. Boyd. Raman spectra of thorium (IV) in fluoride complex ions in fluoride melts. J. Phys. Chem. 77(1973): 2654–2657.
40. E. L. Compere, S. S. Kirslis, E. G. Bohlmann, F. F. Blankenship, and W. R. Grimes. Fission Product Behavior in the Molten Salt Reactor Experiment, ORNL-4865, Oak Ridge National Laboratory, 1975.
41. S. Guo, et al., Corrosion in the molten fluoride and chloride salts and materials development for nuclear applications, Progress in Materials Science, 2018.
42. J.R. Keiser, Status of tellurium - Hastelloy N studies in molten fluoride salts, ORNL/TM-
43. 6002, Oak Ridge National Laboratory, Oak Ridge, TN, USA,1977
44. V. Ignatiev, A. Surenkov, I. Gnidoy, A. Kulakov, V. Uglov, A. Vasiliev, J. Nucl. Mater., 440
45. (2013): 243–249.
46. C. F. Baes Jr Reprocessing of Nuclear Fuels, Conf. 690-801, USAEC, 1969
47. L. Toth, L. L. Gilpatrick, L. Report ORNL-TM-4056, Oak Ridge National Laboratory, 1972.
48. L. E. McNeese, Engineering development studies for molten salt breeder reactor processing No.6, ORNL-TM-3141, 1971.
49. W. Cohen, et al., Molten Fluoride salt and liquid metal multistage extraction model, Progress in Nuclear Energy, 97(2017): 214-219.
50. Jan Uhlir, Martin Straka, Lorant Szatmary, Development of pyroprocessing technology for thorium fueled molten salt reactor, Proceedings of ICAPP 12, Paper 12399, 2012.
51. J. Zhang, N. Li, Analytical solution on the transient corrosion/precipitation in non-isothermal liquid lead bismuth eutectic flow loops, Corrosion 60 (2004): 331-341.
52. J.W. Koger, Alloy compatibility with LiF-BeF2 salts containing ThF4 and UF4, ORNL-TM-4286, Oak Ridge National Laboratory, Oak Ridge, TN, USA, 1972.
53. J. R. Engel, et al., Conceptual design characteristics of a denatured molten salt reactor with once through fueling, ORNL-TM-7207, 1980
54. M. Ambrova, et al, Electrochemical behaviour of the LiF-(CaF2)-La2O3 system, Chemical Papers, 62(2008): 154-159.
55. M. Gibilaro, et al., Direct electrochemical reduction of solid uranium oxide in molten fluoride salt, Journal of Nuclear Materials, 414(2010): 169-173.

4.2. Primary Salt Purification Methods

4.2.1. Liquid/Liquid Separation

A previously developed distribution model for the removal of actinides and rare earths from chloride salt using lithium activated bismuth has been modified and adapted as part of this study [1]. A new model has been developed to simulate a multistage extraction system for the removal of actinides and rare earths from a eutectic mixture of LiF-BeF_2 (66% LiF) salt using the same reductive extractant. The model predicts the distribution of actinides and rare earths between the fluoride salt and liquid metal at each stage using experimentally determined data for the apparent potential and activity coefficients of each contaminant in both phases. All stages are assumed to have a residence time large enough for equilibrium to be reached, and electrochemical kinetics are therefore not considered. However, previous experiments and studies show that the time scale for reaching equilibration in a batch system is on the order of a few hours to a couple days [2, 3]. This is a significant challenge that will need to be addressed in order for the continuous extraction process described in this paper to be advantageous. The development of equipment to decrease the equilibration time will be necessary. Possible solutions could be to use a series of centrifugal contactors or pulse columns [4] to mix the liquids during the separation. The centrifugal contactor and the pulse column have been successfully applied in liquid-liquid separation in PUREX for used fuel reprocessing.

Based on limitations of available electrochemical data in fluoride salt, the model can currently predict the distribution across any number of stages for a combination of up to two actinides (U and Pu) and three rare earths (La, Ce, and Sm). The model has the capability to be expanded to include additional elements, if necessary data becomes available in the future. The remainder this paper will discuss the methods and equations used in the development of the model and the efficacy and plausibility of this multistage extraction system based on the results.

4.2.1.1. Equilibrium Model

In a molten salt/ liquid metal system, reductive extraction can be applied to remove metal elements from the salt phase. For the case of an FHR using LiF-BeF_2 as the primary coolant, lithium activated bismuth can be used to reduce metallic fluorides through the reaction shown below.

$$MF_n + n\,Li \leftrightarrow M + n\,LiF \tag{4-3}$$

where M denotes the metal species being reduced and n is the oxidation state of the oxidized metal. The Nernst equation can be used to describe the equilibrium potential of the reaction:

$$E_{eq} = E^{ap}_{M^{n+}} + \frac{RT}{nF}\ln\left(\frac{X_{M^{n+}}}{\gamma_M Y_M}\right) \tag{4-4}$$

where E_{eq} and $E_{M^{n+}}^{ap}$ are the equilibrium potential and the apparent standard potential, respectively, R is the gas constant, F is Faraday's constant, $X_{M^{n+}}$ is the molar fraction of the metallic fluoride in the molten salt and Y_M is the molar fraction of the metal in the liquid metal.

The distribution coefficient can be defined as the ratio of the concentration of metal M in the salt phase ($X_{M^{n+}}$) to the concentration of metal M in the metal phase (Y). Rearranging the above equation gives:

$$D_M = \frac{X_{M^{n+}}}{Y_M} = \gamma_M \exp\left(\frac{nF}{RT}\left(E_{eq} - E_{M^{n+}}^{ap}\right)\right) \tag{4-5}$$

For a multi-contaminant system with multiple metallic fluorides dissolved in the molten salt, the equilibrium potential, E_{eq}, must be equal for all species. Therefore, the distribution coefficient for each rare earth and actinide is driven by the concentrations of all other elements within the molten salt/liquid metal system. Molar balances across a single stage are shown below, assuming that there is initially no rare earths or actinides in the liquid metal phase and that the change in volume of the molten salt and liquid metal phases as ions are transferred is negligible.

$$Bi_{feed}Y_{M_i} + Salt_{feed}X_{M_i^{n_i+}} = Salt_{feed}X^I_{M_i^{n_i+}} \tag{4-6}$$

$$Bi_{feed}Y_{Li} + Salt_{feed}X_{Li^+} = Salt_{feed}X^I_{Li^+}\ Bi_{feed}Y^I_{Li} \tag{4-7}$$

$$\sum_{i=1}^{m} Bi_{feed}n_iY_{M_i} = Bi_{feed}Y^I_{Li} - Salt_{feed}X_{Li} \tag{4-8}$$

where Bi_{feed} and $Salt_{feed}$ are the volumetric flow rates of the liquid Bismuth phase and molten fluoride salt phase, respectively, the superscript "I" denotes the initial concentration, and m is the total number of metal elements in the system. Combining the molar balance equations with the first half of the equation for distribution coefficient gives:

$$\sum_{i=1}^{m} \frac{n_iX^I_{M_i^{n_i+}}}{Bi_{feed} + Salt_{feed}D_{M_i}} = \frac{Y^I_{Li}D_{Li} - X^I_{Li^+}}{Bi_{feed} + Salt_{feed}D_{Li}} \tag{4-9}$$

With specified initial concentrations for each element (including Lithium), the only unknown variables are the corresponding distribution coefficients at equilibrium. The previously shown equation for distribution coefficient shows that for a specified temperature, the equilibrium potential, E_{eq}, is the only unknown. Since the equilibrium

potential is constant within the system for all present elements, the above equation has only one unknown variable.

In order to accurately predict the distribution of rare earths and actinide elements, the apparent potential of each element in the salt phase must be known. The apparent potential has been shown to be dependent on temperature in previous studies and can be expressed in the form shown below.

$$E_{M^{n+}}^{ap} = A + BT \tag{4-10}$$

where A and B are experimental constants and T is temperature in Kelvin. Data has been collected from previous experiments and are reported in Table 4-2. All literature data is valid for LiF-BeF_2 (66% LiF) within the temperature range of 600 to 800^{0}C.

Table 4-2: Experimentally Determined Apparent Potentials of Rare Earths and Actinides in LiF-BeF_2 Molten Salt

	Oxidation State	Apparent Potential in Salt		Reference
		Const. A (V)	Const. B (V/K)	
U	3	-2.06E+00	6.26E-04	[5]
Pu	3	-2.31E+00	7.88E-04	[6]
La	3	-3.03E+00	8.21E-04	[5]
Ce	3	-2.96E+00	8.17E-04	[7,8]
Sm	3	-2.81E+00	7.95E-04	[7,8]
Li	1	-3.362E+00	8.21E-04	[5]

In addition to the apparent potential in the salt phase, the activity coefficient in the liquid metal phase must also be known. The activity coefficient, which is also temperature dependent, can be expressed using the equation below.

$$\ln \gamma = A - \frac{B}{T} \tag{4-11}$$

where A and B are experimental constants and T is temperature in Kelvin. Data has been collected from previous experiments and are reported in *Table 4-3*. As with apparent potential literature data, all activity coefficient data is valid for liquid bismuth metal within the temperature range of 600 to 800^{0}C.

Table 4-3: Experimentally Determined Activity Coefficients of Rare Earths and Actinides in Liquid Bismuth Metal

	Oxidation State	Activity Coefficient in Bi		Reference
		Const. A	Const. B (K)	
U	3	2.39E+00	1.00E+04	[9]
Pu	3	3.43E+00	1.93E+04	[10]
La	3	3.11E+00	2.63E+04	[11]

Ce	3	3.82E+00	2.61E+04	[11]
Sm	3	4.03E+00	2.71E+04	[11]

The activity coefficient of lithium in bismuth has also been reported in literature [12]. However, the activity coefficient does not follow the form used above for LiF-BeF_2 salt. The expression for activity coefficient can be seen below and is reported to be valid within the temperature range of 775 to 1100 K (approximately 500 to 825^{0}C).

$$\ln(\gamma_{Li}) = -4.262 + .787T - 4.72 * 10^{-4}T^2 + (307.72 - .842T + 2.94 * 10^{-4}T^2) * Y_{Li} \quad (4\text{-}12)$$

Based on the expression, along with temperature, concentration of Li is also significant contributing factor in the activity coefficient in liquid bismuth.

4.2.1.2. Multistage Extraction model

A continuous multistage extraction model is the proposed method for online primary coolant reprocessing. The described process will include multiple equilibrium stages with a fresh liquid metal stream at each stage. The product molten salt stream from each stage will be fed to the inlet of the next stage. A schematic diagram for the extraction cascade can be seen below in Figure 4-1, where N is the total number of stages, $X_{M_i,n}$ is the concentration of element M_i in the molten salt outlet of the nth stage, and $Y_{M_i,n}$ is the concentration of element M_i in the liquid metal outlet of the nth stage.

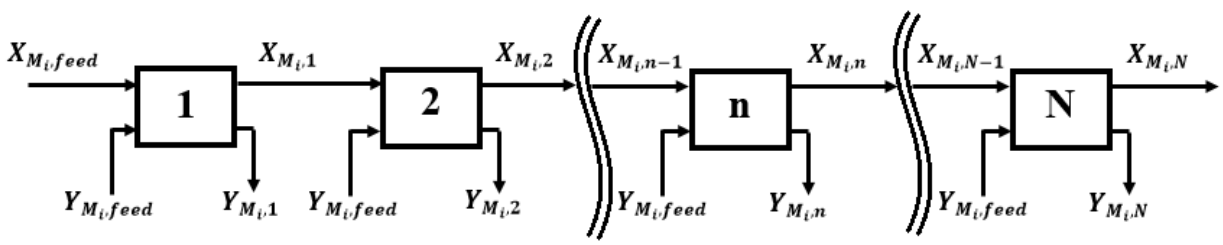

Figure 4-1: Flowchart Diagram of Multistage Extraction System

The distribution coefficient for each element M_i describes the final equilibrium state and can therefore be represented based on the final concentrations in the two phases at the outlet of each stage n.

$$D_n = \frac{X_{M_i,n}}{Y_{M_i,n}} \quad (4\text{-}13)$$

The single stage equations shown in 4.2.1.1 hold valid and can be applied to each stage. The equilibrium potential and distribution coefficients of all solutes at each stage can then be determined. Using the molar balances, the distribution coefficients can be used to

determine the concentrations of solutes in each phase. Then, the recovery yield for each solute at each stage can be expressed by

$$\zeta_{M_i,n} = \frac{X_{M_i,feed} - X_{M_i,n}}{X_{M_i,feed}} * 100 \tag{4-14}$$

The model, which has been developed in MATLAB, can be seen at the end of this report in the Appendix.

During FHR operation, radionuclides from the fuel will inevitably leak into the primary fluoride salt coolant. These contaminants will be present in very low concentrations. Based on previous experiments all contaminants were either less than .002 mole fraction or a major component of the salt (LiF and BeF_2) [13]. Therefore, .001 was used the mole fraction for each actinide and rare earth for this model. The metal phase for each stage was specified to have an initial Lithium concentration of .001 mole fraction. The flow rates of each phase are not empirically set in the model, however the ratio of the molten salt feed stream to liquid Bismuth metal feed must be specified. The liquid metal flow rate was set to 3 times the molten salt flow rate to account for the rare earth and actinide fluorides being trivalent whereas lithium fluoride is monovalent. Temperature specifications in previous experimental studies range from 600 to 800^{0}C, and an initial value of 700^{0}C was chosen for this model [13, 3]. The results from the model can be seen below in Figure 4-2.

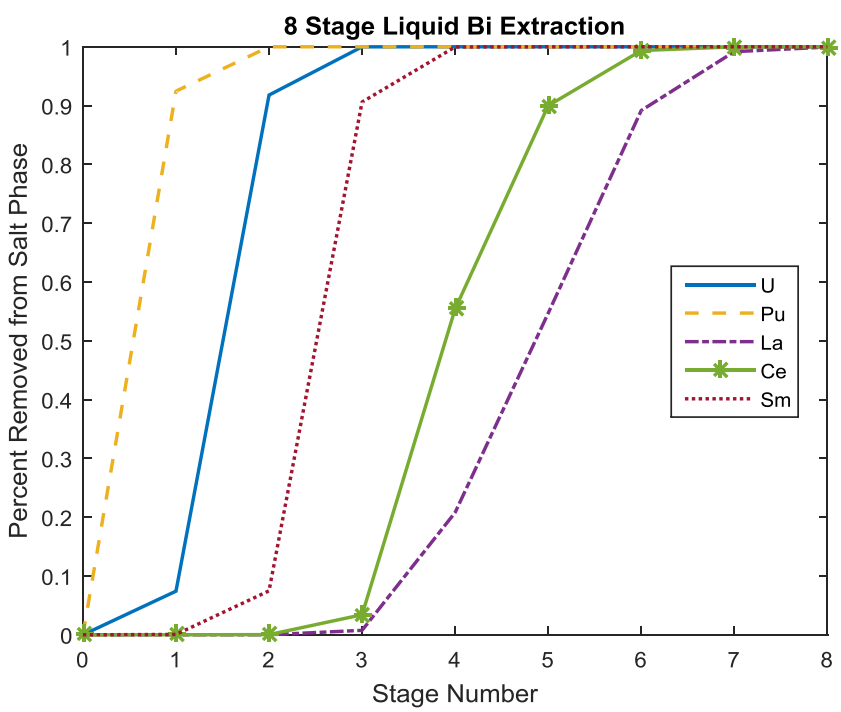

Figure 4-2: Percent Removal of Actinides and Rare Earths across Extraction Cascade at 700 ^{0}C

The figure above shows that as stage number is increased, the percent removal of all contaminants also increases. Therefore, with sufficient stages (8 with the current parameters), it is possible to remove greater than 99% of all contaminants. Additionally, it

can be noted that the actinide elements, uranium and plutonium, are the first to be extracted, followed by the rare earths lanthanum, cerium, and samarium. This result is promising as the majority of the fuel materials can be recycled separately from the fission products. The fuel materials contained in the liquid Bismuth could be removed and reused through another electrochemical transfer step with molten LiCl [2].

The effect of concentration of lithium initially in the metal phase was studied by varying the mole fraction in the model. The initial concentration was assumed to be a constant value across all stages. The model was run for 2 additional lithium mole fractions .0025 and .005 (total molar fraction of contaminants in the salt). Temperature remained at 700^{0}C. The results can be seen below in Figure 4-3 and Figure 4-4.

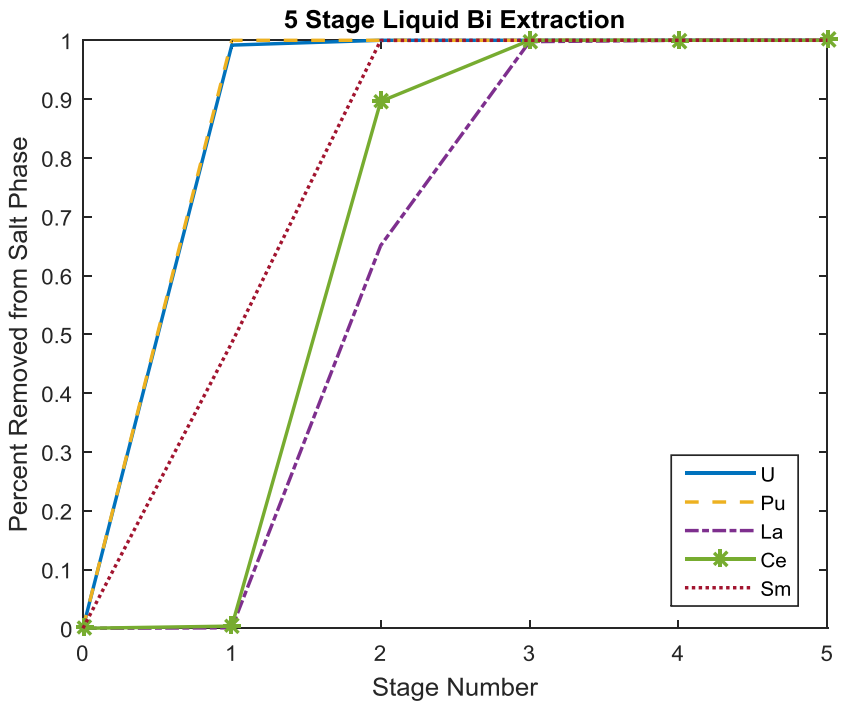

Figure 4-3: Percent Removal across Cascade at 700 ^{0}C and .0025 initial mole fraction of Li in Bi phase

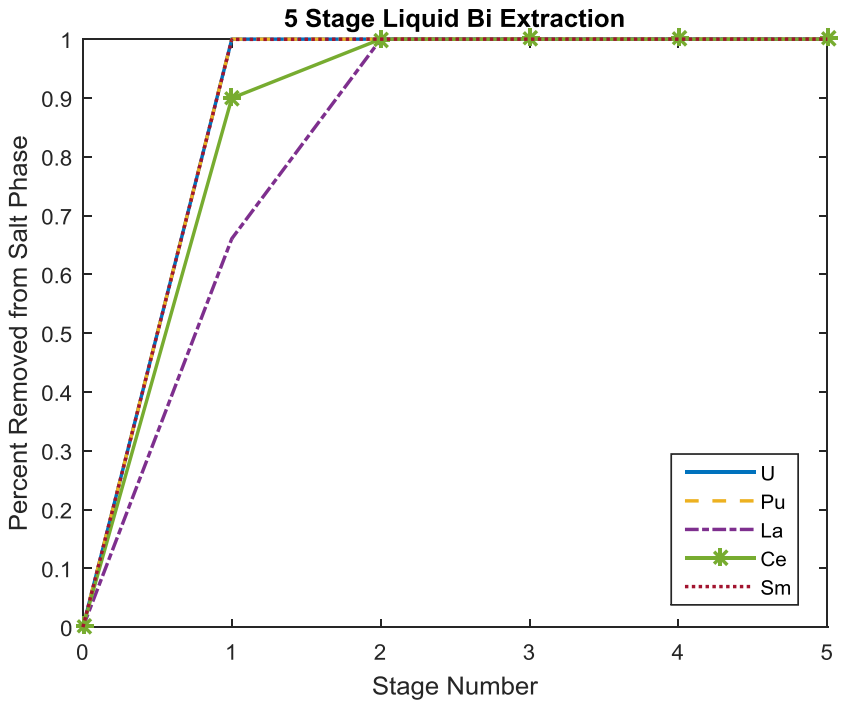

Figure 4-4: % Removal across Cascade at 700 ^{0}C and .005 initial mole fraction of Li in Bi phase

As shown in the figures above, increasing the initial concentration of lithium in the Bi phase results in a higher effective extraction at each stage and therefore, less stages are required to reach a 99% removal of all contaminants from the salt. However, decreasing the number of stages also results in the simultaneous extraction of both rare earths and actinides. This consequence is undesirable as it would be favorable to recycle the fuel materials (U and Pu) separately. This can be solved by varying the initial lithium concentration in the Bi phase at each stage in the cascade. The concentration should be kept lower at the first few stages in order to separate out the U and Pu with as little rare earths as possible. The concentration of lithium can then be increased in the following stages to remove the remaining rare earth contaminants.

The model was used to show the distribution using a stage dependent initial Li concentration in the metal phase. The model was adjusted so that the initial Li mole fraction was .0005 in the first 4 stages, and all latter stages were raised to .0025. The temperature was set to 700^{0}C and all other parameters were left unchanged. Figure 4-5 below shows the results of this model.

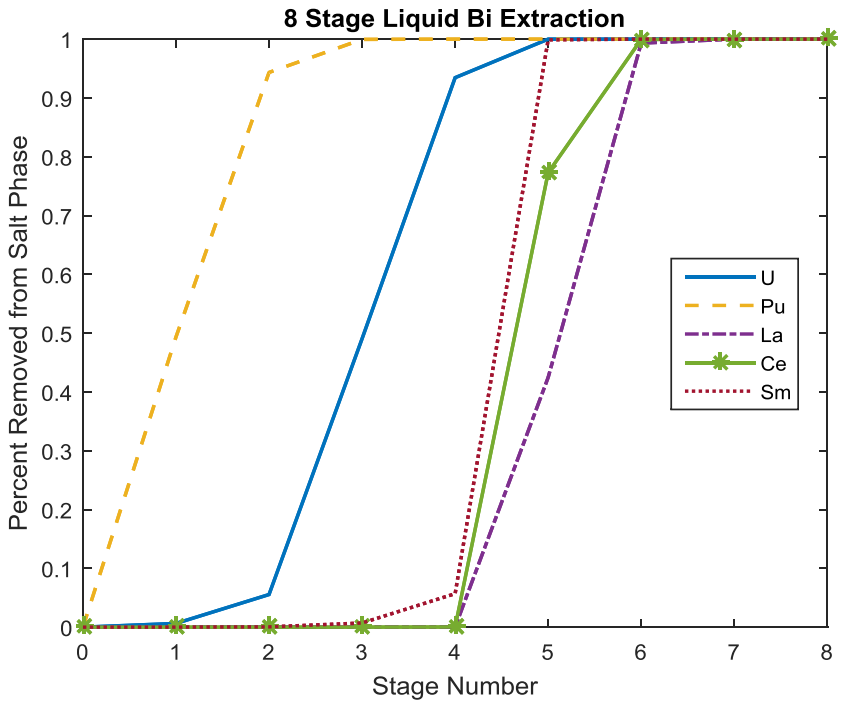

Figure 4-5: % Removal across Cascade at 700 ⁰C with stage dependent initial mole fraction of Li in Bi phase

As shown in the distribution plot above, this model produces a favorable result. Following stage 4, greater than 99% of Pu and 93% of U has been removed, while only 1% of all other contaminants has been extracted. Following stage 4, the initial Li concentration in the metal phase is increased, which allows for a more effective transfer of all other rare earths with less stages. This revised model predicts that 6 stages is sufficient to remove all contaminants, while still being capable of extracting the actinides separately from the rare earths.

The ratio of the molten salt to liquid metal flow rates were also studied in this model by varying the liquid metal flow rate from 1 to 5 times the molten salt flow rate. The metal phase for each stage was specified to have a constant initial Lithium concentration of .001 mole fraction. Additionally, the temperature was set at 700^{0}C. The model was run with all 5 elements set to an initial concentration of .001. The plots below in Figure 4-6 and Figure 4-7 show the distribution results for uranium and cerium for different flow ratios. The results for all other rare earths and actinides in the model show very similar trends.

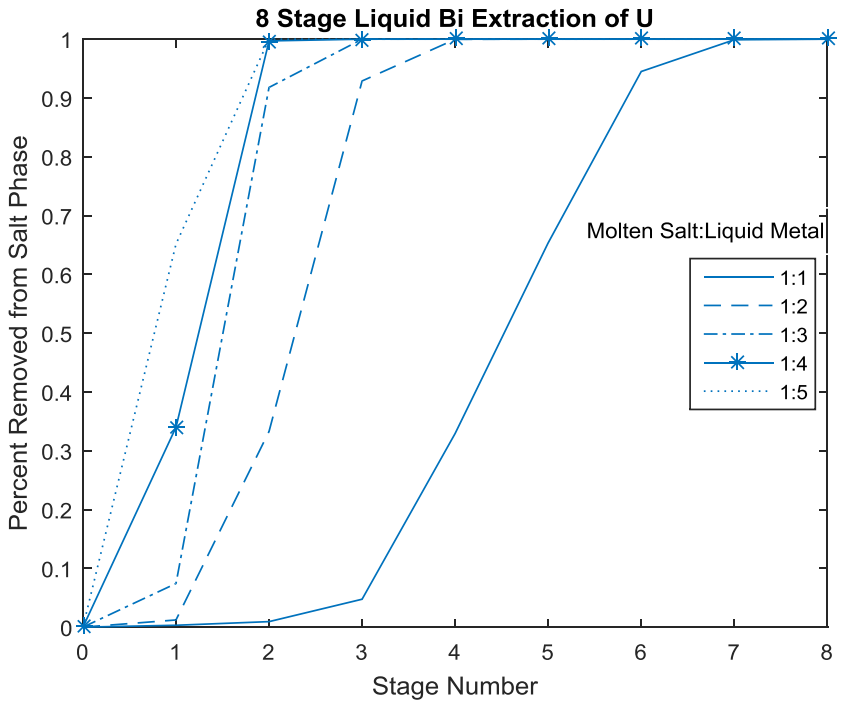

Figure 4-6: % Removal of Uranium across Cascade at 700 ℃ with varying flow rate ratios

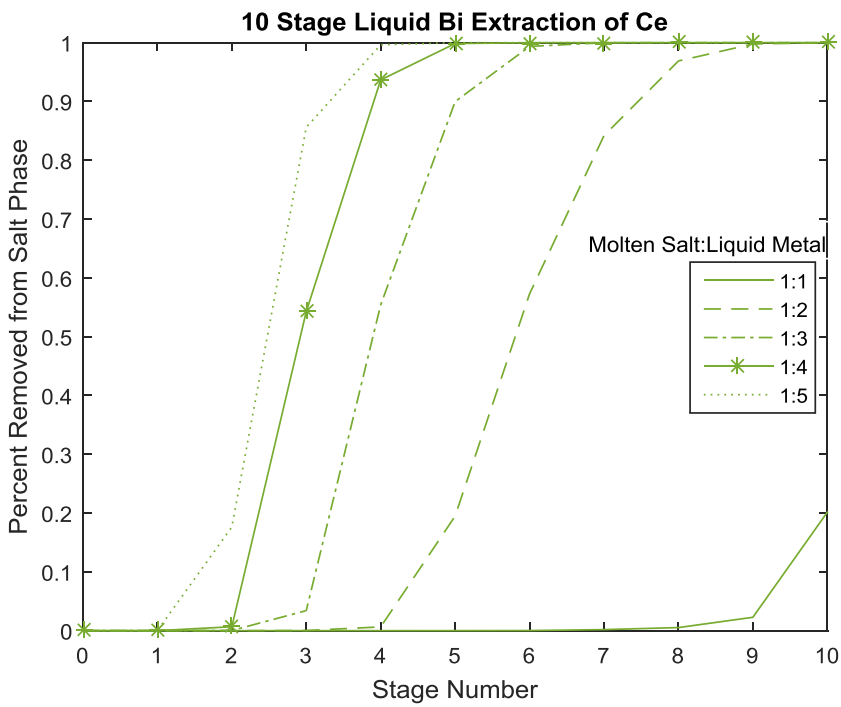

Figure 4-7: % Removal of Cerium across Cascade at 700 ℃ with varying flow rate ratios

As can be seen by the plots for uranium and cerium, increasing the flow rate of the liquid metal phase increased the percent removal of contaminants across each stage. However, the relationship shows a decreasing exponential effect as the flow rate is increased. At low

liquid metal flow rates, increasing the flow rate has a much greater impact on the distribution, but at higher flow rates, the same increase in flow rate has significantly less of an impact on the distribution across the cascade.

Apparent potential and activity coefficient are both significantly affected by temperature based on the literature data provided in Section 4.2.1.1. Therefore, the effect of temperature on extraction across the cascade was also examined by varying the temperature in the model. The initial concentration on lithium in the Bi phase was assumed to be a constant value across all stages, and was set to .001 mole fraction. The model was run for varying temperatures ranging from 600 to 800^{0}C and is plotted in Figure 4-8 shown below.

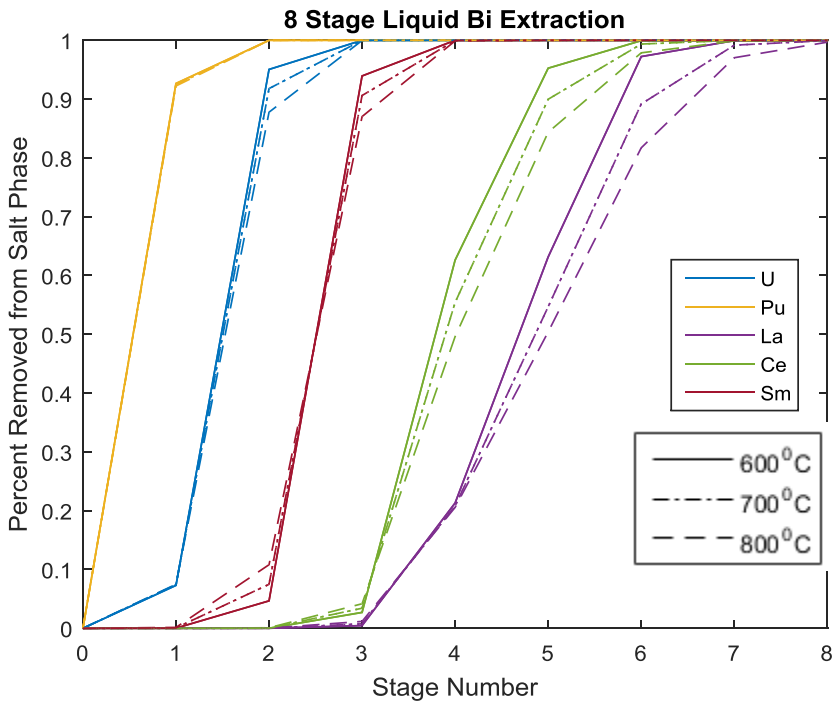

Figure 4-8: Effect of Temperature on Percent Removal across Extraction Cascade

Based on the generated plot for varying temperature, it is evident that increasing the temperature results in a lower percent removal of the majority of contaminants at each stage. Plutonium seems to be the least affected by changing temperature, however the rare earth elements show a much more drastic effect. The results suggest that maintaining a lower system temperature will allow for the most effective extraction and require the least number of stages to achieve the desired removal of contaminants.

4.2.1.3. Summary

The likelihood of contamination into the primary coolant from leaked fuel major is a concern for FHR development. A possible solution to this contamination is to develop an online processing system for the primary coolant using a two phase extraction process with lithium activated bismuth as the extractant. A multistage extraction model has been

developed for determining the distribution of possible actinides and rare earth elements between two phases of lithium activated bismuth and molten LiF-BeF_2 (66 mole % LiF). The model provides good evidence that this multistage system could be an effective method for removing contaminates from the coolant. Based on the results from the model, the major contributing factor in the distribution is the concentration of lithium in the bismuth phase. A higher concentration allows for a greater removal at each stage, however better separation between each actinide and rare earth can be achieved with a lower initial concentration of Li. The results suggest that by varying this initial concentration at each stage, fuel elements (U and Pu) and be removed and recycled separately from the rare earth contaminants. The flow rate ratio between the molten salt and liquid metal phases was also studied, and showed that at lower liquid metal flow rates, increasing the rate has a large positive effect on the extraction of all contaminants; however, at larger flow rates, the effect is much less significant. Temperature effects were also studied and the model shows that lower temperatures result in a better extraction. However, the desired extraction can still be achieved at all temperatures within the designated range of 600 to 800^0C.

This model provides good insight to the development of a multistage extraction system for primary coolant clean-up in FHRs. However, additional improvements should be made to further this concept. First, liquid-liquid extraction kinetics must be considered, as the extraction rates are normally very slow and equipment to reduce equilibration time will need to be developed. Experimental data for other transuranic elements and fission products in LiF-BeF_2 salt and in liquid Bi would allow this model to be extended to more than 5 elements. Currently, this data is not readily available in literature. Additionally, flow rate considerations and other time dependent processes in FHR operation are important parameters that still need to be studied more thoroughly. This model can be further expanded to include electrochemical kinetics in order to consider these parameters.

4.2.2. Electrochemical Separation

Electrochemical separation has applied to separate actinides and lanthanides from molten salt in pryprocessing for process spent metal fuels (U-Zr), and it was also proposed and tested as an on-line method for cleaning molten salt fuels for MSRs [14]. Electrochemical separation not only can separate metal impurities such as lanthanides and corrosion products but also can separate gas impurities such oxygen impurity from dissolution of oxides and leakage of air into the primary salt. The electrochemical separation technology using a sacrificial carbon anode for oxygen removal was successfully demonstrated in the MSBR program [1].

For metal cations, the common separation/deposition reaction is:

$$M^{n+} + \mathrm{ne} = M \qquad (4\text{-}15)$$

For non-metal anions, the common separation ration is:

$$O^{n-} - \mathrm{ne} = O \qquad (4\text{-}16)$$

Therefore, the separation of cations happens at the cathode, while the separation of anions happens at the anode. The deposition or equilibrium potential of the two electrochemical reaction can be expressed by:

$$E_{M^{n+}/M} = E^0_{M^{n+}/M} + \frac{RT}{nF} lna_{M^{n+}} \quad (4\text{-}17)$$

$$E_{O/O^{n-}} = E^0_{O/O^{n+}} - \frac{RT}{nF} lna_{O^{n+}} \quad (4\text{-}18)$$

where E^0 is the standard potential, R is the gas contract, T is temperature in Kelvin, n is the charge number, F is Faraday's number and a is the activity of the ion in molten salt which can be expressed by $a = \gamma X$ with γ the activity coefficient and X the concentration in mole fraction.

Only the element that has a redox potential which is more positive than the major cations (Li^+ and Be^{2+}) and more negative that the major anion (F^-) can be separated using the electrochemical method. If it is just based on the standard redox potential, it indicates that most of the lanthanides cannot be separated from the primary salt using electrochemical method. However, the redox potential depends on both the standard redox potential and the activity of the element in the salt. If the element concentration in the primary salt is known, the redox potential will be determined by the apparent potential which is given by (4-20). One example [15] is the electrochemical deposition of Dy^{3+} and La^{3+} from molten LiF-NaF-KF even both of them have a more negative standard potential than K^+ and Na^+. Unfortunately, the apparent potentials of most of the impurities in the primary salt are not known.

To shift redox potential of the metal impurity to more positive to improve the separation efficiency, a liquid metal electrode or a reactive electrode were used [16]. For a liquid metal electrode (LE), the deposition reaction and the redox potential becomes:

$$M^{n+}(MS) + ne = M(LE) \quad (4\text{-}19)$$

$$E_{M^{n+}/M} = E^0_{M^{n+}/M} + \frac{RT}{nF} ln\frac{\gamma_{M^{n+}}}{\gamma_M} + \frac{RT}{nF} ln\frac{X(Ms)}{X(LE)} \quad (4\text{-}20)$$

where γ_M is the activity coefficient of metal M in the liquid electrode. (4-20) indicates that if γ_M is small, the redox potential at an LE is more positive than that at an inert solid electrode. Another method to move the redox potential to the positive direction is to use reactive electrodes (RE) which can react with the separated metal to form metal compounds. The reactive electrode can be liquid or solid. The deposition reaction and redox potential can be expressed:

$$M^{n+}(MS) + ne + yN = MN_y \quad (4\text{-}21)$$

$$E_{M^{n+}/M} = E^0_{M^{n+}/M} + \frac{RT}{nF} ln\gamma_{M^{n+}}X(MS) - \frac{\Delta G_{MN_y}}{nF} \quad (4\text{-}22)$$

ΔG_{MN_y} is the Gibbs free energy of formation of the metal compound MN_y. Commonly, ΔG_{MN_y} has a negative value, therefore, the redox potential will be more positive when a reactive

electrode is used than an inert electrode, which makes it much easier to separate the elements from the salts.

Demonstration of separation fission products from both molten chloride salts and fluoride salts has been conducted using reactive electrode, for example, Al and Zn electrode for separation of Sm [17,18] from molten chloride salt, Cu electrode for separation of Eu from fluoride salt [19], and Ni electrode for separation of Sm and Gd from molten fluoride salt [20].

The electrochemical cleanup of FHR primary salt is an electrolysis process which leads to metal deposition at cathode electrode and fluorine development at the anode if an inert electrode is used through a reaction:

$$2F^{-} - 2e = F_2 \qquad (4\text{-}23)$$

This reaction leads to not only loss of primary salt but also production of corrosive gas F_2. By using a Bi-Li alloy as an anode, a current will be applied to control the potential in the salt. This special anode can be coupled with an inert or active solid cathode to assist in the removal of not only rare-earth elements and fission products, but also the actinides dissolved in the primary salt due to fuel failure. The current would drive the Li in the Bi-Li alloy into the primary molten salt, where it would act as a reducing agent to impurities in the molten salt from fuel leakage. The solid cathode would then collect the elemental forms of the impurities from the salt. The schematic of the electrochemical system utilizing Bi-Li liquid metal as the sacrificial anode is provided in Figure 4-9. The dissolution of Li into the salt is driven by electrical current, which does not need a special contactor, such as a centrifugal contactor, for completely mixing the two liquids. Therefore, there is no carryover of Bi into the primary salt. The impurities will directly deposit on the solid/liquid cathode. If the products are solid deposits which are much easier to be removed than the liquid deposits resulting from traditional Bi-Li anode methods developed for MSBRs.

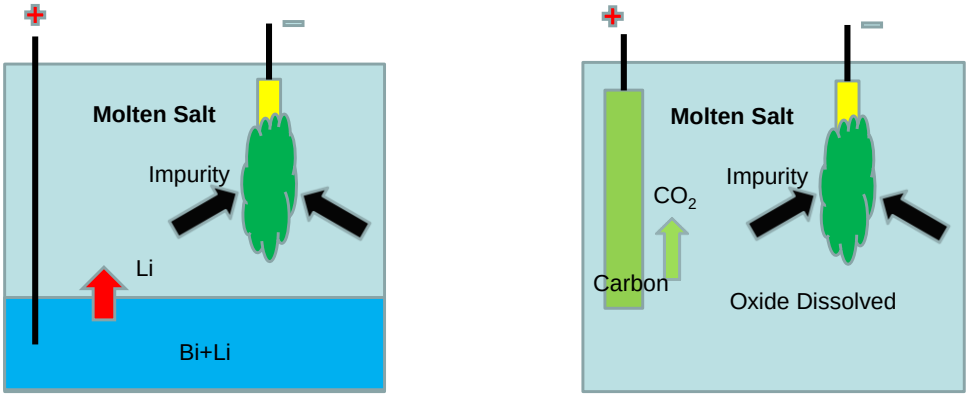

(a) Bi+Li sacrificial anode (b) Carbon sacrificial anode

Figure 4-9: Schematics of the electrochemical processes for contaminant removal

For removing oxygen, oxygen gas can be produced at the anode if an inert anode is used. The oxygen generation is problematic as it causes the back-oxidation of fission products and actinides in the salt mixture. As a result, they precipitate as oxyfluorides and other corrosive species such as fluorine F_2 are formed:

$$MF_3 + 0.5\,O_2 \rightarrow MOF + F_2 \qquad (4\text{-}24)$$

By using a sacrificial carbon electrode (Figure 4-9), oxygen (mainly in oxide forms) in the molten salt can be electrochemically removed as schematic showed in the figure [21] by forming carbon dioxide. The sacrificial carbon anode technology for oxygen removal was successfully demonstrated in the MSBR program [1]. However, the use of a sacrificial carbon anode has not been well tested. One of the major concerns with the sacrificial carbon anode is the formation of carbides due to the reduction of carbonates [22].

4.2.3. Reference

1. Evan Wu, "Distribution model for molten salt clean up and actinide separation", ICAPP 2016. Apr.17-20, San Francisco, CA.
2. V. Zagnit'ko, V.V. Ignat'ev, "Equilibrium Distribution of Lanthanum, Neodymium, and Thorium between Fluoride Salt Melts and Liquid Bismuth", Russian Journal of Physical Chemistry A, 86(2012): 533-538.
3. H. Moriyama, K. Yajima, N. Nunogane, T. Ohmura, K. Moritani, J. Oishi, "Reductive Extraction of Lanthanide and Actinide Elements from Molten LiF-BeF2 Salt into Liquid Bismuth", Journal of Nuclear Science and Technology, 21 (1984): 949-958.
4. J. D. Law, T. A. Todd, "Liquid-Liquid Extraction Equipment", Introduction to Nuclear Chemistry and Fuel Cycle Separations Course, Idaho National Lab, 2008
5. C.F. Baes, The chemistry and thermodynamics of molten-salt-reactor fluoride solutions, Thermodynamics, 1(1965): 427.
6. L. Martinot, Physics and Chemistry of the actinides, Molten-salt chemistry of actinides, chap. 4, 1991.
7. W. R. GRIMES , et al, Chem. Eng. Prog., 55, No. 27 (1959): 65-70.
8. W. T. WARD, et al, USAEC Report ORNL-2749, 1959.
9. M. Kurata, Y. Sakamura, T. Matsui, Thermodynamic quantities of actinides and rare earth elements in liquid bismuth and cadmium, Journal of Alloys and compounds, 234(1996): 83-92.
10. V. A. Lebedev, L. G. Babikov, S. K. Vavilov, I. F. Nichkov, S. P. Raspopin, O. V. Skiba, The thermodynamics of the system plutonium-bismuth, Atomnaya Energiya, 27 (1969): 59-61.
11. J. Zhang, et al., Thermodynamic properties of actinides and fission products in liquid bismuth, Progress in Nuclear Energy, 81 (2015): 67-77.
12. M. S. Foster, et al., Thermodynamics of binary alloys. I. The lithium-bismuth system, Inorganic chemistry, 3 (1964): 1428-1431
13. L. M. Ferris, J. C. Mailen, J. J. Lawrence, F. J. Smith, and E. D. Nogueira, Equilibrium Distribution Of Actinide And Lanthanide Elements Between Molten Fluoride Salts

And Liquid Bismuth Solutions, Journal of Inorganic and Nuclear Chemistry, 32(1970): 2019-2035

14. Pyrochemical separations in nuclear applications, A Status Report, ISBN 92-64-02071-3, OECD 2004.
15. R. Chesser, S. Guo, J. Zhang, Electrochemical behavior of dysprosium and lanthanum in molten LiF-NaF-KF (Flinak) salt, Annals of Nuclear Energy, 120(2018): 246-252.
16. P. Chamelot, L. Mossot, M. Gibilaro, P. Taxil, Lanthanides extraction processes in molten fluoride media, Molten Salt Chemistry: From Lab to Application, 521-540, 2013.
17. Y. Castrillejo, et al., Electrocehmical extraction of samarium from molten chlorides in pyrochemical processes, Electrocehimica Acta, 56(2011): 8638-8644.
18. Ya-Lan Liu, et al., Electrochemical extraction of samarium form LiCl-Kcl melt by forming Sm-Zn alloys, electrochimica Acta, 120(2014): 369-378.
19. M. Gibilaro, et al., Electrochemical extraction of europium from molten fluoride media, electrochimica Acta, 55(2009): 281-287.
20. M. Straka, L. Szatmary, Electrochemistry of selected lanthanides in FliBe and possibilities of their recovery on reactive electrode, Procedia Chemistry, 7(2012): 804-813.
21. M. Ambrova M., Electrochemical behaviour of the LiF-(CaF2)-La2O3 system, Chemical Papers, 62(2008): 154-159.
22. M. Gibilaro,, Direct electrochemical reduction of solid uranium oxide in molten fluoride salt, Journal of Nuclear Materials, 414(2010): 169-173.

4.3. Redox Control for the Mitigation of Material Corrosion in Molten Fluorides

4.3.1. Theory of Redox Control

Redox control technique has been proposed to prevent the corrosion of structural materials in molten fluoride and chloride salts. The idea of the redox control is to introduce another redox couple RA^{k+}/RA^{j+} (k > j, RA stands for redox buffering agent) to make the salt less oxidizing. The corrosion of structural metals is an irreversible electrochemical process at a mixed/corrosion potential that deviates from the equilibrium potentials of the anodic and cathodic partial reactions. However, the equilibrium potentials of the partial electrode reactions will approach an intermediate value with the increase of the product concentrations and consumption of the oxidants with time. Hence the overall corrosion reaction tends to reach an equilibrium where corrosion will be stopped:

$$\mathrm{M} + \mathrm{Ox} \leftrightarrow \mathrm{M}^{n+} + \mathrm{Red} \tag{4-25}$$

If a redox buffering agent RA^{k+}/RA^{j+} is introduced in the system, the equilibrium of reaction (4-25) will be influenced by the following two reactions:

$$\mathrm{RA}^{j+} + \mathrm{Ox} \leftrightarrow \mathrm{RA}^{k+} + \mathrm{Red} \tag{4-26}$$

$$\mathrm{M} + \mathrm{RA}^{k+} \leftrightarrow \mathrm{M}^{n+} + \mathrm{RA}^{j+} \tag{4-27}$$

In the thermodynamic consideration, the equilibrium of reaction (4-25) can be pushed to the left by keeping the concentration ratio of RA^{k+}/RA^{j+} sufficiently low. Hence, the concentration of M^{n+} can be thermodynamically limited by controlling the concentration ratio or redox potential of RA^{k+}/RA^{j+}. Thus, the introduction of a proper redox buffer RA^{k+}/RA^{j+} may mitigate the metal corrosion if the redox buffer makes the salt redox condition more reducing. The redox condition in the molten fluoride salts can be defined as the fluorine potential $\Delta\bar{G}_{F_2}$ [1]:

$$\Delta\bar{G}_{\mathrm{F}_2} = RT \ln p_{\mathrm{F}_2} \tag{4-28}$$

There are at least three methods control the salt redox condition, including the gas phase control (e.g., H_2/HF), major metal control (e.g., Be^{2+}/Be^0), and dissolved salt control (e.g., U^{4+}/U^{3+}). The corresponding equilibrium reactions establishing the fluorine partial pressure p_{F_2} are:

$$\tfrac{1}{2}\mathrm{H}_{2\,(g)} + \tfrac{1}{2}\mathrm{F}_{2\,(g)} \leftrightarrow \mathrm{HF}_{(g)} \tag{4-29}$$

$$\mathrm{Be}^0 + \mathrm{F}_{2(g)} \leftrightarrow \mathrm{BeF}_{2(soln)} \tag{4-30}$$

$$\mathrm{UF}_{3(soln)} + \frac{1}{2}\mathrm{F}_{2(g)} \leftrightarrow \mathrm{UF}_{4\,(soln)} \tag{4-31}$$

And the fluorine potentials are expressed as

$$\Delta\bar{G}_{F_2} = RT \ln p_{\mathrm{F}_2} = 2\Delta G^0_{\mathrm{HF}} + 2RT \ln \frac{p_{\mathrm{HF}}}{\sqrt{p_{\mathrm{H}_2}}} \tag{4-32}$$

$$\Delta\bar{G}_{F_2} = RT\ln p_{\mathrm{F}_2} = \Delta G^0_{\mathrm{BeF}_2} + RT\ln\frac{a_{\mathrm{BeF}_2}}{a_{Be^0}} \tag{4-33}$$

$$\Delta\bar{G}_{F_2} = RT\ln p_{\mathrm{F}_2} = \Delta G^0_{\mathrm{UF}_4} - \Delta G^0_{\mathrm{UF}_3} + 2RT\ln\frac{a_{\mathrm{UF}_4}}{a_{\mathrm{UF}_3}} \tag{4-34}$$

Dividing the fluorine potential by 2F yields to the redox potential versus the standard F/F^- potential:

$$E_{HF/\mathrm{H}_2} = E^0_{\mathrm{HF/H}_2} + \frac{\mathrm{RT}}{\mathrm{F}}\ln\frac{p_{\mathrm{HF}}}{\sqrt{p_{\mathrm{H}_2}}} \tag{4-35}$$

$$E_{\mathrm{BeF}_2/\mathrm{Be}^0} = E^0_{\mathrm{BeF}_2/\mathrm{Be}^0} + \frac{\mathrm{RT}}{2\mathrm{F}}\ln\frac{a_{\mathrm{BeF}_2}}{a_{Be^0}} \tag{4-36}$$

$$E_{\mathrm{UF}_4/\mathrm{UF}_3} = E^0_{\mathrm{UF}_4/\mathrm{UF}_3} + \frac{\mathrm{RT}}{\mathrm{F}}\ln\frac{a_{\mathrm{UF}_4}}{a_{\mathrm{UF}_3}} \tag{4-37}$$

Compared to the fluorine potential, the redox potential can be measured directly or indirectly by an electrochemical sensor using various electrochemical techniques

4.3.2. Dissolved Salt Control Using Eu(III)/Eu(II)

4.3.2.1. Experimental methods

The FLiNaK salt preparation and electrochemical tests were conducted inside of a custom glovebox manufactured by Inert Technology. The glovebox was filled with circulating argon gas to maintain an inert argon atmosphere. Water vapor impurities were limited to 2.6 ± 0.3 ppm, and oxygen impurities were limited to 4.6 ± 0.1 ppm over the course of preparation and experiments. Lithium fluoride, LiF, sodium fluoride, NaF, and potassium fluoride, KF, were procured from Sigma Aldrich at > 99% purity to prepare the FLiNaK salt with a composition of 46.5 mol% LiF, 11.5 mol% NaF and 42 mol% KF. The powders of LiF, NaF, and KF were weighted according to the eutectic FLiNaK salt composition using an analytical balance with an accuracy of 10^{-5} g. All the FLiNaK salt used in this work is from the same batch procured salt. A prepared FLiNaK in pure nickel crucible was heated to 700°C for 36 hours to examine the content of impurities. The salt sample was dissolved in pure nitric acid and then analyzed using inductively coupled plasma mass spectroscopy. The results showed an impurity level of 7.2 ppm Fe, 4.5 ppm of Cr 1.7 ppm of Ni and 1.1 ppm of Mn. The anhydrous europium fluoride, EuF_3, was procured from Sigma Aldrich at >99.9% purity. 0.3 ± 0.0005 g of EuF_3 was added in the 29.7 ± 0.0015 g of prepared FLiNaK salt yielding to a target concentration of 1 wt% EuF_3 in prepared salt. Then the prepared salt mixture was mixed in a pure nickel crucible and placed inside a Kerr Electro-Melt furnace.

Experiments utilized a three electrode electrochemical cell in the furnace. The working and counter electrodes were tungsten rods, 1mm and 3.97 mm diameter respectively. The reference electrode utilized was a 1mm diameter platinum wire with potential associated to $Pt/PtO_x/O^{2-}$ [2]. All the electrodes were suspended in the salt without touching the wall

of the nickel crucible. The active surface area of the working electrode was determined by the direct measurement of the immersion depth after cooldown as the viscous molten salt adhered on tungsten electrode was solidified as a thin and white coating on the electrode after the removal of electrode from the melt. The measured immersion depth of the tungsten working electrode in the melt varied from 7.56 mm to 8.25 mm for the tests in this work. The tungsten electrode is chosen because tungsten is thermodynamically more stable than the major alloy constituent (e.g., Ni, Fe, and Cr) in the molten fluoride salt [3]. The interesting potential window in this study is between the potassium reduction potential and the oxidation potential of Cr so that the tungsten can be considered as an inert electrode.

Cyclic voltammetry (CV) and chronopotentiometry (CP) were taken using the stated electrochemical cell and a Gamry Instruments Interface 1000 potentiostat/galvanostat. Tests were performed at 650°C, 700°C, and 750°C to characterize the range of temperatures at which an FHR reactor would operate. Prior to each test, the salt was heated inside the glovebox to the desired test temperature (e.g., preheated to 650°C for the test at 650°C)) for a minimum of 8 hours to ensure thermal equilibrium and remove water impurities in the salt. It should be acknowledged that the salt might still contain residual water and oxides impurities as additional purification process such as HF sparging was not performed. At least three replicate tests were carried out to obtain cyclic voltammograms at each temperature. Cyclic voltammograms were obtained at a potential scan rate ranging from 60 to 500 mV/s. The CV was performed starting from the lowest scan rate to higher scan rates, and five cycles of voltammograms were collected at each scan rate. During three of all replicate tests at each temperature, CP was performed to determine the potassium reduction potential on the tungsten electrode (vs. Pt quasi-reference electrode) using the dynamic reference electrode method [4]. A 5 s of current pulse was applied between tungsten working electrode and counter electrode to form a thin potassium layer on working electrode, i.e., reduction of potassium ions from FLiNaK. And the potential of working electrode against Pt reference electrode was monitored with time. A pulse current of 5 s was chosen as recommended by Duran-Klie et al. [4] which is necessary to guarantee a reliable and accurate measurement of the potassium reduction potential but short enough to prevent the modification of the salt composition.

X-ray photoelectron spectroscopy (XPS) was applied to examine the concentration ratio of Eu^{3+}/Eu^{2+} in the melt. As the concentration ratio of Eu^{3+}/Eu^{2+} is temperature dependent in molten fluorides [2,5], the time duration for cooling the XPS salt sample from the test temperature (e.g., 700°C) to the room temperature must be minimized to avoid considerable change of Eu^{3+}/Eu^{2+} ratio during the cooldown. This was done by immersing a cold tungsten coupon in the FLiNaK-EuF_3-EuF_2 melt and stirring it in the melt for seconds. Then the tungsten coupon was pulled out from the melt, and the residual melt adhered on the coupon was solidified as a white layer with some small compressed droplets in about 10 seconds. It took approximately another 30-40 seconds to cool down the sample to room temperature. Then the salt sample was sealed in an argon filled bottle and loaded in the vacuum chamber of PHI VersaProbe III. XPS spectra were acquired using monochromatic Al K-alpha X-ray source (1486.6 eV). All the reported binding energies were calibrated with the adventitious C-C at 284.8 eV.

4.3.2.2. Results and discussion

4.3.2.2.1. Dynamic reference electrode

Due to the sensitivity of redox potential measurements in the nuclear coolant system with potential leakage of fuel and fission products, it is not appropriate to reference against a quasi-reference electrode such as the Pt reference electrode that is sensitive to O^{2-} impurity in the salt. A reference electrode with a well-defined potential is preferred for the redox control management in engineering application. Traditional reference electrodes such as NiF_2/Ni electrode constructed with boron nitride (BN) compartment is challenging due to the long-term compatibility of its membrane/insulating material BN with fluoride salt media. One of the most promising reference electrodes is the dynamic reference electrode (DRE) which applies a sufficiently large pulse current on a solid inert electrode to identify the reduction potential of the salt solvent. Duran-Klie et al. [4] have demonstrated a potassium DRE in FLiNaK. The reduction potential of K^+ is more positive than Na^+ and Li^+ in FLiNaK. By applying a current under a controlled potential range, the potassium ions can be electrodeposited on a tungsten wire, and the redox potential of K^+/K^0 can be captured for a while. This reference potential is well-defined by the Nernst equation as long as the mole fractions of the major salt constituents are known.

A 5-second pulse of 5 mA, 50 mA, 100 mA, 200 mA, and 300 mA current (I) was applied between the tungsten working and counter electrodes respectively. Then the evolution of the open circuit potential (OCP) of the tungsten working electrode against platinum quasi-reference electrode is monitored. Chronopotentiometry data at 650°C, 700°C, and 750°C was acquired, as shown in Figure 4-10. The OCP evolution exists as three distinct zones. In zone I, 5-second current pulse is applied, and the potential of the tungsten electrode becomes more negative because a potassium layer is formed on the tungsten electrode surface due to the reduction of K^+. It is seen that 5 seconds of 5 mA current pulse is insufficient to form a fully covered potassium layer. Above 50 mA, a lower OCP is observed at higher pulse current which is attributed to the ohmic drop in the melt between tungsten working electrode and platinum wire. The electrolyte resistance of the molten FLiNaK salt can be achieved by comparing the potential difference (ΔV) between two applied current pulses. The ratio of $\Delta V/\Delta I$ indicates an electrolyte resistance of 0.34 Ω at 650°C, 0.29 Ω at 700°C and 0.24 Ω·cm^2 at 750°C, respectively. These values are pretty close to the FLiNaK electrolyte resistance determined by the same method. In zone II, the OCP steps up once the current pulse is achieved because the ohmic drop associated with the applied pulse current does not exist. This potential corresponds to the equilibrium potential of K^+/K^0, and will remain constant for a certain time. The time duration of this plateau depends on how much potassium is deposited by the current pulse. In zone III, the OCP increases to its initial value due to the dissolution of the potassium layer on the tungsten electrode. The averaged potential values at the plateau under all tested current magnitudes was considered as the redox potential of K^+/K^0 (vs. Pt). Three replicates were performed for each temperature which showed consistent results. The relative constant potential of the Pt quasi-reference might be attributed to the use of same batch of salt and the well-controlled H_2O and O_2 impurity level in the glove box. The average value of the K^+/K^0 redox potential

in FLiNaK and the standard deviation from replicate tests are given in Table 4-4. In this way, the redox potential measured using a Pt quasi-reference can be converted to the potassium reduction potential in FLiNaK.

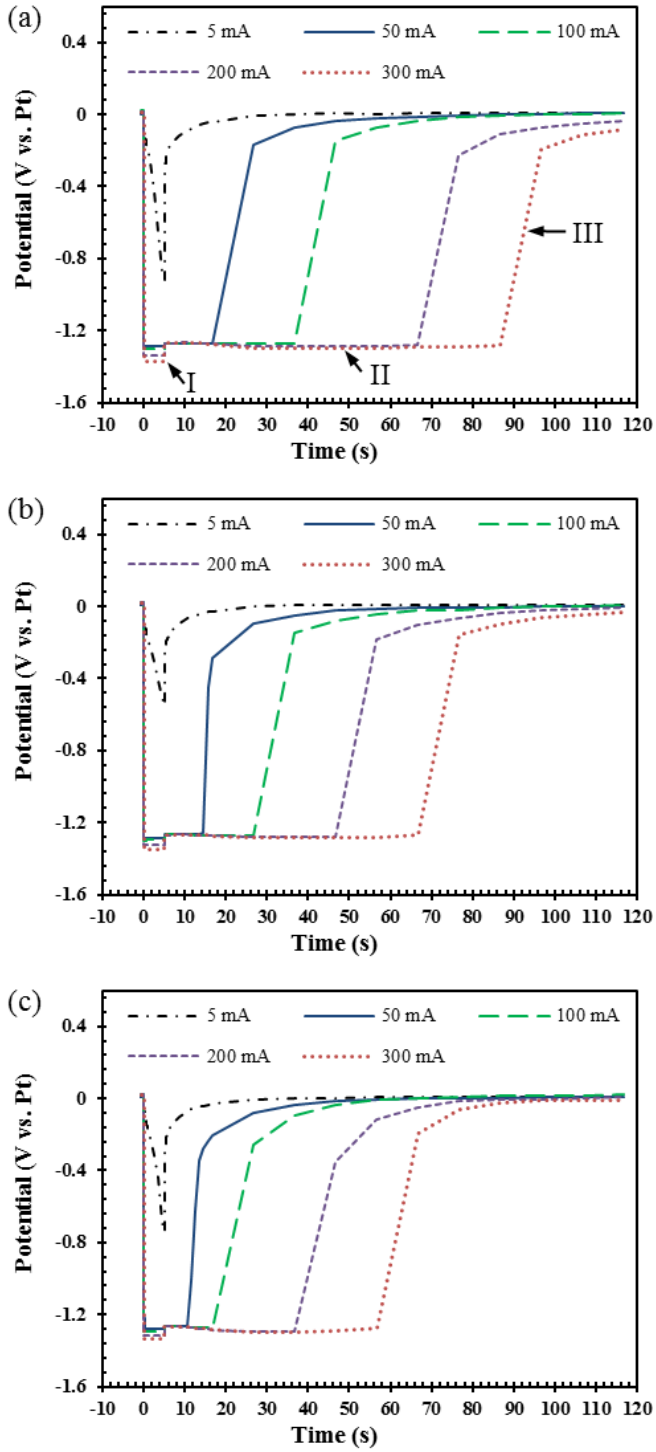

Figure 4-10: Chronopotentiograms giving the potential evolution of the tungsten electrode against Pt wire over time following current pulses at (a) 650°C, (b) 700°C and (c) 750°C.

Table 4-4: Summary of potassium reduction potential in FLiNaK from three replicates at each temperature.

Temperature (°C)	$E^{redox}_{K^+/K^0}$ (V vs. Pt)	Standard Deviation (mV)
650	-1.272	3
700	-1.270	3
750	-1.271	5

4.3.2.2.2. Determining of concentration ratio of Eu^{3+}/Eu^{2+} by CV

An example of a typical cyclic voltammetric curve obtained at a sweep rate of 200 mV/s is shown in Figure 4-11. The tested salts were FLiNaK and FLiNaK with initial addition of 1 wt% EuF_3 before melting. The reference potential has been converted from Pt quasi-reference potential to the redox potential of K^+/K^0 in FLiNaK according to Table 4-4. The pair of intense peaks (R2/O2) around 0 V (vs. K^+/K^0) are attributed to the decomposition of the FLiNaK salt, specifically the reduction of K^+. Similar to Huang et al.'s CV results [5], the R1/O1 peaks located in the potential window of 0.9 - 1.3 V (vs. K^+/K^0) should be attributed to the reduction of Eu^{3+} into Eu^{2+} and oxidation of Eu^{2+} into Eu^{3+} respectively, as expressed by reaction (6). This is further confirmed by the cyclic voltammograms in the same potential window for the FLiNaK melt without the initial addition of EuF_3 which shows only background signals without any redox peaks. A pair of very small peaks R3/O3 are detected near the K^+/K^0 spike. The difference of peak potentials for R3/O3 is about 0.07 V. The corresponding number of exchanged electrons is 2.7 if applying $\Delta E_p = 2.3RT/nF$ that is valid for reversible reaction that has either reactant or product in the salt. Although the origin of the R3/O3 peaks is not clear, it should be attributed to the impurities in the salt rather than the Eu element since they are also observed from the FLiNaK salt without EuF_3 addition. It might be some redox reaction related to O^{2-} or OH^- impurities as HF sparging pretreatment was not performed to remove potential oxides impurities.

$$Eu^{3+} + e^- \leftrightarrow Eu^{2+} \tag{4-38}$$

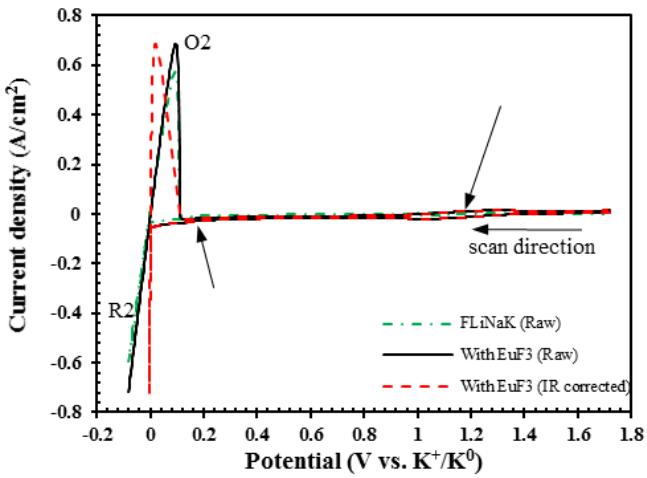

Figure 4-11: Cyclic voltammograms obtained in FLiNaK melt with and without addition of 1 wt% EuF_3 at 700°C, sweep rate of 200 mV/s.

The electrolyte resistance obtained in section 2.2.2.1 was used to correct the potentials for IR drop. A comparison between raw CV plot and IR corrected CV plot is given in Figure 4-11. In this work, only the pair of the Eu^{3+}/ Eu^{2+} redox peaks are interested. Although peak shift is observed for the K^+/K^0 peaks due to the higher magnitude of current, IR correction has very little effect on the shape and magnitude of the europium peaks, as shown in Figure 4-11. This is expected since the magnitude of europium peak current density results in a negligible potential drop (<2 mV). Thus, it is decided to use the raw data rather than the IR corrected data.

Cyclic voltammograms were measured at various scan rates for each temperature of interest to obtain the formal standard potential and concentration ratio of Eu^{3+}/Eu^{2+} in FLiNaK with the addition of 1 wt% EuF_3, as shown in Figure 4-12(a-c). At various scan rates from 60 to 500 mV/s, both the anodic and cathodic peak currents occur at repeatable potentials for all three temperature tested. A reversible reaction's electron transfer rate is faster than its mass transport rate which means that the peak potential will be independent of scan rate. This independence of peak potential with scan rate is exhibited across the scan rate range plotted in Figure 4-12, indicating this couple's reversibility.

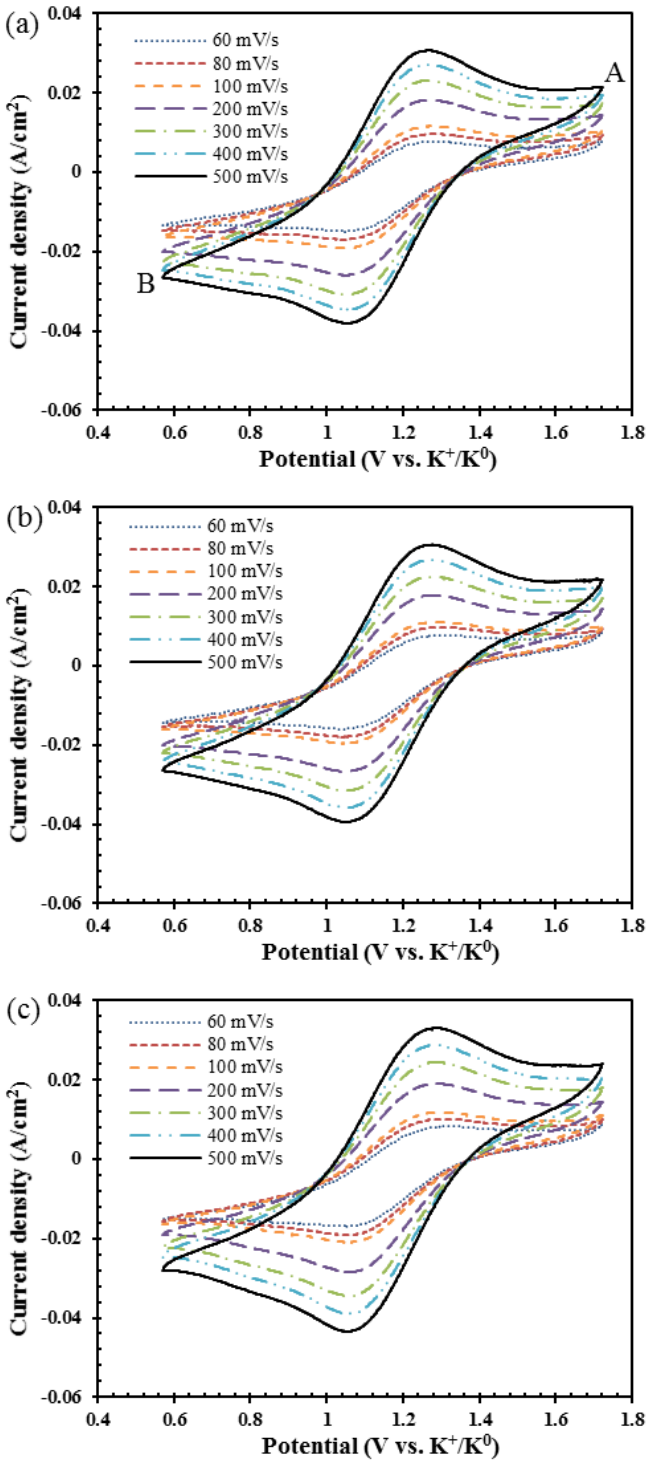

Figure 4-12: Cyclic voltammograms (5th cycle) of the Eu^{3+}/ Eu^{2+} couple in FLiNaK-EuF_3-EuF_2 melt at (a) 650°C, (b) 700°C and (c) 750°C. Potential scans from A to B then back to A.

Cyclic voltammograms (Figure 4-13) were also obtained at various scan rate in FLiNaK without EuF_3 addition to determine the background current. The background current

consists of the charging current, and the faraday current from the redox reactions in the system. The faraday current should be negligible as either the redox reaction of major salt constituents (e.g., K^+/K^0) or the impurities related to R3/O3 peaks occurred at potentials far away from the Eu^{3+}/Eu^{2+} potential window. The charging current is caused by the continuously changing of electrode potential during the potential scan. Figure 4-13 shows the background current increases with scan rate as the magnitude of charging current is proportional to the product of scan rate and double layer capacitance. Depending on the potential scan direction, charging current flows in the anodic or cathodic direction. It is expected the relaxation of charging current occurs when the scan direction switches to the opposite direction, as observed by the exponential evolution of current density at the two ends of the potential window in Figure 4-13. Thus, the linear portion of the background current and its extrapolation were used for the subtraction of background signals from the CV data in Figure 4-12. The peak current densities were then determined at each scan rate. Figure 4-14 shows the good linear correlation between peak current density and the square root of scan rate which further confirmed the diffusion controlled behavior or the reversibility of Eu^{3+}/Eu^{2+} within scan rates of 60-500 mV/s.

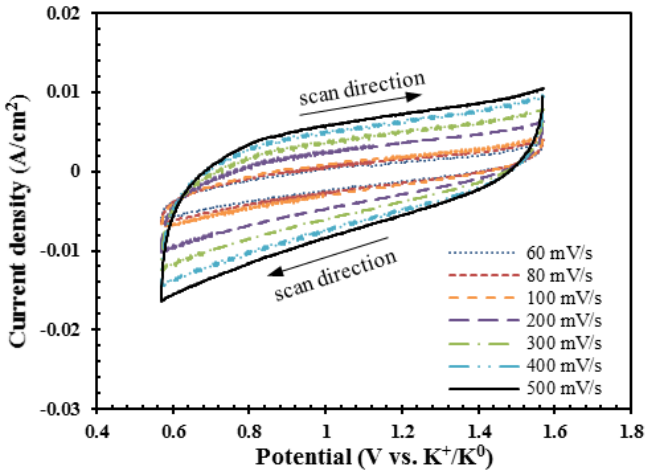

Figure 4-13: Cyclic voltammograms (5th cycle) of FLiNaK melt without EuF_3 addition at various scan rates at 700°C.

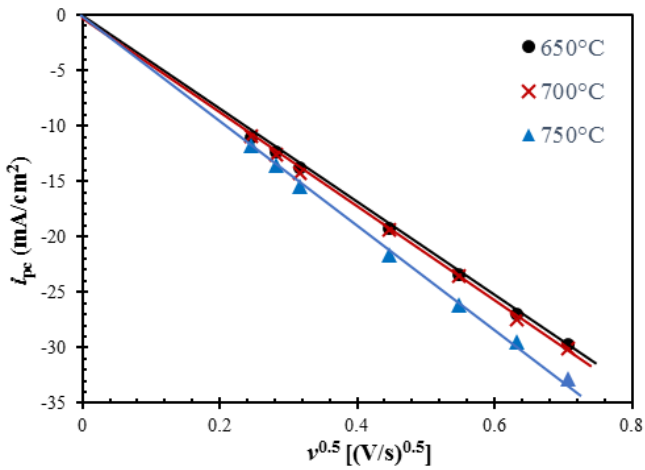

Figure 4-14: Plots of peak current density versus square root of scan rate in FLiNaK-EuF_3-EuF_2 melt.

For the reversible soluble-soluble system, the Randles-Sevcik equation, Eq. (4-39), is typically used to calculate the concentration based on the peak current density from the cyclic voltammogram. The Randles-Sevcik equation was used to calculate the concentration ratio of U^{4+}/U^{3+} from voltammogram during the MSR program at ORNL in 1970s [6]. However, it must be stressed that the Randles-Sevcik equation is valid when only one member (either reactant or product) of a redox couple is present in the electrolyte [7], i.e., either Ox or Red of the redox couple Ox/Red exists in the molten salt. This means the Randles-Sevcik equation is not applicable for the MSR redox buffering system containing both members of the redox couple, e.g., the presence of both $U^{4+}$and U^{3+} in the salt, or presence of both Eu^{3+} and Eu^{2+} in the salt.

$$i_{\mathrm{p}} = AnFC^{b}D^{1/2}\left(\frac{nFv}{RT}\right)^{1/2} \tag{4-39}$$

where A=0.4463; i_{p} is the peak current density, A/cm^2; D is the diffusion coefficient, cm^2/s; C^b is the bulk concentration, mol/cm^3; n is the number of exchanged electrons of the reaction; and v is the scan rate, V/s.

In this study, although only EuF_3 was added in the molten FLiNaK, Eu^{3+} and Eu^{2+} may coexist in the salt. Kuznetsov et al. [8,9] reported both Eu^{3+} and Eu^{2+} were present in the molten chloride salts when only $EuCl_3$ was introduced in the system. The $EuCl_2$ was assumed to be formed during the heat treatment as $EuCl_3$ decomposed to $EuCl_2$ and Cl_2 at temperatures above 300°C according to reaction (4-40). Massot et al. [2] claimed the decomposition of EuF_3 might take place in the LiF-CaF_2 melt in a similar way, as expressed by reaction (4-41). The occurrence of this decomposition reaction was supported by the recent studies from Huang et al. [5] and Wang et al. [10]. The transformation of EuF_3 to EuF_2 was evidenced by the XPS analysis of the FLiNaK-EuF_3 and/or EuF_3 samples before and after melting [5,10]. The presence of Eu^{2+} was also confirmed in our work by XPS analysis. Figure 4-15 shows the high resolution XPS spectra of Eu $3d_{5/2}$ for FLiNaK-EuF_3-EuF_2 melt samples collected at different temperatures. The peak at about 1134 eV is

associated to the EuF_3 while the other peak at about 1124 eV corresponds to EuF_2 [10]. The concentration ratio of Eu^{3+}/Eu^{2+} determined by the ratio of the two peaks' area are 2.16 at 650°C, 2.22 at 700°C, and 2.19 at 750°C.

$$EuCl_3 \leftrightarrow EuCl_2 + \frac{1}{2}Cl_2 \tag{4-40}$$

$$EuF_3 \leftrightarrow EuF_2 + \frac{1}{2}F_2 \tag{4-41}$$

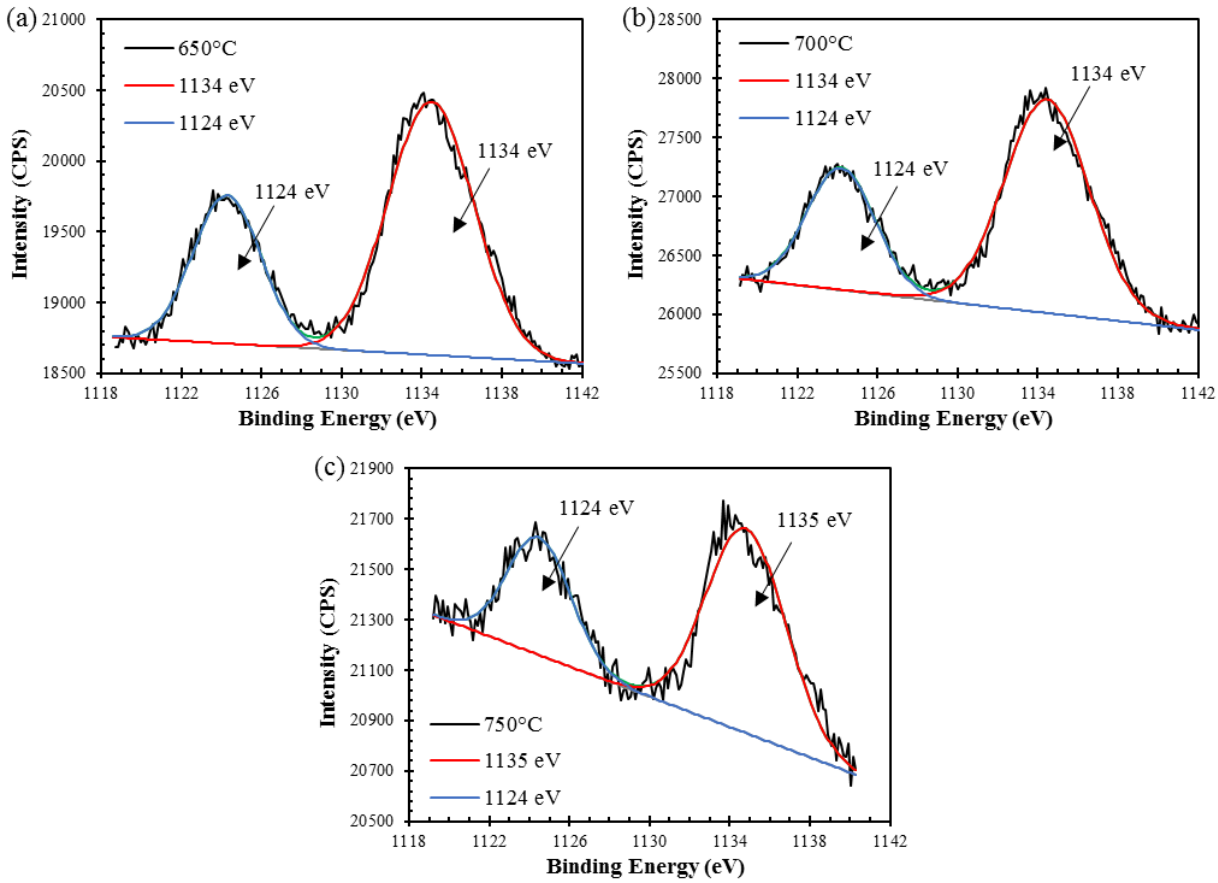

Figure 4-15: XPS spectra of Eu $3d_{5/2}$ of FLiNaK-EuF_3-EuF_2 melt at various temperatures.

To determine the concentrations of Eu^{3+} and Eu^{2+} using CV, the theory developed by Keightley et al. [11] is adopted which is applicable for the reversible cyclic voltammogram when both members of the redox couple are present, e.g., when Eu^{3+} and Eu^{2+} coexist in the salt. In a reversible cyclic voltammogram, the current density during the forward sweep ($\vec{\imath}$) and backward sweep ($\overleftarrow{\imath}$) can be expressed by:

$$\vec{\imath} = nF\left(C_{\mathrm{Red}}^{\mathrm{b}} D_{\mathrm{Red}}{}^{1/2} + C_{\mathrm{Ox}}^{\mathrm{b}} D_{\mathrm{Ox}}{}^{1/2}\right)\left(\frac{\pi n F v}{RT}\right)^{1/2} \chi(\xi;\xi_i) \tag{4-42}$$

$$\tilde{\imath} = nF\left(C_{\mathrm{Red}}^{\mathrm{b}} D_{\mathrm{Red}}{}^{1/2} + C_{\mathrm{Ox}}^{\mathrm{b}} D_{\mathrm{Ox}}{}^{1/2}\right)\left(\frac{nFv}{RT}\right)^{1/2}\left[\chi(2\xi_r - \xi, \xi_i) - \chi(2\xi_r - \xi, \xi_r) - \chi(-\xi, \xi_r)\right] \quad (4\text{-}43)$$

where $\chi\,(x,\alpha) = \frac{\mathrm{d}^{1/2}}{\mathrm{d}x^{1/2}}\frac{1}{2\sqrt{\pi}}\left[\tanh\left(\frac{x+\alpha}{2}\right) - \tanh(\frac{\alpha}{2})\right]$; $\xi = nF(E - E_{1/2})/RT$; $\xi_i = nF(E_i - E_{1/2})/RT$; $\xi_r = nF(E_r - E_{1/2})/RT$; $E_i = E_{1/2} + \frac{RT}{nF}\ln\frac{C_{\mathrm{Ox}}^{\mathrm{b}} D_{\mathrm{Ox}}{}^{1/2}}{C_{\mathrm{Red}}^{\mathrm{b}} D_{\mathrm{Red}}{}^{1/2}}$; E_r is the reversal potential.

If $D_{\mathrm{Ox}}{}^{1/2}/D_{\mathrm{Red}}{}^{1/2}$ is known, the cyclic voltammogram including the peak current densities and the peak potentials at any given ratio of $C_{\mathrm{b}}^{\mathrm{Ox}}/C_{\mathrm{b}}^{\mathrm{Red}}$ can be predicted by Eqs. (4-42) and (4-43). More importantly, the prediction shows the value of $C_{\mathrm{Red}}^{\mathrm{b}} D_{\mathrm{Red}}{}^{1/2}/C_{\mathrm{Ox}}^{\mathrm{b}} D_{\mathrm{Ox}}{}^{1/2}$ solely corresponds to a certain peak potential difference ΔE_{p}between the forward peak and the backward peak regardless of the reversal potential [11]. This means the value of $C_{\mathrm{Red}}^{\mathrm{b}} D_{\mathrm{Red}}{}^{1/2}/C_{\mathrm{Ox}}^{\mathrm{b}} D_{\mathrm{Ox}}{}^{1/2}$ can be determined by the experimental value of ΔE_{p} from the cyclic voltammogram. The value of $\Delta E_{\mathrm{p}} = E_p^a - E_p^c$ was obtained from the measured cyclic voltammogram. The average of ΔE_{p} from all replicate tests are 0.238 ± 0.010 V at 650°C, 0.253 ± 0.010 V at 700°C, and 0.243 ± 0.006 V at 750°C, respectively. The corresponding values of $\frac{nF}{RT}(\Delta E_{\mathrm{p}})$ and $C_{\mathrm{Eu^{2+}}} D_{\mathrm{Eu^{2+}}}{}^{1/2}/C_{\mathrm{Eu^{3+}}} D_{\mathrm{Eu^{3+}}}{}^{1/2}$ for the three replicates at each temperature are listed in Table 4-5.

Table 4-5: Predicted coordinates of cyclic voltammetric peaks and the calculated concentration ratio.

Test #	$\frac{nF}{RT}\Delta E_{\mathrm{p}}$	$\frac{C_{\mathrm{Eu^{3+}}}}{C_{\mathrm{Eu^{2+}}}}\sqrt{\frac{D_{\mathrm{Eu^{3+}}}}{D_{\mathrm{Eu^{2+}}}}}$	$\frac{\lvert i_p\rvert}{C^b}\sqrt{\frac{RT}{n^3F^3vD^b}}$	$\frac{nF}{RT}(E_{1/2} - E_p^c)$	$\frac{C_{\mathrm{Eu^{3+}}}}{C_{\mathrm{Eu^{2+}}}}$
-	2.236	0	0.4463	1.109	-
650°C #1	2.814	1.31	0.5415	1.697	1.21
650°C #2	3.102	2.13	0.5596	1.988	1.96
650°C #3	3.075	2.04	0.5581	1.959	1.88
700°C #1	2.855	1.42	0.5447	1.741	1.29
700°C #2	3.067	2.02	0.5578	1.953	1.83
700°C #3	3.119	2.18	0.5605	2.003	1.98
750°C #1	2.740	1.13	0.5356	1.623	1.08
750°C #2	2.674	0.98	0.5299	1.558	0.93
750°C #3	2.842	1.39	0.5439	1.729	1.33

†Calculated by the determined diffusion coefficient.

The ratio of diffusion coefficients needs to be known to determine the concentration ratio from the CV method. In this work, the concentrations of Eu^{3+} and Eu^{2+} from XPS analysis were used to calculate the diffusion coefficients by the peak current densities using the parameters listed in Table 4-5. The average values of $D_{Eu^{3+}}$ are 1.21 × 10^{-5} cm^2/s at 650°C, 1.37 × 10^{-5} cm^2/s at 700°C, and 1.79 × 10^{-5} cm^2/s at 750°C respectively, while the $D_{Eu^{2+}}$ values are 1.02 × 10^{-5} cm^2/s at 650°C, 1.13 × 10^{-5} cm^2/s at 700°C, and 1.65 × 10^{-5} cm^2/s at 750°C respectively. These numbers are lower than the values predicted by the equations developed by Huang et al. [5] for $D_{Eu^{3+}}$ and $D_{Eu^{2+}}$ in FLiNaK. For example, the $D_{Eu^{3+}}$ predicted by Ref. [5] are 2.59 × 10^{-5} cm^2/s at 650°C, 3.37 × 10^{-5} cm^2/s at 700°C, and 4.29 × 10^{-5} cm^2/s at 750°C. One reason causing the overestimation of diffusion coefficients might be the inappropriate use of Randles-Sevcik equation in Ref. [5]. As shown in Table 4-5, when both Eu^{2+} and Eu^{3+} present in the melt, the parameter A is slightly higher than the 0.4463 in standard Randles-Sevcik equation. The concentration ratio of Eu^{3+}/Eu^{2+} can also be estimated by the value of $C_{Eu^{2+}} D_{Eu^{2+}}{}^{1/2} / C_{Eu^{3+}} D_{Eu^{3+}}{}^{1/2}$ corresponding to the ΔE_p for each test, as listed in the last column of Table 4-5. These numbers are close to the values from XPS analysis, indicating the consistence of the experimental data with the predictions by Eqs. (4-42) and (4-43).

The percent deviations of 14-20% for the concentration ratio obtained from replicate tests are observed in Table 4-5. According to the Nernst equation, the deviation of less than 20% on concentration ratio results in a deviation of less than 14 mV on the calculated redox potential. This number is quite small compared to the adjustable potential window in MSR redox control system. The proposed window for U^{4+}/U^{3+} concentration ratio in MSBR and MSFR are in the magnitude of 10-100 [12,13,14] which corresponds to a potential window of hundreds of millivolts (e.g., U^{4+}/U^{3+} ratio in 10-100 corresponds to a potential window of 203 mV at 750°C). Thus, the accuracy of this method to determine the concentration of redox buffer species such as europium ions should be adequate for redox control. It must be mentioned that the concentration ratio can be calculated from both columns 3 and 4 in Table 4-5.

4.3.2.2.3. Formal standard potential of Eu^{3+}/Eu^{2+}

For reversible systems utilizing linear sweep voltammetry, the formal standard potential can be calculated by the half-wave potential $E_{1/2}$ and the diffusion coefficients: [7]

$$E^* = E_{1/2} + \frac{RT}{nF} ln\left(\frac{D_{Ox}}{D_{Red}}\right)^{\frac{1}{2}} \tag{4-44}$$

$$E_{1/2} = E^\circ + \frac{RT}{nF}\ln\left(\frac{D_{Red}}{D_{Ox}}\right)^{\frac{1}{2}} + \frac{RT}{nF}\ln\left(\frac{\gamma_{Ox}}{\gamma_{Red}}\right) \tag{4-45}$$

where D_{Red} and D_{Ox} are the diffusion coefficients of Eu^{2+} and Eu^{3+}, respectively.

The half-wave potential $E_{1/2}$ can be determined by the difference of the anodic peak potential and cathodic peak potential ΔE_p according to Table 4-5. Comparing the second column with the fifth column in Table 4-5 confirms the value $E_{1/2}$ is not a simple mean of

the anodic peak potential and cathodic peak potential. Then the formal standard potential can be calculated for a given temperature by Eq. (4-44). The results of the three replicates are summarized in Table 4-6:. For the formal standard potentials obtained in this work, the standard deviations from all replicate tests are 6 mV at 650°C, 4 mV at 700°C and 5 mV at 750°C, respectively. The formal potentials of Eu^{3+}/Eu^{2+} in FLiNaK at 550°C form reference [5] and in LiF-CaF_2 (77-33 mol%) salt from reference [2] are also given in Table 4-6. It is seen that, the formal potential (vs. F_2/F^-) increased linearly with the temperature in either FLiNaK or LiF-CaF_2. Although there is no available data in overlapped temperature range to make a solid conclusion, it seems the formal potential of Eu^{3+}/Eu^{2+} (vs. F_2/F^-) increases faster with temperature in LiF-CaF_2 eutectic (increase of 29 mV per 10°C) than in FLiNaK (increase of 11 mV per 10°C) which should be attributed to the difference of activity coefficients in the two salts.

Table 4-6: Summary of formal standard potential from this work and references [2] and [5].

Temperature (°C)	E^* (V vs. F_2/F^-)	Salt	Total concentration of Eu in salt (mol/kg)	Source
550	-3.94 or -3.82†	FLiNaK	0.072	[5]
650	-3.781 ± 0.006	FLiNaK	0.048	This work
700	-3.730 ± 0.004	FLiNaK	0.048	This work
750	-3.677 ± 0.005	FLiNaK	0.048	This work
800	-3.53 ± 0.01	LiF-CaF_2	0.100	[2]
820	-3.46 ± 0.01	LiF-CaF_2	0.100	[2]
840	-3.40 ± 0.01	LiF-CaF_2	0.100	[2]
870	-3.33 ± 0.01	LiF-CaF_2	0.100	[2]

† E^* is -3.82 V versus F_2/F^- if assuming the activity coefficient of NiF_2 in the experimental Ni/NiF_2 reference electrode is 1; E^* is -3.94 V versus F_2/F^- if using the K^+ reduction potential estimated from CV scan as reference.

4.3.2.2.4. Thermodynamic calculation

Corrosion of structural materials in molten salts is an irreversible electrochemical process involving the anodic dissolution of metal (M) and the cathodic evolution of oxidant in the salt:

$$M \rightarrow M^{n+} + ne^- \quad (4\text{-}46)$$

$$Ox + ne^- \rightarrow Red \quad (4\text{-}47)$$

where Ox and Red represent the oxidant and its corresponding reductant, respectively.

To allow the corrosion occur spontaneously, the Gibbs free energy change of the overall corrosion reaction has to be negative. The Gibbs free energy change for an electrochemical corrosion reaction can be expressed as:

$$\Delta G_r = -nF\Delta E \tag{4-48}$$

where ΔG_r is the Gibbs free energy change per mole of reaction, J/mol; $\Delta E = E_{\mathrm{c}}^{\mathrm{redox}} - E_{\mathrm{a}}^{\mathrm{redox}}$; $E_{\mathrm{a}}^{\mathrm{redox}}$ and $E_{\mathrm{c}}^{\mathrm{redox}}$ are the redox potential of the anodic electrode reaction (4-46) and cathodic electrode reaction (4-47) in V, respectively.

If $E_{\mathrm{c}}^{\mathrm{redox}}$ is more positive than $E_{\mathrm{a}}^{\mathrm{redox}}$, i.e., $\Delta G_r < 0$, the metal in molten salt will be corroded spontaneously. The redox potential for the half cell electrode reaction is related to the activities of the involved species according to Nernst equation:

$$E_{\mathrm{a}}^{\mathrm{redox}} = E_{\mathrm{a}}^{\circ} + \frac{RT}{nF}\ln\frac{a_{\mathrm{M^{n+}}}}{a_{\mathrm{M}}} \tag{4-49}$$

$$E_{\mathrm{c}}^{\mathrm{redox}} = E_{\mathrm{c}}^{\circ} + \frac{RT}{nF}\ln\frac{a_{\mathrm{Ox}}}{a_{\mathrm{Red}}} \tag{4-50}$$

where E_{a}° and E_{c}° are the standard electrode potential for reaction (4-46) and (4-47) in V, respectively; a is the activity.

According to Eq. (4-48), if a standard F_2/F^- electrode was selected as the reference, the standard electrode potential of reaction (4-46), $E_{\mathrm{M^{n+}/M^0}}^{\circ}$, can be calculated by the standard Gibbs free energy of formation of $\mathrm{MF_n}$:

$$E_{\mathrm{M^{n+}/M^0}}^{\circ}(\mathrm{vs.\,F_2/F^-}) = \Delta G^{\circ}(\mathrm{MF_n})/nF \tag{4-51}$$

For the fluorides that have higher melting temperature than the eutectic salt temperature, e.g., CrF_2 that has a melting temperature T_{m} of 894°C, the ΔG° at supercooled state rather than the solid state should be used as these fluorides actually present as liquid in the FLiNaK salt. The ΔG° at supercooled state at temperature T is a summation of the ΔG° value at solid state ($\Delta G_{\mathrm{s},T}^{\circ}$) and the Gibbs energy of fusion ($G_{\mathrm{f},T}^{\circ}$) at temperature T. The fusion energy $G_{\mathrm{f},T}^{\circ}$ can be obtained from the following equations:

$$G_{\mathrm{f},T}^{\circ} = H_{\mathrm{f},T}^{\circ} - TS_{\mathrm{f},T}^{\circ} = H_{T,\mathrm{l}}^{\circ} - H_{T,\mathrm{s}}^{\circ} - T(S_{T,\mathrm{l}}^{\circ} - S_{T,\mathrm{s}}^{\circ}) \tag{4-52}$$

$$H_T^{\circ} = H_{T_{\mathrm{m}}}^{\circ} + \int_{T_{\mathrm{m}}}^{T} C_p\, dT \tag{4-53}$$

$$S_T^{\circ} = S_{T_m}^{\circ} + \int_{T_m}^{T} C_p\, dT \tag{4-54}$$

where subscript 's' and 'l' represent the solid and liquid states respectively. The values of H_T°, S_T°, and C_p at both solid and liquid states at various temperatures used in this study are from the database in Outotec HSC Chemistry 6.0.

Then the standard electrode potentials of various M^{n+}/M^0 can be calculated according to Eq. (4-51). If the activity of M^{n+} in the molten salt is known, the redox potential of M^{n+}/M^0 can be obtained from Nernst equation. Figure 4-16 shows the redox potentials of various

redox couples as a function of temperature in fluoride salts. All the standard potentials are calculated based on the ΔG° at liquid or supercooled state except MoF_5, MoF_6, WF_6, and HF which are stable as gas at temperatures of interests. The solid line represents the stability of M^{n+} whereby the metal M dissolves and equilibrates with an $a_{M^{n+}}$ of 10^{-6}. At the potentials below the solid line, the metal can be expected thermodynamically not to corrode, i.e., the maximum molar fraction of dissolved M^{n+} in molten salt will be less than 10^{-6} if assuming the activity coefficient of M^{n+} is 1. For the oxidants in the salts, the redox potentials of major salt constituents such as K^+ and impurity HF are displayed as dotted lines in Figure 4-16: . The activity coefficients of KF, NaF and LiF in FLiNaK salt were assumed to be 1 since FLiNaK salt is totally dissociated and no complexes are formed. For FLiBe, the activity due to chemical reactions must be taken into account considering the formation of a chemical compound $LiBeF_3$ [15]. In this work, the activity coefficients of BeF_2 and LiF in FLiBe are calculated according to the correlations provided by Hitch and Baes [16].

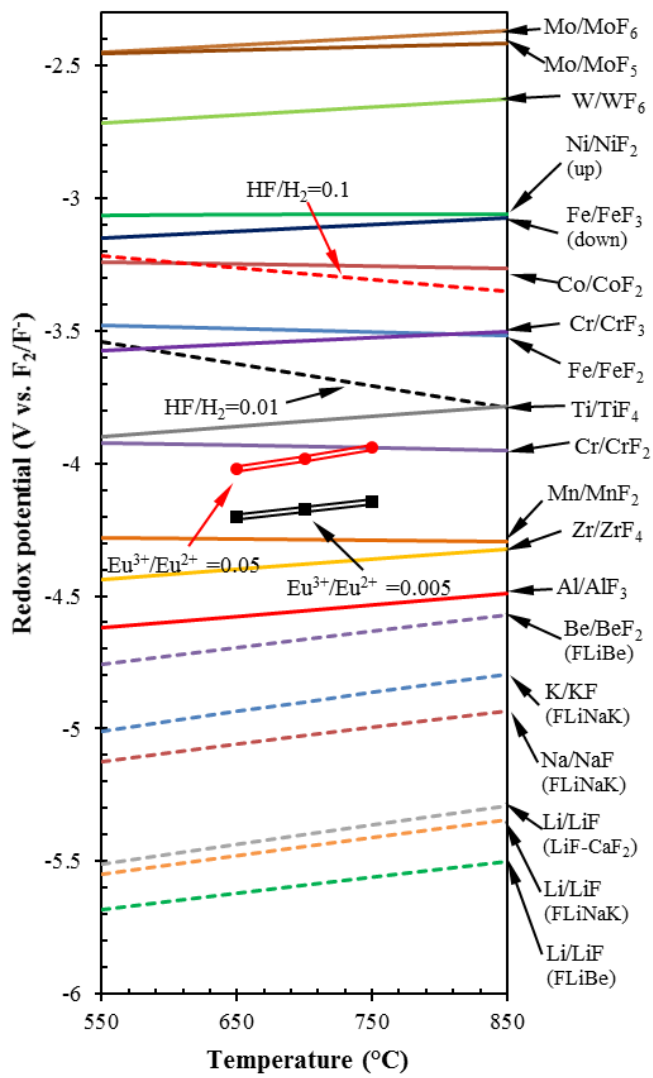

Figure 4-16: Redox potential versus temperature for various redox couples in FLiNaK and FLiBe salts. Solid line: metal dissolution at limit activity of 10^{-6}; Dotted line: reduction of oxidants. HF/H_2=0.1: a mole ratio of HF/H_2=0.1 at 1 atm total pressure. Double solid line: redox potential calculated based on the measured formal potentials.

Thermodynamically, the metal with lower $E^{\mathrm{redox}}_{\mathrm{M/M^{n+}}}$ than the redox potential of an oxidant will be corroded until the concentration of dissolved M^{n+} elevates to the equilibrium level where $E^{\mathrm{redox}}_{\mathrm{M/M^{n+}}} = E^{\mathrm{redox}}_{\mathrm{Red/Ox}}$. It is also indicated that Cr is most corrodible amongst the major alloy elements (Ni, Fe and Cr) as the metal with lower $E^{\mathrm{redox}}_{\mathrm{M/M^{n+}}}$ has a higher tendency for corrosion. This explains the formation of Cr depletion zones and the voids which are commonly observed for Cr containing iron- and nickel- base alloys in molten fluoride salt [17,18]. Figure 4-16 also shows that trace amounts (e.g., activity of 10^{-6}) of metallic impurities such as NiF_2 and FeF_3 can oxidize both Cr and Fe, while FeF_2 and CrF_3 are able to cause the selective corrosion of Cr. These impurities' effects on molten fluoride corrosion have been observed from other researchers' experimental results [19,20,21].

The double solid lines are the redox potentials of Eu^{3+}/Eu^{2+} calculated based on the formal potentials given in Table 4-6. Using the redox potential of Cr/CrF_2 as the limiting baseline, Figure 4-16 has shown that a Eu^{3+}/Eu^{2+} ratio of less than 0.05 will result in a redox potential less than that of chromium across the studied temperature range. For comparison, U^{3+}/U^{4+} ratio between 0.007-0.02 was used to maintain an adequate redox potential for MSRE [13], and U^{3+}/U^{4+} ratio of 0.01-0.1 was proposed for redox control in recent MSFR [14]. This indicates that a ratio of less than 0.05 for the europium couple is a realistic ratio to maintain for an electrochemical couple in an industrial fluoride molten salt application.

Therefore, Eu^{3+}/Eu^{2+} is a promising redox buffering agent for redox control in fluoride molten salt, specifically in the secondary coolant of a molten salt reactor. According to the formal standard potential measured by cyclic voltammetry, the limiting Eu^{3+}/Eu^{2+} concentration ratio can be determined to prevent the corrosion of the least noble alloy constituent such as chromium in the container material. In the presence of oxidant impurities, it is expected that most of these impurities will be consumed by the oxidation of Eu^{2+} into Eu^{3+}. The resulted change of concentration ratio of Eu^{2+} and Eu^{3+} can be characterized by the ΔE_{p} in cyclic voltammogram. The raised Eu^{3+} concentration due to oxidant impurities can be reduced back to Eu^{2+} by contacting a strong reductant metal such as beryllium in FLiBe salt. Thus, the redox potential can be controlled. The accuracy of redox potential measurement relies on a stable reference electrode with well-defined reference potential. This study also shows a quasi-reference electrode with potential calibrated using DRE method can be used as a reliable reference electrode for redox potential measurement.

4.3.3. Kinetic Modeling of Molten Salt Corrosion and Redox Control

4.3.3.1. Kinetic model for corrosion in molten fluoride salts

The rate for an electrode reaction can be represented by the current density according to the Faraday's law. According to the mixed potential theory [22], corosion occurs at the corrosion potential E_{corr} where the net current for all electrode reactions on the metal surface is zero. At this potential, the electrode reactions for both metal oxidation and oxidant reduction are driven by the potential differences between the corrosion potential and their corrsponding equilibrium potentials. With the assumption of no mass-transfer effect, the relation of current density and potential for an electrode reaction is characterized by the Butler-Volmer equation [7]:

$$i = i_0 \left\{ \exp\left[\frac{(1-\alpha)nF}{RT}\eta\right] - \exp(-\frac{\alpha nF}{RT}\eta) \right\} \tag{4-55}$$

where i is current density, A/cm^2; i_0 is the exchange current density, A/cm^2; α is the charge transfer coefficient; overpential $\eta = E - E^{\mathrm{eq}}$; E and E^{eq} are the electrode potential and the equilibrium potential respectively, V.

At the corrosion potential, the rates of the reverse reactions for both the metal dissolution and oxidant reduction are typically negligible. This leads to the elimination of the second exponential term in Eq. (4-55) for metal dissolution as well as the first exponential term for the reduction of oxidants. The reduction rate of an oxidant can be limited by its mass-transfer rate from the bulk solution to the metal surface, i.e., the oxidant in the solution adjacent to the metal surface is depleted by the faster charge-transfer rate. In such situation, the cathodic current density i_{c} representing the reduction rate of oxidant can be expressed as:

$$i_{\mathrm{c}} = -i_{\mathrm{c0}} \frac{c_{\mathrm{Ox}}^{\mathrm{s}}}{c_{\mathrm{Ox}}^{\mathrm{b}}} \exp(-\frac{\alpha_{\mathrm{c}} nF}{RT}\eta_{\mathrm{c}}) \tag{4-56}$$

where c^{s} and c^{b} represent the concentration on the electrode surface and in bulk solution respectively, mol/cm^3.

By considering $i_{\mathrm{c}} = nFk_{\mathrm{m}}\left(c_{\mathrm{Ox}}^{\mathrm{b}} - c_{\mathrm{Ox}}^{\mathrm{s}}\right)$ and the definition of the limiting current density $i_{\mathrm{L}}^{\mathrm{Ox}} = nFk_{\mathrm{m}}c_{\mathrm{Ox}}^{\mathrm{b}}$, the concentration ratio can be correlated with the limiting current density:

$$\frac{c_{\mathrm{Ox}}^{\mathrm{s}}}{c_{\mathrm{Ox}}^{\mathrm{b}}} = \frac{i_{\mathrm{L}}^{\mathrm{Ox}} - i_{\mathrm{c}}}{i_{\mathrm{L}}^{\mathrm{Ox}}} \tag{4-57}$$

Insertion of Eq. (4-57) in Eq. (4-56) derives the following expression for the reduction rate of oxidant when the mass-transfer effect is involved:

$$i_{\mathrm{c}} = -\frac{i_0 \exp(-\frac{\alpha nF}{RT}\eta)}{1 - \frac{i_0}{i_L^{\mathrm{Ox}}}\exp(-\frac{\alpha nF}{RT}\eta)} \tag{4-58}$$

Rather than the homogeneous dissolution, the structural alloys in molten fluorides and chlorides typically suffered from the selective dissolution of the less noble element Cr, as observed from the experimental results. This can be interpreted by the schematic simulation of corrosion of alloys in molten fluoride salts at 700°C as shown in Figure 4-17. Three model alloys 71Fe-17Cr-12Ni, 73Ni-17Cr-10Fe, and 71Ni-16Mo-7Cr-5Fe that have similar contents of major alloying elements as stainless steel 316L, Inconel 600, and

Hastelloy N were chosen. The current-potential curves for the electrode reactions were calculated by Eqs. (4-55) and (4-58). In the simulation, the equilibrium potentials of Cr(II)/Cr, Fe(II)/Fe, and Ni(II)/Ni on the alloys were calculated based on the formal potential values reported in FLiBe [23] and mole fractions of 10^{-4} for Cr(II) and 10^{-5} for Fe(II) and Ni(II) cations in the molten salt. By considering the correlation $i_0 = nFk^0 {C^{\mathrm{b}}_{\mathrm{M(n)}}}^{1-\alpha} {X_{\mathrm{M}}}^{\alpha}$ [7], the exchange current densities of Cr(II)/Cr and Fe(II)/Fe at the simulated cation fractions were calculated by the reaction rate constant k^0 derived from the i_0 and α values measured in FLiNaK [24]. The value of k^0 for Ni(II)/Ni was assumed equal to Fe(II)/Fe and an α value of 0.5 was used. The dissolution of molybdenum was considered negligible. The reduction kinetics of an intrinsic oxidant U(IV) redox in the fuel salt was simulated at a U(IV)/U(III) concentration ratio of 5000 with a total uranium concentration of 0.13 mol%. The current-potential curve was then calculated based on the formal potential of U(IV)/U(III) given in Ref. [23], and the assumptions of α = 0.5 and k^0 = 10^{-3} cm/s as estimated in molten chloride [25]. The reduction kinetics of U(IV) was assumed to be the same on the three model alloys, which in fact may vary with the materials and the surface conditions. The oxidation kinetics of U(III) and Ni(II) were not plotted in Figure 4-17 as they act as oxidants. The maximum transfer rates of metal cations to alloy surface, i.e., the limiting current densities i_{L}, at simulated flow velocity of 3 m/s and 0.1 m pipe diameter were calculated by $Sh = \frac{k_{\mathrm{m}}L}{D} = \mathrm{A}\, Re^{\alpha} Sc^{\beta}$ using the physical properties of FLiBe [26] and the reported diffusion coefficients for related cations [27,28,29].

The corrosion potentials at zero net current are indicated by the horizontal lines in Figure 4-17. As shown in Figure 4-17(a–c), the corrosion of three model alloys in the simulated condition are predominated by the dissolution of Cr. Negligible corrosion of iron is expected for the two modeled Ni-based alloys. Iron dissolution is observed for modeled Fe-based alloy (Figure 4-17a) but remains nearly two orders of magnitude smaller than the chromium dissolution rate. Fe-based alloy 71Fe-17Cr-12Ni and Ni-based alloy 73Ni-17Cr-10Fe with same Cr content show similar Cr dissolution rate of ~9.6 μA/cm^2, while for lower Cr content alloy 71Ni-16Mo-7Cr-5Fe it is decreased by 45%. It seems that the corrosion resistance of alloy is primarily determined by the content of the least noble element Cr in the alloy rather than the base metal at simulated redox conditions. However, if significant amounts of oxidizing impurities such as water, HF, or Ni ions presents in the salt, iron content may become important as well because corrosion of alloys may occur at higher potentials where rate of iron dissolution will approach chromium dissolution. In this simulation, the nickel ion concentration is very low (10^{-5} mole fraction) and its exchange current density is much smaller compared to U(IV)/U(III). Hence, the contribution of Ni(II) reduction to Cr dissolution is much less than the reduction of U(IV) although Ni(II) is thermodynamically more oxidizing.

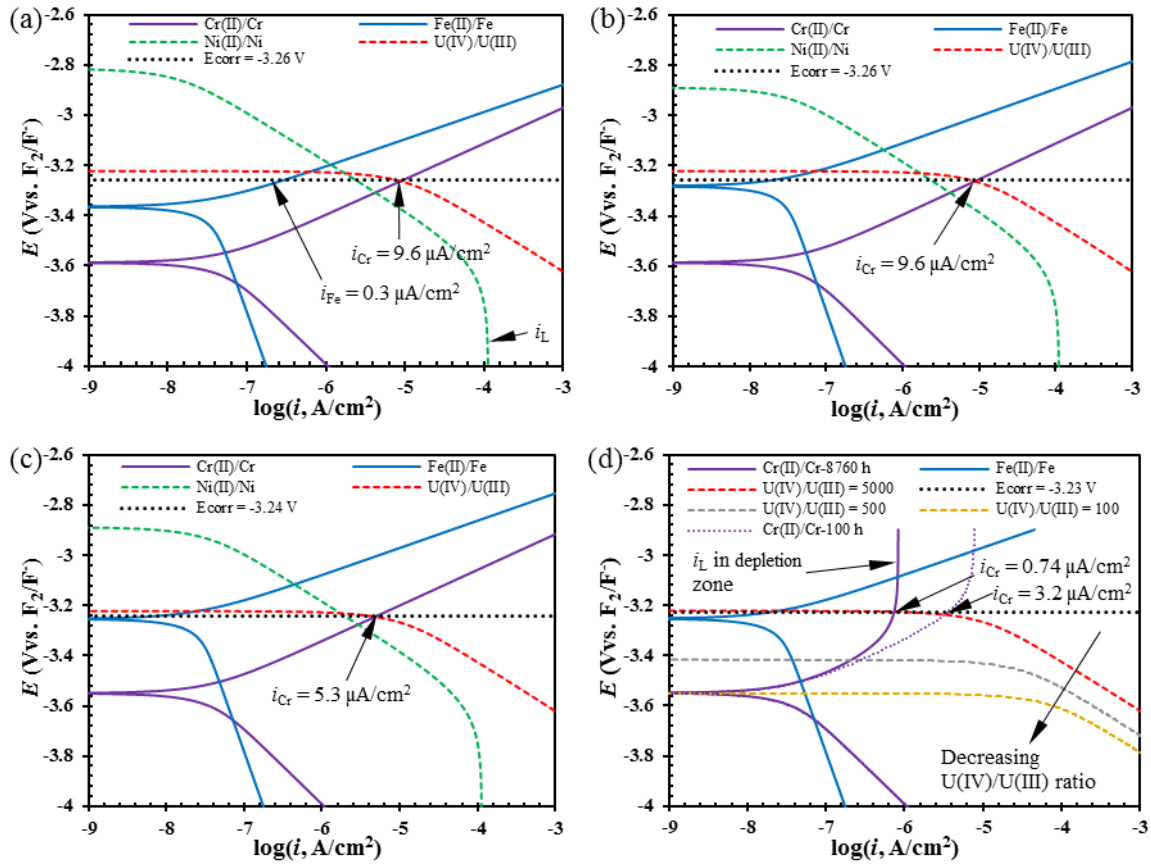

Figure 4-17: Schematic polarization curves for alloy corrosion in molten fluoride salts at 700°C (a) 71Fe-17Cr-12Ni alloy, (b) 73Ni-17Cr-10Fe alloy, (c) 71Ni-16Mo-7Cr-5Fe alloy, (d) 71Ni-16Mo-7Cr-5Fe alloy after 1 year of Cr selective dissolution.

As the corrosion of alloy is predominated by the selective dissolution of Cr, the depletion of Cr in the alloy region near the alloy/molten salt interface is expected. The Cr depletion zone in the alloy will grow deeper with time by the outward diffusion of Cr. The increase of Cr depletion layer thickness will result in the lower diffusion rate of Cr from the alloy matrix to the alloy/molten interface, thus limiting the Cr dissolution rate. Similar to the diffusion of ions in the molten salt, the limiting current density representing the maximum diffusion rate of Cr in the alloy matrix can be defined by [30]:

$$i_{\mathrm{L}}^{\mathrm{M}} = nFc_{\mathrm{b}}^{\mathrm{M}}D_{\mathrm{eff}}^{\mathrm{M}}/\delta_{\mathrm{M}} \tag{4-59}$$

where $i_{\mathrm{L}}^{\mathrm{M}}$ is the maximum diffusion current density of M in the alloy, A/cm²; $c_{\mathrm{b}}^{\mathrm{M}}$ is the concentration of M in the bulk alloy, mol/cm³; δ_{M} is the diffusion length, cm; $D_{\mathrm{eff}}^{\mathrm{M}} = D_{\mathrm{tra}}^{\mathrm{M}}(1-f) + D_{\mathrm{int}}^{\mathrm{M}}f$ [31] is the effective diffusion coefficient of M in the alloy, cm²/s; $D_{\mathrm{tra}}^{\mathrm{M}}$ and $D_{\mathrm{int}}^{\mathrm{M}}$ are the transgranular and intergranular diffusion coefficients respectively; and f represents the fraction of diffusion sites in the grain boundaries.

The effective diffusion coefficient strongly depends on the grain size. As $D_{\mathrm{int}}^{\mathrm{M}}$ is normally 10^4-10^6 times higher than $D_{\mathrm{tra}}^{\mathrm{M}}$ [31], the effective diffusion coefficient can be lowered by

increasing the size of grain, i.e., minimizing the grain boundaries [31,32]. The estimated effective diffusion coefficient of Cr in the Hastelloy N is 2.51×10^{-15} cm^2/s [33] or 8.72×10^{-15} cm^2/s [34] at 700°C. The value for Fe in Hastelloy N is about double of Cr, i.e., 5.56×10^{-12} cm^2/s for Fe diffusion compared to 2.81×10^{-12} cm^2/s for Cr at 850°C [35]. The value of 2.51×10^{-15} cm^2/s for Cr diffusion will be used for 71Ni-16Mo-7Cr-5Fe model alloy in the later simulation.

The diffusion length in Eq. (4-59) can be conservatively estimated by $D_{\mathrm{eff}}^{\mathrm{M}}$ and time t [32,33]:

$$\delta_{\mathrm{M}} = \sqrt{D_{\mathrm{eff}}^{\mathrm{M}} t} \tag{4-60}$$

Then the anodic dissolution rate of the less noble metal alloy element considering the diffusion through the depletion zone can be obtained:

$$i_{\mathrm{a}} = \frac{i_0 \exp\left[\frac{(1-\alpha)nF}{RT}(E-E^{eq})\right]}{1+\frac{i_0}{i_L^M}\exp\left[\frac{(1-\alpha)nF}{RT}(E-E^{eq})\right]} \tag{4-61}$$

Figure 4-17d shows the simulated corrosion kinetics of 88Ni-7Cr-5Fe with a Cr depletion zone at 700°C. The limiting current density for Cr diffusion through the depletion zone was calculated according to Eqs. (4-59) and (4-60) at two exposure durations. As shown in Figure 4-17d, the limiting current density decreased with time, significantly slowing down the Cr dissolution rate at 8760 h (i.e., one year). The initial Ni(II) impurity in the salt should be exhausted and was not considered at 8760 h. The indicated Cr corrosion current density after one year was decreased by seven times compared to its initial condition without depletion zone (Figure 4-17c). This is attributed to the Cr depletion effect which can also be understood by considering the following equation for selective dissolution of alloying element $i = nFk_0\exp\left[X_{\mathrm{Cr}}^{\mathrm{S}}\frac{(1-\alpha)nF}{RT}(E-E^*)\right]$ [7]. It is obvious that the Cr depletion decreases the Cr atoms on the alloy surface $X_{\mathrm{Cr}}^{\mathrm{S}}$, resulting in the decrease of Cr dissolution rate. It should be mentioned that the metal dissolution is normally predominated by the dissolution of kink atoms as their removal requires much less activation energy than terrace atoms. However, the dissolution of atoms from terrace sites may become considerable when the dissolution rate of kink atoms is limited by the diffusion rate through the depletion zone [36]. The other reason that can further decrease the corrosion rate is the decrease of U(IV)/U(III) concentration ratio with time due to consumption of U(IV) ions. As shown in Figure 4-17d, the dissolution of Cr in the alloy will be decreased with the decrease of U(IV)/U(III) concentration ratio. At U(IV)/U(III) ratio below 100, the redox potential will be balanced with Cr(II)/Cr, indicating the termination of corrosion. However, if the dissolved Cr(II) is continually deposited at cold sections of the coolant loop, thermal gradient-driven corrosion will occur at hot sections. Regardless of the simplification of the above corrosion simulation, the predictions indicate an initial corrosion rates of ~50 – 110 μm/year which are in the same order of magnitude with the test results of 300 series stainless steels and Inconel alloys in fluoride fuel salts with initial U(IV)/U(III) concentration ratio of ~5×10^3 – 10^4 [37,38]. The corrosion rates of Hastelloy N determined from ORNL's loop tests were about 0.5 – 2.2 μm/year in the time scale of 10^3

– 10^4 h [37,38], which are lower than the predicted value (~8 μm/year) in Figure 4-17d. This might be due to the decrease of U(IV)/U(III) concentration ratio with time in the loop tests.

4.3.3.2. Kinetic consideration of redox control effects

Similarly, in a redox control system, the evaluation of the actual corrosion inhibition effects should also consider the kinetic factors. Although introducing a reducing redox buffer RA^{k+}/RA^{j} seems thermodynamically favorable to limit the concentration of the dissolved corrosion products in the melt, the kinetic factors must be considered and might be more important. For example, the influence of RA^{k+}/RA^{j+} to reaction (4-25) could be very limited if the two RA^{k+}/RA^{j+} related reactions (4-26) and (4-27)are relatively slow. Moreover, corrosion is an irreversible electrochemical process before reaching such equilibrium. Therefore, it is always valuable to consider the effects of redox control on metal corrosion from the kinetics aspect. Figure 4-18 shows the kinetics of reactions occurring on a corroded metal surface in a redox control system that contains a metal M, an oxidizing impurity Ox, and a redox buffering agent RA^{k+}/RA^{j+}. All electrochemical parameters except the exchange current density of RA^{k+}/RA^{j+} are the same in Figure 4-18a and b. The corrosion potential where the net current is zero is indicated by the horizontal line. It is seen that the inhibition of corrosion by introducing RA^{k+}/RA^{j+} with lower i_0 in the system is very limited. By increasing the i_0 of RA^{k+}/RA^{j+} (Figure 4-18b), the negative shift of corrosion potential becomes more pronounced. At this corrosion potential, oxidation rate of RA^{j+} is several orders of magnitude higher than the dissolution rate of metal M. This means most oxidants will be consumed by the oxidation of RA^{j+} rather than the corrosion of metal. In other word, RA^{j+} acts as a sacrificial material to protect the metal. In addition to the exchange current density, charge-transfer coefficient and diffusion coefficient also affect the sacrificial effect of redox buffers. Back to the thermodynamic consideration, the redox potential of RA^{k+}/RA^{j+} should be controlled below the oxidation potential of M to avoid the corrosion by RA^{k+} after the consumption of the oxidizing impurities. Therefore, the redox control system requires a redox buffer RA^{k+}/RA^{j+} with higher i_0 and lower redox potential. The control of the redox potential can be performed by adjusting the concentration ratio of RA^{k+}/RA^{j+} which may change with time due to the reaction with oxidants in the molten salt.

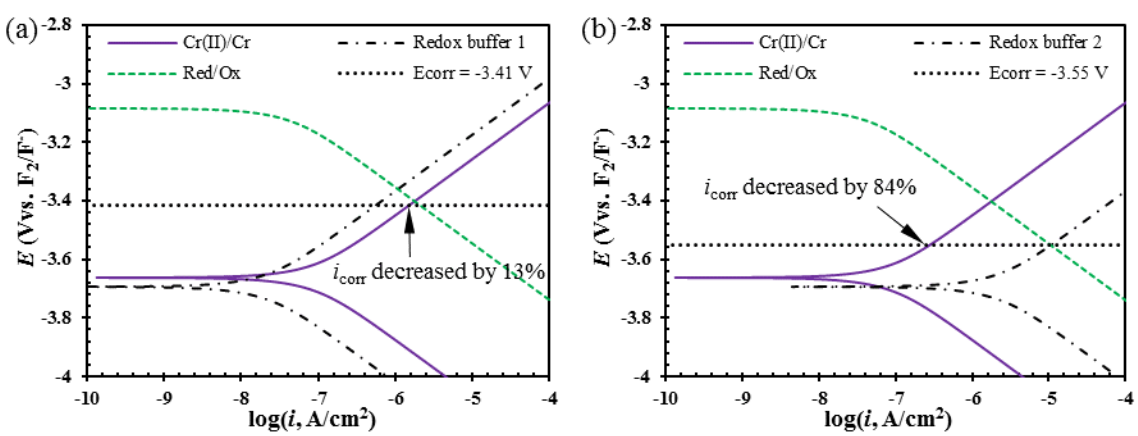

Figure 4-18: Schematic polarization curves for chromium corrosion in the presence of a redox buffer with (a) low $\boldsymbol{i_0}$ and (b) high $\boldsymbol{i_0}$, respectively.

4.3.4. Electrochemical Sensor

4.3.4.1. Sensor Design

One of the goals of this study is to implement the results of the reference electrode investigation to a full electrochemical sensor design which could be employed in an industrial molten salt application such as the FHR. This proposed sensor must be capable of making accurate and precise measurements while maintaining sufficient durability and service life. Design of the sensor cell is performed under the assumption that only a small rod/wire will be used as the reference electrode based on the results discussed prior. An important quality which is considered as the starting point of design is the determination of the electrode's surface area. In the studies described above, the immersion depth of the electrode is measured using a ruler as indicated by the solidified salt. Inaccurate quantification of this immersion depth directly relates to less accurate calculations. This method is also problematic because it prevents real time calculations from being made, negating the purpose of the sensor in the first place. Fixing the working electrode's surface area prior to the sensor insertion is critical to ensuring the desired function and performance. *Figure 4-19* displays a designed component which can achieve this by constraining the exposed electrode depth. The working, counter, and reference electrodes can be inserted into the through holes which correspond to their particular diameters. This component will need to electrically insulate each electrode from each other. This requirement eliminates the use of metallic materials which can withstand fluoride molten salt environment such as a stainless steel or nickel based alloy. Boron nitride is a candidate for this purpose since this ceramic has low electrical conductivity and high durability in low impurity fluoride molten salts.

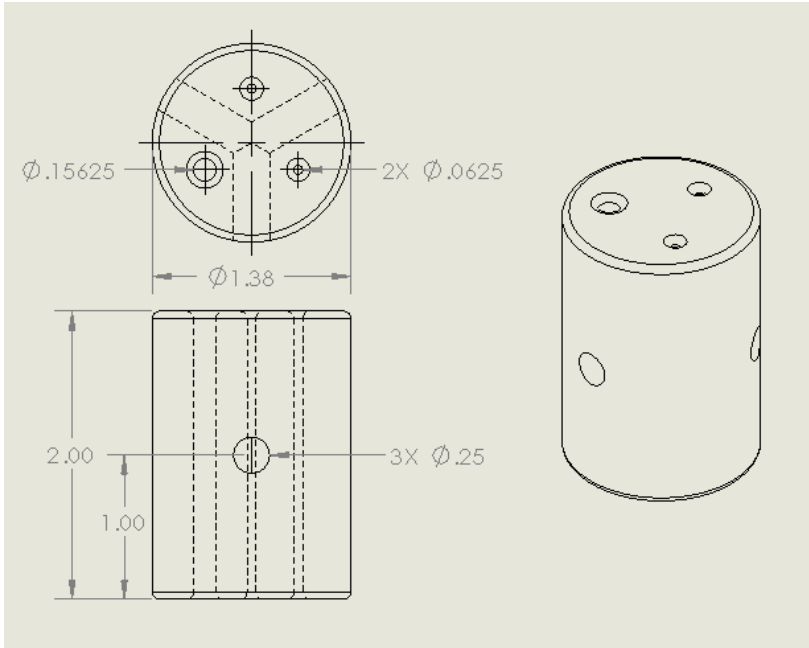

Figure 4-19: Electrochemical sensor housing dimensioned drawing

A high purity boron nitride such as Saint-Gobain's AX05, which does not contain any oxide binders, is selected here having a thermal expansion coefficient of 3.0E-6 m/m-K. Metals such as tungsten and platinum have thermal expansion coefficients of 4.5E-6 and 9E-6 m/m-K respectively [45, 46]. At high temperatures, the thermal expansion coefficients difference will limit any existing gap between the electrode and the boron nitride hole, serving to protect the known immersion depth of the electrodes. The electrodes are prevented from slipping through the housing component by brazing of the electrode with a nickel or stainless steel bushing. This bushing fixes the electrode's vertical position and allows for desired electrical connections to be made to each electrode either by another brazing process or a simple clip. The brazing material must be compatible with the high operating temperatures, possibly nickel, platinum, or gold.

The sensor assembly, Figure 4-20, will be inserted into the molten salt to a level which completely immerses the exposed electrode length. In order to physically accomplish this, the sensor may need to be lowered some distance from an access port, likely flanged. Figure 31 depicts its interface with a 1.25-inch Schedule 40 pipe with a Class 300 flanged connection. This flanged pipe is to be constructed out of the same structural materials which will be utilized for the FHR, likely Hastalloy-N. Three metallic dowels which possess a nominal fit with holes in the pipe and sensor housing maintain the sensor's position inside the end of the pipe. These dowels can also be welded to the pipe for robustness. At the high operating temperature, a nominal fit at room temperature will create a slight interference fit because of the difference in the metal and ceramic thermal expansion coefficients. The pipe length can be varied depending on the specific molten salt surface level of the tank or coolant loop for which measurements are desired. The specific dimensions noted in these figures were specified to interface with a 2-inch diameter

flanged access port for the Liquid Salt Testing Loop's sump tank at ORNL, however the dimensions can be altered as needed to fit any given access port or insertion point. This design can easily be utilized in either stagnant or flowing conditions.

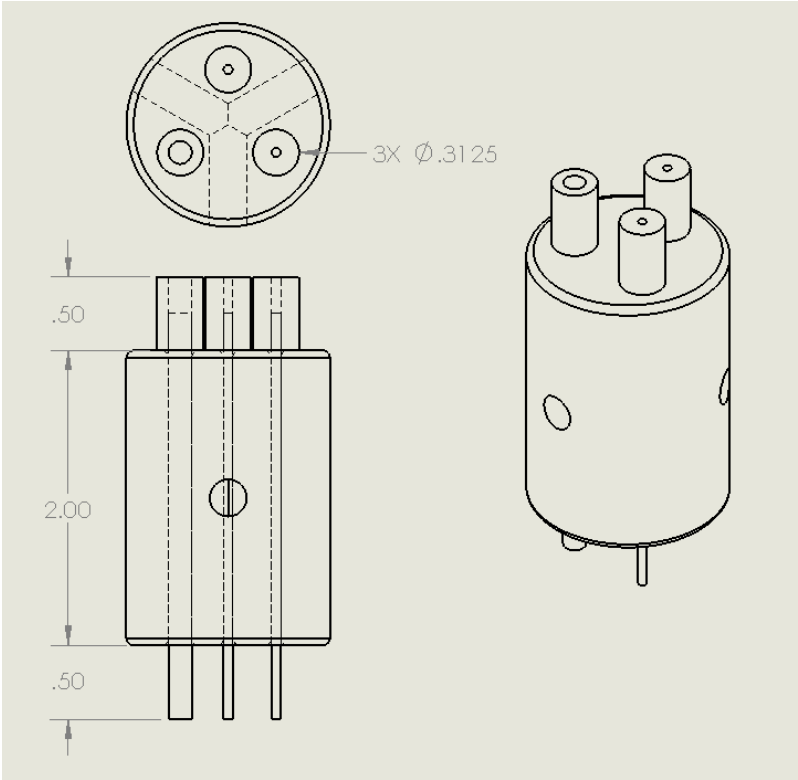

Figure 4-20: Drawing of the complete sensor assembly.

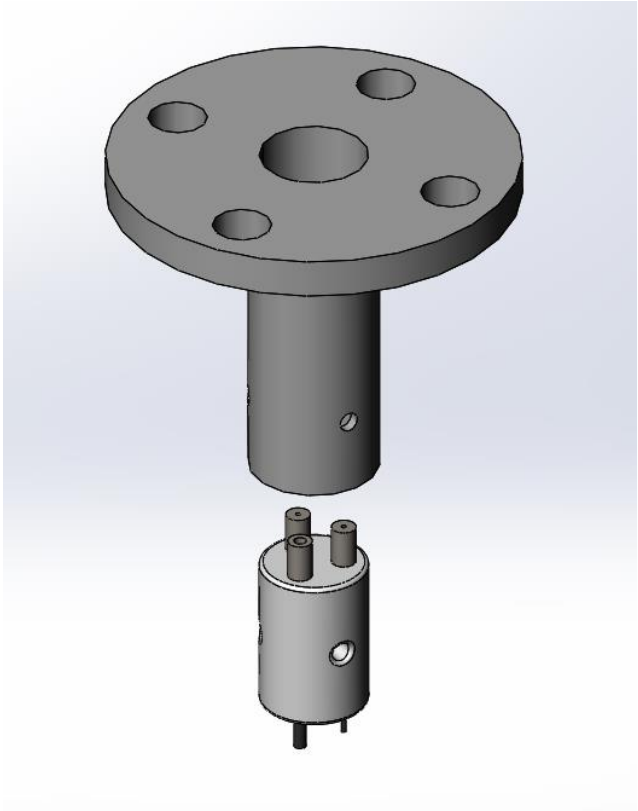

Figure 4-21: Exploded view of the sensor assembly and flanged connection.

Use of the platinum quasi-reference electrode for cyclic voltammetry measurements has allowed for the characterization of the europium(III)/europium(II) standard apparent potential in FLiNaK at 650-750°C. This newly identified information is consequential because it has allowed for a thermodynamic study whose results clearly characterize the equilibrium potential of a variety of redox couples which may be present in a fluoride molten salt. Knowledge of the europium couple's apparent standard potential is able to fully describe its redox potential as a function of temperature and concentration. Assembling this information provides the determination that a Eu^{3+}/Eu^{2+} concentration ratio of lower than 0.05 is sufficient to inhibit corrosion of even a material's most easily oxidized metal, chromium. A concentration ratio of 0.05 is in alignment with the U^{3+}/U^{4+} ratio which the MSRE demonstrated for redox control proving the feasibility of using the Eu^{3+}/Eu^{2+} couple for redox control. With the application of the full sensor design presented, additional redox couples and molten salt media can be investigated with the methods utilized in this study.

The sensor design presented in this study has been investigated and designed with the intent of application for a FHR system in support of redox control, however could be applied to numerous other applications as is or with only slight modifications. All fluoride molten salts are potential applications including FLiNaK and FLiBe. The primary and intermediate loops of the FHR are clear examples of environments in which this sensor can be utilized, however this sensor could find valuable usage in future fusion systems as well

as other MSRs. Additional materials consideration can be performed to even make the sensor useful to chloride molten salts which are used in pyroprocessing of used nuclear fuel. The application of the results of this study mark a significant advancement to the deployment of the Fluoride salt-cooled High-temperature Reactor and will assuredly be applied to further electrochemical investigations and industrial molten salt applications.

4.3.4.2. Reference Electrode discussion

Therefore, the redox potential of the element in the molten salt is the most important parameter that determine if the element can be separated or not. For accurately measuring the redox potential, a function reference electrode is needed. For molten chloride salts such as KCl-LiCl, the Ag/AgCl reference electrode is well developed, while for a fluoride salt such as the primary salt of FHR, the selection of the reference electrode is difficult even studies on how to develop a reference electrode for molten fluoride salt are available. For developing an appropriate reference electrode, the following parameters must be taken into account: the reversibility of the electrode system, stability and reproducibility of the potential, stability of the reference electrode materials, impedance of the reference electrode, and compatibility of the reference electrode with the type of measurement [39]. These are the characteristics that will be used to analyze the usefulness of each presented reference electrode with an emphasis on stability of the potential and stability of the electrode materials, as these characteristics most pertain to the requirements of this application.

Quasi-reference electrode: Inert metals, such as platinum, can serve the function of the reference electrode for molten fluoride salt. Platinum has been used/proposed many times in the literature and appears to be becoming the preferred reference electrode in these systems due to its simplicity [40]. This type of reference electrode has been shown to be reversible, however the quasi-reference electrode does not have a defined potential. Its potential reaches steady state within minutes but potential drift has been observed by experimenters ranging from 1-20 mV within a few days, for which the causes have not been identified. Platinum is very inert in fluoride salt system and resists the temperature and corrosion effects. The impedance of Pt is negligible and it is compatible with cyclic voltammetry and electrochemical cleaning methods that will be applied between measurements to refresh the electrode.

Ni/Ni^{2+} electrode: The Ni/Ni^{2+} reference electrode has been widely used as well in the literature [39, 41]. This reference electrode uses the reaction shown by:

$$Ni \rightleftarrows Ni^{2+} + 2e \qquad (4\text{-}62)$$

A nickel wire is placed in a solution of NiF_2 to achieve this equilibrium reaction. Container materials can be boron nitride, graphite, or lanthanum fluoride. The nickel-nickel reference electrode possesses reversible behavior and a stable and reproducible standard potential. It has been shown that the potential can remain constant for at least 11 days [39]. The previously mentioned container materials are compatible with fluoride molten salts at high

temperatures, although some temperature restrictions have been noted for boron nitride [41] and thermal cycling is an issue for the LaF_3 crystal [39]. Junction potentials are reported to be negligible using both BN and LaF_3 [39]. This reference electrode system is compatible with cyclic voltammetry. Other metal/metal ion reference electrode such as Ag/Ag^+ and Fe/Fe^{2+} have also been proposed and tests [39].

<u>*Ni/NiO electrode:*</u> The Ni/NiO electrode utilizes a nickel wire placed in FLiBe solution saturated with both NiO and BeO. This electrode's potential is defined by the following reaction:

$$NiO + Be^{2+} + 2e \rightleftarrows BeO + Ni \qquad (4\text{-}63)$$

The electrode compartment is either constructed of sintered BeO or SiO_2. This electrode is reversible and is reported to have maintained stable potential measurements of 0.5-10 mV at 500-700 ^oC [39]. This electrode was tested in FLiBe with no reported material issues, however the material composition could be an issue in an online reactor. The presence of oxides can react with any HF gas in the bulk system, accelerating deterioration of the container and affecting the fluorine potential in the near vicinity of the reference electrode according to the reaction [42]:

$$O^{2-} + 2HF(g) \rightarrow H_2O(g) + 2F^- \qquad (4\text{-}64)$$

No information related to impedance is reported. This reference electrode is suitable for cyclic voltammetry.

<u>*Be/Be^{2+} electrode:*</u> The Be/Be^{2+} electrode is reported for fluoride salts which have beryllium constituents such as FLiBe [39] . This electrode consists of a beryllium rod placed in the molten salt with a BeF_2 solution. This mixture is housed within a nickel or silica compartment and corresponding eutectic for ion transfer. This electrode is reversible and possesses a stable potential varying by 0.1 mV in the temperature of 500-900 ^oC. The stability of nickel or silica as a construction material is not an issue. Impedance is not reported. This electrode is also compatible with cyclic voltammetry.

<u>*Dynamic electrode:*</u> A unique dynamic electrode has been reported recently for use in FLiBe [43] . This design is relatively simple; which uses the Be/Be^{2+} reference electrode. The ion transfer diaphragm is eliminated by passing current pulses through the dynamic reference electrode which was selected to be a molybdenum wire. This causes beryllium to plate onto the wire allowing for a potential measurement to take place after which the potential is allowed to relax before repeating. Testing this electrode for reversibility was not reported, however a stable potential was identified over a period of 1200 hours at 700 ^oC. Over this period the potential varied by 5 mV. Stability of construction materials is not an issue because the reference electrode is very simple, possessing no container or diaphragm. No impedance information was reported. This type of reference electrode is compatible with cyclic voltammetry while beryllium is plated onto the electrode. Other dynamic electrode using K/K^+ for LiF-KF-NaF was also tested [44].

For industrial applications, an electrochemical sensor for salt composition measurements and an electrochemical separation cell will be required to maintain as much durability and service life as possible to avoid high operation costs. Therefore, the stability and reproducibility of potential and the stability of its materials will be the most important characteristics by which to compare. This burden is primarily placed upon the reference electrode as the limiting component in any proposed electrochemical cell. Many reference electrodes have been summarized above which have been utilized in fluoride molten salts to some extent. Very few have reported the results of potential stability over the course of a time scale appropriate for industrial application and only one was tested in a convection loop for validation in such an environment. The most promising reference electrodes include the Ni/Ni^{2+}, Be/Be^{2+}, and Be/Be^{2+} dynamic reference electrode. Further research needs to be conducted to properly analysis and compare the variety of reference electrode types and construction to determine an ideal recommendation for an electrochemical sensor design for use in FLiBe.

4.3.5. Summary

In this section, the theory of redox control method was introduced and the feasibility of using the Eu^{3+}/Eu^{2+} couple for redox control in a molten fluoride salt was studied. Cyclic voltammetry measurements were performed at 650°C, 700°C and 750°C which showed reversible and diffusion controlled behavior at scan rates of 60-500 mV/s. Within these scan rates, the voltammograms were utilized to determine the concentration ratio of Eu^{3+}/Eu^{2+} and the formal standard potential of the Eu^{3+}/Eu^{2+} redox couple. Results indicated that both the concentration ratio and the formal standard potential can be measured with sufficient precision for redox control purpose. Determination of the formal standard potential allowed for the determination that a Eu^{3+}/Eu^{2+} concentration ratio of smaller than 0.05 would be sufficient to control the redox potential below that of chromium dissolution. This study's results show that the Eu^{3+}/Eu^{2+} couple is a feasible redox buffering agent for maintaining redox control in any next-generation application of fluoride molten salts and can be precisely measured using simple tools such as cyclic voltammetry. Additionally, the kinetics of alloy corrosion in molten salts and the important of the kinetic factors of redox buffer were discussed using a model that was developed based on the electrode reaction kinetics and mass-transfer in the salt and alloy.

4.3.6. References

1. D. Olander, J. Nucl. Mater., 300 (2002) 270-272.
2. L. Massot, P. Chamelot, L. Cassayre, P. Taxil, Electrochimi. Acta 54 (2009) 6361-6366.
3. S. Delpech, C. Cabet, C. Slim, G. Picard, Mater. Today 13 (2010) 34-41.
4. G. Duran-Klie, D. Robrigues, S. Delpech, Electrochimi. Acta 195 (2016) 19-26.
5. W. Huang, L. Tian, C. She, F. Jiang, H. Zheng, W. Li, G. Wu, D. Long, Q. Li, Electrochimi. Acta 147 (2014) 114-120.

6. M.W. Rosenthal, R.B. Briggs, P.N. Haubenreich, Molten salt reactor program semiannual progress report, ORNL-4782, Oak Ridge National Laboratory, Oak Ridge, TN, USA, 1972, pp. 80.
7. A.J. Bard, L.R. Faulkner, Electrochemical methods: Fundamentals and applications (second edition). John Wiley & Sons, Inc. 2001.
8. S.A. Kuznetsov, M. Gaune-Escard, Electrochimi. Acta 46 (2001) 1101-1111.
9. S.A. Kuznetsov, L. Rycerz, M. Gaune-Escard, J. Nucl. Mater. 344 (2005) 152-157.
10. Z. Wang, H. Fu, Y. Yang, J. Geng, Y. Jia, D. Huang, W. Li, Y. Gong, Q. Dou, Q. Li, J. Radioanal. Nucl. Chem. 311 (2017) 637-642.
11. A.M. Keightley, J.C. Myland, K.B. Oldham, P.G. Symons, J. Electroanal. Chem. 322 (1992) 25-54.
12. C.F. Baes, Jr., J. Nucl. Mater. 51 (1974) 149-162.
13. L.M. Toth, G.D. Del Cul, S. Dai, D.H. Metcalf, Molten Fluoride Fuel Salt Chemistry, AIP Conf. Proc. 346 (1995) 617-626. DOI: 10.1063/1.49142.
14. M. Gibilaro, L. Massot, P. Chamelot, Electrochimi. Acta 160 (2015) 209-213.
15. G. T. Fukuda, P. F. Peterson, D. R. Olander, J. M. Prausnitz, Fluid Phase Equilib. 255 (2007) 1-10.
16. B.F. Hitch, C.F. Baes Jr., Inorg, Chem., 8 (1969) 201-207.
17. L.C. Olson, J.W. Ambrosek, K. Sridharan, M.H. Anderson, T.R. Allen, J. Fluorine Chem. 130 (2009) 67-73.
18. J.W. Koger, Chromium Depletion and Void Formation in Fe-Ni-Cr Alloys During Molten Salt Corrosion and Related Processes, in: M.G. Fontana, R.W. Staehle, Advances in Corrosion Science and Technology, Springer US, 1974, pp. 245-318.
19. Y. Wang, Q. Wang, H. Liu, C. Zeng, Corros. Sci. 103 (2016) 268-282.
20. M. Kondo, T. Nagasaka, V. Tsisar, A. Sagara, T. Muroga, T. Watanabe, T. Oshima, Y. Yokoyama, H. Miyamoto, E. Nakamura, N. Fujii, Fusion Eng. Des. 85 (2010) 1430-1436.
21. V. Pavlik, M. Kontrik, M. Boca, New J. Chem. 39 (2015) 9841-9847.
22. D.A. Jones, Principles and Prevention of Corrosion, Prentice-Hall, Inc. 1996, pp. 86.
23. C.F. Baes Jr., "The chemistry and thermodynamics of molten-salt-reactor fluoride solutions", in: Thermodynamics. Vol. I. Proceedings of the Symposium on Thermodynamics with Emphasis on Nuclear Materials and Atomic Transport in Solids, International Atomic Energy Agency, Vienna, Austria, 1966, pp. 427.
24. W. Wu, S. Guo, J. Zhang, J. Electrochem. Soc., 164 (2017) C840–C844.
25. J. Zhang, J. Appl. Electrochem., 44 (2014) 383–390.
26. O. Beneš, R.J.M. Konings, "Molten Salt Reactor Fuel and Coolant", in: R.J.M. Konings (Ed.), Comprehensive Nuclear Materials, Elsevier Ltd., 2012, Vol. 3, pp. 359–389.
27. C. Hamel, P. Chamelot, A. Laplace, E. Walle, O. Dugne, P. Taxil, Electrochim. Acta, 52 (2007) 3995–4003.
28. W. Wu, S. Guo, J. Zhang, Int. J. Electrochem. Sci., 13 (2018) 225–234.
29. D.L. Manning, G. Mamantov, J. Electroanal. Chem., 7 (1964) 102–108.
30. S. Fabre, C. Cabet, L. Cassayre, P. Chamelot, S. Delepech, J. Finne, L. Massot, D. Noel, J. Nucl. Mater., 441 (2013) 583–591.
31. Y.L. Wang, Q. Wang, H.J. Liu, C.L. Zeng, Corros. Sci., 109 (2016) 43–49.
32. L. Olson, K. Sridharan, M. Anderson, T. Allen, J. Nucl. Mater., 411 (2011) 51–59.
33. F.-Y. Ouyang, C.-H. Chang, J.-Jung Kai, J. Nucl. Mater., 446 (2014) 81–89.

34. G. Zheng, B. Kelleher, L. He, G. Cao, M. Anderson, T. Allen, K. Sridharan, Corrosion, 71 (2015) 1257−1266.
35. X.-X. Ye, H. Ai, Z. Guo, H. Huang, L. Jiang, J. Wang, Z. Li, X. Zhou, Corros. Sci., 106 (2016) 249−259.
36. H. Kaesche, Corrosion of Metals: Physicochemical Principles and Current Problems, Springer-Verlag, 2003, pp. 169.
37. J.W. Koger, Alloy compatibility with LiF-BeF2 salts containing ThF4 and UF4, ORNL-TM-4286, Oak Ridge National Laboratory, Oak Ridge, TN, USA, 1972.
38. J.R. Keiser, Compatibility studies of potential molten-salt breeder reactor materials in molten fluoride salts, ORNL/TM-5783, Oak Ridge National Laboratory, Oak Ridge, TN, USA, 1977.
39. N. Q. Minh, L. Redey, Reference Electrodes for Molten Electrolytes. Molten Salt Techniques, 3(1987): 105-287.
40. M. Tylka, et al. "Method Development for Quantitative Analysis of Actinides in Molten Salts." Journal of The Electrochemical Society, 162 (2015): 625-633.
41. C. G. Kontoyannis, Pyrolytic Boron Nitride Coated Graphite as a Container of Reference Electrodes for Molten Fluorides. Electrochimica Acta Volume 40 (1995): 2547-2551.
42. S. Delpech, Molten fluorides for nuclear applications. Materialstoday Volume 13 (2010): 34-41.
43. V. Afonichkin, et all. Dynamic reference electrode for investigation of fluoride melts containing beryllium difluoride. Journal of Fluorine Chemistry, 130 (2009): 83-88.
44. S. Guo. N. Shay, J. Zhang, Measurement of europium (III)/europium (II) couple in fluoride molten salt for redxo control in a molten salt concept, Journal of Nuclear Materials, 496(2018): 197-206.

4.4. Properties of Fission Products in the FLiNaK Melt

4.4.1. Experimental Setup

The experimental tests were conducted using the experiment set-up as shown in Figure 4-22 inside the glove box with an argon atmosphere (≤5 ppm O_2 and ≤0.1 ppm H_2O) to prevent the reactions with water and oxygen due to the hygroscopic nature of electrolytes. The selected electrolyte for this research is molten LiF-NaF-KF salt (46.5–11.5–42 mol%, respectively). The salt was prepared in the lab by weighing the constituent salts in the given eutectic ratio. Once weighed, the dry mixture was mixed and stirred by hand in the test crucible. The purities of the salt purchased are as follows: Lithium fluoride, LiF, ≥ 99.0 % purity, sodium fluoride, NaF, ≥ 99.0 % purity, potassium fluoride, KF, ≥ 99.5 % purity, lanthanum (III) fluoride, LaF_3, ≥ 99.99 %, and dysprosium fluoride, DyF_3, ≥ 99.99 %. The electrochemical experiments were performed using a standard three-electrode setup and a Gamry Interface 1000 Potentio-stat. The working electrode used is a 1.6 mm diameter tungsten rod, the counter electrode used at the beginning is a 3.2 mm diameter tungsten rod which was proven to be oxidized during the electrochemical test. Thus, the counter electrode was later replaced with a 3.05 mm diameter graphite rod. The reference electrode utilized was a 0.81 mm diameter platinum wire with potential associated to $Pt/PtO_x/O^{2-}$[1]. The crucibles used are nickel crucible and glassy carbon crucible. The bottoms of electrodes were immersed in the FLiNaK salt bath and no touch of electrodes with crucible was confirmed before test. Open circuit potential (OCP) was performed before any electrochemical tests to confirm the stabilization of the system. IR compensation was selected in Gamry Framework software which is programmed with interrupt method during the tests.

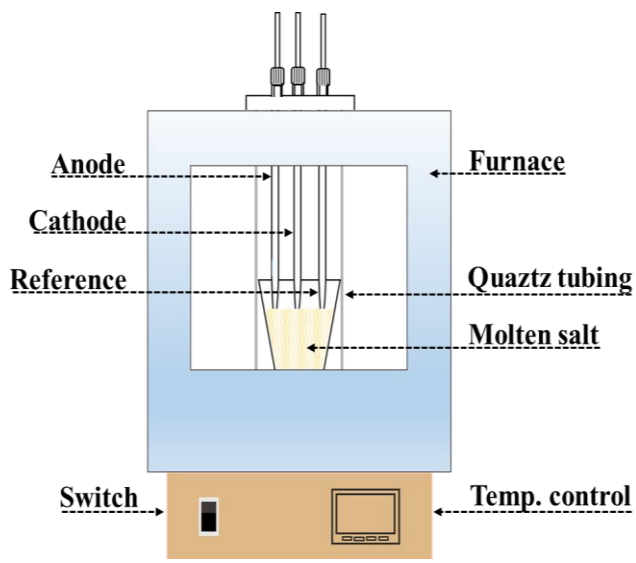

Figure 4-22: Schematic of the experimental setup.

4.4.2. Cyclic Voltammetric Studies of Dy and La in FLiNaK Melt

In order to successfully analyze the electrochemical behavior of a test species in Flinak salt, the redox reaction must occur within the electrochemical window of the molten salt. At sufficiently low potentials, cations constituting the salt will reduce in order of more negative Gibbs free energy of formation (K→Na→Li) while the anion F^- will oxidize to F_2 at a more positive potential The Gibbs free energy of formation for fluorides also demonstrates the ability of tungsten to act as an inert electrode, as the free energy value is much more positive than other materials that may be tested.

Considering the nature of the platinum quasi-reference electrode, the potential scale observed in the experiment has no thermodynamic basis to anchor it along the absolute potential scale. To provide this basis, a known redox couple can be added to the system for reference. Taking advantage of the ionic nature of the molten Flinak system introduces the option to reference the potential to the Flinak electrochemical window (i.e. K/K^+ on the more negative end, F_2/F^- on the more positive end). Figure 4-23 give the basis for converting reference potentials from platinum to potassium. These results were further verified using chronopotentiometry (CP) experiments, as showed in subsection2.2.2.1 before.

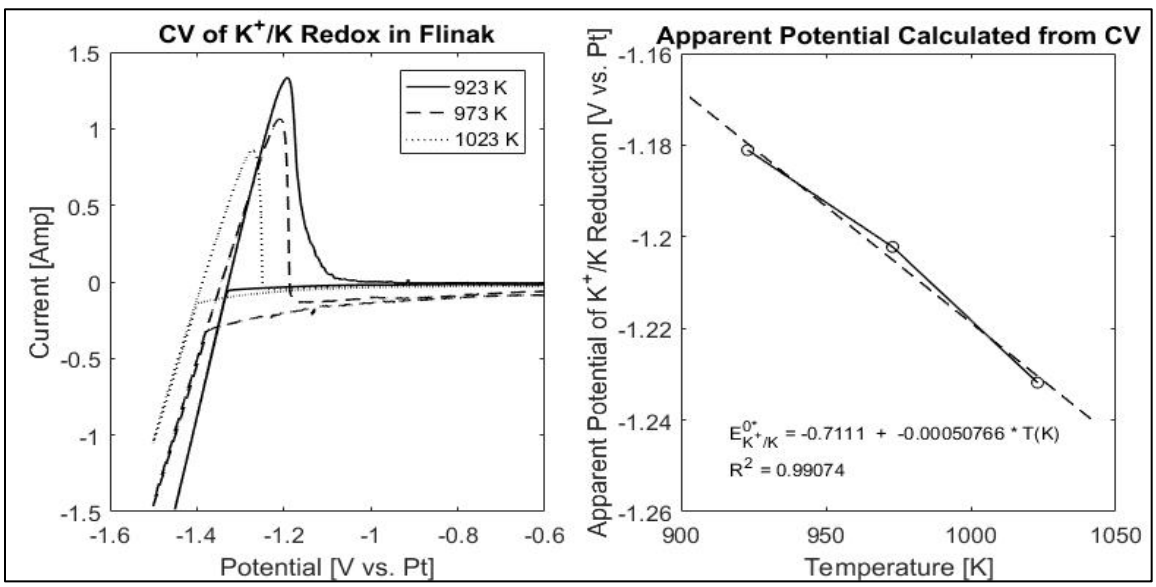

Figure 4-23: Cyclic Voltammetry results (left) used to characterize the redox potential of K^+/K in Flinak. Apparent potentials (right) are calculated from the CV results and consider the concentration of K^+ in the mixture as well as the soluble-insoluble nature of the redox reaction.

Before analysis was conducted on the experimental CV curves, consideration was given to the possibility of an exchange current from the molten media contributing a signal to the Flinak-Ln measurement. To quantify the contribution from the media, a signal was measured with a pure Flinak system. The results of both the Flinak-only "background" and the Flinak-Dy system are illustrated in Figure 4-24 below, after correcting for working

electrode surface area. As expected, no peaks are observed in the pure Flinak system. The contribution from the pure Flinak amounted in <5% of the total peak current. Moving forward it was deemed unnecessary to measure a background signal for each CV test. While the negligibility of the background contribution produces a source of error, this error is much smaller than other issues that are discussed later.

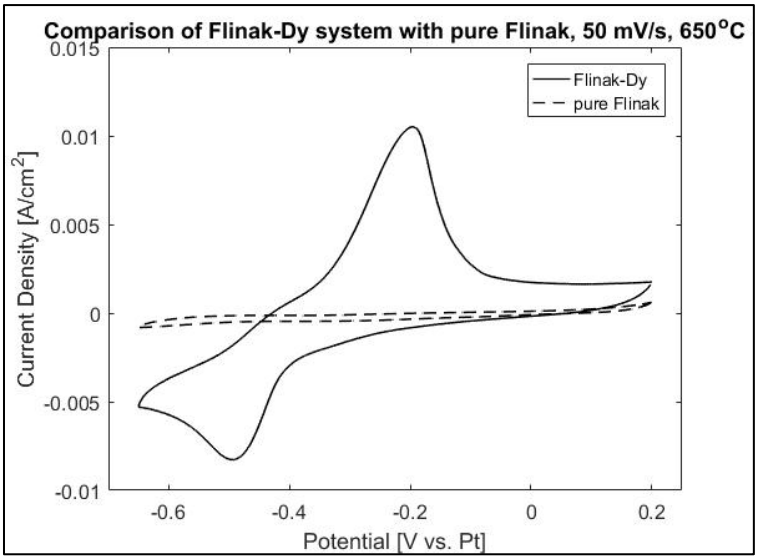

Figure 4-24: Comparison of the Flinak-Dy system with pure Flinak reveals negligible contribution from the molten Flinak media to the experimental CV curve. Disregarding the contribution from Flinak remains a source of error, but much less significant than other sources of error.

Analysis of cyclic voltammetry data was performed through observations of peak current and peak potential. The results were plotted showing effect of scan rate (Figure 4-25) which reveals a shift in the measured peak potential with scan rates above 160 mV/s. This shift is explained by Hamann, Hamnett, and Vielstich in "Electrochemistry" [2]. The peak potential should remain constant and independent of scan rate while the redox reaction exhibits reversible kinetics. When the scan rate is sufficiently high, the time scale of the redox reaction lags. Electron transfer becomes slow relative to the scan rate and the redox reaction becomes quasi-reversible. In the quasi-reversible range, electrochemical equations based on Nernstian kinetics must be modified. Furthermore, peak potential is not independent of scan rate but shifts to more negative cathodic potentials and more positive anodic potentials. This is because the concentration of the depleting redox species (M^{3+} during cathodic reaction, M^0 during anodic reaction) at the working electrode interface is decreasing more slowly than the reversible case. The maximum concentration gradient, and therefore the current peak, occurs slightly later in the time scale of the experiment and appears as a shift in peak potential. The peak current increases linearly with scan rate, maintaining the same trend as the reversible case.

Other works with molten fluoride and chloride salts show scan rate limits of reversibility in the range of 50-500 mV/s [3,4]. It has been suggested that difference in reversibility of the

same reactions may be attributed to experimental temperature, electrode materials, and diffusional property of the media [5]. The order of magnitude difference is interesting and certainly worth investigating.

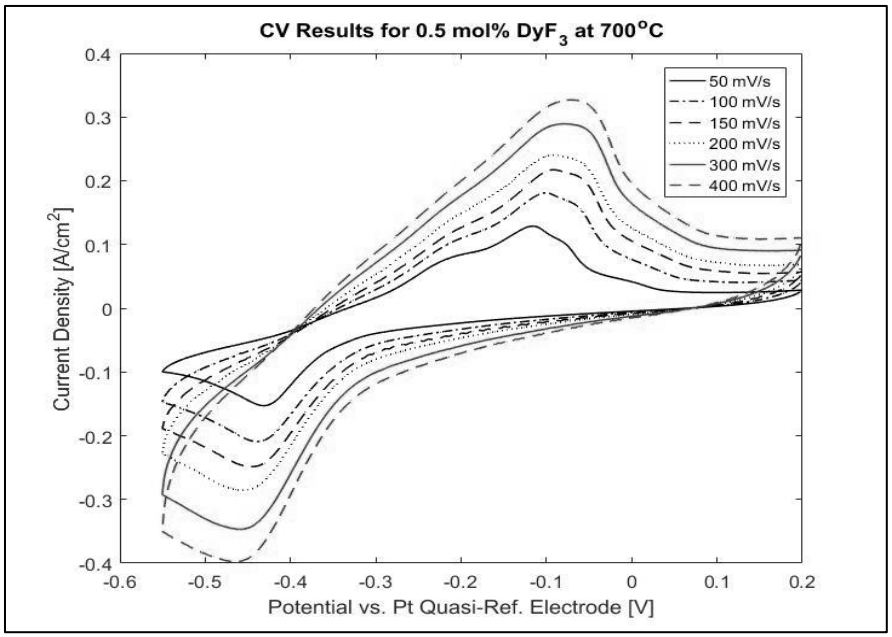

Figure 4-25: The CV curves are generated for Dy in Flinak with scan rates 50-400 mV/s at 700°C. Slight deviation in peak potential is observed with scan rates of 200 mV/s and higher. WE: tungsten [0.0094 cm²].

For the quasi-reversible case, the number of electrons, *n*, can be calculated from the anodic and cathodic peak separation by Eq. (4-65) [5]. A value for the charge transfer coefficient is assumed α=0.5.

$$|E_p - E_{p/2}| = 1.857\ RT/\alpha nF \qquad (4\text{-}65)$$

This analysis provides a value of n=1.86 ± 0.55 for Dy and n=2.21 ± 0.48 for La. These results do not exactly match the expected value of n=3 which calls into question the assumed value of α=0.5. A more extensive investigation could provide insight on the reversible case and quasi-reversible charge transfer coefficient. Furthermore, alternative methods such as Square Wave Voltammetry may provide a more reliable analysis.

For the analysis of soluble-insoluble reactions, the cathodic (reduction: $Ln^{3+} \rightarrow Ln^{0}$) reaction peak is analyzed to determine properties of Ln^{3+}. The peaks from the CV curve correspond to the point at which the redox reaction becomes limited by diffusion of M^{3+} ions to the electrode surface. At this point, the diffusion coefficient of Ln^{3+} can be calculated from the Berzins-Delahay equation (Eq. (4-66)) for soluble species. A common method to validate that the reaction is reversible and diffusion-limited is to plot the peak current density against the square root of the scan rate (Figure 4-26, left). While this trend remains linear, the redox system continues to follow reversible, diffusion-controlled behavior.

$$J_p = 0.6105 * C_{Bulk} * \sqrt{\frac{(nF)^3 Dv}{RT}} \quad (4\text{-}66)$$

Where J_p is the peak current density [A/cm^2], C_{bulk} is the concentration of Dy in the molten salt [mol/cm^3], n is the number of electrons transferred, which is assumed to be three, D is the diffusion coefficient, v is the scan rate [V/s], F is the Faraday constant, R is the gas constant, and T is the temperature [K]. Another test to verify reversibility of the redox reaction is to plot the peak potential against the logarithm of the scan rate. This plot will more evidently reveal potential shifts, and thus quasi-reversibility, as deviations from a horizontal line. Figure 4-26 (right) indicates that the redox system remained in the diffusion-controlled region throughout scan rates of 160 mV/s and below.

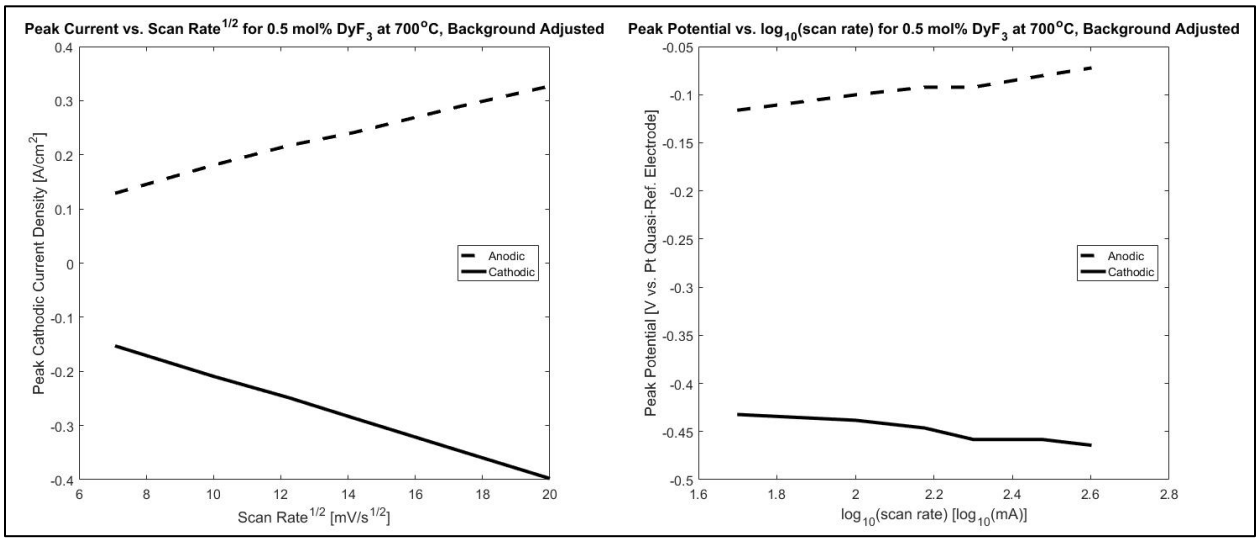

Figure 4-26: Left, peak current density plotted against square root of the scan rate, to confirm reversibility in the diffusion-controlled region (linear). Right, peak potential vs. log(scan rate) to confirm kinetic reversibility (horizontal). Significant deviation is observed in peak potential for scan rates of 200 mV/s and higher while not observed in the current density.

Having verified the diffusion-controlled behavior of the redox reaction, the diffusion coefficient at each temperature was calculated. Figure 4-27 proves the linear trend of ln(D) vs. 1/T[K] fits the Arrhenius Equation (Eq. (4-67)) for both species. The activation energy (E_a) can be calculated from the linear slope of the Arrhenius plot yielding $E_a^{La^{3+}} =$ 127 kJ/mol and $E_a^{Dy^{3+}} =$ 51.5 kJ/mol.

$$D = D^0 * \exp\left(-\frac{E_a}{RT}\right) \quad (4\text{-}67)$$

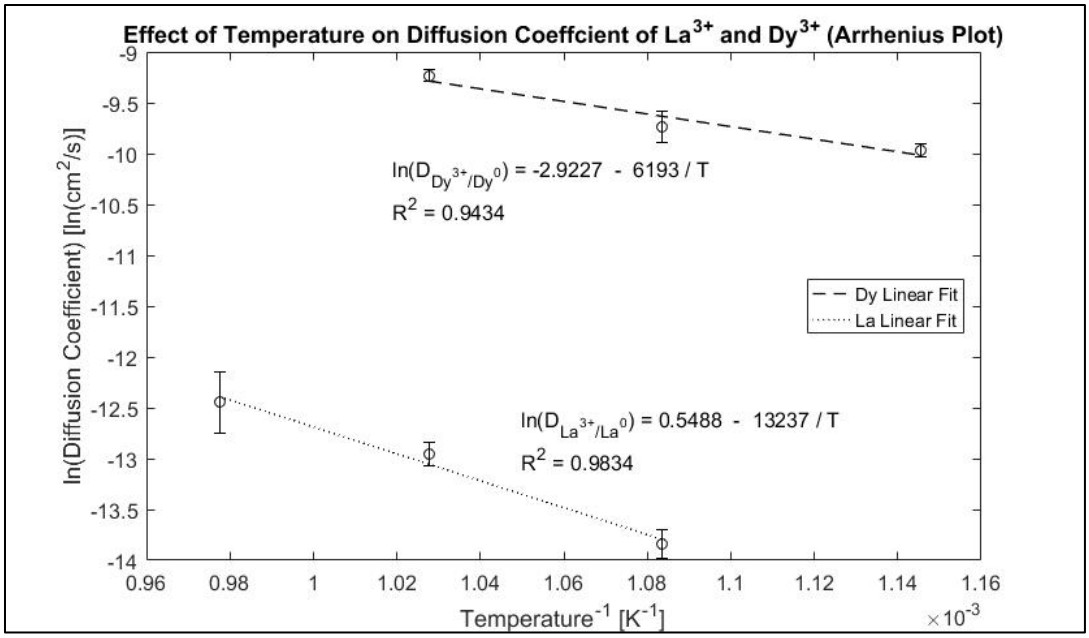

Figure 4-27: Diffusion coefficient results and temperature dependence fit to the Arrhenius Equation for dysprosium (top) and lanthanum (bottom) From the linear slope of the ln(D) vs. 1/T relationship, the activation energy is extrapolated.

The result for Dy seem slightly high while the result for La seems extremely high. Other related research shows activation energies typically near 40 kJ/mol. (Wei Huang, Lifang Tian, Changfeng She, Feng Jiang, Haiyang Zheng, Wenxin Li, Guozhong Wu, Dewu Long, Qingnuan Li, 2014) While the order of magnitude difference seems confusing and unexplainable, it has been previously reported in literature for similar experiments [1]. These experimental extremes may be explained away by experimental conditions or the sensitive and error-prone nature of electrochemical research in molten salts. However, there may be some interesting unaccounted phenomenon worth investigating.

Using the K^+/K reaction as a reference point allows a thermodynamic basis for reporting reaction potentials. Figure 4-28 below shows these results at for La and Dy. The apparent standard reduction potential E^{0^*} can be calculated via Eq. (4-68) [6].

$$E^{0*}_{Ln^{3+}/Ln^0} = E_p - \frac{RT}{nF}\left(\ln(X_{Ln^{3+}}) - 0.854\right) \qquad (4\text{-}68)$$

E_p is the observed cathodic peak potential [V vs. Ref.] and $X_{Ln^{3+}}$ is the mole fraction of Ln^{3+} in the salt. Because $\ln(X_{Ln^{3+}})$ is always negative, the observed potential will always be more negative than the apparent standard potential.

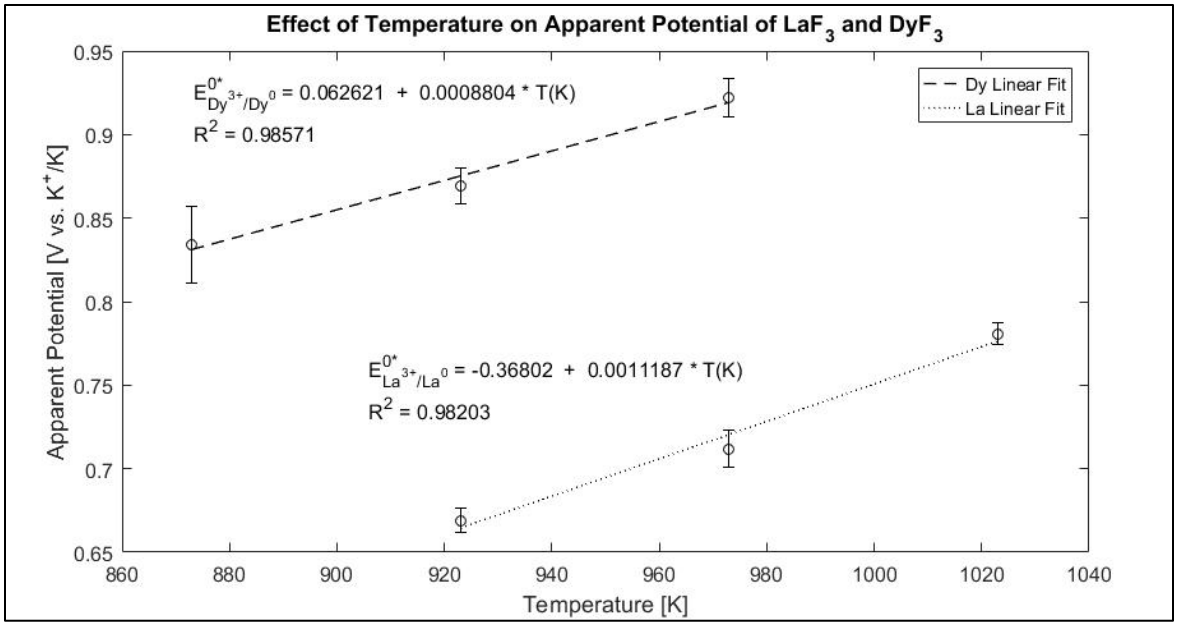

Figure 4-28: Temperature trend of apparent standard reduction potential, E^{o*}, with reference to K^+/K in Flinak. Large error reported at 823 K is the result of a significant shift in potential with scan rate. Given the same time scale (scan rate), lower temperature systems with slower diffusion will eventually exhibit irreversible kinetics and peak potential shift.

4.4.3. Chronopotentiometric and Potentiometric Polarization Studies of La in FLiNaK Melt

The reduction behavior of LaF_3 in FLiNaK was studied by chronopotentiometry (CP) test and then the diffusion coefficients were determined at several temperatures. Figure 4-29 illustrates the typical chronopotentiograms of LaF_3 (1.05×10^{-4} mol/cm^3) in FLiNaK molten salt at the temperatures of 923, 973, and 1023 K when applying different currents. The first plateau shown with time evolution corresponds to the reduction of La ion into La metal. The transition time for the reduction can be determined from chronopotentiograms using the method described in the literature [7]. Figure 4-30 (A) shows the relationship between the applied current and the obtained transition time for the chronopotentiometry data given in Figure 4-29. A fine proportional relation can be observed between I and $\tau^{-1/2}$. It indicates that the Sand's equation is applicable for the reduction of LaF_3 in FLiNaK molten salt. The diffusion coefficient of La^{3+} can be calculated from the slope of the plot of I versus $\tau^{-1/2}$ based on Sand's equation [8] shown below

$$I\tau^{1/2} = 0.5nFC_o{}^*S\pi^{1/2}D^{1/2} \qquad (4\text{-}69)$$

where I is the applied current (A), τ is the transition time (s), $C_o{}^*$ is the bulk concentration (mol/cm^3), D is the diffurion coefficient (cm^2/s), F is the Faraday's constant, S is the working electrode surface area (cm^2) and n is the electron transfer number.

In addition to the chronopotentiometry test of LaF_3 in FLiNaK molten salt at the concentration of 1.05×10^{-4} mol/cm^3, a same test was performed at a higher concentration (2.25×10^{-4} mol/cm^3). The relationship between the applied current I and the obtained

transition time τ was plotted which can be seen in Figure 4-30 (B). The diffusion coefficients at these two different concentrations were calculated based on equation (4-69) and summarized in Table 4-7. Based on the independence of diffusion coefficient on concentration, its average value at 923, 973, and 1023 K was calculated respectively from the data obtained at these two different concentrations. The average diffusion coefficient can be further used to produce the Arrhenius plot as shown in Figure 4-31. Based on the fitted linear relationship in the Arrhenius plot, the diffusion coefficient of La ion in FLiNaK molten salt was formulated as

$$lnD = -1.5945 - 12487/T \tag{4-70}$$

According to the Arrhenius equation as follows

$$D = D_0 \exp\left(-\frac{E_a}{RT}\right) \tag{4-71}$$

where E_a is activation energy (J/mol), R is gas constant and T is temperature (K), the activation energy E_a was acquired with the value of 103.8 KJ/mol.

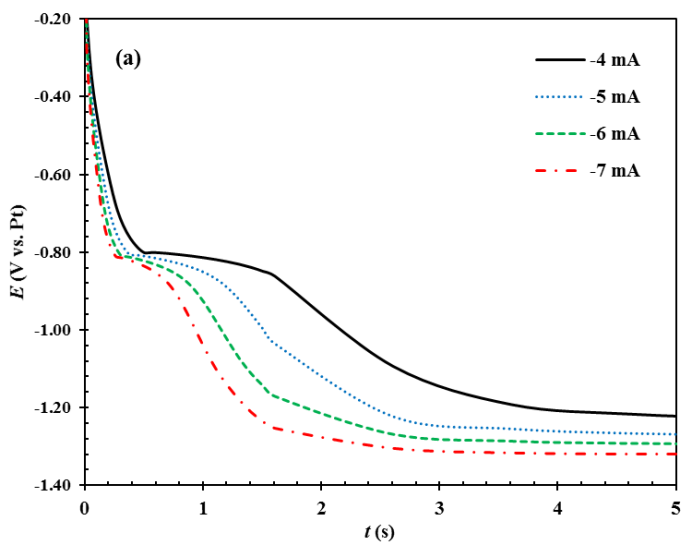

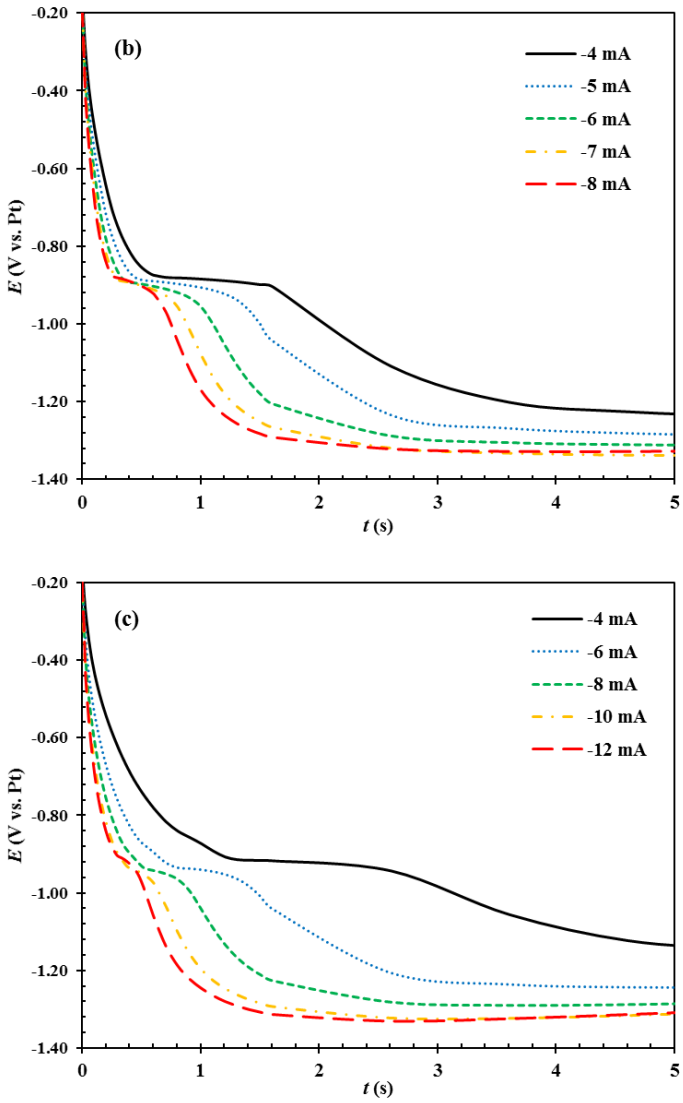

Figure 4-29: Chronopotentiograms of LaF_3 in FLiNaK molten salt at the temperatures of (a) 923 K, (b) 973K, and (c) 1023 K. LaF_3=1.05×10^{-4} mol/cm^3; electrode area=0.296 cm^2.

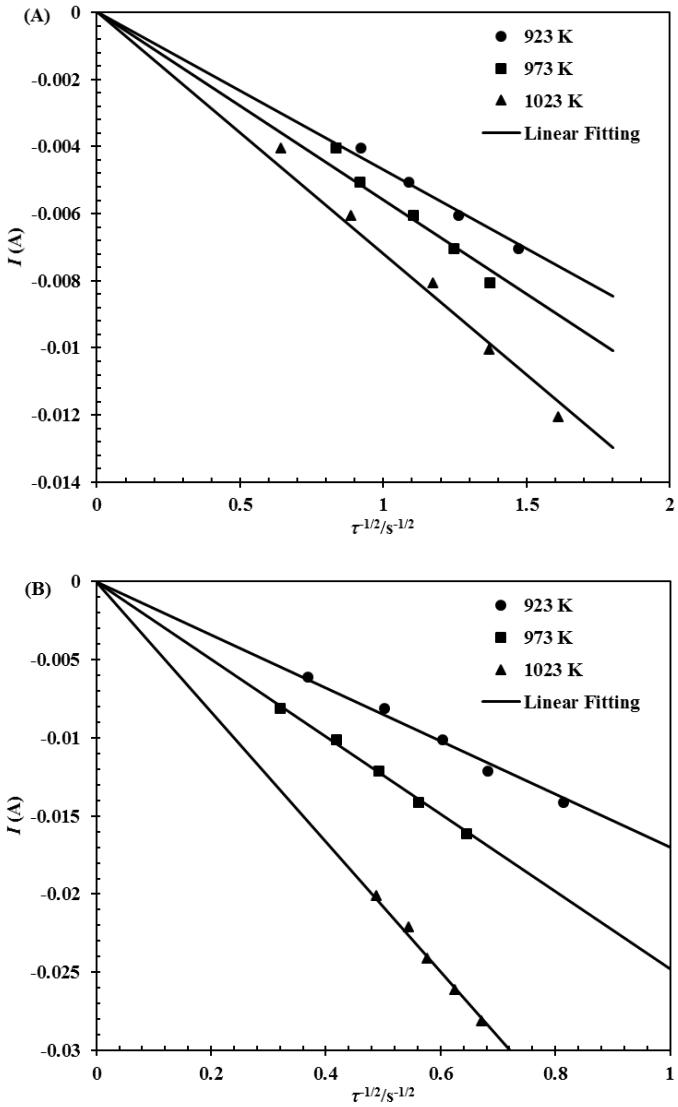

Figure 4-30: Linear relationship of I versus $\tau^{-1/2}$ for the CP test of LaF_3 in FLiNaK molten salt with the concentration of (A) LaF_3=1.05×10^{-4} mol/cm^3 and (B) LaF_3=2.25×10^{-4} mol/cm^3.

Table 4-7: Diffusion coefficients of lanthanum ion in FLiNaK molten salt determined using equation (4-69).

C_o^* (mol/cm^3)	1.05×10^{-4}			2.25×10^{-4}		
T (K)	923	973	1023	923	973	1023
D×10^7 (cm^2/s)	3.47	4.92	8.14	2.24	4.76	13.4

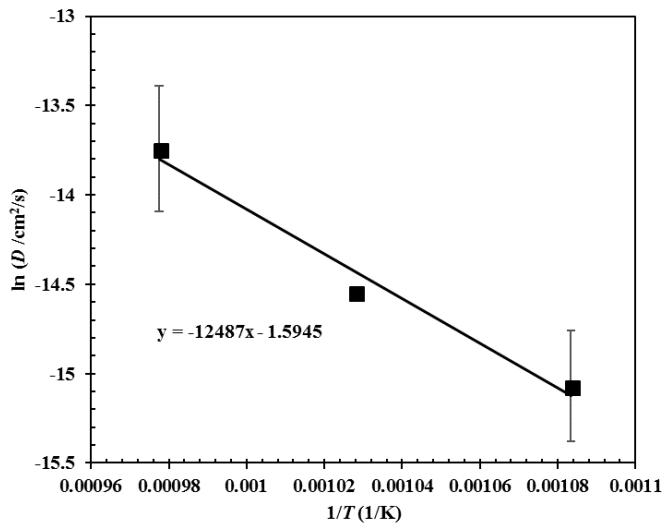

Figure 4-31: Arrhenius plot of diffusion coefficient as a function of temperature.

Kinetic parameters such as exchange current density and charge transfer coefficient are important to understand the reaction kinetics of La ion to La metal in FLiNaK molten salt. Potentiodynamic polarization can be used to determine the values of these kinetic parameters. In order to get these parameters accurately, it is essential to make sure the scan rate of the potentiodynamic polarization is sufficiently low to reach the steady state. Figure 4-32 indicates the potentiodynamic polarization curves at various scan rates and a highly coincidence on the curve during each scan except the distortion part can be observed. The potential applied on the inert working electrode (W) was scanned from the negative overpotential to the anodic direction in the potentiodynamic polarization test. In the negative overpotential section, La ion was reduced to La metal and formed a layer on the tungsten working electrode surface. A distortion on the curve where the initial potential scan started was observed in this section which could be attributed to the initial development of the diffusion layer. In the positive overpotential section, the dissolution of the deposited La occurs and the current increased with the increase of overpotential. The irregular variation was observed after overpotential η reached to the value of around 0.03 V. This is due to the heterogeneous dissolution of deposited La layer which might not be uniform after negative overpotential scan [9]. The dissolution of La layer and the decrease of La coverage area on the electrode with time might be different at different scan rates, as a result, there is an obvious deviation on the distortion area in the positive overpotential scan section for each scan.

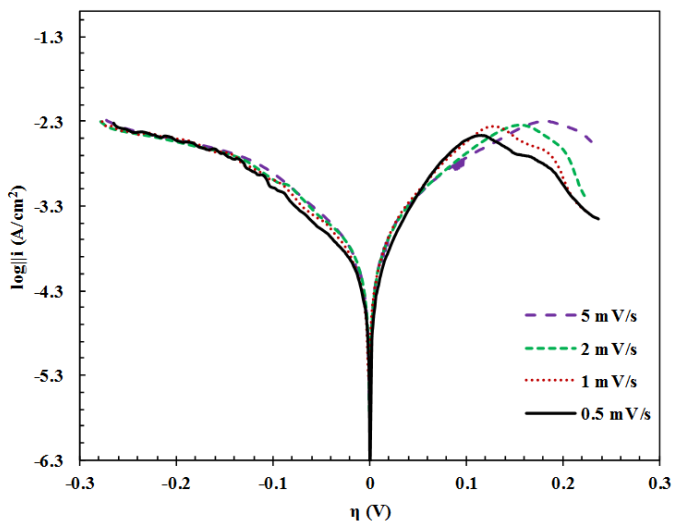

Figure 4-32: Potentiodynamic polarization curves measured at different scan rates for LaF_3 in FLiNaK molten salt. LaF_3=1.58×10^{-4} mol/cm^3; T=923K.

The external current measured during potentiodynamic polarization is a sum of unwanted charging current and faradic current. Charging current comes from the continuous change of the potential during the scan process and is proportional to scan rate. Due to the influence of charging current can be minimized at slow scan rate, potentiodynamic polarization at low scan rate is usually employed to study the kinetic reaction of electrochemical reaction. However, at lower scan rate potentiodynamic polarization test will take longer time, electrode surface may change greatly during this process and bring more noises to the curve obtained. Considering the extremely small difference on the curve obtained at 0.5 mV/s, 1 mV/s, 2 mV/s, and 5 mV/s in Figure 4-32, the potentiodynamic polarizations at 5 mV/s were performed in the following tests.

Figure 4-33 illustrates the potentiodynamic polarization curves obtained at the scan rate of 5 mV/s for FLiNaK molten salt containing different concentrations of LaF_3 at the temperatures of 923, 973, and 1023 K, respectively. From which it can be seen the measured current increases with concentration for each temperature.

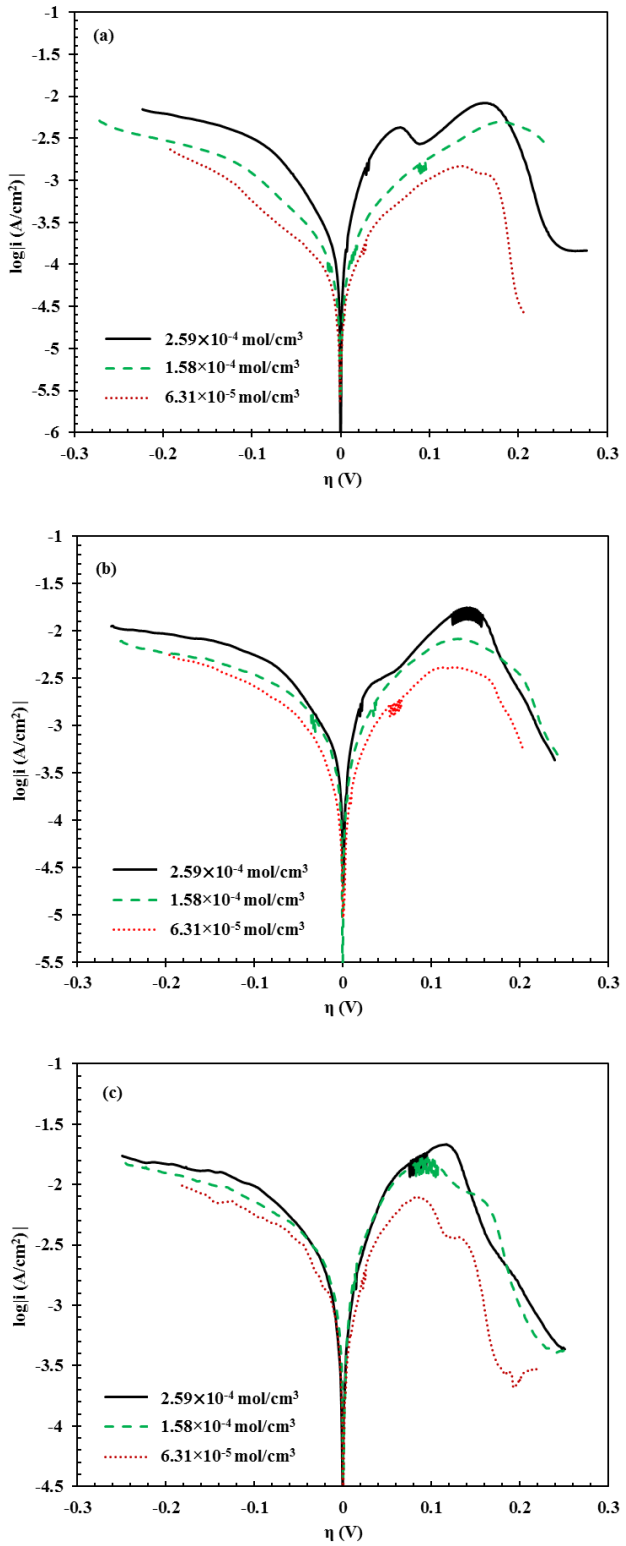

Figure 4-33: Potentiodynamic polarization curves at different concentrations for the temperatures of (a) 923 K, (b) 973 K, and (c) 1023K. Scan rate: 5 mV/s.

In order to determine the kinetic parameters, an analysis method based on the non-simplified electrode kinetic equation was applied here. This method is thought to be more reliable than the conventional Tafel and linear polarization methods [9]. The non-simplified electrode kinetic equation for the redox reaction happens to La can be expressed as follows [9]

$$i = \frac{i_0\left\{exp\left[\frac{(1-\alpha)nF)}{RT}\eta\right] - exp\left(\frac{-\alpha nF}{RT}\eta\right)\right\}}{1 - \frac{i_0}{i_L}exp\left(\frac{-\alpha nF}{RT}\eta\right)} \quad (4\text{-}72)$$

Where i is the current density (A/cm^2), i_0 is the exchange current density (A/cm^2), n is the electron transfer number, α is the charge transfer coefficient, η is the overpotential (V). i_L (A/cm^2) is the limiting diffusion current density which is defined as below

$$i_L = -nFDC_o{}^*/\delta \quad (4\text{-}73)$$

where δ is the diffusion layer thickness (cm).

Equation (4-72) was applied to fit the experimental potentiodynamic polarization curves. The values of the various parameters that best fit the experimental data can be extracted by the least squares fitting procedure through minimizing χ^2 with respect to the 3 fitting parameters: i_0, i_L, and α. Thus, if we refer to the parameters by a vector m= [i_0, i_L, α], then the Chi-square function to be minimized can be expressed by

$$\chi^2\ (m) = \left|i^{sim}(m) - i^{exp}(m)\right|^2 \quad (4\text{-}74)$$

The non-linear least square algorithm can search this 3- dimensional parameter space to find the optimum values that minimize χ^2. Due to the distortion at the both ends of the experimental polarization curve, the data in the overpotential range of -0.2 to 0.05 V was used to do the fitting. Through this way, these three parameters at which the calculated potentiodynamic polarization best fits the experimental one can be obtained. The solid lines in Figure 4-34 are the calculated polarization curves at the optimized values. It can be seen the calculated polarization curves agree very well with the experimental ones in the fitted range (-0.2~ 0.05 V). The optimized values for the parameters are included in Table 4-8. In addition to the parameters talked before, reaction rate constant k^0 is another key kinetic parameter for the understand of reaction kinetics of La ion in FLiNaK molten salt. It is related to the exchange current density i_0 and charge transfer coefficient α by the following correlation [8, 9]:

$$i_0 = nFk^0C_o{}^{*(1-\alpha)} \quad (4\text{-}75)$$

The values of i_0 listed in Table 4-8 were plotted against its corresponded concentration of LaF_3 in mol/cm^3 which can be seen in Figure 4-35. Equation (4-75) was used to fit the data points in Figure 4-35 from which it can be known all data points agree well with the fitted power law trend line. The values of α from the fitted expression using equation (4-75) are 0.47 at 923 K, 0.51 at 973 K, and 0.47 at 1023 K, respectively. These numbers in fact are close to the values of α obtained from the optimization fitting of individual test results (Table 4-8). Table 4-9 lists the values of k^0 determined from the fitted expression by equation (4-75), from which it can be known k^0 increase with temperature.

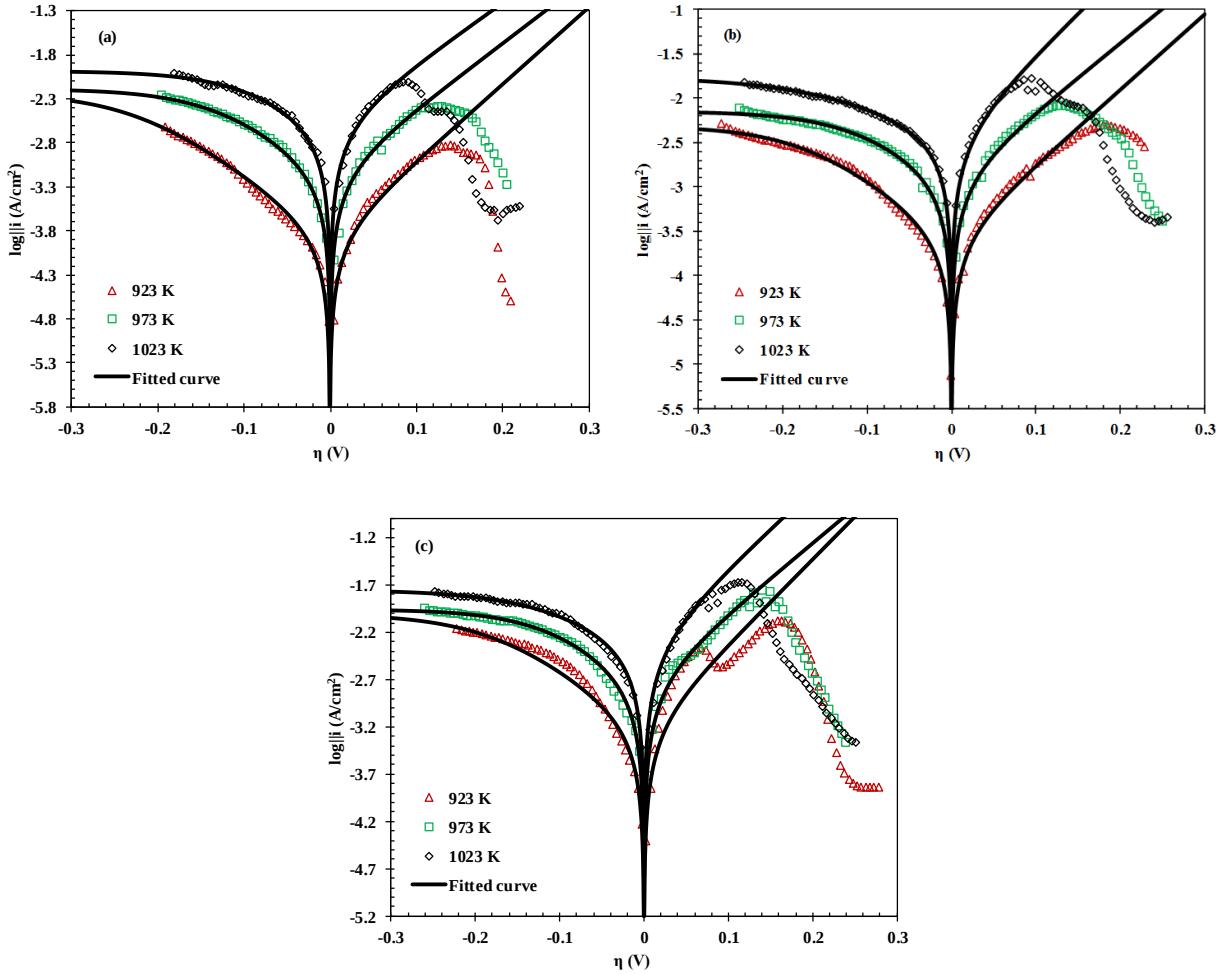

Figure 4-34: Potentiodynamic polarization curves at the scan rate of 5 mV/s for LaF_3 in FLiNaK molten salt at the temperatures of 923, 973, and 1023 K. (a) LaF_3=6.31×10^{-5} mol/cm^3; (b) LaF_3=1.58×10^{-4} mol/cm^3; (c) LaF_3=2.59×10^{-4} mol/cm^3.

Table 4-8: Optimized parameters determined by non-simplified electrode kinetic equation.

Concentration(mol/cm³)	T (K)	i_0 (A/cm²)	α	i_L (A/cm²)
	923	0.00013	0.47	-0.0058
6.31×10^{-5}	973	0.00069	0.52	-0.0065
	1023	0.00250	0.53	-0.0102
	923	0.00025	0.48	-0.0049
1.58×10^{-4}	973	0.00120	0.50	-0.0070
	1023	0.00380	0.37	-0.0169
	923	0.00060	0.45	-0.0010
2.59×10^{-4}	973	0.00180	0.52	-0.0109
	1023	0.00460	0.44	-0.0177

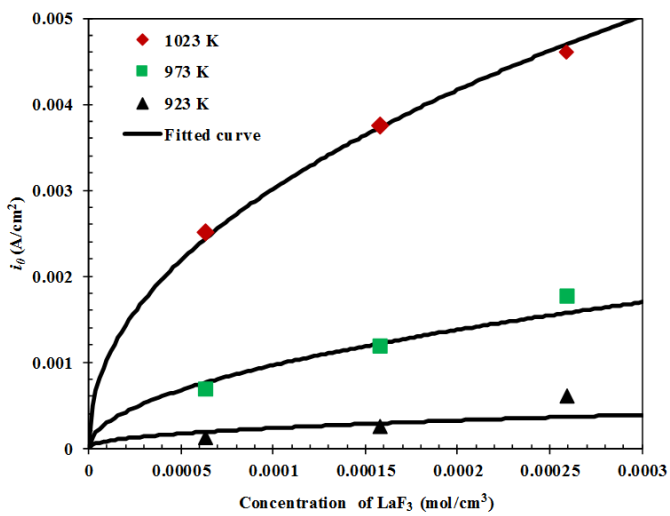

Figure 4-35: The plot of i_0 from Table 4-8 versus LaF_3 concentration.

Table 4-9: The obtained values of K^0 at different temperatures using equation (4-75).

T (K)	K^0 (cm/s)
1023	7.6E-7
973	3.8E-7
923	5.9E-8

4.4.4. Summary

In this section, the thermodynamic and kinetic properties of La and Dy in molten Flinak salt was investigated. Cyclic Voltammetry analysis was applied to study the soluble-insoluble reduction reactions at different temperatures and scan rates. The CV results demonstrated quasi-reversible reaction kinetics for both species considered at scan rates of 160 mV/s and below. At higher scan rates, significant deviation from reversibility was apparent, resulting in increased peak separation. In depth analysis of CV results resulted in experimental determination of reaction mechanism, diffusion coefficient, activation energy, and apparent potential. For both species, the reaction proved to be a single-step electron transfer. The diffusion coefficients follow Arrhenius temperature behavior, yielding the activation energy of 51.5 kJ/mol for Dy and 127 kJ/mol for La. The apparent potential (V vs. K^+/K) was observed as $E^{0*} = 0.0626 + 0.00088*T[K]$ for the Dy^{3+}/Dy^0 reaction and $E^{0*} = -0.368 + 0.001119*T[K]$ for La^{3+}/La^0. The diffusion coefficient of lanthanum in FLiNaK was further studied using chronopotentionmetry technique at different concentrations and temperatures. In addition, the kinetic parameters, i.e., exchange current, charge-transfer coefficient, and rate constant were investigated by analysis of potentiodynamic polariztion using an electron kinetic model.

4.4.5. References

1. L. Massot, et al. Electrochimica Acta 54.26 (2009): 6361-6366.
2. C.H. Hamann, A. Hamnett, W. Vielstich, Electrochemistry, Wiley, April 2007.
3. M. Straka, M. Korenko, F. Lisý, L. Szatmáry, J. Rare Earths, 29 (2011) 798-803
4. S. Guo, N. Shay, Y. Wang, W. Zhou, J. Zhang, J. Nucl. Mater., 496 (2017) 197-206.
5. H. Matsuda and Y. Ayabe, Z. Elektrochem., Ber. Bunsenges. Phys. Chem., 59 (1955) 494-503.
6. L. Masset, et. al., Journal of the Electrochemical Society, (152)2005 A1109-A1115.
7. Laity, Richard W., and James DE McIntyre. Journal of the American Chemical Society 87.17 (1965): 3806-3812.
8. A.J. Bard, L.R. Faulkner, Wiley, New York, 2001.
9. S. Guo, E. Wu, J. Zhang, Electrochimica Acta 259 (2018): 253-261.

4.5. Properties of Corrosion Products in the FLiNaK Melt

4.5.1. Cyclic Voltammetric and Chronopotentiometric Studies of Cr in the FLiNaK

The electrochemical behavior of CrF_2 in FLiNaK molten salt was studied by the electrochemical technique of cyclic voltammetry. Figure 4-36 shows a typical cyclic voltammogram of CrF_2 in FLiNaK melt obtained at the temperature of 923 K and scan rate of 100 mV/s. Two pairs of redox peaks C1/A1 and C2/A2 can be observed in Figure 4-36 Based on the previous studies [1,2,3], this two pairs of redox peaks are attributed to the reactions (4-76) and (4-77).

$$Cr^{3+}+e^{-}\leftrightarrow Cr^{2+} \quad (4\text{-}76)$$

$$Cr^{2+}+2e^{-}\leftrightarrow Cr \quad (4\text{-}77)$$

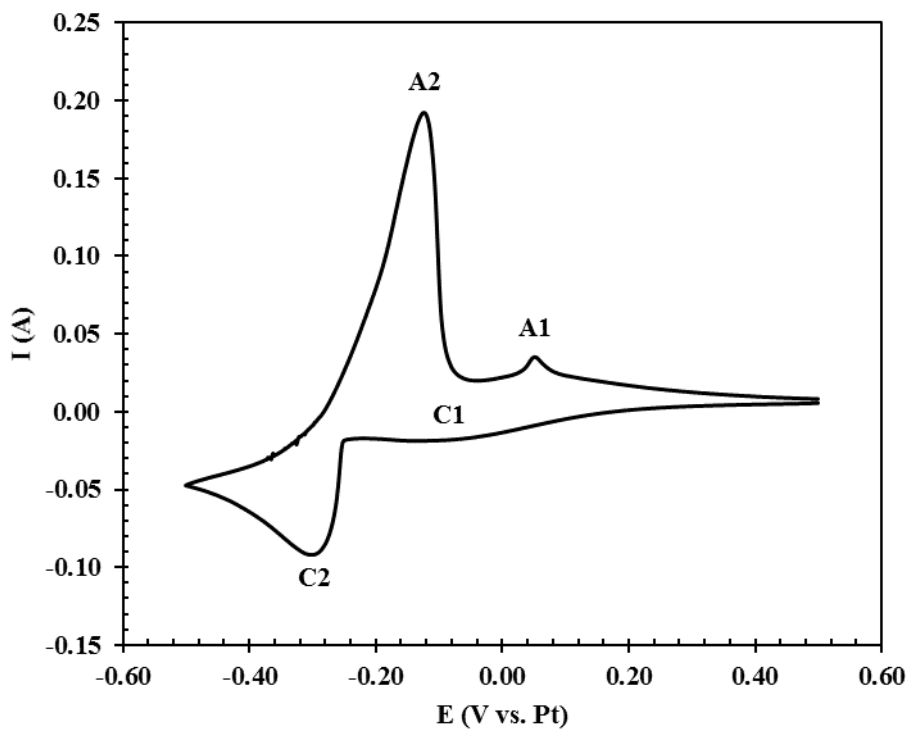

Figure 4-36: Cyclic voltammogram of CrF_2 in FLiNaK molten salt at the temperature of 923 K and scan rate of 100 mV/s. Working electrode: tungsten (s=0.6481 cm^2), reference electrode: platinum, counter electrode: graphite.

The evolution of the open circuit potential of the tungsten working electrode against platinum reference electrode over time at 1023 K is monitored by applying a reduction current of 180 mA for 4s and then an oxidation current of 180 mA for another 4s as well. Figure 4-37 indicates the acquired chronopotentiometry data. Cr (III) is first reduced to Cr (II) after a reduction current is applied, plateau A in Figure 4-37 corresponds to the reduction reaction of Cr (III) to Cr (II). The plateau A is not obvious here because of a large

current (180 mA) is imposed. After the concentration of Cr (III) drops to zero at the electrode surface, the flux of Cr (III) is insufficient to accept the electrons being forced across the electrode-solution interface, the potential shifts to a more negative value where the reduction reaction of Cr (II) to Cr happens. It is reflected in plateau B. The potential transits to the value where the reduction reaction of K (I) to K happens after the depletion of Cr (II) at the electrode surface which is indicated in plaetau C. An oxidation current of 180 mA is applied after 4s, as a result, the OCP steps up as shown in plateau C' which corresponds to the oxidation of the deposited K. Similarly, the plateaus B'and A' correspond to the oxidation of Cr (II) and Cr (III), respectively. The plateau difference of C' and C can be used to calculate the electrolyte resistance by comparing the potential difference between two applied currents. The ratio of $\Delta V/\Delta I$ indicates the electrolyte resistance of 0.15 Ω.

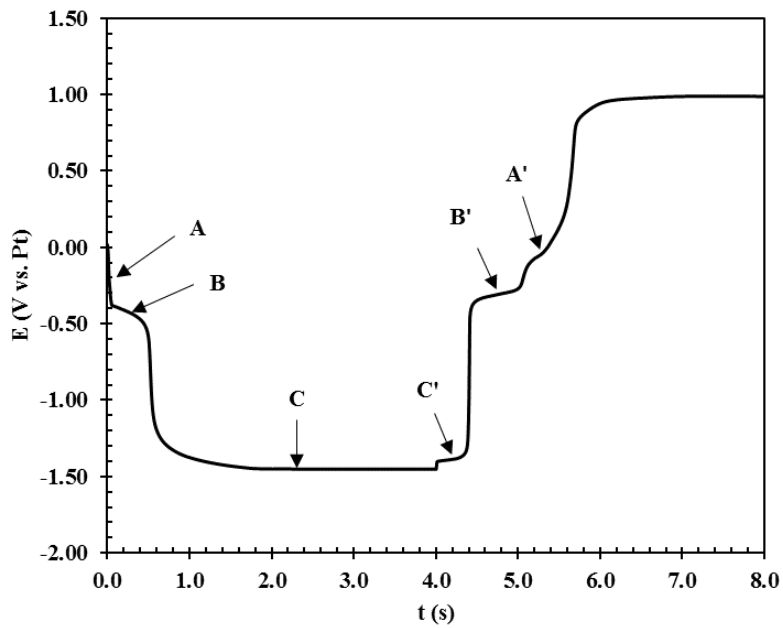

Figure 4-37: OCP evolution of the tungsten working electrode against platinum reference electrode over time by chronopotentiometry test at the temperature of 1023 K.

In order to study the thermodynamic properties of Cr (III) and Cr (II) in FLiNaK molten salt, the cyclic voltammogram of the redox reaction of Cr (III)/Cr (II) is focused and measured. Figure 4-38 shows the cyclic voltammogram of Cr (III)/Cr (II) in FLiNaK with the addition of 2.37×10^{-4} mol/cm^3 CrF_2 at different temperatures and scan rates. The independence of peak potential with scan rate can be observed in Figure 4-38. It means the redox reaction of Cr (III)/Cr (II) is reversible based on that the peak potential is independent of scan rate when electron transfer rate is faster than its mass transport rate [4].

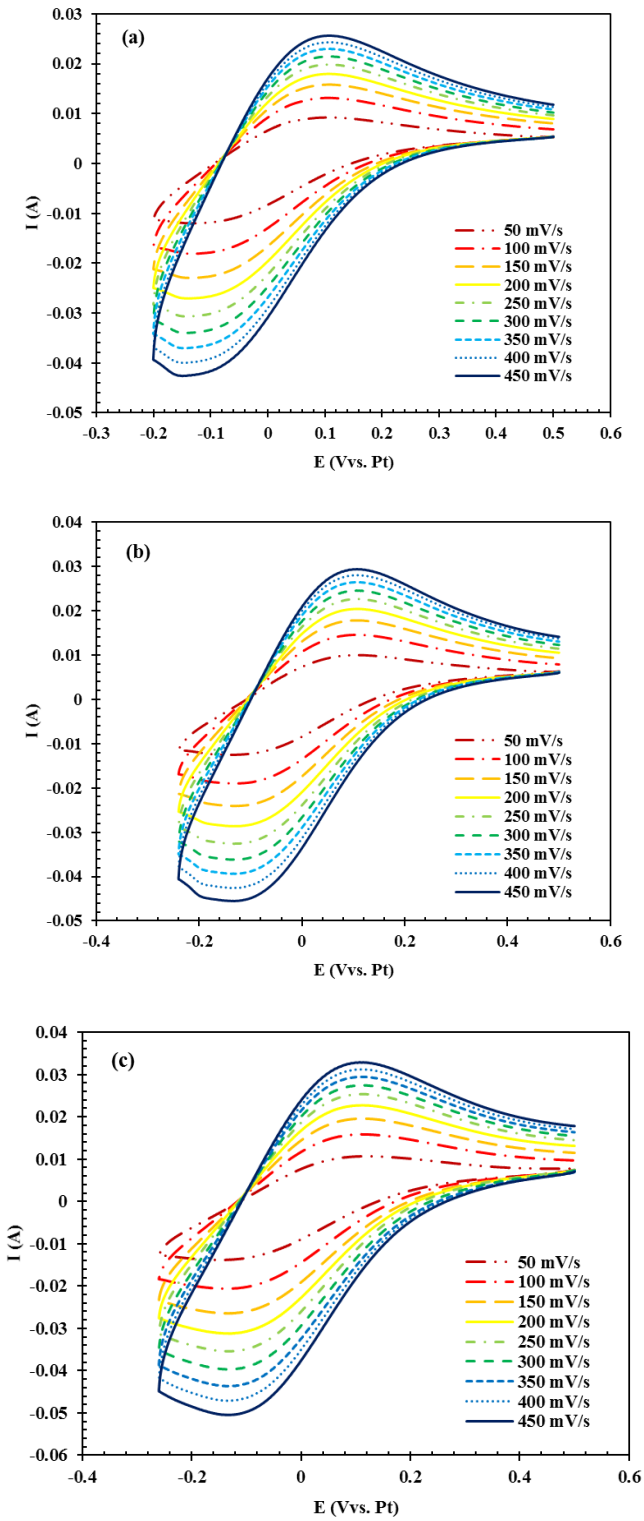

Figure 4-38: Cyclic voltammograms of redox reaction Cr (III)/Cr (II) couple in FLiNaK molten salt at (a) 923 K, (b) 973K, and (C) 1023K. Working electrode: tungsten (s=0.6481 cm^2), reference electrode: platinum, counter electrode: graphite.

The Randles-Sevcik equation (Eq. (4-78)) is typically used for the electrode processes where the electrochemical equilibrium is reversible and achieved between two soluble species.

$$i_{\mathrm{p}} = 0.4463nFAC_{\mathrm{b}}D^{1/2}\left(\frac{nFv}{RT}\right)^{1/2} \tag{4-78}$$

where i_{p} is the peak current density, A; D is the diffusion coefficient, cm^2/s; C_{b} is bulk concentration, mol/cm^3; n is the number of exchanged electrons of the reaction; and v is the scan rate, V/s; A is the electrode area, cm^2. However, it should be noted that the derivation of Randles-Sevcik equation is based on the assumption of no reductant in presence. Peng et al [2] used electrochemical techniques and spectrometry method such as Raman spectroscopy, X-ray powder diffraction (XRD), and Scanning electron microscope (SEM) to investigate the stable chromium species in molten FLiNaK. It is found Cr (III) is more stable than Cr (II) in FLiNaK melt and Cr (II) can be converted to Cr (III) via disproportion: 3 Cr (II) ↔ 2 Cr (III) + Cr. The conversion ratio of Cr (II) to Cr (III) was also confirmed with the values of 86.71% to 88.23% for different concentrations by Peng et al [2] at the temperature of 873 K. Normally, the conversion ratio may fluctuate a little at different temperatures. However, we did not find a good way to measure the conversion ratio in the present study. Thus, the average conversion ratio of Cr (II) to Cr (III), 87.57%, reported in the previous study [2] is used to determine the concentration of Cr (II) and Cr (III) in FLINaK melt which are 2.95×10^{-5} mol/cm^3 and 1.39×10^{-4} mol/cm^3, respectively.

For the system with both oxidant and reductant exist, the theory developed by Keightley et al [5] can be adopted for the data analysis of the reversible cyclic voltammogram. For the reversible cyclic voltammetry in the presence of product, the current density in the forward sweep $\vec{\imath}$ and backward sweep $\overleftarrow{\imath}$ can be expressed by [5,6]

$$\vec{\imath} = nF\left(C_{\mathrm{b}}^{\mathrm{R}}{D_{\mathrm{R}}}^{1/2} + C_{\mathrm{b}}^{\mathrm{O}}{D_{\mathrm{O}}}^{1/2}\right)\left(\frac{nFv}{RT}\right)^{1/2}\chi(\xi;\xi_i) \tag{4-79}$$

$$\overleftarrow{\imath} = nF\left(C_{\mathrm{b}}^{\mathrm{R}}{D_{\mathrm{R}}}^{1/2} + C_{\mathrm{b}}^{\mathrm{O}}{D_{\mathrm{O}}}^{1/2}\right)\left(\frac{nFv}{RT}\right)^{1/2}[\chi(2\xi_r-\xi,\xi_i) - \chi(2\xi_r-\xi,\xi_r) - \chi(-\xi,\xi_r)] \tag{4-80}$$

where $\chi\,(x,\alpha) = \frac{\mathrm{d}^{1/2}}{\mathrm{d}x^{1/2}}\frac{1}{2\sqrt{\pi}}\left[\tanh\left(\frac{x+\alpha}{2}\right) - \tanh(\frac{\alpha}{2})\right]$; $\xi = nF(E-E_{1/2})/RT$; $\xi_i = nF(E_i - E_{1/2})/RT$; $\xi_r = nF(E_r - E_{1/2})/RT$; $E_i = E_{1/2} + \frac{RT}{nF}\ln\frac{C_{\mathrm{b}}^{\mathrm{O}}{D_{\mathrm{O}}}^{1/2}}{C_{\mathrm{b}}^{\mathrm{R}}{D_{\mathrm{R}}}^{1/2}}$; E_r is the reversal potential; $E_{1/2}$ is half wave potential.

Either the forward or the backward branch of the cyclic voltammogram can be calculated by Eqs. (4-79) and (4-80). It is found the value of $C_{\mathrm{b}}^{\mathrm{R}}{D_{\mathrm{R}}}^{1/2}/C_{\mathrm{b}}^{\mathrm{O}}{D_{\mathrm{O}}}^{1/2}$ is solely dependent on the current peak potential difference ΔE_p between the forward current peak and backward current peak [5]. It means the ratio of D_{R} to D_{O} can be predicted by the value of ΔE_p determined from the experimental cyclic voltammetry. *Table 4-10* presents the current peak potential difference in cyclic voltammetry shown in Figure 4-38. ΔE_p are averaged with the values of 0.2490 V at 923 K, 0.2425 V at 973 K, and 0.2492 V at 1023 K. The values

of $\frac{nF}{RT}\Delta E_p$ are calculated and the corresponded values of $\frac{C_{\mathrm{b}}^{\mathrm{Cr(III)}} D_{\mathrm{Cr(III)}}{}^{1/2}}{C_{\mathrm{b}}^{\mathrm{Cr(II)}} D_{\mathrm{Cr(II)}}{}^{1/2}}$ obtained from Eqs. (4-79) and (4-80) are listed in Table 4-11. The shapes and peaks of cyclic voltammograms calculated from Eqs. (4-79) and (4-80) will vary with values of $\frac{C_{\mathrm{b}}^{\mathrm{Cr(III)}} D_{\mathrm{Cr(III)}}{}^{1/2}}{C_{\mathrm{b}}^{\mathrm{Cr(II)}} D_{\mathrm{Cr(II)}}{}^{1/2}}$ and the corresponded $\frac{|i_p|}{nFC_{\mathrm{b}}^{\mathrm{Cr(III)}} D_{\mathrm{Cr(III)}}{}^{1/2}}\left(\frac{RT}{nFv}\right)^{1/2}$ is also listed in Table 4-11.

Table 4-10: Current peak potential difference determined in cyclic voltammetry at different temperatures and scan rates.

Scan rate (mV/s)	ΔE_p (V)		
	923 K	973 K	1023 K
50	0.2340	0.2550	0.2651
100	0.2380	0.2411	0.2630
150	0.2431	0.2341	0.2450
200	0.2431	0.2411	0.2510
250	0.2481	0.2411	0.2541
300	0.2511	0.2421	0.2421
350	0.2515	0.2404	0.2464
400	0.2566	0.2566	0.2446
450	0.2605	0.2435	0.2474

Table 4-11: The predicted coordinates of cyclic voltammetry current peaks at the selected bulk concentration ratios for the cyclic voltammetry results shown in Figure 4-38.

Temperature (K)	$\frac{nF}{RT}\Delta E_p$	$\frac{C_{\mathrm{b}}^{\mathrm{Cr(III)}} D_{\mathrm{Cr(III)}}{}^{1/2}}{C_{\mathrm{b}}^{\mathrm{Cr(II)}} D_{\mathrm{Cr(II)}}{}^{1/2}}$	$\frac{\lvert i_p \rvert}{nFC_{\mathrm{b}}^{\mathrm{Cr(III)}} D_{\mathrm{Cr(III)}}{}^{1/2}}\left(\frac{RT}{nFv}\right)^{1/2}$
-	2.236	0	0.4463
923	3.131	2.216	0.5611
973	2.898	1.533	0.5477
1023	2.825	1.341	0.5425

As known in Table 4-11, for every value $\frac{nF}{RT}\Delta E_p$ obtained from cyclic voltammogram, there is a value for $\frac{|i_p|}{nFC_{\mathrm{b}}^{\mathrm{Cr(III)}} D_{\mathrm{Cr(III)}}{}^{1/2}}\left(\frac{RT}{nFv}\right)^{1/2}$ corresponded and it can be used to calculate the

diffusion coefficient of Cr (III) in FLiNaK $D_{\mathrm{Cr(III)}}$ directly. For the system without the presence of product, the value of $\frac{C_{\mathrm{b}}^{\mathrm{Cr(III)}} D_{\mathrm{Cr(III)}}{}^{1/2}}{C_{\mathrm{b}}^{\mathrm{Cr(II)}} D_{\mathrm{Cr(II)}}{}^{1/2}}$ is 0 and $\frac{|i_p|}{nFC_{\mathrm{b}}^{\mathrm{Cr(III)}} D_{\mathrm{Cr(III)}}{}^{1/2}}\left(\frac{RT}{nFv}\right)^{1/2} = 0.4463$ which is the Randles-Sevcik equation (4-78) commonly used. Figure 4-39 shows in the linear relationship between the cathodic current peaks $i_{p,c}$ and scan rate v at the temperatures of 923 K, 973 K, and 1023 K. The slopes as given in Figure 4-39 are used to determine the diffusion coefficients $D_{\mathrm{Cr(III)}}$ which are 1.19×10^{-5} cm^2/s at 923 K, 1.46×10^{-5} cm^2/s at 973 K, and 1.66×10^{-5} cm^2/s at 1023 K, respectively. Based on the obtained $D_{\mathrm{Cr(III)}}$, the diffusion coefficient for Cr (II) in molten FLiNaK can be obtained from the values of $\frac{C_{\mathrm{b}}^{\mathrm{Cr(III)}} D_{\mathrm{Cr(III)}}{}^{1/2}}{C_{\mathrm{b}}^{\mathrm{Cr(II)}} D_{\mathrm{Cr(II)}}{}^{1/2}}$ listed in the third column of Table 4-11. The acquired $D_{\mathrm{Cr(II)}}$ are 0.53×10^{-4} cm^2/s at 923 K, 1.37×10^{-4} cm^2/s at 973 K, and 2.04×10^{-4} cm^2/s at 1023 K, respectively.

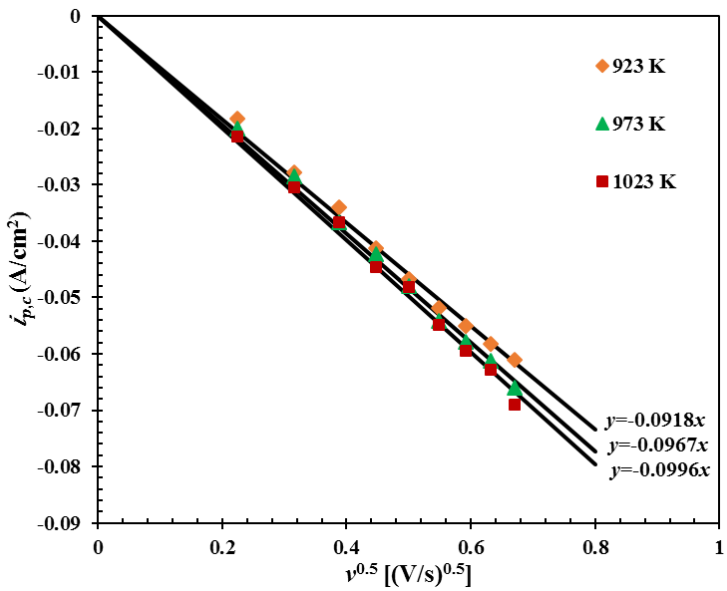

Figure 4-39: Linear relationship of $i_{p,c}$ versus $v^{0.5}$ for the cyclic voltammogram given in Figure 4-38.

Chronopotentiometry test can also be used to study the thermodynamic properties of Cr (III) and Cr (II) in FLiNaK. As discussed before, there are two charge reactions happen for Cr (III) when applying a reduction current: $Cr^{3+}+e^{-}\leftrightarrow Cr^{2+}$ and $Cr^{2+}+2e^{-}\leftrightarrow Cr$. It is found that the plateau for the first charge reaction $Cr^{3+}+e^{-}\leftrightarrow Cr^{2+}$ is not easy to be identified from Figure 4-37. In order to obtain an obvious potential transition and then confirm the transition time for the first charge reaction, small currents were applied here. Figure 4-40 shows the typical chronopotentiograms for charge reaction of $Cr^{3+}+e^{-}\leftrightarrow Cr^{2+}$ obtained at the temperature of 923 K. Whereras, higher currents were applied for obtaining the potential transition of the charge reaction $Cr^{2+}+2e^{-}\leftrightarrow Cr$, a representative of the resulting chronopotentiograms were shown in Figure 4-41.

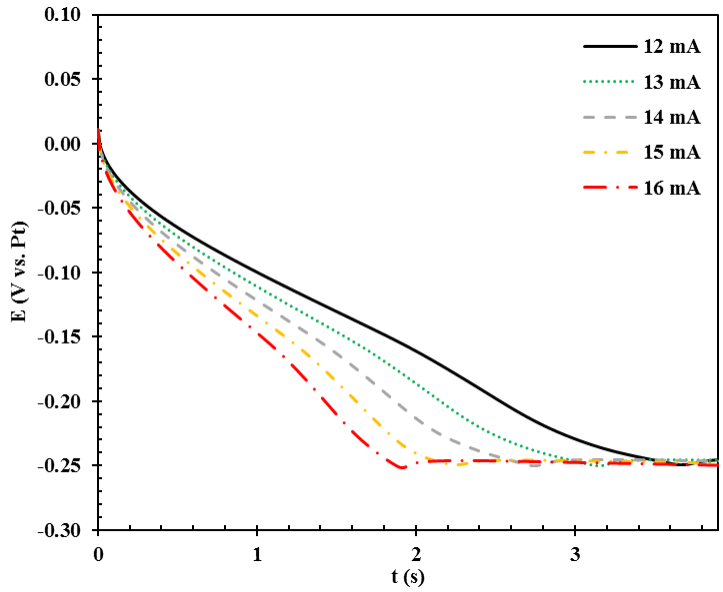

Figure 4-40: Typical chronopotentiograms for reaction of $Cr^{3+}+e^{-} \leftrightarrow Cr^{2+}$ at 923 K for molten FLiNaK with addition of CrF_2.

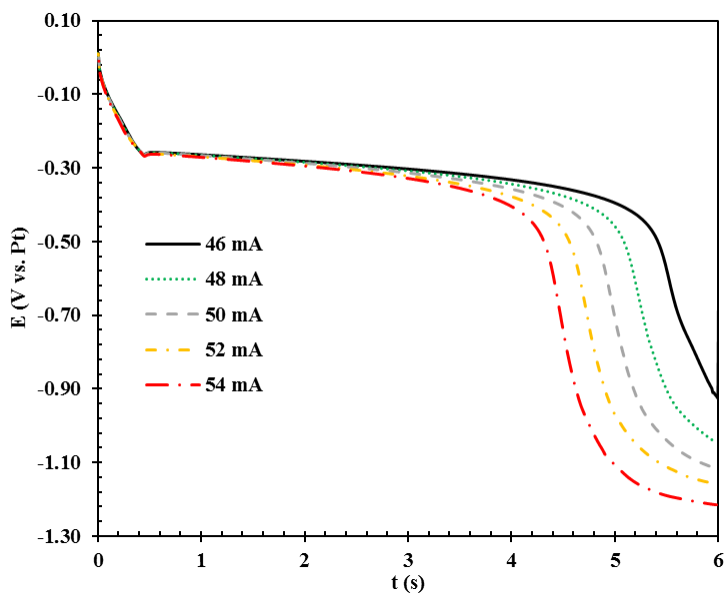

Figure 4-41: Typical chronopotentiograms obtained at 923 K for molten FLiNaK with addition of CrF_2 when applying higher currents.

In chronopotentiometry test, the transition time can be determined from the chronopotentiogram using the method described in the literature [7]. The plots of I versus $\tau^{-1/2}$ in Figure 4-30 exhibit a linear relationship passing through the origin point. It indicates the Sand's equation [8] is applicable for the redox couple Cr (III)/ Cr (II). The diffusion coefficient of Cr (III) in molten FLiNaK can be calculated from the plot slope of I versus $\tau^{-1/2}$ through Sand's equation

$$I\tau^{1/2} = 0.5nFC_{\mathrm{b}}^{\mathrm{Cr(III)}}A\pi^{1/2}D_{\mathrm{Cr(III)}}{}^{1/2} \quad (4\text{-}81)$$

where I is the applied current, A; τ is the transition time, s; A is the working electrode surface area, cm^2.

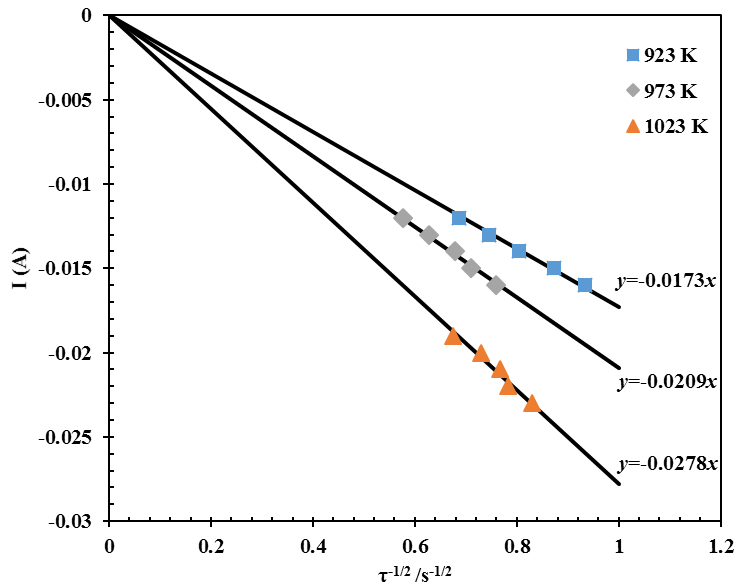

Figure 4-42: Linear relationship of I versus $\tau^{-1/2}$ for the chronopotentiometry test of redox couple Cr (III)/ Cr (II) at different temperatures.

For the second charge reaction Cr (II) +e$^-$↔ Cr, the sand's equation which is applied for one simple charge transfer process cannot be used. For that reason, equations were derived here for two charge reactions with the presence of both reactant and intermediate product in electrolyte initially. The two charge reactions can be expressed by the following elementary processes (4-82) and (4-83):

$$A + n_1 e \leftrightarrow B \quad (4\text{-}82)$$

$$B + n_2 e \leftrightarrow C \quad (4\text{-}83)$$

If the reactant A, intermediate product B, and final product C obey Fick's law, the following initial and boundary conditions can be assumed [9,10]:

$$C_A = C_A{}^*, C_B = C_B{}^*, C_C = 0; t = 0 \quad (4\text{-}84)$$

$$C_A \to C_A{}^*, C_B \to C_B{}^*, C_C \to 0; t > 0; x \to \infty \quad (4\text{-}85)$$

$$(n_1+n_2)D_A\frac{\partial C_A}{\partial x}+n_2D_B\frac{\partial C_B}{\partial x}=\frac{i}{FA};t>0;x=0 \tag{4-86}$$

where ${C_A}^*$ and ${C_B}^*$ are bulk concentrations of species A and B in electrolyte, respectively.

The diffusion equations to be solved for reactions (4-82) and (4-83) are

$$\begin{cases}\frac{\partial C_A}{\partial t}=D_A\left(\frac{\partial^2 C_A}{\partial x^2}\right)\\ \frac{\partial C_B}{\partial t}=D_B\left(\frac{\partial^2 C_B}{\partial x^2}\right)\\ \frac{\partial C_C}{\partial t}=D_C\left(\frac{\partial^2 C_C}{\partial x^2}\right)\end{cases} \tag{4-87}$$

If only species A and B are initially present in the electrolyte, the Laplace transformation of Eq. (4-87) can be expressed by

$$\begin{cases}\overline{C_A}(x,s)=\frac{{C_A}^*}{s}+\left[\overline{C_A}(x=0)-\frac{{C_A}^*}{s}\right]exp\left(-\sqrt{s/D_A}x\right)\\ \overline{C_B}(x,s)=\frac{{C_B}^*}{s}+\left[\overline{C_B}(x=0)-\frac{{C_B}^*}{s}\right]exp\left(-\sqrt{s/D_B}x\right)\\ \overline{C_C}(x,s)=\overline{C_C}(x=0)exp\left(-\sqrt{s/D_C}x\right)\end{cases} \tag{4-88}$$

The Laplace transform of one boundary condition Eq. (4-86) for constant current can be given by

$$(n_1+n_2)D_A\frac{\partial\overline{C_A}(x,s)}{\partial x}+n_2D_B\frac{\partial\overline{C_B}(x,s)}{\partial x}=\frac{i}{sFA} \tag{4-89}$$

The differentiation of Eq.(4-88) with respect to x at x=0 yields the following expression

$$\begin{cases}\left(\frac{\partial\overline{C_A}(x,s)}{\partial x}\right)_{x=0}=-\sqrt{s/D_A}\left[\overline{C_A}(x=0)-\frac{{C_A}^*}{s}\right]\\ \left(\frac{\partial\overline{C_B}(x,s)}{\partial x}\right)_{x=0}=-\sqrt{s/D_B}\left[\overline{C_B}(x=0)-\frac{{C_B}^*}{s}\right]\\ \left(\frac{\partial\overline{C_C}(x,s)}{\partial x}\right)_{x=0}=-\sqrt{s/D_C}\overline{C_C}(x=0)\end{cases} \tag{4-90}$$

Substituting Eq. (4-90) to Eq. (4-89), then Eq. (4-91) can be obtained

$$\begin{aligned}&(n_1+n_2){D_A}^{1/2}\overline{C_A}(x=0)+n_2{D_B}^{1/2}\overline{C_B}(x=0)\\ &=(n_1+n_2){D_A}^{1/2}\frac{{C_A}^*}{s}+n_2{D_B}^{1/2}\frac{{C_B}^*}{s}-\frac{i}{s^{3/2}FA}\end{aligned} \tag{4-91}$$

The inverse Laplace transformation of Eq. (4-91) can be performed and the expression for time-dependent surface concentrations of species A and B is yielded:

$$(n_1 + n_2){D_A}^{1/2}C_A(x = 0) + n_2{D_B}^{1/2}C_B(x = 0) = (n_1 + n_2){D_A}^{1/2}{C_A}^* + n_2{D_B}^{1/2}{C_B}^* - \frac{2it^{1/2}}{\pi^{1/2}FA} \quad (4\text{-}92)$$

After the two potential transitions happen for the two charge transfer reactions, that is, at the overall transition time τ, both $C_A(x = 0)$ and $C_B(x = 0)$ drop to zero, Eq. (4-92) can be rewritten by

$$(n_1 + n_2){D_A}^{1/2}{C_A}^* + n_2{D_B}^{1/2}{C_B}^* = \frac{2i\tau^{1/2}}{\pi^{1/2}FA} \quad (4\text{-}93)$$

Based on Eq. (4-93), the diffusion coefficient of Cr (II) in molten FLiNaK can be obtained after knowing diffusion coefficient of Cr (III) by Sand's equation (4-81). The $i\tau^{1/2}$ in Eq.(4-93) is determined by linear fitting the slope of I versus $\tau^{-1/2}$ with the intercept of zero. The fitting curves for the temperatures of 923 K, 973 K, and 1023 K are shown in Figure 4-43 and the calculated diffusion coefficients of Cr (II) at this different temperatures are summarized and listed in

Table 4-12.

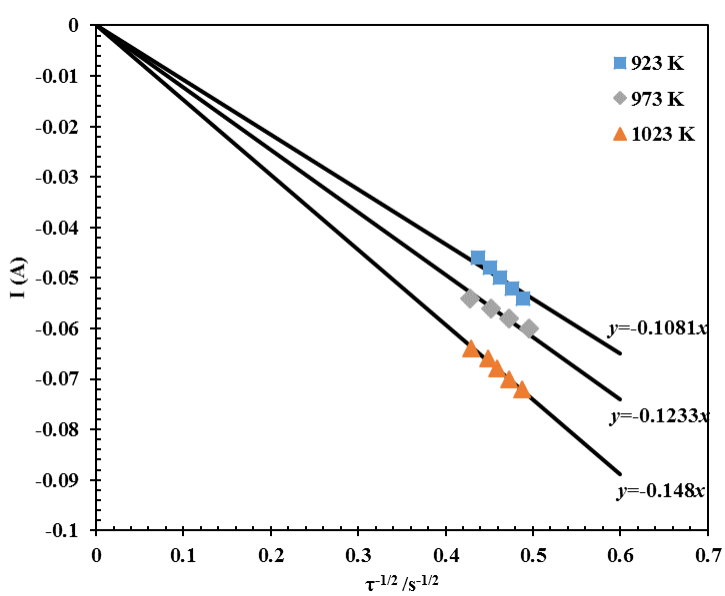

Figure 4-43: Linear relationship of I versus $\tau^{-1/2}$ for the chronopotentiometry overall reaction of Cr (III) to Cr at different temperatures.

Table 4-12: diffusion coefficients of Cr (III) and Cr (II) obtained at different temperatures by CV and CP methods

Temperature (K)	Diffusion coefficient		Method
	Cr (III) ($cm^2/s \times 10^{-5}$)	Cr (II) ($cm^2/s \times 10^{-4}$)	
923	1.19	0.53	CV
	0.51	2.95	CP
973	1.46	1.37	CV
	0.74	3.43	CP
1023	1.66	2.04	CV
	1.31	3.90	CP

4.5.2. Potentiometic Polarization Studies of Cr and Fe in the FLiNaK

4.5.2.1. Experimental methods

All the electrochemical tests and the salt preparation were done in a glove box system manufactured by Inert Technology. The glove box system was equipped with a gas purification system to recirculate argon gas, and sensors to monitor the concentration of H_2O and O_2 impurities in the atmosphere. During all tests in this study, the H_2O and O_2 impurities in the glove box were controlled under 5 ppm.

The anhydrous lithium fluoride (LiF, ≥99% purity), sodium fluoride (NaF, ≥99% purity), and potassium fluoride (KF, ≥99.5% purity) were procured from Sigma Aldrich. For each test, 50 g of FLiNaK salt was prepared according to its eutectic composition, 46.5LiF-11.5NaF-42KF in mol%. The inductively coupled plasma mass spectroscopy analysis of a FLiNaK salt sample detected impurities of 2 ppm Ni, 8 ppm Fe, 5 ppm Cr, and 1 ppm Mn. The salt powders were weighed using an analytical balance (Mettler Toledo MS) with an accuracy of 10^{-5} g in the glove box. Anhydrous chromium difluoride (CrF_2) and iron difluoride (FeF_2) with greater than 99.0% purity were procured from Sigma Aldrich. Additional 0.2 g of FeF_2 or CrF_2 was added in the prepared FLiNaK salt mixture, corresponding to a weight percent of 0.4 wt%. Then the weighed salt powders were mixed in a dry alumina crucible (CoorsTek AD-998). The crucible was placed in an auto electro-melt furnace (Kerr Series 1361), and the salt mixture was dehydrated at 300°C under argon atmosphere for at least 8 hours.

The furnace was equipped with a three-electrode system, as shown in Figure 4-44. The working electrode (WE) was an iron rod (99.9% purity from American Elements) or a chromium rod (99.9% purity from American Elements) with a diameter of 3 mm. The counter electrode (CE) was a pure tungsten rod (Miller Weldcraft) with a dimeter of 4 mm,

and the reference electrode (WE) was a platinum wire. Platinum can serve as a quasi-reference electrode in molten salts with the potential associated with $Pt/PtO_x/O^{2-}$. All the electrodes were polished by gauze, rinsed, and dried before use.

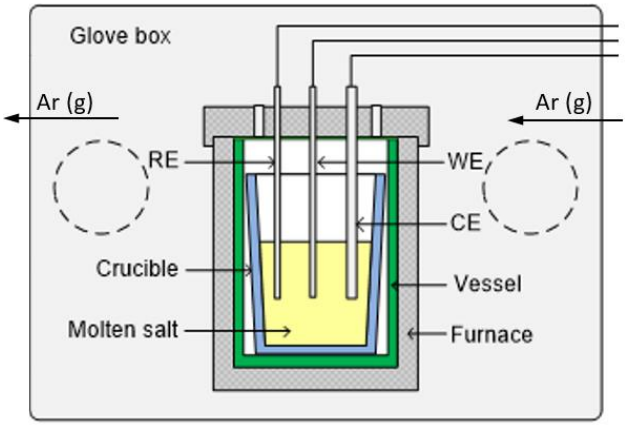

Figure 4-44: Schematic illustration of the electrochemical cell. Dashed circles represent glove ports.

Prior to each test, the melt was heated to the desired test temperature and maintained for 3 hours. Then the CE and RE were loaded into the melt. An ohmmeter connected to WE and CE was used to determine the surface area of the WE exposed to the melt. The WE was slowly moved down, and the ohmmeter was triggered at the length where the WE touched the top surface of the molten salt. The length at the initial touching and final immersion locations were marked, and the immersion depth of the WE in the melt was indicated by the difference. The determined immersion depth of the WEs varied slightly for different tests, and the resulted surface area for all tests in this work was in the range of 1.53 cm^2 to 1.92 cm^2.

The electrodes were connected to a Gamry Interface 1000 Potentiostat/Galvanostat/ZRA. Open circuit potential (OCP) measurement was followed immediately after the immersion of WE. After the stabilization of OCP, the potential was swept at a scan rate of 1 mV/s in the anodic direction. At least one replicate tests were performed at a different scan rate or with the potential swept in the opposite direction, showing nonobvious deviation at different scan directions and scan rates. As the prepared FLiNaK salt was dehydrated at 300°C and only contained ppm levels of metallic impurities, the concentrations of the residual oxidants in the salt were considered to be negligible compared to the 0.4 wt% of CrF_2 or FeF_2 in the FLiNaK salt. Furthermore, the residual oxidizing impurities might be exhausted soon by the oxidation of Cr or Fe metal at the beginning of the test. Therefore, the stabilized OCPs of the WE were assumed to be the equilibrium potentials of Cr^{2+}/Cr^0 or Fe^{2+}/Fe^0.

Additionally, electrochemical impedance spectroscopy (EIS) was carried out at the OCP with an amplitude of 10 mV over a frequency ranging from 50 kHz to 0.1 Hz to estimate the resistance of molten salt electrolyte. The electrolyte resistance in the cell was estimated by the EIS measurement for each test. The product of electrolyte resistance with electrode surface area from various tests was in the range of 0.15-0.31 $\Omega \cdot cm^2$. In fact, the ohmic

potential drop caused by such small resistance will not cause considerable distortion of the measured polarization curves. Nevertheless, during all polarization measurement, the applied potentials were automatically corrected by the current interrupt iR compensation function in Gamry Framework software. Thus, the reported polarization data are free of iR errors.

4.5.2.2. Determining of the exchange current density

Three methods were applied to determine the electrochemical kinetics parameters of the dissolution of chromium and iron in molten FLiNaK based on the measured polarization data. All the methods are based on the Butler-Volmer equation which describes the kinetics of an electrochemical reaction with an assumption of no mass-transfer influence:

$$i = i_0 \left\{ \exp[\frac{(1-\alpha)nF}{RT}\eta] - \exp[\frac{-\alpha nF}{RT}\eta] \right\} \quad (4\text{-}94)$$

where i is the current density, A/m^2; i_0 is the exchange current density, A/m^2; α is the charge-transfer coefficient ranging from zero to unity; n is the number of exchanged electrons: F is the Faraday constant, 96485 C/mol; R is the ideal gas constant, 8.314 J/K/mol; T is the absolute temperature, K; $\eta = E - E_{eq}$ is the overpotential, V; E and E_{eq} are the potential and equilibrium potential, V, respectively.

(1) Optimized fitting

The measured current-potential curve can be fitted by the Butler-Volmer equation (4-94). The optimized fitting was performed by the iterations of α and i_0. The iteration of α was performed in the range of 0.0001-0.999 with a step size of 0.0001, while the i_0 was iterated between the the minimum and maximum values of the measured absolute cathodic current densities at each α. The current density at each α and i_0 were calculated. The absolute difference between the calculated current density and the experimental one at all potentials was summed and set as the deviation of the fitting. The values of α and i_0 resulting in the minimum deviation (i.e., best fitting of the measured polarization curve) were selected as the optimized values.

(2) Tafel method

When $|\eta|$ is sufficiently large, either the first or second exponential term in Eq. (4-94) becomes negligible. Thus, Eq. (4-94) can be re-written as:

$$\lg(|i|) = \lg(i_0) + \frac{(1-\alpha)nF}{2.3RT}\eta;\ \eta > 0 \quad (4\text{-}95)$$

$$\lg(|i|) = \lg(i_0) - \frac{\alpha nF}{2.3RT}\eta;\ \eta < 0 \quad (4\text{-}96)$$

where the terms $\frac{2.3RT}{(1-\alpha)nF}$ and $-\frac{2.3RT}{\alpha nF}$ are defined as the anodic Tafel slope β_a and cathodic Tafel slope β_c, respectively.

Thus, the nearly linear portions are expected in the Tafel regions of the $\lg(|i|) - \eta$ curve. The intersection of this extrapolated linear curve with the equilibrium potential ($\eta = 0$)

line indicates the value of i_0. The charge-transfer coefficient can be calculated from the slope of the $\lg(|i|) - \eta$ curve in the Tafel region, i.e., the Tafel slope.

(3) Linear polarization (LP) method

For very small overpotentials (typically $|\eta| < 10$ mV), a linear correlation of the current density and overpotential can be obtained from Eq. (4-94) by using the Taylor approximation of $e^{f(\eta)}$ to $1 + f(\eta)$:

$$i = i_0 \left(\frac{nF}{RT}\right) \eta \tag{4-97}$$

Then the value of i_0 can be obtained by the slope of linear portion of the measured $i - \eta$ curve in very small overpotentials.

4.5.2.3. Exchange current density of Cr dissolution

Figure 4-45 shows the polarization curves of the chromium electrode in the molten FLiNaK salt containing 0.4 wt% CrF_2. The logarithmic current density is plotted against the overpotential in the range of -150 -150 mV. The solid lines in Figure 4-45(a) are the calculated current-potential curves using the optimized values of i_0 and α from the optimized fitting method. It is seen that the fitted curves agree well with the experimental data at all temperatures. The linear Tafel regions can also be observed in $|\eta| > 70$ mV range. An example of obtaining the i_0 using Tafel method is given at 700°C in Figure 4-45(a). The red dotted lines are the extrapolated lines in the Tafel regions and the equilibrium potential line. The value of the current at the intersection point is the exchange current density. Deviations may exist between the values obtained from anodic and cathodic Tafel extrapolations as indicated by the different i_0 values in Figure 4-45(a). Nevertheless, these deviations are normally small. The slopes of the extrapolated lines in the Tafel regions represent the Tafel slopes β_a and β_c, which are used to calculate the charge-transfer coefficient. The exchange current density can also be obtained by the linear fitting in very small overpotential region. As displayed in Figure 4-45(b), the curves indicate an increase of exchange current density with temperature. The slope of the linear trend line in the $|\eta| <$ 10 mV region was used to calculate the i_0 according to Eq. (4-97).

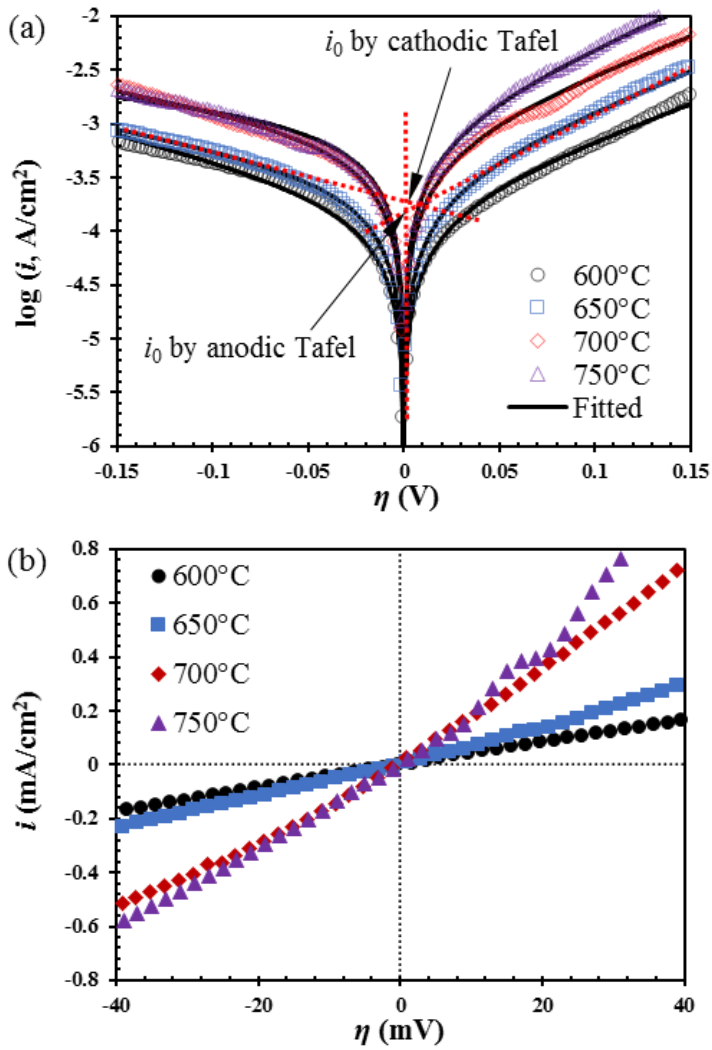

Figure 4-45: Polarization curves of Cr electrode in FLiNaK melt containing 0.4 wt% CrF_2, (a) plot of $\boldsymbol{lg}(|\boldsymbol{i}|) - \boldsymbol{\eta}$, (b) plot of $\boldsymbol{i} - \boldsymbol{\eta}$ in $|\boldsymbol{\eta}| < 40$ mV. Scan rate: 1 mV/s.

The average of the parameters obtained by different methods and the standard deviations from replicate tests are summarized in Table 4-13. For the Tafel method, the deviations of the values obtained from both the anodic and catholic Tafel regions are included. Table 4-13 indicates that the values of the exchange current density from the Tafel method are slightly lower but show a similar temperature dependence with the values from the optimized fitting method. Larger deviation of the i_0 obtained from LP method might be attributed to the fact that the LP method uses much less experimental data than the optimized fitting method. The charge-transfer coefficients obtained from the optimized fitting and Tafel methods are in good agreement. However, the large deviations of α values from the Tafel method at 700°C and 750°C are noticed. This might be due to the uncertainty introduced from the selection of the Tafel region. The term related to the reverse reaction current in Eq. (4-94) may not be negligible if η is not large enough. However, if the η is too large, the accelerated dissolution or deposition rate may cause

considerable change of the electrode surface roughness and the concentration of Cr^{2+}, leading to the distortion of the polarization curve. Thus, the values obtained from the optimized fitting method should be more representative compared to other two methods. This is expected because the theoretical base of all three methods is the same (Eq. (4-94)), and the optimized fitting method uses the most experiment data without introducing any conditional assumption for the simplification of the Butler-Volmer Equation.

Table 4-13: The exchange current densities for Cr^{2+}/Cr^0 couple in FLiNaK eutectic containing 0.4 wt% CrF_2.

T (°C)	i_0 (mA·cm^{-2})			α	
	Optimized fitting	Tafel	LP	Optimized fitting	Tafel
600	0.15	0.12 ± 0.07	0.17	0.42	0.28 ± 0.07
650	0.25 ± 0.01	0.19 ± 0.04	0.20 ± 0.05	0.33 ± 0.01	0.35 ± 0.09
700	0.57 ± 0.04	0.43 ± 0.11	0.54 ± 0.14	0.32 ± 0.02	0.36 ± 0.20
750	0.88	0.61	0.75	0.22	0.24

4.5.2.4. Exchange current density of Fe dissolution

Potentiodynamic polarization was also conducted using iron electrode in molten FLiNaK salt containing 0.4 wt% FeF_2 at different temperatures. As shown in Figure 4-46(a), the fitted curves from the optimized fitting method match well with the experimental data. The linear portion of the curves in the $|\eta|$ ranging from 70 mV to 150 mV were extrapolated to get the exchange current densities by Tafel method, and the charge-transfer coefficient was estimated by the Tafel slopes. The plot of current density versus overpotential displays good linear correlations in the $|\eta| < 10$ mV region, and the slope gradually increases with the increase in temperature, as displayed in Figure 4-46(b). The determined values using the three methods at various temperatures are given in Table 4-14. The exchange current density from all the methods increases with temperature, while the charge-transfer coefficient displays little temperature dependence. The results from the optimized fitting method exhibit good agreement with the values of i_0 obtained from LP methods. Similar to the chromium dissolution, the values of i_0 for iron dissolution from Tafel method are slightly lower than the other two methods and the large uncertainty of α is observed. The small values of α indicate a possibility of the involvement of the mass transfer effect in which case the cathodic reaction rate is limited by the maximum mass transfer rate from the bulk solution the electrode surface. However, as the anodic Tafel slopes also indicate small α values, the mass transfer effect is not considered in this study. Table 4-13 and Table 4-14 show that the exchange current densities of iron dissolution in molten FLiNaK are

about 1 order of magnitude larger than chromium dissolution at the same temperature. This does not mean iron is corroded faster than chromium as the corrosion rate corresponds to the dissolution current density at the corrosion potential rather than the equilibrium potential.

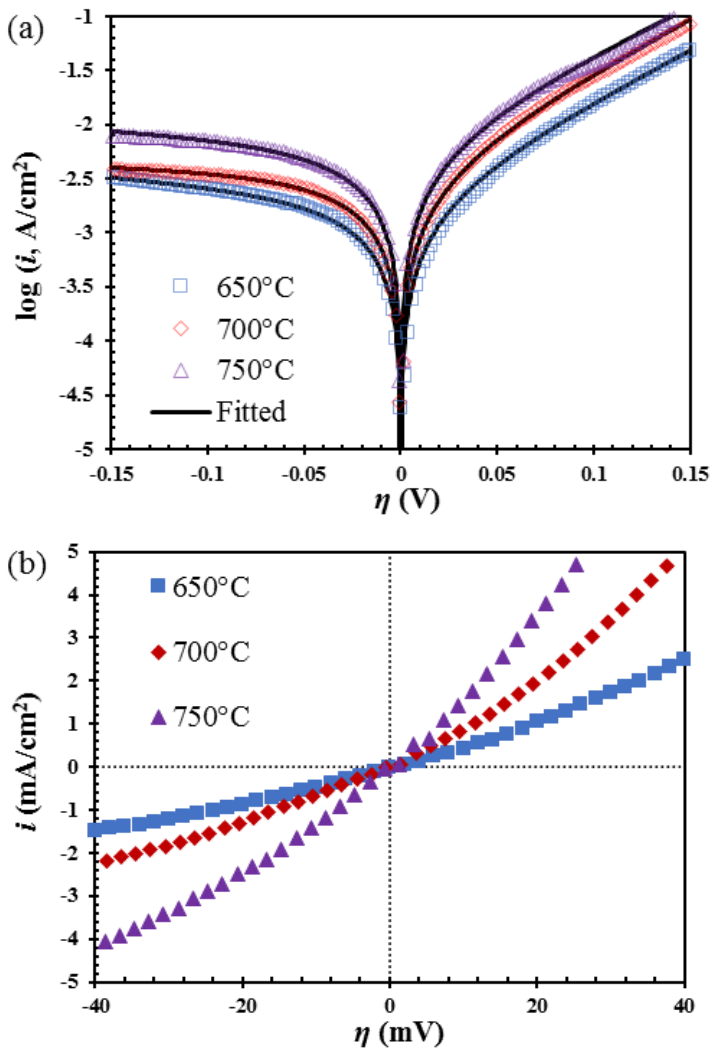

Figure 4-46: Polarization curves of Fe electrode in FLiNaK eutectic containing 0.4 wt% FeF_2 (a) plot of $\boldsymbol{lg}(|\boldsymbol{i}|) - \boldsymbol{\eta}$, (b) plot of $\boldsymbol{i} - \boldsymbol{\eta}$ in $|\boldsymbol{\eta}| < 40$ mV. Scan rate: 1 mV/s.

Table 4-14: The exchange current densities of Fe^{2+}/Fe^{0} couple in FLiNaK eutectic containing 0.4 wt% FeF_2.

T (K)	i_0 (mA·cm^{-2})			α	
	Optimized fitting	Tafel	LP	Optimized fitting	Tafel
923	1.89 ± 0.06	1.39 ± 0.19	1.78 ± 0.03	0.13 ± 0.01	0.13 ± 0.08
973	3.36 ± 0.03	2.73 ± 0.36	3.25 ± 0.09	0.09 ± 0.03	0.08 ± 0.03

1023	6.15	4.61 ± 0.17	6.15	0.11	0.10 ± 0.07

4.5.2.5. *Activation energies for Cr and Fe dissolution in FLiNaK melt*

The temperature dependence of the exchange current density can be expressed by the Arrhenius equation:

$$i_0 = Ae^{-E_a/RT} \tag{4-98}$$

where A is the pre-exponential factor, E_a is the activation energy associated with the Cr/Cr^{2+} or Fe/Fe^{2+} reaction.

To estimate the activation energy for the dissolution reactions of chromium and iron, the exchange current densities obtained from the optimized fitting method are plotted in natural logarithmic scale against the $1/T$, as shown in Figure 4-47. The slopes of the liner trend lines indicate an activation energy of 92.7 kJ/mol for Cr^{2+}/Cr^0, and 90.7 kJ/mol for Fe^{2+}/Fe^0 in molten FLiNaK salt. Fabre et al. [11] reported an activation energy of 127 ± 47 kJ/mol for iron corrosion in LiF-NaF (61-39 mol%) in the temperature range of 800-1100°C. It should be noted that their activation energy was determined by the corrosion current density instead of the exchange current density. As no FeF_2 was added in the melt [11], the reduction current of the residual oxidants in the LiF-NaF melt could be non-negligible, causing the polarization of the electrode away from its equilibrium potential. The larger deviation might be caused by the uncertainty of the coupling with the residual oxidants. Nevertheless, the lower limit of their reported activation energy is comparable with the value obtained from this study.

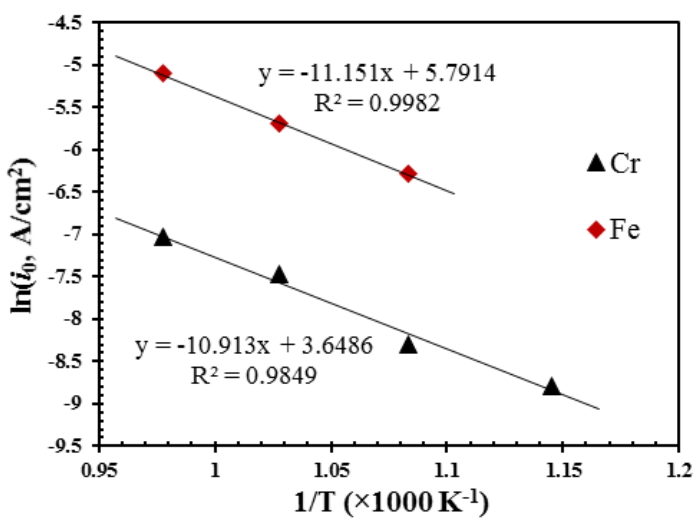

Figure 4-47: Plots of $\boldsymbol{ln(i_0)}$ versus 1/T for the dissolution of chromium and iron in molten FLiNaK melt.

4.5.3. Preliminary Investigation of Corrosion in FLiNaK

The corrosion behaviors of alloys Hastelloy N, SS 316L, Ni-201 and Incoloy 800 were investigated in FLiNaK at 700°C under argon. The composition of the abovementioned test materials is given in Table 4-15.

Table 4-15: Chemical composition of the materials (in weight percent).

	Ni	Cr	Fe	Mo	C	Si	Al	Mn	Ti	Others
Hastelloy N	76.30	7.33	4.00	16.41	0.06	1.00	1.00	1.00	-	balance
SS316	12.00	17.00	65.00	2.50	<0.03	<1.00	-	<2.00	-	balance
Ni 201	99.80	-	0.07	-	0.001	0.11	-	0.002	0.02	balance
Incoloy800	34.18	19.53	43.65	-	0.07	0.53	0.52	0.77	0.60	balance

Table 4-16 shows the test matrix and current status for the baseline corrosion test which is named as series C100. As shown in the table, two tests were designed for each material. The second one without polarization measurement at the end will be used for surface characterization, because the polarization will change the coupon surface. The potentiodynamic polarization curve was used to evaluate the instantaneous corrosion rate (corrosion current density), corrosion potential and Tafel slopes. The cross-sectional morphologies of the samples will be observed using scanning electron microscopy (SEM), and the composition will be analyzed by energy dispersive spectrometry (EDS). The test duration is 24 hours, and the temperature is 700 °C.

Table 4-16: Test matrix for series C100 and test status

Test #	Material	Salt	Measurements
C101	Hastelloy N	FLiNaK	OCP, EIS, Polarization
C102	Hastelloy N	FLiNaK	OCP, EIS, Cross-section SEM
C103	SS316	FLiNaK	OCP, EIS, Polarization
C104	SS316	FLiNaK	OCP, EIS, Cross-section SEM
C105	Ni-201	FLiNaK	OCP, EIS, Polarization
C106	Ni-201	FLiNaK	OCP, EIS, Cross-section SEM
C107	Incoloy 800	FLiNaK	OCP, EIS, Polarization
C108	Incoloy 800	FLiNaK	OCP, EIS, Cross-section SEM

Figure 4-48 shows the potentiodynamic polarization curves of four tested materials. Electrochemical parameters and the Tafel slopes (b_a and b_c) of the anodic and cathodic curves are estimated using Tafel extrapolation method are listed in Table 4-17. The corrosion potential values of SS316L, Incoloy-800, Hastelloy-N and Ni-201 are approximate -304.3, -335.0, -282.5, -221.6 mV (vs. Pt), respectively. The corresponding corrosion current densities (I_{corr}) are around at 21.2, 24.0, 15.8 and 9.9 μA/cm^2, respectively

The results indicate that the Tafel slope of the cathodic reaction of each material, βc, is similar (approximate 120 mV·dec-1), suggesting that cathodic reactions involved in FLiNaK salt are the same and follows the same mechanism. However, the exchange current densities of the cathodic reaction on the surface of different materials are very different. The Tafel slope of the anodic reaction of each material, βa, is obviously different, and has an order of Ni-201 > Hastelloy-N > Incoloy 800 > 316L. The corrosion current density of Ni 201 is the lowest while 316L and Incoloy 800 shows relatively higher corrosion current density.

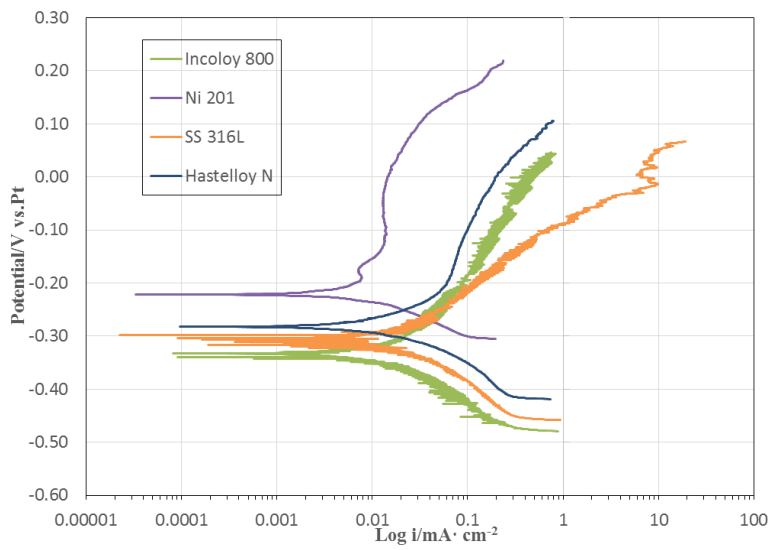

Figure 4-48: Polarization curves of alloys in molten FLiNaK salt at 700 °C

Table 4-17: Electrochemical parameters of potentiodynamic polarization tests.

Alloys	E_{corr}(mV)	I_{corr}(μA/cm²)	b_a	b_c	CR(mm/y)
SS316L	-304.3	21.2	139.2	126.1	0.23
Incoloy-800	-335.0	24.0	194.5	138.0	0.18
Hastelloy-N	-282.5	15.8	215.5	138.4	0.16
Ni-201	-221.6	9.9	235.4	112.7	0.10

Figure 4-49 shows the EIS data for tested materials. The results show the EIS plots of all alloys consist of a depressed semicircle that represents the charge transfer resistance. There is no dramatic change of resistance during the 24 hour test. Results also indicated that the impedance of the materials in FLiNaK salt changes in the following order: Ni-201 > Hastelloy-N > Incoloy 800 > 316L. These results indicate that Ni-201 has the best corrosion resistance in molten FLiNaK salt at 700 °C, followed by Hastelloy-N, Incoloy 800, and 316L.

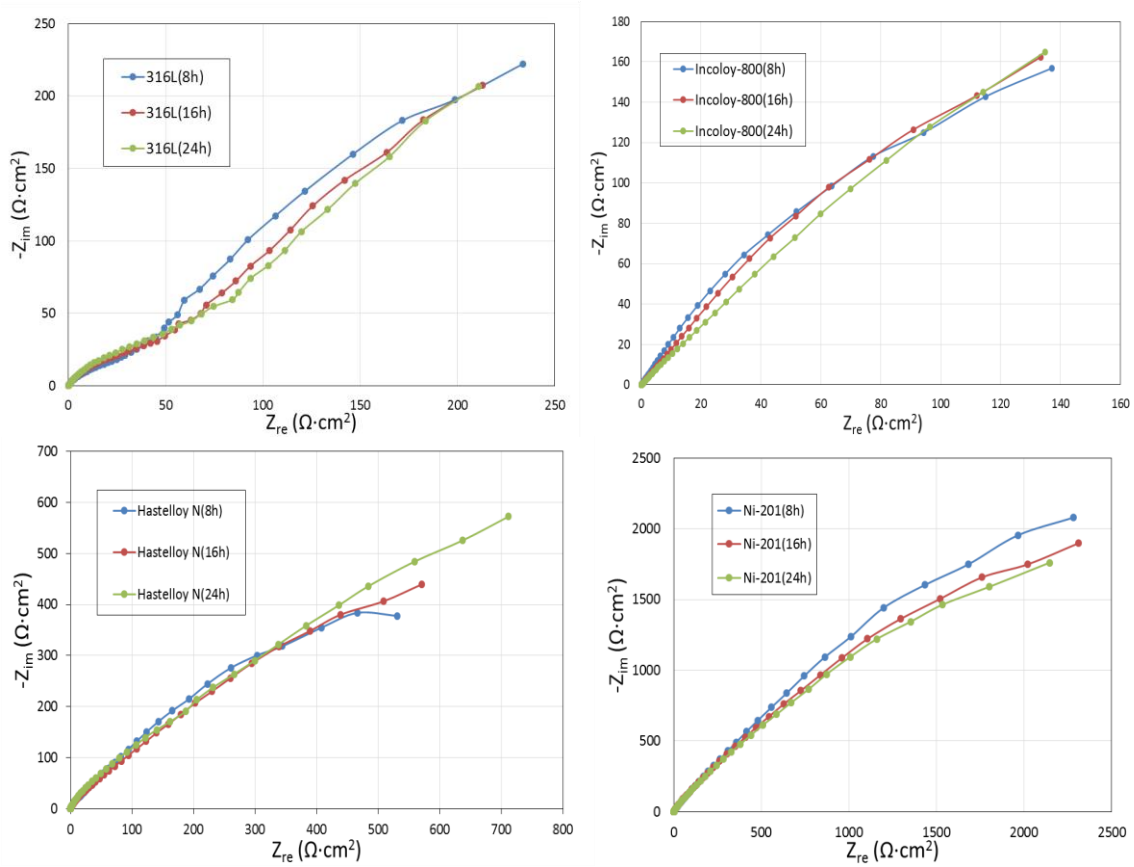

Figure 4-49: EIS of alloys in molten FLiNaK salt at 700 °C at different exposure time.

Fig. 6 shows the SEM photographs of the cross sections of the corroded samples covered with the remaining salts. The results indicate that there are not deposition on the surface of each alloy in this study. Hastelloy-N and Ni-201 have no obvious corrosion attack at the alloy/melt interface, while Incoloy-800 presents a change in content of metallic elements near the interface. SS316L shows a remarkable depletion layer of Fe and Cr near the interface.

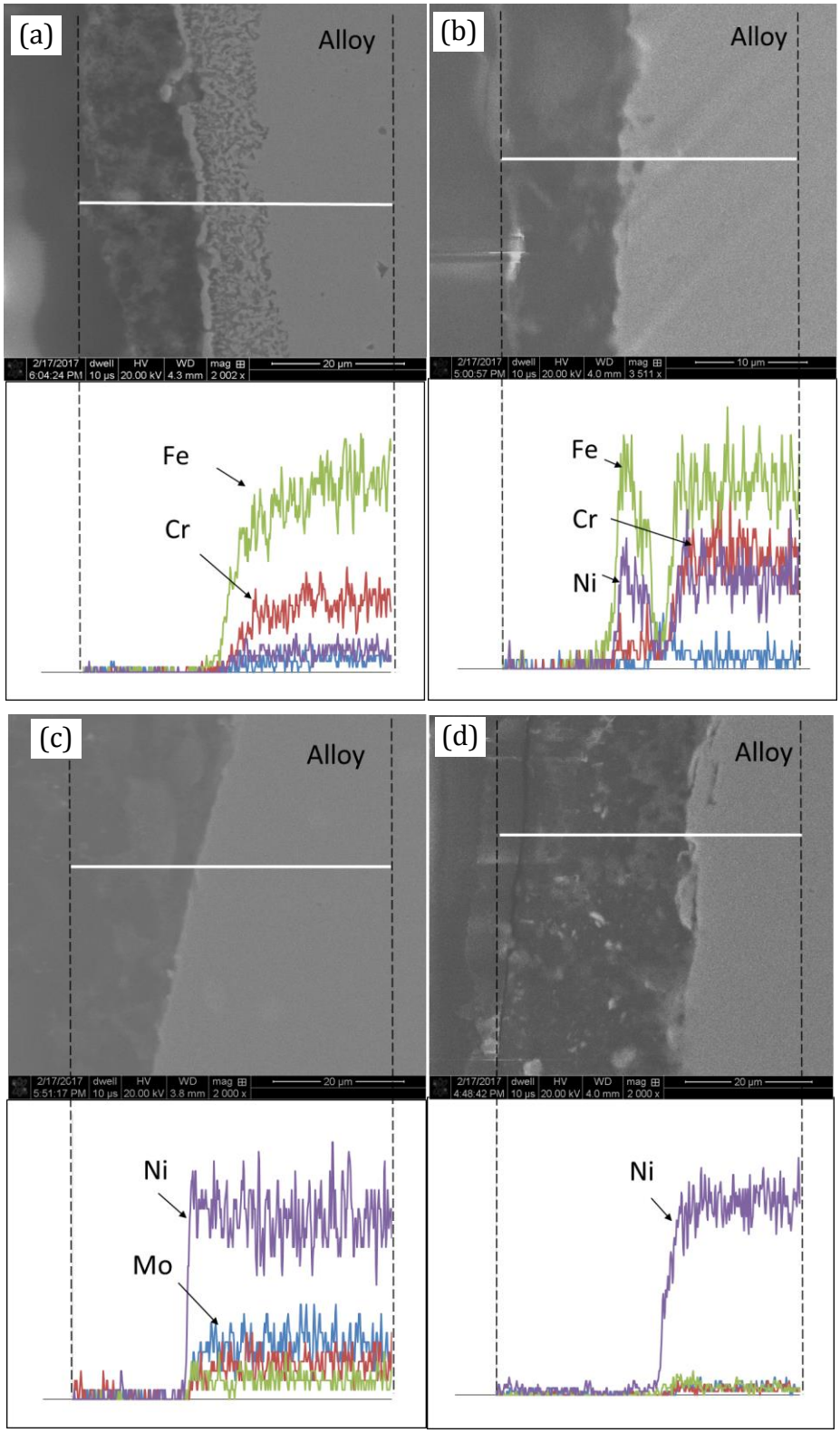

Figure 4-50: SEM photographs and alloying element distributions of different alloys after immersion experiments for 24 hours. (a) SS316L, (b) Incoloy-800, (c) Hastelloy-N, (d) Ni-201.

4.5.4. Summary

In this section, the diffusion coefficient of Cr (III) and Cr (II) in molten FLiNaK salt was studied by CV and CP methods at three temperatures. A new approach of analysis of the diffusion coefficients for two-step charge electrochemical reactions was utilized and the temperature dependence of Cr (III) and Cr (II) diffusion coefficients were determined.

Optimized fitting method, Tafel method, and LP method were used to calculate the exchange current density and the charge-transfer coefficient for Cr^{2+}/Cr^0 and Fe^{2+}/Fe^0 couples in molten FLiNaK salt. The i_0 and α values obtained from the three methods were in good agreement while optimized fitting method showed smaller uncertainty. The evaluated activation energy of the exchange current density was 91 ± 19 kJ/mol for Cr/Cr^{2+}, and 93 ± 6 kJ/mol for Fe/Fe^{2+}, respectively. The value of α for iron dissolution showed little temperature dependence, while α of Cr^{2+}/Cr^0 decreased with the increase in temperature in molten FLiNaK.

The corrosion resistance of Incoloy-800, Ni-201, SS316L and Hastelloy-N alloys were investigated in FLiNaK at 700°C using potentiodynamic polarization, EIS and cross-sectional SEM examination. The results of polarization curves shows the anodic dissolution rate of materials follows an order of Ni-201 > Hastellloy N > Incoloy-800 > SS316L, while the EIS showed opposite change of the impedance. The SEM results indicate nonobvious corrosion of Hastelloy-N and Ni-201 and severe void attack of SS316L up to a depth of 10 μm in 24 hours.

4.5.5. References

1. Yoko, Toshinobu, and Ronald A. Bailey. Journal of The Electrochemical Society 131.11 (1984): 2590-2595.
2. Peng, Hao, et al. RSC Advances 5.94 (2015): 76689-76695.
3. Wu, Wei, Shaoqiang Guo, and Jinsuo Zhang. Int. J. Electrochem. Sci 13 (2018): 225-234.
4. Heinze, J. Angewandte Chemie International Edition in English, 23(1984), 831-847.
5. Keightley, Angela M., et al. Journal of Electroanalytical Chemistry 322.1-2 (1992): 25-54.
6. Guo, Shaoqiang, et al. Journal of Nuclear Materials 496 (2017): 197-206.
7. Laity, Richard W., and James DE McIntyre. Journal of the American Chemical Society 87.17 (1965): 3806-3812.
8. A.J. Bard, L.R. Faulkner. New York, 2001.
9. Macdonald, Digby D. Springer, Boston, MA, 1977. 119-184.
10. Testa, A. C., and W. H. Reinmuth. Analytical Chemistry 33.10 (1961): 1320-1324.
11. S. Fabre, C. Cabet, L. Cassayre, P. Chamelot, S. Delepech, J. Finne, L. Massot, D. Noel, J. Nucl. Mater., 441 (2013) 583.

4.6. Separation and Properties of La_2O_3 in Molten FLiNaK Salt

4.6.1. Solubility Study of La_2O_3 in Molten FLiNaK Salt

4.6.1.1. Introduction

This work is a part of a project dealing with the electrochemical separation of impurities leaking into the primary molten salt coolant in the high temperature molten salt reactors with solid reactor fuel pellets. Here, lanthanum oxide dissolved in the molten fluoride salt was chosen as a model system. In this part, it will demonstrate the solubility and phase patterns at different temperatures to mimic the actual operation condition in the real reactor operation. As for the solubility of lanthanum oxide in the molten fluoride salt, the studies in this field is still limited. Until now only a few studies have been done. In 2008, Ambrová., et al [1] studied the solubility of lanthanum oxide in molten alkali fluorides with thermal analysis and concluded that the solubility of La_2O_3 in molten FLiNaK is 1.5 mol% which was lower than in pure LiF and NaF but higher than in KF. In R. M. Wheat's study[2], the isothermal saturated method was applied. It was demonstrated that the solubility of lanthanum oxide, samarium oxide and holmium oxide increased with the temperature and showed linear relationship between the nature logarithm of the solubility and the reciprocal temperature. In 2014, another study was conducted by X. L. Guo [3]. In his work, the available data on the rare earth oxide solubility in molten fluoride salt was summarized and analyzed which proposed that the rare earth oxide solubility increases with rare earth metal fluoride salt. However, the solubility of lanthanum oxide in these studies didn't accord with each other which indicated that more researches are still needed to further understand the solubility mechanism of lanthanum oxide in the molten fluoride salt. Besides the lanthanum oxide, there have been several studies on other lanthanide oxides which could give us a glance in this field and provide some references on the study of the lanthanum oxide. In E. Stefanidaki's research on the electrodeposition of neodymium from LiF-NdF_3-Nd_2O_3 melts, it was proposed that the neodymium oxyfluorides would be formed if neodymium oxide was added to the molten LiF [4]. S. I. Berul and N. K. Voskresenskaya studied the solubility of CeO2 and Sm2O3 in molten NaF-KF. They found that samarium oxide could form SmF3 and SmOF during the dissolving and there was also Na3SmF6 existed in NaF-KF melt [5].

4.6.1.2. Experiment Set up

Four experiments at four different temperatures are implemented to study the solubility at the corresponding temperature. Since the operation temperature of fluoride cooled high temperature reactor is between 600 C and 800°C, the experiment temperature in this study was set at 600°C, 650°C, 700°C and 750°C respectively to mimic the real operation condition in the reactors. LiF (BioUltra, ≥99.0%, Sigma), NaF (ACS regent, ≥99.0%, Sigma-Aldrich), KF (ACS regent, ≥99.0%, Sigma-Aldrich) and La_2O_3 (≥99.9%, Aldrich) were used in this experiment. Without special noting, all the operations are done in the glove box with <2.5ppm O2 level and <1.0ppm H2O level. Before the heating process, 1.5000g La_2O_3 was placed on the bottom of the Nickle crucible which serves as the salt container first. After

that, 14.6054g LiF, 5.8472g NaF, 29.5474g KF were mixed well before putting into the Nickle crucible which would lay at the top of the La_2O_3 to ensure the result accuracy of the experiment. Also, the furnace was preheating at 200°C for 1 hour to remove the possible moisture or other impurities that hidden in the furnace parts. Then, the alumina safety crucible and the Nickle crucible with salt inside were placed into the furnace. The temperature was kept at 200°C for another 2 hours to ensure that the moisture in the salt and other low boiling points impurities could be evaporated in this process. The heating temperature was increased to 400°C 2 hours later to remove those impurities with higher boiling points. Finally, after totally 5 hours' impurities removal process, the heating temperature would be set at the goal temperature, e. g. 600°C, 650°C, 700°C and 750°C and kept for different days as shown in Table 4-18 . During the heating process, samples were taken for Inductively Coupled Plasma Mass Spectrometry (ICP-MS) to analyze the on-site La^{3+} concentration in the molten salt. Moreover, the mass of ICP-MS samples taken each time was controlled at about 0.01g±0.005g to minimize the effect of sample mass measurement variance on the La^{3+} concentration. The ICP-MS samples were taken at the specific intervals as shown in Table 4-18.

The samples of the molten salt were also analyzed by the X-Ray powder diffraction (XRD) (PANalytical X'Pert PRO, Cu-Kβ, $\lambda = 1.387$Å) from 20-95° 2θ to determine the phase patterns.

Table 4-18 Solubility Experiment information

Heating temperature °C	Heating time Hours	Interval of samples taken Hours
600°C	384	6
650°C	336	6
700°C	73/282	6
750°C	336	6

4.6.1.3. Results and Analysis

During the experiments, it was found that there was still a large amount of insoluble material on the bottom of the crucible as shown in Figure 4-51, even after being heated for 384 hours. Therefore, XRD analysis was done to identify the phase patterns of the insoluble material and the melting mixture. As shown in Figure 4-52 which represents the phase patterns of the insoluble materials on the bottom, the sample consists LaOF and undissolved La_2O_3 besides FLiNaK. The formation of LaOF can be described by the reactions *(4-99)*, *(4-100)*, *(4-101)* and the corresponding Gibbs free energy of the reaction is also calculated which demonstrate that the reaction between La_2O_3 and alkali eutectic happens in the order of LiF, NaF and KF.

$$La_2O_3 + 2LiF = 2LaOF + Li_2O \qquad (4\text{-}99)$$

$$\Delta G_1 = -1141.05kJ$$

$$La_2O_3 + 2NaF = 2LaOF + Na_2O \quad (4\text{-}100)$$

$$\Delta G_2 = -1048.99kJ$$

$$La_2O_3 + 2KF = 2LaOF + K_2O \quad (4\text{-}101)$$

$$\Delta G_3 = -1005.11kJ$$

Also, the XRD phase patterns shown in Figure 4-53 contains the same components as those in the insoluble materials which are a small amount of LaOF, La_2O_3 and large amount of FLiNaK. Known that the sample mass of the insoluble materials and the melting salt taken for the XRD analysis are almost the same (0.02706g and 0.02699g), comparing the peaks of LaOF and La2O3 in Figure 4-52 and Figure 4-53, it was found that the peak intensity of those two components in the insoluble materials are much stronger than that in the salt melt. As for the stronger peak intensity of the La_2O_3, it is not difficult to understand that it results from the large quantity of undissolved La_2O_3 accumulated on the bottom due to its higher density than FLiNaK. While for the stronger peak of LaOF, since the sample was taken during the heating process before the experiment completed and then quenched to keep the initial crystal structures, if LaOF is a kind of material that is easy to dissolve in the molten fluoride salt, most of it should exist in the melt, not on the bottom. Therefore, it's possible that most of the LaOF formed in the reaction of *(4-99)*, *(4-100)* and *(4-101)* would deposit on the bottom and only a small amount of LaOF dissolved into the melt which would contribute to the La concentration increasing in the system.

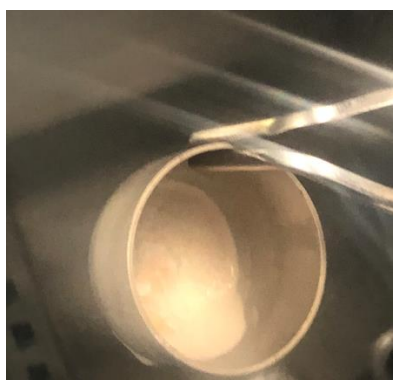

Figure 4-51 Insoluble material on the bottom

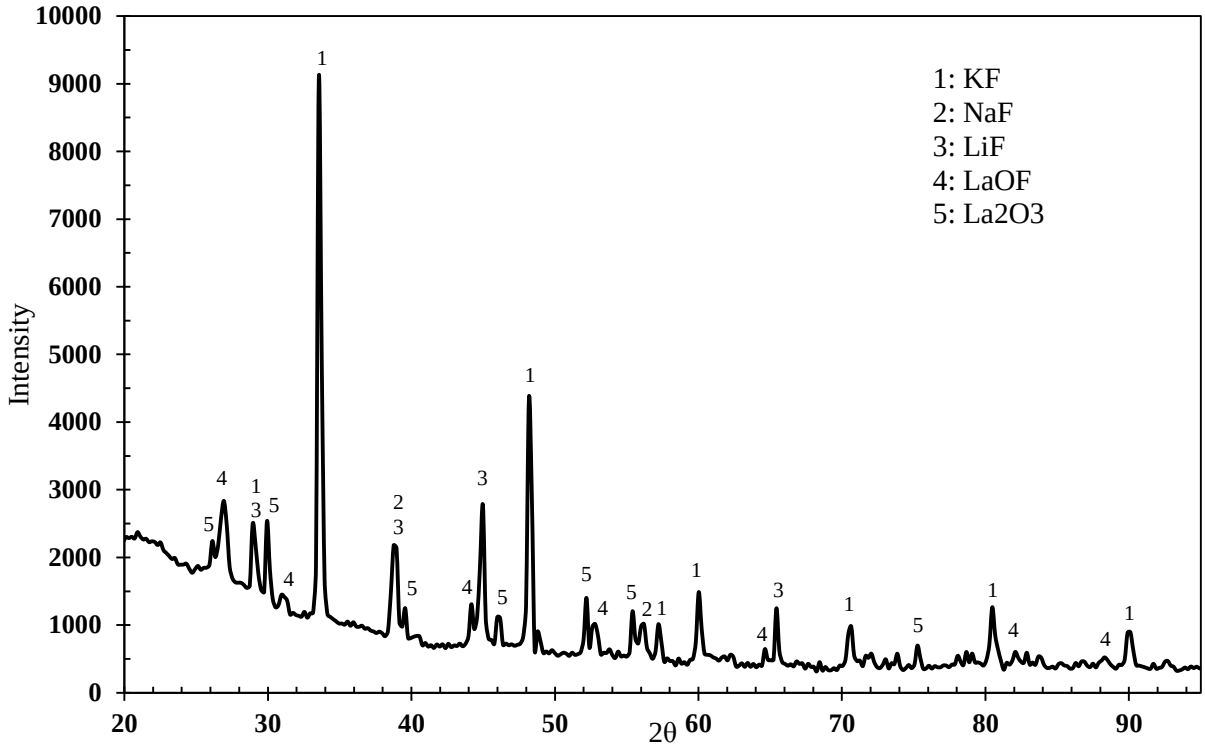

Figure 4-52 XRD of the insoluble materials on the bottom

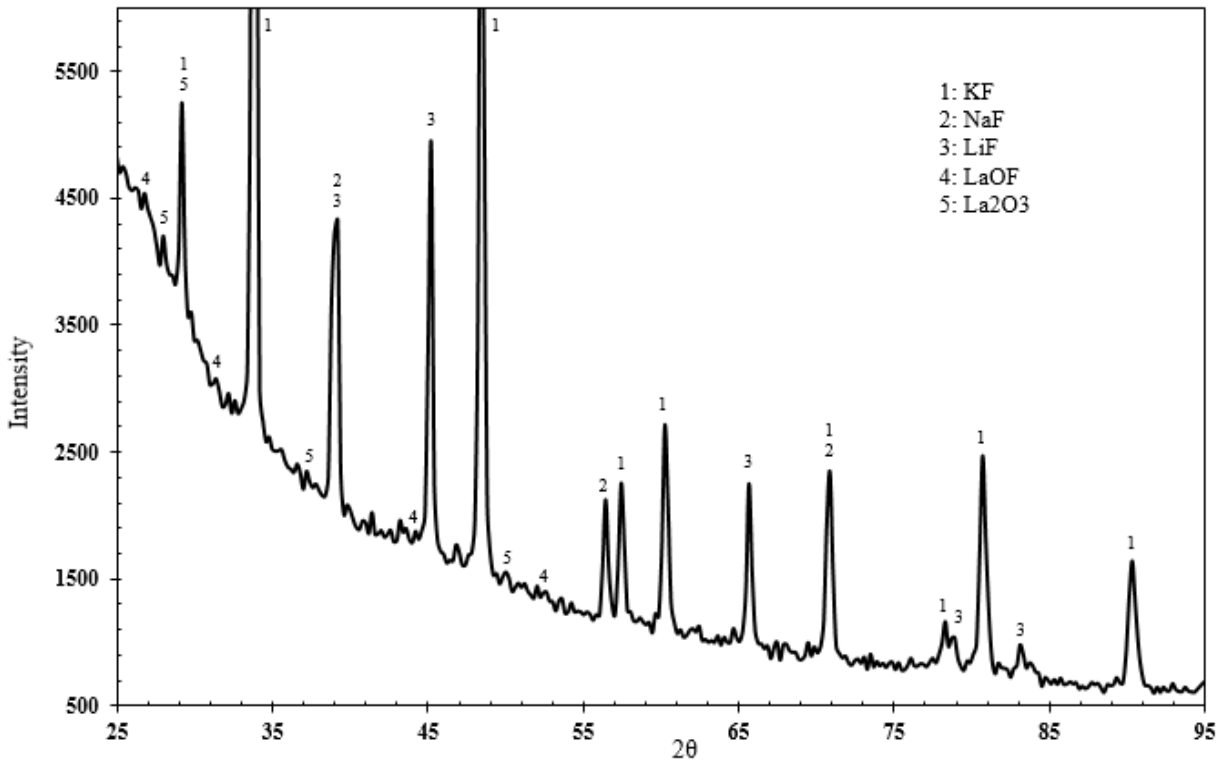

Figure 4-53 XRD of melting salt during heating

The ICP-MS analysis results at different temperatures are shown in Figure 4-54 and Figure 4-55. It's obvious that the La concentration is less than 0.04% both at 650°C and 600°C, while the concentration is between 0.05% and 0.1% both at 750°C and 700°C, which demonstrated that the solubility of lanthanum oxide is actually much smaller than those reported by M. Ambrová [1] and R. M. Wheat [2]. As for the La concentration at 650°C and 600°C shown in Figure 4-54, both of the La concentration at these two different temperatures are stable in terms of heating time. Since the molten salt mixture have been kept at the corresponding temperature for more than 300 hours, the whole system can be regarded as equilibrium. Therefore, the final stable La concentration could represent the corresponding solubility at each temperature as shown in Table 4-19.

while for the La concentration at 750°C shown in Figure 4-55, the relation between the La concentration and heating time becomes more complicated comparing with the results at 650°C and 600°C. A turning point A located between 150hrs and 170hrs is observed after which the curve goes up and keep stable.

It is known that the melting point of FLiNaK is 454°C and will increase due to the addition of Lanthanum oxide into the mixture. But considering that the amount of the La dissolving in the melt is very small according to the results in Table 4-19, the magnitude of the increasing may be neglected which means that the 4 experiment temperatures in this study will be greatly larger than the melting point of the mixture La_2O_3-FLiNaK. Therefore, it is unavoidable that there will be evaporation phenomenon occurred during the heating process. As showed in Figure 4-56, there is no visible trace of evaporated salt on the crucible surface at 600°C, then a small amount of salt can be observed on the surface when

the temperature goes up to 650°C. Finally, if the heating temperature is set at 700°C and 750°C, the evaporated salt can even form large salt spots which demonstrate the sever evaporation during the heating process. Since the evaporation only occurs at higher temperature, it's possible that the fluctuation shown in Figure 4-55 could result from that. Moreover, if combining the evaporation phenomenon with the fact that the La concentration increases after the turning point A in Figure 4-55, the assumption of the supersaturated solution is proposed. As is known, the dissolution of La_2O_3 in molten FLiNaK is a physical-chemical interaction, among which, one of the mechanism is built on the equilibrium process between solid La_2O_3 and La^{3+}, O^{2-} ions given by,

$$La_2O_{3(solid)} \overset{K}{\leftrightarrow} 2La^{3+} + 3O^{2-} \qquad (4\text{-}102)$$

Another one is the chemical reaction between the fluoride salt and lanthanum oxide which is given by,

$$La_2O_3 + 2MF = 2LaOF + M_2O \qquad (4\text{-}103)$$

$$LaOF \leftrightarrows LaO^+ + F^- \qquad (4\text{-}104)$$

$$LaO^+ \leftrightarrows La^{3+} + O^{2-} \qquad (4\text{-}105)$$

Where M is Li, Na, K.

And the equation *(4-104)* and *(4-105)* can be combined and given by,

$$LaOF \leftrightarrows La^{3+} + O^{2-} + F^- \qquad (4\text{-}106)$$

Since the temperature was stable during the heating process, the equilibrium of La dissolution in the molten salt could not be undermined. Therefore, it was assumed that only materials related to alkali elements was evaporated to steam, then cooled on the outside surface of the nickel crucible to form the salt spots after the furnace was turned off and the temperature decreased, while the La element that has already been dissolved in the evaporated molten salt was still remained in the solution thus the super-saturated solution of La was formed. As more sever evaporation occurred, more La would be left over in the solution which shown in Figure 4-55 was that the La concentration increased after the turning point A and then kept stable when more La can no longer be dissolved in the molten salt.

The XRD analysis of the evaporated salt was done to identify the components in the salt. As shown in Figure 4-57, there is no LaOF or La_2O_3 present in this sample and only FLiNaK and the corresponding alkali oxide produced in *(4-99)*, *(4-100)*, *(4-101)* were identified as expected thus further confirming the assumption on the super-saturated solution.

The dependence of reciprocal of temperature in K and the natural logarithm of solubility in mole fraction shows linear relationship in Figure 4-58.

$$lnS = -\frac{7520.7}{T} - 1.823 \qquad (4\text{-}107)$$

Where S: solubility in mole fraction, T: temperature in K

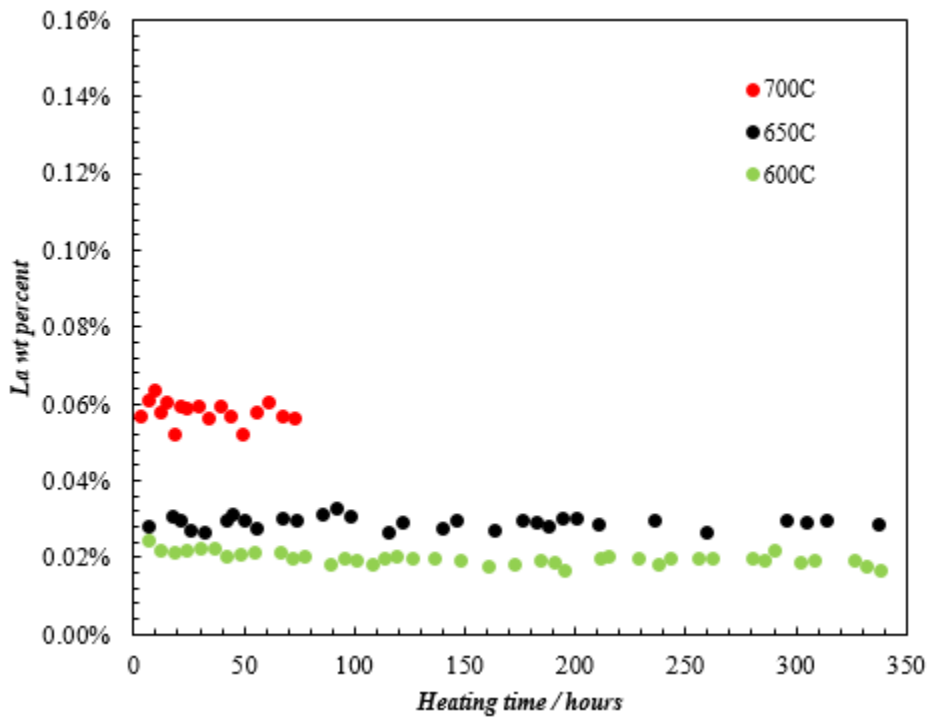

Figure 4-54 La concentration distribution at 600°C, 650°C and 700°C

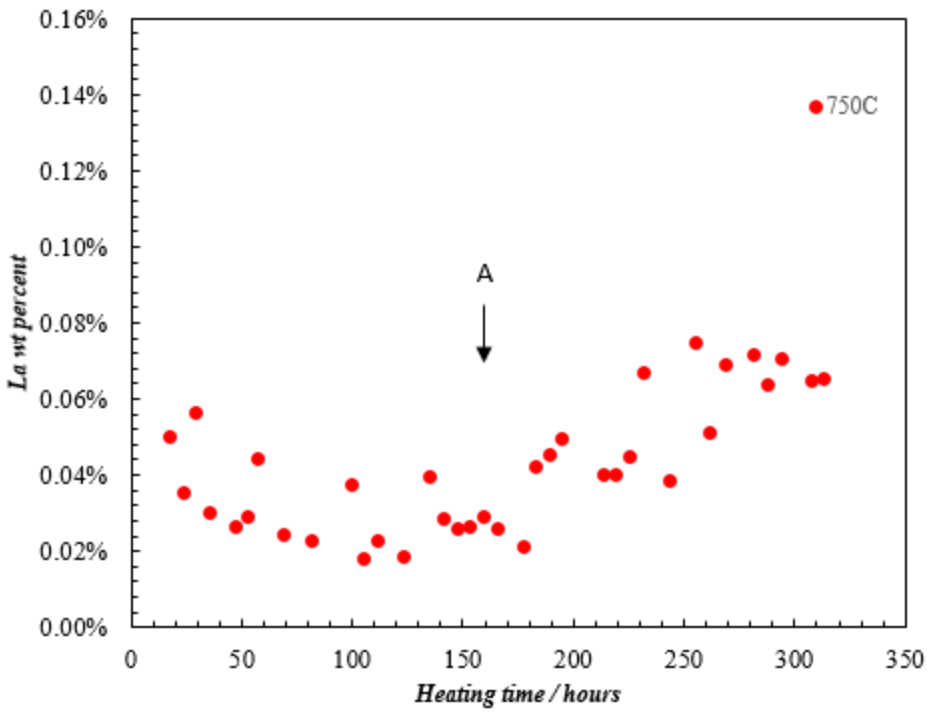

Figure 4-55 La concentration distribution at 750°C

Figure 4-56 Evaporation Phenomenon at different temperatures, from left to right, A: 600°C, B: 650°C, C: 700°C, D: 750°C

Table 4-19 La concentration and La2O3 solubility at 600°C, 650°C, 700°C, 750°C

	Heating Temperature			
	600°C	650°C	700°C	750°C
La Concentration (Weight percent)	0.02% ± 0.000231%	0.0293% ± 0.000273%	0.0528% ± 0.00359%	0.0667% ± 0.00384%
La_2O_3 Solubility (Mole Fraction)	2.9729×10^{-5}	4.3557×10^{-5}	7.8508×10^{-5}	9.9157×10^{-5}

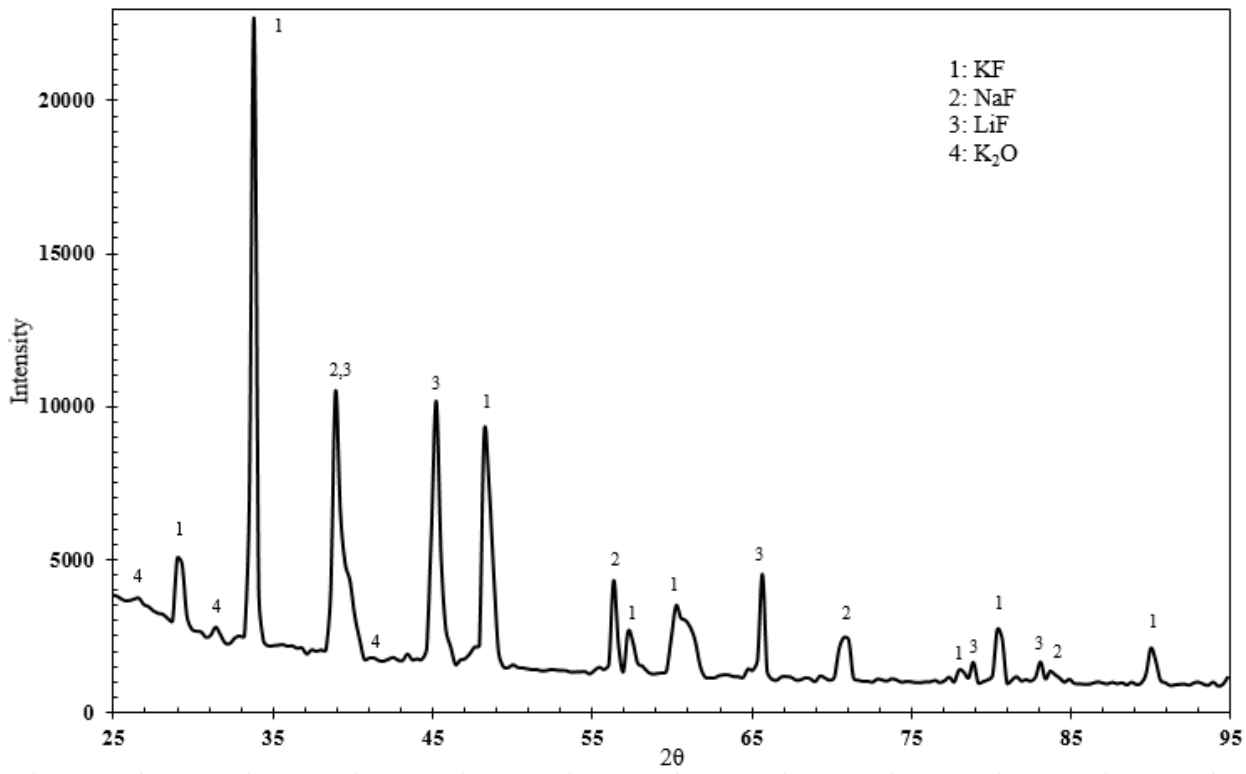

Figure 4-57 XRD of evaporated salt on the surface of the crucible

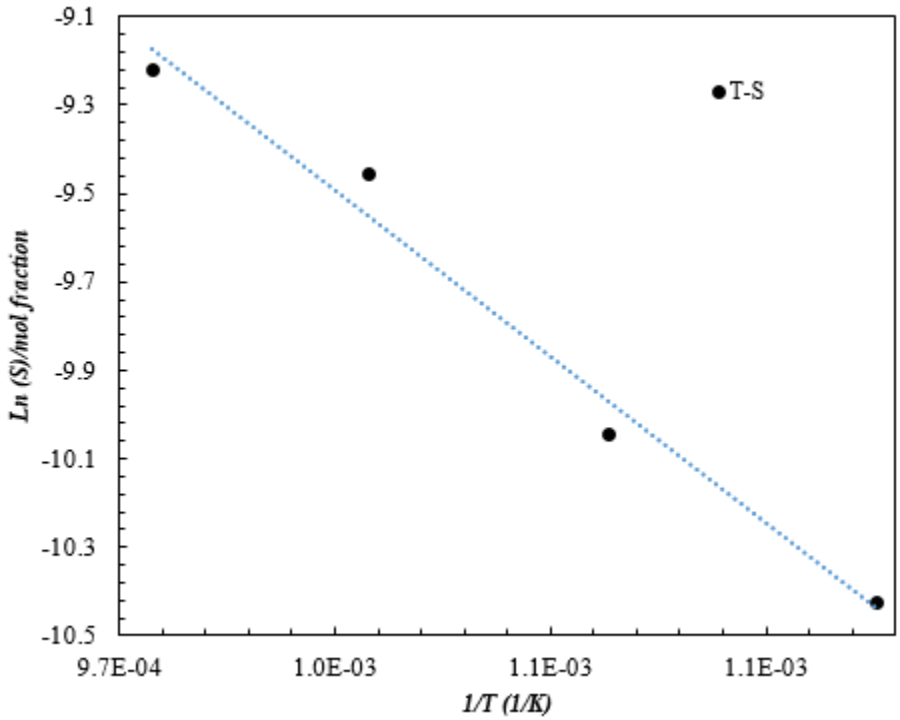

Figure 4-58 linear relationship between natural logarithm of solubility and reciprocal of temperature in Kelvin

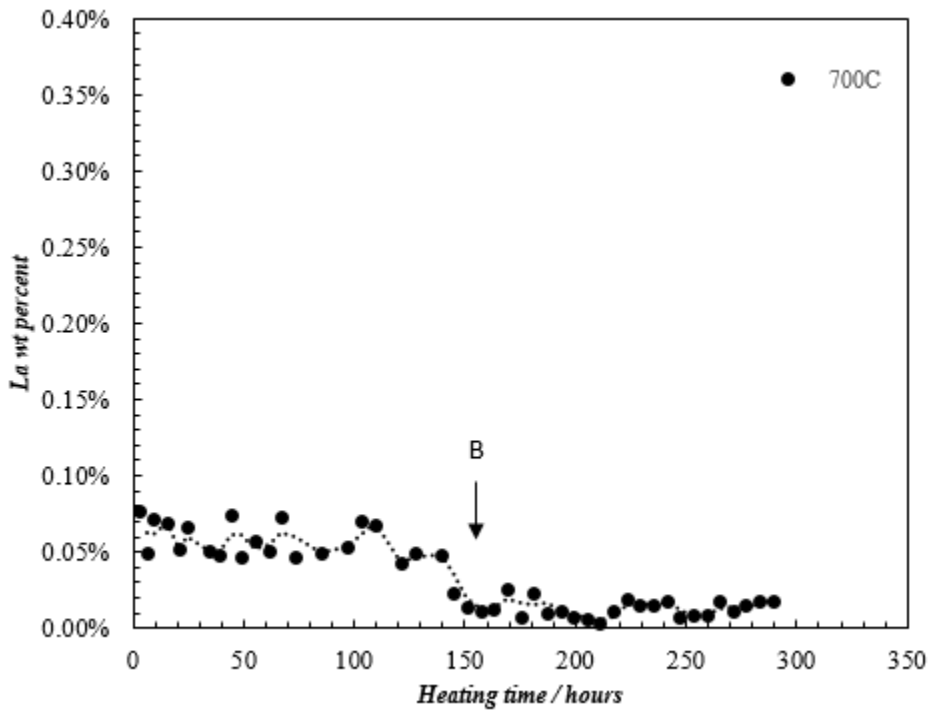

Figure 4-59 La concentration distribution at 700°C

Since the experiment at 700°C in Figure 4-54 only lasted for 72 hours, another experiment operated for 282 hours were also conducted. The corresponding La concentration curve is shown in Figure 4-59. Comparing with Figure 4-55, there is still fluctuation which may result from the evaporation as discussed before.

In addition, the La concentration decreases to as low as 0.0132% $\pm$ 0.00127% after being heated for 220 hours which is beyond expectation. The super-saturated solution of La could not be applied to explain the La concentration curve trend shown in Figure 4-59, which, in the other hand, indicates the complicated dissolution mechanism of La_2O_3 in molten fluoride salt deserves more studies.

4.6.1.4. Conclusions and Future work

The solubility of lanthanum oxide in molten fluoride salt has been studied in this part. Without considering the second experiment at 700°C, the La_2O_3 solubility increases with temperature. There is a simple linear relationship between the nature logarithm of the solubility in mole fraction and the reciprocal of the temperature in Kelvin. Based on the analysis, It was also found that most of LaOF formed in reaction *(4-103)* could deposit on the bottom due to its higher density. Moreover, the evaporation does exist during the heating process and it becomes more and more sever with temperature increasing, thus

leading to the formation of La super-saturated solution which makes the La concentration increase after turning point A shown in Figure 4-55. However, although the super-saturated solution theory performs well on the solubility study at 750°C, there is still one issue existed that it cannot be applied to explain the La concentration curve trend with longer heating time at 700°C. Therefore, more studies are urgent to be conducted in the future to further explore the dissolution mechanism of La_2O_3 in molten FLiNaK salt.

4.6.2. Electrochemcial Separation Study of La_2O_3 in Molten FLiNaK Salt

4.6.2.1. Introduction

Until recently, there is still not enough studies on the electrochemical behavior of lanthanum oxide in fluoride melt. M. Ambrova [6] studied the electrochemical behavior of La_2O_3 in LiF-CaF_2 system and concluded that the electro-deposition of lanthanum on metal cathodes cannot be achieved in molten LiF or in LiF-CaF_2 without depolarization. But with active cathodes copper and nickel, a liquid alloy could be formed on the copper cathode, while intermetallic compounds $LaNi_x$ was formed on the nickel cathode. In 2001, Stefanidak [4] studied the electrodeposition of neodymium in LiF-NdF_3, LiF-Nd_2O_3 and LiF-NdF_3-Nd_2O_3 melts. It was found that neodymium oxyfluoride was formed in the LiF melts. The electroreduction of neodymium fluorides to neodymium metal in LiF-NdF_3-Nd_2O_3 on tungsten cathode was detected. During the oxidation of neodymium oxyfluoride, oxygen was evolved on the anode at less positive potentials with respect to the fluorine evolution. There are also several studies on the electrochemical methods with graphite electrode which provide good references for our study. In 2003, Huan Qiao et al [7] proposed that the anodic products of oxygen ion at glassy carbon anode electrode at 3.0V (vs. K+/K) were confirmed to be CO_2 and CO gases and the anodic process was proved to be an irreversible process. Later in 2010, Z. Huang's study [8] on the anode process of carbon electrode in LiF-NaF-KF melt demonstrated that the anode effect occurred at the potential higher than 3.7V (vs. K+/K) and would produce perfluorocarbons such as CF_4 and C_2F_6 on the anode electrode.

To further understand the electrochemical behavior of La_2O_3 in the LiF-NaF-KF as well as the electrodes' effect on the electrolysis process, a detailed investigation was implemented in this part. Different kinds of electrodes were applied to verify if the lanthanum and oxygen elements can be separated from the molten salt.

4.6.2.2. Experimental Setup

LiF (BioUltra, ≥99.0%, Sigma), NaF (ACS regent, ≥99.0%, Sigma-Aldrich), KF (ACS regent, ≥99.0%, Sigma-Aldrich) and La_2O_3 (≥99.9%, Aldrich) were used in this experiment. Without special noting, all the operations are done in the glove box with O_2 level < 1.7 ppm and H_2O level < 2.0ppm. 1.0104g La_2O_3 was placed on the bottom of the Nickle crucible which serves as the salt container first. After that, 14.5893g LiF, 5.8299g NaF, 29.5528g KF were mixed well before putting into the Nickle crucible which would lay on the top of the La_2O_3 to ensure the system reach equilibrium as soon as possible. Then the possible

impurities consisted in the fluoride salt and hidden in the furnace parts were removed following the procedures in 4.6.1.2. Finally, the temperature would be set at 700°C and keep heating for more than 48 hours before any measurements were carried out.

Tungsten (≥99.5%, 3.2mm and 1.6mm) and graphite (99.999%, 3mm) were used as electrodes. Totally, 4 electrochemical experiments were designed to study the behavior of La_2O_3 in the molten salt. The single difference between these 4 experiments was the materials of the working electrodes and counter electrodes as shown in Table 4-20.

The electrode distribution in the furnace was also shown in Figure 4-60. The three-electrode cell was utilized in the experiment at 700°C. All voltammetric experiments were carried out in the furnace capable of sustaining a constant temperature. Insulation materials are used to keep a lower gradient over the melt during the experiment operation. The quartz tubes were used for the isolation between electrodes and the stainless steel tubes. The electrodes bathed in the dilution water were cleaned in the ultrasonic machine for 40 minutes. Then, both the electrodes and the quartz tubes were heated in the furnace for more than 24 hours before being inserted into the melt.

All the electrochemical experiments were performed with Gamry interface 1000 which was controlled by the Gamry Instruments Framework software. The transient electrochemical techniques, such as cyclic voltammetry (CV) and chronopotentiometry (CP) were used to examine the electrochemical behavior and the reaction on the working electrodes in the molten fluoride salt. In addition, without special noting, all the potential shown in the curves are relative to the tungsten reference electrode. X-ray powder diffraction analysis (XRD) was also done to identify the new material phase patterns on the surface of the working electrodes.

Table 4-20 Electrodes implied in the electrochemical experiments

	1st experiment	2nd experiment	3rd experiment	4th experiment
Working electrode	tungsten	tungsten	graphite	graphite
Counter electrode	tungsten	graphite	tungsten	graphite
Reference electrode	tungsten	tungsten	tungsten	tungsten

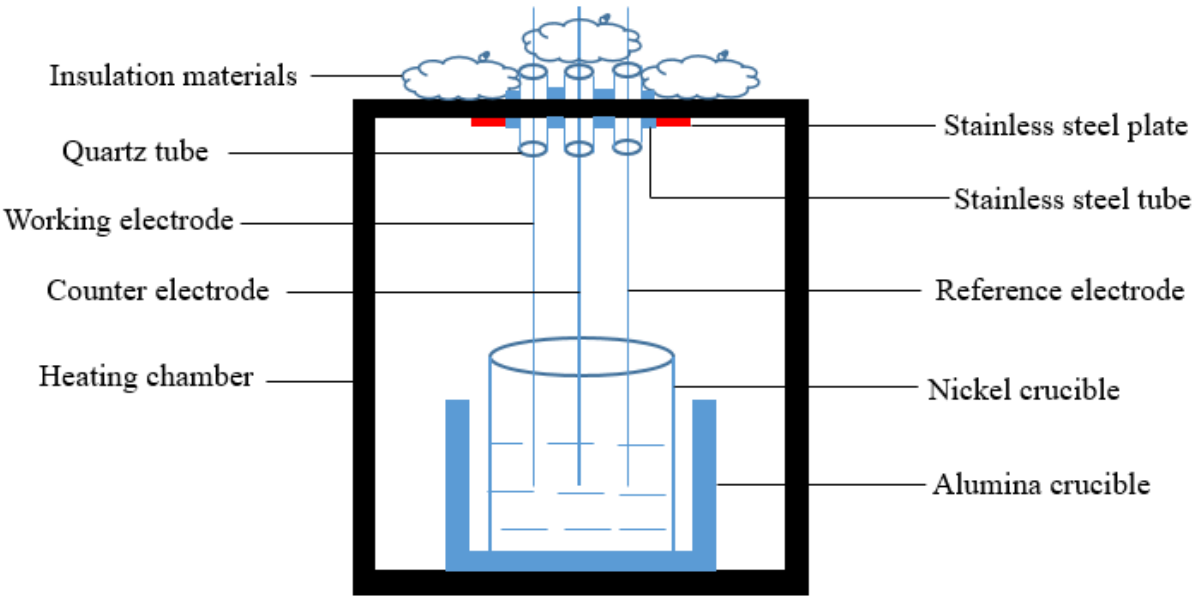

Figure 4-60 Electrochemical experimental setup sketch

4.6.2.3. Results and Analysis

4.6.2.3.1. 1st Experiment with Tungsten as Working, Counter and Reference Electrode

A typical curve of cyclic voltammetry from -1V to 0V of the tungsten working electrode in La_2O_3-FLiNaK system is shown in Figure 4-61. Two pairs of peaks A/A' and B/B' are presented. According to the redox potential of K^+/K, Na^+/Na and Li^+/Li vs. F_2/F^- at 700°C, it's known that the potential of K^+/K is less negative than the other two pairs [9]. Also, T. Yamamura et al. has demonstrated that redox potential of La^{3+}/La is less negative than that of K^+/K [10]. Therefore, peak B/B' would correspond to K^+/K. As shown in Figure 4-61, a cathodic peak A at -0.44V and the corresponding anodic peak A' were observed. Since it's not known if the reaction is reversible or irreversible, the number of the electrons involved in the anodic peak was calculated from the difference of the potential giving peak current E_p and the potential giving the half of the peak current $E_{p/2}$ based on the equations given by,

$$reversible: \left|E_p - E_{\frac{p}{2}}\right| = 0.774\frac{RT}{nF} \qquad (4\text{-}108)$$

$$irreversible: \left|E_p - E_{\frac{p}{2}}\right| = 1.857\frac{RT}{\alpha nF} \qquad (4\text{-}109)$$

Where, $\alpha = 0.5$ [11].

For peak A, the calculated electrons number is 3.09 for reversible reaction and 14.83 for irreversible reaction, which is the evaluated electrons number transferred in this reactions. Moreover, the electrode reaction for the reduction of La^{3+} can be expressed by,

$$La^{3+} + 3e^- = La \qquad (4\text{-}110)$$

Which matches well with the transferred electron number 3.09, therefore, the peak A/A' in Figure 4-61 corresponds to the reaction of La^{3+}/La.

Since tungsten serves as working electrode in this experiment and La_2O_3 exists in the molten fluoride salt, the following reaction of the Gibbs free energy formation is calculated by,

$$W + O_2 = WO_2, \qquad \Delta G = -412.342kJ \tag{4-111}$$

$$W + \frac{3}{2}O_2 = WO_3, \qquad \Delta G = -592.298kJ \tag{4-112}$$

$$W + 3F_2 = WF_6, \qquad \Delta G = -1434.379kJ \tag{4-113}$$

The Gibbs free energy of formation in these three reactions is less than 0, which indicates that once tungsten rod was exposed to O_2 or F_2 it's possible that the tungsten oxide and tungsten fluoride would be produced. Since the Gibbs free energy of reaction in *(4-113)* is more negative than the other two reactions. Therefore, in the electrochemical experiment, it is assumed that the following reaction would dominate the anodic reactions under positive potentials, which is given by,

$$W + 6F^- - 6e^- = WF_6 \tag{4-114}$$

As shown in Figure 4-62, the scan potential of the cyclic voltammetry is from 0.2V to 1.5V, the curve is characterized by the strong fluctuation. If the scan maximum potential limit is increased from 1.5V to 2V and 2.2V as shown in Figure 4-63 and Figure 4-64, the corresponding maximum current will quickly increase from 0.33A to 0.79A and 1.00A (the maximum current that the Gamry can stand before overload). Since the assumption that tungsten could combine with fluorine ions to produce the tungsten fluoride was proposed, it's possible that the fluorine gas production would adhere on the surface of the working electrode before reacting with tungsten rod thus resulting in the passivation on the surface of working electrode which lead to the fluctuation in the curve. In addition, the tungsten fluoride would dissolve in the molten fluoride salt. As long as the potential goes up more than 0.8, the combination between tungsten and the fluorine ions will keep taking place. After the electrochemical experiment, it was found that the diameter of the tungsten working electrode was about 0.815 mm less than that before the experiment which further confirmed that the tungsten reacted with the fluoride ions to produce tungsten fluoride thus leading to its dissolving.

Shown in Figure 4-62, Figure 4-63 and Figure 4-64, it's obvious that all the cyclic voltammetry curves coincide with the assumption, the fluctuation peaks observed in the curve represent the production of tungsten fluoride.

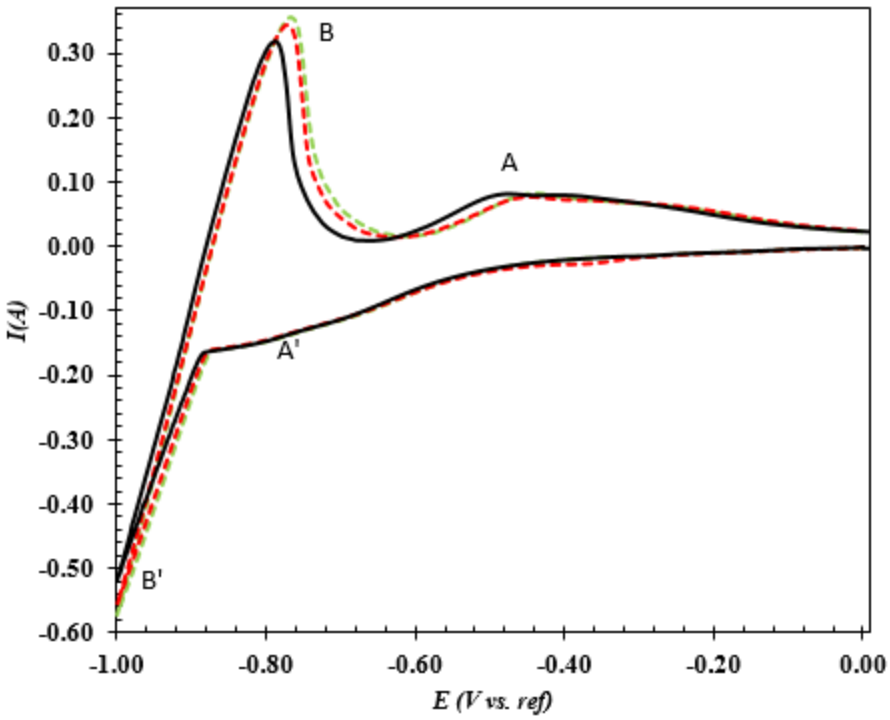

Figure 4-61 cyclic voltammetry, scan rate: 100 mv/s, working electrode: tungsten, counter electrode: tungsten, reference electrode: tungsten

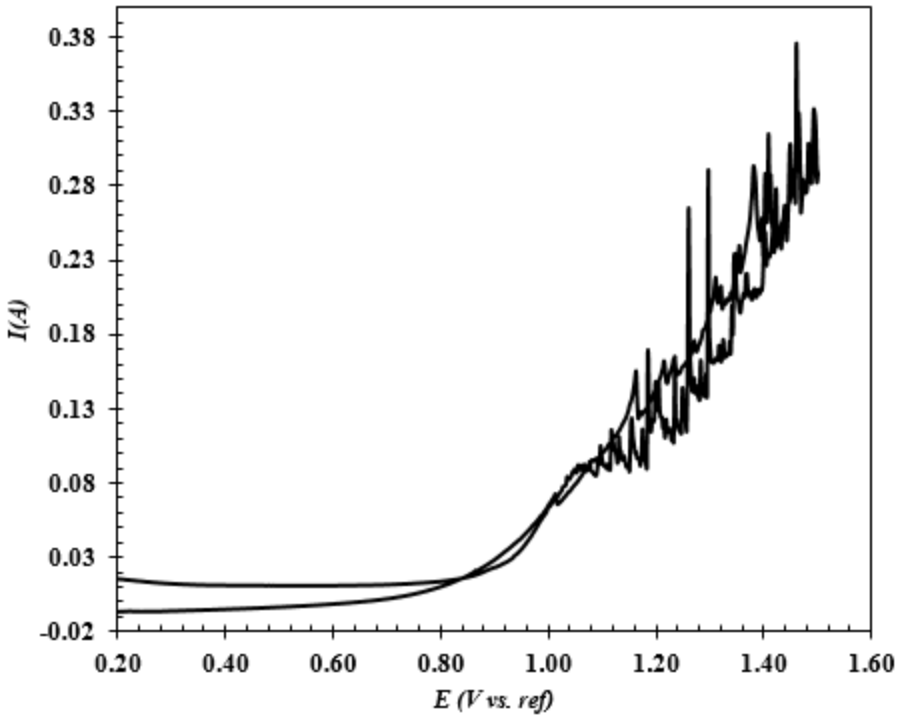

Figure 4-62 cyclic voltammetry, scan rate: 100 mv/s, working electrode: tungsten, counter electrode: tungsten, reference electrode: tungsten

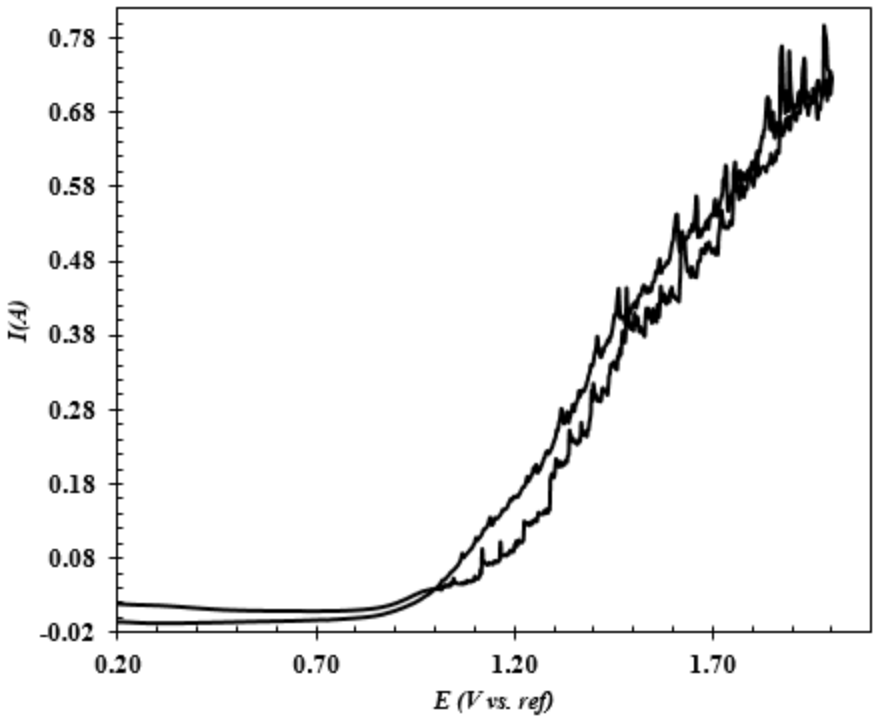

Figure 4-63 cyclic voltammetry, scan rate: 100 mv/s, working electrode: tungsten, counter electrode: tungsten, reference electrode: tungsten

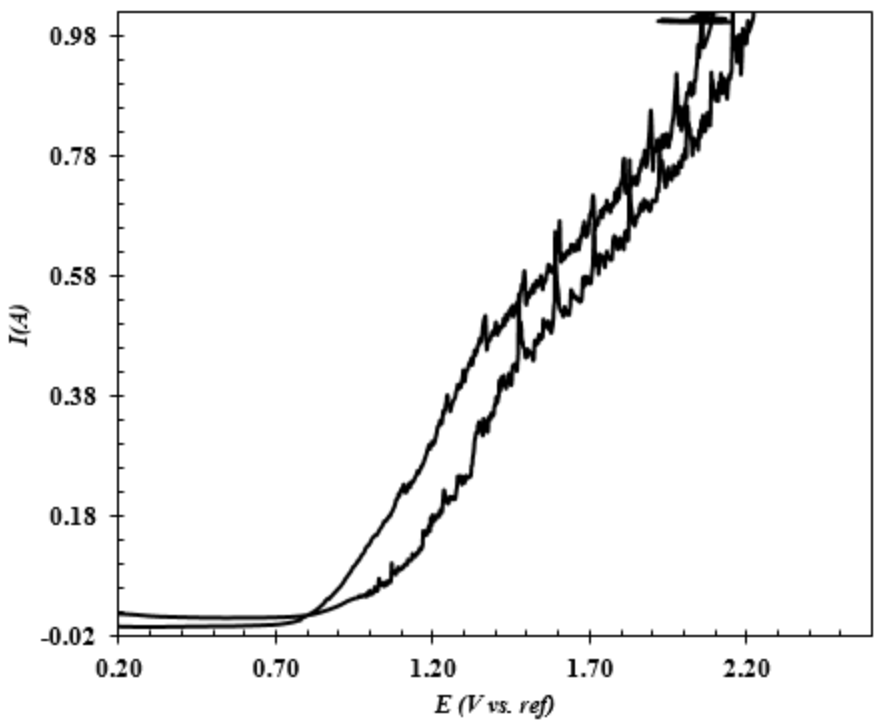

Figure 4-64 cyclic voltammetry, scan rate: 100 mv/s, working electrode: tungsten, counter electrode: tungsten, reference electrode: tungsten

4.6.2.3.2. 2nd Experiment with Tungsten as Working, Reference Electrode and graphite as counter electrode

Based on 1st experiment, it has been confirmed that the tungsten rod could combine with the fluorine ions to form tungsten fluoride during the anodic process. Since the tungsten serves as the counter electrode in the 1st experiment, it has not been clear that whether the counter electrode materials could affect the electrochemical analysis result if that corresponding counter electrode has possibility to react with the ions in the melt. Therefore, the 2nd experiment with graphite as counter electrode was designed the verify the assumption.

In the 2nd experiment, the experiment setup was kept as same as the 1st one except that the counter electrode was changed from tungsten to graphite. The obtained cyclic voltammetry curve with 100mv/s scan rate is shown in Figure 4-65. Comparing with the curve in Figure 4-61, it is obvious that these two cyclic voltammetry curves share the same trend and characteristics, both of which has two cathodic peaks and anodic peaks. To further clearly observing the difference between these two experiments' curves, the two cyclic voltammetry curve results were drawn in one single figure as shown in Figure 4-66. Here, it's obvious that the two pairs of peaks A/A' and B/B' both in two experiments are located at the same potential. The only difference is that the peak current at B with tungsten

counter electrode is about 0.2A larger than that with graphite counter electrode, which may result from the working electrode surface area immersed into the melt (surface area in 1st experiment was 50.265 mm^2, while the surface area in 2nd experiment was 80.425mm^2) and the different internal resistance of the tungsten and graphite rod. Therefore, same to the analysis in 1st experiment, the B/B' corresponds to the reaction of K^+/K, while the peak A/A' represents the redox reaction of lanthanum in the melt. The different counter material's effect on the separation of lanthanum can be neglected except the peak current at redox reaction of potassium which is possibly related to that.

As shown in Figure 4-67, the scan potential was set from -1.0V to 1.5V, the black curve is the cyclic voltammetry with graphite as counter electrode, while the red curve represents that with tungsten counter electrode. As expected, when the potential arrives in the range more than 0.7V, the current in the black curve begins to increase, then appears unstable fluctuation just as the same trend shown in the red curve due to the fluorine gas formation on the working electrode and the tungsten dissolving to produce the tungsten fluoride as discussed before. Therefore, it can be concluded that with different counter electrode, e. g., tungsten or graphite, both methods demonstrated the possibility of the lanthanum separation, while the fluorine ions would react with the tungsten at the anodic reaction to produce the tungsten fluoride. Meanwhile, the formation of the fluorine gas will lead to the passivation effect which casts on the cyclic voltammetry curve is the continuous and strong fluctuation and the tungsten fluoride produced at higher applied potential could result in large current until overload. Hence, according to results of 1st and 2nd experiment, there is no significant evidence to confirm that the counter materials applied in the experiment (tungsten and graphite) can affect the separation of lanthanum. Both works well in the La_2O_3-FLiNaK melt system.

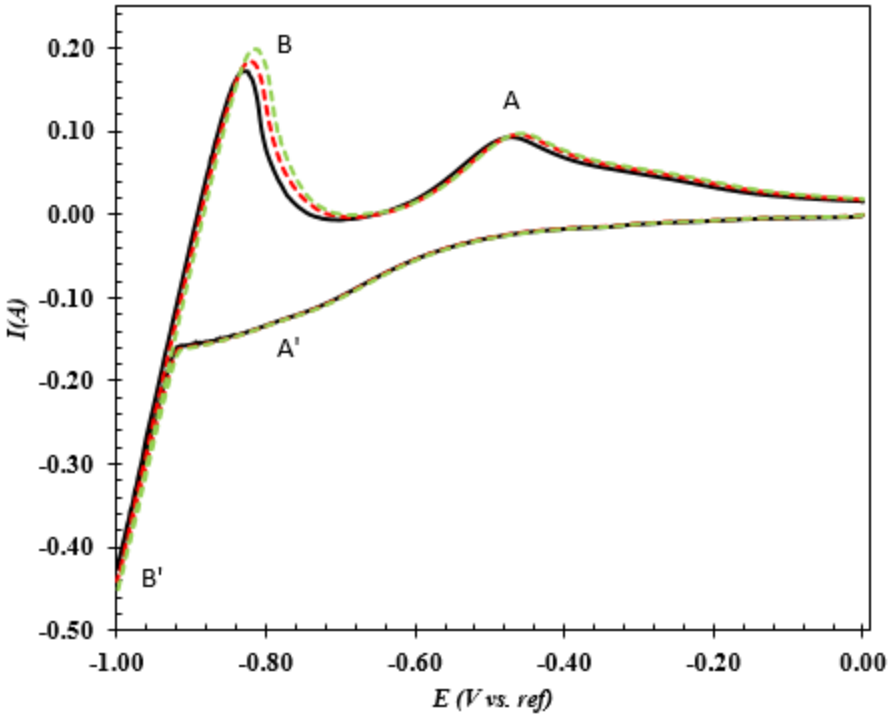

Figure 4-65 cyclic voltammetry, scan rate: 100 mv/s, working electrode: tungsten, counter electrode: tungsten, reference electrode: tungsten

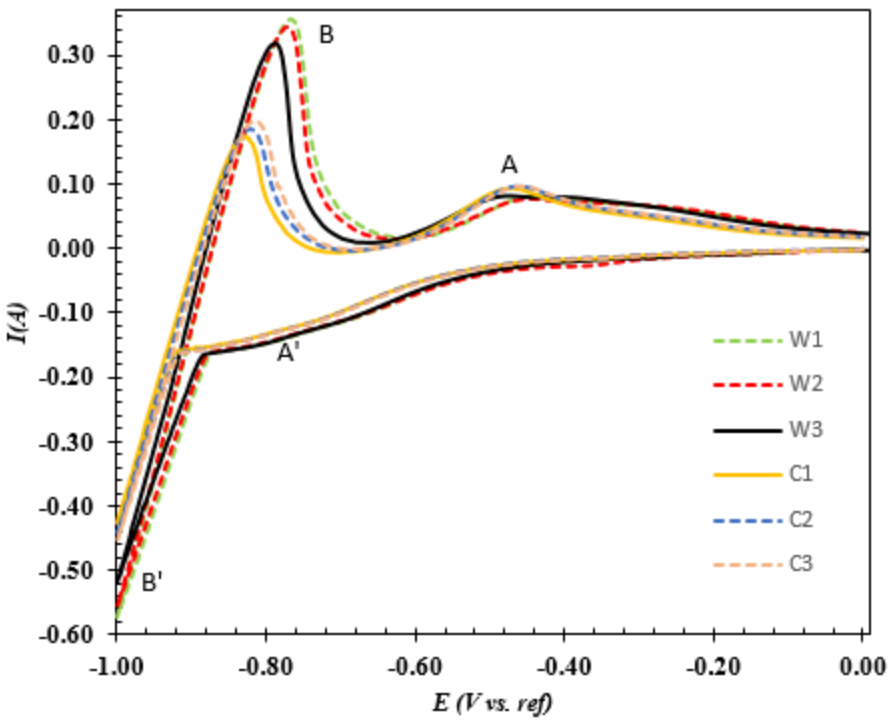

Figure 4-66 cyclic voltammetry, scan rate: 100 mv/s, working electrode: tungsten, counter electrode: tungsten (W1, W2, W3) and graphite (C1, C2, C3), reference electrode: tungsten. Surface area of tungsten: 80.43mm2, surface area of graphite: 50.27mm2

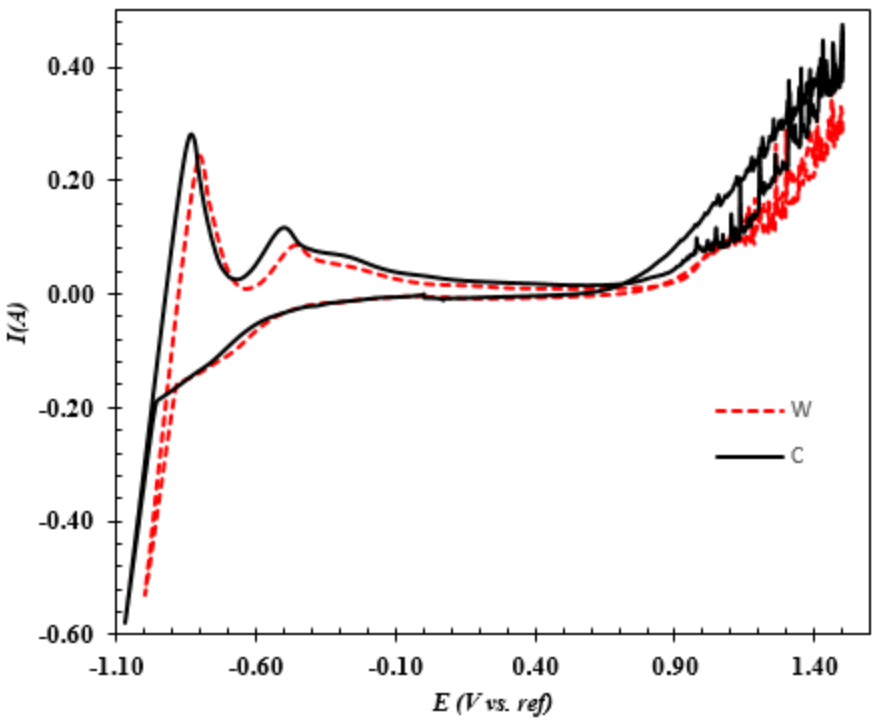

Figure 4-67 cyclic voltammetry, scan rate: 100 mv/s, working electrode: tungsten, counter electrode: graphite (C) and tungsten (W), reference electrode: tungsten

4.6.2.3.3. 3rd Experiment with Graphite as Working Electrode, Tungsten as Counter Electrode and Reference Electrode

In this part, the pure graphite rod was applied instead of tungsten to serve as the working electrode. As discussed before, the graphite rod plays the role of the sacrifice electrode which was expected to react with the oxygen ions in the melt to remove the impurities which has been studied in [7] and [8]. When the potential was set from 0V to -3.2V, the cyclic voltammetry with different scan rates were obtained as shown in Figure 4-68. Comparing with the curves in Figure 4-61, Figure 4-65, Figure 4-66 and Figure 4-67, it is obvious that there is only one reduction peak when the potential scans from positive to negative direction with graphite working electrode. Moreover, the reduction potential vs. W at peak B' is much more positive than that with tungsten as working electrode. Considering that two oxidation peaks appear in the curve, therefore, it was assumed that reduction peak corresponding to peak A may be immersed into the peak B', in other words, the potential of corresponding reduction peak at A is close to the reduction peak at B, which lead to the absence of the reduction peak.

Another cyclic voltammetry experiment with pure FLiNaK was conducted. As shown in Figure 4-69, the black dash line represents the cyclic voltammetry result without La_2O_3 addition. In the cyclic voltammetry curve of pure FLiNaK, the peak at C/C' correspond to the K^+/K due to its less negative potential than Na^+/Na and Li^+/Li. The potential at oxidation peak B is the same as K^+/K, which indicates that the peak B corresponds to the

oxidation reaction of K^+/K. As for the peak A, the Gibbs free energy and the potential of the following reactions were calculated before further analysis which are given by,

$$\Delta G = -nEF \tag{4-115}$$

$$6KF + 1.5C + La_2O_3 = 2LaF_3 + 1.5CO_2 + 6K, \tag{4-116}$$

$$\Delta G_1 = 819.444kJ$$

$$\Delta E_1\ vs.\ o^{2-}/co2 = -1.4155V$$

$$La_2O_3 + 5.5C = 1.5CO_2 + 2LaC_2, \tag{4-117}$$

$$\Delta G_2 = 713.745kJ$$

$$\Delta E_2\ vs.\ o^{2-}/co2 = -1.2329V$$

$$La_2O_3 + 1.5C = 1.5CO_2 + 2La, \tag{4-118}$$

$$\Delta G_3 = 923.185kJ$$

$$\Delta E_3\ vs.\ o^{2-}/co2 = -0.3811V$$

$$La + 2C = LaC_2, \tag{4-119}$$

$$\Delta G_3 = -104.694kJ$$

The potential difference vs. O^{2-}/CO_2 in reactions between *(4-116)* and *(4-117)*, *(4-116)* and *(4-118)* is is 0.18V, which is close enough to make reduction peaks overlapping possible. As shown in Figure 4-69, since Peak B overlaps with peak C in the pure FLiNaK cyclic voltammetry, the reaction occurs at the peak B would be the oxidation reaction of K. Then, based on the calculated potential difference, if the peak A was the oxidation of La, the difference between peak B and A should be close to theoretical value 1.0344, however, in Figure 4-68, the potential difference between these two peaks are about 0.15V, which is far less than 1.0344V, but can match the potential difference value between *(4-116)* and *(4-117)*. To further confirm the reaction at peak A, the electron transferred number is calculated with equation *(4-108)* and *(4-109)* since both LaC_2 and La metal is hardly soluble in the molten salt and it is not known if the reaction is reversible or irreversible. After ohmic drop is corrected, the number of electrons involved in the electrode reactions can be estimated to be 1.44 for reversible reaction and 6.91 for irreversible reaction. Since 1.44 is smaller, but close to 1.5, the reaction at peak A should correspond to C/LaC_2, not La/La^{3+}. In addition, since the peak B represents the oxidation reaction of K^+/K, it is surely that the corresponding reduction is included in peak B'. There are two evidence can support this assumption. First, potential difference vs. O^{2-}/CO_2 in *(4-116)* and *(4-117)* is very small which is only 0.1826V and the Gibbs free energy of *(4-117)* is smaller than *(4-116)* that would made the production of LaC_2 easier than deposition of K. Therefore, when the applied potential scans from positive to negative, at the beginning, the La^{3+} will be reduced to La metal at the graphite rod surface then immediately react with C to form LaC_2, since the lanthanum carbide LaC_2 is a metallic conductor and hardly dissolve in the molten fluoride salt, it will adhere on the surface of the working electrode. Thus, the interface property will be changed due to the deposition of LaC_2. As shown in Figure 4-69, the slope of B' is larger than that of C', which demonstrated the possibility that the reaction rate has

increased after the interface property change due to the kinetics of electrode reactions increasing. As a result, the formation of LaC_2 would make the over-potential of K reduction lower which indicates that the potential of K^+/K ("fake" reduction potential -0.3V) right now becomes much less negative than the "real" reduction potential of K^+/K (-0.85V) in the pure FLiNaK without La_2O_3.

Another assumption is that the potential shift of K^+/K is due to the referent electrode potential shift in the electrochemical. The open circuit potential (OCP) was measured before the cyclic voltammetry as shown in Figure 4-70. It's obvious that the potential shift between different experiments is less than 0.01V which is much less than 0.15V, which demonstrates that the reference electrode shift cannot result in the potential shift of K^+/K and further confirm that the assumption that the production of LaC_2 is the main cause of the peak overlap shown in Figure 4-68.

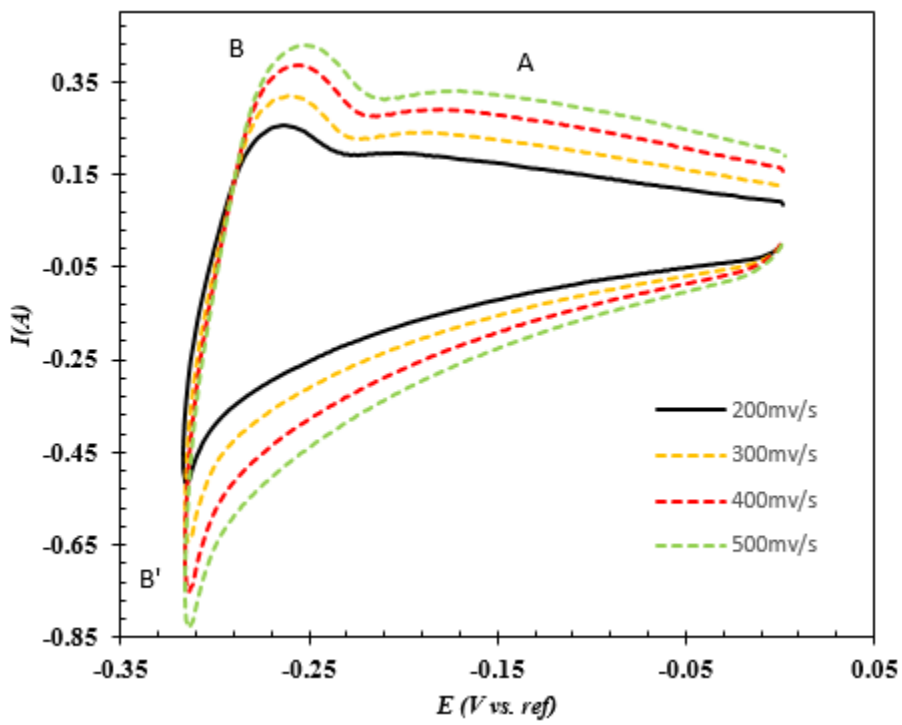

Figure 4-68 cyclic voltammetry, working electrode: graphite, counter electrode: tungsten, reference electrode: tungsten

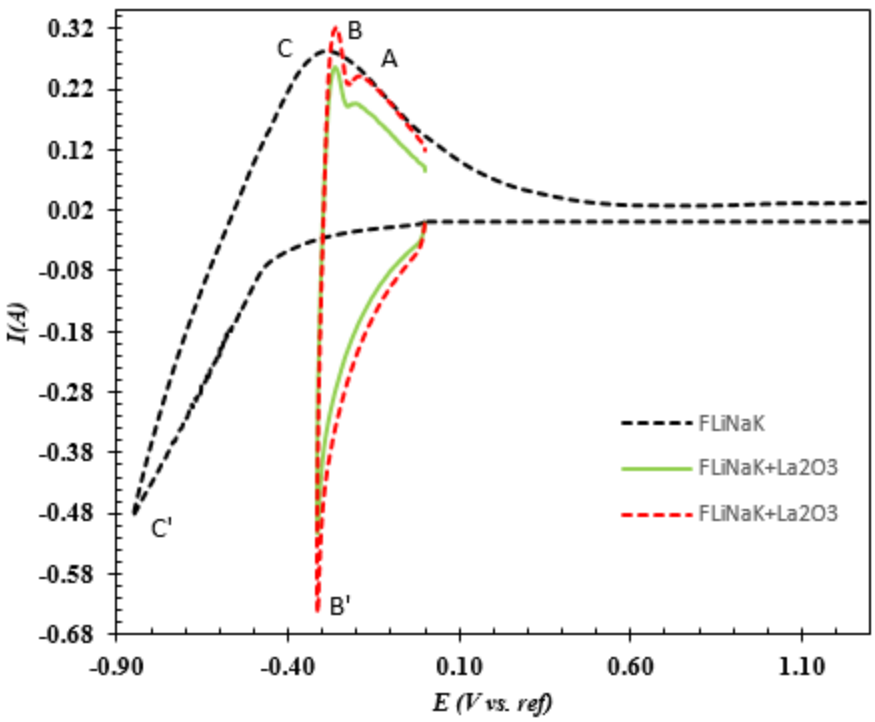

Figure 4-69 cyclic voltammetry, working electrode: graphite, counter electrode: tungsten, reference electrode: tungsten, red curve is FLiNaK without La_2O_3, green and red curve are FLiNaK with La2O3. Electrode surface area in pure FLiNaK: 89.54mm2, electrode surface area in FLiNaK-La_2O_3 is 87.65mm2.

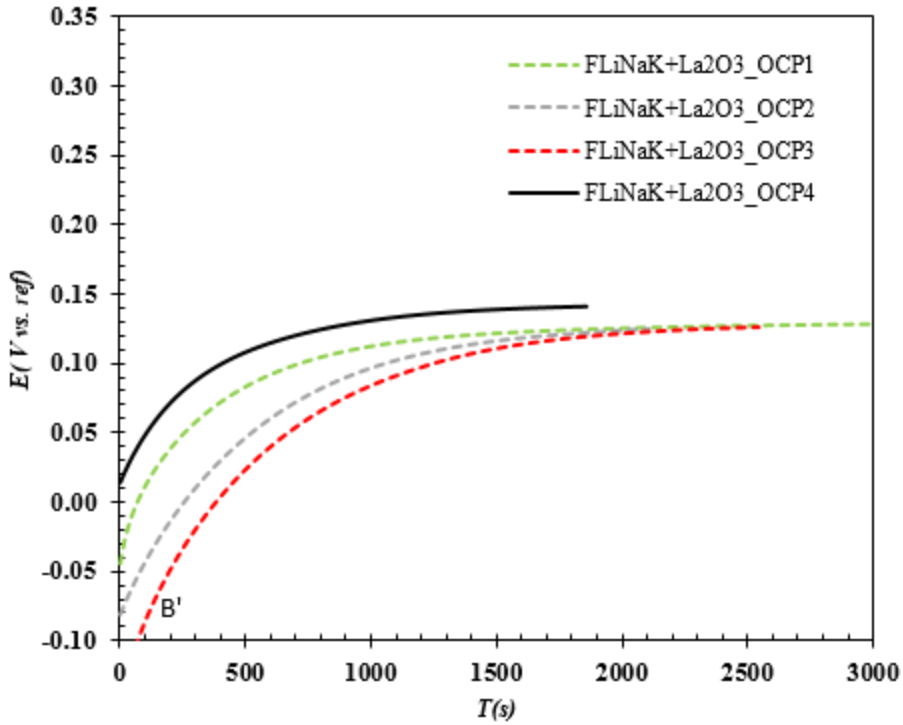

Figure 4-70 Open circuit potential at different time in the electrochemical experiment with working electrode: graphite, counter electrode: tungsten, reference electrode: tungsten

When the cyclic voltammetry curve was scanned from 0V to more positive in the experiment, theoretically, the major contribution to anodic reactions should come from the dominant fluorine ions due to its large amount in the molten fluoride salt. Oxygen ions could also be involved for its less positive potential than fluorine ions. Therefore, the most possible reactions on graphite anode are given by,

$$C + O^{2-} - 2e^- \rightarrow CO \qquad (4\text{-}120)$$

$$C + O^{2-} - 4e^- \rightarrow CO_2 \qquad (4\text{-}121)$$

$$C + 4F^- - 4e^- \rightarrow CF_4 \qquad (4\text{-}122)$$

$$2C + 6F^- - 6e^- \rightarrow C_2F_6 \qquad (4\text{-}123)$$

$$2F^- - 2e^- \rightarrow F_2 \qquad (4\text{-}124)$$

As shown in Figure 4-71, the applied potential is scanned from 0V to 3.5V, an anodic peak was observed around 2.5V in region C. Since the similar result has been reported by Y. Ito and T. Yamamura [10] [12], this anodic peak should be contributed to the oxidation of oxygen ions with the gaseous production CO/CO_2.

When the maximum scan potential increases to 5.5V, 6V, 6.5V, 8V and 11V, the corresponding cyclic voltammetry are shown in Figure 4-72. It was found that the peak current in reverse scans doesn't change at all with maximum scan potential less than 6.5V,

otherwise, it decreases. Bases on studies in [8] [13], the decreasing current could result from reaction between C and F^- with production of C_xF_y.

The whole reaction process can be described as: when the applied potential scans from 0V to 3.5V, at the beginning, the oxygen ions would discharge and react with graphite to produce CO/CO_2 as shown in *(4-120)* and *(4-121)*, since the bubbles would accumulate on the electrode surface thus decreasing the contact chance between the graphite and oxygen ions, which would lead to the current decreasing slowly until the oxygen ions around were consumed totally. As the applied potential keeps increasing, after it cross the threshold value which is about 6.5V in this study, the main reaction would be changed to the reaction between the graphite and the fluorine ions in the melt. The production in this region is much more complicated, such as, the CF_4 gas, C_2F_6 gas and CF_x film et al.

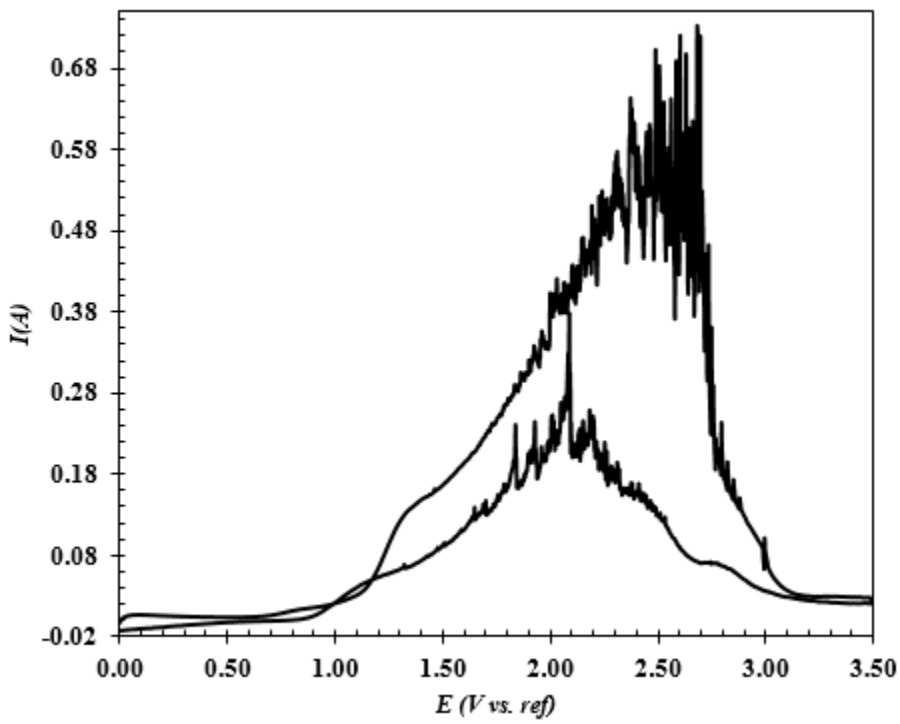

Figure 4-71 cyclic voltammetry, scan rate: 200 mv/s, working electrode: graphite, counter electrode: tungsten, reference electrode: tungsten

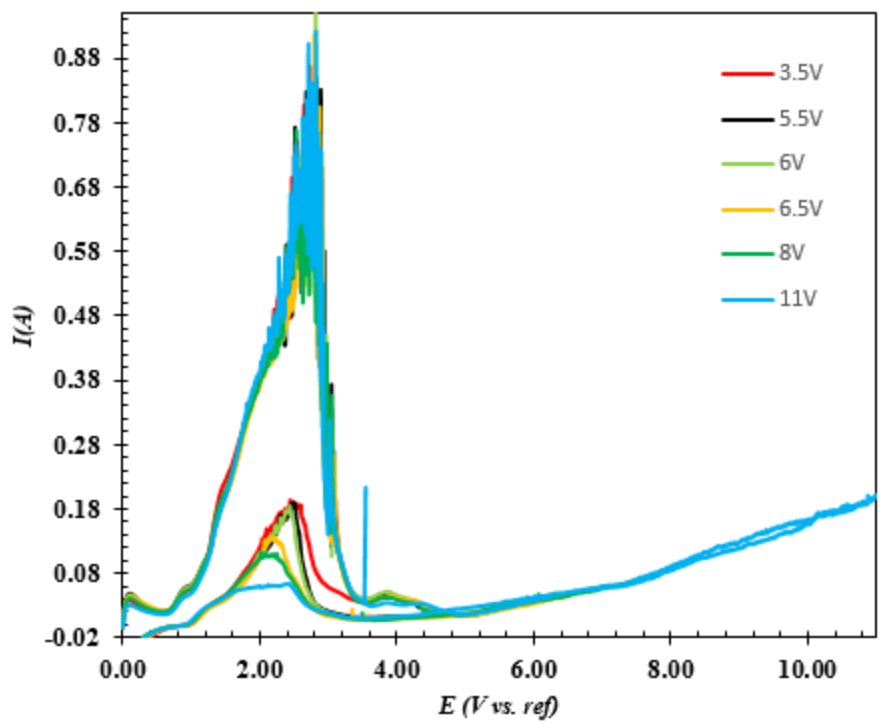

Figure 4-72 cyclic voltammetry, scan rate: 1000 mv/s, working electrode: graphite, counter electrode: tungsten, reference electrode: tungsten

4.6.2.3.4. 4th Experiment with Graphite as Working Electrode and Counter Electrode, Tungsten as Reference Electrode

Another electrochemical experiment was also conducted with graphite as working electrode and counter electrode, tungsten rod as the reference electrode. The difference between the 3rd experiment is that the graphite counter electrode instead of tungsten electrode. A typical cyclic voltammetry curves were obtained with 100mV/s, 200 mV/s, 300 mV/s and 400 mV/s in *Figure 4-73*. A cyclic voltammetry curve was also obtained with pure FLiNaK (no La_2O_3 addition) and the comparison between the pure FLiNaK and the FLiNaK-La_2O_3 curves were shown in Figure 4-74. Comparing the curves in *Figure 4-73* and Figure 4-74 with that in Figure 4-68 and Figure 4-69, it is obvious that the cyclic voltammetry curves share the same characteristics as that with the tungsten counter electrode. In addition, the corresponding open circuit potential is also shown in Figure 4-75 which indicates the reference electrode potential shift is less than 0.01V, demonstrating that the reduction peak of La^{3+}/LaC_2 and peak K^+/K has overlapped in the single peak B' as discussed before. Also, the peak of K^+/K has been shifted to less negative due to the interface property change on the graphite working electrode and the kinetics of the electrode reaction.

Moreover, chronopotentiometry with constant currents of 9mA and 10mA was done to further verify the two reduction reactions overlapped in peak B'. As shown in Figure 4-76, two plateaus A and B present in the curves individually. According to the calculated Gibbs

free energy in *(4-116)* and *(4-118)* and the corresponding potential at each plateau, plateau A at about 0.35V indicates that the reaction of La^{3+}/LaC_2 is undergoing, while plateau B at about 0.40V is the reflection of the reduction reaction of K^+/K which happens right following the reaction of La^{3+}/LaC_2.

In addition, since the Gibbs free energy of reaction *(4-116)* is greater than 0 kJ/mol, it is thermodynamically impossible that LaC_2 would be produced without external charge in the heating process. Therefore, the XRD samples were taken from the graphite working electrode surface after the chonopotentiometry with 10mA constant current to identify the phase patterns. As shown in Figure 4-77, LaC_2 was found in the samples which further demonstrates that the reaction of La^{3+}/LaC_2 does happen in the electrochemical process and the peak A in both of Figure 4-68 and *Figure 4-73* represent the oxidation reaction of LaC_2.

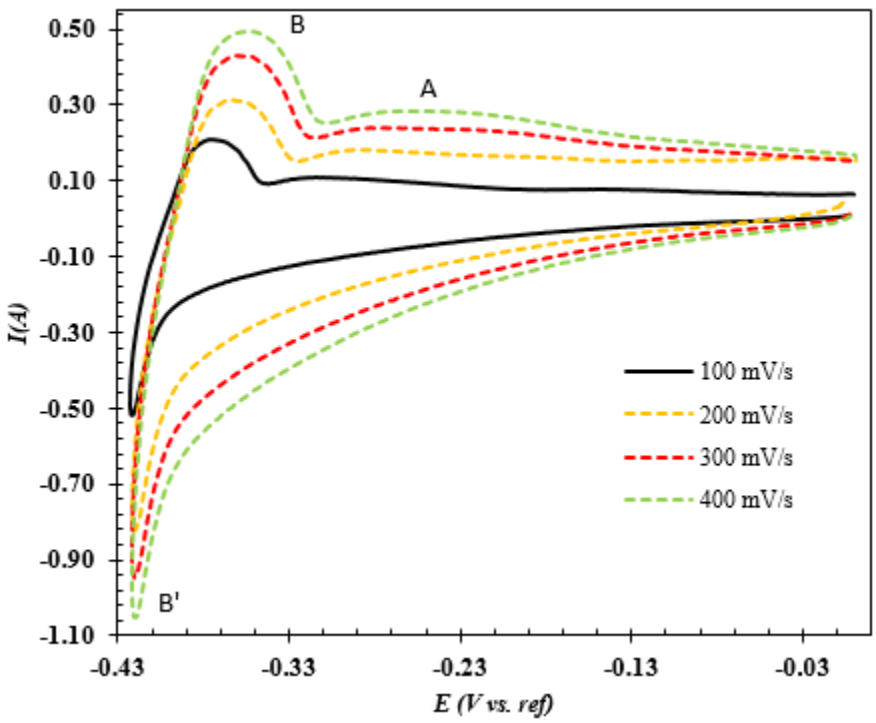

Figure 4-73 cyclic voltammetry, working electrode: graphite, counter electrode: graphite, reference electrode: tungsten

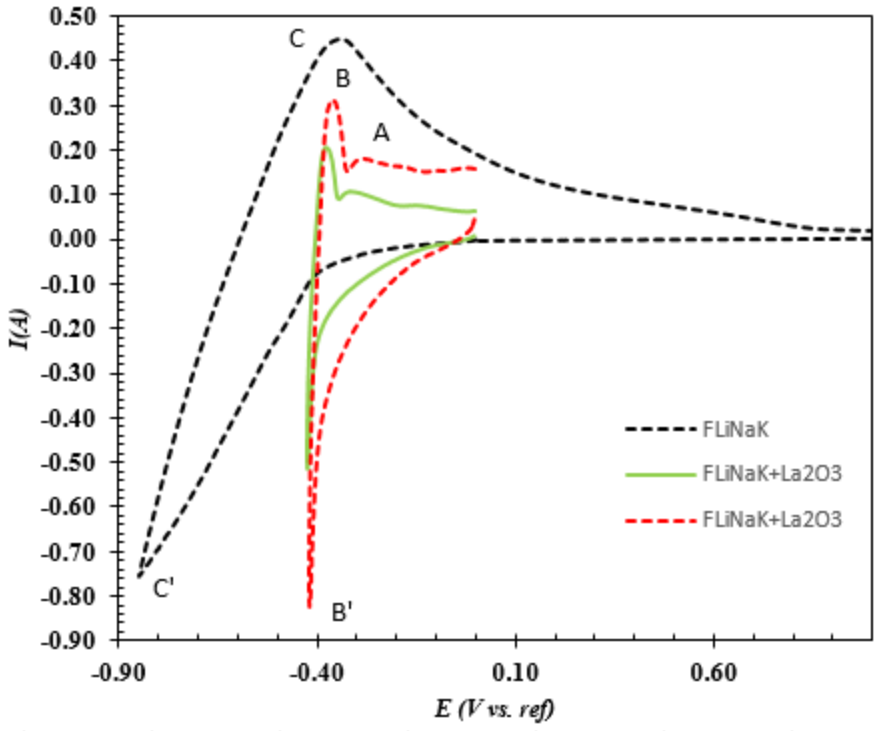

Figure 4-74 cyclic voltammetry, working electrode: graphite, counter electrode: graphite, reference electrode: tungsten. Electrode surface area in pure FLiNaK is 94.25mm2, electrode surface area in FLiNaK-La_2O_3 is 44.88mm2

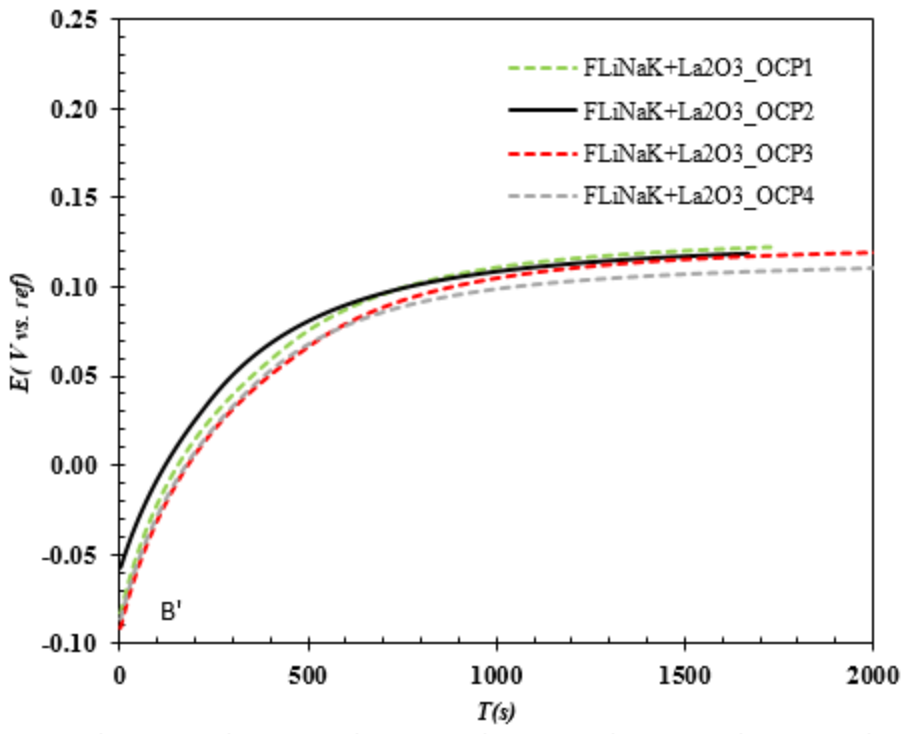

Figure 4-75 Open circuit potential at different time in the electrochemical experiment with working electrode: graphite, counter electrode: graphite, reference electrode: tungsten

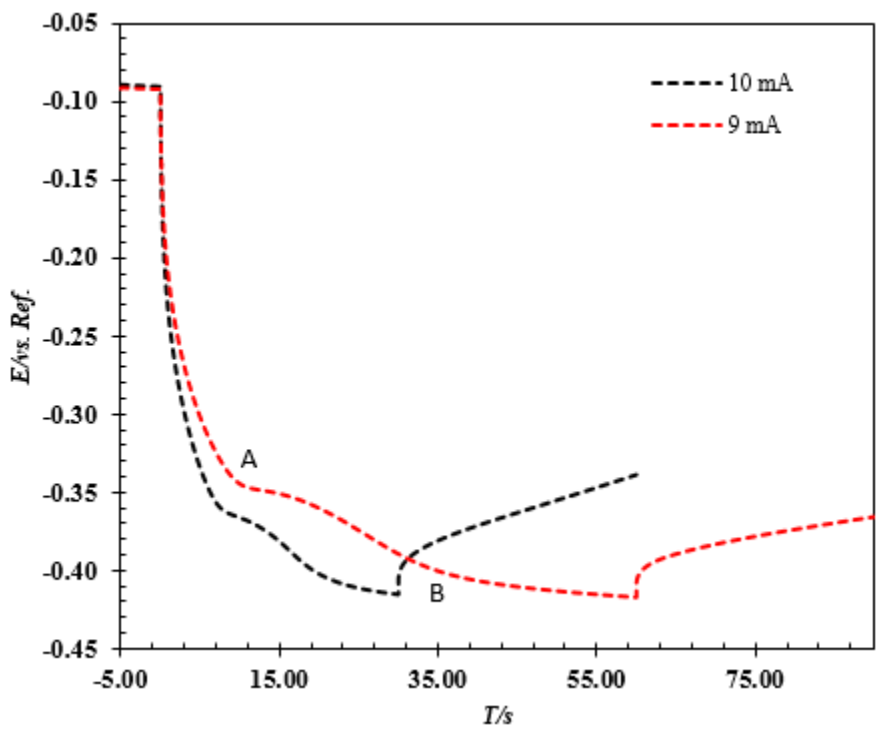

Figure 4-76 chronopotentiometry, working electrode: graphite, counter electrode: graphite, reference electrode: tungsten

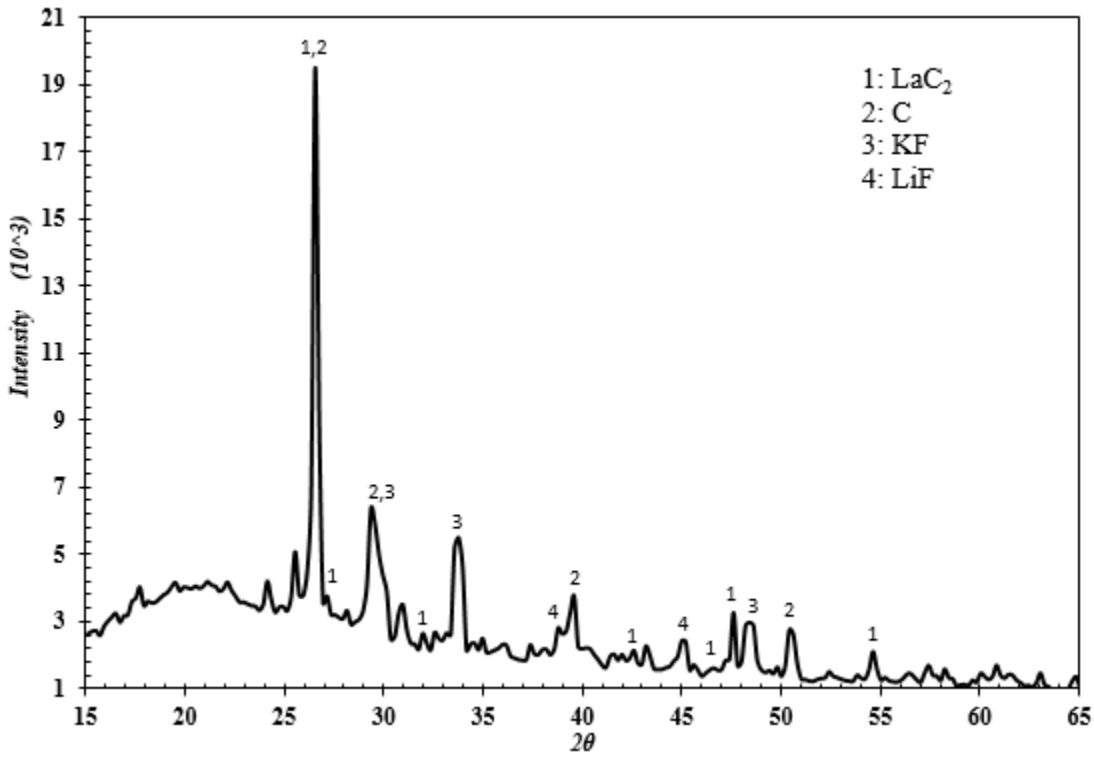

Figure 4-77 X-ray powder diffraction analysis on the graphite surface after deposition

When the potential from 0V to a more positive value were applied, the cyclic voltammetry curves were obtained as shown in Figure 4-78, Figure 4-79. Comparing with the curves in the 3rd experiment, there is no significant difference. The applied maximum potential is 3.5V shown in Figure 4-78, which corresponds to the reaction of C and O^{2-}. Then, the maximum scan potential increased to 5.0V, 6.0V, 6.5V, 8V and 11V as shown in Figure 4-79, it was observed that the reverse scan current peak decreased when potential was more than 6V, indicating that the reaction between C and F^- happened after. However, it need to be noted that the threshold of C-F^- reaction here is 6V which is different from 6.5V in 3rd experiment. It's possible that it could result from reference potential shift or the different counter materials.

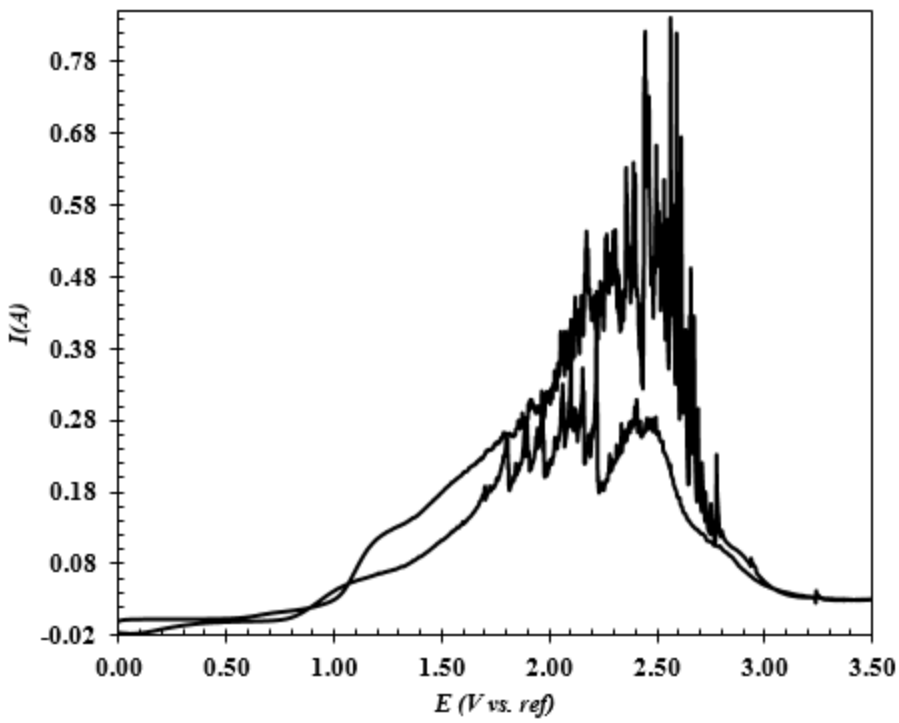

Figure 4-78 cyclic voltammetry, scan rate: 200mv/s, working electrode: graphite, counter electrode: graphite, reference electrode: tungsten

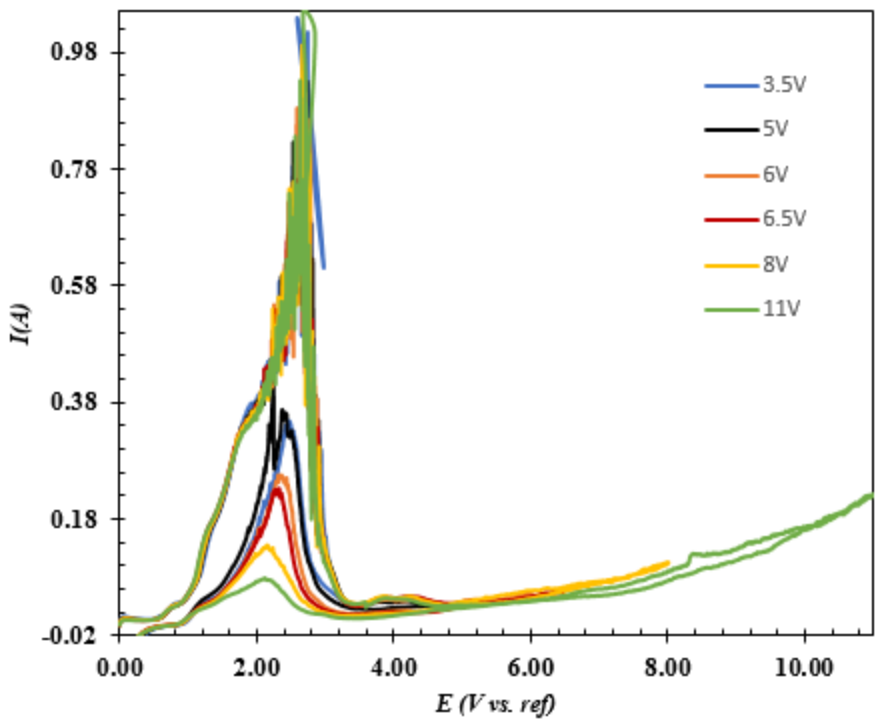

Figure 4-79 cyclic voltammetry, working electrode: graphite, counter electrode: graphite, reference electrode: tungsten

4.6.2.4. Conclusions and Future work

The electrochemical behavior of lanthanum oxide was investigated by cyclic voltammetry and chronopotentiometry at 700°C in fluoride molten salt with tungsten or graphite as working or counter electrode and tungsten as reference electrode.

The lanthanum ions can be reduced to lanthanum metal on the tungsten cathode electrode, while the fluorine ions would react with the tungsten anode electrode to form the tungsten fluoride thus leading to the dissolving of the tungsten anode electrode to introduce new impurity, such as WF_6, to the molten salt. Therefore, tungsten electrode is not a good choice when applied to oxygen ions removal. As for the graphite electrode, it performed well both for the lanthanum and oxygen element separation. In the electrochemical experiments, the lanthanum ions could be reduced in the form of LaC_2 and the oxygen ions would be oxidized to CO/CO_2 which was easy to separate from the solution with low cost. More work will be done to further study the electrochemical behavior of La_2O_3 in molten FLiNaK salt.

4.6.3. First Principle Molecular Dynamics Study of Molten FLiNaK and FLiNaK-La_2O_3 Salt

4.6.3.1. Introduction

Recently more and more molecular dynamics simulation tools have been developed, which, in the other hands, also helped to speed up the development and application of the first principle molecular dynamics (FPMD). There are several softwares that are often implemented in FPMD, e. g., Vienne Ab-initio Simulation Package (VASP) [14] [15] [18], CPMD [16] and Cambridge serial total energy package (CASTEP) [17] [18]. In addition, due to the rapid development of the supercomputer performances, FPMD is now able to be practically applied in the simulations of liquid systems [19] [20] [21] [22]. More and more work has also been done with these tools to study the properties of the molten salt, liquid metal and many other materials. H.O. Nam et al [23] studied two types of molten fluoride salt, LiF-BeF_2 and LiF-NaF-KF with Cr, Cr^{2+} and Cr^{3+} ions. In his work, the thermo-kinetic properties of the fluoride salt, i.e., equilibrium volume, density, bulk modulus, coefficient of thermal expansion and self-coefficient, as well as the effect of Cr valence on diffusivity and local structure in the salt were calculated in detail which provided a good reference for the FPMD's application. Moreover, J. Dai et al [24] also applied the FPMD in the simulation of identified clusters in gas phase and the salts in condensed phase, through which to have an insight on the structure and vibrational spectra of the local structures in LiF-BeF_2 molten salts. In 2017, J. Song et al [25] combined classical molecular dynamics and FPMD to evaluate the densities of molten salt mixtures in NVT ensemble [26] and local coordination structures in terms of radial distribution functions, and self-diffusion coefficients and ion conductivities from the mean square displacements based on Einstein relation. X. Lv et al performed FPMD simulations to studied the ionic structure and transport properties of LiF-NaF-AlF_3 [27] and Na_3AlF_6 [28] with CASTEP code in 2016 and 2018 respectively.

In this part, the FPMD is employed directly to model the molten fluoride salt at high temperature. The FLiNaK system composed of 46.5 mol% LiF, 11.5 mol% NaF and 42 mol% KF would be studied to determine the local ionic structure. Firstly, details of computational method to simulate the molten fluoride salt system by FPMD are proposed. Basic structure information of pure fluoride salts was calculated and compared with the results in literatures to validate the FPMD modeling of fluoride salts. Then the Gibbs free energy of mixing was calculated to further understand the properties of the molten salt.

4.6.3.2. Computational Methods

4.6.3.2.1. First Principle Molecular Dynamics Method

Before the FPMD simulation, the initial configuration of ions for the molecular dynamics were prepares by packing the ions randomly in the simulation cubic box via Packmol package [29]. For the model of FLiNaK, based on the industry component, 46.5 mol% LiF, 11.5 mol% NaF and 42 mol% KF, the model was comprised of 23 Li atoms, 6 Na atoms, 21 K atoms and 50 F atoms with total 100 atoms. The cubic simulation model box was built with a density of $2 \times 10^3 kg/m^3$ according to experimental data and lattice constant 11.83

Å. The obtained initial configuration was then run in the VASP to reach equilibrium. The equilibrium simulation was done in a canonical ensemble with fixed particle number, volume and temperature (NVT) using the algorithm of Nose [30]. A conjugate-gradient algorithm was used to relax the ions into their instantaneous groundstate [31]. PAW-PBE potentials were used to simulate F(s2p5), Li(s1p0), Na(s1p0) and K(p6s1). Within the parenthesis the valence electrons for each pseudopotential wad specified. The projector augmented wave (PAW) method and a plane wave basis set with the energy cutoff of 400 eV with the energy convergence of 10^{-4} which is enough in most cases due to the fact that the convergence speed is exponential in the simulation. A $2 \times 2 \times 2$ k-point mesh was applied with KSPACING equal to 0.5. Finally, the configuration obtained from the equilibrium procedure was applied in the molecular dynamics simulations with $1 \times 1 \times 1$ k-point mesh and time step of 2fs. The FPMD simulation data were obtained after 30ps which would be used to obtain the electronic structures. After that, 2 lanthanum atoms and 3 oxygen atoms were added to simulate the FLiNaK-La_2O_3 mixture thus obtaining the local ionic structure in the system.

4.6.3.2.2. Radial Distribution Function

The radial distribution function analysis was conducted from the molecular dynamics trajectories to study the local structure surrounding a certain ion. In statistical mechanics, the radial distribution function $g(r)$ in a system of particles describes how density varies as a function of distance from a reference particle. It is the probability distribution for particles surrounding another particle which is given by,

$$g(r[i]) = \frac{n_{pair}[i]}{v[i]} \cdot \frac{V}{N_{pair}} \qquad (4\text{-}125)$$

Where, $n_{pair}[i]$: the number of pairs in bin $(r_i, r_{i+1} = r_i + dr)$

$v[i]$: volume of bin

N_{pair}: number of pairs

V: volume of simulation cell

While the first shell coordination numbers (CNs) is the average coordination number for one atom around the reference atom [32]. It is estimated by numerical integration of the radial distribution function within a cut-off radius which corresponds to the first peak interval of the RDF. By integrating equation *(4-125)*, the first shell coordination number is obtain given by,

$$N_{ij} = 4\pi\rho_j \int_0^{R_{cut-off}} r^2 g_{ij}(r)\, dr \qquad (4\text{-}126)$$

Where, $g_{ij}(r)$: the RDF between atom i and atom j

ρ_j: the average number density of reference atom in the center.

4.6.3.2.3. Enthalpy of Formation $\Delta \boldsymbol{H_{mix}}$

Assuming that a multicomponent solution of LiF-NaF-KF are mixed well in homogeneous state at 700°C, 1mol of solution contains $X_{Li}mol$, $X_{Na}mol$, $X_K mol$ and $X_F mol$ of Li, Na, K and F ions ($X_{Li}mol\ LiF, X_{Na}mol\ NaF, X_K mol\ KF$) in the molten salt. There are two steps of mixing: first ($X_{Li}mol$ pure LiF, $X_{Na}mol$ pure NaF and $X_K mol$ KF are brought together, then pure LiF, NaF and KF are mixed evenly to make a homogeneous solution. After the first step, the Gibbs free energy of the system is given by,

$$G_1 = X_{Li}G_{LiF} + X_{Na}G_{NaF} + X_K G_{KF} \tag{4-127}$$

Where, G_1: Gibbs free energy after step 1

G_{LiF}: Gibbs free energy of pure LiF

G_{NaF}: Gibbs free energy of pure NaF

G_{KF}: Gibbs free energy of pure KF

After step 2 the free energy of the system is given by,

$$G_2 = G_1 + \Delta G_{mix} \tag{4-128}$$

$$\Delta G_{mix} = \Delta H_{mix} - T\Delta S_{mix} \tag{4-129}$$

$$\Delta H_{mix} = H_2 - H_1 \tag{4-130}$$

Where, ΔG_{mix} is the Gibbs free energy change due to the mixing

ΔH_{mix}: heat of formation of the molten salt solution

ΔS_{mix}: entropy of formation of the molten salt solution

For the heat of formation ΔH_{mix}, the quasi-chemical model is applied in which the heat of mixing only dependent on the bond energy between the adjacent atoms, indicating that the interatomic distances and bond energies are independent of composition. In the molten FLiNaK salt, 10 types of bonds are included, i.e., Li-F, Li-Li, Li-Na, Li-K, Na-F, Na-Na, Na-K, K-F, K-K and F-F. Then, the internal energy of the solution is given by,

$$E = B_{Li-F}E_{Li-F} + B_{Li-Li}E_{Li-Li} + B_{Li-Na}E_{Li-Na} + B_{Li-K}E_{Li-K} + B_{Na-F}E_{Na-F} + B_{Na-Na}E_{Na-Na} + B_{Na-K}E_{Na-K} + B_{K-F}E_{K-F} + B_{K-K}E_{K-K} + B_{F-F}E_{F-F} \quad (4\text{-}131)$$

Where, E: the internal energy of the molten salt

$B_{Li-F}, B_{Li-Li}, B_{Li-Na}, B_{Li-K}, B_{Na-F}, B_{Na-Na}, B_{Na-K}, B_{K-F}, B_{K-K}, B_{F-F}$: the bonds number of each type.

$E_{Li-F}, E_{Li-Li}, E_{Li-Na}, E_{Li-K}, E_{Na-F}, E_{Na-Na}, E_{Na-K}, E_{K-F}, E_{K-K}, E_{F-F}$: the bonds energy of each type.

$$N_{Li}z_{Li} = 2B_{Li-Li} + B_{Li-F} + B_{Li-Na} + B_{Li-K} \quad (4\text{-}132)$$

$$N_{Na}z_{Na} = 2B_{Na-Na} + B_{Na-F} + B_{Li-Na} + B_{Na-K} \quad (4\text{-}133)$$

$$N_{K}z_{K} = 2B_{K-K} + B_{K-F} + B_{Na-K} + B_{Li-K} \quad (4\text{-}134)$$

$$N_{F}z_{F} = 2B_{F-F} + B_{Na-F} + B_{Li-F} + B_{K-F} \quad (4\text{-}135)$$

Where, N_{Li}, N_{Na}, N_K, N_F: the number of Li, Na, K, F

z_{Li}, z_{Na}, z_K, z_F: the coordination number of each atom in terms of reference atom in the solution

Therefore,

$$B_{Li-Li} = \frac{N_{Li}z_{Li}}{2} - \frac{B_{Li-F} + B_{Li-Na} + B_{Li-K}}{2} \quad (4\text{-}136)$$

$$B_{Na-Na} = \frac{N_{Na}z_{Na}}{2} - \frac{B_{Na-F} + B_{Li-Na} + B_{Na-K}}{2} \quad (4\text{-}137)$$

$$B_{K-K} = \frac{N_{K}z_{K}}{2} - \frac{B_{K-F} + B_{Na-K} + B_{Li-K}}{2} \quad (4\text{-}138)$$

$$B_{F-F} = \frac{N_{F}z_{F}}{2} - \frac{B_{Na-F} + B_{Li-F} + B_{K-F}}{2} \quad (4\text{-}139)$$

Substitute the equation *(4-136)*, *(4-137)*, *(4-138)* and *(4-139)* into *(4-131)*, then,

$$E = \frac{N_{Li} z_{Li} E_{Li-Li}}{2} + \frac{N_{Na} z_{Na} E_{Na-Na}}{2} + \frac{N_K z_K E_{K-K}}{2} + \frac{N_F z_F E_{F-F}}{2} + B_{Li-F}\left(E_{Li-F} - \frac{E_{Li-Li} + E_{F-F}}{2}\right) + B_{Li-F} E_{Li-F} - E_{Li-Li} \frac{B_{Li-F} + B_{Li-Na} + B_{Li-K}}{2} + B_{Li-Na} E_{Li-Na} + B_{Li-K} E_{Li-K} + B_{Na-F} E_{Na-F} - E_{Na-Na} \frac{B_{Na-F} + B_{Li-Na} + B_{Na-K}}{2} + B_{Na-K} E_{Na-K} + B_{K-F} E_{K-F} - E_{K-K} \frac{B_{K-F} + B_{Na-K} + B_{Li-K}}{2} - E_{F-F} \frac{B_{Na-F} + B_{Li-F} + B_{K-F}}{2} \tag{4-140}$$

Since in equation *(4-140)*,

$$\frac{N_{Li} z_{Li} E_{Li-Li}}{2} + \frac{N_{Na} z_{Na} E_{Na-Na}}{2} + \frac{N_K z_K E_{K-K}}{2} + \frac{N_F z_F E_{F-F}}{2} = energy\ of\ the\ unmixed\ component \tag{4-141}$$

Then, the heat of formation ΔH_{mix} can be expressed by,

$$\Delta H_{mix} = H_2 - H_1 = B_{Li-F}\left(E_{Li-F} - \frac{E_{Li-Li} + E_{F-F}}{2}\right) + B_{Li-F} E_{Li-F} - E_{Li-Li} \frac{B_{Li-F} + B_{Li-Na} + B_{Li-K}}{2} + B_{Li-Na} E_{Li-Na} + B_{Li-K} E_{Li-K} + B_{Na-F} E_{Na-F} - E_{Na-Na} \frac{B_{Na-F} + B_{Li-Na} + B_{Na-K}}{2} + B_{Na-K} E_{Na-K} + B_{K-F} E_{K-F} - E_{K-K} \frac{B_{K-F} + B_{Na-K} + B_{Li-K}}{2} - E_{F-F} \frac{B_{Na-F} + B_{Li-F} + B_{K-F}}{2} \tag{4-142}$$

Therefore, the enthalpy of formation can be calculated by equation *(4-142)*.

4.6.3.3. Results and Analysis

4.6.3.3.1. Structure Information of FLiNaK

As shown in Figure 4-80, it is a snapshot of the local ionic structure in the simulation box for FLiNaK. From the statistical calculation of ions' trajectories, the important structure information including the radial distribution function and coordination number distribution were obtained based on the analysis in section 4.6.3.2.2.

Since the structure is extremely sensitive to the simulation model, the structural information of constituent ions of FLiNaK was analyzed and compared with the literature and experimental measurements to validate the FPMD modeling of molten fluoride salts. The radial distribution functions (RDF) of different ion pairs and corresponding coordination numbers in molten FLiNaK salt are shown in Figure 4-81, Figure 4-82, Figure 4-83 and *Figure 4-84*. The comparison summary between the predicted structure data in this study with the literature [23] and experimental data [33] are also shown in Table 4-21 and Table 4-22. As shown in Table 4-22, the average bond length which correspond to the first peak radius of Li-F, Na-F, K-F and F-F ion pairs were in good agreement with the literature and experiment data. The first shell coordination numbers which were determined by the integral of the RDF in terms of corresponding first peak interval were also compared in Table 4-22. The coordination number predicted in this FPMD agrees well with the literature, but shows greater values than the experiment data. As for the Na-F, K-F and F-F, the lower interval values as pointed by the arrow in Figure 4-82, Figure 4-83 and *Figure 4-84* shows a wide flat zone which make the range of the first peak larger thus leading to the large difference between the FPMD and experiment data. But, since our FPMD results match well with the literature FPMD study, it has demonstrated that our method has a good performance in the simulation model.

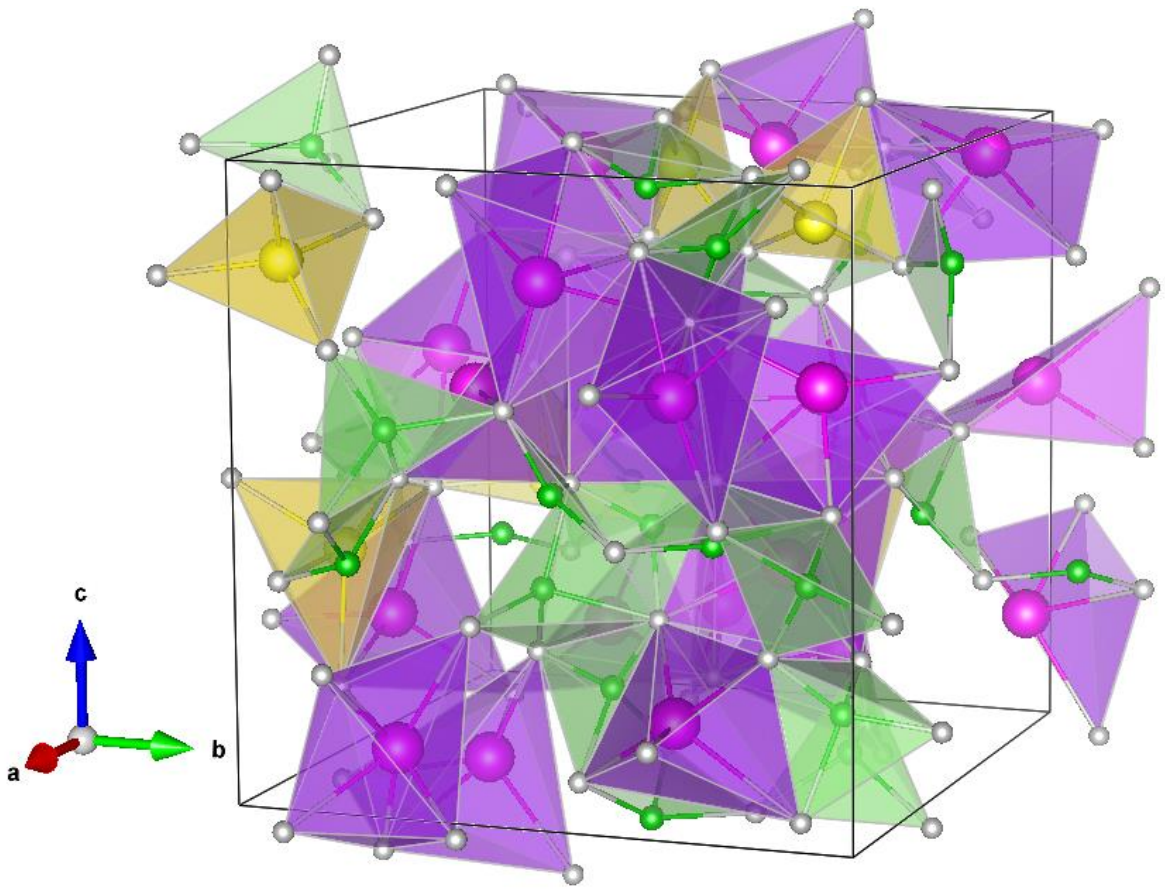

Figure 4-80 Snapshot of the local ionic structure in FLiNaK molten salt at 700°C, grey balls are fluorine ions, green balls are lithium ions, yellow balls are sodium ions, pink balls are potassium balls.

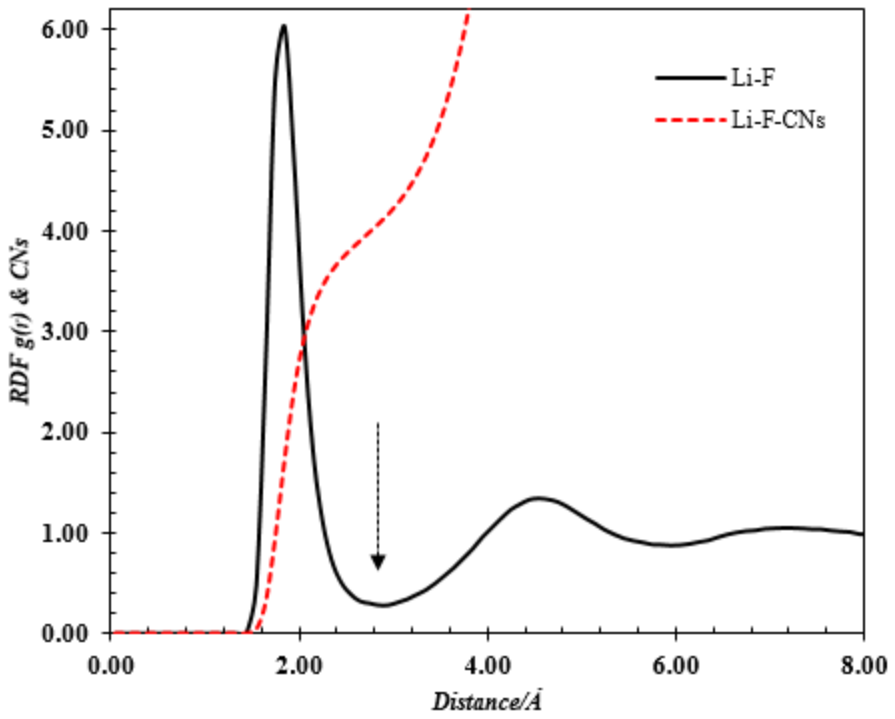

Figure 4-81 Radial distribution function (RDF) of Li-F in FLiNaK at 700°C

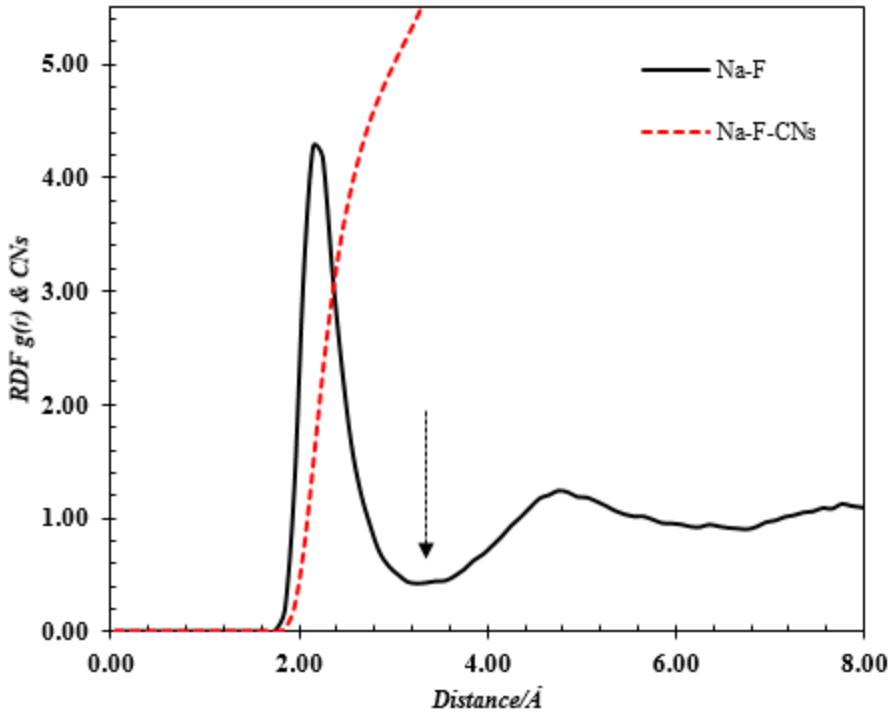

Figure 4-82 Radial distribution function (RDF) of Na-F in FLiNaK at 700°C

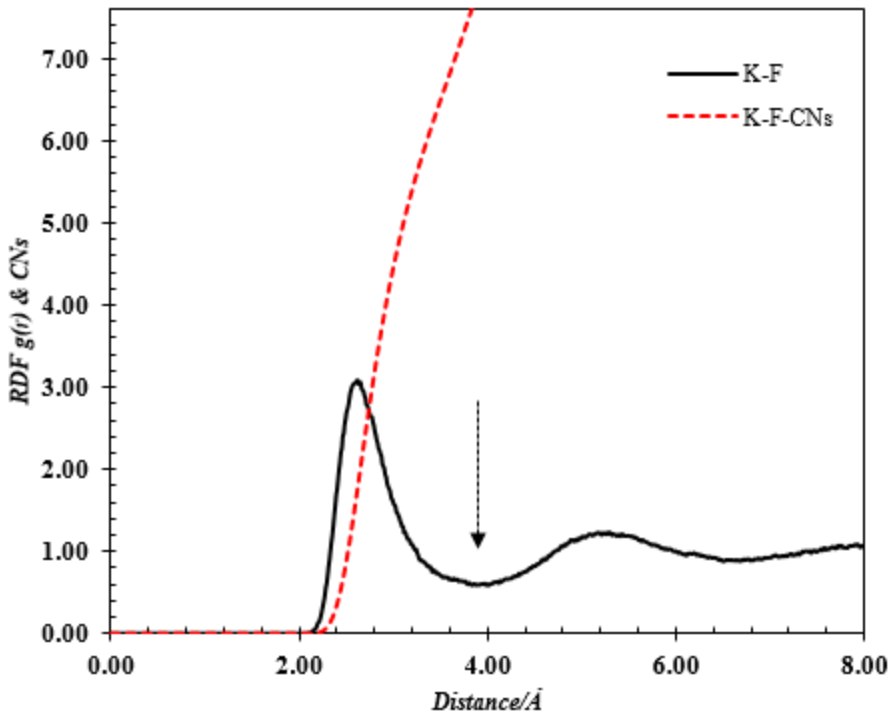

Figure 4-83 Radial distribution function (RDF) of K-F in FLiNaK at 700°C

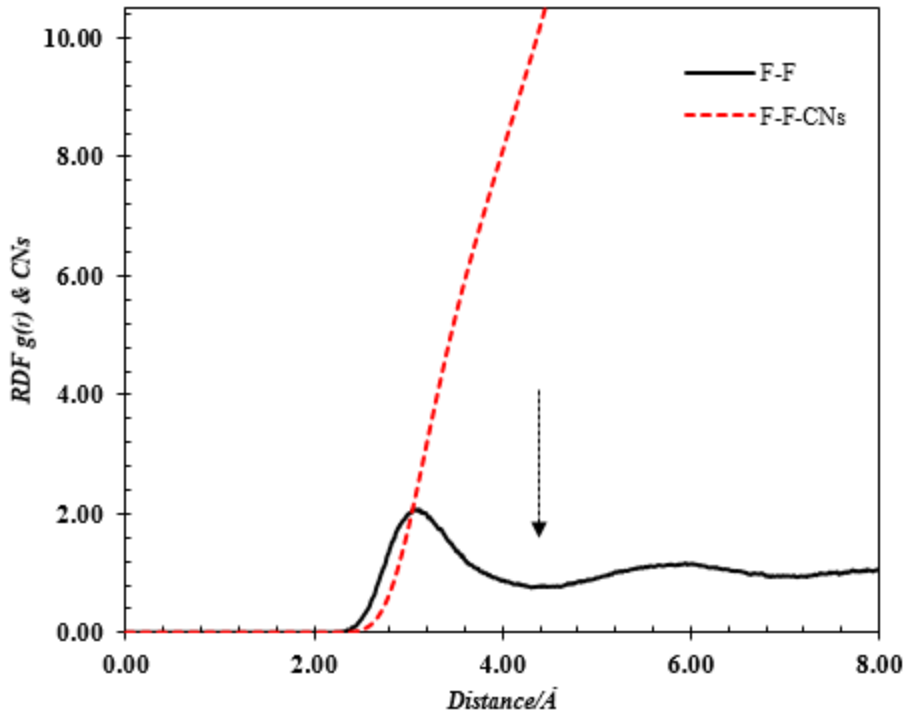

Figure 4-84 Radial distribution function (RDF) of F-F in FLiNaK at 700°C

Table 4-21 Comparison of the first peak radius for ion pairs in FLiNaK with literature data and experiment data. FPMD simulations for FLiNaK were performed at 700°C

Ion pair	First peak radius Å		
	FPMD (700°C)	Literature (700°C)[23]	Experiment (520°C)[33]
Li^+-F^-	1.85	1.86	1.83
Na^+-F^-	2.17	2.19	2.18
K^+-F^-	2.62	2.59	2.59
F^--F^-	3.07	3.13	3.05

Table 4-22 Comparison of first shell coordination numbers for ion pairs in FLiNaK with literature data and experiment data. FPMD simulations for FLiNaK were performed at 700°C

	Coordination number		
Ion pair	FPMD	Literature FPMD	Experiment
Li^+-F^-	4.0	4.0	3.3
Na^+-F^-	5.4	5.4	3.8
K^+-F^-	7.5	7.3	4.0
F^--F^-	10.3	10.2	8.9

4.6.3.3.2. *Structure Information of FLiNaK-La_2O_3*

The local ionic structure of the FLiNaK-La_2O_3 was shown in Figure 4-85. Since there are only two lanthanum atoms included in the simulation box. It is observed that the one La ion is bonded with five fluorine ions to form a pentahedron structure, while the other one is bonded with both fluorine ions and oxygen ions which should be the LaOF as discussed in 4.6.1.3.

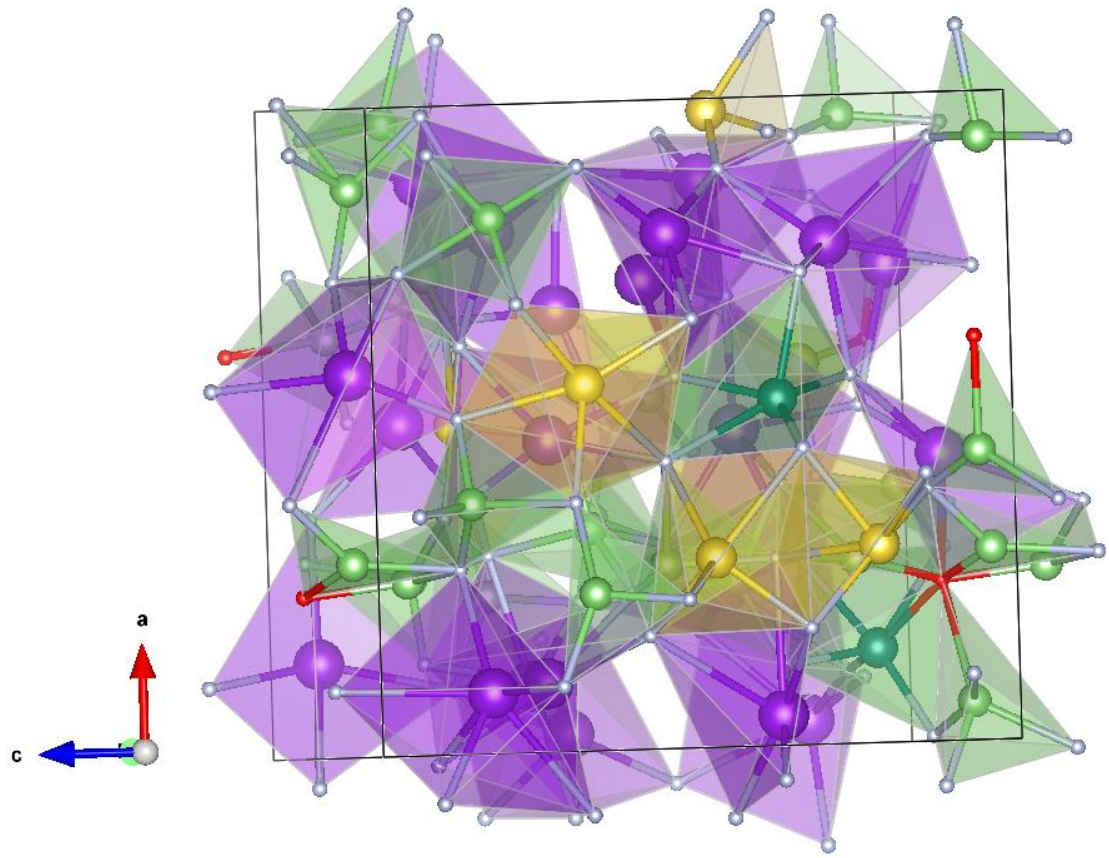

Figure 4-85 Snapshot of the local ionic structure in FLiNaK-La_2O_3 molten salt at 700°C, grey balls are fluorine ions, light green balls are lithium ions, yellow balls are sodium ions, purple balls are potassium ions, deep green balls are lanthanum ions, red balls are oxygen ions.

The first peak radius and first shell coordination number were also calculated in the FLiNaK-La_2O_3 system. The comparison with the data of pure FLiNaK was shown in Table 4-23. There is no significant difference between them in the first peak radius and coordination number for the ionic pairs of Li^+-F^-, Na^+-F^-, but the first peak radius and coordination number of ions pair K^+-F^- and F^--F^- have slight decrease due to the bond of La^{3+}-F^-.

Table 4-23 comparison of first peak radius and first shell coordination numbers for ions pairs in FLiNaK and FLiNaK- La_2O_3. FPMD simulations for FLiNaK were performed at 700°C

Ion pair	FLiNaK-La_2O_3		FLiNaK	
	First peak radius Å	Coordination number	First peak radius Å	Coordination number
Li^+-F^-	1.85	4.0	1.85	4.0
Na^+-F^-	2.17	5.4	2.17	5.4
K^+-F^-	2.57	7.4	2.62	7.5
F^--F^-	3.05	9.1	3.07	10.3
La^{3+}-F^-	2.35	7.6	-	-
Li^+-O^{-2}	1.85	0.28	-	-
Na^+-O^{-2}	2.25	0.22	-	-
K^+-O^{-2}	2.65	0.25	-	-
F^--O^{-2}	3.25	0.41	-	-
La^{3+}-O^{-2}	2.15	0.15	-	-

Note: for the corresponding radial distribution function curves, please see the Appendix.

4.6.3.3.3. Enthalpy of formation $\Delta \boldsymbol{H_{mix}}$

The total energy from the FPMD simulation with the 100-atom unit cell which include 23Li, 6Na, 21K and 100F and the 105-atom unit cell which include 23Li, 6Na, 21K, 100F, 2La and 3O were used to estimate heat of formation in the molten salt ΔH_{mix} as shown in Table 4-24.

Table 4-24 Comparison of enthalpy of formation in FLiNaK and FLiNaK-La_2O_3

	ΔH_{mix}	Literature
	kJ/mol	kJ/mol
FLiNaK	-583.207 ± 0.840	-
FLiNaK+La_2O_3	-398.397 ± 2.557	-

There is no available literature data to compare with the obtained enthalpy of formation ΔH_{mix} data. But since the validity of simulation method has been confirmed in 4.6.3.3.1, our result of the Gibbs free energy should be acceptable. In addition, the Gibbs free energy of LaOF and LaF_3 at 1200°C were also calculated with the quasi-harmonic approximation as shown in Table 4-25. More work will be done in the future to study further in this field.

Table 4-25 Gibbs free energy of LaOF and La_2O_3 at 1200°C

	Gibbs free energy	Literature [34]
	kJ/mol	kJ/mol
LaOF	-2101.916 ± 0.343	-
LaF_3	-2049.677 ± 1.374	-1974.437

4.6.3.4. Conclusions and Future work

In this part, the local ionic structure information of FLiNaK and FLiNaK-La_2O_3 was obtained and compared with the literature and experiment data. As for the FLiNaK, the first peak radius agrees well with the literature FPMD and experiment data, while the coordination number can only match well with the literature FPMD, but much larger than the experiment due to the flat zone of the first peak interval which is an issue that also existed in the literature FPMD. As for the enthalpy of formation, a multicomponent solution model was built in 4.6.3.2.3. The total energy from the FPMD simulation was used to estimate the heat formation of the solution. As for the FLiNaK-La_2O_3 model, the local ionic structure and the corresponding first peak radius and the first shell coordination number were calculated and compared with the obtained pure FLiNaK at 700°C. The kinetic properties, such as self-diffusion coefficient, will be studied in the future to further understand the properties of the FLiNaK and the effect of La_2O_3 on its properties.

4.6.4. Appendix

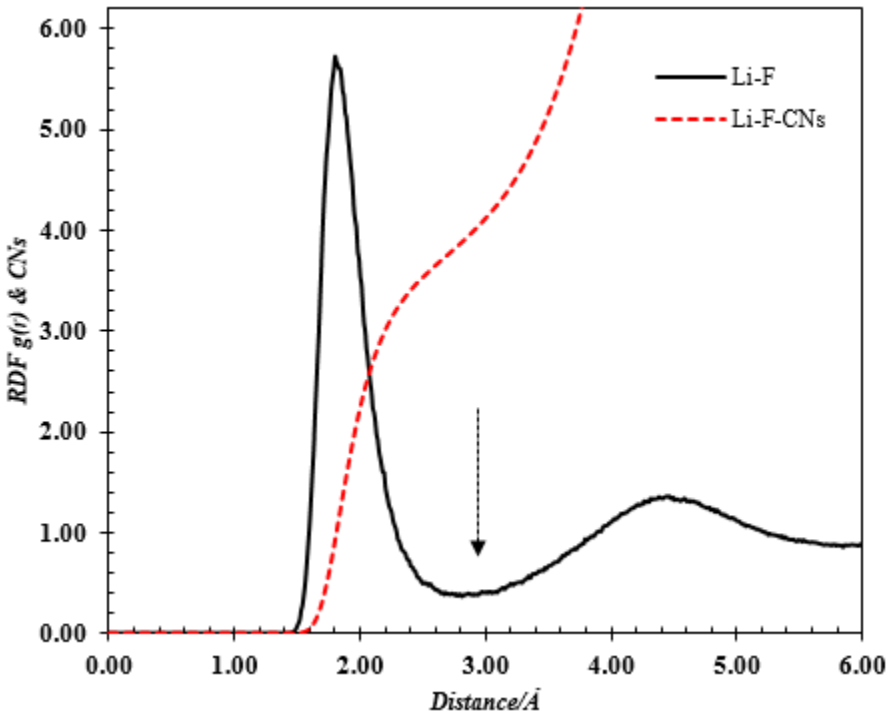

Figure 4-86 Radial distribution function (RDF) of Li-F in FLiNaK-La_2O_3 at 700°C

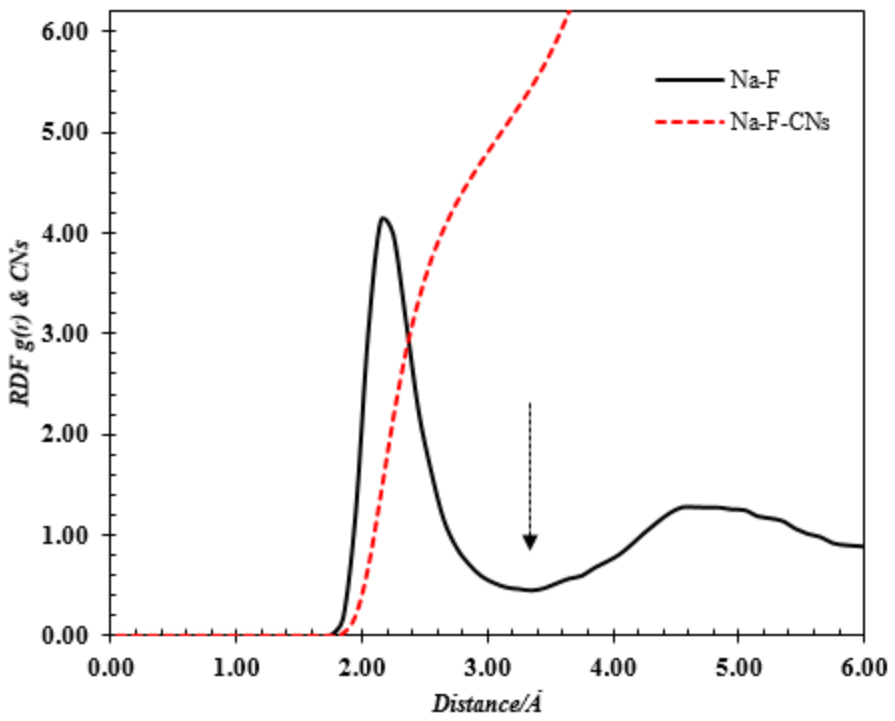

Figure 4-87 Radial distribution function (RDF) of Na-F in FLiNaK-La_2O_3 at 700°C

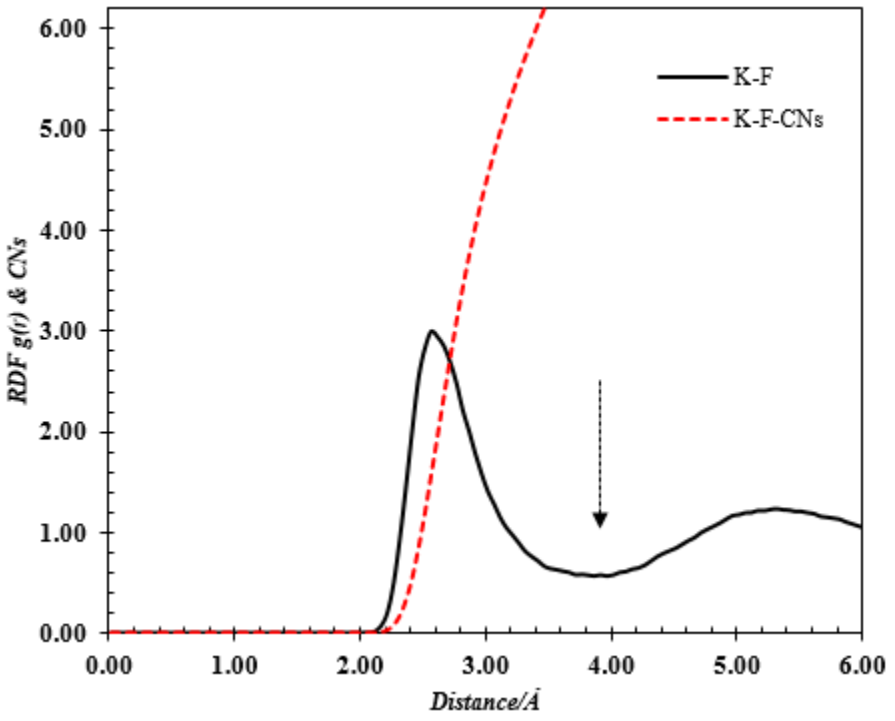

Figure 4-88 Radial distribution function (RDF) of K-F in FLiNaK-La_2O_3 at 700°C

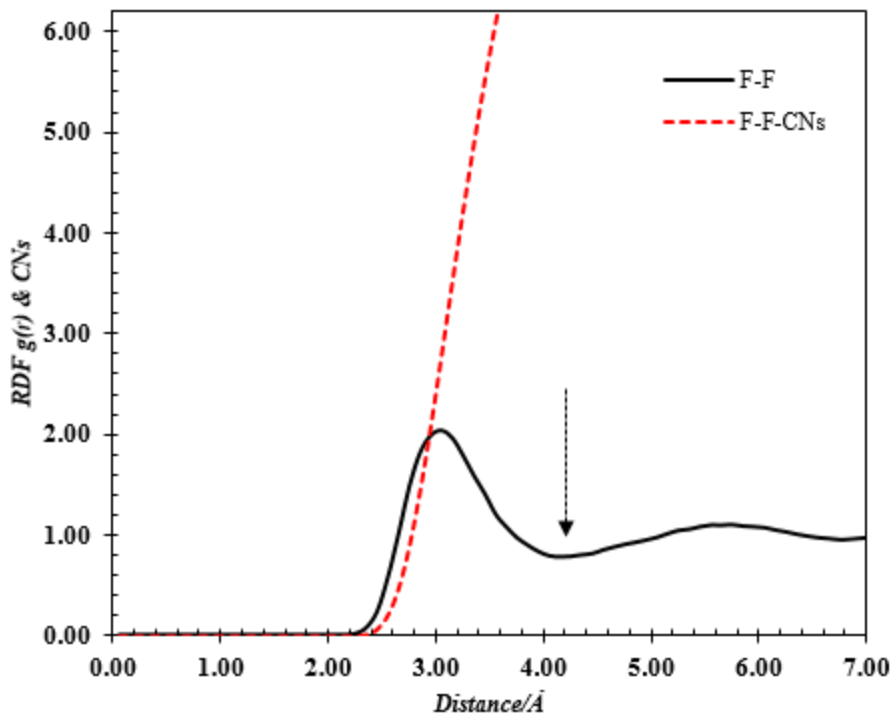

Figure 4-89 Radial distribution function (RDF) of F-F in FLiNaK-La_2O_3 at 700°C

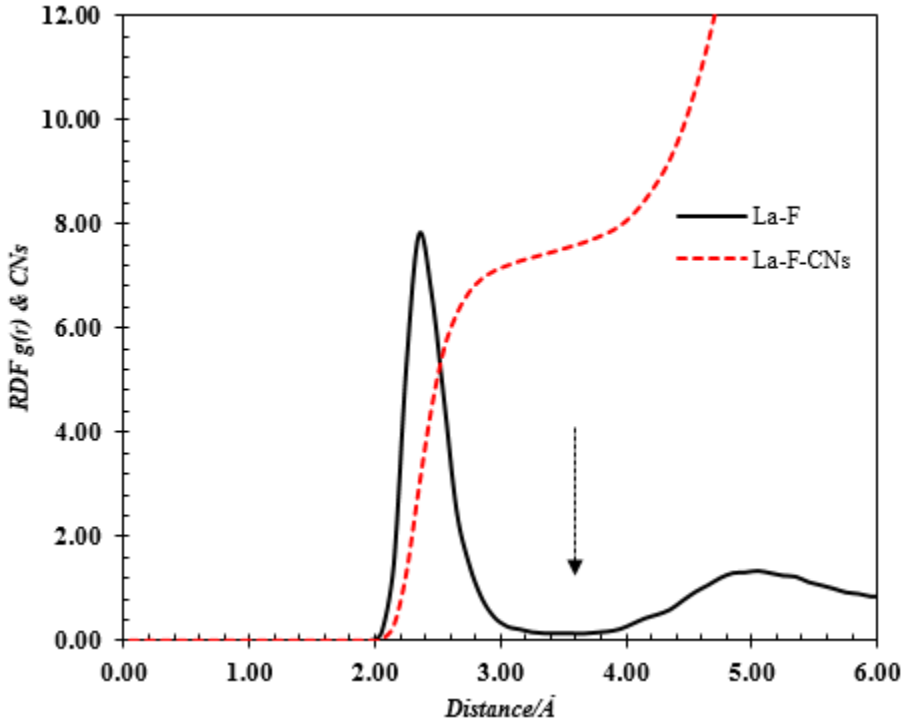

Figure 4-90 Radial distribution function (RDF) of La-F in FLiNaK-La_2O_3 at 700°C

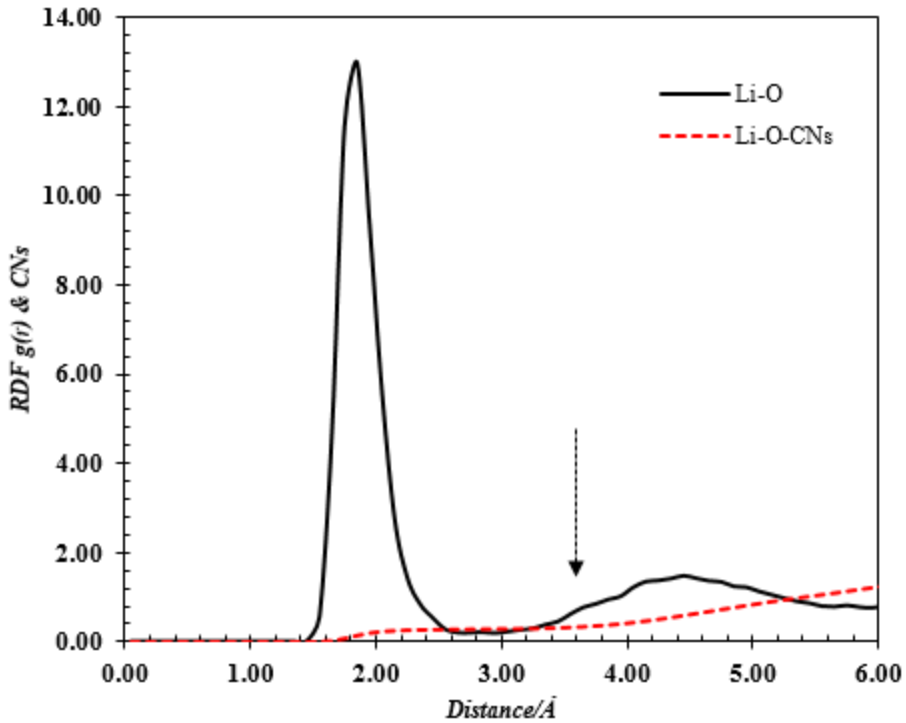

Figure 4-91 Radial distribution function (RDF) of Li-O in FLiNaK-La_2O_3 at 700°C

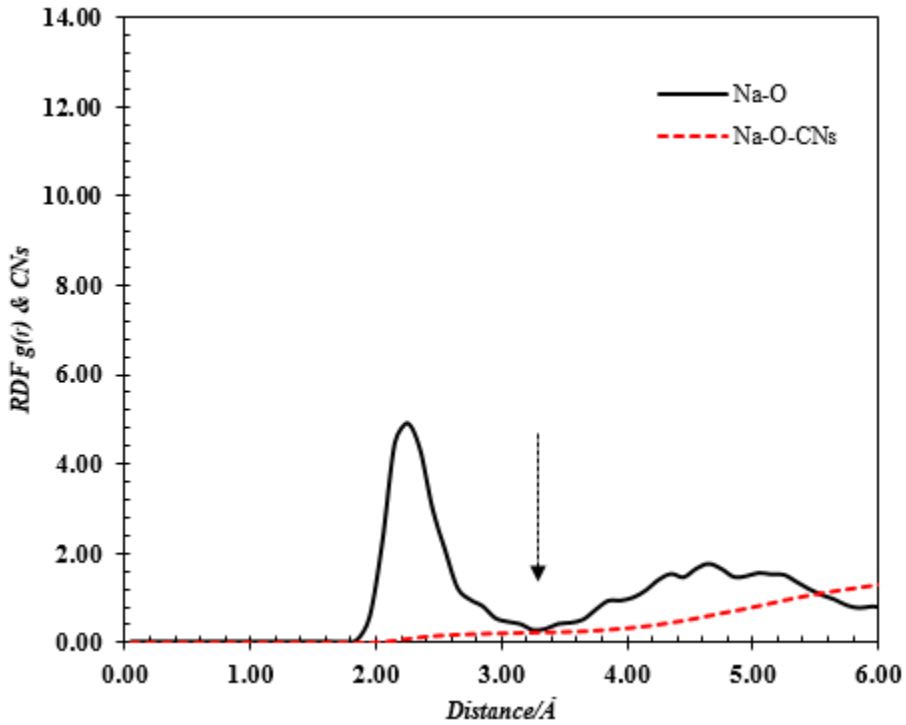

Figure 4-92 Radial distribution function (RDF) of Na-O in FLiNaK-La_2O_3 at 700°C

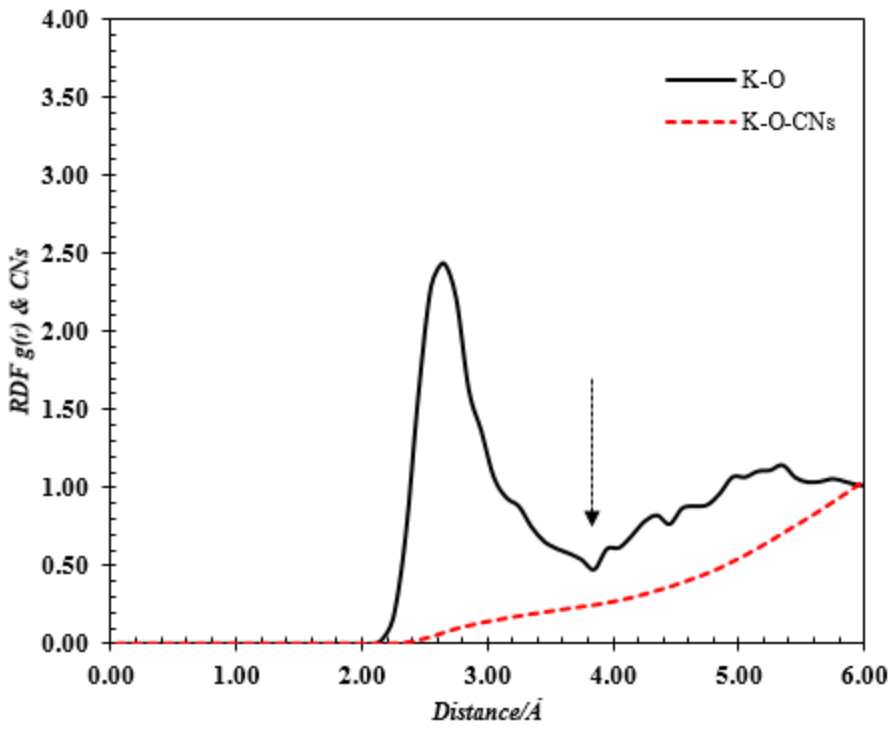

Figure 4-93 Radial distribution function (RDF) of K-O in FLiNaK-La_2O_3 at 700°C

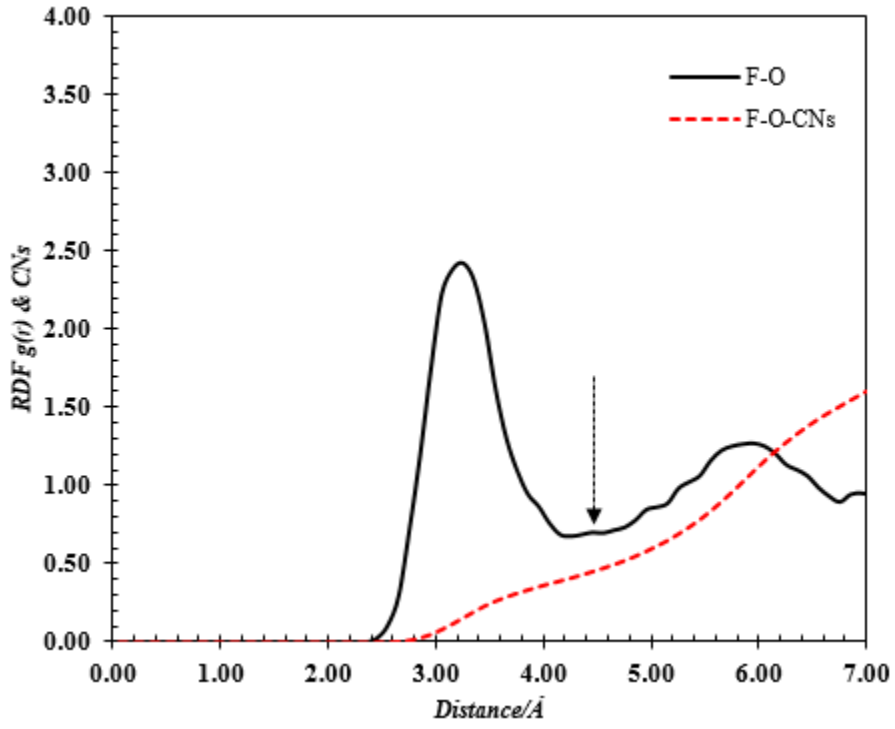

Figure 4-94 Radial distribution function (RDF) of F-O in FLiNaK-La_2O_3 at 700°C

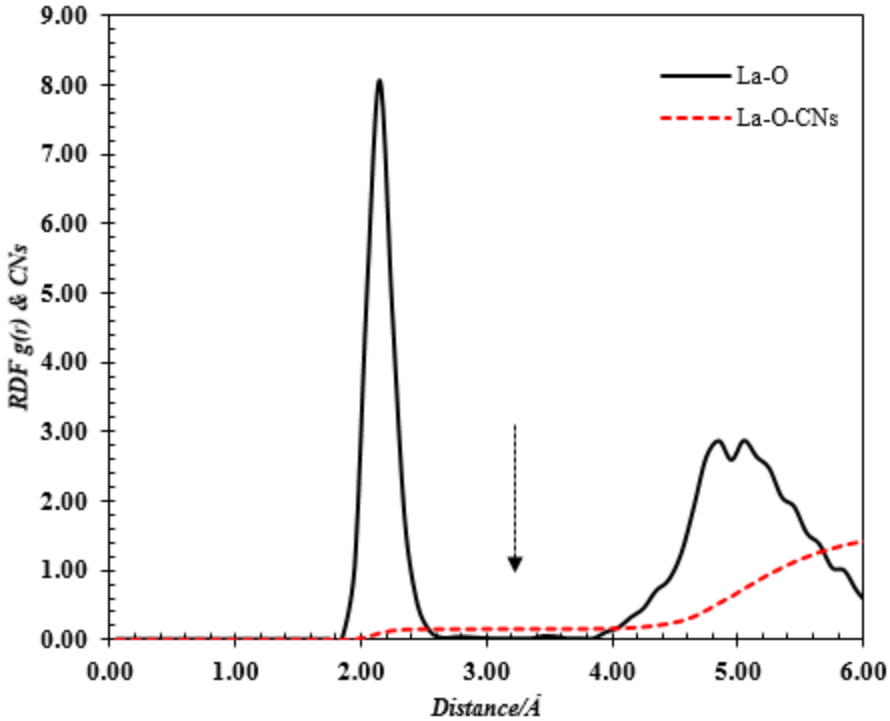

Figure 4-95 Radial distribution function (RDF) of La-O in FLiNaK-La_2O_3 at 700°C

4.6.5. References

1. M. Ambrová., et al, "On the Solubility of Lanthanum Oxide in Molten Alkali Fluorides" , Journal of Thermal Analysis and Calorimetry, 91(2008): 569-573.
2. R. M. Wheat., et al, "Solubility of Lanthanum Oxide, Samarium Oxide and Holmium Oxide in the eutectic melt LiF-NaF-KF", Report of the National Academy of Sciences of Ukraine, 4(2011): 132-138.
3. X. L. Guo, J. Sietsma, Y. X. Yang, "Solubility of Rare Earth Oxides in Molten Fluorides", ERES2014: 1st European Rare Earth Resource Conference, 2014
4. E. Stefanidaki, C. Hasiotis, C. Kontoyannis, "Electrodeposition of neodymium from LiF-NdF3-Nd2O3", Electrochinica Acta, 46(2001): 2665-2670.
5. S. I. Berul, N. K. Voskresenskaya, Zh. Neorg. Khim, 8(1963): 1431.
6. M. Ambrova, J. Jurisova, A. Sykorova., et al, "Electrochemical behavior of the LiF-CaF2-La2O3 system", Chemical Papers, 62(2008): 154-159.
7. Huan Qiao, T. Nohira, Y. Ito, "Electrochemical Behavior of Oxide Ion at a Glassy Carbon Electrode in a LiF-NaF-KF Eutectic Melt", 71(2003): 530-535.
8. Zuoju Huang, Zhanmin Cao, Guihua Wang, Hongmin Zhu, "An Electrochemical Study of Electrode Process on Carbon Electrode in LiF-NaF-KF Melt", Electrochemistry, 78(2010): 510-512.
9. Shaoqiang Guo, N. Shay, Y. Wang, W. Zhou, J. Zhang, "Measurement of Europium(III)/Europium(II) Couple in Fluoride Molten Salt for Redox Control in a Molten Salt Reactor Concept", Journal of Nuclear Materials, 496(2017): 197-206.

10. T. Yamamura, M. Mehmood, H. Maekawa, Y. Sato, "Electrochemical Processing of Rare-Earth and Rare Metal by Using Molten Salts", Chemistry for Sustainable Development, 12(2004): 105-111.
11. Devin Rappleye and Michael F. Simpson, "Electrochemical Signal Measurement and Analysis for Metal Deposition in Molten LiCl-KCl Eutectic," in INMM 56th Annual Meeting, Palm Springs, CA, July 2015.
12. Y. Ito, T. Takenaka, K. Ema, J. Oishi, Electrochemistry, 51(1983):864.
13. G. Chen, Z. N. Shi, et al, "Anodic Passivation of a Graphite Electrode in LiF-KF Melt at 773K", Journal of The Electrochemical Society, 162(2015): C197-C204.
14. G. Kresse, J. Hafner, "Ab Initio Molecular Dynamics for Liquid Metals", Physical Review B, 47(1993): 558-561.
15. G. Kresse, J. Furthmüller, "Efficiency of Ab-initio Total Energy Calculations for Metals and Semiconductors Using a Plan-wave Basis Set", Computational Materials Science 6 (1996) 15–50.
16. CPMD, http://www.cpmd.org/, jointed copyright by IBM Corporation and Max-Planck Institut, Stuttgart.
17. G. Kresse, D. Joubert, "From Ultrasoft Pseudopotentials to the Projector Augmented-Wave Method", Physical Review B, 59(1999): 1758-1775.
18. G. Kresse, J. Furthmuller, "Efficient Iterative Schemes for Ab Initio Total Energy Calculations Using a Plan-wave Basis Set", Physical Review B, 54(1996): 169-186.
19. D. Alfe, M. J. Gillan, "First-Principles Calculation of Transport Coefficients", Physical Review Letters, 81(1998): 5161-5164.
20. H.Z. Fang, W.Y. Wang, P.D. Jablonski, Z.K. Liu, "Effects of Reactive Elements on the Structure and Diffusivity of Liquid Chromia", Physical Review B, 85(2012): (014207)1-(014207)10.
21. P. Ganesh, M. Widom, "Liquid-Liquid Transition in Supercooled Silicon Determined by First-Principles Simulation", Physical Review Letters, 102(2009): (075701)1-(075701)4.
a. Bengtson, H.O. Nam, S. Saha, R. Sakidja, D. Morgan, "First-principles Molecular Dynamics Modeling of the LiCl-KCl Molten Salt System", Computational Materials Science, 83(2014): 362-370.
22. H.O. Nam, A. Bengtson, K. Vortler, S. Saha, R. Sakidja, D. Morgan, "First-principles Molecular Dynamics Modeling of the Molten Fluoride Salt with Cr Solute", Journal of Nuclear Materials, 449(2014): 148-157.
23. J. Dai, H. Han, Q. Li, P. Huai, "First-principle Investigation of the Structure and Vibrational Spectra of the Local Structures in LiF-BeF2 Molten Salt"
24. J. Song, S. Shi, X. Li, L. Yan, "First Principle Molecular Dynamics Modeling of UCl3 in LiCl-KCl Eutectic", Journal of Molecular Liquids, 234(2017): 279-286.
25. S. Nosé, "A Unified Formulation of the Constant Temperature Molecular Dynamcis Methods", J. Chem. Phys. 81 (1984) 511–519.
26. X. Lv, Z. Han, J. Chen, L. Jiang, Z. Xu, Q. Liu, "First-principles Molecular Dynamics Studies of Ionic Structure and Transport Properties of LiF-NaF-AlF3 Molten Salt", Chemistry
27. Physics Letters, 706(2018): 237-242.
28. X. Lv, Z. Xu, J. Li, J. Chen, Q. Liu, "First-principles Molecular Dynamics Investigation on Na3AlF6 Molten Salt", Journal of Fluorine Chemistry, 185(2016): 42-47.

29. L. Martínez, R. Andrade, E.G. Birgin, J.M. Martínez, "Packmol: A Package for Building Initial Configurations for Molecular Dynamcis Simulatins" J. Comput. Chem. 30 (2009)
30. 2157–2164.
31. Shuichi Nose, "A Unified Formulation of the Constant Temperature Molecular Dynamics Methods", J. Chem. Phys. 81(1984): 511-519.
32. W.H. Press, B.P. Flannery, S.A. Teukolsky and W.T. Vetterling, "Numerical Recipes: The Art of Scientific Computing (Third Edition)", Cambridge University Press, New York, 1986.
33. J.M. Ziman, Principles of the Theory of Solids Cambridge, Cambridge University Press, Cambridge University, 1972.
34. K. Igarashi, Y. Okamoto, J. Mochinaga, H. Ohno, "X-Ray Diffraction Study of Molten Eutectic LiF-NaF-KF Mixture", J. Chem. Soc., Faraday Trans. 1: Phys. Chem. Condens. Phases, 84(1988): 4407–4415.
35. HCP Chemistry 6, Barin 95.

4.7. Electrochemical Investigation on Lanthanide Separation

4.7.1. Lanthanum Separation in Molten Fluoride salts by Electrochemical Methods

Lanthanum is one of the abundant fission products in nuclear reactors [35] and the ions of which dissolved in the molten salt is commonly taken as a model system for electrochemical separation study of fission products in molten salt. Electrochemical behavior of La (III)/La and thermodynamic properties of La (III) in molten salt is widely studied before. For instance, in the investigation of pyroprocessing of spent nuclear fuel, concentration and temperature-dependent reduction potentials of La (III) in LiCl-KCl molten salt was reported before [36,37,38,39]. In addition, there were extensive researches studied the fundamental properties such as diffusivity and activity coefficient using different methods [38,39,40,41,42,43,44]. Electrochemical studies of La (III)/La in molten fluoride salt is rarely conducted before. As far as we know in the literature, only Marta et al [45] used LiF and LiF-CaF_2 eutectic for lanthanum electrochemical studies. Qiao et al [46] conducted the electrochemical study of LaF_3 in LiF-NaF-KF molten salt and found there were no cathodic and anodic peaks shown up in their cyclic voltammetry (CV) test when using inert working electrode. The conclusion was made that electrochemical separation of La (III) in FLiNaK cannot be realized because of the more negative standard reduction potential of La (III) comparing with K (I). Recently, Chesser et al [47] recently found there is redox reaction related to lanthanum happened prior to the redox reaction of K(I)/K in FLiNaK molten salt. It is interesting that the results reported in the two previous literatures [46,47] for one same electrochemical cell are different. In order to further confirm the electrochemical behavior of LaF_3 in molten salt, the present study was carried out.

4.7.1.1. Experimental methods

The electrochemical tests were carried out inside the glove box with an argon atmosphere (≤0.1 ppm O_2 and ≤0.1 ppm H_2O) to prevent the reactions with water and oxygen due to the

hygroscopic nature of electrolytes. Electrolytes were prepared with the chemicals as follows: Lithium fluoride, LiF, ≥ 99.0 % purity, sodium fluoride, NaF, ≥ 99.0 % purity, potassium fluoride, KF, ≥ 99.5 % purity, and lanthanum (III) fluoride, LaF_3, ≥ 99.99 % purity which were all procured from Sigma Aldrich. The powders of LiF, NaF, and KF were weighted using an analytical balance with the accuracy of 10^{-4} g. The prepared fluoride chemicals were placed in the nickel crucible (55 mL) and heated in a muffle furnace. Electrochemical tests in the study utilized a three-electrode electrochemical cell in the furnace, the working electrode used was a 3.2 mm diameter tungsten rod and a 3.17 mm diameter molybdenum rod. The counter electrode used was a 3.05 mm diameter graphite rod. The reference electrode utilized was a 0.81 mm diameter platinum wire with potential associated to $Pt/PtO_x/O^{2-}$ [48]. The bottoms of electrodes were immersed in the FLiNaK salt bath and no touch of electrodes with nickel crucible was confirmed before test. The top ends of electrodes were connected to the Gamry Interface 1000 potentiostat to perform electrochemical measurements. Open circuit potential (OCP) was performed before CV and CP tests to confirm the stabilization of the system. IR compensation was selected in Gamry Framework software which is programmed with interrupt method during the tests.

4.7.1.2. Electrochemical Separation Study of LaF_3 in Molten FLiNaK Salt Melt

The electrochemical behavior of lanthanum in FLiNaK molten salt was studied by cyclic voltammetry and chronopotentiometry test. Figure 4-96 shows the obtained cyclic voltammograms in pure FLiNaK and FLiNaK-LaF_3 systems, respectively. The redox peaks at the left of the electrochemical window C1 and A1 correspond to the redox reaction of K (I)/K and this has been verified by Qiao et al [46] through the potential measurements of Li^+/Li, Na^+/Na, and K^+/K using alkali-metal electrodes in the FLiNaK melt. Different from the cyclic voltammogram obtained in pure FLiNaK molten salt, there is an extra pair of redox peaks C2 and A2 show up when LaF_3 was added into FLiNaK molten salt. A plateau P1 also appeared in the obtained chronopotentiogram Figure 4-96 (b) after LaF_3 was dissolved in. Thus, both cyclic voltammetry and chronopotentiometry test show there is a redox reaction occurs prior to the redox reaction of K (I)/K in FLiNaK-LaF_3 molten salt system.

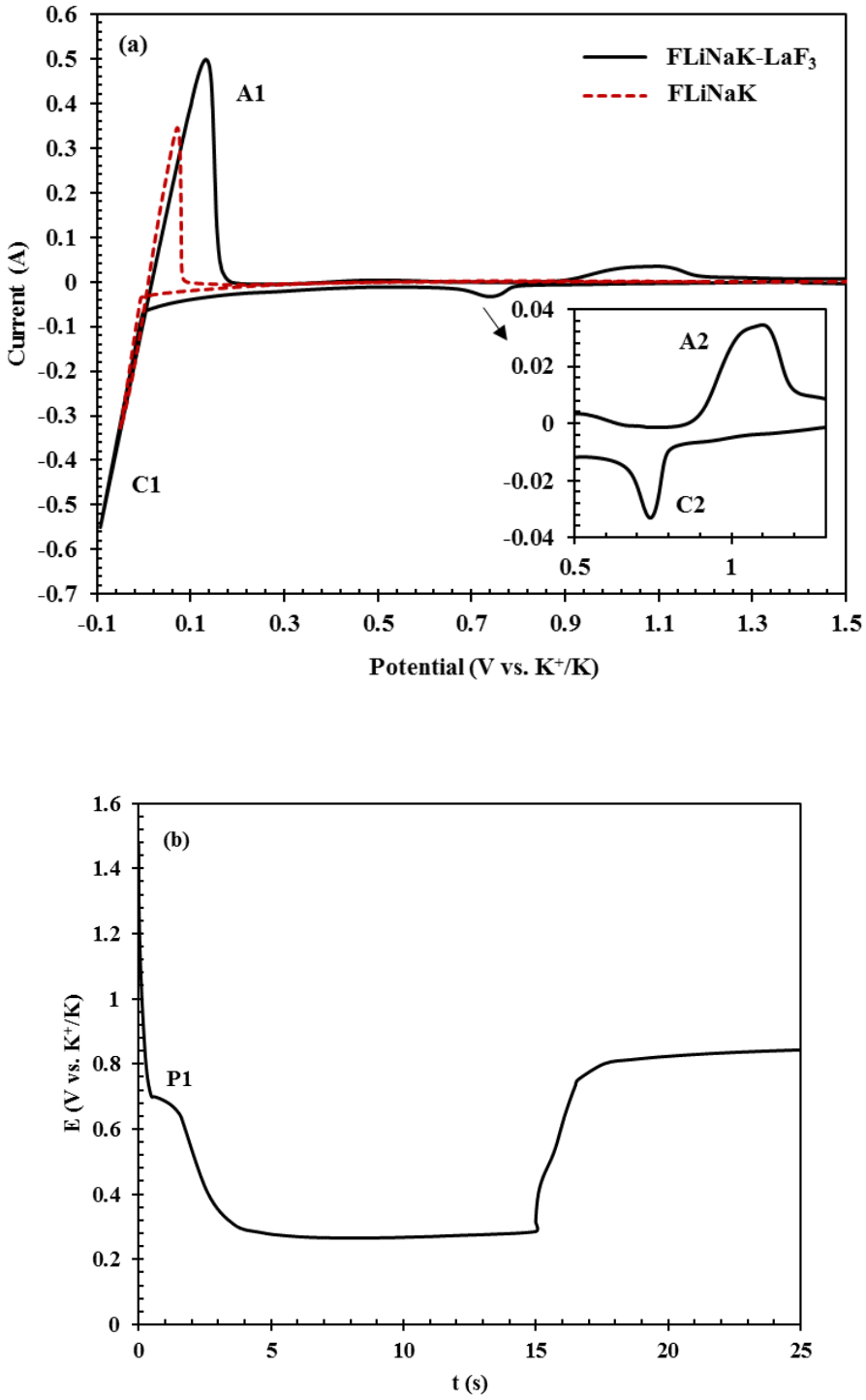

Figure 4-96.(a) Typical cyclic voltammograms obtained in FLiNaK-LaF_3 (working electrode area=0.673 cm^2) and pure FLiNaK molten salts at the scan rate of 100 mV/s. (b) Typical chronopotentiogram obtained in FLiNaK-LaF_3 molten salt with the applied current of -4 mA for 15s (working electrode area=0.673 cm^2). Working electrode: tungsten; counter electrode: tungsten; LaF_3=1.02 wt%; T=923 K.

In order to identify the reaction occurs prior to the redox reaction of K (I)/ K, the chronopotentiometry electrolysis was performed by applying a reduction current of 2 mA on the tungsten working electrode for 3500s to proceed that reduction reaction. During this process, the open circuit potential was monitored and controlled such that the reduction potential of K (I) was guaranteed not to be reached. Figure 4-97 shows the open circuit potential evolution with time when the reduction current was applied, from which it can be known that only the reduction reaction prior to that of K (I) occurs during the period when the current was applied. The electrode was taken out immediately after the chronopotentiometry electrolysis to do SEM test.

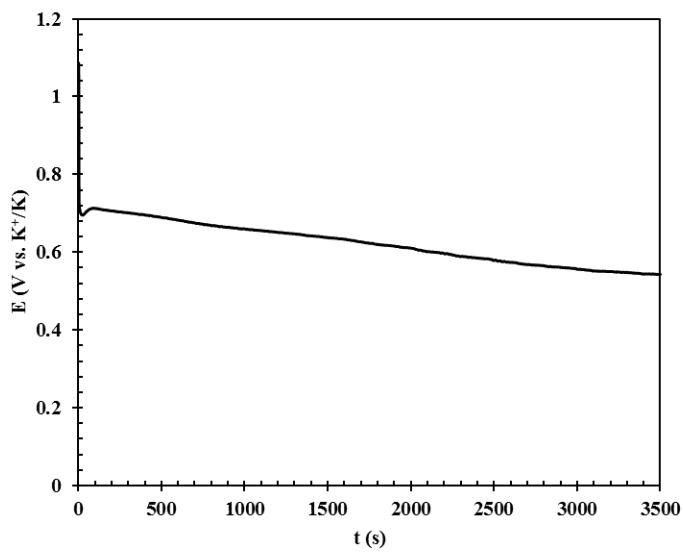

Figure 4-97. Open circuit potential evolution with time when a stable reduction current of 2 mA was applied on the tungsten electrode in FLiNaK-LaF_3 molten salt for 3500s. Working electrode: tungsten (electrode area=1.186 cm^2); counter electrode: graphite; T=973 K; LaF_3=1.68 wt%.

Figure 4-98 shows the obtained SEM results on the cross section of the tungsten electrode after chronopotentiometry electrolysis test. Figure 4-98 (a) depicts the BSE image, from which it can be seen lots of lanthanum is concentrated at the center. The extremely weak signal of element F in the point scans of the lanthanum concentrated area indicates that the product produced is lanthanum metal. Additionally, the absence of element F in the lanthanum rich area as shown in the EDS mapping (Figure 4-98 (c-f)) illustrates the same result. Based on the results obtained from electrochemical techniques and SEM method, it can be known that the reduction reaction of La ion to La metal occurs prior to the reduction of K (I) in FLiNaK-LaF_3 molten salt. This investigation conflicts with the previous study by

Qiao et al [46] in which they declared that the reduction reaction of lanthanum could not happen on inert electrode.

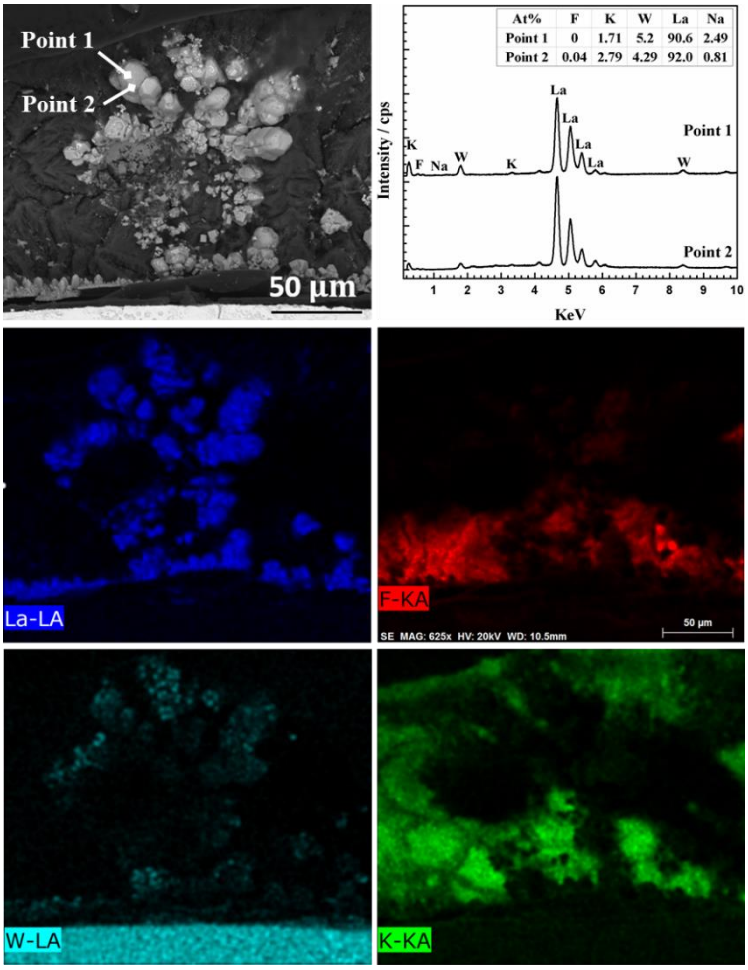

Figure 4-98. (a) Backscattered electrons (BSE) image of the cross section of polished tungsten rod electrode after electrolysis in FLiNaK-LaF_3 molten salt; (b) EDS point scan results of point 1 and point 2 in Figure 4-98a; (c)-(f) EDS mapping results of Figure 4-98a.

Given that the working electrode used by Qiao et al [46] was molybdenum not tungsten. The same electrochemical and SEM tests were also carried out on molybdenum working electrode although the electrochemical behaviors on different kinds of inert working electrodes normally are expected to be the same. Figure 4-99 shows the obtained cyclic voltammogram and chronopotentiogram on molybdenum working electrode in FLiNaK-LaF_3 system from which the redox reduction of lanthanum can be observed to occur prior to that of potassium. Chronopotentiometry electrolysis was also performed on the molybdenum working electrode by applying a reduction current of 6 mA for 1800s to deposit lanthanum. Figure 4-100 shows the open circuit potential evolution during the process of chronopotentiometry electrolysis from which it can be known the reduction potential of K (I) was not reached and only the reduction reaction of lanthanum ion happened. The molybdenum working electrode was taken out immediately out from

molten salt after chronopotentiometry electrolysis which is shown in Figure 4-101 from which it can be seen lots of dark substance deposited on it. Figure 4-102 presents the obtained SEM results on the molybdenum working electrode from which the lanthanum metal was also identified.

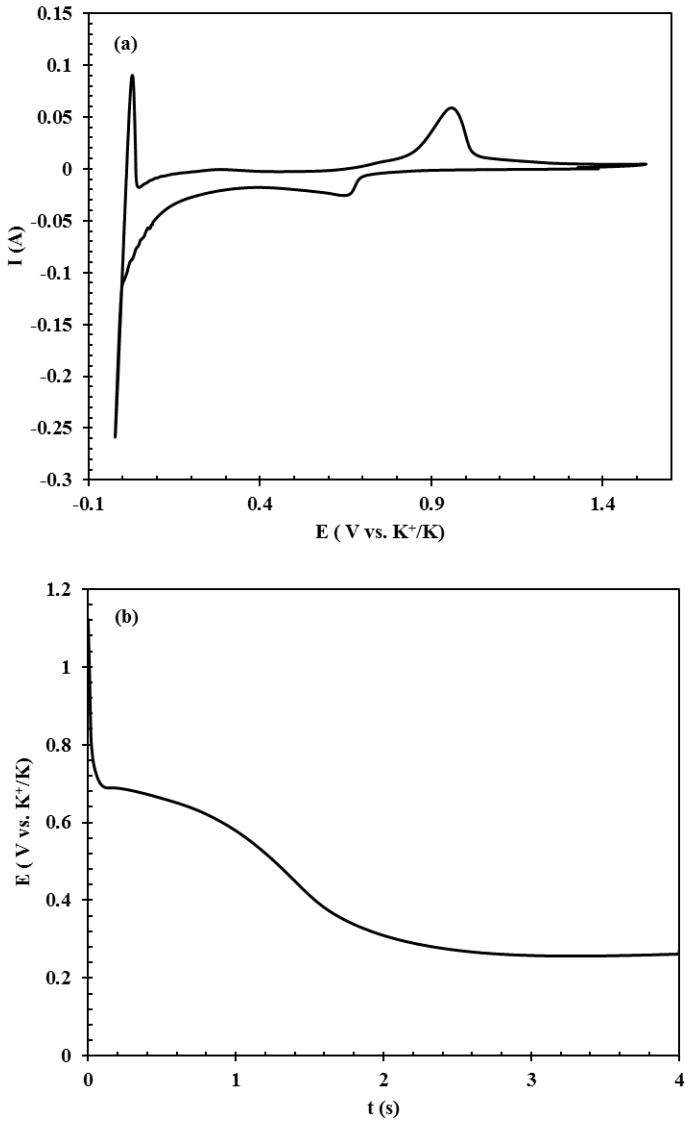

Figure 4-99. (a) Typical cyclic voltammograms obtained in FLiNaK-LaF_3 (working electrode area=1.273 cm^2) and pure FLiNaK molten salts at the scan rate of 200 mV/s. (b) Typical chronopotentiogram obtained in FLiNaK-LaF_3 molten salt with the applied current of -20 mA for 4s (working electrode area=1.273 cm^2). Working electrode: molybdenum; counter electrode: graphite; LaF_3=3.64 wt%; T=973 K.

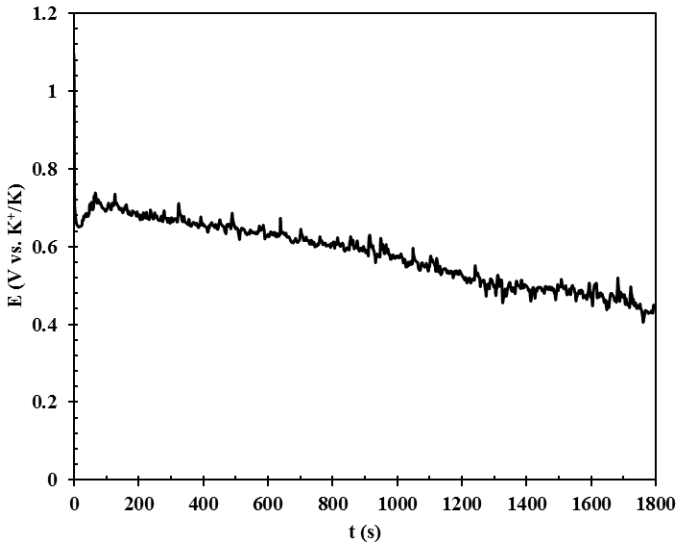

Figure 4-100. Open circuit potential evolution with time when a stable reduction current of 6 mA was applied on the molybdenum electrode in FLiNaK-LaF_3 molten salt for 1800s. Working electrode: tungsten (electrode area=1.174 cm^2); counter electrode: graphite; T=973 K; LaF_3=3.45 wt%.

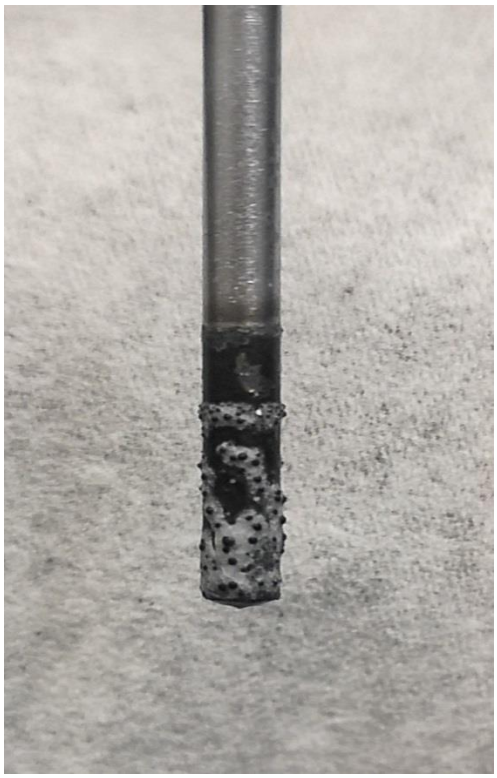

Figure 4-101. Picture of the molybdenum working electrode after chronopotentiometry electrolysis.

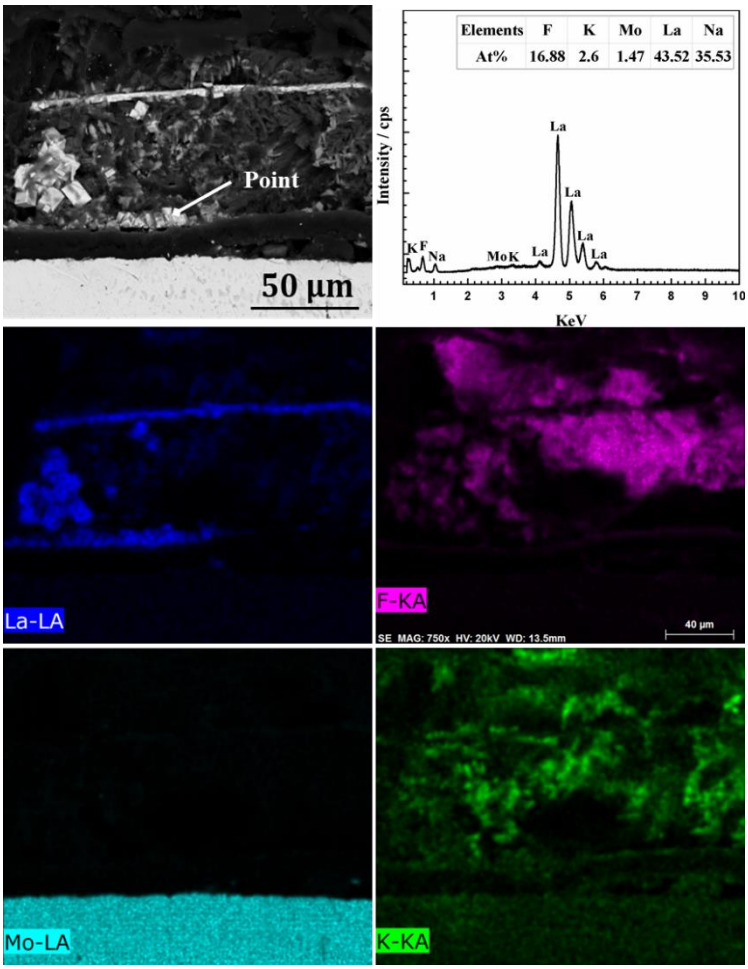

Figure 4-102. (a) Backscattered electrons (BSE) image of the cross section of polished molybdenum rod electrode after electrolysis in FLiNaK-LaF_3 molten salt; (b) EDS point scan results of the point in Figure 4-98a; (c)-(f) EDS mapping results of Figure 4-98a.

Based on the same results obtained on the tungsten and molybdenum working electrodes, it can be concluded that the reduction of lanthanum ion to lanthanum metal occurs prior to the reduction of K (I) to K metal and the electrochemical separation of lanthanum from FLiNaK molten salt can be realized by merely using an inert electrode. It is surprising that lanthanum can be separated out from FLiNaK molten salt since the standard reduction potential of La (III)/La is more negative than that of K(I)/K and other investigators always think that the deposition of La metal on inert electrode from FLiNaK-LaF_3 system is impossible [46,49]. This study will correct the pervious study on the electrochemical separation of LaF_3 in FLiNaK molten salt and provide a new insight on the electrochemical separation of other lanthanides in FLiNaK molten salt.

4.7.1.3. Electrochemical Extraction of Lanthanum in Molten Fluoride Salts Assisted by KF or NaF

Electrodeposition is a process that uses a current to reduce dissolved cations so they can form a thin coherent layer and coat on an electrode. For the cation which has a more anodic equilibrium potential than the electrolyte constituent cations, it can be electrodeposited by simply using an inert electrode. However, for the active element which has a more cathodic standard electrode potential, two main ways were investigated before: (1) electrodeposition assisted by liquid electrode, and (2) electrodeposition assisted by reactive electrode.

To understand the principle of electrodeposition assisted by liquid electrode, it is important to recognize the equilibrium potential

$$E_{eq(in\ liquid\ metal)} = E_{A^{n+}/A} - \frac{RT}{nF}\ln(\alpha_A(in\ liquid\ metal)) \quad (4\text{-}143)$$

where $E_{A^{n+}/A}$ is the equilibrium potential when pure A is deposited on inert material, R is the gas constant, T is the temperature, F is the faraday constant, n is the electron transfer number and α is the activity. If the activity of the target element in liquid metal is extremely small, then the electrodeposition potential of the target element into liquid metal will shift to a more positive value greatly. This method has been successfully applied for the electrodeposition of Ba^{2+} in $BaCl_2$-LiCl-$CaCl_2$-NaCl molten salt [50], and lanthanides in LiF-BeF_2 molten salt [51].

The formation of alloy between the target element and the reactive electrode could allow the target species to be reduced at a potential more anodic. The overall reaction of the electrodeposition on a reactive electrode can be expressed by

$$xA^{n+} + nxe^- + yR \leftrightarrow A_xR_y \quad (4\text{-}144)$$

where R represents reactive electrode. Then the equilibrium potential of A^{n+}/A_xR_y could be expressed by

$$E_{A^{n+}/A_xR_y} = E_{A^{n+}/A} - \frac{1}{x}\frac{\Delta G(A_xR_y)}{nF} \quad (4\text{-}145)$$

where $\Delta G(A_xR_y)$ is the Gibbs energy of formation of intermediate compound A_xR_y. The value of E_{A^{n+}/A_xR_y} will be larger than $E_{A^{n+}/A}$ if the value of $\Delta G(A_xR_y)$ is positive and the electrodeposit of A^{n+} will happen at a potential more anodic. Electrodepositions of Eu in LiCl-KCl molten salt [52] and lanthanides in LiF-CaF_2 molten salt [53] were realized through this method.

Based on the study of LaF_3 in FLiNaK molten salt, the electrodeposition of La (III) in molten fluorides can be achieved by a new method. According to the database in Outotec HSC Chemistry 6.0 [54] and thermodynamic calculation method reported before [55], the standard reduction potentials of LaF_3/La, LiF/Li, NaF/Na, KF/K are shown in Figure 4-103. It can be known La would not be electrodeposited prior to Na and K unless the activity of La (III) is far larger than that of Na (I) and K (I). However, this possibility is pretty low considering the concentration of K (I) is much larger than that of La (III). It is found lanthanum predominantly exists in the species of LaF_6^{3-} instead of La^{3+} in LaF_3-KF [56] and NaF-LiF-LaF_3[57] salts at the liquid states. In that case, the redox reaction happens to La in LaF_3-KF molten salt, for example, would be

$$K_3LaF_6 \leftrightarrow 3KF + La + \frac{3}{2}F_2 \tag{4-146}$$

Comparing with the redox reaction of LaF_3/La, the standard reduction potential $E^o_{K_3LaF_6/La}$ for redox reaction K_3LaF_6/La can be expressed by

$$E^o_{K_3LaF_6/La} = E^o_{LaF_3/La} + \frac{\Delta G_f(K_3LaF_6)}{nF} \tag{4-147}$$

where $E^o_{LaF_3/La}$ is the standard reduction potential for redox reaction LaF_3/La, $\Delta G_f(K_3LaF_6)$ is the Gibbs energy of formation for K_3LaF_6. Providing the value on the Gibbs energy of formation for K_3LaF_6 which is reported as -295 KJ/mol in the previous literature [58], the electrodeposition potential for La will shift positively by 1.02 V with the existence of KF.

Based on the discuss above, the electrodeposition of La in molten fluorides will be much easier with the existence of KF or NaF. The electrochemical behaviors of La in molten LiF fluoride salt, LiF fluoride salt with the addition of KF, and LiF fluoride salt with the addition of NaF will be investigated separately to confirm our theory.

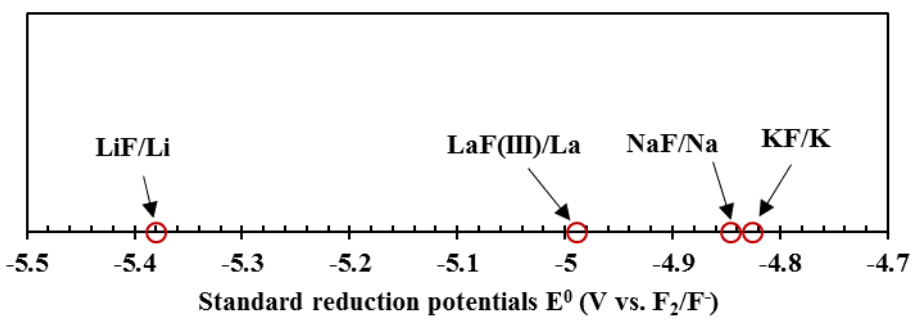

Figure 4-103. Standard reduction potentials of LaF_3/La, LiF/Li, NaF/Na, KF/K.

The typical cyclic voltammograms of LiF and LiF-LaF_3 recorded on Mo working electrode are shown in Figure 4-104. As can be seen in Figure 4-104, in addition to the redox peaks of Li(I)/Li, the cyclic voltammogram shows a new pair of redox peaks when LaF_3 was dissolved in molten LiF salt which is attributed to the reaction of La (III) ↔La [59]. The cyclic voltammetry results obtained on inert Mo electrode also indicates that the reduction of La (III) to La metal proceeds just prior to the solvent reaction (Li (I)/Li). In such a case, the co-electrodeposition of La and Li is easier to occur and the extraction of La from LiF molten salt may not be possible under these conditions. To realize the electrodeposition of La, Marta et al [59] used reactive Ni electrode and realized the electrodeposition of La through which the intermediate compounds between La and Ni were formed on the electrode. The disadvantage coming with this method is the pure La metal cannot be obtained.

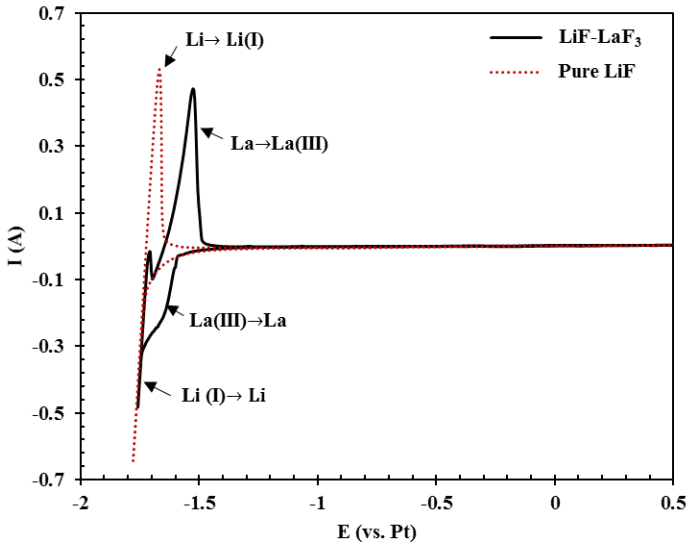

Figure 4-104. Cyclic voltammograms obtained in LiF-LaF_3 (working electrode area=0.385 cm^2) and pure LiF molten salts. Scan rate: 100 mV/s; working electrode: Mo; counter electrode: graphite; LaF_3=3.33 wt%; T=1173 K.

It is found La will exist in the form of LaF_6^{3-} species instead of La^{3+} species when KF or NaF is added into molten salts [56,57]. As discussed before, the existence of LaF_6^{3-} could make the electrodeposition of La proceed at a considerably more anodic potential. In that case, the electrochemical test was first carried out in LiF-LaF_3 molten salt system with KF added to check the feasibility of the extraction of La. Figure 4-105 shows the cyclic voltammogram and chronopotentiogram recorded on the inert Mo working electrode. According to the standard reduction potential shown in Figure 4-103, the reduction of K(I) is easier to occur than that of Li (I) in fluoride salts. Thus, the cathodic and anodic limit C1 and A1 at the left side of the electrochemical window should be attributed to the redox reaction of K (I)/K, the redox reaction of Li (I)/Li is supposed to happen at a more cathodic potential which cannot be seen from Figure 4-105. Unlike the system that LaF_3 dissolved in LiF molten salt in which the reduction potential of La is extremely close to that of Li, there is a pair of redox peaks C2 and A2 in cyclic voltammogram as shown in Figure 4-105 (a) and a plateau P1 in chronopotentiogram as shown in Figure 4-105 (b) which is far away from the redox reaction of K(I)/K and even farther from Li (I)/Li redox reaction. Considering there is no redox peaks show up prior to redox reaction of K(I)/K in pure LiF-KF molten salt, the cathodic peak C2 (also plateau P1) should be attributed to the electrodeposition of La.

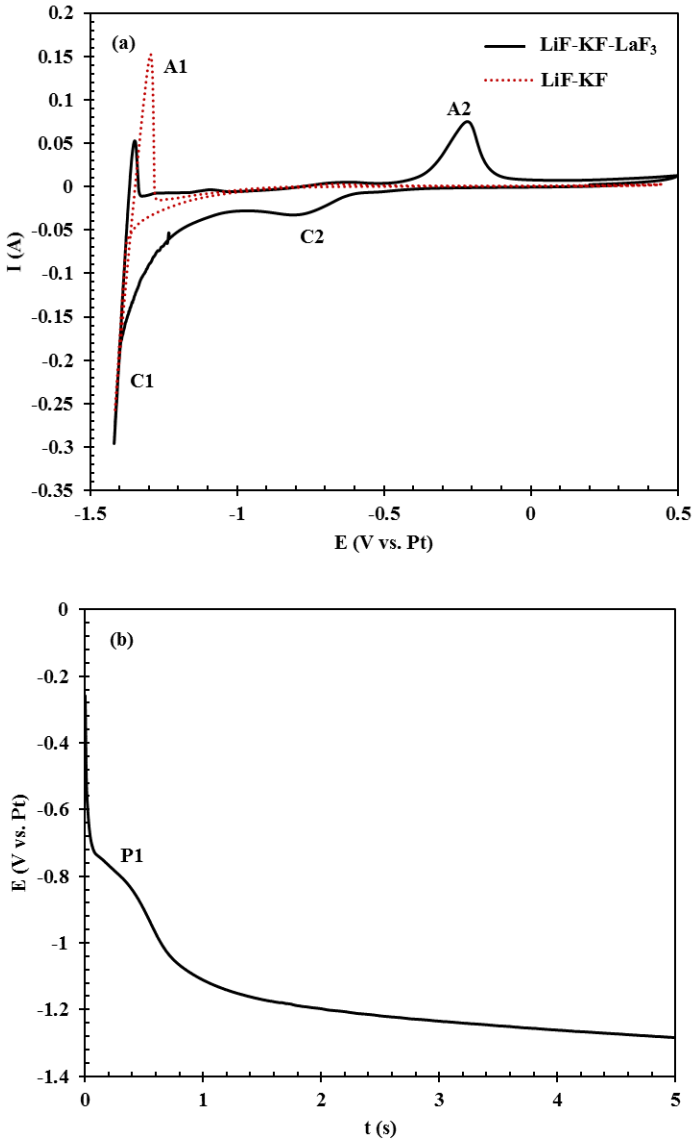

Figure 4-105. (a) Cyclic voltammograms obtained in LiF-KF eutectic molten salt with LaF_3 dissolved in (working electrode area=2.24 cm^2) and pure LiF-KF eutectic molten salt at the scan rate of 200 mV/s. (b) Chronopotentiogram of the system of LiF-KF-LaF_3 with the applied current of -50 mA (working electrode area=2.24 cm^2). Working electrode: Mo; counter electrode: graphite; LaF_3=2.73 wt%; T=973 K.

In order to affirm the electrodeposition of La occurs at a more anodic potential when KF was added in. A stable current of -4 mA was provided for 1800s on a Mo working electrode to do chronopotentiometry electrolysis. The cathode potential was monitored and controlled not to reach the reduction potential of alkali species during the electrolysis process. The Mo electrode was taken out from the electrochemical cell immediately after chronopotentiometry electrolysis to do SEM test. Figure 4-106 shows the SEM results obtained on the cross section of the polished Mo rod electrode after electrolysis. Figure

4-106 (a) depicts the backscattered electrons (BSE) image in which the grey bottom part and the top black part are Mo electrode and solidified salt, respectively. Plenty of La was reduced and accumulated after electrolysis which can be seen in the middle of the image as shown in Figure 4-106 (a). The point scans of the La rich part show the signal for La element is very strong while extremely weak for the element of F. It means the substance deposited is La metal. Figure 4-106 (c-f) shows the EDS mapping results from which the absence of F at the place where La is concentrated can be observed and it further confirms that the deposited material after chronopotentiometry electrolysis is La metal. Therefore, the addition of KF indeed greatly assists the extraction of La from molten salts.

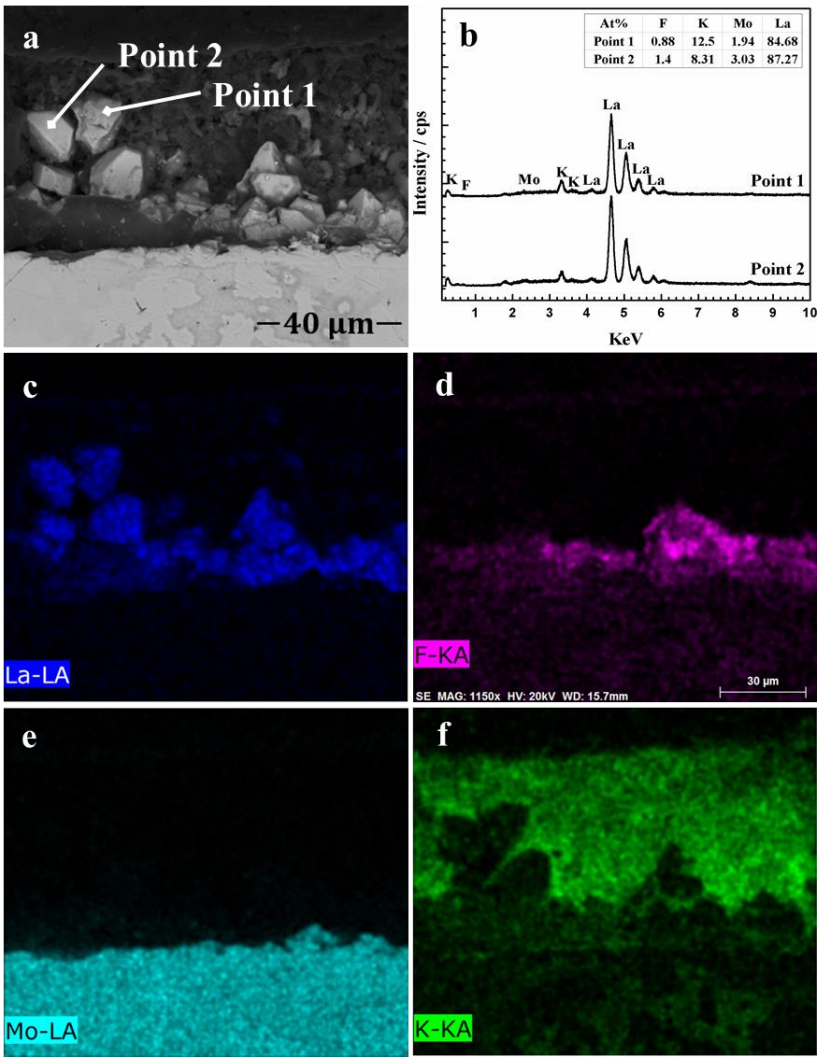

Figure 4-106. (a) Backscattered electrons (BSE) image of the cross section of polished Mo rod electrode after electrolysis in LiF-KF-LaF_3 molten salt; (b) EDS point scan results of point 1 and point 2 in Figure 4-106a; (c)-(f) EDS mapping results of Figure 4-106a.

Given that La also predominantly exists in the form of LaF_6^{3-} species when NaF is added into molten salts [57], electrochemical test was performed in LiF-LaF_3 molten salt system with NaF added in as well.

Figure 4-107 shows the cyclic voltammogram and chronopotentiogram obtained on Mo working electrode in the LiF-NaF-LaF_3 molten salt system. Based on the calculated standard reduction potential in Figure 4-103, C1 in

Figure 4-107 (a) and P2 in

Figure 4-107 (b) should be attributed to the reduction of Na (I). Similar as the results obtained in LiF-LaF_3 molten salt when KF was added in, a pair of redox peaks far away from the redox reaction of alkali species was observed. This reaction was also identified from the chronopotentiogram (

Figure 4-107 (b)) in which a plateau P1 can be seen. A same process was conducted as done in LiF-KF-LaF_3 system to identify this redox reaction in which a stable current of -4 mA was applied on the Mo rod electrode for 1800s to do chronopotentiometry electrolysis. Then the Mo rod electrode was polished and a SEM test was performed on its cross section. Figure 4-98 shows the obtained SEM result. It can be identified that the element of F rarely exists in the La rich part and which indicates the product produced by the electrolysis is La metal. A strong signal of La can also be observed in the point scans of the La concentrated part. There are some amounts of F were also found in the point scans which could be attributed to the salt stuck to the La metal surface. Combing the electrochemistry and SEM test results, it can be concluded that the extraction of La in molten salt can also be assisted by the addition of NaF.

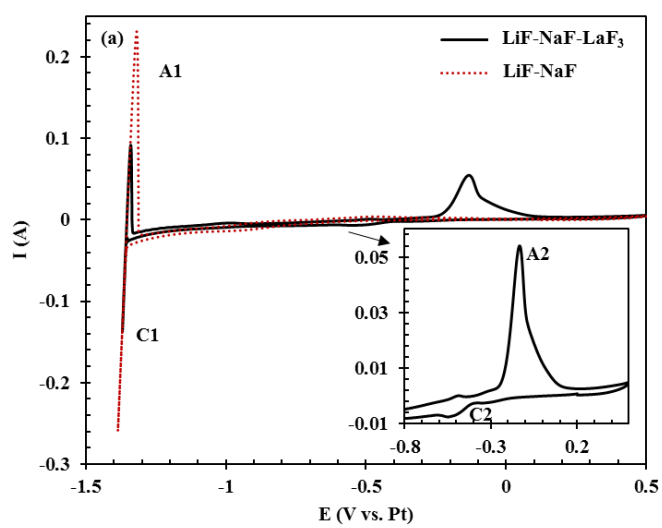

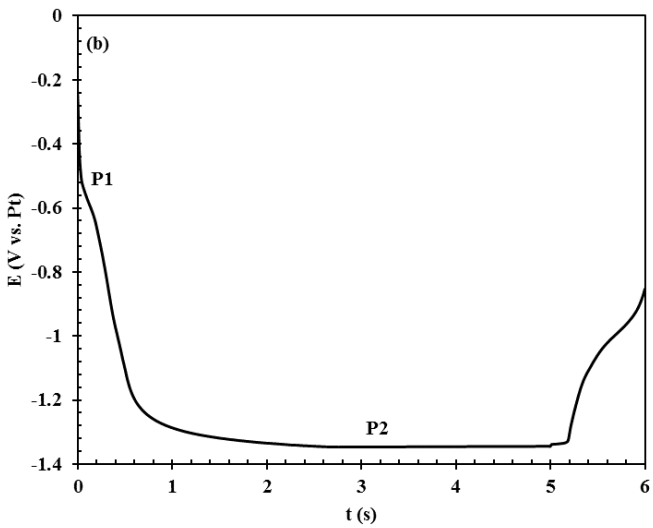

Figure 4-107. (a) Cyclic voltammograms obtained in LiF-NaF eutectic molten salt with LaF_3 dissolved in (working electrode area=0.577 cm^2) and pure LiF-NaF eutectic molten salt at the scan rate of 200 mV/s. (b) Chronopotentiogram of the system of LiF-NaF-LaF_3 with the applied current of -20 mA (working electrode area=0.577 cm^2). Working electrode: Mo; counter electrode: graphite; LaF_3=3.02 wt%; T=1023 K.

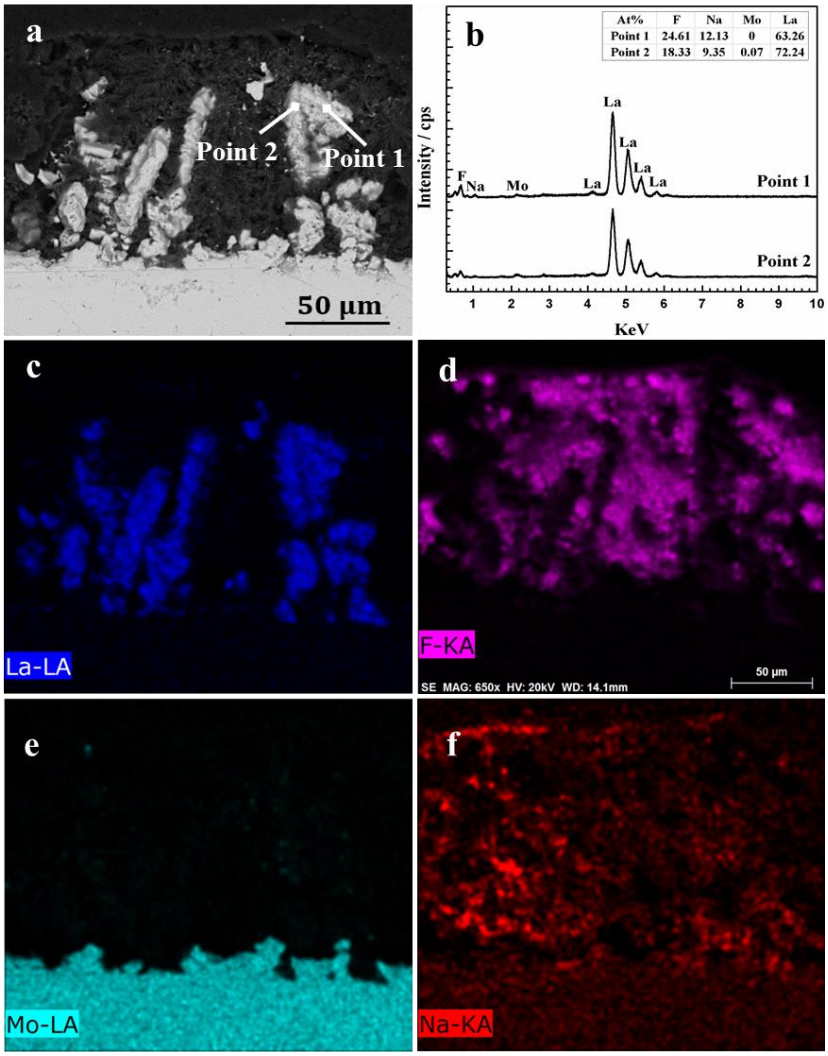

Figure 4-108. (a) Backscattered electrons (BSE) image of the cross section of polished Mo rod electrode after electrolysis in LiF-NaF-LaF_3 molten salt; (b) EDS point scan results of point 1 and point 2 in Figure 4-98a; (c)-(f) EDS mapping results of Figure 4-98a.

4.7.2. Electrochemical Investigation of CeF_3 in Molten FLiNaK Salt on W, Cu, and Ni Electrodes

Cerium is an important fission product. The electrochemical behaviors of Ce (III) in molten FLiCa, FLiNa, and FLiNaCa have been studied [60,61,62], which indicates that the reduction of Ce (III) to Ce metal is an one-step reaction and the reduction potential is close to that of Li (I) in molten FLiCa. However, there is no study on Ce (III) in FLiNaK and FLiBe. According to the database in Outotec HSC Chemistry 6.0 [63], the standard reduction potentials for the elements in FLiNaK-CeF_3 and FLiBe-CeF_3 systems at 973 K are given in Figure 4-109 which shows the standard reduction potential of Ce (III)/Ce is more cathodic than Na (I)/Na, K (I)/K, and Be (II)/Be. Therefore, unless the activity coefficient of Ce (III) is extremely large and that of K(I), Na(I), and Be (II) are extremely small in FLiNaK and

FLiBe, it is impossible to separate Ce from molten FLiNaK or FLiBe by using an inert cathodic electrode.

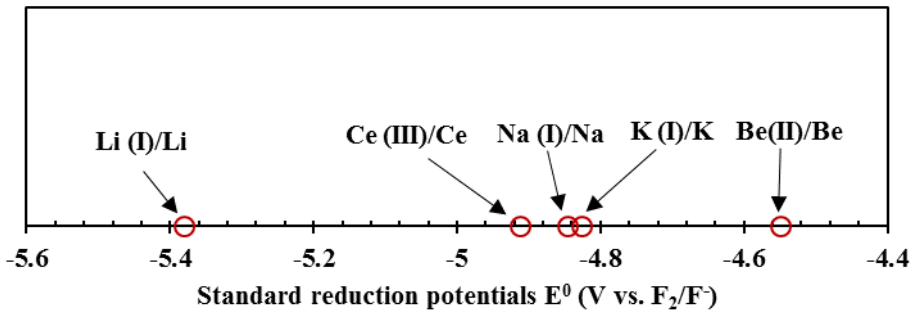

Figure 4-109. Standard reduction potentials of the alkali elements and Ce vs. F_2/F^- in fluoride salt melt at the temperature of 973 K.

In this subsection, electrochemical behaviors of Ce (III) in FLiNaK was examined at 973K which is a typic operation temperature of the FHR. A new redox reaction Ce (III)/Ce (II), which has not been reported in other molten salts, was identified. Therefore, Ce (II) can be another stable ion in FLiNaK. The study also verified that it is impossible to deposit Ce metals on tungsten and copper electrode, however, Ce can be deposited on a Ni electrode because of the formation of an intermetallic compound between Ce and Ni. The intermetallic compound was identified to be $CeNi_5$ by XRD and SEM analyses.

4.7.2.1. Experimental methods

Sample preparation and experiments were performed in a glove box (PureLab HE, Innovative Technologies) which was filled with argon gas. The moisture and oxygen level inside the glovebox were both maintained under 5 ppm. The LiF-NaF-KF (46.5 mol% LiF, 11.5 mol% NaF, and 42 mol% KF) was prepared by mixing the lithium fluoride (>99.0% purity, Sigma Aldrich), sodium fluoride (>99.0% purity, Sigma Aldrich) and potassium fluoride (>99.5% purity, Sigma Aldrich). A small amount of cerium fluoride (99.99% purity, Sigma Aldrich) was added to the prepared LiF-NaF-KF salt sample to provide Ce (III). The test salt was mixed well before transferred to a nickel crucible and placed in a muffle furnace (Thermofisher Scientific FB1315M) for which the temperature can be maintained within $\pm$1°C during the experiment. The salt mixture was dehydrated at 473 K for 24 hours before heating to 973 K.

The electrochemical experiments were carried out using a Gamry Interface 1000 Potentiostat and a standard three-electrode setup. The working electrodes used are 1.6 mm diameter tungsten rod (Midwest Tungsten Service, >99.5% purity), 2.9 mm diameter copper rod (Surepure Chemetals,99.99% purity), and 3.2 mm diameter nickel rod (Fisher Scientific, 99% purity). The inert counter electrode was a 3 mm diameter graphite rod. The reference electrode utilized was a 0.81 mm diameter platinum wire (Surepure Chemetals) with potential associated to $Pt/PtO_x/O^{2-}$ [64]. It has been proved to be a reliable quasi-reference electrode in molten salts [64,65]. However, there is a potential shift with time for

Pt reference electrode, therefore, for all the data analyses in this study, the reference potential is converted from Pt quasi-reference potential to the redox potential of K (I)/K. For working electrode, the surface area of it was measured according to its depth exposed to the salt melt. IR compensation that programed in Gamry Framework software was selected during the electrochemical experiment [66].
To study the valence state of Ce in FLiNaK salt melt, the molten salt sample was taken out from crucible before electrochemical test, quenched in the room temperature argon atmosphere, and grounded into powder for X-ray diffraction (XRD) analysis. The cathode depositions were prepared by potentiostatic electrolysis and chronopotentiometry electrolysis. All the XRD samples were sealed in a Kapton tape to avoid the exposure to air during XRD test. The cathode depositions were also characterized using scanning electron microscopy (SEM, FEI Quantan 600) to examine its composition and morphology.

4.7.2.2. Electrochemical Behavior of CeF_3 in FLiNaK Melt on Tungsten Electrode

The typical cyclic voltammograms on tungsten working electrode for FLiNaK and FLiNaK-CeF_3 are shown in Figure 4-110 (a). The cathodic limit at the left of the electrochemical window is the deposition of K (I), which has been verified by Qiao et al [67] through the potential measurements of Li (I)/Li, Na (I)/Na, and K (I)/K using each alkali-metal electrode in the FLiNaK melt. Different from pure FLiNaK, there is a redox reaction observed prior to the reduction of K (I) in FLiNaK-CeF_3 melt. To identify this reaction, the inversion potential was set to 0.43 V (vs. K (I)/K) and the obtained cyclic voltammetry plot is inserted in *Figure 4-110* (a). From which it can be known, there are one anodic peak and one small shoulder which might be owed to the desorption effect of Ce (III) [68]. The redox reaction is also observed in the chronopotentiogram shown in Figure 4-110 (b).

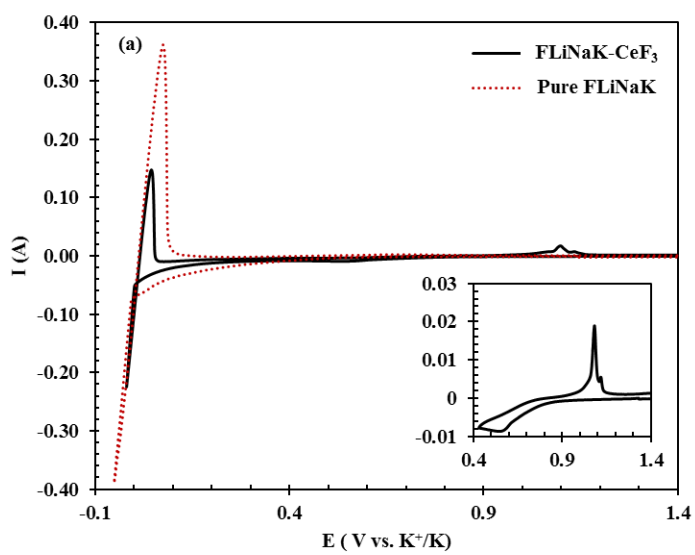

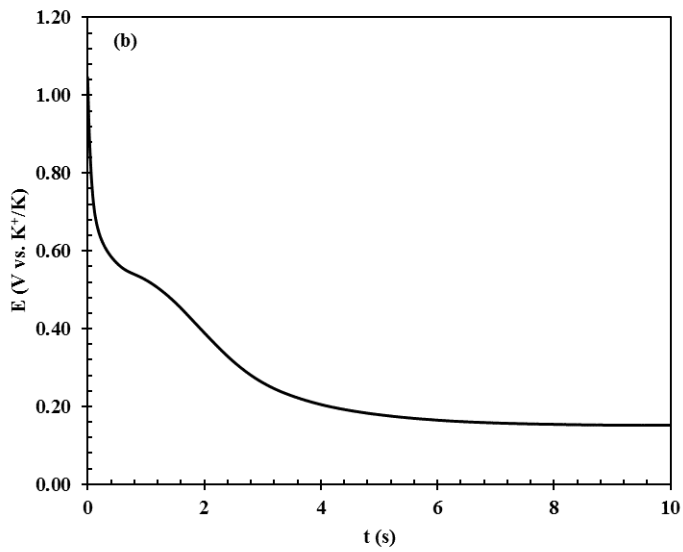

Figure 4-110. (a) Cyclic voltammograms obtained in FLiNaK-CeF_3 (working electrode area=0.698cm^2) and pure FLiNaK salt melt at the scan rate of 100 mV/s. (b) Chronopotentiogram of the system FLiNaK-CeF3 with the applied current of -10 mA (working electrode area=0.698cm^2). Working electrode: W. counter electrode: graphite. CeF_3=2.47×10^{-4} mol/cm^3; T=973K.

To identify the redox reaction, both FLiNaK-CeF_3 bulk salt before performing electrochemical measurement and the salt adjacent to tungsten foil electrode after potentiostatic electrolysis with applied voltage of 0.4 V (vs. K^+/K) for 1500 s were collected for XRD analysis. Figure 4-111 (a) shows the XRD analysis result of the quenched FLiNaK-CeF_3 salt and Ce was found to exist in the forms of $NaCeF_4$ and K_3CeF_6. It means Ce (III) is the stable ion in bulk FLiNaK. To get the salt sample adjacent to electrode after potentiostatic electrolysis, a tungsten foil electrode was used and taken out from electrolyte immediately after the electrolysis test. The salt sample adhered to tungsten foil was grounded into powder after cooled down for XRD analysis. Figure 4-111 (b) shows the XRD pattern obtained on the potentiostatic electrolysis products. It turned out that CeF_2 is the electrolysis product, so the redox reaction observed in cyclic voltammetry and chronopotentiometry test discussed above should attribute to the following process:

$$Ce^{3+} + e^- \leftrightarrow Ce^{2+} \tag{4-148}$$

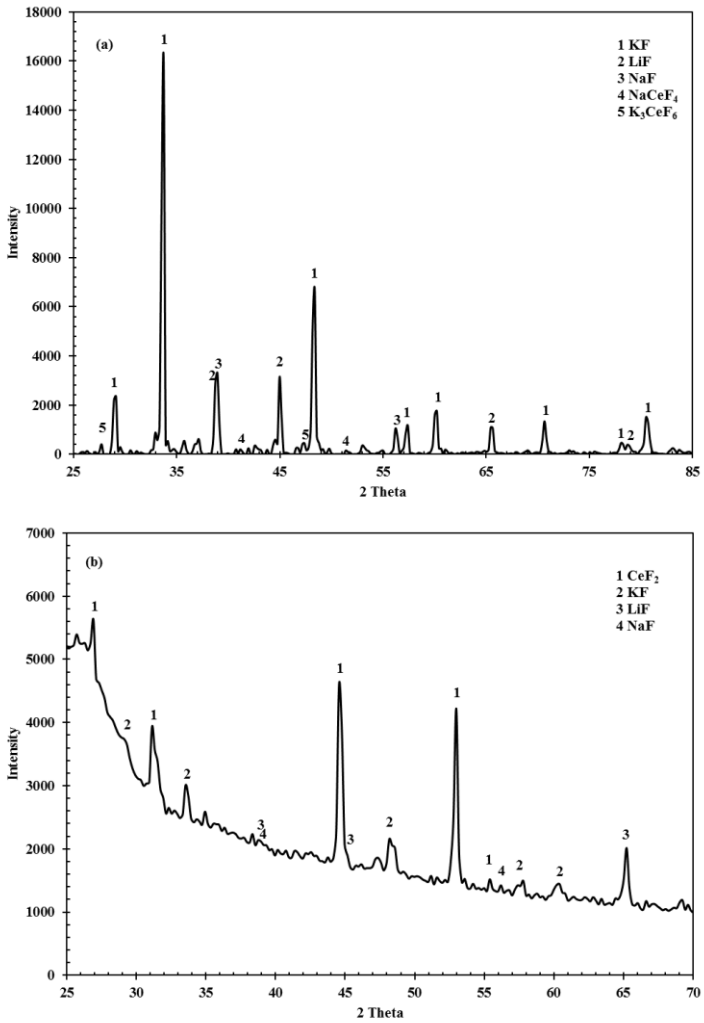

Figure 4-111. (a) XRD analysis result of the quenched FLiNaK-CeF_3 salt. (b) XRD analysis result of the potentiostatic electrolysis products of FLiNaK-CeF_3 melt on the tungsten foil electrode.

Further SEM and EDS analyses also confirmed the absence of Ce metal and the formation of CeF_2 at the electrode surface during electrolysis, as shown in Figure 4-112. Figure 4-112a depicts the backscattered electrons (BSE) image of the cross section of the polished tungsten rod electrode, of which the white bottom part and black top part are tungsten electrode and solidified molten salt, respectively. As seen in EDS mapping results (Figure 4-112c-f), no cerium is detected except a cerium rich spot inside the molten salts in Figure 4-112a. A strong signal of cerium and fluoride can be observed in the point scans of the cerium rich spot (Figure 4-112b), which is consistent with the EDS mapping results. Therefore, Ce at the spot is in the form of Ce fluoride. Considering the XRD analysis result, it is CeF_2. The presence of oxygen should be attributed to the exposing of electrode sample to air. Therefore, all the results demonstrate that, at a tungsten working electrode surface, the redox reaction is Ce (III)/Ce (II) and deposition of Ce metal is not observed.

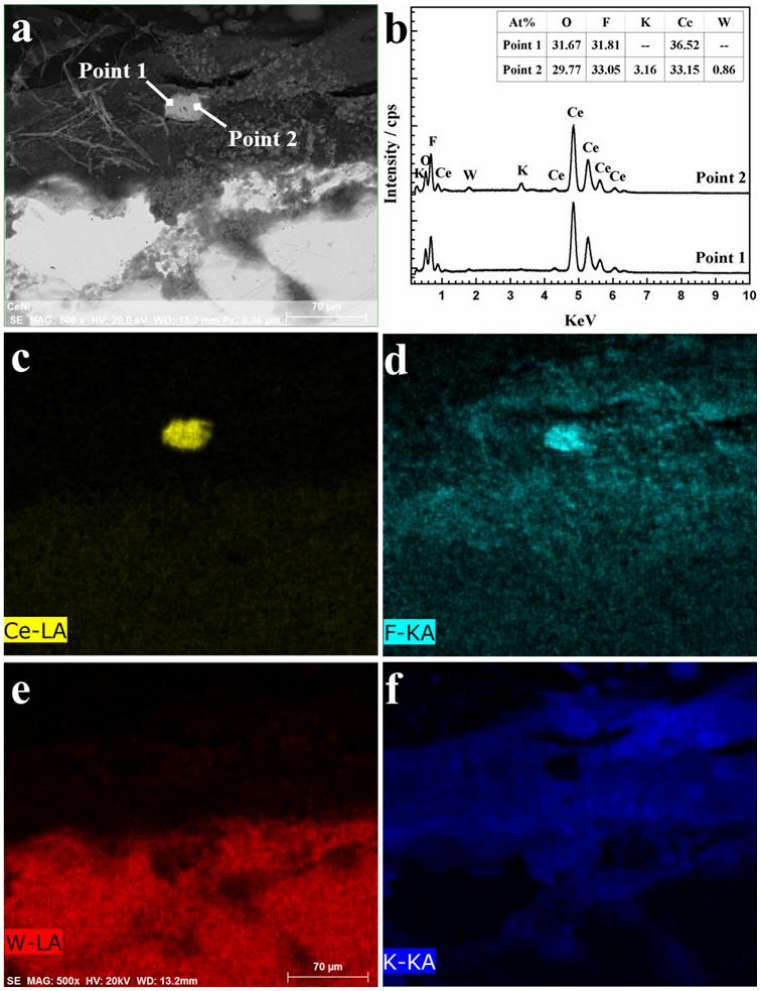

Figure 4-112. (a) Backscattered electrons (BSE) image of the cross section of polished tungsten rod electrode after electrolysis; (b) EDS point scan results of point 1 and point 2 in Figure 4-112a; (c)-(f) EDS mapping results of Figure 4-112a.

There are two factors could determine the electrochemical behavior of M^{x+} ion in molten salt: (1) the standard Gibbs free energy of formation of MF_x, and (2) activity of M^{x+} in molten salt. For example, the reduction of ThF_4 to Th metal is a single-step process with exchanging 4 electrons in LiF-CaF_2 melt [69] while two-step process in FLiNaK [70]. At 973 K, the Gibbs free energy of formation for the equilibrium reaction of Th/ThF_4 is -1807 KJ/mol and then the corresponded standard reduction potential (Th^{4+}/Th) is -4.68 V (vs. F_2/F^-), while for the equilibrium reaction of ThF_3/ThF_4, the values are -548 KJ/mol for Gibbs free energy and -5.67 V (vs. F_2/F^-) for reduction potential [54]. Because of the more positive value of the standard reduction potential of Th^{4+}/Th, the reduction of Th^{4+} to Th metal is easier to happen than that of Th^{4+} to Th^{3+}. It explained why the electrochemical behavior of ThF_4 in LiF-CaF_2 is a single-step process with 4 electrons transferred. However, standard reduction potential can only provide some hints on the favorability of reduction reaction. Equilibrium potential is the final decisive factor which is expressed by:

$$E_{eq} = E^0 + \frac{RT}{nF} ln \frac{\alpha_{ox}}{\alpha_R} \tag{4-149}$$

where E_{eq} is the equilibrium potential, E^0 is the standard reduction potential, R is the gas constant, T is the temperature in kelvin, n is the electron transfer number, α_{ox} and α_R are the activity of oxidant and reductant, respectively. This equation indicates that the activity of Th^{4+} and Th^{3+} in electrolyte could also affect the electrochemical behavior. If the activity of Th^{4+} is much larger than that of Th^{3+}, the equilibrium potential will shift to the positive direction significantly and the reduction of Th^{4+} to Th $^{3+}$ could happen prior to reaction of Th^{4+} to Th metal. It is probably the reason that the reduction of ThF_4 to Th metal in FLiNaK is a two-step process. The same principle could apply to the system of FLiNaK-CeF_3 as well. There may be a great difference on the activity of Ce^{3+} and Ce^{2+} in FLiNaK, as a result, the electrochemical reaction of Ce (III)+ $e^- \leftrightarrow$Ce (II) was observed here while not in other salt systems [61,62].

4.7.2.3. Electrochemical Behavior of CeF_3 in FLiNaK Melt on Reactive Electrodes

The electrochemical behavior of CeF_3 in FLiNaK on the inert tungsten electrode indicates Ce (III) is reduced to Ce (II), whereas no Ce metal deposition occurs. The formation of intermetallic compound between Ce and a reactive electrode allows Ce ion to be reduced at a potential more anodic than that for the deposition of a pure metal. Ni and Cu are metals with which Ce can form several intermetallic compounds whereas alkali metal cannot [71]. Thus, the reduction potential of Ce (II) will move to anodic direction and may be separated out at a potentail which is more anodic than the reduction potential of K (I)/K by using Ni and Cu as the working electrodes.

(1) Studies on Cu electrode

Figure 4-113 shows the cyclic voltammogram of FLiNaK-CeF_3 on a Cu working electrode. It can be observed that only the reaction: $Ce^{3+} + e^- \leftrightarrow Ce^{2+}$ occurs prior to the redox reaction of K (I)/ K, which is same to the results obtained when W is used as the working electrode. The reason for this phenomenon could attribute to the not big enough Gibbs free energy of formation of $Ce_x\mathrm{Cu}_y$ such that the intermetallic compound deposition is still more cathodic than K (I).

Potentiostatic electrolysis was also carried out on Cu working electrode by setting a voltage of 0.4 V (vs. K^+/K) for 3000 s. The electrode was taken out immediately after the test for XRD analysis and SEM test. Figure 4-114 shows the XRD pattern on Cu electrode from which the CeF_2 was found, therefore, the reduction during electrolysis is $Ce^{3+} + e^- \leftrightarrow Ce^{2+}$. No Ce metal or Ce-Cu intermetallic compound was found by XRD analysis.

Consistently, the SEM and EDS analysis illustrates the absence of the formation of intermetallic compound after potentiostatic electrolysis, as shown in Figure 4-106. When the copper electrode was lifted from molten salt, a black solidified salt layer can be observed on the electrode. The backscattered electrons (BSE) image of the cross section of copper rod electrode was shown in Figure 4-106a, where substantial white spots can be seen. In the point scans (Figure 4-106b), cerium as well as fluoride element are detected. Since the white spots may be covered by a thin layer of salt, the signal of potassium element has a very high intensity. Also, as shown in EDS mapping analysis (Figure 4-106c-f), cerium element as well as fluoride element is well distributed on the white spots in

Figure 4-106a whilst no overlapping of copper and cerium is found. This demonstrates the absence of intermetallic compound between cerium and copper metal.

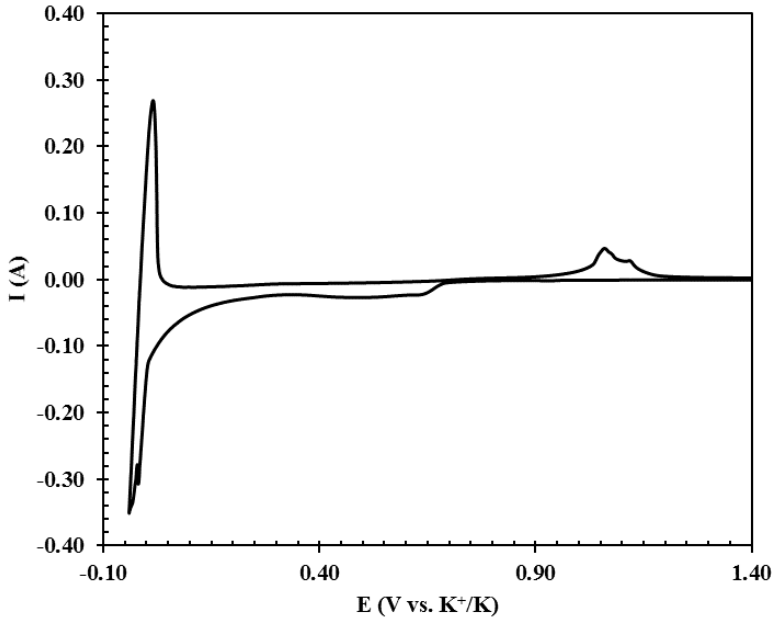

Figure 4-113. Cyclic voltammogram of CeF_3 in FLiNaK molten salt recorded on Cu working electrode (area=1.389 cm^2). Counter electrode: graphite. CeF_3=1.4×10^{-4} mol/cm^3; T=973K; Scan rate: 100 mV/s.

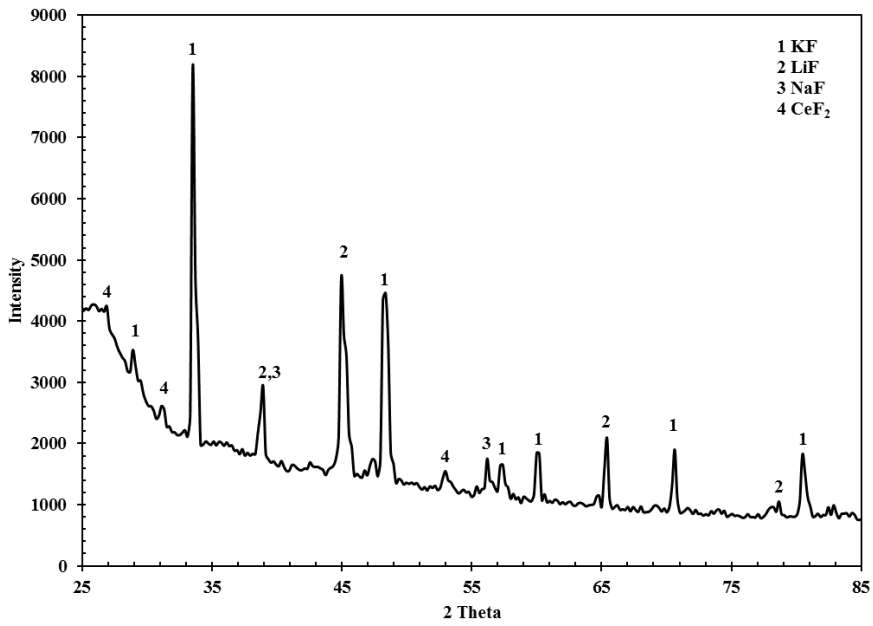

Figure 4-114. XRD analysis result of the potentiostatic electrolysis products of FLiNaK-CeF_3 melt on Cu electrode.

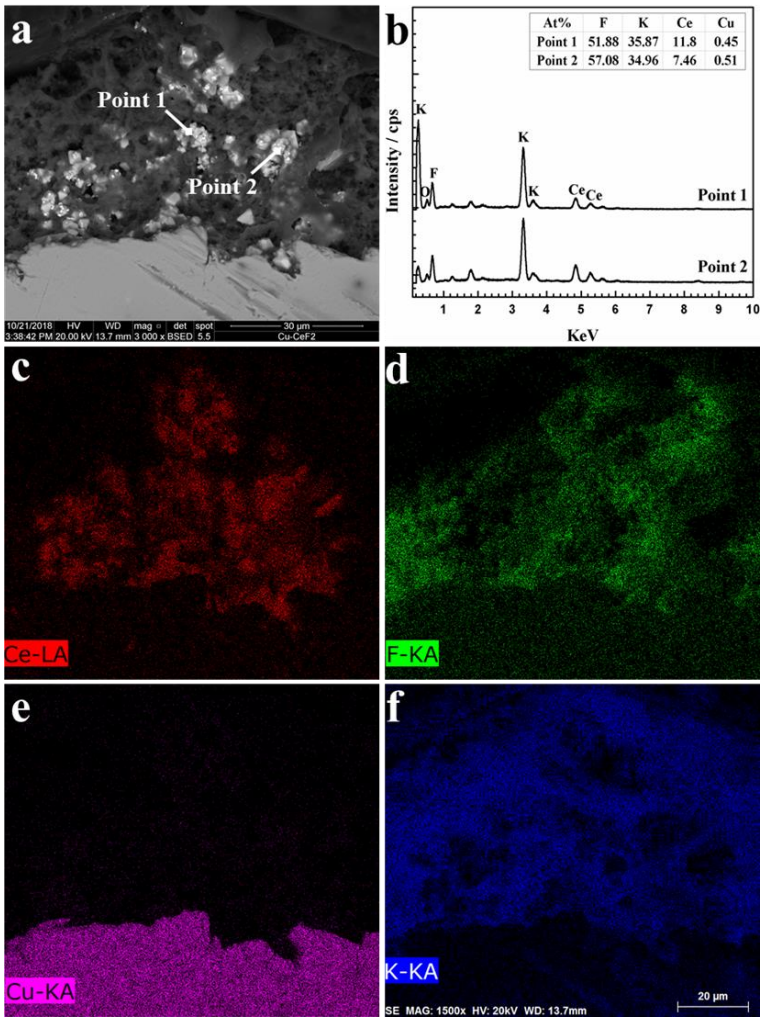

Figure 4-115. (a) Backscattered electrons (BSE) image of the cross section of polished copper rod electrode after electrolysis; (b) EDS point scan results of point 1 and point 2 in Figure 4-106a; (c)-(f) EDS mapping results of Figure 4-106a.

(2) Studies on Ni electrode

Figure 4-116 shows the typical cyclic voltammogram of FLiNaK-CeF_3 molten salt system recorded on Ni working electrode at the temperature of 973 K. Different from the results obtained on W and Cu electrode, several cathodic and anodic peaks, in addition to the redox peaks of Ce (III)/Ce (II), are observed prior to the redox reaction of K (I)/K which correspond to the formation and dissolution of Ce-Ni intermetallic compounds. In order to find out the cathodic peaks to their corresponding anodic peaks, several cyclic voltammetry tests at various switching potentials were subsequently conducted and the results are shown in Figure 4-117. Same to the cyclic voltammogram recorded on W and Cu electrode, the redox reaction of $Ce^{3+} + e^- \leftrightarrow Ce^{2+}$ is observed (Peaks C_I /A_I). It should be noticed that the position of A_I shifts when setting different inversion potential which may due to the surface change on the working electrode when intermetallic compound is formed. Cathodic peak C_{II} corresponds to an intermetallic compound formation between Ni and Ce.

Only one anodic peak A_{III} can be observed when the inversion potential is set to be 0.05 V (vs. K^+/K) whereas two anodic peaks A_{III} and A_{II} are indicated when the inversion potential of 0.02 V (vs. K^+/K) is applied. It means the dissolution of the formed intermetallic Ce-Ni compound when more Ce is deposited could be multi-step reactions. The same phenomenon was also observed in the $LiF-CaF_2-CeF_3$ system on Ni working electrode [60].

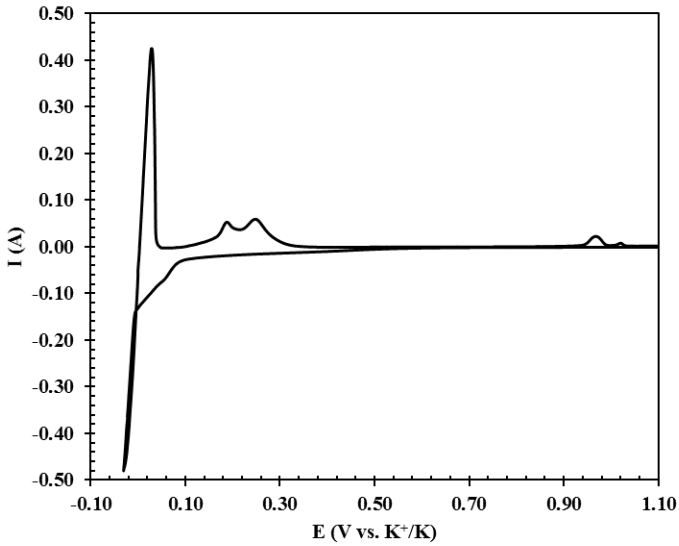

Figure 4-116. Cyclic voltammogram of CeF_3 in FLiNaK molten salt recorded on Ni working electrode (area=1.085 cm^2). Counter electrode: graphite. CeF_3=1.95×10^{-4} mol/cm^3; T=973K; Scan rate: 100 mV/s.

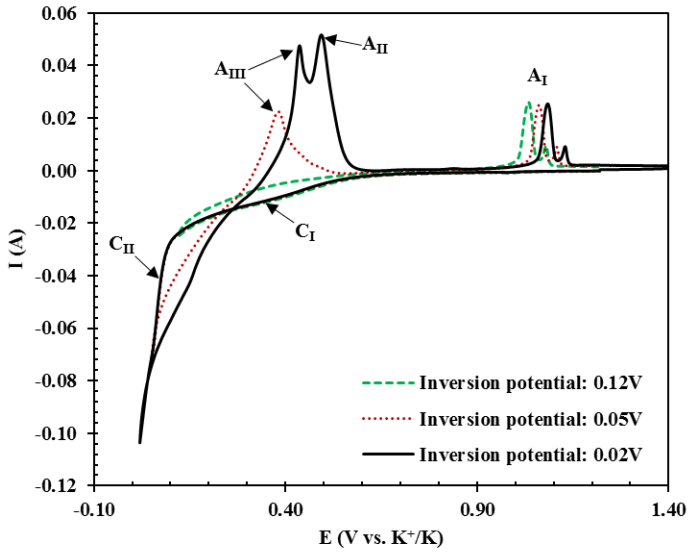

Figure 4-117. Cyclic voltammograms of CeF_3 in FLiNaK molten salt at various reverse potentials on Ni working electrode (area=1.085 cm^2). Counter electrode: graphite. CeF_3=1.95×10^{-4} mol/cm^3; T=973K; Scan rate: 100 mV/s.

The electrochemical behavior of Ce (III) in FLiNaK was also studied by chronopotentiometry technique. The chronopotentiogram obtained on Ni electrode by applying a reduction current of 100 mA for 4 s and an oxidation current of 40 mA for another 4s is shown in Figure 4-118. No obvious transition plateau for Ce (III) reduction and compound formation is observed when the reduction current of 100 mA is applied which probably because the applied current is too large. The slight rise of the plateau of K over time can be seen from Figure 4-118, which may attribute to the nucleation of K on the electrode. An oxidation current of 40 mA was applied after 4 s and several plateaus can be identified: A corresponds to the oxidation of the deposited K on the electrode surface; B and C corresponds to the dissolution of Ce-Ni intermetallic compounds; D is due to the oxidation of Ce (II) to Ce (III), and E is attributed to the desorption effect of Ce (III). These plateaus can be found correspondingly on the oxidation peaks obtained in cyclic voltammogram (Figure 4-116).

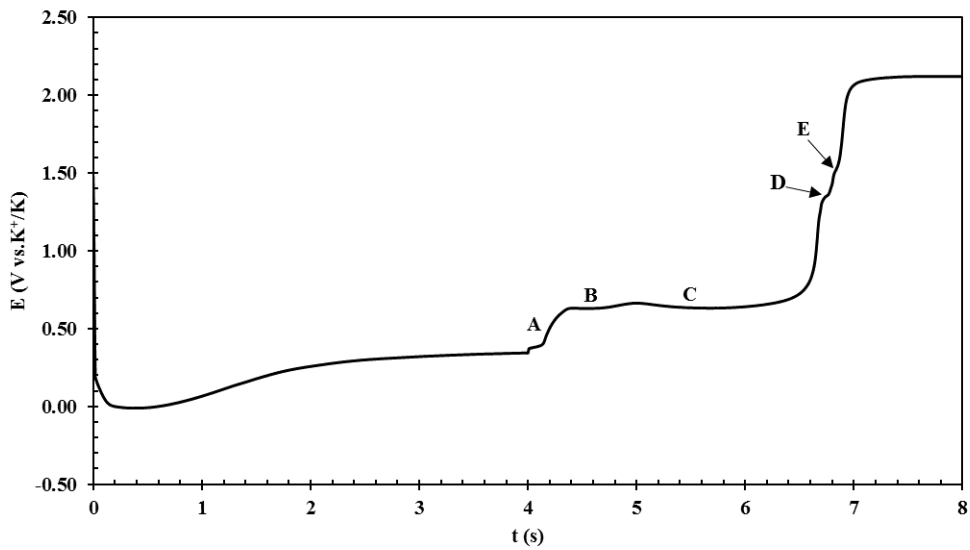

Figure 4-118. OCP evolution of the Ni working electrode (area=0.698cm^2) against Pt reference electrode over time by chronopotentiometry test at the temperature of 973 K through applying a reduction current of 100 mA for 4s and an oxidation current of 40 mA for another 4s.

Considering that the reduction potentials of potassium and Ce-Ni intermetallic compound are very close as shown in Figure 4-116, a stable reduction current of 30 mA was provided for 1 hour on a Ni foil to do chronopotentiometry electrolysis. The cathode potential was monitored and controlled not to reach the reduction potential of K (I) during the electrolysis. The Ni foil was taken out from electrochemical cell immediately after the chronopotentiometry electrolysis for XRD analysis. Figure 4-119 shows the results of XRD analysis, which are different from the results of using W and Cu electrodes. One intermetallic compound $CeNi_5$ in addition to CeF_2 are observed here and it is the same as what we expected from our electrochemistry tests.

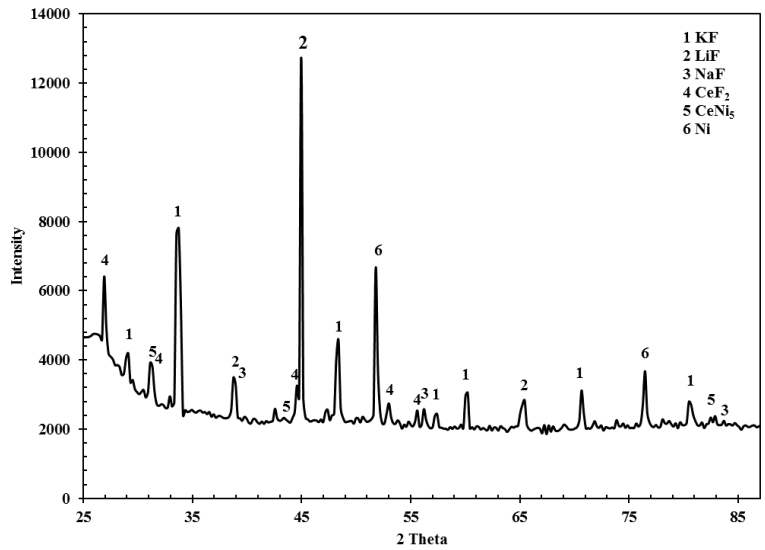

Figure 4-119. XRD analysis result of the chronopotentiometry electrolysis products of FLiNaK-CeF_3 melt on Ni electrode.

To further confirm the formation of CeF_2 and $CeNi_5$ intermetallic compound, SEM and EDS analysis were conducted to characterize the cross section of the nickel working electrode after chronopotentiometry electrolysis. The electrolysis products of CeF_2 and $CeNi_5$ intermetallic compound are shown in Figure 4-120 and Figure 4-121, respectively. The BSE image of the cross section of the nickel electrode with attached CeF_2 is depicted in Figure 4-120a. Subsequent point scan (Figure 4-120b) as well as EDS mapping results (Figure 4-120c-f) illustrate the co-existence of cerium and fluoride, which is in consistent with the XRD result. In Figure 4-121a, an evident white strip can be seen on the top of nickel electrode, EDS mapping results (Figure 4-121c-f) obtained on this strip reveal the well overlapping of cerium and nickel. It implies the formation of intermetallic compound. Further EDS analyses of point 1 and point 2 (Figure 4-121b) on that strip give an atom ratio of ~1:5 between Ce and Ni for the formed Ce-Ni intermetallic compound. Thus, the formed Ce-Ni intermetallic compound should be $CeNi_5$ which in fact is also found from the XRD analysis.

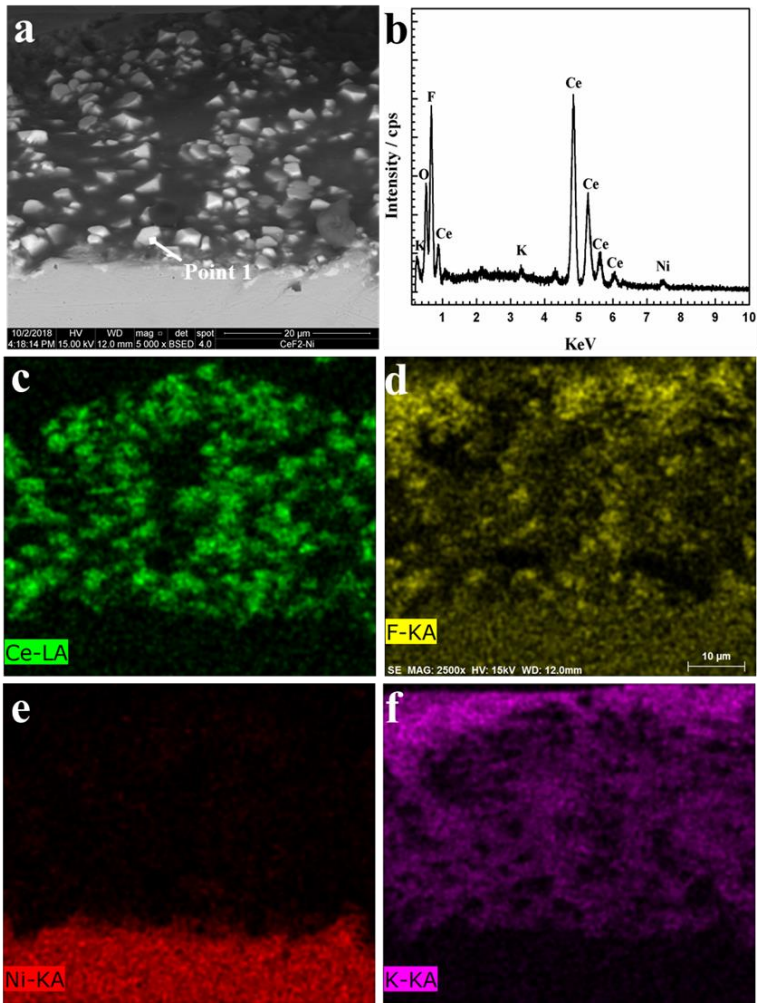

Figure 4-120. (a) Backscattered electrons (BSE) image of the cross section of polished nickel rod electrode with attached CeF_2 salts after electrolysis; (b) EDS point scan results of point 1 in Figure 4-120a; (c)-(f) EDS mapping results of Figure 4-120a.

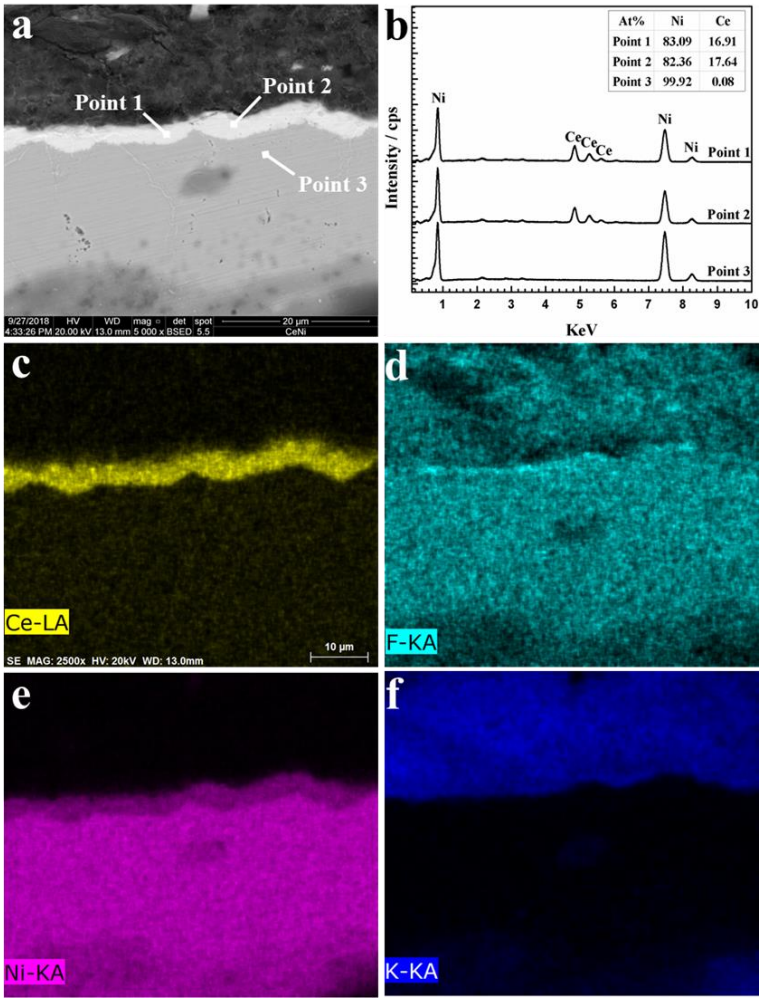

Figure 4-121. (a) Backscattered electrons (BSE) image of the deposited $CeNi_5$ intermetallic compound at nickel rod electrode; (b) EDS point scan results of point 1, point 2 and point 3 in Figure 4-121a; (c)-(f) EDS mapping results of Figure 4-121a.

4.7.3. Summary

The study explored the electrochemical behavior of CeF_3 in FLiNaK melt at 973 K on tungsten (inert), copper and nickel (reactive) working electrodes. The mechanism for the Ce (III) electroreduction in FLiNaK melt was determined by both cyclic voltammetry and chronopotentiometry and further confirmed by characterization methods including XRD and SEM analyses. It is found the reaction of Ce (III)+ $e^- \leftrightarrow$Ce (II) happens prior to the redox reaction of K (I)/ K. It means the electroreduction mechanism of Ce (III) in FLiNaK melt is unlike other salt systems in which Ce (III) has a one-step process with three-electron transfer: Ce (III)+ $3e^- \leftrightarrow$Ce. To realize the separation of Ce ions from FLiNaK electrolyte, copper and nickel electrodes were attempted with the possibility of intermetallic compound formation. However, intermetallic compound electrodeposition only occurs on

nickel working electrode at the current test condition which is probably ascribed to the not big enough Gibbs free energy of formation of $Ce_x Cu_y$ such that the intermetallic compound deposition potential is still more cathodic than potassium. The reduction of Ce (III) on nickel electrode results in the formation of intermetallic compound which was verified to be $CeNi_5$ by XRD and SEM analyses. The unique reaction of Ce (III)+ $e^- \leftrightarrow$Ce (II) was found out through the combination of electrochemical techniques and material characterization methods in the study, it will provide a new insight for the investigations of other lanthanides in FLiNaK melt based on the similar properties among lanthanides. In addition, the separation of cerium from FLiNaK melt is realized and it will facilitate the development of primary coolant clean-up system in FHR reactor.

4.7.4. References

1. Ackerman, John P. Industrial & Engineering Chemistry Research 30.1 (1991): 141-145.
2. S.P. Fusselman, J.J. Roy, D.L. Grimmett, L.F. Grantham, C.L. Krueger, C.R. Nabelek, T.S. Storvick, T. Inoue, T. Hijikata, K. Kinoshita, Y. Sakamuraet, K. Uozumi, T. Kawai, N. Takahashial. Journal of the Electrochemical Society, 146 (1999) 2573-2580.
3. Y. Castrillejo, M.R. Bermejo, E. Barrado, A. Martinez, P. Diaz Arocas. Journal of Electroanalytical Chemistry 545 (2003) 141-157.
4. F. Lantelme, Y. Berghoute. Journal of the Electrochemical Society, 146 (1999) 4137.
5. H. Tang, B. Pesic. Electrochimica Acta, 119 (2014) 120-130.
6. Y. Castrillejo, M.R. Bermejo, A.M. Martinez, P. Diaz Arcas. Journal of Mining and Metallurgy 39 (2003) 109-135.
7. P. Masset, R.J.M. Konings, R. Malmbeck, J. Serp, J.-P. Glatz. Journal of Nuclear Materials, 344 (2005) 173-179.
8. S. Vandarkuzhali, N. Gogoi, S. Ghosh, B.P. Reddy, K. Nagarajan. Electrochimica Acta, 59 (2012) 245-255.
9. C.P. Fabian, V. Luca, P. Chamelot, L. Massot, C. Caravaca, G.R. Lumpkin. Journal of The Electrochemical Society 159 (2012) F63-F67.
10. Z.-H. Wang, D. Rappleye, M.F. Simpson. Electrochimica Acta, 191 (2016) 29-43.
11. Ambrová, Marta, Jana Jurišová, and Vladimír Danielik. Chemical Papers 62.6 (2008): 559-565.
12. Qiao, Huan, Toshiyuki Nohira, and Yasuhiko Ito. Journal of alloys and compounds 359.1-2 (2003): 230-235.
13. Chesser, Ryan, Shaoqiang Guo, and Jinsuo Zhang. Annals of Nuclear Energy 120 (2018): 246-252.
14. Massot, Laurent, et al. Electrochimica Acta 54.26 (2009): 6361-6366.
15. Chuchvalcova Bimova, K., et al. Atalante, Montpellier (France) (2008).
16. Kim, Hojong, et al. Electrochimica Acta 220 (2016): 237-244.
17. Ferris, L. M., J. C. Mailen, and F. J. Smith. Journal of Inorganic and Nuclear Chemistry 33.5 (1971): 1325-1335.
18. Bermejo, M. R., et al. Journal of Electroanalytical Chemistry 603.1 (2007): 81-95.
19. Chamelot, Pierre, et al. Journal of Nuclear Materials 360.1 (2007): 64-74.
20. http://www.hsc-chemistry.com/
21. Guo, Shaoqiang, et al. Journal of Nuclear Materials 496 (2017): 197-206.

22. Dracopoulos, V., B. Gilbert, and G. N. Papatheodorou. Journal of the Chemical Society, Faraday Transactions 94.17 (1998): 2601-2604.
23. Sokol'skii, V. E., et al. Inorganic Materials 48.4 (2012): 416-422.
24. Beneš, O., and R. J. M. Konings. Calphad32.1 (2008): 121-128.
25. Ambrová, Marta, Jana Jurišová, and Vladimír Danielik. Chemical Papers 62.6 (2008): 559-565.
26. Chandra, Manish, et al. Electrochimica Acta 58 (2011): 150-156.
27. Ray
28. V. Constantin, A.M. Popescu, S. Zuca, Z. Naturforsch. 58a (2003) 57.
29. http://www.hsc-chemistry.com/
30. Massot, Laurent, et al. Electrochimica Acta 54.26 (2009): 6361-6366.
31. Masset, Patrick, et al. Journal of The Electrochemical Society152.6 (2005): A1109-A1115.
32. http://www.egmont.com.pl/gamry/katalog/PHE200.pdf
33. Qiao, Huan, Toshiyuki Nohira, and Yasuhiko Ito. Electrochimica acta 47.28 (2002): 4543-4549.
34. Bard, Allen J., et al. Vol. 2. New York: wiley, 1980.
35. Chamelot, Pierre, et al. Electrochimica Acta 55.16 (2010): 4758-4764.
36. Zvejskova, R., F. Lisy, and P. Soucek. No. INIS-FR--3043. Nuclear Research Institute Rez, 2004.
37. Massalski, Thaddeus B., et al., eds. Binary alloy phase diagrams. Vol. 2, 2nd ed., 1990.

4.8. Separation of Iodine from the Salt

4.8.1. Available data Review

Fluoride salt-cooled high temperature reactor (FHR) is an emerging reactor class that uses solid particle fuel and a liquid fluoride salt coolant at a high working temperature. This reactor class combines attractive advantages from previously developed reactors and power plants, for example, at a low operating pressure and with a fully passive decay heat rejection, which enables FHRs to generate electrical energy in a more economical and reliable way. [72-73] An important part of this reactor system deals with the design of the primary coolant cleanup system resulted from the possible leaking of fission products and fissile material into the primary coolant. Scientists and engineers make efforts to build this cleanup system for three basic adverse effects caused by leaking contaminants. Firstly, the escape of tritium from the primary coolant into cover gas and intermediate coolant increases the possibility of plant radionuclide release. Secondly, part of the contaminants (e.g., tellurium) makes the primary coolant more corrosive and then reduces the service lifetime of the system. Thirdly, a higher radioactivity requires extra maintenance of electronics and components employed in system. [74] While the negative effects discussed here apply to almost all of these contaminants, the main emphasis in this chapter is on the study of the electrochemical behavior and separation of iodide in molten salt.

In an FHR reactor, several types of radioactive iodine isotopes are formed as fission products in nuclear fuel and are remained within the fuel matrix as iodide. [75] Since the main concern is the leak of ^{129}I from defect TRISO fuel particles, it is of great importance to

efficiently remove all the radioactive iodide contaminants in the primary coolant. In general, 7LiF-BeF_2 binary salt (FLiBe) is selected as the primary coolant in FHR system for its viable application in Molten Salt Reactor Experiment (MSRE). However, the toxicity of beryllium makes the ternary LiF-NaF-KF salt (FLiNaK) a substitute for FLiBe and also the serving salt in this study. Electrochemical separation is a common method that utilizes an electrolysis step to concentrate and separate a substance from solution onto the surface of a solid electrode or into the small volume of a liquid electrode. This method has been widely employed as a tool in the study of the separation (or deposition) of lanthanide metals (e.g., La, Dy, Eu, Ce) from molten FLiNaK. [76,77,78,79,80] Conversely, only limited work has been reported on the progress of the electrochemical separation of iodide from high temperature molten salts. N. Shrestha et al studied the electrochemical behavior of iodide in LiCl-KCl salt with a tungsten working electrode and observed an anionic chemla effect between I^- and Cl^-. [4] Currently people still lack a basic understanding of electrochemical properties of I^- in molten FLiNaK and more efforts are needed to study its behavior in the salt.

In the present work, we are concerned with the electrochemistry of NaI in molten FLiNaK under different conditions. Tungsten electrode, as a stable electrode for metal deposition, was firstly employed as working electrode to study the mechanism of iodide oxidation in molten FLiNaK while the counter electrode and reference electrode were graphite and Pt, respectively. In addition, anodic passivation of a graphite electrode in molten fluorides has been observed when a positive potential is applied and current passes. [81-82] This phenomenon provides an anodic background limit positive enough to allow the occurrence of iodide oxidation reaction. Therefore, a graphite working electrode was selected and tested for the electrochemical system envisioned. The factors (e.g., temperatures, concentration) that may affect the electrochemical behavior of I- were also studied.

4.8.2. Electrochemical Analysis
4.8.3. Tungsten as a working electrode

To electrochemically separate and oxidize the I^- from molten salts, a positive potential is needed to obtain iodine. Typical anodic reactions on a tungsten working electrode in the molten FLiNaK-NaI mixture are as follows:

Tungsten dissolution reaction:

$$\mathrm{W} - \mathrm{ne} + X^- = WX_n \quad (n = 1,2 \ldots ,6; X = F^- or\ I^-) \tag{4-150}$$

Iodine formation reaction:

$$I^- - 2\mathrm{e} = I_2\ (g) \tag{4-151}$$

Fluorine formation reaction:

$$F^- - 2\mathrm{e} = F_2\ (g) \tag{4-152}$$

Correspondingly, the alkali metal deposition occurs at the cathode given below. It should be noticed that sodium metal deposition is selected as the most favorable reaction at the

cathode according to the standard free energy even though the concentration of NaF is only ~11.5 mol%.

Sodium metal deposition:

$$2Na^{+} - 2e = 2Na\ (l) \qquad (4\text{-}153)$$

And if the Na^{+}/Na redox couple is set as the reference electrode, the standard anodic potential of reaction (4-150),(4-151) and (4-152), E_{X_2/X^-} or $E_{WX_n/W}$, can be calculated by the standard Gibbs free energy. For the fluorides that have higher melting temperature than the eutectic salt temperature, e.g., NaF that has a melting temperature T_m of 996 °C, the ΔG^0 at supercooled state rather than the solid state should be used as these fluorides actually present as liquid in the FLiNaK salt. The ΔG^0 at supercooled state at temperature T is a summation of the ΔG^0 value at solid state ($\Delta G^0_{s,T}$) and the Gibbs energy of fusion ($\Delta G^0_{f,T}$) at temperature T. This calculation has been reported in our previous paper [76] and the standard electrode potentials of reaction (4-150),(4-151) and (4-152) have been calculated according to supercooled theory and HSC 6.0, as shown in Figure 4-122.

The potential of F_2 formation reaction is most positive among all the anodic reactions while the potential of WF_6 formation is most negative. Also, the potential of iodine evolution reaction is very close to the potential of WF_6 formation, indicating the potential possibility of separation of iodide from molten FLiNaK. Figure 4-123 First cycle of CVs recorded from a tungsten WE (area: 0.5 cm2) in both FLiNaK and FLiNaK-NaI (1.5 wt%) melts at 600 °C under argon atmosphere. Scan rate: 100 mV/s. CE and RE: Graphite and Pt.shows the CVs recorded from a tungsten electrode in blank FLiNaK and FLiNaK-1.5 wt% NaI mixture. As can be seen in Figure 4-123, for blank FLiNaK molten salt, there is no obvious oxidation peak during the

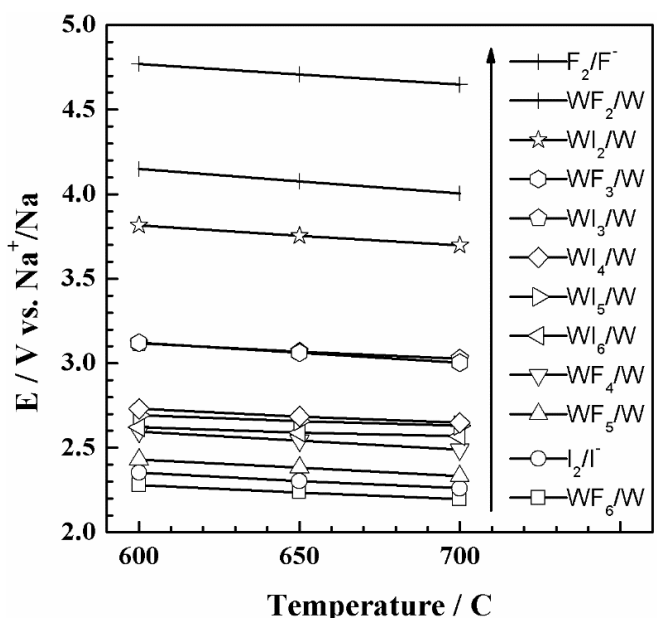

Figure 4-122 Redox potential (E vs. $E_{Na+/Na}$) at different temperatures for various redox couples in molten FLiNaK-NaI salt with a tungsten electrode.

sweep range between -1.35 V and 1.5 V (vs. Pt), proving the absence of electrochemical reactions. A very small reduction of R1 can be observed due to the dissolution of tungsten in the anodic sweep. With the addition of NaI, a couple of redox peaks (O2 and R2) appear and the oxidation peak O1 should be attributed to the oxidation of the deposited metal. Apparently, the peak O2 (1.4 Vvs. Pt) represents either oxidation of tungsten to form tungsten iodide or iodine formation given by Reaction (4-150) and Reaction (4-151). However, the appearance of reduction peak R2 with a high peak current indicates the absence of iodine, which should be in gas status and easily come out from the molten salt. Furthermore, since

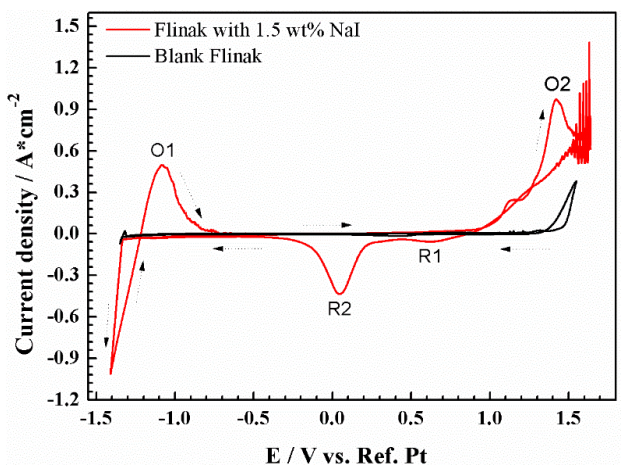

Figure 4-123 First cycle of CVs recorded from a tungsten WE (area: 0.5 cm²) in both FLiNaK and FLiNaK-NaI (1.5 wt%) melts at 600 °C under argon atmosphere. Scan rate: 100 mV/s. CE and RE: Graphite and Pt.

the current don't fall to zero at potential beyond the potential of peak O2 in the positive potential scan, the anodic current is the sum of multiple oxidation reactions taking place at the tungsten electrode.

Intriguingly, in molten FLiNaK-NaI (1.5 wt%) mixture, the second cycle of CV test and subsequent scans are quite different form first cycle, as shown in Figure 4-124a. One oxidation peak O3 before peak O2 can be observed. The mechanism of peak O3 formation was investigated in detail by cyclic voltammograms by controlling the cathodic potential limit (from 0.9 V to 1.05 V), the different shapes of the CVs were obtained at 600 °C and the results are displayed in Figure 4-124b. When the anodic limit potential is set at 0.9 and 1.0 V, no peak O3 can be observed. The presence of a small signal of peak O3 at a more positive potential shows the complicated anodic reactions and implies the changes of the electrode surface that allows a new oxidation reaction at the tungsten electrode. Also, when the potential is fixed at 1.1 V (vs. Pt) for almost half an hour, a severe tungsten dissolution can be observed after the experiment, implying that the O2 peak is related to the tungsten dissolution. Since so many potential kinds of tungsten dissolution reactions is proposed in

the anodic sweep, it's difficult to accurately decide which reaction will take place at tungsten working electrode for peak O2.

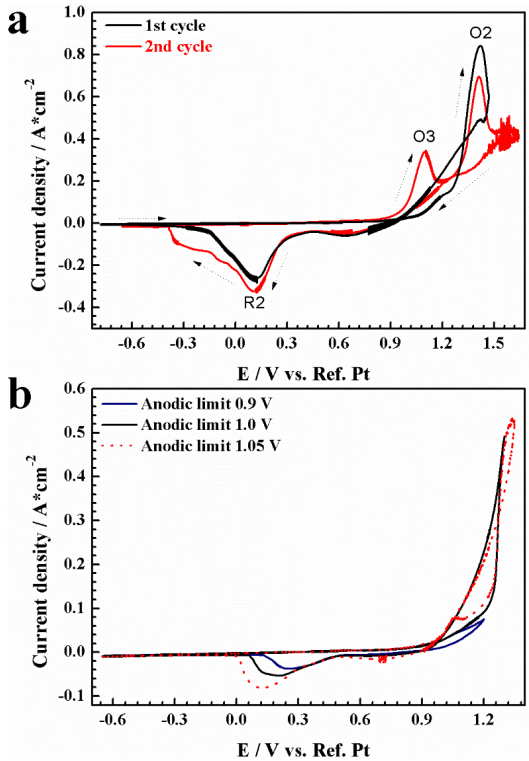

Figure 4-124 (a) First cycle and Second cycle of CVs recorded from a tungsten WE (area: 0.5 cm²) in FLiNaK-NaI (1.5 wt%) melts at 600 °C; (b) CVs recorded under different anodic potential limits.

For a CV test, a potentiostat controls E + iR_u rather than the true potential of the working electrode. Since current *i* varies with time as the peak is traversed, the error in potential varies correspondingly. The practical effect of Ru is to flatten the wave and to shift the reduction peak toward more negative potentials. Uncompensated resistance can thus have the insidious effect of mimicking the response found with heterogeneous kinetic limitations. An approach to fix this is the interrupter method, where the current flowing during a faradaic reaction is switched off for a few microseconds (i.e., the cell is taken to open circuit), and the instantaneous change in the potential, as the current drops to zero, is used to find *iRu*. This method is based upon the fact that the relaxation of potential from faradaic processes and diffusion is slower, so that the instantaneous change in potential can be totally assigned to iR_u. [83] A 10 s pulse of 50 mA, 100 mA and 200 mA current was applied between a tungsten working electrode and a graphite counter electrode. Then the evolution of the open circuit potential (OCP) was conducted and the changes of the instantaneous potential change were recorded and shown in Figure 4-125. The calculated R_u at 50 mA, 100 mA and 150 mA are 0.412 Ω, 0.376 Ω and 0.374 Ω. The little difference of R_u between low current and high current should be attributed to a fact that the relaxation time for lower current is a little shorter than 1ms due to a more positive polarization potential. Therefore, Ru in molten FLiNaK-NaI mixture is selected as 0.375 Ω.

Figure 4-126 shows the CVs recorded in FLiNaK-1.5 wt% NaI mixture at 600 °C and different scan rates before and after IR drop corrected. It can be seen that after IR-drop corrected, the potentials of peak O2 and O3 show almost no change with various scan rates, implying the reversibility and the fast kinetics of tungsten dissolution reaction.

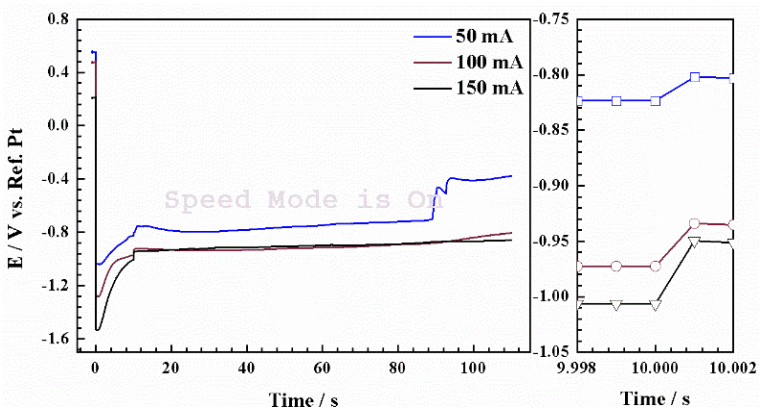

Figure 4-125 Chronopotentiograms at different currents for 10 s. Time interval: 1 ms.

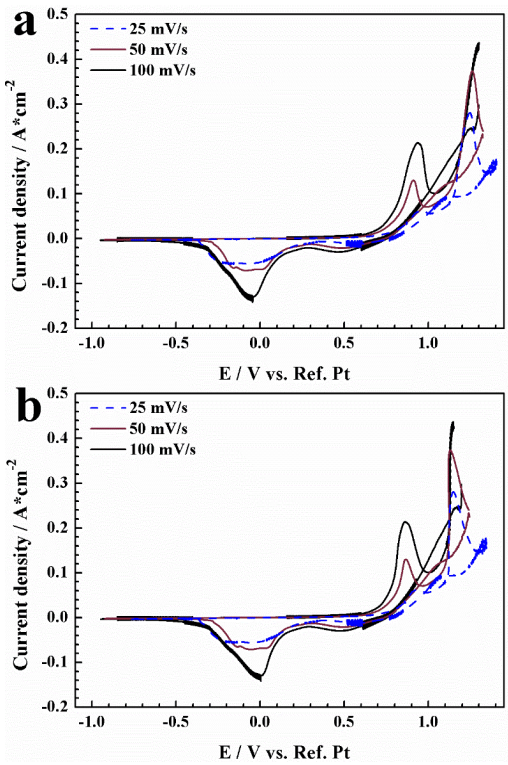

Figure 4-126 CVs recorded in FLiNaK-1.5 wt% NaI mixture at 600 ℃ and different scan rates before (a) and after (b) IR drop corrected.

An interesting phenomenon is that peak O2 gradually vanishes as temperature increases, as presented in Figure 4-127. As explained before, more than one oxidation reaction took place at the anode surface. Then the reason for the disappearance of peak O2 is the shrink of the difference between different reaction redox potentials. In that case, the individual waves are merged into an increasing oxidation current. Also, when the potential is set at 1.0 V (vs. Pt), tungsten working electrode dissolved into molten salt, which is similar to the result obtained at 600 °C. All the results demonstrated the unsuccessful separation of iodide from molten FLiNaK with a tungsten electrode.

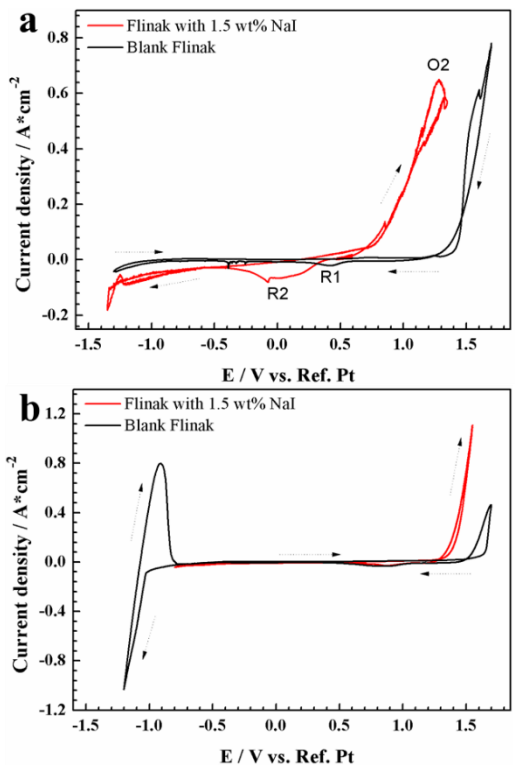

Figure 4-127 CVs recorded from a tungsten WE (area: 0.5 cm²) in both FLiNaK (black line) and FLiNaK-NaI (1.5 wt%, red line) melts at 650 (a) and 700 ℃ (b) under argon atmosphere. Scan rate: 100 mV/s. CE and RE: Graphite and Pt

.

4.8.4. Graphite as a working electrode

The separation of iodide from this FLiNaK system can be perfect when the working electrode is inert even at a sufficiently positive potential. Unfortunately, many electrodes including alloys and conductive metal oxides do not satisfy this requirement in high temperature molten salt, and their behaviors are just the same as that of the tungsten electrode. [13] Instead of finding an inert anode, graphite electrode is considered as a substitute in this work because of its so-called 'anode effect' at positive potential at which a

passivation CF_x layer forms and blocks the electron-transfer reaction. [14,15,16,17] With this passivation layer, the carbon fluoridation reaction does not occur at values one would predict from thermodynamics. Instead considerably higher energies (more positive potentials to even 9 V *vs.* K^+/K in molten FLiNaK [15]) must be applied to make the carbon fluoridation reactions occur at a measurable rate. More to this point, in molten cryolite ($NaAlF_6$) for aluminum production, the addition of aluminum oxide relieves this blocking effect, enabling the successful production of aluminum metal, which implies the possible separation of iodide from molten FLiNaK with this graphite electrode.[18,19,20]
As before, thermodynamic analysis of a graphite working electrode was conducted first in just the way when tungsten was employed as working electrode. Typical anodic reactions on a graphite working electrode is similar to those with a tungsten electrode expect the carbon oxidation reactions, which are written as follows (4-154):

Graphite oxidation reactions:

$$\mathrm{C} - \mathrm{ne} + X^- = CX_n \quad (X = F^- or\ I^-) \tag{4-154}$$

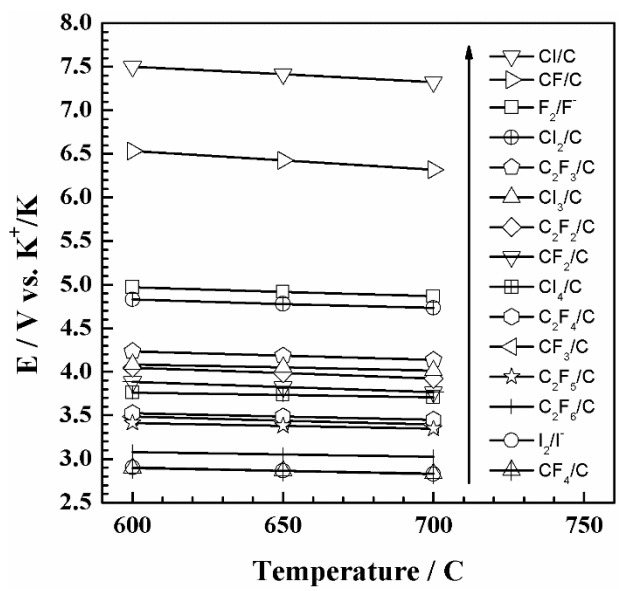

Figure 4-128 Redox potentials (E vs. $E_{K+/K}$) at different temperatures for various redox couples in molten FLiNaK-NaI salt with a graphite electrode.

If the K^+/K redox couple is set as the reference electrode, the standard redox potentials, $E_{CF_n/C}$, were calculated by their standard Gibbs free energies of formation and the results were shown in Figure 4-128 after calibrated by the supercooled theory. [5] The potential of I_2 formation reaction is 2.83 V *vs.* K^+/K at 700 °C, least positive among all the anodic reactions while the potentials of CF_4 and C_2F_6 formation reactions are 2.83 V and 3.02 V vs. K^+/K at 700 °C, respectively. Although the potential of the formation CF_4 is very close to that of the formation of I_2 gas, there is still a potential to separate iodide ions from this system as discussed earlier.

Before embarking on the detailed consideration of the electrochemical behavior of I^- with a graphite working electrode in molten FLiNaK, we will consider the 'anode effect' of

graphite electrode to illustrate its main features for further comparison. Typical CV recorded from a graphite electrode in FLiNaK at 700 °C with a scan rate of 500 mV/s was presented in Figure 4-129. The formation of CF_4 and C_2F_6 have been identified as the related reactions giving rise to the observed O3 and O4 peaks respectively, concluded from thermodynamic prediction. However, there is considerable uncertainty in their related reactions. In H. Zhanju's work [11], a large amount of CF_4 and C_2F_6 gas won't be detected by GC gas analysis until a potential more than 9 V *vs.* K^+/K at 700 °C in the FLiNaK salt. A big additional potential (beyond the thermodynamic requirement) is needed to drive carbon fluoridation reactions across the passivation layer at a certain rate and thus the carbon electrode shows high over-potentials for this two reactions. Also, both CO_2 and CO were generated at 3.0 V *vs.* K^+/K and thus the peak O3 and O4 is actually caused by the oxygen impurities even under argon atmosphere. However, in C. Gong's work [15], only argon gas was detected when the potential was set at 1.0 V vs. Pt for 8 h (~2.7 V vs. K^+/K in this reference) in LiF-KF salt, and the peak should be related to the formation of a solid carbon fluoride compound C_xF. This controversy makes it

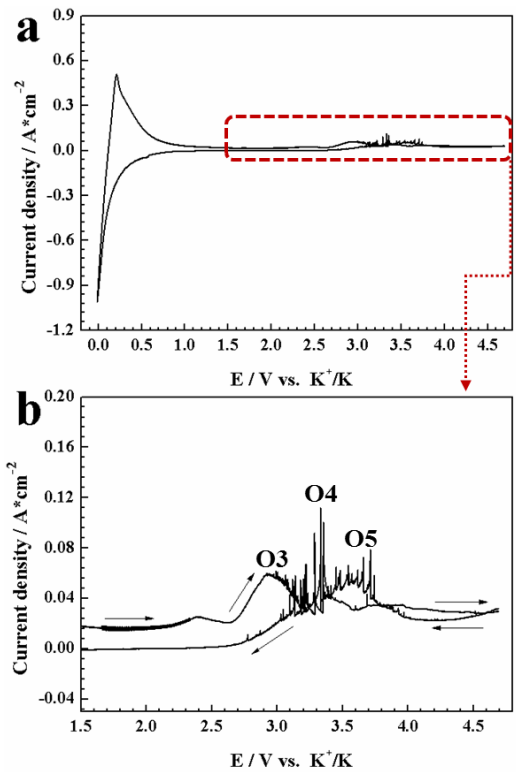

Figure 4-129 (a) CV curve recorded from a graphite WE (area: 0.21 cm²) in FLiNaK melt at 700 °C under argon atmosphere; (b) the enlargement of the curve in Figure 4a. Scan rate: 500 mV/s. CE and RE: Graphite and Pt (the potential of Pt reference electrode is converted to the redox K^+/K couple for easier comparison with thermodynamic calculation).

difficult to illustrate reaction mechanism. Literally, only very little amount of the formed CF_4 or C_2F_6 gas (or the solid carbon fluoride compound) could cover the electrode surface, remain at the electrode and then cut off the circuit at positive potential, which means that the concentration of the formed gas may be too low to be detected by the GC gas analysis technique. In our experiment, the electrolysis curves always suffer a severe vibration such

as the current dropping off to zero, and this might be caused by the formation and decomposition of this passivation layer. Furthermore, it should be noted that in H. Zhanju's work, the detection of large amounts of CO and CO_2 gas in blank FLiNaK salt implied the existence of oxygen impurities that may have an uncertain influence on the result even under the argon atmosphere. Therefore, we prefer that the O3 and O4 peaks correspond to either the evolution of CF_4 and C_2F_6 gases or the formation of solid carbon fluoride compounds on the electrode. Intriguingly, another oxidation peak (O5) is observed in Figure 4-129b as the curve is traversed, which is uncommon especially compared to the reduction current observed from a typical CV test.

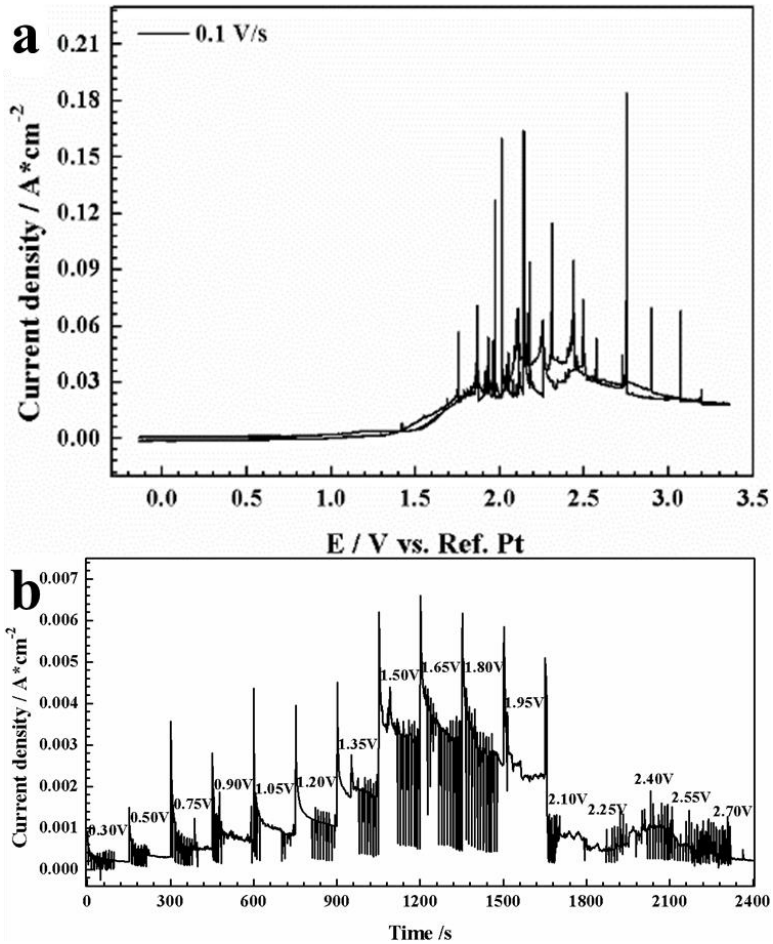

Figure 4-130 (a) CV result with graphite electrode in molten FLiNaK at 700 °C. Scan rate: 100 mV/s; (b) Chronopotentiograms recorded in FLiNaK at 700 °C at different potentials (vs. Ref. Pt). Electrolysis time interval: 150s. OCP interval: 300 s. OCP curves are not shown here.

Chronoamperometry and cyclic voltammetry method with a slow scan rate were employed to estimate this uncommon phenomenon in CV test, as shown in Figure 4-130. With a scan rate of 100 mV/s, the forward and the reverse curves overlap precisely, showing the irreversibility of this reaction that takes place at the graphite electrode. Now we consider a series of potential-step experiments employed in this system, as shown in Figure 4-130a. Between each experiment the open-circuit potential is measured for 300 s, so that the initial conditions are always the same. Initially, the potential is chosen to be at a relatively negative value where no faradaic processes occur. The change from experiment to

experiment is in the step potential. In the experiment where potential is set at 0.3 V and 0.5 V *vs.* Pt, they yield almost no faradaic current. Then the current slightly increases with the applied potential. At a more positive potential such as 1.5 V, 1.65 V and 1.8 V *vs.* Pt, these experiments yield the same current. However, when the potential is set at a value higher than 1.95 V, the current decreases as the potential is shifted positive. Usually, for a typical diffusion-controlled reaction in CV test, the surface concentration at extreme potentials (either sufficiently negative or positive) is zero and hence the reactant arrives as fast as diffusion can bring it, and the current is limited by the rate of its diffusion. [12] Thus at such a condition that applies, it should no longer influence the electrolytic current, which is opposite to our results. This phenomenon should be attributed to a 'passivation layer' on the electrode during the anodic scan. In fact, the small oxidation currents flowing through the system in these tests (Figure 4-130b) are indicative of formation of a passivation layer especially in this FLiNaK system full of fluorine ions, and one can expect it to exert effects on the electrochemical behavior of the ion transfer in these tests. This layer could be made up of either carbon fluoridation gas or solid film (or from both of them), and we observe that it could decompose and then recover the electrode after several minutes of OCP test. Since the currents always maintain at a very low level in this potential range, the formation of this layer should occur at the initial stage, and thus the current might be limited by the diffusion of F^- penetrating through this layer. The decrease in current at higher value of potential suggests a thicker passivation layer that covers the electrode surface and exacerbates the blocking effect. Then, as stated earlier, the overlapping of the forward and reverse scan in CV implies that the change in the thickness of this passivation film reaches a quasi-steady state at such a slow scan rate of 100 mV/s.

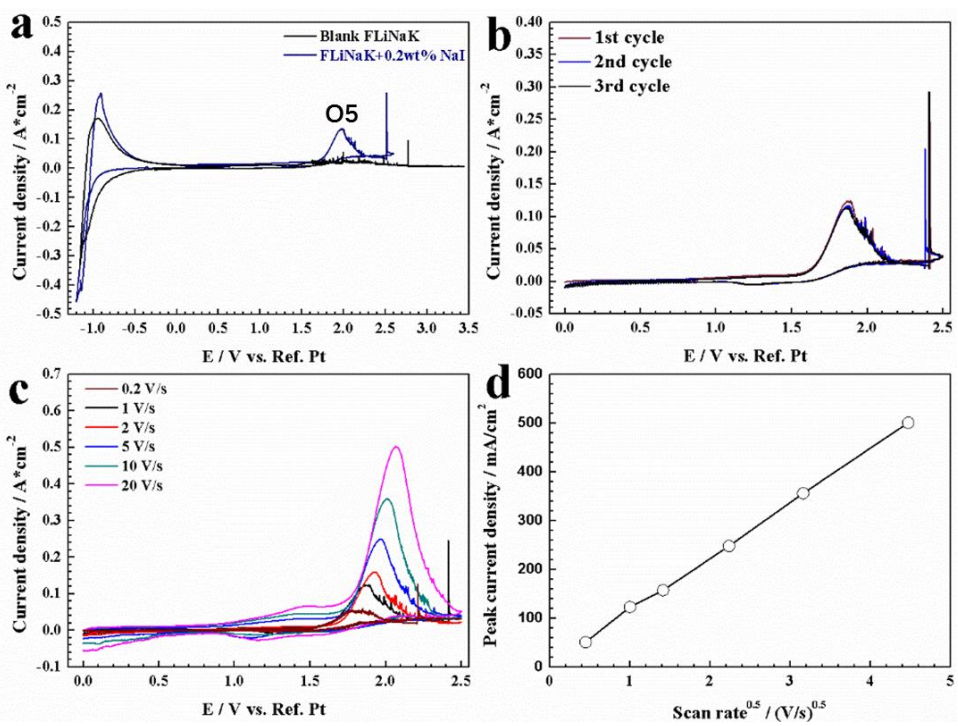

Figure 4-131 CVs recorded from a graphite WE in FLiNaK-0.2 wt% NaI (0.0267 mol/L) at 700 °C. (a) The typical CV test results in the FLiNaK and FLiNaK-0.2 wt%NaI. Scan rate: 1 V/s; (b) Three consecutive CV cycles in FLiNaK-0.2 wt% NaI; (c) CV tests at different scan rates

(from 0.2 V/s to 20 V/s); (d) The current peaks obtained at different scan rates (from (c)); CE and RE: Graphite and Pt.

The typical CV tests with the addition of 0.2 wt% NaI at 700 °C into molten FLiNaK were firstly carried out, as shown in Figure 4-131. The emerging of an oxidation peak O5 at ~2.0 V *vs.* Pt in Figure 4-131a shows the influence of the addition of NaI. This cathodic background limit for potassium deposition in Figure 4-131b is ~1.1 V *vs.* Pt, and then the redox potential that occurs at peak O5 is ~3.1 V vs. K^+/K, which is quite different from the potential of the redox couple of I_2/I^- from thermodynamic consideration. Thus the peak O5 might be either the formation of I_2 (2.26 V *vs.* K^+/K from Figure 4-128) or CI_4 (3.14 V *vs.* K^+/K from Figure 4-128). More details on this reaction will be discussed later. Since the CV test in Figure 4-127b yields almost no oxidation current in the reverse scan, this reaction shows a strong irreversibility due to the release of I_2 gas or CI_4 gas. The potential peak, O5, is a function of scan rate, shifting in a positive direction as the scan rates increase, which yields the typical irreversible waves as presented in Figure 4-131c. In addition, the peak current varies with $v^{1/2}$ and shows a good linearity at higher scan rate characteristic of a diffusion-controlled process (Figure 4-131d). [21,22] The CV results obtained in FLiNaK-0.2 wt%NaI implies that there is no relationship between the passivation layer and the oxidation of iodide ions. However, its influence on the ongoing electrode reaction was revealed in the chronoamperometry tests.

Potential-step electrolysis analogous to that employed in blank FLiNaK were conducted, as shown in Figure 4-132. Between each experiment the open-circuit potential is measured for 300 s, so that the initial conditions are always the same. The behaviors also follows in an analogous manner to that decribed earlier in the FLiNaK salt. As can be seen, the current continues increasing with increasing potential until a peak is reached at 2.1 V *vs.* Pt. Then the current decreases with the increasing potential. This trend is in well consistent with the CV tests, and illustrates that this passivation layer at a sufficiently positive potential blocks the oxidation of iodide. More interestingly, the blocking effect of this passivation layer produces selectivity toward a particular process (here inhibiting the carbon fluoridation reactions) at a proper potential and thus allow the oxidation (or separation) of iodide from the system. Then the diffusion-controlled behavior in Figure 4-131d might be explained as below. At a higher scan rate (such as 2 V/s and 10 V/s), the duration time is relatively short and the passivation layer could be regarded as stable. In this case, the oxidation of iodide ions is controlled by the mass transfer of iodide ions.

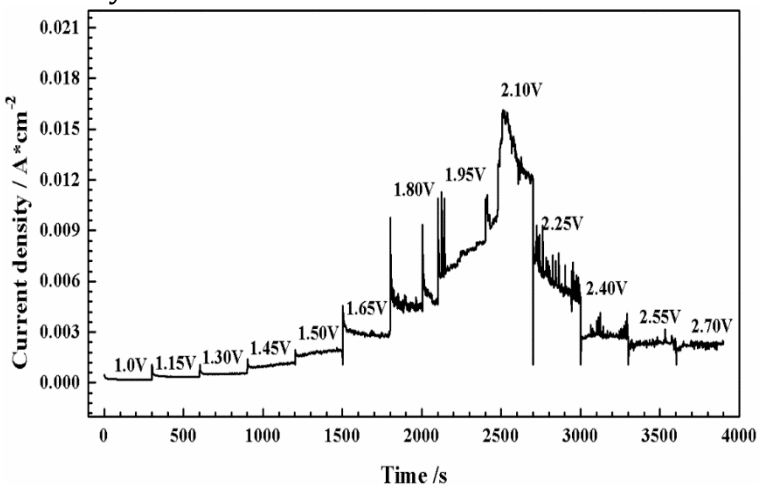

Figure 4-132 Chronopotentiograms recorded in FLiNaK-0.2 wt% NaI at 700 °C and different potentials (vs. Ref. Pt). Electrolysis time interval: 300 s. OCP interval: 300 s. OCP curves are not shown here.

When the concentration of NaI increased to 0.5 wt%, the performance of the system in CV test was slightly different from that with 0.2 wt% NaI, and oxidation peaks were observed in the both forward and backward scans (Figure 4-133a). Similarly, the chronopotentiogram results (Figure 4-133b) behave in a manner analogous to previous tests. While the effect of this passivation layer discussed above still apply to the oxidation of iodide ions, the rate of the iodide ions passing through the film, instead of the mass transfer of iodide ions, becomes rate-limiting with a higher concentration of NaI and control the experiment, thus leading to the emerging of an oxidation current in the reverse scan.

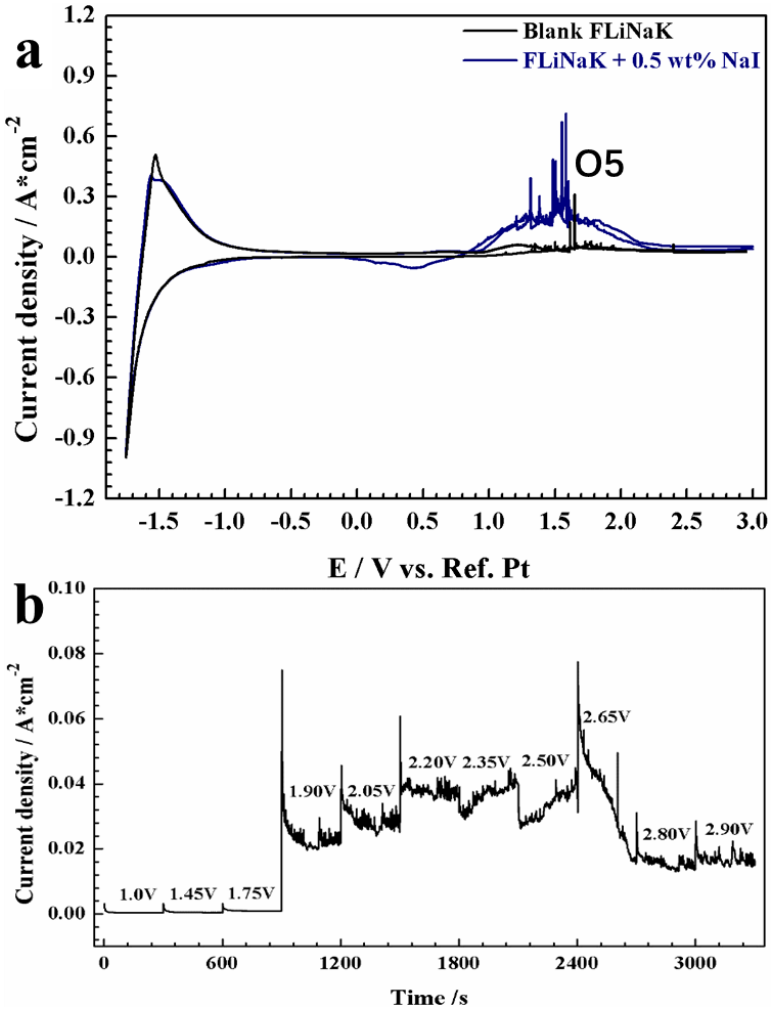

Figure 4-133 (a) CV result with graphite electrode in molten FLiNaK-0.5 wt% NaI at 700 °C. Scan rate: 500 mV/s; (b) Chronopotentiograms recorded in FLiNaK-0.5 wt% NaI at 700 °C at different potentials (vs. Ref. Pt). Electrolysis time interval: 300 s. OCP interval: 300 s. OCP curves are not shown here.

In both the experiment with 0.2 wt% and 0.5 wt% NaI in this FLiNaK system, there is no direct evidence that I_2 or CI_4 gas comes out from the system during the electrolysis (CA tests) due to the lack of GC gas analysis. However, a certain amounts of green powder that

attached to the inside of the crucible after the experiments can be observed, providing the possibility to reveal the potential reaction pathways. The XRD result (Figure 4-134) of this green powder illustrates the presence of large amounts of KI and other fluorides and the absence of carbon. The possible pathways for the formation of KI are written as below:
Pathway 1:

$$2I^- - 2\mathrm{e} = I_2\ (g) \quad (4\text{-}155)$$

$$\mathrm{Ni} + I_2 = NiI_2 \quad (4\text{-}156)$$

$$\mathrm{Ni}I_2 + \mathrm{KF} = KI + NiF_2 \quad (4\text{-}157)$$

Pathway 2:

$$4I^- - 4\mathrm{e} + \mathrm{C} = CI_4\ (g) \quad (4\text{-}158)$$

$$2\mathrm{Ni} + \mathrm{C}I_4 = 2NiI_2 + C \quad (4\text{-}159)$$

$$\mathrm{Ni}I_2 + \mathrm{KF} = KI + NiF_2 \quad (4\text{-}160)$$

Since no carbon was detected from the XRD analysis, the iodine element in KF might be from the I_2 gas through pathway 1. Furthermore, the existence of NiF_2 might arise from the following reactions ((4-161), (4-162) and (4-163)), as shown below. Usually, a very high overpotential (no less than 6 V *vs.* K^+/K) is required to drive the fluorine gas out from the system at a measurable rate.[12-13] Thus with the modest condition we applied in our experiment the concentration of fluorine gas should be negligible, and combined with the absence of carbon in these green powder, the formation of NiF_2 should also be attributed to

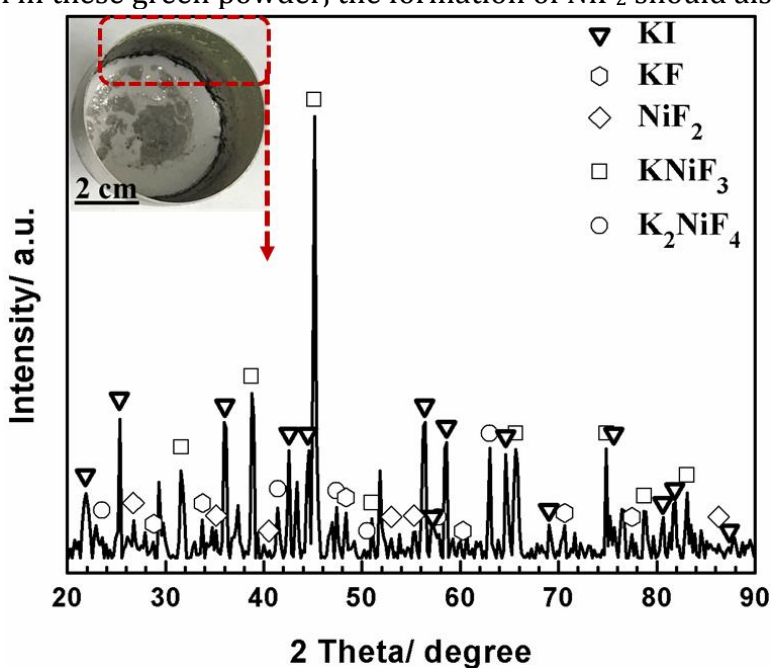

Figure 4-134 XRD result of the green powder inside the crucible after CA tests in FLiNaK-0.5wt% NaI salt; Insert graph: the digital photo of the crucible after experiment.

the pathway 1. These results imply that the potential reaction for peak O4 in previous CV test should correspond to the formation of iodine gas instead of CI_4 gas.

$$4F^- - 4\mathrm{e} + \mathrm{C} = CF_4\ (g) \quad (4\text{-}161)$$

$$2\mathrm{Ni} + \mathrm{C}F_4 = 2NiF_2 + C \quad (4\text{-}162)$$

Or

$$\mathrm{Ni} + F_2 = NiF_2 \quad (4\text{-}163)$$

Further SEM and EDS analysis of the green powder also confirmed the absence of carbon, as shown in Figure 4-135. Figure 4-135a depicts the second electron image of the green

powder, which are made up of various irregular particles with the size in the range of 0.5 to 8 μm. A strong signal of potassium, fluorine, nickel and iodine can be observed in the point scans of the particles (Figure 4-135b), which is in consistent with the XRD result. Note that the atomic concentration of the iodide is much smaller than that in the XRD result, and this error is caused by a low working voltage (20.00 KV) that is not in capable of stimulating the electrons in K shell of the iodine element. As can be seen in EDS mapping results (Figure 4-135c-f), the partial overlapping of these four elements indicated the coexistence of the chemical compounds as provided by XRD analysis.

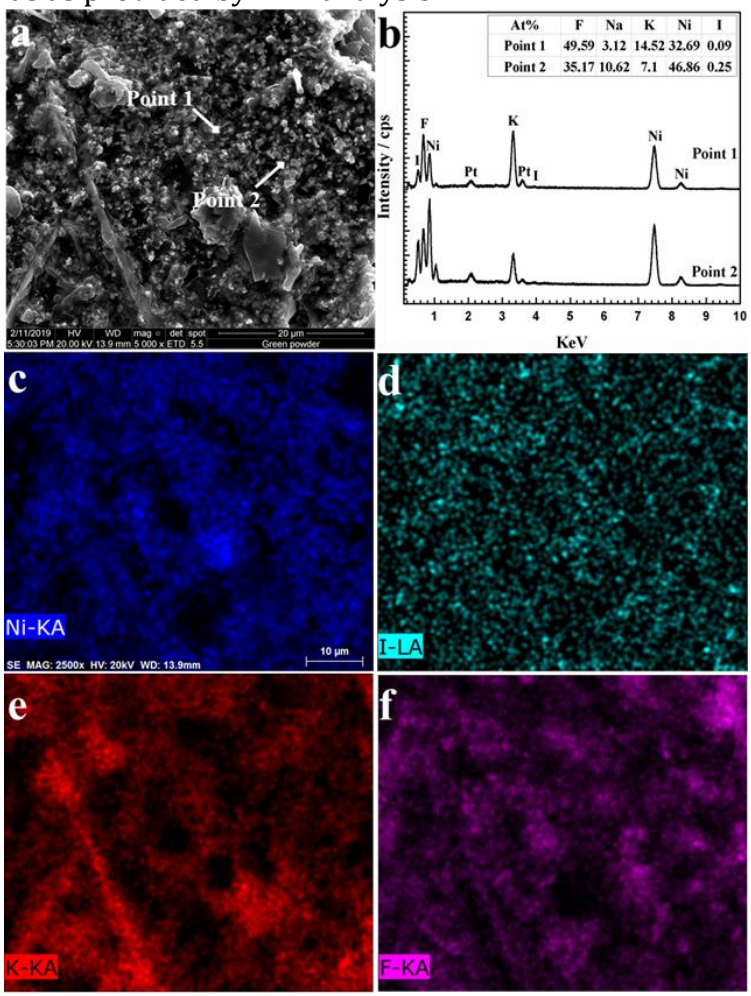

Figure 4-135 (a) Second electron (SE) image of the green powder; (b) EDS point scan results of point 1 and point 2 in Figure 10a; (c)-(f) EDS mapping results of Figure 10a.

The analogous behavior of the graphite electrode in CA tests to previous results can be observed when the concentration of NaI within the cell reaches 1.5 wt% (Figure 4-136). Still, between each experiment the open-circuit potential is measured for 300 s, so that all the components in the salt will be in equilibrium with each other. One can still observe the blocking effect caused by the passivation film (Figure 4-136a). In this series of CA tests, the duration time is set at 1000 s to slightly alter the composition of the salt. Thus, a decrease in peak current before and after electrolysis could be observed and it illustrates the consumption of iodide ions (Figure 4-136b). The shifting of the peak potential to a more

negative value in both CV and CA tests compared to previous tests could be regarded as a consequence of the employment of an unstable Pt quasi-reference electrode.

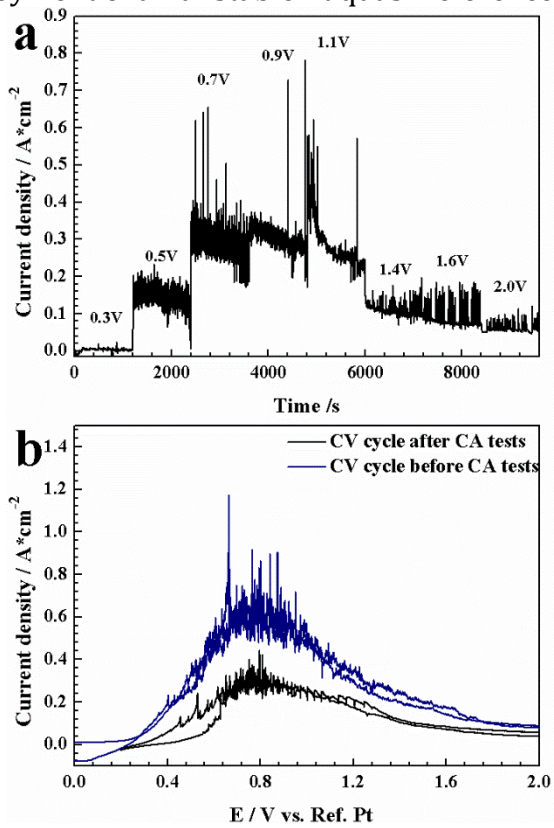

Figure 4-136 (a) Chronopotentiograms recorded in FLiNaK-1.5 wt% NaI at 700 °C at different potentials (vs. Ref. Pt). Electrolysis time interval: 1000s. OCP interval: 300 s. OCP curves are not shown here. (b) CV results in molten FLiNaK-1.5wt% NaI before and after consecutive CA tests. Scan rate: 100 mV/s.

When the electrolyte contains a higher concentration of NaI such as 5 wt%, the cell shows a different electrochemical behavior compared to those observed at low concentrations (Figure 4-137a). The current varies almost linearly with the applied potential in the region where the oxidation reaction starts until a steep decrease in oxidation current is attained. Moreover, as the concentration of NaI is increased, the potential difference between E_p and $E_{0.5p}$ (Where E_p is the potential of the peak potential; $E_{0.5p}$ is the potential where the current is at the half peak value) becomes larger. Similar behavior was also observed in the cryolite salt containing alumina oxide, without further explanation for this phenomenon. [84] The situation is more complicated than that the above passivation layer suggests, since the passivation layer usually refers to an insulative film that leads to a termination of the test. The performance of the whole system is actually determined by an uncertain interrelation of the added NaI and this passivation layer. The addition of iodide ions might produce small displacement of the passivation layer formed on the electrode surface and then inhibit the anode effect, which is equivalent to the relay of its effective potential to a more positive value and the production of a higher current. Thus at a more positive potential, the oxidation rate of iodide ions could be very fast, and to a certain extent, the continuously increased potential would lead to a limiting current, a subsequent deficiency of iodide ions and then final formation of an integral passivation layer. The complicated mechanism

makes it difficult to obtain the electrochemical properties of the redox couple at the graphite electrode. Figure 4-137b shows good reproducibility of the CV curves. The CV tests obtained at different scan rates in Figure 4-137c

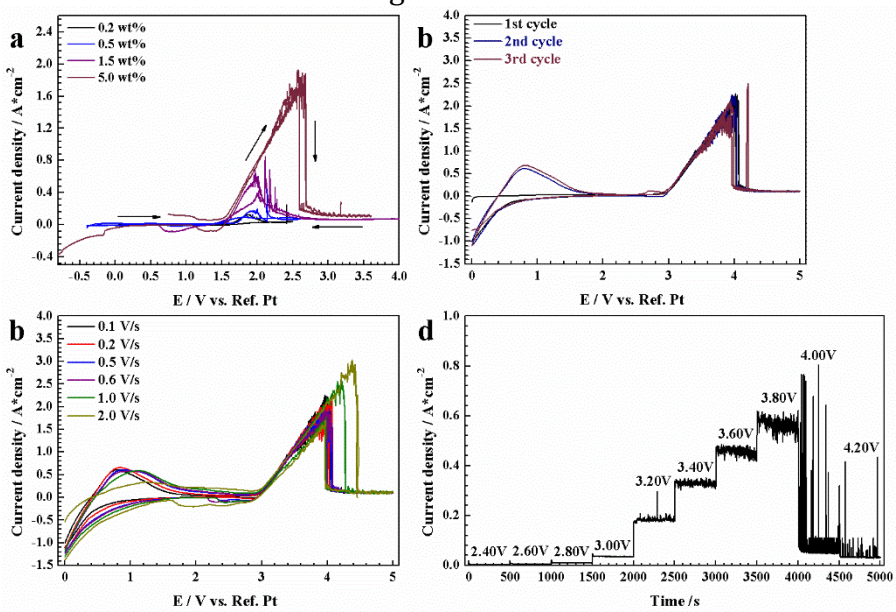

Figure 4-137 (a) CV tested recorded at different concentrations of NaI at 700 °C; Scan rates: 500 mV/s; (b) Subsequent cycles of the CV test recorded in the FLiNaK-5 wt% NaI melt; Scan rate: 500 mV/s; (c) CV tests at different scan rates (from 0.1 V/s to 2.0 V/s); (d) The CA results in FLiNaK-5.0 wt% NaI salt at 700 °C; Electrolysis time interval: 500s. OCP interval: 1000 s. OCP curves are not shown in figure.

present the irreversibility of this iodine formation reaction since a shift in potential can be observed with the increase in scan rate. The typical CA tests (Figure 4-137d) is in accordance with the previous CV tests, the vibration of the current at 4.0 or 4.2 V (vs. Pt) implies the formation of carbon fluorides gases that block the electron transfer through the electrode/solution interface.

In both the experiments with 1.5 wt% and 5 wt% NaI, a lot of white powder and red powders as well as the green powder inside the crucible (Figure 4-138b, Figure 4-138c and Figure 4-138d) could be observed on the after CA tests while both the crucible and the salt without the electrolysis show clean surfaces (Figure 4-138a). The black spot inside the salt in Figure 4-138a is the graphite bar immersed into the salt for exact comparison. Further XRD analysis (Figure 4-138e) of the powders collected by a tape shows the existence of KI and KF. Since the clean surface of the crucible and salt proved that the formation of the powders is yielded by the electrolysis, the deposit of KI on the clamp after the electrolysis implies another possible pathway for the separation of iodide from the system, and that is a following chemical reaction occurring (or the generation of an unstable intermedieate) after the electrochemical reaction as written below. Initially, the small amount of red powder was regarded as the deposition of iodine. However, the XRD result didn't reveal the existence of iodine in the powder deposits and the reason for this is that the temperature at the electrode maintained at a very high level unable to physically deposit most of the generated iodine vapor. Thus the concentration within the powder is too low to be detected

by the XRD analysis. After the electrolysis, the surface is covered by a layer of graphite powder because of the insertion of potassium metal into the graphite counter electrode.

$$\mathrm{KF} + \mathrm{NaI} = KI + NaF \quad (4\text{-}164)$$

$$2I^- - 2\mathrm{e} = I_2\ (g) \quad (4\text{-}165)$$

$$\mathrm{KI} + I_2 \xrightarrow{high\ temperature} KI_3\ (g) \quad (4\text{-}166)$$

$$\mathrm{KI} + I_2 \xleftarrow{low\ temperature} KI_3\ (g) \quad (4\text{-}167)$$

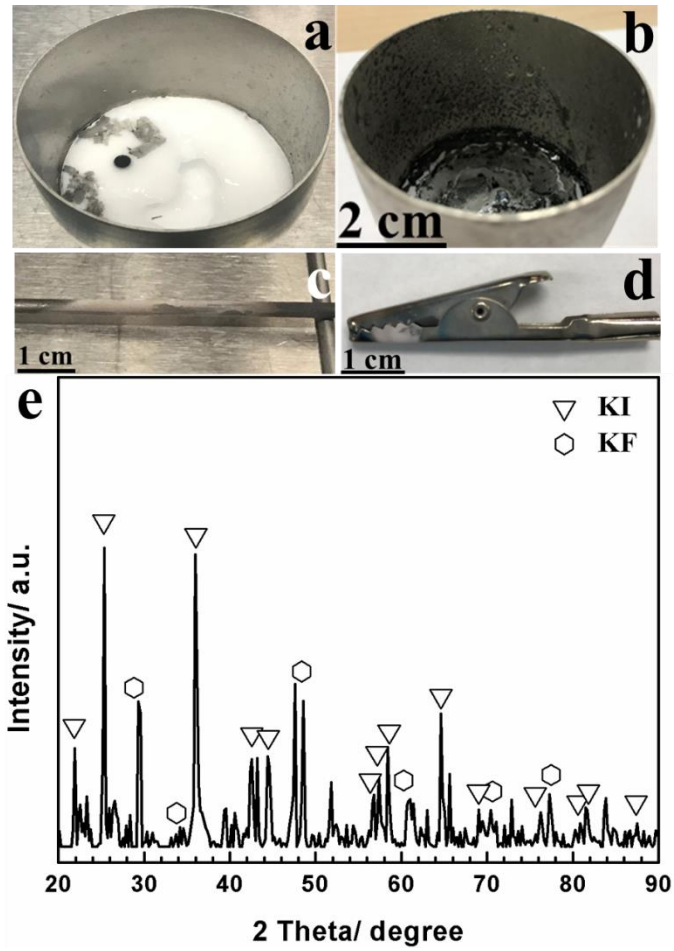

Figure 4-138 (a) the photo of the crucible containing FLiNaK-5 wt% NaI held at 700 °C for 8 h without any tests; black spot: the graphite rod that immersed into the salt; (b) The typical photo of the crucible after the CA tests in the salt containing either 1.5 wt% or 5 wt% NaI; (c) The photo of the upper part of the graphite electrode after the CA tests in the FLiNaK-1.5 wt% NaI; (d) The photo of the clamp fixing the working electrode after the CA tests in the FLiNaK-5wt% NaI; (e) The XRD result of the powders on the clamp.

4.9. Summary

The electrochemical behavior of NaI has been studied in molten FLiNaK with a tungsten and graphite electrode at various conditions. With a tungsten electrode, a severe dissolution of tungsten working electrode was observed when the potential is set at positive values of 1.35 V vs. Pt at 650 °C and 1.0 V vs. Pt at 700 °C, strongly interfering the separation of iodide. In the case of a graphite electrode, the observation of NiF_2 or KI after

the long time electrolysis is much evidence favoring the formation of I_2 and KI_3 coming out from the system during the electrolysis, which provides an opportunity for iodide separation from molten salt reactor. The decrease in the peak current of CV test after long time electrolysis in the FLiNaK-1.5 wt% NaI also confirmed the consumption of the iodide ions. By carrying out the CV and CA measurements, the behavior of iodide ions in the salt suggested a complex mechanism influenced by multiple factors such as the concentration and the applied potential. At a low concentration of 0.2 wt% NaI, the process that occurs at the electrode is mainly controlled by the mass transfer of the iodide ions, while with a concentration of NaI at 0.5 wt% or above that, it is dominated by the anode effect of a passivation graphite electrode. The anode effect of a passivation film at the graphite electrode inhibits the transport of the charge across the solution-electrode interface especially at a sufficiently positive potential, leading to a decrease in ongoing current. This passivation layer complicates the interpretation of the results of the electrochemical test and also the elucidation of the pathway of the overall reaction. For example, the uncommon current curve observed in the CV test in FLiNaK-5 wt% NaI system depends linearly upon the potential applied to the system. Thus in-situ technique, such as real-time gas monitoring, could be introduced to further illustrate of the reaction mechanism.

4.10. References

[1] D.E. Holcomb, G.F. Flanagan, G.T. Mays, W.D. Pointer, K.R. Robb and G.L. Yoder Jr., Fluoride Salt-cooled High-temperature Reactor Technology Development and Demonstration Roadmap, ORNL/TM-2013/401, Oak Ridge National Laboratory, Oak Ridge, TN, USA, September 2013.
[2] R. O Scarlat, M. R. Laufer, E. D. Blandford, N. Zweibaum, D. L. Krumwiede, A. T. Cisneros, C. Andreades, C. W. Forsberg, E. Greenspan, L. W. Hu and P. F. Peterson, Progress in Nuclear Energy, 77 (2014) 406-420.
[3] E. L. Compere, S. S. Kirslis, E. G. Bohlmann, F. F. Blankenship, and W. R. Grimes, Fission Product Behavior in the Molten Salt Reactor Experiment, ORNL-4865, Oak Ridge National Laboratory, Oak Ridge, TN, October 1975.
[4] N. Shrestha, B. Day, V. Utgikar, K. S. Raja, G. Fredrickson and S. Frank, ECS Transactions, 85(4) (2018) 15-23.
[5] S. Guo, N. Shay, Y. Wang, W. Zhou and J. Zhang, Journal of Nuclear Materials, 496 (2017) 197-206.
[6] H. Tang and B. Pesic. Electrochimica Acta, 119 (2014) 120-130.
[7] C.P. Fabian, V. Luca, P. Chamelot, L. Massot, C. Caravaca and G.R. Lumpkin. Journal of The Electrochemical Society, 159 (2012) F63-F67.
[8] Constantin, Virgil, Ana-Maria Popescu, and Mircea Olteanu. Journal of Rare Earths, 28(3) (2010) 428-434.
[9] C. Ryan, S. Guo, and J. Zhang. Annals of Nuclear Energy, 120 (2018) 246-252.
[10] G. Chen, Z. Shi, J. Yu, J. Xu, X. Hu, Z. Wang and B. Gao, Journal of Electrochemical Society, 162(4) (2015) C197-C204.
[11] Z. Huang, Z. Cao, G. Wang and H. Zhu, Electrochemistry, 78(6) (2010) 510-512.
[12] Bard, Allen J., et al. Vol. 2. New York: wiley, 1980.
[13] D. R. Sadoway. JOM, 53(5) (2001) 34-35.
[14] H. Yin, L. Gao, X, Zhu, X. Mao, D. Wang. Electrochimica Acta, 56 (9) (2011) 3296-3302.

[15] G. Chen, Z. Shi, J. Yu, J. Xu, X. Hu, Z. Wang and B. Gao, Journal of Electrochemical Society, 162(4) (2015) C197-C204.
[16] H. Chen, X. Jin, L. Yu, G. Z. Chen. Journal of Solid State Electrochemistry 18 (2014) 3317-3325.
[17] L. Tian, W. Huang, F. Jiang, H. Zheng et al. Electrochimica Acta, 225 (2011) 392-398.
[18] J. Thonstad, F. Nordmo, K. Vee. Electrochimica Acta, 18 (1973) 27-32.
[19] A. J. Calandar, C. E. Castellano, C. M. Ferro. Electrochimica Acta, 30(11) (1985) 1449-1454.
[20] S. Jarek, J. Thonstad. Electrochimica Acta, 32(5) (1987) 743-747.
[21] J. Vatamanu, L. Cao, O. Borodin, D. Bedrov and G. D. Smith, The Journal of Physical Chemistry Letters, 2 (2011) 2267-2272.
[22] R. S. Nicholson and I. Shain, Analytical Chemistry, 36(4) (1964) 706-723.
[23] H. Imoto, K. Ueno, N. Watanabe, 51 (10) (1978) 2822-2825.

4.11. Properties of fission products in Liquid Bi

4.11.1. Available Data Review

The activity coefficients of some actinides (U, Th, Np, Pu, Am) and fission products (Y, La, Ce, Pr, Nd, Sm, Eu, Gd, Tb, Dy, and Er) were recently summarized in reference [1] and the relationship between solubility and activity coefficient of a metal in liquid Bi is also given in the reference. The correlations between solubility and temperature for elements Be, Mg, Ca, Sr, Ba, Al, Si, Ce, Lu, Th, Ti, Zr, Hf, V, Cb, Ta, Cr, Mo, W, Mn, Fe, Ru, Os, Co, Rh, Ni, Pd, and Pt were summarized in reference [2,3]. When the solubility is low, the solution can be an infinite dilution, and the activity coefficient is non-concentration dependent and it can be calculated by using the correlation between solubility and activity coefficient that is given in reference [1]. Recently, the concentration-dependent activity coefficients of Dy, Gd, Ho, La, Lu, Nd, Tb and Tm were calculated based on CALPHAD [4]. The Bi-fission-product binary or ternary system were also investigated experimentally or theoretically using thermodynamic analysis [5,6].

4.11.2. Thermodynamic Properties of Fission Products in Liquid Bismuth by Thermodynamic Assessment

CALPHAD (CALculation of PHAse Diagrams) is a powerful method to analyze thermodynamic properties of the binary systems with fission products and bismuth. Several bismuth-fission products systems have been thermodynamically studied by the method of CALPHAD such as Bi-La [7], Bi-Lu [8], Bi-Nd (Tm) [9], Bi-Tb [10], Bi-Gd (Dy, Ho, Er) [11,12], and Bi-Tm [13]. Pr, Ce, and Er are three important fission products. Thermodynamic assessment of Bi-Pr which has never been reported before was conducted in the present study. Li et al [14] and Wang et al [15] did the thermodynamic assessments of Bi-Ce and Bi-Er, but the optimizations of the solid solutions were not considered. Thus, the Bi-Ce and Bi-Er systems were also studied in the present work with an improved optimization. In addition to the phase diagram optimization as done in available studies,

the following fundamental data was obtained in the present study: enthalpy of formation, entropy of formation, enthalpy of mixing, concentration-dependent activity coefficient and activity, and temperature-dependent solubility for all the three systems. Based on the previous studies of other lanthanides in liquid bismuth [7-13], the activity coefficients for these elements were also reported here.

4.11.2.1. Thermodynamic models

The liquid and solid solution (e.g. BCC, FCC, HCP) were described using a sub-regular solution model based on the random mixing of the constituent atoms with the Redlich-Kister formula [16]. The Gibbs energy of liquid phase can be expressed by

$$G^{liq} = \sum_{i=A,B} x_i G_i^{liq,0} + RT \sum_{i=A,B} x_i ln x_i + x_A x_B \sum_{n=0}^{m} L_n^{liq} (x_A - x_B)^n \qquad (4\text{-}168)$$

where $G_i^{liq,0}$ is the Gibbs free energy of pure component i at liquid state taken from SGTE database [17], x_i is the mole fraction of component i, R is the gas constant, T is the temperature in Kelvin. L_n^{liq} is the binary interaction parameter and can be expressed by

$$L_n^{liq} = a_n + b_n T + c_n T ln T \qquad (4\text{-}169)$$

where the coefficients a_n, b_n and c_n are the parameters that would be optimized in the present work based on experimental data using Thermo-Calc software [18].

The intermetallic compounds in the Bi-Pr, Bi-Ce, and Bi-Er binary systems were treated as stoichiometric compounds because of their narrow homogeneity [14,15]. The Gibbs free energy of these intermetallic compounds can be written by two-sublattice model [19], it was formulated as

$$G^{A_m B_n} = \frac{m}{m+n} G_A^{SER,0} + \frac{n}{m+n} G_B^{SER,0} + a + bT \qquad (4\text{-}170)$$

where m and n are the stoichiometric coefficients of the compound $A_m B_n$, $G_A^{SER,0}$ and $G_B^{SER,0}$ are the molar Gibbs free energies of the pure components A and B at their standard element reference states, respectively. a and b are the parameters to be optimized in the present work.

4.11.2.2. Available input information

Input data was needed for all the binary systems in order to develop the phase diagrams based on CALPHAD.

For the Bi-Pr system, the phase equilibria data was only measured in the Pr-rich part (up to 7 at% Bi) by Griffin et al [20] using the methods of X-ray diffraction, thermal, chemical and metallographic analyses. Yoshihara et al [21] studied the structure data of Pr_5Bi_3 and Pr_2Bi while Gambino et al [22] reported the crystal structure of Pr_4Bi_3. The solubility data for Pr in liquid Bi at the temperature range of 300 to 700 °C was determined by Schweitzer et al [23]. Regarding the results obtained by [20,21,22,23], Okamoto et al [24] published an

assessed phase diagram. In the whole composition range of Bi-Pr system, five intermetallic compounds (PrBi, $PrBi_2$, Pr_4Bi_3, Pr_5Bi_3, and Pr_2Bi) and three terminal solution phases (rhombohedral (Bi), DHCP (Pr), and BCC_A2 (Pr)) were reported. There are two eutectic reactions of the L ↔ rhombohedral (Bi) + $PrBi_2$ at 544 K and L ↔ Pr_2Bi+ BCC_A2 (Pr) at 1167 K. Also, four peritectic reactions of the L + PrBi ↔ $PrBi_2$ at 1773 K, L + PrBi ↔ Pr_4Bi_3 at 1923 K, L + Pr_4Bi_3 ↔ Pr_5Bi_3 at 1498 K, and L + Pr_5Bi_3 ↔ Pr_2Bi at 1373 K exist. The solubility of Bi in BCC_A2 (Pr) solution phase is about 0.8 at% [20], and this solution phase would be assessed using the sub-regular solution model. However, the other two terminal solution phases were treated as pure element phases because of their very limited solubility. There are several studies reporting the thermodynamic properties of Bi-Pr system. Colinet et al [25] studied the enthalpies of formation of the intermetallic compounds based on the Miedema model [26]. Borsese et al [27] determined the enthalpies of formation of PrBi and Pr_4Bi_3 at 300 K by the method of direct isoperibol calorimeter. All the data of phase equilibria [20], solubility [23] and enthalpy of formation [25,27] were used as the input information. Due to the lack of phase equilibria data, some digital data from the assessed phase diagram [24] was also used in the optimization.

For the Bi-Ce system, Vogel et al [28] firstly measured the phase-equilibrium of Bi-Ce binary system experimentally in which four stable intermetallic compounds were reported: Ce_3Bi, Ce_4Bi_3, CeBi, and $CeBi_2$. Pleasance et al [29] studied the solubility of Ce in liquid Bi. Yoshihara et al [21] investigated the whole range of Bi-Ce alloys using X-ray diffraction and metallographic methods and confirmed the first compound existing at the Ce-rich side is Ce_2Bi but not Ce_3Bi as Vogel et al [28] reported. Gschneidner et al [30] assessed the phase diagram for the Bi-Ce binary system based on the previous studies [21,28,29]. In Bi-Ce binary system, CeBi, $CeBi_2$, Ce_4Bi_3, Ce_5Bi_3, and Ce_2Bi were shown to be the stable compounds. Except for Ce_4Bi_3, which melts congruently at 2013 K, all other four stable compounds are formed through peritectic reactions: L + CeBi ↔ $CeBi_2$ at 1183 K, L + Ce_4Bi_3 ↔ CeBi at 1903 K, L + Ce_4Bi_3 ↔ Ce_5Bi_3 at 1670 K, and L + Ce_5Bi_3 ↔ Ce_2Bi at 1518 K. There are also two eutectic reactions: L ↔ rhombohedral (Bi) + $CeBi_2$ and L ↔ Ce_2Bi + BCC_A2 (Ce) reported at the temperature of 544 K and 1023 K, respectively. The Bi-Ce system consists of three terminal solution phases: rhombohedral (Bi), FCC_A1 (Ce), and BCC_A2 (Ce). The solution phase BCC_A2 (Ce) would be assessed with sub-regular solution model in the present work because of the 1 at% solubility of Bi in Ce [30]. Whereas rhombohedral (Bi), FCC_A1 (Ce) would be treated as pure element phases as the solubility of Bi inside is very limited. In addition, the enthalpies of formation of the intermetallic compounds were determined by Borzone et al [31]. In the present optimization, all the experimental data [21,28,29,31] discussed above was used as the input information. Additionally, due to the lack of the phase information beyond 80 at% of Ce from experiments, some digital data was picked up from the assessment by Gschneidner et al [30] for a better optimization.

For the Bi-Er system, Abulkhaev has drawn a phase diagram using results of DTA, X-ray phase analysis, and microstructural analysis [32], which was reproduced by H. Okamoto [33]. In the Bi-Er binary system, two stable intermetallic compounds: ErBi and Er_5Bi_3 exist. There are two eutectic reactions: L ↔ rhombohedral (Bi) + ErBi at 542 K and L ↔ Er_5Bi_3 + HCP_A3 (Er) at 1434 K and one peritectic reaction: L + ErBi ↔ Er_5Bi_3 at 1700 K. ErBi congruently melts at the temperature of 2080 K. Two terminal solution phases: rhombohedral (Bi) and HCP_A3 (Er) exist in this binary system and HCP_A3 (Er) would be assessed using the sub-regular solution model in the present study. The enthalpy of

formation of ErBi was measured by Borzone et al [34] using direct calorimetry method. Besides, enthalpies of formation of ErBi and Er_5Bi_3 were also determined by EMF method [35,36]. All the data collected was used for the optimization.

4.11.2.3. Results and discussion

Based on the available input data, the evaluation of the thermodynamic parameters was carried out by using the PARROT module in the Thermo-Calc software [37]. The optimization process in the Thermo-Calc software was realized by minimizing the sum of squares of the differences between the experimental values and computed ones. Each piece of the input information was given a certain weight based on the uncertainty of the input data. The interaction parameters were developed through carefully assessing the phase relations in the binary systems. The step by step optimization was employed until the output information including phase diagram agreed well with the input ones. The final thermodynamic parameters and the Gibbs free energy expressions for different phases can be obtained after the optimization, then the phase diagrams can be calculated accordingly in the POLY module of Thermo-Calc. Thermodynamic properties such as enthalpy of formation, entropy of formation, enthalpy of mixing of liquid, activity coefficient and activity can also be obtained based on the assessed Gibbs free energy expressions of different phases.

4.11.2.3.1. Phase diagram development

The calculated phase diagram of Bi-Pr binary system by the sub-regular solution model and two sub-lattice model is shown in *Figure 4-139*. The figure shows that the assessed phase diagram is in good agreement with the literature data [20,23,24]. The calculated compositions and temperatures for the invariant reactions and the literature data are listed in Table 4-26 which also shows a great consistence. The interaction parameters were developed by assessing the phase relations in the Bi-Pr binary system based on the calculated and experimental data of phase diagram and thermodynamic properties. The optimized parameters of thermodynamic models are shown in Table 4-27.

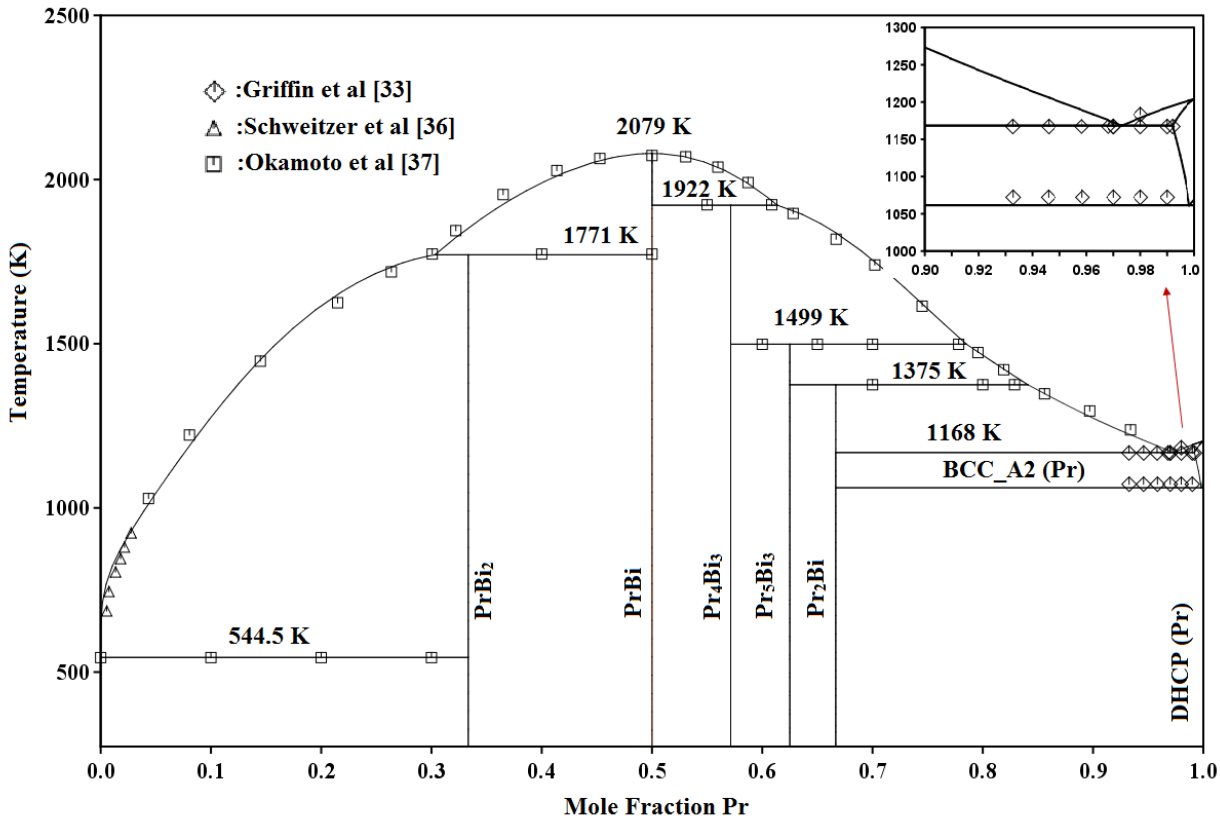

Figure 4-139.Calculated Bi-Pr phase diagram compared with literature data [20,23,24].

Table 4-26.Invariant reactions in Bi-Pr binary system.

Invariant Reaction	Reaction Type	x_{Pr}^{L}	T/K	Ref.
L ↔ rhombohedral (Bi) + $PrBi_2$	Eutectic	0.00	544	[24]
		5.2E-6	544.5	This Work
L + PrBi ↔ $PrBi_2$	Peritectic	~0.30	1773	[24]
		0.3031	1771	This Work
L + PrBi ↔ Pr_4Bi_3	Peritectic	~0.61	1923	[24]
		0.6137	1922	This Work
L + Pr_4Bi_3 ↔ Pr_5Bi_3	Peritectic	~0.78	1498	[24]
		0.7851	1499	This Work
L + Pr_5Bi_3 ↔ Pr_2Bi	Peritectic	~0.83	1373	[24]
		0.8410	1375	This Work
L ↔ Pr_2Bi+ BCC_A2 (Pr)	Eutectic	~0.97	1167	[20]
		0.9730	1168	This Work

Table 4-27. Thermodynamic parameters of the Bi-Pr system obtained by CALPHAD method.

Phase	Thermodynamic Parameters (J/mol)
Liquid (Bi, Pr)	$L_0^{liq} = -7956.29 - 789.84T + 83.32Tln(T)$
	$L_1^{liq} = -2015.64 + 166.08T$
	$L_2^{liq} = 1061.90 - 69.63T$
BCC, formula (Bi, Pr)	$L_0^{BCC} = -37.37 + 151.00T$
	$L_1^{BCC} = -152.31 + 337.21T$
$PrBi_2$	$G^{PrBi_2} = -78697.64 - 5.92T + 0.3333G_{Pr}^{SER,0} + 0.6667G_{Bi}^{SER,0}$
PrBi	$G^{PrBi} = -97648.70 - 7.56T + 0.5000G_{Pr}^{SER,0} + 0.5000G_{Bi}^{SER,0}$
Pr_4Bi_3	$G^{Pr_4Bi_3} = -92876.62 - 8.33T + 0.5714G_{Pr}^{SER,0} + 0.4286G_{Bi}^{SER,0}$
Pr_5Bi_3	$G^{Pr_5Bi_3} = -88136.16 - 4.64T + 0.6250G_{Pr}^{SER,0} + 0.3750G_{Bi}^{SER,0}$
Pr_2Bi	$G^{Pr_2Bi} = -81399.78 - 2.82T + 0.6667G_{Pr}^{SER,0} + 0.3333G_{Bi}^{SER,0}$

Figure 4-140 shows the comparison between the calculated Bi-Ce phase diagram and the available literature data [21,28,29,30] and they agree well with our assessed phase diagram. The comparisons of compositions and temperatures in the calculated invariant reactions with the experimental data for Bi-Ce system are shown in Table 4-28, which shows the accuracy of our optimization. The thermodynamic parameters obtained are given in Table 4-29.

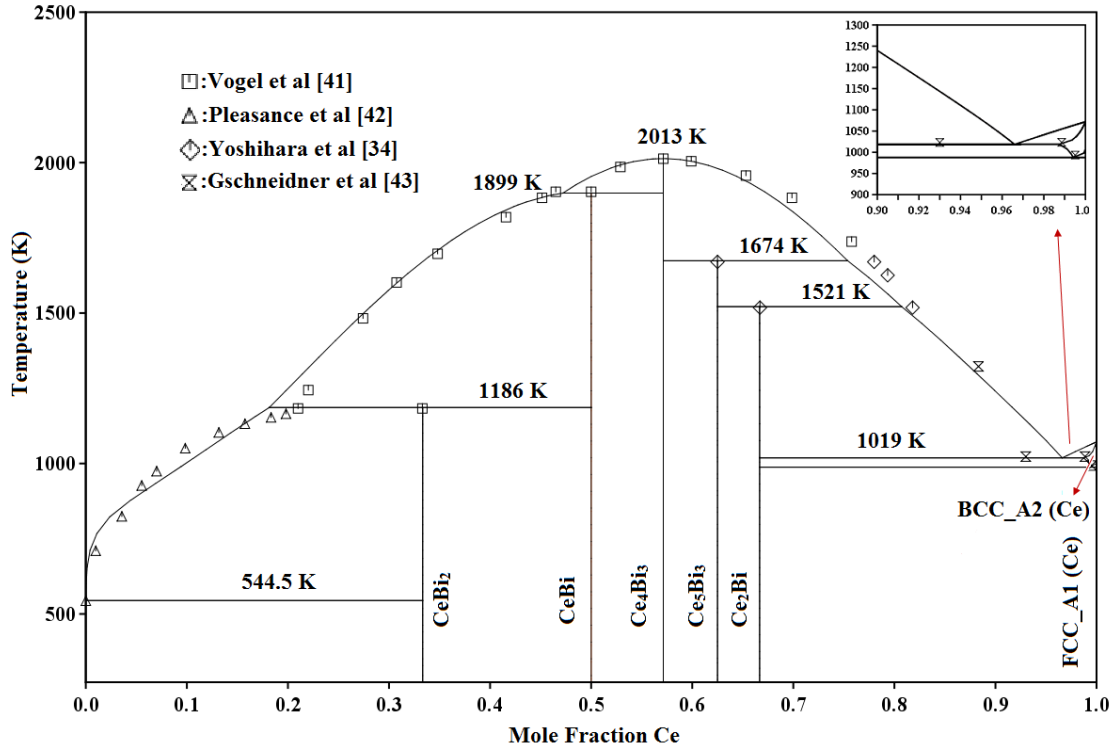

Figure 4-140. Calculated Bi-Ce phase diagram compared with literature data [21,28,29,30].

Table 4-28. Invariant reactions in Bi-Ce binary system.

Invariant Reaction	Reaction Type	x_{Ce}^{L}	T/K	Ref.
L ↔ rhombohedral (Bi) + $CeBi_2$	Eutectic	~0.000	544	[29]
		7.5E-5	544.5	This Work
L + CeBi ↔ $CeBi_2$	Peritectic	~0.21	1183	[28]
		0.1815	1186	This Work
L + Ce_4Bi_3 ↔ CeBi	Peritectic	~0.465	1903	[28]
		0.4721	1899	This Work
L + Ce_4Bi_3 ↔ Ce_5Bi_3	Peritectic	~0.78	1670	[21]
		0.7537	1674	This Work
L + Ce_5Bi_3 ↔ Ce_2Bi	Peritectic	~0.818	1518	[21]
		0.8072	1521	This Work
L ↔ Ce_2Bi+ BCC_A2 (Ce)	Eutectic	~0.93	1023	[30]
		0.9659	1019	This Work

Table 4-29. Thermodynamic parameters of the Bi-Ce system obtained by CALPHAD method

Phase	Thermodynamic Parameters (J/mol)
Liquid (Bi, Ce)	$L_0^{liq} = -237286.39 + 6.19T$
	$L_1^{liq} = 3681.43$
	$L_2^{liq} = 46794.67$
BCC, formula (Bi, Ce)	$L_0^{BCC} = -2674.67$
	$L_1^{BCC} = 615475.61$
	$L_2^{BCC} = 441332.95$
$CeBi_2$	$G^{CeBi_2} = -77578.29 + 6.20T + 0.3333G_{Ce}^{SER,0} + 0.6667G_{Bi}^{SER,0}$
CeBi	$G^{CeBi} = -114315.74 + 15.50T + 0.5000G_{Ce}^{SER,0} + 0.5000G_{Bi}^{SER,0}$
Ce_4Bi_3	$G^{Ce_4Bi_3} = -101540.52 + 8.88T + 0.5714G_{Ce}^{SER,0} + 0.4286G_{Bi}^{SER,0}$
Ce_5Bi_3	$G^{Ce_5Bi_3} = -91762.01 + 8.17T + 0.6250G_{Ce}^{SER,0} + 0.3750G_{Bi}^{SER,0}$
Ce_2Bi	$G^{Ce_2Bi} = -81420.73 + 6.36T + 0.6667G_{Ce}^{SER,0} + 0.3333G_{Bi}^{SER,0}$

For Bi-Er system, the comparison between our assessed phase diagram and the experimental data in literature [32] is shown in Figure 4-141. It shows that the liquidus and invariant reactions boundaries are nearly identical to the experimental data. All the calculated invariant reactions in the Bi-Er are given in Table 4-30. In addition, the experimental invariant reactions are also listed and compared in Table 4-30 where a good consistence is obtained. The evaluated parameters of thermodynamic models and Gibbs free energy expressions for Bi-Er system are shown in

Table 4-31.

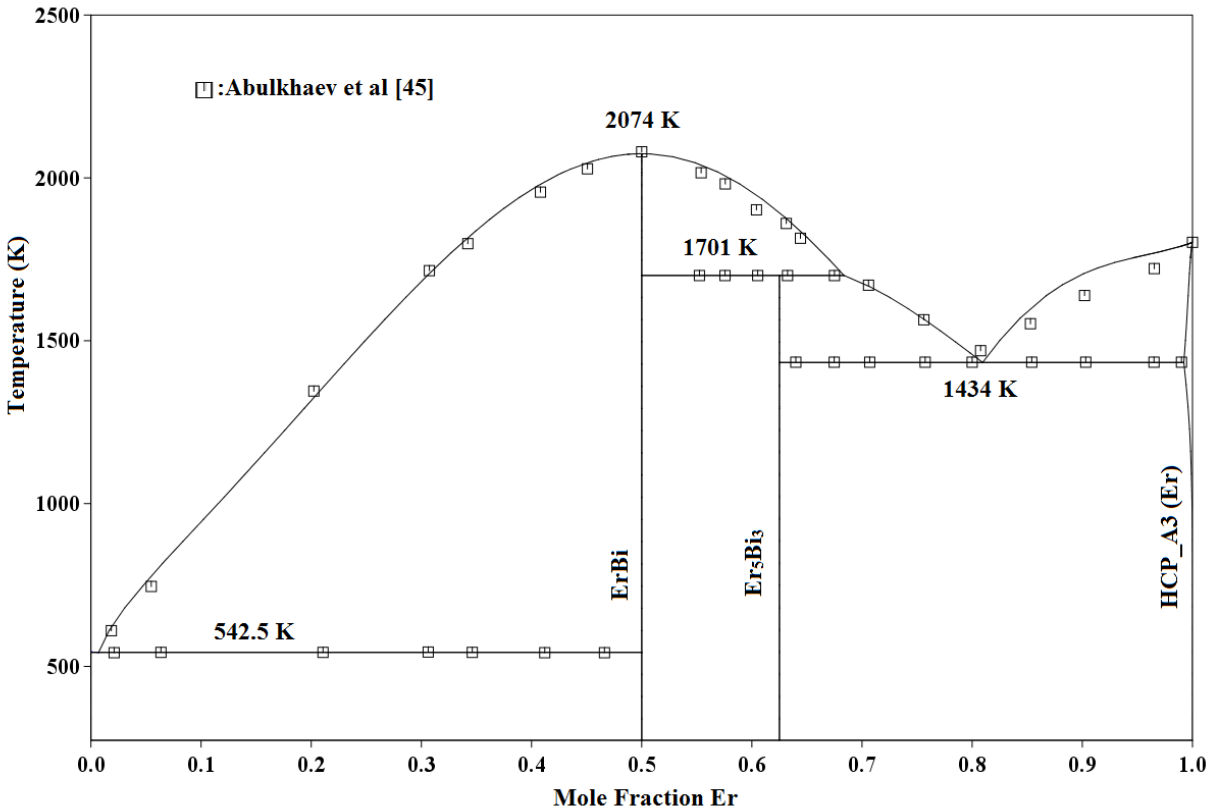

Figure 4-141. Calculated Bi-Er phase diagram compared with literature data [32].

Table 4-30. Invariant reactions in Bi-Er binary system.

Invariant Reaction	Reaction Type	x_{Er}^{L}	T/K	Ref.
L ↔ rhombohedral (Bi) + ErBi	Eutectic	~8.4E-3	542	[32]
		8.6E-3	542	This Work
L + ErBi ↔ Er_5Bi_3	Peritectic	~0.68	1700	[32]
		0.6832	1701	This Work
L ↔ Er_5Bi_3 + HCP_A3 (Er)	Eutectic	~0.80	1434	[32]
		0.8078	1434	This Work

Table 4-31. Thermodynamic parameters of the Bi-Er system obtained by CALPHAD method.

Phase	Thermodynamic Parameters (J/mol)
Liquid (Bi, Er)	$L_0^{liq} = -188097.29$
	$L_1^{liq} = 5429.67$
	$L_2^{liq} = 48809.49$
	$L_3^{liq} = -16792.89$
HCP, formula (Bi, Er)	$L_0^{BCC} = -104311.13$
ErBi	$G^{ErBi} = -80350.02 + 1.93T + 0.5000G_{Er}^{SER,0} + 0.5000G_{Bi}^{SER,0}$
Er_5Bi_3	$G^{Er_5Bi_3} = -66485.80 + 2.54T + 0.6250G_{Er}^{SER,0} + 0.3750G_{Bi}^{SER,0}$

4.11.2.3.2. Thermodynamic study

<u>Heat capacity, enthalpy of formation and entropy of formation</u>

In the optimization, Gibbs free energy of formation of intermetallic compounds is written by equation (4-171) according to the equation (4-170)

$$G_f = a + bT = \Delta H_f - T\Delta S_f \quad (4\text{-}171)$$

where ΔH_f and ΔS_f are enthalpy of formation and entropy of formation, respectively. It can be known from equation (4-171) that a and b are corresponding to ΔH_f and $-\Delta S_f$, and the obtained ΔH_f and ΔS_f in the study are temperature-independent. Thus, heat capacity is 0 for all these three binary systems.

The optimized results for a and b in equations (4-170) and (4-171) give the values of enthalpy of formation and entropy of formation. Enthalpies of formation of the intermetallic compounds in Bi-Pr, Bi-Ce, and Bi-Er systems together with the results reported in literature are listed in Tables 4-32, 4-33, and 4-34 respectively. The exothermic enthalpies indicate the heat release when forming these compounds. It can be known from the quantitative comparison with the literature data that the agreement is satisfactory on the whole. Based on the comparison of these three binary systems, a fairly monotonic decrease was found on the value of the Gibbs energy of formation with the increasing atomic number of the lanthanide. The similar phenomenon is also found by other investigators [25]. It is also found that the value of Gibbs energy of formation of the intermetallic compound at equiatomic composition is the largest in one binary system. It means the biggest change of Gibbs energy accompanying the formation of a substance happens at equiatomic composition.

Table 4-32. Enthalpies of formation of the intermetallic compounds in Bi-Pr system.

Composition	x_{Pr}	ΔH_f (kJ/mol)		
		Colinet et al. [25]	Borsese et al. [27]	This Work
$PrBi_2$	0.333	-79	-	-78.698
PrBi	0.500	-97	-100	-97.649
Pr_4Bi_3	0.571	-94	-94	-92.877
Pr_5Bi_3	0.625	-88	-	-88.136
Pr_2Bi	0.667	-81	-	-81.400

Table 4-33. Enthalpies of formation of the intermetallic compounds in Bi-Ce system

Composition	x_{Ce}	ΔH_f (kJ/mol)		
		Colinet et al. [25]	Borzone et al. [31]	This Work
$CeBi_2$	0.333	-84	-77.5	-77.578
CeBi	0.500	-102	-114.7	-114.32
Ce_4Bi_3	0.571	-99	-101.3	-101.54
Ce_5Bi_3	0.625	-92	-91.7	-91.762
Ce_2Bi	0.667	-84	-81.6	-81.421

Table 4-34. Enthalpies of formation of the intermetallic compounds in Bi-Er system.

Compositon	x_{Er}	ΔH_f (kJ/mol)				
		Colinet et al. [25]	Petrashgkevich et al [35]	Borzone et al [34]	Yamshchikov et al [36]	This Work
ErBi	0.500	-75	-109	-90	-103	-80.350
Er_5Bi_3	0.625	-69	≤ -81	-	≤ -77	-66.486

The entropies of formation of the intermetallic compounds in Bi-Pr, Bi-Ce, and Bi-Er systems are given in Table 4-35. There is no available literature data for comparison. However, when considering the values reported for other lanthanides-bismuth binary systems [7-15], our optimization gave realistic and reasonable values for this property.

Table 4-35. Entropies of formation of intermetallic compounds for Bi-Pr, Bi-Ce, and Bi-Er systems.

Compositon	x (fission products)	ΔS_f (J/mol)
$PrBi_2$	0.333	5.92
PrBi	0.500	7.56
Pr_4Bi_3	0.571	8.33
Pr_5Bi_3	0.625	4.64
Pr_2Bi	0.667	2.82
$CeBi_2$	0.333	-6.20
CeBi	0.500	-15.50
Ce_4Bi_3	0.571	-8.88
Ce_5Bi_3	0.625	-8.17
Ce_2Bi	0.667	-6.36
ErBi	0.500	-1.93
Er_5Bi_3	0.625	-2.54

Enthalpy of mixing of liquid

Figure 4-142, Figure 4-143, and Figure 4-144 show the enthalpies of mixing of the liquid phase for Bi-Pr, Bi-Ce, and Bi-Er systems respectively at 2500 K in comparison with other literature. The presented thermodynamic data agrees well with the values reported previously. It also can be seen enthalpy of mixing changes with concentration and which decreases firstly and then increases with the increment of concentration. The calculation of enthalpies of mixing at different concentrations greatly extends the experimental data and will provide abundant data for the future study.

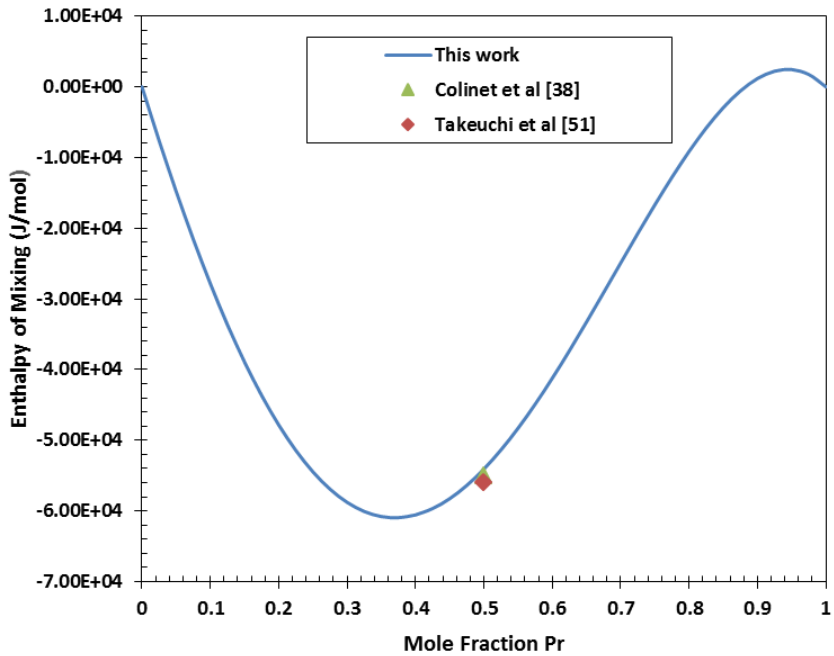

Figure 4-142. The calculated enthalpy of mixing of the liquid phase in Bi-Pr system compared with literature data [25,38].

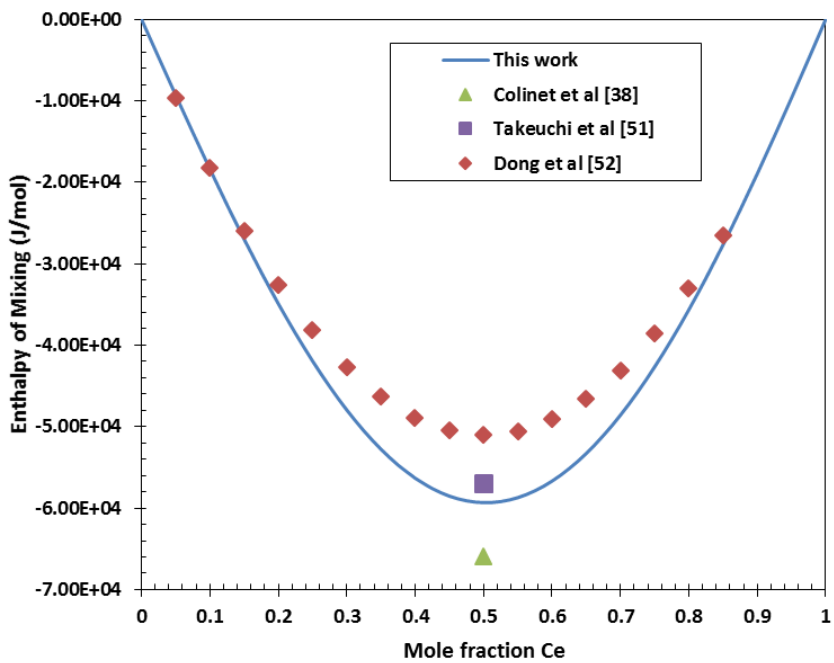

Figure 4-143. The calculated enthalpy of mixing of the liquid phase in Bi-Ce system compared with literature data [25,38,39].

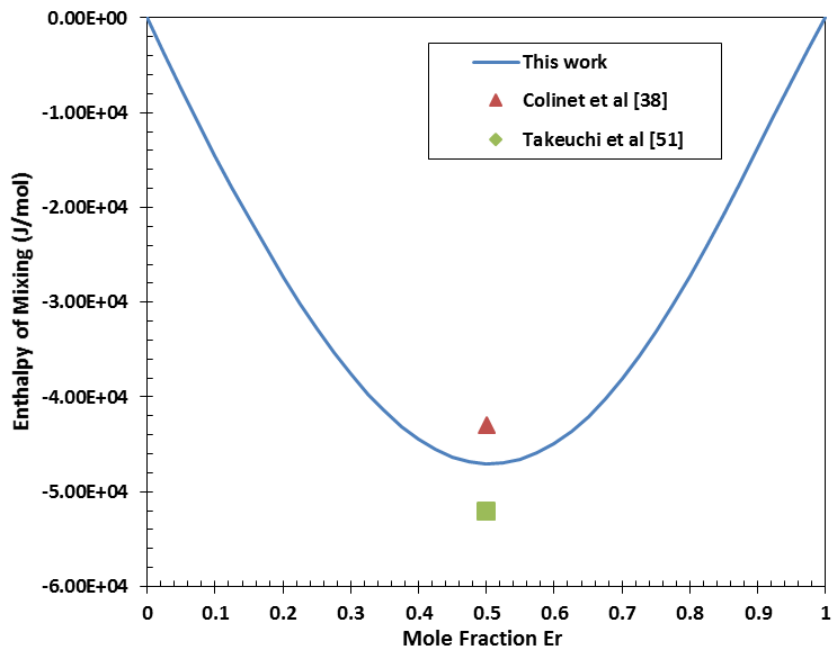

Figure 4-144. The calculated enthalpy of mixing of the liquid phase in Bi-Er system compared with literature data [25,38].

Activity coefficient and activity

Based on equation (4-168), the molar excess Gibbs free energy can be written by

$$G_{excess} = x_A x_B \sum_{n=0}^{m} L_n^{liq} (x_A - x_B)^n \tag{4-172}$$

Then the activity coefficient of A, for example, can be calculated by

$$RT ln\gamma_A = \left(\frac{\partial G_{excess}}{\partial n_A}\right)_{n_B,p,T} \tag{4-173}$$

The activity coefficients of Pr in liquid bismuth at different concentrations under the temperatures of 873, 923 and 973 K are shown in Figure 4-145. For all the calculations of the activity coefficients in this study, the reference states were supercooled states. Figure 4-145 shows that the activity coefficient of Pr in liquid bismuth increases with the increment of concentration and temperature. The value of the activity coefficient of Pr in liquid bismuth is extremely small and in the order of magnitude of 10^{-13} to 10^{-11} at the temperature range of 873 K to 973 K. It is a little smaller than the value with the order of magnitude of 10^{-12} at the temperature of 823 K reported by Zhang et al [40] previously. However, if considering the value of activity coefficient is extremely small at this concentration and temperature ranges, this discrepancy is acceptable.

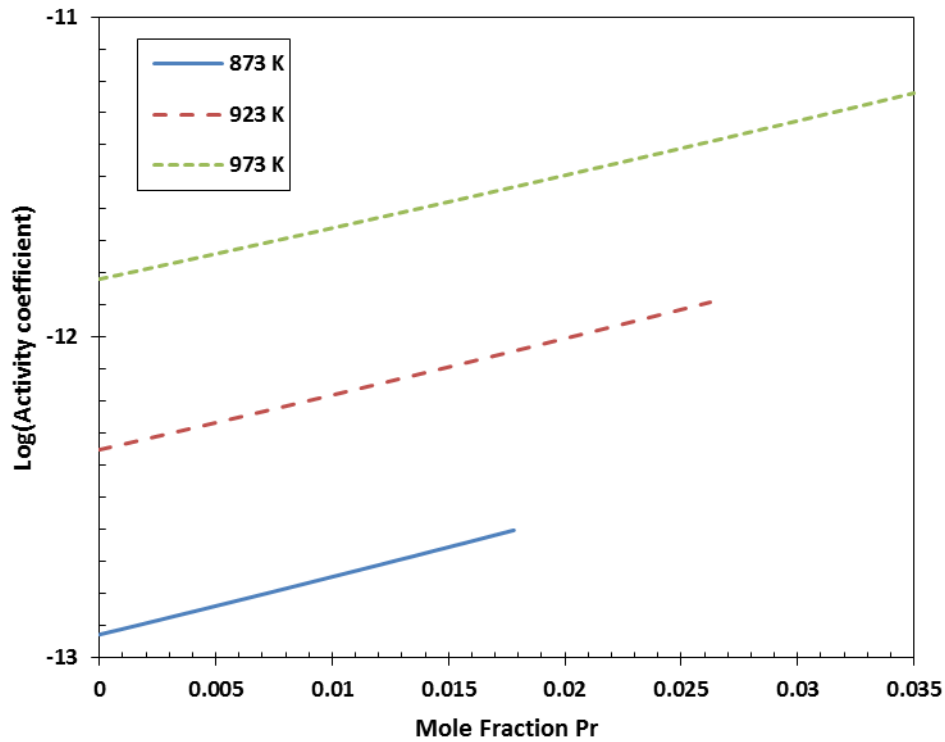

Figure 4-145. Activity coefficient of Pr in liquid Bi at different concentrations under three temperatures: 873, 923, and 973 K.

Figure 4-146 presents the activity coefficient of Ce in liquid bismuth at different concentrations under the temperatures of 873, 923 and 973 K. It shows a slight decrease with the increase of mole fraction of Ce in liquid bismuth at low concentration. The value of activity coefficients starts to increase gradually at the mole fraction around 0.02 at%. In addition, temperature also plays an important role on the activity coefficient, and the value of which at higher temperature is larger than the one at lower temperature for the same concentration. The calculated activity coefficients at the temperatures of 823 K and 873 K are compared with the literature values reported before and shown in Table 4-36, from which it can be seen the calculated values are close to the literature data. It verified the reliability of our calculated activity coefficients at different concentrations and temperatures.

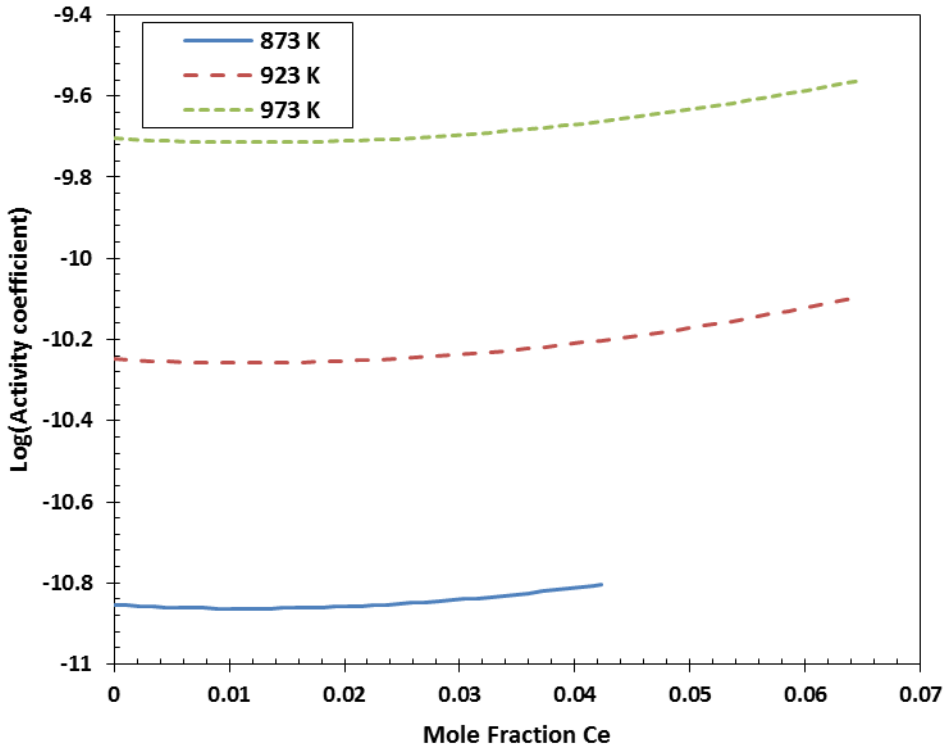

Figure 4-146. Activity Coefficients of Ce in liquid Bi at different concentrations under three temperatures: 873, 923, and 973 K.

Table 4-36. Comparison between the calculated activity coefficients and literature values for Bi-Ce system.

Temperature	Concentration	Log(activity coefficient)	Ref.
873 K	Dilution	-11.03	[41]
	Dilution	-11.31	[40]
	0~4.23 at%	-10.85~-10.80	This Work
923 K	Dilution	-10.32	[41]
	Dilution	-10.61	[40]
	0~6.42 at%	-10.25~-10.10	This Work

The activity coefficients of Er in liquid bismuth at different concentrations under the temperatures of 873, 923 and 973 K were also investigated in the present work. Figure 4-147 presents our calculated results of the activity coefficients of Er in liquid bismuth at the concentration range of 0 to 8 at%. It can be seen the activity coefficient increases with the increment of mole fraction of Er in liquid bismuth and temperature as well. The calculated activity coefficients are compared with the literature data in Table 4-37, which shows an excellent agreement.

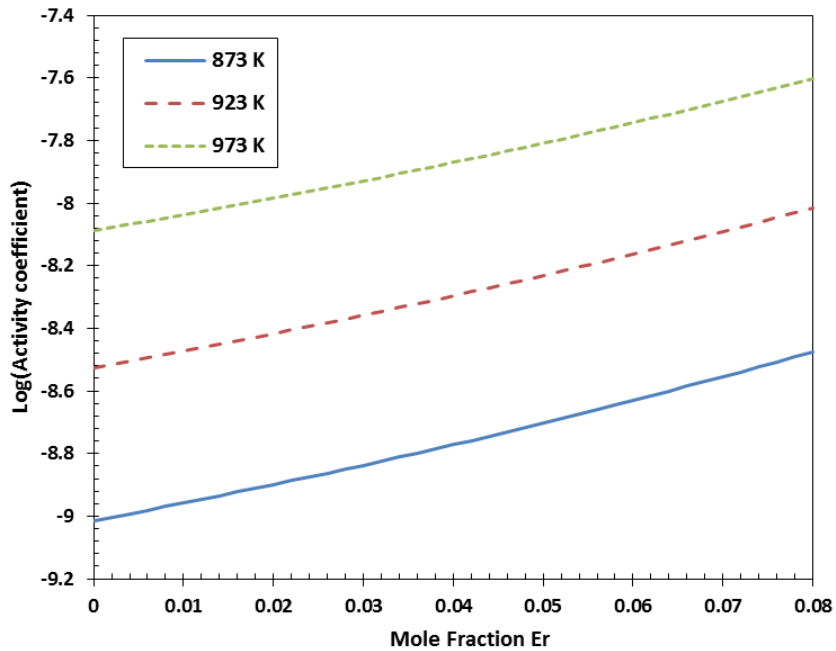

Figure 4-147. Activity Coefficients of Er in liquid Bi at different concentrations under three temperatures: 873, 923, and 973 K.

Table 4-37. Comparison between the calculated activity coefficients and literature values for Bi-Er system.

Temperature	Concentration	Log(activity coefficient)	Ref.
873 K	Dilution	-9.21	[42]
	Dilution	-9.14	[43]
	0~8 at%	-9.01~-8.47	This Work
923 K	Dilution	-8.62	[42]
	Dilution	-8.73	[43]
	0~8 at%	-8.52~-8.02	This Work
973 K	Dilution	-8.08	[42]
	Dilution	-8.37	[43]
	0~8 at%	-8.09~-7.60	This Work

Figures 4-145, 4-146, and 4-147 show that the dependence of the activity coefficient of the element on its concentration is different for different element. Based on equations (4-172) and (4-173), it can be found that interaction parameter L_i^{liq} and maximum power m affect

the concentration-dependence of the activity coefficient. L_i^{liq} works as a constant and is independent on the mole fraction of species. However, the maximum power m sufficiently to fit a system may be different for different cases in the practical optimization. It explains why the dependence of the activity coefficients on the concentrations for Bi-Pr, Bi-Ce, and Bi-Er is different.

Activity is product of activity coefficient and mole fraction

$$a = \gamma x \tag{4-174}$$

Because of the similar patterns of the activity coefficients at three temperatures for each lanthanide, here only the activities at 973 K were plotted and analyzed to avoid the redundancy. The activities of the three elements considered are shown in Figure 4-148. It is shown that under these concentration ranges calculated, the activity is far away from the Raoult's law [44,45], which should be a unit-slope diagonal line in the coordinate system. It indicates dramatically negative deviations of these systems from the ideal ones. The interactions between unlike atoms should be therefore significantly different from these between like atoms. Generally more energy should be released for the attraction set up between unlike atoms than that needed to break the original atom pairs, which results in an exothermic enthalpy of mixing. This conclusion is consistent with the negative enthalpy of mixing in Figures 4-142, 4-143, and 4-144.

If the low concentration part is focused, the activities show linear relationships up to concentrations of 0.8%, 2.0%, and 1.6%, respectively, for the Ce, Pr, and Er. The phenomenon can be explained by Henry's law [46], which states

$$P_{Ln} = x_{Ln} K_{Ln} \tag{4-175}$$

where P_{Ln} is the partial pressure of the lanthanide, K_{Ln} is the Henry's constant. At very dilute solute, K_{Ln} is related to the vapor pressure of the pure lanthanide by a limiting activity coefficient

$$\gamma_{Ln}^{\infty} = K_{Ln}/P_{Ln}^{0} \tag{4-176}$$

P_{Ln}^{0} is the vapor pressure of pure lanthanide, it indicates an almost constant activity coefficient and a linear relationship between activity and concentration. However, beyond these concentrations, neither Raoult's law nor Henry's law is followed. The activity increases faster than a linear relationship and shows a dependence on the concentration. Further studies theoretically or experimentally are needed to understand the properties thoroughly.

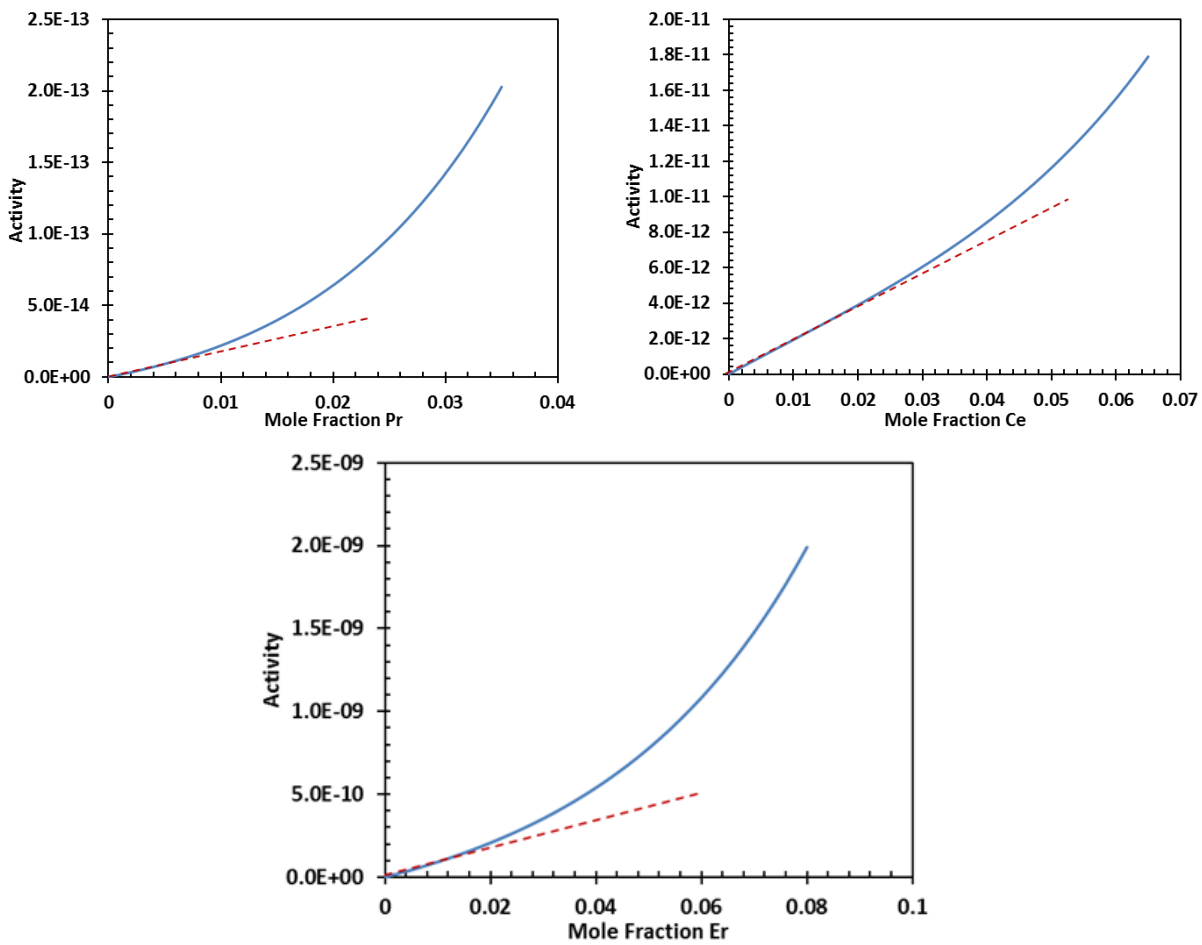

Figure 4-148. Activity of Pr, Ce, and Er in liquid bismuth at the temperature of 973 K. Solid line is the activity at different concentration while the dashed line is the linear relationship of the activity with concentration at dilution.

<u>Solubility</u>

The solubility of Pr, Ce, and Er in liquid bismuth at the temperature range of 873 K to 973 K was also studied in this work. Generally, the solubility S in the unit of mole fraction can be expressed by [47]

$$logS = k_1 + k_2/T \tag{4-177}$$

where k_1 and k_2 are constants. The data of solubility was selected from the calculated phase boundary where $PrBi_2$ and liquid coexist in Bi-Pr system, $CeBi_2$ and liquid coexist in Bi-Ce system, and ErBi and liquid coexist in Bi-Er system. Figure 4-149 shows the calculated solubility of Pr, Ce, and Er in liquid bismuth together with the fitting curve, then the correlation between $logS$ and $1/T$ is given in Table 4-38. The correlation obtained in this study can bring much convenience to other investigators to get the solubility at the desired temperature.

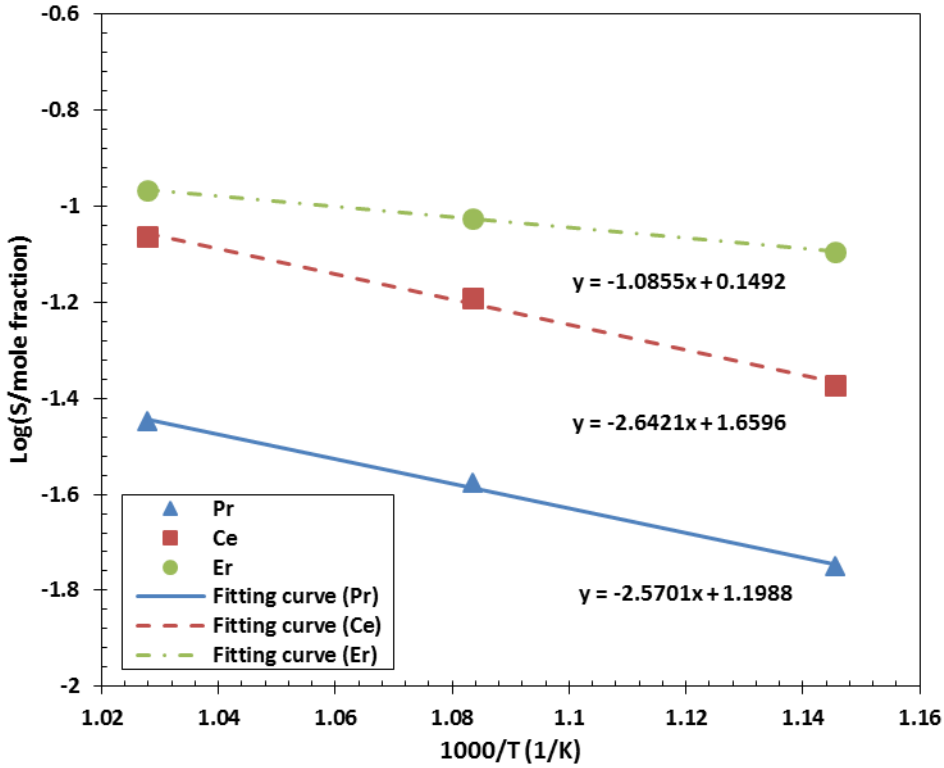

Figure 4-149. Calculated solubility of Pr, Ce, and Er in liquid bismuth with the fitting curve.

Table 4-38. Solubility of Pr, Ce, and Er in liquid bismuth.

Elements	Solid in equilibrium with the liquid	Fitting correlation
Pr	$PrBi_2$	$logS = 1.1988 - 2570.1/T$
Ce	$CeBi_2$	$logS = 1.6596 - 2642.1/T$
Er	ErBi	$logS = 0.1492 - 1085.5/T$

4.11.3. Concentration-dependent Activity Coefficients of Lanthanides in Liquid Bismuth

Based on the computed parameters published for the expression of L_i^{liq} [7-13], the activity coefficients of Dy, Gd, Ho, La, Lu, Nd, Tb, and Tm in liquid bismuth were calculated by equation (4-173). In these references, L_i^{liq} was temperature-dependent and can be expressed with equations (4-178) by assuming that the excess heat capacity is zero [48].

$$L_i^{liq} = a_i + b_i T \qquad (4\text{-}178)$$

where a_i and $b_i$are constants. Given the finding of that excess Gibbs energy is linearly temperature-dependent in the experiment [49], this common assumption should be close to the real situation. The substitution of L_i^{liq} in Eq. (5) to Eq (3) reveals ΔG_{excess} is linearly temperature-dependent, corresponding to the expression of $\Delta G_{excess} = \Delta H_{mix} - \Delta S_{excess} T$.

Thus, ΔH_{mix} and ΔS_{excess} can be considered as constants at a given concentration, and the relationship between the activity coefficient and temperature can be expressed by

$$ln\gamma = \frac{\Delta H_{mix}}{RT} - \frac{\Delta S_{excess}}{R} = a(x) + \frac{b(x)}{T} \quad (4\text{-}179)$$

where $a(x)$ and $b(x)$ are concentration-dependent variables. Based on the reported expressions for L_i^{liq} [7-13], the expressions of $a(x)$ and $b(x)$ can be obtained which are shown in Table 4-39. The correlations in Table 4-39 can be used to evaluate the activity coefficients of these eight lanthanides in liquid bismuth at concentrations below solubility limit.

Table 4-39. Correlations for the activity coefficients of lanthanides in liquid bismuth.

Element	$ln\gamma = a(x) + \frac{b(x)}{T}$	
	$a(x)$	$b(x)$
Dy	$0.219389x^5 + 5.27833x^4 - 15.7205x^3 + 15.5663x^2 - 6.18138x + 0.837864$	$120098x^5 - 300974x^4 + 231603x^3 - 60666.7x^2 + 29930.5x - 19990.7$
Gd	$-11.1026x^5 + 41.0031x^4 - 59.3434x^3 + 41.2856x^2 - 13.0403x + 1.19763$	$115468x^5 - 305701x^4 + 273066x^3 - 114351x^2 + 54968.9x - 23450.6$
Ho	$-12.3558x^5 + 45.0757x^4 - 64.071x^3 + 43.8425x^2 - 13.9959x + 1.50447$	$69284.8x^5 - 144059.x^4 + 58422.4x^3 + 19092.5x^2 + 16359.7x - 19100.4$
La	$4.57907x^3 - 9.96467x^2 + 6.19213x - 0.806531$	$88108.5x^4 - 232720x^3 + 176307x^2 - 6888.48x - 24807.3$
Lu	$3.3197x^2 - 6.6394x + 3.3197$	$49045x^4 - 134680x^3 + 105114x^2 - 2367.81x - 17111$
Nd	$31.7537x^4 - 84.6764x^3 + 75.5352x^2 - 24.0558x + 1.44335$	$76978.6x^5 - 197258x^4 + 150830x^3 - 42278.1x^2 + 36204x - 24476.8$
Tb	$11.5468x^4 - 30.7914x^3 + 27.9047x^2 - 9.62232x + 0.962232$	$55280.3x^4 - 140197x^3 + 92097.7x^2 + 15275.4x - 22456.1$
Tm	$14.4335x^4 - 37.7195x^3 + 36.1418x^2 - 16.859x + 4.00325$	$57012.3x^4 - 152995x^3 + 116039x^2 - 1142.89x - 18913.8$

Figure 4-150 presents the calculated results of activity coefficients of Dy, Gd, Ho, La, Lu, Nd, Tb, and Tm in liquid bismuth at the temperatures of 973, 923, and 873 K. Equations (4-172) and (4-173) shows molar excess Gibbs energy and the activity coefficient will keep constant with the increasing mole fraction when the solute (lanthanides) reaches the solubility limit and intermetallic compounds were formed between bismuth and solute

(lanthanides). The solubility limit of the lanthanides studied is provided in Table 4-40. The activity coefficient was calculated at the concentration up to solubility limit in the study. Figure 4-150 indicates that activity coefficients of most of those elements except Lu and Tb increase with the increment of mole fraction. Activity coefficients of Lu and Tb decrease initially and then increase with the increasing mole fraction. Good linearity between the logarithmic activity coefficient and the mole fraction was observed for Dy, Gd, and Nd at all temperatures, as shown in Figure 4-150.

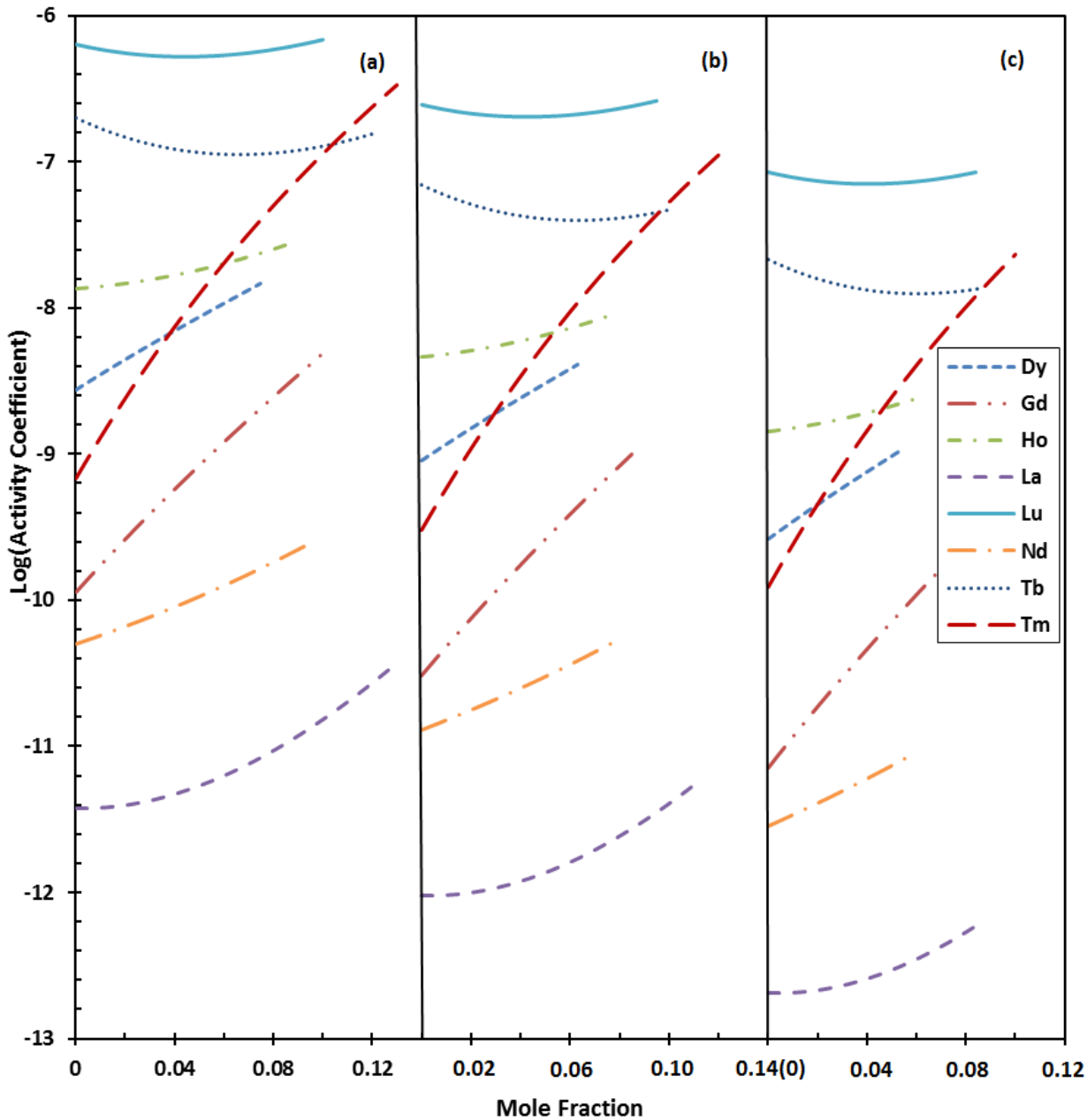

Figure 4-150.Relationship between logarithms of activity coefficient and mole fraction of lanthanides in liquid bismuth at the temperatures of 973 K (a), 923 K (b), and 873 K (c).

Table 4-40. Solubility limit of lanthanides in liquid bismuth at the temperatures of 873 K, 923 K, and 973 K.

Ref.	Element	Solubility limit (mole fraction %)		
		873 K	923 K	973 K
[12]	Dy	5.3	6.3	7.5
[11]	Gd	7.0	8.5	10.0
[11]	Ho	6.0	7.5	9.0
[7]	La	8.7	11.0	13.0
[8]	Lu	8.4	9.5	10.0
[9]	Nd	5.8	8.0	9.5
[10]	Tb	8.5	10.0	12.0
[9]	Tm	10.0	12.0	13.0

Two parameters influencing the concentration-dependence of the activity coefficient are interaction parameter L_i^{liq} and maximum power m in equation (4-172) Obviously, L_i^{liq} is independent on the mole fraction of species. It works as a constant term affecting the relationship between the activity coefficient and concentration at a given temperature. However, the value of maximum power m required to characterize a system can be different to fit a system in the practical optimization. These two factors explain why the variation trends of activity coefficients for different elements are different in Figure 4-150. The difference on the value of maximum power m for different cases determines that there is no common definite correlation to express the relationship between the activity coefficient and concentration for all the elements studied.

Figure 1 also shows the important role of temperature on the value of the activity coefficient. For all of these eight lanthanides in liquid bismuth, the mixing enthalpy of liquid decreases with the mole fraction of lanthanides in bismuth at concentrations below solubility. As a result, the value of ΔH_{mix} or b in equation (4-179) is negative. That is why activity coefficients of these lanthanides in liquid bismuth at a higher temperature appear larger value.

The Calculated activity coefficients of Dy, Gd, Ho, La, Lu, Nd, Tb, and Tm in liquid bismuth at the concentration up to its solubility limit are summarized and compared with the available literature data in Tables 3 to 5, respectively. Considering activity coefficients of these elements are very small, the calculated results should be reasonable and acceptable if the calculated activity coefficients are at the same order of magnitude as the published literature data. Table 4-41 to

Table 4-43 show that the calculated activity coefficients of Dy, Gd, Ho, La, and Nd in liquid bismuth are in good agreement with the values reported by others. The overestimated activity coefficient of terbium (Tb) may be attributed to the not very good optimized

parameters for L_i^{liq} [10]. Based on the authors' knowledge, there was no reported data for Lu and Tm in liquid bismuth.

Table 4-41. Activity coefficients of lanthanides in liquid bismuth at 873 K.

Element	Mole fraction	Log(activity coefficient)	Studies
Dy	0~0.053	-9.58~-8.98	This study
	0.005	-9.85	[50]
	0.005	-10.16	[51]
Gd	0~0.070	-11.15~-9.78	This study
	0.0006	-10.12	[52]
	0.005	-10.18	[51]
	Dilution	-10.4	[53]
	Dilution	-10.06	[54]
	Dilution	-9.78	[55]
	Dilution	-10.10	[56]
Ho	0~0.060	-8.85~-8.62	This study
	0.005	-9.7	[57]
	0.001	-9.43	[58]
La	0~0.087	-12.69~-12.20	This study
	0.005	-11.79	[51]
	Dilution	-11.84	[59]
	Dilution	-11.65	[60]
	Dilution	-11.73	[55]
	Dilution	-11.75	[56]
Lu	0~0.084	-7.15~-7.07	This study
Nd	0~0.058	-11.55~-11.06	This study
	0.005	-12.03	[57]
	Dilution	-10.78	[61]
	Dilution	-10.94	[53]
Tb	0~0.085	-7.90~-7.67	This study
	0.005	-9.95	[51]
Tm	0~0.100	-9.91~-7.63	This study

Dilution: mole fraction is less than 1 at%.

Table 4-42. Activity coefficients of lanthanides in liquid bismuth at 923 K.

Element	Mole fraction	Log(activity coefficient)	Studies
Dy	0~0.063	-9.04~-8.39	This study
	0.005	-9.26	[50]
	0.005	-9.53	[51]
Gd	0~0.085	-10.51~-9.00	This study
	Dilution	-9.47	[52]
	0.005	-9.53	[51]
	Dilution	-9.75	[53]
	Dilution	-9.45	[54]
	Dilution	-9.22	[55]
	Dilution	-9.48	[56]
Ho	0~0.075	-8.33~-8.06	This study
	0.005	-9.09	[57]
	0.001	-8.88	[58]
La	0~0.110	-12.02~-11.27	This study
	0.005	-11.07	[51]
	Dilution	-11.15	[59]
	Dilution	-10.93	[60]
	Dilution	-11.01	[55]
	Dilution	-11.04	[56]
Lu	0~0.095	-6.69~-6.58	This study
Nd	0~0.080	-10.89~-10.27	This study
	0.005	-11.28	[57]
	Dilution	-10.10	[61]
	Dilution	-10.23	[53]
	Dilution	-8	[62]
Tb	0~0.100	-7.40~-7.16	This study
	0.005	-9.30	[51]
Tm	0~0.120	-9.52~-6.95	This study

Dilution: mole fraction is less than 1 at%.

Table 4-43. Activity coefficients of lanthanides in liquid bismuth at 973 K.

Element	Mole fraction	Log(activity coefficient)	Studies
Dy	0~0.075	-8.56~-7.84	This study
	0.005	-8.73	[50]
	0.005	-8.96	[51]
Gd	0~0.100	-9.95~-8.31	This study
	Dilution	-8.92	[52]
	0.005	-8.94	[51]
	Dilution	-9.17	[53]
	Dilution	-8.90	[54]
	Dilution	-8.72	[55]
	Dilution	-8.93	[56]
Ho	0~0.090	-7.87~-7.54	This study
	0.005	-8.54	[57]
	0.001	-8.39	[58]
La	0~0.130	-11.42~-10.43	This study
	0.005	-10.42	[51]
	Dilution	-10.53	[59]
	Dilution	-10.28	[60]
	Dilution	-10.37	[55]
	Dilution	-10.40	[56]
Lu	0~0.100	-6.28~-6.16	This study
Nd	0~0.095	-10.30~-9.61	This study
	0.005	-10.61	[57]
	Dilution	-9.48	[61]
	Dilution	-9.59	[53]
Tb	0~0.120	-6.95~-6.70	This study
	0.005	-8.72	[51]
Tm	0~0.130	-9.17~-6.48	This study

Dilution: mole fraction is less than 1 at%.

The relationships between the activity and the concentration were also investigated. Here only the activities at 973 K were plotted and analyzed in Figure 4-151 because of the similar change patterns of activity coefficients with concentrations at three temperatures for each lanthanide as shown in Figure 4-150. Similar to our study of Pr, Ce and Er, a unit-slope diagonal line is not indicated in the coordinate of Figure 4-151, it means the change of the activity with concentration is far away from the Raoult's law [63,64]. Raoult's law [63,64] states that the activity of a component in liquid mixture is related to its activity of pure substance and its mole fraction in the solution.

$$\alpha = x\alpha^0 \tag{4-180}$$

where α^0 is the activity of the pure component and can be taken as unity, and x is the mole fraction of the component. It is only applicable to ideal solution where there is no intermolecular interaction between particles or each intermolecular interaction equals to those of the pure components [63,64]. The systems investigated with relatively low concentration in the study do not obey to this law. For a real solution of lanthanide-bismuth mixture, the activity coefficient γ_{Ln} needs to be introduced. It denotes the deviation from the ideal solution. Now we have

$$\alpha_{Ln} = x_{Ln}\gamma_{Ln}\alpha_{Ln}^0 \tag{4-181}$$

When the mole fraction of solute approaches 1, the solution can be treated approximately as ideal solution and the activity coefficient of solute approaches unity. When comparing equations (4-180) and (4-181) and considering activity coefficients of these lanthanides in liquid bismuth are extremely low, there is thus a dramatically negative deviation of these systems from the ideal ones. Therefore, the interactions between the unlike atoms are significantly different from these between like atoms. Generally, more energy would be released for the attraction set up between unlike atoms in comparing with breaking the originally like atom pairs. It results in an exothermic enthalpy of mixing and explains the negative values of enthalpies of mixing for these binary systems reported before [7-13].

It should be noted that at infinite dilution (x_{Ln} approaches 0), the activity coefficient will have a constant value of γ_{Ln}^{∞}. In this region, the system can be depicted by Henry's law [65]

$$\alpha_{Ln} = x_{Ln}K_H \tag{4-182}$$

where Henry's constant K_H is used. Comparing equation (4-181), the activity coefficient γ_{Ln}^{∞} can be expressed by

$$\gamma_{Ln}^{\infty} = K_H/\alpha_{Ln}^0 \tag{4-183}$$

It indicates the activity coefficient is a constant in infinite dilution and there is a linear relationship between the activity and concentration. As shown in Figure 4-151, if focusing on the infinite dilution, activities show linear relationships with concentrations at infinite dilution. Upon the infinite dilution, neither Raoult's law nor Henry's law is necessarily followed. Another interesting thing observed is that the activities increase faster than the linear relationship at low concentration for all elements except Lu and Tb. Further theoretical or experimental studies maybe needed to thoroughly understand it.

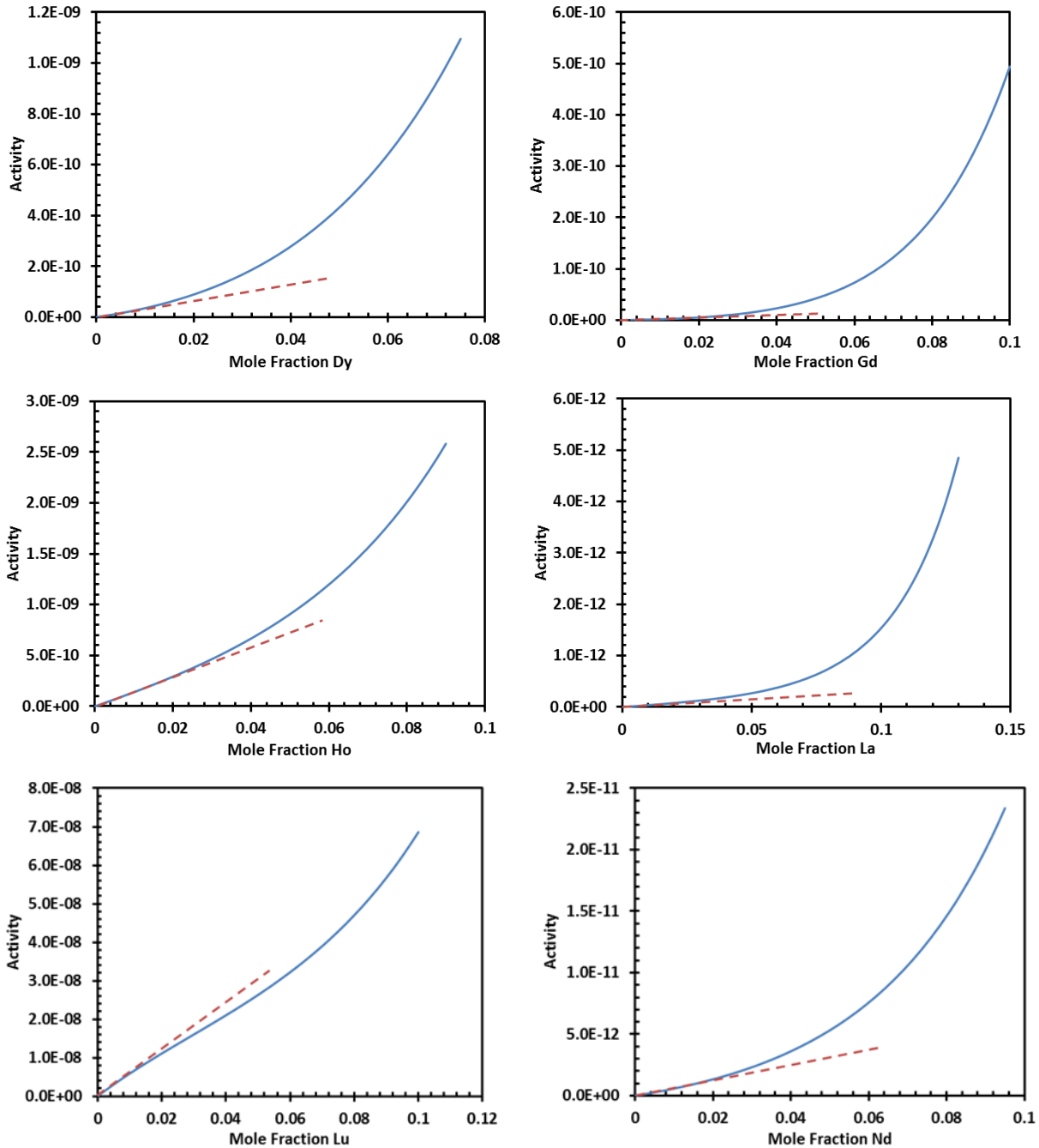

Figure 4-151. The activities of lanthanides in liquid bismuth at the temperature of 973 K. Solid line is the activity at different concentration while the dashed line is the linear relationship of the activity with concentration at dilution.

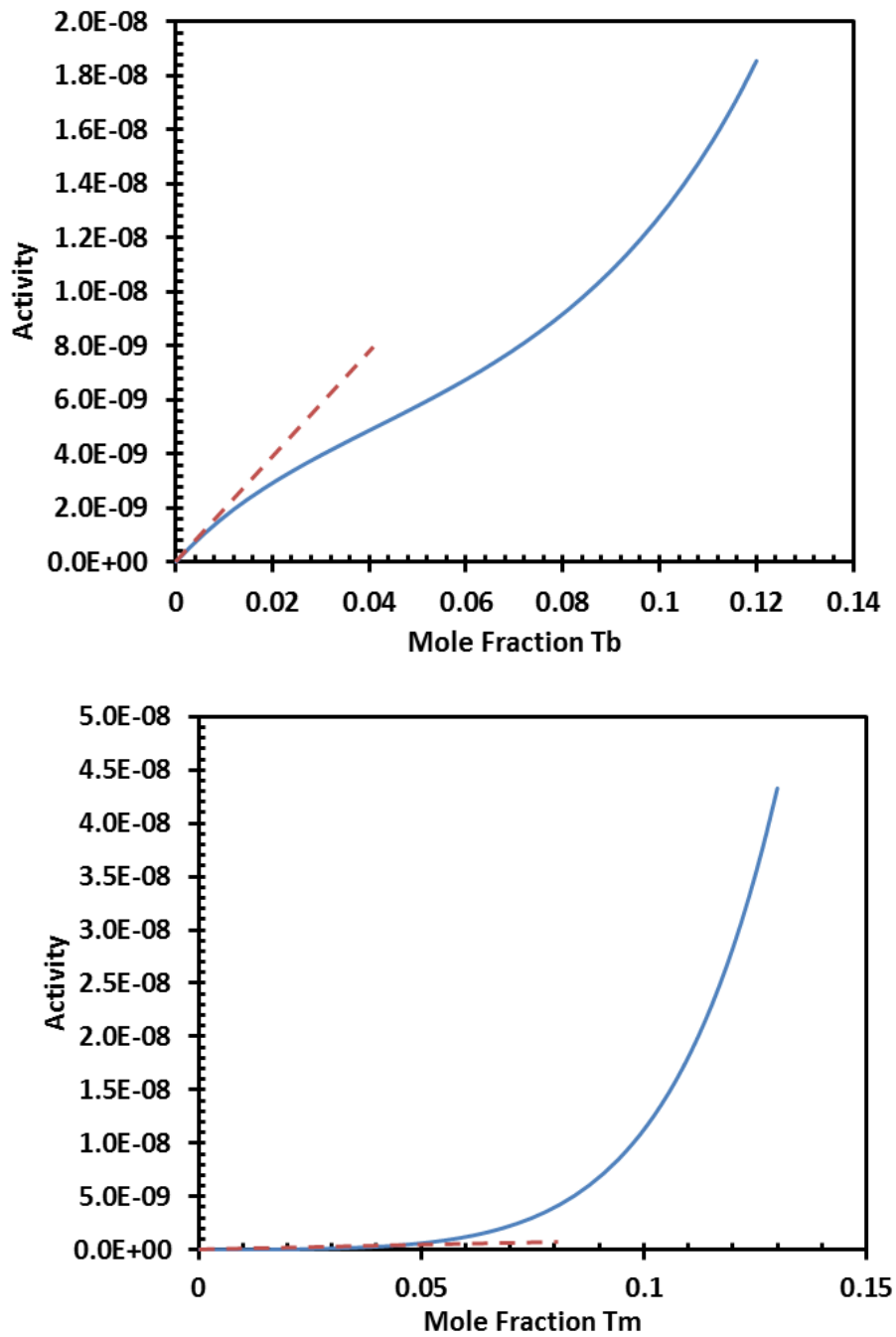

Figure 4-151 The activities of lanthanides in liquid bismuth at the temperature of 973 K. Solid line is the activity at different concentration while the dashed line is the linear relationship of the activity with concentration at dilution. (CONTINUED)

4.11.4. Summary

Thermodynamic assessments for the Bi-Pr, Bi-Ce, and Bi-Er have been carried out through CALPHAD method using sub-regular model and two-sublattice model. These three binary systems were mainly evaluated based on the available phase information and other thermodynamic properties published in literatures. The calculated phase diagrams show a great consistence with the experimental ones. Entropies and enthalpies of formation for metallic compounds and enthalpies of mixing for liquid phase were obtained after the acquirement of thermodynamic parameters in the Gibbs free energy expressions for all phases. The assessed enthalpies of formation and enthalpies of mixing were illustrated to have a good agreement with the literature values. The study about the enthalpies of mixing for liquid phase greatly extends the existed experimental data.

The solubility of fission products (Pr, Ce, and Er) and the correlations between solubility and temperature were obtained. Furthermore, the activity coefficients of fission products in liquid bismuth at different concentrations and temperatures were also evaluated based on the assessed thermodynamic parameters. It is found that the activity coefficient is a function of temperature and concentration, and it increases with the element concentration and temperature on the whole. The change pattern of the activity with concentration were also analyzed and discussed which greatly enhanced our understanding of the three binary systems.

Based on the assessed results for Gibbs energy of solution by CALPHAD method reported in the previous literatures [7-13], activity coefficients of other lanthanides except Pr, Er, and Ce in liquid bismuth at different concentrations and temperatures were also studied. It is found that the activity coefficients of Dy, Gd, Ho, La, Nd, and Tm in liquid bismuth increase with the increasing concentration, while the activity coefficients of Lu and Tb increase firstly and then decrease with the increment of concentration. Correlations for the activity coefficients were also obtained for the concentration range up to solubility limit and the temperature range of 873-973 K. The obtained activity coefficients over a wide concentration and temperature would greatly contribute to the FHR primary coolant cleanup system development.

4.11.5. Reference

1. J. Zhang, E. A. Lahti, E. Wu, Thermodynamic properties of actinides and fission products in liquid bismuth, Progress in Nuclear Energy, 81(2015): 67-77.
2. J. R. Week, Lead, bismuth, tin and their alloys as nuclear coolant, Nuclear engineering and Design, 363-372, 1971
3. H. Shimotake, J. C. Hesson, Corrosion by fused salts and heavy liquid metals-A survey, In Advances in chemistry, American Chemical Society, Wasington DC., 1967.
4. Y. Wang, et al., Concentration-dependent activity coefficients of lanthanides in liquid bismuth for the FHR primary coolant cleanup, Annals of Nuclear Energy, 113(2018): 89-95.
5. M. Tan, et al., Experimental investigation of phase relations in BI-Te-RE (Yb, La, Ce) Ternary systems, Calphad, 61(2018): 62-71.

6. N. D. Smith, et al., Thermodynamic properties of strontium-bismuth alloys determined by electromotive force measurements, Electrochimica Acta, 225(2017): 584-591.
7. Tang, Ying, et al. Journal of Phase Equilibria and Diffusion 34.4 (2013): 297-306.
8. Wang, S. L., et al. Calphad 35.3 (2011): 421-426.
9. Wang, C. P., et al. Journal of Alloys and Compounds 502.1 (2010): 43-48.
10. Wang, S. L., et al. Journal of Phase Equilibria and Diffusion 32.5 (2011): 441-446.
11. Wang, Jinsan, et al. CALPHAD 41 (2013): 1-5.
12. Wang, Jinsan, et al. Thermochimica Acta 566 (2013): 44-49.
13. Djaballah, Y., et al. CALPHAD 48 (2015): 72-78.
14. Li, Juan, et al. CALPHAD 38 (2012): 133-139.
15. Wang, Jinsan, et al. Thermochimica Acta 566 (2013): 44-49.
16. Redlich, Otto, and A. T. Kister. Industrial & Engineering Chemistry 40.2 (1948): 345-348.
17. Dinsdale, A_T. "SGTE Data for Pure Elements." CALPHAD 15.4 (1991): 317-425.
18. Andersson, Jan-Olof, et al. CALPHAD 26.2 (2002): 273-312.
19. Hillert, M., and L. I. Staffansson. Acta Chem. Scand. 24.10 (1970): 3618-3626.
20. Griffin, R.B., Gschneidner jr., K.A.: Metall. Trans. 2 (1971) 2517.
21. K Yoshihara, J.B Taylor, L.D. Calvert, J.G. Despault, J. Less-Common Met. 41 (1975) 239–245.
22. Gambino, R.J.: J. Less-Common Met. 12 (1967) 344.
23. Schweitzer, D. G., and J. R. Weeks. Trans. Am. Soc. Metals 54 (1961).
24. Bi-Pr Binary Phase Diagram (http://materials.springer.com/isp/phase-diagram /docs/c_0900459).
25. Colinet, C., et al. Journal of the Less Common Metals 102.2 (1984): 239-249.
26. Miedema, A. R. Journal of the Less Common Metals 32.1 (1973): 117-136.
27. Borsese, A., Ferro, R., Capelli, R., Delfino, S.: Thermochim. Acta 11 (1975) 205.
28. Vogel, Rudolf. "Über die Legierungen des Cers mit Silicium und Wismut." Zeitschrift für anorganische Chemie 84.1 (1913): 323-339.
29. R.J. Pleasance, J. Inst. Met. 88 (1959) 45–50.
30. K.A. Gschneidner, F.W. Calderwood, Bull. Alloy Phase Diagram 10 (1989) 427–430.
31. Borzone, G., et al. Journal of the Less Common Metals 58.1 (1978): 31-36.
32. Abulkhaev, V.D.: Neorg. Mater. 28 (1992) 2111.
33. Okamoto, H.: J. Phase Equil. 18 (1997) 671.
34. G. Borzone, N. Parodi, R. Ferro, J. Phase Equilib. 14 (1993) 485–493.
35. S.E. Petrashkevich, V.A. Degtyar, L.A. Vnuchkova, V.V. Serebrennikov, Reaction of Erbium with Bismuth and Aluminium, Nauch. Soobshch. II Vses. Konf. Bo stroeniyu I Svoistvam Metal. I Shlak. Rasplavov. 2 (1976) 12.
36. L.F. Yamshchikov, V.A. Lebedev, I.F. Nichkov, S.P. Raspopin, B.A. Karmanov, Thermodynamics Properties of Molten Alloys of Erbium with Low-melting Metals, in: L.F. Kozin IIzd (Ed.), Termodin. Svoistva Met. Rasplavov, Mater. Vses Soveshch. Termodin. Met. Splavov (Rasplavy), 4th, 2, Nauka Kazakhskoi SSR, USSR, Alma-Ata, 1979, pp. 181–185.
37. Sundman, Bo, Bo Jansson, and Jan-Olof Andersson. CALPHAD 9.2 (1985): 153-190.
38. Takeuchi, Akira, and Akihisa Inoue. Materials Transactions 46.12 (2005): 2817-2829.

39. Dong, Wen, et al. Journal of Materials Science 43.9 (2008): 3240-3244.
40. Zhang, J., E. A. Lahti, and E. Wu. Progress in Nuclear Energy 81 (2015): 67-77.
41. Kober, V.I., Lebedev, V.A., Nichkov, I.F., Raspopin, S.P., 1971b. Zh. Fiz. Khim. 45, 569 (in Russian; TR: Russ. J. Phys. Chem., 45, 313, 1971).
42. Yamana, Hajimu, et al. Journal of nuclear materials 294.3 (2001): 232-240.
43. Gschneidner, K. A., and F. W. Calderwood. "The Bismuth-rare Earth Systems." Bulletin of Alloy Phase Diagrams 10.4 (1989): 419-427.
44. Raoult, Francois-Marie. CR Hebd, Seances Acad. Sci 104 (1887): 1430-1433.

45. Staverman, A. J., and J. H. Van Santen. Recueil des Travaux Chimiques des Pays-Bas 60.2 (1941): 76-84.
46. Henry, William. Philosophical Transactions of the Royal Society of London 93 (1803): 29-276.
47. Zhang, Jinsuo. Progress in Nuclear Energy 70 (2014): 287-297.
48. Kaptay, George. Calphad 28.2 (2004): 115-124.
49. Yamana, Hajimu, et al. Journal of nuclear materials 294.3 (2001): 232-240.
50. Sheng, Jiawei, Hajimu Yamana, and Hirotake Moriyama. Journal of nuclear materials 301.2 (2002): 220-222.
51. Yamana, Hajimu, et al. Journal of nuclear materials 294.3 (2001): 232-240.
52. Sheng, Jiawei, Hajimu Yamana, and Hirotake Moriyama. PhysChemComm 4.9 (2001): 40-43.
53. Lebedev, V. A. Metallurgiya, Chelyabinsk 21 (1993).
54. Kober, V.I., Nichkov, I.F., Raspopin, S.E., Kuziminyx, V.M., 1983. In: Special Physical Characteristics of Dilute Alloys. Nauka, Moscow, pp. 132-135 (in Russian).
55. Kurata, Masaki, Yoshiharu Sakamura, and Tsuneo Matsui. Journal of alloys and compounds 234.1 (1996): 83-92.
56. Zhang, J., E. A. Lahti, and E. Wu. Progress in Nuclear Energy 81 (2015): 67-77.
57. Yamana, Hajimu, Jiawei Sheng, and Osamu Shirai. Journal of nuclear materials 344.1 (2005): 146-151.
58. Sheng, Jiawei. Journal of materials science 40.23 (2005): 6333-6336.
59. Gschneidner, K. A., and F. W. Calderwood. Bulletin of Alloy Phase Diagrams 10.4 (1989): 419-427.
60. Castrillejo, Y., et al. Journal of nuclear materials 360.1 (2007): 32-42.
61. V.A. Lebedev, MV. Effemov and V.I. Kober, in Special Physical and Chemical Characteristics of Dilute Alloys Nauka, Moscow, 1975, pp. 96-99 (in Russian).
62. Ferris, L. M., J. C. Mailen, and F. J. Smith. Journal of the Less Common Metals 25.1 (1971): 83-88.
63. Raoult, Francois-Marie. CR Hebd, Seances Acad. Sci 104 (1887): 1430-1433.
64. Staverman, A. J., and J. H. Van Santen. Recueil des Travaux Chimiques des Pays-Bas 60.2 (1941): 76-84.
65. Henry, WilliamPhilosophical Transactions of the Royal Society of London 93 (1803): 29-276.

4.12. Activity and activity coefficient investigation of K and Li in liquid Bi determined by EMF measurements

Liquid bismuth has broad applications in pyrochemical process for the separation of actinides and fission products from spent nuclear fuel and molten salt reactor coolant clean-up [1,2,3]. In the pyroprocessing of spent nuclear fuel, liquid bismuth is typically used as the cathode to extract the fission product of which the electrodeposition potential is close to or more negative than that of the constitutes in LiCl-KCl molten salt electrolyte when using inert solid electrode [3,4]. By using liquid Bi electrode, the electrodeposition of the target fission product could proceed greatly to a more positive potential and its separation can be realized. In molten salt breeder reactor (MSBR), liquid bismuth with dissolved lithium is used as the extraction media to reprocess the fuel salt through the selective reduction of actinides and fission products [5,6]. A liquid bismuth contacting system similarly to what used in MSBR is also being considered for the primary salt coolant clean-up to separate the fission products resulting from fuel leakage in fluoride salt cooled high temperature reactor (FHR) [7,8]. Recently, liquid Bi-Li metal mixture is proposed as the sacrificial anode for the contaminant removal from primary salt coolant in FHR. In that case, the reaction occurs on the anode during the contaminant removal is $Li - e^- \leftrightarrow Li^+$ through which the production of F_2 gas existed when using carbon material can be avoided.

Activity and activity coefficient are essential knowledges for assessing the viability of bismuth in separating actinides and fission products species from molten salt electrolytes. When using liquid bismuth electrode, the equilibrium potential of a reduction reaction can be expressed by

$$E^{eq}_{M^{n+}/M} = E^{o}_{M^{n+}/M} + \frac{RT}{nF}\ln(\frac{\alpha_{M^{n+}}}{\alpha_M}) \qquad (4\text{-}184)$$

where $E^{o}_{M^{n+}/M}$ is the standard reduction potential, R is gas constant, T is temperature in kelvin, F is faraday constant, n is electron transfer number, $\alpha_{M^{n+}}$ is the activity of M^{n+}in molten salt electrolyte, and α_M is the activity of M in liquid bismuth. Thus, the value of α_M will affect the equilibrium potential and the electrodeposition of M^{n+} from molten salt electrolyte. The knowledges of the activity and activity coefficient can help instruct the conditions needed to be applied for a desired electrochemical separation. Consequently, massive studies have been carried out to study the activity and activity coefficient of fission products and actinides in liquid bismuth [1,6,8,9,10,11]. However, considering the equilibrium reduction potential of K^+ and Li^+ which are the main constituent species of the molten salt used in the applications discussed above will also change when using liquid bismuth electrode, the activity and activity coefficient of K and Li in liquid bismuth also need to be known for identifying whether the target fission products and actinides can be preferentially deposited over Li and K.

Several relevant experimental studies have been conducted to report the activity and activity coefficient of K in liquid bismuth. A Petric et al [12] investigated the variation of the activity coefficient of K in liquid bismuth in the composition range of 0~66 mol% K at

the temperature of 873 K using electromotive force measurement (EMF). The activity coefficient of K in liquid bismuth at high concentration for the temperatures of 848 K and 1023 K are reported by R. Hultgren et al [13] and Egan et al [14], respectively. The activity and activity coefficient studies of Li in liquid bismuth have been limited to a few concentration points by Foster et al [15] and Demidov et al [16] at the temperatures of 800, 850, and 1000 K. To meet the requirement of the application of bismuth in nuclear field, the activity and activity coefficient of K and Li in liquid bismuth at the temperatures of 973 K and 1023 K are studied in the present work which are the typical operation temperatures for molten salt reactors. By coulometric titrating different quantities of K and Li into liquid bismuth from molten salt electrolyte, the various concentrations of K and Li in liquid bismuth can be acquired. Based on the EMF measurement followed by each titration, the variations of activity and activity coefficient of K and Li in liquid bismuth with concentration lower than 20 mol% were investigated in this study.

4.12.1. Experimental methods

All experiments and sample preparations were carried out under argon atmosphere in a glovebox (Inert Technology) where the moisture and oxygen levels were maintained under 0.5 ppm and 5 ppm, respectively.

Preparation of the electrolyte

For the investigation of the activity of K in liquid Bi, the LiF-NaF-KF (46.5 mol% LiF, 11.5 mol% NaF, and 42 mol% KF) salt melt was used as electrolyte, which was prepared by mixing lithium fluoride (>99.0% purity, Sigma Aldrich), sodium fluoride (>99.0% purity, Sigma Aldrich) and potassium fluoride (>99.5% purity, Sigma Aldrich). In the salt preparation, the LiF, NaF, and KF salt powder was mixed well before transferred to a nickel crucible and placed in a muffle furnace (Thermofisher Scientific FB1315M) for which the temperature can be maintained within ± 1°C during the experiment. To remove the moisture and oxygen inside the salt powder, the salt mixture was dehydrated at 673 K for 24 hours before heating to the target temperature (973 K and 1023 K). For the activity study of Li in liquid Bi, the LiF-LiCl (52 mol% LiF-48 mol% LiCl) salt melt was used as electrolyte. It was prepared by mixing lithium fluoride (>99.0% purity, Sigma Aldrich) and lithium chloride (>99.0% purity, Sigma Aldrich). In order to do the moisture and oxygen removal, a same dehydration process as done in LiF-NaF-KF salt was performed in this salt mixture.

Electrochemical apparatus and electrodes

The electrochemical tests were carried out using a Gamry Interface 1000 Potentiostat and a standard three-electrode setup. A 3.05 mm diameter graphite rod (99.9995% purity, Alfa Aesar) was used as the counter electrode for all the electrochemical experiments in this study. To perform the activity measurement of K in liquid Bi, a new reference electrode was designed as shown in Figure 4-152. Considering the low melting and boiling points of K, it is easy for K metal to vaporize away if the Bi-K liquid mixture is simply prepared by mixing K and Bi solid metals and heating up. To solve this issue, a sophisticated preparation procedure was proposed here. Bi (granule, ≥ 99.99 purity, Sigma Aldrich) metal was heated individually to 673 K in a glassy carbon crucible using a muffle furnace. K (ingot, 99.95% purity, Sigma Aldrich) metal was then added into the liquid bismuth and the formed Bi-K melt mixture was kept at 673 K for 2 hours to get Bi and K uniformly mixed. After that, the well mixed Bi-K was cooled down and grounded into granules using mortar and pestle.

Thus, the well mixed Bi-K granule was obtained, and the concentration of K was identified to be 3.8 mol% by ICP-MS test. A small amount of the prepared Bi-K granules (~1.5g) was placed at the bottom of the alumina tube (9 mm OD×6 mm ID, LSP Industrial Ceramics, Inc.) which has a hole drilled on the wall. At high temperature, Bi-K granules will melt, and the molten salt electrolyte can contact the Bi-K liquid metal through the drilled hole when the whole equipment in is immersed into molten salt. An inert material: tungsten which does not have any reaction with Bi or K was chosen as the electrical wire. The tungsten electrical wire was immersed into the Bi-K melt allowing the current to flow through during the electrochemical tests. An alumina insulation tube (CoorsTek, 2 mm OD×1.02 mm ID) was sheathed on this electrical wire to avoid its contact with molten salt. Two kinds of working electrodes were utilized for the activity study of K in liquid Bi, the first one is a 1 mm diameter tungsten rod (Midwest Tungsten Service, >99.5% purity) while the other one is liquid bismuth which is contained in the same equipment for reference electrode as shown in Figure 4-152. To guarantee the free diffusion of ions from molten salt to liquid Bi working electrode, unlike the only one hole drilled at the bottom of alumina tube shown in Figure 4-152, two holes were drilled for the equipment used to contain liquid Bi. For the activity measurement of Li in liquid Bi, the same procedure and equipment as employed for the study of K were used for the preparation of Bi-Li reference electrode (x(K)=10.5 mol%) and liquid Bi working electrode. In addition, another working electrode: tungsten rod (1 mm D, Midwest Tungsten Service, >99.5% purity) was used for the activity study of Li in liquid Bi.

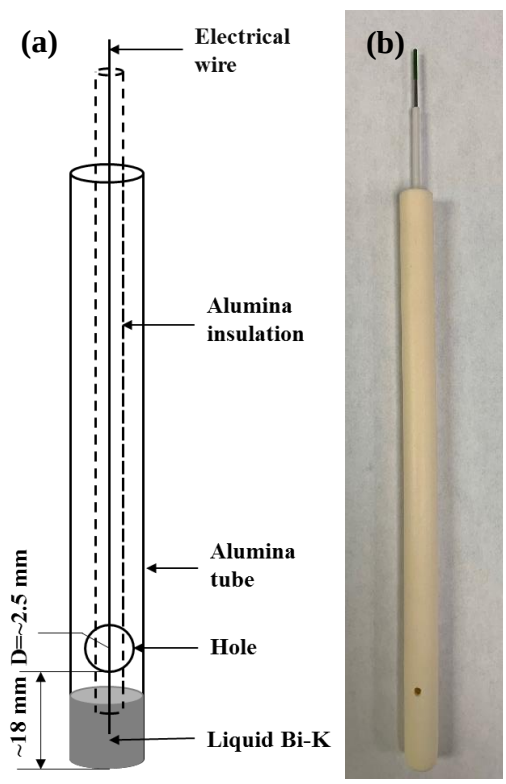

Figure 4-152. Schematic diagram of the designed Bi-K liquid reference electrode.

4.12.2. Results and Discussions

4.12.2.1. The Bi-K system

To obtain the information about the activity of K in the reference electrode, EMF measurement was carried out on a tungsten working electrode. The basic cell reaction can be expressed by

K-Bi (reference electrode) || FLiNaK electrolyte || W (working electrode).

During the EMF measurement, a 5-s current pulse was applied between the tungsten working electrode and graphite counter electrode in FLiNaK molten salt system. Figure 4-153 shows the potential evolution of the tungsten working electrode against K-Bi reference electrode over time when different current pulses were applied at the temperatures of 973 K and 1023 K. In the period of a 5-s current pulse was applied, the potential of the working electrode dropped to a more negative value sharply because a potassium layer was formed on the tungsten electrode surface due to the reduction of K (I). The formed plateau during the first 5 s period in *Figure 4-153* means a potassium layer is fully covered on the tungsten working electrode. A lower potential value for the plateau was observed at a higher pulse current which is attributed to the ohmic drop in the electrolyte between the tungsten working electrode and K-Bi reference electrode [17]. After 5 s, the potential steps up since the ohmic drop associated with the applied current pulse does not exist. This potential value corresponds to the equilibrium potential of K(I)/K referring to K-Bi reference electrode which can be expressed by

$$EMF = E^{eq}_{K^+/K} - E^{eq}_{K^+/K-Bi(RE)} = \frac{RT}{F}\ln(\alpha_{K\ in\ RE}) \tag{4-185}$$

where $E^{eq}_{K^+/K}$ and $E^{eq}_{K^+/K-Bi(RE)}$ are the equilibrium potential of K(I)/K and K(I)/K-Bi (reference electrode) which are written as

$$E^{eq}_{K^+/K} = E^o + \frac{RT}{F}\ln\left(\frac{\alpha_{K^+\ in\ FLiNaK}}{1}\right) \tag{4-186}$$

$$E^{eq}_{K^+/K-Bi(RE)} = E^o + \frac{RT}{F}\ln\left(\frac{\alpha_{K^+\ in\ FLiNaK}}{\alpha_{K\ in\ RE}}\right) \tag{4-187}$$

in which E^o is the standard reduction potential, α is activity.

It means if the stepped-up potential value after the cease of the applied current pulse is known, the activity $\alpha_{K\ in\ RE}$ can be obtained directly. The activity of K in the reference electrode were calculated and listed in Table 4-44 based on equation (4-185) and the measured stepped-up potential value. The stepped-up potential will keep constant for a while and the duration time depends on the quantity of potassium deposited on the tungsten working electrode. After a certain time, the potential increases back to its initial

value because of the dissolution of the deposited potassium layer on the tungsten electrode.

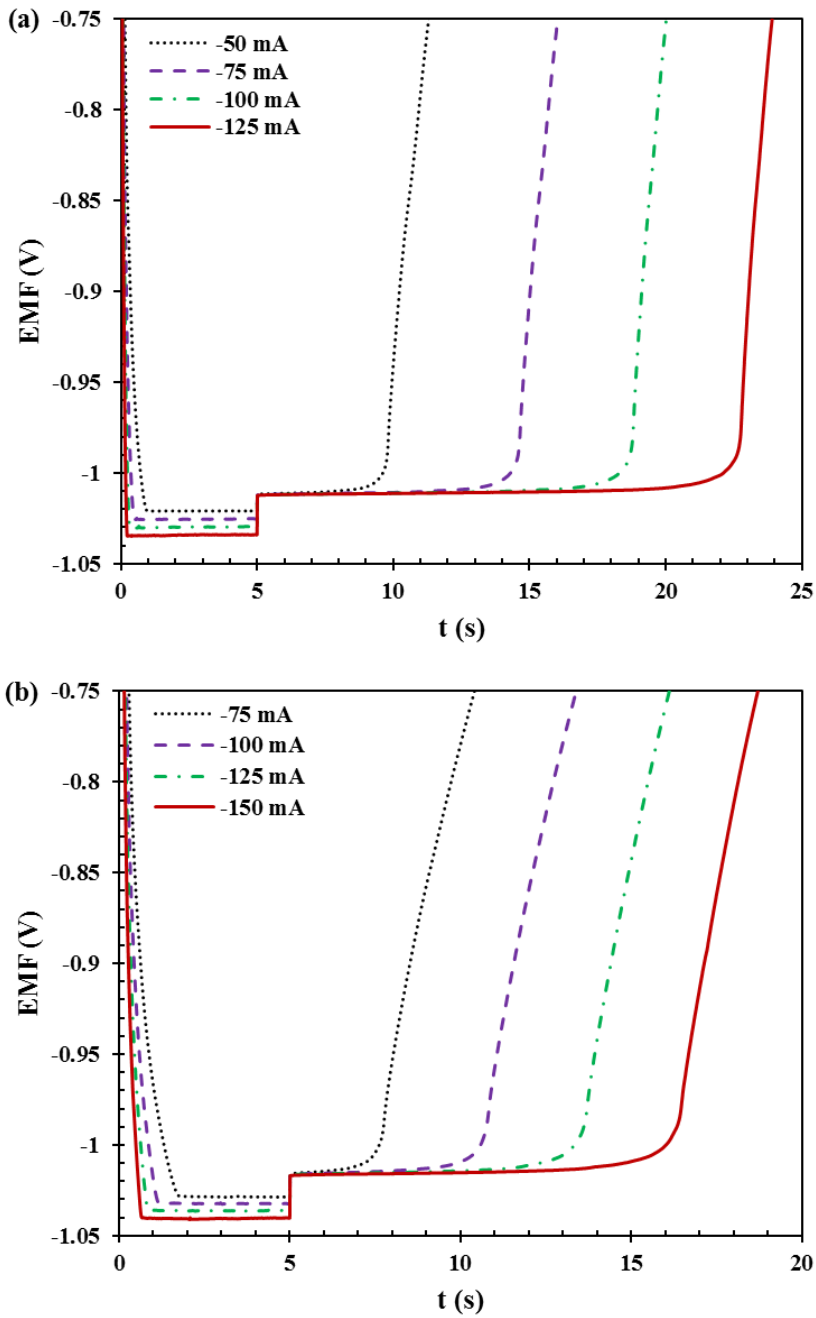

Figure 4-153. Potential evolution of the tungsten working electrode against K-Bi reference electrode over time in FLiNaK molten salt when a 5-s pulse current was applied at (a) 973 K and (b) 1023 K.

Table 4-44. Activity and activity coefficient of K in reference electrode at the temperatures of 973 K and 1023 K.

T (K)	EMF (V)	$\alpha_{K\ in\ RE}$	$x_{K\ in\ Bi}$	$\gamma_{K\ in\ RE}$
973	-1.012	5.73×10^{-6}	0.0379	1.51×10^{-4}
1023	-1.016	9.87×10^{-6}	0.0379	2.60×10^{-4}

Once the activity of K in the reference electrode was known, the working electrode was replaced with liquid Bi. The basic cell reaction then can be expressed as

K-Bi (reference) || FLiNaK electrolyte || liquid Bi (working).

To get different Bi-K ratios, coulometric titration was used to titrate K into the liquid Bi working electrode by applying a constant current during the EMF measurement. The accuracy of the coulometric titration method in molten salt system has been verified in the previous study [18]. Figure 4-154(a) shows the typical coulometric titration EMF data at the temperature of 973 K in which a constant current of -50 mA was applied for 100 s to titrate K into liquid Bi working electrode (1.745 g) and a subsequent 1800s open circuit potential was measured following each titration. Similarly, coulometric titration of K into liquid Bi (1.289 g) in FLiNaK molten salt electrolyte at current of -35 mA for 100 s followed by a 3600s open circuit potential measurement was also performed at the temperature of 1023 K (*Figure 4-154* (b)). From the open circuit potential measurement following each titration, the equilibrium electrode potentials as a function of K mole fraction are extracted and shown in Figure 4-155. The equilibrium electrode potential which refers to K-Bi reference electrode (K=3.79 mol%) can be expressed as

$$EMF = E^{eq}_{K^+/K-Bi(WE)} - E^{eq}_{K^+/K-Bi(RE)} = \frac{RT}{F}\ln\frac{\alpha_{K\ in\ RE}}{\alpha_{K\ in\ Bi}} \tag{4-188}$$

where $E^{eq}_{K^+/K-Bi(WE)}$ is the equilibrium potential of K(I)/K-Bi (working electrode) which can be written as

$$E^{eq}_{K^+/K-Bi(WE)} = E^o + \frac{RT}{F}\ln\left(\frac{\alpha_{K^+\ in\ FLiNaK}}{\alpha_{K\ in\ Bi}}\right) \tag{4-189}$$

Combining equation (4-189) and the known $\alpha_{K\ in\ RE}$ listed in Table 4-44, the activity of K in liquid Bi $\alpha_{K\ in\ Bi}$ at different concentrations for the temperatures of 973 K and 1023 K are obtained and shown in *Figure 4-156* (a). *Figure 4-156* (b) shows the calculated activity coefficient of K in liquid Bi $\gamma_{K\ in\ Bi}$ based on equation (4-190).

$$\gamma_{K\ in\ Bi} = \alpha_{K\ in\ Bi}/x_{K\ in\ Bi} \tag{4-190}$$

where the molar fraction of K in liquid Bi can be derived from the quantity of the titrated K by

$$x_{K\ in\ Bi} = \frac{It/F}{It/F + n_{Bi}} \tag{4-191}$$

in which I is the titration current applied, t is the time duration of the applied current, and n_{Bi} is the mole number of Bi for the working electrode used.

As can be seen from *Figure 4-156*, both $\alpha_{K\ in\ Bi}$ and $\gamma_{K\ in\ Bi}$ varies with concentration. It increases with the increasing concentration for $\alpha_{K\ in\ Bi}$ while initially decreases and subsequently increases for $\gamma_{K\ in\ Bi}$. To validate the results obtained in this study, the activity and activity coefficient of K in liquid Bi as a function of concentration at 873 K measured by A Petric et al [12] are also presented in Figure 4-156 for comparison. Recently, Niu et al [19] performed the thermodynamic assessment of the Bi-K system using the CALculation of PHAse Diagrams (CALPHAD) method. Based on the assessed expression of Gibbs free energy, the activity and activity coefficient of K in liquid Bi in the concentration range of 0 to 18 mol% for the temperatures of 973 K and 1023 K were calculated and shown in Figure 4-156. The comparison exhibited in Figure 4-156 (a) indicates the activity $\alpha_{K\ in\ Bi}$ obtained through the experiment in this study agrees well with the ones attained from model and A Petric et al [12]. Figure 4-156 (b) shows the variation trend of activity coefficient $\gamma_{K\ in\ Bi}$ with concentration at the low concentration in our study is a little different with the ones attained from model and A Petric et al [12]. However, considering the values of activity coefficient $\gamma_{K\ in\ Bi}$ shown in Figure 4-156 (b) are all at the same order, the activity coefficient obtained in this study is still reasonable.

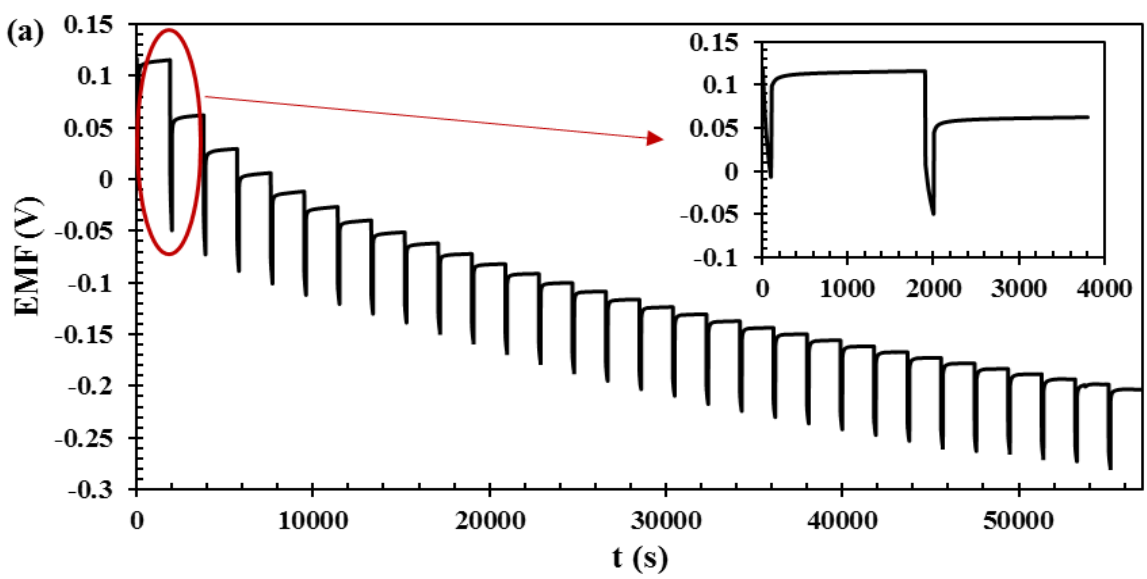

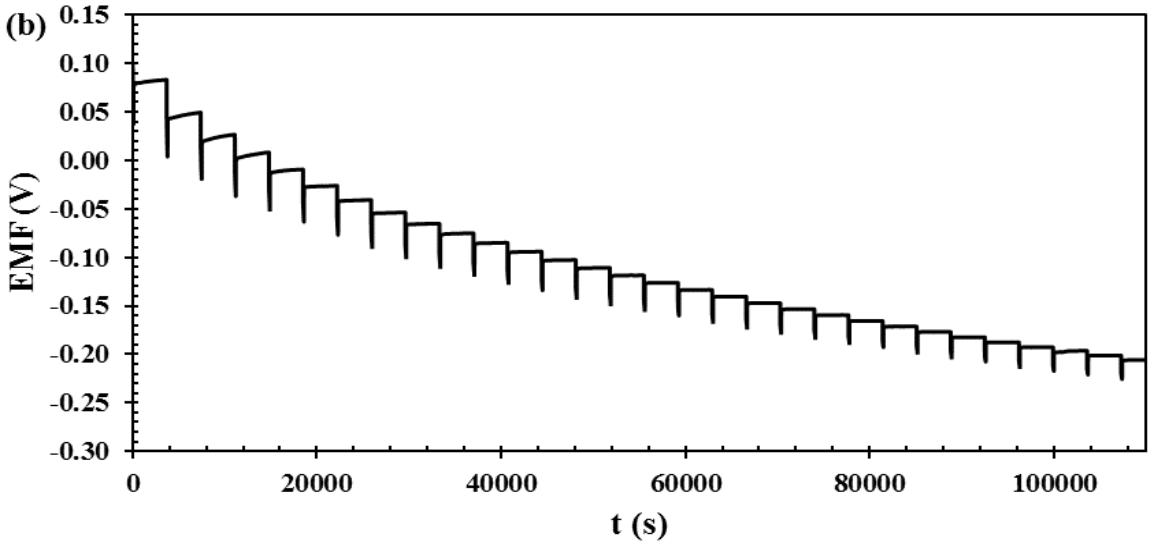

Figure 4-154. Coulometric titration of K into liquid Bi working electrode in FLiNaK electrolyte at (a) 973 K and (b) 1023K.

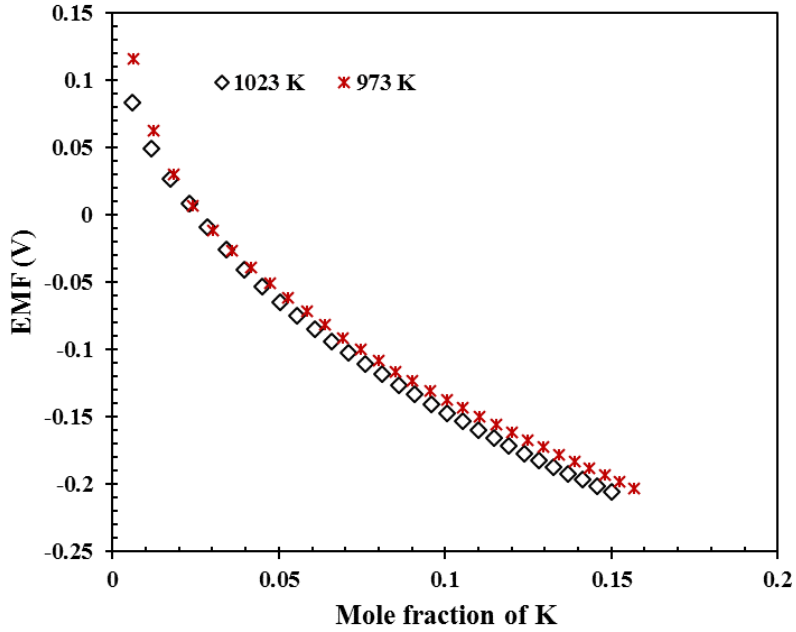

Figure 4-155. Equilibrium electrode potential as a function of K mole fraction upon K deposition at 973 K and 1023K.

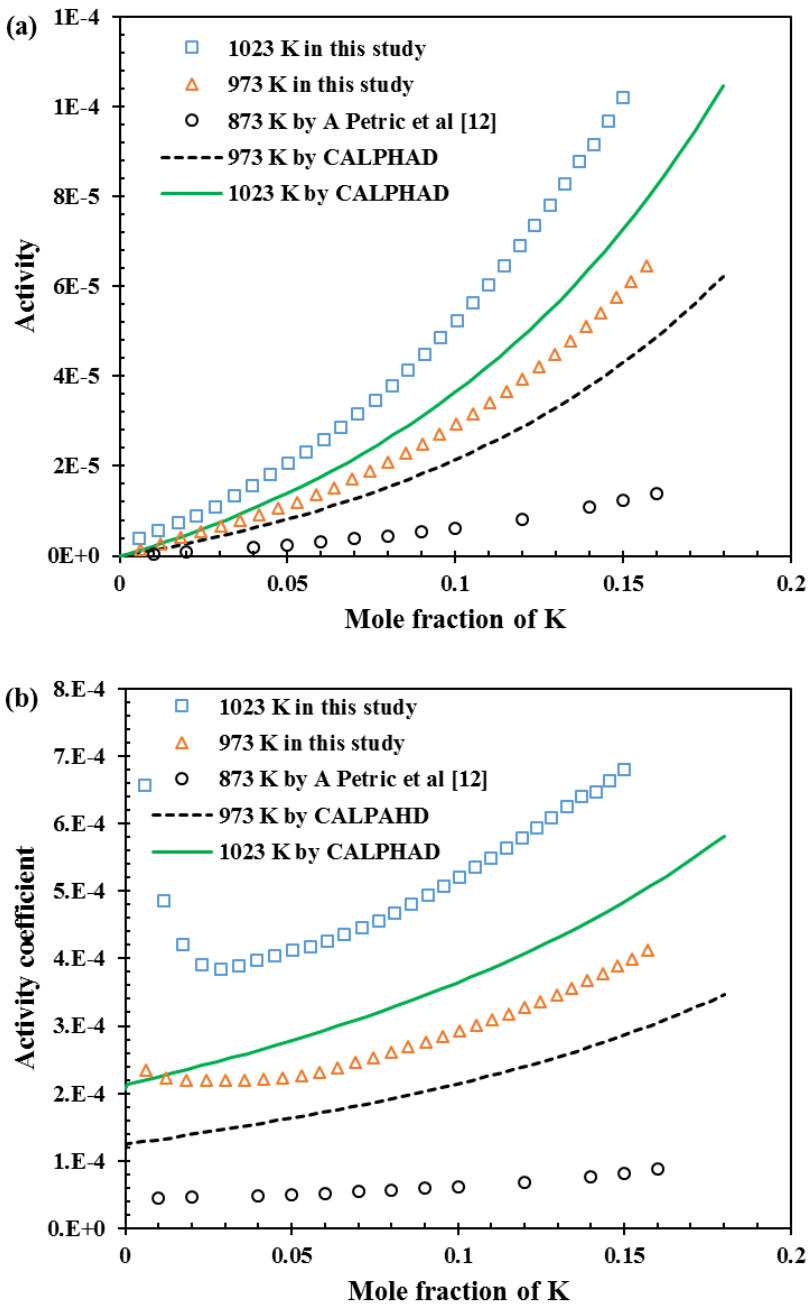

Figure 4-156. Activity and Activity coefficient of K in liquid Bi at different concentrations for the temperatures of 973 K and 1023 K.

4.12.2.2. The Bi-Li system

To study the activity of Li in liquid Bi, a same experiment procedure as done in Bi-K system was performed in the Bi-Li system. The test was carried out on a tungsten working electrode firstly and the basic cell reaction was expressed as

Li-Bi (reference electrode) || LiF-LiCl electrolyte || W (working

electrode).

Figure 4-157 shows the potential evolution of the tungsten working electrode against Li-Bi reference electrode over time in LiF-LiCl molten salt at the temperatures of 973 K and 1023 K. From the measured value of open circuit potential right after the termination of the application of the 5-s current pulse, the activity of Li in the reference electrode was calculated based on equation (4-185) and listed in Table 4-45.

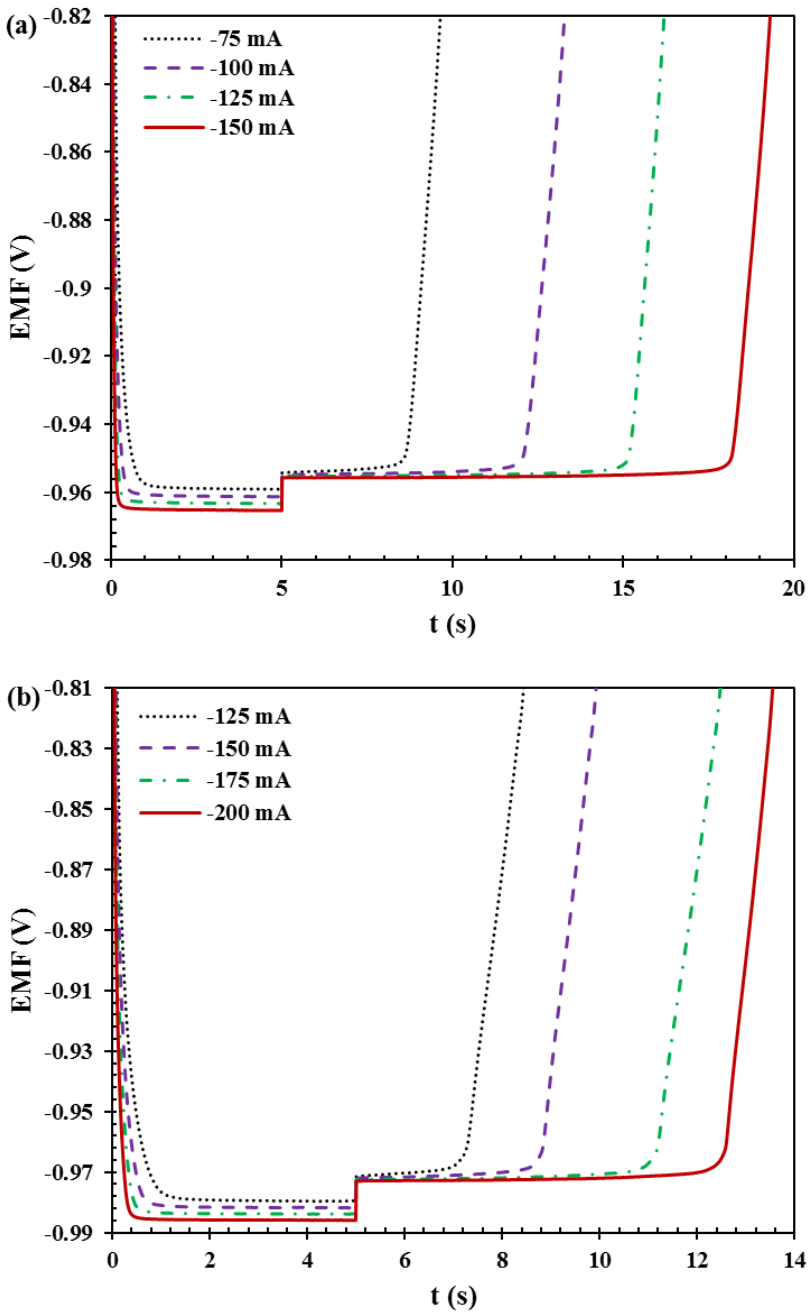

Figure 4-157. Potential evolution of the tungsten working electrode against Li-Bi reference electrode over time in LiF-LiCl molten salt when a 5-s pulse current was applied at (a) 973 K and (b) 1023 K.

Table 4-45. Activity and activity coefficient of Li in reference electrode at the temperatures of 973 K and 1023 K.

T (K)	EMF (V)	$\alpha_{Li\ in\ RE}$	$x_{Li\ in\ Bi}$	$\gamma_{Li\ in\ RE}$
973	-0.955	1.13×10^{-5}	0.1054	1.07×10^{-4}
1023	-0.972	1.62×10^{-5}	0.1054	1.54×10^{-4}

After the activity of Li in reference electrode was known, the working electrode was replaced with liquid Bi and the basic cell reaction then can be expressed as

Li-Bi (reference) || LiF-LiCl electrolyte || liquid Bi (working).

In Figure 4-158 (a), a constant current of -35 mA was applied on the liquid Bi electrode (1.263 g) for 100 s to titrate Li into it at 973 K. Followed by the titration, an open circuit potential measurement was performed for 2000 s to wait the titrated Li uniformly mixed with the liquid Bi. The same process was repeated for 30 times to get the equilibrium electrode potentials at different Li-Bi ratios. Similarly, Figure 4-158(b) shows the obtained coulometric titration EMF data at the temperature of 1023 K in which a constant current of -35 mA was applied on the liquid Bi electrode (1.241 g) to titrate Li for 100 s and a subsequent 3600 s open circuit potential measurement was conducted after each titration. Based on the measured open circuit potential followed by each titration, the equilibrium electrode potential referring to Li-Bi reference electrode was extracted and shown in Figure 4-159. Given that 3.63×10^{-5} mol Li was pre-deposited (-35 mA for 100 s) into liquid Bi working electrode before the coulometric titration at 1023 K, the equilibrium electrode potential at 1023 K shown in Figure 4-159 starts from the mole fraction of 1.21 mol%. From the obtained equilibrium electrode potential at different concentrations and $\alpha_{Li\ in\ RE}$ listed in Table 4-45, the variations of activity and activity coefficient of Li in liquid Bi with concentration were acquired and indicated in Figure 4-160. These results are also compared with the ones reported in other literatures from which it can be known our results are reasonable and consistent with them if taking account of the temperature influence on the activity and activity coefficient.

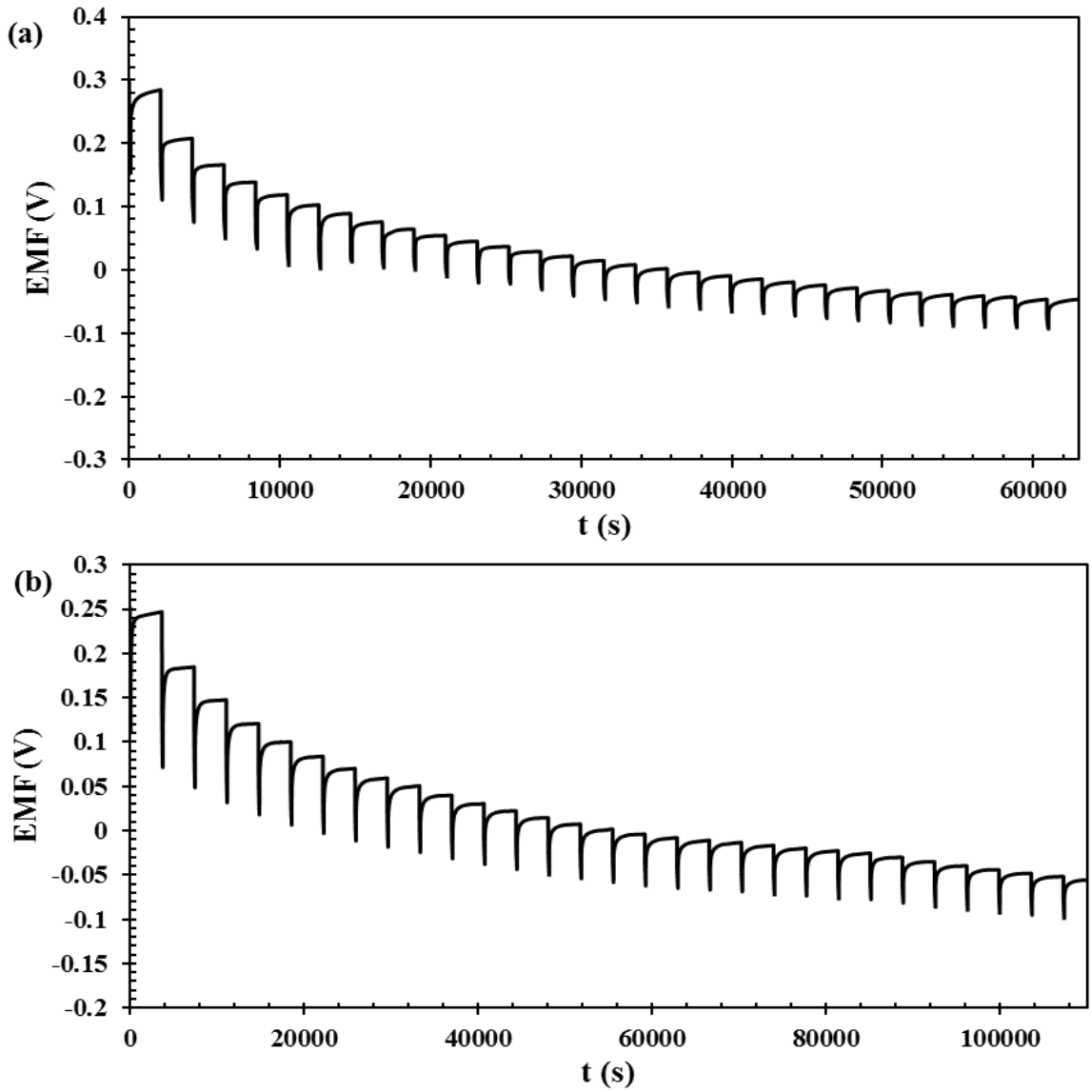

Figure 4-158. Coulometric titration of Li into liquid Bi working electrode in LiF-LiCl electrolyte at (a) 973 K and (b) 1023K.

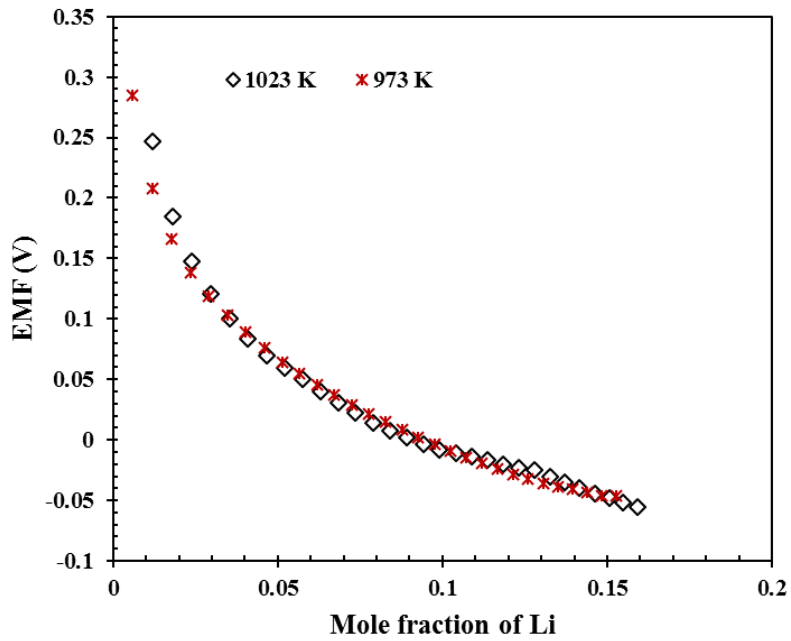

Figure 4-159. Equilibrium electrode potential as a function of Li mole fraction upon Li deposition at 973 K and 1023K.

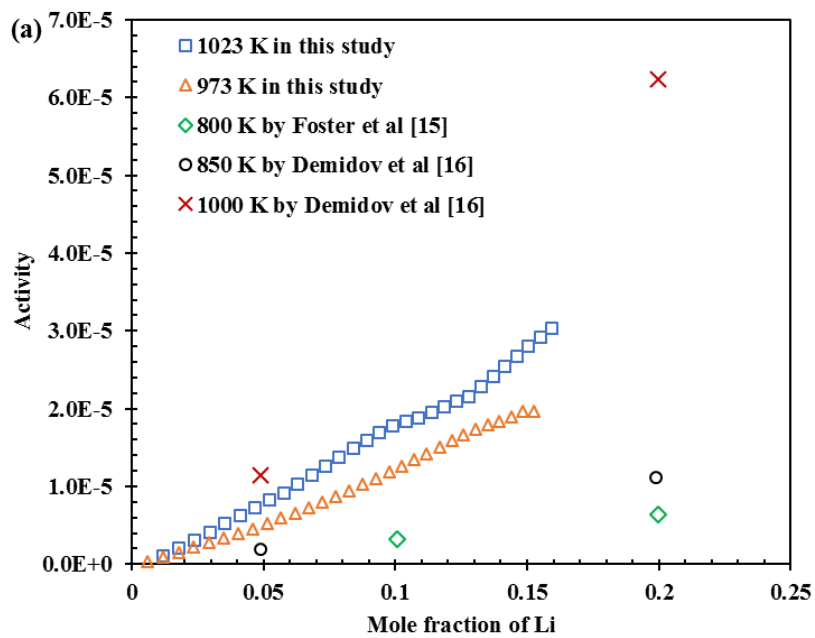

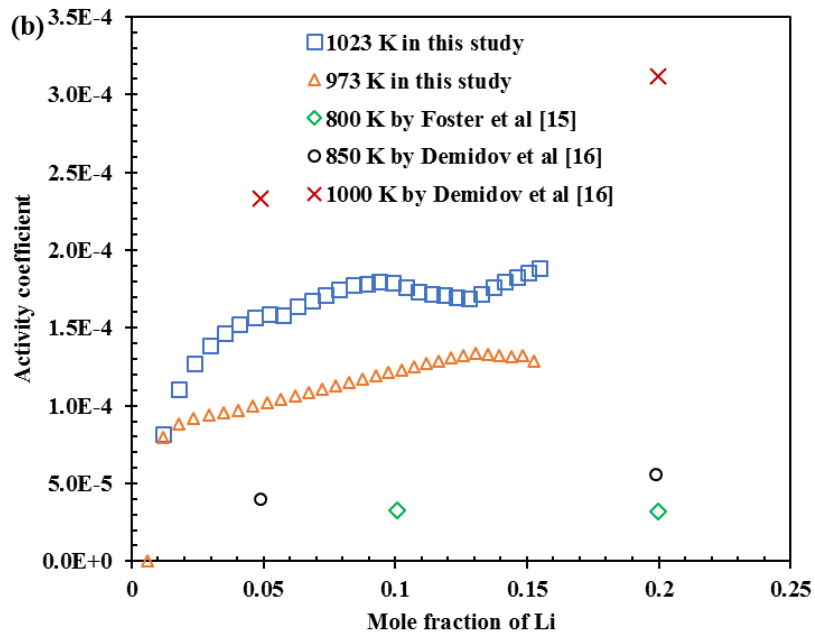

Figure 4-160. Activity and Activity coefficient of Li in liquid Bi at different concentrations for the temperatures of 973 K and 1023 K.

4.12.3. Summary

The activity and activity coefficient of K and Li in liquid bismuth at the temperatures of 973 K and 1023 K were obtained by the EMF measurement. Through coulometric titrating K and Li into liquid bismuth and performing EMF measurement after each titration, the variations of activity and activity coefficient of K and Li in liquid bismuth with concentration in the composition range lower than 20 mol% were also acquired. It is found that the activity of both K and Li increases with the increasing concentration. For the activity coefficient, it is observed that the activity coefficient of K in liquid bismuth initially decreases and subsequently increases with the increasing concentration, while the activity coefficient of Li in liquid bismuth generally increases with the increment of concentration. Given that the various Bi-K (or Bi-Li) compositions were obtained by coulometric titrating different quantities of K (or Li) into liquid bismuth from molten salt electrolyte, the way to track the variations of the activity and activity coefficient for K and Li in liquid bismuth with concentrations reported in this study will be more accurate comparing with the EMF measurement on the different simply mixed Bi-K (Li) compositions.

4.12.4. References

[1] Wang, Yafei, et al. "Thermodynamic properties of fission products (Pr, Ce, Er) in liquid bismuth by thermodynamic assessment." Journal of Nuclear Materials 495 (2017): 181-191.

[2] Taylor, Robin, ed. Reprocessing and recycling of spent nuclear fuel. Elsevier, 2015.

[3] Castrillejo, Y., et al. "Electrochemical extraction of samarium from molten chlorides in pyrochemical processes." Electrochimica Acta 56.24 (2011): 8638-8644.

[4] Kim, Beom Kyu, and Byung Gi Park. "Characterization of Ce-Bi intermetallic compound formations by electrolytic reduction in molten LiCl-KCl eutectic." Electrochimica Acta 295 (2019): 270-277.

[5] Ferris, L. M., et al. "Equilibrium distribution of actinide and lanthanide elements between molten fluoride salts and liquid bismuth solutions." Journal of Inorganic and Nuclear Chemistry 32.6 (1970): 2019-2035.

[6] Zhang, J., E. A. Lahti, and E. Wu. "Thermodynamic properties of actinides and fission products in liquid bismuth." Progress in Nuclear Energy 81 (2015): 67-77.

[7] Grimes, W. R. "Molten-salt reactor chemistry." Nuclear Applications and Technology 8.2 (1970): 137-155.

[8] Wang, Yafei, et al. "Concentration-dependent activity coefficients of lanthanides in liquid bismuth for the FHR primary coolant cleanup." Annals of Nuclear Energy 113 (2018): 89-95.

[9] Kurata, Masaki, Yoshiharu Sakamura, and Tsuneo Matsui. "Thermodynamic quantities of actinides and rare earth elements in liquid bismuth and cadmium." Journal of alloys and compounds 234.1 (1996): 83-92.

[10] Dong, Wen, et al. "The activity coefficient of low-level cerium in liquid bismuth." Materials Letters 62.6-7 (2008): 957-959.

[11] Yamana, Hajimu, et al. "Thermodynamic properties of lanthanide metals in liquid bismuth." Journal of nuclear materials 294.3 (2001): 232-240.

[12] Petric, A., A. D. Pelton, and M. L. Saboungi. "Thermodynamic properties of liquid K-Bi alloys by electromotive force measurements." Journal of Physics F: Metal Physics 18.7 (1988): 1473.

[13] R. Hultgren, P.D. Desai, D.T. Hawkins, M. Gleiser, K.K. Kelley, Selected Values of the Thermodynamic Properties of Binary Alloys, ASM, Metals Park, OH, 1973, pp. 421–423.

[14] Egan, J. J. "Coulometric titrations using calcium fluoride solid electrolytes to study some ionic alloys." High temperature science 19.2 (1985): 111-125.

[15] Foster, Melvin S., Scott E. Wood, and Carl E. Crouthamel. "Thermodynamics of binary alloys. I. The lithium-bismuth system." Inorganic Chemistry 3.10 (1964): 1428-1431.

[16] Demidov, A. I., and A. G. Morachevsky. "Thermodynamic Properties of Liquid Li-Bi Alloys." Elektrokhimiya 9.9 (1973): 1393-1394.

[17] Durán-Klie, Gabriela, Davide Rodrigues, and Sylvie Delpech. "Dynamic Reference Electrode development for redox potential measurements in fluoride molten salt at high temperature." Electrochimica Acta 195 (2016): 19-26.

[18] Kim, Hojong, et al. "Thermodynamic properties of calcium–bismuth alloys determined by emf measurements." Electrochimica Acta 60 (2012): 154-162.

[19] Niu, Chunju, et al. "Thermodynamic assessment of the Bi–K binary system." Thermochimica acta 528 (2012): 9-14.

5. Identification and Prioritization of V&V Needs via PIRT Panel

PIRT panels with internal and inverted external experts have been organized on key issues addressed in this project to identify and prioritize verification and validation (V&V) needs. Four panels were convened to address issues related to the following areas: neutronics, thermal hydraulics, materials and multiphysics modeling and simulation. This chapter documents the overall PIRT process, ranking methods, voting procedures, rationale for all rankings, discussion of the next steps for phenomena that require further consideration, and a record of the comments and suggested path forward from the panelists.

5.1. Neutronics PIRT

5.1.1. Introduction

5.1.1.1. Background

The widespread deployment of FHR technology promises many benefits: improved safety, through passive safety systems and proliferation-resistant waste forms; improved economics, through higher operating temperatures and thus higher operating efficiency; and a diversification of the nation's energy portfolio, through expanding the role of nuclear power beyond baseload electricity to meeting peaking electricity demand and supplying industrial process heat. However, significant challenges remain before this class of reactors can be deployed, mostly related to its technology readiness. A panel of experts was commissioned to identify and rank the phenomena presented by FHRs relating to the verification and validation (V&V) of neutronics tools, codes, and methodologies for core and system design in support of licensure of FHRs. Since FHRs vary greatly in reactor design, the phenomenon identification and ranking table (PIRT) was developed using the Advanced High-Temperature Reactor (AHTR) design as the basis.

5.1.1.2. PIRT Panel Membership

The PIRT panel consisted of thirteen voting members, covering a wide range of expertise in areas relevant to FHR neutronics validation and verification, including reactor physics, cross section development, national and international regulators, industry, and code and method developers. Table 5-1 provides a list of voting panelists and their organizations. In addition to the voting members of the panel, observers included several graduate students from both the Georgia Tech and MIT led IRPs, as well as Kim Stein, of AREVA Federal Services, LLC. David Diamond led the PIRT Panel and acted as the facilitator for the process.

Table 5-1: Neutronics PIRT panelists and organization.

Name	Organization
David Diamond (Facilitator)	Brookhaven National Laboratory

Christopher Edgar	Georgia Institute of Technology
Max Fratoni	University of California – Berkeley
Hans Gougar	Idaho National Laboratory
Ayman Hawari	North Carolina State University
Jianwei Hu	Oak Ridge National Laboratory
Nathanael Hudson	Nuclear Regulatory Commission
Dan Ilas	Oak Ridge National Laboratory
Ivan Maldonado	University of Tennessee – Knoxville
Bojan Petrovic	Georgia Institute of Technology
Farzad Rahnema	Georgia Institute of Technology
Dumitru Serghiuta	Canadian Nuclear Safety Commission
Dingkang Zhang	Georgia Institute of Technology

5.1.1.3. PIRT Overview

The PIRT process consisted of nine major steps:

1. Define the issue
2. Define objectives of the PIRT
3. Define hardware, scenario, methodology, etc.
4. Define evaluation criteria (figures-of- merit)
5. Identify, obtain, review database
6. Identify phenomena (processes, parameters, etc.)
7. Rank importance and provide rationale
8. Assess uncertainty/knowledge level
9. Document results and conclusions

Step 1: Define the Issue
Research on and eventual licensing of FHR technologies requires the availability of verified and validated neutronics tools, codes, and methodologies to provide modeling solutions which are well representative of the actual physics in the real system. These tools, codes, and methodologies may not currently exist and/or have a low level of knowledge and/or quantifiable accuracy.

Step 2: Define the Objectives of the PIRT
The objective of the PIRT panel was to determine the important phenomena that impact the fidelity of neutronics analysis for the FHR and determine where new databases, modeling, and detailed analysis need to be added to validate computer codes and methods.

Step 3: Define Hardware, Scenario, Methodology, etc.
This step involved the preparation of a white paper [1] by students and faculty at Georgia Tech discussing the details of the AHTR (GT's chosen FHR for evaluation) and the current status of research activities applicable to FHR technology. The whitepaper was released to the panelists ahead of the PIRT session to provide a design basis and present the current state of neutronics evaluations. Additionally, expert panelists shown in *Table 5-2* gave presentations on the opening day of the PIRT Panel, covering several key areas of interest

related to FHR neutronics analyses. Several members of the panel were primary authors on the major literature currently published and these presentations expanded on the details presented in their publications.

Table 5-2: List of Presentation on the PIRT Panel.

Name	Presentation
Christopher Edgar	AHTR Design Features
Jianwei Hu	SCALE Updates for FHR Applications
Dan Ilas	Use and Application of the SCALE Code System to AHTR Problems
Ivan Maldonado	Use and Application of SERPENT to AHTR Problems

Step 4: Define Evaluation Criteria (Figures-of-Merit)
In order to assess and rank the identified phenomena, two figures-of-merit (FoMs) were selected by the panel. These FoMs were selected such that the ability/inability of a tool, code, or method to accurately and correctly resolve the FoMs would allow for a basis to say the tool, code, or method is/is not verified. The two FoMs identified by the panel were:

- FoM_1: $k_{effective}$
- FoM_2: Plate piece wise fission density or neutron flux

These two FoMs were selected because they provide items of interest when considering licensure of a plant. The eigenvalue provides the reactivity (or change in reactivity) that can be used for design of reactivity control systems and analysis of various reactivity feedback characteristics. The plate wise fission density provides a spatial and time distribution of the fission density (and therefore reaction rates, flux, power, etc.), information necessary for fuel design, thermal hydraulics, safety systems, safety analysis, fuel management and operation.

Step 5: Identify, Obtain, Review Database
This step was performed by the panelists when they reviewed the whitepaper together with a list of relevant references, which identified and obtained any relevant research on FHRs. The expert presentations added additional depth and direct engagement between the panel and individuals who performed many of the previous neutronics analysis of FHR technologies.
Step 6: Identify Phenomena
In this step, panelists identified a list of phenomena and defined each of these for ranking and knowledge level classification. These phenomena are found in Appendices A-D. This portion of the process is effectively a brainstorming session and no consideration of whether the phenomenon would affect the chosen FoMs or the knowledge level was made at this step.

Step 7: Rank Importance and Provide Rationale

After phenomena identification was completed, panelists ranked the importance of each phenomenon identified, in relation to its effect on the FoMs. A vote was taken, whereby each voting member of the panel chose to assign high, medium, or low importance to the phenomenon's effect on the FoMs. Votes were then averaged to assign an overall importance. *Table 5-3* depicts the ranking and associated description. The rationale for each agreed upon importance was provided by the panel and is found in Appendices A-D.

Table 5-3 Phenomena importance rankings and descriptions

Ranking	Description
High (H)	Significant or dominant influence on FoM
Medium (M)	Moderate influence on FoM
Low (L)	Small influence on FoM

Voting Process for Assigning Importance Ranking

Each of the voting members were asked to vote if they felt the phenomena had a significant or dominant influence (High), moderate influence (Medium), or small influence (Low) on the Figure-of-Merit. Votes for High, Medium, and Low importance were assigned numerical score of 8, 5, and 2, respectively. If the average of the score was 6.5 or higher, the importance was assigned as High. If the average was above 3.5 and below 6.5, the importance was assigned as Medium. Finally, if the average was below 3.5, the importance was set to Low. This process was repeated for each phenomenon as it relates to each FoM.

Step 8: Assess Knowledge Level

In a similar manner to the importance ranking, the knowledge level of each phenomenon was voted on by the panel. During this process, each of the phenomena was classified as known, partially known, or unknown via a voting process. *Table 5-4* provides the definition of each knowledge level ranking. The knowledge level ranking was assigned based on the majority vote of the panelists, after the discussion period. Once this step was completed, phenomena were identified for further consideration based on their combination of importance and knowledge level rankings (see section 2.3.3 for description on how phenomena were identified for further consideration).

Table 5-4 Knowledge level ranking and descriptions

Ranking	Description
Known (K)	Phenomenon is well understood and can be accurately modeled
Partially Known (P)	Phenomenon is understood, however, can only be modeled with moderate accuracy
Unknown (U)	Phenomenon is not well understood. Modeling is currently either not possible or is possible only with large uncertainty

Step 9: Document Results and Conclusions
This publication represents the primary objective and fully covers the overall PIRT process, ranking methods, voting procedures, rationale for all rankings, discussion of the next steps for phenomena that require further consideration, and a record of the comments and suggested path forward from the panelists.

5.1.2. PIRT Preliminaries

Several important preliminary steps were taken before the identification and ranking efforts undertaken by the panel. The PIRT organizers (Farzad Rahnema, Christopher Edgar, David Diamond, and Bojan Petrovic) discussed the overall objective of the PIRT, based on the needs of the FHR-IRP. Once the objective was settled, a whitepaper was commissioned describing the geometry of the AHTR, as well as providing panelists with a literature review of applicable published works relating to the AHTR or FHRs in general.

5.1.3. FHR Neutronics Core Physics PIRTs

The PIRT tables representing core physics of neutronics calculations were broken down into four main categories and are presented in Appendices A-D of the topical report on PIRT. The subsequent sections provide a description of these categories, the format of the PIRT tables, and the criteria for deciding if a phenomenon requires further consideration. A path forward recommended by the panel for each phenomenon identified as requiring further consideration is summarized *Table 5-6*. This table in effect identifies the phenomena (issues) that require further work and/or research and development in support of licensing of the modeling and simulation tool(s) for neutronics analysis of FHR.

5.1.3.1. Category Descriptions

The PIRT panel identified and ranked phenomena for importance relative to the Figures-of-Merit in the following four categories, each of which is discussed in its corresponding subsection below.

Fundamental Cross-Section Data
Phenomena in this category include cross-sections, uncertainty in nuclear data, moderation and thermalization by isotopes and compounds, absorption rates, and reaction rates.

Material Composition
Phenomena in this category relate to fuel particle distributions in fuel plates, impurities present in materials, dimensional changes, and changes in conductivity.

Computational Methodology
Phenomena in this category were classified further into subcategories based on classes of computational methods, as follows:

- Stochastic continuous energy methods

- Stochastic multi-group methods
- Deterministic transport methods
- Two step stochastic transport-diffusion

Phenomena presented in each subcategory relate to issues faced by that computational methodology in relation to the FHR of interest. There are phenomena which cross over multiple computational methods and tables are provided in each subcategory for all phenomena discussed. Therefore, the reader may observe the same phenomena appearing in multiple subcategories.

General Depletion
Phenomena in this category represent effects presented in general for depletion calculations and relate to control depletion, spectral history effects, and isotope tracking.

5.1.3.2. Structure of the PIRT Tables

The structure of the PIRT tables found in Appendices A-D is as follows:

- Column 1 – Subcategory of the phenomena being addressed in that table
- Column 2 – Phenomenon that is being ranked
- Column 3 – The definition, rationale, importance, knowledge level, comments, and path forward for the phenomenon (if it meets the further consideration requirements presented in the next section)

5.1.3.3. Phenomena Identified for Further Consideration

After the identification and ranking process for each phenomenon was performed, the panel selected the phenomena requiring further consideration. This selection was based on the knowledge level ranking and importance ranking pertaining to each Figure-of-Merit. *Table 5-5* depicts the combinations of knowledge level and importance ranking requiring further action.

Table 5-5: Knowledge level and importance ranking combinations for further consideration.

		Importance Ranking (IR)		
		H (high)	**M** (medium)	**L** (low)
Knowledge Level (KL)	**K** (known)			
	P (partially known)	YES		
	U (unknown)	YES	YES	

If a phenomenon met the knowledge level and importance ranking requirements to be considered further, a path forward was provided by the panel and is presented in the Path Forward section of Column 3 of the PIRT and summarized below.

Table 5-6: Phenomena Requiring Further Consideration.

Phenomena	**Importance**		**Knowledge Level**	**Path forward**
	FoM_1	**FoM_2**		
	Fundamental Cross Section Data			
Moderation by FLiBe	H	L	P	Do a formal review of existing libraries; Compare ENDF to other cross-sections; Do a critical review of covariances for this design.
Thermalization by FLiBe	H	M	U	There is currently S(α,β) data under development for FLiBe and scheduled to be released in the Fall of 2016.
Thermalization in Carbon	H	H	U	Development of S(α,β) data of ENDF quality is recommended for C-C composite
Absorption in FLiBe	M	L	U	The uncertain impact on the temperature reactivity coefficient needs to be determined
Absorption in Carbon	H	M	P	Transmission measurements of typical samples for total cross-section, correlated for impurities, and over several thermal energies representative of graphite temperatures are recommended.
	Material Composition			
Fuel Particle Distribution	M	L	U	Interact with fuel fabricators to determine realistic particle distributions in the plate. If unusual non-uniformity is a possibility, then study the effect on $k_{effective}$ and local peaking factor
Computational Methodology				
Solution Convergence	L	H	P	Study the underestimate of statistical uncertainty and the magnitude of the fission density tilt. Develop methods to improve fidelity.
Granularity of Depletion Regions	H	H	U	The analysis needs to be performed to determine what the effects on the FoMs are.
Multiple Heterogeneity Treatment for Generating MG Cross-Sections	H	H	U	Develop methods for generating multi-group cross-sections. Stochastic continuous energy response methods may prove to be a good candidate for this purpose.

Selection of Multi-group Structure	H	H	U	Perform a sensitivity study at the assembly level with control rods and burnable absorbers to determine the minimum number of energy groups and structure. Consider generalized condensation theory as a candidate.
Boundary Conditions for MG x-section Generation	H	H	U	Develop methods for generating multi-group cross-sections. Stochastic continuous energy response methods may prove to be a good candidate for this purpose.
Burnable Poison Cell	H	H	U	Review the burnable absorber candidates and develop models for treatment of the most probable choice.
Scattering Kernel	H	H	P	Develop methods for generating multi-group cross-sections. Stochastic continuous energy response methods may prove to be a good candidate for this purpose.
Spatial Mesh	M	H	U	Explore various subdivisions of the fuel assembly.
Diffusion Approximation	H	H	P	Test methods to determine level of accuracy compared to full transport. If method is not satisfactory, explore higher order diffusion.
Dehomogenization	L	H	U	Develop a method to reconstruct the plate power and compare to detailed results.
	General Depletion			
Spectral History Effects	H	H	U	Adapt methods currently employed in Light Water Reactors to FHR and test.

It can be seen from *Table 5-6* that each of the four categories has at least one phenomenon that requires further consideration. In the fundamental cross section data category, five phenomena were identified, three of which are related to the FLiBe and two are related to the carbon. In the material composition category, fuel particle distribution in the fuel plate requires further investigation. In the computational methodology, 10 phenomena were identified. These can be summarized as issues related to solution convergence, multigroup treatment, and approximations made in the solution methods. Finally, spectral history effect was the only phenomenon identified in the general depletion category.

References

Abdukadyrova, I. K. ((2005)). Effect of Neutron Irradiation on the Structure and Optical Properties of Sapphire. *Inorganic Materials, 41*(10), 1080-1084.

Ames, D. E., & Tsvetkov, P. V. ((2008)). Benchmark Efforts to Support Studies of Advanced VHTRs. *Proc. 4th Intern. Conf. HTRs, HTR2008-58206.* ASME.

Anderson, E. E., Langer, S., Baldwin, N. L., & Vanslager, F. E. (ANS (1971)). An In-Core Furnace for the High-Temperature Irradiation Testing of Reactor Fuels. *Nucl. Techn., 11*, 259.

Arakani, M., & Gharib, M. ((2007)). *Design and Construction of an Independent Channel for Tehran Research Reactor Power Measurement Using Cherenkov Detector.* Tehran: MS Thesis, Azad University, Research and Science Department.

Arakani, M., & Gharib, M. ((2009)). Reactor Core Power Mesurement Using Cherenkov Radiation and Its Application in Tehran Research Reactor. *Ann. Nucl. Eng., 36*, 869-900.

Boland, J. F. ((1970)). *Nuclear Reactor Instrumentation (In-Core).* New York, NY: Gordon and Breach.

Connolly, K. J., Rahnema, F., & Tsvetkov, P. V. (Elsevier (2015)). Prismatic VHTR Neutronic Benchmark Problems. *Nucl. Eng. Design, 285*, 207.

Drinkwater, B. W., & Wilcox, P. D. ((2006)). Ultrasonic Arrays for Non-destructive Evaluation: A Review. *NDT&E International, 39*, 525-541.

Durkee, J. W. ((2013)). *MCNP6 Cherenkov Radiation.* Los Alamos, New Mexico: 2013-07-17, Los Alamos National Laboratory.

Generation IV International Forum. ((2016)). *Generation IV Annual Report.* GIF.

Giford, D., Soller, B., Wolfe, M., & Froggatt, M. ((2009)). Distributed Fiber-Optic Temmperature Sensing Using Rayleigh Backscatter. *LUNA Technologies*.

Hashemian, H. M. (InTech (2011)). Nuclear Power Plant Instrumentation and Control. In *Nuclear Power - Control, Reliablity, and human Factors* (pp. 49-66). Rijeka, Croatia.

Holcomb, D. E., Ilas, D., Varma, V. K., Cisneros, A. T., Kelly, R. P., & Gehin, J. C. (2011). *Core and Refueling Design Studies for the Advanced High Temperature Reactor (ORNL/TM-2011/365).* Oak Ridge, TN: Oak Ridge National Laboratory.

Holcomb, D. E., Peretz, F. J., & Qualls, A. L. ((2011)). *Advanced High Temperature Reactor Systems and Economic Analysis: September 2011 Status.* ORNL/TM2011/364: ORNL.

INL. ((2007)). *Next Generation Nuclear Plant Pre-conceptual Design Report, INL/EXT-07-12967.* Idaho: INL.

(2014). *Integrated Approach to Fluoride High Temperature Reactor (FHR) Technology and Licensing Challenges.* U.S. Department of Energy Nuclear Energy University Programs.

International Atomic Energy Agency. ((1999)). *Modern Instrumentation and Control for Nuclear Power Plants - a Guidebook.* Vienna, Austria: IAEA.

Jang, K. W., Yagi, T., Pyeon, C. H., Yoo, W. J., Shin, S. H., Misawa, T., & Lee, A. B. ((2013)). Feasibility of Fiber-Optic Radiation Sensor Using Cerenkov Effect for Detecting Thermal Neutrons. *Optics Express, 21*(12).

Janz, G. J. ((1967)). *Molten Salts Handbook.*

Jiang, X., Kim, K., Zhang, S., Johnson, J., & Salazar, G. ((2014)). High-Temperature Piezoelectric Sensing. *Sensors, 14*, 144-169.

Johns, J. ((2011)). A Distributed Fiber Optic Sensor Network for Online 3D Temperature and Neutron Fluence Mapping in a VHTR Environment. *Texas A&M University*.

Leppanen, J. ((2010)). Performance of Woodcock Delta-Tracking in Lattic Physics Applkications Using the Serpent Monte Carlo Reactor Physics Burnup Calculation Code. *Ann. Nucl. Eng., 37*(5), 715-722.

Luna. ((2016)). *Luna Sensors.*

Measurement of the Refractive Index of Distilled Water from the Near-Infrared Region to the Ultraviolet Region. ((2007)). *Applied Optics, 46*(18), 3811-3820.

Perrotton, C. ((2013)). A Reliable, Sensitive and Fast Optical Fiber Hydrogen Sensor Based on Surface Plasmon Resonance. *Optics Express, 21*(1), 382-390.

Petrie, C. M. ((2013)). *Characterization of the Performance of Sapphire Optical Fiber in Intense Radiation.* The Ohio State University.

physics.nist.gov ESTAR database. (n.d.).

Pioro, I. ((2016)). *Handbook of Generation IV Nuclear Reactors.* Woodhead Publishing, Elsevier.

Principles of Optics. ((1980)). New York: Pergamon Press.

Quickenden, T. I., & Irving, J. A. ((1980)). The Ultraviolet Absorption Spectrum of Liquid Water. *The Journal of Chemical Physics, 72*(4416).

Rahnema, F., & Others. (2018). Phenomena, Gaps, and Issues for Neutronics Modeling and Simulation of FHRs. *Annals of Nuclear Energy*(IN THIS ISSUE).

Rahnema, F., Edgar, C., Zhang, D., & Petrovic, B. (2016). *Phenomena Identification and Ranking Tables (PIRT) for Fluoride High-Temperature Reactor (FHR) Neutronics.* Atlanta, GA: Georgia Institute of Technology. Retrieved from https://smartech.gatech.edu/handle/1853/55812

Rahnema, F., Petrovic, B., Edgar, C., Zhang, D., Avigni, P., Huang, M., & Terlizzi, S. (2015). *Whitepaper: The Current Status of the Tools for Modeling and Simulation of Advanced High Temperature Reactor Neutronics Analysis Modeling.* Atlanta, GA.

Rippon, S. E. ((1963)). Cherenkov Detectors for the Measurement of Reactor Power. *Nucl. Instr. Methods, 21*, 192-196.

Ritchie, J. ((2010)). *Pressure Measurement in a High Temperature Molten Salt Loop.* Knoxville, TN: University og Tennessee.

Segelstein, D. J. ((1981)). *The Complex Refractive Index of Water, MS Thesis in Physics.* Kansas City, Missouri: University of Missouri-Kansas City.

Singh, P., & Others. (2018). Phenomena Identification and Ranking Tables (PIRT) Study for Advanced High Temperature Reactor Structural Materials. *Annals of Nuclear Energy*(IN THIS ISSUE).

Singh, P., Chan, K., & Rahnema, F. (2017). *Phenomena Identification and Ranking Tables (PIRTs) Report for Material Selection and Possible Material Degradation Mechanisms in FHR.* Atlanta, GA.

Sun, X., & Others. (2018). A Thermal Hydraulic Phenomena Identification and Ranking Table Study for Advanced High Temperature Reactor. *Annals of Nuclear Energy*(IN THIS ISSUE).

Sun, X., Yoder, G., Christensen, R., Shi, S., Lin, H.-C., Wu, X., & Zhang, S. (2016). *Thermal Hydraulic Phenomena Identification and Ranking Tables (PIRTs) for Advanced High-Temperature Reactor (AHTR).*

Tsvetkov, P. V., Bragg-Sitton, S. M., Johns, J. M., Lewis III, T. G., Alajo, A. B., & Johnson, M. P. (USA (2011)). Distributed Sensor Networks for Online 3D In-Core Monitoirng in VHTR Environments. *Trans. Amer. Nucl. Soc., 104*, 931.

Varma, V. K., Holcomb, D. E., Peretz, F. J., Bradley, E. C., Ilas, D. Q., & Zaharia, N. M. (2012). *AHTR Mechanical, Structural, and Neutronic Preconceptual Design (ORNL/TM-2012/320).* Oak Ridge, TN: Oak Ridge National Laboratory.

Varma, V., Holcomb, D., Peretz, F., Bradley, E., Ilas, D., Qualls, A., & Zaharia, N. (2012). *AHTR Mechanical, Structural, and Neutronic Preconceptual Design.* Oak Ridge, TN: ORNL.

Wei Huang, Lifang Tian, Changfeng She, Feng Jiang, Haiyang Zheng, Wenxin Li, Guozhong Wu, Dewu Long, Qingnuan Li. (2014). Electrochemical Behavior of Europium(III)-Europium(II) in LiF-NaF-KF Molten Salt. *Electrochimica Acta, 147*, 114-120.

Wen, J., Peng, G. D., Luo, W., Xiao, Z., Chen, Z., & Wang, T. ((2011)). Gamma Irradiation Effect on Rayleigh Scattering in Low Water Peak single-Mode Optical Fibers. *Optics Express*.

X-5 Monte Carlo Team. (Los Alamos National Laboratory (2018)). MCNP - A General Monte Carlo N-Particle Transport Code, Version 6, User Manual.

Yang, M., & Dai, J. ((2014)). Fiber Optic Hydrogen Sensors: a Review. *Photonic Sensors, 4*(4), 300-324.

Zhou, Q. a. ((2011)). Pressure Sensor Based on the Fiber-Optic Extrinsic Fabry-Perot Interferometer. *Photonic Sensors, 1*(1), 72-83.

5.2. Thermal Hydraulics PIRT-like Panel

5.2.1. PIRT Methodology

A detailed PIRT process consists of nine steps [5.1]. They are described for the current TH-PIRT process in the following:

Step 1: Define the Issue

The objective of this step is to define the potential issue for the AHTR future licensing applications. The issue is identified to be a lack of adequate thermal hydraulic modeling methodologies, tools, and codes that can be validated to support research and development, and eventual licensing for the FHRs with sufficient accuracy.

Step 2: Define the Specific Objectives

The objective of the TH-PIRT study panel is to determine the important phenomena that impact the fidelity of thermal hydraulics analysis for the AHTR and determine where new databases, modeling and detailed analysis need to be performed to validate computer codes and methods. In addition, it also provides insights in establishing the requirements for separate-effect and integral-effect experimental programs in support of the AHTR licensing.

Step 3: Define the Hardware and Scenario

The AHTR design is the subject of this PIRT study. Four scenarios, including SBO, simultaneous withdrawal of all control rods, reactor core partial flow blockage, and loss of coolant accidents (LOCAs), were initially proposed together with a number of other events. Due to time constraint of the PIRT workshop and based on potential severity of the accidents, two of the identified scenarios, namely, the SBO and simultaneous withdrawal of all control rods, were selected for detailed discussion.

Step 4: Define the Evaluation Criterion

Figures of Merit (FOMs) are used to define the evaluation criteria for different scenarios. For the event of SBO, four FOMs were identified by the panel: (a) peak vessel temperature; (b) Direct Reactor Auxiliary Cooling System (DRACS) coolant (salt) temperature in the natural draft DRACS heat exchangers (NDHXs); (c) peak temperature of the DRACS heat exchangers (DHXs); and (d) average temperature increase of carbonaceous materials in the

reactor core. For the event of simultaneous withdrawal of all control rods, two FOMs were identified: a) hot-leg salt temperature and b) maximum fuel kernel temperature.

Step 5: Identify, Compile, and Review the Current Knowledge Base
The PIRT panel members reviewed the prepared whitepaper and relevant references prior to the TH-PIRT workshop. In addition, three presentations were given at the beginning of the meeting to summarize the AHTR design, discuss the whitepaper, and introduce the PIRT process, which helped the panelists develop a good understanding of current knowledge base related to the AHTR technologies and the PIRT process.

Step 6: Identify Plausible Phenomena
Phenomena are identified by the panelists based on the systems and components in the AHTR, which were defined and classified as follows:

- Core: fuel and primary coolant
    - Heat capacity of the carbonaceous materials
    - Thermal conductivity of the carbonaceous materials
    - Heat capacity of the fuel stripe
    - Thermal conductivity of the fuel stripe
    - Heat capacity of the fuel kernel
    - Thermal conductivity of the fuel kernel
    - Geometry of the fuel plate
    - Energy generation rate in the fuel kernel
    - Energy generation rate outside the kernels but within the fuel plates
    - Radiative heat transfer
    - Surface condition
    - Fuel temperature coefficient of the reactivity
    - Assembly (graphite) coefficient
    - Heat capacity of FLiBe
    - Thermal conductivity of FLiBe
    - Viscosity of FLiBe
    - Core heat transfer coefficient
    - Optical properties
    - Form loss coefficients
    - Wall friction
    - Core flow asymmetry
    - Bypass flow fraction
    - Direct energy deposition
- Reactor vessel/internals/cavity: upper plenum, lower plenum, fluidic diode, reactor vessel, and cavity
    - Upper plenum mixing
    - Fluidic diodicity
    - Cover gas entrainment
    - Thermal heat capacity of the vessel
    - Thermal conductivity of the vessel
    - Heat transfer to the upper plenum structures

    - Heat transfer to the fusible links
    - Heat transfer coefficient to the vessel wall
    - Friction factor on the vessel wall in the downcomer
    - Mixing in the lower plenum
    - Heat transfer to the cover gas and vessel top flange
    - Thermal properties of the insulation
    - Heat transfer across the vessel to the gas space
    - Heat transfer across the second gap to the concrete
    - Conduction in the concrete
- Primary loop: pump, piping, and tube side of the primary to the intermediate heat exchanger (P-IHX)
    - Pump performance
    - Pump resistance or the *K* factor
    - Form losses in the loop
    - Wall friction in the loop
    - P-IHX performance
    - Heat losses through and from, thermal inertia of piping
    - Impact of the cover gas entrainment on the pump
- Intermediate loop: pump, piping, and shell side of the P-IHX, tube side of the intermediate to power cycle heat exchanger (I-PHX)
    - Pump performance
    - Pump coast down
    - Pump resistance or the *K* factor
    - Form losses in the loop
    - Wall friction in the loop
    - I-PHX performance
    - Heat losses from piping
    - P-IHX performance
- Power conversion loop
    - I-PHX performance
    - Power cycle performance
- DRACS: DHX, NDHX, DRACS salt, chimney, and piping
    - DRACS piping
    - DHX performance
    - NDHX performance
    - Piping heat losses
    - Chimney natural circulation and performance
    - $KF\text{-}ZrF_4$ thermophysical properties
    - Thermal inertia of DRACS and chimney

Step 7: Develop Importance Ranking

After the phenomena had been identified, phenomena importance rankings were decided based on their effects on each of the identified FOMs by the panelists Table 5-7 shows the phenomena importance rankings. Considering the importance of each phenomenon to an

FOM in a specific scenario, the panelists then voted for the phenomenon and the importance ranking of the phenomenon was then solidified by averaging the votes.

Table 5-7. Phenomena importance rankings

Ranking	Description
High (H)	Significant or dominant influence on FOMs
Medium (M)	Moderate influence on FOMs
Low (L)	Small influence on FOMs (including the possibility that the phenomenon is not present or possible)

Step 8: Assess Knowledge Level
Similar to Step 7, the panelists voted for the knowledge level (KL) of each phenomenon. In this step, the knowledge levels were graded as Known (K), Partially known (P), and Unknown (U). Table 5-8 shows the knowledge level rankings. The knowledge level of a phenomenon was set to Known if more than 75% of the voting members ranked it as Known, Unknown if less than 25% of the knowledge base is established, and Partially known otherwise.

Table 5-8. Knowledge level ranking definitions

Ranking	Description
Known (K)	Phenomenon is well understood and can be accurately modeled
Partially Known (P)	Phenomenon is understood, however, can only be modeled with moderate uncertainty
Unknown (U)	Phenomenon is not well understood. Modeling is currently either not possible or is possible only with large uncertainty

After the phenomenon importance and knowledge level ranking, phenomena that need further consideration were then determined. Table 5-9 shows the rules to determine phenomena that need further consideration. As can be seen from the table, the phenomena under three combinations of importance ranking and knowledge level require further consideration: (a) the importance ranking is High (H) and knowledge level is Partially known (P), (b) the importance ranking is High (H) and knowledge level is Unknown (U), and (c) the importance ranking is Medium (M) and knowledge level is Unknown (U).

		Importance Ranking (IR)		
		H	**M**	**L**
Knowledge Level	**K**			
	P	YES		
	U	YES	YES	

Table 5-9. Determination of phenomena for further consideration

Step 9: Document PIRT Results
The PIRT study results, including the phenomenon definitions, importance rankings, knowledge level rankings, rationale for all rankings, path forward regarding the phenomena needing further consideration and prioritization of next steps were documented in this step. This report presents a simplified version of the TH-PIRT chats due to the space limit. More detailed information, such as commentary of each phenomenon, can be found in the TH-PIRT report [5.2-3].

5.2.2. AHTR PIRT for Event of Station Blackout

An SBO event involves the complete loss of all offsite and onsite alternating current (AC) power. This event was identified as one of the main contributors to overall plant risk and overall core damage frequency (CDF) for LWRs [5.4]. which was also selected as the main event for the current FHR analysis. Per design, when the external AC electrical power is lost, onsite emergency diesel generators will start to provide AC electrical power for operation of safety related systems and accident recovery. However, when the diesel generators also fail, the nuclear power plant is then left in the SBO.

The protected SBO (SBO with reactor scram) is focused on by this PIRT panel, i.e., all the pumps trip and coast down due to the loss of electric power supply when the event is initiated. Therefore, forced coolant circulations are gradually lost and active cooling systems, such as the power conversion cycle loops and the maintenance cooling system, are out of commission. As an emergency response, the reactor will scram. One major concern in such a situation is the generation and removal of decay heat. The decay heat removal entirely relies on natural circulation/convection in the DRACS and the three DRACS loops are designed to remove a total of 0.75% of the nominal reactor thermal power from the primary coolant to the ambient air. For the AHTR design, the fuel and coolants have large thermal margins from failure under the reactor normal operation. However, even with the superior inherent safety features, the SBO scenario still needs to be analyzed to ensure reactor safety for the AHTR design.

5.2.3. Proposed FOMs for Event of Station Blackout

During the SBO, the reactor vessel temperature may increase dramatically and potentially affect its integrity. DHX is submerged in the primary salt between the core barrel and reactor vessel, therefore, the phenomena related to the peak vessel temperature are also relevant to the DHX peak temperature, which indicates where the structural material may be challenged for integrity since the tube walls in the DHXs are relatively thin compared to other components in the reactor vessel. DRACS is the main decay heat removal system during SBO and its decay heat removal performance is largely affected by the two types of heat exchangers, namely the DHXs and NDHXs. One of the scenarios that should be carefully examined is the potential DRACS salt freezing due to potential overcooling by air in the NDHXs. It is therefore important to monitor the DRACS salt temperature at the exit of the NDHXs. In addition, the average temperature increase of carbonaceous materials in the

core during the accident characterizes the stored energy, which may delay the vessel temperature increase and reduce the magnitude of the increase. Temperature increase in the carbonaceous materials will also lead to potential tritium release from the carbonaceous materials. The amount of tritium released depends on the original amount of tritium retained in the carbonaceous materials. Based on the above discussion, the following FOMs are selected for the SBO scenario in developing the TH-PIRT:

- Peak vessel temperature
- Average temperature increase of the carbonaceous materials in the core
- DRACS salt temperature in the NDHXs
- Peak temperature of the DHXs

The TH-PIRT charts identified by the panel for the event of SBO are summarized in Table 5-10 to Table 5-17, which state the definition of the phenomena and their importance level with regard to each of the individual FOMs and our current state of knowledge of the phenomena. It is noted that the knowledge level for some of the phenomena is not provided (noted with "--") due to their low importance level to the FOMs. In addition, the importance level for some of the FOMs is left blank. All the identified phenomena are discussed in detail with respect to the first FOM by the panelists, but due to the time constraint, if the importance level of a specific phenomenon for the other FOMs is not considered to be higher than that with respect to the first FOM, then this phenomenon is not ranked for the other FOMs.

5.2.4. TH-PIRT for Event of Station Blackout

Table 5-10. TH-PIRT chart for SBO (Core/fuel)

System: Core/fuel		FOMs				
Phenomenon	Definition	Peak vessel temp.	Average temp. increase of carbonaceous materials in the core	DRACS salt temp. in the NDHX	Peak temp. of the DHX	KL
Heat capacity of the carbonaceous materials	As a function of the temperature and irradiation (includes the density and specific heat capacity)	M	H			K
Thermal conductivity of the carbonaceous materials	As a function of the temperature and irradiation	M				P
Heat capacity of the fuel stripe	As a function of the temperature and irradiation (includes the density and specific heat capacity)	M	H			K
Thermal conductivity of the fuel stripe	As a function of the temperature and irradiation	M				P
Heat capacity of the fuel kernel	As a function of the temperature and irradiation (includes the density and specific heat capacity)	L				--
Thermal conductivity of the fuel kernel	As a function of the temperature and irradiation	L				--
Geometry of the fuel plate	Deviation from its original geometry. Distortion due to irradiation	M				U
Energy generation rate in the fuel kernel	Heat generation rate due to accumulation of the fission products and actinides at steady-state or at shutdown during accidents (decay power)	H				K
Radiative heat transfer	From surface of the fuel plate	L				--
Surface condition	Surface roughness, degradation or erosion	M				P

Note: temp: temperature

Table 5-11. TH-PIRT chart for SBO (Core/primary coolant flow)

System: Core/Primary coolant flow		FOMs				
Phenomenon	Definition	Peak vessel temp.	Average temp. increase of carbonaceous materials in the core	DRACS salt temp. in the NDHX	Peak temp. of the DHX	KL
Heat capacity of FLiBe	As a function of the temperature (includes the density and specific heat capacity)	H				K
Thermal conductivity of FLiBe	As a function of the temperature	H				P
Viscosity of FLiBe	As a function of the temperature	H				P
Core heat transfer coefficient	Forced/ natural convection	M	M			P
Optical properties	Absorption and transmission as a function of the temperature and wavelength	L				--
Form loss coefficients	Entrance and exit loss coefficients as a function of the area ratio and Reynolds number	M				P
Wall friction	Taking into account spacer ridges on the fuel plates	H				P
Core flow asymmetry	Due to components in the vessel	M				U
Bypass flow fraction	Ratio of the inter-assembly flow to the total core flow	L				--
Direct energy deposition	Direct heating of the coolant from fuel as a function of the axial and radial positions in the core for steady state and decay loads	L	M			P

Table 5-12. TH-PIRT chart for SBO (Reactor vessel)

System: Reactor vessel		FOMs				
Phenomenon	Definition	Peak vessel temp.	Average temp. increase of carbonaceous materials in the core	DRACS salt temp. in the NDHX	Peak temp. of the DHX	KL
Upper plenum mixing	Pluming and stratification and impact on the upper internal structures	H				U
Fluidic diodicity	Pressure loss as a function of flow direction and flow rate	H				P
Cover gas entrainment	Due to frothing at the free surface	L				--
Heat capacity of the vessel	As a function of the temperature (includes the density and specific heat capacity); to determine heat transfer across the vessel wall	L				--
Thermal conductivity of the vessel	As a function of the temperature and irradiation; to determine heat transfer across the vessel wall	L				--
Heat transfer to the upper plenum structures	Heat transfer to the control rod drives and guide tubes	L				--
Heat transfer coefficient to the vessel wall	Natural/Forced convection heat transfer coefficient (inside the vessel)	M				K
Friction factor on the vessel wall in the downcomer	As a function of the Reynolds number; to determine the frictional pressure drop in the downcomer	M				K
Mixing in the lower plenum	Mixing of the salt flow from eight downcomer segments	M				U
Heat transfer to the cover gas and vessel top flange	Radiative and convective heat transfer of the cover gas	M				P

Table 5-13. TH-PIRT chart for SBO (Cavity)

System: Cavity		FOMs				
Phenomenon	Definition	Peak vessel temp.	Average temp. increase of carbonaceous materials in the core	DRACS salt temp. in the NDHX	Peak temp. of the DHX	KL
Thermal properties of the insulation	Density, thermal conductivity and heat capacity	L				--
Heat transfer across the vessel to the gas space	Net resistance to heat transfer	L				--
Heat transfer across the second gap to the concrete	Heat convection and radiation	L				--
Conduction in the concrete	Wall heat transfer; concrete thermal conductivity and temperature gradient in the wall	L				--

Table 5-14. TH-PIRT chart for SBO (Primary loop)

System: Primary loop		FOMs				
Phenomenon	Definition	Peak vessel temp.	Average temp. increase of carbonaceous materials in the core	DRACS salt temp. in the NDHX	Peak temp. of the DHX	KL
Pump performance	Relationship between the driving force and flow rate, efficiency, including coastdown (speed vs. time)	L				--
Pump resistance or the *K* factor	Pressure drop across the pump	L				--
Form losses in the loop	Pressure losses due to bends, fittings, valves, etc., presented in the flow loop	L				--
Wall friction in the loop	Function of the Reynolds number	L				--
P-IHX performance	Heat transfer and pressure drop on the primary side	L				--
Heat losses through and from, thermal inertia of piping	Through thermal insulation	L				--
Impact of the cover gas entrainment on pump	Due to frothing at the free surface	L				--

Table 5-15. TH-PIRT chart for SBO (Intermediate loop)

System: Intermediate loop		FOMs				
Phenomenon	Definition	Peak vessel temp.	Average temp. increase of carbonaceous materials in the core	DRACS salt temp. in the NDHX	Peak temp. of the DHX	KL
Pump performance	Relationship between the driving force and flow rate, efficiency	L				--
Pump coastdown	Pump speed versus time	L				--
Pump resistance or the *K* factor	Pressure drop across the pump	L				--
Form losses in the loop	Pressure losses due to bends, fittings, valves, etc.	L				--
Wall friction in the loop	Frictional pressure drop, friction factor is a function of the Reynolds number	L				--
I-PHX performance	Heat transfer and pressure drop in I-PHX on the intermediate loop side	L				--
Heat loss from piping	Heat loss through the thermal insulation on piping	L				--
P-IHX performance	Heat transfer and pressure drop in P-IHX on the intermediate loop side	L				--

Table 5-16. TH-PIRT chart for SBO (Power cycle)

System: Power cycle		FOMs				
Phenomenon	Definition	Peak vessel temp.	Average temp. increase of carbonaceous materials in the core	DRACS salt temp. in the NDHX	Peak temp. of the DHX	KL
I-PHX performance	Heat transfer and pressure drop in the I-PHX on the power cycle side	L				--

Table 5-17. TH-PIRT chart for SBO (DRACS)

System: DRACS		FOMs				
Phenomenon	Definition	Peak vessel temp.	Average temp. increase of carbonaceous materials in the core	DRACS salt temp. in the NDHX	Peak temp. of the DHX	KL
DRACS piping	Friction and form losses	H		H	H	K
DHX performance	Heat transfer and pressure drop in DHX on both sides	H		H	H	P
NDHX performance	Heat transfer and pressure drop in NDHX on both sides	H		H	H	P
Piping heat losses	Heat losses through thermal insulation	H		H	H	P
Chimney natural convection and performance	Pressure loss coefficients under different conditions	H		H	H	P
KF-ZrF_4 thermo-physical properties	Specific heat capacity, thermal conductivity, viscosity, density	H		H	H	U
Thermal inertia of DRACS and chimney	Heat stored in the structures, thermal insulation, and chimney	M		M	M	P

5.2.5. AHTR PIRT for the Event of Simultaneous Withdrawal of All Control Rods

In the AHTR design, control rods (control blades) are driven by control drives located above the reactor vessel upper flange. Each control rod is independently driven and connected to a leader rod [5.5]. The control drive design determines the time needed to withdraw all control rods, which has a significant effect on the time response of the core in terms of reactor power change. Different from the SBO, forced flow circulation and active cooling are still available in the event of simultaneous withdrawal of all control rods. The heat transfer from the primary loop to the power conversion cycle loop is the major heat transfer path for this scenario. Therefore, the performance of the primary and intermediate loop pumps and other active cooling components are critical in this event. One of the important safety mechanisms in the AHTR design is the fusible link on the control rod: each fusible link is connected to a control rod and is immersed in the upper plenum salt. If the temperature of a fusible link rises and exceeds the set point, the fusible link will melt and the connected control rod will drop down into the core. The non-uniform temperature distributions in the reactor core and upper plenum would result in the control rod insertion at different times. The fusible links just above the hot channels are expected to melt first and the associated control rods to drop first.

5.2.6. Proposed FOMs for the Event of Simultaneous Withdrawal of All Control Rods

The AHTR was found inherently safe with large negative temperature feedback (-0.01 $/°C) so that the reactor power is limited by the Doppler effect [5.6]. With the safety characteristics of large thermal inertia in the AHTR, the reactor vessel can be kept at lower temperatures even if the fuel temperatures increase in a short period of time. For this event, when all control rods are withdrawn from the reactor core at the same time, a positive reactivity is introduced, making the reactor supercritical. Although the primary pumps keep operating, the coolant temperature may still increase significantly due to the over power event. The salt hot-leg temperature is the maximum temperature of the entire primary loop. It may exceed the structural material damage or failure temperature limit and therefore affect the primary loop integrity. The maximum fuel kernel temperature was selected as one of the FOMs for this event because of its significant influence on the kernel integrity of the fuel particles. Based on the issues described above, the following FOMs are selected for the event of simultaneous withdrawal of all control rods in developing the PIRT:

- Hot-leg salt temperature
- Maximum fuel kernel temperature

The TH-PIRT charts identified for the event of simultaneous withdrawal of all control rods by the panel are listed in Table 5-18 to Table 5-25.

5.2.7. TH-PIRT for the Event of Simultaneous Withdrawal of All Control Rods

Table 5-18. TH-PIRT chart for simultaneous withdrawal of all control rods (Core/fuel)

System: Core/fuel		FOMs		
Phenomenon	Definition	Hot-leg salt temp.	Maximum fuel kernel	KL

			temp.	
Heat capacity of the carbonaceous materials	As a function of the temperature and irradiation (includes the density and specific heat capacity)	H		K
Thermal conductivity of the carbonaceous materials	As a function of the temperature and irradiation	H		P
Heat capacity of the fuel stripe	As a function of the temperature and irradiation (includes the density and specific heat capacity)	H		K
Thermal conductivity of the fuel stripe	As a function of the temperature and irradiation	H		P
Heat capacity of the fuel kernel	As a function of the temperature and irradiation (includes the density and specific heat capacity)	H		K
Thermal conductivity of the fuel kernel	As a function of the temperature and irradiation	H		K
Geometry of the fuel plate	Deviation from its original geometry. Distortion due to irradiation	L		U
Energy generation rate in the fuel kernel	Heat generation rate due to accumulation of the fission products and actinides at steady-state or at shutdown during accidents (decay power)	H		K
Energy generation rate outside the kernel but within the fuel plate	Heat generation rate axially and transversely (radially) due to accumulation of the fission products and actinides at steady-state and decay power	M	M	K
Radiative heat transfer	From the surface of the fuel plate	L		--
Surface condition	Surface roughness, degradation or erosion	L		P
Fuel temperature coefficient of the reactivity	The change in reactivity per degree of the change in the temperature of the nuclear fuel	H		K
Assembly (graphite) coefficient	The change in reactivity per degree of the change in the temperature of the assembly (graphite)	M		K

Table 5-19. TH-PIRT chart for simultaneous withdrawal of all control rods (Core/primary coolant flow)

System: Core/primary coolant flow		FOMs		
Phenomenon	Definition	Hot-leg salt temp.	Maximum fuel kernel	KL

			temp.	
Heat capacity of FLiBe	As a function of the temperature (includes the density and specific heat capacity)	H		K
Thermal conductivity of FLiBe	As a function of the temperature	H		P
Viscosity of FLiBe	As a function of the temperature	H		P
Core heat transfer coefficient	Forced/Natural convection	H		P
Optical properties	Absorption and transmission as a function of the temperature and wavelength	L		--
Form loss coefficients	Entrance and exit loss coefficients as a function of the area ratio and Reynolds number	L	M	P
Wall friction	Taking into account the spacer ridges on the fuel plate	M		P
Core flow asymmetry	Due to the existence of the components in the vessel	L	M	U
Bypass flow fraction	Ratio of the inter-assembly flow to the total core flow	M	H	U
Direct energy deposition	Direct heating of the coolant from the fuel as a function of the axial and radial positions in the core for steady state and decay loads	L	M	P

Table 5-20. TH-PIRT chart for simultaneous withdrawal of all control rods (Reactor vessel)

System: Reactor vessel		FOMs		
Phenomenon	Definition	Hot-leg salt temp.	Maximum fuel kernel temp.	KL
Upper plenum mixing	Pluming and stratification, and impact on upper internal structures	H		U
Fluidic diodicity	Pressure loss as a function of the flow direction and flow rate	M		P
Cover gas entrainment	Due to frothing at the free surface	L		--
Heat capacity of the vessel	As a function of the temperature (includes the density and specific heat capacity); to determine heat transfer across the vessel wall	L		--
Thermal conductivity of the vessel	As a function of the temperature and irradiation; to determine heat transfer across the vessel wall	L		--
Heat transfer to the upper plenum structures	Heat transfer to the control rod drives and guide tubes	L		--
Heat transfer to the fusible links	Heat transfer to the fusible links, which helps determine when the fusible links melt	H		U
Heat transfer coefficient to the vessel wall	Natural/Forced convection heat transfer coefficient (inside the vessel)	L		K
Friction factor on the vessel wall in the downcomer	As a function of the Reynolds number; to determine the frictional pressure drop in the downcomer	L		K
Mixing in the lower plenum	Mixing of the salt flow from eight downcomer segments	L		U
Heat transfer to the cover gas and vessel top flange	Radiative and convective heat transfer of the cover gas	L		P

Table 5-21. TH-PIRT chart for simultaneous withdrawal of all control rods (Cavity)

System: Cavity		FOMs		
Phenomenon	Definition	Hot-leg salt temp.	Maximum fuel kernel temp.	KL
Thermal properties of the insulation	Density, thermal conductivity, and specific heat capacity	L		--
Heat transfer across the vessel to the gas space	Net resistance to heat transfer	L		--
Heat transfer across the second gap to the concrete	Heat convection and radiation	L		--
Conduction in the concrete	Wall heat transfer; concrete thermal conductivity and temperature gradient in the wall	L		--

Table 5-22. TH-PIRT chart for simultaneous withdrawal of all control rods (Primary loop)

System: Primary loop		FOMs		
Phenomenon	Definition	Hot-leg salt temp.	Maximum fuel kernel temp.	KL
Pump performance	Relationship between the driving force and flow rate, efficiency and coastdown (pump speed vs. time)	H		P
Pump resistance or the *K* factor	Pressure drop across the pump	L		--
Form losses in the loop	Pressure losses due to bends, fittings, valves, etc., presented in the flow loop	L		--
Wall friction in the loop	Friction factor as a function of the Reynolds number and wall roughness	L		--
P-IHX performance	Heat transfer and pressure drop on the primary side	H		U
Heat losses through and from, thermal inertia of piping	Through thermal insulation	L		--
Impact of the cover gas entrainment on pump	Due to frothing at the free surface	L		--

Table 5-23. TH-PIRT chart for simultaneous withdrawal of all control rods (Intermediate loop)

System: Intermediate loop		FOMs		
Phenomenon	Definition	Hot-leg salt temp.	Maximum fuel kernel temp.	KL
Pump performance	Relationship between driving force and flow rate, efficiency	H		P
Pump coastdown	Pump speed versus time	L		--
Pump resistance or the *K* factor	Pressure drop across the pump	L		--
Form losses in the loop	Pressure losses due to bends, fittings, valves, etc.	L		--
Wall friction in the loop	Frictional pressure drop, friction factor is a function of the Reynolds number	H		U
I-PHX performance	Heat transfer and pressure drop in the I-PHX on the intermediate loop side	L		--
Heat losses from piping	Heat losses through the thermal insulation on piping	L		--
P-IHX performance	Heat transfer and pressure drop in the P-IHX on the intermediate loop side	H		U

Table 5-24. TH-PIRT chart for simultaneous withdrawal of all control rods (Power cycle)

System: Power Cycle		FOMs		
Phenomenon	Definition	Hot-leg salt temp.	Maximum fuel kernel temp.	KL
I-PHX performance	Heat transfer and pressure drop in the I-PHX on the power cycle side	H		U
Power cycle performance	Overall performance of the Steam Rankine cycle, including the major components of turbines, condenser, feedwater heaters, feedwater pump, and auxiliary systems	H		U

Table 5-25. TH-PIRT chart for simultaneous withdrawal of all control rods (DRACS)

System: DRACS		FOMs		
Phenomenon	Definition	Hot-leg salt temp.	Maximum fuel kernel temp.	KL
DRACS piping	Friction and form losses	L		K
DHX performance	Heat transfer and pressure drop in DHX on both sides	L		P
NDHX performance	Heat transfer and pressure drop in NDHX on both sides	L		P
Piping heat losses	Heat losses through intact insulation	L		P
Chimney natural convection and performance	Pressure loss coefficients under different conditions	L		P
KF-ZrF_4 thermo-physical properties	Specific heat capacity, thermal conductivity, viscosity, and density	L		U
Thermal inertia of DRACS and chimney	Heat stored in the structures, thermal insulation, and chimney	L		P

5.2.8. Modeling the Two Events and Path Forward

The commentary notes on the key phenomena identified for the two events and path forward suggested by the panelists are summarized Table 5-26. More detailed information can be found in the TH-PIRT report [5.1-2].

Table 5-26. Commentary and path forward for key phenomena identified for both events

Phenomenon	Commentary and Path Forward
Heat capacity of the carbonaceous materials	• The carbonaceous materials are used inside fuel stripes and as a structural material in the fuel assemblies • After the reactor scrams, a fraction of the captured tritium in carbonaceous materials will be released to the salt with temperature increase • The heat capacity related to the stored energy in the materials affects the transient of the structure and coolant temperature changes
Thermal conductivity of the carbonaceous materials	• Cooperation with material scientists to better understand the property is required
Thermal conductivity of the fuel stripe	• Cooperation with material scientists to better understand the property is required
Heat capacity of the fuel kernel	• The mass ratio of the fuel kernel to the primary salt is low, therefore this phenomenon is ranked as Low for the peak vessel temperature FOM in SBO
Thermal conductivity of the fuel kernel	• Cooperation with material scientists to better understand the property is required
Geometry of the fuel plate	• The change of the geometry will affect the pressure drop and heat transfer from the fuel to the primary salt as well as the coolant flow distribution in the core • Deviation from the original plate geometry may affect the alignment between fuel plate and supporting structure • Vibration in the long fuel plates may cause potential structural issues • To better understand the effect of fuel plate swelling with temperature and irradiation, cooperation with material scientist is required
Energy generation rate in the fuel kernel	• Energy generation is the heat source of the transient. Its rate is determined by the reactivity or the decay heat rate

Radiative heat transfer	• Radiative heat transfer from the fuel plates to the primary salt is low compared to the heat conduction and convection • FLiBe is nearly transparent to thermal radiation
Fuel plate surface condition	• The fuel plate surface condition is one of the design parameters • Surface condition of fuel plates has impact on natural circulation flow in the core during SBO • Cooperation with material scientists is required to characterize the fuel plates
Thermal conductivity and viscosity of FLiBe	• Measured values of the properties have large variations in the literature • Instrumentation limitation results in high measurement uncertainties, therefore a comprehensive review of the measurement uncertainties in the literature is needed. It is also important to study the sensitivities of the uncertainties in these properties to the final quantities of interest • New measurements of the molten salt properties should be carried out on demand
Core heat transfer coefficient	• Perform separate-effect tests for correlation/model improvement (and/or development) and validation with experimental data for different flow regimes (laminar/transition/turbulent) in the core
Form loss coefficients	• The form loss coefficient depends on the core design. A small change in the design could potentially lead to large differences in the pressure drop across the core
Wall friction in the core	• Wall friction is the resistance to the flow, which affect the mass flow rate and temperature difference between the core inlet and outlet • Scaled experiment in an appropriate flow regime with molten salt as coolant can assist correlation/model development and code validation
Core flow asymmetry	• Core flow asymmetry can occur due to change of the flow distribution in the core, because of loss of a DRACS loop, a primary pump trip, or fuel plate deformation • The peak salt temperature and peak vessel temperature locations will change due to core flow asymmetry • Computational fluid dynamics (CFD) calculations of core flow asymmetry might be needed • Scaled integral-effect tests are recommended

Bypass flow fraction (Inter-assembly)	• The pressure drop through the inter-assemblies and structural vibration should be considered • The inter-assembly gap deforms with the temperature and irradiation • Cooperation with material scientists to better understand this phenomenon is required • Detailed analysis and parametric study are required to solidify the design. • Integrated CFD and structural analyses should be performed to investigate the fuel plate swelling/distortion
Heat transfer to the fusible links	• The knowledge level is ranked as Unknown due to lack of design specificity • The sodium fast reactor (SFR) design strategies and Curie point design can be referenced [5.7-8] • The core outlet temperature distribution is needed for modeling the heat transfer from the primary salt to the fusible link • Tests on each specific design and control rod reliability should be performed
Upper plenum mixing	• CFD calculations upper plenum mixing are needed • Separate-effect tests for correlation/model development and validation with scaled experimental data are required
Fluidic diodicity	• Flow resistance in the reverse direction affects the pumping power of the primary pump and bypass flow to the DHX primary side • Flow resistance in the forward direction affects DRACS performance during accident conditions
Heat capacity of the vessel	• The thin vessel wall leads to small thermal inertia compared to the thermal inertia of the primary salt
Mixing in the lower plenum	• Mixing in the lower plenum determines the boundary condition for the core inlet • CFD calculations of lower plenum mixing are needed • Separate-effect tests for correlation/model development and validation with scaled experimental data are required
Pump performance	• Analyses that inform pump design inputs/parameters should be carried out • Investigation on design and testing of salt pumps should be conducted

DHX performance	• The design uncertainties of heat exchangers due to uncertainties in heat transfer correlations/models lead to uncertainties in predicting heat exchanger performance • DHX peak temperature may indicate potential damage to the heat exchanger structure • Analyses that inform design inputs/parameters should be performed • Design and testing of the DHXs should be carried out • Scaled integral-effect tests should be conducted
NDHX performance	• The design uncertainties of heat exchangers due to uncertainties in heat transfer correlations/models lead to uncertainties in predicting heat exchanger performance • The salt temperature at the NDHX outlet should be kept from freezing to ensure the natural circulation flow is not blocked • Analyses that inform design inputs/parameters should be performed • Design and testing of the NDHX should be carried out • Scaled integral-effect tests should be conducted
DRACS piping heat loss	• Experimental data are needed to validate the heat loss calculations
KF-ZrF_4 thermophysical properties	• Measured property values have large variations from different experiments • Instrumentation limitation results in high measurement uncertainties, therefore a comprehensive review of the measurement uncertainties in the literature is needed. It is also important to study the sensitivities of the uncertainties in these properties to the final quantities of interest • New measurement of the molten salt properties should be carry out on demand
Chimney natural convection and performance	• The wind direction may affect natural convection in the chimneys • Detailed analyses and parametric studies should be carried out to solidify the chimney design • After the AC power is lost or under SBO scenarios, louvers o the chimneys have to open to ensure DRACS decay heat removal performance. The opening mechanism must be passive and electricity independent

	• Scaled integral-effect tests are suggested
P-IHX and I-PHX	• The design uncertainties of the heat exchangers due to uncertainties in heat transfer correlations/models lead to uncertainties in predicting heat exchanger performance • Design and testing of the components should be carried out • Analysis that informs design inputs/parameters should be performed • Scaled integral-effect tests should be conducted
Power cycle performance	• Design specifications and parametric studies are needed

To better understand the key phenomena in the SBO event, analyses using both system-level analysis codes and CFD codes are necessary. To support the code modeling, simulation, and analysis, additional experimental studies, including scaled separate-effect and integral-effect tests, are still needed to establish validated reactor safety analyses. There currently exist large discrepancies for the molten salt thermophysical and transport properties (e.g., thermal conductivity and viscosity) in the literature, which could result in large uncertainties in final analysis results, such as predictions of the mass flow rates and temperatures. Therefore, a comprehensive review of the molten salt thermophysical properties is required. In addition, analyses need to be carried out to investigate the effects of structural material swelling and distortion in the core on the core flow channels and therefore flow distributions in the reactor core. The flow resistance due to the form losses and wall friction also affects the core natural circulation flow during SBO. To better understand the core asymmetry phenomenon, CFD models of the reactor core with the downcomer, upper plenum, and lower plenum flow mixing, and fluidic diodicity should be further investigated since these phenomena show high or medium significance on the peak vessel temperature both with Unknown (U) or Partially known (P) knowledge level in the PIRT results. During SBO, most of the phenomena in the DRACS loops are ranked as of high importance to the identified FOMs since DRACS is the main passive decay heat removal path. System-level analyses of DRACS decay heat removal capability can help achieve a better understanding of transient responses of the phenomena listed in the PIRT charts for SBO, such as the DHX and NDHX performance, chimney natural convection flow and performance. The scaled experimental tests of these components can also assist correlation/model development and code validation.

For the event of withdrawal of all control rods simultaneously, further studies to develop system–level and multidimensional CFD analysis models with the capability of neutronic coupling for calculations of the core salt flow and temperature distributions are recommended by the panel. Even though the AHTR and other FHR designs generally operate with sufficient margins to the thermal limits of the fuel and structural components,

it is critical to investigate the coupling of the thermal hydraulics and reactor physics analysis tools, such as considering the thermal reactivity feedback under different core power distributions and core conditions. The AHTR designs of long fuel plates, assemblies, and coolant channels (without significant mixing mechanisms) warrant detailed thermal-hydraulic analyses for individual fuel assembly or groups of fuel assemblies, accounting for the power profiles of the fuels across the core. It is essential to simulate the hot channels and determine the peak coolant temperature since the outlet of the hot channels is potentially the location of the highest salt temperature in the core, which can be treated as a reference for the safety limit for integrity of the structural components. The salt flow and temperature distributions at the core outlet from a multidimensional CFD analysis serve as the boundary conditions for investigating salt flow mixing and potential flow stratification in the upper plenum. Furthermore, the application of fusible links to each of the fuel assemblies requires accurate prediction of coolant and fuse temperatures at the spots of the fusible links, in order to determine the margins of the fusible links during reactor normal operation and the times at which the fusible link protection can be credited during a transient or accident. If the temperature exceeds the melting point of the fusible links connected to the control rods, the associated control rods will drop into the core and introduce perturbations to neutronics, which need to be coupled with the thermal hydraulics analysis. Finally, in this event, the core flow is still under forced convection and the power conversion cycle is the ultimate heat sink. It becomes imperative to accurately model the heat transfer from the fuel plates to the primary coolant, the primary coolant to the intermediate loop coolant, and then to the power conversion cycle working fluid.

5.2.9. Summary

The purpose of this study is to support FHR modeling, safety analysis, and ultimately licensing by identifying key phenomena that potentially impose significant challenges on thermal hydraulics modeling and simulation of an FHR reference design, i.e., AHTR. A TH-PIRT panel was assembled to perform the PIRT study focused on the thermal hydraulics of the AHTR. Two accident scenarios, namely, the SBO and simultaneous withdrawal of all control rods, were discussed in detail by the panel during a 2.5-day PIRT study. For the event of SBO, four FOMs were identified, namely the peak vessel temperature, DRACS coolant temperature in the NDHX, peak temperature of the DHX, and average temperature increase of the carbonaceous materials in the core. For the event of simultaneous withdrawal of all control rods, the hot-leg salt temperature and maximum kernel temperature were defined as the FOMs. During the TH-PIRT study, phenomena identification, importance rankings, and knowledge level rankings were performed. In addition, the phenomena that were recommended by the panel for further consideration are discussed and for some of those phenomena, corresponding path forward is also proposed. It is suggested that further research be carried out to increase our knowledge levels, improve the current AHTR design, and perform design evaluation and safety analysis for the AHTR. Furthermore, the panel strongly suggested multidimensional CFD simulations and system-level analyses coupled with neutronics analysis be performed for AHTR safety margin quantification during reactor normal operation as well as transient and accident conditions.

For the event of SBO, the following phenomena are categorized as Yes in Table 5-9, which need further investigation:

- Geometry of the fuel plates, i.e., those deviations from their original geometry
- Thermal conductivity of FLiBe
- Viscosity of FLiBe
- Wall friction in the core
- Core flow asymmetry
- Upper plenum mixing
- Fluidic diodicity
- Lower plenum mixing
- DHX performance
- NDHX performance
- DRACS piping heat loss
- Chimney natural circulation and performance
- KF-ZrF_4 thermo-physical properties

For the event of simultaneous withdrawal of all control rods, the following phenomena are categorized as Yes in Table 5-9, and therefore, are recommended for further investigation:

- Thermal conductivity of the carbonaceous materials
- Thermal conductivity of fuel stripe
- Thermal conductivity of FLiBe
- Viscosity of FLiBe
- Core heat transfer coefficient
- Primary coolant flow bypass fraction
- Upper plenum mixing
- Heat transfer to fusible links for the control rods
- Primary pump performance
- P-IHX performance
- Intermediate pump performance
- I-PHX performance
- Power cycle performance

It should be noted that while the AHTR was used as the reference design for the current TH-PIRT study, the identified TH-PIRTs are expected to be generally cross-cutting to other FHR designs.

References

[5.1] Ball, S.J., Corradini, M., Fisher, S.E., Gauntt, R., Geffraye, G., Gehin, J.C., Hassan, Y., Moses, D.L., Renier, J.P., Schultz, R. and Wei, T., "Next Generation Nuclear Plant Phenomena Identification and Ranking Tables (PIRTs) Vol. 2: Accident and Thermal Fluids Analysis PIRTs," ORNL/TM-2007/147, Oak Ridge National Laboratory, Oak Ridge, TN (2008).

[5.2] Sun, X., Yoder, G.L., Christensen, R.N., Shi, S., Lin, H.C., Wu, X. and Zhang, S., "Thermal Hydraulics Phenomena Identification and Ranking Table (PIRT) for Advanced High Temperature Reactor (AHTR)," University of Michigan, Ann Arbor, MI (2017).

[5.3] H.C. Lin, S. Zhang, D. Diamond, S. Bajorek, R. Christensen, Y. Guo, G. Yoder, S. Shi, Q. Lv and X. Sun, "Phenomena identification and ranking table study for thermal hydraulics for Advanced High Temperature Reactor," *Annals of Nuclear Energy*, **124,** pp. 257-269(2019)

[5.4] Eide, S.A., Gentillon, C.D., Wieman, T.E., "Reevaluation of Station Blackout Risk at Nuclear Power Plants," Vol. 2. NUREG/CR-6890, U.S. Nuclear Regulatory Commission, Washington DC (2005).

[5.5] Varma, V.K., Holcomb, D.E., Peretz, F.J., Bradley, E.C., Ilas, D., Qualls, A.L. and Zaharia, N.M., "AHTR Mechanical, Structural, and Neutronic Preconceptual Design," ORNL/TM-2012/320, Oak Ridge National Laboratory, Oak Ridge, TN (2012).

[5.6] Ingersoll, D.T., Forsberg, C.W., Ott, L.J., Williams, D.F., Renier, J.P., "Status of Preconceptual Design of the Advanced High-Temperature Reactor (AHTR)," ORNL/TM-2004/104, Oak Ridge National Laboratory, Oak Ridge, TN (2004).

[5.7] Ichimiya, M., Mizuno, T. and Kotake, S., "A Next Generation Sodium-Cooled Fast Reactor Concept and Its R&D Program," *Nuclear Engineering and Technology*, **39(3)**,171-186 (2007).

[5.8] Aoto, K., Uto, N., Sakamoto, Y., Ito, T., Toda, M. and Kotake, S., "Design Study and R&D Progress on Japan Sodium-Cooled Fast Reactor," *Journal of Nuclear Science and Technology*, **48(4)**, 463-471 (2011).

5.3. Phenomena Identification and Ranking Table (PIRT) Study for Metallic Structural Materials for Advanced High-Temperature Reactor (AHTR)

5.3.1. Introduction

Material selection and identification of the possible degradation mechanisms for the selected materials in FHRs is important for the licensure and the safe operation of Fluoride High-Temperature Reactors (FHRs) [1]. In order to address this task, this integrated research project (IRP) hosted a Phenomena Identification and Ranking Table (PIRT) panel of internal and invited external experts to address degradation mechanisms and other materials related issues of importance to the FHRs. The PIRT panel for the FHR-IRP on Materials met on November 28-30, 2016 at Georgia Tech. The panel consisted of experts from different fields of materials science and engineering, mechanical behavior of materials, nuclear materials, and environmental degradation of materials participated in the PIRT.

Materials, ones that come in contact with FLiBe or FLiNaK molten salts or other related environments like high temperature steam etc., were considered in this PIRT. There is limited experience with molten salts, so identifying and ranking of the possible degradation mechanisms in these environments was the primary objective of this PIRT. Secondary objective was to rank the degradation mechanisms in more known environments, like in

high temperature steam. Focus of this PIRT was the metallic alloys used in FHRs, and it was acknowledged that non-metallic materials like graphite, pyrolytic carbon, and ceramics require a separate PIRT exercise. There are a number of possible phenomenon that can degrade a metallic material over time. This may fall in the category of chemical degradation, mechanical degradation, radiation degradation, and synergistic effect of these mechanisms. Material property degradation may negatively impact operations or may cause some safety concerns for the major structural components of FHRs. Specific degradation mechanisms will depend on the material as well as the operational environment for that component.

This PIRT exercise was dedicated to identifying and ranking of the possible degradation mechanisms for metallic materials in FHR environments that may come in contact with FLiBe or FLiNaK molten salts or other FHR related environments like high temperature steam etc.. Names and affiliation of panelists are given in Table 5-27 List of panelists for the FHR Materials PIRT panel held at the Georgia Institute of Technology, Atlanta, GA on November 28 to 30, 2016..

Table 5-27 List of panelists for the FHR Materials PIRT panel held at the Georgia Institute of Technology, Atlanta, GA on November 28 to 30, 2016.

Name	Organization
David Diamond *(Facilitator)*	*Brookhaven National Laboratory*
Preet M. Singh	*Georgia Institute of Technology*
Chaitanya Deo	*Georgia Institute of Technology*
Farzad Rahnema	*Georgia Institute of Technology*
Jinsuo Zhang	*Virginia Tech*
Graydon Yoder	*Oak Ridge National Laboratory*
Weiju Ren	*Oak Ridge National Laboratory*
James R. Keiser	*Oak Ridge National Laboratory*
Dane Wilson	*ThorCon Power*
T. L. Sham	*Argonne National Laboratory*
William Corwin	*Department of Energy, Nuclear Energy*
Vinay Deodeshmukh	*Haynes International*

Scope of PIRT Exercise – *Selection of Materials and Environments of Relevance*

Degradation mechanisms will depend on the materials used and the mechanical, chemical or radiation conditions. Therefore, as a starting point for the PIRT process, the panelists defined the AHTR design concept and its environmental parameters as the basis for the PIRT exercise. For this PIRT exercise the Oak Ridge National Laboratory (ORNL) pre-conceptual design for the AHTR was selected as the candidate design. During this process, panelists considered published literature in the field of materials performance and degradation in FHR related environments. This literature covers topics including effects of alloy composition, salt chemistry and impurities, radiation effects, processing related variables like cladding and welding, as well as individual degradation mechanisms considered in this PIRT report. Since the publication of this PIRT report, papers have been

published which addressed some phenomena identified as important. This PIRT report is available on Georgia Tech's SMARTech website:
https://smartech.gatech.edu/bitstream/handle/1853/56668/fhr-materials_pirt_report-final-4-16-2017.pdf?sequence=1&isAllowed=y

Although different classes of materials (i.e. metallic alloys, carbonaceous materials like graphite, pyrolytic carbon, and ceramics like SiC and BC) will be used for different components of FHR and were discussed in this PIRT exercise, the main emphasis during the PIRT meeting was on the metallic materials and their degradation mechanisms. Panel acknowledged that a number of new commercial or model materials are available or may become available with time for the FHRs applications. However, code approval of structural materials is very important for their selection or usage for the AHTR applications. Therefore, the majority of metallic alloys considered during this PIRT exercise were the ones that are permitted for the construction of elevated temperature Class A components, contained in Section III Division 5 of the ASME Boiler and Pressure Vessel Code. Main components which were considered included vessel and primary piping, primary heat exchangers, steam generator vessel, steam generator tubes, intermediate loop piping, valves and pumps. Welds in all structural components were identified as an important class of material, which varies in composition and properties, and needs more attention.

Environments considered for the degradation phenomenon were based on the pre-conceptual AHTR reactor design parameters. Where the environmental parameters for a component were not available, important degradation mechanisms under extreme conditions were considered. A list of possible degradation mechanisms, including chemical degradation, mechanical degradation, thermal degradation, and radiation damage was listed and the effect of different environmental variables was summarized. Most of the important degradation mechanism was included for the panel discussion, but the list of phenomena may not represent every possible degradation phenomenon or their synergistic effects on the material behavior. This list may also include some phenomena which are deemed to have minimal impact on material degradation of selected classes of materials in FHR related environments.

5.3.2. PIRT Process

Once the reactor design parameters and the scope of materials was defined, the following process was used to identify metallic material degradation phenomena, rank their importance in terms of their impact, and provide their level of understanding.

Step 1: Define the Issue
Materials used in the FHR, ones that come in contact with FLiBe or FLiNaK molten salts or other related environments like high temperature steam etc., need to be capable of providing functionality with high reliability, to provide safe and economical operation.

Step 2: Define objectives of the PIRT

Objectives of this PIRT exercise were to determine the materials and their associated degradation mechanisms that might negatively impact operation of the FHR and determine new experimental databases, modeling, and detailed analyses that needs to be carried out. The initial focus was on structural materials, with secondary focus on core, control rod, and instrumentation materials. In this PIRT, 'operation' was defined to include normal operation as well as transients and accidents.

There is limited experience with molten salts, so identifying and ranking of the possible degradation mechanisms in these environments was the primary objective of this PIRT exercise. Secondary objective was to rank the degradation mechanisms in more known environments, like in high temperature steam. Degradation mechanisms considered in this PIRT included Chemical Degradation, Mechanical Degradation, Radiation Degradation, and synergistic effect of these mechanisms, that may negatively impact operations or cause some safety concerns for the major structural components of FHRs.

Step 3: Define Hardware, Scenario, Methodology

The environmental parameters, including salt chemistry, salt impurities, temperature, stress state, irradiation fluence and flux etc. for this PIRT exercise were defined based on: (a) Georgia Tech (GT) White Paper on AHTR materials (structural, core, etc.). Review of this AHTR conceptual design is also presented in section 3 of this report; (b) presentations by various panel experts on different aspects of AHTR design, materials, and mechanical behavior; and (c) consensus opinions of the panel. Each table defines the environment considered for that particular component considered in this PIRT exercise. Normal operation as well as transients/accident conditions for most of critical components of FHR were considered.

Step 4: Define Evaluation Criteria, Figures-of-Merit (FoM)

Figure of merit (FoM) was defined for each component according to the risks involved with the failure of that component and its expected service life. Various criteria for unacceptable degradation, used as FoM for the PIRT exercise included the following:

- Any crack (e.g stress corrosion, corrosion fatigue, fatigue cracking)
- "Excessive" embrittlement (radiation induced, hydrogen embrittlement and other embrittlement sources)
- Decrease in fracture toughness, increase in yield strength
- "Excessive" deformation
- Loss of functionality
- others

Step 5: Identify, Obtain, Review Database

Important references related to the FHR material selection were sent to the panel. Whitepaper for the PIRT exercise also included the AHTR design information along with the degradation mechanisms.

Step 6: Identify Phenomena (processes, parameters, etc.)

Phenomena discussed included a number of degradation mechanisms that can potentially cause enough damage to cause local failure in the components considered in this PIRT exercise. Details of these mechanisms are given in a separate section after PIRT in this

report. However, the phenomena could be grouped under following degradation categories:

- Chemical Degradation
- Mechanical Degradation
- Radiation Degradation
- Synergistic Effect

Possibility of any selected alloy or material to fail by the degradation mechanism will depend on the environmental factors as well as other influencing factors listed here.

- Environment (including salt chemistry, salt impurities, temperature, stress state, irradiation fluence and flux etc.)
- Fabrication method (e.g welding)
- Geometry

Step 7: Rank Importance and Rationale

Importance of any degradation mechanism for a given component was ranked based on its influence on the (FoM) for that particular component. Table 5-28: Description of degradation mechanism FoM ranking designations. describes the lettered ranking used in this PIRT exercise.

Table 5-28: Description of degradation mechanism FoM ranking designations.

Ranking	**Description**
High (H)	Significant or dominant influence on FoM
Medium (M)	Moderate influence on FoM
Low (L)	Small influence on FoM *(including the possibility that the phenomenon is not present or possible). For the phenomenon with* "Low" FoM ranking, knowledge level is not considered.

Step 8: Assess Uncertainty (Knowledge Level)

Based on the data and the information available to the experts participating in the PIRT exercise, each phenomenon (degradation mechanism for a given material in a given environment) was ranked. Table 5-29 describes the lettered ranking of knowledge level for each phenomenon considered in this PIRT exercise.

Table 5-29: Description of knowledge level ranking designations.

Ranking	***Description***
Known (K)	Phenomenon is well understood, and can be accurately modeled/analyzed/assessed.

Partially Known (P)	Phenomenon is understood, however, can only be modeled with moderate uncertainty.
Unknown (U)	Phenomenon is not well understood. Modeling the phenomenon is currently either not possible or is possible only with large uncertainty.

5.3.3. PIRT Results and Conclusions

There is limited experience with molten salts, so identifying and ranking of the possible degradation mechanisms in these environments was the primary objective of this PIRT. Secondary objective was to rank the degradation mechanisms in more known environments, like in high temperature steam. Main components which were considered included vessel and primary piping, primary heat exchangers, steam generator vessel, steam generator tubes, intermediate loop piping, valves and pumps. Welds in all structural components were identified as an important class of material, which varies in composition and properties, and needs more attention.

Based on panel discussions, data available, and the knowledge of experts on the PIRT panel, gap analysis was done to identify research needs for each specific phenomenon considered. Details of these results can be found in the complete PIRT report which contains unabridged tables and is available online [2]. Results from the PIRT panel are also available in a recent paper [3].

References

[1] D.E. Holcomb, G.F. Flanagan, G.T. Mays, W.D. Pointer, K.R. Robb, G.L. Yoder, "Fluoride Salt-Cooled High-Temperature Reactor Technology Development and Demonstration Roadmap", Oak Ridge National Laboratory, ORNL/TM-2013/401, 2013.

[2] P.M. Singh, K.J. Chan, F. Rahnema, "Phenomena Identification and Ranking Table (PIRT) report for metallic materials use in Fluoride High-Temperature Reactors (FHRs)", Atlanta, GA: Georgia Institute of Technology, 2017, https://smartech.gatech.edu/handle/1853/56668.

[3] P.M. Singh, K.J. Chan,, C. S. Deo, V. Deodeshmukh, J. R. Keiser, W. Ren, T. L. Sham, D. F. Wilson, G. Yoder, J. Zhang, Phenomena Identification and Ranking Table (PIRT) study for metallic structural materials for advanced High-Temperature reactor, Annals of Nuclear Energy, Vol. 123, Jan 2019, pp 222-229, 2019.

5.4. Phenomena Identification and Categorization by the Required Level of Multiphysics Coupling in FHR Modeling and Simulation

5.4.1. Introduction

The Fluoride-Salt-Cooled High-Temperature Reactor (FHR) concept is an advanced reactor design concept in which molten salt is used as coolant in the primary loop with a core containing some form of solid fuel. This allows for high-temperature operation at near-atmospheric pressure, allowing for higher thermal efficiency in electricity generation, usable industrial process heat, etc. On the path to deployment for this, and indeed any, reactor concept, modeling tool verification and validation is a crucial step. To aid in this process for FHRs, an Integrated Research Project was funded under the Nuclear Energy University Program of the U.S. Department of Energy [1]. This university-led project assembled four panels to begin the process of identifying phenomena that are important to FHR modeling in different areas. The first three panels studied individual physics areas: neutronics [2], thermal-hydraulics [3], and reactor material [4]. The fourth panel examined the ways in which the individual physics areas interact with each other, called Multiphysics modeling.

One challenge in simulating various reactor operation scenarios is to capture the feedback from various physics. Often, the underlying physical phenomena that govern reactor operation are broadly grouped into physics areas such as neutronics, T-H and materials as above. However, many of these phenomena depend on feedback from multiple other physics areas. In order to model these phenomena accurately, the simulations cannot be performed as a sequence of isolated single physics calculations. Instead, capturing these phenomena requires coupling multiple physics codes/modules, since simulation of one physics area depends on parameters that are functions of other physics.

In some cases, this co-dependence can be handled via pre-calculation of a set of parameters in one physics area, and iteration/interpolation of this table of values for another area. In other cases, however, this pre-calculation method is insufficient or impractical, and will not produce satisfactory results. For these more complicated phenomena, simulations must use detailed feedback models (e.g., direct coupling) between two or more physics areas. In this paper, two categories of required coupling level will be referred to as “loose” and “tight” coupling, where “loose” coupling involves sharing of precalculated parameters, and “tight” coupling involves detailed feedback models.

For current operating light water reactor (LWR) designs, multiphysics tools that handle the operative phenomena are relatively mature. However, these tools are not applicable for modeling of advanced reactors, as many design aspects pose challenges to the LWR focused physics models. In an attempt to identify and then categorize physical phenomena into these “tight” and “loose” coupling categories for FHR modeling, a panel of subject matter experts was assembled. This panel included experts in the physics areas of neutronics, thermal-hydraulics, and materials. This panel assembled a list of multiphysics phenomena that are important to FHR modeling of both normal operation and accident scenarios, grouped them into the “tight” and “loose” categories, and provided commentary on this categorization. The panel performed this exercise for the Advanced High-Temperature Reactor (AHTR), a pre-conceptual FHR design [5] developed at Oak Ridge National Laboratory.

5.4.2. Phenomena Coupling Categorization Process

The following process was used to identify phenomena relevant to multiphysics modeling and categorize the level of coupling required to accurately model the phenomena.

1. Define the issue
   - The issue was defined to be a lack of adequate multiphysics modeling tools, codes, and methodologies to model FHRs with sufficient accuracy.
2. Define objectives of the study
   - The objectives were defined to be:
     - The identification of the phenomena that impact the accuracy of FHR multiphysics analysis, as well as what new data/analysis is necessary to adequately model the phenomena.
     - A categorization of the coupling required to model these phenomena with sufficient accuracy, according to the evaluation criteria defined in Step 4.
3. Define hardware, scenario, methodology, etc.
   - The context for this panel was provided to the panelists through reports on three previous Phenomena Identification and Ranking (PIRT) exercises, one each on the physics areas of neutronics [6], thermal hydraulics [7], and materials [8]. Additionally, whitepapers that were distributed to those individual physics PIRT panelists were also distributed to the multiphysics PIRT panelists. These whitepapers provided background information on the state-of-the-art for the relevant physics area, as well as detailed information on the reference reactor.
   - Three scenarios were selected for consideration in this exercise: station blackout, simultaneous withdrawal of all control rods, and normal operation. The first two (transient) scenarios were selected because they were discussed in-depth in the thermal-hydraulics PIRT panel [3].
   - Additionally, a set of relevant AHTR systems and components was assembled.
4. Define evaluation criteria
   - Only one evaluation criterion was used: the tightness of coupling required to model the phenomenon.
     - **Tight coupling** is when a phenomenon requires iterative feedback between two different physics (e.g., thermal-hydraulics and neutronics) in order to provide spatial and temporal information. Note that tight coupling means coupling of physics models irrespective of numerical coupling/framework.
     - **Loose coupling** is when a phenomenon requires only data that can be precalculated (e.g., in tabular or functional form) without any iterative feedback from other physics.
5. Identify, obtain, review database
   - This was performed by the panelists as for Step 3.
6. Identify phenomena (processes, parameters, etc.)
   - This step is effectively a brainstorming session where possible phenomena are assembled and defined in writing.
7. Categorize phenomena and provide rationale

- At this stage, phenomena were categorized by the panel into requiring tight or loose coupling, according to the definitions in Step 4.

The panelists for this study held at the Georgia Institute of Technology in Atlanta, GA on November 30 – December 2, 2016 were:

Table 5-30: Multi-physics PIRT Members

Name	Organization	Expertise
David Diamond (Facilitator)	Brookhaven National Laboratory	Thermal hydraulics, Materials
Steven Bajorek	Nuclear Regulatory Commission	Thermal Hydraulics
Max Fratoni	University of California – Berkeley	Neutronics
Yunjun Guo	Canadian Nuclear Safety Commission	Thermal hydraulics
Ali Haghighat	Virginia Tech	Neutronics
David Holcomb	Oak Ridge National Laboratory	Thermal hydraulics, Materials
Dan Ilas	Oak Ridge National Laboratory	Reactor Physics
Kevin Robb	Oak Ridge National Laboratory	Thermal Hydraulics
Bojan Petrovic	Georgia Institute of Technology	Neutronics
Farzad Rahnema	Georgia Institute of Technology	Neutronics
Preet Singh	Georgia Institute of Technology	Materials
Carl Stoots	Idaho National Laboratory	Thermal Hydraulics
Gerhard Strydom	Idaho National Laboratory	Neutronics
Xiaodong Sun	Ohio State University	Thermal Hydraulics
Grady Yoder	Oak Ridge National Laboratory	Thermal hydraulics, Materials
Dingkang Zhang	Georgia Institute of Technology	Neutronics
Jinsuo Zhang	Ohio State University	Materials

5.4.3. Overview of System Components and Operation Scenarios

Systems and components in AHTR were defined and classified as follows:

- Core: Fuel, primary coolant
- Vessel/internals/cavity: Upper plenum, lower plenum, fluidic diode, reactor vessel, cavity
- Primary loop: Pump, piping, primary to intermediate heat exchanger (P-IHX)
- Intermediate loop: Pump, piping, P-IHX, intermediate to power loop heat exchanger (I-PHX)
- Power conversion loop: I-PHX
- DRACS: Piping, DHX, NDHX, DRACS salt, chimney

Multiphysics phenomena were considered in the context of three scenarios: station blackout, simultaneous withdrawal of all control rods, and normal operation.

5.4.4. Station Blackout

For the station blackout conditions, active cooling systems, such as the cavity air cooling system, the maintenance cooling system, are assumed out of commission. For this scenario, the primary concern is removing decay heat. Thus, the main concern is that the DRACS system operates as intended. Phenomena for this scenario were classified further based on the system and component where they occur.

- Core
- Vessel
- Primary loop
- Intermediate loop
- Power conversion loop
- DRACS

5.4.4.1. Rod Withdrawal

Rod withdrawal refers to the scenario in which all control rods are withdrawn simultaneously. For this scenario, the reactor is not necessarily scrammed until the fusible links on the control rods melt. Phenomena for this scenario were classified further based on the system and component where they occur.

- Same as in the station blackout scenario

5.4.4.2. Normal Operation

Normal operation means the nuclear plant is operating without significant changes that would impair its ability to meet its performance objectives. For this scenario, the reactor continues operating as normal, and DRACS Phenomena for this scenario were classified further based on the system and component where they occur.

- Same as in the station blackout scenario

5.4.4.3. Others

This scenario contains those phenomena that cannot be appropriately classified as belonging to the three scenarios discussed above.

5.4.5. Phenomena Requiring Tight Coupling

Table 5-31 below contains those phenomena that were determined by the panel to require tight coupling, grouped by operation scenario for three scenarios discussed in the study. The first column contains a short description of the phenomenon in bold. The relevant system and/or component is provided in italics. The second column contains commentary about the modeling of the specific phenomenon.

Table 5-31: Phenomena requiring tight coupling

Phenomenon: *System*	**Commentary**
Scenario: Station Blackout	
No phenomena in the Station Blackout scenario were determined to require tight coupling. All phenomena in this scenario can be found in the Loose Coupling table.	
Scenario: Rod Withdrawal	
Energy generation rate in fuel kernel: *Core/Fuel*	• Thermal-hydraulics (T-H) requires fission density distribution for direct coupling • Need the plate-wise axial power distribution • May need local power distribution for high-fidelity calculations, in particular for real-life nonuniform kernel distribution
Fuel temperature reactivity coefficient: *Core/Fuel*	• Fuel kernel temperature can be inferred from the power distribution • Need the plate-wise axial power distribution • May need local power distribution for high-fidelity calculations
Bypass fraction: *Core/Primary Coolant Flow*	• Inter-assembly flow is a function of the core geometry, forced circulation flow in the core, and core power • Core geometry changes with graphite dimensional changes • High-fidelity T-H tools may be needed to determine inter-assembly flow
Graphite temperature reactivity coefficient: *Core/Fuel*	• Graphite temperature can be calculated by T-H • The level of required fidelity needs to be investigated
Coolant reactivity coefficient: *Core/Fuel*	• Coolant temperature can be calculated by T-H • The level of fidelity needs to be investigated
Upper plenum mixing: *Vessel*	• Need high-fidelity computational fluid dynamics (CFD) modeling in upper plenum • Possibly need similar fidelity in the core to calculate core coolant outlet temperature distribution and coolant flow distribution
Heat transfer coefficient to fusible links: *Vessel*	• Need high-fidelity CFD modeling in upper plenum • Possibly need similar fidelity in the core to calculate both fuel and coolant core outlet temperature distribution and coolant flow distribution
Scenario: Normal Operation	

Energy generation rate in fuel kernel*: Core/Fuel*	• T-H requires the fission density distribution for direct coupling • Need the plate-wise axial and span-wise power distribution • May need local power distribution for high-fidelity calculations
Fuel temperature reactivity coefficient*: Core/Fuel*	• Fuel kernel temperature can be inferred from the power distribution • Need the plate-wise axial and span-wise power distribution • May need local power distribution for high-fidelity calculations
Bypass fraction*: Core/Primary Coolant Flow*	• Inter-assembly flow is a function of the core geometry, forced circulation flow in the core, and core power • Core geometry changes with graphite dimensional changes • High-fidelity T-H tools may be needed to determine inter-assembly flow
Graphite temperature coefficient of reactivity*: Core/Fuel*	• Graphite temperature can be calculated by T-H • The level of fidelity needs to be investigated
Coolant reactivity feedback*: Core/Fuel*	• Coolant temperature can be calculated by T-H • The level of fidelity needs to be investigated
Upper plenum mixing*: Vessel*	• Need high-fidelity CFD modeling in upper plenum • Possibly need similar fidelity in the core to calculate both fuel and coolant core outlet temperatures and coolant flow distribution
Heat transfer coefficient to fusible links*: Vessel*	• Need high-fidelity CFD modeling in upper plenum • Possibly need similar fidelity in the core to calculate both fuel and coolant core outlet temperatures and coolant flow distribution

5.4.6. Phenomena Requiring Loose Coupling

Table 5-32 contains those phenomena that were determined by the panel to require loose coupling, grouped by operation scenario. The first column contains a short description of the phenomenon in bold. The relevant system and/or component is provided in italics. The second column contains commentary about the modeling of the specific phenomenon.

Table 5-32: Phenomena Requiring Loose Coupling

Phenomenon: *System*	**Commentary**
Scenario: Station Blackout	
Heat capacity of carbonaceous materials: *Core/Fuel*	• Heat capacity is a function of temperature and irradiation • Experimental tests may be needed to validate heat capacity correlations/models
Thermal conductivity of carbonaceous materials: *Core/Fuel*	• Thermal conductivity is a function of temperature, irradiation, and materials characteristics (such as allotropes) • Experimental tests may be needed to validate thermal conductivity (heat capacity) correlations/models
Heat capacity of fuel stripe: *Core/Fuel*	• Heat capacity is a function of temperature and irradiation • Model needs to be developed for fuel stripe of different irradiation (burnup) levels • Experimental tests may be needed to validate the model
Thermal conductivity of fuel stripe: *Core/Fuel*	• Thermal conductivity is a function of temperature and irradiation • Model needs to be developed for fuel stripe of different irradiation (burnup) levels • Experimental tests may be needed to validate the model
Heat capacity of fuel kernel: *Core/Fuel*	• Heat capacity is a function of temperature and irradiation • Experimental tests may be needed to develop model • High-fidelity modeling may be needed if experiments not possible
Thermal conductivity of fuel kernel: *Core/Fuel*	• Thermal conductivity is a function of temperature and irradiation • Experimental tests may be needed to develop model • High-fidelity modeling may be needed if experiments not possible
Density (carbonaceous materials, fuel stripe, kernel): *Core/Fuel*	• Density is a function of temperature and irradiation
Decay heat generation rate in fuel and structure: *Core/Fuel*	• Spatial distribution of heat generation rate due to accumulation of fission products and actinides at steady-state and decay power • Decay heat is precalculated as an input to T-H

	• Need the isotope distribution from burnup calculations
Geometry evolution of the fuel plate (Deviation from original geometry)*: Core/Fuel*	• Distortion due to thermal expansion, irradiation, and fuel fabrication defects • Fabrication deviation from nominal dimensions needs to be identified prior to loading the fuel (as initial condition) • Model development to account for thermal expansion and irradiation effects
Radiative Heat Transfer*: Core/Fuel*	• Radiative heat transfer from the surface of the fuel plate • Can be precalculated • Primary salt absorption coefficient needs to be modeled
Surface condition*: Core/Fuel*	• Surface roughness, degradation or erosion • Affects T-H calculations (friction and convective heat transfer) • Important for flow distribution into coolant channels in the core during natural circulation
Heat capacity of FLiBe*: Core/Primary Coolant flow*	• Heat capacity is a function of the temperature • Can be precalculated using existing correlations/models
Density of FLiBe*: Core/Primary Coolant flow*	• Density is a function of the temperature
Viscosity of FLiBe*: Core/Primary Coolant flow*	• Viscosity is a function of the temperature
Thermal conductivity of FLiBe*: Core/Primary Coolant flow*	• Thermal conductivity is a function of the temperature
Core heat transfer coefficient*: Core/Primary Coolant flow*	• Forced/mixed/natural convection: Need to determine flow regime in the core • Primary coolant pump coastdown curve is needed to determine the initial flow following reactor scram • Natural circulation flow is coupled to heat transfer from the fuel to FLiBe and from FLiBe to DHXs
Optical properties*: Core/Primary Coolant flow*	• Absorption and transmission of the coolant as a function of temperature and wavelength • Models may need to be developed for FLiBe absorption and transmission to thermal radiation of

	typical wavelengths • Experiments may be necessary to develop this model
Form loss coefficients*:* *Core/Primary Coolant flow*	• Entrance and exit loss coefficients as a function of area ratio and Reynolds number • May not be easy to precalculate even with the CFD method. May need at least pre-confirmatory measurements
Wall friction*:* *Core/Primary Coolant flow*	• Wall friction factor is a function of the Reynolds number and surface roughness (for turbulent flow) • Spacer ridges on the fuel plates need to be accounted for • Experimental testing to assist correlation/model development
Core flow asymmetry*:* *Core/Primary Coolant flow*	• Occurs in the core due to asymmetry in core structures, such as that due to fuel plate deformation, and asymmetric performance in DRACS loops • Flow distribution in the core may need to be calculated using high-fidelity tools
Bypass fraction*:* *Core/Primary Coolant flow*	• Inter-assembly flow is a function of the core geometry, flow in the core (forced/mixed/natural convection), and coolant temperature • High-fidelity T-H tools may be needed to determine inter-assembly flow • T-H can be loosely coupled to neutronics here for station blackout, since it is the decay heat distribution that is relevant, which can be precalculated
Direct energy deposition*: Core/Primary Coolant flow*	• Gamma heating of coolant from fuel as a function of the axial and radial positions in the core for steady-state and decay loads
Upper plenum mixing*:* *Vessel*	• Pluming and stratification and impact of upper internal structure • May require high fidelity (e.g., CFD) calculation
Cover gas entrainment*:* *Vessel*	• Due to frothing at the free surface • Function of core flow rate and core geometry

Heat capacity of vessel*: Vessel*	• To determine heat transfer across vessel wall • Function of vessel temperature and irradiation • Correlations/models
Thermal conductivity of vessel*: Vessel*	• To determine heat transfer across vessel wall • Function of vessel temperature and irradiation • Correlations/models
Heat transfer to upper plenum structures*: Vessel*	• Heat transfer to control rod drives (are there Guide tubes for the control blades in AHTR?) • Thermal radiation from the salt pool surface and vessel wall • Natural convection in the gas space
Heat transfer coefficient to vessel wall*: Vessel*	• Forced/Mixed/Natural convection heat transfer • Natural circulation flow in the core and downcomer
Friction factor on vessel wall in downcomer*: Vessel*	• Downcomer pressure drop • Friction factor is a function of the Reynolds number and vessel wall inner surface roughness (for turbulent flow) • Important for primary loop natural circulation flow
Mixing in lower plenum*: Vessel*	• From eight downcomer segments • Boundary condition to the core inlet • High-fidelity tools are needed to calculate mixing in lower plenum
Heat transfer to cover gas and vessel upper flange*: Vessel*	• Radiative heat transfer for the salt free surface • Convective heat transfer from the cover gas to the upper flange due to natural circulation in the cover gas • Cover gas thermophysical properties
Thermal properties of insulation*: Vessel/Cavity*	• Density, thermal conductivity and heat capacity • Functions of insulation temperature
Heat transfer across vessel to gas space*: Vessel/Cavity*	• Thermal resistance to heat transfer from reactor vessel wall to gas space through thermal insulation
Heat transfer across second gap to concrete*: Vessel/Cavity*	• Thermal radiation from the guard vessel wall to concrete • Convective heat transfer in the cavity due to natural

	convection in the second gap between the guard vessel and concrete
Conduction in concrete*: Vessel/Cavity*	• Wall heat transfer and concrete thermal conductivity • Heat sink for concrete • Concrete property changes with time (e.g., water content)
Pump performance*: Primary Loop*	• Pump performance (four quadrant), coastdown curve, and pump efficiency • Vendor provided information • Coastdown characteristics designed based on specified requirement
Pump resistance or K factor*: Primary Loop, Intermediate Loop*	• Pressure drop across pump • Vendor provided K factor information
Form loss in the loop*: Primary Loop, Intermediate Loop*	• Pressure losses due to bends, fittings, valves, flow area abrupt changes, and obstacles • Function of flow loop geometry and Reynolds number
Wall friction in the loop*: Primary Loop, Intermediate Loop*	• Function of the Reynolds number (and wall roughness for turbulent flow) • Function of piping wall roughness for turbulent flow
P-IHX performance*: Primary Loop*	• Heat transfer and pressure drop on primary side • Heat exchanger modeling
Heat loss through and thermal inertia of piping*: Primary Loop, Intermediate Loop*	• Piping/component geometry and material of construction • Heat transfer to the ambient from pipe thermal insulation
Impact of cover gas entrainment on pump*: Primary Loop*	• Potential pump cavitation, reducing pump head
Pump curve*: Intermediate Loop*	• Pump performance curve, coastdown curve, and pump efficiency • Vendor provided information

Pump coastdown*: Intermediate Loop*	• Speed versus time • Vendor provided information
I-PHX performance*: Intermediate Loop, Power Cycle*	• Heat transfer and pressure drop in the intermediate loop • Loop geometry in the intermediate loop and power cycle loop
P-IHX performance*: Intermediate Loop*	• Heat transfer and pressure drop in the intermediate loop • Loop geometry in the intermediate loop
Thermal conversion efficiency*: Power Cycle*	• Steam Rankine cycle is proposed for AHTR power cycle • No detailed design available for AHTR • Must mature analysis
DRACS piping*: DRACS*	• Friction and form losses in the piping • Heat losses to the ambient
DHX performance*: DRACS*	• Heat transfer and pressure drop on both sides • Natural circulation flows on both sides • Function of the DHX design and FLiBe coolant temperature • Experimental testing may be needed for a given DHX design to assist model development
NDHX performance*: DRACS*	• Heat transfer and pressure drop on both sides • Natural circulation/convection flows on both sides • Function of the NDHX design, DRACS salt and ambient air temperatures • Experimental testing may be needed for a given NDHX design to assist model development
Piping heat loss*: DRACS*	• Entire system both inside and outside • Function of the thermal insulation, salt temperature and ambient air temperature
Chimney natural convection and performance*: DRACS*	• Loss coefficients under different conditions (e.g. louver opening) • Function of chimney design, NDHX design, DRACS salt temperature and ambient air temperature • Validation measurements needed

KF-ZrF_4 thermo-physical properties*: DRACS*	• Heat capacity, conductivity, viscosity, and density • Function of salt temperature • Validation experiments may be needed to improve existing correlations
Thermal inertia of DRACS and chimney*: DRACS*	• Heat stored in the structures, heat exchangers, insulation and chimney • Function of DRACS design and geometry, and materials temperatures
Scenario: Rod Withdrawal	
Heat capacity of carbonaceous materials*: Core/Fuel*	• Heat capacity is a function of temperature and irradiation • Experimental tests may be needed to validate heat capacity correlations/models
Thermal conductivity of carbonaceous materials*: Core/Fuel*	• Thermal conductivity is a function of temperature, irradiation, and materials characteristics (such as allotropes) • Experimental tests may be needed to validate thermal conductivity (heat capacity) correlations/models
Heat capacity of fuel stripe*: Core/Fuel*	• Heat capacity is a function of temperature and irradiation • Model needs to be developed for fuel stripe of different irradiation (burnup) levels • Experimental tests may be needed to validate the model
Thermal conductivity of fuel stripe*: Core/Fuel*	• Thermal conductivity is a function of temperature and irradiation • Model needs to be developed for fuel stripe of different irradiation (burnup) levels • Experimental tests may be needed to validate the model
Heat capacity of fuel kernel*: Core/Fuel*	• Heat capacity is a function of temperature and irradiation • Experimental tests may be needed to develop model • High-fidelity modeling may be needed if experiments not possible
Thermal conductivity of fuel kernel*: Core/Fuel*	• Thermal conductivity is a function of temperature and irradiation • Experimental tests may be needed to develop model • High-fidelity modeling may be needed if experiments not possible

Density (carb. mat., fuel stripe, kernel)*: Core/Fuel*	• Density is a function of temperature and irradiation
Energy generation rate inside kernel*: Core/Fuel*	• Energy generation inside the kernel due to fission • This is important
Energy generation rate outside kernel but within plate*: Core/Fuel*	• Energy generation rate outside kernel but within plate due to gamma (and neutron) transport • Gamma heating using the precalculated information • No Gamma transport needed
Geometry evolution of the fuel plate (Deviation from original geometry)*: Core/Fuel*	• Distortion due to thermal expansion, irradiation, and fuel fabrication defects • Fabrication deviation from nominal dimensions needs to be identified prior to loading the fuel (as initial condition) • Model development to account for thermal expansion and irradiation effects
Radiative Heat Transfer*: Core/Fuel*	• Radiative heat transfer from the surface of the fuel plate • Can be precalculated • Primary salt absorption coefficient needs to be modeled
Surface condition*: Core/Fuel*	• Surface roughness, degradation or erosion • Not important. Since there is forced circulation flow through the core, the surface condition is not as important as for natural circulation flow under SBO.
Heat capacity of FLiBe*: Core/Primary Coolant Flow*	• Heat capacity is a function of the temperature • Can be precalculated using existing correlations/models
Density of FLiBe*: Core/Primary Coolant Flow*	• Density as a function of the temperature
Viscosity of FLiBe*: Core/Primary Coolant Flow*	• Viscosity as a function of the temperature
Thermal conductivity of FLiBe*: Core/Primary Coolant Flow*	• Thermal conductivity as a function of the temperature

Core heat transfer coefficient*: Core/Primary Coolant Flow*	• Forced/mixed/natural convection: Need to determine flow regime in the core • Primary coolant pump coastdown curve is needed to determine the initial flow following reactor scram • Natural circulation flow is coupled to heat transfer from the fuel to FLiBe and from FLiBe to DHXs
Optical properties*: Core/Primary Coolant Flow*	• Absorption and transmission of the coolant as a function of temperature and wavelength • Models may need to be developed for FLiBe absorption and transmission to thermal radiation of typical wavelengths • Experiments may be necessary to develop this model
Form loss coefficients*: Core/Primary Coolant Flow*	• Entrance and exit loss coefficients as a function of area ratio and Reynolds number • May not be easy to precalculate even with the CFD method. May need at least pre-confirmatory measurements
Wall friction*: Core/Primary Coolant Flow*	• Wall friction factor is a function of the Reynolds number and surface roughness (for turbulent flow) • Spacer ridges on the fuel plates need to be accounted for • Experimental testing to assist correlation/model development
Core flow asymmetry*: Core/Primary Coolant Flow*	• Occurs in the core due to asymmetry in core structures, such as that due to fuel plate deformation • Flow distribution in the core may need to be calculated using high-fidelity tools
Direct energy deposition*: Core/Primary Coolant Flow*	• Gamma heating of coolant from fuel as a function of the axial and radial positions in the core for steady-state and decay loads
Fluidic diodicity/Bypass Flow*: Vessel*	• Bypass flow to the core through the DRACS DHX loops is a function of the DRACS design, pump head, and fluidic diodicity • Modeling of fluid diode performance • Experimental verification of fluidic diode performance

Cover gas entrainment*: Vessel*	• Due to frothing at the free surface • Function of core flow rate and core geometry
Heat capacity/conductivity of vessel*: Vessel*	• To determine heat transfer across vessel wall • Function of vessel temperature and irradiation • Correlations/models
Heat transfer to upper plenum structures*: Vessel*	• Heat transfer to control rod drives (are there Guide tubes for the control blades in AHTR?) • Thermal radiation from the salt pool surface and vessel wall • Natural convection in the gas space
Heat transfer coefficient to vessel wall*: Vessel*	• Forced/Mixed/Natural convection heat transfer • Natural circulation flow in the core and downcomer
Friction factor on vessel wall in downcomer*: Vessel*	• Downcomer pressure drop • Friction factor is a function of the Reynolds number and vessel wall inner surface roughness (for turbulent flow) • Important for primary loop natural circulation flow
Mixing in lower plenum*: Vessel*	• From eight downcomer segments • Boundary condition to the core inlet • High-fidelity tools are needed to calculate mixing in lower plenum
Heat transfer to cover gas and vessel upper flange*: Vessel*	• Radiative heat transfer for the salt free surface • Convective heat transfer from the cover gas to the upper flange due to natural circulation in the cover gas • Cover gas thermophysical properties
Thermal properties of insulation*: Vessel/Cavity*	• Density, thermal conductivity and heat capacity • Functions of insulation temperature
Heat transfer across vessel to gas space*: Vessel/Cavity*	• Thermal resistance to heat transfer from reactor vessel wall to gas space through thermal insulation
Heat transfer across second gap to concrete*: Vessel/Cavity*	• Thermal radiation from the guard vessel wall to concrete • Convective heat transfer in the cavity due to natural convection in the second gap between the guard

	vessel and concrete
Conduction in concrete*: Vessel/Cavity*	• Wall heat transfer and concrete thermal conductivity • Heat sink for concrete • Concrete property changes with time (e.g., water content)
Pump performance*: Primary Loop, Intermediate Loop*	• Pump performance (four quadrant), coastdown curve, and pump efficiency • Vendor provided information • Coastdown characteristics designed based on specified requirement
Pump resistance or K factor*: Primary Loop, Intermediate Loop*	• Pressure drop across pump • Vendor provided K factor information
Form loss in the loop*: Primary Loop, Intermediate Loop*	• Pressure losses due to bends, fittings, valves, flow area abrupt changes, and obstacles • Function of flow loop geometry and Reynolds number
Wall friction in the loop*: Primary Loop, Intermediate Loop*	• Function of the Reynolds number (and wall roughness for turbulent flow) • Function of piping wall roughness for turbulent flow
P-IHX performance*: Primary Loop, Intermediate Loop*	• Heat transfer and pressure drop on primary side • Heat exchanger modeling
Heat loss through and thermal inertia of piping*: Primary Loop, Intermediate Loop, DRACS*	• Piping/component geometry and material of construction • Heat transfer to the ambient from pipe thermal insulation
Impact of cover gas entrainment on pump*: Primary Loop*	• Potential pump cavitation, reducing pump head
Pump curve*: Intermediate Loop*	• Pump performance curve, coastdown curve, and pump efficiency • Vendor provided information

I-PHX performance*: Intermediate Loop, Power Cycle*	• Heat transfer and pressure drop in the intermediate loop • Loop geometry in the intermediate loop and power cycle loop
Thermal conversion efficiency*: Power Cycle*	• Steam Rankine cycle is proposed for AHTR power cycle • No detailed design available for AHTR • Must mature analysis
DRACS piping*: DRACS*	• Friction and form losses in the piping • Heat losses to the ambient
DHX performance*: DRACS*	• Heat transfer and pressure drop on both sides • Natural circulation flows on both sides • Function of the DHX design and FLiBe coolant temperature • Experimental testing may be needed for a given DHX design to assist model development
NDHX performance*: DRACS*	• Heat transfer and pressure drop on both sides • Natural circulation/convection flows on both sides • Function of the NDHX design, DRACS salt and ambient air temperatures • Experimental testing may be needed for a given NDHX design to assist model development
Chimney natural circulation and performance*: DRACS*	• Loss coefficients under different conditions (e.g. louver opening) • Function of chimney design, NDHX design, DRACS salt temperature and ambient air temperature • Validation measurements needed
KF-ZrF_4 thermo-physical properties*: DRACS*	• Heat capacity, conductivity, viscosity, and density • Function of salt temperature • Validation experiments may be needed to improve existing correlations
Thermal inertia of DRACS and chimney*: DRACS*	• Heat stored in the structures, heat exchangers, insulation and chimney • Function of DRACS design and geometry, and materials temperatures
Scenario: Normal Operation	

Heat capacity of carbonaceous materials*: Core/Fuel*	• Heat capacity is a function of temperature and irradiation • Experimental tests may be needed to validate heat capacity correlations/models
Thermal conductivity of carbonaceous materials*: Core/Fuel*	• Thermal conductivity is a function of temperature, irradiation, and materials characteristics (such as allotropes) • Experimental tests may be needed to validate thermal conductivity (heat capacity) correlations/models
Heat capacity of fuel stripe*: Core/Fuel*	• Heat capacity is a function of temperature and irradiation • Model needs to be developed for fuel stripe of different irradiation (burnup) levels • Experimental tests may be needed to validate the model
Thermal conductivity of fuel stripe*: Core/Fuel*	• Thermal conductivity is a function of temperature and irradiation • Model needs to be developed for fuel stripe of different irradiation (burnup) levels • Experimental tests may be needed to validate the model
Heat capacity of fuel kernel*: Core/Fuel*	• Heat capacity is a function of temperature and irradiation • Experimental tests may be needed to develop model • High-fidelity modeling may be needed if experiments not possible
Thermal conductivity of fuel kernel*: Core/Fuel*	• Thermal conductivity is a function of temperature and irradiation • Experimental tests may be needed to develop model • High-fidelity modeling may be needed if experiments not possible
Density (carb. mat., fuel stripe, kernel)*: Core/Fuel*	• Density is a function of temperature and irradiation
Energy generation rate in fuel and structure*: Core/Fuel*	• Energy generation rate outside kernel but within plate due to Gamma transport • Gamma heating using the precalculated information • No Gamma transport needed
Geometry evolution of the fuel plate (Deviation from original geometry)*: Core/Fuel*	• Distortion due to thermal expansion, irradiation, and fuel fabrication defects • Fabrication deviation from nominal dimensions needs to be identified prior to loading the fuel (as initial condition)

	• Model development to account for thermal expansion and irradiation effects
Radiative Heat Transfer*:* *Core/Fuel*	• Radiative heat transfer from the surface of the fuel plate • Can be precalculated • Primary salt absorption coefficient needs to be modeled
Surface condition*:* *Core/Fuel*	• Surface roughness, degradation or erosion • Affects T-H calculations (friction and convective heat transfer) • Important for flow distribution into coolant channels in the core during natural circulation
Heat capacity of FLiBe*:* *Core/Primary Coolant flow*	• Heat capacity is a function of the temperature Can be precalculated using existing correlations/models
Density of FLiBe*:* *Core/Primary Coolant flow*	• Density as a function of the temperature
Viscosity of FLiBe*:* *Core/Primary Coolant flow*	• Viscosity as a function of the temperature
Thermal conductivity of FLiBe*: Core/Primary Coolant flow*	• Thermal conductivity as a function of the temperature
Core heat transfer coefficient*: Core/Primary Coolant flow*	• Forced/mixed/natural convection: Need to determine flow regime in the core • Primary coolant pump coastdown curve is needed to determine the initial flow following reactor scram • Natural circulation flow is coupled to heat transfer from the fuel to FLiBe and from FLiBe to DHXs
Optical properties*:* *Core/Primary Coolant flow*	• Absorption and transmission of the coolant as a function of temperature and wavelength • Models may need to be developed for FLiBe absorption and transmission to thermal radiation of typical wavelengths • Experiments may be necessary to develop this model

Form loss coefficients*:* *Core/Primary Coolant flow*	• Entrance and exit loss coefficients as a function of area ratio and Reynolds number • May not be easy to precalculate even with the CFD method. May need at least pre-confirmatory measurements
Wall friction*:* *Core/Primary Coolant flow*	• Wall friction factor is a function of the Reynolds number and surface roughness (for turbulent flow) • Spacer ridges on the fuel plates need to be accounted for • Experimental testing to assist correlation/model development
Core flow asymmetry*:* *Core/Primary Coolant flow*	• Occurs in the core due to asymmetry in core structures, such as that due to fuel plate deformation, and asymmetric performance in DRACS loops • Flow distribution in the core may need to be calculated using high-fidelity tools
Direct energy deposition*: Core/Primary Coolant flow*	• Gamma heating of coolant from fuel as a function of the axial and radial positions in the core for steady-state and decay loads
Fluidic diodicity/Bypass Flow*: Vessel*	• Fluidic diodicity/Bypass Flow
Cover gas entrainment*:* *Vessel*	• Due to frothing at the free surface • Function of core flow rate and core geometry
Thermal heat capacity/conductivity of vessel*: Vessel*	• To determine heat transfer across vessel wall • Function of vessel temperature and irradiation • Correlations/models
Heat transfer to upper plenum structures*:* *Vessel*	• Heat transfer to control rod drives (are there Guide tubes for the control blades in AHTR?) • Thermal radiation from the salt pool surface and vessel wall • Natural convection in the gas space
Heat transfer coefficient to vessel wall*: Vessel*	• Forced/Mixed/Natural convection heat transfer • Natural circulation flow in the core and downcomer

Friction factor on vessel wall in downcomer*:* *Vessel*	• Downcomer pressure drop • Friction factor is a function of the Reynolds number and vessel wall inner surface roughness (for turbulent flow) • Important for primary loop natural circulation flow
Mixing in lower plenum*:* *Vessel*	• From eight downcomer segments • Boundary condition to the core inlet • High-fidelity tools are needed to calculate mixing in lower plenum
Heat transfer to cover gas and vessel upper flange*: Vessel*	• Radiative heat transfer for the salt free surface • Convective heat transfer from the cover gas to the upper flange due to natural circulation in the cover gas • Cover gas thermophysical properties
Thermal properties of insulation*: Vessel/Cavity*	• Density, thermal conductivity and heat capacity • Functions of insulation temperature
Heat transfer across vessel to gas space*:* *Vessel/Cavity*	• Thermal resistance to heat transfer from reactor vessel wall to gas space through thermal insulation
Heat transfer across second gap to concrete*:* *Vessel/Cavity*	• Thermal radiation from the guard vessel wall to concrete • Convective heat transfer in the cavity due to natural convection in the second gap between the guard vessel and concrete
Conduction in concrete*:* *Vessel/Cavity*	• Wall heat transfer and concrete thermal conductivity • Heat sink for concrete • Concrete property changes with time (e.g., water content)
Pump performance*:* *Primary Loop, Intermediate Loop*	• Pump performance (four quadrant), coastdown curve, and pump efficiency • Vendor provided information • Coastdown characteristics designed based on specified requirement

Pump resistance or K factor: *Primary Loop, Intermediate Loop*	• Pressure drop across pump • Vendor provided K factor information
Form loss in the loop: *Primary Loop, Intermediate Loop*	• Pressure losses due to bends, fittings, valves, flow area abrupt changes, and obstacles • Function of flow loop geometry and Reynolds number
Wall friction in the loop: *Primary Loop, Intermediate Loop*	• Function of the Reynolds number (and wall roughness for turbulent flow) • Function of piping wall roughness for turbulent flow
P-IHX performance: *Primary Loop, Intermediate Loop*	• Heat transfer and pressure drop on primary side • Heat exchanger modeling
Heat loss through and thermal inertia of piping: *Primary Loop, Intermediate Loop: DRACS*	• Piping/component geometry and material of construction • Heat transfer to the ambient from pipe thermal insulation
Impact of cover gas entrainment on pump: *Primary Loop*	• Potential pump cavitation, reducing pump head
Pump curve: *Intermediate Loop*	• Pump performance curve, coastdown curve, and pump efficiency • Vendor provided information
I-PHX performance: *Intermediate Loop, Power Cycle*	• Heat transfer and pressure drop in the intermediate loop • Loop geometry in the intermediate loop and power cycle loop
Thermal conversion efficiency: *Power Cycle*	• Steam Rankine cycle is proposed for AHTR power cycle • No detailed design available for AHTR • Must mature analysis
DRACS piping: *DRACS*	• Friction and form losses in the piping • Heat losses to the ambient

DHX performance*: DRACS*	• Heat transfer and pressure drop on both sides • Natural circulation flows on both sides • Function of the DHX design and FLiBe coolant temperature Experimental testing may be needed for a given DHX design to assist model development
NDHX performance*: DRACS*	• Heat transfer and pressure drop on both sides • Natural circulation/convection flows on both sides • Function of the NDHX design, DRACS salt and ambient air temperatures Experimental testing may be needed for a given NDHX design to assist model development
Chimney natural circulation and performance*: DRACS*	• Loss coefficients under different conditions (e.g. louver opening) • Function of chimney design, NDHX design, DRACS salt temperature and ambient air temperature Validation measurements needed
KF-ZrF_4 thermo-physical properties*: DRACS*	• Heat capacity, conductivity, viscosity, and density • Function of salt temperature Validation experiments may be needed to improve existing correlations
Thermal inertia of DRACS and chimney*: DRACS*	• Heat stored in the structures, heat exchangers, insulation and chimney Function of DRACS design and geometry, and materials temperatures

5.4.7. Others

This section contains events and phenomena that were determined to be important to FHR modeling in general but did not fit well into the above discussed operation scenarios and/or systems/components. The first column contains a short description of the phenomenon. The second column contains an initial assessment of the required coupling level determined by the panel. The third column contains commentary about the modeling of the specific phenomenon.

Phenomenon	Required Coupling	Commentary
Tube rupture in P-IHX	Loose	• Need activation calculation and evaluation of gamma instrumentation to detect leak – accident condition

Overcooling due to inadvertent DRACS operation or restart/shut down of primary pumps	Tight	• Tight coupling if the effect is important/to be determined • Preliminary calculations indicated very small reactivity effects due to coolant temperature perturbation • Need to understand the source of cooling and coolant feedback effects
Secondary shut down system/kinetics and fluid mixing and dissolution in lower plenum	Tight	• Coupling level depends on the initiating events • Requires high-fidelity T-H
Salt deposition on control rod drive mechanism	Loose	• This affects the operation of control rods, due to temperature differential (150°C in the upper support plate vs the 700°C coolant temperature), and therefore salt deposition must be tracked. This is an operational issue • An experiment is recommended to determine salt deposition
Grid disconnection event	Tight	• Need coupling between neutronics and T-H analyses
Partial flow blockage accident	Tight	• Need coupling among neutronics, T-H, and materials analyses
Online salt redox control and clean up	Loose	• The salt temperature (computed by T-H) needed for online salt redox control and clean up • Loose, one direction coupling
Graphite conductivity and dimensional changes	Loose	• Feedback of graphite conductivity and dimensional changes due to irradiation and temperature on T-H and neutronics • Long-term (irradiation/fluence) and short-term (sudden change in temperature) effects • Graphite dimensional change will affect fuel particles
Materials temperature and density change	Loose	• The impacts of materials temperature and density (T-H) change on neutronics • Coupling level will depend on the scenario type • Effect should be studied

T-H and neutronics spatial resolution coupling	Loose	• T-H and neutronics spatial resolution coupling • Sub-channel calculations for T-H – T-H spatial resolution needed is coarser than that of neutronics. i.e., fuel-stripe resolved neutronics versus sub-channel T-H
Salt impurity transport effect	Loose	• Salt impurity transport effect on neutronics and T-H • Effect should be studied • Depends on the scenario type
Effect of tritium	Loose	• Effect of tritium in salt and (trapped) in graphite or corrosion from materials due to an event (e.g., a sudden change of temperature) • The design is to remove tritium via, e.g., heat exchangers, i.e., negligible effect on neutronics
Impacts of instrumentation	Loose	• The impacts of instrumentation on neutronics, T-H and materials • Negligible effect since the design does not include in-core instrumentation as in BWR. Currently, the core is designed for instrumentation in the central assembly.
Irradiation effects on corrosion	Loose	• Irradiation effects have impact on corrosion • Not necessary for core calculation
Effects of fuel plate deformation	Loose	• Fuel plate deformation (e.g., radiation induced swelling, fuel fabrication defects, and thermal expansion) effect on the plate power, coolant flow, heat transfer from the fuel plate to the coolant, and flow-structure interactions during reactor normal operation • Loose coupling with respect to neutronics as this effect is long term. However, structural and T-H coupling can be important • Investigate the need for tight coupling between T-H and structural analyses

5.4.8. Summary

The required coupling between different physics areas for the modeling and simulation of FHR operation and accident scenarios is identified in this paper. A list of multiphysics phenomena was created and then categorized into the groups of “tight” and “loose”

required coupling. "Tight" coupling refers to phenomena that require iterative feedback between multiple physics modules/methods while "loose" coupling refers to phenomena that require only data that can be pre-calculated and shared in tabular or functional forms.

This study is a necessary step prior for developing new or extending existing multiphysics modeling and simulation tools. For the station blackout scenario, it was determined that no identified phenomena required tight coupling. This stems from the fact that this scenario mainly focuses on the removal of decay heat. Thus, the nature of the feedback between neutronics and T-H is inherently only loosely coupled, as the main parameter required of neutronics is the decay heat generation rate distribution. This can be precalculated. For the rod withdrawal and normal operation scenarios, it is found that there is a large number of phenomena that require tight coupling of neutronics and thermal hydraulics physics. Although, tight multiphysics coupling is not necessary for licensing of a first-of-a-kind reactor such as the FHRs it is believed that multiphysics methods/codes with the appropriate tight coupling for the phenomena identified in this study will have the sufficient accuracy for design optimization of the AHTR or similar reactors. Additionally, such a method/code can be also used for design and optimization of supporting experimental programs and facilitate a smoother regulatory review.

References

[1] Integrated Approach to Fluoride High Temperature Reactor (FHR) Technology and Licensing Challenges. U.S. Department of Energy Nuclear Energy University Programs, 2014.

[2] Rahnema, F., Edgar, C., Zhang, D., & Petrovic, B. (2016). Phenomena Identification and Ranking Tables (PIRT) for Fluoride High-Temperature Reactor (FHR) Neutronics. Atlanta, GA: Georgia Institute of Technology. Retrieved from https://smartech.gatech.edu/handle/1853/55812

[3] Sun, X., Yoder, G., Christensen, R., Shi, S., Lin, H.-C., Wu, X., & Zhang, S. (2016). Thermal Hydraulic Phenomena Identification and Ranking Tables (PIRTs) for Advanced High-Temperature Reactor (AHTR)

[4] Singh, P., Chan, K., & Rahnema, F. (2017). Phenomena Identification and Ranking Tables (PIRTs) Report for Material Selection and Possible Material Degradation Mechanisms in FHR. Atlanta, GA.

[5] Varma, V. K., Holcomb, D. E., Peretz, F. J., Bradley, E. C., Ilas, D. Q., & Zaharia, N. M. (2012). AHTR Mechanical, Structural, and Neutronic Preconceptual Design (ORNL/TM-2012/320). Oak Ridge, TN: Oak Ridge National Laboratory.

[6] Rahnema, F., & Others. (2018). Phenomena, Gaps, and Issues for Neutronics Modeling and Simulation of FHRs. Annals of Nuclear Energy(IN THIS ISSUE).

[7] Sun, X., & Others. (2018). A Thermal Hydraulic Phenomena Identification and Ranking Table Study for Advanced High Temperature Reactor. Annals of Nuclear Energy(IN THIS ISSUE).

[8] Singh, P., & Others. (2018). Phenomena Identification and Ranking Tables (PIRT) Study for Advanced High Temperature Reactor Structural Materials. Annals of Nuclear Energy(IN THIS ISSUE).

5.5. Conclusion

As a starting point to determine the phenomena that potentially need to be addressed in support of licensing of the FHR M&S tools, the Georgia Tech led IRP convened Phenomena Identification and Ranking Table (PIRT) panels of both internal and external experts. The results of the PIRT panel meetings for neutronics, thermal hydraulics, materials, and multiphysics are provided in PIRT reports. All the PIRT reports have been published. The relevant PIRT phenomena are summarized in each chapter. These results represent the broader, global issues related to M&S of FHRs specifically, and are expected to facilitate more accurate modeling as they are addressed.

6. Instrumentation

This effort was focused on development, demonstration and evaluations of novel FHR instrumentation options and visual/optical reactor performance characterization capabilities taking advantage of the TRIGA reactor configuration as a prototypic optically (visually) accessible reactor environment. The actual reactor operation data have been compiled and used to support sensitivity studies as well as model validation efforts. Performed simulations indicate significant noise levels that potentially may complicate reconstructions of localized values of in-core parameters in FHRs.

The project accomplishments include developing two 3D reconstruction methods, assessment of emulation options for scaling experimental results from TRIGA to FHR conditions, and design of the multiphysics sensor probe concept realizing optical and mixed-field sensing capabilities within a single integrated probe configuration. One of the developed 3D reconstruction methods assumes exclusive fiberoptics-based technology options. The 2nd method is based on the integration of multi-field distributed sensing approaches using fiberoptics-based and optical (image-based) technology options.

The work is significant well beyond applications for FHRs. As already noted above, the project addressed the grand challenge of 3D high-resolution characterization needs to support development and licensing of advanced reactors. Findings and developed solutions are directly applicable to all advanced reactors. They have particular benefits for systems with optical in-core access.

6.1. Visual Instrumentation and Fiberoptics as Synergistic Options

Because of transparency of fluoride salts and their performance range in FHRs being far below boiling conditions, it becomes possible to take advantage of visual measurements. Visual instrumentation approaches allow locating sensor materials outside of the FHR core environment while gathering in-core data.

The technical issue to resolve is to make sure visual instruments have reliable access to the FHR core internals. In-vessel visual access ports (windows, mirrors, etc.) must remain transparent or reflective, and maintain their functional alignment with respect to in-core features. Sensors and instrumentation systems are needed to provide local data supporting material performance characterization, safety studies and benchmarks.

The set of operating parameters characterizing conditions in the reactor primary system includes temperatures, neutron fluxes and fluences, local power levels, coolant flow rates, pressure, coolant level/inventory, coolant composition, and structural conditions (mechanical changes, surface conditions, vibration phenomena, degradation characteristics, and etc.). These are the parameters of interest in the present work.

The objective is to assess capabilities and limitations of visual instrumentation approaches in combination with novel sensing technologies providing complementary local data for predictive assessments assuring reliable operation of FHRs. The visual ability to monitor important regions of the reactor vessel from the interior while the reactor remains online and the entire vessel periodically during maintenance outages can provide assurance that unacceptable corrosion will not have occurred over the previous inspection interval.

Performance and applicability of novel in-core sensing technologies is assessed, namely fiberoptics sensing, as complimentary means to monitor local phenomena and changes. Fiberoptics sensors offer driftless accuracy and high sensitivity, light weight and small size, ease of installation, low power requirements, immunity to electromagnetic interference, potential for multiplexing (several sensors can be used with a single transmission cable), large bandwidth, and reliability and environmental ruggedness. This task is directly linked to the reactor physics and transient test subtasks.

Instrumentation systems and the corresponding performance demonstration experiments utilize equivalent scaling and are assessed under fully prototypical conditions to support the design of startup testing protocols for validating transient response models as well as for use in the licensing program.

6.2. Research Reactors as Generation IV Environment Emulators

The mostly-decommissioned first generation included various proof-of-concept and prototype systems which were more like experiments themselves than deployable power systems. Notably, the first generation already included nearly all viable nuclear reactor designs found in active development today.

The global majority of the operating nuclear reactors belongs to the so-called Generation II. It includes LWRs, both PWRs and BWRs, CANDU, and naval reactors. Upgrades and evolutionary advancements of those belong to Generation III+. (Generation IV International Forum, (2016); Pioro, (2016))

Generation IV includes designs that are on the vanguard of technological advances in nuclear reactors. It consists of reactors that were conceptually initiated in the '40-'60s – VHTRs, FHR and MSRs, SCWR, GFR, LFR, SFRs, as Generation I, and takes those designs to the 21st century technological state-of-the art taking advantage of developments in relevant areas since Generation I.

Nuclear power units with Generation IV reactors offer significant advances in performance, safety, security and economics; thus, emerging as a strong competitor to contemporary power technologies including the current LWR fleet. (Generation IV International Forum, (2016)) To assure successful commercialization and deployment of these systems in the coming decades, extensive research and development (R&D) efforts are underway to advance relevant technologies.

The Generation IV R&D programs are challenged by extreme in-core operating conditions due to expected high temperatures and the high energy radiation environments. The reactors advance from water as a well-known coolant. Instead, they utilize gas (VHTR and GFR), salts (FHR and MSR), and liquid metals (LFR and SFR). These conditions dramatically depart from the LWR in-core environments bringing new design challenges due to materials and operational considerations.

The novelty of the Generation IV systems results in a limited number of the representative facilities supporting experimental studies. The challenge is further exacerbated by the fact that large scale integral prototype facilities exist only for some of the Generation IV designs (VHTR and SFR) and do not exist for others (GFR, FHR and MSR, LFR).

Close international collaborations are paramount for the successful development, deployment and commercialization of the Generation IV systems because capabilities, technologies and available prototype facilities are scattered globally. (Generation IV International Forum, (2016)) Scarcity of actual prototypic environments is one of the leading factors demanding more R&D time and significantly contributing to the R&D cost.

Responding to these challenges, this project is exploring research reactors, namely TRIGA reactors, as in-core environment emulators and their ability to support Generation IV reactors. This will facilitate further R&D efforts and expand available experimental capabilities for advanced reactor development efforts. Developing approaches to experimentally evaluate the Generation IV reactor features using existing facilities, before investing in exact prototypic environments, dramatically improves the Generation IV reactor R&D economics and consequently reduces the deployment and commercialization risk factors.

The scaling analysis is performed to provide full alignment of the TRIGA-based experiments to the FHR in-core conditions. Taking advantage of normal and pulsed modes of TRIGA reactor operation, this subtask allows developing startup testing protocols for validating transient response models as well as for use in the licensing program to demonstrate efficiency of visual instrumentation.

6.3. ORNL FHR Design

The work is focused on Fluoride High-Temperature Reactors (FHR) which belong to the MSR group but utilize molten fluoride salt only as a coolant while using solid fuel forms. The FHR core layout is shown in Figure 6-1 as modeled using MCNP in the present effort. The layout is depicted with the MCNP VISED editor.

It is assumed that the considered reactor unit is operating at 600 MWth. The design features have been aggregated for the purposes of the present analysis based on the ORNL FHR design. (Holcomb, Peretz, & Qualls, (2011))

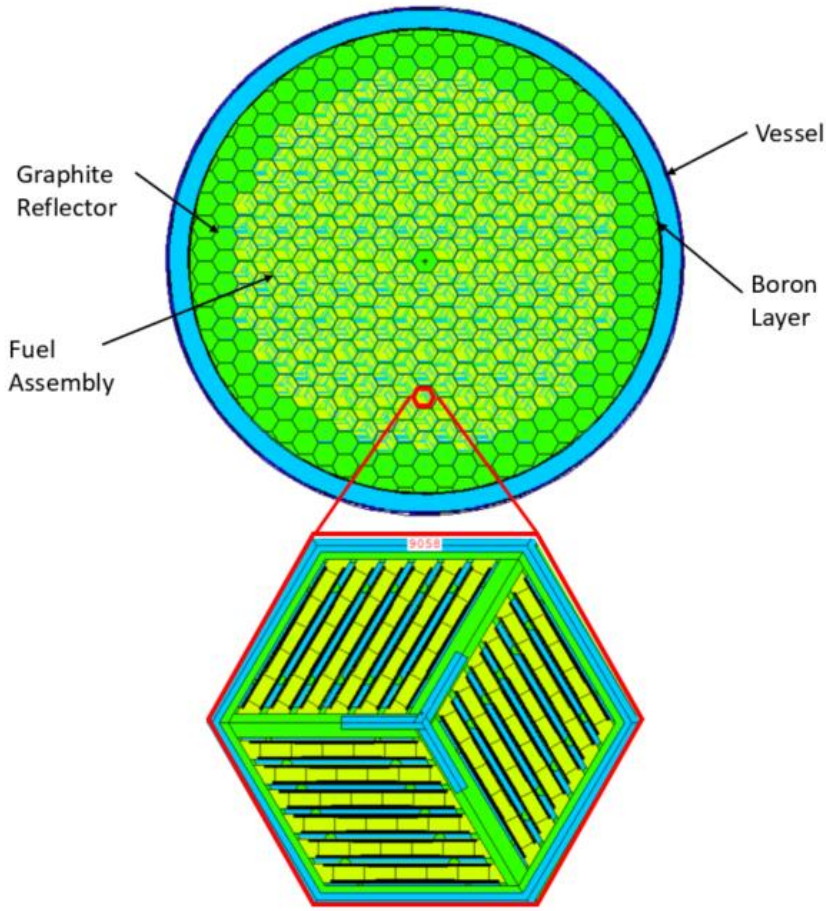

Figure 6-1 Details of the FHR core layout rendered using MCNP VISED editor.

The reactor vessel is made of alloy 800H with a 1-cm boron layer between the core and the vessel. There are 252 hexagonal fuel assemblies in the active core surrounded by graphite reflector blocks.

The fuel assembly lattice pitch is 45 cm. Within each assembly, the blue-colored Y-shaped center region represents the control rod slot which is filled with flibe. The yellow sections represent graphite at 1200 K with semi-circle spacers for coolant flow.

The black strips represent graphite matrix regions filled with TRISO fuel particles enriched to 9 wt. % 235U. In addition, small Eu_2O_3 (^{151}Eu and ^{153}Eu) spheres are embedded within the graphite matrix to act as burnable absorbers. The core is 5.25 m in diameter.

Relevant features of this FHR design are summarized in Table 6-1. The complete set of design parameters and performance characteristics of the ORNL FHR design can be found in the corresponding design specifications. (Holcomb, Peretz, & Qualls, (2011))

Table 6-1 Representative characteristics of the considered FHR design.

Reactor Characteristics	Design Value
Power ($MW_{th.}$)	600
Fuel Temperature (K)	1200
Lattice	Hexagonal
Thermal Flux Peak Energy (MeV)	1.91E-7
Thermal Flux Peak (n/cm^2s)	6.79E11
Moderator	Graphite
Coolant	Flibe
Fuel	UO_2
Fuel Design	TRISO
Enrichment (wt. %)	9.0
Core diameter/ Active core diameter (m)	10.5/9.6
Core height/Active core height (m)	19.5/5.5
Burnable Absorber	^{203}Eu
Control Rod Material	Mo and Hf

The Serpent model was developed based on the FHR MCNP model to aid in scoping calculations. The Serpent model will not be used for Cherenkov studies as Serpent lacks the relevant modeling capabilities, but it can be used to supplement studies into the correct placement of fiber optic probes and cables for neutron/gamma detection. Figure 6-2 shows MCNP and Serpent models.

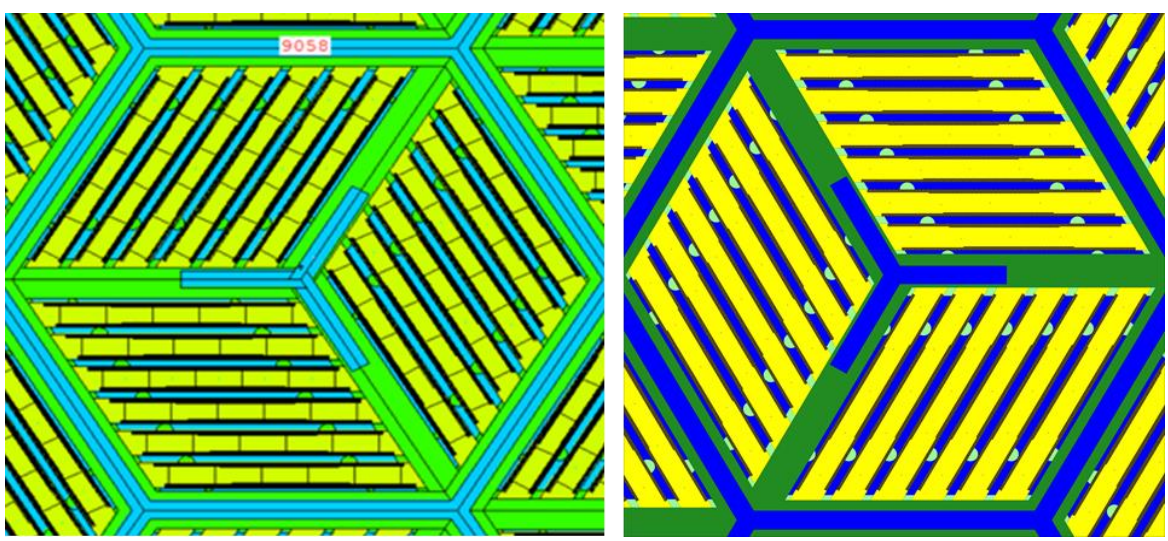

Figure 6-2 MCNP (left) and Serpent (right) models of the FHR active core features.

Figure 6-3 shows the whole-core Serpent model. Comparisons between the Serpent and MCNP calculations confirm accuracy of both computational tools while the Serpent model yield shorter computational times compare to the MCNP model.

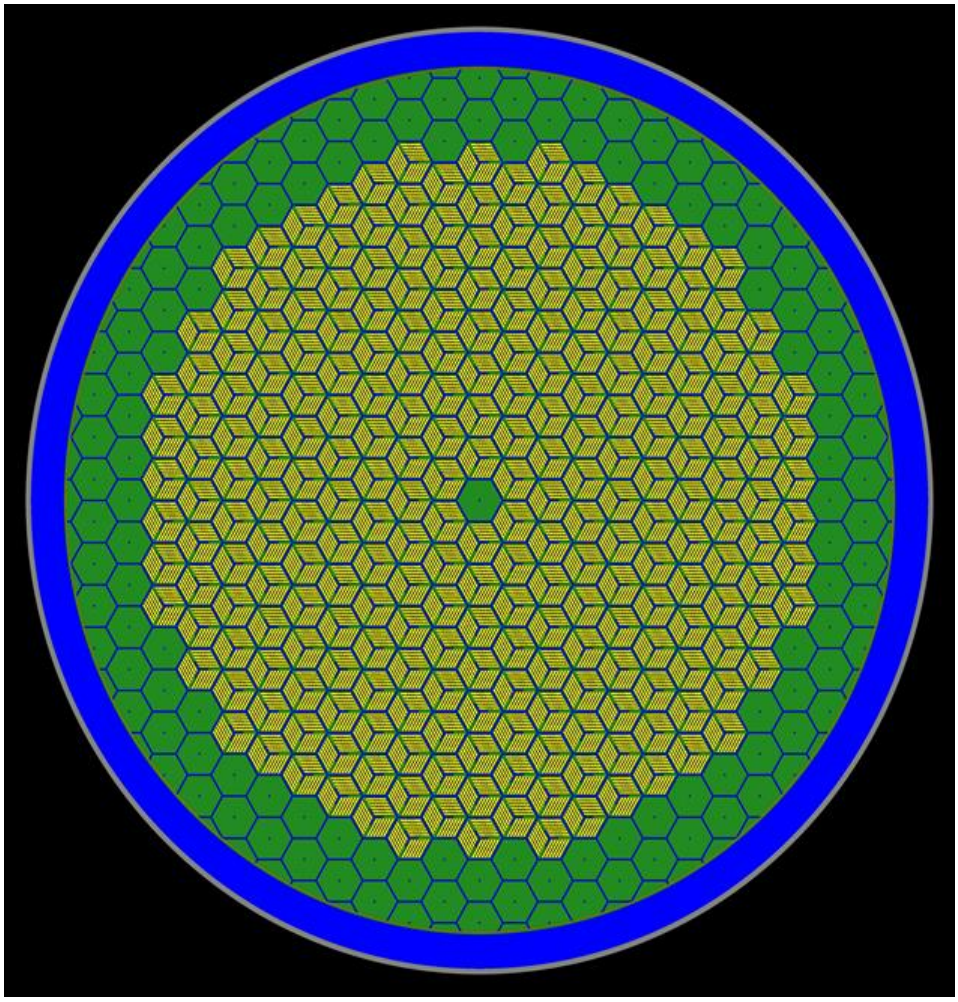

Figure 6-3 Full core model of the FHR core for use with Serpent.

6.4. Validation Approach Using the VHTR Configuration

The Very High-Temperature Reactor (VHTR) is taken into consideration for validation purposes. (Ames & Tsvetkov, (2008); Connolly, Rahnema, & Tsvetkov, Elsevier (2015); Tsvetkov, et al., USA (2011)) The design features have been aggregated for the purposes of the present analysis based on the NGNP VHTR design and the corresponding benchmark problems. (Connolly, Rahnema, & Tsvetkov, Elsevier (2015); INL, (2007)) The considered VHTR core layout is shown in Figure 6-4 as modeled using MCNP. The layout is depicted with the MCNP VISED editor.

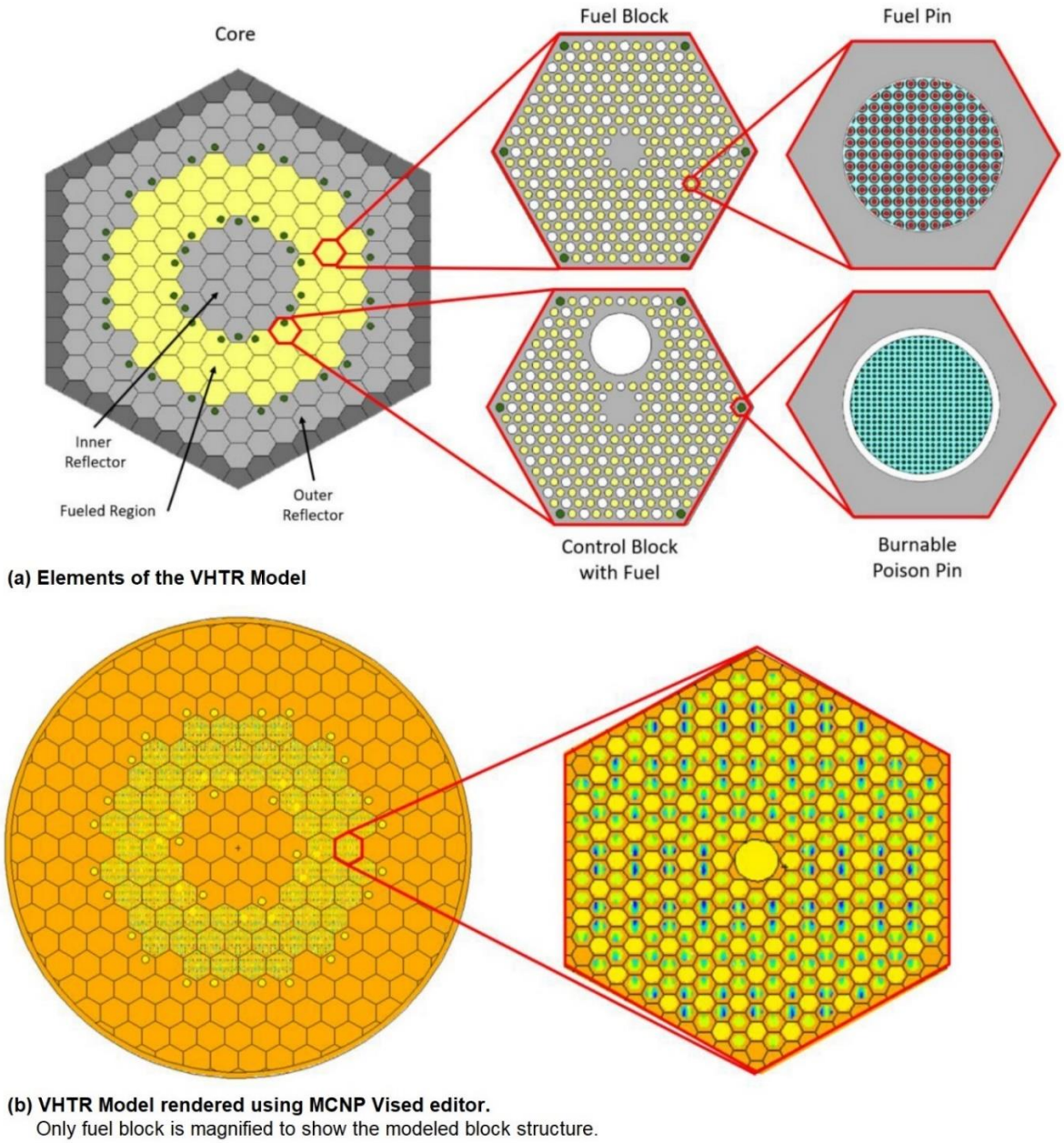

Figure 6-4 Details of the VHTR core layout rendered using MCNP VISED editor.

The active core of the VHTR has ten axial levels of 79.3 cm per level. Each level is formed by hexagonal blocks as shown in Figure 6-4. The effective core radius is 304.9 cm. Most notably, the core consists of three main sections: the inner graphite reflector, annular fuel region, and the outer graphite reflector.

The fuel utilizes TRISO particles with an effective enrichment of 15.5 wt.%. Similarly to the FHR unit, it is assumed that the VHTR unit is operating at 600 MWth.. Relevant features of this VHTR design are summarized in Table 6-2. The complete set of design parameters and

performance characteristics of the NGNP VHTR design can be found in the corresponding design specifications. (Connolly, Rahnema, & Tsvetkov, Elsevier (2015); INL, (2007))

Table 6-2 Representative characteristics of the considered VHTR design

Reactor Characteristics	Design Value
Power (MW_{th})	600
Fuel Temperature (K)	1200
Lattice	Hexagonal
Thermal Flux Peak Energy (MeV)	2.53E-07
Thermal Flux Peak (n/cm^2s)	1.3457E+13
Moderator	Graphite
Coolant	Helium
Fuel, Fuel Design	UO_2, TRISO
Enrichment (wt. %)	15.5
Core diameter (m)	6.1
Core height (m)	10.7
Control Rod Material	Boron
Core Geometry	Annular
Inner Reflector Eff. Radius (m)	1.48
Active Core Eff. Radius (m)	2.41
Outer Reflector Eff. Radius (m)	3.33

The use of graphite in VHTRs and FHRs is expected to yield similarities in reactor physics characteristics, neutron distributions in their respective core environments, which is significant for the purposes of the present analysis seeking to replicate reactor physics of these reactors in a research reactor with very different native environment. As already noted above, the objective of the present effort is to emulate advanced reactor conditions using TRIGA reactor. Recognizing principal design differences, local modification options in the TRIGA core are being evaluated and discussed with the objective of emulating advanced reactors. The considered modifications include various moderators, absorbers, and localized elevated temperatures in thermally isolated in-core enclosures.

6.5. Instrumentation Options for FHRs

The high-temperature, molten fluoride-salt coolant provides a hostile environment for nuclear reactor state and diagnostic sensors. Reactor instrumentation provides information for plant operation, automated control, and corrective action in abnormal situations. Reactor systems necessitate multiple systems measuring extensive parameters (temperature, pressure, neutron flux, etc.) to guard against single point failures and inadvertent reactor shutdown. (International Atomic Energy Agency, (1999))

The same instrumentation technologies that are developed for the molten salt reactor will find application in any industry that utilizes molten salt heat transfer loops. These include, but are not limited to renewable energy power generation and storage, petrochemical production, and materials manufacturing. Much, if not all, of commercially available nuclear reactor instrumentation is devoted to water cooled reactor technology. Instrumentation will need to be able to measure temperature, pressure, mass flow rate, flow velocity, two phase void fraction, and liquid levels.

Fiber optic sensors have the potential for low-profile, robust instrumentation in the harsh environments of high-temperature, molten salt loops. They are immune from electromagnetic interference (EMI) at the location of measurement, and many sensors can be combined into a single fiber bundle to provide redundancy, greater awareness, or both.

Fiber optic sensors have two broad classifications: extrinsic/hybrid or intrinsic/all-fiber. Extrinsic fiber sensors are similar to the conventional counterparts except that the measure of deflection is performed by light. Intrinsic fiber sensors use a change in the fiber itself as the measurement. (Hashemian, InTech (2011))

6.5.1. Neutron Flux Monitoring

Neutron flux monitoring is an important tool used for reactor control and safety functions. Spatial neutron flux profile awareness is necessary to safely maximize the reactor thermal output and signal deviations into flux tilting and shifting conditions.

The technology of neutron flux detection has remained relatively unchanged for the past few decades, but signal processing methods have improved dramatically. New fission chamber designs have enabled single fission chambers to measure the entire working neutron flux range of power reactors. (International Atomic Energy Agency, (1999))

This class of neutron and gamma detectors produces a positive charge on one electrode by the emission of energetic electrons when exposed to radiation and do not need an external power supply for quantity measurement. (Boland, (1970)) Major issues of the self-powered detectors are the vulnerability to spurious EMI and sensitivity burnup swing.

The neutron flux monitor is derived from the Cherenkov radiation that is emitted from the fission daughter products, but it can be made more sensitive to neutrons by adding a short-

lived beta emitter such as Cd or Gd to increase the Cherenkov signal due to the neutron flux. (Jang, et al., (2013))

Since the beta flux from fission is substantial, it would be simplest to use an uncoated, fiber bundle. The bundle would be sheathed in Hastelloy-N with a flexible lead bellows, also made from Hastelloy-N. The fibers themselves would be made from sapphire fiber coated with a micron-thick nickel clad.

Developed in the present effort, Figure 6-5 shows a conceptual drawing of the proposed detector with the dimensions exaggerated for clarity. The power profile is deduced by the difference in the Cherenkov signals between adjacent fibers.

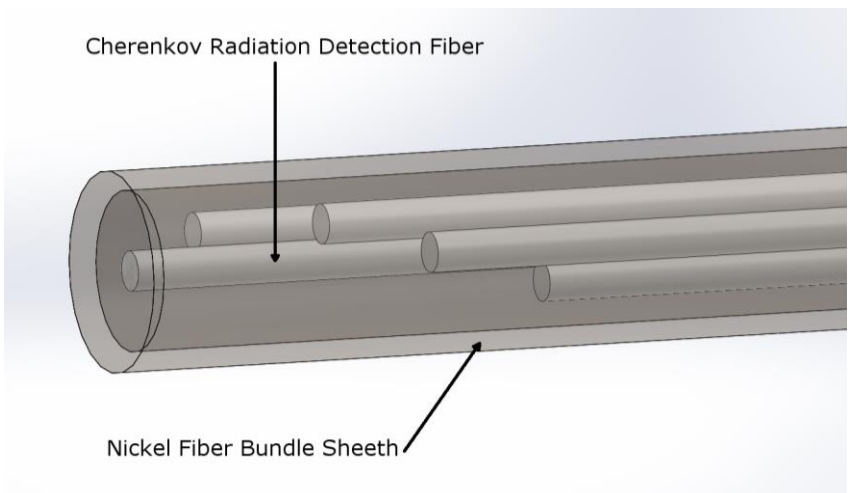

Figure 6-5 Cherenkov axial power profile detector.

Sapphire is a durable material that is able to remain relatively transparent even under the harsh radiation environment of a nuclear reactor core and should remain transparent up to 10^{19} n/cm^3. (Abdukadyrova, (2005); Petrie, (2013)) The defects should be able to be annealed out of the fiber at temperatures above 600ºC.

6.5.2. Temperature Measurements

Thermocouples, resistance temperature detectors (RTD) are widely used for temperature measurement. Fiber-Bragg grating temperature sensors are the most mature fiber-based technology and commercially available fibers can withstand operational temperatures up to 900ºC. (Luna, (2016))

6.5.3. Liquid Level Monitoring

Ultrasonic measurements of the liquid level in a vessel or other containers are currently an accepted method of fluid height monitoring.

6.5.4. Corrosion and Vessel Thickness Monitoring

A high temperature piezoelectric material such as single crystal AlN clad in nickel should provide a robust sensor capable of withstanding the harsh molten salt environment. The acoustic waves can be used to monitor vessel and piping thickness, and to a limited degree the corrosion layer immediately inside the vessel wall. (Jiang, Kim, Zhang, Johnson, & Salazar, (2014))

This technology can be used to a greater degree if ultrasonic phased-arrays are employed to generate a 3D picture of vessel wall and its molten salt interface. (Drinkwater & Wilcox, (2006))

6.5.5. Pressure Measurements

Most pressure transducers use the deflection of a pressure sensing element to infer the pressure reading. The deflection can be measured using piezoresistive, piezoelectric, capacitive electromagnetic, resonant, and optical techniques. The diaphragm and measurement system can incorporate inherent errors due to hysteresis, temperature, and corrosion. The fiber optic techniques are best suited for the corrosive, high-radiation environments at higher temperatures. (Ritchie, (2010))

The Fabry-Perot interferometer pressure transducer detects pressure disk deflections with sub-micron accuracy using the inherent length change measurements from multiple-bounce light-interference that is then transmitted via multimode optical fiber to a fringe pattern CCD sensor that translates the moving fringe pattern into pressure-disk deflections. (Zhou, (2011))

6.5.6. Flow Measurements

Flow measurement can be achieved from differential pressure measurement on flow through a venturi, ultrasonic particle velocimetry (using suspended microbubbles as the particles). The pressure measurements can be performed by the fiber optic methods mentioned above.

6.5.7. Omni-Directional, Light-Pipe Visual Inspection Periscope

Aluminum nitride shows some promise as a potential window material for molten fluoride salts at lower temperatures than the maximum outlet temperature at full power. The temperature of the salt should remain below 700°C for inspection of the core internals.

A small-scale test apparatus could be constructed to demonstrate prototypic conditions. This small-scale device would consist of a sealed furnace and crucible of candidate molten fluoride salt in which an AlN-clad, sapphire fiber-bundle would be immersed. This furnace could then be loaded into the TEES NSC reactor irradiation location for testing at temperature and radiation fields that would approximate the environment of a FHR.

6.5.8. Fiber Optic Material Analysis

Spectroscopic interrogations of materials have been performed using fiber optics as the light delivery and collection medium.

Fiber-Optic Laser-Induced Breakdown Spectroscopy (FO-LIBS) is a technique that is based on creating plasma from an intense laser pulse and reading the atomic spectrographic emission information from the collected light as the plasma decays. Fiber optic cables can be used to generate the laser pulses, confer the light to the target and collect the emitted light to transfer it back to a spectrometer. An all fiber monitoring system is possible, and this advance could dramatically increase the reliability of in-the-field spectroscopy analysis for molten salt systems.

Fiber Optic Raman Spectroscopy aims to measure molecular rotational and vibrational energy states and can thus differentiate between isotopes in molecules. Using this signal, it would be possible to measure the transition states in tritium containing molecules, enabling rapid tritium detection at a potentially lower cost and a more robust instrumentation system.

The presence of hydrogen within the reactor hall or secondary heat transfer loops or protective jackets can be detected with fiber optic sensors, which have several different sensing methods. The methods are generally grouped into surface reactions with thin films, changes in the intensity of reflected light, emission and/or absorption spectra, or surface plasmon resonance. (Yang & Dai, (2014); Perrotton, (2013))

It is possible to measure the ratio of ^{235}U to ^{238}U signals using molecular spectra and thus determine the isotope enrichment for continuous enrichment processes. This could be used for faster measurements than would be achievable through gamma spectroscopy (depending on light source strength and the signal to noise ratios). These systems could also be person portable. Such a fast measurement technique would help the IAEA in their global nonproliferation goals.

6.6. Modeling Approach

Whole-core 3D exact-geometry models of TRIGA internals and VHTR and FHR hexagonal-block configurations with detailed component representations have been developed and implemented for computational studies with MCNP. (X-5 Monte Carlo Team, Los Alamos National Laboratory (2018))

In-core neutron distributions in FHRs, VHTRs and TRIGA are analyzed through detailed modeling efforts using these models. Figure 6-1, Figure 6-4, and *Figure 6-97* illustrate details accounted for.

The MCNP6.1.1 Beta is being used to model the reactor and the production of Cherenkov radiation from the electrons produced from fission, decay etc. The MCNP6.1.1 Beta is the first version of MCNP to incorporate photon transport for energies down to 1 eV, corresponding to infrared light.

The MCNP6.1.1 has the capability of modeling refraction in materials and the corresponding production of Cherenkov radiation when electrons or other high velocity particles pass through a refracting medium.

As a result, these simulations are able to accurately estimate the production of visible and Ultraviolet Cherenkov photons from the reactor when it is in operation, allowing photon tallies to be taken at various locations in or near the core to simulate the visual instrumentation options and the use of fiber optic probes.

The FHR model includes the active core region and the surrounding reactor vessel. A detailed top-down view of the active core region is shown in Figure 6-1. The green and yellow colors represent graphite at different temperatures. The green graphite is at 900 K while the yellow graphite is at 1200 K. The light blue color represents the flibe.

The VHTR model is constructed to be consistent with the FHR model. The model details are shown in Figure 6-4. It shows the model elements and their internals capturing reactor component details as well as the overall model rendering using MCNP VISED editor.

The rendering colors represent different materials: yellow is for helium, multi-color regions in the fuel block are for fuel, and orange is for graphite. The VHTR model has been used to validate the overall modeling approach and is developed based on the NGNP VHTR design specifications. (Connolly, Rahnema, & Tsvetkov, Elsevier (2015); INL, (2007))

The detailed high fidelity TRIGA reactor model is capable to simulate performance characteristics represented by both reactor internal instrumentation data feeds and external visual equipment data feeds.

The model utilizes Monte Carlo MCNP and Serpent. *Figure 6-6* provides the core-level view of the TRIGA model.

The top-down view of the TRIGA reactor model is shown in *Figure 6-97*. The fuel rods, graphite blocks, and water are shown by the color designations: white, green, and blue, respectively.

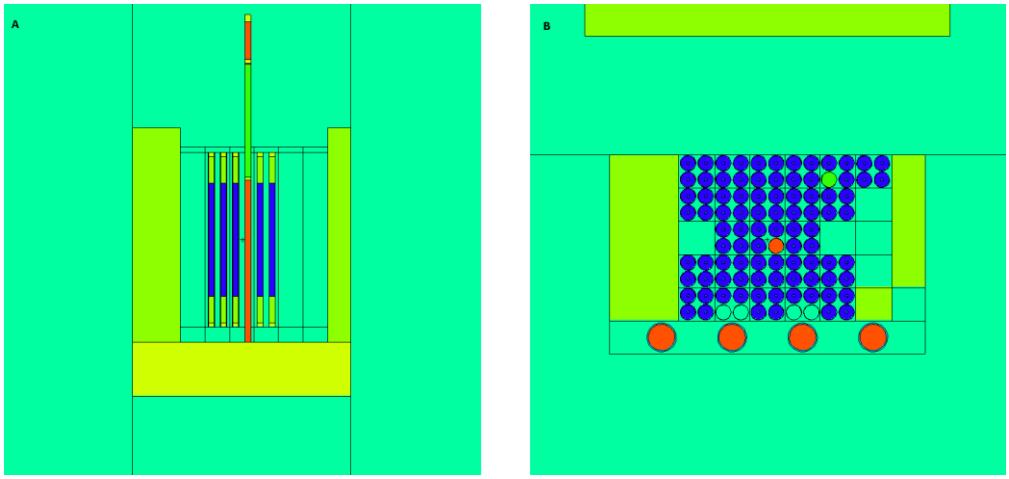

Figure 6-6 TRIGA reactor model, core-level view.

It is comprised of 86 regular fuel pins filling some of the locations in a 12x10 lattice. Each fuel pin was modeled with a zirconium rod in the center surrounded by the Zr-H fuel with stainless steel cladding. Graphite regions are placed axially above and below each fuel pin within the cladding, and aluminum caps are at the top and bottom of each pin.

There are four safety shim control rods in the (4,4), (4,8), (8,4), and (8,8) locations in the core. The safety shims are moveable rods that consist of a fuel region similar to the fuel pins with a boron carbide absorber region above it.

The safety shims are fuel following to increase their reactivity worth and are used to make large reactivity adjustments in the core. A translation card in the end of the input deck can be used to easily adjust the degree to which the safety shims are inserted or removed.

The in-core irradiation location D3 (Location 1) is selected as the primary reference location for use in the present analysis, see *Figure 6-97*.

The majority of the TRIGA tallies are taken in D3. It is a compromise solution taking advantage of the higher flux value. Locations 2 and 3 are investigated comparing neutron distributions in these locations to Location 1.

The applied approach allows tracking environments in fuel regions and coolant channels. Within the considered locations, multiple material configurations and temperatures are taken into account to explore options to get closer to the FHR and VHTR environments.

As illustrated in *Figure 6-7*, the model fidelity is sufficient to recognize fine scale adjustments within the sample locations towards needed spectral conditioning. The distributed sensing using fiberoptics is modeled as illustrated in *Figure 6-8*.

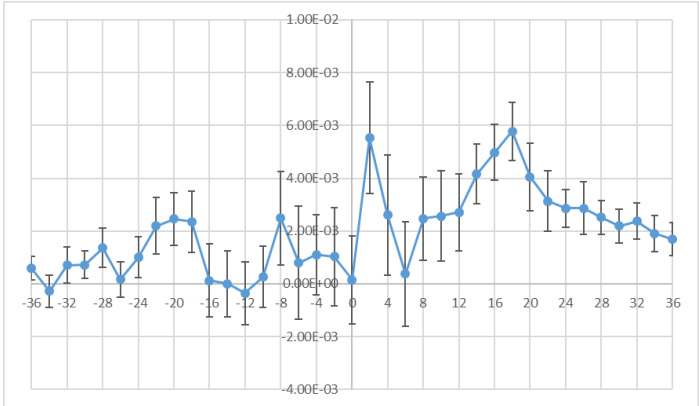

Figure 6-7 Differences in the photon fluxes for a critical system following the regulating rod movement from its fully removed position and to its fully inserted position.

The computational methods, including use of libraries, geometry details and simulation parameters, have been validated in previous efforts. The TRIGA reactor model will be discussed further in later sections of this report. (Ames & Tsvetkov, (2008); Connolly, Rahnema, & Tsvetkov, Elsevier (2015))

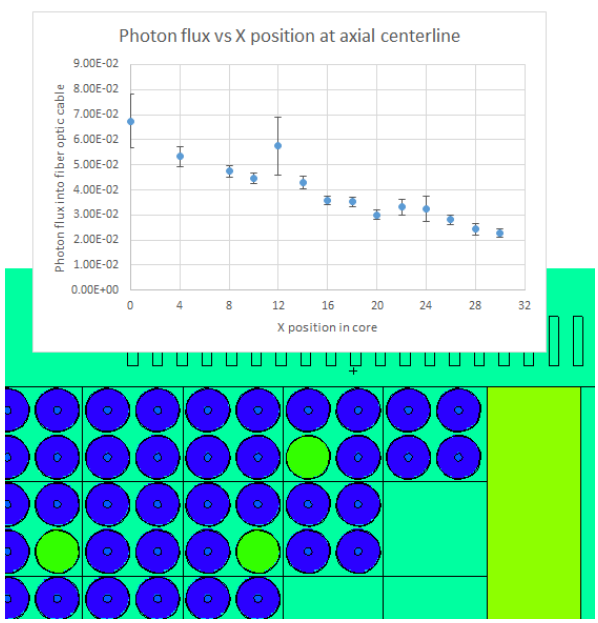

Figure 6-8 Photon flux into fiber optic probe vs position at the core's axial centerline.

6.7. Radiation Field Analysis, Reconstruction, and Feature Characterization

6.7.1. Modeling and Visualization of Mixed Radiation Fields

In this research effort, a standardized method is developed and used for calculating and presenting mixed (neutron, gamma and beta) radiation fields in a reactor. An MCNP mesh tally is used to provide a graphical representation of the flux of a given type of radiation. The mesh tallies are produced using the TMESH feature of MCNP.

This feature allows the user to define mesh tallies in rectangular, cylindrical or spherical coordinates. In rectangular coordinates, the X, Y, and Z components of the mesh are defined using the CORA, CORB and CORC cards with the points corresponding to the boundaries of each mesh cell.

For example, the input lines in an MCNP deck are shown here:

```
TMESH
RMESH1:n
CORA1 -20 99i 30
CORB1 -52 99i -2
CORC1 -30 30
ENDMD
```

The command creates a mesh tally for neutrons over a 50 cm x 50 cm x 60 cm rectangle with the x mesh spanning from x= -20 cm to 30 cm, the y mesh spanning from y= -52 cm to -2 cm and the z mesh spanning z = -30 cm to 30 cm. The x and y dimensions are each split into 100 mesh cells, and each mesh cell is averaged over the entire 60 cm of the z axis. Running an MCNP deck with this will perform an F4 type neutron path length tally in each cell of the mesh. This gives the average neutron flux in $n/cm^2/s$ per source particle in each of the 10,000 mesh cells.

The flux in each cell also has a corresponding Monte Carlo uncertainty which is reported by MCNP as a proportional uncertainty; an uncertainty of 0.1 corresponds to a sigma equal to 10% of the flux value. The results of the mesh tally are placed in an MCTAL file, named MCTAL by default. In the MCTAL file, each tally has its parameters described, and then the keyword “vals” is followed by a pair of numbers corresponding to each mesh cell’s flux value and uncertainty.

Then, a python script is used to extract the data from the MCTAL file. Each mesh tally has a corresponding object created that reads the dimensions, flux value, and uncertainty from the MCTAL file in each mesh cell. The mesh tally can then be manipulated, compared to other tallies, and plotted in the code.

In each MCNP run, three separate mesh grids are used, one for each directional plane, XY, XZ and YZ. To decrease uncertainties, each mesh tally is relatively fine in two dimensions

and is averaged over the entire meshed region of the reactor in the third dimension as shown in the example above. This results in more scores in each tally bin but does not allow one to take a thin planar slice out of the reactor.

In the model of the TRIGA reactor, the meshed region is the 50 cm x 50 cm x 60 cm region used in the example ranging from -20 to 30, -52 to -2 and -30 to 30 in X, Y and Z. However, for the XZ mesh, the X dimension is split into 50 bins, 1 cm across, with the z dimension split into 60 bins 1cm tall. The YZ mesh also has 1 cm bins for both the y and z dimensions, as opposed to the half cm mesh cell sizes in the XY plots.

For each reactor configuration run, a total of 9 mesh plots can be generated; the meshes would be one for neutrons, gammas, and electrons in each of the three planes. In this report, cases will often have only a selection of the mesh plots presented to show relevant reactor changes.

The XY mesh plots are often the most useful and easy to understand. Each XY mesh point is averaged over the entire height of the fuel and some space above and below the fuel, so an alteration to a given pin in the core is most noticeable in an XY mesh. Of the three radiation types tallied in the meshes, the neutrons are generally the most tightly coupled to alterations in the reactor, and the gamma fluxes are slightly more blurred than the neutrons.

Alternatively, the electron maps can show the geometry of the reactor. This is because the electron generation in a material is approximately proportional to the density of that material multiplied by the gamma flux at that location. Thus, the denser materials in the core, such as the fuel, will have a higher electron flux in the mesh plots when compared to less dense materials like water.

In addition to reactor flux mesh plots in various states, plots can be produced showing the difference in the fluxes between two reactor states. Difference plots are produced by subtracting the flux of one reactor state from the flux in another reactor state at each mesh point. This produces a visual representation of how and where the flux in the reactor is increased or decreased by a given change.

Some composition and cladding thickness changes are tested, but the primary alterations analyzed are changes in the degrees of insertion for the various control rods in the reactor. Some of the models have rod positions corresponding to the rod positions during an experiment performed at the reactor.

The difference plots are also shown with relative difference plots. The relative difference plots show the difference in the flux at each mesh point divided by the average flux at that mesh point. In this report, the mesh plots over the reactor core are often displayed in sets of four plots comparing two reactor states. The top left and right plots are the fluxes in the reactor in each state, while the bottom left is the absolute difference and the bottom right is the relative difference.

6.7.2. Cherenkov Radiation and Its Characterization Potential

Taking advantage of the optically detectable variations in the in-core processes, the primary means of using optical (visual) instrumentation analyzed here, in this context, is the use of Cherenkov radiation measurements. To this end, most of the modeling efforts are focused on modeling Cherenkov radiation production in the reactor.

Cherenkov radiation occurs when a charged particle passes through a dielectric medium at a velocity greater than the phase velocity of light in that medium. The phase velocity of light in a medium is the speed of light divided by the refractive index for light of that wavelength in the medium.

Cherenkov radiation is emitted in a cone travelling outwards and in the direction of the particle, similar to the effect of a sonic boom produced by an object exceeding the speed of sound in air or some other sound propagating medium.

In a real system, there is a diffraction effect where different wavelengths of light are emitted at different angles from the particle's path based upon their indices of refraction. The emission rate is approximately proportional to the frequency causing the intensity to peak in the upper blue and ultraviolet ranges for Cherenkov radiation produced in water.

This results in the distinctive blue glow that can be seen in operating reactors and other beta emitting sources kept under water. Further into and beyond the ultraviolet range, the frequency dependent index of refraction drops below one preventing the production of Cherenkov photons with higher frequencies.

As previously stated, Cherenkov radiation is the production of photons when particles are moving faster than the phase velocity of light through a medium. In a nuclear reactor, this primarily occurs when betas are moving through the coolant. The threshold energy for betas creating Cherenkov radiation in water is 261 keV.

This energy threshold is a function of the index of refraction of the medium such that the velocity of the particle is greater than the speed of light divided by the medium's index of refraction. In general, betas above the threshold will produce Cherenkov radiation while those below it will not.

The index of refraction is a function of the frequency of the light. In the far UV and lower x-ray range, the index of refraction drops below one, and no Cherenkov radiation is produced.

Where the index of refraction is dropping significantly with increasing frequency, the production of photons should be dependent on the beta energies beyond a simple ~ 260 keV threshold as the energy threshold would increase with frequency up to infinity at the point where the index of refraction reaches unity.

The index of refraction is one where the wavelength is close to 60 nm. The final drop in the refractive index occurs after the wavelength decreases below about 100 nm. (Segelstein, (1981))

Therefore, the physics of the Cherenkov radiation determines its practical use for the purposes of in-core process analysis, reconstruction and in-core feature characterization with the objective to predictively detect anomalies affecting reliability and performance of the reactor. Universally, a Cherenkov-based process signature approach can be developed to meet this objective in a variety of applications.

Measurements for a specific reactor core state could give a Cherenkov frequency spectrum which may be a function of the fuel enrichment, actinide content, pin design, or other factors. Therefore, a radiation signature could be obtained for accountability or safeguards purposes similar to the use of Cherenkov detectors in spent fuel pools for verification of burnup, cooling time, and the presence of all pins in an assembly.

The primary transitional range for the beta energy dependence on Cherenkov productions of specific wavelengths occurs between 100 nm and 60 nm, just beyond what is conventionally defined as ultraviolet light.

If an effective system for detecting light by its frequency in this frequency range could be designed, it may be possible to measure the higher energy beta fluxes in the coolant as a function of the energy by observing the Cherenkov radiation produced.

The prevalence of high energy betas in the coolant could provide information about thinning or breaches in the cladding or the presence of specific high energy beta emitters.

One of the straightforward applications is the use of the Cherenkov-based in-core characterization to assist in calibration of power-measuring instruments, power profile reconstruction including local hot spot detection:

- The production of Cherenkov radiation is linearly related to the fission rate density and thus power in the intermediate power range and above. In higher power ranges without rapid changes in power, Cherenkov based measurements could be used to quickly measure the power of the whole core with a distant monitor or of specific regions with focused monitors allowing for a quick determination of the power profile. Due to the changes in the core over time, these sensors should be periodically calibrated using other slower, more thoroughly benchmarked power measurements.
- In the source range, Cherenkov production from the beta decay of medium lived fission products, such as Sr-90 and Cs-137, becomes significant and causes nonlinearity. The contribution to the Cherenkov production from medium lived fission products is affected by the burnup of the core. Also, nonlinearity can result from rapid power changes as the production of betas from fission is not entirely prompt with short lived fission products making significant contributions.

Cherenkov measurements could provide another diverse and redundant power measurement system for reactor safety and operations. (Rippon, (1963); Arakani & Gharib, Design and Construction of an Independent Channel for Tehran Research Reactor Power Measurement Using Cherenkov Detector, (2007); Arakani & Gharib, Reactor Core Power Mesurement Using Cherenkov Radiation and Its Application in Tehran Research Reactor, (2009)) Next chapter of this report will discus the Cherenkov radiation physics features and modeling details.

6.7.3. In-Core 3D Reconstruction Using 2D Data Sets

The in-core reconstruction approaches were tested with MCNP6.1.1 Beta. Neutron, gamma, and beta mesh tallies were produced using three separate grids with two high resolution dimensions and one dimension with only one mesh bin.

This gave three separate, orthogonal data sets from which to reconstruct the interior core features. The data sets were extended into the 3rd dimension and padded with the values of the representative pixels on the face of that 3D representation.

An example from the top view of the reactor core is given in *Figure 6-9*; an example from the side view of the reactor core is given in *Figure 6-10*; an example from the front view of the reactor core is given in *Figure 6-11*.

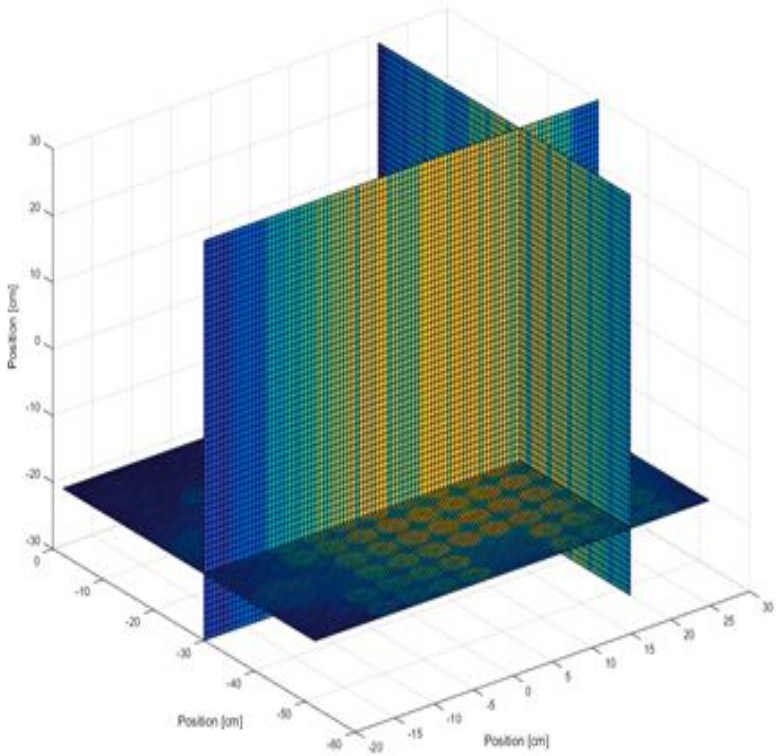

Figure 6-9 Projection of electron flux tallies to the top of the reactor core.

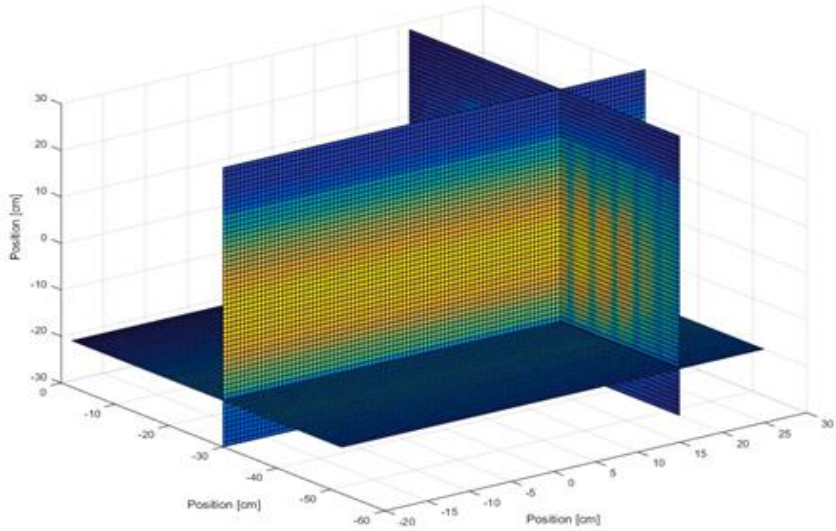

Figure 6-10 Projection of the electron flux to the side of the reactor core

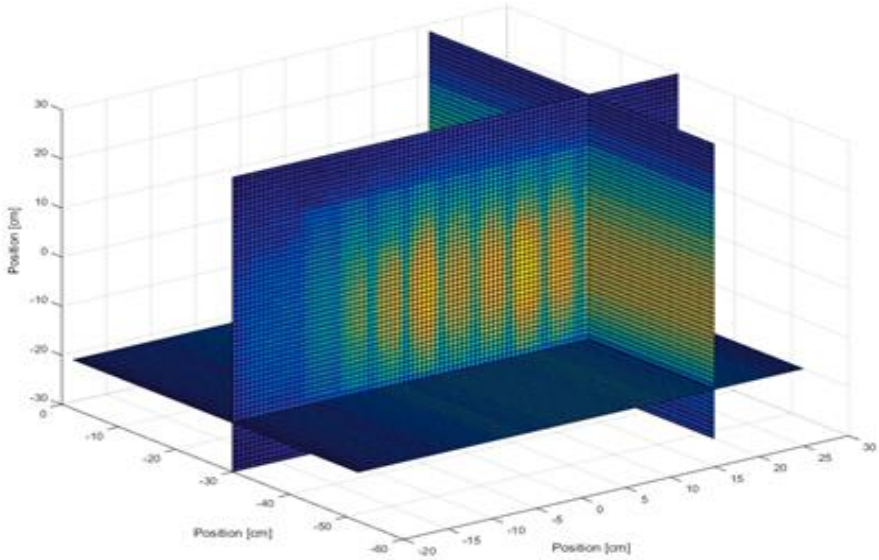

Figure 6-11 Projection of the electron flux through the front of the reactor core.

Using the gathered projection data, the corresponding core reconstruction is given in *Figure 6-12*. It is noteworthy to point out the reconstruction artefacts in the reconstruction volume: the electron intensity features continue beyond the edge of the core where they should rapidly decay. This artefact is due to the necessary averaging of the low-resolution wavelet decompositions in which a combination of low-resolution data and high-resolution data are combined in a wavelet bin that optimally should contain only low-resolution wavelet data.

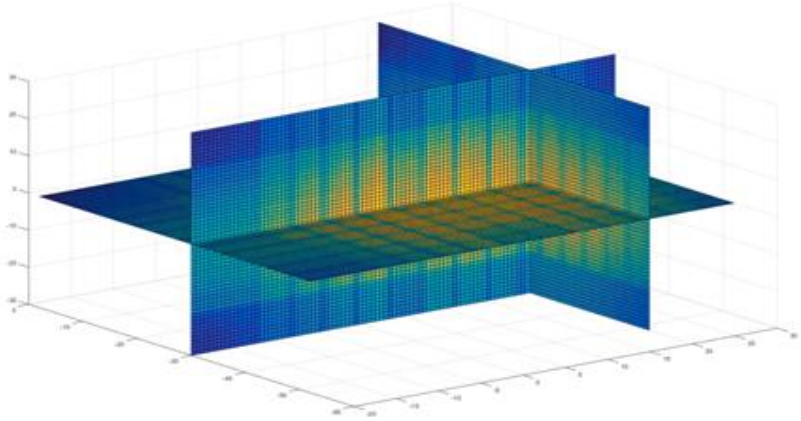

Figure 6-12 Reconstructed total electron flux for the reference TRIGA core.

Figure 6-13 shows the reconstructed total neutron flux. The neutron flux reconstruction adopts the same approach as the one used for electrons. The result is a volumetric reconstruction based on quasi 2D data sets. Notably, the reconstruction artefacts are much less noticeable in this case.

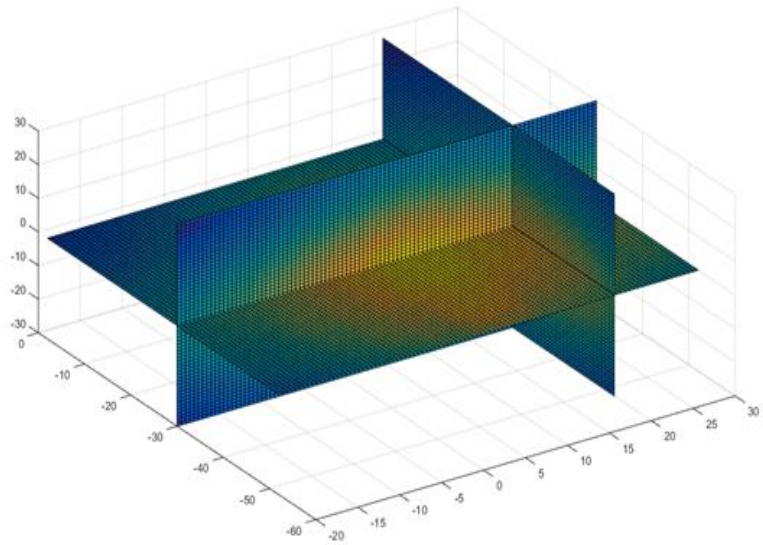

Figure 6-13 Reconstructed total neutron flux for the reference TRIGA core.

The same reconstruction approach is used for the photon flux reconstruction. The corresponding volumetric reconstruction based on the quasi 2D data sets is shown in *Figure 6-14*. Similar to neutron reconstructions, the reconstruction artefacts are much less noticeable for the photon reconstructions. In both, photon and neutron cases, reduction in artifacts may be due to longer mean free paths for these particles within the reactor core.

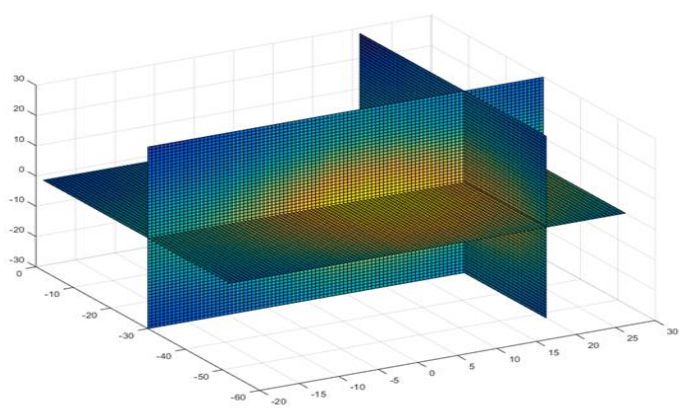

Figure 6-14 Reconstructed total photon flux for the reference TRIGA core.

Further application of wavelet transforms allows handling combinations of low resolution and high-resolution data sets. This will allow further utilization of the mixed resolution data sets to form improved data representations reducing reconstruction artefacts.

6.7.4. Feature Characterization Using 3D Reconstructed Mixed Field Data

The 3D reconstructed mixed field approach takes advantage of the existing option to survey the FHR in-core domain via imaging in the visible light wavelength focusing on the core topological signatures of the observable features. In addition, optical access allows capturing Cherenkov radiation data.

This adds additional layer of information to the topological signature providing performance characterization capabilities based on the detectable performance of the core via Cherenkov radiation signature evaluations. Lastly, the mixed-field multi-modal radiation signature evaluation taking advantage of the distributed sensing via fiberoptics provides the full characterization capabilities capturing the physics phase space of the core performance through sensing of temperature, neutron, gamma and electron fields.

With a response function distributed over a spatial range, the use of fiber optics could offer a significant advance in radiation sensing. Providing a multitude of radiation measurement data points could support a new type of reactor power monitoring with reconstruction capabilities in 3D from a 3D layout of fiber optics.

6.8. Cherenkov Radiation Physics, Modeling and Analysis

6.8.1. Cherenkov Radiation Modeling in MCNP 6.1.1.

The MCNP 6.1.1 Beta is the first version of MCNP able to perform photon transport with photon energies as low as 1 eV and to model refraction in materials. It also includes a Cherenkov production feature. This version of MCNP allows the user to input an index of refraction for each material using either a constant index of refraction, Cauchy coefficients, or Sellmeier coefficients. There is an option on the physics card to toggle Cherenkov production on and set a biasing scheme for how many Cherenkov photons will be produced.

With Cherenkov production turned on, the minimum energy cutoff for photons reduced to 1 eV, and indices of refraction input for materials, MCNP 6.1.1 will produce Cherenkov photons. The lower energy photons produced by Cherenkov have energies in the infrared, visible, and ultraviolet ranges.

The majority of the Cherenkov photons are in the blue and ultraviolet ranges. These photons are affected by refraction in transparent mediums and are transported as such.

Due to an issue in MCNP 6.1.1 involving the treatment of refraction in lattice structures, refraction in lattices can cause particles to be lost and crash the code. To circumvent this problem in MCNP 6.1.1, an input deck that has no universe/lattice structure was created so that the Cherenkov photons can be modeled successfully.

Also, due to the number of Cherenkov photons produced per particle and the complexity of modeling refracting photon transport, code run times are much longer when using Cherenkov production thus requiring the number of source particles to be reduced substantially.

To achieve acceptable uncertainties in tallies for neutrons, electrons, and gammas, separate runs are performed with Cherenkov production disabled so that more particles can be run within computational time constraints.

Tallies for Cherenkov production are primarily performed using a segmented surface tally. The plane tallied is an XZ plane that is 8 cm away from the core in the +y direction (east). For the Cherenkov tallies, only the photons with an angle of incidence on the plane such that the cosine of the angle is greater than 0.8 are counted. This corresponds to a 36.9 degree cone of accepted photons.

The mesh for the surface segment tally is produced by separately counting the photons crossing circles with 2 cm radii spaced in a grid 4 cm apart. The incident Cherenkov flux at the center point of each circle is taken to be the flux through the circle. Also, the Cherenkov flux tally only counts photons with energies less than 50 eV.

This is done to capture all the photons produced by Cherenkov while ignoring gamma rays and other higher energy photons. Further energy discrimination or energy spectrum production on the segment tally is not feasible due to runtime and uncertainty constraints.

The physics of Cherenkov photon production and transport is assessed in this effort. Loss of information caused by attenuation of Cherenkov photons, coolant activation noise, and spatial blurring effects caused by electron transport are included in the discussion below. An analysis of the Cherenkov energy spectrum produced in MCNP is also performed in the present effort, as a comparison between the use of Cauchy and Sellmeier coefficients for the index of refraction of water.

6.8.2. Cherenkov Radiation Attenuation, Noise and Blurring Effects

Cherenkov radiation occurs primarily in the ultraviolet range with noticeable production in the blue and violet wavelengths as well. The attenuation coefficient in a medium is a function of the wavelength. In pure water, the attenuation coefficient for UV light falls from 1.26 m^{-1} at a wavelength 190 nm to 0.0100 m^{-1} at a wavelength of 320 nm. (Quickenden & Irving, (1980))

However, the attenuation coefficient can increase by two orders of magnitude if small quantities of organic contamination are present in the water. As the water in the TRIGA reactor pool is likely to have some contamination by organic molecules that could absorb UV light, an accurate estimation of the attenuation of UV in the pool may be feasibly obtained by taking measurements with a light sensor at various distances from the core while it is operating.

The attenuation coefficients are much larger for the shorter wavelength and harder UV light, so distance from the source of Cherenkov photons would notably soften the UV spectrum by decreasing the shorter wavelength Cherenkov photon fluxes more than the longer wavelength fluxes. Unless accurately calibrated, this shifting would greatly hinder any attempts to measure the beta energy spectrum and obtain information other than the fission rate density or total above threshold energy beta energy production rate.

Activation of the coolant could cause noise and additional Cherenkov radiation that is not linearly related to the fission rate. However, this must involve betas with energies greater than the threshold energy for Cherenkov production in the coolant. Data for the optical properties of FLiBe is lacking, so LiF is assumed to be similar enough for comparison. The index of refraction of molten LiF salt is 1.32 (Janz, (1967)), and the index of refraction for water is 1.33. This corresponds to a beta threshold energy of 261 keV for water or 271 keV for molten LiF salt.

The primary activation in a molten salt coolant is the production of tritium which decays with a 12.32 year halflife and a maximum beta energy of 18.59 keV. This beta energy is far below the threshold for Cherenkov production in the coolant, so tritium decay should not create any issues with Cherenkov based measurements. No other beta decay producing activations in the coolant have sufficiently large cross sections to create issues. However, if

sodium were present in the core, such as in a FLiNaK cooled reactor or a water cooled reactor with sodium contamination, the activation of sodium produces much higher energy betas which would create Cherenkov noise.

Cherenkov photons in a reactor are produced by particles travelling at near the speed of light in the coolant. Nearly all of the particles with the required velocity are electrons. The primary contribution to the electron flux in the coolant is the production of free electrons by gammas interacting with the water, with electrons produced by fission in the fuel passing through the cladding and entering the coolant making a much smaller contribution to the total Cherenkov flux. The Cherenkov production density in the coolant is therefore closely correlated to the total electron production and thus the total gamma flux at any given location.

The electron density can be blurred somewhat by the transport of the electrons from where they are created. The amount or length scale of the blurring can be estimated by the electron's range in the coolant. A plot of the range of electrons in water vs energy can be seen in *Figure 6-15*. (physics.nist.gov ESTAR database) As there are few electrons in the coolant with energies greater than 2 MeV, the upper end of the expected range for electrons is about 1g/cm^2 in water with a density of 1 g/cm^3 which results in a distance of 1 cm.

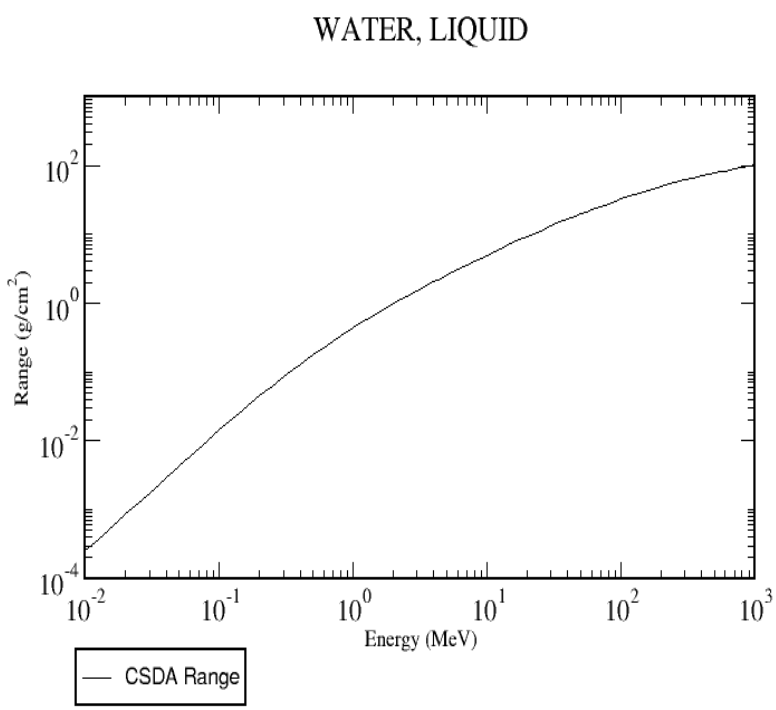

Figure 6-15 Range of electrons in water vs electron energy.

This blurring caused by electron transport is fairly small especially when the Cherenkov detection mesh has 4 cm wide bins to get enough particles. Blurring effects from the electron's path length in the coolant are thus considered to be negligible.

6.8.3. Spectral Analysis of Cherenkov Radiation

The energy dependence of Cherenkov photon production in MCNP is more closely analyzed by running simpler models with electrons in a sphere of water which is similar to the MCNP validation tests performed by Los Alamos. (Durkee, (2013)) The model consists of a sphere of water with a radius of 5 cm surrounded by a void.

Electrons are spawned in the center of the sphere, and the photon flux at the edges of the sphere are tallied. The results presented here have 0.2 eV wide photon energy bins ranging from 1 eV to 10 eV.

The bin widths in the following model are constant and linear as opposed to models elsewhere that have logarithmic bin spacing with larger bins at higher energies.

There is some skewing of the flux profile when comparing a profile using constant energy width bins to constant lethargy bins used in logarithmic spacing.

Also, there is a reversal of the flux profile when plotted against the photon wavelength instead of the energy because the wavelength is inversely proportional to the photon energy.

An energy of 1.6 eV, or 775 nm, roughly corresponds to the lower limit of red visible light, and 3.2 eV, 387 nm, corresponds to the upper limit of visibility for violet light for people.

Energetic photons at 6.2 eV have a wavelength of 200 nm which is the transition point between photons being classified as near UV and far UV. Near UV, UVA and UVB photons have energies between 3.2 eV and 6.2 eV.

The range of increasing photon energy at which the index of refraction begins its final descent to below unity is for photons with wavelengths of about 100 to 60 nm which corresponds to an energy range of 12 eV to 20eV.

The following spectrum analysis is performed using the Cauchy index of refraction instead of Sellmeier. As the Sellmeier model is more accurate for liquids, it is used in later models of the reactor instead of the Cauchy model.

The plot showing the photon energy spectra produced in the sphere of water can be seen in *Figure 6-16*. All of the curves show the photon fluxes monotonically increasing with photon energy until a sharp cutoff at 6.2 eV above which the total photon flux drops by orders of magnitude. This likely occurs because of the way MCNP produces Cherenkov radiation and the use of the Cauchy equation to approximate the refractive properties of water.

The photons in the model above 6.2 eV are produced from bremsstrahlung only and thus are far less numerous than those produced by Cherenkov.

Unfortunately, it appears that the method of refractive index input and physics for Cherenkov production in MCNP provide no mechanism for distinguishing higher energy electrons by the production of Cherenkov photons near the limit where the refractive index drops back towards unity of which occurs above the hard 6.2 eV cutoff for MCNP's Cherenkov photon production.

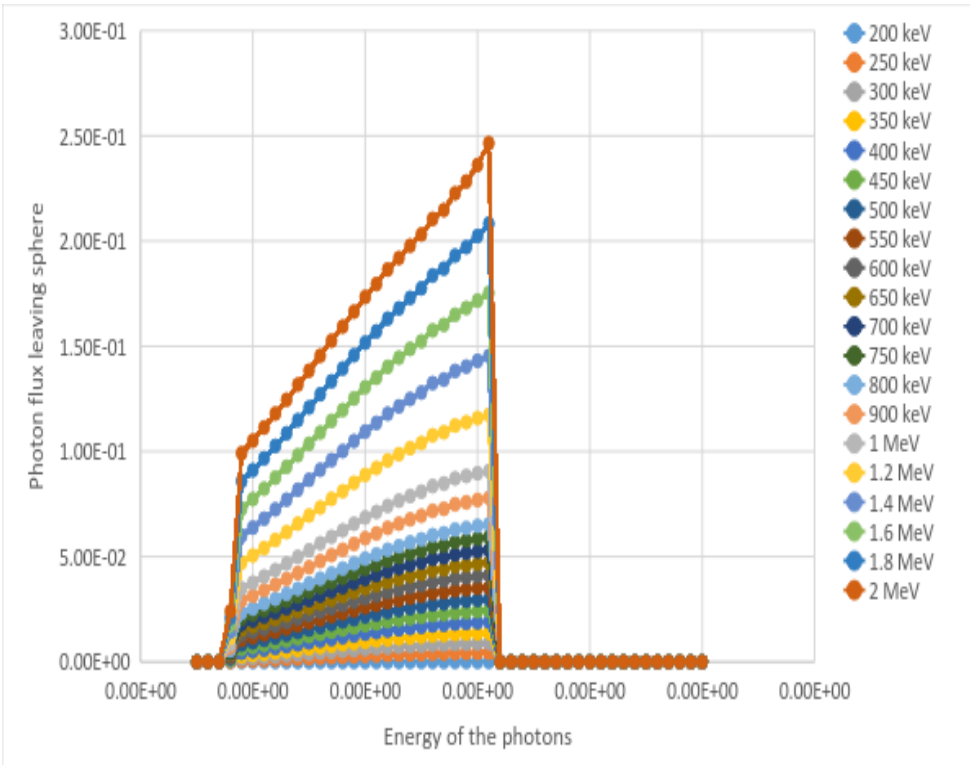

Figure 6-16 Photon flux vs photon energy leaving a 5 cm sphere of water produced by source electrons of various energies.

The upper energy cutoff for Cherenkov production in the MCNP models does not provide any information about the energy of the initial electrons producing the Cherenkov radiation.

Therefore, an analysis was done comparing the normalized photon spectra for various initial electron energies to better determine if higher or lower energy electrons produce a larger portion of their Cherenkov photons at either end of the energy spectrum.

The resulting plot can be seen in *Figure 6-17*. From this plot, it appears that the higher energy electrons produce a larger portion of their Cherenkov photons in the lower photon

energy range (in the redder portion of the visible spectrum) and a lower portion in the highest part of the energy range (near UV).

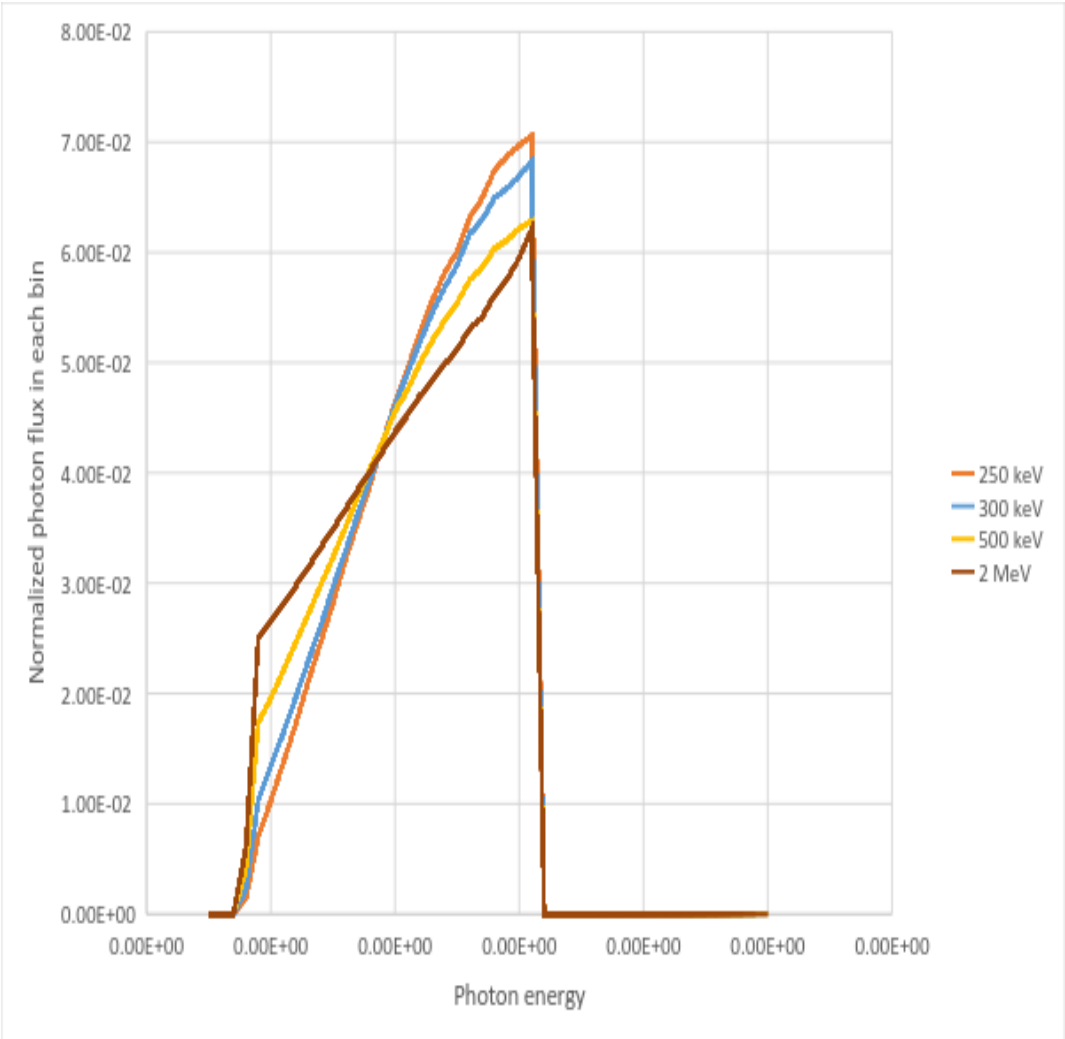

Figure 6-17 Normalized photon fluxes vs photon energy for various initial electron energies.

This effect could be because the Cauchy approximation for the wavelength dependent refractive index of water increases to above 1.4 in the ultraviolet range which causes the minimum electron energy cutoff for Cherenkov production to be lower. This decreases from a cutoff of 260 keV for longer wavelengths to the lowest threshold energy of 200 keV for shorter wavelength UV Cherenkov photon production.

Due to the 5 cm radius of this model, every electron produced slows down to well below the Cherenkov production limit before being killed, so most 300 keV electrons also end up being 250 and 200 keV electrons before stopping. The higher energy initial electrons will take longer to slow down to the low energy range in which only the higher index of

refraction wavelengths of Cherenkov photons are produced, and thus this phenomenon would have a reduced effect on the output spectrum.

There appears to be some potential for selectively identifying higher energy electrons by their increased production of the lower energy, redder photons. While this does not have the same hard cutoffs hoped for with the highest energy ranges, it does have the advantage of a noticeable difference occurring across the visible spectrum (1.6 eV to 3.2 eV) which should be easier to detect with conventional photon detection instruments.

An analysis was done comparing the use of the Cauchy and Sellmeier refractive indices for water using the 5 cm radius sphere in a vacuum. The simpler Cauchy equation has been used for all previous models. The Cauchy equation is ideally used for gasses and nonconductive mediums with indices of refraction close to 1, so there may be some error present in using it for water. The Sellmeier equation approximation is supposed to be more accurate and the preferred option for liquids and solids. (Principles of Optics, (1980)) The Cauchy coefficients used were the same as in reference (Durkee, (2013)) and are A = 1.3199, B = 6.878e-2, C = 1.132e-3, D = 1.14e-4. The Sellmeier coefficients used are B_1 = 5.6840e-1, C_1 = 5.1018e-3, B_2 = 1.7262e-1, C_2 = 1.8211e-2, B_3 = 2.0862e-2, C_3 = 2.6207e-2, obtained from reference. (Measurement of the Refractive Index of Distilled Water from the Near-Infrared Region to the Ultraviolet Region, (2007))

The plot showing the Cherenkov spectra with the Cauchy and Sellmeier coefficients can be seen in *Figure 6-18*.

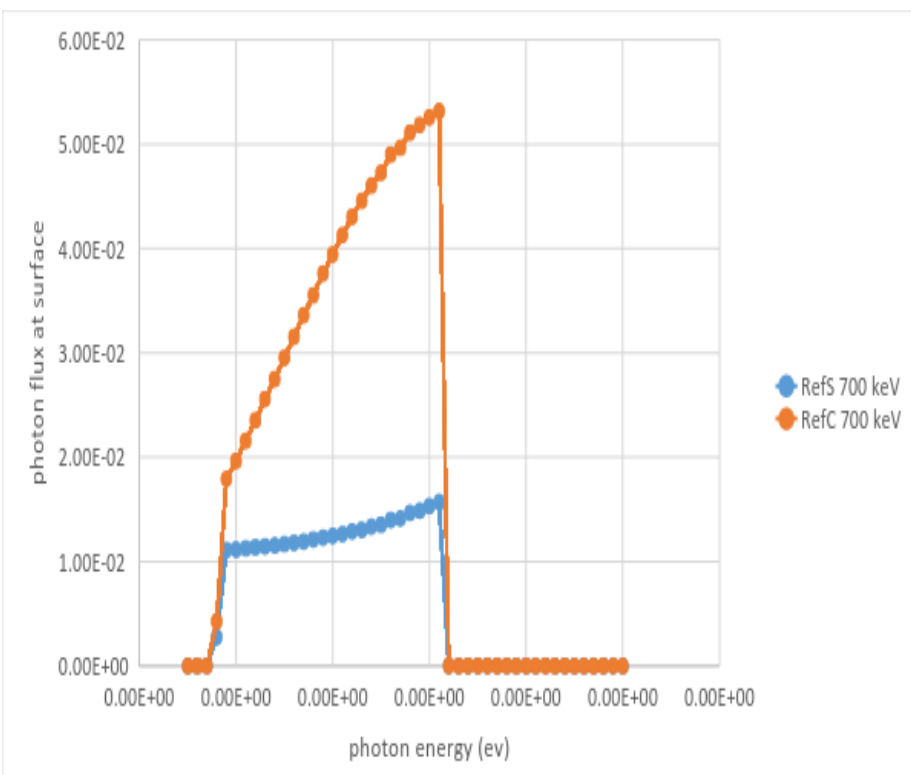

Figure 6-18 Photon flux vs photon energy for 700 keV electrons using the Cauchy (RefC) and Sellmeier (RefS) coefficients for the index of refraction in the water.

The Cauchy method seems to overestimate the total production of Cherenkov photons when compared to the Sellmeier method, particularly for the higher energy UV photons. The approximately 1.8 eV and 6.2 eV cutoffs for the production of Cherenkov photons remain unchanged. A similar overestimation of the photon production using the Cauchy equation is noted elsewhere. (Durkee, (2013))

Using a 1 mm radius sphere and 4 MeV electrons instead to more closely mirror the test done in the literature (Durkee, (2013)), the results yielded the plot in *Figure 6-19*. Despite the larger uncertainties, a similar difference can still clearly be seen, with the Cauchy predicting more photons, and the plots diverging further as the photon energy increases.

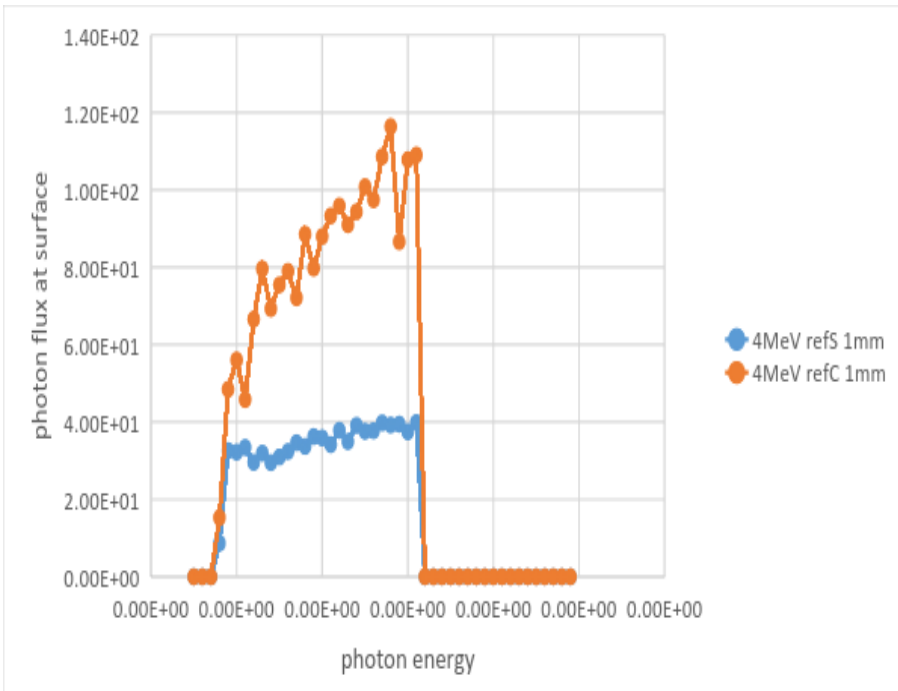

Figure 6-19 Photon flux vs photon energy for 4 MeV electrons in a 1mm radius sphere using the Cauchy (refC) and Sellmeier (refS) coefficients for the index of refraction in the water.

It is also notable that while the Sellmeier equation produces substantially less photons, the calculation run times were about an order of magnitude faster, so the Sellmeier equation usage may be slightly more computationally efficient when trying to model enough Cherenkov photons to get acceptable uncertainties in a full core model. The energy spectra produced using the Sellmeier equation appear to be less distinguishable than those produced using the Cauchy equation, as the profiles are much flatter for all electron energies that were tested.

6.8.4. Uncertainty Reduction Options in Cherenkov Radiation Simulations

One of the major issues with mapping the Cherenkov flux in the core is the presence of fairly large uncertainties when using finer meshes. Some alterations to the methodology of modelling the Cherenkov radiation to decrease the uncertainty are considered.

Increasing the number of particles run and thus the code runtime is one option. This can be done for a few specific cases to improve their statistics, but greatly increasing runtimes is not feasible in the majority of the more exploratory/diagnostic cases being modelled.

Additionally, for a given decrease in uncertainty, a quadratic increase in runtime is required, i.e. to decrease the uncertainty by a factor of 2, the number of particles and thus runtime must be increased by a factor of 4. This can help, but other changes are still needed.

Increasing the area of the tally is another potential option for improving the statistics. The current method used is only tallying photons crossing circular regions of a plane, causing the particles crossing the surface outside of the circles not to contribute to any bin. In the XZ mesh on the side of the reactor, this results in approximately pi/4 = 0.785 of the particles being tallied, with 0.215 of them being wasted. In the XY mesh above the reactor, the circles are smaller to avoid collisions with withdrawn control rods and to focus only on the light from a single channel.

Switching to a larger tallying surface for each mesh point could potentially improve the statistics, but it would also introduce inconsistencies with the areas covered by each segment, as there are differences in what rods are present to block the light. Also, any increase in the size of the surface segments tallies will decrease the number of points in the mesh and thus the resolution of the resulting image. The mesh is already an 11 x 9 grid, so any further decrease would preferably be avoided.

Another option available in the XY mesh is to transition from using a surface tally above the core to using a volume tally throughout the core. If the electron flux in these regions is assumed to be isentropic, the Cherenkov radiation production will also be isentropic. The total electron flux in a coolant channel can thus be approximately correlated to the amount of Cherenkov light leaving through the top of the channel. This could allow the code to be run in “mode n p e” with the Cherenkov production disabled. This can drastically reduce the runtime in the code, as producing and transporting all of the Cherenkov photons is computationally expensive. The accuracy of this approximation could be increased by instead using an energy dependent Cherenkov production cross section to tally the electron flux.

The Cherenkov production cross section would probably have to be computed using a separate, simplified model and then validated against a model producing Cherenkov photons. This could be done to obtain an energy dependent Cherenkov production cross

section to convert an electron flux in a coolant channel into a Cherenkov photon flux leaving the top of the core.

Additionally, an approximate correction for attenuation of the Cherenkov light through the water could be investigated and potentially added to the model if necessary, by using different weighting schemes for different axial regions in the fuel. It is not expected that the attenuation within the height of the fuel will be relevant, as any photon energies that are appreciably attenuated by the 40 cm or so of water in the core are not likely to reach a camera positioned meters above the core, and should probably be rejected from the tallies anyways.

Another benefit of this method is the potential ability to discriminate between Cherenkov photon energies/wavelengths. As many of the actual Cherenkov photons are in the ultraviolet range, it is not feasible to reject the ultraviolet Cherenkov photons in a direct Cherenkov tally because there are too few particles reaching the tally as is.

However, if the Cherenkov photons are only directly modeled in a small scale cross section determination model, then a more stringent energy segregation can be imposed. A cross section for the production of visible Cherenkov photons instead of any Cherenkov photon could be computed without causing a significant penalty in the statistics of the main run.

6.9. MCNP TRIGA Model and Reference Radiation Field Analysis

6.9.1. TRIGA Core Topology and its Representation in Field Simulations

As already discussed, the TRIGA reactor at Texas A&M is used for modelling and experimentation as a surrogate for the FHR salt cooled reactor design. The TRIGA is selected because it is a versatile research reactor and it is accessible for use in visual experimentation. It has a maximum rated steady state power of 1 MW and is a "swimming pool" type reactor cooled by natural convection.

The core resides in a large pool of water and can be moved to different locations in the pool for various experiments. It is visible from the surface of the pool, and the blue Cherenkov glow of the reactor can be seen during operation.

The core contains cylindrical fuel elements and graphite reflecting elements on two sides. One side of the core has instrumentation and irradiation tubes while the final side has fuel elements directly open to the water. This allows for fairly direct imaging of some fuel in the core during operation.

Notably, one primary limitation of MCNP6.1.1 Beta is that the use of refractive indices in a system with a lattice geometry structure causes low energy photons to be lost which results in the code stopping after 10 lost particles. To avoid losing particles, it was found that the lower cutoff energy for photons must be 6.2 eV or higher.

This corresponds to the far UV range and cuts out a large portion of the Cherenkov radiation that is generally peaked in the blue and near UV range at around 3 eV. This loss of information is unacceptable, so a workaround was required.

The only feasible workaround is to reconstruct the model in a non-lattice geometry which required individually modeling each pin and surface in the core. The model used for most purposes in this research effort is this reconstructed version without any lattice or universe structures.

The reactor is oriented with the z axis corresponding to the vertical axis of the core and the +y direction corresponding to the side of the reactor facing the graphite coupler box (East in the real world).
The cells and surfaces for the pins and control rods are numbered based upon which position in the lattice they occupy such that every surface and cell involved in a lattice location (x,y)will be defined as xxyy#.

The first 4 digits denote the position in the core, and the remaining digits define each surface for the pin, control rod, or other object in that location. An axial cross section of the reactor can be seen in *Figure 6-20*.

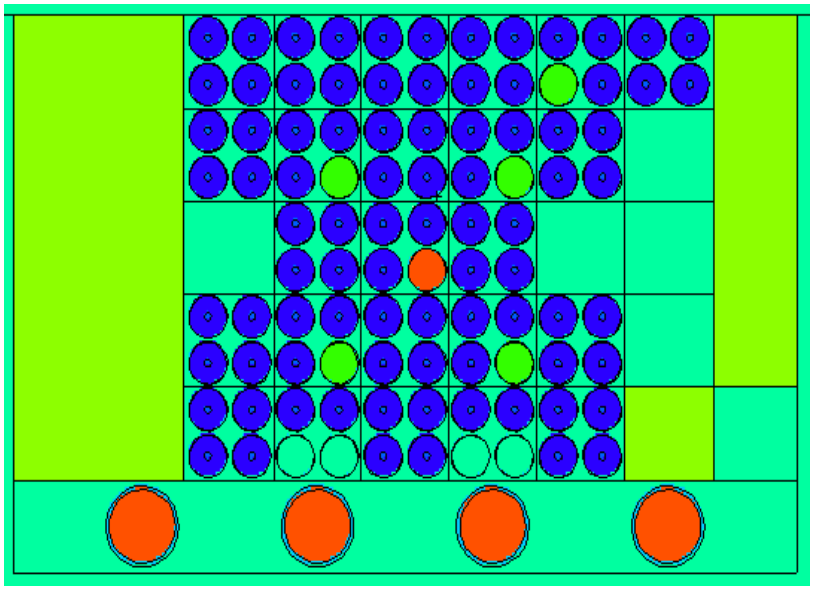

Figure 6-20 Axial cross section of the core. The top is the +y direction, corresponding to East in the real world. North is on the left side of this plot.

A more detailed diagram of the actual core can be seen in *Figure 6-21*. Note that in every XY plot shown of the core, north is on the left side of the plot (the -x direction) and the top of the plot (the +y direction) is east. Also, +x is south, -y is west, +z is away from the center of the earth and -z is towards the center of the earth.

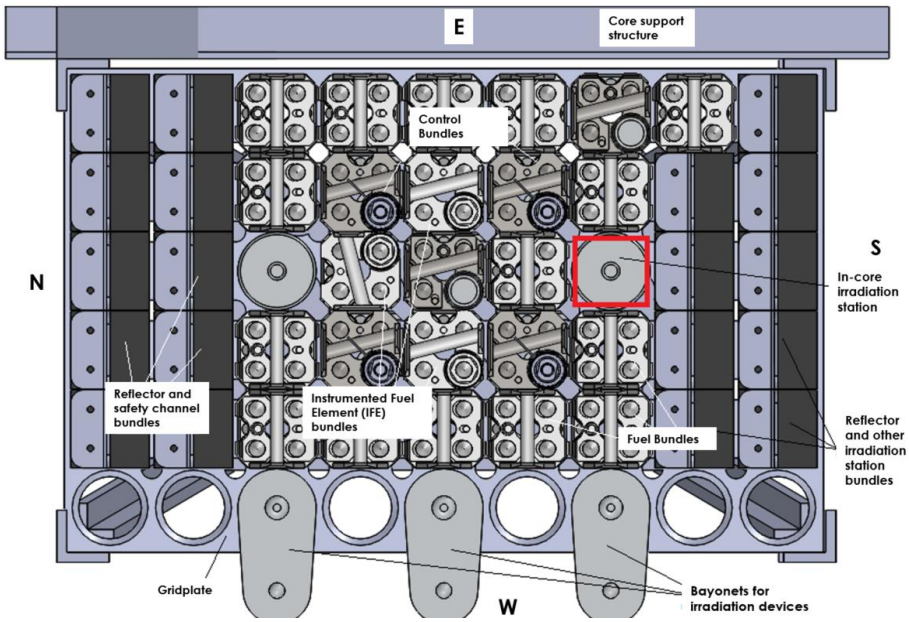

Figure 6-21 The TRIGA core map corresponding to the XY picture, showing various features and directions.

The TRIGA reactor model captures all 3D component details as illustrated by Figure 6-20, Figure 6-21 and other depictions of the TRIGA model features throughout this report. Quantitatively, the TRIGA model is comprised of 86 regular fuel pins filling some of the locations in a 12x10 lattice. Each fuel pin was modeled with a zirconium rod in the center surrounded by the Zr-H fuel with stainless steel cladding.

Graphite regions are placed axially above and below each fuel pin within the cladding, and aluminum caps are at the top and bottom of each pin. There are four safety shim control rods in the (4,4), (4,8), (8,4), and (8,8) locations in the core.

The safety shims are moveable rods that consist of a fuel region similar to the fuel pins with a boron carbide absorber region above it. The safety shims are fuel following to increase their reactivity worth and are used to make large reactivity adjustments in the core. A translation card in the end of the input deck can be used to easily adjust the degree to which the safety shims are inserted or removed.

To further characterize and present the TRIGA model, a vertical cross section of the 4th row of pins, showing fuel rods and two of the safety shims, can be seen in the left side of *Figure 6-22*.

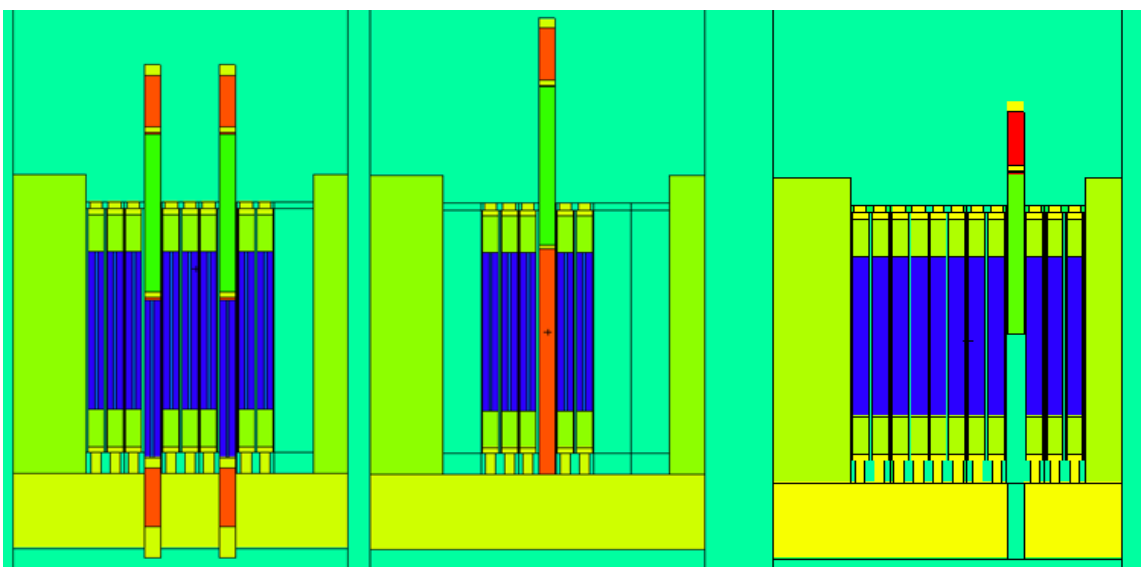

Figure 6-22 Vertical XZ cross sections of row 4 (left) and row 6 (middle) and row 2 (right) displaying fuel pins, safety shims, the transient control rod, and the regulating rod North is to the left of this plot, South is to the right.

The transient control rod is located in the center of the core at location (6,6). This is modeled as a moveable cylinder of boron carbide with aluminum endcaps within stainless steel cladding with air regions above and below it. The length of the boron region is the same as that of the fuel pins. When the transient rod is moved, the boron region with its caps moves within the air region while the rest of the rod remains in place. The transient

rod extends above the fueled region of the core, so when the transient rod is withdrawn, the bottom of the absorber is slightly above the top of the fueled regions of the fuel rods. A vertical cross section of row 6, displaying the transient rod at full withdrawal, can be seen in the middle section of *Figure 6-22*.

The regulating rod is a movable control rod at location (2,9) in the second row of fuel pins. This control rod is not fuel following and is located near the periphery of the core, so it has a lower total reactivity worth. The regulating rod is primarily used for small reactivity changes and is meant to be adjusted automatically to regulate the reactor power and maintain it at a set level. Due to its location near the most exposed face of the core, changes in the position of the regulating rod are one of the primary reactor changes studied for their effect on the observable Cherenkov fluxes.

The core has graphite blocks beside it in the +x and -x directions that act as reflectors. In this model, they are approximated as continuous rectangular prisms without anything but graphite inside of them. The lower grid plate and the structures by which the pins are supported by the plate were approximated as a solid aluminum block with a few simple square and cylindrical holes in it for control rods and other tubes and instruments.

The four irradiation tubes next to the core in the –y direction are also modeled as cylinders of air with steel cladding. Due to the way that MCNP calculates geometries and transports particles, cells with large numbers of bounding surfaces can drastically increase runtime, so it was necessary to place planes to divide the water regions in the core into smaller regions that each contained only 4 pins to reduce the runtime.

6.9.2. Fidelity of Radiation Filed Simulations

The computational methods, including use of libraries, geometry details and simulation parameters, of the TRIGA core model have been validated in previous efforts. (Ames & Tsvetkov, (2008); Tsvetkov, et al., USA (2011)) One of the primary sources of error in the criticality estimation in this model is the usage of a single homogenous material for all of the fuel pins. Differences in the modeling of the materials and regions inside of the graphite block on the –x side of the core also contribute to a difference in the k_{eff} estimates produced by this model.

The higher fidelity lattice-based neutron-only input deck with many separately depleted zones in each fuel pin and a more detailed treatment of the graphite source region is used when more precise criticality estimates are needed.

Using the neutronics only model, the reactor is critical with the transient rod fully withdrawn, the safety shims withdrawn 28.4 cm, and the regulating rod withdrawn by 19.8 cm. Modeling the reactor with these rod positions in the Cherenkov compatible model produces a k_{eff} estimate of 1.00556 ± .00037.

This degree of deviation, while significant from an operational standpoint, is acceptable for the modeling of Cherenkov fluxes because MCNP will run the number of neutrons specified when using a kcode regardless of the actual criticality value.

Despite a difference of nearly 1$ of reactivity, the difference in photons produced is proportional to the difference in the number of fissions and therefore should be on the order of 0.5%. However, due to this discrepancy, the more accurate lattice-based model with heterogeneously burned fuel is used for determining different critical rod positions.

6.9.3. Radiation Field Simulations for the Reference TRIGA Core Configuration

The present effort is focused on the multi-modal (neutron, gamma and beta) radiation field evaluations to identify and characterize in-core features. Integration of multiple radiation field modalities allows developing mixed-field analysis methods to quantify in-core features accounting for sensitivity dependencies of such measurable quantities as temperature, stress, neutron and gamma fluences.

In the present effort, neutron, photon, and electron mesh plots are produced for a given core state to characterize in-core processes. These mesh plots are used to emulate an actual multi-modal sensor network that would gathering data for the integrated mixed-field method to reconstruct, analyze, identify and ultimately predictively characterize in-core features. The multi-modal mesh plots are gathered in this section for the reference TRIGA core configuration that represents the base state of the system.

The reference TRIGA core configuration is the critical reactor state with:

- the transient rod fully removed,
- the safety shims all at 28.4 cm withdrawal, and
- the regulating rod at 19.8 cm withdrawal.

As mentioned previously, the meshed region is 50 cm x 50 cm x 60 cm, with

- the x mesh spanning from x= -20 cm to 30 cm,
- the y mesh spanning from y= -52 cm to -2 cm, and
- the z mesh spanning z = -30 cm to 30 cm.

For the XY mesh plots, the x and y dimensions are each split into 100 mesh points 0.5 cm apart and the Z bin is tallied over the entire 60 cm height. For the XZ mesh, the X dimension is split into 50 bins 1 cm across with the z dimension split into 60 bins 1 cm tall. The YZ mesh also has 1 cm bins for both the y and z dimensions.

The area of the TRIGA core covered by the mesh plots is shown in *Figure 6-23*. In the right side of *Figure 6-23*, the rods with X's are the fuel following control rods, two of which can be seen as partially inserted in the left side (see also *Figure 6-22*).

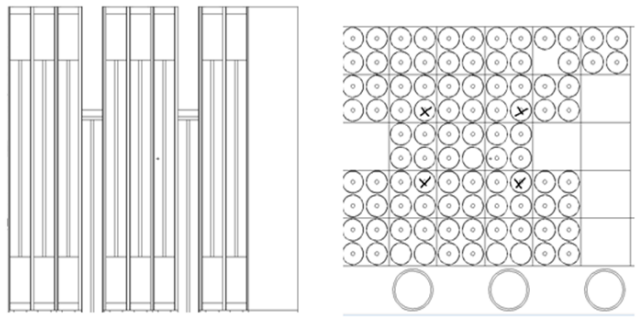

Figure 6-23 XZ and XY cross sections of TRIGA showing the region covered by the mesh tallies.

The data matrix formed by an illustrative set of 9 mesh plots, as generated through MCNP simulations of the reference TRIGA core configuration, is shown in *Table 6-3*. In the actual application, this matrix would be a big data set composed of reconstructed multi-modal 3D in-core information flows based on high-resolution scans of the in-core domain.

Table 6-3 Emulation of a multi-modal sensor network via simulated mesh plots

XY Mesh Plots	**XZ Mesh Plots**	**YZ Mesh Plots**
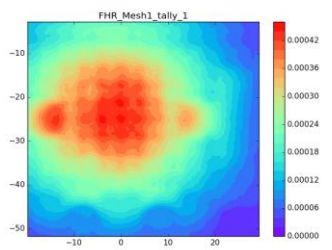	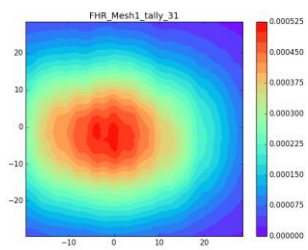	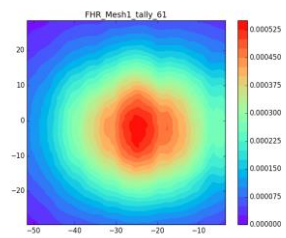
Neutron Field	Neutron Field	Neutron Field
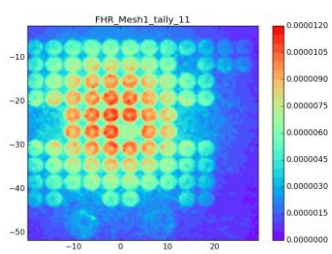	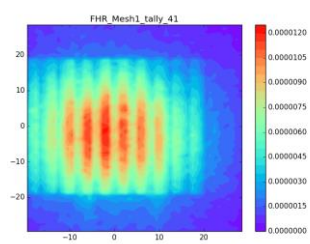	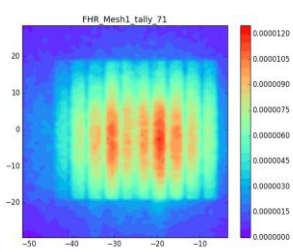
Electron Field	Electron Field	Electron Field
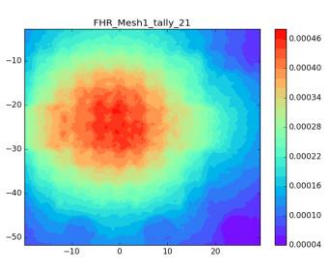	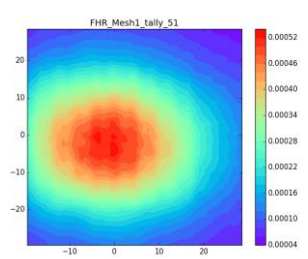	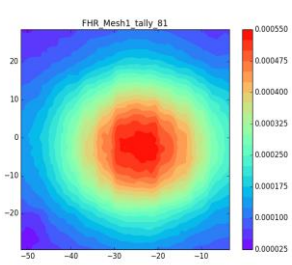
Photon (Gamma) Field	Photon (Gamma) Field	Photon (Gamma) Field

The neutron spectrum averaged over the entire reference TRIGA core configuration is shown in *Figure 6-24*. The fission portion and thermal peak can both be clearly seen. This plot includes neutrons in the fuel, coolant, and all other components.

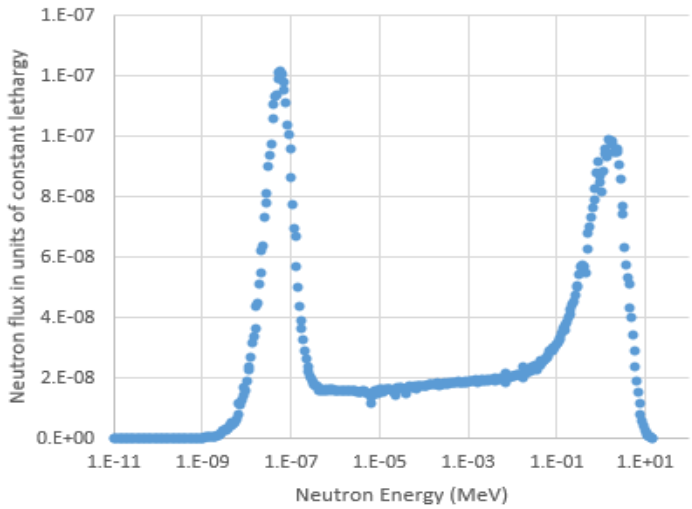

Figure 6-24 Neutron flux per unit lethargy (arbitrary units) averaged over the entire in-core domain of the efference TRIGA core.

Cherenkov radiation is produced primarily by the electrons in the coolant. The main source of these electrons are gamma rays interacting with the coolant. Therefore, an approximate energy spectrum was obtained for the neutron, gamma, and beta fluxes in the coolant within the reactor core domain as described below.

The reactor was modeled in the reference critical configuration, and the energy dependent fluxes were tallied for the sum of multiple coolant regions. The tally encompasses the water around all of the fuel pins from the bottom of the fuel to the top including the sections within the core parallelepiped region that do not contain pins.

Notably, MCNP initially gave fatal errors when tallying this because it is unable to calculate the volumes, so the volume in each 4-pin sized coolant region was manually set to 1. Different amounts of coolant are present in regions that do not have all 4 pins, so this approximation may introduce some error by unequally weighting different coolant regions though it could just cancel out.

The arbitrary vol=1 card caused the flux to be normalized incorrectly, so that the magnitude of the spectrum is shifted. However, the shape of the spectra is accurate and can be seen for neutrons (a), photons (b), and electrons (c) in *Figure 6-25*. The flux in the plots is the total flux of the respective particles with energies within the bin divided by the width of the bin.

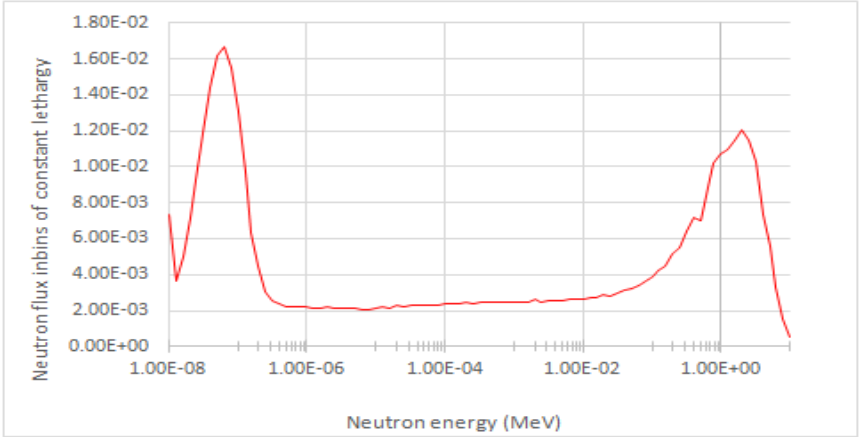

(a) Neutron flux per unit lethargy (arbitrary units) in the coolant

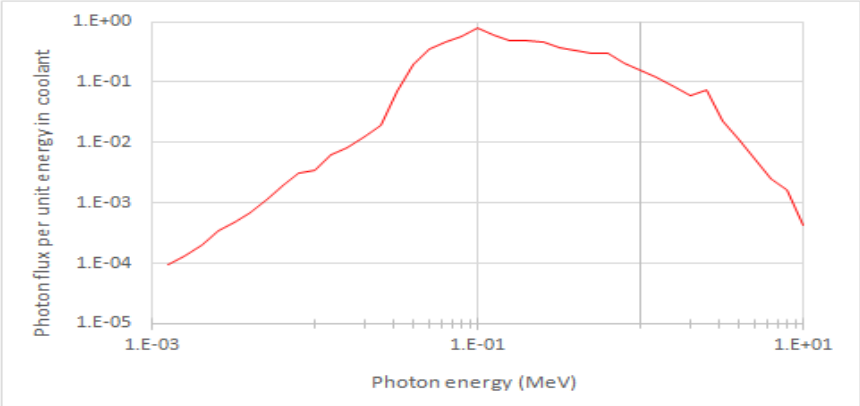

(b) Photon flux per unit energy (arbitrary units) in the coolant

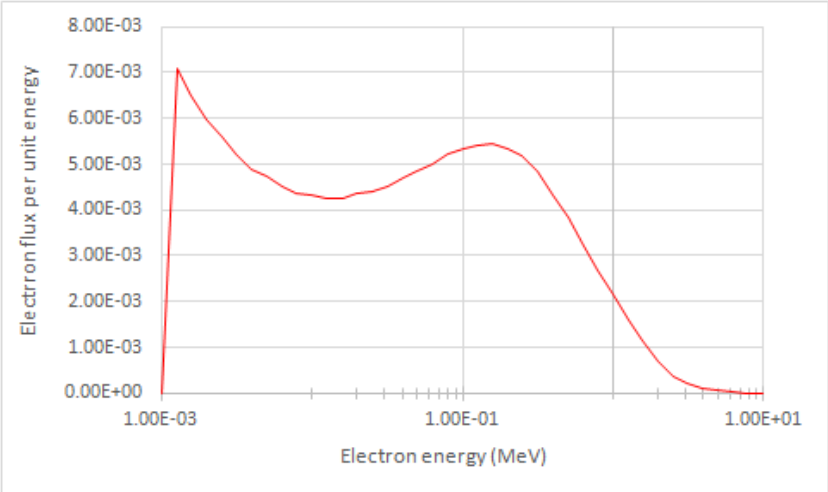

(c) Electron flux per unit energy (arbitrary units) in the coolant

Figure 6-25 Average energy spectra of neutron, gamma, and electrons in the coolant within the reactor core domain of the reference TRIGA configuration.

In *Figure 6-25*, the photon energy spectrum only includes the gamma rays. The Cherenkov photons were not modeled in this run but would produce a much larger peak at far lower energies, in the few eV range. Furthermore, the electron flux energy spectrum drops to zero at 1 keV because the energy cutoff in MCNP is at that energy and all electrons dropping below that energy are killed. This is well below the energy of interest for Cherenkov production with a cutoff energy of ~ 260 keV in water.

Figure 6-26 shows the energy spectrum as it was taken for all photons crossing the Cherenkov tallying plane of 8 cm into the + y direction from the real-world eastern edge of the reference core. The photon flux in the 1.5 eV to 6 eV range is substantially higher than in any other energy bin because this is the region where Cherenkov photons are primarily produced. All energy bins, which are shown in this plot without a flux value included, had no photon counts. The higher energy tail in the 6-15 eV bins is caused by the production of Cherenkov photons by higher energy electrons where the electron energy threshold for photon production increases with decreasing wavelength. The high value at 10-12 eV has an uncertainty of 0.57, so it may not be statistically significant that it is higher than the two points before it.

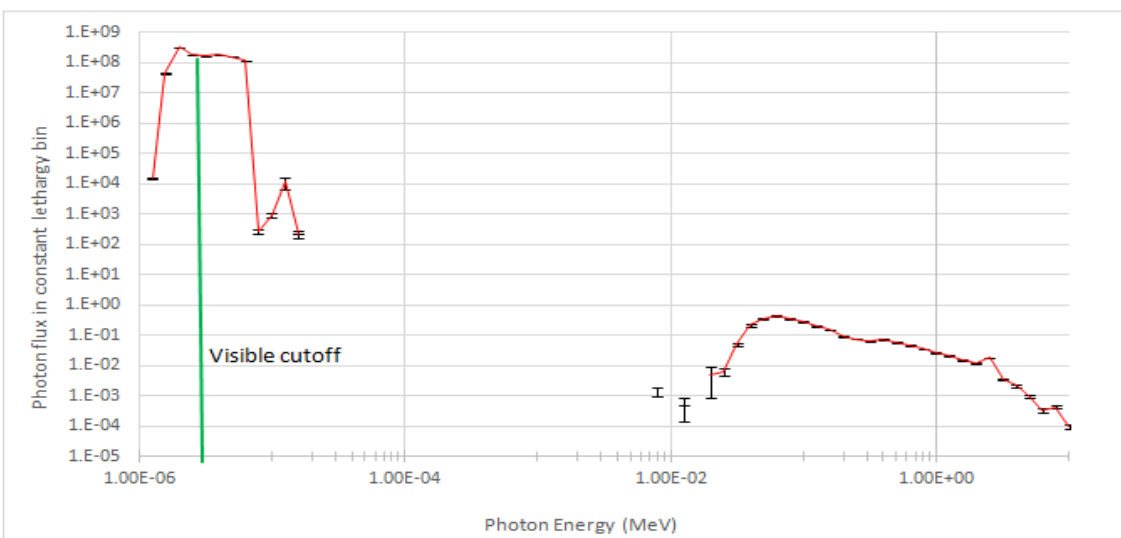

Figure 6-26 Energy spectrum of photons crossing the Cherenkov tallying plane of 8 cm from the face of the reference TRIGA core with directions within a 0.8-cone.

The physically expected curve, as shown in *Figure 6-26*, for the energy spectrum in the 6-15 eV range is monotonically decreasing with increasing photon energy until it reaches zero near the absolute Cherenkov cutoff in water where the index of refraction drops below unity. The green line labeled "Visible cutoff" is at 3.1 eV which corresponds to a wavelength of 400 nm which is the minimum wavelength for visible light. Only the photons with energies below the cutoff line will be visible; photons above or to the right of the red line are in the ultraviolet region.

6.10. Analysis of Select TRIGA Operation Cases for Feature Identification

The TRIGA reactor is modelled in several operational core configurations. The list of considered configuration cases y is as follows:

- Reference (normal) configuration (shims are all at 28.4 cm, regulating rod is at 19.8, transient rod is fully withdrawn at 40 cm).
  - Pin 1, 4 (first row 4th pin) is replaced with water hole.
  - Pin 1, 4 (first row 4th pin) is replaced with borated aluminum absorber material.
- Regulating rod is fully inserted (0 cm) with shims adjusted (32.0 cm) for criticality.
- Regulating rod is fully withdrawn (40 cm) with shims adjusted (26.9 cm) for criticality.
- Transient rod is fully inserted (0 cm), other rods are at their reference (normal) positions (28.4 cm and 19.8 cm). Subcritical.
  - Transient rod is ¾ withdrawn (30 cm), other rods are at their reference (normal) positions (subcritical).
  - Transient rod is ½ withdrawn (20 cm), other rods are at their reference (normal) positions (subcritical).
  - Transient rod is ¼ withdrawn (10 cm), other rods are at their reference (normal) positions (subcritical).
- Cladding on a peripheral pin (1,4) is removed.
- Cladding on peripheral pin (1,4) is coated with boron layer.
- Cladding on central pin (7,6) is coated with boron layer.
- Regulating rod is ¼ withdrawn (10 cm), shims are adjusted (30.5 cm) for criticality.
- Regulating rod is ¾ withdrawn (30 cm), shims are adjusted (28.0 cm) for criticality.
- All rods are in their reference (normal) positions, cladding is removed from pins (1,2 through 1,6) and replaced with water.
- Case matching the conducted TRIGA experiment (video 1 state 2), reactor at 520 kW, Regulating Rod is at 70% (28 cm), shims are at 25.2 cm.
- Case matching the conducted TRIGA experiment (video 2 state 2), reactor at 530kW, Regulating Rod is at 30% (12cm), shims are at 26.52 cm.

In the initial version of the TRIGA model, the core was modeled in its reference (normal) critical configuration. Cherenkov production was successfully implemented, and the Cherenkov photon fluxes were computed using the flat faces of small cylindrical cells of water next to the core. An F2 type surface tally for the number of photons crossing the surface of the cylinder facing the core is used to estimate the amount of light that would be detected by a sensor or fiber optic cable leading to a sensor at the location of the cylinder.

The tally surfaces are initially placed at a distance of 4 cm from the +y side of the core. As an example, the energy distribution of the photons crossing these surfaces is shown in *Figure 6-27*. This is the plot of the photon flux at the axial and x-direction core center of 4 cm into the +y direction from the +y face of the core.

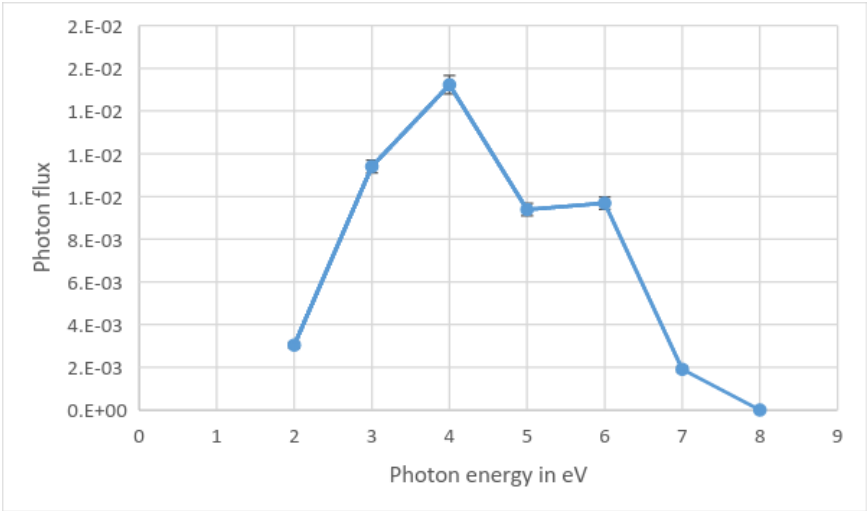

Figure 6-27 Photon flux (arbitrary units) energy spectrum at 4 cm from the center of the +y face of the reference TRIGA core configuration.

The energy bins, as shown in *Figure 6-27*, correspond to 99.38% of the total flux with 0.62% of the total photon flux coming from higher energy photons such as gamma rays. The vast majority of the photons have energies in the visible and ultraviolet range, so the total flux can be closely approximated as the total Cherenkov flux.

The energy of 3.1 eV corresponds to the upper edge of the visible spectrum with a wavelength of 400 nm. Photons above this are ultraviolet, so most of the Cherenkov radiation crossing the plane is actually in the ultraviolet region.

Figure 6-28 shows the photon surface flux tally for the surface closest to the core in each cylindrical tallying region. To better illustrate the relationship between the core geometry and the photon flux, an overlay presentation is created combining the core geometry and the energy spectrum into a single composition illustration. This overlay illustration provides an explicit illustration of the existing relationship between the core geometry features and the photon flux spectrum. Realized computationally, this overlay approach offers a method to analyze and characterize the in-core behavior while providing an opportunity to identify features of interest. The approach also provides a highly visual way of justifying observed spectral characteristics.

For example, there appears to be a spike in the photon flux at the 12 cm position. This could be because it is very close to the bottom of the regulating rod which is represented by the green cylinder in the 2nd row in *Figure 6-28*.

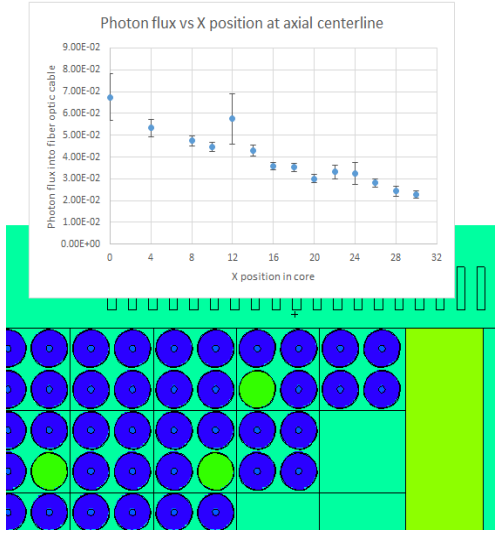

Figure 6-28 Photon flux vs x-position at the core's axial centerline level as an overlay presentation illustrating the core geometry relation.

The open water gap below the regulating rod could be producing more Cherenkov photons to add to the tally than other spaces with fuel pins in them. Other than that, this feature, *Figure 6-28* seems to follow what would be expected for the power profile in a reactor core with the peak in the center and a minimum near the edge. The data collected from the a second run for the photon flux as a function of the x position at 10 cm above the axial centerline can be seen in *Figure 6-29*.

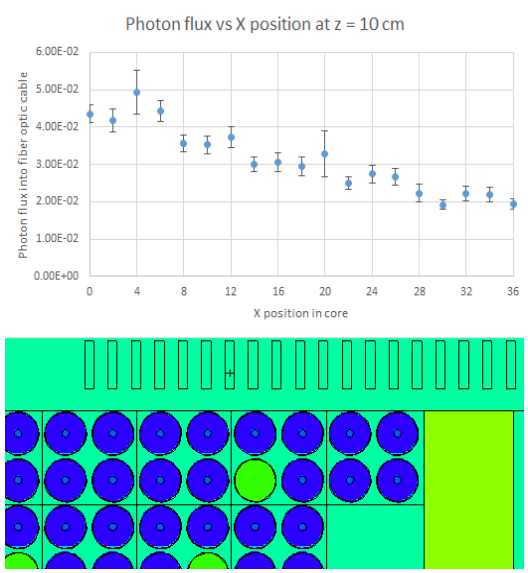

Figure 6-29 Photon at 10 cm above core centerline level as an overlay presentation illustrating the core geometry relation.

Plotting the photon flux as a function of the axial distance above the centerline at a location slightly east (in the +y direction) of the edge of the x axis center of the core yields the spectrum plot shown in *Figure 6-30*. The transition from fuel to graphite occurs at a z position of 19.1 cm.

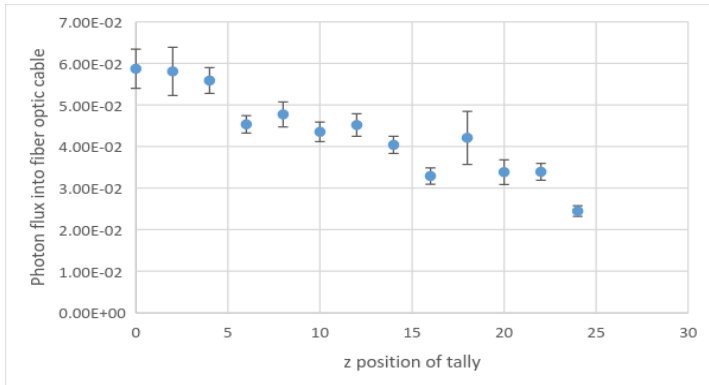

Figure 6-30 Photon flux at axial positions above the centerline facing the +y side.

The corresponding higher fidelity results are shown in Figure 6-31. The variances are much lower due to a larger number of particles run.

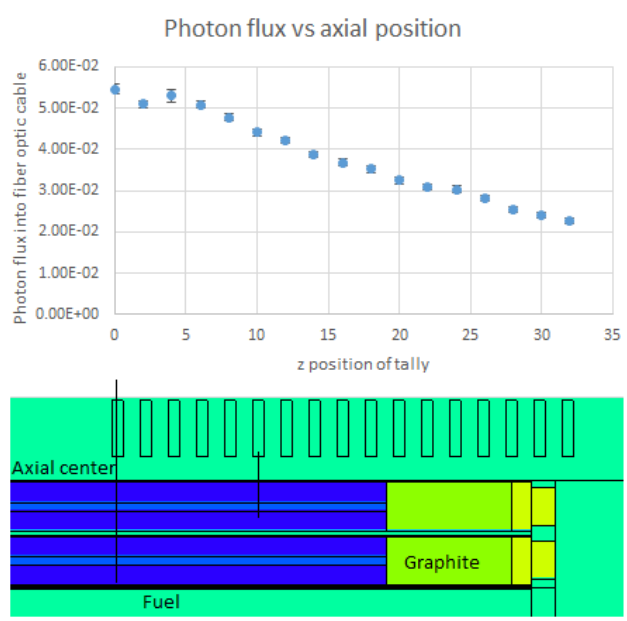

Figure 6-31 High fidelity photon flux at axial positions above the centerline facing the +y side.

It can be concluded that the data sets for the photon fluxes do seem to follow a general trend of decreasing towards the edges of the core. This is to be expected. The fluxes tallied at positions well beyond the end of the fueled region are approximately half the tallied

photon flux at the center of the core. It was expected that the photon fluxes into the simulated fiberoptics probes would be much lower at positions where the probes are looking at graphite or water beyond the active fueled regions. Some phenomenon in either the physics or the tallying method is causing an unexpectedly large degree of blurring of the "image" of the core power levels that the Cherenkov detection system should be producing.

In an attempt to improve the spatial sensitivity of the modeling approach, the tallies in MCNP were altered using a *c0 cosine* card to only tally photons crossing the surfaces with an angle that is within a cone with mu = 0.9 which corresponds to about 25 degrees of the +y direction. This should only tally photons coming from a small cone in front of each surface thus providing a better representation of what is occurring spatially by decreasing the effect of events happening elsewhere on the photon flux tallies.

Additionally, the number of tallies was increased to capture data from the entire width of the core in the x direction as opposed to one half of the core which had been done previously. A set of surfaces arranged along the axial centerline of the core 4 cm in the +y direction of the core face is placed with one tally surface every 2 cm along the x axis ranging from an x position of -36 cm to +36 cm. This configuration is used to test the sensitivity of the new photon tallies to changes in the reactor state by running more models with various alterations made to the configuration. The configuration of the applied tallies can be seen in the right side of *Figure 6-32*, with a closeup of the effective view field on the left. This alteration does seem to provide improved analysis capabilities to assess spatial features. A similar approach is taken in the later Cherenkov mesh models by placing the tallying plane 8 cm away and using 2 cm radius circles with 36.9-degree cone.

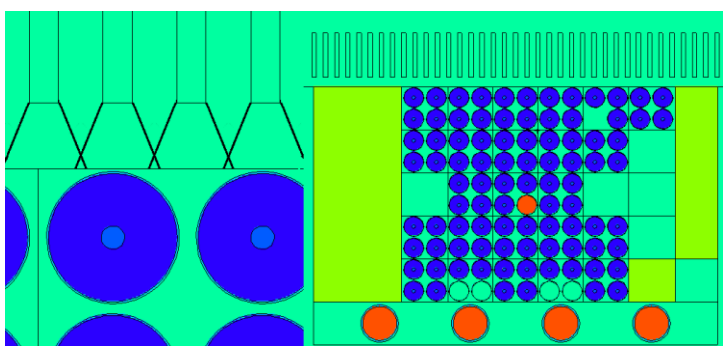

Figure 6-32 Reactor core cross section with tallying surfaces explicitly displayed (right) with a closeup of the effective view field (left).

The system's ability to detect fairly drastic changes in the core is tested by modeling the reactor with a complete alteration of one of its pins. For this comparison, the reactor was modeled once with no alterations, once with the 4th pin in the first row (pin 1,4) completely replaced with water, and a third time with the pin replaced with a borated aluminum material, referred to as Boral.

This pin was chosen because it is against the external face of the reactor to magnify the effect on the tallies, and the 4th column was chosen because this is where one row of the safety shim control rods are. This would result in a somewhat similar perturbation of a control shim rod further into the reactor.

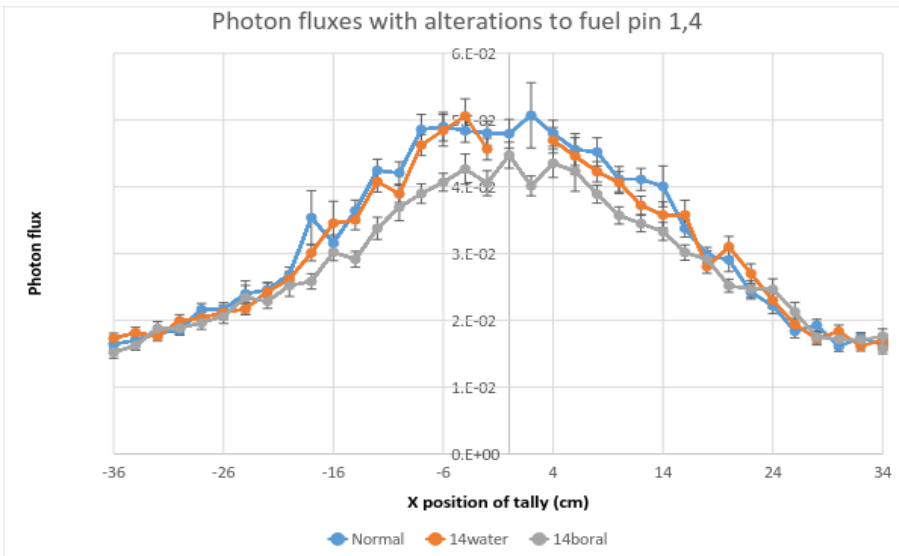

Figure 6-33 Photon fluxes with the composition of the pin 1,4 altered.

The model was run for each case with electron and Cherenkov photon production to produce photon flux estimates at the same locations. Plots of the data from these comparisons can be seen in *Figure 6-33*. The uncertainties are quite large, and at many points, the differences between the altered reactors are smaller than the one sigma error bars. Note that the location of pin 1, 4 is at the edge of the reactor approximately 2 cm away from the tally surface and at an x location of -6. The most immediate changes in the flux should be around -6 on the charts.

Replacing the pin with an absorber causes a large decrease in both the neutron population and fluxes in the vicinity of the pin. Removing the fuel pin and filling the space with water seems to have a much smaller effect on the fluxes, and due to uncertainties, it cannot be determined if this actually increases or decreases the photon flux at the location of the simulated fiber optic cable's lens. It is suspected that this would create a small increase in the Cherenkov flux right in front of the pin due to the increase in the amount of water present to produce Cherenkov photons.

To advance the project towards the possibility of relating the model to an experiment, comparisons between realistic configurations of the reactor core are performed. Neutron-only criticality models are run to determine what positions the 4 safety shims need to be in for the reactor to be critical with the regulating rod both fully inserted and fully removed.

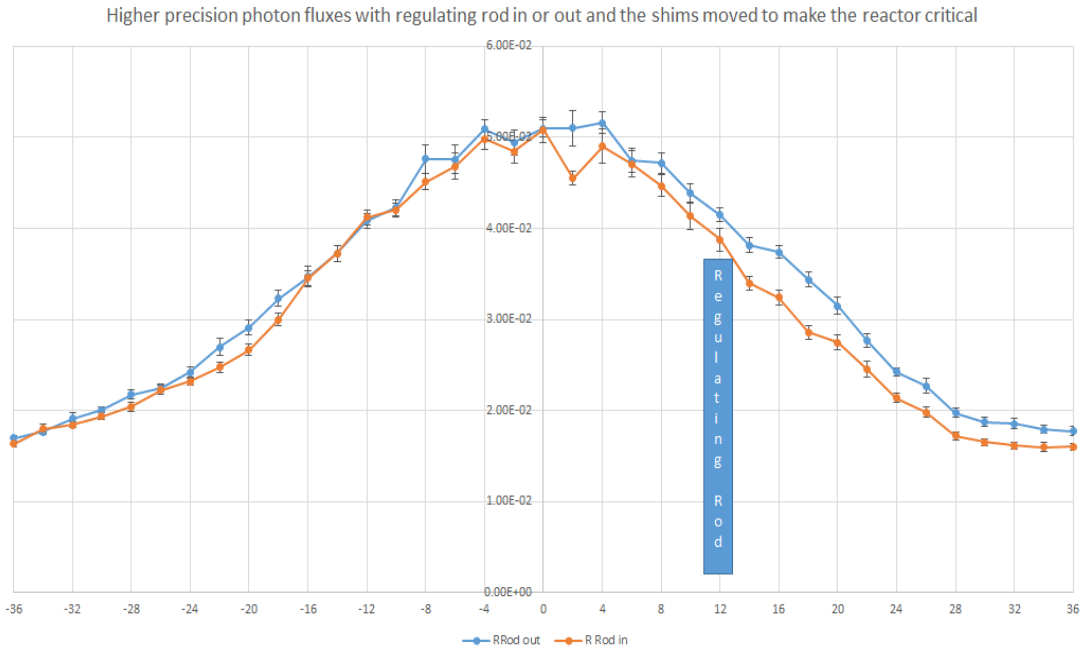

Figure 6-34 Photon fluxes vs x for two critical configurations of the core with the regulating rod fully inserted and removed.

Two much longer MCNP runs were performed with photon production to determine the fluxes more precisely. One run had the regulating rod fully inserted and the shims adjusted to maintain criticality, and the other had the regulating rod fully removed and the shims inserted slightly further to maintain a critical configuration. The results of these models can be seen in *Figure 6-34*, *Figure 6-35*, and *Figure 6-36*.

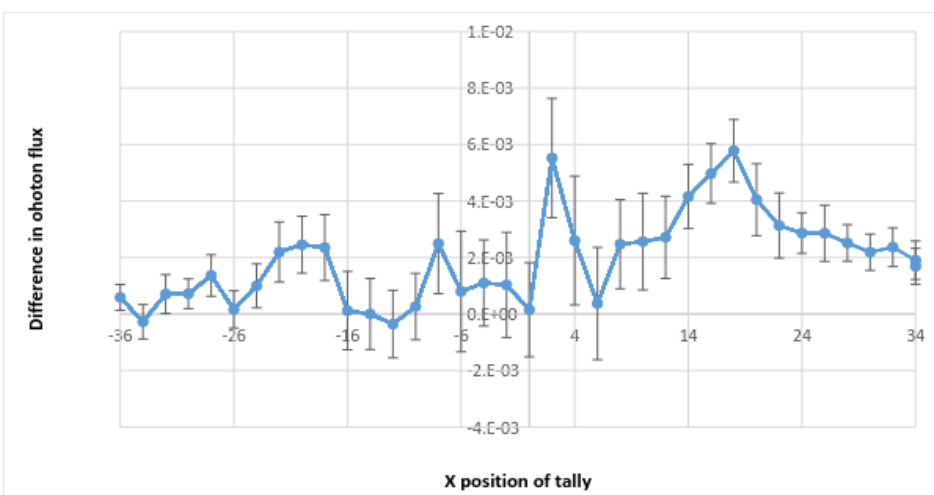

Figure 6-35 Difference in the photon fluxes for a critical system with the regulating rod fully removed and inserted.

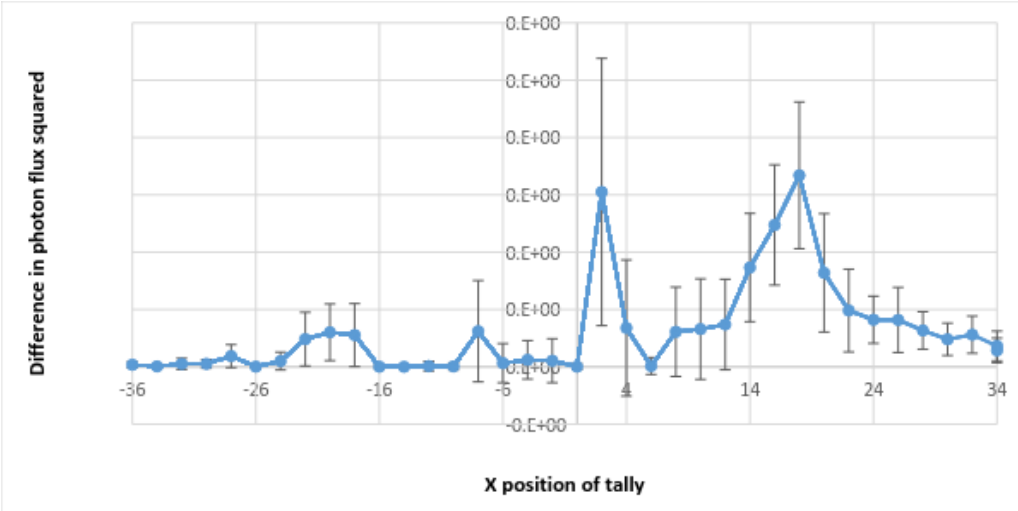

Figure 6-36 Square of the difference in the measured photon fluxes with the regulating rod fully removed and inserted.

The regulating rod is at an x position of +12 and is in the 2nd row of pins. There is clearly a change in the photon flux on the right side of the reactor when the regulating rod is inserted or removed. It is expected that the removal/insertion of the regulating rod would cause a power tilt in the reactor, and the simulated Cherenkov photon detectors show a distinct depression in the photon flux and thus fission rates in the +x, +y corner of the reactor. While the changes produced by this alteration are detectable in the photon tallies, the difference is relatively small.

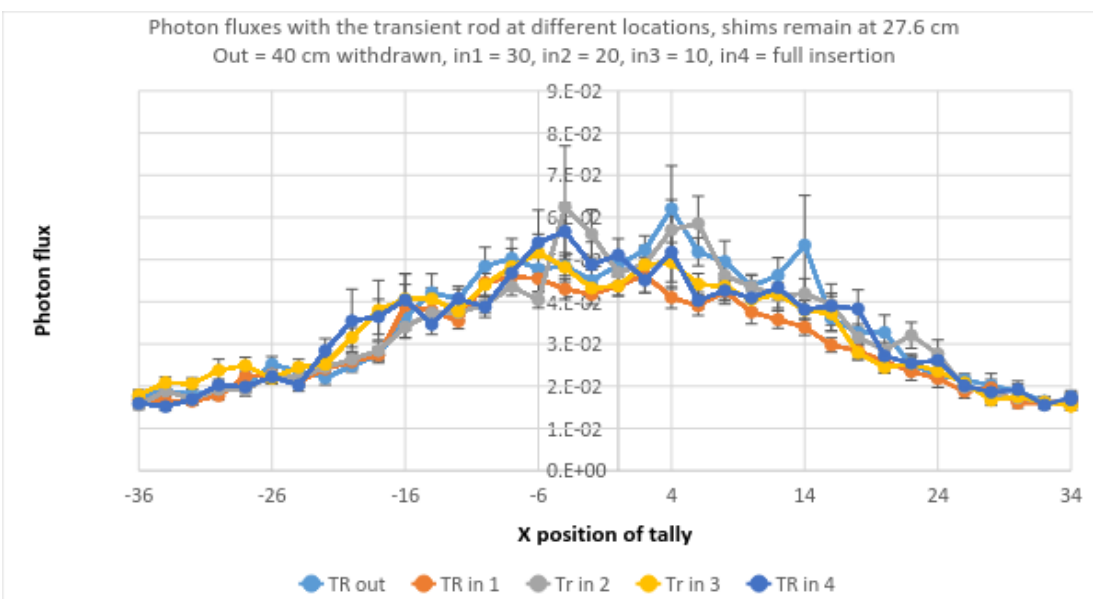

Figure 6-37 Photon fluxes with alterations to the degree of transient rod insertion.

For other alterations further from the edge of the core, the differences may be even smaller thus increasing the required sensitivity to effectively resolve them. The single row of photon detectors can distinguish between a critical reactor with the regulating rod inserted and with it removed.

The regulating rod perturbation approach is also performed again in later versions of the model and is used in the TRIGA experiment. Changes were made to the location of the central transient control rod, with other reactor parameters remaining constant. The safety shims remained at 27.6 cm which corresponds to a critical configuration with the transient rod removed. The runs with an inserted transient rod are subcritical, but the model is still held at the same total particle production rate. The neutron and photon fluxes near the +y face of the reactor are shown in *Figure 6-37* and *Figure 6-38*.

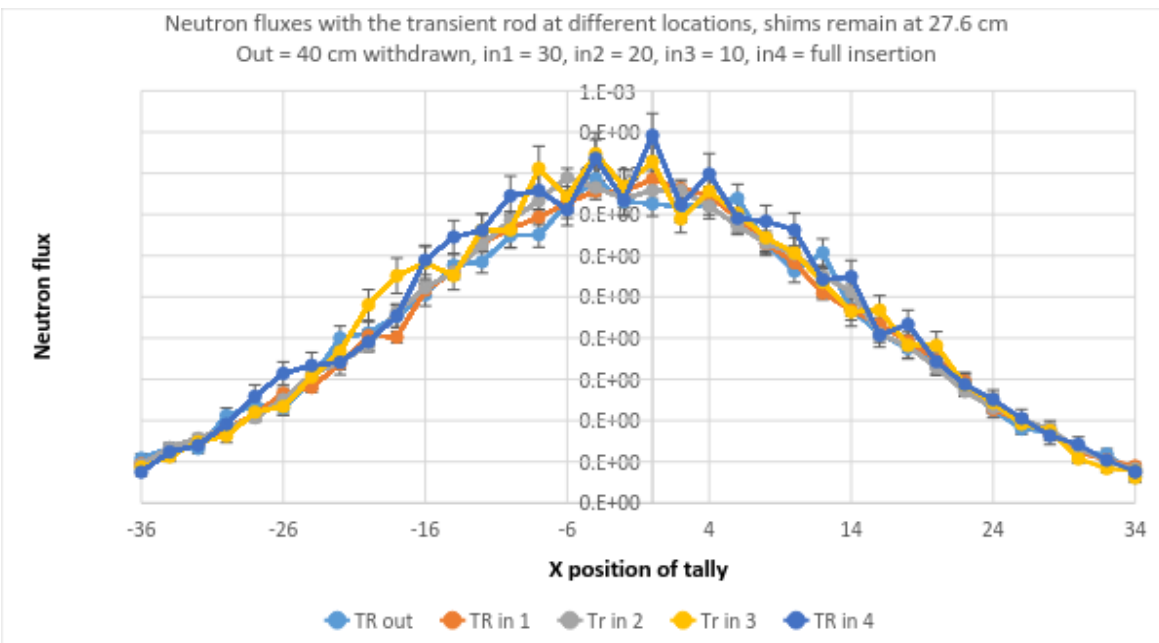

Figure 6-38 Neutron fluxes with alterations to the degree of transient rod insertion.

A more direct comparison of the results for the extreme cases where the transient rod is fully withdrawn which corresponds to a normal critical configuration and where the transient rod is fully inserted can be seen in the plots in *Figure 6-39* and *Figure 6-40*. They show the difference in the photon and neutron fluxes for these two extreme cases.

The ability to confidently resolve these differences in the system with the external tally data is limited. The large sizes of the uncertainties relative to the differences in the fluxes hinders the distinction between physical perturbation results and the Monte Carlo statistical noise.

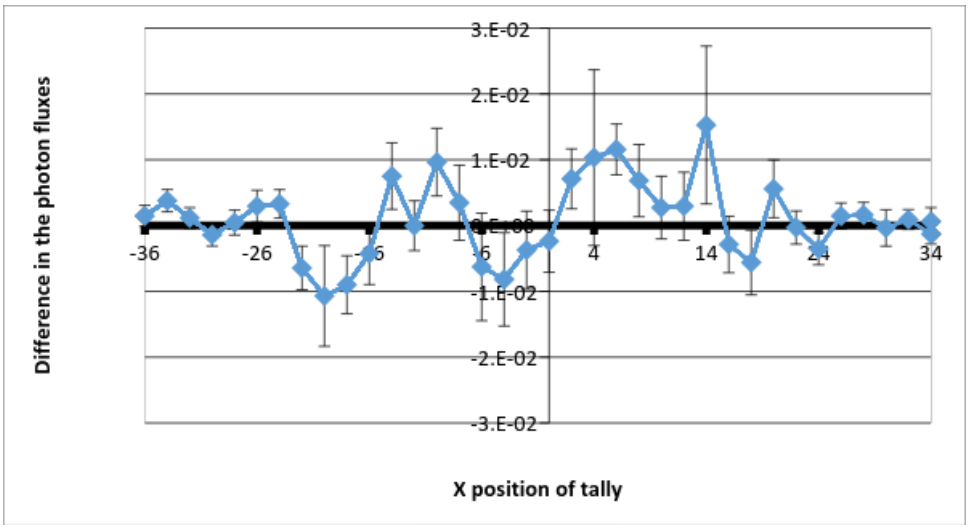

Figure 6-39 Difference in the photon fluxes with the transient rod removed and fully inserted.

The discussed metrics led to the use of mesh plots in the analysis of differences within the in-core domain. The sets of 2D meshes for neutrons, gammas, and electrons averaged over one dimension of the core are produced in accordance with the already introduced characterization approach.

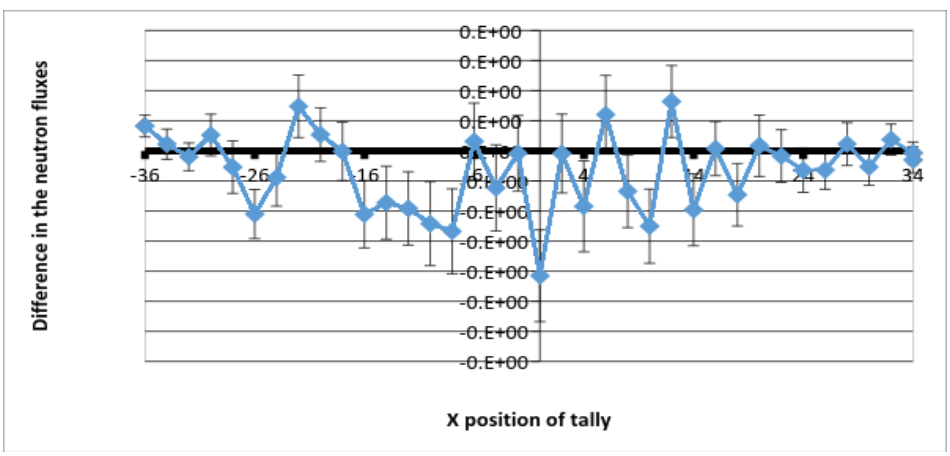

Figure 6-40 Difference in the neutron fluxes with the transient rod removed and fully inserted.

For estimating the Cherenkov radiation, two methods are used. In the runs with more particles and no Cherenkov production, an XZ mesh tally for electrons is created for the volume of water between the east face of the core and the plane 8 cm away where the Cherenkov radiation is normally tallied. In the runs with Cherenkov radiation modelled directly, there are segment tally type meshes for the Cherenkov flux crossing the plane at 8 cm to the East of the core. Both of these XZ meshes have 4 cm between mesh points in the x and z directions. A python script was developed to pull data out of the MCTAL files that MCNP produces, manipulate it, and then plot it. This allows for difference tallies to be

plotted. Plots for the neutron, gamma, and electron fluxes for an XY plane averaged over the entire Z dimensional height of the core can be seen in *Figure 6-41*, *Figure 6-42*, and *Figure 6-43* for the reactor in the normal critical state and in a subcritical state with the transient rod fully inserted.

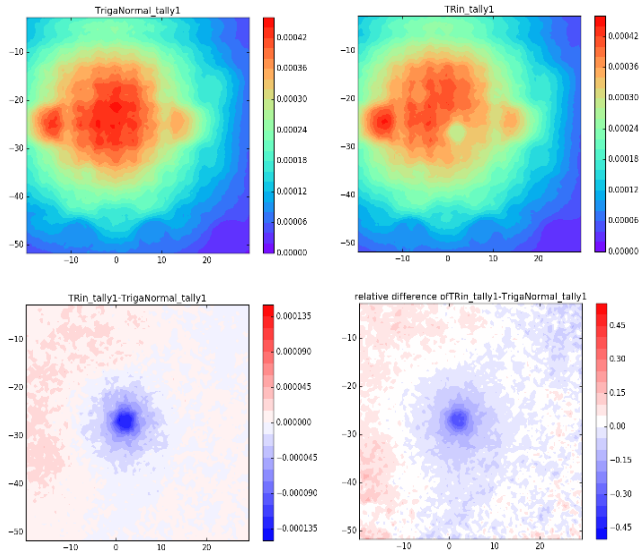

Figure 6-41 XY plane neutron mesh tally results with the reactor in the reference state (top left), with the transient rod inserted (top right), the absolute difference of the perturbed case minus the reference case (bottom left) and the relative difference divided by the value of the reference case at each mesh point (bottom right).

The calculated values of k_{eff} for these two runs are 1.0056 for the normal reactor state and 0.9886 with the transient rod inserted. The normal state is slightly supercritical in this model because fuel burnup inhomogeneity is not accounted for.

The XY plane is a 100x100 mesh with mesh points spaced 0.5 cm apart. These plots show fluxes and behavior of the entire core which can help to understand what is happening but may not be readily measurable in a real system. In *Figure 6-41*, the effect of inserting the transient rod on the neutron population is evident. The transient rod creates a large depression in the neutron flux.

The slight increase in the flux near the edges of the reactor is caused by the normalization because MCNP normalizes the flux per source particle regardless of what k_{eff} is. A similar, though less localized, effect can be seen in *Figure 6-42* for the gamma fluxes with a depression in regions near the transient rod decreasing in magnitude as one looks further away.

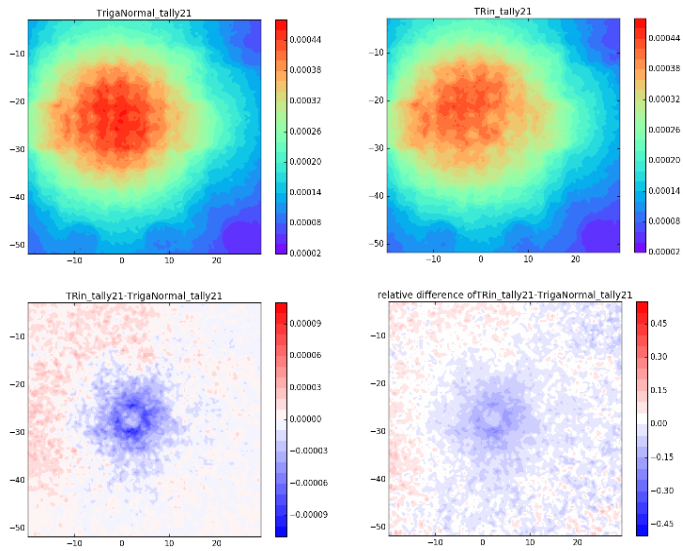

Figure 6-42 XY plane gamma mesh tally results with the reactor in the reference state (top left), with the transient rod inserted (top right), the absolute difference of the perturbed case minus the reference case (bottom left) and the relative difference divided by the value of the reference case at each mesh point (bottom right).

The electron map in *Figure 6-43* also shows a large absolute flux change near the inserted transient rod though the relative flux plot emphasizes the noise in the lower flux regions near the periphery. Bin uncertainty values are much larger in the electron mesh tally with most in the range of 10 to 30%.

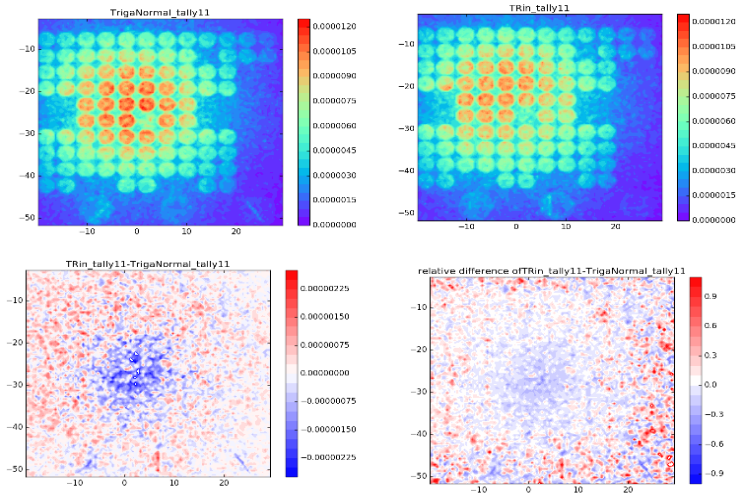

Figure 6-43 XY plane electron mesh tally results with the reactor in the reference state (top left), with the transient rod inserted (top right), the absolute difference of the perturbed case minus the reference case (bottom left) and the relative difference divided by the value of the reference case at each mesh point (bottom right).

In an attempt to more closely correlate the gamma and electron fluxes to the Cherenkov fluxes, a much coarser mesh with mesh points spaced 4 cm apart was produced to tally the fluxes in the region of water just east of the core (in the +y direction).

This XZ mesh has a 4 cm spacing for the mesh points and a thickness of 8 cm which captures the fluxes in the water next to the edge of the core.

Two mesh runs were performed: first, a run with the reactor in its base critical configuration and second, a run with the regulating rod fully inserted and the safety shims slightly removed to maintain approximate criticality.

The critical rod positions were obtained by running multiple cases with neutrons only and perturbing the safety shims until the k_{eff} value for the run closely matches the value of 1.007 ± 0.0005 that is obtained with the reactor in the normal, critical configuration.

The critical configuration is slightly supercritical because the fuel depletion is homogenized. It is being assumed that the homogenization adds a fixed 0.007 worth of reactivity regardless of the control rod positions which does introduce a source of error.

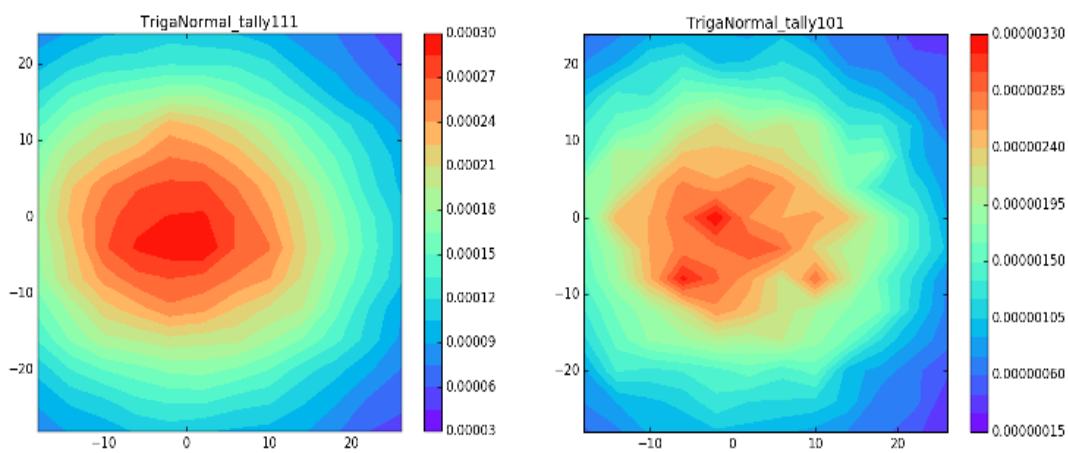

Figure 6-44 Gamma (left) and electron (right) fluxes in an XZ mesh east of the core.

A plot of the gamma and electron fluxes in the water east of the core with the reactor in the base configuration is shown in *Figure 6-44*. A plot showing just the electron flux in both the base state and with the regulating rod inserted with the absolute and relative differences at each point is shown in *Figure 6-45*.

The insertion of the regulating rod position causes a clear decrease in the electron flux in the water near the regulating rod's position with some mesh points seeing decreases of 30%.

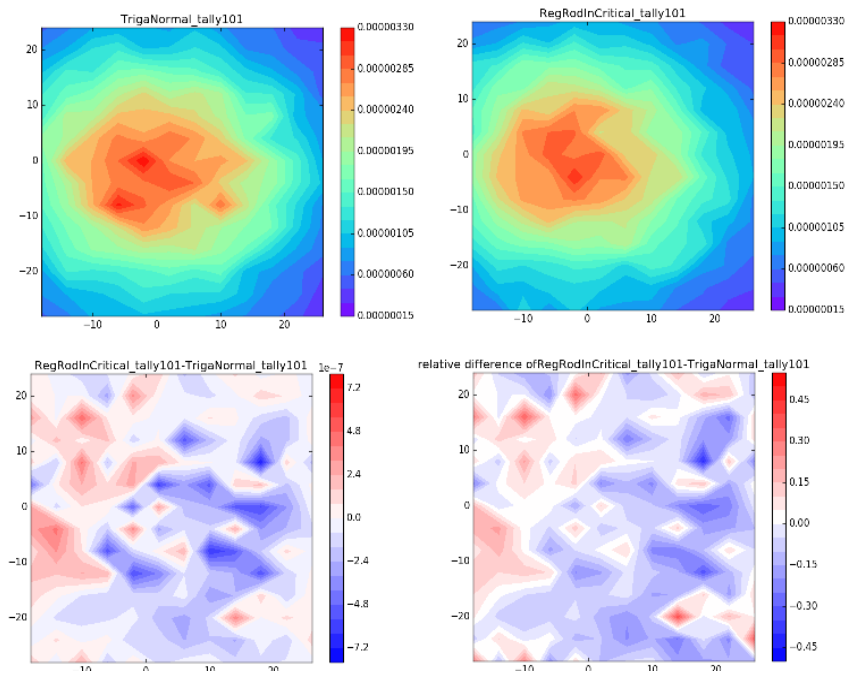

Figure 6-45 XZ plane electron mesh tally results with the reactor in the reference state (top left), with the regulating rod fully inserted and shims adjusted to maintain a critical configuration (top right), the absolute difference of the perturbed case minus the reference case (bottom left) and the relative difference (bottom right).

In addition to this electron and gamma mesh, another set of runs were performed with Cherenkov production turned on and a pseudo mesh is tallied of photons crossing the y=2 plane approximately 8 cm east of the core. The Cherenkov tally is performed by using a segment tally of photons crossing the surface binning those crossing through 2 cm radius circles spaced 4 cm apart to form a mesh of the fluxes at the center points of the circles.

Additionally, the photon flux is binned by energy, and only the photons with energies below 50 eV are counted as Cherenkov photons. The angle of incidence onto the surface is accounted for such that only photons with an angle of incidence where the cosine of the angle is greater than 0.8 are counted.

This rejects photons with an angle greater than 36.9 degrees away from direct incidence on the surface to simulate a field of view for each photon collection point and to more strongly correlate the flux at a mesh point to what is happening in front of that mesh point. This is done to measure the same change as the one seen in *Figure 6-45* by explicitly modeling the Cherenkov radiation production and transport.

Figure 6-46 is qualitatively similar to *Figure 6-45* which is to be expected as the Cherenkov photons crossing the plane 8 cm from the core are primarily produced by the electrons in the region between the core and the tallying plane.

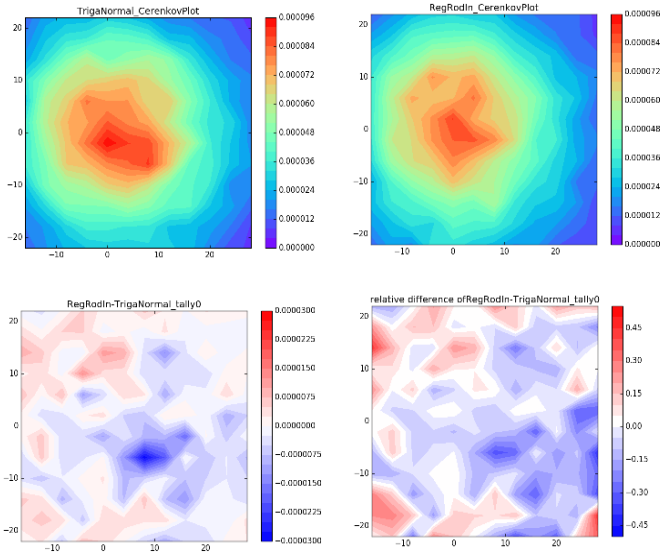

Figure 6-46 Cherenkov radiation 8 cm east of the core for the reference case (top left) the critical case with the regulating rod fully in (top right) the absolute difference in the flux (bottom left) and the relative difference in the flux when compared to the reference case (bottom right).

The cladding of a peripheral pin, specifically pin 1, 4, was removed to analyze the effects on the fluxes. An XZ plot of the neutron flux is shown in *Figure 6-47*.

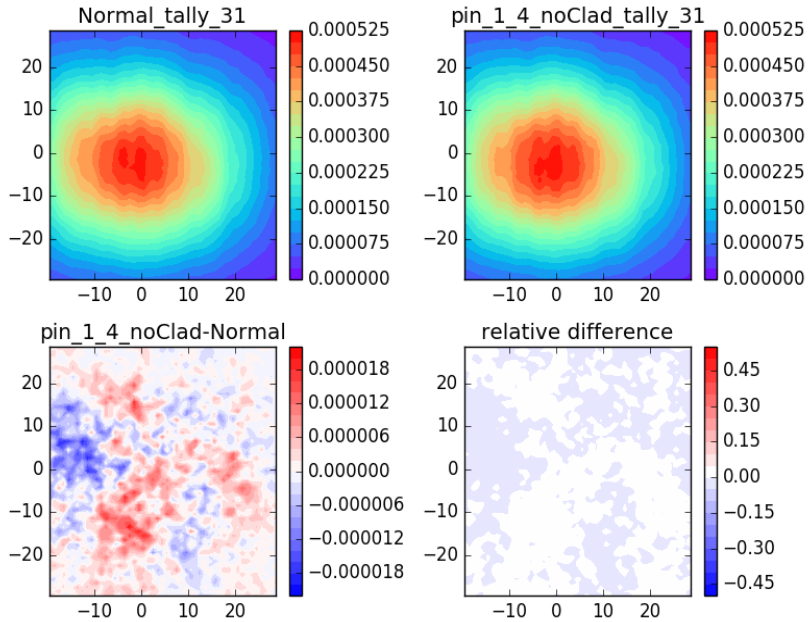

Figure 6-47 XZ plot of the neutron flux with the cladding of a peripheral pin removed compared to the reference (normal) reactor state.

The corresponding XY plots of the neutron, electron, and gamma fluxes are shown in *Figure 6-48*, *Figure 6-49*, and *Figure 6-50*, respectively.

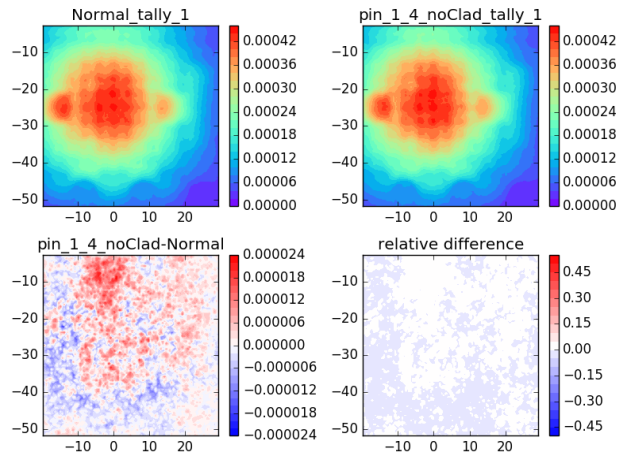

Figure 6-48 XY plot of the neutron flux with the cladding of a peripheral pin removed compared to the reference (normal) reactor state.

There is a little real discernible difference in the flux plots. Any expected difference would be near the top and at about -4 cm on the X axis where the pin had its cladding removed. The fluxes in the model are not very sensitive to the removal of cladding beyond the possible small increase in the neutron flux in that region due to decreased parasitic absorption.

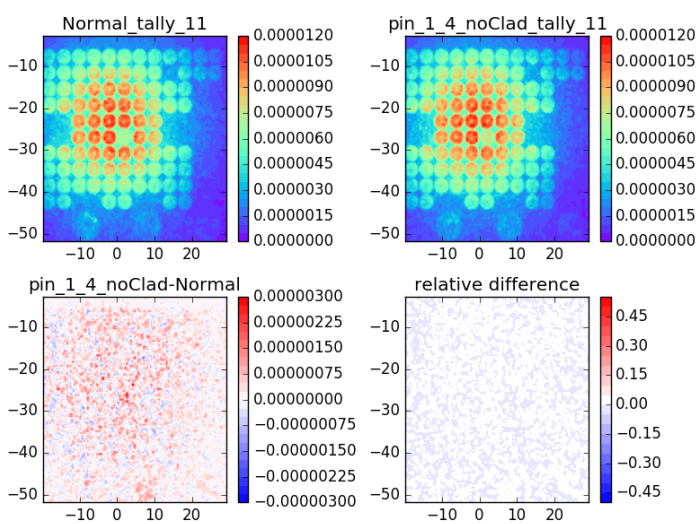

Figure 6-49 XY plot of the electron flux with the cladding of a peripheral pin removed compared to the reference (normal) reactor state.

However, removing the cladding from a pin creates no noticeable difference in the neutron, gamma, or electron fluxes. It is therefore assumed that no noticeable Cherenkov production difference would be produced by removing cladding from a single pin.

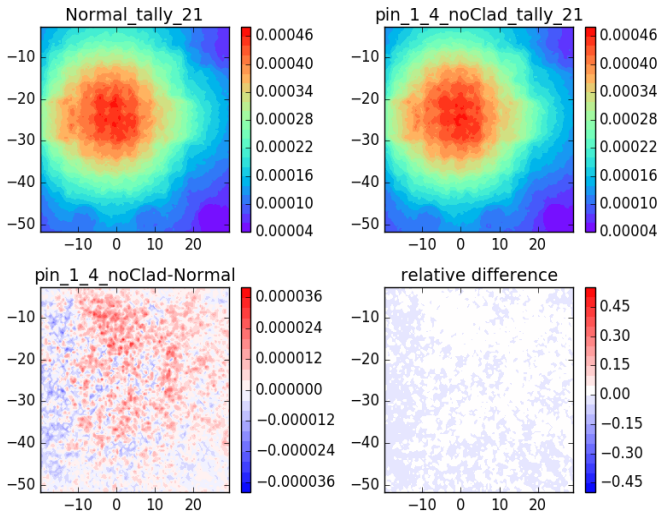

Figure 6-50 XY plot of the gamma flux with the cladding of a peripheral pin removed compared to the reference (normal) reactor state.

Thus, using Cherenkov-radiation-based in-core signatures to analyze and characterize responses due to cladding-level localized phenomena requires ultra-high resolution optical (visual) sensing capabilities allowing detection of very small-scale variations in optical characteristics. The attained resolution of the MCNP emulations of such capabilities has not been sufficient to identify selected representative changes in a sample pin at the localized cladding level.

Higher fidelity simulations or conducting actual experiments to explore sensitivity needs for sensing instruments are needed. The detectability is also evidently a function of location within the in-core domain.

Because removing cladding created little to no noticeable difference, another alteration to simulate an absorber being plated on a pin was performed. The same peripheral pin at 1,4 has the outer 1/10th of its cladding thickness replaced with B_4C at the density of the cladding (8 g/cc).

This is a fairly significant amount of absorber though still far less than an actual control rod. The B_4C was replacing the outer 1/10th of the cladding instead of plating on the outside to avoid issues with surface definitions and cell overlap. The XY plots of the neutron and electron fluxes are shown in *Figure 6-51* and *Figure 6-52*.

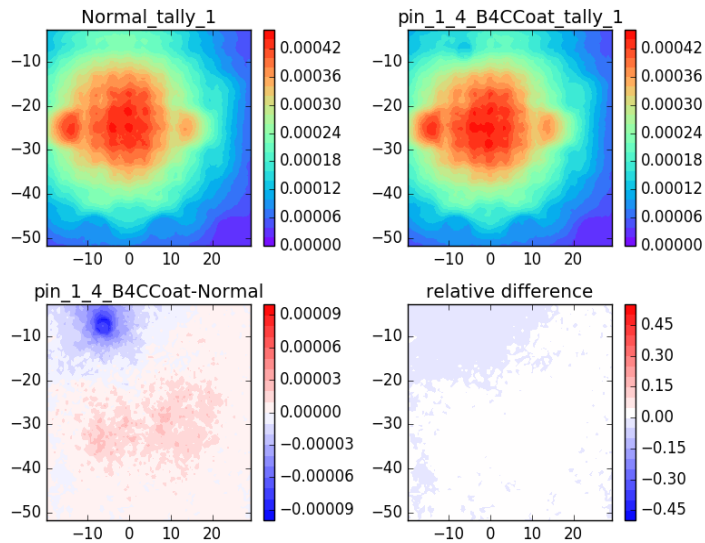

Figure 6-51 XY plot of the neutron flux with 1/10 of the cladding of a peripheral pin as B_4C compared to the reference (normal) state.

Clearly according to *Figure 6-51*, there is a very noticeable depression in the neutron flux at the pin with boron buildup on the cladding. The electron flux is also significantly lower in this region. Additionally, the neutron and electron fluxes are both slightly higher in the opposite side of the core due to the shifting of the flux profile and the constraint that the total neutron population remains the same.

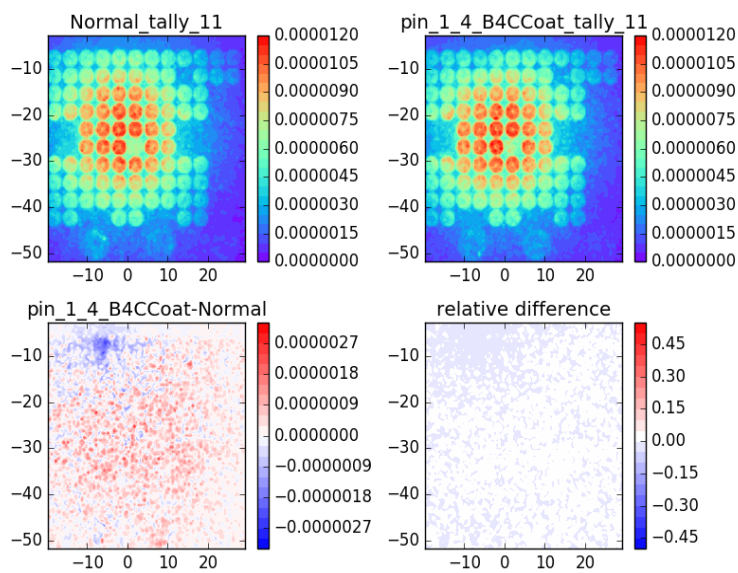

Figure 6-52 XY plot of the electron flux with 1/10 of the cladding of a peripheral pin as B_4C compared to the reference (normal) state.

In another case, a more central pin at 7, 6 had the boron coating placed on the cladding. The XY neutron and electron flux plots are shown in *Figure 6-53* and *Figure 6-54*.

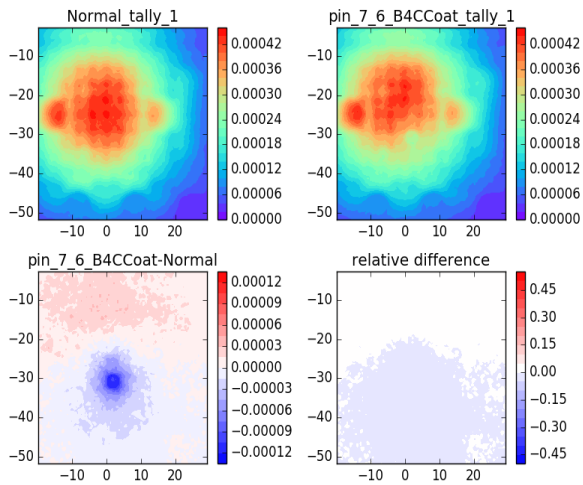

Figure 6-53 XY plot of the neutron flux with 1/10 of the cladding of a central pin as B_4C compared to the reference (normal) state.

The depression in the flux at the perturbed pin is noticeable in *Figure 6-53*, even without looking at the difference plots. The electron flux also shows a decrease near the boron coated pin. Both fluxes are slightly higher in the opposite side of the reactor due to the nature of MCNP's *kcode* simulations and the way it causes the flux to be shifted such that the same total number of particles is run.

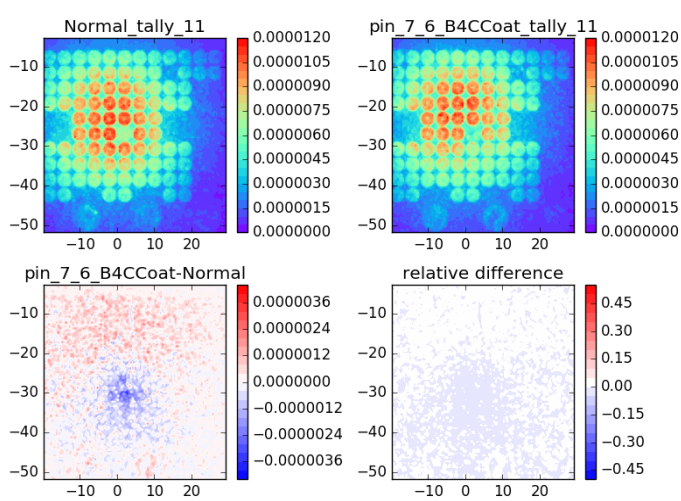

Figure 6-54 XY plot of the electron flux with 1/10 of the cladding of a central pin as B4C compared to the reference (normal) state.

Due to the large uncertainties present in the fluxes at many mesh points, it was decided to attempt to quantify the certainty with which the differences can be observed in the simulation. MCNP gives tally outputs with a tally value and an uncertainty relative to the value which ranges from 0 to 1. The flux tally output is an average of many random, independent particle histories so it can be approximated as a Gaussian with its mean at the tally value and a sigma of the value multiplied by the percent uncertainty. The comparison between the fluxes at the same mesh point for two reactor configurations is therefore a comparison between two Gaussians. As the goal is to determine the certainty of the difference with large uncertainties, another metric was needed. For two distributions, a combined uncertainty can be approximated by taking the square root of the sum of the squares of the distributions' uncertainties. Then, dividing the difference in the means by the combined uncertainty.

The deviations or sigmas of difference method is used in the comparison of the runs with the regulating rod at 10 cm (1/4) withdrawal and 30 cm (3/4) withdrawal. The Cherenkov flux and difference plots are shown in *Figure 6-55*.

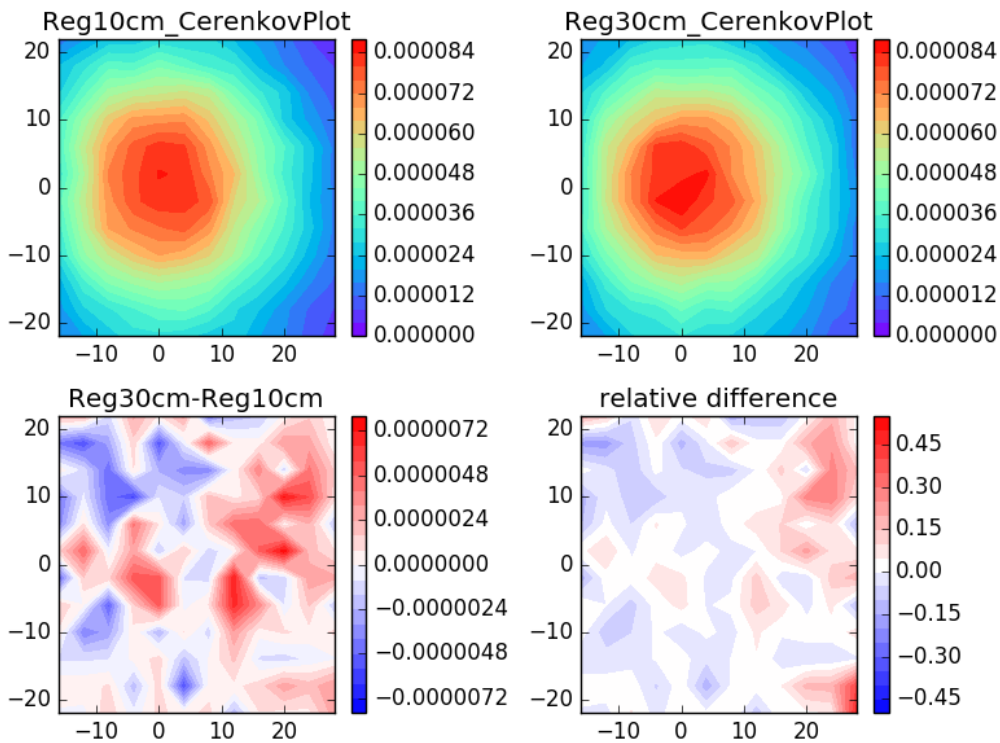

Figure 6-55 Comparison of the Cherenkov flux with the regulating rod at 10 cm (top left) and 30 cm (top right).

The number of deviations worth of difference at each point is shown in *Figure 6-56*. At two of the mesh points near the middle right and top right, there is a 3.5 sigma difference in the means of the distributions which should correspond to a 99.95% confidence that there is a detectable difference in the two fluxes at those locations. This metric attempts to isolate

changes that are statistically significant from those that are the result of high uncertainties in specific bins due to noise.

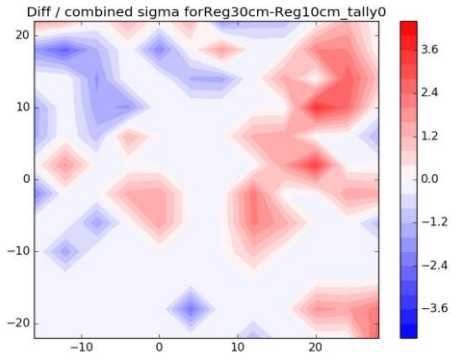

Figure 6-56 Number of combined sigmas of difference between the cases with the regulating rod at 10 and 30 cm.

Another comparison of the reactor states with the regulating rod fully withdrawn and fully inserted is shown in *Figure 6-57*; note the random spike in the flux at the top right that exceeds the plot scale, causing it to be whited out, and the corresponding high point in both difference plots. In the top right plot of the Cherenkov flux with the regulating rod withdrawn, there is a very large spike in the flux at the (x,z) point (0,-4). This spike causes the area to appear white in the flux plot as the value at this mesh point is outside of the range being plotted. This is likely a random artifact of the weight window biasing where a single history caused a very large number of hits in that bin or something similar. This also causes the uncertainty in that bin to be very large.

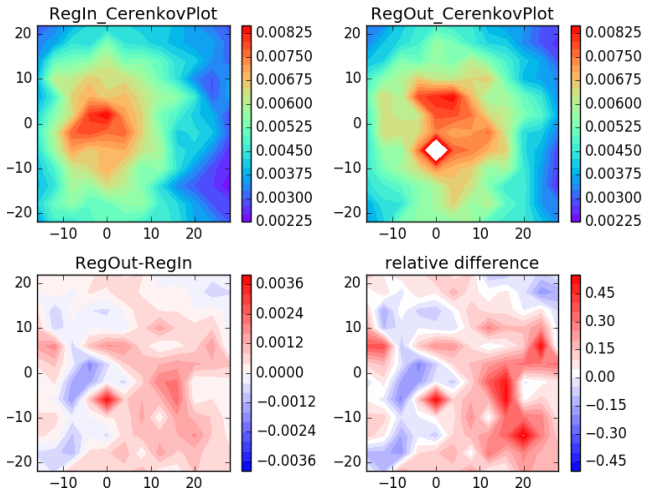

Figure 6-57 Comparison of the Cherenkov flux with the regulating rod at fully inserted (top left) and fully withdrawn (top right).

Fortunately, the difference over sigma plot, as shown in *Figure 6-58*, effectively filters out the erroneously large, high uncertainty point in *Figure 6-57*. The erroneous spike in the previous plots is very small here, due to its large uncertainty. This is good because the point is clearly not supposed to have such a high flux or a large difference between the two reactor configurations as none of the other runs have shown a similar spike. This particular comparison of data sets shows how the sigmas of difference method can filter out some aspects of noise. Future Cherenkov comparisons also include the plot of the numbers of sigmas of difference.

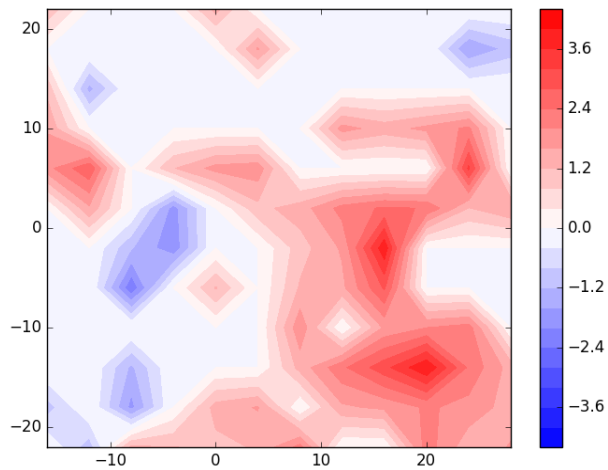

Figure 6-58 Number of sigmas of difference when the regulating rod is fully inserted and fully withdrawn.

6.11. Fiberoptics Probe Tests

The objective of this project area is to assess capabilities and limitations of visual instrumentation approaches in combination with novel sensing technologies providing complementary local data for predictive assessments assuring reliable operation of FHRs.

The visual ability to monitor important regions of the reactor vessel from the interior while the reactor remains online and the entire vessel periodically during maintenance outages can provide assurance that unacceptable corrosion will not have occurred over the previous inspection interval. Performance and applicability of novel in-core sensing technologies will be assessed, namely fiberoptics sensing, as complimentary means to monitor local phenomena and changes.

Fiberoptics sensors offer driftless accuracy and high sensitivity, light weight and small size, ease of installation, low power requirements, immunity to electromagnetic interference, potential for multiplexing (several sensors can be used with a single transmission cable), large bandwidth, and reliability and environmental ruggedness.

Fiber optics have been shown to exhibit increased Rayleigh scattering as a result of being dosed by a radiation field. (Wen, et al., (2011)) Optical Frequency Domain Reflectometers can measure the backscattering through the fiber as a distributed measurement in high spatial resolution. (Giford, Soller, Wolfe, & Froggatt, (2009))

One such experiment was conducted at Texas A&M University in the TRIGA reactor to test fiber optic sensors in a high radiation, high temperature environment. (Tsvetkov, et al., USA (2011); Johns, (2011)) The results of the effect of radiation on the fiber's backscattered light can be seen in *Figure 6-59*.

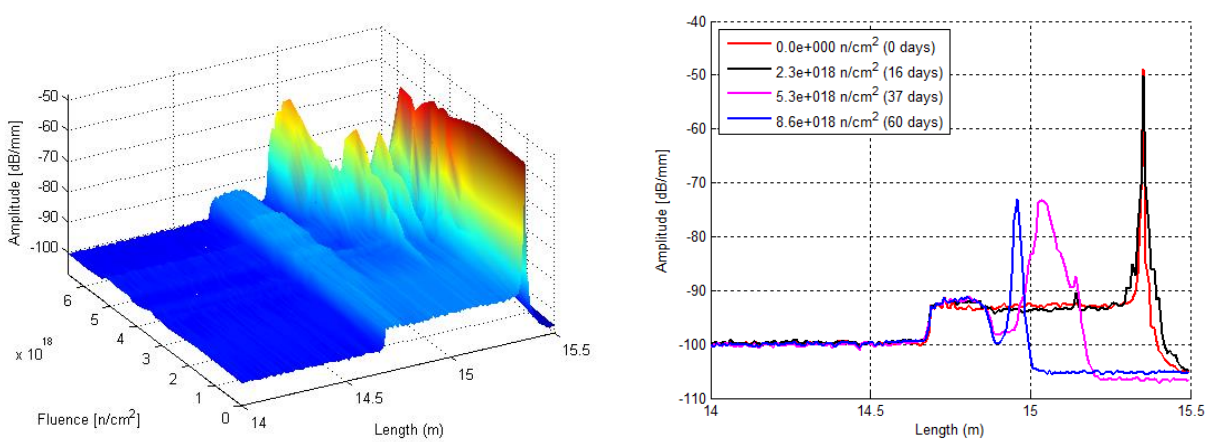

Figure 6-59 Response to radiation in TRIGA experiments.

The fiber dose does not yield a clear predictable response as a scattering amplitude increase. There was no response early on in the irradiation up to a certain point (around a fluence of 5e18 n/cm^2), and then the scattering amplitude increased rapidly until the point of probe failure. However, the setup was limited in its measurement range due to the fiber termination near the irradiated portion of the probe. The limited length of the irradiated region is shown in *Figure 6-60*.

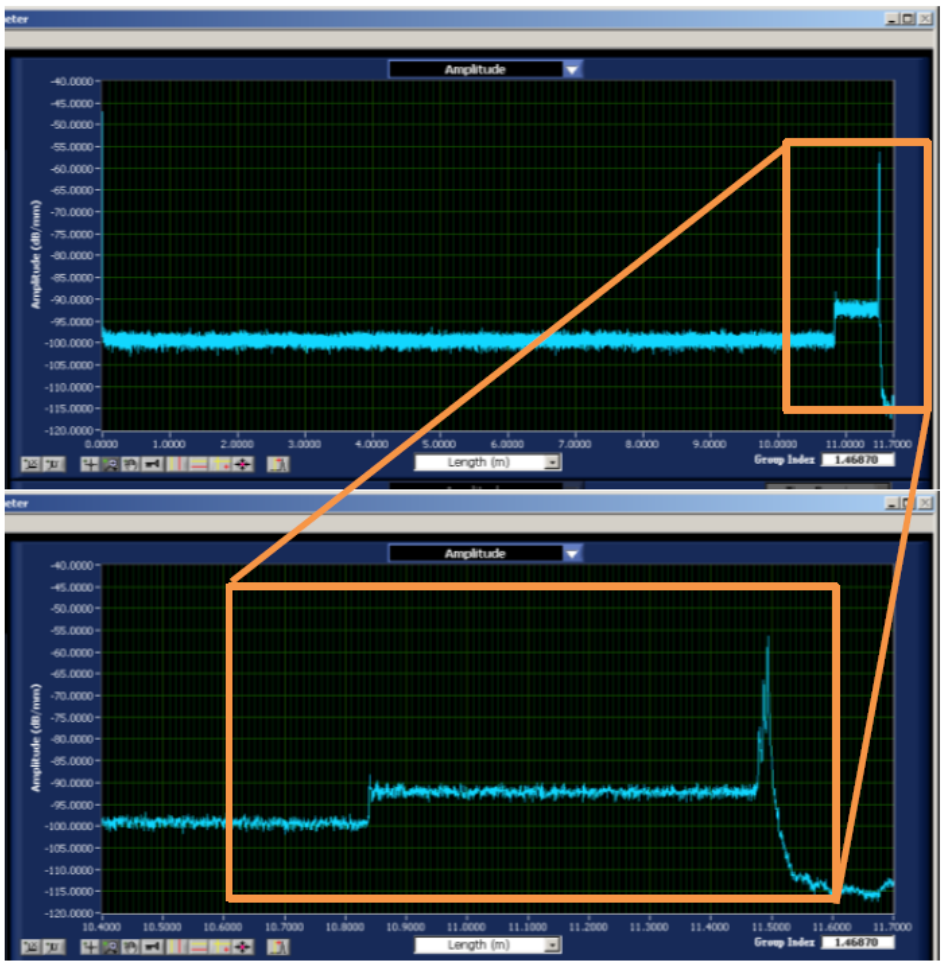

Figure 6-60 Comparison of the irradiated region to the entire fiber length.

Limited scope irradiation tests have been conducted using radiation sources as well as HFIR at ORNL. The tests used fibers and manufactured sensor probes developed for the completed project that was focused on fiberoptics use in VHTRs.

This task takes advantage of the collected data for relevant probe evaluations. Further probe tests will be conducted in the benchtop experiments to assess the probe functionality and losses due to radiation effects. The experimental configuration (temperature measurements) and fiberoptics equipment used in the project are showing in *Figure 6-61*

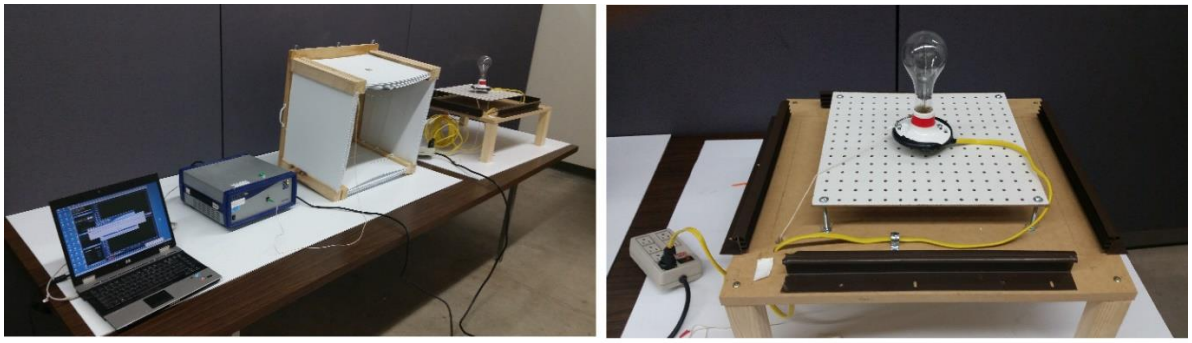

Figure 6-61 Fiberoptics benchtop testing configuration.

In an experimental setup to improve on the developing a response function for distributed radiation measurement, a test rig design was created to maximize the length of irradiated fiber.

This involved coiling the fiber within the rig as seen in *Figure 6-62*. This test rig would not be designed with accessibility during irradiation as was the case for the TRIGA test probe. (Tsvetkov, et al., USA (2011))

Gamma radiation was to be used exclusively rather than a reactor irradiation which allowed the test rig to be handled post irradiation without concern of induced radioactive elements by neutron activation.

Since the goal was to characterize any radiation response, it was acceptable that only one type of radiation would be measured.

Figure 6-62 Coiled fiber optic test rig.

Several of these test rigs were created to evaluate the effect of radiation on fiber optics as a distributed measurement. The lowest dose was achieved using a Co-60 pool source at the University of Cincinnati. The rig was lowered in an air tight container as seen in Figure 6-63.

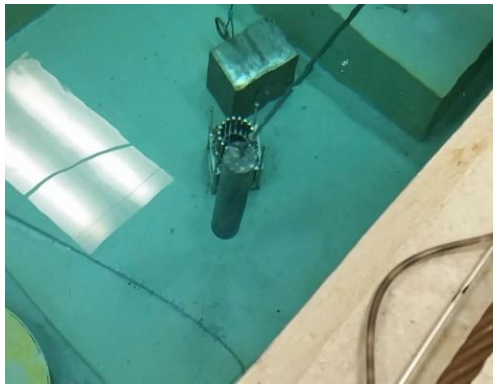

Figure 6-63 Cobalt-60 pool source irradiation.

The higher doses were achieved using the Oak Ridge National Laboratory Gamma Radiation Facility. This facility uses an intense radiation field created by spent fuel from the High Flux Isotope Reactor. The test rigs exhibited a distinct color change in their structural materials corresponding to their respective dose range as can be seen in *Figure 6-64*.

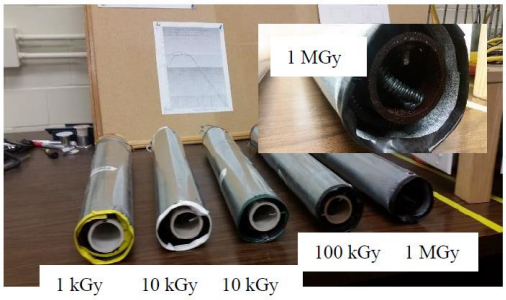

Figure 6-64 Color comparison for test rig dose ranges.

Each rig had three different fiber material types and each fiber had around 7 meters (23 ft) of measurement. This should offer a significantly improved range for characterizing the radiation response function for the fiber scattering amplitude. A sample scan of the fibers for low dose range is seen in *Figure 6-65*.

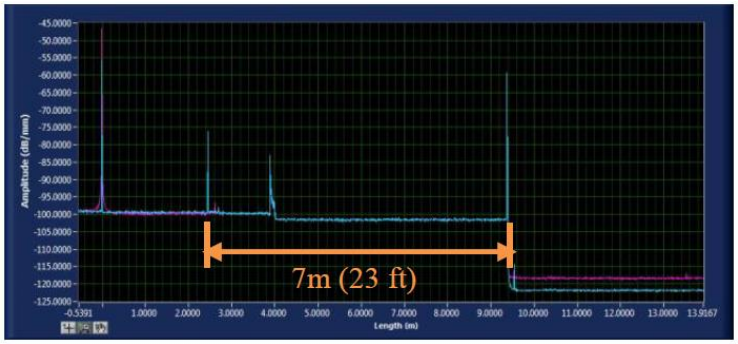

Figure 6-65 Sample scan of a gamma-irradiated fiber.

The higher dose range has the same length of irradiated fiber and should have a detectable increase in scattering for this range.

The results for the low dose range experiments conducted at the University of Cincinnati are seen in *Figure 6-66*.

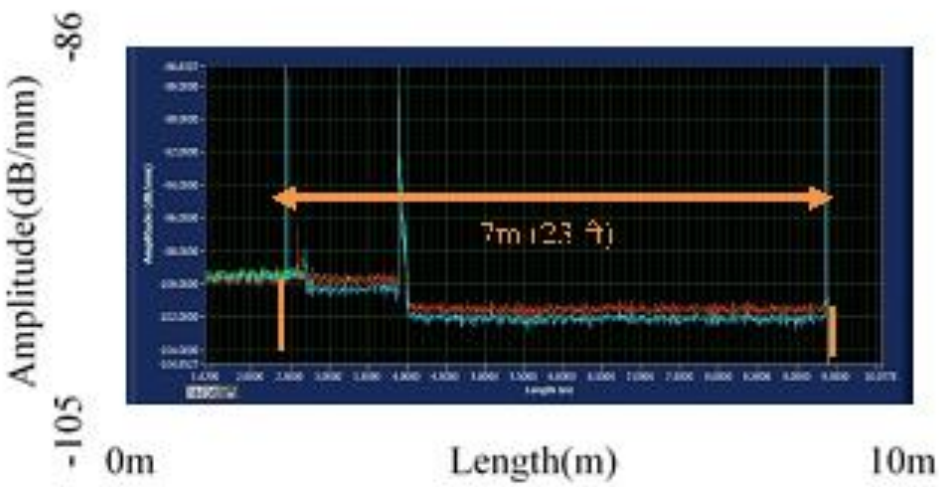

Figure 6-66 University of Cincinnati irradiation results.

Here the green line (100 Gy) matches exactly to the red line (0 Gy). This follows that the measurement is not sensitive enough for the lowest dose. The blue line (1 kGy) is seen below the other lines, this is on the contrary to what is expected by the literature that the scattering amplitude should increase.

However, the blue line experiences a greater loss through the first connection, so some additional computation must be done to make a comparison of the scattering within the irradiated region of the fiber to see if a detectable increase is present. What was successful in these measurements is the clear advantage of the coiled test rig to achieve a full 7 meters

of measurement. It is anticipated that the higher dose ranges will have a clearer detectable increase in scattering than the lower ranges.

With a response function distributed over a spatial range, the use of fiber optics could offer a significant advance in radiation sensing. Providing a multitude of radiation measurement data points could support a new type of reactor power monitoring with reconstruction capabilities in 3D from a 3D layout of fiber optics.

6.12. Experimental Optical In-Core Data Capture from the Core Side Observational Position

An experiment was performed at the Nuclear Science Center using the TRIGA reactor. This experiment was intended to validate the Cherenkov models and demonstrate the potential for Cherenkov radiation measurements in reactor instrumentation. This experiment is performed using a video camera to image the reactor while changes in the rod positions and reactor state are induced from the control room. Corresponding MCNP models are then run to compare the effects observed in MCNP to the changes in the Cherenkov radiation detected in the video.

The TRIGA reactor at the NSC hangs suspended in the pool from a movable bridge. This allows the reactor to be moved to different locations in the pool for various experiments and purposes. In this experiment, the reactor was positioned some distance away from the graphite coupler box approximately at the outer edge of the reactor stall within the pool as seen in the right half of *Figure 6-67*. The waterproof camera was suspended in the pool above the graphite coupler box using a pole attached to the ceiling crane. A string attached to the front of the camera was attached to the bridge above the reactor to stabilize the camera and adjust its angle to ensure that it is pointing at the reactor. The setup can be seen in the left half of *Figure 6-67*.

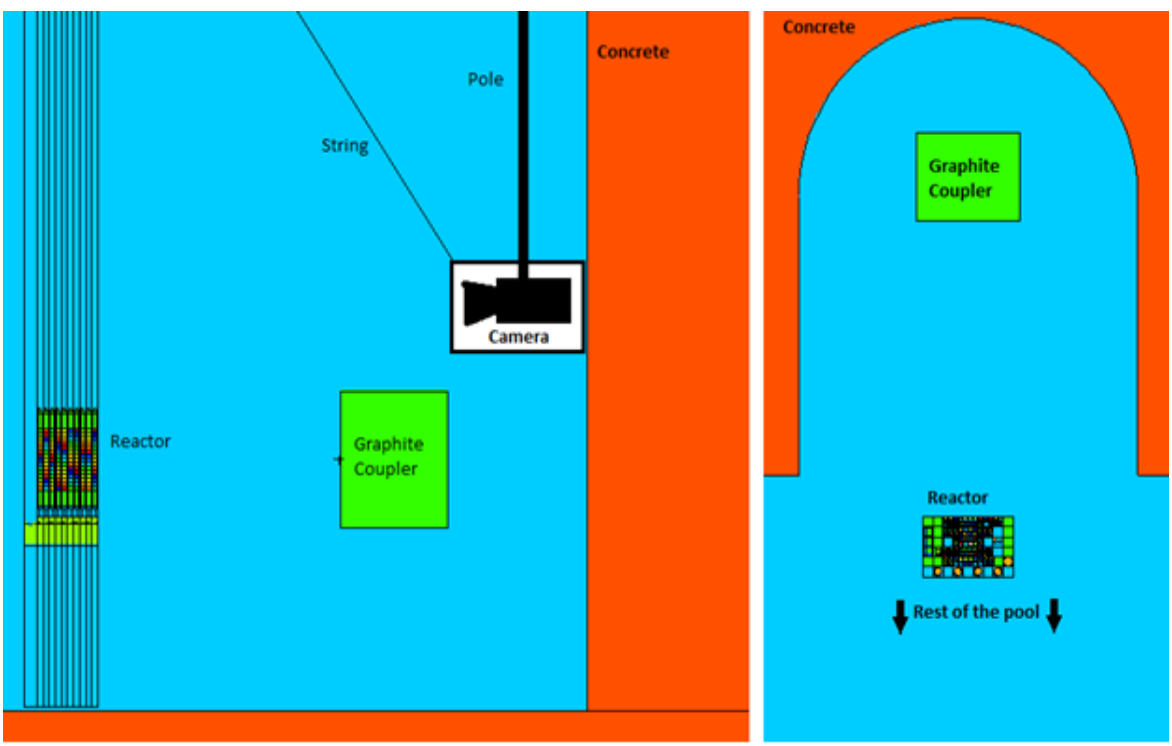

Figure 6-67 Approximate setup of the camera and the reactor (left) and location of the reactor in the pool (right) during the video experiment.

The video feed from the camera was connected to a computer so that the video could be seen in real time as the experiment progressed. A snapshot of the reactor and its Cherenkov glow taken from the video can be seen in *Figure 6-68*. The camera was at a slight angle and the resolution limited, but the fuel rods are evident in the middle of the picture as are the black graphite reflectors on each side of the core. The bright lines are the Cherenkov radiation from the water further inside the core escaping between the pins. Also, the general shape of the Cherenkov glow from the water in front of the reactor can be vaguely seen as the diffuse blue glow.

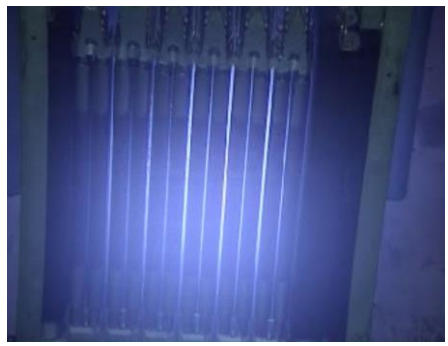

Figure 6-68 Snapshot of the TRIGA reactor core taken from the experiment video.

Two videos were taken each of which covered multiple reactor states. The reactor was initially in a stable state at 400 kW with the safety shims at 63% withdrawal and the regulating rod at 55.5%. The video was run in this state for a period of at least 60 seconds with the start and end time recorded. Control rods were then moved to bring the reactor into the second state imaged, and once the neutronics fluctuations in the system were considered to have stabilized, the time was recorded, and the reactor was held in this state for a minute with the end time also recorded. Thus, the reactor was imaged in multiple states, with the times recorded so that the states could be correlated to the footage from the video.

The first video covers four reactor states. The second video covers a total of 9 states, though the first state in the second video (state 4) is the same as the last state in the first video. States 1-5 were imaged with the intent to connect them to the Cherenkov modelling comparisons, while states 6-12 were images to test the linearity of the relationship between the total Cherenkov production in the core and the total reactor power:

- State 1, as previously mentioned, has the reactor at 400 kW with the shims at 63% and the regulating rod at 55% withdrawal.
- State 2 has the reactor at 520 kW with the safety shims at 63% withdrawal and the regulating rod at its maximum allowable withdrawal position of 70% withdrawal. The operating procedures for the TRIGA limit the regulating rod movement to keep it between 30% and 70% withdrawal so that its reactivity worth stays sufficient to control the core. This state is one of the two states modeled in MCNP for the Cherenkov comparison.

- State 3 holds the shims at 63% and moves the regulating rod to 50%, lowering the power to 368 kW.
- State 4 holds the shims at 63% and inserts the regulating rod to its maximum allowable insertion of 30%. This lowers the power to 235 kW. This state does not work as an effective Cherenkov flux shape comparison to state 2 because the reactor power is vastly different.
- State 5 holds the regulating rod at 30% and removes the safety shims to 66.3%, bringing the power back up to 530 kW. This is the state that was intended to be compared to state 2 to detect the change in the Cherenkov flux caused by a shift in the power profile of the reactor with the total power remaining close to constant.
- States 6-12 hold the regulating rod at approximately 50%, while moving the shims to place the reactor at different power levels:
  - State 6 has the reactor at 500 kW.
  - State 7 has the reactor at 400 kW.
  - State 8 has the reactor at 300 kW.
  - State 9 has the reactor at 200 kW.
  - State 10 has the reactor at 100 kW.
  - State 11 has the reactor at 50 kW.
  - State 12 is the one dynamic state and comprises the 15 seconds immediately following the reactor being tripped and dropping to near zero power.

An MCNP model was produced to compare the expected Cherenkov fluxes from states 2 and 5 from the experiment. As the tallying plane is in the same direction from the core as the camera and the tally only counts photons that are moving within a 36.9 degree cone of the direction of the graphite coupler that the camera was above, it is assumed that the general shape of the Cherenkov flux should be similar. Both state 2 and 5 had models run for both the Cherenkov fluxes and the neutron, gamma, and electron mesh plots. The other states are not currently modeled and compared in MCNP. This is because the power levels are quite different, and most of them are intended for other uses.

The MCNP model does not really account for the power as it normalizes the fluxes to the flux per source particle and the reactor power only factors in as a scalar multiplier that is applied uniformly to every tally to convert them into units of actual flux.

It is possible to correct for the differences in power in the MCNP model by scaling each case to its own power, and this is done in the comparison of states 2 and 5 at 520 and 530 kW which results in a difference plot that corresponds more closely to the video. Comparing states with vastly different power levels using this correction results in the difference caused by the power correction overwhelming any differences in the spatial profile.

The comparison between states 2 and 5 shows the difference caused by moving the regulating rod from 70% (28 cm) withdrawal to a 30% (12 cm). The shims are adjusted from 63% (25.2 cm) to 66.3% (26.52 cm) to keep the reactor at close to the same power.

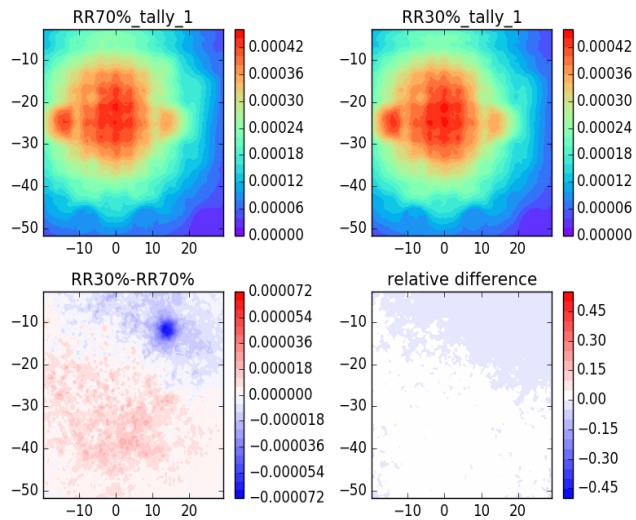

Figure 6-69 XY neutron flux mesh plot comparing video states 2 and 5 with the regulating rod moved, showing state 2 (top left) state 5 (top right) the absolute difference (bottom left) and the relative difference (bottom right).

The 530 kW power level in state 5 was deemed to be close enough to the 520 kW in state 2 and was used for the video due to time constraints and the high level of sensitivity in the reactor to any changes in the shim rod positions when the regulating rod is locked into a specific place. The XY plane mixed field comparative mesh plots for states 2 and 5 can be seen in *Figure 6-69*, *Figure 6-70*, and *Figure 6-71*. These plots are not renormalized to the reactor power level and simply show the differences in the flux shapes.

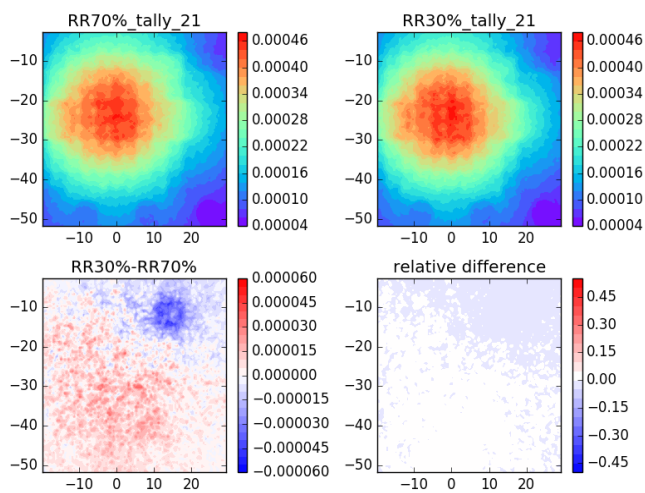

Figure 6-70 XY gamma flux mesh plot comparing video states 2 and 5 with the regulating rod moved, showing state 2 (top left) state 5 (top right) the absolute difference (bottom left) and the relative difference (bottom right).

As expected, there is a clear depression in the neutron flux where the regulating rod is inserted, as seen by the blue dot in the absolute difference plot in *Figure 6-69*. The gamma and electron plots show a similar flux decrease in the general area around the regulating rod though the electron plot is noisier. From these results, it is expected that there should be a noticeable decrease in the Cherenkov flux in front of and near the regulating rod.

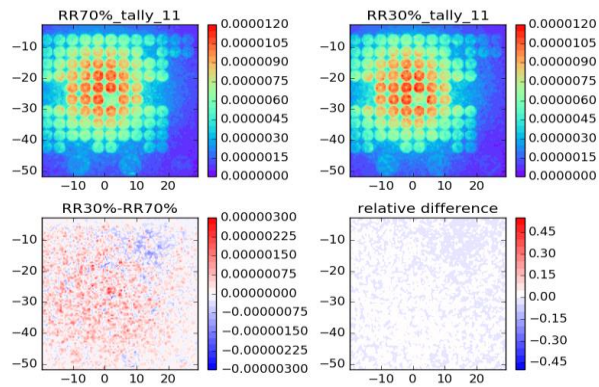

Figure 6-71 XY electron flux mesh plot comparing video states 2 and 5 with the regulating rod moved, showing state 2 (top left) state 5 (top right) the absolute difference (bottom left) and the relative difference (bottom right).

The Cherenkov photon producing models corresponding to states 2 and 5 from the experiment were run and the output files produced. The comparison between these two models was then done both with and without the implementation of a scaling factor to adjust for the difference in reactor power. In the case without the scaling factor, seen in *Figure 6-72*, the fluxes in each spatial bin are simply subtracted from one another in the same manner used previously.

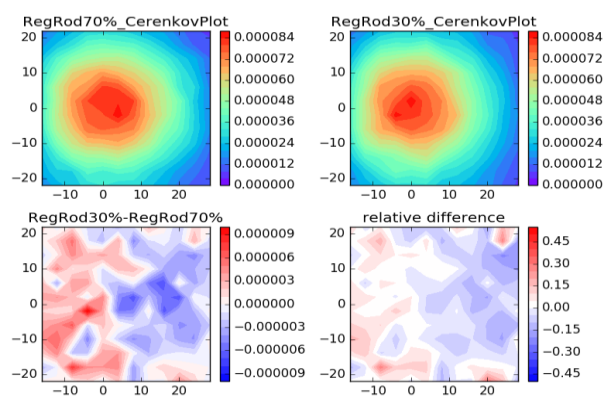

Figure 6-72 Cherenkov flux plots comparing video states 2 and 5 with no scaling, showing state 2 (top left) state 5 (top right) the absolute difference (bottom left) and the relative difference (bottom right)

The plot showing the sigmas of difference is shown in *Figure 6-73*. In the scaled comparison, the Cherenkov flux in state 2 is multiplied by 520/530, or 0.98113, to account for the change in power.

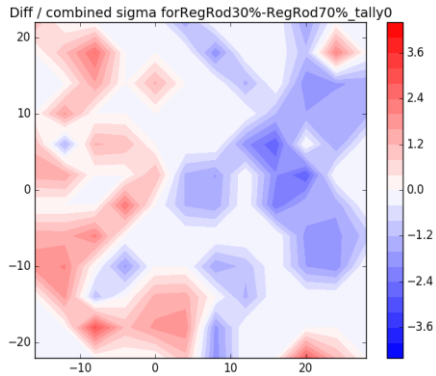

Figure 6-73 Sigmas of difference comparing video states 2 and 5 with no scaling.

The differences in this comparison, shown in *Figure 6-74*, are the flux in state 5 minus (520/530) times the flux in state 2. The corresponding sigmas of difference plot can be seen in *Figure 6-75*.

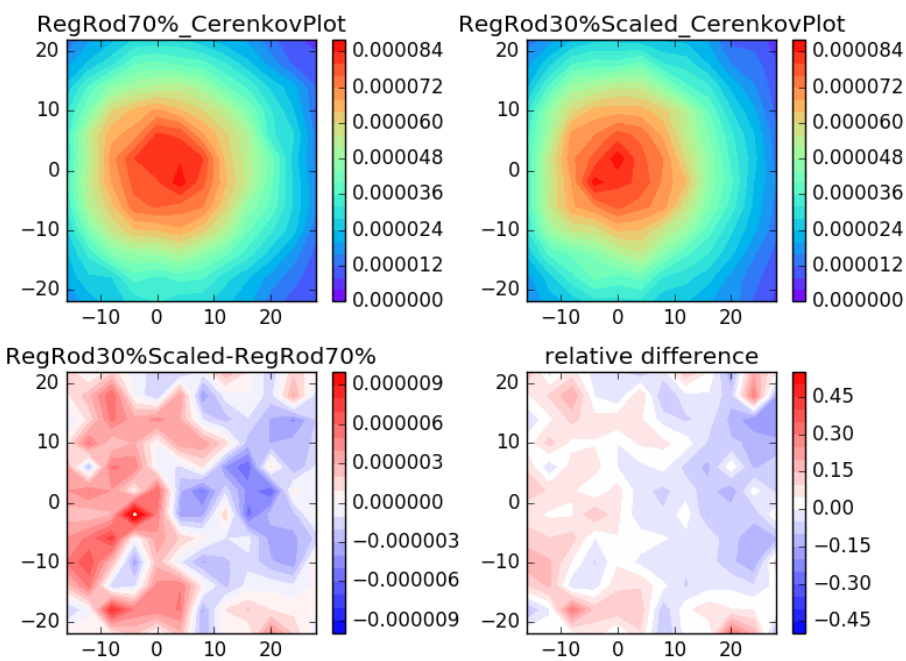

Figure 6-74 Cherenkov flux plots comparing video states 2 and 5 with scaling, showing state 2 (top left) state 5 (top right) the absolute difference (bottom left) and the relative difference (bottom right).

The use of the scaling factor causes only a small difference in the appearance of the plots. One specific change can be seen in the absolute difference plot in the scaled case. The scaled difference plot has slightly darker reds and lighter blues because the total Cherenkov flux in state 5 at 530 kW is higher than in 520 kW state 2. The two power levels are close enough that the spatial effect of the Cherenkov reduction in the right side of the plot near the regulating rod is not swallowed by the total power scaling difference. This is expected for this comparison because the 10 kW difference in power is less than 2% of the power in the base state.

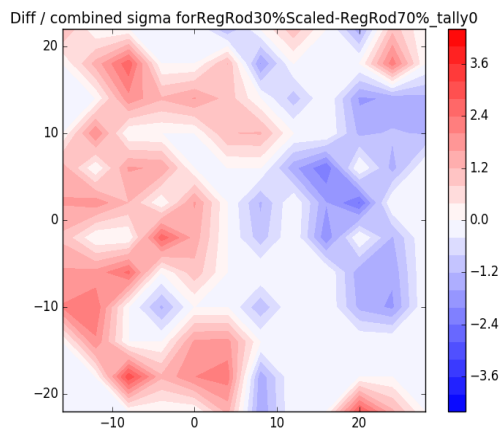

Figure 6-75 Sigmas of difference comparing video states 2 and 5 with the scaling factor.

The python script, used to post-process and compare the MCNP results, compares states at different power levels without requiring another time-consuming MCNP run. Further post processing tests are performed to determine how increasing the power difference between the two regulating rod cases changes what can be seen from the Cherenkov shape comparison and at what percent power difference the spatial effects of the regulating rod movement are no longer evident.

The effects of the power scaling on the Cherenkov comparison in this model are entirely based upon the ratio of powers in the two states and not the absolute power in either state. This means that comparing 500 kW to 550 kW will produce the same observable flux perturbations at comparing 100% to 110%. To better generalize the observable power shifting effects, further comparisons in this section will be presented as the comparison with the case with the regulating rod at 70% as the basis having 100% power. The case with the regulating rod at 30% has its fluxes scaled in the comparison and is reported as having a different power. I.e. the first comparison has the flux with the regulating rod at 30% at 110% power minus the case with the regulating rod at 70% at 100% power. Additionally, as the base Cherenkov flux profiles are not changing, merely the difference plots, the differences will be the only plots shown.

As small movements to the safety shims in the TRIGA can result in large differences in the stable power level and fuel temperature. The critical shim heights in states 2 and 5 are

assumed to be accurate enough for subsequent power scaling scoping analysis on the Cherenkov fluxes.

Power at 110% in the RR30% case is compared to the base RR70% in *Figure 6-76* with the sigmas of difference plot shown in *Figure 6-77*. The Cherenkov flux in the state with the elevated power is significantly greater than in the other case.

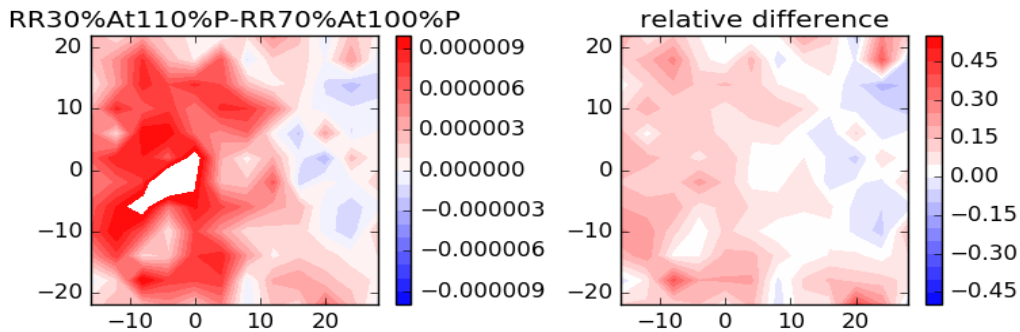

Figure 6-76 Comparison between the Cherenkov fluxes with the regulating rod at 70% and with the regulating rod at 30% with the power increased to 110%.

The absolute difference plot has the white area on the left where the difference exceeds the plot's bounds. This is because the bounds for this plot are fixed to be the same as in the non-perturbed case for the sake of comparison.

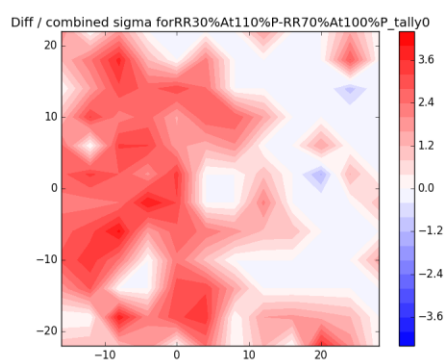

Figure 6-77 Sigmas of difference for the comparison between the Cherenkov fluxes with the regulating rod at 70% and with the regulating rod at 30% with the power increased to 110%.

From the relative difference and sigmas of difference plots, it appears that the Cherenkov flux is higher in nearly every location except directly in front of the regulating rod. These plots suggest that a 10% change in the total reactor produces approximately the same change in the Cherenkov flux in front of the regulating rod as moving the regulating rod from 30% to 70% withdrawal does.

Power at 120% in the RR30% case is then compared to the RR70% baseline and the results shown in *Figure 6-78* with the corresponding sigmas of difference plot in *Figure 6-79*Figure 7.74.

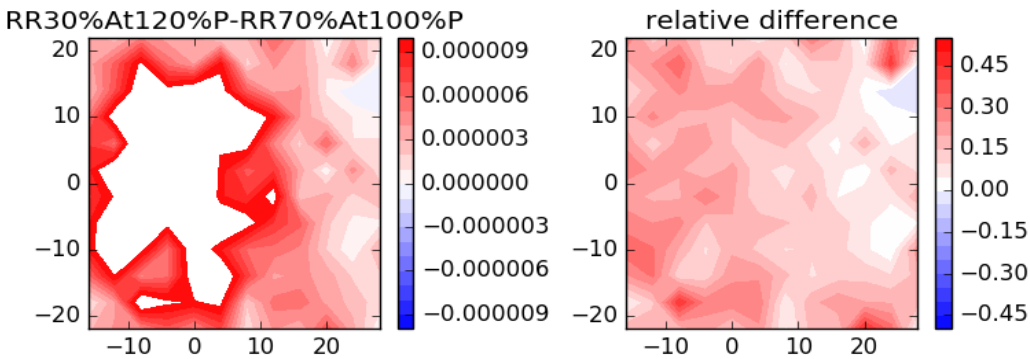

Figure 6-78 Comparison between the Cherenkov fluxes with the regulating rod at 70% and with the regulating rod at 30% with the power increased to 120%. The absolute difference plot (left) and relative difference plot (right) are shown.

In this comparison, a large portion of the absolute difference plot is outside of the bounds of the color scale, and the relative difference plot shows that the flux is higher in essentially all locations in the higher power case. The few points where the flux may be lower are less than one combined sigma lower as shown in the *Figure 6-79*.

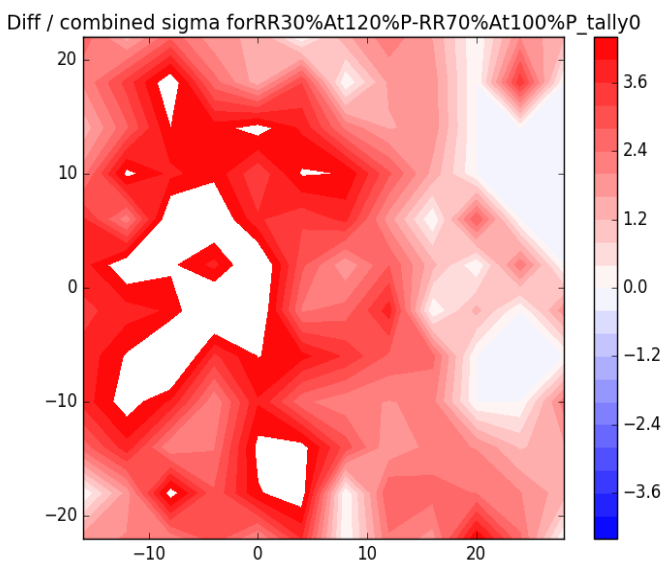

Figure 6-79 Sigmas of difference for the comparison between the Cherenkov fluxes with the regulating rod at 70% and with the regulating rod at 30% with the power increased to 120%.Figure 6-78

The scaled experimental comparison and the two previous altered power comparisons look at an increased power in the reactor with the regulating rod at 30% when compared to 70%. This results in a competing effect between the depression in the flux caused by the insertion of the regulating rod and the increase in the flux caused by the increased power. The following comparisons look instead at decrease in the power in the state with the regulating rod at 30% compared to the state at 70%. Here the local effect of the Cherenkov reduction caused by the insertion of the regulating rod is compounded by the effect of the decrease in power. The analysis with a 10% decrease in the power for the case with the regulating rod at 30% withdrawal can be seen in *Figure 6-80* and *Figure 6-81*.

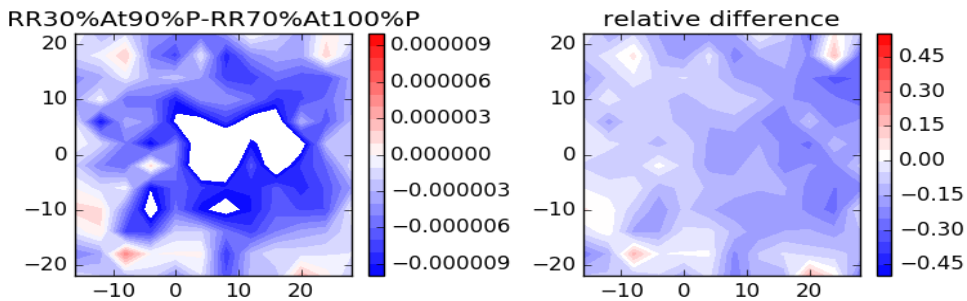

Figure 6-80 Comparison between the Cherenkov fluxes with the regulating rod at 70% and with the regulating rod at 30% with the power decreased to 90%. The absolute difference plot (left) and relative difference plot (right) are shown.

With only a 10% decrease in the power, a large portion of the absolute difference plot is already outside of the previously defined bounds. From the relative difference plot, it can be seen that there is a very large decrease in the Cherenkov flux at the right side of the reactor that exceeds 0.25 relative difference at some points.

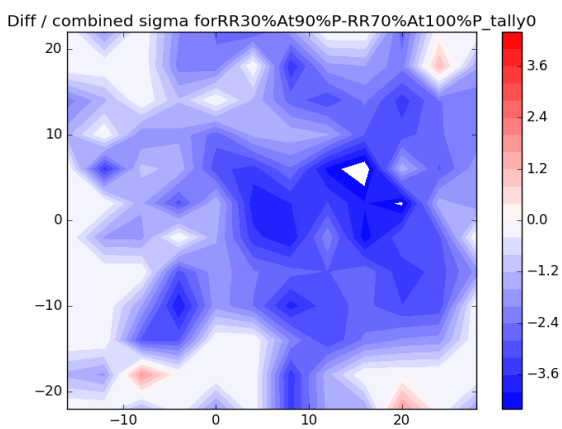

Figure 6-81 Sigmas of difference for the comparison between the Cherenkov fluxes with the regulating rod at 70% and with the regulating rod at 30% with the power decreased to 90%.

Also, the left portion of the plot, which was red in the equal power level comparison, denoting a higher flux in the reg rod 30% case is now almost entirely blue, corresponding to a decrease in the flux. The slight increase in the flux at the left side of the eastern face of the core is overwhelmed by the 10% decrease in the total reactor power.

As already previously discussed and analyzed through simulations using MCNP, Cherenkov radiation emission from the reactor core is concentrated in the areas between the fuel pins and resembles a collection of line sources of light. The goal of the present effort is to explore signature capabilities based on the Cherenkov radiation images. The difference in the intensity of these emissions helps determine changes in local and/or global fission density.

Figure 6-82 is obtained as described above by placing a camera in front of the operating TRIGA reactor. The experimental setup is shown in *Figure 6-67*. The brighter the area means the greater the change in local power density. The variations in brightness in the difference image, therefore, show the difference in power by region (due to the camera auto brightness adjustment, total power cannot be determined in this specific experiment).

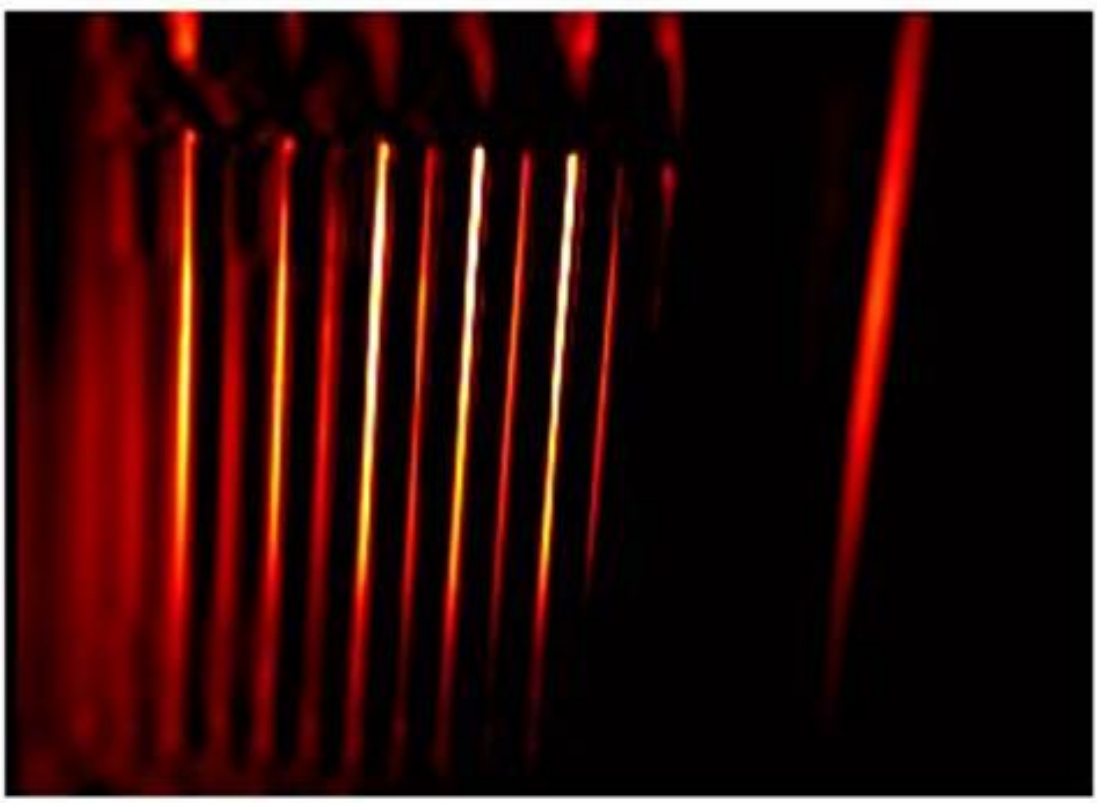

Figure 6-82 False color image (MatLab 'Hot') of the Cherenkov radiation profile from the TAMU NSC 1MW TRIGA reactor. Power is transitioning from 520kW to 368kW due to the regulating rod moving from the 70% position to the 50% position.

The obtained images were manually aligned with one another due to the resistance of this data to the video stabilization software.

Figure 6-83 False color image (MatLab 'Bone') of the Cherenkov radiation profile from the TAMU NSC 1MW TRIGA reactor. Power is transitioning from 520kW to 368kW due to the regulating rod moving from the 70% position to the 50% position.

The brighter the location in the image, the greater the difference in the power levels. There is a limited range of linear power interpretation between the steps the camera equipment makes between aperture settings on the lens. This feature, however, was not experimentally verified. Further image analysis is shown in *Figure 6-83* and *Figure 6-84*.

Figure 6-84 False color image (MatLab 'Bone') of the Cherenkov radiation profile from the TAMU NSC 1MW TRIGA reactor. Power is transitioning from 520kW to 235kW due to the regulating rod moving from the 70% position to the 30% position.

The largest power change appears to be coming from the main fuel region of the core and this is interesting to note due to the fact that the regulating rod is on the opposite side of

the core. When viewing the core from a plan view, it is easy to observe that the majority of the fuel mass does indeed reside on the other side of the regulating rod and should be responsible for the relative decrease in light output from the North (right) end of the reactor core.

Unfortunately, there is a great deal of error introduced into these images due to the data acquisition setup. The video camera was mounted on the end of a 10 m aluminum pole from a gantry crane located in the containment building. There is some flow and circulation in the pool which caused the camera to sway back and forth slightly during the experiment. This allowed the camera field of view to oscillate back and forth across the core, thus, blurring the final average image. Many attempts were made with regard to image stabilization, but the low resolution, aliasing, and geometry of the image features thwarted every image stabilization algorithm available in MatLab. Without an effectively stabilized image, a comparison between two states from the video would involve large differences caused by the camera movement.

The section of the experiment aiming to test the assumed linear relationship between the reactor power and the total Cherenkov flux was foiled by the auto adjustment of the camera's aperture during the video. The camera automatically increased the aperture size as the level of light decreased to let more light in. This is a common and often helpful feature in cameras under normal circumstances, but here it disrupts the direct correlation of the brightness in the video to the total amount of light striking the camera. The video footage does not keep track of what the aperture size of the camera is, so it is not possible to use it to accurately calculate what the total luminosity is in the footage relative to other parts of the video where the aperture size is different.

A proposed plan for a future experiment is to first move the reactor further away from the stall and into the pool. This would allow room for a tripod to be set up on the bottom of the pool to hold and stabilize the camera. It will be necessary to move the core so that the camera can remain far enough away from the reactor to minimize its dose and the resulting damage to the electronics. Also, a different camera with higher resolution at low light levels and an option to fix the aperture size and exposure time would be used instead of the camera used previously.

These two alterations should allow for another experiment similar to the first to be performed more successfully so that useful data can be extracted and used to validate the models and assumptions used in this project. The stable platform for correct spatial Cherenkov profiling will be particularly useful as it has not been experimentally validated elsewhere before. The linear relationship between the Cherenkov flux and the reactor power has been established in another system used elsewhere. (Rippon, (1963); Arakani & Gharib, Reactor Core Power Mesurement Using Cherenkov Radiation and Its Application in Tehran Research Reactor, (2009)) This experiment demonstrates the ability to determine local and global power changes in the reactor core. The next steps in research are to improve the resolution of the data acquired by employing a higher resolution camera and increase camera stability to reduce the reliance on image stabilization software and processing techniques.

6.13. In-Core Data Capture from the Core Top Observational Position

Another future experiment at the TRIGA reactor would be to image the Cherenkov light coming from the top of the core. This will create some added difficulty as there are various structures and drive mechanisms in the way. It may require multiple cameras or camera positions to effectively capture the desired data.

Ideally, there would be a view that is direct or close to directly in line with each gap between the fuel pins which would allow the amount of Cherenkov light produced in each region between pins to be observed.

If this is possible, it could be coupled with a new version of the MCNP model that observes the Cherenkov production and flux above the reactor. The added information from such a setup should allow for an improved mapping of the core power profile and for changes anywhere in the core to be detected more easily. Changes near the bottom of the core may be harder or impossible to detect though.

An additional benefit of a top down viewing of the core would be that it could more closely be replicated in the FHR core. The FHR core has FLiBe coolant channels that run vertically for the length of the core. Optical instruments above and in line with these channels could theoretically view the cumulative Cherenkov production along the entire length of the channel which would allow an array of instruments or fiber optic cables leading back to an instrument to map the power profile of the reactor and to quickly detect anything causing expected or unexpected changes.

A new Cherenkov tallying method was devised that looks at the Cherenkov flux coming out of the top of the reactor instead of the exposed side. The channel between each of the four pins is a straight shot through the height of the active core, and thus the Cherenkov radiation visible at the top of that channel should be closely correlated to the gamma and electron flux in the coolant in the channel. As seen in the left half of *Figure 6-85*, the tallying plane coincides with the plane ending the top tips of the aluminum caps on the regular fuel pins.

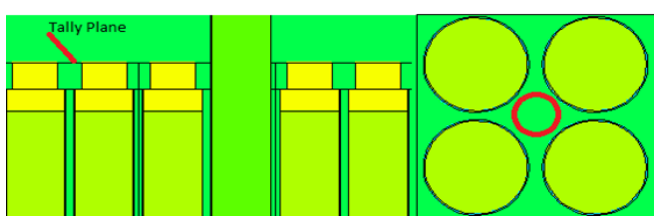

Figure 6-85 Tallying plane coinciding with the tips of aluminum rod caps (left) and approximate diagram showing circular area of one segment in the tally in the main fueled region.

In the core, the fuel pins are spaced 4.050030 cm apart in the x direction and 3.85445 cm in the y direction. The outer radius of the cladding is 1.79195 cm. The largest circle that can fit within the channel without touching the cladding has a radius of 1.003904 cm. For simplicity and to avoid any unwanted surface interactions, a 1cm radius is used for the tally. The segment tallies are spaced in an 11 x 9 array to view each coolant channel.

The full mesh shown overlaid across the core can be seen in *Figure 6-86*. Some of the points in the bottom right of the array are either partially or fully obstructed by a graphite block. The python script used for extracting and plotting Cherenkov mesh data was altered to accommodate and plot the top down geometry with its 11 x 9 mesh, and these obstructed points are left in so that the mesh can remain rectangular and the python script can accept it.

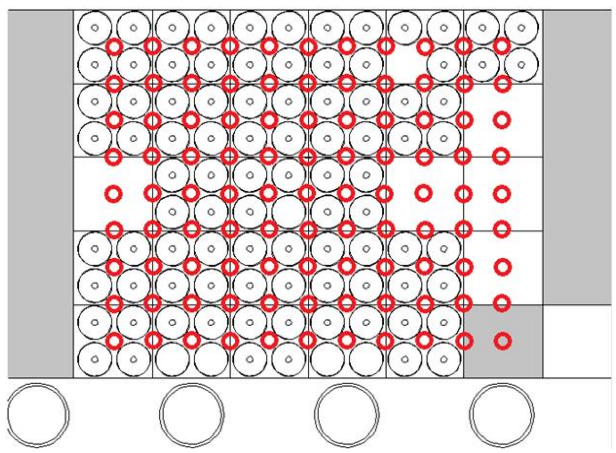

Figure 6-86 Top down Cherenkov detection array shown through a cross section of the center of the core. The 11x9 array of segment tallies (shown in red) are "viewing" each internal coolant channel.

The tally is set to only accept photons with directions within a mu = .8 (36.9 degree) cone of the +z direction (vertically out of the reactor), similarly to the previous setup for the XZ Cherenkov tallies. Also, the only photons counted by the tally are again those with energies below 50 eV, so that Cherenkov photons are counted but gamma rays are not.

A visible/UV cutoff is again not implemented because the majority of the Cherenkov photons are in the UV range rather than the visible range and rejecting them would cause there to be too few particles to get reasonably good statistics.

The 1 cm radius used in the tallies is half the size of the tallying circles previously used in the XZ Cherenkov tallying plane on the side of the reactor, resulting in ¼ the area and thus ¼ as many particle hits. This will approximately double the uncertainty for a similar length MCNP run, so some alternative methods of Cherenkov flux estimation to reduce variance are being investigated.

The first top down Cherenkov model run was with the reactor in the reference (normal) state with the safety shims at 28.4cm and the regulating rod at 19.8 cm. The results of the trial run for Cherenkov flux leaving the top of the core can be seen in the top left portion of *Figure 6-87*.

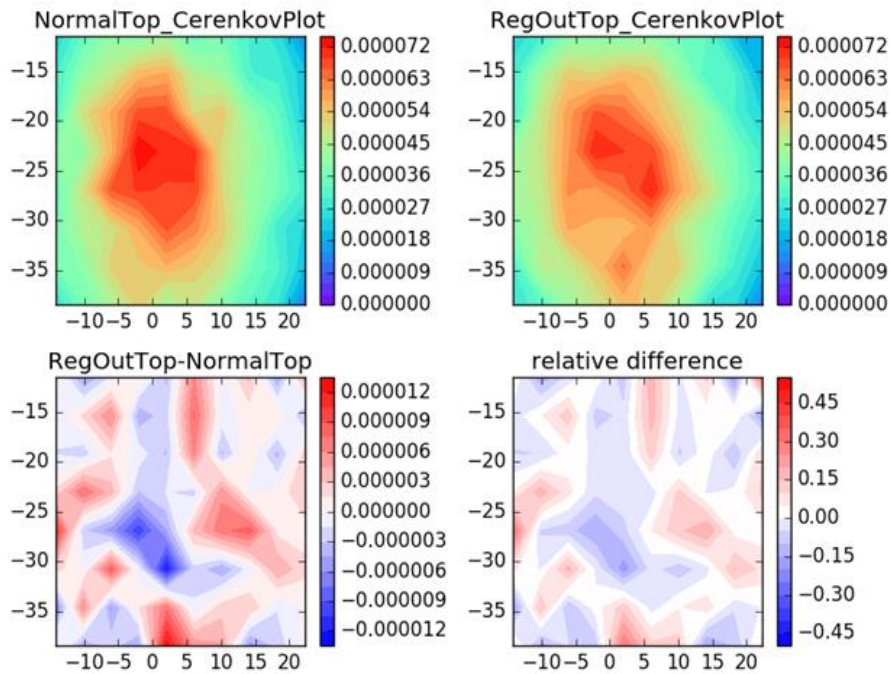

Figure 6-87 Comparison between the XY plots of Cherenkov flux leaving the top of the reactor with the reactor in the reference (normal) state (top left) and with the regulating rod fully removed and the shims adjusted for criticality (top right). The absolute (bottom left) and relative (bottom right) difference plots are also shown.

The plot appeared rather noisy, so to both ensure that the plot is being produced correctly and that the noise is sufficiently low, a second run was performed with the regulating rod fully withdrawn and the safety shims adjusted to 26.9 cm to maintain criticality. The rest of *Figure 6-87* shows this run and the comparison between it and the reference (normal) case.

The regulating rod is near the top right portion of the plot, so it was expected that there would be a noticeable increase in the Cherenkov flux in that region. Unfortunately, this is not the case. This could be due solely to issues with the uncertainties and noise being greater than the change.

Figure 6-88 shows the sigmas of difference for the comparison. There are only 3 points that have more than 2 sigmas of difference, so it is likely simply an issue of noise. Another possibility is that there could be an issue with the orientation of the tally, as the script extracting it has been changed.

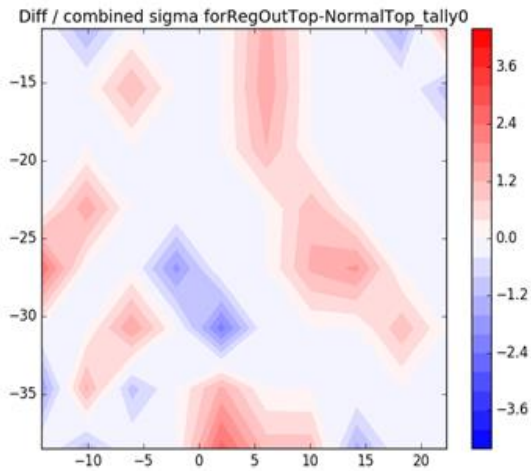

Figure 6-88 Sigmas of difference for the XY Cherenkov mesh above the core comparing the reactor in the reference (normal) state with the regulating rod fully removed.

To test both of these potential errors, a third input was run with an artificial full insertion of the safety shim at 4,4 (in the upper right quadrant of the core when viewed on an XY plane). This configuration is very subcritical and has a large perturbation. The resulting comparison can be seen in *Figure 6-89* and *Figure 6-90*.

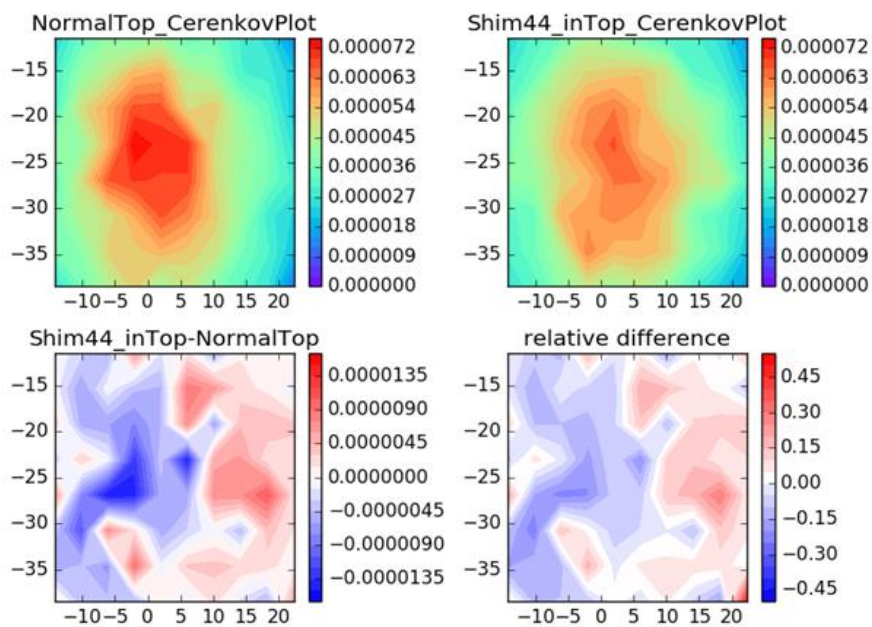

Figure 6-89 Comparison between the XY plots of Cherenkov flux leaving the top of the reactor with the reactor in the reference (normal) state (top left) and with the safety shim at 4,4 fully inserted (top right). The absolute (bottom left) and relative (bottom right) difference plots are also shown.

There is a pronounced decrease in the Cherenkov flux in the portion of the core nearest to the altered control rod. The sigmas of difference plot shows that there is a statistically significant change, and that it is in the correct location. This implies that the noise caused by large uncertainties is what caused the problem with the regulating rod movement comparison.

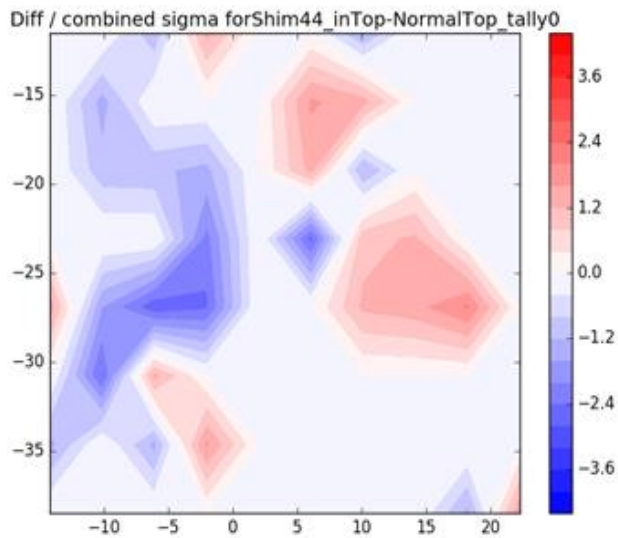

Figure 6-90 Sigmas of difference for the XY Cherenkov mesh above the core comparing the reactor in the reference (normal) state with the safety shim at 4,4 (the near the left side of the plot) fully inserted.

An analysis technique has been developed that uses spatial and energy dependent electron flux measurements to estimate the Cherenkov fluxes at a point directly above the core using a correlation. The correlation relates the electron flux within a space with an energy within a specific range to the visible Cherenkov flux at a distant point that is produced by the electrons. A correlation is generated for 23 electron energy bins ranging from 200 eV to 5MeV and 16 spatial bins.

The spatial region considered for the tally is a 1cm radius cylinder in the coolant channel, nearly touching the 4 neighboring pins. This region is segmented into 16 spatial bins along the vertical (z) axis, each 4 cm long, ranging from z=-32 cm to z=28cm below and above the core midplane. This produces a total of 16*23 = 368 bins for which a correlation is found. The Cherenkov flux is tallied at a location 200 cm above the core midplane and only counts photons with energies between 1.76eV and 3.17eV, corresponding to visible light.

A greatly simplified model is run with only photons and electrons to obtain reasonably precise correlation factors. This model consists of a tube of water surrounded by a region of zero photon importance in which photons are killed. The electron importance is set to zero everywhere except for in the spatial region that the correlation is being calculated for, and the electron physics card is set to kill all electrons with energies below the lower

energy for the bin. Then, the source definition card is set to homogenously spawn electrons in the region of interest with an initial energy distribution that approximately results in a flat energy profile within the energy bin range.

The electron flux is tallied to ensure that only electron within the energy bin are present and that there is a close to flat energy profile within the bin. A photon tally counts the photons crossing the plane at z = 200 cm and the flux of photons with energies in the visible range calculated.

The visible Cherenkov flux estimate is then divided by the electron flux tally result to get the correlation for the Cherenkov flux produced per unit of electron flux in that spatial and energy bin. This is done for all 368 combinations of energy ranges and spatial segments in the coolant channel.

The set of correlations between the electron and photon fluxes can then be used to estimate the Cherenkov flux without requiring the actual production and tracking of Cherenkov photons. To verify this, a model consisting of only 4 pins in an infinite lattice is produced with no Cherenkov production using a surface source write (SSW) card that records all of the gammas passing out of the cladding and into the coolant.

Then a separate model is run with zero photon importance in all materials except the coolant to simulate opacity. This second model uses a surface source read (SSR) card to take the gammas leaving the pins and transport them through the coolant to produce electrons.

The second model tallies the electrons in the 1cm cylinder comprising most of the coolant channel with spatial and energy bins corresponding to the correlations previously calculated. The second model also has Cherenkov production enabled and tallies the Cherenkov photons crossing a plane at z= 200 cm.

The Cherenkov tally used only counts photons with energies in the visible range travelling in a direction that is within a mu = .99995 cone of the +z direction. The pseudo-arbitrary angle restriction exists to screen out photons that have come from regions of the core other than the coolant channel of interest and to mimic the way a real photon detector such as a camera would be able to distinguish where the light is coming from using lenses and small apertures.

This method ties the response for the Cherenkov detection at each location to the light produced within a single specific coolant channel, so that the electron flux in that channel can be remotely measured with little to no interference from neighboring regions.

The measurement of Cherenkov radiation directly above a coolant channel can detect changes in the fission rate in pins near the channel, or a blockage of the channel by any opaque object. This is illustrated in *Figure 6-91*.

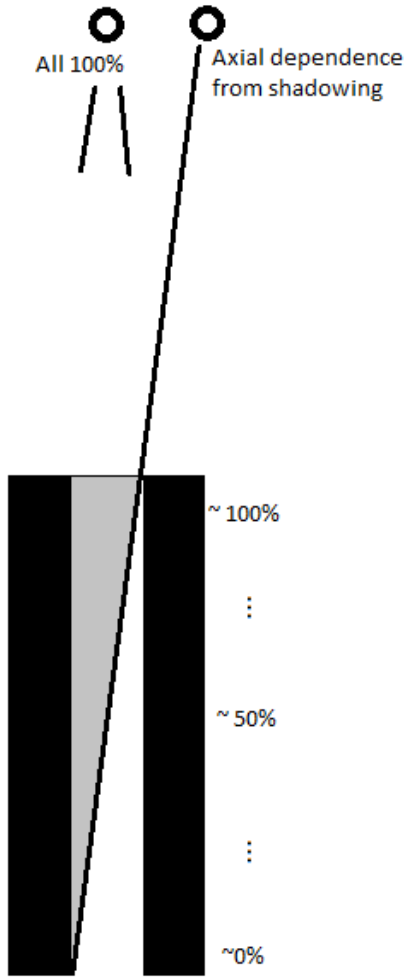

Figure 6-91 Top view geometrical constraints for the in-core 3D feature reconstruction.

However, as illustrated in *Figure 6-91*, it is not possible to determine at what axial location in the channel the blockage is present. A second Cherenkov measurement from a location that is laterally offset from the center of the channel can provide additional information as to where axially a change is. The contribution that a given region's electron flux makes to the measured Cherenkov flux at an offset location is far more dependent upon the axial position of the region.

If the coolant channel is approximated as a 58cmx2cmx2cm square prism, the contribution to the Cherenkov flux at a 7 cm horizontal offset at a height of z=200 cm will range from nearly zero for the bottommost bin from z=-28 to -24 cm, to 50% for the bin ranging from z= 0 to 4 cm, up to nearly 100% for z= 20 to 24 cm at the top.

This is due to the change in the portion of each axial slice of the fuel channel that is visible from an offset location. For a larger offset, regions at the bottom of the fuel channel will not contribute to the Cherenkov flux at all.

A combination of a measurement of the Cherenkov flux directly above a fuel channel and measurements offset from the fuel channel could potentially be used to unfold the different contributions from different axial regions. This would then give information about changes in the electron fluxes in different axial regions, or information about where in the channel a blockage is occurring and how complete the blockage is.

Two or more "viewpoints" for the same coolant channel can be compared. Directly above the channel will have all segments contributing fully. At an offset, there will be a shadowing effect as shown in *Figure 6-91*, reducing contribution from lower segments.

Models of the TRIGA with the new electron flux-based Cherenkov estimation method in place are run with the reactor in different critical configurations. This can evaluate the ability of the Cherenkov measurement-based system to detect horizontal flux tilts caused by changes in control rod positions and changes in the reactor's location within the pool.

Placing the reactor next to the graphite coupler box can create a large power tilt towards the coupler box due to increased neutron economy caused by replacing a water boundary condition with a graphite boundary. Inserting or removing the regulating rod partially and slightly moving the shims to maintain criticality can create a power tilt away from or towards the regulating rod. It is hoped that the newer method of Cherenkov estimation will be able to obtain uncertainties small enough to effectively distinguish between these changes using the measurable Cherenkov fluxes. A square coolant channel approximation will be used for calculating the shadowing effect as illustrated in *Figure 6-92*.

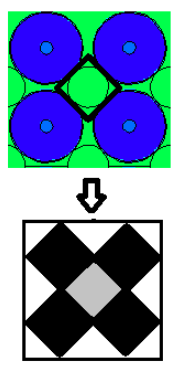

Figure 6-92 Coolant channel approximation for 3D power distribution evaluations.

Blocked coolant channel can be approximated by negating the contribution of all segments below the blockage to the Cherenkov response. Above blockage, the contribution will be assigned normally based upon the viewing location. As a result, reductions in Cherenkov responses will become detectable contributing data needed in the reconstruction process.

6.14. FHR vs. TRIGA Analysis

Nuclear power units with Generation IV reactors offer significant advances in performance, safety, security and economics; thus, emerging as a strong competitor to contemporary power technologies including the current LWR fleet. To assure successful commercialization and deployment of these systems in the coming decades, extensive research and development (R&D) efforts are underway to advance relevant technologies.

The Generation IV R&D programs are challenged by extreme in-core operating conditions due to expected high temperatures and the high energy radiation environments. These conditions dramatically depart from the LWR in-core environments.

The novelty of the Generation IV systems and limited number of the representative facilities supporting experimental studies are the factors demanding more time and significantly contributing to the R&D cost.

Responding to these challenges, this project is exploring research reactors, namely TRIGA reactors, as in-core environment emulators and their ability to support Generation IV reactors.

The work is focused on the Fluoride High-Temperature Reactor (FHR). The Very High-Temperature Reactor (VHTR) is taken into consideration for validation purposes. In-core neutron distributions in FHRs, VHTRs and TRIGA are analyzed through detailed modeling efforts using MCNP. The objective of the present effort is to emulate advanced reactor conditions using TRIGA reactor.

Recognizing principal design differences, local modification options in the TRIGA core are being evaluated and discussed with the objective of emulating FHRs. The considered modifications include various moderators, absorbers, and localized elevated temperatures in thermally isolated in-core enclosures.

The in-core neutron environments of FHRs, VHTRs and TRIGA reactors are determined by their geometry, materials, and operational characteristics. To understand differences and similarities between TRIGA and FHR, the corresponding reactor models were run. *Figure 6-93* and *Figure 6-94* show energy spectra in active cores of these systems.

Figure 6-93 shows the results for the reference TRIGA core configuration produced with MCNP as well as the results for the FHR cores produced with MCNP and Serpent. (X-5 Monte Carlo Team, Los Alamos National Laboratory (2018); Leppanen, (2010))

The consistency between MCNP and Serpent simulations allows for complimentary applications of these codes in the present effort.

As shown in *Figure 6-93*, the thermal peak of the TRIGA reactor is significantly higher than FHR. In part, this is the visual artifact of model normalization differences and scaling due to

geometry differences. However, this also makes sense accounting for physical considerations due to the lack of fuel in the in-core irradiation slot in the TRIGA case.

his is beneficial because it allows leveraging thermal neutron fluence irradiations as it yields the capability to produce the same thermal neutron fluence levels over a shorter amount of time during experiments. It also provides room for the implementation of flux traps when necessary.

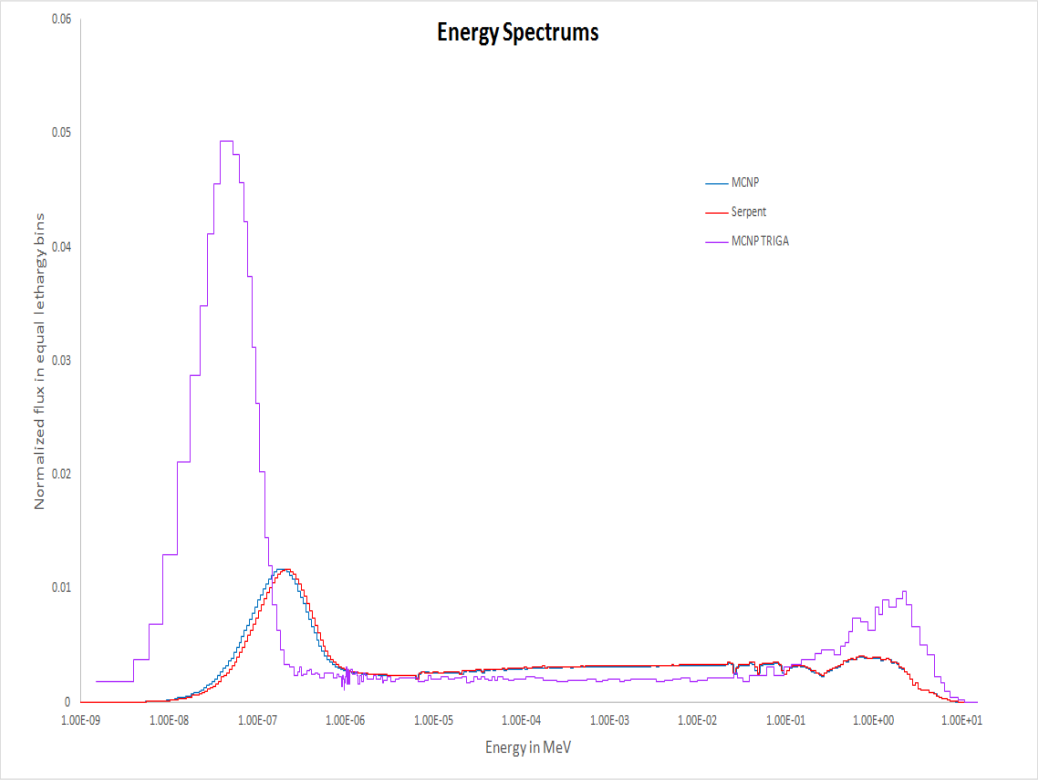

Figure 6-93 Energy spectra in FHR and TRIGA.

Graphite is the common material, but coolants and fuel forms are very different comparing the TRIGA configuration to the VHTR and FHR environments. *Figure 6-94* clearly illustrates that flibe contributes much more significantly to in-core neutron moderation rates in FHRs compare to helium in VHTRs.

To alter the neutronics of the TRIGA reactor to represent the FHR, theoretically possible and physically possible situations must both be considered. The theoretically best-comparison results may be impossible to implement physically in a TRIGA experimental setup. For this reason, some of the cases will produce the best-comparison results, and others will not have optimal results but are physically realizable.

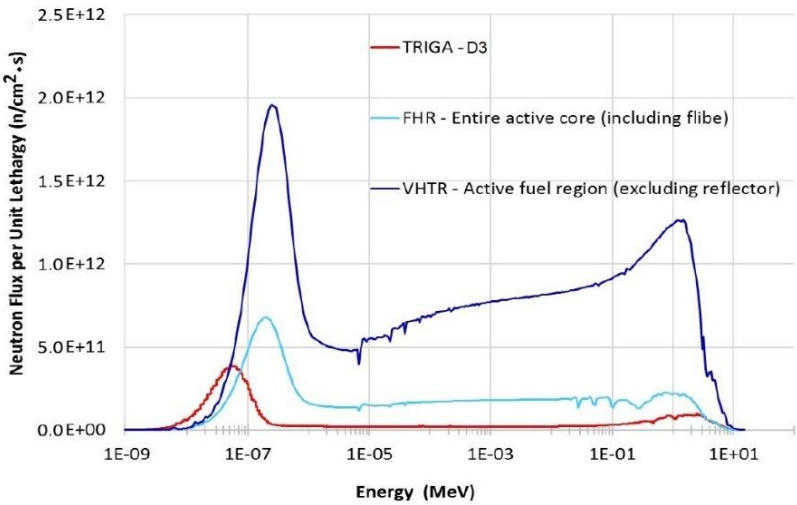

Figure 6-94 Representative energy spectra in FHR and VHTR and in TRIGA.

The spatial flux profile in the FHR core is analyzed through detailed simulations using MCNP. The mesh was created in a similar manner to the mesh used in the TRIGA flux mapping, though the FHR mesh is much larger to encompass the larger core. The mesh extends from -400 cm to + 400 cm in the X, Y and Z directions with 160 mesh bins in each direction, resulting in a 5 cm mesh spacing. The neutron mesh plot of the FHR core is shown in *Figure 6-95*.

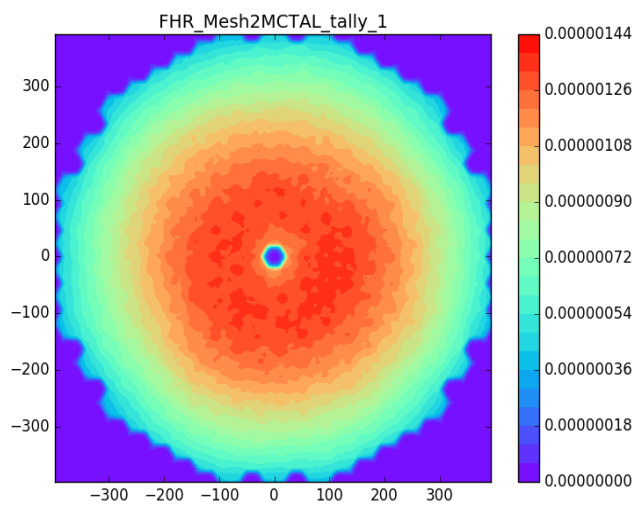

Figure 6-95 XY neutron mesh plot of the FHR core averaged over entire height of core.

Figure 6-96 shows the gamma-field mapping result of the flux mapping run with MCNP for FHR core to tally the gamma fluxes. This run simulated both neutron fields and photon (gamma) fields.

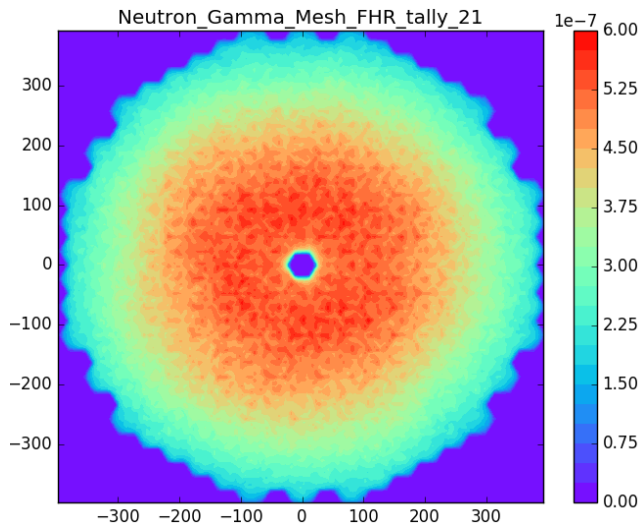

Figure 6-96 XY gamma mesh plot of the FHR core averaged over entire height of core.

Figure 6-96 shows an increase in the gamma fluxes in the FLiBe regions between the hexagonal fuel blocks, and in the region of FLiBe in the center of the blocks. This is likely because the FLiBe has a lower absorption cross section for gammas, thus allowing the gammas that reach it to persist for a longer periods of time. The gammas within these coolant regions will be the source for electrons that produce the Cherenkov radiation which could potentially be measured by an optical device or an array of devices placed above the core.

The scaling analysis is performed to provide full alignment of the TRIGA-based experiments to the FHR in-core conditions. Taking advantage of normal and pulsed modes of TRIGA reactor operation, this subtask allows developing startup testing protocols for validating transient response models as well as for use in the licensing program to demonstrate efficiency of visual instrumentation.

Recognizing principal design differences, local modification options in the TRIGA core are being evaluated and discussed with the objective of emulating advanced reactors. The considered modifications include various moderators, absorbers, and localized elevated temperatures in thermally isolated in-core enclosures.

The Texas A&M University's TRIGA (Training, Research, Isotope production, and General Atomics) Mark I research rector with a nominal operational power of 1MW is used as a representative example of a research reactor to emulate in-core conditions in VHTRs and in FHRs. *Figure 6-97* illustrates the TRIGA core layout showcasing availability of multiple irradiation locations; for example, D1, D2, D3 and D7. The light water environment is shown in blue.

The in-core locations provided by D3 and D7 offer opportunities to surround samples with fuel. The outer reflector locations D2 and D3 are configurable and offer less intrusive

irradiations in the graphite environment with higher degree of configurability. The principal locations of interest are designated as 1, 2, 3 in *Figure 6-97*:

- Location 1 (D3) is the fuel-surrounded sample location offering high neutron fluxes but more water-defined environments (graphite is only on one side);
- Location 2 (D2) is the graphite-surrounded sample location where neutron fluxes are somewhat lower, but the environment is fully defined by interactions in graphite;
- Location 3 (D1) is nearly equally influenced by proximity to graphite and water regions and is further from the fuel which means much lower fluxes and mixed energy distributions.

Native presence and proximity to graphite regions allow achieving flux profiling to emulate the in-core conditions of FHRs and VHTRs.

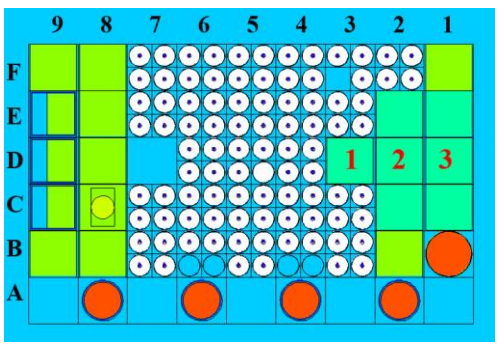

Figure 6-97 Details of the TRIGA core layout rendered using MCNP VISED editor.

Several factors can change neutronics. Some of the few are utilizing different moderators, varying the temperature of materials, introducing neutron absorbers and chemical shims, and finally, changing the tally location in the core will yield different spectrums. These factors were altered, results analyzed, and best-comparison and physically realizable determinations made. Since experiments are to represent in-core operating conditions of the FHR, the TRIGA core was altered in the D3 location. Various locations in the FHR were tallied so experiments can represent conditions seen at various points in the core.

The first alteration tested various moderators and the effects of the energy spectrum in the D3 location. For this, commonly used moderators were selected: graphite, beryllium, and deuterium oxide (heavy water). In addition, a small flux trap consisting of TRISO fuel particles was placed in location D3 to determine whether the effects were worth researching further. The altered TRIGA spectrums were not comparable to the FHR because the thermal peak energy was not sufficiently close to the FHR data. However, due to the FHR's graphite moderator, the graphite simulations most accurately represented the FHR spectrum shape in all cases, thus it remained in the D3 location as the moderator for future simulations.

Specific advantages of the TRIGA configuration are its operation without a pressure boundary, at ambient atmospheric pressure, and optical transparency of its pool environment, open water pool, that support testing of advanced optical sensors exploring feasibility of visual sensing options for FHRs and other advanced reactors with optically transparent environments. Relevant features of the TRIGA reactor are summarized in *Table 6-4*.

Table 6-4 Representative characteristics of the TRIGA reactor

Reactor Characteristics	Design Value
Power (MW_{th})	1
Pressure (atm)	1
Fuel Temperature (K)	600
Lattice	Square
Thermal Flux Peak Energy (MeV)	5.06E-8
Thermal Flux Peak (n/cm^2s)	3.93E11
Coolant	Light Water
Fuel	U-ZrH
Fuel Design	pin
Enrichment (wt %)	<20

Within the TRIGA core and its surrounding environment, the realistically achievable neutron fluxes range from 1E12 n/cm^2s to 1.4E13 n/cm^2s, with the peak in the D3 location of 3.93E11n/cm^2s. These rather low flux values challenge TRIGA applications for those studies where significant fluences are needed. Attaining large fluence values requires simply too long time. The TRIGA-based emulations of advanced reactors are sufficient for the studies aiming at demonstrating the presence of certain effects without pushing to find the corresponding performance limits.

Notably, because the TRIGA reactor is a light water reactor operating at much lower operational temperatures than any of the Generation IV reactors, engineering feasibility of a specialized test device has been investigated and has been proven in prior research efforts. (Tsvetkov, et al., USA (2011))

The so-called high temperature test furnace has been developed, constructed and successfully operated to emulate the VHTR high temperature gas-environment conditions within the TRIGA core. The furnace design was an adaptation of the original General Atomics furnace developed in 1970s for HTR fuel testing efforts in TRIGA reactors. (Tsvetkov, et al., USA (2011); Anderson, Langer, Baldwin, & Vanslager, ANS (1971))

The completed experimental program involving the test furnace is used for validation of the efforts presented in this paper. The demonstrated feasibility of this test device providing high temperature environments serves as the engineering basis for the

considered configuration options emulating advanced reactor environments in the present analysis.

The experimental test matrix includes the following efforts:

- TRIGA operational data. Capture and archiving operational data of the TRIGA reactor during its startup, normal operation and shutdown sequences using the reactor internal instrumentation and external visual instrumentation equipment.
- TRIGA pulse data. Capture and archiving operational data of the TRIGA reactor during its pulse mode operation using the reactor instrumentation and external visual instrumentation.
- TRIGA-FHR scaling. Bench top experiments and evaluations to develop a scaling approach between TRIGA conditions (single phase water) and FHR conditions (fluoride) recognizing optical characteristics as well as temperature differences.

The modeling and analysis efforts include:

- TRIGA model. Developing a detailed high fidelity TRIGA reactor model (Monte Carlo) that is capable to simulate performance characteristics represented by both reactor internal instrumentation data feeds and external visual equipment data feeds.
- TRIGA model validation. Validation efforts to demonstrate applicability of the developed coupled model and quantify uncertainties via comparison to the obtained experimental data.
- Visual vs. internal instrumentation. Development of the reconstruction approach and evaluation of visual instrumentation capabilities vs. reactor internal instrumentation to characterize reactor in-core states under transient conditions. Ability to capture local and global phenomena within the core will be assessed.

The archived data sets characterizing TRIGA operational characteristics collected and analyzed for completeness for use in support of visual instrumentation development efforts. The focus is on validation and capabilities needed for performance demonstration. The TRIGA operational data are used to capture operational states of the reactor.

Absorption hardening is a phenomenon that occurs in reactors when absorbers are present. When neutrons are absorbed due to the presence of absorbers, the thermal peak shifts and centers over a higher thermal energy.

This is because the lower energy neutrons are absorbed before reaching those lower energies; therefore, the probability distribution of neutron energies shifts to a higher energy before the absorption energy. For these reasons, absorber materials were placed in the irradiation location to determine whether the absorption hardening affect was great enough to shift the TRIGA's spectrum to represent the FHR.

Two common thermal absorbers were used in simulations to determine the usability of the absorption hardening phenomenon: ^{10}B and ^{113}Cd. The graphite in location D3 was doped with 0.01% and 0.001% of both absorbers to determine their effectiveness. Unfortunately, the thermal peaks did not shift enough to center around the FHR thermal energies.

Since previous attempts did not shift the thermal peak energies enough, changing the location of the tally was tested. Locations D3, D2, and D1 (locations 1#, #2, and #3 respectively) are shown in *Figure 6-98*.

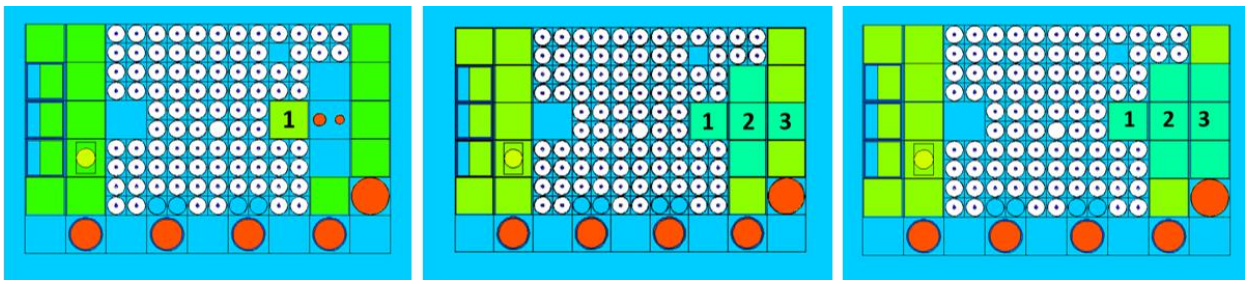

Figure 6-98 Top-down view of TRIGA reactor showing tally locations #2 and #3.

Additional high-temperature graphite at 900 K and 2500 K was inserted into empty locations shown by turquoise blocks. This was done to better represent graphite-moderated cores. The results of these runs are shown in *Figure 6-99*.

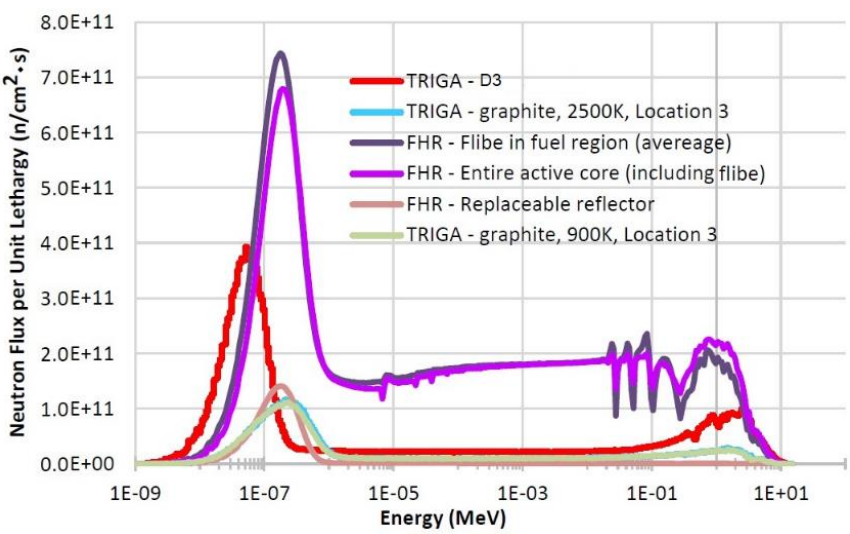

Figure 6-99 Various tally locations and temperatures in TRIGA compared to FHR. Best-comparison and physically realizable comparisons in TRIGA compared to FHR.

Tallying in D1 (location #3) at both 900 K and 2500 K most closely matches thermal energies with the FHR benchmark data in all cases (active core region, flibe, assembly

graphite, and reflectors). From this, it is concluded that adding graphite and increasing the temperature of the graphite in an experimental setup will obtain the operating characteristics needed for FHR comparison. This is shown visually in *Figure 6-99* where the peaks nearly line up vertically.

The 2500 K run in D1 lines up best with the FHR flibe and FHR reflectors while the 2500 K run with additional high-temperature graphite compares best with the FHR active core and FHR graphite comparisons. However, the 900 K run with additional high-temperature graphite is the best, physically realizable comparison. The centerline energy of this run is slightly higher than the true FHR comparisons, but the experimental setup can be adjusted to center around the corresponding centerline energies by either decreasing the amount of surrounding graphite or slightly decreasing the temperature.

The ratio of fluxes is a particular interest because it facilitates the conversion between TRIGA experimental results and FHR predicted results. *Figure 6-100* shows the best, physically realizable similarity factors between the comparable TRIGA data and the FHR regions of interest. Most factors in all regions fall below 20 with the permanent reflector factors below one even in the thermal region.

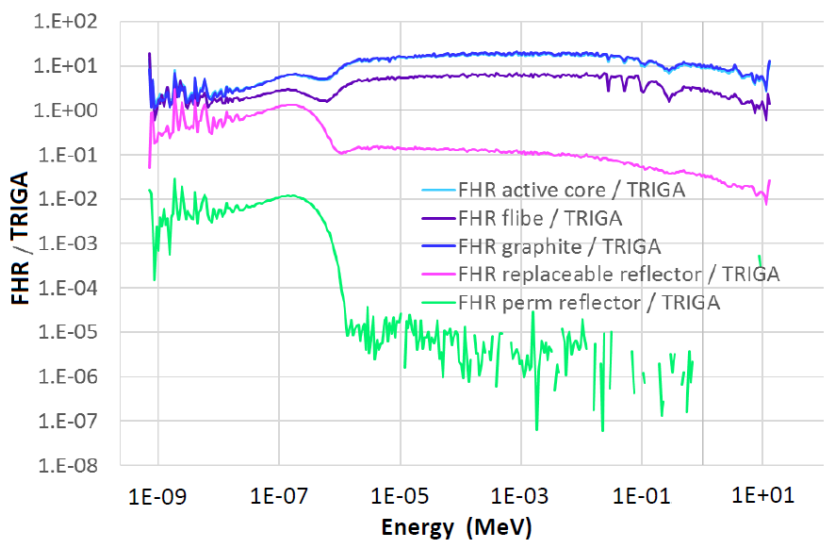

Figure 6-100 : Physically realizable similarity factors for FHR vs. TRIGA.

The average similarity factor between 8.18E-8 ≤ E ≤ 1.30E1 MeV and without zero indices (excluding the permanent reflector similarity factors) is 6.60. This is only 2% different from the best-comparison average similarity factor thus validating that the physically realizable case can be used instead of the best-comparison case.

Thus, TRIGA reactor can be used for experiments focused on FHRs given the nature of the reactor's core design, and it will provide adequate and consistent neutronics (for at least two years). The TRIGA core must be altered to represent the FHR features. The data shows

that the addition of high-temperature graphite, both at 900 K and 2500 K, in the TRIGA's D1 and D2 locations can adequately represent the FHR. The reactor physics similarity factors calculated from the best and most physically realizable results will facilitate converting experimental results into useful data. This will aid in determining the strenuous operating environment equipment for advanced reactors will see.

Based on the collected data and performed evaluations, the FHR and VHTR in-core characteristics could be reliably emulated in graphite enclosures maintained at 900 K. It is possible to use the same location to represent various regions and features within the advanced reactor core. Conversion factors can be introduced to relate TRIGA results to advanced reactor features. Overall, the effort evaluated a readily available and accessible academic pathway towards advanced reactors supporting critically needed validation and licensing efforts.

6.15. Conclusions

The completed 3-year effort was focused on development, evaluations, and demonstrations of the FHR instrumentation options together with visual/optical reactor performance characterization methods using the TRIGA reactor a prototypic optically (visually) accessible reactor environment. The actual reactor operation data have been compiled and used to support sensitivity studies as well as model validation efforts. Performed simulations indicate significant noise levels that potentially may complicate reconstructions of localized values of in-core parameters in FHRs.

Focusing specifically on Cherenkov radiation characteristics, resolution of local 3D in-core features and perturbations through Cherenkov radiation measurements has been investigated. The optical under-water imaging experiments were conducted in Year 2 in the TRIGA pool to assess capabilities to capture and characterize in-core transient conditions. The TRIGA/FHR scaling and similarities evaluations are performed to take advantage of the TRIGA tests in the FHR design development efforts. Fiber optics sensing is a basis instrumentation approach allowing integration of mixed radiation fields quantifying performance and to account for sensitivity dependencies of such measurable quantities as temperature, stress, neutron and gamma fluences in sensor performance simulations. Fiber optics experimental data are being used in the project to quantify probe performance uncertainties.

Based on the collected data and performed evaluations, the FHR and VHTR in-core characteristics could be reliably emulated in graphite enclosures maintained at 900 K. It is possible to use the same location to represent various regions and features within the advanced reactor core. Conversion factors can be introduced to relate TRIGA results to advanced reactor features. Overall, the analysis offers a readily available and accessible academic pathway towards advanced reactors supporting critically needed validation and licensing efforts.

The project accomplishments include developing two 3D reconstruction methods, assessment of emulation options for scaling experimental results from TRIGA to FHR

conditions, and design of the multiphysics sensor probe concept realizing optical and mixed-field sensing capabilities within a single integrated probe configuration. One of the developed 3D reconstruction methods assumes exclusive fiberoptics-based technology options. The 2nd method is based on the integration of multi-field distributed sensing approaches using fiberoptics-based and optical (image-based) technology options.

With a response function distributed over a spatial range, the use of fiber optics could offer a significant advance in radiation sensing. Providing a multitude of radiation measurement data points could support a new type of reactor power monitoring with reconstruction capabilities in 3D from a 3D layout of fiber optics.

The obtained results demonstrate efforts towards developing methods allowing taking advantage of optical transparency while recovering in-core 3D information with high feature resolution. Results obtained for fiberoptics sensors suggest future use of this sensor type to supplement optical sensing. However, extensive R&D efforts are required. Similarity achievability has been investigated to assess usefulness of research reactor environments such as TRIGA in FHR-related R&D. The obtained results support developing methods allowing conversion and correlation of TRIGA data to FHRs.

The work is significant well beyond applications for FHRs. As already noted above, the project addressed the grand challenge of 3D high-resolution characterization needs to support development and licensing of advanced reactors. Findings and developed solutions are directly applicable to all advanced reactors. They have particular benefits for systems with optical in-core access.

6.16. References

Abdukadyrova, I. K. ((2005)). Effect of Neutron Irradiation on the Structure and Optical Properties of Sapphire. *Inorganic Materials, 41*(10), 1080-1084.

Ames, D. E., & Tsvetkov, P. V. ((2008)). Benchmark Efforts to Support Studies of Advanced VHTRs. *Proc. 4th Intern. Conf. HTRs, HTR2008-58206.* ASME.

Anderson, E. E., Langer, S., Baldwin, N. L., & Vanslager, F. E. (ANS (1971)). An In-Core Furnace for the High-Temperature Irradiation Testing of Reactor Fuels. *Nucl. Techn., 11*, 259.

Arakani, M., & Gharib, M. ((2007)). *Design and Construction of an Independent Channel for Tehran Research Reactor Power Measurement Using Cherenkov Detector.* Tehran: MS Thesis, Azad University, Research and Science Department.

Arakani, M., & Gharib, M. ((2009)). Reactor Core Power Mesurement Using Cherenkov Radiation and Its Application in Tehran Research Reactor. *Ann. Nucl. Eng., 36*, 869-900.

Boland, J. F. ((1970)). *Nuclear Reactor Instrumentation (In-Core).* New York, NY: Gordon and Breach.

Connolly, K. J., Rahnema, F., & Tsvetkov, P. V. (Elsevier (2015)). Prismatic VHTR Neutronic Benchmark Problems. *Nucl. Eng. Design, 285*, 207.

Drinkwater, B. W., & Wilcox, P. D. ((2006)). Ultrasonic Arrays for Non-destructive Evaluation: A Review. *NDT&E International, 39*, 525-541.

Durkee, J. W. ((2013)). *MCNP6 Cherenkov Radiation.* Los Alamos, New Mexico: 2013-07-17, Los Alamos National Laboratory.

Generation IV International Forum. ((2016)). *Generation IV Annual Report.* GIF.

Giford, D., Soller, B., Wolfe, M., & Froggatt, M. ((2009)). Distributed Fiber-Optic Temmperature Sensing Using Rayleigh Backscatter. *LUNA Technologies*.

Hashemian, H. M. (InTech (2011)). Nuclear Power Plant Instrumentation and Control. In *Nuclear Power - Control, Reliablity, and human Factors* (pp. 49-66). Rijeka, Croatia.

Holcomb, D. E., Ilas, D., Varma, V. K., Cisneros, A. T., Kelly, R. P., & Gehin, J. C. (2011). *Core and Refueling Design Studies for the Advanced High Temperature Reactor (ORNL/TM-2011/365).* Oak Ridge, TN: Oak Ridge National Laboratory.

Holcomb, D. E., Peretz, F. J., & Qualls, A. L. ((2011)). *Advanced High Temperature Reactor Systems and Economic Analysis: September 2011 Status.* ORNL/TM2011/364: ORNL.

INL. ((2007)). *Next Generation Nuclear Plant Pre-conceptual Design Report, INL/EXT-07-12967.* Idaho: INL.

(2014). *Integrated Approach to Fluoride High Temperature Reactor (FHR) Technology and Licensing Challenges.* U.S. Department of Energy Nuclear Energy University Programs.

International Atomic Energy Agency. ((1999)). *Modern Instrumentation and Control for Nuclear Power Plants - a Guidebook.* Vienna, Austria: IAEA.

Jang, K. W., Yagi, T., Pyeon, C. H., Yoo, W. J., Shin, S. H., Misawa, T., & Lee, A. B. ((2013)). Feasibility of Fiber-Optic Radiation Sensor Using Cerenkov Effect for Detecting Thermal Neutrons. *Optics Express, 21*(12).

Janz, G. J. ((1967)). *Molten Salts Handbook.*

Jiang, X., Kim, K., Zhang, S., Johnson, J., & Salazar, G. ((2014)). High-Temperature Piezoelectric Sensing. *Sensors, 14*, 144-169.

Johns, J. ((2011)). A Distributed Fiber Optic Sensor Network for Online 3D Temperature and Neutron Fluence Mapping in a VHTR Environment. *Texas A&M University*.

Leppanen, J. ((2010)). Performance of Woodcock Delta-Tracking in Lattic Physics Applkications Using the Serpent Monte Carlo Reactor Physics Burnup Calculation Code. *Ann. Nucl. Eng., 37*(5), 715-722.

Luna. ((2016)). *Luna Sensors.*

Measurement of the Refractive Index of Distilled Water from the Near-Infrared Region to the Ultraviolet Region. ((2007)). *Applied Optics, 46*(18), 3811-3820.

Perrotton, C. ((2013)). A Reliable, Sensitive and Fast Optical Fiber Hydrogen Sensor Based on Surface Plasmon Resonance. *Optics Express, 21*(1), 382-390.

Petrie, C. M. ((2013)). *Characterization of the Performance of Sapphire Optical Fiber in Intense Radiation.* The Ohio State University.

physics.nist.gov ESTAR database. (n.d.).

Pioro, I. ((2016)). *Handbook of Generation IV Nuclear Reactors.* Woodhead Publishing, Elsevier.

Principles of Optics. ((1980)). New York: Pergamon Press.

Quickenden, T. I., & Irving, J. A. ((1980)). The Ultraviolet Absorption Spectrum of Liquid Water. *The Journal of Chemical Physics, 72*(4416).

Rahnema, F., & Others. (2018). Phenomena, Gaps, and Issues for Neutronics Modeling and Simulation of FHRs. *Annals of Nuclear Energy*(IN THIS ISSUE).

Rahnema, F., Edgar, C., Zhang, D., & Petrovic, B. (2016). *Phenomena Identification and Ranking Tables (PIRT) for Fluoride High-Temperature Reactor (FHR) Neutronics.* Atlanta, GA: Georgia Institute of Technology. Retrieved from https://smartech.gatech.edu/handle/1853/55812

Rahnema, F., Petrovic, B., Edgar, C., Zhang, D., Avigni, P., Huang, M., & Terlizzi, S. (2015). *Whitepaper: The Current Status of the Tools for Modeling and Simulation of Advanced High Temperature Reactor Neutronics Analysis Modeling.* Atlanta, GA.

Rippon, S. E. ((1963)). Cherenkov Detectors for the Measurement of Reactor Power. *Nucl. Instr. Methods, 21*, 192-196.

Ritchie, J. ((2010)). *Pressure Measurement in a High Temperature Molten Salt Loop.* Knoxville, TN: University og Tennessee.

Segelstein, D. J. ((1981)). *The Complex Refractive Index of Water, MS Thesis in Physics.* Kansas City, Missouri: University of Missouri-Kansas City.

Singh, P., & Others. (2018). Phenomena Identification and Ranking Tables (PIRT) Study for Advanced High Temperature Reactor Structural Materials. *Annals of Nuclear Energy*(IN THIS ISSUE).

Singh, P., Chan, K., & Rahnema, F. (2017). *Phenomena Identification and Ranking Tables (PIRTs) Report for Material Selection and Possible Material Degradation Mechanisms in FHR.* Atlanta, GA.

Sun, X., & Others. (2018). A Thermal Hydraulic Phenomena Identification and Ranking Table Study for Advanced High Temperature Reactor. *Annals of Nuclear Energy*(IN THIS ISSUE).

Sun, X., Yoder, G., Christensen, R., Shi, S., Lin, H.-C., Wu, X., & Zhang, S. (2016). *Thermal Hydraulic Phenomena Identification and Ranking Tables (PIRTs) for Advanced High-Temperature Reactor (AHTR).*

Tsvetkov, P. V., Bragg-Sitton, S. M., Johns, J. M., Lewis III, T. G., Alajo, A. B., & Johnson, M. P. (USA (2011)). Distributed Sensor Networks for Online 3D In-Core Monitoirng in VHTR Environments. *Trans. Amer. Nucl. Soc., 104*, 931.

Varma, V. K., Holcomb, D. E., Peretz, F. J., Bradley, E. C., Ilas, D. Q., & Zaharia, N. M. (2012). *AHTR Mechanical, Structural, and Neutronic Preconceptual Design (ORNL/TM-2012/320).* Oak Ridge, TN: Oak Ridge National Laboratory.

Varma, V., Holcomb, D., Peretz, F., Bradley, E., Ilas, D., Qualls, A., & Zaharia, N. (2012). *AHTR Mechanical, Structural, and Neutronic Preconceptual Design.* Oak Ridge, TN: ORNL.

Wei Huang, Lifang Tian, Changfeng She, Feng Jiang, Haiyang Zheng, Wenxin Li, Guozhong Wu, Dewu Long, Qingnuan Li. (2014). Electrochemical Behavior of Europium(III)-Europium(II) in LiF-NaF-KF Molten Salt. *Electrochimica Acta, 147*, 114-120.

Wen, J., Peng, G. D., Luo, W., Xiao, Z., Chen, Z., & Wang, T. ((2011)). Gamma Irradiation Effect on Rayleigh Scattering in Low Water Peak single-Mode Optical Fibers. *Optics Express*.

X-5 Monte Carlo Team. (Los Alamos National Laboratory (2018)). MCNP - A General Monte Carlo N-Particle Transport Code, Version 6, User Manual.

Yang, M., & Dai, J. ((2014)). Fiber Optic Hydrogen Sensors: a Review. *Photonic Sensors, 4*(4), 300-324.

Zhou, Q. a. ((2011)). Pressure Sensor Based on the Fiber-Optic Extrinsic Fabry-Perot Interferometer. *Photonic Sensors, 1*(1), 72-83.

7. Qualification of Alloys for Structural Applications

7.1. Corrosion Resistance of Alloys in Molten FLiBe and FLiNaK

7.1.1. Experimental Procedures

7.1.1.1. Materials Tested

Static exposure tests of selected commercial nickel based alloys and austenitic stainless steels in molten FLiNaK were conducted. Apart from commercial alloys used in this study, pure elements were also tested to characterize their corrosion resistance in FLiNaK. The nickel based alloys were Haynes 230, Haynes 244, Hastelloy N, Inconel 600 and commercially pure nickel Ni 200. The austenitic stainless steels were 304L, 316L, 321, and 347. Alumina forming austenitic (AFA) stainless steels developed at Oak Ridge National Laboratory, designated OC-5, OC-8 and OC-T were also included.The composition each alloy are listed in *Table 7-1*.

*Table 7-1 Nominal compositions of Ni based alloys and stainless steels and other materials tested in this study * indicates XRF measurement*

	Ni	Cr	Mo	W	Co	Fe	Mn	Si	C
Haynes 230	59.8	21.9	1.23	14	0.22	0.97	0.51	0.37	0.1
Haynes 244	61.9	7.97	22.6	6.13	<0.05	0.97	0.27	0.05	<0.001
Hastelloy N	70.7	7.2	16.8	<0.1	<0.1	4.09	0.48	<0.302	0.06
Inconel 600$^{(nom)}$	72.0	15.5	0	0	0	8.0	1.0	0.5	0.15

	Fe	Cr	Mo	Ni	Mn	Ti	Nb	Si	C
SS 304L*	70.8	18.1	0.36	8.1	1.7			0.5	
SS 321*	71.2	17.0	0.34	9.0	1.5	0.2		0.4	
SS 347*	70.3	17.5	0.24	9.0	1.4		0.6	0.6	
SS 316L	67.8	17.6	2.2	11.4	0.97			0.59	0.02

	Fe	Cr	Mn	Ni	Cu	Al	Nb	Ti	Mo
OC-5	bal	13.84	1.99	25.02	0.51	3.06	1.02	0.05	2.00
OC-8	bal	18.69	0.15	32.06	0.15	3.10	3.32	0.05	0.15
OC-T	bal	13.80	0.10	35.07	0.11	3.04	2.92	2.02	0.11
Ni-200									
Cr†		99.9							

7.1.1.2. FLiNaK Salt Preparation

High purity LiF (99.85%), NaF (99.99%), and KF (99%) powders were individually heated to 200°C for 4 hours to drive off residual moisture. These salts were then weighed and mixed in the proper proportions to create FLiNaK. The mixed powder was placed in a graphite crucible and fused by heating to 600°C for 2 hours. After cooling, the resulting FLiNaK puck was removed from the crucible and crushed into small pieces. The entire This homogenized FLiNaK was used for the corrosion tests.FLiNaK production procedure was done in an oxygen and moisture controlled glovebox.

7.1.1.2.1. FLiNaK moisture content control and measurement

Ouyang et.al have shown that higher moisture content in FLiNaK increases corrosion of Ni based alloys [2]. Because FLiNaK is hygroscopic, measurement and control of FLiNaK moisture content is necessary. Heating as a method of drying FLiNaK was investigated. DSC and TGA of FLiNaK was conducted in order to determine the melting temperature and measure mass loss during heating. This information is useful for identifying appropriate drying temperatures and estimating the original moisture content in the FLiNaK.
High purity LiF, NaF, and KF powders (46-11.5-42 mol%) were weighed and mixed in laboratory air, then poured into a 10ml alumina crucible and heated to 750°C in laboratory air for 24h. After heating, the FLiNaK was retrieved from the crucible, crushed, and stored in an airtight glass vial. A small amount of this FLiNaK was placed into an alumina DSC pan for analysis in a PerkinElmer Simultaneous Thermal Analyzer (STA) 6000 with N_2 cover gas. The sample was heated from 35 to 750°C at a constant 10°C/min ramp rate.
Figure 7-1 shows the percent weight change and heat flow during the temperature scan. Significant mass loss was observed up to 115°C with a corresponding endothermic heat flow. Above this temperature, only slight mass loss occurred. This indicates that sustained heating at temperatures above 115°C will remove the majority of water absorbed in FLiNaK.

A Mettler-Toledo v20 volumetric Karl-Fischer titrator was used to quantify moisture content in FLiNaK and in separate component salts. Anhydrous methanol solvent and AQUASTAR Combititrant 5 were used. A 0.2 g sample of salt was dissolved in the solvent for each measurement.

The dried FLiNaK described in the previous section was 0.12 wt% H_2O measured by this method. However, the true FLiNaK moisture content is expected to be lower because of contamination by atmospheric moisture and because the measurement is at the lower limit of the instrument's measurement range.

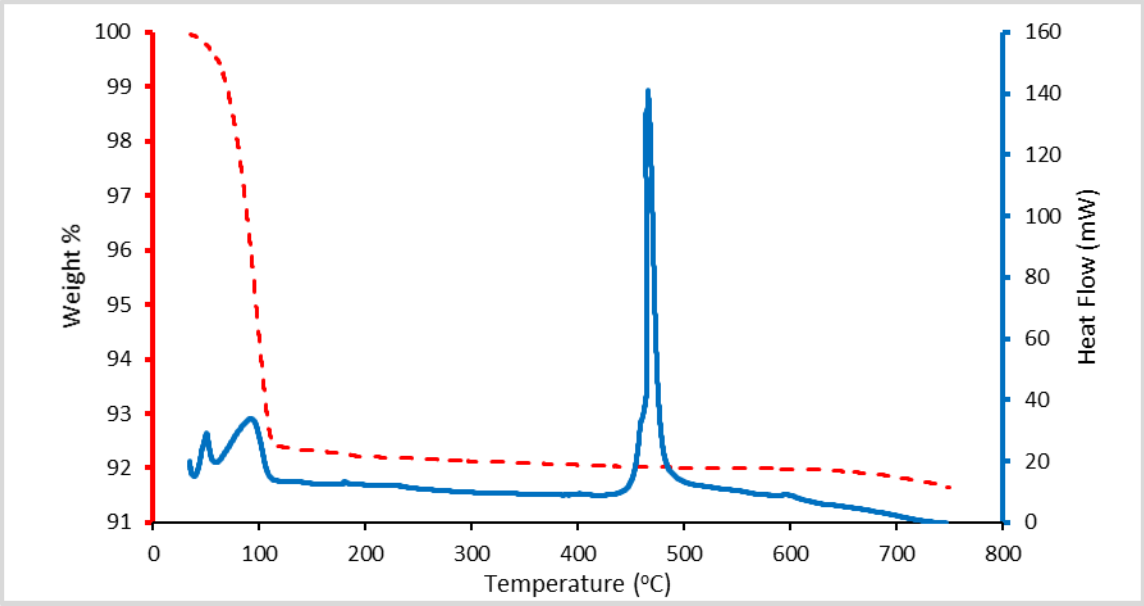

Figure 7-1 Figure 8-2 DSC and TGA of FLiNaK. Maximum heat flow was measured at 465.9°C.

7.1.1.2.2. Atmosphere control

A Vacuum Atmospheres Company HE-43-2 glovebox was acquired
Figure *7-2*. Moisture and oxygen levels are controlled to less than 1ppm by use of gas analyzers and a catalyst bed. In the initial stages of this project, while this glovebox was being commissioned, as a temporary measure, glove bags and a rudimentary glove box were used instead for initial tests to establish procedures requiring inert atmosphere.

Static exposure tests were conducted under argon cover gas in capsules. Crucibles containing FLiNaK, prepared under inert atmosphere, and an alloy sample were placed into a capsule and sealed in the glove box under argon. The capsule design consists of a SS 304 pipe nipple sealed by end caps (
Figure 7-3). The sealed capsules were placed inside the SS 304 box shown in
Figure *7-4*. During these early tests, a positive pressure of argon was maintained in the box by feeding the gas through an inlet on the lid.

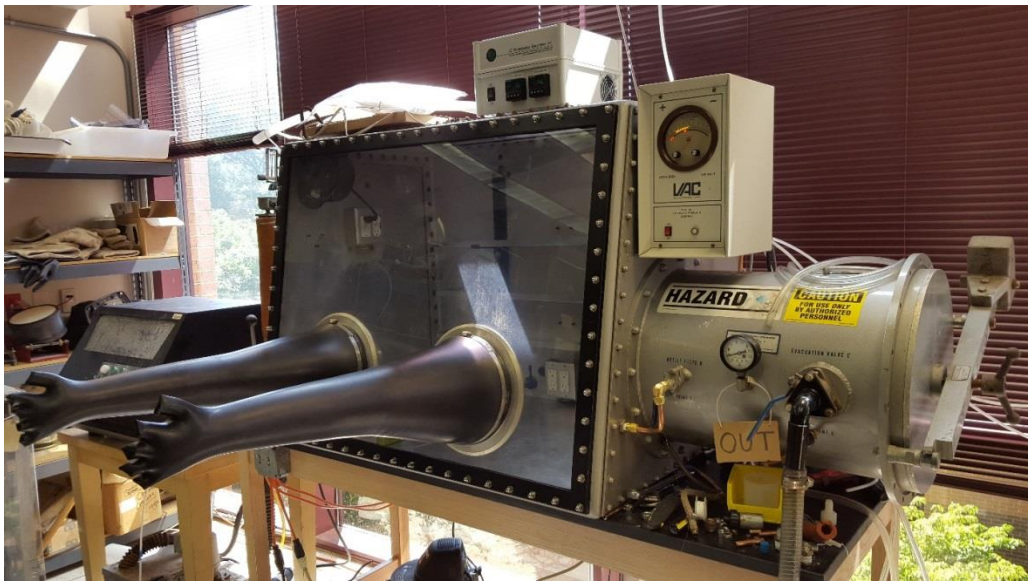

Figure 7-2Vacuum Atmospheres Company HE-43-2 glovebox with catalyst bed and gas analyzer.

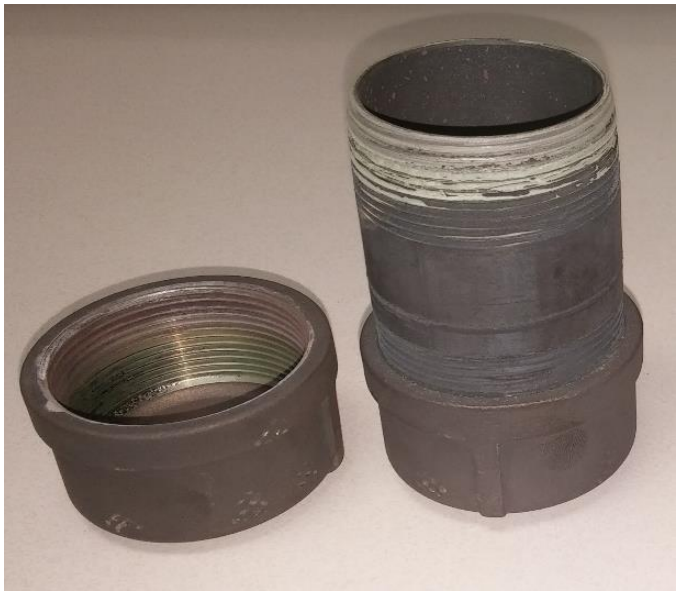

Figure 7-3 SS 304 capsule for static exposure tests.

Figure 7-4 SS 304 box with inlet for argon cover gas.

7.1.1.3. Static Corrosion Tests

Sample materials were cut into 1 cm by 1 cm samples. All samples were ground from 120 to 1000 grit, then rinsed with deionized water and acetone. Initial dimensions and weight of each alloy sample were recorded. Selected samples were pre-oxidized as described in later sections.

Unless otherwise specified LiF (99.85%), NaF (99.99%), and KF (99%) purity were used for making FLiNaK for corrosion tests in this study. The entire FLiNaK production procedure was done in an oxygen and moisture controlled glovebox.

The samples and high purity graphite crucibles (8ml, 5ppm ash) were heated in a 60°C oven for 1 hour just before they were introduced into the glovebox to drive off adsorbed moisture. To further eliminate moisture sources, the graphite crucibles were then fired at 900°C under a flow of a reducing gas mixture (4% H_2 – balance Ar) for 8 hours. A sample was placed into each crucible and covered in 9.17g of FLiNaK pieces. The crucibles were loaded into a crucible rack, which was lowered into a vertical furnace at room temperature. This experimental setup is shown in *Figure 7-5*. The furnace setpoint was raised to 700°C, and held for the desired duration.

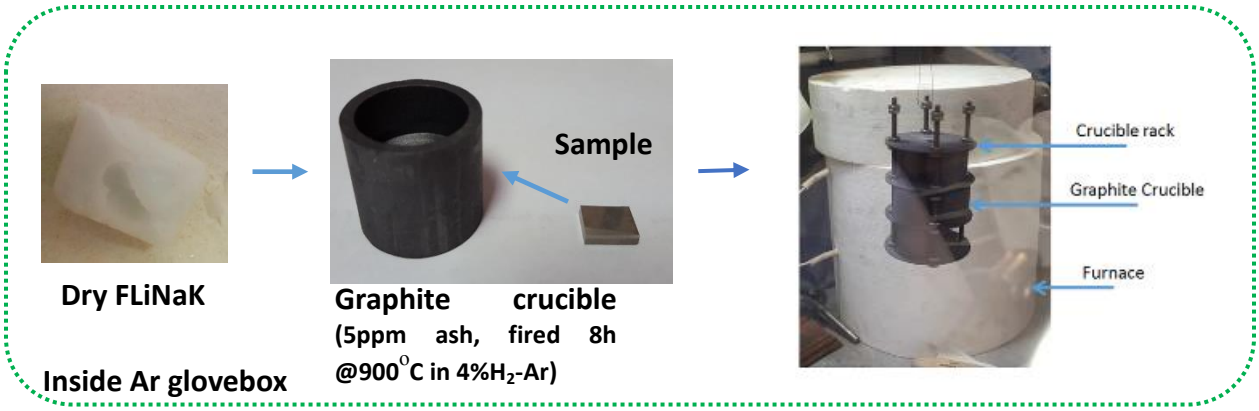

Figure 7-5 Experimental setup for exposure tests inside an Ar atmosphere glovebox.

After cooling to room temperature, the crucibles were removed from furnace and crushed with a hammer to fragment the FLiNaK. The alloy samples were retrieved from the FLiNaK and cleaned ultrasonically in deionized water, acetone, and then ethanol. After drying, the samples were weighed using a high precision balance. Selected samples were analyzed by SEM, EDS, Raman spectroscopy and XRD.

7.1.2. Results - Corrosion Resistance of Alloys in Molten FLiNaK

7.1.2.1. Static Exposure Test of Alloys in FLiNaK in Glovebox using High Purity Salts

Impurity content in molten fluorides is known to have a large influence on corrosion rates. [1] In an effort to minimize impurity effects in corrosion tests, FLiNaK was produced from 99.85% or higher purity salts, and a new experimental setup was devised to conduct tests inside an oxygen and moisture controlled glove box. Ni base alloys Hastelloy N, Haynes 244, Haynes 230, and austenitic stainless steels 316L, 304L, 321, and 347 were selected for this series of exposure tests to compare with our previous results. The exposure duration was 100 hours and followed the procedure described in 7.1.1.

The SEM cross section of Hastelloy N shown in *Figure 7-6*, shows very little attack. Cr depletion depth was under 1μm. Some voids were observed, but were only sparsely distributed near the surface.

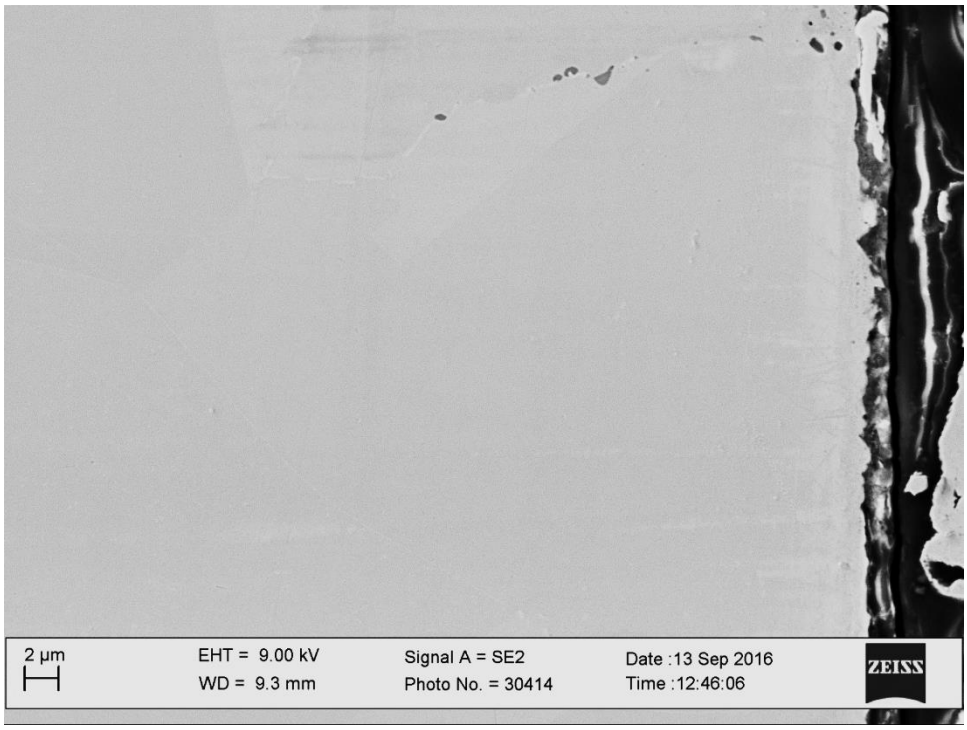

Figure 7-6 Cross sectional SEM image of Hastelloy N exposed to FLiNaK at 700°C.

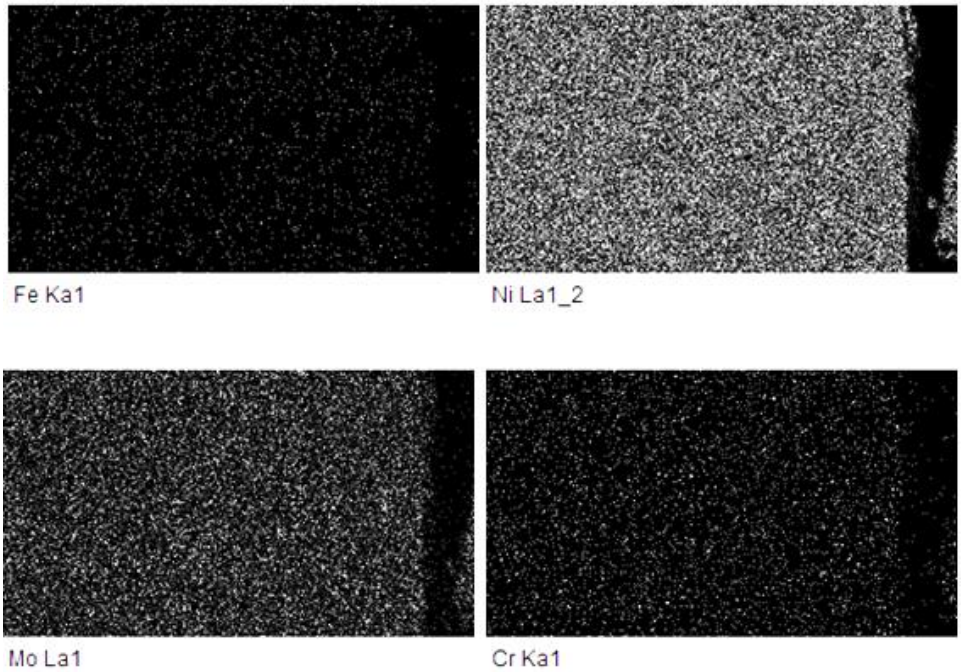

Figure 7-7 EDS map of Hastelloy N cross section for Fe, Cr, Mo, and Ni.

As shown in Figure 7-8, voids formed to a depth of roughly 10 μm in Haynes 244. These voids do not appear to have formed along grain boundaries, indicating that the Cr transport to the surface is dominated by bulk diffusion. Cr depletion was observed in the void layer on the EDS map (Figure 7-8). However, the depth of the void layer was not uniform. In some areas, the void layer was under 1μm in thickness.

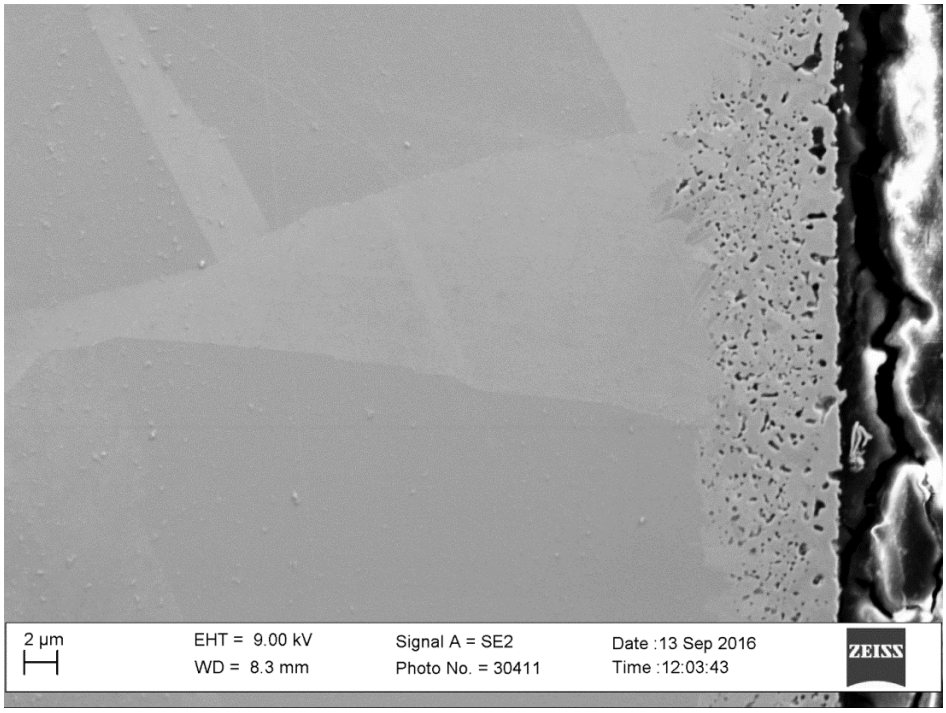

Figure 7-8 Cross sectional SEM image of Haynes 244 exposed to FLiNaK at 700°C.

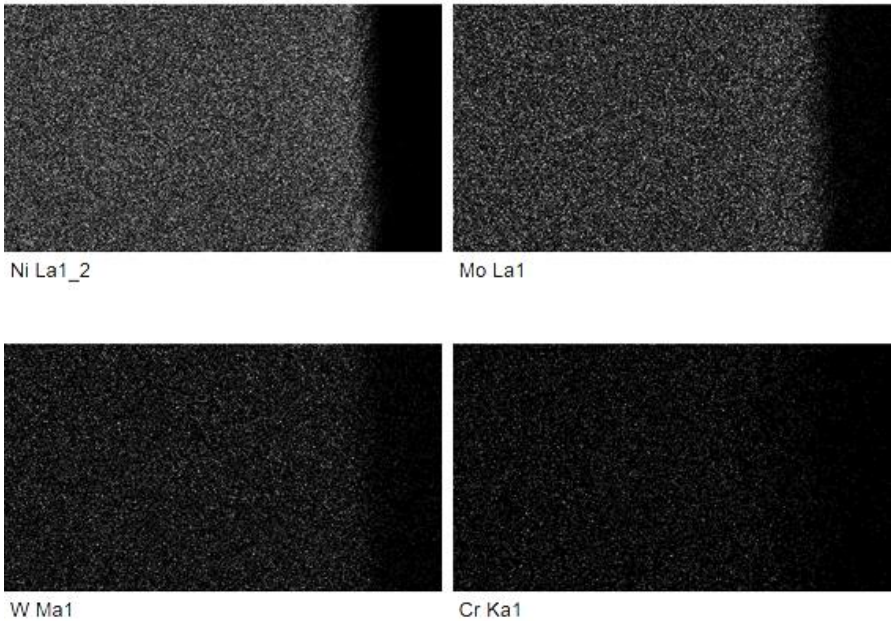

Figure 7-9 EDS map of Haynes 244 cross section for Mo, Cr, W, and Ni.

As shown in *Figure 7-9*, Haynes 230 experienced much deeper attack than Hastelloy N and Haynes 244, as shown in *Figure 7-10* due to its greater Cr content. Like in Haynes 244, generally the voids do not appear to have formed along grain boundaries, indicating that the Cr transport to the surface is dominated by bulk diffusion.

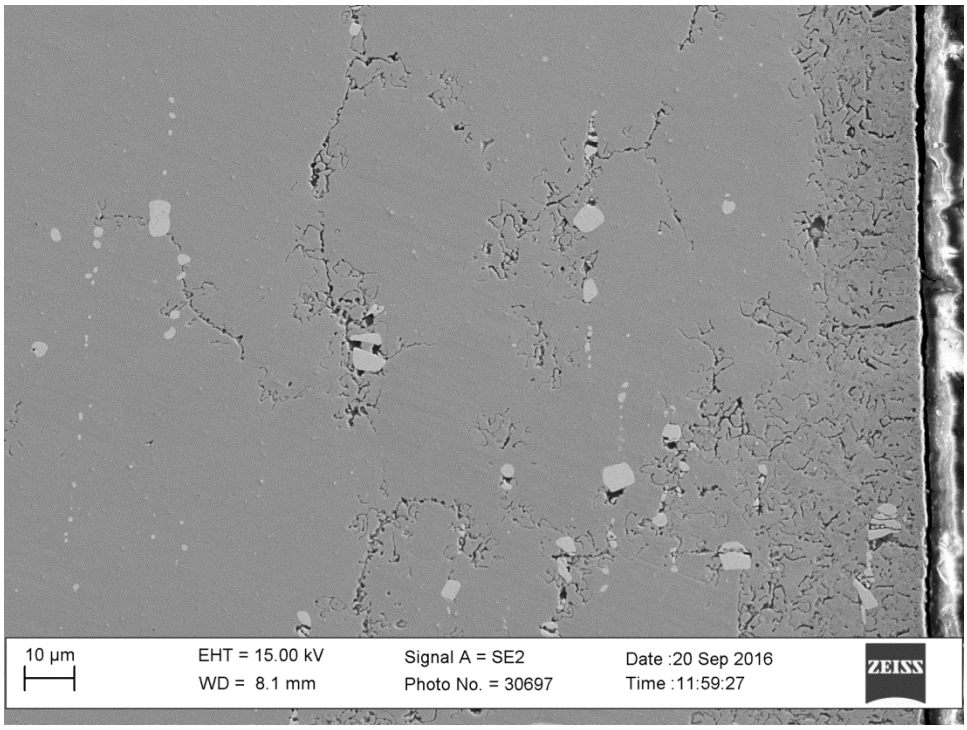

Figure 7-10 Cross sectional SEM image of Haynes 230 exposed to FLiNaK at 700°C.

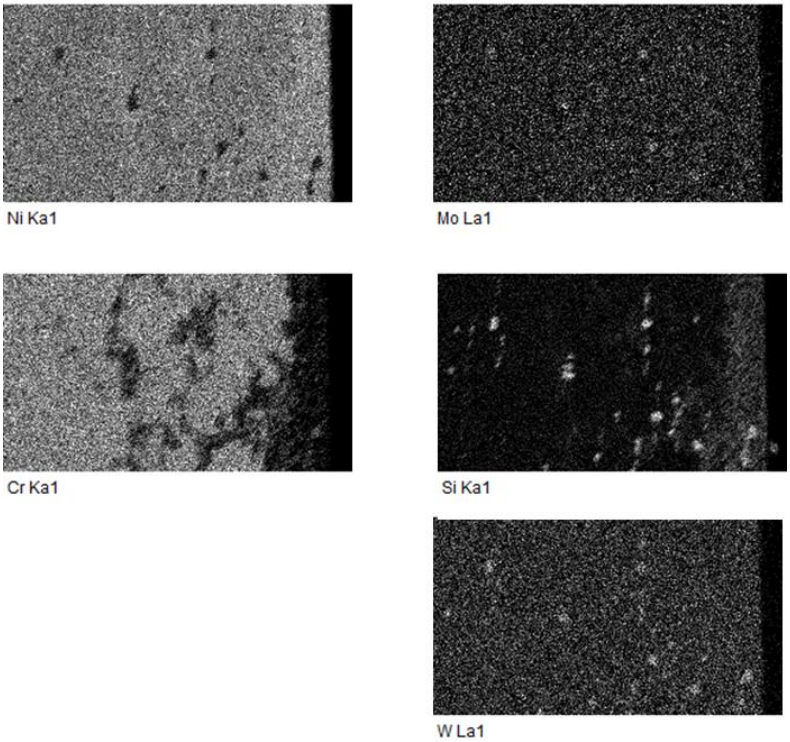

Figure 7-11 EDS map of Haynes 230 cross section for Mo, Cr, W, Si, and Ni.

SS 316L (*Figure 7-12*) experienced significant grain boundary attack. The EDS maps shown in *Figure 7-13* reveal that grain boundaries near the surface showed depletion of all alloying elements except Ni, which was instead enriched. Cr depletion appears to be controlled by transport through grain boundaries and not significantly through bulk diffusion.

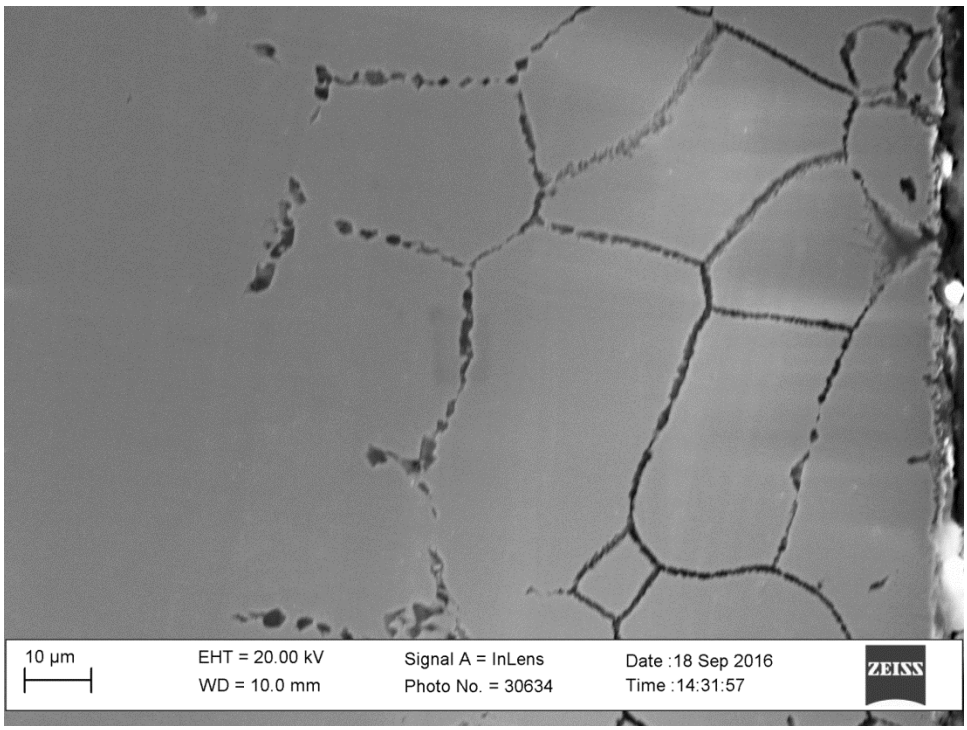

Figure 7-12 Cross sectional SEM image of SS 316L exposed to FLiNaK at 700°C.

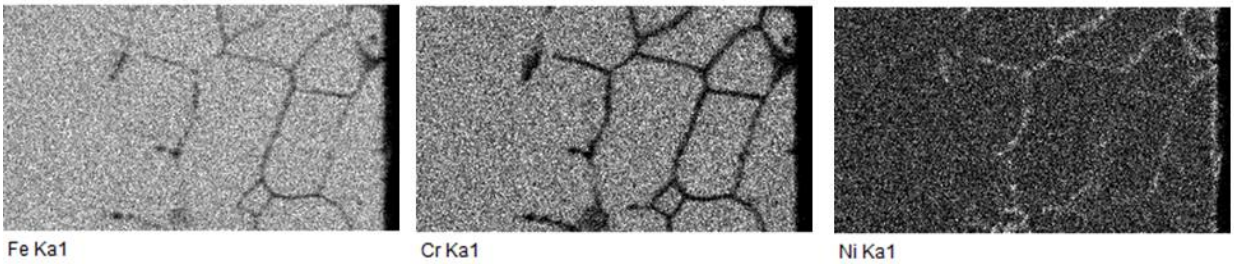

Figure 7-13 EDS map of SS 316L cross section for Fe, Cr, and Ni.

SS 304L (*Figure 7-14*) also experienced significant grain boundary attack, however the depth of attack was less than that of 316L. Voids tended to grow at grain boundaries. Cr depletion was observed in the voids located at the grains. The EDS maps shown in *Figure 7-15* reveal that grain boundaries near the surface showed depletion of all alloying elements

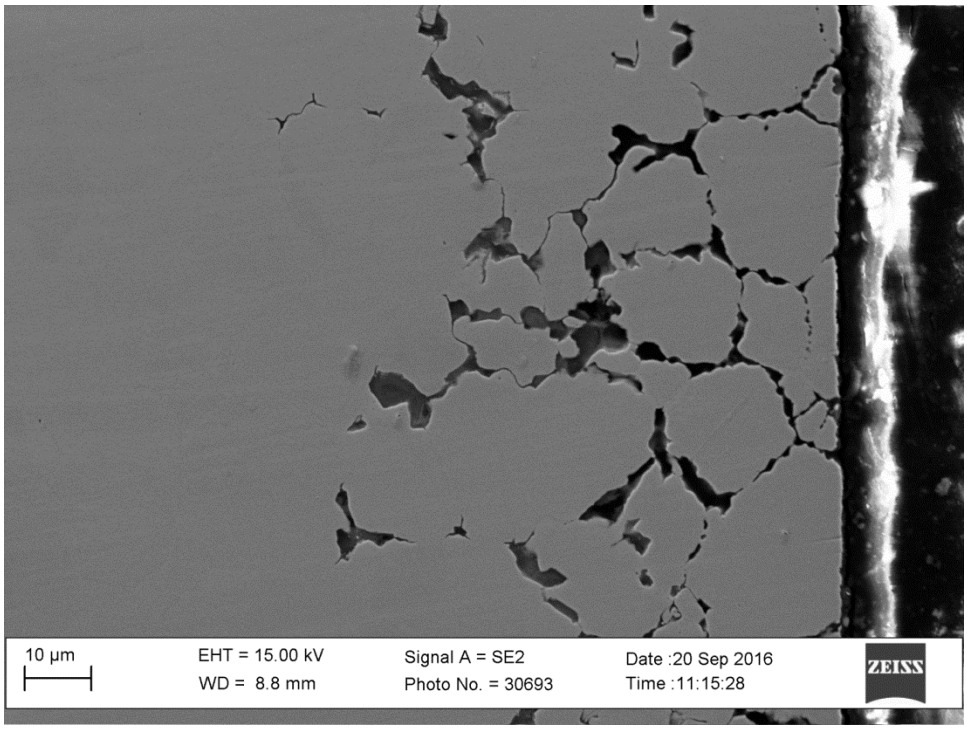

Figure 7-14 Cross sectional SEM image of SS 304L exposed to FLiNaK at 700°C.

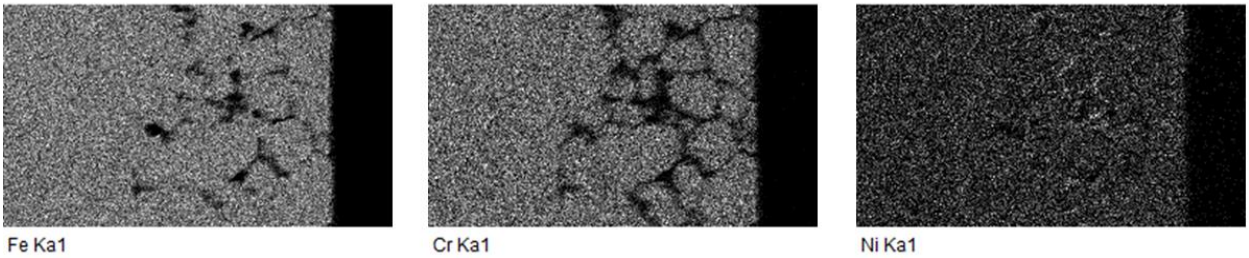

Figure 7-15 EDS map of SS 304L cross section for Fe, Cr, and Ni.

SS 321 and SS 347 (*Figure 7-16* to *Figure 7-19*), which are stabilized versions of SS 304 experienced less mass loss and significantly less grain boundary attack than the low carbon SS 304L. The cross section of 347 was appeared more similar to those of Ni base alloys exposed to lower purity FLiNaK. Most significantly, the Cr depletion was more uniform as observed in the EDS map shown in Figure 7-19 EDS map of SS 347 cross section for Fe, Cr, Mn, and Nb

. However, there was some difference in the morphology of intergranular attack for SS 321 and SS 347. One of the reasons may be the difference in grain size for the two alloys tested. This is further being investigated.

During the exposure test, the samples are held at 700°C for 100h, which is well within the sensitization temperature range of 400°C to 800°C and long enough for sensitization to develop, even in low carbon and stabilized stainless steels. [2] The greater performance of

stabilized stainless steels suggests that sensitization effects can increase corrosion of stainless steels in molten fluoride.

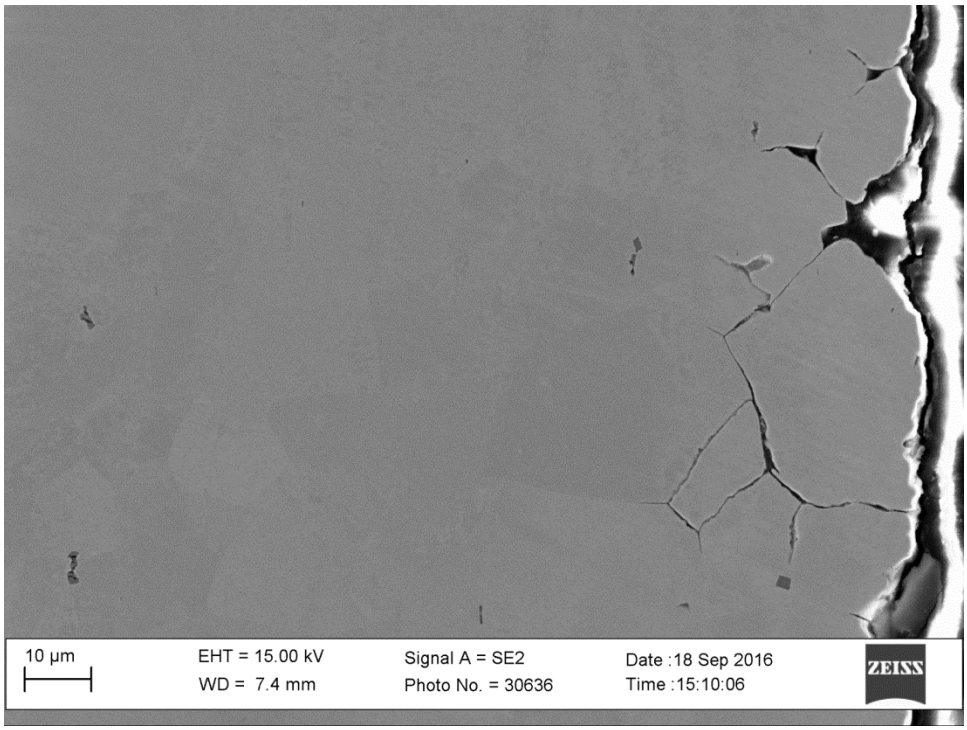

Figure 7-16 Cross sectional SEM image of SS 321 exposed to FLiNaK at 700°C.

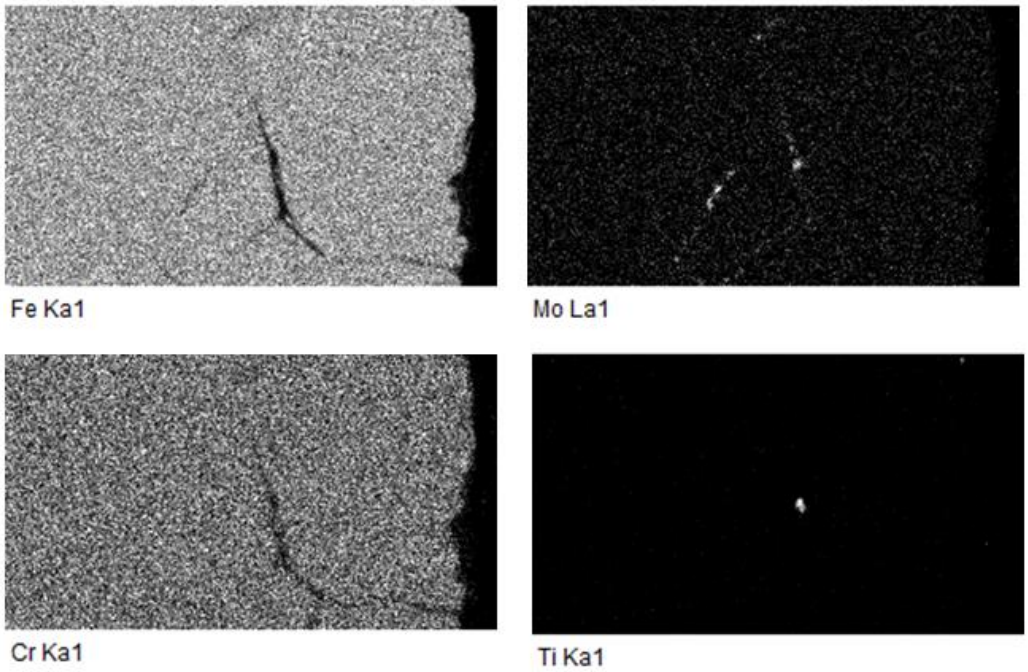

Figure 7-17 EDS map of SS 321 cross section for Fe, Cr, Mo, and Ti.

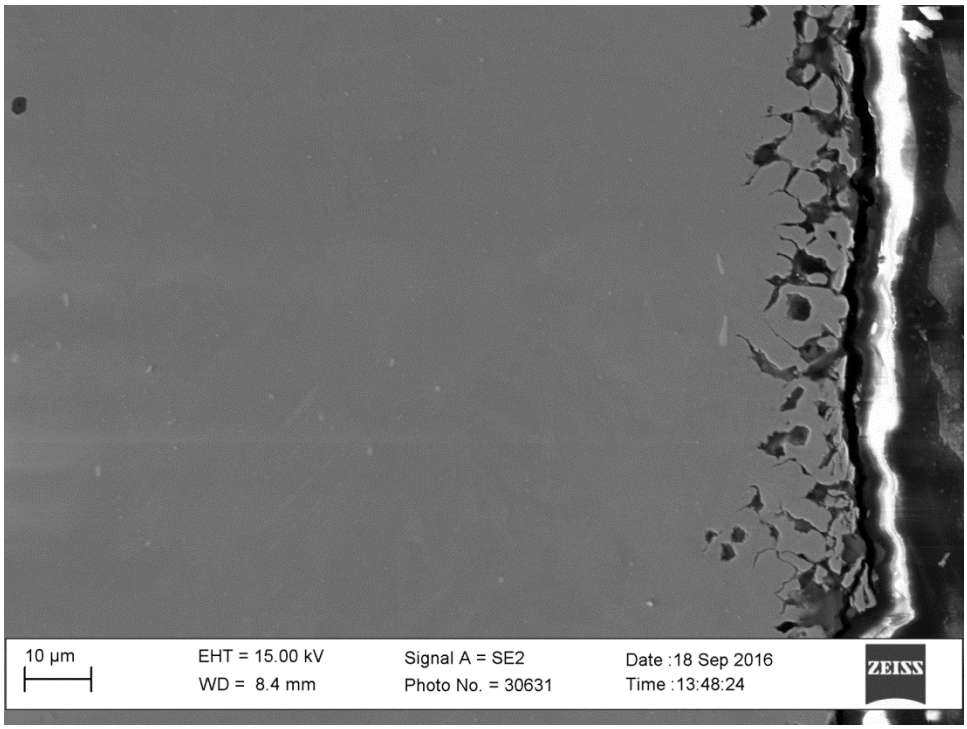

Figure 7-18 Cross sectional SEM image of SS 347 exposed to FLiNaK at 700°C.

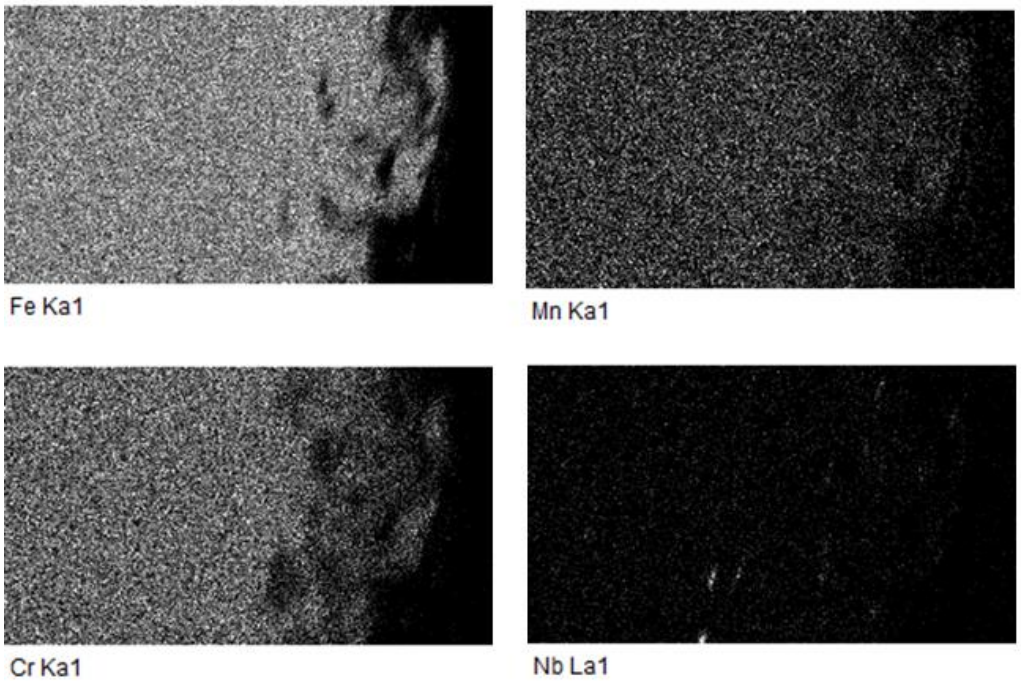

Figure 7-19 EDS map of SS 347 cross section for Fe, Cr, Mn, and Nb

7.1.2.2. The role of carbon content in corrosion of type 316 stainless steel (316L vs 316H)

SS 316H, the material used in the construction of the FLiNaK flow loop at the University of Michigan for this IRP was tested using GA Tech facilities. Samples provided by the University of Michigan were tested done to compare the corrosion resistance of SS 316H to that of SS316L, which was more widely examined in previous studies of molten fluoride corrosion. The elevated carbon content of SS 316H over SS 316L was also used to test some hypotheses about the role of carbide formation in the corrosion in austenitic stainless steels. In a study of SS 316L corrosion in molten FLiBe in the presence of graphite, Zheng speculated that carbide formation in SS 316L (and other austenitic stainless steels) may affect their corrosion resistance in molten fluoride environments, possibly by impeding grain boundary diffusion of Cr. Chromium carbides are known to grow in the grain boundaries of austenitic stainless steels in the temperature range of 425-815°C. This phenomena, usually referred to sensitization, results in the depletion of Cr in grain boundaries as chromium carbides form. However Cr depletion in grain boundaries caused by this process is usually mitigated if adequate time is allowed for bulk Cr to diffuse to and repopulate the grain boundaries. The time dependent nature of sensitization can be represented in a time-temperature-sensitization diagram (*Figure 7-20*). An experiment was designed to explore this line of thought. [1]

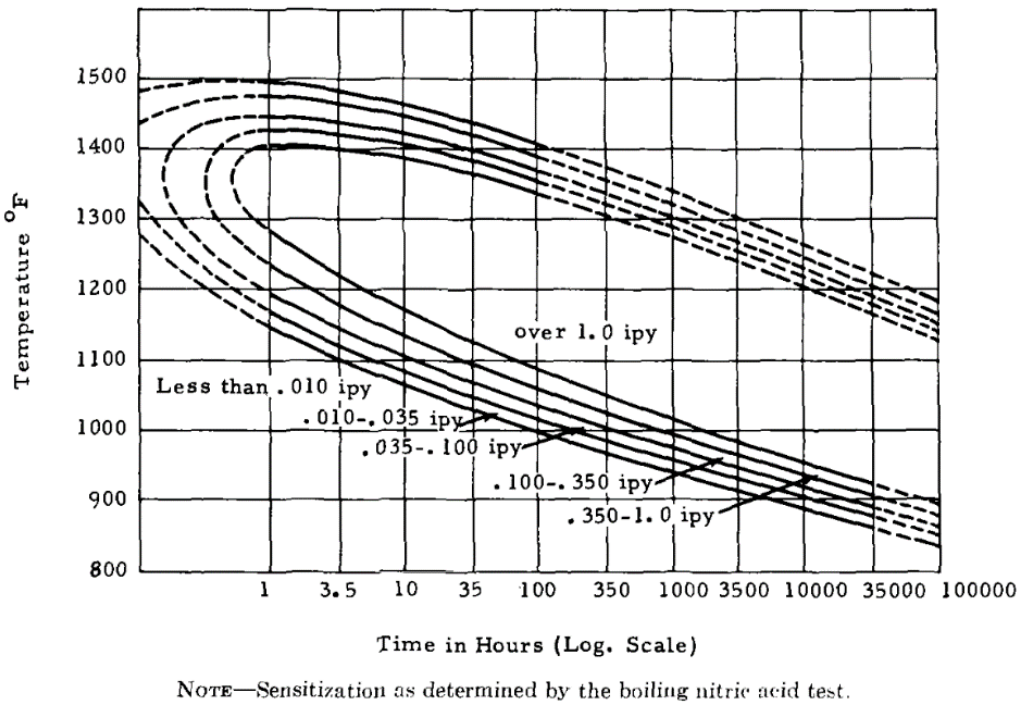

Figure 7-20 Time-temperature-sensitization diagram of SS 316L heat containing 0.023% C. [2]

All SS 316 stock material was annealed at 1100°C for 1 hour, with rapid air cooling. 1 cm by 1 cm samples of SS 316L were prepared. Due to thickness difference in the stock material, SS 316H samples were cut to have similar surface area as 316L samples. All samples were ground from 120 to 1000 grit, then rinsed with deionized water and acetone. Initial dimensions and weight of each sample were recorded. Samples were then processed in one of four ways:

1) No secondary heat treatment
2) Secondary heat treatment: 700°C in air for 25 hours
3) Secondary heat treatment: 700°C in Ar <2ppm O_2 for 25 hours
4) Secondary heat treatment: 700°C in Ar <2ppm O_2 for 25 hours w/ surface reground after heat treatment

After heat treatment, samples were rinsed with deionized water and acetone, and reweighed. Then samples were tested in FLiNaK according to the procedure described in section 2.1.1. Sample surfaces of selected materials were observed by SEM. XRD and a ferrite scope were used to characterize surface phase changes.

Results

The mass loss results for this series of tests are summarized in *Figure 7-21*. The mass loss of samples which did not undergo secondary heat treatment (controls) showed greater mass loss for 316H samples than 316L samples. The same trend was observed when all

316L and 316H samples, including samples with every secondary heat treatment were averaged. This result is in spite of lower Cr content in the 316H samples and suggests that the higher C content may enhance corrosion.

Selected samples were subjected to one of four pre-exposure treatments. Secondary heat treatment was done with the intent to induce sensitization and check for any effects by surface changes during heat treatment. The individual values of the center group in *Figure 7-21* represent the average of 316L and 316H samples subject to the same pre-exposure treatment. These results do not suggest that the secondary heat treatment affected the corrosion resistance of these steels. Cross sections of these samples will be examined to characterize the extent of carbide formation. The mass loss of samples heat treated in air was greater due to the dissolution of surface oxides which were formed during the heat treatment.

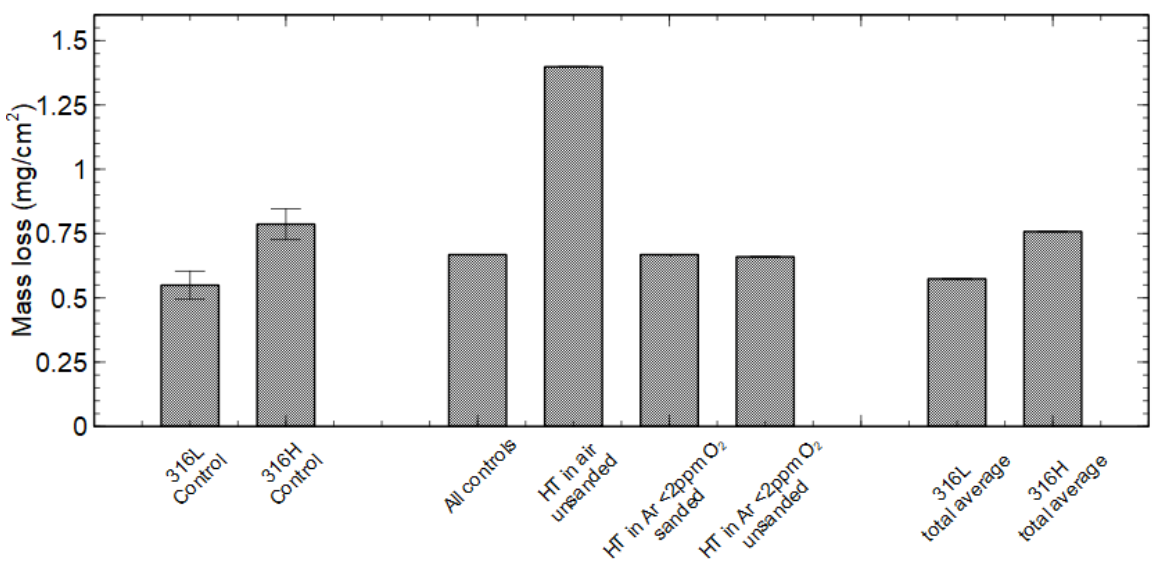

Figure 7-21 Mass loss of 316L and 316H samples exposed to FLiNaK for 100 hours at 700°C.

The ferrite number of each sample was measured using a ferrite scope before and after the test at multiple locations on the surface. Before exposure, the ferrite number of each sample was below 0.5%. However after exposure, the ferrite number was in range of 2-3%. The change in ferrite number after exposure indicates a phase transformation from the non-magnetic austenite phase to a magnetic phase, either ferrite or martensite.
A representative XRD pattern of samples taken after FLiNaK exposure is shown in *Figure 7-22* This pattern was collected at a glancing angle $\Omega = 5^{o}$, with an estimated penetration depth of ~2 μm. The patterns for all samples taken at this angle were similar. The pattern is consistent with both BCC ferrite and BCT martensite. Distinguishing between BCC and BCT is difficult because their lattice parameters are very similar. However we have assigned this phase as martensite due to expected chromium depletion. According to Butler, chromium depletion in austenitic stainless steel reduces the stability of the austenite phase and can result in formation of martensite. [3]

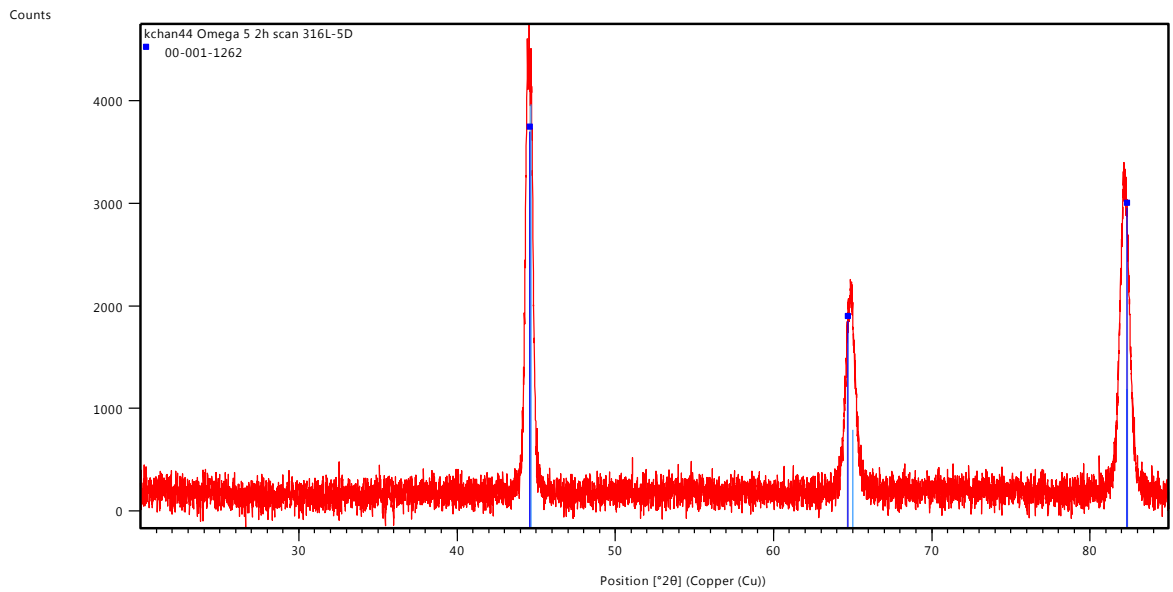

Figure 7-22 Glancing Angle XRD of 316L control sample after FLiNaK exposure. Ω = 5°

7.1.2.3. Exposure Tests of Pure Alloying Elements in FLiNaK

Active metals experience higher thermodynamic driving force for corrosion than do noble metals. Cr is the most active alloying element used in the structural alloys under consideration. Alloys with higher Cr content are expected to experience more severe corrosion, as we and others have shown [2]. Exposure tests of pure alloying elements Mo, Ni, Fe, and Cr in FLiNaK were done to experimentally verify thermodynamic predictions.

The mass loss results are shown in *Figure 7-23*. The relative corrosion rates generally followed thermodynamic predictions, with Cr experiencing much higher corrosion rates than the other elements, with Fe experiencing the second highest corrosion rates. These results are explain the relative corrosion behavior of alloys with different amount of active elements.

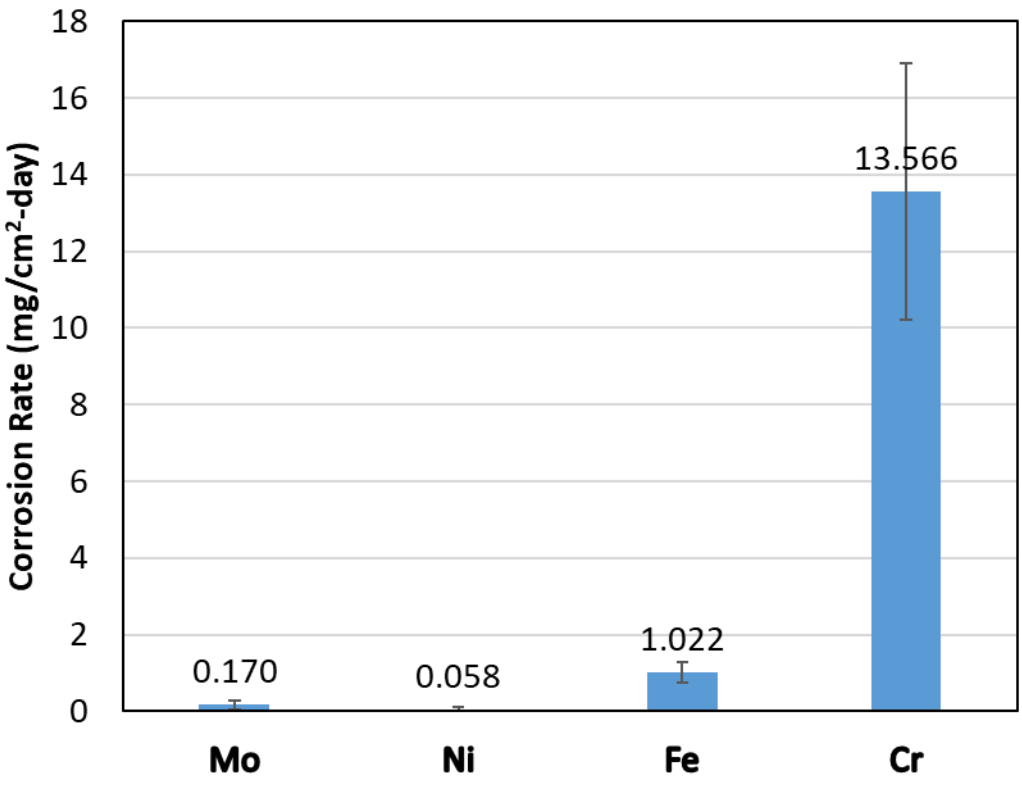

Figure 7-23 Corrosion rates of pure alloying elements exposed to FLiNaK at 700°C.

7.1.2.4. Static Exposure Tests of Alumina Forming Austenitic Stainless Steels in FLiNaK

The corrosion resistance of alumina forming austenitic (AFA) stainless steels provided by Dr. Michael Brady from ORNL were tested and characterized. Three samples each of the AFA alloys OC-5, OC-8, and OC-T were tested alongside one sample each of Hastelloy N, Haynes 244, SS 316L, SS 304L, and SS 321 for comparison with an exposure duration of 100 hours. The exposure test procedure was as described in section 7.1.1. AFA alloy OC-5 was also included in the 500 hour test described in the previous.

The mass loss and penetration depth results and are summarized in *Figure 7-24* and *Figure 7-25*. While the mass loss of OC-5 and OC-T were comparable to those of the other materials, OC-8 showed significantly higher mass loss. This could be explained by the higher Cr content of OC-8: 18.7% Cr while OC-5 and OC-T had 13.8% Cr. The penetration depths measured for these AFA stainless steels were greater than that of other materials. The surface SEM image of exposed OC-T (*Figure 7-26*) reveals grain boundary attack. However this is not also observed on the surfaces of OC-5 and OC-8 (*Figure 7-27* and *Figure 7-28*).

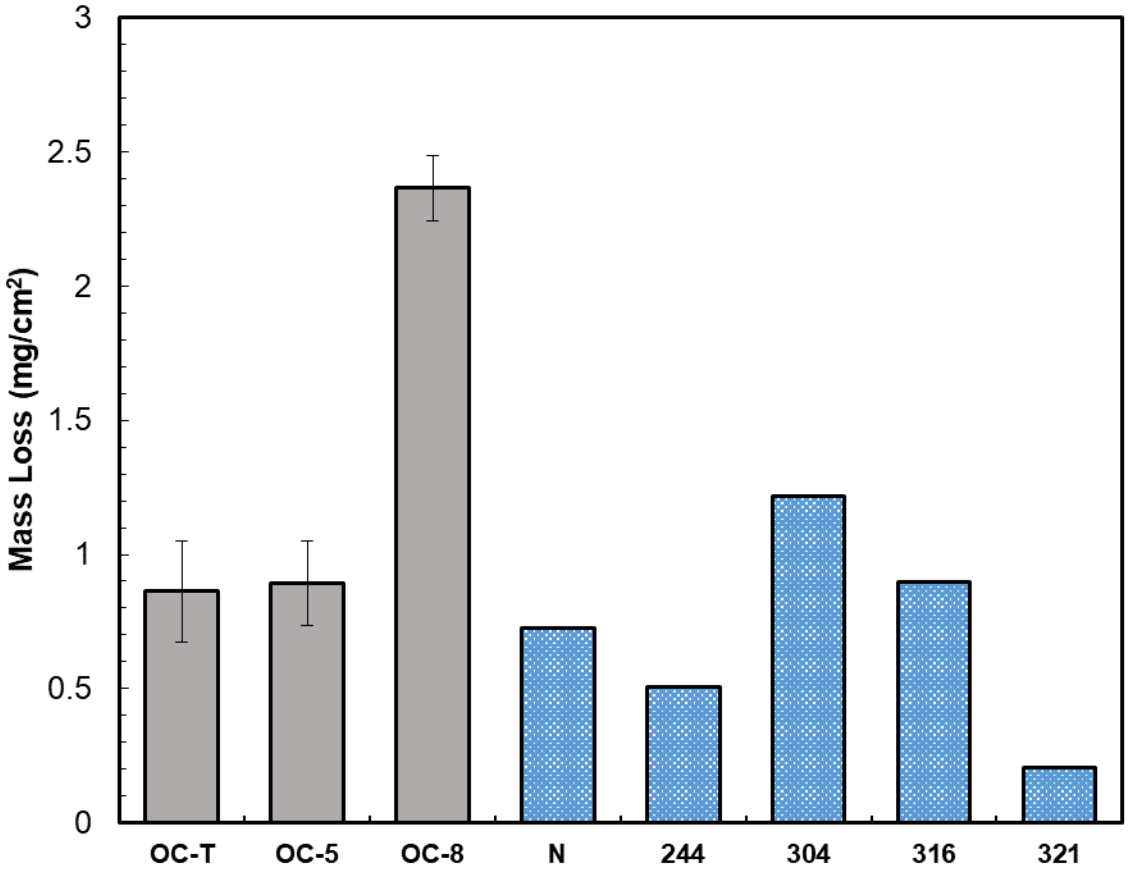

Figure 7-24 Mass loss of AFA stainless steels, Ni based alloys, and conventional stainless steels exposed to FLiNaK at 700°C for 100h.

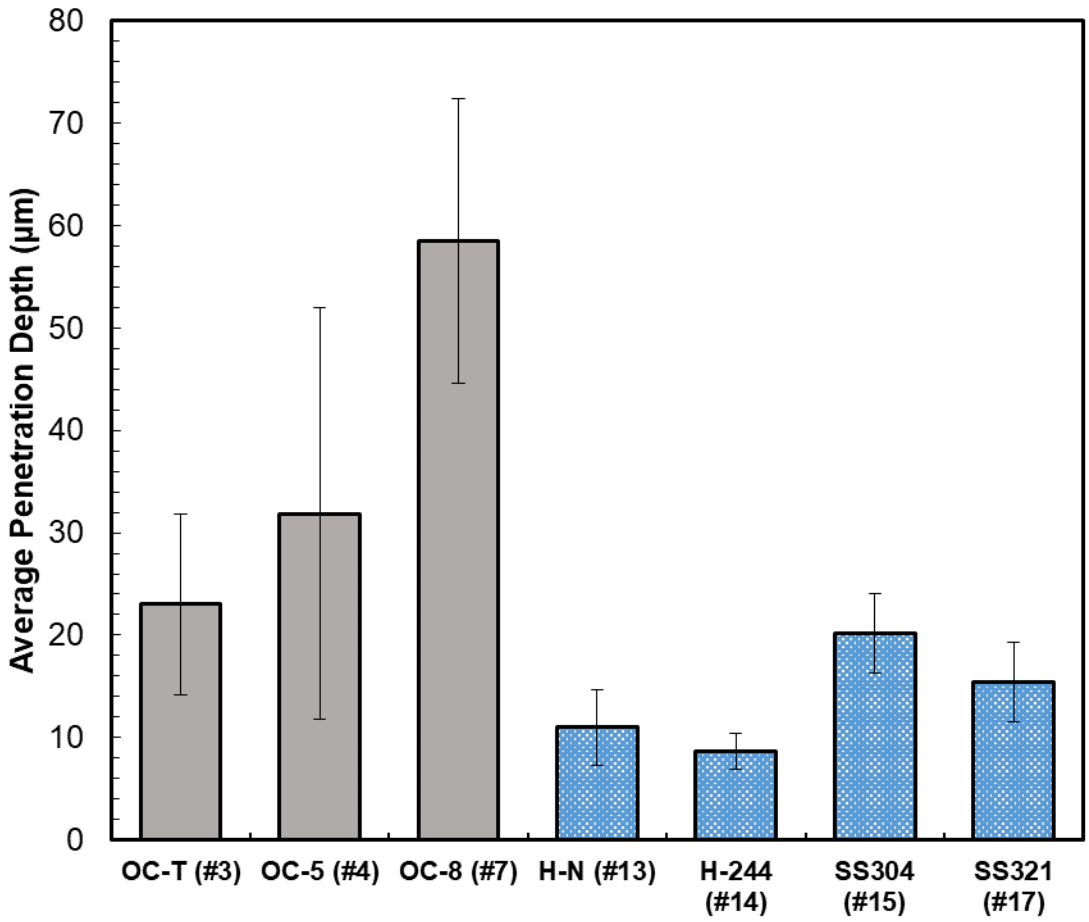

Figure 7-25 Penetration depth of AFA stainless steels, Ni based alloys, and conventional stainless steels exposed to FLiNaK at 700°C for 100h. Depths were measured at multiple locations in the cross section of one sample for each alloy.

In the 500 hour test, OC-5 was found to experience mass loss comparable to the conventional austenitic stainless steels. Pre-oxidation of OC-5 did not have a significant effect on mass loss. The no traces of the alumina film were observed after exposure.

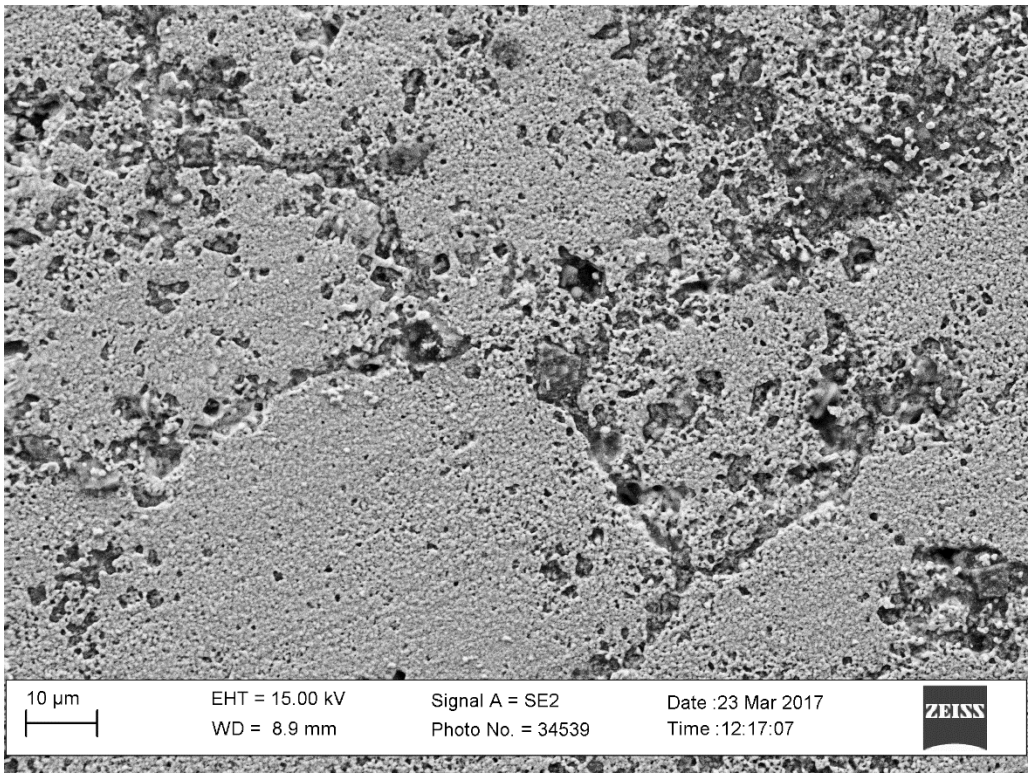

Figure 7-26 Plan view of OC-T after 100h FLiNaK exposure.

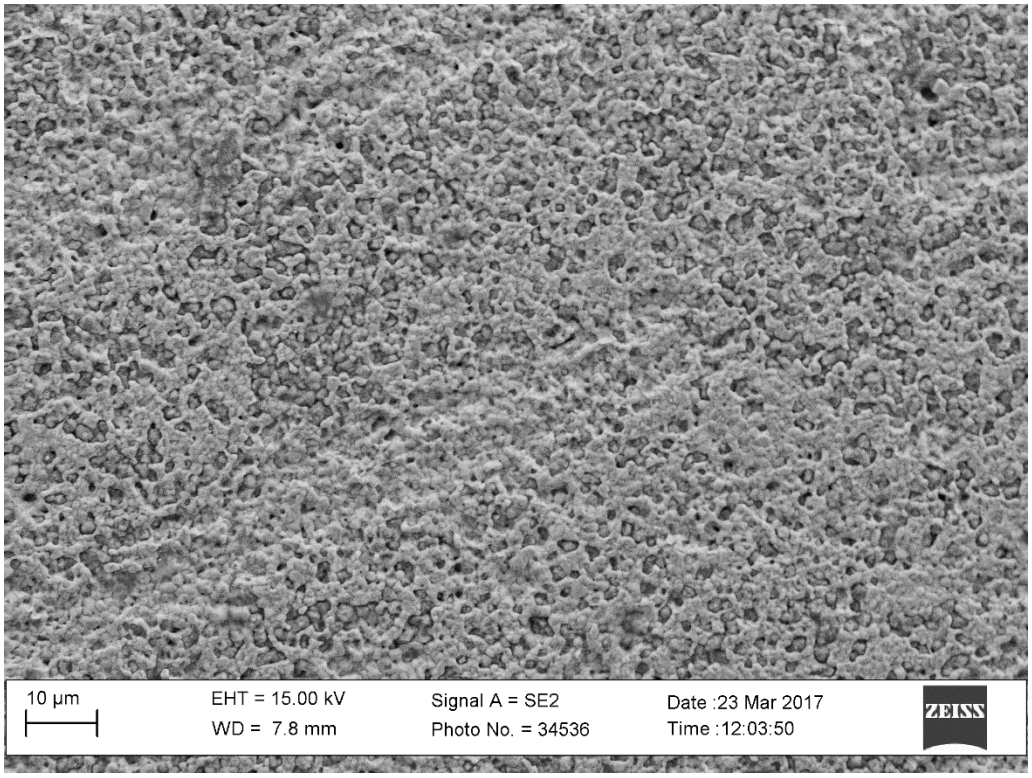

Figure 7-27 Plan view of OC-5 after 100h FLiNaK exposure.

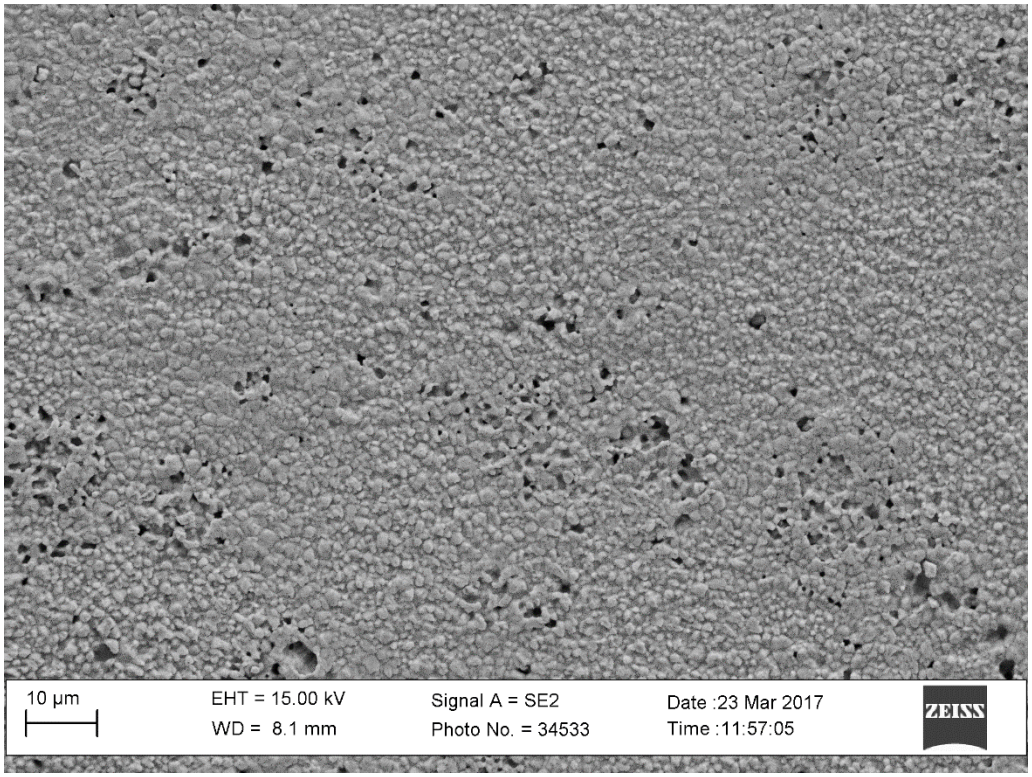

Figure 7-28 Plan view of OC-8 after 100h FLiNaK exposure.

7.2. Corrosion Tests in FLiNaK – Liquid Salt Test Loop (LSTL)

Corrosion tests of structural alloys under dynamic flow conditions were started in the Liquid Salt Test Loop (LSTL) at ORNL. Due to space limitations, the samples were placed in the sump tank, and inserted through a 2" tube port. The design and operation of the sample holder are shown in *Figure 7-29*. The test materials were machined into either washer or tube shapes, with the tube samples used to create give space between the washer samples. The flange was modified to allow the sample holder rod to penetrate the sump tank, and allow the vertical position of the sample holder to be adjusted without removing the flange. A 316L SS Conax compression fitting was welded to standard blank Conflat flange, shown in *Figure 7-30*. The fitting uses a graphite element which seals around the sample holder rod. The sample holder rod could then be used to raise or lower the sample holder. Due to uncertainty in the salt level during operation, the lengths of all sample holder components were adjusted to maximize clearance in the transfer (upper) position. The sample holder was inserted into the sump tank on September 21, 2018 while the LSTL was cold. A custom glove bag was used during installation to minimize air ingress (*Figure 7-31*). The sample materials were Ni 200, Hastelloy N, Haynes 244, Inconel 600, Inconel 625, 316L SS, and 321 SS. Exposure of these samples is scheduled to complete after the completion of this IRP.

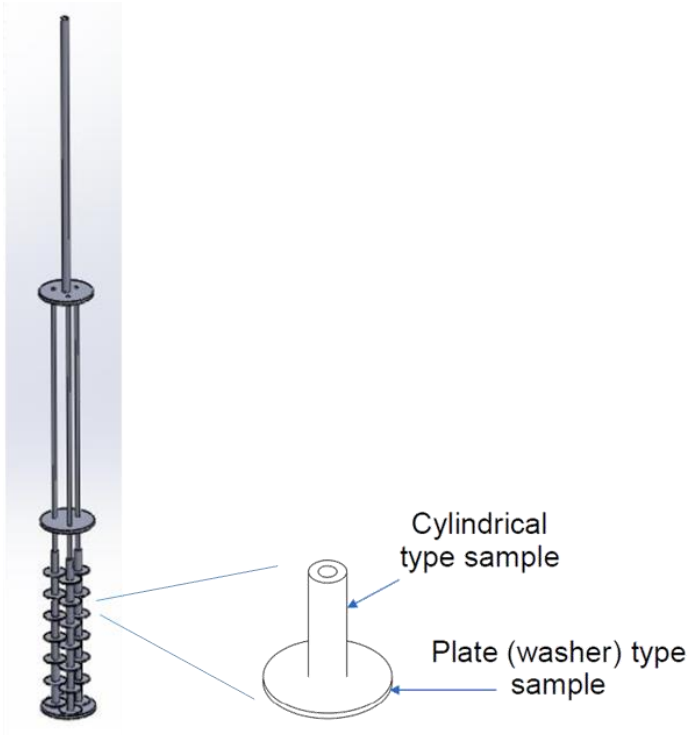

Figure 7-29 Sample shape and sample holder for dynamic corrosion tests in the LSTL at ORNL

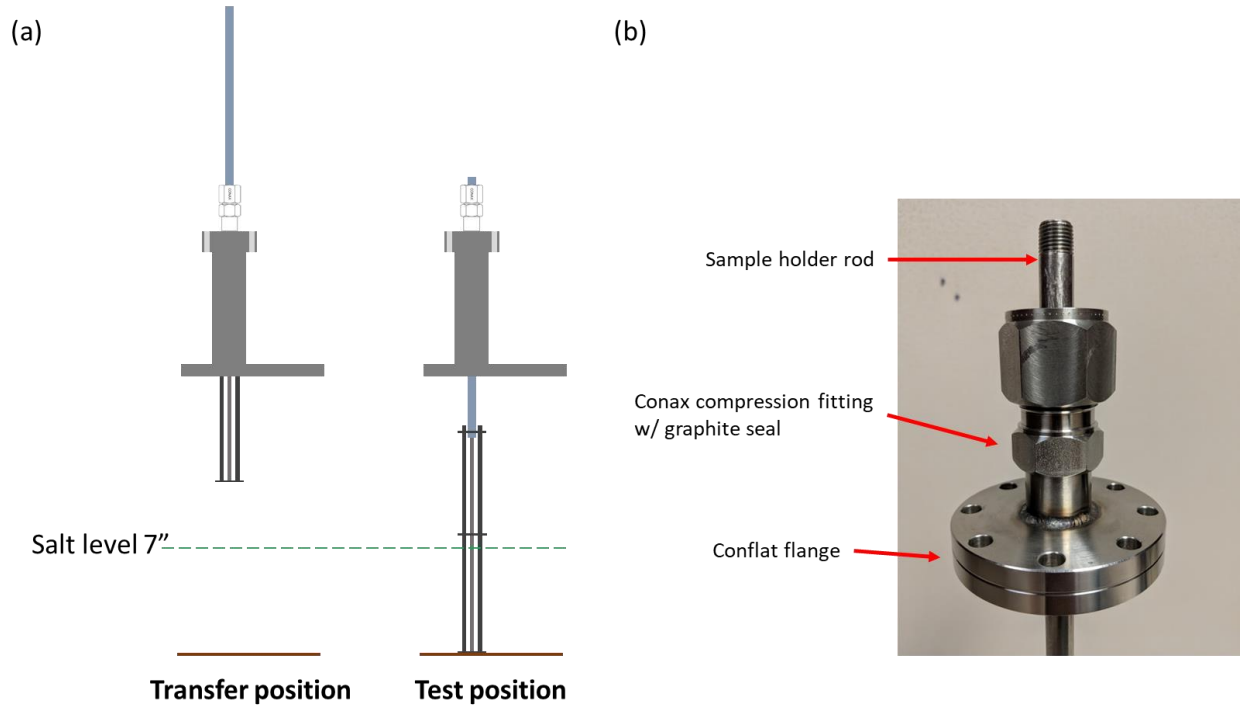

Figure 7-30 Modifications made to flange of a 2” sump tank port.

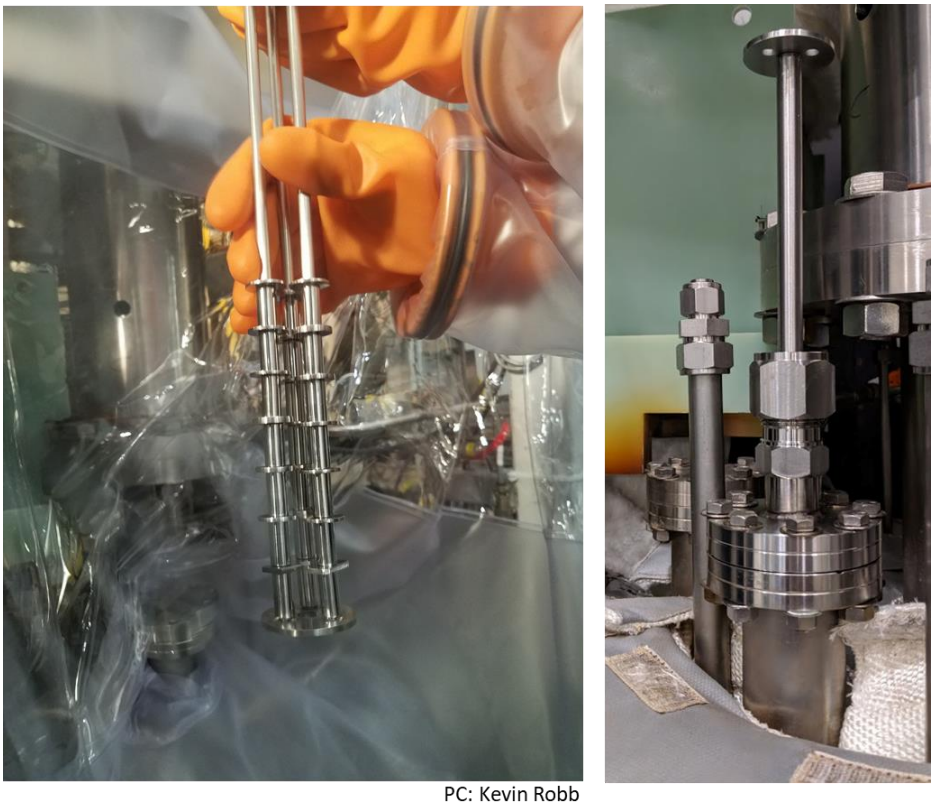

PC: Kevin Robb

Figure 7-31 Assembled sample holder with samples during and after installation into the LSTL sump tank.

7.3. Effect of Molten Salt Impurities and Redox Conditions on Corrosion Alloys

7.3.1.1. Effect of Impurities

7.3.1.1.1. Effect of Salt Volume

There was some concern that the small volume of FLiNaK we had been using in our exposure tests could be limiting the extent of corrosion observed. If the Cr solubility limit in FLiNaK is reached during the test, further attack would be thermodynamically limited. However, if the solubility limit is not reached, the extent of corrosion is expected to be controlled by impurities present in the FLiNaK. This is because larger quantities of FLiNaK are expected to hold a proportionally larger quantity of impurities.

Exposure tests of Hastelloy N using from 4.5g to 9.17g FLiNaK at 700°C were done. These tests were conducted using the same procedure as described in section 7.1.1, except using lower purity FLiNaK. FLiNaK batches of two different purities were used: the first was

made from 98%+ LiF, 99%+ NaF, and 99%+ KF, and the second was made from 99.85% LiF, 99.99% NaF, and 99%+ KF (assay 99.9%).

The mass loss results are shown in *Figure 7-32*. For the same FLiNaK batch used, lower FLiNaK volumes resulted in lower mass loss. Exposure tests using lower purity FLiNaK resulted in significantly higher mass loss compared to tests using higher purity FLiNaK. Corrosion does not appear to be limited by the solubility of corrosion products in FLiNaK. Instead, the total quantity of impurities in the salt appears to be a much more significant factor in controlling corrosion rates for these static exposure tests.

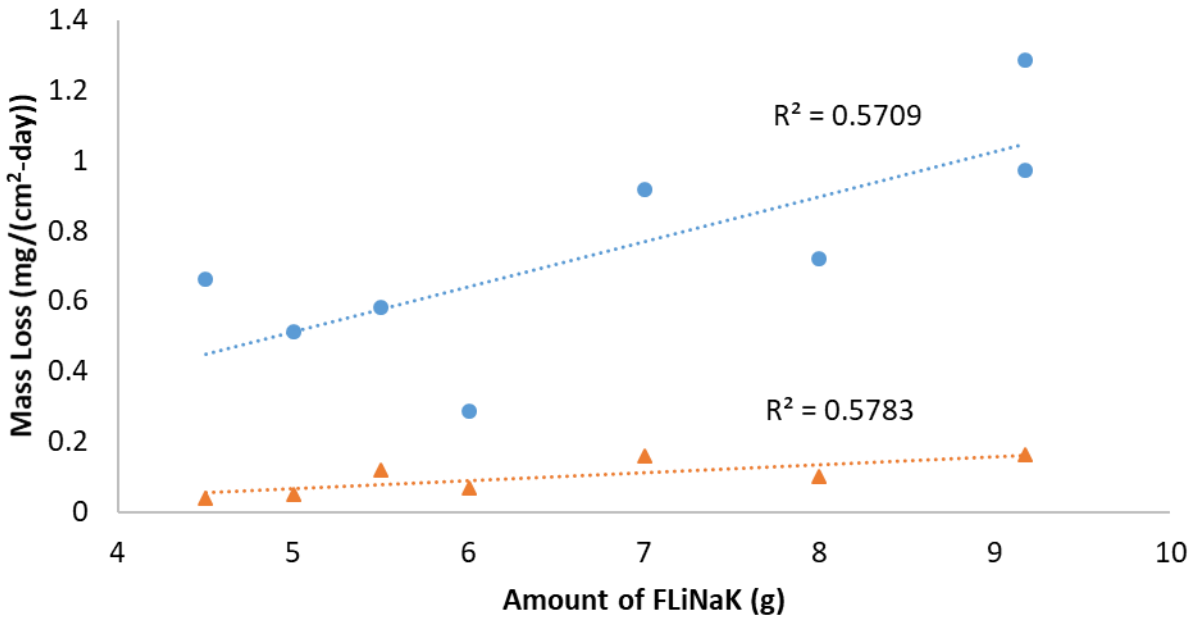

Figure 7-32 Mass loss results of Hastelloy N exposure at 700°C in varying amounts of FLiNaK. Data for higher purity (orange triangles) and lower purity (blue circles) are shown.

7.3.1.1.2. Effect of Moisture

Static exposure tests of Hastelloy N in FLiNaK with added moisture were conducted at 700 °C. The procedure for these tests was nearly identical to that described in section 7.1.1, except measured amounts of water were added to the FLiNaK just prior to heating. For these tests, ten 1 cm by 1 cm coupons cut from 1/16" Hastelloy N sheet were prepared. All coupons were ground to 1000 grit, then rinsed with deionized water and acetone. Each sample was weighed and measured for their initial surface area. In a moisture and oxygen controlled argon atmosphere glove box, dried FLiNaK was divided into high purity 8ml graphite crucibles each containing a Hastelloy N coupon and sealed in capsules made from 304L NPT pipe nipples and caps. Initial dried FLiNaK moisture content at room temperature was measured at a maximum of 0.12% by Karl-Fischer Titration. Each crucible was filled with 9.17g dried FLiNaK, followed by an amount of deionized water in the range of 0 to 140mg. The capsules were transferred outside the glove box and welded shut. They were then enclosed in a SS 304 box and transferred to a furnace outside the

glovebox. An argon line was connected to the box, which delivered 0.5 L/min of argon throughout these exposure tests. The furnace was run at 700°C for 100h.

Following the test, the crucibles were removed from the capsules and crushed with a hammer to fragment the FLiNaK. The coupons were retrieved from the FLiNaK and cleaned ultrasonically in 1M $Al(NO_3)_3$ solution for 2.5 min, deionized water for 1.5 min, and acetone for 1.5 min. After drying, the coupons were weighed using a high precision balance to determine the mass loss. Cross sections of each coupon were examined via optical microscopy and SEM/EDS.

The mass loss results are shown in *Figure 7-33*. Mass loss tended to decrease with increasing amounts of added moisture. This trend was mirrored by the depth of affected material, as measured by SEM.

SEM/EDS analysis revealed three distinct layers of affected material, as shown in *Figure 7-34*, *Figure 7-35*, and *Figure 7-36* for 0.6 wt% moisture addition. Arranged from the original surface to the bulk material, they are: (1) A porous layer, (2) A layer of internal oxidation, and (3) A layer containing Mo rich phases.

Cr depletion was observed just in all three layers, with normal Cr concentrations just below the Mo rich phases. The porous first layer was depleted of Cr and Mo, and enriched in Ni and Fe. In this layer, carbides were detected in the voids and pores. Carbon transport appeared to occur through the porous region, but was limited through the alloy matrix.

The oxides in the second layer, formed in the presence of moisture, could decrease the diffusion rate and therefore the corrosion rate of these alloys, which would otherwise be shortcuts for outward diffusion of Cr and Mo. The tests with higher moisture content may have increased the extent of this obstruction.

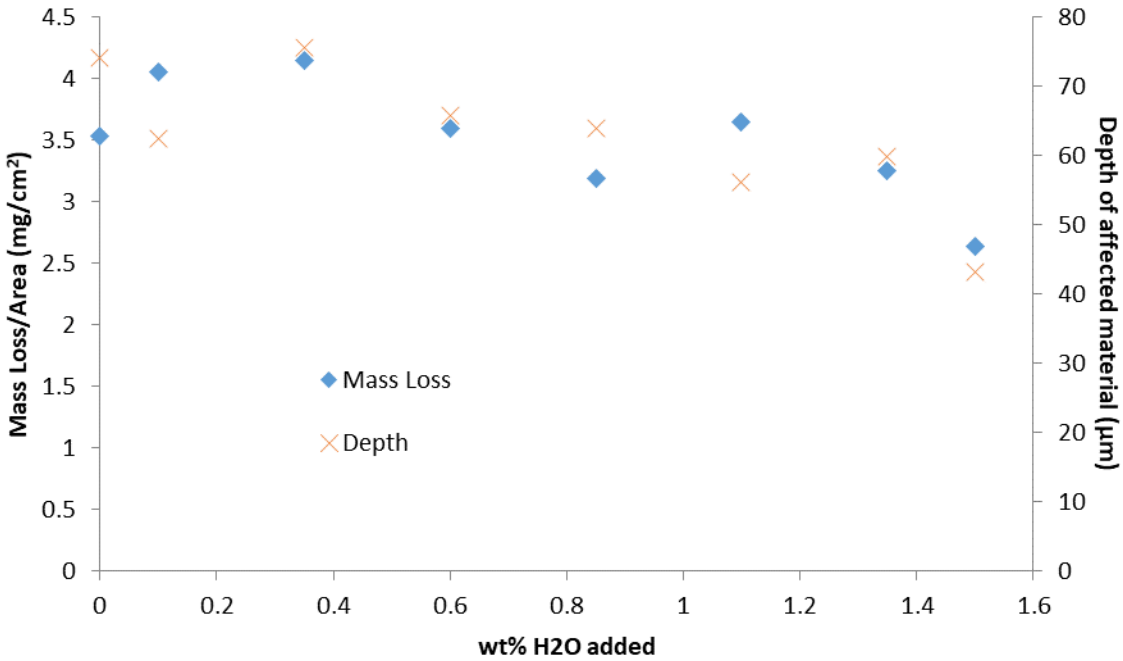

Figure 7-33 Mass loss per surface area and attack depth for varying amounts of added water.

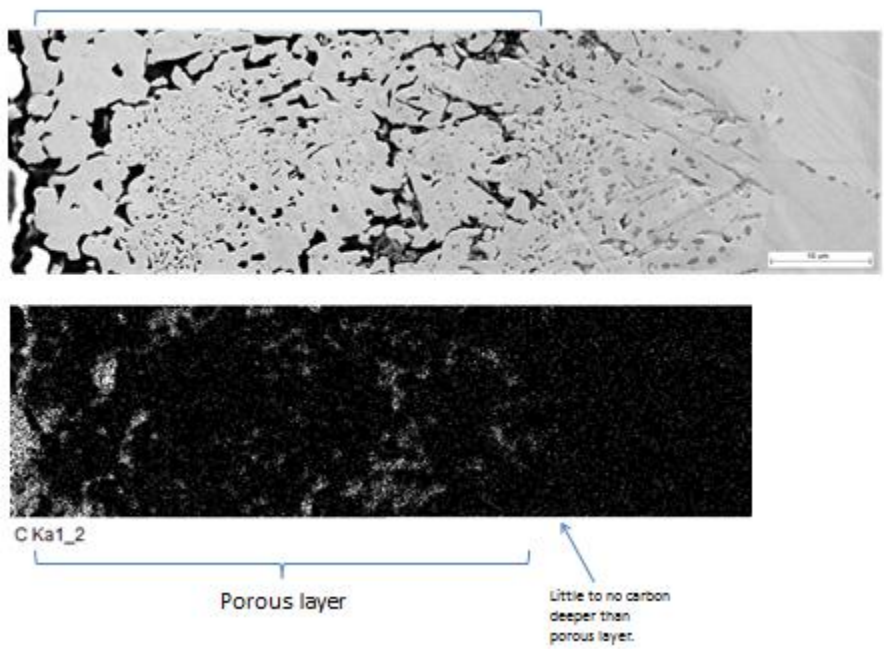

Figure 7-34 SEM/EDS analysis of Hastelloy N sample exposed to FLiNaK with 0.6 wt% moisture addition showing extent of carbon ingress.

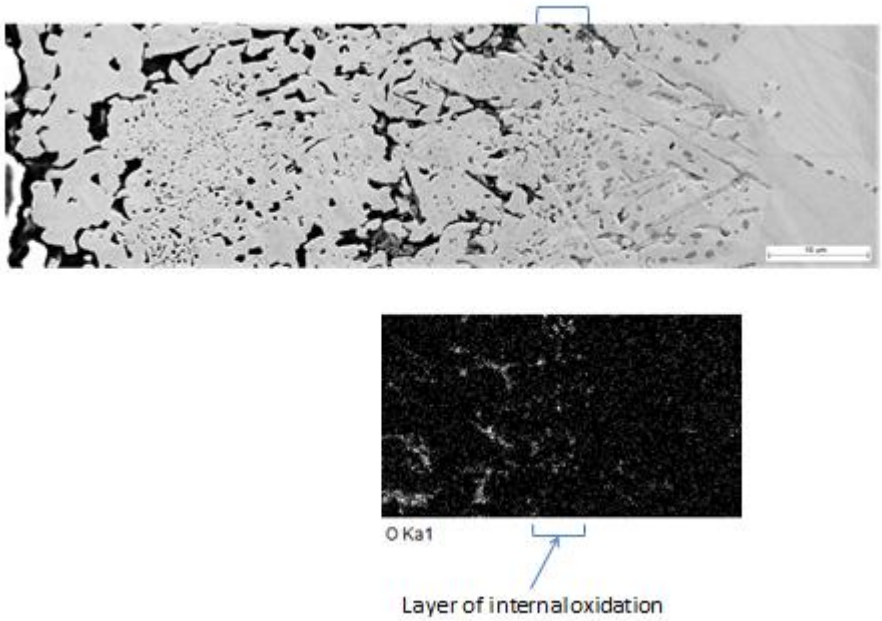

Figure 7-35 SEM/EDS analysis of Hastelloy N sample exposed to FLiNaK with 0.6 wt% moisture addition showing internal oxidation layer.

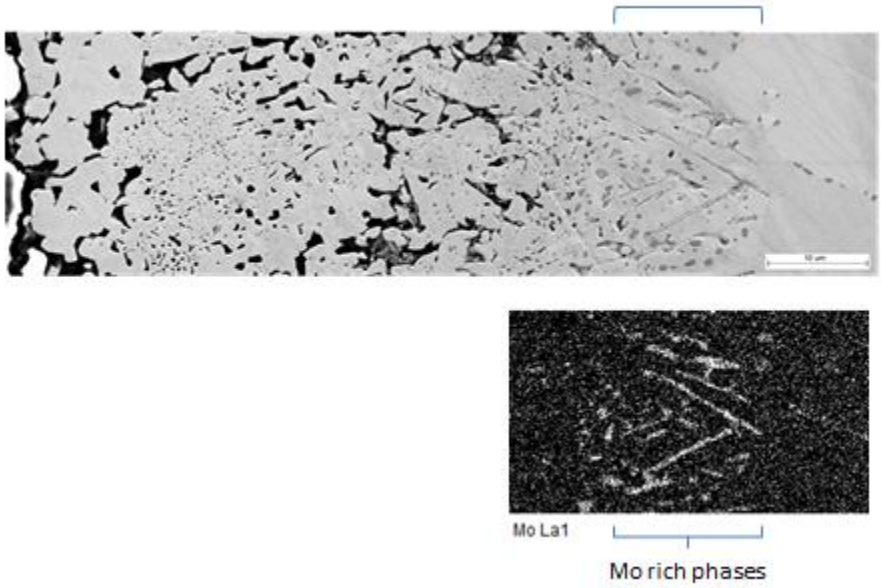

Figure 7-36 SEM/EDS analysis of Hastelloy N sample exposed to FLiNaK with 0.6 wt% moisture addition showing layer containing Mo rich phases.

7.3.1.1.3. Effect of Metal Fluoride Addition

To see the effect of access metal fluoride impurities on corrosion, static exposure tests of Hastelloy N in FLiNaK with NiF_2 impurity added were conducted. The procedure was identical to that of the moisture impurity test, except 0.1 wt% or 1 wt% of NiF_2 were added to the FLiNaK. The mass loss results are shown in *Figure 7-37*. The surface of the coupon exposed to 1 wt% NiF_2 FLiNaK had significant porosity, easily visible to the naked eye. The depth of affected material was very large, over 400 µm (*Figure 7-38*).

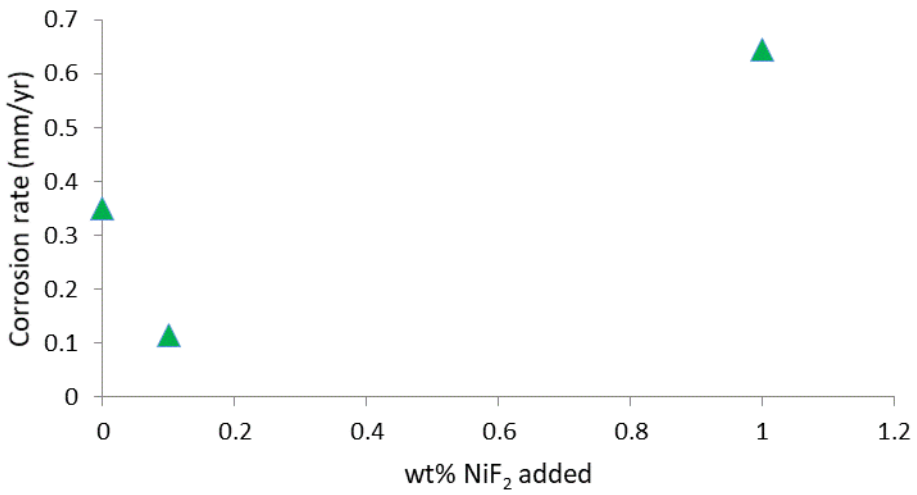

Figure 7-37 Mass loss data for 100h Hastelloy N exposure test in FLiNaK with NiF2 impurity addition.

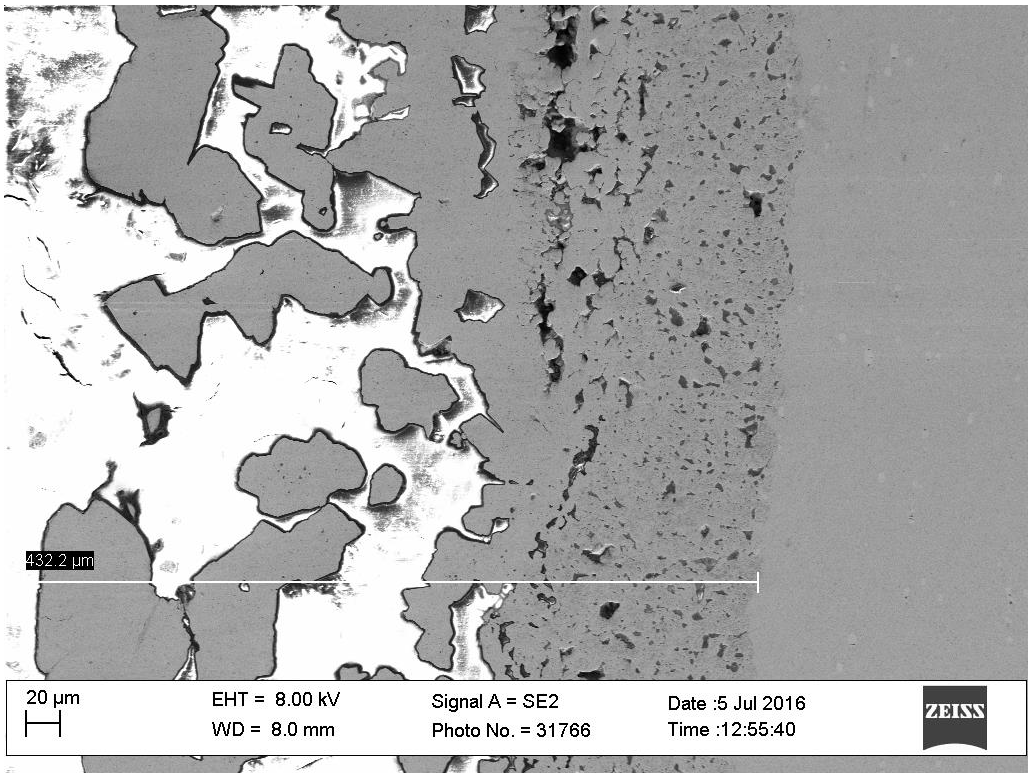

Figure 7-38 Cross sectional SEM of Hastelloy N sample exposed to FLiNaK with 1.0 wt% NiF2 impurity.

7.3.1.1.4. Evaluation of Salt Purification by H_2 Gas Sparge

Corrosion experiments done at Georgia Tech thus far have used FLiNaK made by combining high-purity salt components from chemical suppliers. However, FLiNaK produced by this method still contain impurities which have large effects on corrosion. To minimize the effects of impurities, a purification process must be implemented. The hydrofluorination process, which is typically used to purify fluoride salts involves bubbling a mixture of HF and H_2 gas through the liquid salt. HF is needed to oxygen containing anions, including O^{2-} and SO_4^{2-}, but larger ratios of HF to H_2 impart a more oxidizing fluorine potential to the salt being purified. We evaluated the effect of purifying FLiNaK salt with a H2 sparge with no HF. While oxygen containing anions were not expected to be eliminated, some highly oxidizing impurities may be reduced. By the following relation defined by Olander, a fluorine potential can be estimated from the partial pressures of HF and H_2. [10]

$$\Delta\bar{G}_{F_2} = 2RTln\left(\frac{p_{HF}}{\sqrt{p_{H_2}}}\right) + 2\Delta G^0_{HF}$$

where $\Delta\bar{G}_{F_2}$ is the standard free energy of formation of HF(g). For $p_{HF}/\sqrt{p_{H_2}} = 10^{-3}$ at 900K, the fluorine potential would be -156.9 kcal/mol. At this fluorine potential, metals cations less noble than Fe should be reduced.

LiF (99.85%), NaF (99.99%), and KF (99%) powders were individually heated to 200C for 4 hours to drive off residual moisture. These salts were then weighed and mixed in the proper proportions to create FLiNaK. Two equally sized salt batches were prepared. One batch of mixed salts was placed in a graphite crucible and fused by heating to 600°C for 24 hours. The second batch was fused in a similar manner, except with a SS 316L dip tube inserted which delivered Ar-4%H_2 gas at 1 L/min for 24 hours. The FLiNaK pucks produced from these two batches were broken into small pieces and used in an exposure test.

1cm by 1cm samples of Hastelloy N and SS 316L samples were prepared in manner similar to what was described in 2.1.1. Two samples of each alloy were tested in each batch of salt. Samples were exposed for 100 hours at 700°C. The mass loss results for these samples are shown in *Figure 7-39*. From these results, we could not conclude that there was any significant difference in corrosion between the two batches of FLiNaK.

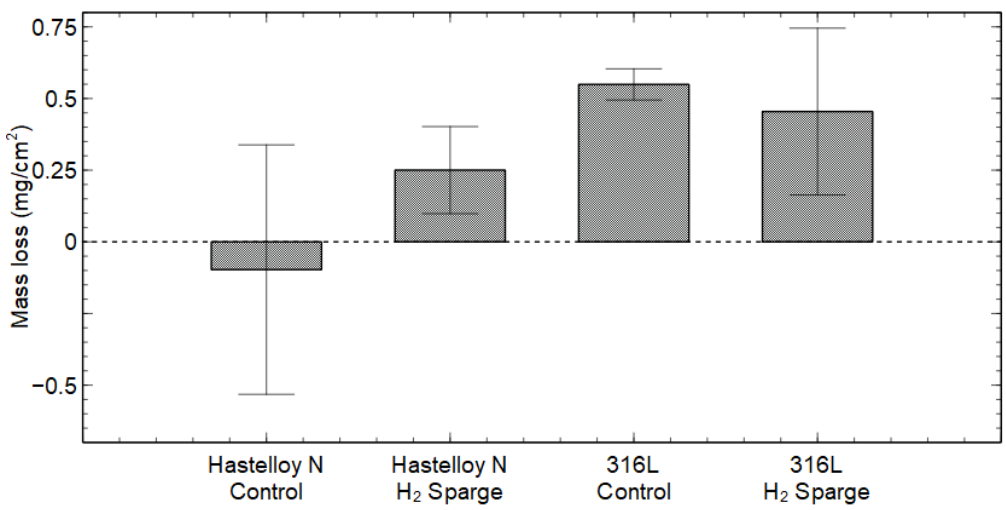

Figure 7-39 Mass loss of alloys tested in H2 sparged FLiNaK.

7.3.1.2. Static Exposure Tests of Pre-Oxidized Alloys in FLiNaK

General wisdom of corrosion in molten fluoride is that oxide films cannot be relied upon to protect the underlying metal. The primary reasons for the lack of protection are the low availability of oxygen in the molten fluoride environment and solubility of oxides that compose these oxide scales. Under these conditions a protective oxide layer cannot be formed. However there is the possibility that oxide layers formed prior to exposure to molten fluoride may have some protective effect. To test this idea, a preliminary experiment was conducted: SS 316L samples were pre-oxidized in air at 700°C for 100 hours before exposure in static molten FLiNaK. In the cross section shown in *Figure 7-40*, it can be seen that the pre-oxidized sample was attacked to a much smaller extent than a surface-sanded sample tested under identical conditions.

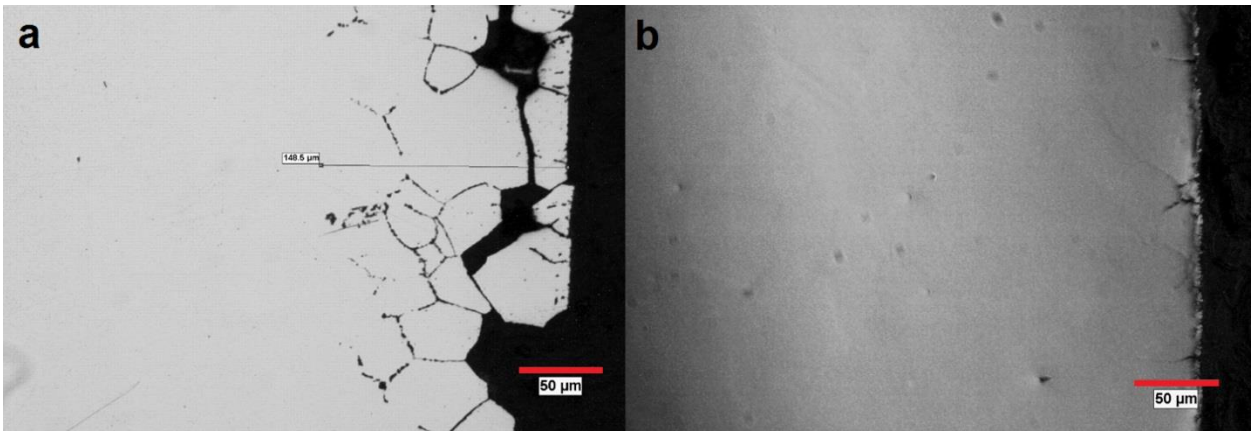

Figure 7-40 Cross sectional micrographs of (a) surface-sanded and (b) pre-oxidized SS 316L after 100 hour exposure in static FLiNaK at 700°C.

7.3.1.3. Effect of Test Time

The effect of pre-oxidation on the corrosion resistance of austenitic stainless steels was further investigated. In the first, the corrosion resistance of pre-oxidized SS 316L samples was compared to that of freshly-polished SS 316L and other alloys in side-by-side exposure tests. Samples were pre-oxidized in air at 700°C for 25 hours. The samples were exposed for 25, 100, and 500 hours.

The mass loss results for Hastelloy N, Haynes 244, SS 316L, pre-oxidized SS 316L, and SS 321 for this series of tests are summarized in *Figure 7-41*. These materials were tested in each test in the series. The mass loss presented here was calculated as the difference in mass before any pre-oxidation step and the post-exposure mass. Both Hastelloy N and Haynes 244 experienced lower mass loss as the test duration was increased. This decreasing mass loss was unexpected, and could be explained by the formation of carbides on sample surfaces. In contrast, mass loss of the stainless steels SS 316L and SS 321 increased over the test duration. In his static corrosion tests in FLiBe, Zheng observed that SS 316L experienced mass loss proportional to the square root of the corrosion time. [4] This indicates that the corrosion processes was controlled by thermal diffusion. However as shown in *Figure 7-42*, this proportionality was not clearly observed in our results.

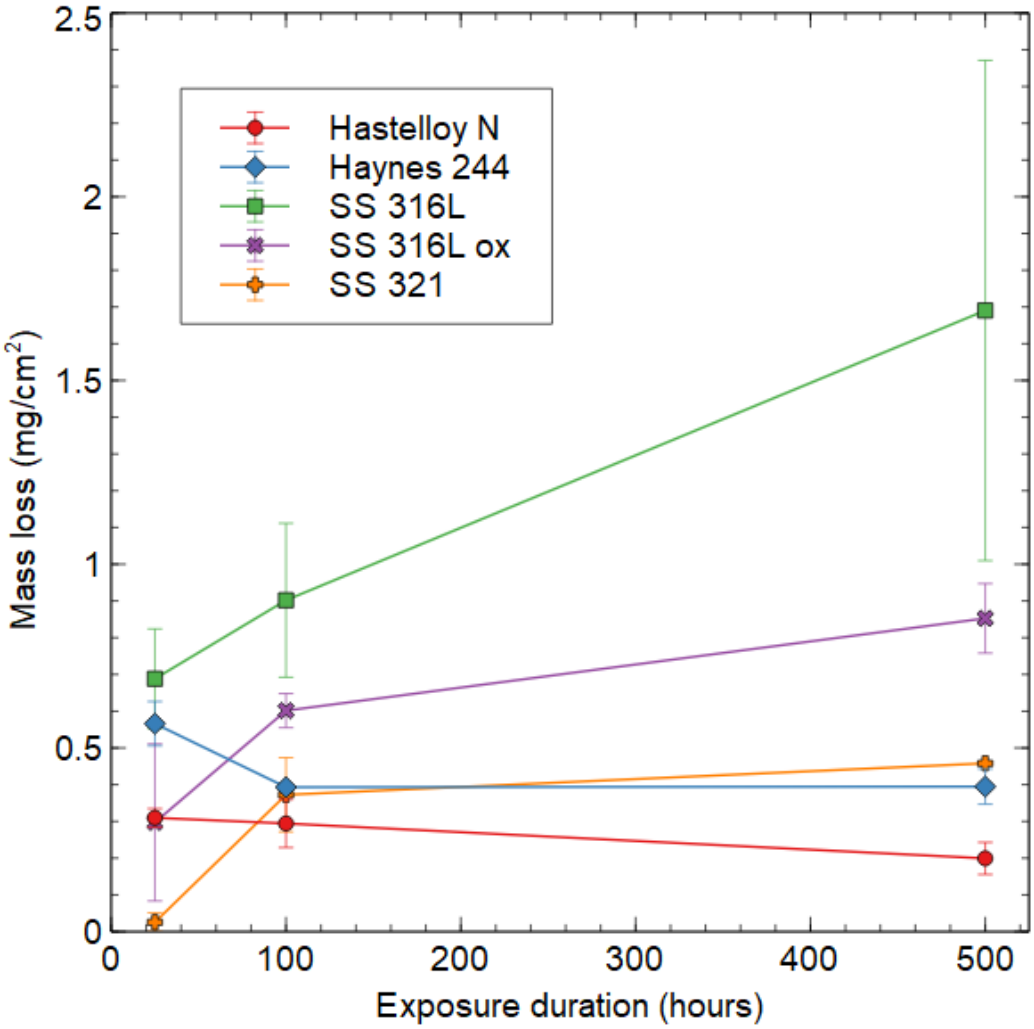

Figure 7-41 Mass loss of alloys exposed to FLiNaK for 25, 100, and 500 hours.

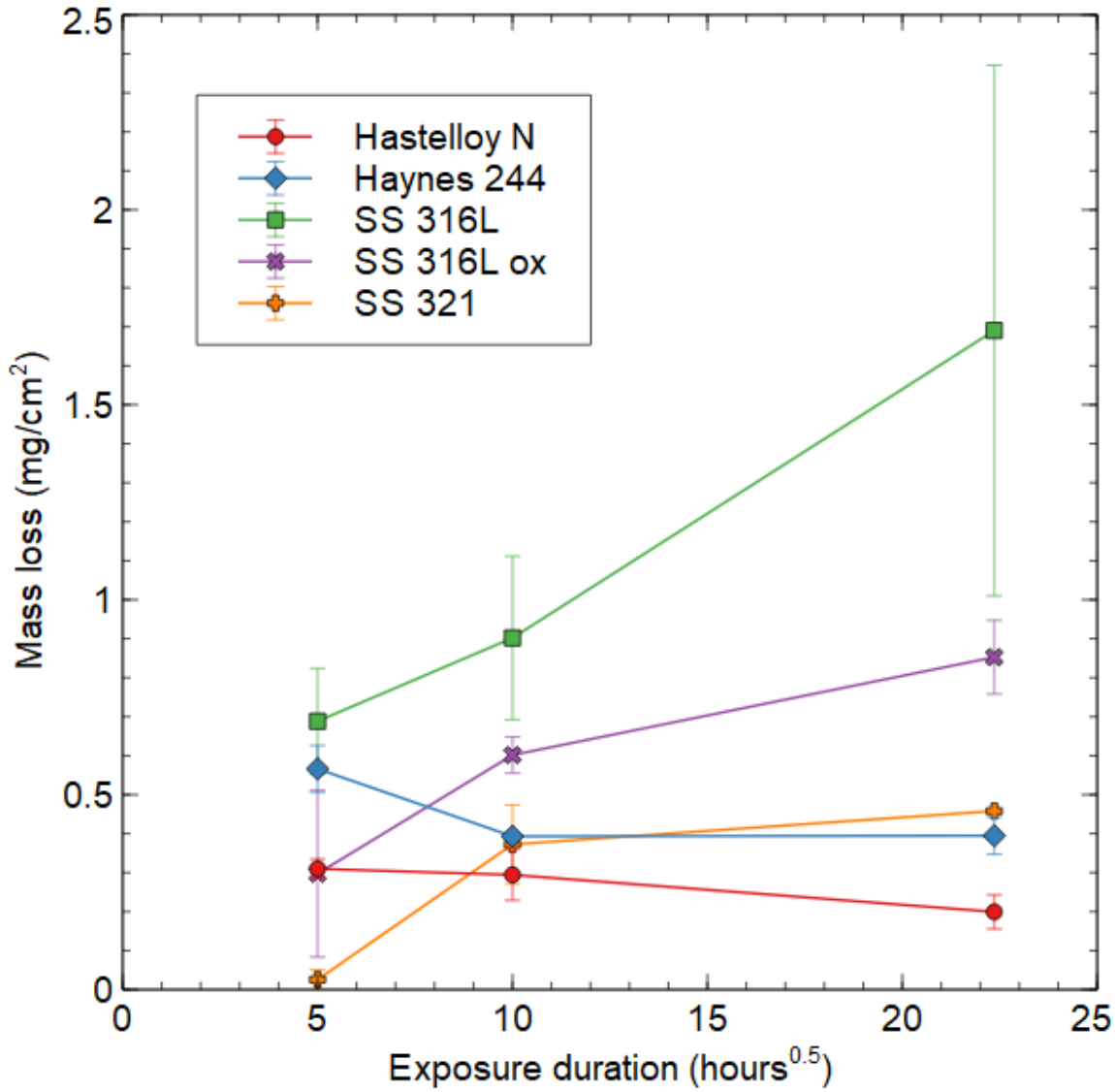

Figure 7-42 Mass loss of alloys exposed to FLiNaK for 25, 100, and 500 hours. Horizontal axis is shown as the square root of exposure duration.

Mass loss results for the 500 hour test only are shown in Figure 7-43. These include materials which were only tested for this test duration. Of the Ni-based alloys, low Cr Hastelloy N and Haynes 244 experienced the least mass loss, while Inconel 600 experienced the highest mass loss of this test. Of the stainless steels tested, SS 321 experienced the least mass loss, which was consistent with all our previous tests.
SS 316L samples which were pre-oxidized in air or steam experienced lower mass loss than those which did not go through these processes. However, inspection of pre-oxidized SS 316L surfaces after exposure by SEM showed no residual oxides after 500 hours (Figure 7-44). Such oxides were clearly visible on the pre-oxidized SS 316L after 25 hour exposure (Figure 7-45). This suggests that the reduction in mass loss in the pre-oxidized samples was not due to the oxide film.

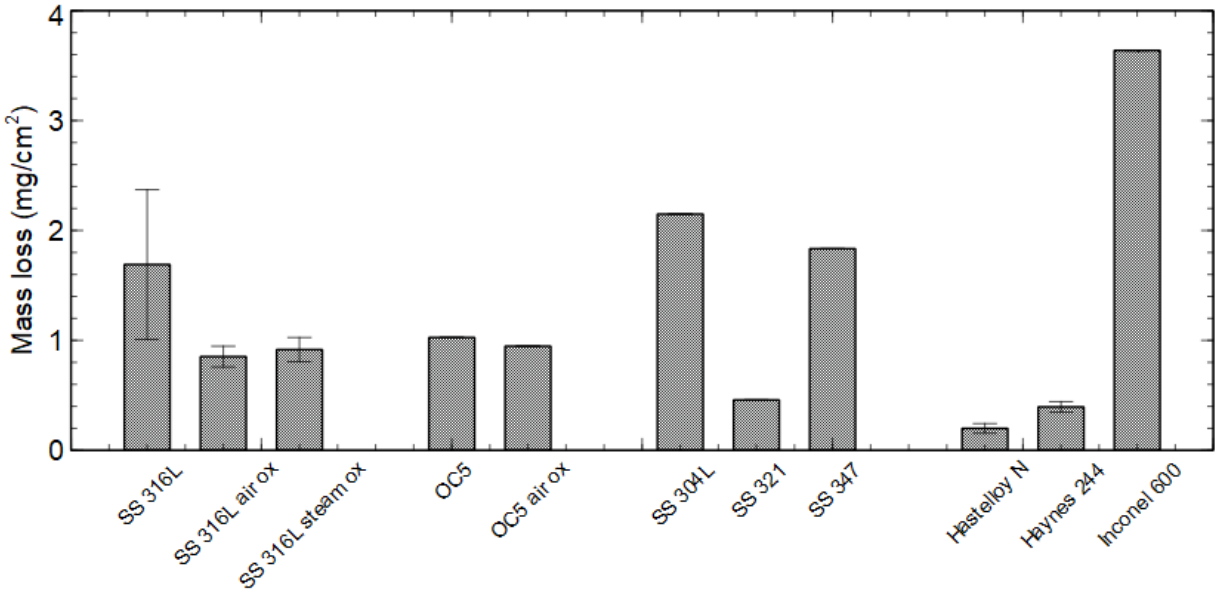

Figure 7-43 Mass loss of alloys exposed to FLiNaK at 700°C for 500 hours. Error bar indicates multiple samples.

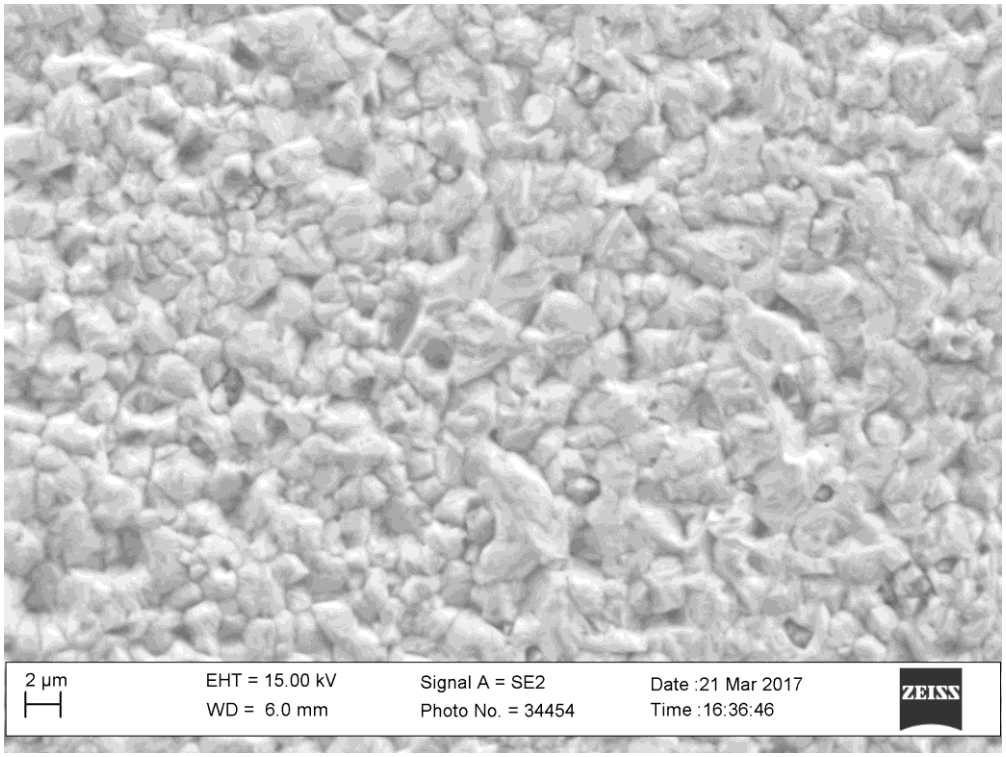

Figure 7-44 Plan view of pre-oxidized 316L sample after 500 hour FLiNaK exposure.

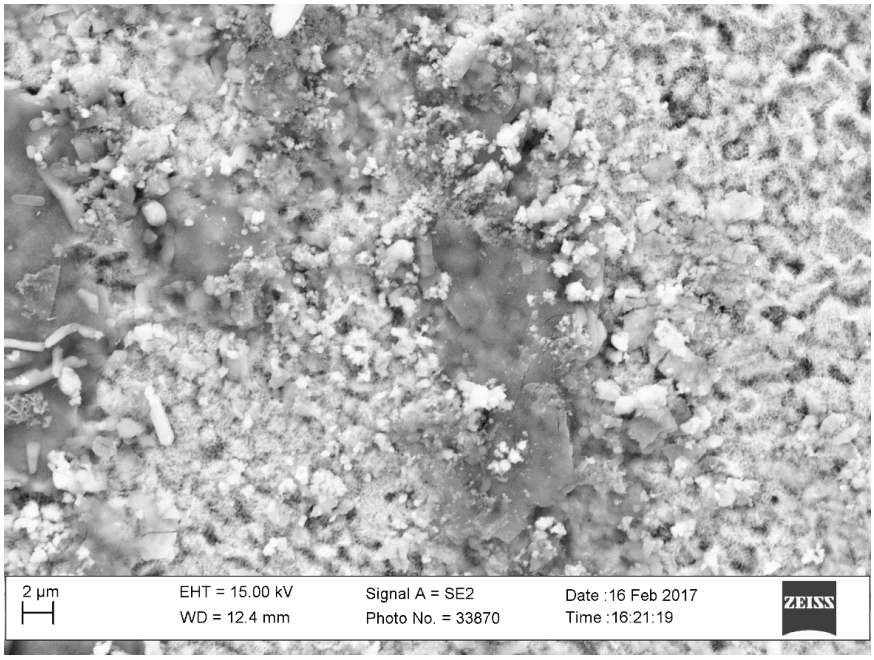

Figure 7-45 Plan view of pre-oxidized 316L sample after 25 hour FLiNaK exposure in an area with visible oxides.

An experiment was also conducted to explore effects of oxide film thickness. SS 304L, SS 306L, and SS 321 were pre-oxidized in a stagnant furnace in air for 25, 50, 100, or 200 hours. A sample of each grade of steel for each pre-oxidation time was set aside for analysis of pre-exposure oxide films. Samples were then exposed to FLiNaK following the procedures described in section 7.1.1 with 200-hour exposure time. The mass change results (
Figure 7-46) do not suggest that pre-oxidation duration had any effect on corrosion resistance.

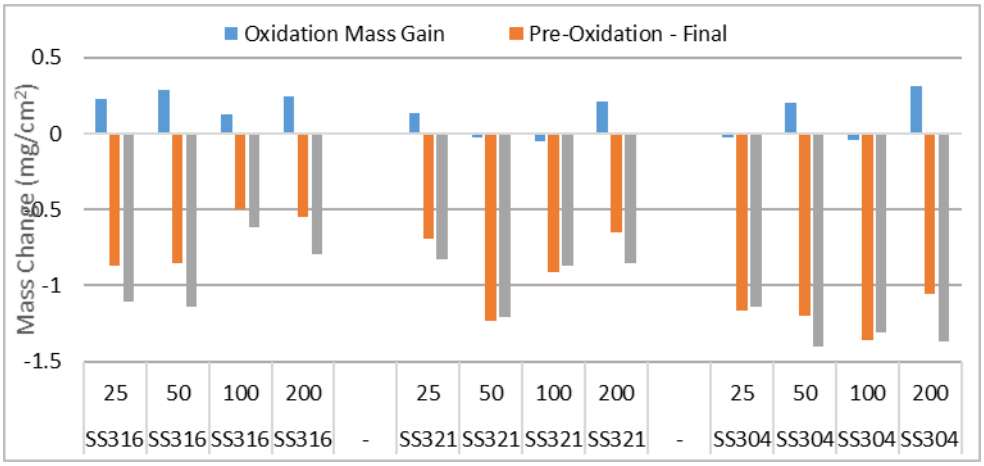

Figure 7-46 Mass change results for austenitic stainless steels which were pre-oxidized for varying durations at 700°C.

7.3.2. Reference Electrode for Electrochemical Measurements in Molten Fluoride Salts

7.3.2.1. Ni/Ni^{2+} Reference Electrode

A reference electrode compatible with molten fluorides is necessary to make redox potential measurements, but no suitable reference electrode is commercially available. To satisfy this need, a reference electrode based on work by Bronstein and Manning is being developed at Georgia Tech. [4] This design uses the Ni/Ni^{2+} redox couple in order to sustain a constant reference potential. This reference electrode system can be described as

$$Ni \left| \begin{matrix} LiF & 46.5 \\ NaF & 11.5 \\ KF & 42 \end{matrix} \; mol\%, \;\; NiF_{2(s)} \; saturated \right| LaF_{3(s)} \Bigg|$$

in electrochemical cell notation.

A sketch of the electrode design is shown in *Figure 7-47*, and a picture of the completed electrode is shown in *Figure 7-48*. A high purity Ni wire electrode is placed in FLiNaK saturated with NiF_2. This saturated FLiNaK solution is contained in hole cut in a cylindrical LaF_2 single crystal, which acts an F^- conductive membrane. Several layers of fine Ni mesh between the LaF_2 crystal and the external environment slows etching of the crystal.

Development of fluoride salt reference electrode at Georgia Tech is mirrored by similar efforts by the MIT-led FHR team at the University of Wisconsin, Madison.

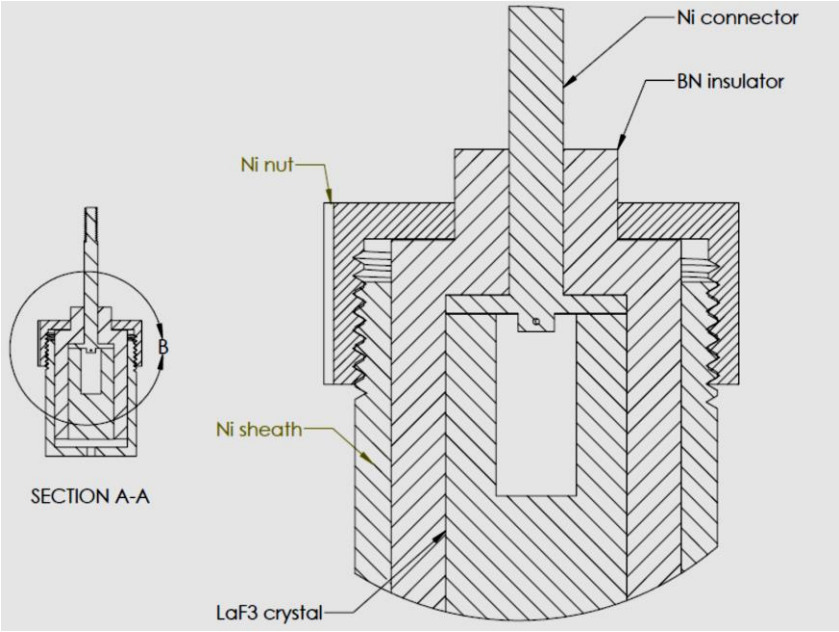

Figure 7-47 Schematic of Ni/Ni2+ reference electrode.

Figure 7-48 Completed Ni/Ni2+ reference electrode.

During testing however, the LaF_2 crystal was found to readily dissolve in FLiNaK salt. Therefore the reference electrode was modified to instead use graphite as the membrane material. Graphite membranes for Ni/Ni^{2+} reference electrodes in molten fluoride were demonstrated by Kontoyannis, Del Cul et al., and Ludwig et al. Isostatically pressed graphite stock (Grade GM-10, 3/8" diameter rod) was machined to the specifications shown in *Figure 7-49*. [12-14]

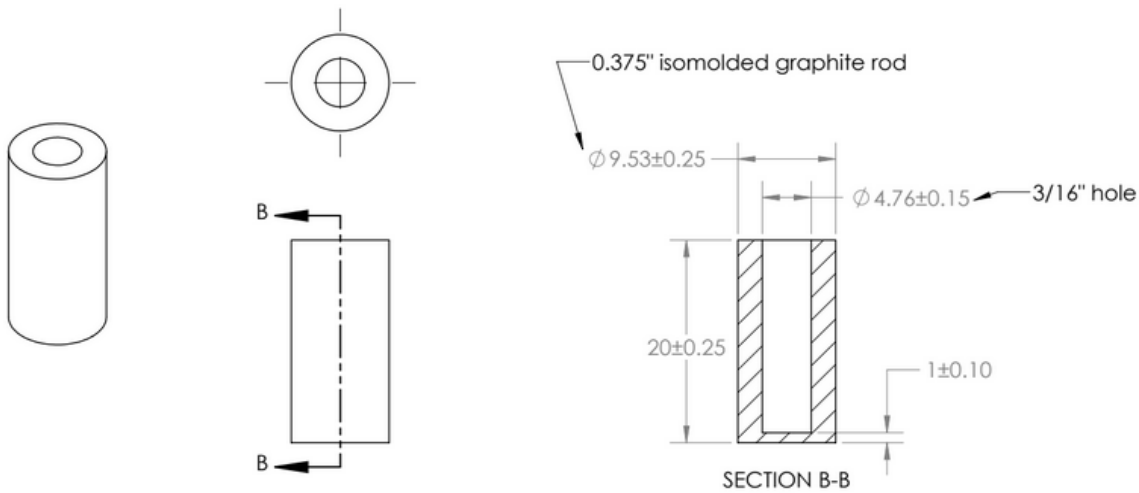

Figure 7-49 CAD drawing of graphite membrane for Ni/Ni2+ reference electrode.

The modified electrode was tested using a 2 electrode setup at 500°C under Ar atmosphere with a nickel crucible acting as the second electrode. The internal salt was FLiNaK with 1 mol% NiF_2 and the crucible salt was FLiNaK with 0.1 mol% NiF_2. Additional boron nitride spacers were placed between the graphite cup and the nickel sheath to provide electrical insulation. As shown in *Figure 7-50*, a stable potential was achieved, which was sustained for over 7 hours.

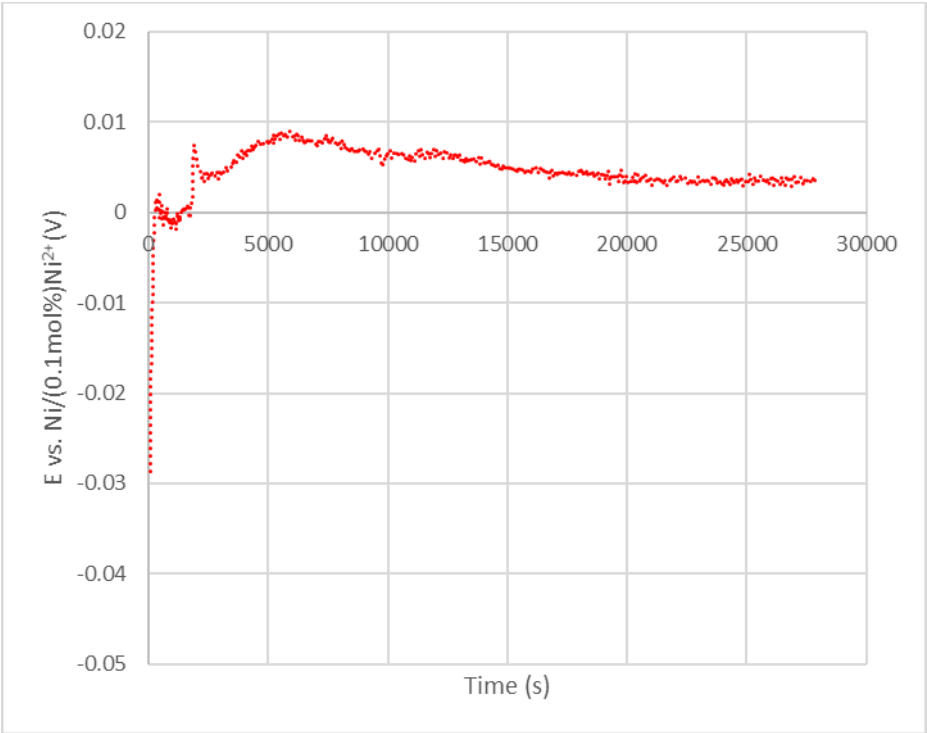

Figure 7-50 Open circuit voltage of Ni/Ni2+ reference electrode vs 0.1mol% Ni2+ reference point.

7.3.2.2. Dynamic Reference Electrode in FLiNaK

A dynamic reference electrode (DRE) for redox potential measurement in FLiNaK was tested. This work was based on a study by Durán-Klie et al., in which a DRE in FLiNaK was demonstrated. [11]

0.1 mol% NiF_2 was added to FLiNaK, which was mixed from 99% grade LiF, NaF, and KF. These salts were combined and fused in a Ni 200 crucible. The crucible and electrodes were placed in a closed cell in a furnace. The three electrodes used were (1) platinum wire working electrode, (2) graphite counter electrode, (3) Ni crucible reference electrode. The equilibrium between the dissolved NiF_2 and the Ni crucible established a stable reference potential. The cell was ramped to 500°C over 12 hours, during which a 2 L/min flow of Ar was supplied. After the cell reached 500°C, the Ar flow was increased to 4 L/min and allowed to stabilize for 1 hour. Electrodes were then inserted, and the DRE was able to be used.

DRE operation is divided into modes, active and inactive. To activate the DRE, a 6 second current pulse was applied between the working electrode and the counter electrode in order to electrochemically plate potassium thin layer of on the working electrode. After the current stopped, the electrode became active, maintaining a stable potential for a few minutes before decaying. *Figure 7-51* shows how the DRE voltage is changes through this

process. The potential during the active mode was maintained the same potential (±0.001 V) for >85% of the voltage plateau.

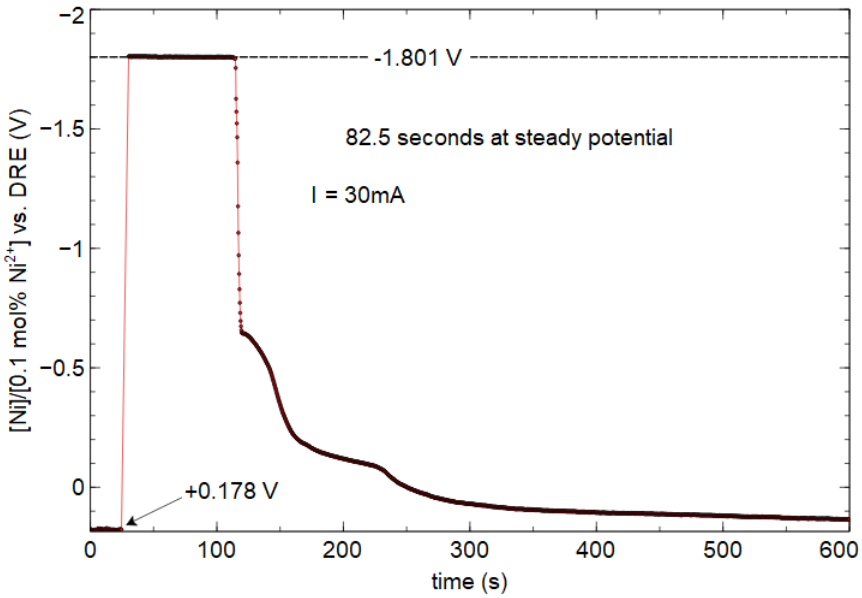

Figure 7-51 Chronopotentiogram of Ni crucible potential against dynamic reference electrode.

7.3.2.2.1. Cyclic Polarization of Hastelloy N in FLiNaK

Electrochemical experiments, including redox potential measurements and cyclic polarization will be conducted inside an oxygen and moisture controlled glove box. However, initial electrochemical tests were conducted outside the glovebox to test the experimental setup as well as to gain experience. Because of the practical difficulty of working inside a glovebox, the experimental technique and experimental setup needed to be refined before attempting the experiment inside. A cyclic polarization experiment of Hastelloy N in FLiNaK was conducted outside the glovebox.

In laboratory air, 99% purity LiF, NaF, and KF powders were weighed and mixed in the proper proportions to make 100g of FLiNaK. This mixture was placed in an alumina crucible and fused by heating to 600°C.

Cyclic polarization was conducted using Princeton Applied Research 263A potentiostat with a three-electrode electrochemical setup. The working electrode was a 1cm by 1cm piece of Hastelloy N ground to 1000grit and spot welded to a 99.99% purity Ni wire for electrical connection. The reference electrode was a Pt pseudo-reference, which was selected for simplicity. Future electrochemical experiments inside the glove box will utilize the Ni/Ni^{2+} reference electrode described in our previous reports. A Ni 200 rod polished to 1000 grit was used as the counter electrode. The cell was heated to 500°C with a constant flow of N_2 to displace air. After the temperature was stable for 30 minutes, the electrodes were lowered into the FLiNaK. The open circuit potential was measured for 5 minutes before the cyclic polarization scan was started.

The cyclic polarization curve is shown in *Figure 7-52*. The initial open circuit potential was -0.100 V vs. Pt, however the open circuit potential changed to -0.060V at the conclusion of the experiment. This change in OCP was likely occurred because we did not wait long enough after inserting the electrodes in the salt and before starting the scan. Chromium depletion at the surface of the Hastelloy N electrode over time could also account for the positive potential shift. XRF measurement (Oxford X-MET8000 Expert) using a revealed a drop in surface Cr% from 7.79% to 0.79%.

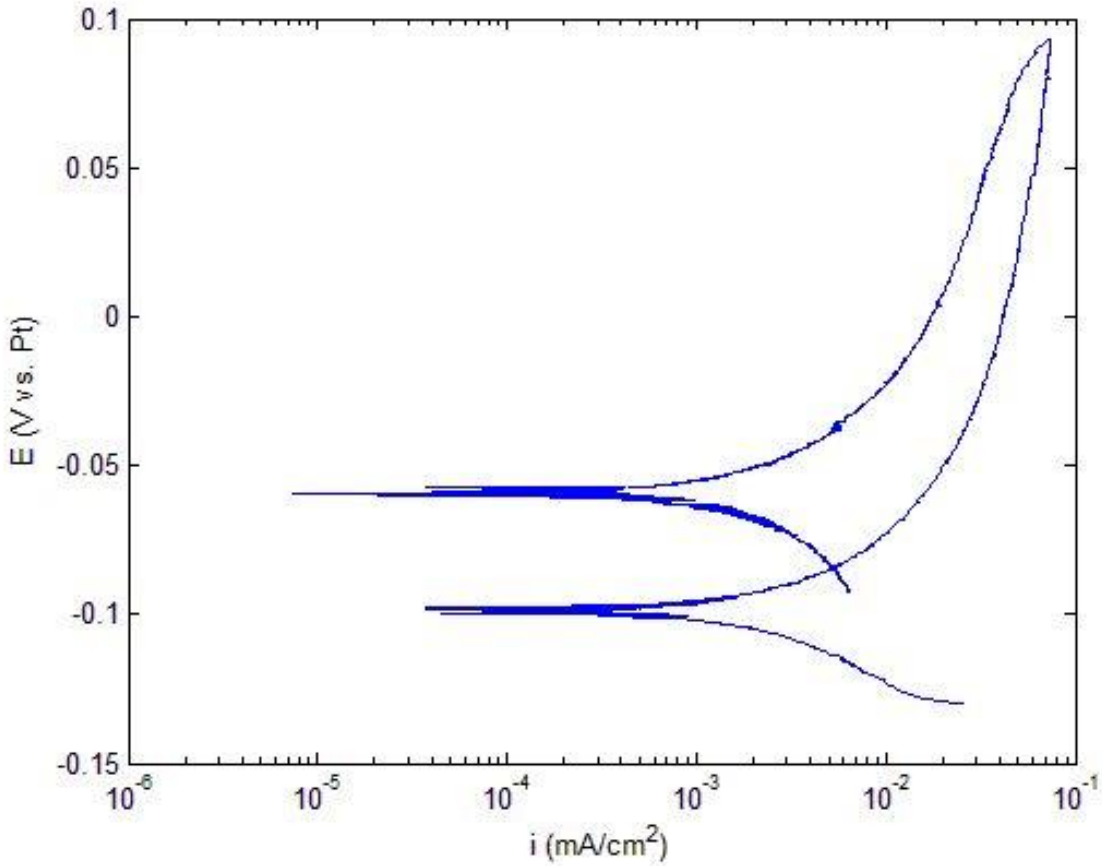

Figure 7-52 Cyclic polarization curve of Hastelloy N in FLiNaK at 500°C.

7.3.2.3. Effect of Carbon on Corrosion of Alloys in FLiNaK

7.3.2.3.1. Effect of Carburization on Corrosion Resistance of Pure Chromium

Chromium carbides coatings are applied to improve the wear and erosion-corrosion resistance of materials in high temperature applications. Chromium carbide coatings for FHR applications were explored by Nagle. They explored several methods for generating this coating on nickel alloys, and settled on a procedure in which materials were first

coated with chromium metal via electrodeposition then carburized in a methane environment. However, they were unable to produce a dense adherent coating. We produced a carbide layer on pure chromium samples and tested their corrosion resistance in molten FLiNaK. We approached this problem from another angle. Because methods for deposition of chromium films is well established, we focused on the carburization of pure chromium and the resulting film properties. [2.4]

Pure chromium samples were carburized in a reducing hydrocarbon environment. The reactor containing the samples was ramped to 800°C over one hour with 200 SCCM ultra-high purity argon flow. Upon reaching 800°C, the gas composition was changed to 116 SCCM H_2 + 84 SCCM C_3H_8. After the prescribed time (12-200 hours) had passed, the heaters were turned off. When the reactor cooled below 40°C, gas lines were closed and samples were retrieved. After carburization, samples were cleaned ultrasonically in water and methanol before being reweighed. Selected samples were set aside for characterization. The remaining samples were exposed in FLiNaK for 100h at 700°C.

The characterization of chromium samples after carburization is summarized in *Figure 7-53*. Chromium samples formed a multi-layered structure during the carburization process. The surface was covered by a carbon film (*Figure 7-53*a). The Raman spectrum of this film is shown in *Figure 7-53*c with D and G bands labeled at 1320 cm^{-1} and 1610 cm^{-1}, which indicates that it is nanocrystalline graphite. The XRD pattern (*Figure 7-53*d) collected at a glancing angle (Ω=5°) for a sample carburized for 100 hours displays peaks belonging to Cr_2O_3 and Cr_3C_2. The cross section shown in *Figure 7-53*b reveals the existence of four distinct layers: nanocrystalline graphite, Cr_2O_3, Cr_3C_2, and the bulk chromium phase. [2.5]

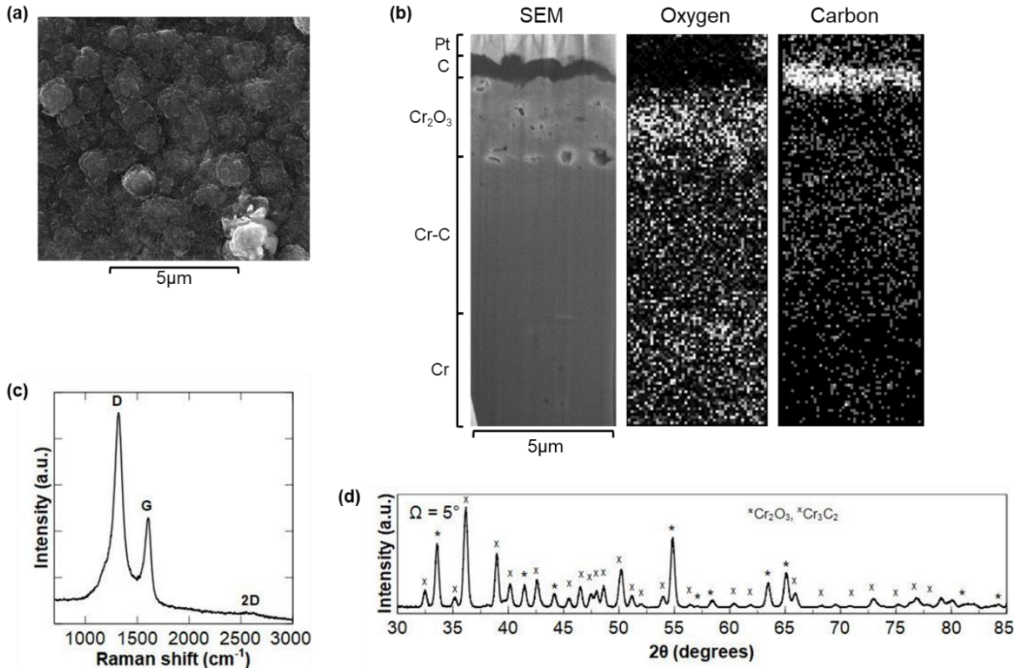

Figure 7-53 Characterization of 200-hour carburized chromium sample before corrosion test: (a) SEM image of sample surface (b) SEM/EDS of FIB cross section (c) Raman spectra of sample surface (d) GAXRD analysis.

The surface of the sample after the corrosion test (*Figure 7-54*a) was covered by the original carbon layer formed during carburization with some redeposition of corrosion products on top. The Raman spectra of the surface exhibits the D and G bands of graphite at 1300 cm^{-1} and 1600 cm^{-1}. The film is partially reflective due to the deposited corrosion product, which caused the high background signal. XRD patterns taken at Ω=5° were dominated by Cr_2O_3 and Cr_3C_2 peaks similar to pre-corrosion samples, however for Ω=20°, the peaks of salt component NaF was high in intensity. The FIB cross section (*Figure 7-54*b) of a chromium sample carburized for 200 hours and exposed to molten fluoride shows how the layers were changed by corrosion.

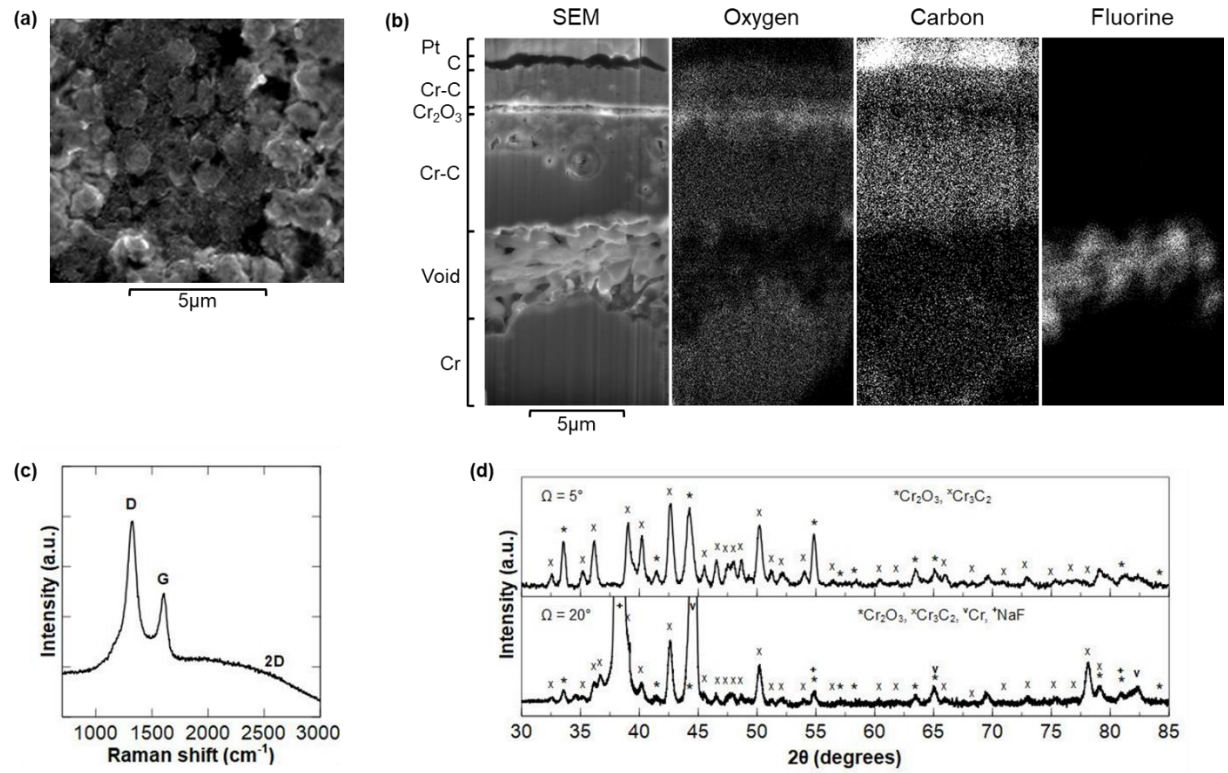

Figure 7-54 Characterization of 200 hour carburized chromium sample after 100 hour exposure to FLiNaK at 700° C: (a) SEM image of sample surface (b) SEM/EDS of FIB cross section (c) Raman spectra of sample surface (d) GAXRD analysis.

A carbide layer largely replaced the Cr_2O_3 layer just below the surface carbon film. This upper carbide layer was formed by the carburization of the Cr_2O_3 layer. Carbon for carburization reactions was provided from the surface carbon film above and the carbide layer below according to Equations 1 and 2.

$$Cr_2O_3 + C \rightarrow Cr_xC_y + CO_{2(g)} \text{ (Eq. 1)}$$
$$Cr_2O_3 + Cr_3C_2 \rightarrow Cr_xC_y + CO_{2(g)} \text{ (Eq. 2)}$$

Compared to the Cr_2O_3 layer before exposure, the (new) upper carbide layer was less porous. This suggests that the new Cr_3C_2 layer nucleated at the interface of the Cr_2O_3 layer and surface carbon film and grew downwards, rather than by carburization the Cr_2O_3 layer in-place. Void formation within the lower carbide layer was caused by the diffusion of carbon driven by reaction in Equation 2.

The lower carbide layer appears to be about the same thickness as in the uncorroded sample. Chromium carbide is significantly more resistant to corrosion by molten fluorides than chromium metal. The voids beneath the chromium carbide layer were infiltrated by the fluoride salt. These formed due to defects in the carbide layer, which allowed undercut

corrosion to occur. The lack of fluorine EDS signal within any of the upper layers suggests that the chromium carbide would be impermeable to fluoride salts if free of defects.

The surface carbon film plays a key role in stabilizing chromium carbide. Because carbon is a product of chromium carbide corrosion by molten fluoride, this layer can be expected to regenerate if damaged. Corrosion of chromium carbide causes the local carbon activity to increase, which makes further corrosion less favorable. This is described by the reaction,

$$Cr_3C_2 + 3F_2 \leftrightarrow 3CrF_2 + 2C \text{ (Eq. 3)}$$

In this way, the chromium carbide film is self-stabilizing. The carbon film also acts as a diffusion barrier which may also limit the interaction between chromium carbide and the fluoride salt.

The mass loss data for these tests (*Figure 7-55*) show that longer carburization generally results in reduced mass loss, significantly lower than unprocessed chromium. This would suggest that the thicker carbide film produced by longer carburization duration is what increases corrosion resistance.

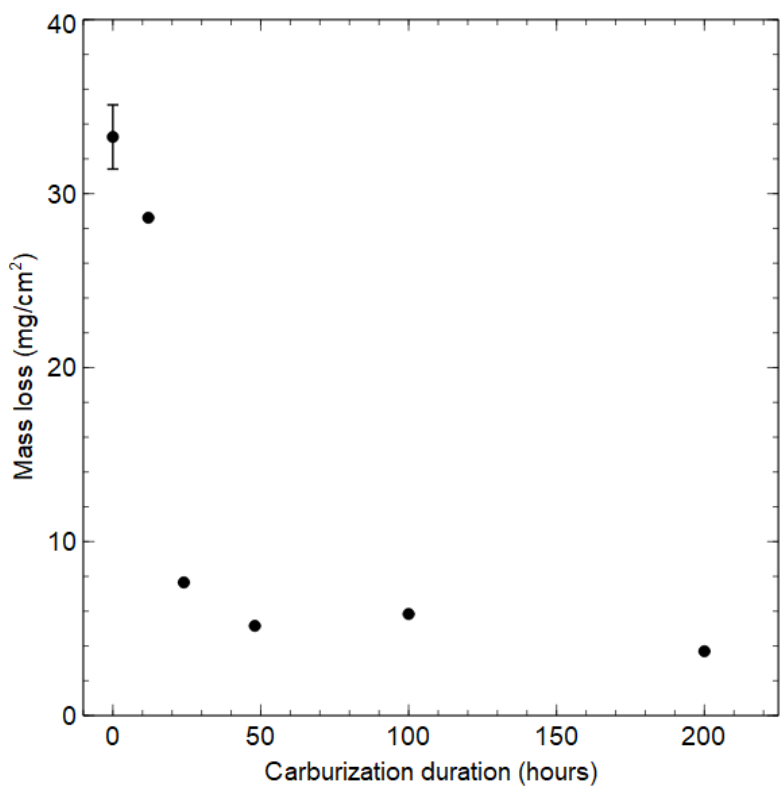

Figure 7-55 Mass loss of carburized pure chromium samples exposed to FLiNaK for 100 hours.

7.3.2.3.2. Effect of Carburization on Corrosion Resistance of Haynes 230

We had previously examined the effect of carburization on the corrosion resistance of pure chromium. A dense chromium carbide layer was formed during the carburization process, which appeared to limit corrosion. The effect of carburization on nickel-based alloy Haynes 230 was studied. Haynes 230 was selected due to its high Cr content (22 wt.% nominal).

Haynes 230 samples were carburized in a reducing hydrocarbon environment. The reactor containing the samples was ramped to 800°C over one hour with 200 SCCM ultra-high purity argon flow. Upon reaching 800°C, the gas composition was changed to 116 SCCM H_2 + 84 SCCM C_3H_8. After 200 hours had passed, the heaters were turned off. When the reactor cooled below 40°C, gas lines were closed and samples were retrieved. After carburization, samples were cleaned ultrasonically in water and methanol before being reweighed. The samples were exposed in FLiNaK for 100h at 700°C. These samples were characterized by glancing angle X-ray diffraction (GAXRD) and Raman spectroscopy. Cross sections were prepared by both conventional and focused ion beam methods, and examined by light microscopy and SEM/EDS.

GAXRD patterns, taken with glancing angle Ω = 5° (~2.5μm) and Ω = 20° (~10μm) are shown in *Figure 7-56*. In addition to the bulk FCC phase, various carbides phases were identified. M_6C and $M_{23}C_6$ type carbides are intentionally present in Haynes 230 to increase resistance to grain coarsening and creep, respectively. In the Ω = 5° pattern (*Figure 7-56*a), MC, M_2C, and $M_{23}C_6$ type carbides were identified, however M_6C carbides were absent. At greater depths (*Figure 7-56*), the Ω = 20° pattern showed MC, M_6C, and $M_{23}C_6$ carbides, with M_2C carbides absent. Both MC and M_2C carbides are more likely to form when carbon activity is high, as is the case after carburization. Salt components LiF, NaF, and KF were detected in the Ω = 20° pattern, which indicates penetration by the salt. [6]

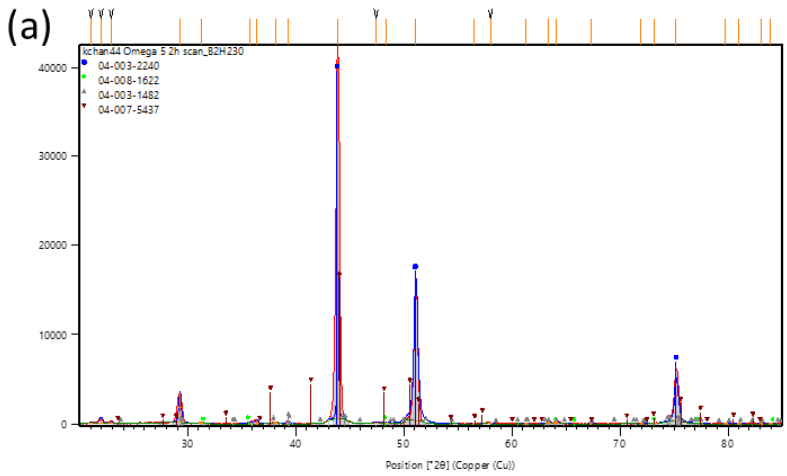

Reference #	Identified phase
04-003-2240	Bulk FCC phase
04-008-1622	MC
04-003-1482	M2C
04-007-5437	M23C6

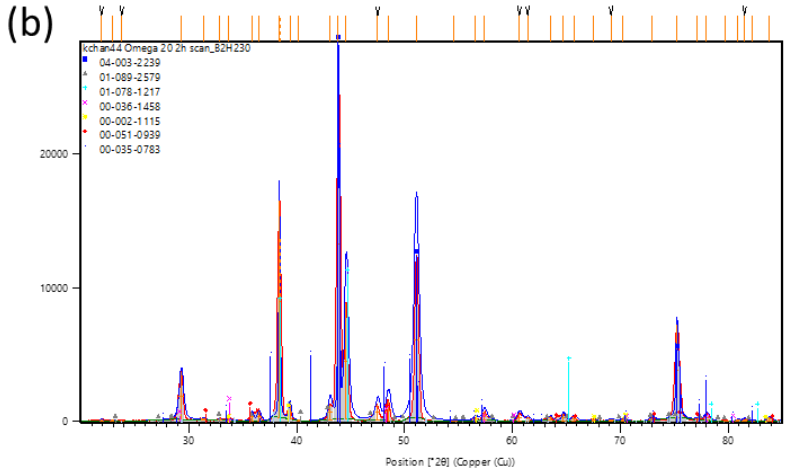

Reference #	Identified Phase
04-003-2239	Bulk FCC phase
01-089-2579	M6C
00-051-0939	MC
00-035-0783	M23C6
01-078-1217	LiF
00-036-1458	NaF
00-002-1115	KF

Figure 7-56 GAXRD patterns of Haynes 230 after exposure to FLiNaK at 700C for 100 hours for (a) Ω = 5° and (b) Ω = 20°.

The SEM image of the FIB cross section, as well as EDS elemental maps are shown in *Figure 7-57*. At this location, chromium depletion was observed to a depth of 6µm. In the chromium depletion zone, nickel enrichment was also observed. From 6µm to 13µm, a layer of carbides were observed.

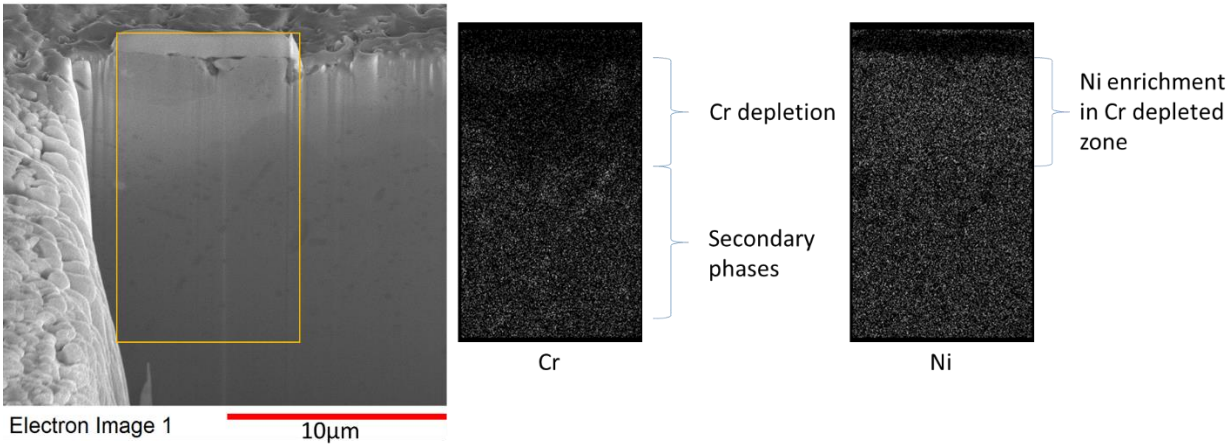

Figure 7-57 SEM and EDS analysis of FIB cross section of pre-carburized Haynes 230 after exposure to FLiNaK at 700C for 100 hours.

The FIB cross section and traditional cross sections are compared to those of Haynes 230 that was not carburized before exposure in *Figure 7-58*. The depths of attack in both cases were similar, however carburized Haynes 230 experienced less matrix attack. The additional carbon activity provided by the carburization step may stabilize chromium by inducing the formation of carbides.

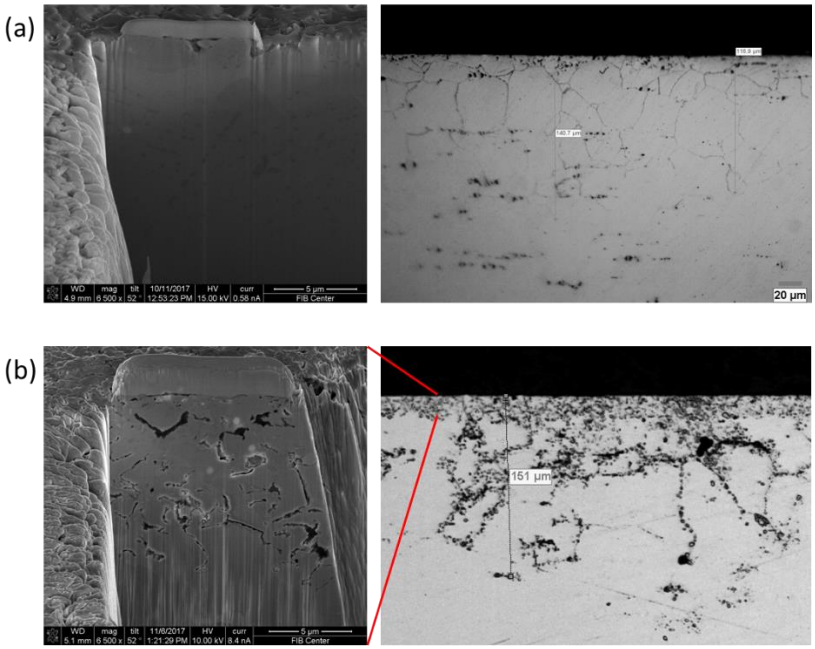

Figure 7-58 Cross sections of (a) pre-carburized and (b) not pre-carburized Haynes 230 after exposure to FLiNaK at 700C for 100 hours.

7.3.2.3.3. Effect of Carburization on Corrosion Resistance of Ni Alloys

We had previously examined the effect of carburization on the corrosion resistance of pure chromium. In this quarter, the effect of carburization on nickel alloys Hastelloy N, Haynes 244, Inconel 800H, and Haynes 230 were studied.

Hastelloy N, Haynes 244, Inconel 800H, and Haynes 230 samples were carburized in a reducing hydrocarbon environment. The reactor containing the samples was ramped to 800°C over one hour with 200 SCCM ultra-high purity argon flow. Upon reaching 900°C, the gas composition was changed to 116 SCCM H_2 + 84 SCCM C_3H_8. After 200 hours had passed, the heaters were turned off. When the reactor cooled below 40°C, gas lines were closed and samples were retrieved. After carburization, samples were cleaned ultrasonically in water and methanol before being reweighed. The samples, and samples of the same materials that were not carburized were exposed in FLiNaK for 100h at 700°C according the procedure described in previous quarterly reports. These samples were characterized by glancing angle X-ray diffraction (GAXRD) and Raman spectroscopy.

GAXRD patterns are shown in *Figure 7-59*. In addition to the bulk FCC phase, various carbides phases were identified. $Cr_{23}C_6$ carbides were detected in all four alloys, which is expected because all these alloys contain significant Cr. Mo_2C type carbides were detected in Hastelloy N, Haynes 244, and Haynes 230. WC type carbides were detected in Haynes 244 and Haynes 230. Salt components were detected in Haynes 230 and Incoloy 800H, which indicates penetration by the salt. [1]

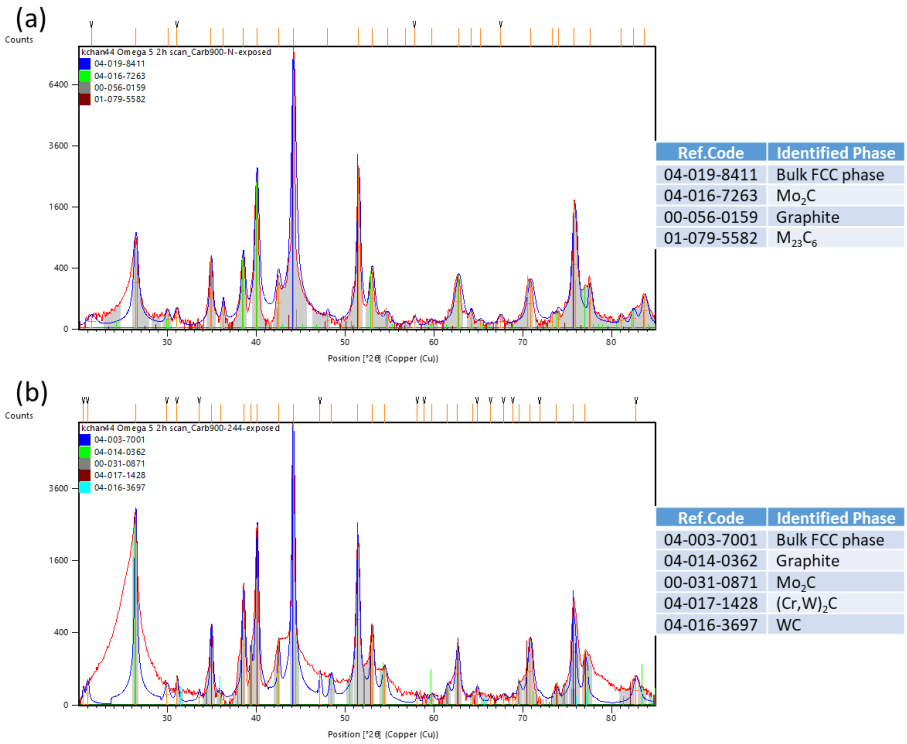

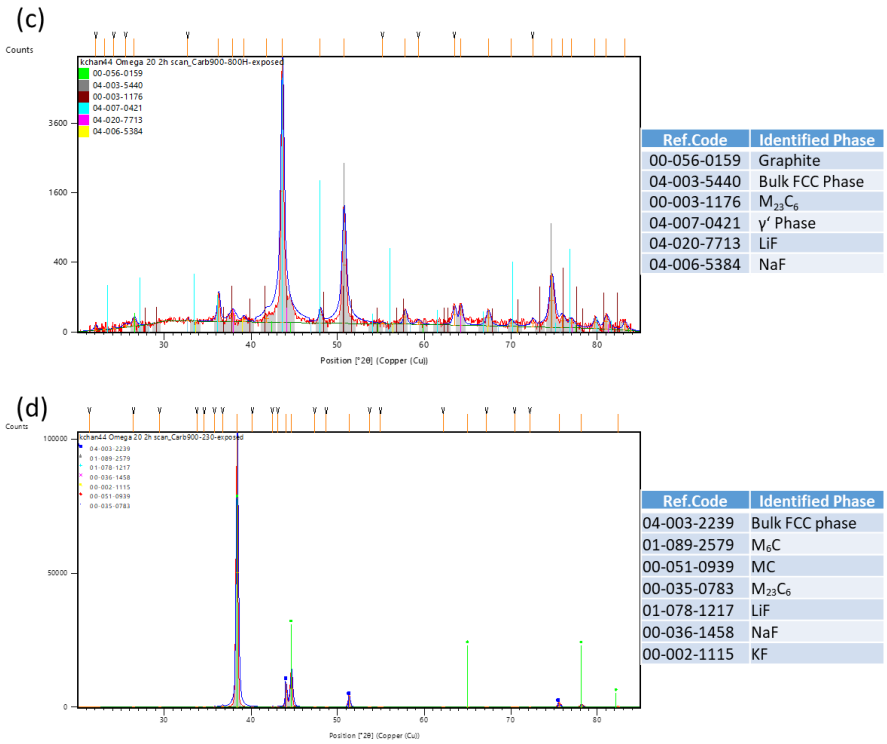

Figure 7-59 GAXRD patterns of pre-carburized nickel based alloys a) Hastelloy N (5°), b) Haynes 244 (5°), c) Inconel 800H (20°), and d) Haynes 230 (20°) after exposure to FLiNaK at 700C for 100 hours.

The mass change for carburized samples was compared to those of untreated samples that were not carburized in *Figure 7-60*. The relative mass loss of untreated samples were within expectation, with Hastelloy N having the least mass loss and Haynes 230 with the greatest. The mass loss of carburized samples was greater, however some of the mass loss can be attributed to damage of the fragile carbon film which was generated during carburization. The post-exposure mass of each carburized alloys was greater than the pre-carburization mass. Therefore mass loss should be used to evaluate corrosion of carburized alloys.

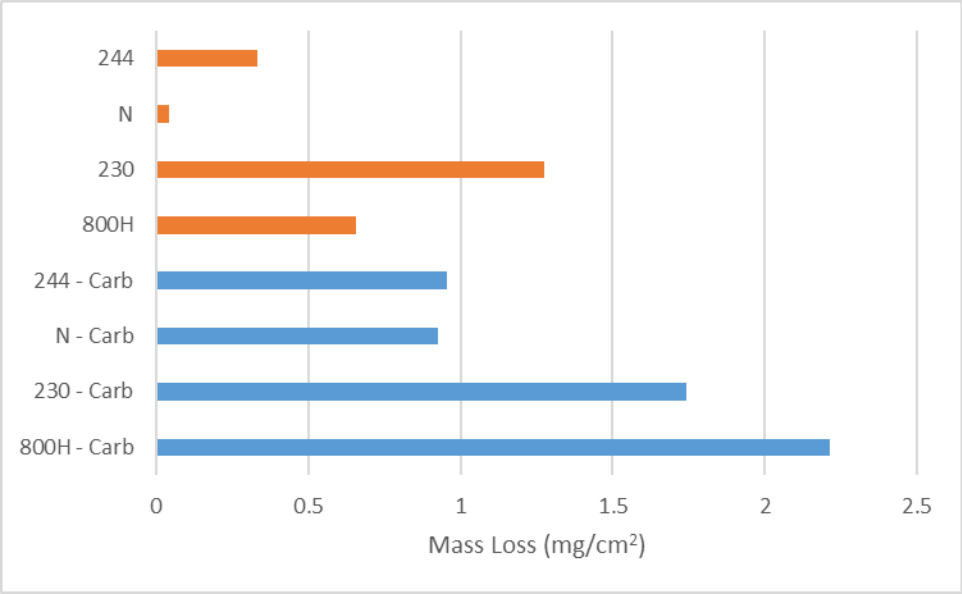

Figure 7-60 Mass loss of alloys exposed to FLiNaK at 700C for 100h in graphite crucibles.

Cross sections of carburized alloys not exposed to FLiNaK salt are shown in *Figure 7-61* and *Figure 7-62*. Hastelloy N and Haynes 244 samples appeared to be carburized through the entire thickness, while Haynes 230 and Incoloy 800H samples were carburized to depths of 350 µm and 1200 µm, respectively. Up to a depth of roughly 300 µm, Hastelloy N and Haynes 244 samples carbide domains were finely dispersed within grains, but at greater depths these were coarser and more prominent along grain boundaries.

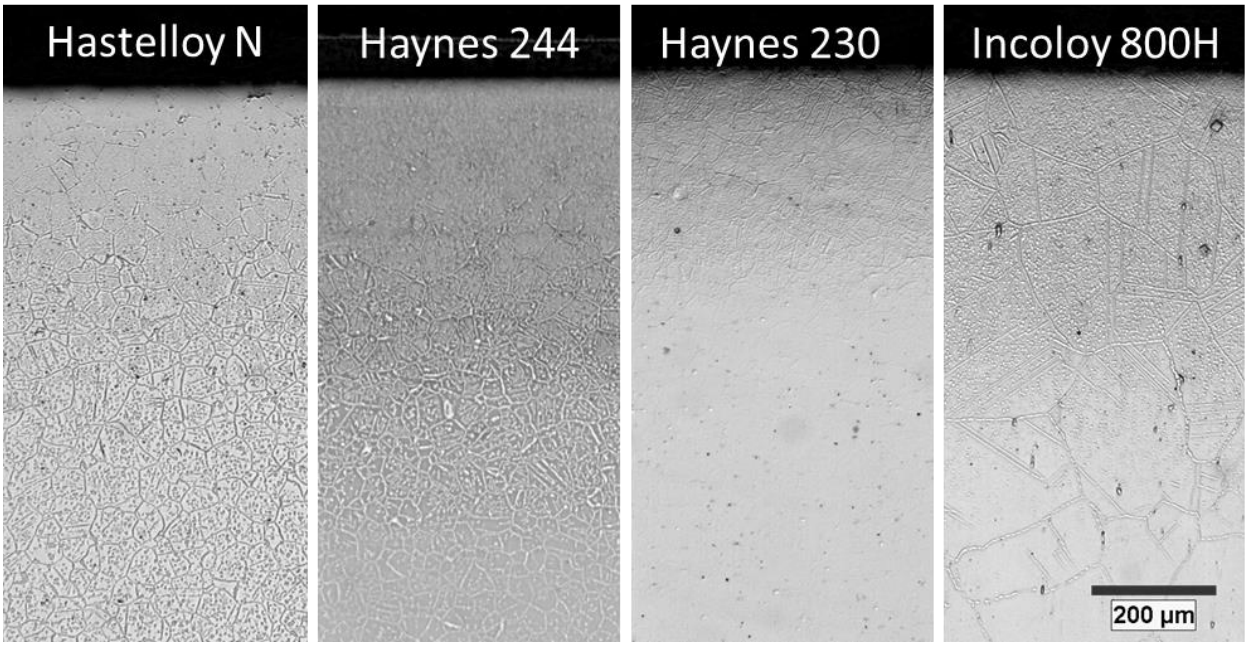

Figure 7-61 Cross sections of carburized Ni based alloys. OM image, 50x magnification.

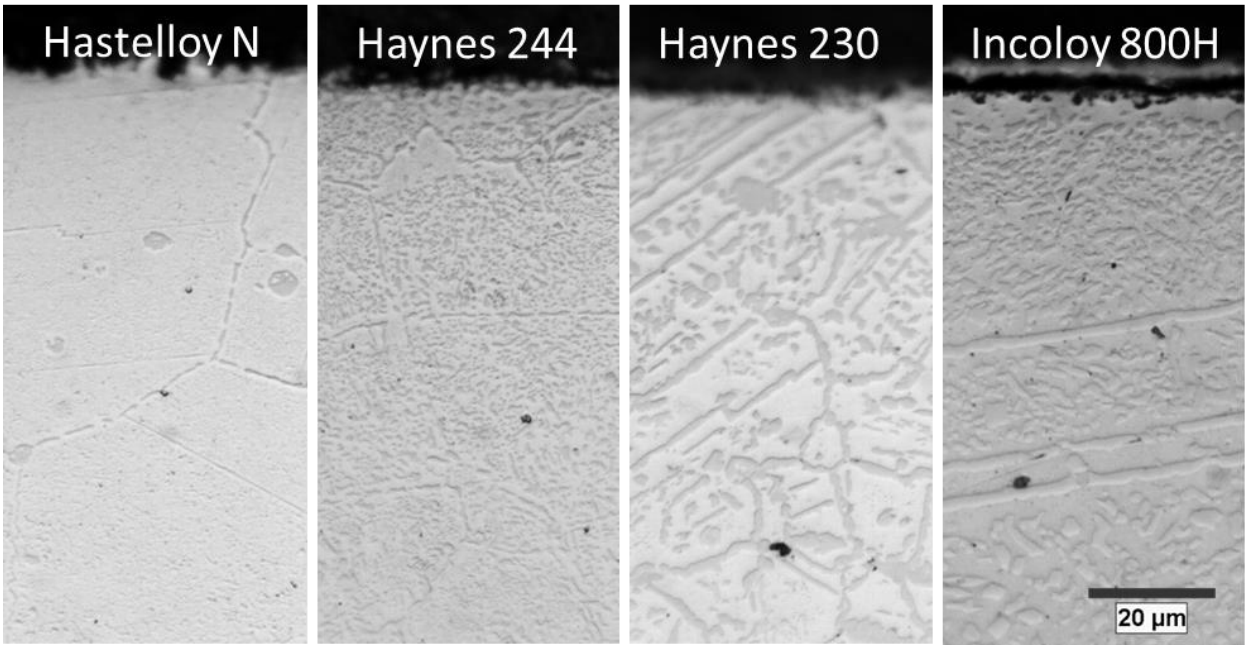

Figure 7-62 Cross sections of carburized Ni based alloys. OM image, 500x magnification.

Cross sections of pre-carburized samples after exposure are shown in *Figure 7-63*, and cross sections samples after exposure which were not pre-carburized are shown in *Figure 7-64* for comparison. Maximum depth of attack measurements for both matrix and grain

boundary type attack are summarized in *Table 7-1Table 7-1*. Subsurface voids, which form due to matrix attack were observed in Haynes 244, Haynes 230 and Incoloy 800H samples without pre-treatment. Grain boundary attack was also observed in Haynes 244 and Haynes 230 samples. Corrosion of pre-carburized samples was only observed for high Cr containing alloys, Haynes 230 and Incoloy 800H. The attack followed along carbide domains, primarily those along grain boundaries.

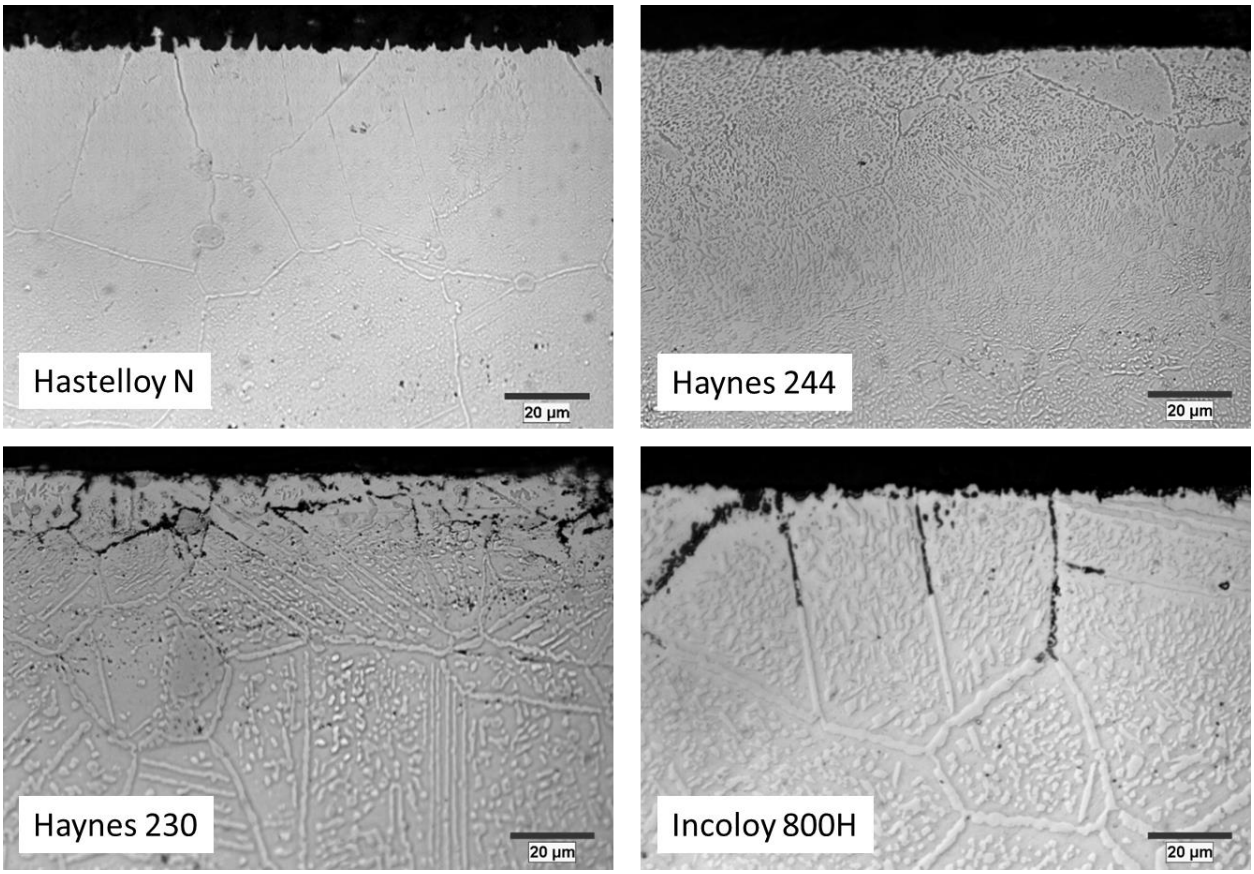

Figure 7-63 Cross sections of pre-carburized Ni based alloys samples after exposure to molten FLiNaK at 700°C for 100 hours.

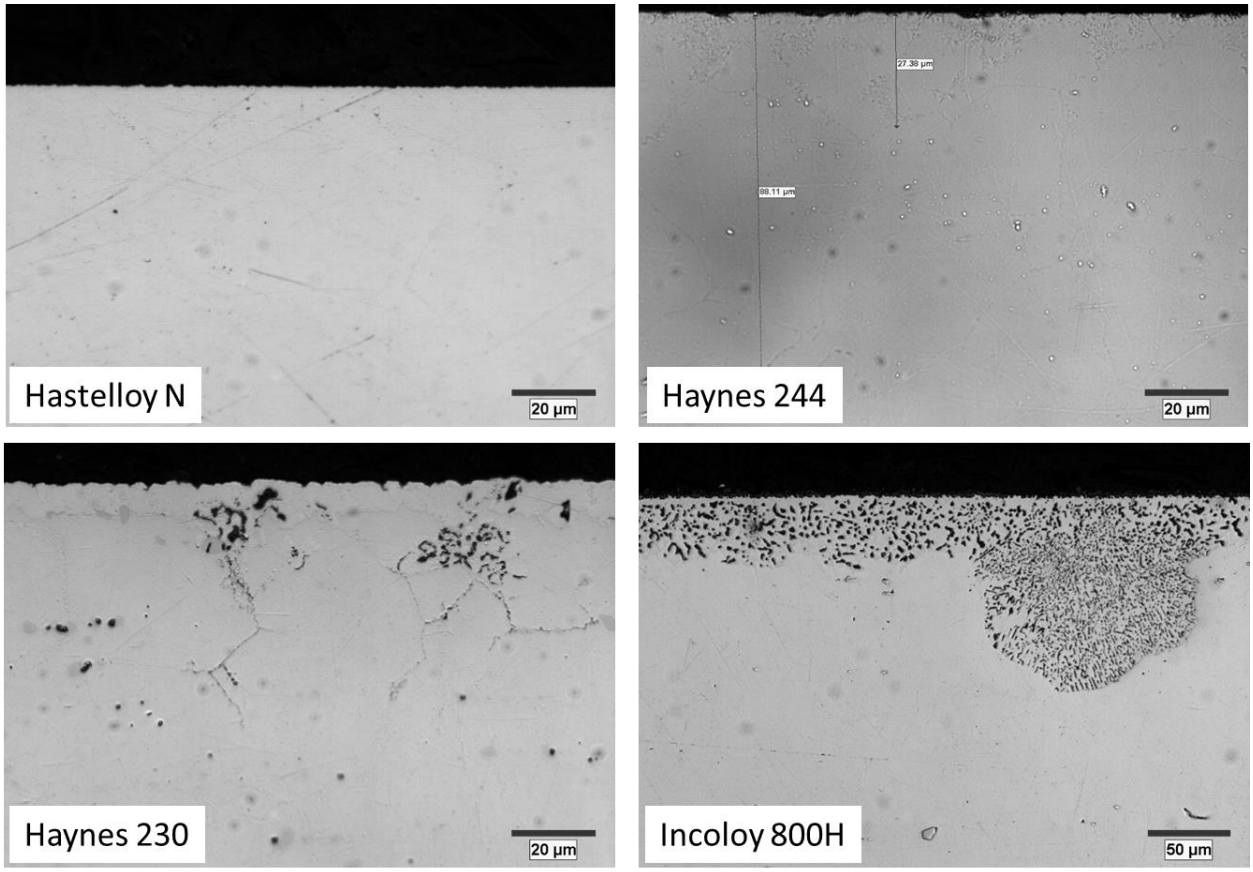

Figure 7-64 Cross sections of Ni based alloy samples after exposure to molten FLiNaK at 700°C for 100 hours.

Table 7-2 Maximum depth of attack of pre-carburized Ni based alloys after exposure to molten FLiNaK. 'NM' indicates attack was not measurable using OM images.

	No pre-treatment		**Pre-carburized**	
attack type	*GB*	*Matrix*	*GB*	*Matrix*
Hast. N	NM	NM	NM	NM
HA 244	90	30	NM	NM
HA 230	59	25	20	NM
Inc. 800H	NM	119	40	NM

7.3.3. In-situ Carburization of Alloys in Molten Salts

7.3.3.1. Pure metals exposed to molten FLiNaK with added carbonate

Several researchers have observed carburization of alloys after exposure to fluoride salt when graphite is present. This occurred even when there was no direct contact between the metal samples and the carburized surface. However, the mechanism for carbon transport is not obvious, because elemental carbon is not known to be soluble in molten fluorides. Possible transport mechanisms, including both physical and chemical type mechanisms were considered. [15-18]

Due to imperfect cleaning or wear during operation, some amount of carbon particles can be expected to break free from graphite components in contact with the molten salt. These particles may become suspended and be carried by the flowing salt elsewhere in the system. Carbon would then be transferred to alloy surfaces when these particles come in contact. Work by Zheng et al. and Xie et al. examined graphite particles found in molten FLiBe that was in contact with graphite and found graphite particles roughly 50nm or greater. [1, 19]

Carbon could be soluble in molten fluoride if it first reacts to form an ionic molecule. The most reasonable candidate molecule is the carbonate (CO_3^{2-}) ion. Carbonate ions can form from oxide (O^{2-}) impurities in the salt if CO_2 is present, or possibly by direct reaction between oxide and elemental carbon. Carbonate would then be reduced on metal surfaces and deposit carbon.

Our previous experience was used to guide which mechanism should be pursued. We considered the morphology of a carbon film found on a W sample exposed to molten FLiNaK in a graphite crucible. This carbon film was found to be highly uniform in both thickness and grain structure, which was characteristic of chemically deposited films. We therefore decided to investigate the possibility of a chemical transport mechanism. [18]

Carbonate reduction in molten alkali fluoride salt has been studied previously by several groups. These studies showed that an applied potential beyond the cathodic limit of the salt was necessary to reduce carbonate ions and suggest that reduction would not be expected without such an applied potential. Nevertheless, an initial experiment was conducted to determine if carbonate reduction was possible in the absence of any applied potential. [20-22]

Pure Fe, Ni, Cr, Mo, and W were cut into 1 cm by 1 cm samples. All samples were wet ground up with up to 400 grit SiC paper, then rinsed with deionized water and acetone. Initial dimensions and weight of each sample were recorded. LiF (99.85%), NaF (99.99%), and KF (99%) and Li_2CO3 (99%) powders were directly mixed in 15ml Ni 205 crucibles to ensure that carbonate was the only source of carbon. Each crucible contained 9g of salt with cation ratio 46.5-11.5-42 mol% Li^+-Na^+-K^+ and anion ratio 95-5 mol% F^--CO_3^{2-}. FLiNaK salt without carbonate was also prepared. These salts were fused by heating to 600C for 1 hour, followed by furnace cooling. As depicted in *Figure 7-65*, each sample was suspended

above the crucible floor using Ni wire (99.95%) and electrically insulated from the crucible using an alumina ring. The crucibles were loaded into a crucible rack, which was lowered into a vertical furnace at room temperature. Crucibles with salt both with and without added carbonate were placed in the furnace at the same time. The furnace set point was raised to 700°C and held for 100 hours. Salt preparation and the experiment were done in an oxygen and moisture controlled glovebox.

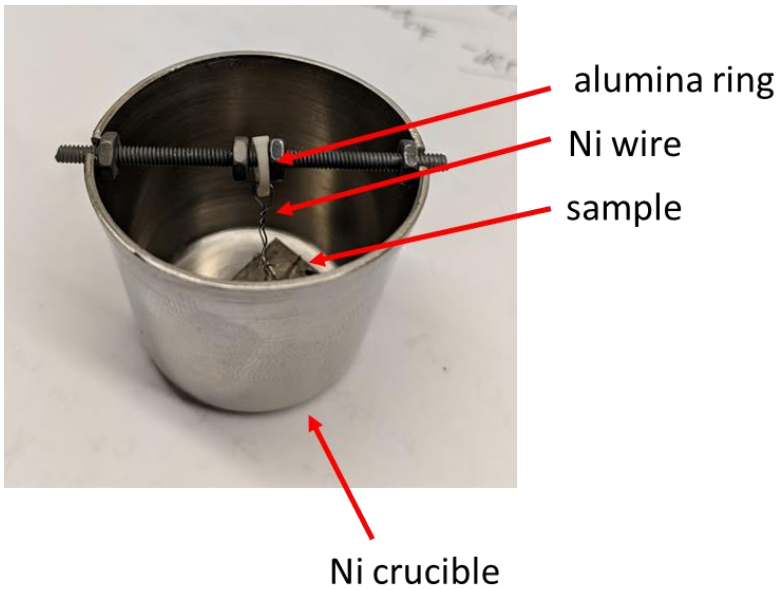

Figure 7-65 Exposure test configuration in Ni 205 crucible.

After cooling to room temperature, the crucibles were removed from furnace and the salt was crushed with a hammer to fragment the FLiNaK and retrieve the samples. The alloy samples were cleaned ultrasonically in deionized water, acetone, and then methanol. After drying, the samples were weighed using a high precision balance. Samples were analyzed by SEM, XRD, and Raman spectroscopy.

Results

Glancing angle XRD was used for post-exposure phase identification. Only the FCC matrix phase was detected for the nickel samples (*Figure 7-66*). $LiFeO_2$ was identified along with the BCC matrix on Fe samples exposed to FLiNaK with added carbonate (*Figure 7-67*). Strong peaks for $LiCrO_2$ were detected on exposed Cr samples (*Figure 7-68*). With added carbonate, the Cr_7C_3 carbides were also identified. The dominant phase on Mo samples was Mo_2C carbide (*Figure 7-69*). MoC, LiF, and K_2MoO_4 were also identified. WC was detected on W samples (*Figure 7-70*).

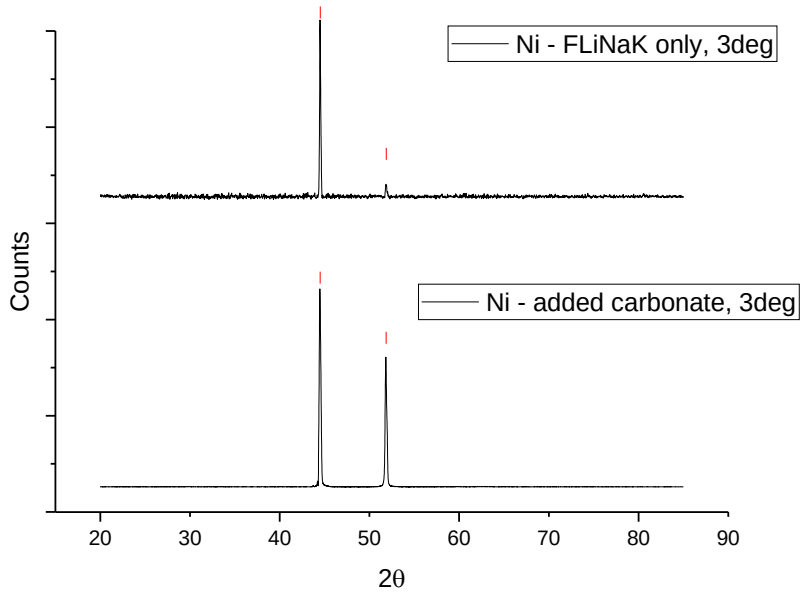

Figure 7-66 GAXRD pattern of Ni samples.

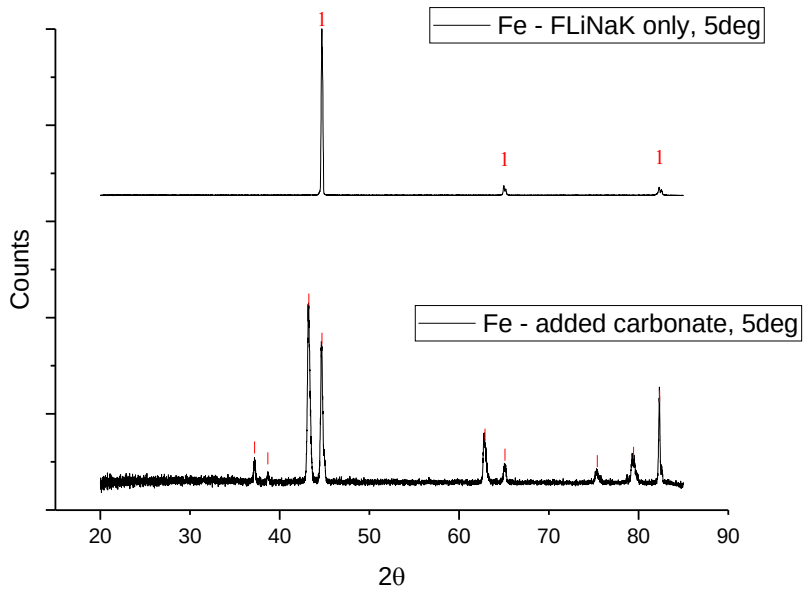

Figure 7-67 GAXRD pattern of Fe samples.

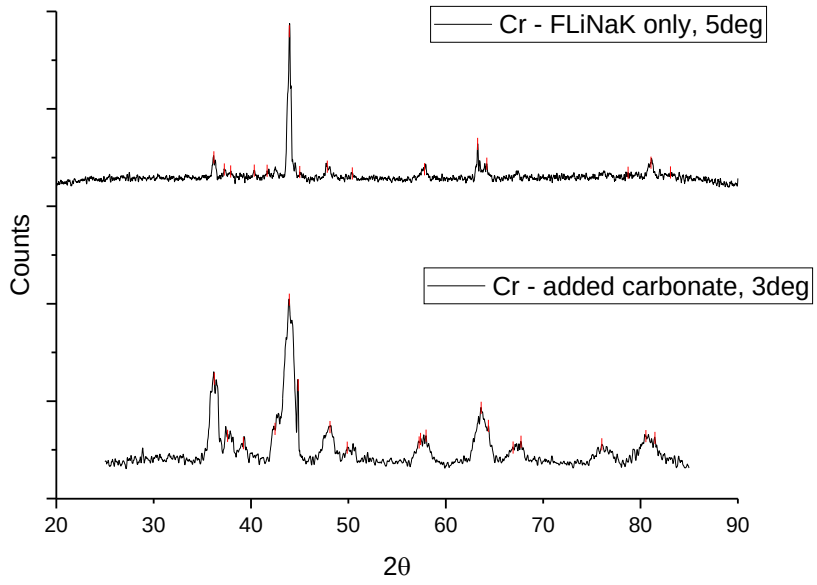

Figure 7-68 GAXRD pattern of Cr samples.

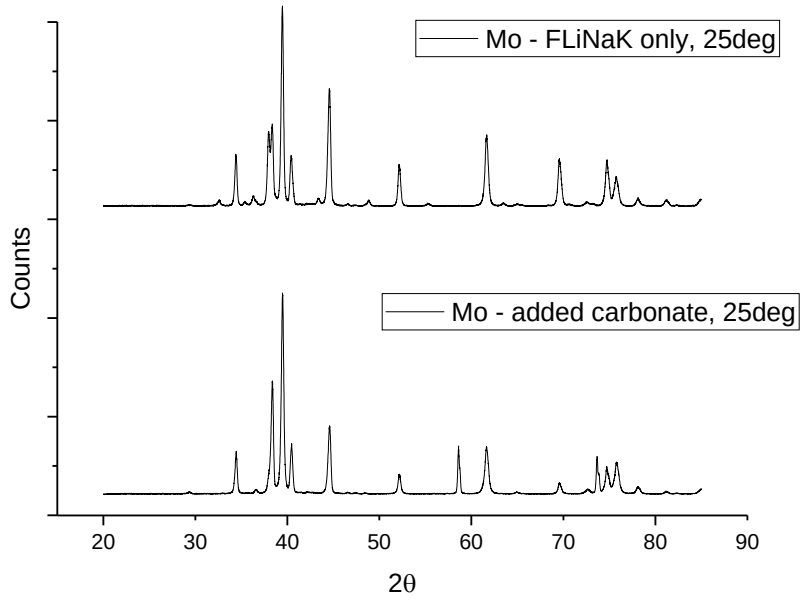

Figure 7-69 GAXRD pattern of Mo samples.

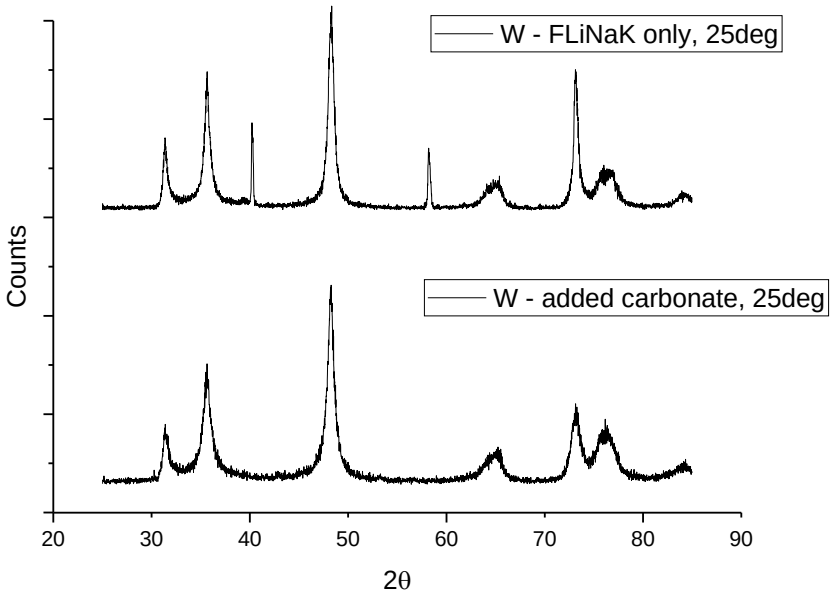

Figure 7-70 GAXRD pattern of W samples.

Raman spectroscopy was used to identify carbon and oxide phases on the sample surface. Secondary phase particles found on the surface of Ni samples exhibit the D (1345cm^{-1}) and G (1603cm^{-1}), and 2D (2900cm^{-1}) which indicate graphite or similar carbon phase (*Figure 7-71*). The Fe sample (*Figure 7-72* exposed to FLiNaK with added carbonate had $LiFeO_2$ peaks in spectra taken on the surface (438, 607cm^{-1}). Particles adherent to the surface appear to be graphite based on their Raman spectra. Spectra for Cr samples both with (*Figure 7-73*), and without added carbonate (*Figure 7-74*) had peaks corresponding to $LiCrO_2$ (446, 580cm-1). Graphite peaks were also found in the spectra for the Cr sample with added carbonate. The spectra for Mo without added FLiNaK showed no peaks besides those from instrument contamination (*Figure 7-75*), however Mo with added carbonate showed signs of a graphite phase (*Figure 7-76*). Spectra of the film on W samples both with and without added carbonate (*Figure 7-77*, *Figure 7-78*) also indicated a graphite phase. Spectra of particles found on the film have peaks corresponding to a carbonate phase (679, 1016, 1061cm^{-1}).

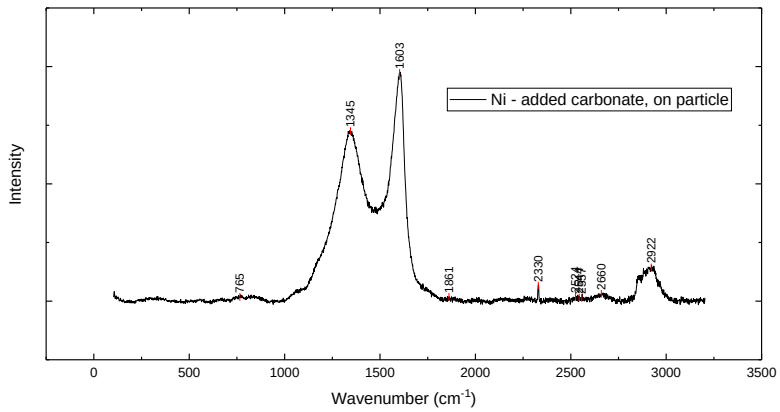

Figure 7-71 Raman spectrum of Ni sample exposed to FLiNaK with added carbonate.

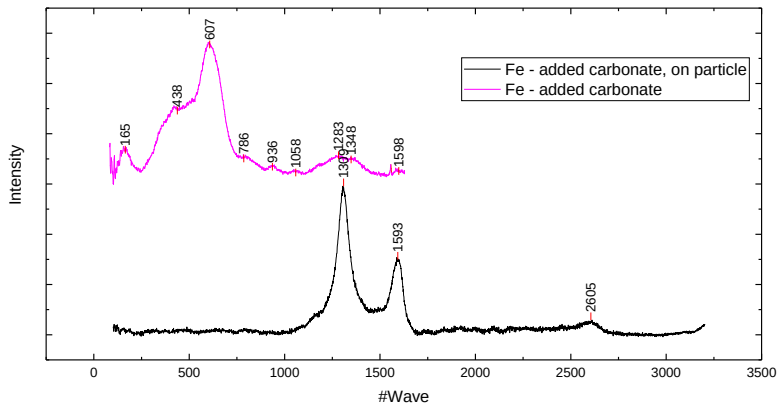

Figure 7-72 Raman spectrum of Fe sample exposed to FLiNaK with added carbonate.

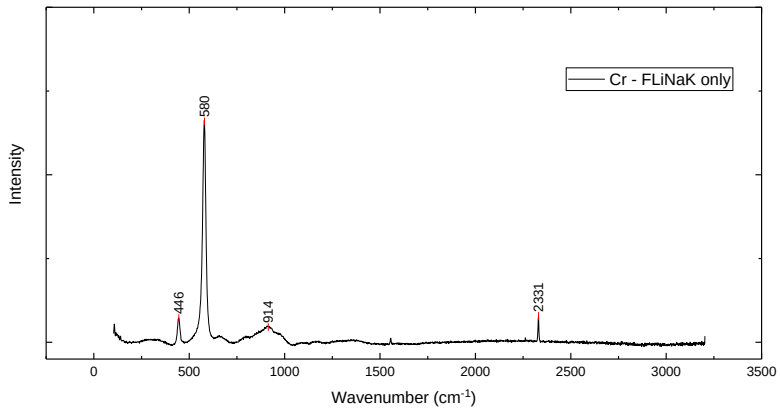

Figure 7-73 Raman spectrum of Cr sample exposed to FLiNaK.

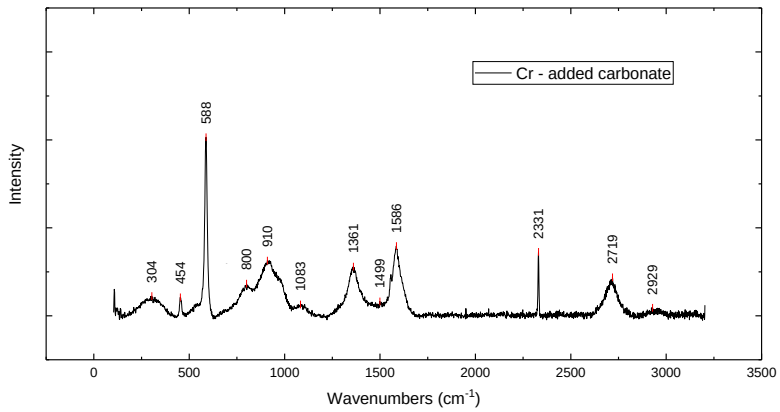

Figure 7-74 Raman spectrum of Cr sample exposed to FLiNaK with added carbonate.

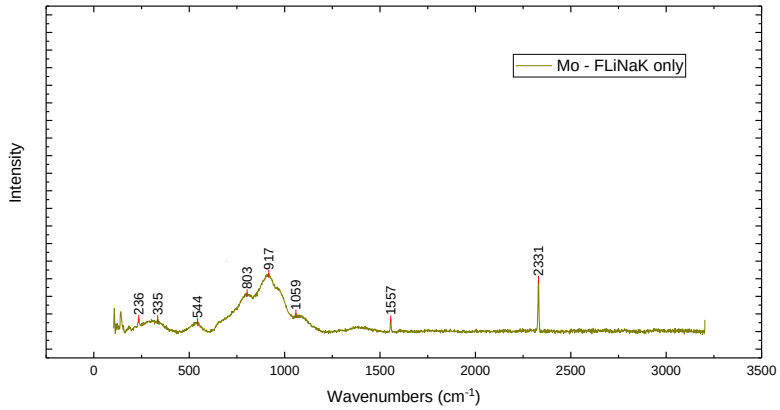

Figure 7-75 Raman of Mo sample exposed to FLiNaK.

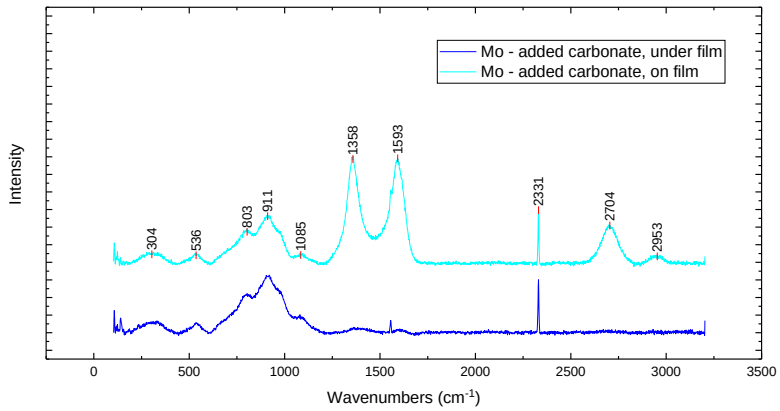

Figure 7-76 Raman of Mo sample exposed to FLiNaK with added carbonate.

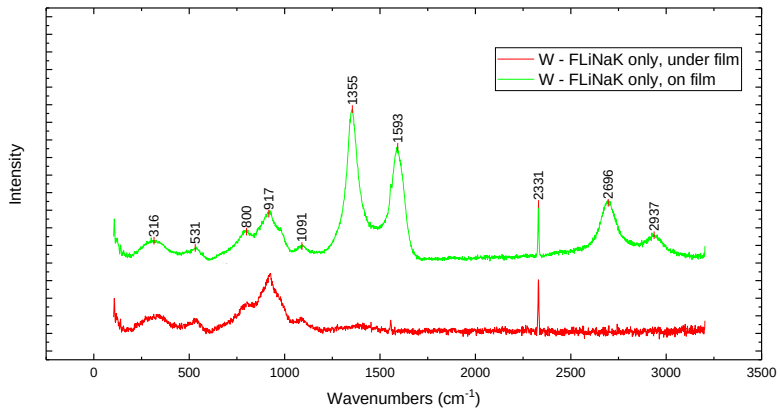

Figure 7-77 Raman of W sample exposed to FLiNaK.

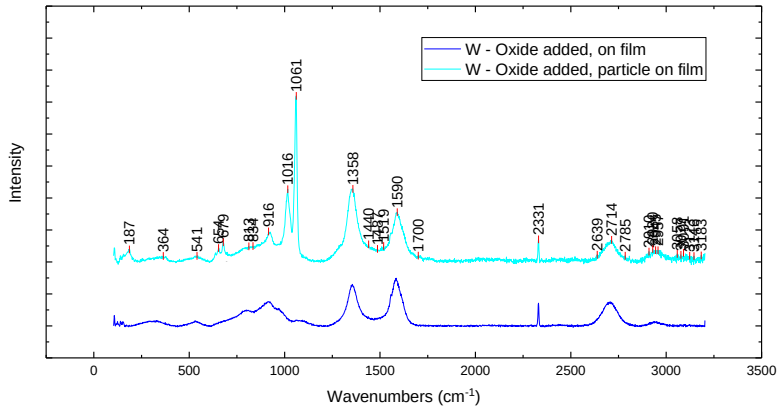

Figure 7-78 Raman of W sample exposed to FLiNaK with added carbonate.

Surface SEM images (*Figure 7-79*) show signs of carburization of all tested elements after exposure to FLiNaK with added carbonate. Ni (*Figure 7-79*a) showed graphitization in backscatter mode, particularly along grain boundaries. Fe (*Figure 7-79*b) darkened in color and had adherent graphite particles dispersed on the surface. Cr (*Figure 7-79*c) had dark carbon splotches, and formed a continuous film on the surface. A film also formed on Mo samples (*Figure 7-79*d), though it tended to spall off in places after removal from the salt. The film on W samples (*Figure 7-79*e) was relatively thick and very brittle, with some particles on the surface.

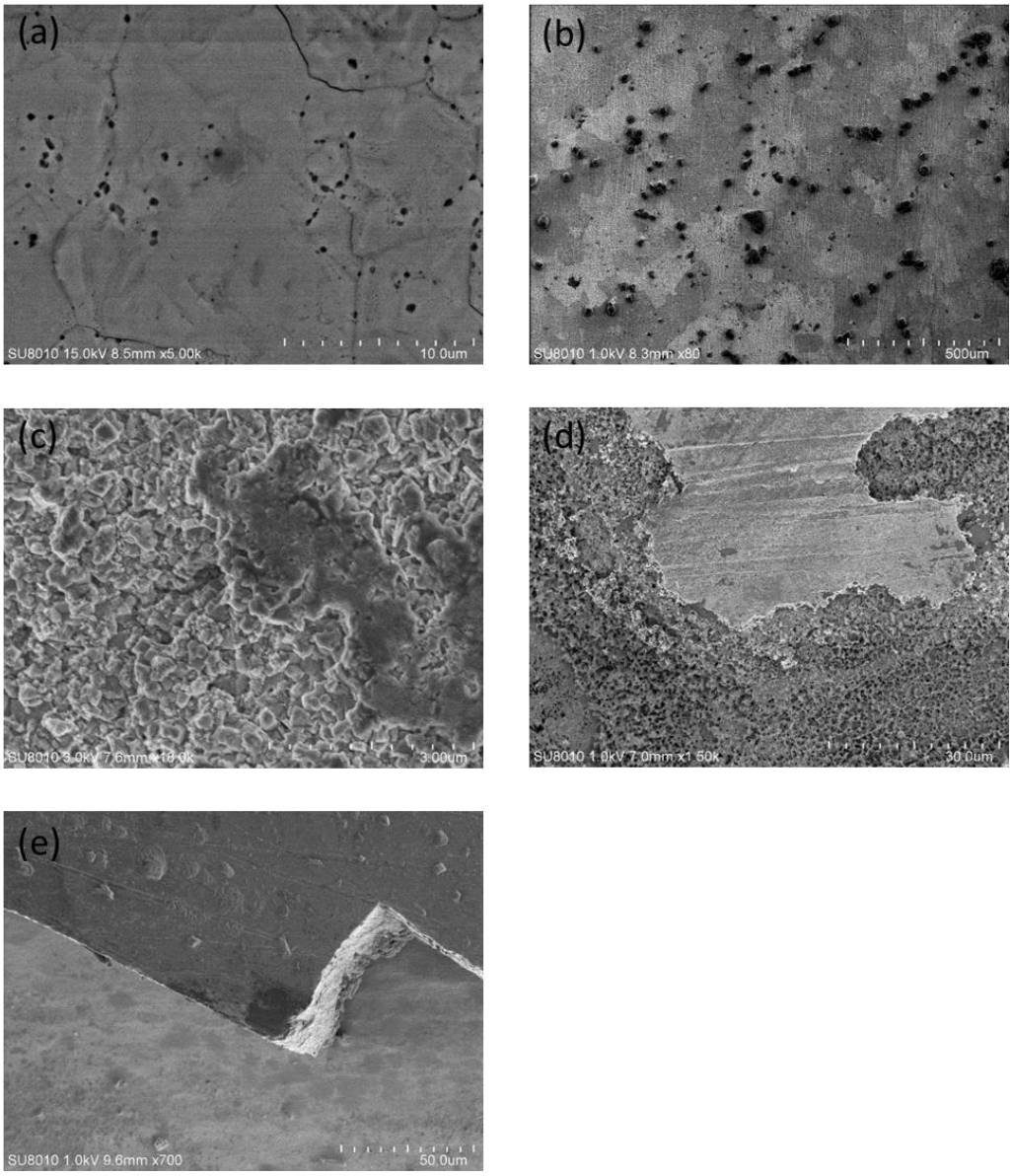

Figure 7-79 SEM images of sample surfaces after 100 hour exposure to FLiNaK with added carbonate.

Mass change results (*Figure 7-80*) showed that W and Mo experienced much greater mass loss after exposure to FLiNaK with added carbonate. This is due to significant spalling of carbide layers which were generated on the sample surfaces. Cr, experienced less mass loss due to the lack of spalling of its surface film. The mass change for Ni and Fe samples were within the measurement error of our analytical balance.

Surprisingly, both Mo and W without added carbonate also experienced significant mass loss. This was again due to spalling of carbide films on Mo and W surfaces. Furthermore, $LiMO_2$ type oxides were found on all Fe and Cr samples, though less was found on samples

without added carbonate. These results indicate that either there was some cross contamination of FLiNaK, or there was some transport of carbonate or CO_2 from crucibles with added carbonate to those without carbonate during the exposure test.

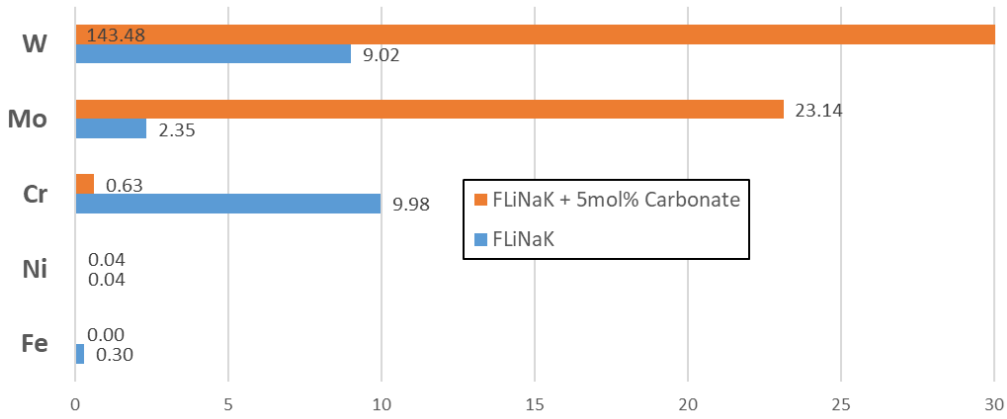

Figure 7-80 Mass loss of pure element samples after 100 hour exposure to FLiNaK with added carbonate.

The Vickers hardness of the film on the Cr sample with added carbonate was measured (*Figure 7-81*). The loading force was varied from 50gf to 2000gf to achieve a range of indent depths. The film hardness was 520HV, while the bulk hardness was 290HV.

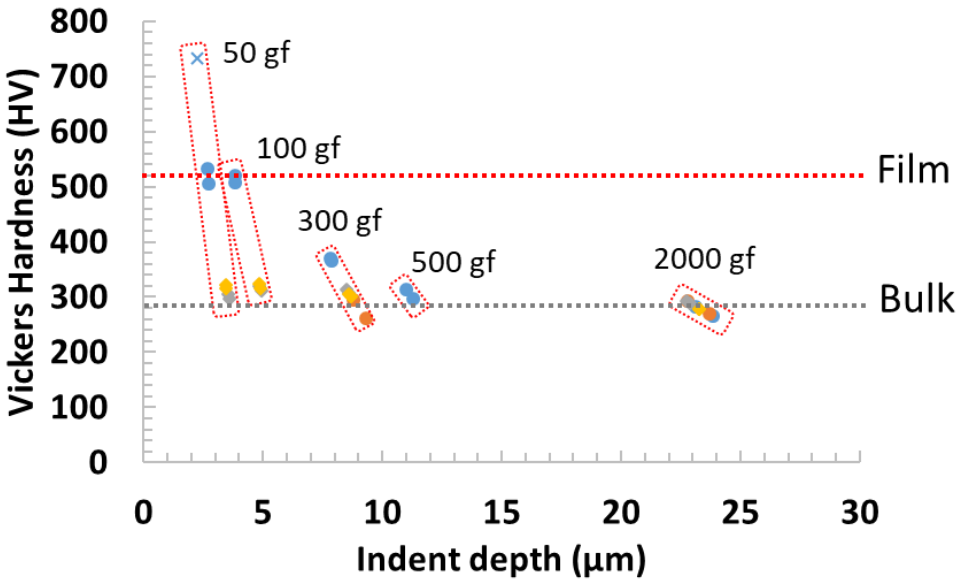

Figure 7-81 Vickers hardness measurements of Cr sample exposed to FLiNaK with added carbonate.

7.4. References

[1] G. Zheng et al., "Corrosion of 316 stainless steel in high temperature molten Li_2BeF_4 (FLiBe) salt", Journal of Nuclear Materials, **461**(2015) p.143–150

[2] H. F. Ebling and M. A. Scheil, "Time-Temperature-Sensitization (TTS) Diagrams for Types 347, 304L, and 316L Stainless Steels," *STP43752S Advances in the Technology of Stainless Steels and Related Alloys*, STP43752S, A. Committee, Ed., ASTM International, West Conshohocken, PA, (1965) p. 275-284,

[3] E. P. Butler, M. G. Burke, "Chromium Depletion and Martensite Formation at Grain-Boundaries in Sensitized Austenitic Stainless-Steel" Acta Metall Mater **34**(1986) p.557-570.

[4] D. Nagle and D. Zhang *"*Carbide Coatings for Nickel Alloys, Graphite and Carbon/Carbon Composites to Be Used in Fluoride Salt Valves*",* Johns Hopkins University (2015) NEUP Project No. 10-857

[5] A. C. Ferrari and J. Robertson, "Interpretation of Raman Spectra of Disordered and Amorphous Carbon", Phys Rev B **61**(2000) p. 14095-14107

[6] J. Veverkova, A. Strang, G. R. Marchant, G. M. McCovlin, H. V. Atkinson "High temperature microstructural degradation of Haynes alloy 230", Superalloys (2008)

[7] V. K. Varma, D. E. Holcomb, F. J. Peretz, E. C. Bradley, D. Ilas, A. L. Quals, N. M. Saharia, "AHTR Mechanical, Structural, and Neutronic Preconceptual Design", Oak Ridge National Laboratory, Oak Ridge National Laboratory (2012).

[8] M. Wieligor *et al* "Raman spectra of silicon carbide small particles and nanowires" *J. Phys.: Condens. Matter* **17**(2005) p. 2387

[9] F.L. Galeener, J.C. Mikkelsen Jr. "Raman studies of the thermal oxide of silicon. Solid State Commun" **37**(1981) p. 719–723.

[10] D. Olander, "Redox condition in molten fluoride salts, Definition and control", Journal of Nuclear Materials **300**(2002) p.270-272

[11] G. Durán-Klie, D. Rodrigues, S. Delpech, "Dynamic Reference Electrode development for redox potential measurements in fluoride molten salt at high temperature", Electrochimica Acta **195**(2016) p.19-26

[12] C. G. Kontoyannis, "Pyrolytic boron nitride coated graphite as a container of reference electrodes for molten fluoride", Electrochimia Acta **41**(1995) p. 2547-2551

[13] G. D. De Cul, D. F. Williams, L. M. Toth, and J. Caja, "Redox potential of novel electrochemical buffers useful for corrosion prevention in molten fluoride", Proceedings of the Electrochemical Society **19**(2002) p.431-436

[14] D. Ludwig, L. Olson, K. Srindaran, M. Anderson, and T. Allen "High temperature electrochemistry of molten fluoride salt for measurement of dissolved chromium", Corrosion Science, Engineering and Technology **46**(2011) p. 360-364

[15 L. C. Olson, J. W. Ambrosek, K. Sridharan, M. H. Anderson, and T. R. Allen, "Materials corrosion in molten LiF-NaF-KF salt," *Journal of Fluorine Chemistry,* 2009.

[16] G. Zheng, "Corrosion Behavior of Alloys in Molten Fluoride Salts," 2015.

[17] G. Zheng *et al.*, "High-Temperature Corrosion of UNS N10003 in Molten Li2BeF4 (FLiBe) Salt," (in English), *Corrosion,* vol. 71, no. 10, pp. 1257-1266, Oct 2015.
[18] K. J. Chan, R. Ambrecht, J. M. Luong W. T. Choi, and P. M. Singh, "Carburization effects on the corrosion of Cr, Fe, Ni, W, and Mo in fluoride cooled high temperature reactor (FHR) coolant," *Annals of Nuclear Engineering*, vol. 120, pp. 279-285, 2018
[19] M. Xie, L. Li, Y. Ding, G. Zhang, "Study on the mechanism of deoxidation and purification for Li2BeF4 molten salt via graphite nanoparticles," *Journal of Nuclear Materials*, vol. 487, pp. 317-322, 2017
[20] L. Massot, P. Chamelot, F. Bouyer, and P. Taxil, "Electrodeposition of carbon films from molten alkaline fluoride media," *Electrochimica Acta,* vol. 47, no. 12, pp. 1949-1957, 2002/05/07/ 2002.
[21] G. Chen *et al.*, *Research on electro-deposition of carbon from LiF-NaF-Na2CO3 molten salt system*. 2010.
[22] M. Deanhardt, K. H. Stern, and A. Kende, "Thermal decomposition and reduction of carbonate ion in fluoride melts," *Journal of the Electrochemical Society,* vol. 133, no. 6, pp. 1148-1152, 1986.
[23] D.E. Holcomb, G.F. Flanagan, G.T. Mays, W.D. Pointer, K.R. Robb, G.L. Yoder, "Fluoride Salt-Cooled High-Temperature Reactor Technology Development and Demonstration Roadmap", Oak Ridge National Laboratory, ORNL/TM-2013/401, 2013.
[24] V.K. Varma, D.E. Holcomb, F.J. Peretz, E.C. Bradley, D. Ilas, A.L. Quals, N.M. Saharia, "AHTR Mechanical, Structural, and Neutronic Preconceptual Design", Oak Ridge National Laboratory, ORNL/TM-2012/320, 2012.
[25] S. Delpech, C. Cabet, C. Slim, G.S. Picard, "Molten fluorides for nuclear applications", Materials Today, 13, 34-41, 2010.
[26] M. Gibilaro, L. Massot, P. Chamelot, "A way to limit the corrosion in the Molten Salt Reactor concept: the salt redox potential control", Electrochimica Acta, 160, 209-213, 2015.
[27] V. Ignatiev, A. Surenkov, "Alloys compatibility in molten salt fluorides: Kurchatov Institute related experience", Journal of Nuclear Materials, 441, 592-602, 2013.
[28] J.W. Koger, Evaluation of Hastelloy N Alloys After Nine Years Exposure to Both a Molten Fluoride Salt and Air at Temperatures from 700 to 560 C., Oak Ridge National Laboratory, ORNL/TM-4189, 1972.
[29] J.W. Koger, "Fluoride Salt Corrosion and Mass Transfer in High Temperature Dynamic Systems", CORROSION, 29, 115-122, 1973.
[30] J.W. Koger, "Corrosion Product Deposition in Molten Fluoride Salt Systems", CORROSION, 30, 125-130, 1974.
[31] J.W. Koger, Chromium Depletion and Void Formation in Fe-Ni-Cr Alloys During Molten Salt Corrosion and Related Processes, in: M.G. Fontana, R.W. Staehle (Eds.), Advances in Corrosion Science and Technology, Springer, Boston, MA, 1974, pp. 245-318.
[32] J.W. Koger, A.P. Litman, "Kinetic Behavior of Chromium and Iron in Some Iron- and Nickel-Base Alloys Exposed to Fluoride Salts", Jom-J Min Met Mat S, 20, A26, 1968.
[33] M. Kondo, T. Nagasaka, T. Muroga, A. Sagara, N. Noda, Q. Xu, D. Ninomiya, N. Masaru, A. Suzuki, T. Terai, "High performance corrosion resistance of nickel-based alloys in molten salt flibe", Fusion Science and Technology, 56, 190-194, 2009.

[34] M. Kondo, T. Nagasaka, A. Sagara, N. Noda, T. Muroga, Q. Xu, M. Nagura, A. Suzuki, T. Terai, "Metallurgical study on corrosion of austenitic steels in molten salt LiF-BeF2 (FLiBe)", Journal of Nuclear Materials, 386-388, 685-688, 2009.

[35] M. Liu, J. Zheng, Y. Lu, Z. Li, Y. Zou, X. Yu, X. Zhou, "Investigation on corrosion behavior of Ni-based alloys in molten fluoride salt using synchrotron radiation techniques", Journal of Nuclear Materials, 440, 124-128, 2013.

[36] H.E. McCoy, B. McNabb, Post-Irradiation Examination of Materials from the MSRE, Oak Ridge National Laboratory, Oak Ridge National Laboratory, ORNL/TM-4174, 1972.

[37] G. Muralidharan, D.F. Wilson, L.R. Walker, M.L. Santella, D.E. Holcomb, Cladding Alloys for Fluoride Salt Compatability, Oak Ridge National Laboratory, ORNL/TM-2011/95 , 2011.

[38] R.S. Sellers, W.J. Cheng, B.C. Kelleher, M.H. Anderson, K. Sridharan, C.J. Wang, T.R. Allen, "CORROSION OF 316L STAINLESS STEEL ALLOY AND HASTELLOY-N SUPERALLOY IN MOLTEN EUTECTIC LiF-NaF-KF SALT AND INTERACTION WITH GRAPHITE", Nuclear Technology, 188, 192-199, 2014.

[39 W.J. Ren, G. Muralidharan, D.F. Wilson, D.E. Holcomb, "Considerations of Alloy N for Fluoride Salt-Cooled High-Temperature Reactor Applications", Proceedings of the Asme Pressure Vessels and Piping Conference, Pvp 2011, Vol 6, a and B, 725-736, 2012.

[40] R.S. Sellers, W.J. Cheng, B.C. Kelleher, M.H. Anderson, K. Sridharan, C.J. Wang, T.R. Allen, "CORROSION OF 316L STAINLESS STEEL ALLOY AND HASTELLOY-N SUPERALLOY IN MOLTEN EUTECTIC LiF-NaF-KF SALT AND INTERACTION WITH GRAPHITE", Nuclear Technology, 188, 192-199, 2014.

[41] J. Serp, M. Allibert, O. Beneš, S. Delpech, O. Feynberg, V. Ghetta, D. Heuer, D. Holcomb, V. Ignatiev, J.L. Kloosterman, L. Luzzi, E. Merle-Lucotte, J. Uhlíř, R. Yoshioka, D. Zhimin, "The molten salt reactor (MSR) in generation IV: Overview and perspectives", Progress in Nuclear Energy, 77, 308-319, 2014.

[42] M.S. Sohal, M.A. Ebner, P. Sabharwall, P. Sharpe, Engineering Database of Liquid Salt Thermophysical and Thermochemical Properties, Idaho National Laboratory, INL/EXT-10-18297, 2013.

[43] Y.L. Wang, Q. Wang, H.J. Liu, C.L. Zeng, "Effects of the oxidants H2O and CrF3 on the corrosion of pure metals in molten (Li,Na,K)F", Corrosion Science, 103, 268-282, 2016.

[44] D.F. Williams, L.M. Toth, K.T. Clarno, Assessment of Candidate Molten Salt Coolants for the Advanced High-Temperature Reactor (AHTR), Oak Ridge National Laboratory, ORNL/TM-2006/12, 2006.

[45] X.X. Ye, H. Ai, Z. Guo, H. Huang, L. Jiang, J. Wang, Z. Li, X. Zhou, "The high-temperature corrosion of Hastelloy N alloy (UNS N10003) in molten fluoride salts analysed by STXM, XAS, XRD, SEM, EPMA, TEM/EDS", Corrosion Science, 106, 249-259, 2016.

[46] P.M. Singh, K.J. Chan, F. Rahnema, “Phenomena Identification and Ranking Table (PIRT) report for metallic materials use in Fluoride High-Temperature Reactors

(FHRs)", Atlanta, GA: Georgia Institute of Technology, 2017, https://smartech.gatech.edu/handle/1853/56668.

[47] P.M. Singh, K.J. Chan,, C. S. Deo, V. Deodeshmukh, J. R. Keiser, W. Ren, T. L. Sham, D. F. Wilson, G. Yoder, J. Zhang, Phenomena Identification and Ranking Table (PIRT) study for metallic structural materials for advanced High-Temperature reactor, Annals of Nuclear Energy, Vol. 123, Jan 2019, pp 222-229, 2019.

8. Heat Exchangers

The advanced high temperature reactor (AHTR) is a conceptual design of fluoride salt-cooled high-temperature reactors (FHRs) with $^{7}LiF-BeF_2$ (66-34 mol%) as its primary coolant [8.1]. The AHTR layout as shown in *Figure 8-1* consists primary loops, intermediate loops, Direct Reactor Auxiliary Cooling System (DRACS) loops, and one power conversion loop. The heat generated in the reactor core is transferred through the primary-to-intermediate heat exchanger (P-IHX) from the primary salt FLiBe to the intermediate salt $KF-ZrF_4$ and then through the intermediate-to-power cycle heat exchanger (I-PHX) from the intermediate salt to water/steam in Rankine cycle or helium/super critical CO_2 ($S-CO_2$) in Brayton cycle for power generation. FHRs employ a passive decay heat removal system, namely, DRACS, in which the decay heat is transferred through the DRACS in-vessel heat exchanger (DHX) from the primary salt FLiBe to the DRACS intermediate salt $KF-ZrF_4$ and then through the natural draft DRACS heat exchanger (NDHX) from the DRACS intermediate salt $KF-ZrF_4$ to the ambient air. The DRACS salt density difference provides the driven force for salt circulation in the DRACS system to remove the decay heat when the reactor is shutdown under accident conditions. In addition, a fluidic diode is adopted in the current AHTR design to reduce heat loss to the DHX during reactor normal operation.

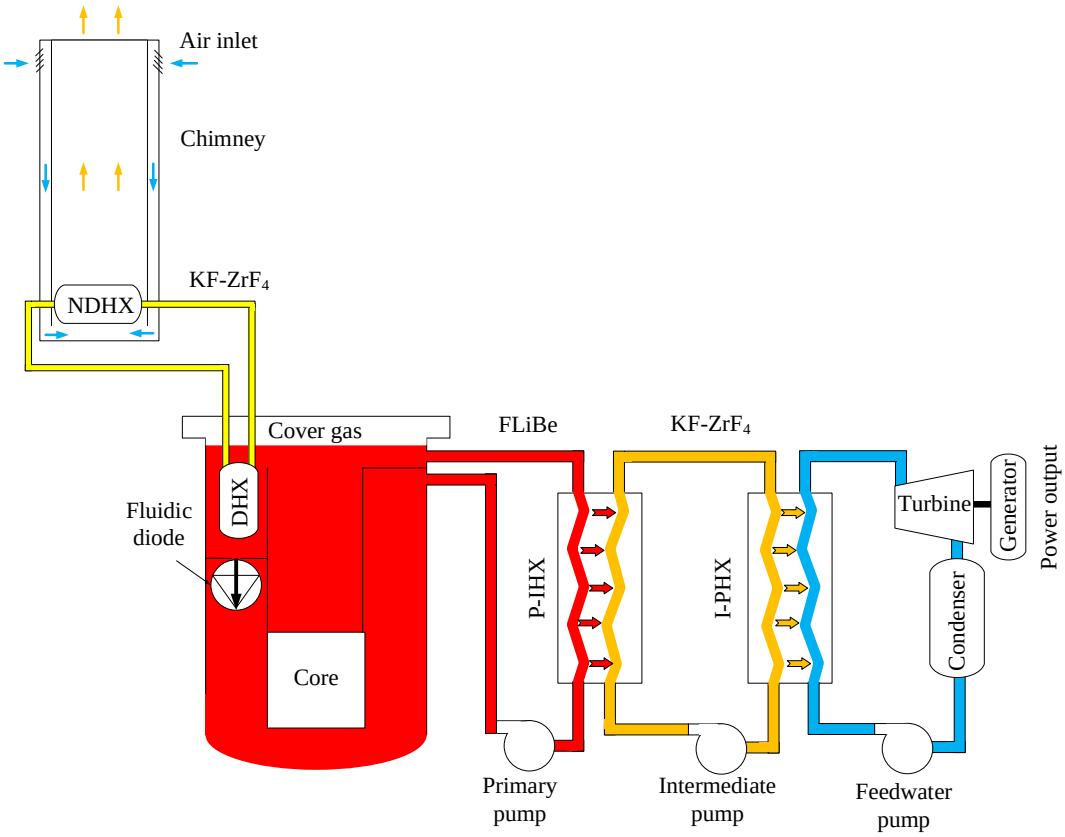

Figure 8-1 A schematic of AHTR

AHTR is one of the promising Generation IV reactor designs due to the improved safety and improved economics. However, tritium control is a critical issue in AHTR because of its extremely high tritium production rate by reactions of $^{6}Li(n, ^{3}H)^{4}He$, $^{7}Li(n, ^{3}H)^{5}He$, and $^{19}F(n, ^{3}H)^{17}O$ [8.2]. It was estimated that AHTR could produce tritium at several orders of magnitude higher than pressurized water reactors (PWRs) with the same electricity output rate [8.3]. Therefore, tritium control should be carefully considered in the AHTR design and other FHR and potentially molten salt reactor (MSR) designs in general.

There are several major paths for the tritium transport in the AHTR: (a) Be trapped by the carbonaceous materials in the core; (b) Escape into the argon cover gas in the reactor vessel; (c) Permeate through the reactor vessel; (d) Permeate through the DHXs; (e) Permeate through the maintenance heat exchangers (HXs); (f) Permeate through the P-IHXs; (g) Permeate through the primary pump; and (h) Permeate through the piping. Among all these paths, HXs, i.e., P-IHXs and DHXs, provide major paths for tritium leakage due to the high working temperatures and large surface areas.

To significantly reduce tritium leakage through P-IHXs, tritium should be removed either upstream of or within P-IHXs. To remove tritium upstream of a P-IHX, a tritium mitigation and control system could be applied as a potential approach, which has been discussed in detail by Wu, et al. [8.4]. To remove tritium within a P-IHX, a double-wall heat exchanger (DWHX) design that adopts a three-fluid design concept as shown in Figure 8-2 can be adopted. Each unit of the heat transfer tubes forms three flow passages, i.e., the inner channel, annular channel, and outer channel. The inner fluid FLiBe, and outer fluid KF-ZrF_4 flow in an inner tube and outside an outer tube in a double-wall tube unit of a P-IHX, respectively. The annular fluid flows in the annulus formed by the inner and outer tubes. A fraction of the tritium carried by the primary salt permeating through the inner tube is taken away by the annular fluid to reduce tritium leakage to the outer fluid. This DWHX design concept was originally proposed for fusion reactors [8.5, 8.6]. However, few such DWHXs have been specifically designed for FHRs with heat and mass transfer performance taken into account simultaneously. A DWHX is therefore adopted and investigated in the current study for the AHTR P-IHX design. In addition, due to the adopted tritium control in P-IHXs, the I-PHXs can be a single-wall HX (SWHX) design due to the significantly reduced tritium concentration in the intermediate salt in AHTR.

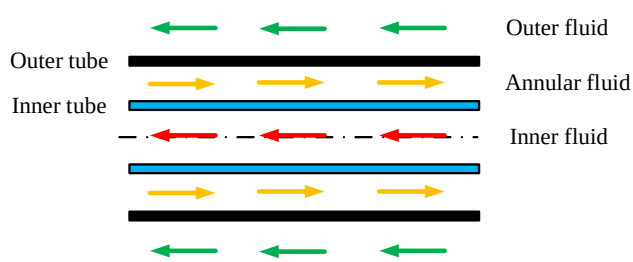

Figure 8-2 A three-fluid design concept for a double-wall heat exchanger

The same DWHX design concept can be applied for NDHXs to significantly reduce tritium leakage through NDHXs to the atmosphere. In addition, the tritium leakage to the atmosphere can be prevented in the air chimney with a controlled chimney environment. Under this condition, both the DHXs and NDHXs can be SWHXs without the need of considering tritium control. These two approaches, tritium control in NDHXs (double-wall design) and air chimneys, will be investigated and discussed in this report.

A coupled heat and mass transfer model was developed to assist a DWHX design and then benchmarked against the experimental data in the literature. In addition, different tube surfaces, i.e., plain and fluted surfaces, were investigated to determine a best double-wall configuration of the inner plain tube with outer plain tube (IPOP), inner plain tube with outer fluted tube (IPOF), inner fluted tube with outer plain tube (IFOP), and inner fluted tube with outer fluted tube (IFOF) designs. As case studies, P-IHX, I-PHX, and DRACS (DHX and NDHX) were designed for AHTR. In addition, the design of a high-temperature fluoride salt test facility (HT-FSTF) for the purpose of component testing and investigation of molten salt thermal hydraulic phenomenon was discussed.

8.1. A Coupled Heat and Mass Transfer Model

Figure 8-3 shows a double-wall (or double-tube) configuration, which consists of an inner fluid, inner tube, annular fluid, outer tube, and outer fluid. A large fraction of the tritium carried by the inner fluid, i.e., FLiBe for P-IHXs, permeates through the inner tube and is then removed by the annular fluid to reduce the tritium leakage to the outer fluid, i.e., KF-ZrF_4 for P-IHXs and air for NDHXs. The annular fluid takes tritium out of the DWHX to a tritium getter bed that is filled with a tritium getter for tritium capture. The "clean" annular fluid then returns to the DWHX to complete one cycle. To achieve good heat transfer performance, a triangular arrangement of double-wall units as shown in *Figure 8-3* is adopted for the analysis. The hexagonal sub-channel is simplified and treated as a circular channel with an equivalent diameter to keep the flow areas the same. A coupled heat and mass transfer model was developed based on this double-wall configuration.

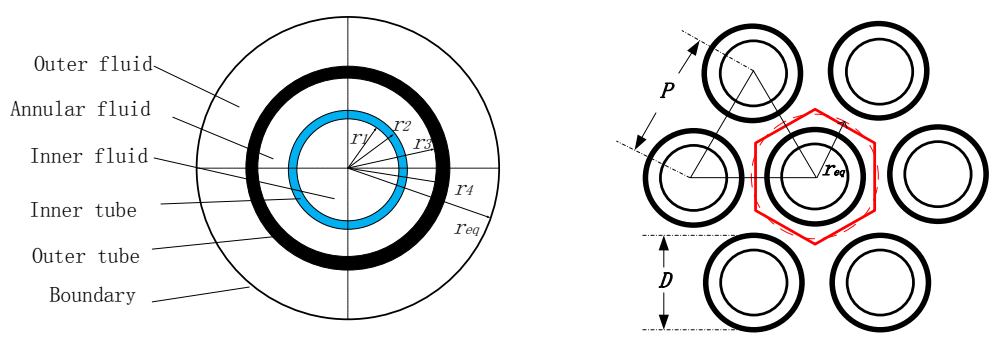

Figure 8-3 A double-wall configuration for (from left to right): (a) one unit and (b) seven units with a triangular arrangement

8.1.1. Heat Transfer Model

If we only consider the thermophysical property changes along the flow direction and neglecting the changes in radial direction, the heat transfer process may be described by a one-dimensional heat transfer model. The heat transfer process from the inner fluid finally to the outer fluid as shown in Figure 8-4 is separated into several steps: (1) Heat transfers from the inner fluid to the inner surface of the inner tube by convective heat transfer; (2) Heat transfers from the inner surface of the inner tube to the outer surface of the inner tube by the conductive heat transfer; (3) Heat transfers from the outer surface of the inner tube to the annular fluid by the convective heat transfer and to the inner surface of the outer tube by the radiative heat transfer; (4) Heat transfers from the annular fluid to the inner surface of the outer tube by the convective heat transfer; (5) Heat transfers from the inner surface of the outer tube to the outer surface of the outer tube by the conductive heat transfer; and (6) Heat transfers from the outer surface of the outer tube to the outer fluid by the convective heat transfer.

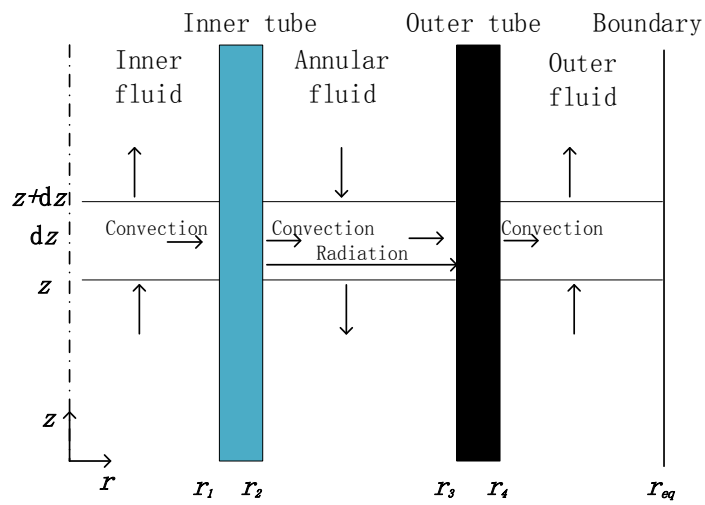

Figure 8-4 Heat transfer model for a double-wall unit

Energy balance for the inner, annular, and outer fluids can be written as

$$\frac{\partial T_{bif}}{\partial z} = -\frac{h_{iit}\left(T_{bif} - T_{iit}\right)}{c_{p,if}\dot{m}_{if}}\frac{\mathrm{d}A_{iit}}{\mathrm{d}z} \tag{8-1}$$

$$\frac{\mathrm{d}T_{baf}}{\mathrm{d}z} = -\frac{1}{c_{p,af}\dot{m}_{af}}\left[h_{oit}\left(T_{oit} - T_{baf}\right)\frac{\mathrm{d}A_{oit}}{\mathrm{d}z} - h_{iot}\left(T_{baf} - T_{iot}\right)\frac{\mathrm{d}A_{iot}}{\mathrm{d}z}\right] \tag{8-2}$$

$$\frac{\mathrm{d}T_{bof}}{\mathrm{d}z} = \frac{h_{oot}\left(T_{oot} - T_{bof}\right)}{c_{p,of}\dot{m}_{of}}\frac{\mathrm{d}A_{oot}}{\mathrm{d}z} \tag{8-3}$$

Thermal conduction equations for the inner and outer tubes can be written as

$$\frac{\mathrm{d}}{\mathrm{d}r}\left(k_{it} r \frac{\mathrm{d}T_{it}}{\mathrm{d}r}\right) = 0 \tag{8-4}$$

$$\frac{\mathrm{d}}{\mathrm{d}r}\left(k_{ot} r \frac{\mathrm{d}T_{ot}}{\mathrm{d}r}\right) = 0 \tag{8-5}$$

The subscripts *bif*, *baf*, *bof*, *it*, and *ot* are variables of the bulk inner fluid, bulk annular fluid, bulk outer fluid, inner tube, and outer tube, respectively. The subscripts *iit*, *oit*, *iot*, and *oot* are variables at the inner surface of the inner tube, outer surface of the inner tube, inner surface of the outer tube, and outer surface of the outer tube, respectively.

If the annular fluid is opaque, non-transparent to the thermal radiation between the inner and outer tubes, the boundary conditions for the tube walls and fluids can be given as

$$-k_{it}\left(\frac{\mathrm{d}T_{it}}{\mathrm{d}r}\right)_{r=r_1} = h_{iit}\left(T_{bif} - T_{iit}\right) \tag{8-6}$$

$$-k_{it}\left(\frac{\mathrm{d}T_{it}}{\mathrm{d}r}\right)_{r=r_2} = h_{oit}\left(T_{oit} - T_{baf}\right) \tag{8-7}$$

$$-k_{ot}\left(\frac{\mathrm{d}T_{ot}}{\mathrm{d}r}\right)_{r=r_3} = h_{iot}\left(T_{baf} - T_{iot}\right) \tag{8-8}$$

$$-k_{ot}\left(\frac{\mathrm{d}T_{ot}}{\mathrm{d}r}\right)_{r=r_4} = h_{oot}\left(T_{oot} - T_{bof}\right) \tag{8-9}$$

$$T_{in,\,bif} = T_{bif,0} \tag{8-10}$$

$$T_{in,baf} = T_{baf,\,0} \tag{8-11}$$

$$T_{in,\,bof} = T_{bof,\,0} \tag{8-12}$$

If the annular fluid is totally transparent to thermal radiation, the boundary conditions for the outer surface of the inner tube and inner surface of the outer can be written as

$$-k_{it}\left(\frac{\mathrm{d}T_{it}}{\mathrm{d}r}\right)_{r=r_2} = h_{oit}\left(T_{oit} - T_{baf}\right) + \varepsilon_{it-ot}\sigma\left(T_{oit}^4 - T_{iot}^4\right) \tag{8-13}$$

$$-k_{ot}\left(\frac{\mathrm{d}T_{ot}}{\mathrm{d}r}\right)_{r=r_3}=h_{iot}\left(T_{baf}-T_{iot}\right)+\frac{A_{oit}}{A_{iot}}\varepsilon_{it-ot}\sigma\left(T_{oit}^4-T_{iot}^4\right) \tag{8-14}$$

More details for the heat transfer model were discussed in separate papers [8.7, 8.8]. The axial temperature profiles estimated by the heat transfer model will be applied as inputs for the mass transfer model to be discussed next.

8.1.2. Mass Transfer Model

Tritium produced in FHR reactor cores exists in the form of tritium ion T+ in TF and molecular tritium T_2, depending on the redox environment of the primary salt. Redox control is widely used in recent studies for tritium management since tritium control becomes extremely important for tritium permeation and material corrosion in FHRs [8.9]. Tritium is mainly in the form of T_2 when the redox control method is adopted. In this study, it is assumed that tritium in molten salts is in the form of T_2, which is a conservative assumption to estimate tritium permeation rates since tritium ion T^+ has a much lower permeation rate through HX structural materials [8.10].

The transport process for tritium permeation through a tube consists of several steps: (1) Mass transfer of molecular tritium T_2 from the bulk fluid to the fluid-solid interface; (2) Dissociative chemisorption of molecular tritium T_2 to two tritium atoms 2T on the fluid-solid interface; (3) Bulk diffusion of tritium atoms through the bulk solid (tube wall); and (4) Re-combinative desorption from 2T to T^2 on the solid surface.

The tritium permeation rate depends on the tritium mass transfer rate in the bulk fluid containing tritium, dissociative chemisorption rate on the fluid-solid interface, bulk diffusion rate in the solid, and re-combinative desorption rate on the solid surface. In general, the dominating parameter affecting the tritium permeation rate is the one with the smallest value. If none dominates, it will become a multi-rate-determining process. It is assumed that the tritium mass transfer in the bulk salt and diffusion in the bulk solid processes are the rate-determining processes [8.11].

The steady-state tritium concentration balance equations for the bulk inner fluid, bulk annular fluid, and bulk outer fluid can be written as

$$\frac{\mathrm{d}}{\mathrm{d}z}\left(\frac{C_{T,bif}\dot{m}_{if}}{\rho_{if}}\right)\cdot\mathrm{d}z=-J_i \tag{8-15}$$

$$\frac{\mathrm{d}}{\mathrm{d}z}\left(\frac{C_{T,baf}\dot{m}_{af}}{\rho_{af}}\right)\cdot\mathrm{d}z=-\left(J_i-J_o\right) \tag{8-16}$$

$$\frac{\mathrm{d}}{\mathrm{d}z}\left(\frac{C_{T,bof}\dot{m}_{of}}{\rho_{of}}\right)\cdot\mathrm{d}z=J_o \tag{8-17}$$

where C and J are the tritium concentration and permeation rate, respectively.

Under steady-state conditions, permeation rates J_i in the following three processes, which are expressed as Eqs. (8-18) to (8-20), are identical: tritium mass transfer from a bulk inner fluid to the inner-fluid-inner-tube interface; tritium diffusion through a bulk inner tube; and tritium mass transfer from the inner-tube-annular-fluid interface to a bulk annular fluid.

$$J_i = k_{m,iit} \cdot \mathrm{d}A_{iit} \cdot \left(C_{T,bif} - C_{T,if-it} \right) \tag{8-18}$$

$$J_i = \frac{k_{Pi} \left(p_{T,it-if}^{1/2} - p_{T,it-af}^{1/2} \right) \cdot 2\pi \cdot \mathrm{d}z}{\ln\left(r_2 / r_1 \right)} \tag{8-19}$$

$$J_i = k_{m,oit} \cdot \mathrm{d}A_{oit} \cdot \left(C_{T,af-it} - C_{T,baf} \right) \tag{8-20}$$

The subscripts *if-it*, *it-if*, *it-af*, and *af-it* are interface between the inner fluid and inner tube but close to the inner fluid, interface between in the inner fluid and inner tube but close to the inner tube, interface between the inner tube and annular fluid but close to the inner tube, and interface between the inner tube and annular fluid but close to the annular fluid, respectively.

Similarly, permeation rates J_o, expressed as Eqs. (8-21) to (8-23), are identical.

$$J_o = k_{m,iot} \cdot \mathrm{d}A_{iot} \cdot \left(C_{T,baf} - C_{T,af-ot} \right) \tag{8-21}$$

$$J_o = \frac{k_{Po} \left(p_{T,ot-af}^{1/2} - p_{T,ot-of}^{1/2} \right) \cdot 2\pi \cdot \mathrm{d}z}{\ln\left(r_4 / r_3 \right)} \tag{8-22}$$

$$J_o = k_{m,oot} \cdot \mathrm{d}A_{oot} \cdot \left(C_{T,of-ot} - C_{T,bof} \right) \tag{8-23}$$

Permeation rates J_i and J_o estimated by Eqs. (8-19) and (8-22) are theoretically derived from Fick's First Law and Sieverts' Law for a diatomic gas. The half-order partial pressure dependence of the permeation rate has been validated for clean surfaces by experiments [8.12, 8.13] and it is adopted in this report. The average wall temperature is used to estimate the permeability of heat transfer tubes at each axial location.

Stempien et al. [8.14] assumed that the tritium partial pressure rather than tritium concentration was continuous on the fluid-solid interface. Under this assumption, the modeling results agreed well with the experimental data [8.14]. The same assumption of continuous tritium partial pressure at a fluid-solid interface is adopted in the development of the mass transfer model in this report. The tritium partial pressures on the inner-fluid-inner-tube interface, inner-tube-annular-fluid interface, annular-fluid-outer-tube interface, and outer-tube-outer-fluid interface have the following relationships:

$$p_{T,if-it} = p_{T,it-if} \tag{8-24}$$

$$p_{T,it-af} = p_{T,af-it} \tag{8-25}$$

$$p_{T,af-ot} = p_{T,ot-af} \tag{8-26}$$

$$p_{T,ot-of} = p_{T,of-ot} \tag{8-27}$$

Per Henry's law, the tritium concentrations in various regions are expressed as Eqs. (8-28) to (25). If a gas is used as the annular fluid, ideal gas law will be applied to relate the concentration to the partial pressure.

$$C_{T,if-it} = k_{H,T,if} \cdot p_{T,if-it} \tag{8-28}$$

$$C_{T,af-it} = k_{H,T,af} \cdot p_{T,af-it} \tag{8-29}$$

$$C_{T,af-ot} = k_{H,T,af} \cdot p_{T,af-ot} \tag{8-30}$$

$$C_{T,of-ot} = k_{H,T,of} \cdot p_{T,of-ot} \tag{8-31}$$

Boundary conditions for the mass transfer model can be written as

$$C_{T,bif}\left(z=0\right) = C_{bif,0} \tag{8-32}$$

$$C_{T,baf}\left(z=L\right) = \left(1-\eta_{TGB}\right) \cdot C_{T,baf}\left(z=0\right) \tag{8-33}$$

$$C_{T,bof}\left(z=0\right) = 0 \tag{8-34}$$

If an open loop is used for the annular fluid, $C_{T,baf}\left(z=L\right)=0$ (or $\eta_{TGB}=100\%$) will be applied. If a closed loop is adopted, $C_{T,baf}\left(z=L\right)>0$ (or $\eta_{TGB}<100\%$) will be used. In the actual application, a closed loop will be most likely to be used for the annular fluid if a DWHX design is adopted in FHRs due to the economic consideration.

Utilizing Eqs. (8-1) to (8-34), temperature and tritium concentration profiles of the liquids can be determined. More details for the heat transfer model were discussed in separate papers [8.7, 8.8].

8.1.3. Model Benchmark

To assess the model performance and achieve reasonable model accuracy, it is necessary to benchmark the coupled heat and mass transfer model. The heat and mass transfer are coupled processes. The heat transfer determines the axial temperature profile, which

affects the mass transfer parameters, i.e., the diffusivity. In addition, the mass transfer determines the property change of each fluid, which affects the heat transfer process. However, the property change due to the tritium permeation can be neglected since the amount of tritium is extremely small. In other words, each of the fluids is assumed being single phase, single composition when evaluating the thermophysical properties of the inner fluid, annular fluid, and outer fluid. Therefore, we can assume the heat transfer process affects the mass transfer process, while the mass transfer has negligible effect on the heat transfer. It is therefore acceptable to benchmark the heat and mass transfer separately against available experimental data in the literature.

Heat transfer model

The predicted results by the heat transfer model are compared with the experimental data from tests in a triple-tube heat exchanger using water as the working fluid as well as computational fluid dynamics (Fluent) simulation results [8.15]. As shown in Figure 8-5, the low-temperature cold water acting as an inner fluid and intermediate-temperature normal water acting as an outer fluid flowed co-currently. Both the co-current and counter-current flow patterns were investigated by changing the flow direction of the annular fluid high-temperature hot water.

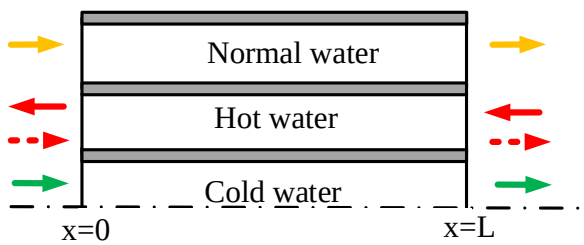

Figure 8-5 Flow directions of three fluids [2.9]

The predicted fluid temperature profiles were compared against the experimental data as show in Figure 8-6. The fluid axial temperature profiles for the counter-current flow pattern are plotted in a dimensionless coordinate system with the origin located at the tube entrance. As predicted by the heat transfer model for the counter-current flow pattern, the hot-water temperature decreases from 70.0 to 52.3 °C with the normal- and cold-water temperatures increasing from 18.0 to 27.6 °C, and 10.0 to 18.1 °C, respectively.

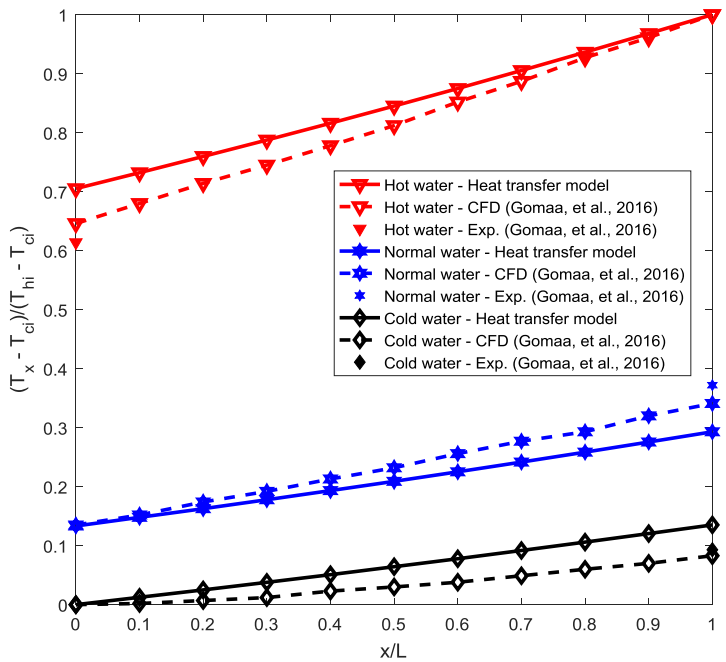

Figure 8-6 Comparisons of the fluid temperatures among the model calculations, experimental data, and Fluent simulation results for a counter-current flow pattern

The relative discrepancies of average heat transfer coefficients obtained by the model and experimental data are within 17%, 24%, and 23% for the hot water, normal water, and cold water, respectively. In addition, the relative differences of temperatures obtained by the model and experimental data are 12%, 15%, and 16% for the hot water, normal water, and cold water, respectively. These discrepancies are acceptable considering the large measurement uncertainty for the cold-water temperature in the experiment and the ±20% uncertainty of the heat transfer correlation [8.16], Eq. (8-35), used for the annulus in the heat transfer model. More details for the heat transfer model benchmark was discussed in a separate paper [8.8].

$$\mathrm{Nu} = 0.022\,\mathrm{Pr}^{0.5}\,\mathrm{Re}^{0.8}, \quad \mathrm{Re} < 5\times10^{3} \tag{8-35}$$

<u>Mass transfer model</u>

There appears no available tritium mass transfer experimental data published for a DWHX. Predictions by the mass transfer model were compared against the experimental data from a hydrogen separation experiment performed by Wang, et al. [8.17]. A mixture of hydrogen and helium gases acting as a feeding gas flowed on the shell side of a nickel hollow fiber tube and nitrogen gas acting as a sweep gas co-currently flowed on the tube side as shown in Figure 8-7. The nickel hollow fiber tube was housed by a quartz tube, which itself was housed and heated by a tubular furnace. Since the furnace temperature varied significantly along the axial direction, the measured temperature profiles under different furnace temperature settings were used for the mass transfer model benchmark. Hydrogen permeated from the shell-side feeding gas to the tube-side sweep gas and the

corresponding permeation rate was measured by a gas chromatograph as shown in Figure 8-7.

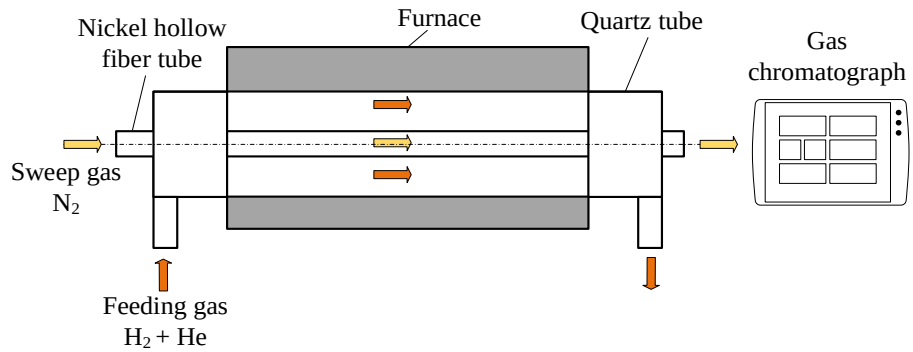

Figure 8-7 A schematic of the experimental setup by Wang, et al. [8.17]

The mass transfer correlation [8.18] used to benchmark the mass transfer model is expressed as Eq. (8-36)

$$\mathrm{Sh} = 1.86\left(\frac{D}{L}\mathrm{Re}\,\mathrm{Sc}\right)^{1/3}, \quad 10 \le \mathrm{Re} \le 2\times10^{3} \tag{8-36}$$

where Sh, *D*, *L*, Re, and Sc are the Sherwood number, tube inner diameter, tube length, Reynolds number, and Schmidt number, respectively. Since the tritium diffusivities in some fluids are not available, the classical rate theory, which states that the diffusivities of hydrogen isotopes in the same material are inversely proportional to the square root of their molecular masses, is used to determine the tritium diffusivities in these fluids.

Figure 8-8 shows the comparisons of the predicted hydrogen permeation rates with the experimental data under various nitrogen flow rates and testing temperatures. Under a given temperature, i.e., 1000 ℃, the hydrogen permeation rate increases with the increase of the sweep gas flow rate. This is because as the increase of the sweep gas flow rate, tritium is more quickly taken out of the hollow fiber tube and consequently the hydrogen partial pressure difference across the tube wall increases, which results in larger hydrogen permeation rates. Under a given sweep gas flow rate, such as 5×10^{-5} mol/s as shown in Figure 8-8, hydrogen permeation rates of the experiment are much larger than those of the model, especially at high temperatures. This is because the permeability of the tube wall is larger at higher temperatures.

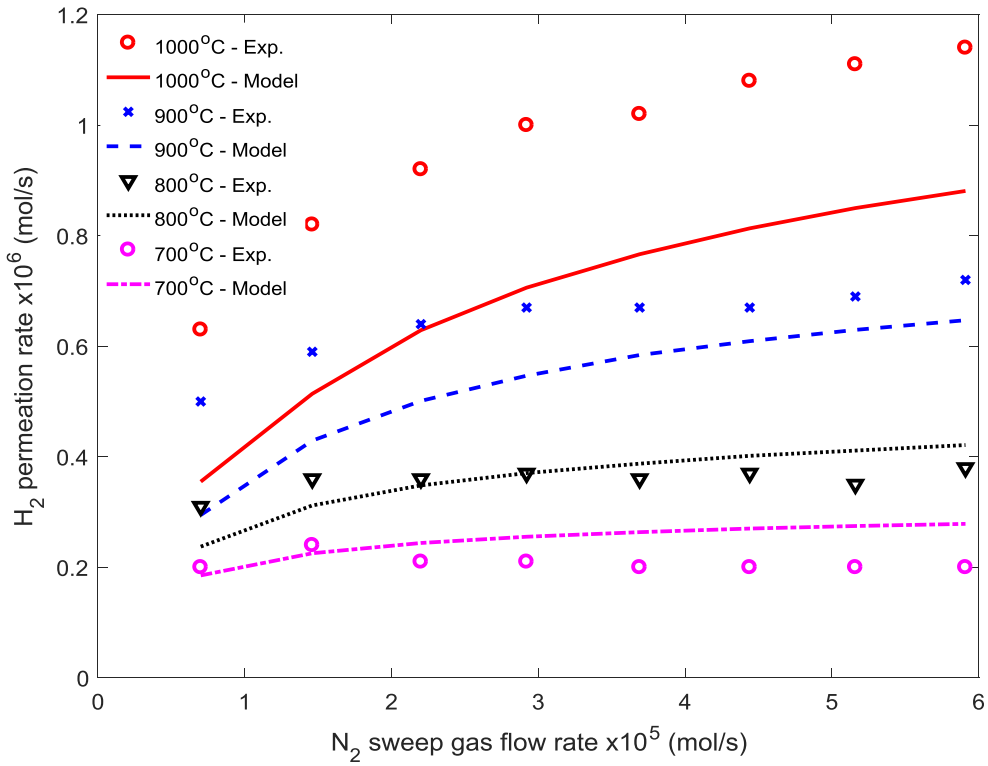

Figure 8-8 Comparisons of the hydrogen permeation rates under different temperatures and sweep gas flow rates

In addition, the trend of the hydrogen permeation curve is predicted well by the model, especially at 700 and 800 °C as shown in Figure 8-8, which is very encouraging as the maximum salt temperature in FHRs is expected to be at such temperatures. A quantitative analysis shows that the maximum relative difference between the hydrogen permeation rates predicted by the mass transfer model and experimental results at 700, 800, 900, and 1000 °C are 35, 23, 41, and 44%, respectively. The much larger permeation rates in the experiments at higher temperatures, for example 1000 °C, most likely result from the additional mass transfer area (quartz tubes on the two ends of the test section), which is not considered in the current model. If the additional area were considered in the model, the discrepancies would be much smaller. To verify this hypothesis, we need to know the temperature profile and the permeability of the quartz tube. However, none of them was provided in the experiment (therefore not considered in the current model). In a simplified analysis, it is assumed that the permeation rate is merely proportional to the mass transfer length/area. The actual mass transfer length should be the entire length between the inlet and outlet of the feeding gas, which is about 33 cm. Since only the nickel tube length, 23 cm, is considered as the mass transfer length in the model, the experimental data should be about 43% higher than the predicted results, which accounts for the much larger experimental data points at high temperatures, i.e., 1000 °C. More details for the mass transfer model benchmark was discussed in a separate paper [8.8].

8.2. A DWHX with Various Tube Surface Configurations and Annular Fluids

The inner and outer tubes of a DWHX may have different tube surface configurations, i.e., fluted and plain surfaces. In addition, the annular fluid could be a gas or a liquid. It is a cost-effective way to determine a best tube surface configuration and a best annular fluid prior to carrying out a DWHX design optimization.

8.2.1. Tube Surface Configuration

There are four tube configurations initially considered for a DWHX unit: IPOP, IPOF, IFOP, and IFOF. Figure 8-9 shows schematically the cross-sectional views of these four double-wall configurations.

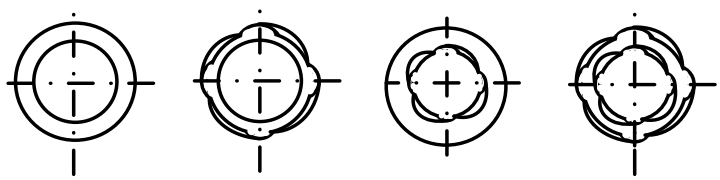

Figure 8-9 Four possible double-wall designs (from left to right): IPOP, IPOF, IFOP, and IFOF

Both the heat transfer and tritium mass transfer performance should be considered to determine a best double-wall configuration for a DWHX. For the heat transfer performance of a double-wall configuration, it is expected to achieve a large heat transfer rate. In addition, the majority of the heat removal from the inner fluid is expected to be taken by the outer fluid rather than the annular fluid. If most of the heat removal is taken by the annular fluid, the annular fluid outlet temperature will increase significantly, which requires an additional cooler to cool down the annular fluid. For the mass transfer performance of a double-wall configuration, it is expected to achieve a large mass transfer rate from the inner fluid. In addition, the majority of tritium is expected to be removed by the annular fluid.

As an example, heat and mass transfer performance of these four double-wall configurations for a double-wall P-IHX are investigated under different Reynolds numbers of the annular fluid as shown in Figure 8-10 to Figure 8-11. As a starting point, the inner, annular, and outer fluids of a double-wall P-IHX are FLiBe, helium, and KF-ZrF_4, respectively. The heat transfer and tritium mass transfer rates are normalized to their individual maximum value.

Figure 8-10 and *Figure 8-11* show the effect of the annular-fluid Reynolds number on the heat transfer and tritium mass transfer rates, respectively. For a certain double-wall configuration, such as IFOF as shown in *Figure 8-10*, the heat transfer rate in the inner fluid increases with the increase of the annular-fluid Reynolds number. This is because the overall heat transfer coefficient increases with the increase of the annular-side heat transfer coefficient. For these four designs, both the IFOF and IFOP designs have at least 48% larger heat transfer rates than the IPOF design and at least 127% larger heat transfer rates than the IPOP design. This is because both the IFOF and IFOP designs use fluted tubes

as the inner tubes, which significantly increases the heat transfer area and heat transfer coefficient. The IFOF configuration has a larger heat transfer rate than the IFOP due to the larger heat transfer area and heat transfer coefficient of the outer tube. For all these four designs, larger than 85% of the heat removal is taken by the outer fluid and the remaining taken by the annular fluid. The heat transfer rates for these four designs under different annular-fluid Reynolds numbers are IFOF > IFOP >> IPOF >> IPOP, which is the priority sequence for selection as well if only the heat transfer performance is considered.

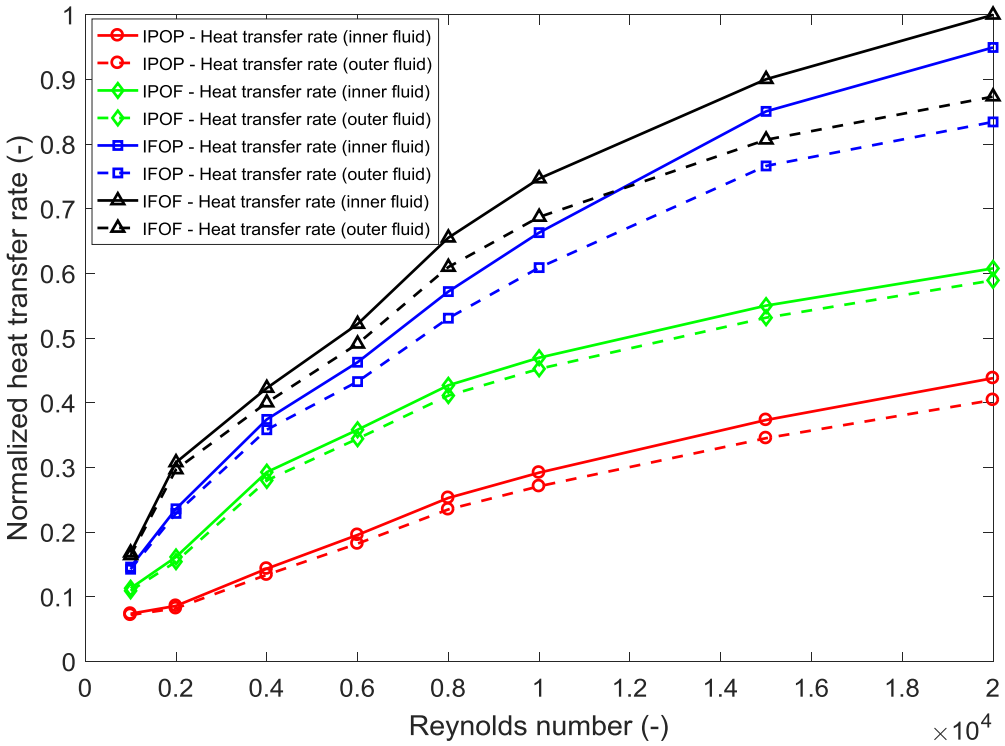

Figure 8-10 Effect of the salt Reynolds number on the heat transfer rate

In addition to the heat transfer, the tritium mass transfer needs to be considered as well. For a certain double-wall configuration, such as IFOF shown in Figure 8-11, the mass transfer rate increases with the increase of the annular-fluid Reynolds number. This is because the overall mass transfer coefficient increases with the increase of the annular-side mass transfer coefficient. For the tritium mass transfer performance, both the IFOF and IFOP designs have at least 375% larger mass transfer rates than those of the IPOP and IPOF designs as shown in Figure 8-11. This is because the IFOF and IFOP designs use fluted tubes as the inner tubes, which significantly increases the mass transfer area and mass transfer coefficient. At least 95% of tritium is taken by the annular fluid and the remaining taken by the outer fluid for all these four configurations. The tritium mass transfer rates for these four configurations under different annular-fluid Reynolds numbers are IFOF> IFOP >> IPOF ≈ IPOP, which is the priority sequence for selection if only the mass transfer performance is considered.

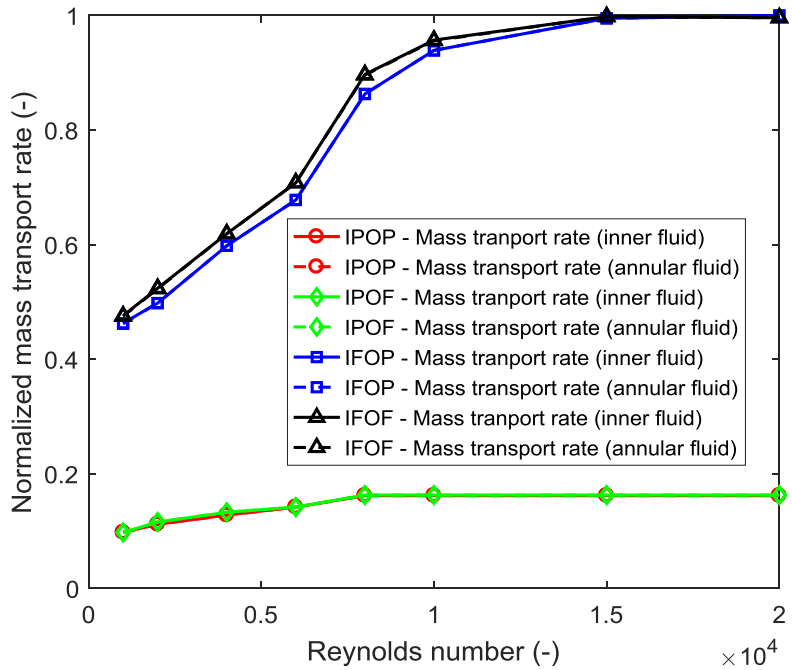

Figure 8-11 Effect of the salt Reynolds number on the tritium mass transfer rate

Considering the heat and mass transfer rates, IFOF is superior than IFOP, IPOF, and IPOP designs. Therefore, IFOF is the base configuration for a DWHX.

8.2.2. Annular Fluid Species

Helium, FLiBe, FLiNaK, and KF-ZrF_4 are considered as potential choices for an annular fluid in a DWHX with IFOF configuration. The mono-atomic gas helium [8.19], fluoride salts FLiBe and FLiNaK are considered as transparent medias to the thermal radiation, while the fluoride salt KF-ZrF_4 is considered as thermally non-transparent due to the significantly large absorption coefficient [8.20].

The mass-transfer properties of helium, FLiBe, FLiNaK, and KF-ZrF_4 are summarized in Table 8-1. The diffusivities and solubilities of tritium (or hydrogen) in FLiBe and FLiNaK are on an order of 10^{-9} m^2/s and 10^{-4} $mol/m^3/Pa$ at 600-700 ˚C, respectively [8.22-8.25]. Since the diffusivity and solubility of tritium (or hydrogen) in KF-ZrF_4 are currently not available, as a starting point, it is appropriate to assume that the diffusivity and solubility of tritium in KF-ZrF_4 are 10^{-9} m^2/s and 10^{-4} $mol/m^3/Pa$ at 600-700 ˚C, respectively. In addition, two additional assumptions are used in the analysis: (1) The rate theory [8.26] that isotope diffusivities in the same material are inversely proportional to the square root of their molecular masses, is applied to convert the hydrogen diffusivity to the tritium diffusivity; and (2) The solubilities of hydrogen and tritium are the same.
-

Table 8-1 Diffusivities and solubilities of potential annular fluids

T_2/H_2	Diffusivity (m^2/s)	Solubility ($mol/m^3 \cdot Pa$)	Refs.

Gas	He	$D_{H_2,He} = \frac{2.7\times10^{-6}T(\mathrm{K})^{1.51}}{\left[\ln\frac{T(\mathrm{K})}{5.34\times10^{-6}}\right]^2}$	$K_{T_2,He} = \frac{n}{pV} = \frac{1}{R_g T\ K}$	[8.21]
Liquid fluoride salts	FLiBe	$D_{T_2,FLiBe} = 9.3\times10^{-7}\cdot \mathrm{e}^{-\frac{42154}{R_g T\ \mathrm{K}}}$	$K_{T_2,FLiBe} = 7.892\times10^{-2}\cdot \mathrm{e}^{-\frac{35403}{R_g T\ K}}$	[8.22]
	FLiNaK*	$D_{H_2,FLiNaK} = 1.877\times10^{-12}\cdot e^{0.01T\ \mathrm{K}}$	$K_{H_2,FLiNaK} = 2.335\times10^{-3}\cdot e^{-0.0044T\ \mathrm{K}}$	[8.23-8.25]
	$KF\text{-}ZrF_4$**	10^{-9}	10^{-4}	N/A

Notes:
*: New fit based on the experimental data in the literature [8.23-8.25]
**: Rough estimation based on diffusivities and solubilities of FLiBe and FLiNaK.

Figure 8-12 shows the comparison of the heat transfer rates using different annular fluids. The heat transfer rate in the inner fluid is the total heat transfer rate, which is defined as the total heat loss from the inner fluid to the annular and outer fluids per unit time. If the Reynolds number is fixed, the total heat transfer rate of using FLiBe as the annular fluid is 69%, 120%, and 633% larger than those of using FLiNaK, $KF\text{-}ZrF_4$, and helium as the annular fluid at low Reynolds number. At high Reynolds number, the total heat transfer rate of using FLiBe is 4%, 9%, and 115% larger than those of using FLiNaK, $KF\text{-}ZrF_4$, and helium as the annular fluid. Therefore, FLiBe as the annular fluid significantly increases the heat transfer rate and reduces the HX volume compared with FLiNaK, $KF\text{-}ZrF_4$, and helium. In addition, the heat transfer rate in the outer fluid occupies 48% to 70% if FLiBe is the annular fluid. The remaining taken by the annular fluid needs to be recycled.

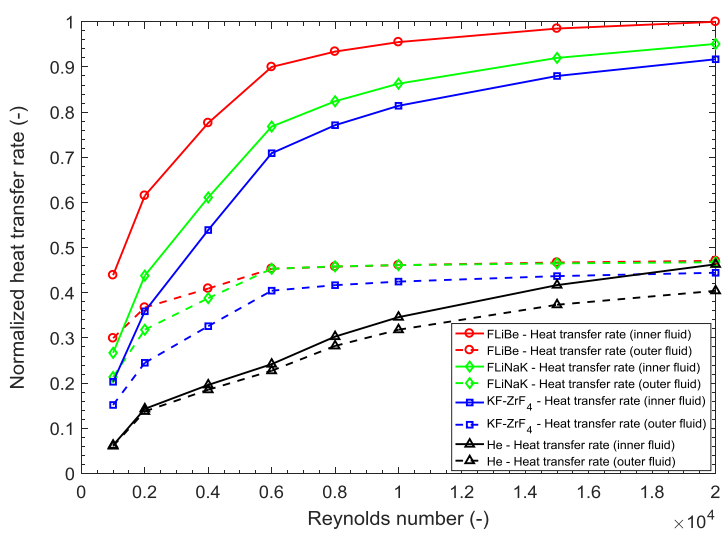

Figure 8-12 Comparison of the heat transfer rates using different annular fluids

Figure 8-13 shows the comparison of the mass transfer rates using different annular fluids. The mass transfer rate in the inner fluid is the total mass transfer rate, which is defined as

the total tritium mass loss from the inner fluid to the annular and outer fluids per unit time. As a fixed Reynolds number, the total mass transfer rate of using helium as the annular fluid is about 4, 20, and 16 times larger than those of using FLiBe, FLiNaK, and KF-ZrF_4 at low Reynolds number. At high Reynolds number, the total heat transfer rate of using helium is about 60%, 200%, and 413% larger than those of using FLiBe, FLiNaK, and KF-ZrF_4 as the annular fluid. In addition, at least 95% of tritium is taken by the annular fluid and the remaining is taken by the outer fluid.

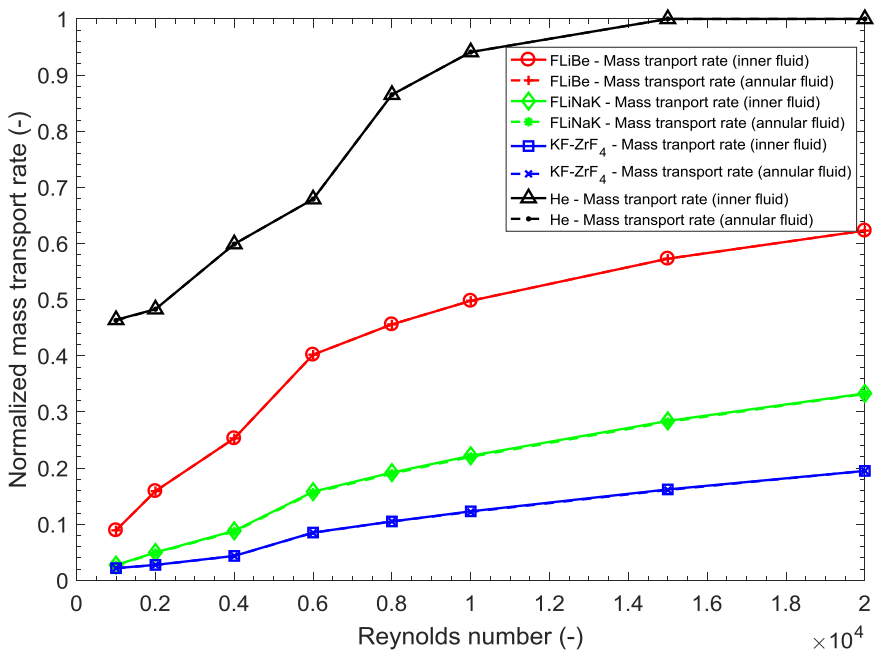

Figure 8-13 Comparison of the mass transfer rates using different annular fluids

The heat transfer rates for these four potential annular fluids under different annular-fluid Reynolds numbers are FLiBe > FLiNaK > KF-ZrF_4 >> He, which is the priority sequence for selection as well if only the heat transfer performance is considered. The mass transfer rates for these four potential annular fluids are He >> FLiBe >> FLiNaK > KF-ZrF_4. If both heat and mass transfer performance are considered, FLiBe is the best choice for the annular fluid. However, the required pumping power for FLiBe may be much larger than that for helium, which results in much larger operation cost. A comprehensive cost-benefit analysis is therefore necessary to determine the best choice as the annular fluid between FLiBe and helium.

8.3. AHTR P-IHX Design

AHTR developed by the Oak Ridge National Laboratory (ORNL) is a design concept for a large-output FHR. The AHTR concept currently remains at a conceptual level. This report addresses AHTR technology gaps by focusing on HXs, i.e., P-IHX, I-PHX, DHX, and NDHX. Figure 8-14 shows overall schematic of the AHTR. P-IHX, which is outside the reactor

vessel and inside the reactor building, removes heat from the primary salt FLiBe to the intermediate salt KF-ZrF_4. I-PHX, which is outside the reactor building takes heat from the intermediate salt to water/steam for Rankine cycle. DHX, which is in the reactor vessel transfers decay heat from the primary salt to the DRACS intermediate salt KF-ZrF_4 and then through NDHX located in an air chimney to the ambient air. Key AHTR design parameters are summarized in Table 8-2. This chapter discusses P-IHX design optimization. Designs of I-PHX, DHX, and NDHX will be discussed in the next a couple of chapters.

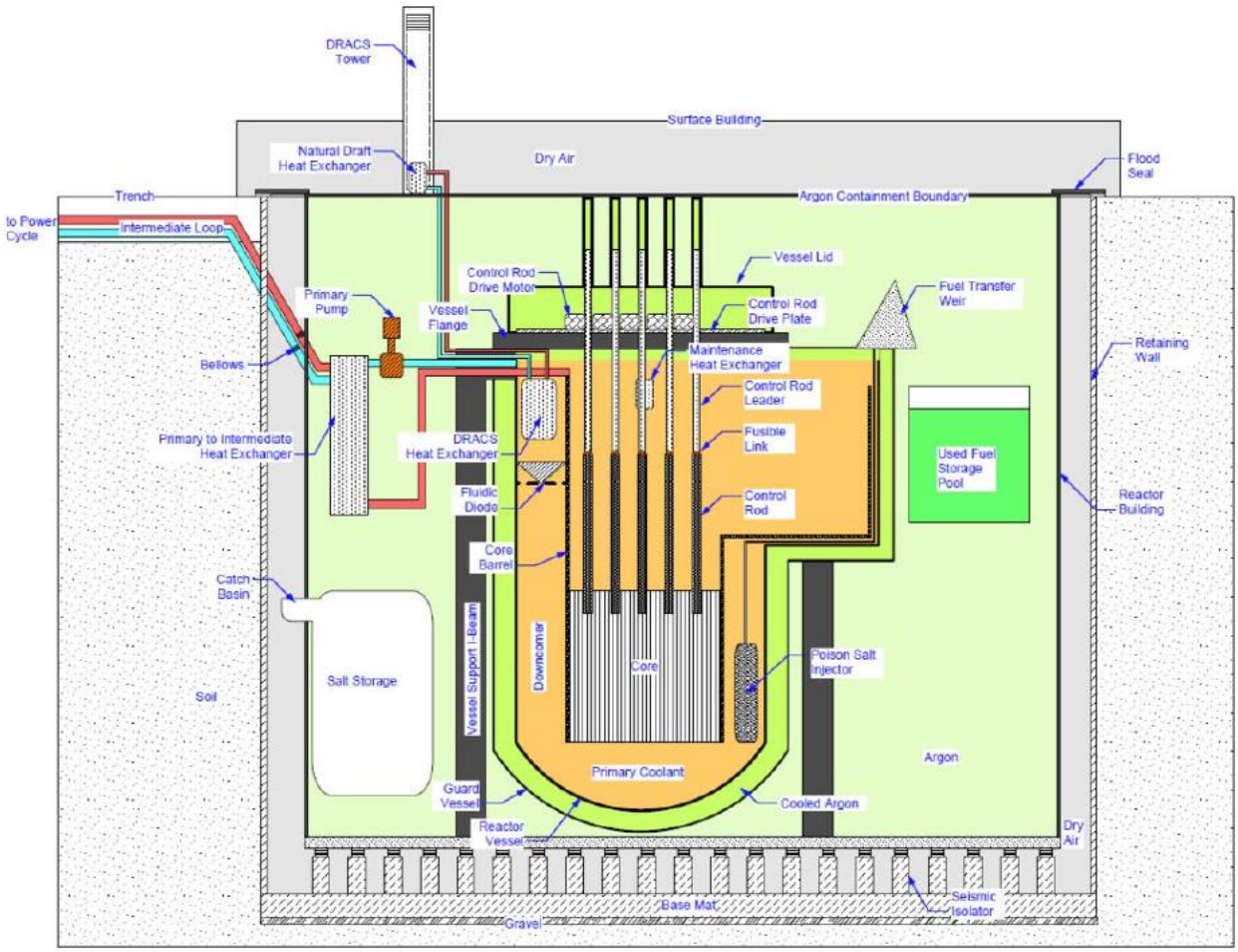

Figure 8-14 Overall schematic of the AHTR reactor building [8.1]

Table 8-2 Key design parameters of AHTR [8.1]

Parameters	Value	Units
Overall parameters		
Core thermal power	3400	MW
Net electrical power	1530	MW
Primary coolant circuit parameters		
Primary coolant salt	LiF-BeF_2	-

Average reactor outlet temperature	700	°C
Primary coolant return temperature	650	°C
Primary coolant flow rate	28500	kg/s
Number of loops	3	-
Primary coolant pressure	Atmospheric	-
Intermediate coolant circuit parameters		
Intermediate coolant	$KF\text{-}ZrF_4$	-
Intermediate coolant supply temperature	675	°C
Intermediate coolant return temperature	600	°C
Intermediate coolant flow rate	43200	kg/s
Number of loops	3	-
Intermediate coolant pressure	Atmospheric	-
Power cycle parameters		
Fluid to high pressure turbine	Supercritical steam	
Turbine supply temperature	650	°C
Turbine supply pressure	24	MPa
Decay heat removal		
DRACS heat transfer coolant	KF-ZrF4	
DRACS maximum power	8.75	MW
Number of loops	3	-

Figure 8-15 shows layout of a double-wall P-IHX unit (totally three P-IHX units for AHTR). The double-wall P-IHX can be one tube-side pass or several tube-side passes as shown in Figure 8-15. The tube-side FLiBe flows through the double-wall P-IHX with inlet and outlet temperatures of 650 and 700 °C, respectively. The outer shell-side $KF\text{-}ZrF_4$ flows through the double-wall P-IHX with temperature increasing from 600 to 675 °C. The annular-side fluid temperature and mass flow rate are design parameters to be discussed next. The one-tube side pass configuration is initially used for the P-IHX design optimization.

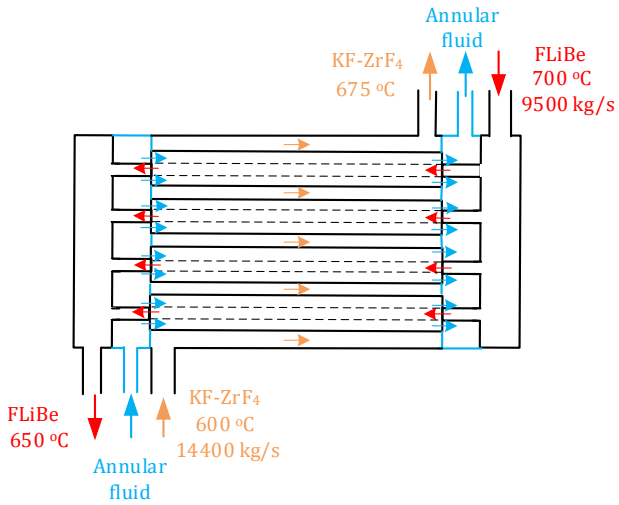

(a)

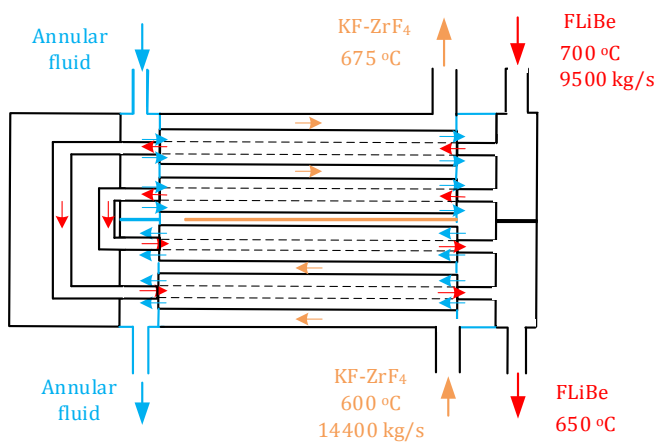

(b)

Figure 8-15 Layout of a double-wall P-IHX unit: (a) one tube-side pass and (b) two tube-side passes

8.3.1. Objectives for P-IHX Design Optimization

Two objectives were used for a double-wall fluted-tube P-IHX design optimization, i.e., heat exchanger surface area per unit power output as defined in Eq. (8-37) and the total cost as defined in Eq. (8-38), which consists of the cost of the P-IHX and the total operation cost.

$$AP = \frac{A_t}{\dot{Q}_t} \tag{8-37}$$

$$C_t = C_{HX} + C_{op_i} + C_{op_a} + C_{op_o} \tag{8-38}$$

where A_t, $\dot{Q}_t$, C_{HX}, C_{op_i}, C_{op_a} and C_{op_o} are the total surface area of a double-wall fluted-tube P-IHX, thermal power of one P-IHX unit, heat exchanger cost, operation cost of the inner fluid, annular fluid, and outer fluid, respectively.

For the HX cost estimation, it is difficult to predict the cost of a fluted-tube HX, i.e., fluted-tube P-IHX in the current design. The cost evaluation for a shell and tube (smooth tube) HX expressed as Eq. (8-39) [8.27] is therefore adopted to estimate the cost of a double-wall fluted-tube P-IHX. An additional factor, F_i, is included to account for the effect of the inflation.

$$C_{HX} = C_b F_d F_p F_m F_i \tag{8-39}$$

where C_b, F_d, F_p, F_m and F_i are the base cost, exchanger type cost factor, design pressure cost factor, material of construction cost factor, and inflation cost factor, respectively.

The operation cost is evaluated by Eq. (8-40) and the pumping power is defined as Eq. (8-41).

$$C_{\mathrm{op}} = \dot{Q}_{pump} \tau_t C_e \tag{8-40}$$

$$\dot{Q}_{\mathrm{pump}} = \frac{\dot{m} \cdot \Delta p}{\eta \rho} \tag{8-41}$$

where τ_t, C_e, $\dot{m}$, Δp, η and ρ are the total hours of operation during the HX life time, price of the electricity, mass flow rate, pressure drop, pump efficiency, and fluid density, respectively. 20 years operation time, 0.12 $/kWh, and 90% pump efficiency are used for the P-IHX design optimization.

Non-dominated sorting in genetic algorithms (NSGA) [8.28] usually used for a multi-objective optimization problem is adopted in this study. To illustrate the optimization methodology, an example with two conflict objectives which should both be minimized is shown in Figure 8-16. The number of designs is called population and different designs develop a population region. The red line shown in Figure 8-16, starting from the point having a minimum f_2 value and ending at the point having a minimum f_1 value, is called the Pareto front, where some optimum designs are located. For an optimum design located on the Pareto front, it has a lower f_2 value than any other designs in the population region when f_1 is fixed. Similarly, the design on the Pareto front has a lower f_1 value than any other points in the population region when f_2 is fixed. This NSGA method is used for the double-wall fluted-tube P-IHX design optimization. In addition, the least squares in regression analysis is applied to determine one optimum design.

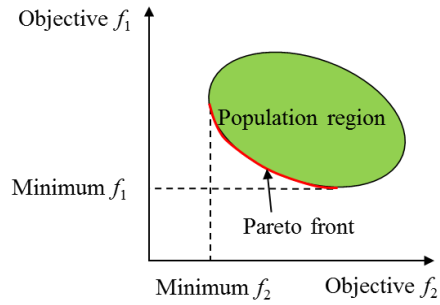

Figure 8-16 NSGA optimization method

8.3.2. Optimum Design

Several parameters have been determined for the P-IHX in the pre-conceptual AHTR design [8.27], i.e., the primary salt FLiBe inlet and outlet temperatures, FLiBe total mass transfer rate, intermediate salt KF-ZrF_4 inlet and outlet temperatures, and KF-ZrF_4 total mass transfer rate. However, these design parameters cannot be satisfied simultaneously because in our current design, P-IHXs are three-fluid HXs instead of the conventional two-fluid HX design in the previous pre-conceptual AHTR. The input parameters for the design optimization of the double-wall fluted-tube P-IHX with either helium or FLiBe as the annular fluid are summarized in Table 8-3 .

Table 8-3 Inputs for a double-wall fluted-tube P-IHX design optimization

Item	Value
Heat load (MW/one unit)	1133.3
Inner fluted tube size (mm)	D_{bi} = 8.08, D_{eo} = 12.83, T_w = 0.406, p = 6.1, N_s = 4
Outer fluted tube size (mm)	D_{bi} = 14.96, D_{eo} = 19.94, T_w = 0.711, p = 15.24, N_s = 4
Inner fluid FLiBe inlet temperature (°C)	700
Inner fluid FLiBe total mass flow rate (kg/s)	9500
Inner fluid FLiBe mass flow rate per tube (kg/s)	0.1 - 1
Annular fluid helium mass flow rate per tube (kg/s)	10^{-5} - 10^{-3}
Annular fluid helium inlet temperature (°C)	600 - 650
Annular fluid FLiBe mass flow rate per tube (kg/s)	10^{-2} - 1
Annular fluid FLiBe inlet temperature (°C)	600 - 650
KF-ZrF_4 inlet temperature (°C)	600
KF-ZrF_4 mass flow rate (kg/s)	14400
Pitch/D_{eo}	1.0 to 2.0

Comparison of the optimum results using either helium or FLiBe as the annular fluid is summarized in Table 8-4. Both the heat exchanger surface area per unit power output (AP) and the total cost (C_t) are smaller if FLiBe instead of helium is used as the annular fluid.

However, the annular fluid FLiBe takes 74.3% of the total heat, which should be recycled through a separate HX. Considering the additional cost for the separate HX, the P-IHX with FLiBe as the annular fluid design may be close to or higher than the cost of helium as the annular fluid design. In addition, 79.0% of the tritium is removed from the inner fluid in the helium-annular-fluid design, while 14.0% of tritium is removed in the FLiBe-annular-fluid design. Helium is therefore selected as the annular fluid for the double-wall fluted-tube P-IHX. The optimum results are summarized in Table 8-5.

Table 8-4 Comparison of the optimum results of a double-wall fluted-tube P-IHX using helium and FLiBe as the annular fluid

Annular fluid	AP (m²/W)	C_t (M$)	$\dot{Q}_{if}$ (MW)	$\dot{Q}_{af}$ (MW)	$\dot{Q}_{of}$ (MW)	$\eta_{T_2,if}$ (%)	$\eta_{T_2,af}$ (%)	$\eta_{T_2,of}$ (%)
Helium	4.45×10^{-6}	70.5	1133.3	2.3	1131.0	79.0	75.8	3.2
FLiBe	1.74×10^{-6}	48.6	1133.3	842.3	291.0	14.0	13.7	0.3

Table 8-5 Optimum double-wall P-IHX design

Tube arrangement	Triangular and horizontal
Tube type	Fluted tube
Tube material	Hastelloy N
Inner tube size (mm)	D_{bi} = 8.08, D_{eo} = 12.83, T_w = 0.406, p = 6.1, N_s = 4
Outer tube size (mm)	D_{bi} = 14.96, D_{eo} = 19.94, T_w = 0.711, p = 15.24, N_s = 4
Tube length (m)	28.7
Tube number	65517
Pitch to diameter ratio	1.2
Inner fluid	FLiBe
Inner-fluid mass transfer rate (kg/s)	9500
Inner-fluid inlet/outlet temperature (°C)	700/651
Annular fluid	Helium
Annular-fluid mass transfer rate (kg/s)	7.93
Annular-fluid inlet/outlet temperature (°C)	632/689
Outer fluid	KF-ZrF_4
Outer-fluid mass transfer rate (kg/s)	14400
Outer-fluid inlet/outlet temperature (°C)	600/675
Heat load (MW/one unit)	1133.3
Percentage of the heat loss to the outer fluid per unit time (%)	99.8
Percentage of the tritium weight loss from the inner fluid (%)	79.0
Percentage of the tritium weight loss to the annular fluid (%)	75.8
Percentage of the tritium weight loss to the outer fluid (%)	3.2

8.4. AHTR I-PHX Design

The intermediate loops in AHTR adopt I-PHXs for the heat exchange between the intermediate salt and water/steam for the Rankine cycle. The helical coil type HX as shown in Figure 8-17 was suggested by Sabharwall, et al. for the AHTR I-PHX design [8.29]. Considering the superior heat transfer performance of fluted tubes compared with plain tubes, helical-coiled fluted tubes were used for the AHTR I-PHX design optimization as shown in Figure 8-18. The intermediate salt, KF-ZrF_4, flows in the shell side and water/steam flows in the tube side of a I-PHX due to the high working pressure.

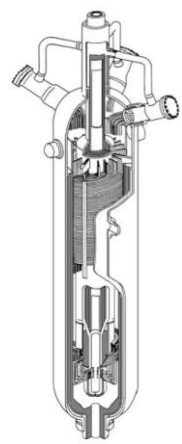

Figure 8-17Helical coil heat exchanger [8.29]

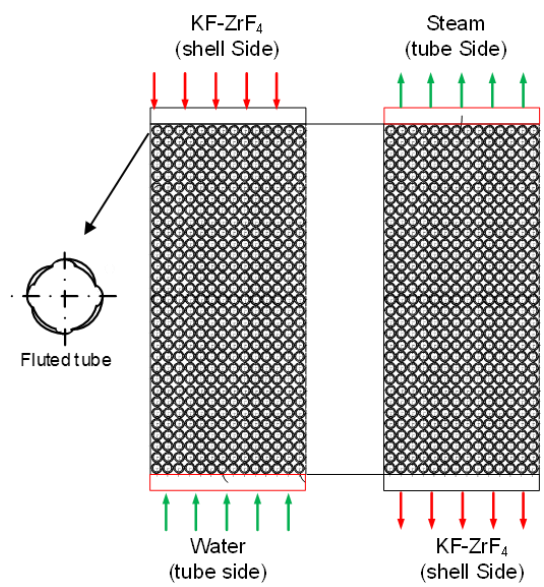

Figure 8-18 Helical-coiled fluted-tube I-PHX

Inputs for the I-PHX design optimization are summarized in Table 8-6. The HX effectiveness and cost are two objectives used for the I-PHX design optimization. Similar to the P-IHX design, the NSGA optimization method is applied for the fluted-tube I-PHX design and optimum results are summarized in Table 8-7.

Table 8-6 Inputs for I-PHX design optimization

Item	Value
Heat load (MW)	1133.3
Tube size (mm)	D_{bi} = 8.08, D_{eo} = 12.83, T_w = 0.406, p = 6.1, N_s = 4
Pitch to diameter ratio	1.0
Tube-side fluid inlet temperature (°C)	20 to 600
Tube-side fluid outlet temperature (°C)	650
Shell-side fluid mass flow rate (kg/s)	14400
Shell-side fluid inlet/outlet temperatures (°C)	675/600
Inner shell diameter (m)	0.2 to 1
Outer shell diameter (m)	2 to 5
One tube bundle height (m)	1 to 5

Table 8-7 Optimum I-PHX design

Tube arrangement	Helical coiled
Tube type	Fluted tube
Tube material	Hastelloy N
Tube size (mm)	D_{bi} = 8.08, D_{eo} = 12.83, T_w = 0.406, p = 6.1, N_s = 4
Tube-side fluid	Water/steam
Shell-side fluid	$KF\text{-}ZrF_4$
Pitch to diameter ratio	1.0
Tube-side fluid mass transfer rate (kg/s)	466.7
Tube-side fluid inlet/outlet temperature (°C)	277/650
Shell-side fluid mass transfer rate (kg/s)	14400
Shell-side fluid inlet/outlet temperature (°C)	675/600
Tube average length (m)	40.2
Tube number	3465
Inner shell diameter (m)	0.84
Outer shell diameter (m)	2.0
Shell height (m)	9.0

8.5. AHTR DRACS Design

DRACS is a passive decay heat removal system in AHTR. The decay heat is transferred from the core to the DHX by the primary salt FLiBe natural circulation in the reactor vessel, then

to the NDHX by the DRACS salt KF-ZrF_4 natural circulation in the DRACS, and finally to the ambient air.

As discussed earlier, HXs, i.e., DHXs, provide paths for tritium leakage. To reduce tritium leakage and parasitic heat loss on normal conditions, it is beneficial to keep chimney closed. On accident conditions, chimney should be open to ensure the air cooling. Dr. Holcomb from ORNL suggested a single-wall NDHX with a controlled outside environment design as shown in Figure 8-19.

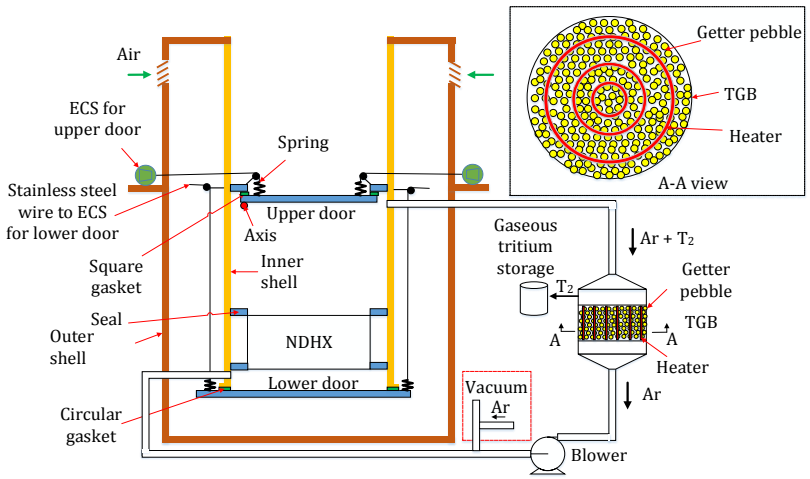

(a)

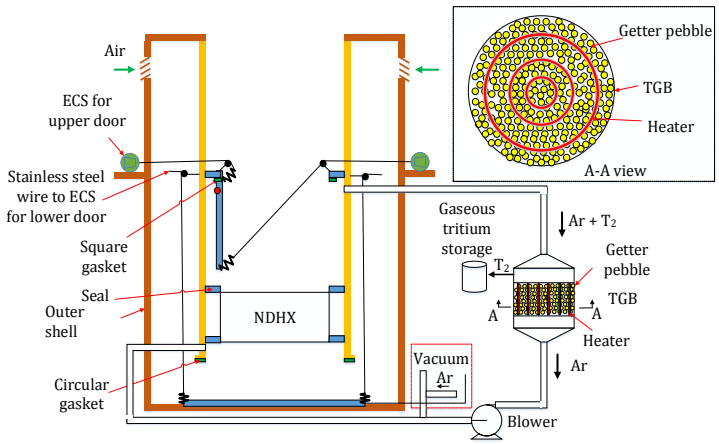

(b)

Figure 8-19 Conceptual design of a passively-open tritium-control chimney: (a) normally closed and (b) accidentally open conditions

On normal conditions, the upper and lower doors, which are located above and under the NDHX, are lift by electromagnetic control systems (ECSs) with continuously energizing to provide closed environment for the NDHX. On accident conditions, such as station blackout (SBO), reactor trip signals including the primary pump trip signal trigger the ECSs de-

energizing function and initiate freely fall of the two doors for an emergency open of the chimney, which enables air flow.

The normally closed chimney is filled with argon inert gas. Tritium leakage on normal conditions can be controlled by circulating argon and tritium gas mixture through a tritium getter bed (TGB) which is located outside the chimney as shown in Figure 8-19. Tritium is captured by the tritium solid getters, i.e., ZrCo, which have sphere shape to achieve a large surface to volume ratio. Tritium gas reacts with the tritium getters to form metal tritides. Heaters in the TGB are used to heat metal tritides to elevated temperatures and the released tritium gas is stored in special containers.

In addition to the single-wall DRACS design, specifically, single-wall DHX and NDHX designs, a double-wall NDHX design is another option for tritium control. Both these two options will be discussed next.

8.5.1. Single-wall DRACS Design

To reduce the heat loss to the DHX on normal conditions, it is beneficial to install a fluidic diode beneath the DHX. The fluidic diode should be properly oriented to provide significant flow resistance in its reverse direction on normal conditions and much smaller resistance in its forward direction on accident conditions. Since the primary salt natural circulation in the reactor vessel, the DRACS salt KF-ZrF_4 natural circulation in the DRACS, and air natural convection in the chimney are coupled, DRACS and fluidic diode designs should be coupled as well.

<u>Fluidic Diode</u>

A CFD code, STAR CCM+, was used to determine the mass flow rates of the forward/reverse flows and the corresponding pressure drops for a given fluidic diode size. Since the three-dimensional flow in the fluidic diode is complex, it is necessary to select an appropriate model with carefully selected prism layer parameters. The simulation results using $k - \varepsilon$ and $k - w$ SST models were compared against the experimental data [8.29] as shown in Figure 8-20.

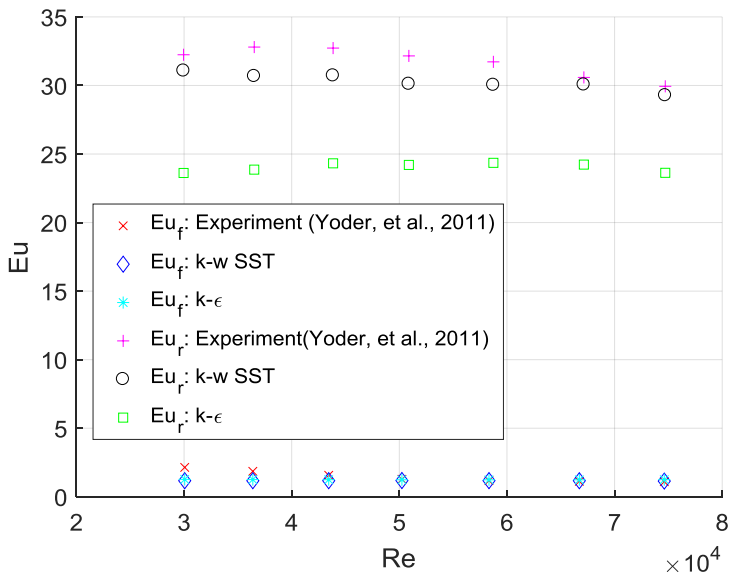

Figure 8-20 Comparison of experimental data and STAR CCM+ predictions

Euler number of the forward flow, Eu_f, obtained by $k-\varepsilon$ and $k-w$ SST models matches well with the experimental data. Euler number of the reverse flow, Eu_r, obtained from the $k-w$ SST turbulent model is slightly larger (within 6%) than the experimental data, while the realizable $k-\varepsilon$ turbulent model underestimates Eu_r significantly. The $k-w$ SST turbulent model is therefore used for the fluidic diode design. A fluidic diode with a chamber diameter of 0.5 m, inlet/outlet port diameters of 0.25 m are initially used for the DRACS design optimization. If the core by-pass mass flow rate through the DHX is large under normal conditions, another fluidic diode design will be used for the DRACS design optimization until an optimum design.

<u>Design Objectives</u>

Both the DHX and NDHX are cross-flow HXs as shown in Figure 8-21. The DHX shell-side salt FLiBe flows downward across the horizontal DHX heat-transfer tubes on accident conditions. The NDHX shell-side air flows upward across NDHX heat-transfer tubes. The arithmetic average heat exchanger effectiveness of the DHX and NDHX, and the total cost are two objectives used for the DRACS design optimization.

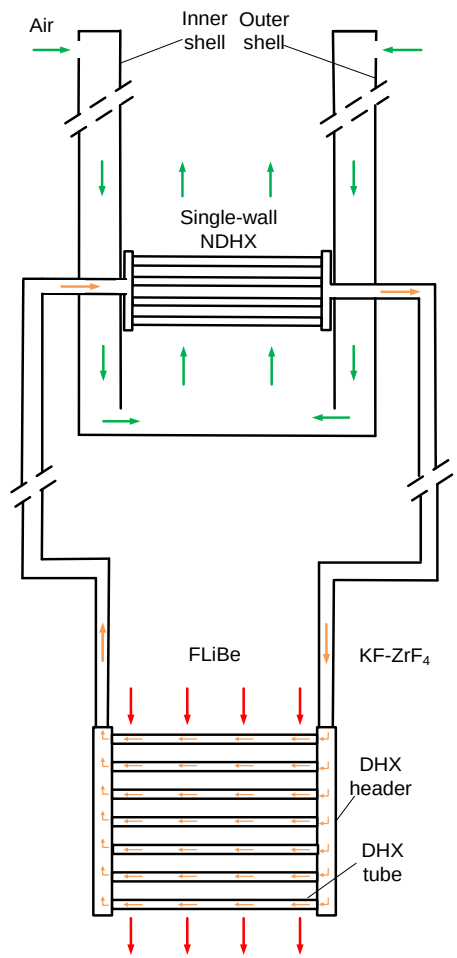

Figure 8-21 Layout of DRACS

The effectiveness of a cross-flow HX is estimated by Eq. (8-42) [8.31].

$$\varepsilon = 1 - \exp\left[\left(\frac{1}{C_r}\right) \text{NTU}^{0.22} \exp\left[-C_r \text{NTU}^{0.78}\right] - 1\right] \tag{8-42}$$

where ε is effectiveness. C_r is defined as $(c\dot{m})_{min}/(c\dot{m})_{max}$. $(c\dot{m})_{min}$and $(c\dot{m})_{max}$ are the smaller and larger one of $(c\dot{m})_h$and $(c\dot{m})_c$, respectively. $(c\dot{m})_h$means a product of thermal capacity and mass flow rate of hot fluid. Similarly, $(c\dot{m})_c$ means a product of thermal capacity and mass flow rate of cold fluid. NTU is the number of heat transfer unit.

The total cost consists of the chimney cost, DRACS salt cost, and HXs cost, as expressed by Eq. (8-43). For a preliminary cost estimation of the chimney, material and construction cost as summarized in Table 8-8 are considered. The DRACS salt cost is estimated by a quote provided by SynQuest Labs, Inc. A shell and tube heat exchanger cost evaluation approach [8.27] previously used to estimate the P-IHX cost is adopted for the cost evaluation of both DHX and NDHX.

Table 8-8 Unit price for the AHTR chimney and DRACS salt

Chimney material cost ($/m³)	Chimney construction cost ($/m³)	KF-ZrF_4 cost ($/kg)
150	350	124

Notes:
1. Chimney material cost evaluation is based on the concrete price in USA in 2016 provided by ConcreteNetwork.com
2. Chimney construction cost evaluation is based on the construction, concrete cover and labor cost provided by Fluri, et al. [8.32]

$$C_t = C_{chi} + C_{salt} + C_{HX} \tag{8-43}$$

The same NSGA optimization method used for the P-IHX design optimziation is applied for the DRACS design optimization. Figure 8-22 shows the flowchart of the DRACS design optimization. For the DHX design, input variables, i.e., mass flow rates, heat removal capacities, and inlet temperatures of the shell-side FLiBe and tube-side KF-ZrF_4 are initially specified. For the NDHX and air chimney designs, input variables, i.e., mass flow rates, inlet temperatures of the NDHX shell-side air and tube-side KF-ZrF_4 are initially specified. The heat removal capacities of FLiBe, KF-ZrF_4, and air are set the same under steady-state condition. The $H_{DHX\text{-}NDHX}$ and $H_{NDHX\text{-}chimney}$, which are respectively defined as the centerline distance between the DHX and NDHX, the NDHX centerline and air inlet location on the chimney, are determined by equalizing the buoyancy with flow resistance. The $H_{core\text{-}DHX}$, centerline distance between the core and DHX, is a fixed parameter which is used to estimate the DHX shell-side FLiBe mass flow rate. A large $H_{core\text{-}DHX}$ is beneficial for the heat removal since it increases the DHX shell-side heat transfer coefficient by increasing the distance between the cold and hot fluids (primary and DRACS salts). A maximum achievable value for $H_{core\text{-}DHX}$ is about 10 m, which is adopted in the DRACS design optimization.

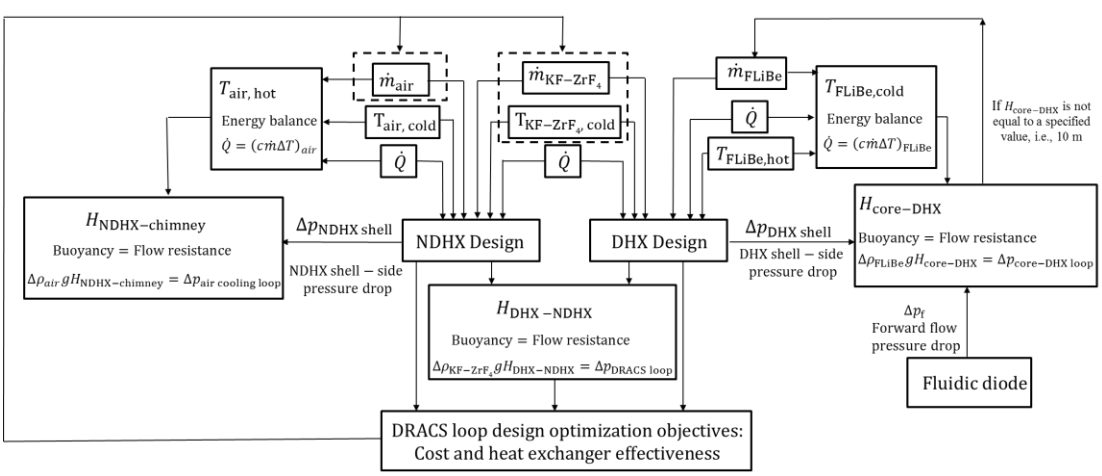

Figure 8-22 Flowchart of DRACS design

Optimum Design

Each of the three DRACS loops is intended to remove 0.25% of the full power at 700 °C salt temperature [8.33]. The heat load for each DRACS loop is therefore 8.5 MW. The inlet temperature of the DHX shell-side salt is set 700 °C. The NDHX tube length is a design variable, while the DHX tube length is a fixed variable due to the limited space in the AHTR downcomer. Considering the available angular space in the downcomer for the DHXs, the average length of one DHX heat-transfer tube is set 3 m. The inlet temperature of the DHX tube-side salt is another design variable, which should be much larger than its melting temperature 390 °C [8.34] to acquire a large safety margin. The TRACE simulation results [8.35] are used as references to set ranges for other variables, i.e., DHX tube-side salt and air mass flow rates as summarized Table 8-9. In addition, the least squares in regression analysis is applied to determine one optimum design of the DRACS. Key design parameters of the DHX and NDHX are summarized in

Table 8-10 and Table 8-11, respectively.

Table 8-9 Inputs for the DRACS design optimization (single-wall design)

Item	Value
Heat load (one DRACS unit)	8.5 MW
Fluted tube size (mm)	D_{bi} = 10.67, D_{eo} = 16.64, T_w = 0.508, p = 8.23, N_s = 4
Transverse and longitudinal tube pitch ratios	1.5
$H_{\text{core-DHX}}$ (m)	10
DHX tube average length (m)	3
DHX shell-side salt inlet temperature (°C)	700
DHX tube-side salt inlet temperature (°C)	550 - 650
DHX tube-side salt mass flow rate per tube (kg/s)	0.01 – 0.1
NDHX tube length (m)	1 - 5
Air inlet temperature (°C)	20
Air mass flow rate per tube (kg/s)	0.001 – 0.01
DRACS piping diameter (m)	0.3 - 0.5

Table 8-10 Key parameters of an optimum DHX design

Tube arrangement	Horizontal, triangular
Tube type	Fluted tube
Tube material	Hastelloy N
Tube size (mm)	D_{bi} = 10.67, D_{eo} = 16.64, T_w = 0.508, p = 8.23, N_s = 4, L = 3000
Tube number	2100
Number of rows/columns	140/15
Pitch to diameter ratio	1.5
Tube-side fluid	KF-ZrF_4
Shell-side fluid	FLiBe
Tube-side pressure drop (Pa)	1554
Shell-side mass flow rate (kg/s)	68.9
Shell-side inlet/outlet temperature (°C)	700/649
Shell-side pressure drop (Pa)	176.4
Overall heat transfer coefficient (W/m^{2}K)	373.6
Heat removal capacity (MW)	8.5
DHX-NDHX vertical height difference (m)	8.15
DRACS loop piping diameter (m)	0.3
DRACS loop piping length (m)	56.3
Core-DHX vertical height difference (m)	10

Table 8-11 Key parameters of an optimum NDHX design

Tube arrangement	Inline horizontal
Tube type	Fluted tube
Tube material	SS 316H
Tube size (mm)	D_{bi} = 10.67, D_{eo} = 16.64, T_w = 0.508, p = 8.23, N_s = 4, L = 3000
Tube number	2625
Row/Column	25/105

Pitch to diameter ratio	1.5
Tube-side fluid	$KF\text{-}ZrF_4$
Shell-side fluid	Air
Tube-side mass transfer rate (kg/s)	102.3
Tube-side inlet/outlet temperature (°C)	625/546
Tube-side pressure drop (Pa)	1004
Shell-side mass transfer rate (kg/s)	24.1
Shell-side inlet/outlet temperature (°C)	20/365
Shell-side pressure drop (Pa)	68.2
Overall heat transfer coefficient (W/m^2K)	92.0
Heat removal capacity (MW)	8.5
NDHX-chimney vertical height difference (m)	18.3
Chimney inner/outer shell diameter (m)	3.7/4.7

It is necessary to check the core by-pass mass flow rate through the DHX under normal conditions. Applying a simplified assumption that the pressure drop is proportionally to the square of the velocity, the total core by-pass mass flow rate for the three DHXs is estimated as 501 kg/s, which occupies 1.8% of the primary salt nominal mass flow rate in AHTR. Therefore, the fluidic diode geometry initially used for the DRACS design optimization is acceptable.

8.5.2. Double-wall DRACS Design

A double-wall NDHX design is another approach to reduce the tritium leakage from the AHTR DRACS. Similar to the double-wall fluted-tube P-IHX design optimization, the heat exchanger surface area per unit power output and the total cost are two objectives for a double-wall NDHX design optimization. The inlet temperature of the NDHX tube-side salt should be much larger than its melting temperature to acquire a large safety margin. Other inputs for a double-wall NDHX design optimization are summarized Table 8-12 and optimum results are summarized in Table 8-14.

Table 8-12 Inputs for a double-wall NDHX design optimization

Item	Value
Heat load (one unit)	8.5 MW
Inner fluted tube size (mm)	D_{bi} = 8.08, D_{eo} = 12.83, T_w = 0.406, p = 6.1, N_s = 4
Outer fluted tube size (mm)	D_{bi} = 14.96, D_{eo} = 19.94, T_w = 0.711, p = 15.24, N_s = 4
Transverse and longitudinal tube pitch ratios	2.0
NDHX tube-side salt inlet temperature (°C)	550-650
NDHX tube-side salt mass flow rate per tube (kg/s)	0.01-0.05
NDHX annular-side helium mass flow rate per tube (kg/s)	10^{-5} – 10^{-4}
NDHX annular-side helium inlet temperature (°C)	500 - 550
NDHX annular-side FLiBe mass flow rate per tube (kg/s)	0.01 - 1
NDHX annular-side FLiBe inlet temperature (°C)	500 - 550
NDHX tube length (m)	1 - 5

Air inlet temperature (°C)	20
Air mass flow rate per tube (kg/s)	0.001 – 0.01

Comparison of the optimum results using either helium or FLiBe as the annular fluid is summarized in Table 8-13. Both the heat exchanger surface area per unit power output (AP) and the total cost (C_t) are smaller if the FLiBe instead of the helium is used as the annular fluid. However, the annular fluid FLiBe takes 67.5% of the total heat, which should be recycled through a separate HX. Considering the additional cost for the separate HX, the P-IHX with FLiBe as the annular fluid design may be close to or higher than the cost of helium as the annular fluid design. In addition, 58.8% of the tritium is removed from the inner fluid in the helium-annular-fluid design, while 17.2% of tritium is removed in the FLiBe-annular-fluid design. Helium is therefore selected as the annular fluid for the double-wall fluted-tube NDHX. The optimum results are summarized in Table 8-14.

Table 8-13 Comparison of the optimum results of a double-wall fluted-tube NDHX using helium and FLiBe as the annular fluid

Annular fluid	AP (m²/W)	C_t (M$)	$\dot{Q}_{if}$ (MW)	$\dot{Q}_{af}$ (MW)	$\dot{Q}_{of}$ (MW)	$\eta_{T_2,if}$ (%)	$\eta_{T_2,af}$ (%)	$\eta_{T_2,of}$ (%)
Helium	5.95×10^{-5}	0.81	8.5	1.2	7.3	58.8	57.4	1.4
FLiBe	2.66×10^{-5}	0.53	8.5	5.7	2.8	17.2	16.7	0.5

Table 8-14 Optimum double-wall NDHX design

Tube arrangement	Triangular
Tube type	Fluted tube
Tube material	SS 316H
Heat load (MW)	8.5
Tube length (m)	3.45
Double-wall unit number	6574
Pitch to diameter ratio	2.0
Tube-side fluid	KF-ZrF_4
Tube-side salt mass flow rate (kg/s)	163
Tube-side salt inlet/outlet temperature (°C)	611/561
Annular fluid	Helium
Annular fluid mass flow rate (kg/s)	3.3
Annular fluid inlet/outlet temperature (°C)	522/590
Shell-side fluid	Air
Air mass flow rate (kg/s)	18.2
Air inlet/outlet temperature (°C)	20/416
Percentage of the heat loss to the outer fluid per unit time (%)	86.2
Percentage of the tritium weight loss from the inner fluid (%)	58.8
Percentage of the tritium weight loss to the annular fluid (%)	57.4
Percentage of the tritium weight loss to the outer fluid (%)	1.4

8.6. High Temperature Fluoride Salt Test Facility

A high-temperature fluoride salt test facility (HT-FSTF) is needed to test the lab-scale fluted-tube heat exchangers, i.e., fluted-tube DHX and NDHX. In the original IRP proposal, the existing high-temperature DRACS test facility (HTDF) was proposed to be used for this heat exchanger testing task. The construction of HTDF was completed at The Ohio State University (OSU), but was disassembled for transferring to UM as Dr. Xiaodong Sun's research group joined UM in January 2017. The facility has been transferred from OSU, however, Dr. Sun's research lab at UM was under renovation and was not available for reconstructing HTDF at that time. We started planning to build a new high-temperature fluoride salt (FLiNaK) test facility, i.e., HT-FSTF, in a temporary lab space at UM. This new facility is primarily used for testing HXs and some thermal-hydraulics phenomena related to FHRs, such as forced and natural circulation flows.

Figure 8-23, Figure 8-24, and Figure 8-25 show a schematic, three-dimensional layout, and photo of HT-FSTF, respectively. It primarily consists of a reservoir tank for salt storage and three closed loops, namely, a primary molten salt loop (red line), a secondary molten salt loop (orange line), and an air loop (blue line). The primary molten salt loop consists of a simulated core for heating, DHX shell side, primary molten salt pump, high-temperature valves, and stainless steel 316H piping. The secondary molten salt loop consists of the DHX tube side, NDHX tube side, secondary molten salt pump, high-temperature valves, and stainless steel 316 piping. The air loop consists of the NDHX shell side, air-to-water HX shell side, air circulator, and stainless steel 304 piping. Chilled water in the tube side of the air-to-water HX serves as the ultimate heat sink for HT-FSTF. Key design parameters of HT-FSTF are summarized in Table 8-15.

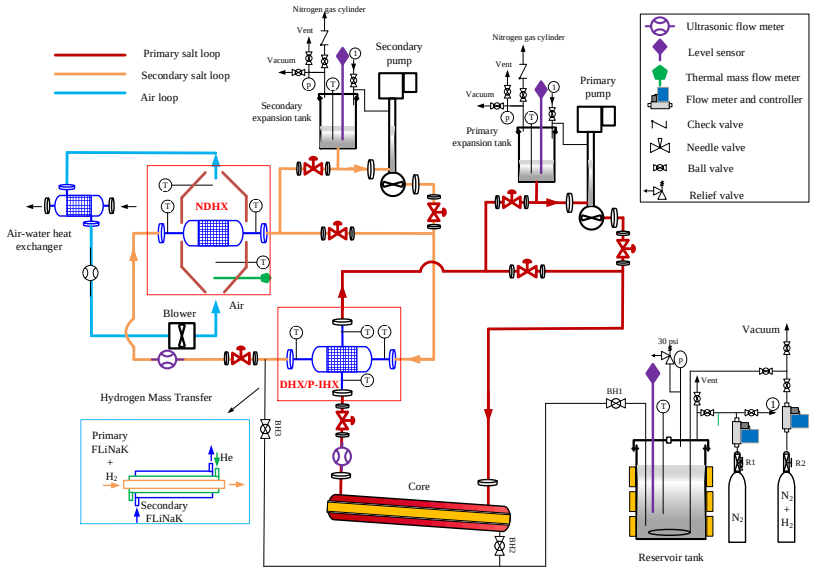

Figure 8-23 A schematic of HT-FSTF at UM

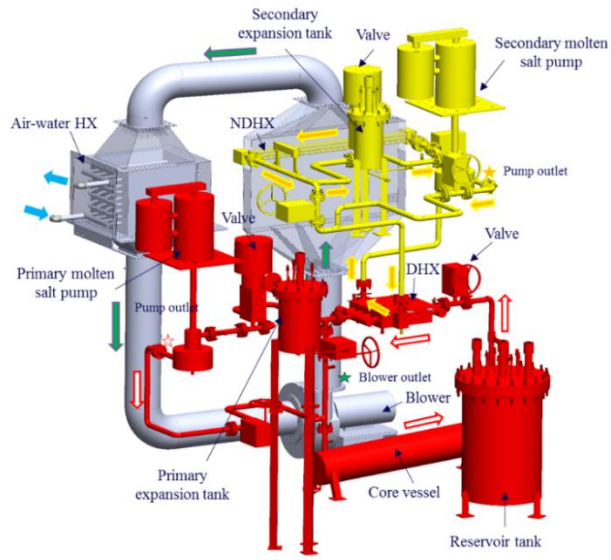

Figure 8-24 Three-dimensional layout of HT-FSTF

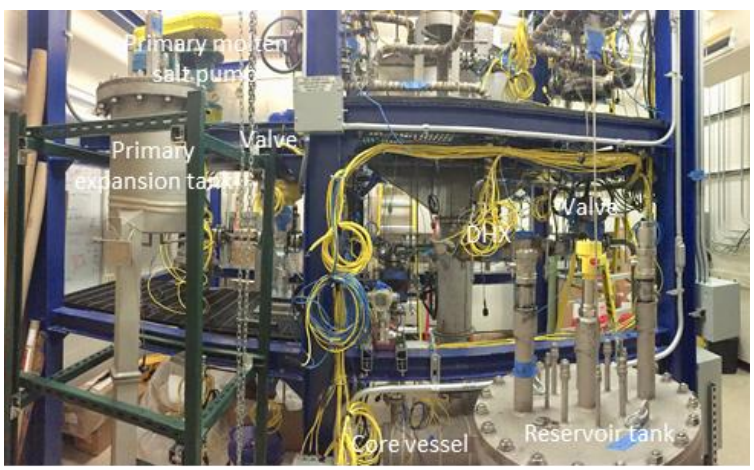

Figure 8-25 Photo of HT-FSTF

Table 8-15 Key design parameters of HT-FSTF

	Primary fluid	Secondary fluid	Total heating power (kW)	Primary fluid inlet/outlet temperature (°C)	Secondary fluid inlet/outlet temperature (°C)	Primary mass flow rate (kg/s)	Secondary mass flow rate (kg/s)
Natural circulation	FLiNaK	FLiNaK	46	700/676	570/550	0.5	0.7
Forced circulation	FLiNaK	FLiNaK	46	--	--	2.1	1.4

8.6.1. Key Components

Heaters

There are three types of heaters applied in HT-FSTF: 1) Nineteen cartridge heaters in the simulated core vessel to provide a total of 38 kW main heating power; 2) Three band heaters (total 9 kW) to be wrapped around the reservoir tank for salt melting; 3) Twenty tape heaters (total 8 kW) to be wrapped on piping and vessels/tanks for trace heating. To control and monitor these heaters, electric panels were designed and fabricated as shown in Figure 8-26.

Figure 8-26 Control panels for HT-FSTF

Molten Salt Pumps

The UM TH research team has been working with Nagle Pumps Inc. for the pump in HTDF. The vertical cantilever dry pit pump as shown in Figure 8-27 is used for HT-FSTF. The pump wetted parts are made of SS 316. In addition, each of the two molten salt pumps supplies 26' FLiNaK head under 30 GPM, which is sufficient for the HX testing.

Figure 8-27 Vertical cantilever dry pit pump

Vessels/Tanks

Stainless steel 316H has been selected as the material for the reservoir tank, two expansion tanks, and core vessel considering the ASME Section VIII code requirement, relatively low cost, and good corrosion resistance with FLiNaK at high temperatures [8.36].

Considering the required FLiNaK inventory in the primary and secondary molten salt loops, the dimensions for the reservoir tank are NPS 24, height 40", and volume 9.82 ft^3. The total volume of the liquid FLiNak in the primary and secondary loops is about 5.15 ft^3 which is equivalent to 17.09 ft^3 FLiNaK in power form. Since FLiNaK is initially in powder form in the reservoir tank when transferred from the glove box, it is necessary to have two-time complete uploading for FLiNaK into the reservoir tank.

To accommodate the change of the molten salt volume during transient tests, a primary expansion tank and a secondary expansion tank were installed in the primary and secondary molten salt loops, respectively. The dimensions of the primary and secondary expansion tanks are NPS 12, height 20", volume 1.3 ft^3, and NPS 8, height 18", volume 0.5 ft^3, respectively.

The core vessel is actually a container for nineteen cartridge heaters which are the main heat sources in HT-FSTF. Considering the size and quantity of cartridge heaters, and the lab space constraint, the dimensions of the core vessel are NPS 10, length 68", and volume 3.1 ft^3.

Valves

HT-FSTF requires a total of eight valves to be installed for HX testing and investigation of the molten salt natural circulation. To ensure the valves working properly at high temperatures, a dual-gasket system is used. The first set of the seal is a primary gasket, which is a spiral-wound construction with a SS 316 winding and a flexible graphite filler. The second set of the seal is a secondary gasket made of Flexitallic Thermiculite 715 material. The dual-gasket system significantly reduces the possibility of leakage.

HXs

To achieve similar convective heat transfer on the tube-side and shell-side fluids between the prototypic and lab-scale (model) HXs, it is necessary to keep the Prandtl number and Reynolds number the same between the model and prototype as written as

$$\mathrm{Pr}_R \equiv \frac{\mathrm{Pr}_{model}}{\mathrm{Pr}_{prototype}} = \left(\frac{\mu c_p}{k}\right)_R = 1.0 \tag{8-44}$$

$$\mathrm{Re}_R \equiv \frac{\mathrm{Re}_{model}}{\mathrm{Re}_{prototype}} = \left(\frac{\rho u d}{\mu}\right)_R = 1.0 \tag{8-45}$$

Lab-scale fluted-tube HXs, i.e., DHX and NDHX, have been developed as shown in Figure 8-28 based on the scaling analysis. In addition, hydrostatic tests were performed for the

fabricated lab-scale HXs. The design gauge pressures at the design temperatures for the NDHX tube/shell sides and DHX tube/shell sides are 7.7/5.0 and 7.2/5.4 psig, respectively. The corresponding minimum test gauge pressures at the room temperature 20 °C for the NDHX tube/shell sides and DHX tube/shell sides are 23.4/7.9 and 21.9/39.8 psig per ASME B31.3-2014 [8.37], respectively. For conservative consideration, 50 psig has been selected as the test gauge pressure for both the NDHX tube and shell sides and 80 psig for both the DHX tube and shell sides. No leakage was observed after one-hour hydrostatic test for these two lab-scale HXs.

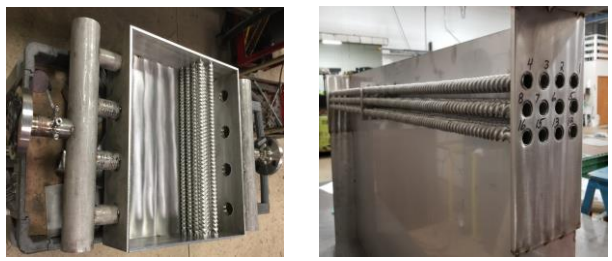

Figure 8-28 Lab-scale DHX (left) and NDHX (right)

8.6.2. Corrosion Tests

The main purpose of this study is to evaluate the corrosion characteristics of FLiNaK with the 99% purity level at the elevated temperature to help assess the operation life of a test facility, i.e., HT-FSTF, which will use the same type of salt with the same or very similar impurity level. A corrosion test system as shown in Figure 8-29 and Figure 8-30 is capable of testing the corrosion rate of various materials in a static liquid in an inert environment. It was used to study the corrosion rate of SS 316H coupons in liquid FLiNaK at 722 °C for 100 hours.

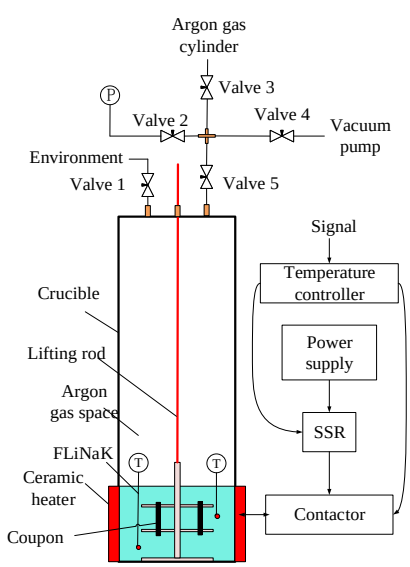

Figure 8-29 A schematic of the corrosion test system

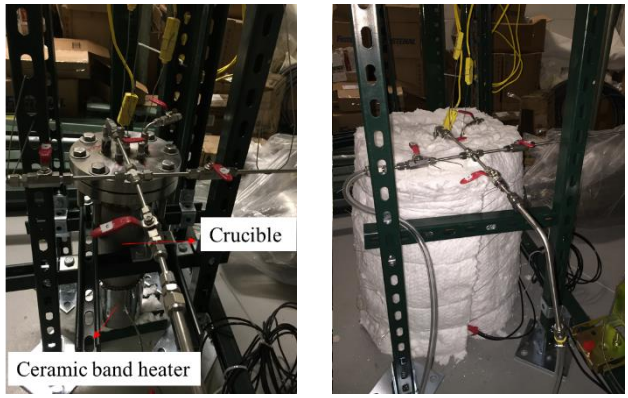

Figure 8-30 Corrosion test system before and after installation of thermal insulation

Coupons made of SS 316H (2.6×5.1×0.67 cm^3) were fastened on a supporting frame that was located at the bottom of a circular crucible (inner diameter 10.2 cm). To avoid causing electrochemical corrosion and introducing impurities, the supporting frame and crucible were made of the same material as the coupons. To ensure that the coupons were completely submerged in the 0.7 kg FLiNaK pool when the salt temperature reached a preset testing temperature, the supporting frame was connected to a lifting rod which penetrated through the top of the crucible.

A series of ball valves with a pressure transducer, an argon gas cylinder (argon concentration >99.998%), and a vacuum pump were utilized to ensure: 1) no air remained in the crucible prior to testing; 2) argon gas covered the salt during the testing duration; and 3) pressure inside the crucible was monitored during the tests. To automatically control and maintain the FLiNaK temperature over a relatively long testing duration, a ceramic band heater located on the outside of the crucible was installed with a contactor, a solid-state relay (SSR), and a temperature controller.

Since the corrosion behavior is sensitive to the moisture and oxygen, the fluoride salt FLiNaK was prepared and processed in a glove box with an inert environment before the test. The glovebox uses nitrogen gas as its cover gas with moisture and oxygen concentrations under 0.1 ppm. Each of the three constituent salts, LiF, NaF, and KF, purchased from SynQuest Labs, Inc., has a purity level of 99%. To remove most of the moisture and oxygen contents in the as-received salts, HF/H_2 gas mixture sparge is a good choice. However, HF was not used in our experiment due to its toxicity. LiF, NaF, and KF were initially dried at 250 °C in the glove box for several hours separately until little change in their mass was observed. To accelerate moisture release, stirring the salt was performed during the dehydrating process. The three salts were then mixed completely in the glove box based on their individual mole percentages of 46, 11.5, and 42.5 for LiF, NaF, and KF, respectively. The prepared FLiNaK was dried at 250 °C for four hours to further remove oxygen and moisture.

To eliminate the air effect on the corrosion performance of SS 316H coupons in FLiNaK, argon was used as the cover gas inside the crucible. Major procedure for the test consists

of: 1) loading FLiNaK and coupons in the crucible in a glove box; 2) vacuuming the corrosion test system, heating FLiNaK to the testing temperature; 3) inserting two test coupons (coupon A and B) into the FLiNaK pool to ensure their total submersion; 4) maintaining testing temperature for a certain testing duration with an argon gas gauge pressure of 10 psi to avoid the air ingress; 5) lifting the coupons out of the FLiNaK pool after the scheduled testing duration is reached; 6) disconnecting power supply for the heaters to allow the liquid FLiNaK to cool down naturally; and 7) finally taking the coupons out for analysis at the room temperature.

The mass loss rates of the two SS 316H coupons after exposure in FLiNaK at 722 °C for 100 hours were 0.90 and 0.97 mg/cm^2-d, corresponding to 1.14 and 1.23 μm/d thickness loss, respectively. The corrosion rates in our test was nearly one half of a literature value 1.79 mg/cm^2-d that was obtained by testing SS 316L in FLiNaK with a graphite crucible at 700 °C for 100 hours in the glove box [8.38]. Less impurities existed in our as-received salt after dehydrating might be one reason resulting in smaller corrosion rates. In addition, the larger corrosion rate in the literature [8.38] could be caused by the use of the graphite crucible that accelerated corrosion process by way of forming Cr-carbide phases for the Cr-containing alloys [8.39].

A second corrosion test under the same conditions (722 °C for 100 hours) was performed as well. However, there was air ingress due to the incorrect operation. The incoming air (oxygen and moisture) in the second corrosion test significantly accelerated the corrosion rate to about 1.85 mg/cm^2-d, which was twice of the average corrosion rate in the first corrosion test (without air). Therefore, it is necessary to remove oxygen and moisture during salt preparation.

8.6.3. Salt Preparation

The fluoride salts, especially the ingredient KF, are sensitive to the moisture and must be dehydrated in an inert environment, which can be provided by a glove box as shown in Figure 8-31. The glovebox is equipped with a purification system that removes the moisture and oxygen continuously. To determine the moisture content in each binary salts, i.e., LiF, NaF, and KF, the dehydrating test for each salt was necessary.

Figure 8-31 Glove box and binary salts, LiF, NaF, and KF

Since KF is hygroscopic, it is in chunk form initially as shown in Figure 8-32. KF was grinded into power prior to heating. To reduce HF production, the dehydrating temperature was set 250 °C. The initial moisture level in the glove box was 4.9 ppm, and initial weights of LiF, NaF, and KF were 622.69, 1008.87, and 995.61 g, respectively. The capacity and accuracy of the scale used in the dehydrating test were 3 kg and 0.01 g, respectively. During the dehydrating test, the weights of the three binary salts were recorded every twenty minutes after stirring. Figure 8-32 to Figure 8-34 show the weight reduction with time for LiF, NaF, and KF, respectively. The moisture contents in LiF, NaF, and KF were 0.307, 0.175, and 0.53 wt%, respectively. In addition, the periods for 99 wt% of the moisture to be removed from LiF, NaF, and KF in the testing conditions were 180, 180, and 240 minutes, respectively.

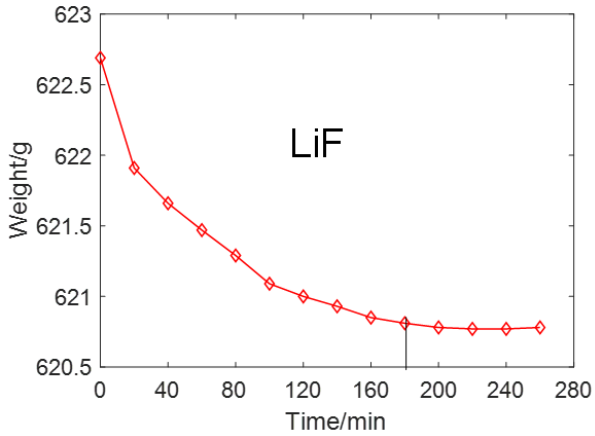

Figure 8-32 Weight change of LiF

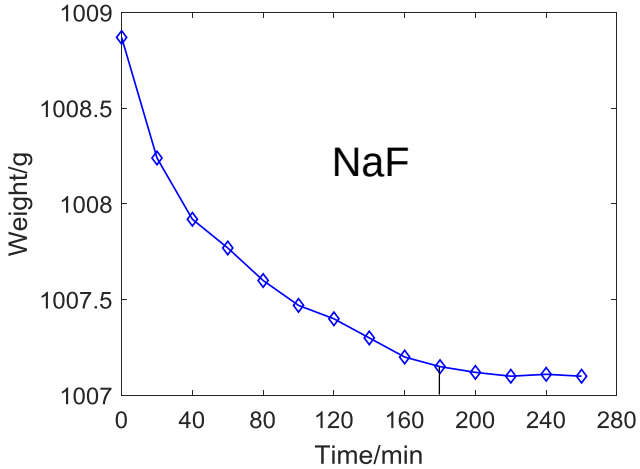

Figure 8-33 Weight change of NaF

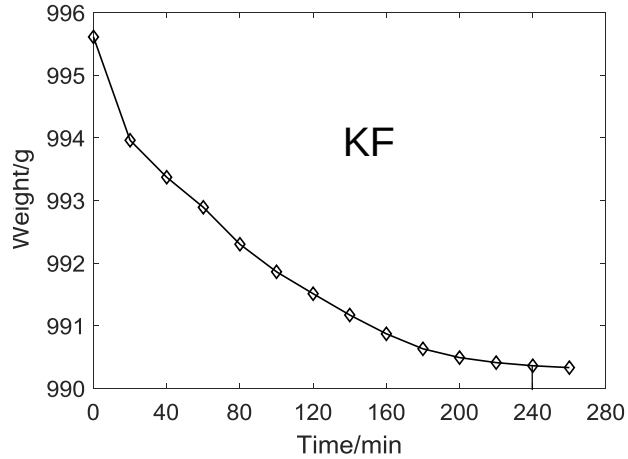

Figure 8-34 Weight change of KF

A methodology for processing FLiNaK is therefore developed, which consists of the following steps: 1) Dehydrating LiF, NaF, and KF at 250 °C for 180, 180, and 240 minutes, respectively, in the glove box; 2) Stirring to accelerate moisture release every 20 minutes; and 3) Weighing and mixing the binary salts NaF, KF, and LiF according to the specific mole ratio NaF-KF-LiF (11.5-42.0-46.5 mol%). After processing FLiNaK, it will be transferred to a reservoir tank for further dehydrating. FLiNaK will then be melted in the reservoir tank and charged into the primary and secondary molten salt loops.

8.7. Summary

Tritium production rates in FHRs could be several orders of magnitude higher than those in PWRs, which makes tritium control a critical issue for these advanced reactors. A DWHX with an annular fluid design, which adopts a three-fluid design concept, is proposed as one of the strategies for tritium control in AHTR.

A coupled heat and mass transfer model was developed and benchmarked against the experimental data in the literature to assist a DWHX design. In addition, four double-wall configurations, i.e., IPOP, IPOF, IFOP, and IFOF, were initially considered for a DWHX. Four fluids, i.e., FLiBe, FLiNaK, KF-ZrF_4, and helium, were initially considered as the annular fluid in a DWHX. The analysis indicated that the IFOF configuration with helium as the annular fluid design had the best mass transfer performance (tritium removal), while the IFOF with the annular fluid FLiBe design had the best heat transfer performance (heat removal). Both FLiBe and helium were investigated as an annular fluid option for the double-wall P-IHX and NDHX designs.

If FLiBe is used as the annular fluid for the P-IHX, 74.3% of the heat is transferred from the inner fluid to the annular fluid. The significant heat loss to the annular fluid FLiBe should be recycled by a separate HX, which results in an increase of the total cost of the system. In addition, the helium-annular-fluid design for the P-IHX removes 79.0% of the tritium contained in the inner fluid, while the annular fluid FLiBe removes 14.0%. Considering the total cost and heat and mass transfer performance, helium is suggested as the annular fluid for the double-wall P-IHX. Similarly, if FLiBe is adopted as the annular fluid for the NDHX, 67.5% of the heat is transferred from the inner fluid to the annular fluid, which should be recycled. In addition, the helium-annular-fluid design removes 58.8% of tritium, while the annular fluid FLiBe removes17.2%. Helium is therefore suggested as the annular fluid for the double-wall NDHX.

The NSGA optimization method was applied for the HX design optimization. As case studies, designs of four AHTR HXs, i.e., double-wall P-IHX, single-wall I-PHX, single-wall DHX, and single/double-wall NDHX, were optimized and summarized in this report.

Finally, a high-temperature fluoride salt test facility (HT-FSTF) was designed and constructed primarily for testing HXs and some thermal-hydraulics phenomena related to FHRs, such as forced and natural circulation flows. Lab-scale fluted-tube DHX and NDHX were fabricated and are planned to be tested in HT-FSTF. In the original proposal, HXs testing was proposed to be performed in a different molten salt test facility, which became unavailable due to the research group's relocation to the University of Michigan. The HT-FSTF was therefore constructed, which resulted in the delay in the HX testing task. Experimental data from the HX tests will be used to validate the HX design model, while experimental data from the natural circulation experiments will be used for the additional benchmark and validation of system analysis codes, namely, RELAP5 and SAM.

References

[8.1] V. K. Varma, D. E. Holcomb, F. J. Peretz, E. C. Bradley, D. Llas, A. L. Qualls, and N. M. Zaharia, "AHTR Mechanical, Structural, and Neutronic Preconceptual Design," ORNL/TM-2012/320, Oak Ridge National Laboratory (2012).
[8.2] H. Schmutz, P. Sabharwall, C. Stoots, "Tritium Formation and Mitigation in High Temperature Reactors," INL/EXT-12-26758 (2012).
[8.3] M. Atlas, N. Brickner, et al., "Tritium Management Approach for FHRs Using Supercritical Steam, Open-Air Brayton, and Closed Gas Brayton Power Cycles," Report UCBTH-12-006, Berkeley (2012).
[8.4] X. Wu, S. Shi, S. Zhang, D. Arcilesi, R. Christensen, P. Sabharwall, and X. Sun, "Mass Transport Analysis for Tritium Removal in FHRs," *Annals of Nuclear Energy*, **121**, pp. 250-259 (2018).
[8.5] B. Badger, L. Guebaly, R. Engelstad, A. Hassanein, A. Klein, G. Kulcinski, E. Larsen, K. Lee, E. Lovell, G. Moses, "HIBALL: A Conceptual Heavy Ion Beam Driven Fusion Reactor Study Volume 2," ISSN 0303-4003, Karlsrube (1981).
[8.6] M. Rufer, P. Murphy, "Laser Program Annual Report," W-7405-ENG-48, DOE (1986).
[8.7] S. Zhang, S. Shi, X. Wu, X. Sun, and R. Christensen, "Double-wall Natural Draft Heat Exchanger Design for Tritium Control in FHRs," Proceedings of the 2017 25th International Conference on Nuclear Engineering, July 2-6, 2017, Shanghai, China.
[8.8] S. Zhang, X. Wu, S. Shi, X. Sun, R. Christensen, and G. Yoder, "A Coupled Heat Transfer and Tritium Mass Transport Model for A Double-wall Heat Exchanger Design for FHRs," *Annals of Nuclear Energy*, **122**, pp. 328-339 (2018).
[8.9] S. Fukada, R. Anderl, A. Sagara, and M. Nishikawa, "Diffusion Coefficient of Tritium through Molten Salt FLiBe and Rate of Tritium Leak from Fusion Reactor System," *Fusion Science and Technology*, **48**, pp. 666-669 (2005).
[8.10] A. Suzuki, T. Terai, and S. Tanaka, "Tritium Release Behavior from Li2BeF4 Molten Salt by Permeation through Structural Materials," *Fusion Engineering and Design*, **51-52**, pp. 863-868 (2000).
[8.11] S. Fukada and A. Morisaki, "Hydrogen Permeability through A Mixed Molten Salt of LiF, NaF, and KF (FLiNaK) as A Heat-Transfer Fluid," *Journal of Nuclear Materials*, **358**, pp. 235-242 (2006).
[8.12] R. Strehlow and H. Savage, "The Permeation of Hydrogen Isotopes through Structrual Metals at Low Pressures and through Metals with Oxide Film Barriers," *Nuclear Technology*, **22**, pp. 127-137 (1974).
[8.13] J. Bell, J. Redman, and H. Bittner, "Tritium Permeation through Clean Incoloy 800 and Sanicro 31 Alloys and through Steam Oxidized Incoloy 800," *Metallurgical Transactions A*, **11A**, pp. 775-782 (1980).
[8.14] J. Stempien, R. Ballinger, and C. Forsberg, "An Integrated Model of Tritium Transport and Corrosion in Fluoride Salt-Cooled High-Temperature Reactors (FHRs) – Part I: Theory and Benchmarking," *Nuclear and Engineering Design*, **310**, pp. 258-272 (2016).
[8.15] A. Gomaa, M. Halim, and A. Elsaid, "Experimental and Numerical Investigations of A Triple Concentric-Tube Heat Exchanger," *Applied Thermal Engineering*, **99**, pp. 1303-1315 (2016).
[8.16] S. Ahn, "Experimental Studies on Heat Transfer in the Annuli with Corrugated Inner Tubes," *KSME International Journal*, **17**, pp. 1226-1233 (2003).

[8.17] M. Wang, J. Song, and Y. Li, "Hydrogen Separation at Elevated Temperatures using Metallic Nickle Hollow Fiber Membranes," *American Institute of Chemical Engineers*, **63**, pp. 3026-3034 (2017).
[8.18] J. Welty, C. Wicks, R. Wilson, and G. Rorrer, "Fundamentals of Momentum, Heat, and Mass Transfer: 5th Edition," John Wiley & Sons, Inc. (2007).
[8.19] M. Thirumaleshwar, "Fundamentals of Heat and Mass Transfer, 2nd Edition" Pearson Education (2009).
[8.20] E. Chaleff, N. Antolin, W. Windl, and T. Blue, "Ab-Initio Calculation of Spectral Absorption Coefficients in Molten Fluoride Salts with Metal Impurities," *Nuclear Technology*, **204**, pp. 59-65 (2018).
[8.21] Marrero T., Mason, E., "Gaseous Diffusion Coefficient," *Journal of Physical and Chemistry Reference Data*, **1**, pp.3-118 (1972).
[8.22] P. Calderoni, P. Sharpe, M. Hara, Y. Oya, "Measurement of Tritium Permeation in FLiBe (2LiF-BeF2)", INL/CON-07-13267, October 2007.
[8.23] S. Fukada and A. Morisaki, "Hydrogen Permeability Through A Mixed Molten Salt of LiF, NaF, and KF (FLiNaK) As A Heat-Transfer Fluid," *Journal of Nuclear Materials*, **358**, pp.235-242 (2006).
[8.24] A. Nakamura, S. Fukada, R. Nishiumi, "Hydrogen Isotopes Permeation in a Fluoride Molten Salt for Nuclear Fusion Blanket," *Journal of Plasma fusion*, **11**, pp.25-29 (2015).
[8.25] Y. Zeng, S. Wu, Y. Qian, G. Wang, L. Du, W. Liu, and Z. Xia, "Apparatus for Determining Permeability of Hydrogen Isotopes in Molten-Salt," *Nuclear Science and Techniques*, **25**, pp.040602 1-6 (2014).
[8.26] R. Causey, R. Karmesky, and C. Marchi, "Tritium barriers and tritium diffusion in fusion reactors," *Comprehensive Nuclear Material*, **4**, pp. 11-49 (2012).
[8.27] A. Corripio, K. Chrien, and L. Evans, "Estimate Costs of Heat Exchangers and Storage Tanks via Correlations," *Chemical Engineering*, **89**, pp. 125-127 (1982).
[8.28] N. Srinivas and K. Deb, "Multi-objective Optimization Using Non-Dominated Sorting in Genetic Algorithms," *Evolutionary Computation* **2**, pp. 221-248 (1994).
[8.29] P. Sabharwall, E. Kim, A. Siahpush, N. Anderson, M. Glazoff, B. Phoenix, R. Mizia, D. Clark, M. McKellar, and M. Patterson, "Feasibility Study of Secondary Heat Exchanger Concepts for the Advanced High Temperature Reactor," INL/EXT-11-23076, Idaho National Laboratory, September 2011.
[8.30] G. Yoder, Y. Elkassabgi, etc., "Vortex Diode Analysis and Testing for Fluoride Salt-Cooled High-Temperature Reactors," ORNL/TM-2011/425, Oak Ridge National Laboratory (2011).
[8.31] ESDU 86018, "Effectiveness-NTU Relations for the Design and Performance Evaluation of Two-steam Heat Exchangers," Engineering Science Data Unit 86018 with Amendment, London ESDU International plc, pp. 92-107 (1991).
[8.32] T.P. Fluri, J.P. Pretorius, C.V. Dyk, T.W. Von Backstrom, D.G. Kroger, G.P.A.G. Van Zijl, "Cost Analysis of solar chimney power plants," *Solar Energy*, **83**, pp. 246-256 (2009).
[8.33] D. Holcomb, G. Flanagan, G. Mays, W. Pointer, K. Robb, and G. Yoder, "Fluoride Salt-Cooled High-Temperature Reactor Technology Development and Demonstration Roadmap," ORNL/TM-2013/401, Oak Ridge National Laboratory (2013).
[8.34] R.E. Thoma, "Phase Diagrams of Nuclear Reactor Materials," ORNL-2548, Oak Ridge National Laboratory (1959).

[8.35] D. Wang, G. Yoder, D. Pointer, and D. Holcomb, "Thermal Hydraulics Analysis of the Advanced High Temperature Reactor," *Nuclear Engineering and Design*, **294**, pp. 73-85 (2015).
[8.36] S. Zhang, M. Chen, S. Shi, X. Sun, and R. Christensen, "Corrosion Behavior of StainlessSteel SS 316H in LiF-NaF-KF (FLiNaK) at High temperatures," ANS Winter Meeting & Expo, Washington, D.C., Octobor 29 – November 2 (2017).
[8.37] "Process Piping, ASME Code for Pressure Piping, B31," ASME B31.3-2014.
[8.38] F. RAHNEMA, "Integrated Approach to Fluoride High Temperature Reactor Technology and Licensing Challenges," 2nd Molten Salt Reactor Workshop, Oak Ridge, TN, October 4-5 (2016).
[8.39] L.C. OLSON, "Materials Corrosion in Molten LiF-NaF-KF Eutectic Salt," PhD dissertation, University of Wisconsin-Madison (2009).

9. Verification and Validation of Neutronics Codes, Tools, and Methodologies in Support of Licensing

Fluoride-cooled High-temperature Reactor (FHR) designs offer benefits that include the promise of improved safety, proliferation-resistant waste, and improved thermodynamic efficiency due to higher operating temperatures. Deployment of this technology would expand the role of nuclear power in the modern energy marketplace, as well as allow it to meet the future demand for industrial process heat.

There is an increased demand for comprehensive modeling and simulation (M&S) tools for design, safety analysis, and operation in support of licensing of these reactors. These tools can also be used to design experiments. Current FHR conceptual designs pose unique challenges to existing tools. To address these challenges, one of the primary objectives of this project is to verify and validate (V&V) neutronics and thermal hydraulics tools, codes and methodologies for core and system design to support licensing of FHRs. It should be noted that FHRs vary greatly in reactor design. As a result, the ultimate goal of the studies and results presented in this chapter is to contribute to Verification and Validation (V&V) of neutronics codes and methodologies needed to support design and licensing of FHRs.

9.1. Gaps in codes/methodologies needed to support licensing

To identify the gaps in existing neutronic codes/methodologies,

9.1.1. Overview of existing codes

This section contains a high-level overview of many codes, as well as information about their past and possible applicability to FHRs.

9.1.1.1. SCALE

The SCALE Code System is a production level suite of tools that has been continuously deployed, enhanced, and supported since 1980 under sponsorship from the U.S. Nuclear Regulatory Commission and the U.S. Department of Energy. SCALE includes a number of computational modules integrated into sequences that address a wide variety of applications, including reactor physics, criticality safety, spent fuel characterization, source term analysis, radiation shielding, and sensitivity/uncertainty quantification. SCALE also includes continuous energy (CE) and multi-group (MG) cross section libraries in several group structures; best available nuclear data for depletion, decay and activation analysis; as well as the best available covariance libraries describing nuclear data uncertainties and correlations.

SCALE 6.2, the latest release, brings improved accuracy and significant reductions in both run-time and memory requirements for many sequences, as well as improved efficiency for parallel Monte Carlo computations. A new unified graphic user interface called Fulcrum is

available for simplified and consistent user input to essentially all sequences. Fulcrum also coordinates user input with rendering of Monte Carlo models and plots output results and nuclear data.

Most sequences in SCALE 6.2 can be applied directly to FHR simulations, though enhancements and extensions may be necessary in some cases. Although CE data are applicable to all system types, MG nuclear data libraries tailored to FHR spectra and physics also should be processed. SCALE 6.2 provides many capabilities that will facilitate the analysis of FHRs.

1. SCALE 6.1 and earlier versions provide MG self-shielding of doubly-heterogeneous tristructural-isotropic (TRISO) fuel that are improved and extended in SCALE 6.2 to include plate fuel geometry in FHRs, in addition to spherical, cylindrical geometry for regular, asymmetric, and annular fuel elements.
2. SCALE 6.2 introduces problem-dependent Doppler broadening in CE Monte Carlo calculations for resolved and unresolved resonances as well as thermal scattering data to address spatial variations of temperature in FHR fuel as well as parallel calculation capabilities in KENO.
3. SCALE 6.2 provides MG and CE shielding analysis with hybrid deterministic-Monte Carlo calculations, which can reduce the Monte Carlo execution time by orders of magnitude.
4. The characterization of tritium production from lithium based salts has been substantially improved in SCALE 6.2 and compared with the limited validation data available from the Molten Salt Reactor Experiment.
5. SCALE 6.2 introduces sensitivity/uncertainty analysis with the new Sampler tool as well as CE Monte Carlo analysis of eigenvalues as well as reaction rates with TSUNAMI-3D. SCALE's library of nuclear data uncertainties have also been significantly updated to include the latest data available from ENDF/B-VII.1. These tools can be applied to quantify uncertainties in FHR calculations as well as identify applicable neutronics benchmarks for validation.
6. Processing of MG and CE data for SCALE are performed with the AMPX code system, which is now distributed with SCALE 6.2. AMPX can be used to easily generate specialized libraries for FHR analysis, which will be important for determining optimized group structures.

9.1.1.2. MCNP

The Monte Carlo N-Particle (MCNP) transport code is developed and provided by the Radiation Safety Information Computation Center (RSICC). MCNP uses continuous energy cross-sections and because of its generalized geometry capability can model multitude of complicated core and reactor geometries. MCNP is a stochastic neutron, photon, and electron transport code that can perform both fixed sources and criticality (eigenvalue) calculations. As a result, the code has many applications in areas such as radiation protection and dosimetry, radiation shielding, reactor physics, and medical physics (MCNP, 2013). In particular, MCNP also has the capability to model the physics performance of instrumentation and sensors for reactors including FHRs.

MCNP limitations for FHR modeling and simulation are mainly two-fold: (1) fission source convergence in eigenvalue problems, and (2) computational efficiency, particularly when detailed (local) solutions (tally) is required, as is the case in realistic reactor analysis. A common problem with all codes is the lack of cross section data for certain materials used in FHR designs (e.g., scattering kernel for graphite and FLiBe).

9.1.1.3. NEAMS Toolkit

The mission of the US Department of Energy's Nuclear Energy Advanced Modeling and Simulation (NEAMS) Program is to develop, apply, deploy, and support state-of-the-art predictive modeling and simulation tools for the design and analysis of current and future nuclear energy systems using computing architectures from laptops to leadership-class facilities. The tools in the NEAMS ToolKit will enable transformative scientific discovery and insights otherwise not attainable or affordable and will accelerate the solutions to existing problems as well as the deployment of new designs for current and advanced reactors. These tools will be applied to solve problems identified as significant by industry and consequently will expand validation, application, and long-term utility of these advanced tools.

The NEAMS program is organized along three product lines: the Fuels Product Line (FPL), the Reactors Product Line (RPL) and the Integration Product Line (IPL). The NEAMS FPL provides advanced tools for the analysis of current and future fuel types with the BISON and MARMOT tools based on the Multiphysics Object-Oriented Simulation Environment (MOOSE) from Idaho National Laboratory (INL). These tools have been validated for light water reactor fuels and demonstrated for the analysis of TRISO fuels. The NEAMS RPL includes the PROTEUS neutronics system (including neutron transport code, multi-group cross section generation codes, and spatial mesh generation tools), the SAM system analysis code, and the NEK5000 computational fluid dynamics code from SHARP tools from Argonne National Laboratory. The SHARP tools were initially developed for sodium-cooled fast reactor (SFR) technologies but could be applied for applications to advanced reactors such as FHRs. The NEAMS IPL, led at ORNL, is responding to the needs of design and analysis communities by integrating the advance NEAMS multiphysics capabilities and current production tools in an easy-to-use common analysis environment that enables end users to apply high-fidelity simulations to inform lower-order models for the design, analysis, and licensing of advanced nuclear systems, especially through the NEAMS Workbench. Ongoing development of the Warthog multiphysics tool will provide the ability to use the PROTEUS neutron transport solver through a MOOSE application and include cross sections generated with SCALE for double-heterogeneity fuel, described in another section of this report, along with BISON fuel performance calculations.

The NEAMS ToolKit integrates various codes for advanced reactor analysis including the ability to prepare multi-group cross sectional data, perform neutronics calculations, generate depletion/source terms, run thermal hydraulics systems, analyze fuel performance, perform structural analysis, and calculate uncertainty quantities. Current challenges with the NEAMS toolset, particularly in neutronics, are as follows: (1) Modeling

complicated geometries with multiple heterogeneities typical to the two FHR designs considered in this whitepaper. This issue may present itself in multi-group cross section generation (using MC^2-3, the cross section API, or Monte Carlo codes) and a potential need for homogenization due to excessive spatial meshing required to model the heterogeneities, (2) Computational efficiency associated with deterministic transport methods in modeling large reactor systems/cores, (3) Accessibility of the tools in the community and limited but growing user base.

9.1.1.4. ARGONNE REACTOR CODES

The Argonne Reactor Codes (ARC) system comprises a consistent compilation of MC^2-3, DIF3D, REBUS-3, VARI3D, PERSENT, and associated utilities. MC^2-3 is the multi-group cross section generation tool for DIF3D as well as PROTEUS. DIF3D is the diffusion and transport theory solver for neutrons and gammas. REBUS-3 is a generic fuel cycle analysis code built around DIF3D. PERSENT and VARI3D are perturbation and sensitivity analysis tools built around DIF3D. Based on homogeneous assemblies, the ARC system has been well verified and validated for fast reactor design and analysis and in addition were updated for prismatic-type Very High Temperature Reactor (VHTR) analysis.

With additional updates, the ARC system could be applied to analyzing prismatic-type FHRs, but spatial homogenization and multi-group cross sections would be challenging issues in accurately modeling FHRs. The Workbench may allow users to easily access and combine useful features and capabilities from external tools such as SCALE.

9.1.1.5. COMET

COMET is an advanced continuous energy hybrid stochastic deterministic transport code with stochastic method fidelity such as that of MCNP but with computational speeds several orders of magnitude faster. COMET works by decomposing a large, heterogeneous system into a set of smaller fixed source local problems. For each unique local problem (e.g., fuel assembly types) that exists, a solution called the response function is obtained. These response functions are pre-computed as a library for future use by resolving the set of smaller fixed source problems. The overall solution to the global problem is then obtained by repeatedly generating local solutions via a linear superposition of responses for the unique local problems.

COMET's computational efficiency and ability to model complex geometries make it an ideal candidate for neutronics modeling of AHTR or other reactor core design with high heterogeneity. COMET has been shown to be highly accurate for current Light and Heavy Water Reactors (LWR and CANDU), the Very High Temperature Reactor (VHTR), the Hight Temperature Test Reactor (HTTR), and the Advanced Burner Test Reactor (ABTR) at steady state.

Two new modules/codes have been developed to advance the COMET framework – the Stochastic Particle Response Calculator (SPaRC) and the Application Programming Interface for Depletion Analysis (APIDA). These modules will extend COMET for lattice and core depletion calculations. Recently, further efficiency improvements have been made through adaptive flux expansion and parallel computing in COMET. The observed speedup

on 40 processors for the parallel version is about 25 (depending on the reactor configuration) with an additional speedup factor of 2-4 times when the adaptive method/option is used.

9.1.1.6. SERPENT

SERPENT is a three-dimensional continuous-energy Monte Carlo particle transport code. Its advantages and limitations are similar to MCNP. However, it is computationally more efficient because of the use of unionized energy grid and it is geared more for reactor physics calculation including depletion. Because SERPENT is a recently developed computational tool, the validation base for SERPENT is limited but growing worldwide. SERPENT was originally developed for cross section generation and conducting depletion calculations, but has continued to mature to include multi-physics capabilities, higher-energy capabilities for fusion applications, and dose rates for medical physics. For any Monte Carlo code being applied specifically toward this project though, the most important question comes down to the ease of accurately treating the TRISO fuel particles. From a coding implementation standpoint, SERPENT can relatively easily model randomly dispersed TRISO particles. SERPENT has a separate command line routine which creates a separate random particle location geometry file, which is then read when executing a transport simulation.

However, like most other Monte Carlo codes, modeling the double heterogeneity of the TRISO fuel still presents computational challenges for SERPENT. In order to accurately capture the effect of having randomly dispersed particles, fuel kernel locations need to be explicitly declared through the input geometry. This can require a moderately higher amount of computational overhead depending on the model complexity and also increases the execution time versus a lattice calculation.

9.1.2. Neutronics and Multiphysics PIRTs

To determine the phenomena that potentially need to be addressed in support of licensing of the FHR M&S tools, this project convened Phenomena Identification and Ranking Table (PIRT) panels of both internal and external experts. The results of the PIRT panel meetings for neutronics and multiphysics are provided in PIRT reports. The PIRT phenomena relevant to neutronics modeling and simulation are summarized below.

9.1.2.1. PIRT – Neutronics

The PIRTs related to neutronics were broken into four categories: fundamental cross section data, material composition, computational modeling, and spectral history effects. Of these, issues relating to both fundamental cross section data and material composition are universal to all codes. Computational methodology and general depletion issues can vary from code set to code set. (Rahnema, Edgar, Zhang, & Petrovic, 2016)

9.1.2.1.1. Fundamental Cross Section Data

There are five phenomena related to fundamental cross section data:

- Moderation in FLiBe
- Thermalization in FLiBe
- Absorption in FLiBe
- Thermalization in carbon
- Absorption in carbon

The PIRT report describes the specific pathway for each of these phenomena, but the net result associated with addressing these phenomena is a cross section library containing improvements in areas of specific interest to FHRs. As mentioned above, these five issues are universal to all code sets, as they all are inherently limited by the quality of the underlying cross section data.

9.1.2.1.2. Material Composition

The only issue identified under the category of material composition is that of the fuel particle distribution. Relevant to both the AHTR and Mk1 PB-FHR designs, the distribution of TRISO particles in real fabricated fuel is not well known. This could have implications in key reactor parameters like k_{eff} and peaking factors.

Obtaining data on this distribution is relevant to all codes, as this affects the geometry of the underlying model. However, the ability of the code to accurately and quickly model this distribution can vary, and should be considered.

9.1.2.1.3. Computational Methodology

At ten identified phenomena, computational methodology is the largest area of improvement:

- Solution convergence
- Granularity of depletion regions
- Multiple heterogeneity treatment for generating multi-group cross sections
- Selection of multi-group structure
- Boundary conditions for multi-group cross section generation
- Burnable poison cell
- Scattering kernel
- Spatial mesh
- Diffusion approximation
- Dehomogenization if relevant

These phenomena can be roughly grouped into issues of solution convergence, multi-group treatment, and solution method approximations. Addressing these phenomena would result in a base of knowledge about how to use existing codes to accurately model FHRs, or an adapted version of an existing code that is optimized for FHRs.

9.1.2.1.4. General Depletion

The only identified issue related to general depletion is that of spectral history effects. While well understood in LWRs, these methods have yet to be adapted to FHRs. Sensitivity analyses relating to the effect of the spectral history of the reactor must be performed, and these methods must be adapted to FHR modeling codes.

9.1.2.2. PIRT – Multiphysics

A PIRT panel was established for this project to examine the challenge of modeling coupled multiple simultaneous physical phenomena in FHRs. This area, called "multiphysics modeling", is desirable because it has the potential to significantly improve model fidelity and more accurately predict responses during reactor transients. The PIRT panel focused on three main operation scenarios: Normal Operation, Station Blackout, and Simultaneous Withdrawal of All Control Rods, as well as another category for phenomena that didn't fit one of these categories. Phenomena were defined as either requiring "Tight" or "Loose" coupling. Tight coupling is defined as requiring detailed iterative feedback between two codes/models. Loose coupling is defined as requiring the sharing of precalculated information between two codes. Phenomena identified as requiring "tight" coupling are examined below.

9.1.2.2.1. Normal Operation

For the normal operation scenario, there were five phenomena identified as requiring "tight" coupling to accurately model:

- Energy generation rate in fuel kernel
- Assembly (graphite) reactivity feedback
- Coolant reactivity feedback
- Upper plenum mixing
- Heat transfer to fusible links

These five phenomena involve "tight" coupling between neutronics and thermal-hydraulics codes. The relative value of the accuracy gained from this "tight" coupling needs to be investigated.

9.1.2.2.2. Station Blackout

All phenomena identified in the station blackout scenario only require "loose" coupling. As such, they are not listed here.

9.1.2.2.3. Simultaneous Withdrawal of All Control Rods

Within the simultaneous withdrawal of all control rods scenario, five phenomena were identified as requiring "tight" coupling:

- Energy generation rate in kernel
- Fuel Temperature reactivity coefficient
- Assembly (graphite) reactivity coefficient
- Upper plenum mixing
- Heat transfer to fusible links

Much like the phenomena identified in the normal operation scenario, these phenomena require "tight" coupling of neutronics and thermal-hydraulics codes.

9.1.2.2.4. Other

Six "other" phenomena were identified as requiring "tight" coupling:

- Tube rupture in P-IHX
- Overcooling due to inadvertent DRACS operation or restart/shut down of primary pumps
- Secondary shut down system/kinetics and fluid mixing and dissolution in lower plenum
- Salt deposition on control rod drive mechanism
- Grid disconnection event
- Partial flow blockage accident

9.2. Identification and Evaluation of Experimental Data for Benchmark Problem Development

In support of the qualification of codes for licensing applications, high quality benchmark problems must be developed for the purpose of code validation. A difficulty in this for FHR applications is that there is little experimental data surrounding the use of these materials and technologies in a reactor environment, and thus little data to work with in developing a benchmark problem. Consequently, it is important to make the most of all data that is available.

As a result, the physics experiments done on the MSRE were selected for examination. Specifically, the zero-power critical experiments were identified for initial evaluation, both with U-235 and U-233 fuel salts. Although the MSRE uses liquid fuel (as opposed to TRISO fuel particles) and is only "singly" heterogeneous, it is relevant for examination due to its combination of FLiBe salt and graphite in a reactor environment. Additionally, the fuel salt had been stagnant in the reactor for 90 minutes prior to the experiment, so the reactivity effect of salt motion does not apply.

During the life cycle of this project, a separate NEUP project was funded at the University of California, Berkeley to examine the U-235 set of experiments. As a result, this project pivoted to focusing on the U-233 experiment. Work on the model is ongoing, and it is

expected that a description of the experiment will be submitted to the IRPhEP committee by the end of the year.

9.2.1. Background Information

9.2.1.1. MSRE Core Description

The MSRE, seen in *Figure 9-1*, was an experimental, graphite-moderated, molten salt reactor operated at Oak Ridge National Laboratory from 1965 to 1969 (ORNL-TM-0728). During operation, a primary salt loop circulated fuel-containing FLiBe salt through a graphite core. Structural components of the MSRE were made of Hastelloy N.

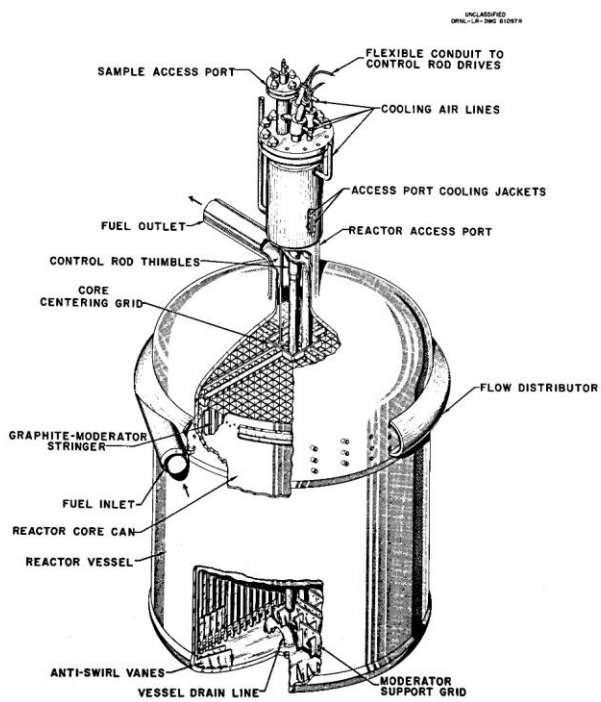

Figure 9-1. MSRE Core Cutaway (ORNL-TM-0728)

Fuel salt flows into the core via the inlet pipe to a half-toroidal flow distributor. The salt then flows downward via a fuel annulus to the lower head. The salt then flows upward via 1140 fuel channels in a bank of graphite moderating stringers to the upper head and then out the outlet pipe. At the center of the core, there are thimbles for three flexible control rods, as well as a sample basket into which samples of graphite and Hastelloy N were placed for examination.

9.2.1.2. Experiment Description

After successful completion of the phase of MSRE operation with U-235 fuel, the fuel salt was drained, cleaned, and charged with U-233 feed material (ORNL-4396). On October 2, 1968, the zero-power critical experiment was performed for the U-233 fuel salt (ORNL-TM-3963). The reactor was brought to critical via additions of U-233 feed material via the pump bowl (ORNL-TM-2304). The salt was stationary for 90 minutes prior to the experiment.

9.2.2. Model Overview

This model of the MSRE is built in MCNP 6.1. The geometric information for the core is pulled from ORNL documentation, largely ORNL-TM-0728, ORNL-TM-0730, and other related documentation.

9.2.2.1. Model Features

The model, shown in *Figure 9-2*, features the MSRE core and a section of outlet pipe suspended in cans of thermal shield and insulator.

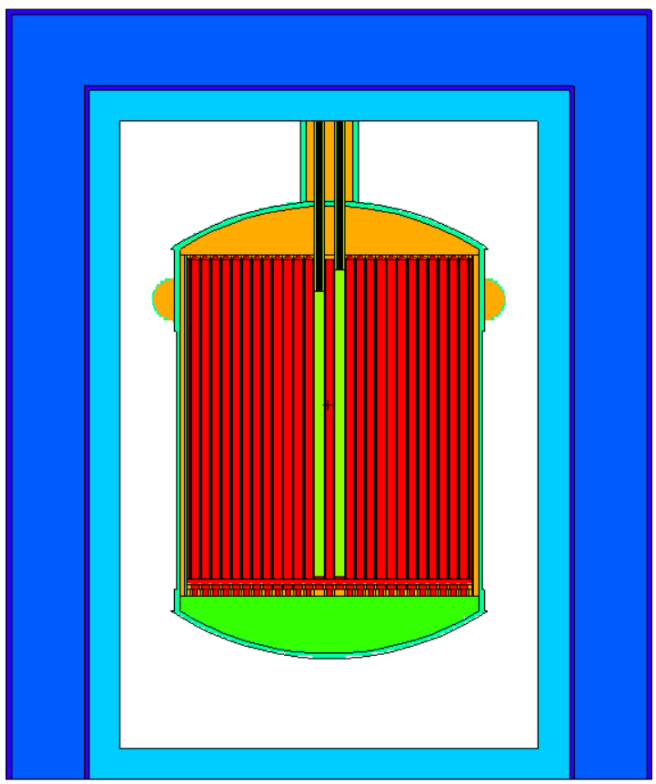

Figure 9-2. MCNP Model XZ Cross Section (y = 2 in.)

Key features of the model include:

- Vertical graphite stringers in main core, including some fractional bars at periphery (*Figure 9-3*)
- Two layers of horizontal graphite upon which the vertical stringers rest when not immersed in salt (*Figure 9-4*)

- Control rods consisting of control element "beads" threaded on steel cable (*Figure 9-5*)
- Sample basket containing bars of graphite and samples of structural material (*Figure 9-5*)
- Part-spherical upper and lower heads (*Figure 9-2*)
- Half-toroidal inlet flow distributor around top of reactor vessel (*Figure 9-2*)

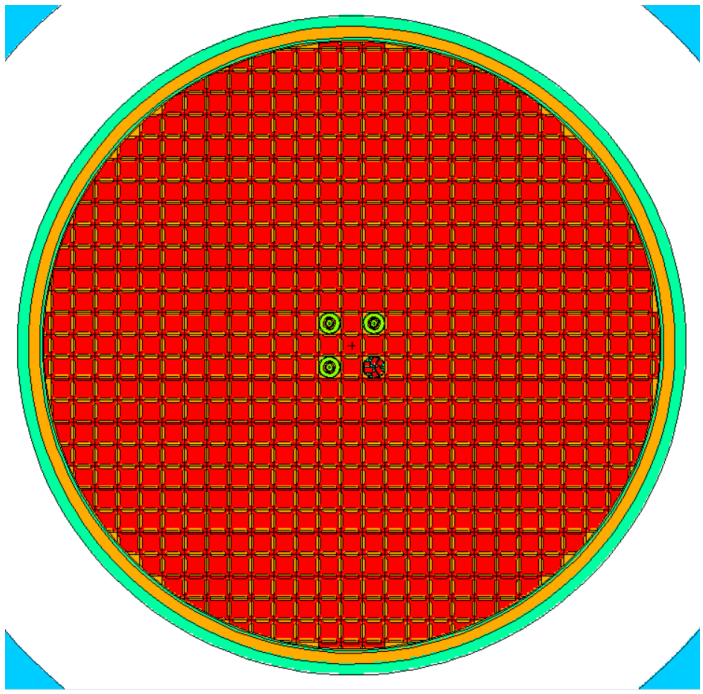

Figure 9-3. XY Cross Section in Graphite Stringer Section

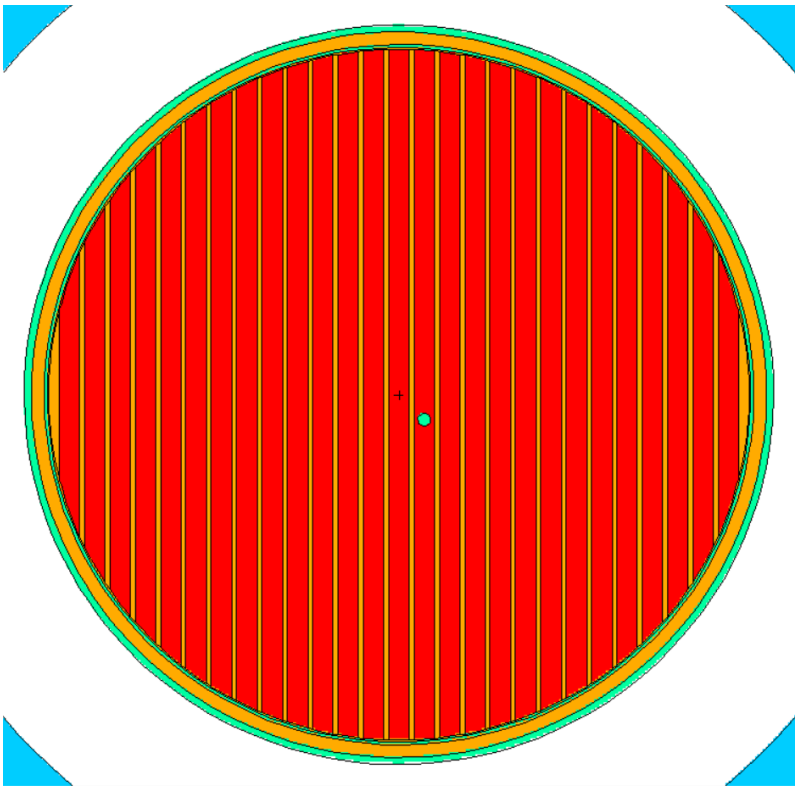

Figure 9-4. XY Cross Section in Horizontal Graphite Section

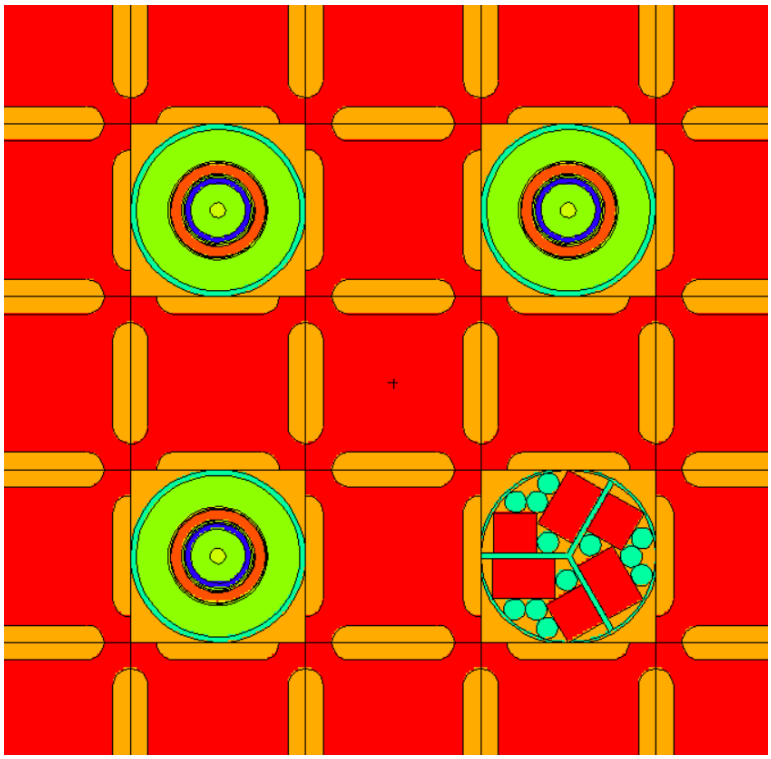

Figure 9-5. XY Cross Section, Control Rods Detail

9.2.2.2. Model Gaps/Simplifications

The ORNL documentation available is missing some geometry information that prevents the model from capturing the entire reactor construction exactly. Noticeable gaps include:

- Information about the anti-swirl vanes in the lower head
- Information about the core centering grid (shown in *Figure 9-1*)
- Locations for the holes in the reactor vessel inside the half-toroidal inlet flow distributor
- Inconsistency in the information about the sample basket and its contents
- Information about the grid support plates in the lower head, above the anti-swirl vanes
- Information about the centering fins within the control rod thimbles

9.2.3. Preliminary Results

Model testing is still ongoing. A major setback is the lack of a clear description of the salt isotopic composition at the time of experiment. There are various reported isotopic values at times surrounding the experiment, and it is possible to come up with a few different defensible compositions based on literature, resulting in a difference of up to 1000 pcm. Moreover, best estimates put the model with a k-effective of about 2500 pcm, with an uncertainty of ~500 pcm. Work is being done to review the literature more finely and come up with a more accurate salt description and narrow down the uncertainty. However, it is projected that this salt isotopic composition will remain the sticking point in the benchmark problem endeavor.

References

ORNL-TM-0728: "MSRE Design and Operations Report Part I: Description of Reactor Design"

ORNL-TM-0730: "MSRE Design and Operations Report Part III: Nuclear Analysis"

ORNL-TM-3963: "Zero-Power Experiments with ^{233}U in the MSRE"

ORNL-TM-2304: "MSRE Design and Operations Report Part XI-A: Test Program for U-233 Operation

ORNL-4396: "Molten-Salt Reactor Program Semiannual Progress Report for Period Ending Feb. 28, 1969"

9.3. Benchmark Problem Development

To verify neutronics tools, it is necessary to create new heterogeneous benchmark problems that retain the important neutronic characteristics of the AHTR such as the detailed geometric and material configurations of the Tristructural-Isotropic (TRISO) fuel and burnable poison particles, fluoride salt coolant, graphite moderator, and reflectors. However, the structural details and the randomness of the fuel particles distribution are simplified for ease of modeling and the lack of the capability of existing codes (including stochastic transport) to model random particle distributions in large systems (e.g., AHTR). These simplifications have relatively small neutronic effects as compared to that of the multiple heterogeneity. This stylized benchmark problem set facilitates numerical verification of deterministic transport and diffusion methods in which the multigroup approximation is a common practice, cross section sensitivity analysis, and evaluation of various approximations used in neutronic modeling at both lattice (fuel assembly) and core levels.

9.3.1. Core specification

The AHTR concept was designed to have a thermal power of 3,400 MW with the overall thermal efficiency of 45%. The core parameters are shown in *Table 9-1*. The primary coolant used in the core is FLiBe ($2LiF\text{-}BeF_2$). The TRISO particles with an enrichment of 9 wt% were used for the most recent AHTR design (Varma, et al., 2012).

Table 9-1. AHTR core parameters

Parameter	Value
Core Thermal Power	3,400 MW
Overall Thermal Efficiency	45%
Heavy Metal (HM) mass in the core	17.48 Mt
Fuel Type	Tristructural-Isotropic (TRISO)
Enrichment	9 wt%
Moderator/ Reflector Material	Graphite
Core Height	6.0 m

Primary Coolant	FLiBe ($2LiF-BeF_2$)

9.3.2. Radial and axial layout

The radial and axial configurations of the stylized AHTR benchmark problem are shown in *Figure 9-6* and *Figure 9-7*, respectively. The AHTR core, from the center outwards, consists of a center replaceable reflector, eight rings of fuel assemblies, one ring of replaceable reflectors, and one ring of permanent reflectors. The total number and dimension of fuel assemblies and replaceable and permanent reflectors are summarized in *Table 9-2*.

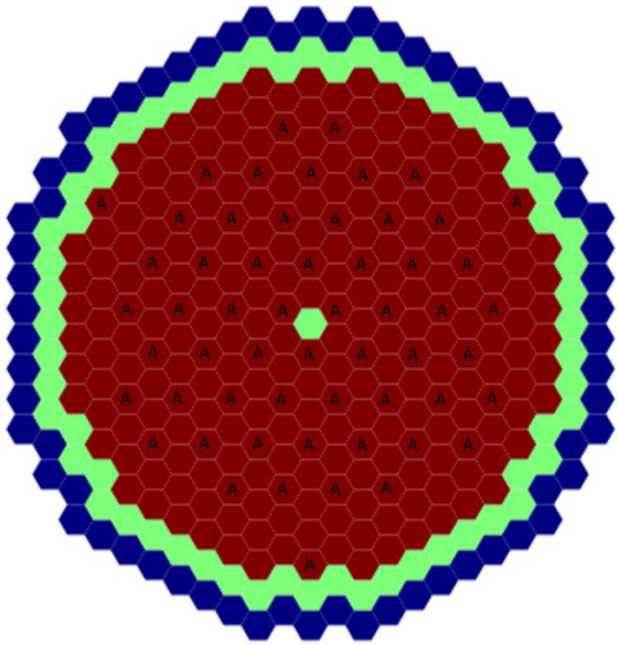

Figure 9-6. The radial configuration of the stylized FHR benchmark problem (Red: Fuel Assembly; Green: Replaceable Reflector; Blue: Permanent Reflector)

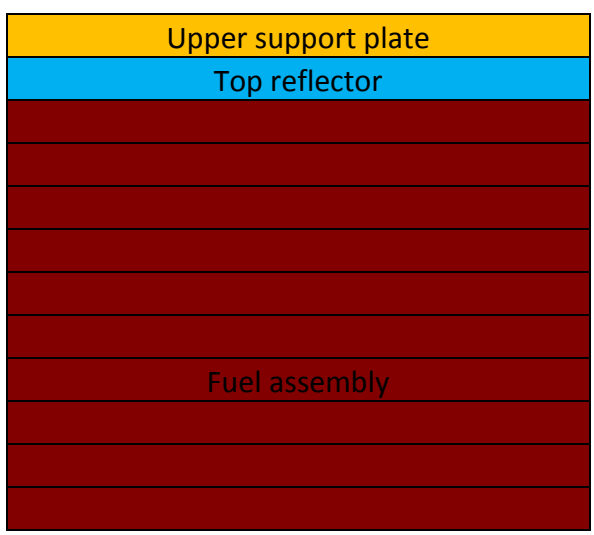

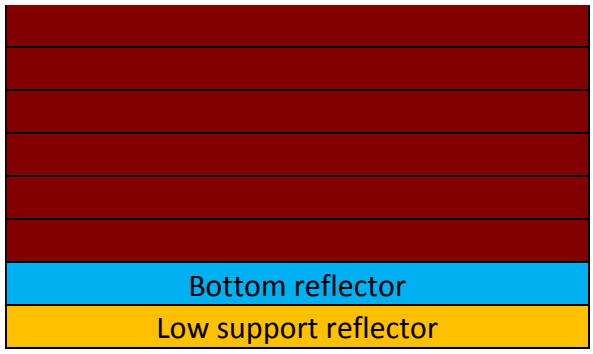

Figure 9-7. The axial configuration of the stylized FHR benchmark problem

Table 9-2. Total number and dimension of fuel assemblies and replaceable and permanent reflectors

Block	Shape	Apothem	Total Number
Fuel Assembly	Hexagon	23.4 cm*	252
Replaceable Reflector	Hexagon	23.4 cm*	49
Permanent Reflector	Hexagon	23.4 cm	54

*The apothem of fuel assemblies and replaceable reflector includes 0.9 cm FLiBe in the gap between fuel assemblies or Replaceable Reflectors

The AHTR axial core configuration, from the bottom to the top, consists of 5 axial zones: a lower support plate, a bottom reflector, a fuel zone, a top reflector, and an upper support plate. The fuel zone is further subdivided into 16 axial segments. The height for each axial segment is listed in *Table 9-3*. The symbol "A" in Figure 2 indicates that the control blade is fully inserted from the upper support plate down through the bottom reflector.

Table 9-3. Height of each axial segment

Axial Segment	Height (cm)
Low support plate	35
Bottom reflector	25
Each Fuel region	34.37686*
Top reflector	24.97024*
Top support plate	35

*Avoiding partial particles at the fuel/reflector interface leads to these dimensions rather than the specified values of 34.375 cm and 25 cm for the fuel and top reflector height, respectively.

9.3.3. Core configuration

The control blade pattern in the core was not specified in Varma, et al. (2012) or Holcomb, et al. (2011). In this paper, two single assembly and three full core configurations are defined as follows.

- Uncontrolled single assembly benchmark problem: This is a full-length single assembly including the top and bottom reflectors and lower and upper support plates. Vacuum boundary condition is used at the top and bottom external surfaces. The boundary condition at the outermost radial surface (the half-gap coolant as shown in *Figure 9-8*) is 120° periodic. This boundary condition preserves the correct fuel plate orientation in the core. However, the specular reflective boundary condition which is more commonly found in most codes is used to provide a reference solution using the MCNP code (X-5 Monte Carlo Team, 2005). The effect of the change in the boundary condition on the solution is found to be small but negligible.
- Controlled single assembly benchmark problem: In this problem, the control blade is fully inserted.
- Full core critical benchmark problem: This is a full core critical benchmark problem in which control blades at locations labelled with "A" in *Figure 9-6* are fully inserted. This configuration was developed (Rahnema and Zhang, 2018a) by a binary search using the hybrid continuous-energy stochastic deterministic transport code COMET (Rahnema and Zhang, 2018b).
- Controlled full core benchmark problem: All control blades are fully inserted.
- Uncontrolled full core benchmark problem: All control blades are fully withdrawn.

9.3.4. AHTR fuel assembly specification

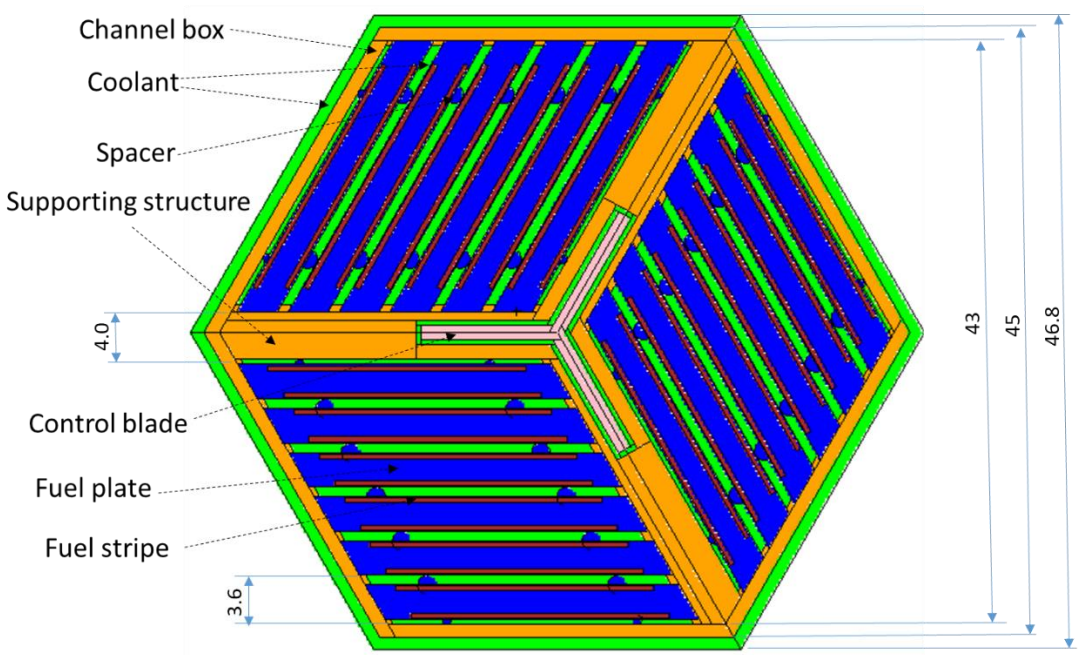

Figure 9-8. Geometrical configuration of AHTR fuel assembly

As shown in *Figure 9-8*, the AHTR fuel assembly has 120º rotation symmetry and is separated into three identical sectors by the 4 cm thick Y-shaped supporting structure

which is made of C-C composite with a density of 1.95 g/cm^3. Each sector consists of six fuel plates. The gap between two fuel plates is 0.7 cm while the gap between a fuel plate and the Y-shaped supporting structure is 0.35 cm. Each of those gaps, maintained by two semi-cylinder spacers, is filled with the primary coolant FLiBe. The fuel plates are enclosed in a 1 cm thick hexagonal C-C fuel channel box. The outer apothem of the box is 22.5 cm. Control blades are in the center of the fuel assembly. They have a molybdenum hafnium carbide Y-shaped structure with the wing length of 10 cm and thickness of 1 cm. The gap between adjacent assemblies is 1.8 cm. For convenience in modeling the benchmark problem, half of the gap is treated as a part of each assembly as shown in *Figure 9-8*. The outer apothem of the resulting assembly is 23.4 cm.

Each parallelepiped fuel plate contains two fuel stripes and a central carbon slab. The dimension and density of the assembly and the fuel plate are listed in *Table 9-4* and *Table 9-5*, respectively. Five burnable poison particles, each with radius of 350 micron, consisting of Eu_2O_3 powder are equally spaced at the center of the plate as shown in *Figure 9-9*. The pitch in the transverse (x) and axial (z) directions is 4 cm and 993.656 μm, respectively. The burnup poison parameters are summarized in *Table 9-6*. Each fuel stripe is filled with a rectangular lattice of TRISO fuel particles with enrichment of 9 wt%.

Table 9-4. Total number and dimension of fuel assemblies, replaceable and permanent reflectors

Components	Shape	Dimension (cm)	Number per assembly
Fuel plate	Parallelogram	Length: 23.5; Thickness: 2.55	18
Fuel stripe	Rectangle	Length: 19.00012; Thickness: 0.36512	36
Control blade hole	"Y"	Wing Length: 10.38; Thickness: 1.76	1
Control blade	"Y"	Wing Length: 10; Thickness:1	0/1
Supporting Structure	"Y"	Thickness: 4	1
C-C Box	Hexagon	Outer Apothem: 22.5; Thickness: 1	1
Large spacer	Semi cylinder	Radius: 0.7	30
Small spacer	Semi cylinder	Radius: 0.35	12
Fuel assembly with surrounding coolant	Hexagon	Outer Apothem: 23.4	---

Table 9-5. Material density for AHTR fuel assembly

Component	**Material**	**Density (g/cm^3)**
Channel Box	C-C composite	1.95
Supporting Structure	C-C composite	1.95
Spacer	Carbon matrix	1.75
Coolant	FLiBe	1.9503*
Control blade	Molybdenum hafnium carbide	10.28
Central carbon slab	Carbon matrix	1.75

*The FLiBe density is dependent on the temperature and can be calculated as ρ (g/cm^3)=2.280000-0.000488*T(C)

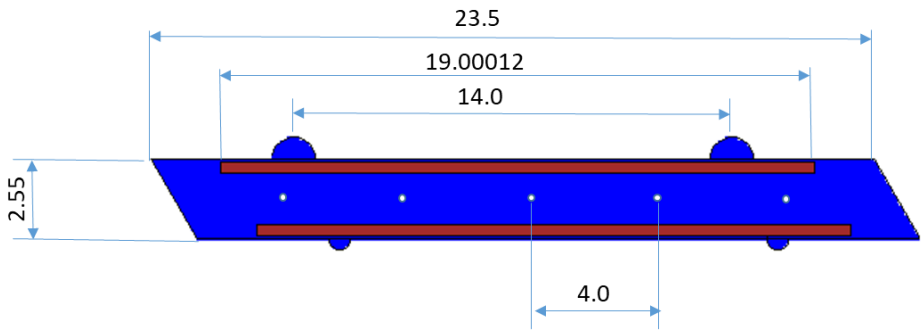

Figure 9-9. Dimension of the AHTR fuel plate

Table 9-6. Parameters for burnable poison

BP (Eu_2O_3)	Value	Unit
Density	5.0	g/cm^3
Radius	350	µm
x-pitch	4	cm
z-pitch	993.656	µm

As shown in *Figure 9-10* the TRISO fuel particle consists of a uranium oxycarbide fuel sphere (kernel) with a diameter of 427 µm and four additional spherical layers. These layers, moving outward from the kernel, are a carbon buffer, an inner pyrocarbon (IPyC), silicon carbide (SiC), and an outer pyrocarbon (OPyC). As mentioned in section 2, to maintain the packing fraction of 40%, the pitch of the TRISO fuel lattice in the x, y and z directions was chosen to be 940.5 µm, 912.8 µm and 926.6 µm, respectively. The parameters of TRISO particle lattice are summarized in *Table 9-7*.

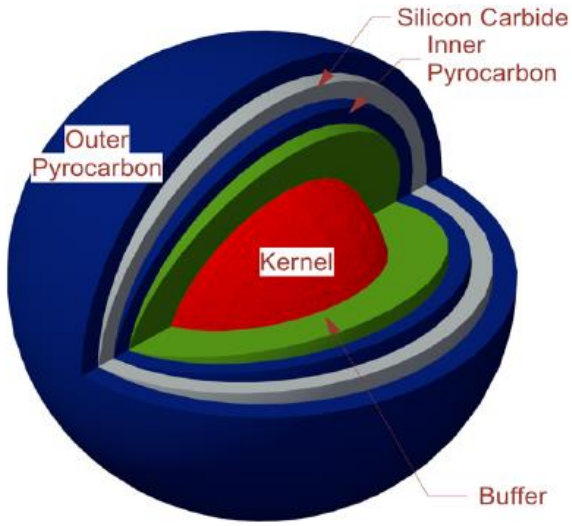

Figure 9-10. TRISO particle geometry configuration, taken from (Varma V. K., et al., 2012)

Table 9-7. Parameters of TRISO fuel lattice

Region	Dimension (μm)	Material	Density (g/cm^3)
Kernel	Diameter: 427	UCO	10.9
Buffer	Thickness: 100	Porous graphite	1
IPyC	Thickness: 35	Pyrolitic graphite	1.9
SiC	Thickness: 35	SiC	3.2
OPyC	Thickness: 40	Pyrolitic graphite	1.87
Fuel lattice	x-pitch: 940.6	--	--
	y-pitch: 912.8	--	--
	z-pitch: 926.6	--	--

9.3.5. Specification of reflectors and support plates

9.3.5.1. Reflectors

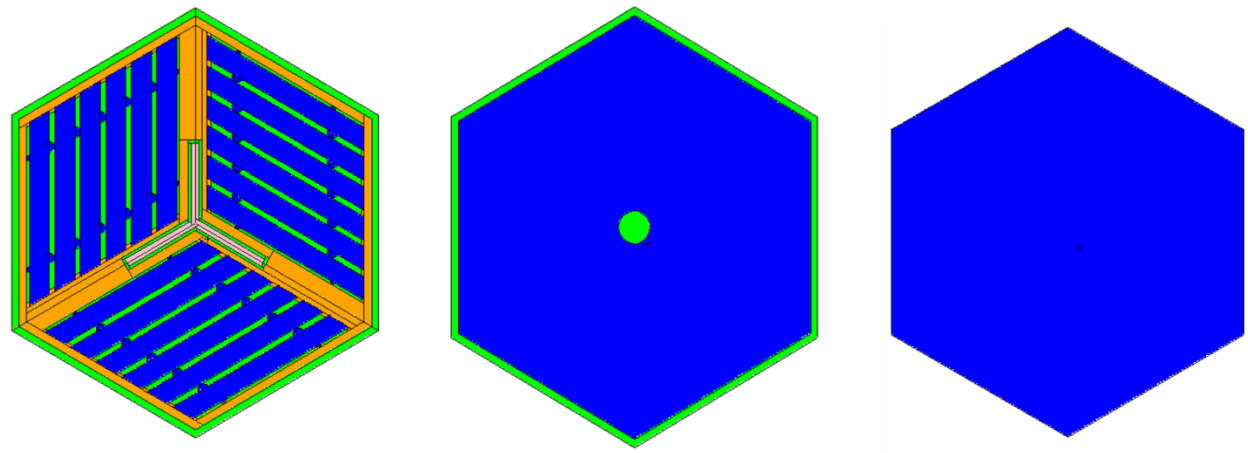

(a) Top/bottom reflector (b) Replaceable reflector (c) Permanent reflector

Figure 9-11. Geometric configuration of reflectors

Reflectors used in the AHTR conceptual design can be classified in four types based on their location and geometric configurations shown in *Figure 9-11*. The outer apothem of all reflectors is 23.4 cm.

- Top reflector: The top reflector is immediately above the fuel assemblies as shown in Figure 3. Like the fuel assembly, the top reflector consists of 18 plates, 42 spacers, a Y-shaped supporting structure, a hexagonal C-C channel box, a 0.9-cm thick surrounding FLiBe, and a Y-shaped control blade if inserted. The radial dimension of each component is the same as that of the fuel assembly while its height is 25 cm. The plate is made of carbon matrix. The densities of materials are the same as those listed in *Table 9-5*.
- Bottom reflector: The bottom reflect is immediately below the fuel assemblies. Its geometric configuration and material composition are the same as those of the top reflector except that the density of FLiBe is 1.9625 since its temperature is 650 °C.
- Replaceable reflector: As shown in *Figure 9-6*, the replaceable reflectors are located at the center of the core or immediately surrounding the fuel assemblies. The replaceable reflector consists of a center cooling channel filled with FLiBe, a graphite hexagonal prism and the surrounding FLiBe (half of the gap between replaceable reflectors). The corresponding dimension and material are listed in *Table 9-8*.

Table 9-8. Dimension of replaceable reflector

Components	Cooling channel	Graphite	Surrounding coolant
Shape	Cylinder	Hexagonal prism	Hexagonal prism
Dimension (cm)	Radius: 2 Height: 670	Outer Apothem: 22.5 Height: 670	Outer Apothem: 23.4 Height: 670
Material	FLiBe	Graphite	FLiBe

Density (g/cm^3)	1.9625	1.75	1.9625

- Permanent reflector: The permanent reflector is constituted by hexagonal blocks of graphite with the density of 1.75 g/cm^3 surrounding the replaceable reflector ring. The apothem and height of each block are 23.4 cm and 670 cm, respectively.

9.3.5.2. Upper/Lower Support plates

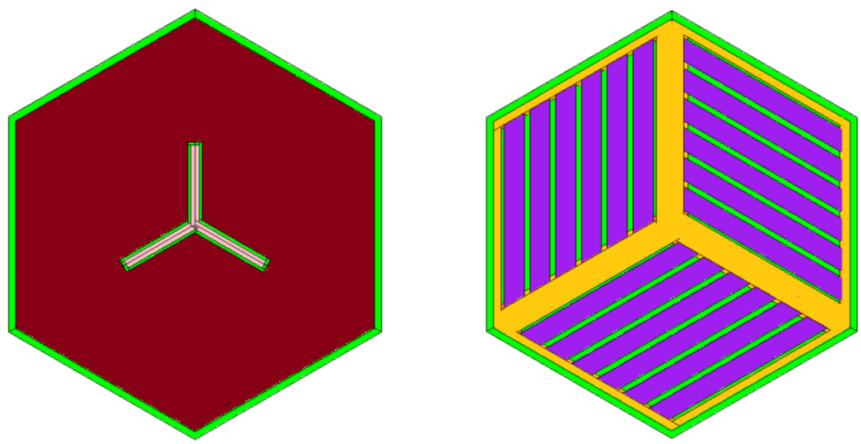

(a) Simplified upper support plate (b) Lower support plate

Figure 9-12. Geometric configuration of support plates

The geometric configurations of the upper support plate and the lower support plate are shown in *Figure 9-12*. The upper support plate is 35-cm high and located immediately above the top reflector. As mentioned above, the upper support plate is represented by a Y-shaped control blade hole, a hexagonal block of the mixture of 43% FLiBe and 57% SiC-SiC composite in volume, surrounding FLiBe, and a Y shaped control blade if inserted. The 35-cm high lower support plate provides support to the core and the reflector. It consists of 18 plates made of SiC-SiC composite, a Y-shaped C-C support structure, a hexagonal C-C channel box, and surrounding FLiBe representing half of the gap between assemblies. The radial dimension of each component is the same as that of the bottom reflector. The material property of the upper and lower support plates is listed in *Table 9-9*.

Table 9-9. Material density for support plates

Support plate	**Component**	**Material 77**	**Density (g/cm^3)**
Lower	Channel Box	C-C composite	1.95
	Support Structure	C-C composite	1.95
	Plate	SiC-SiC composite	3.1
	Coolant	FLiBe	1.9625
Upper	Mixture block	57% SiC-SiC + 43% FLiBe in volume	2.4377
	Control blade	Molybdenum hafnium carbide	10.28
	Coolant	FLiBe	1.9503

9.4. Solution to full core benchmark problems

9.4.1. COMET model

The continuous energy coarse mesh transport method COMET (Rahnema and Zhang, 2018) was used to obtain the whole-core solution to these benchmark problems with very high accuracy. COMET is a hybrid stochastic/deterministic transport method based on the incident flux response expansion theory (Mosher and Rahnema, 2006; Zhang and Rahnema, 2012) and is capable to model the material heterogeneities down to fuel and burnable poison particles without spatial homogenization or energy condensation. These features make COMET very suitable for AHTR full core calculations because of its formidable computational speed and high fidelity.

The following 15 unique coarse meshes were used to construct the stylized AHTR core configurations: two fuel assembly (controlled and uncontrolled), a lower support, two (controlled and controlled) bottom reflector, two (controlled and controlled) top reflector, two (controlled and controlled) upper support, three replaceable reflector, and three permanent reflector coarse meshes. The properties and dimensions of these coarse meshes are listed in *Table 9-10*.

Table 9-10. Properties and dimensions of unique AHTR coarse meshes.

Index	Coarse Mesh Type	Dimension: Apothem × Height (cm)
1	Uncontrolled Fuel Assembly with BP	23.4 × 34.37686
2	Controlled Fuel Assembly with BP	23.4 × 34.37686
3	Lower Support	23.4 × 35
4	Uncontrolled Bottom Reflector	23.4 × 25
5	Controlled Bottom Reflector	23.4 × 25
6	Uncontrolled Top Reflector	23.4 × 25
7	Controlled Top Reflector	23.4 × 25
8	Uncontrolled Upper Support	23.4 × 35
9	Controlled Upper Support	23.4 × 35
10	Replaceable Reflector	23.4 × 25
11	Replaceable Reflector	23.4 × 34.37686
12	Replaceable Reflector	23.4 × 35
13	Permanent Reflector	23.4 × 25
14	Permanent Reflector	23.4 × 34.37686
15	Permanent Reflector	23.4 × 35

The first step of the COMET method is to generate/pre-compute response functions for each unique coarse mesh. The energy spectrum is expanded in eight energy bins with bin boundaries: 0, 1.4572E-7, 6.2506E-7, 3.9279E-6, 1.3007E-4, 9.1188E-3, 8.2085E-1, 2.2313, and 20 MeV. The expansion order in the other phase space variables is {4,4,2,2}, representing 4th order in the two spatial (x,y) variables and 2nd order in the two angular (polar and azimuthal) variables. Ten million particle histories are modeled for each

response function calculation. The total computation time to generate all the response coefficients is about 0.5 days on a 38-CPU cluster, or equivalently about 450 hours on a single CPU. These response functions are then complied into a library.

Given the large number of assemblies or fuel stripes in the benchmark problems, the following four statistical quantities are used to summarize the difference between COMET and the Monte Carlo code MCNP (X-5 Monte Carlo team, 2005) fission density distributions (FDDs): the average (AVG), the mean relative (MRE), the root mean square (RMS), and the maximum (MAX). These quantities are also used to summarize the MCNP statistical uncertainty.

9.4.2. Solutions to the full core benchmark problems

The continuous energy COMET with the expansion order {4,4,2,2} was used to compute the eigenvalue and the assembly averaged and stripe-wise FDs for the three full core benchmark problems. As shown in this section later, significant computation resource is required for MCNP to tally the fission density in all fuel stripes for the full core problems. As a result, only assembly averaged FDs were tallied in MCNP calculations for these three benchmark problems. The MCNP reference calculations were performed with 200 million particles for the initial source convergence and 800 million neutron source particles (2,000 active and 200 skipped cycles with 400,000 particles per cycle) for active tallies. We note that the number of active histories is clearly not sufficient and that to obtain a satisfactory solution would impractically require a prohibitive computation time (see the footnote in Table 5). The comparison of the eigenvalue and computation time are presented in *Table 9-11*. It can be seen from Table 5 that the eigenvalues computed by COMET for the three full core benchmark problems are in good agreement with those computed by MCNP, with a difference of 17 – 88 pcm.

Table 9-11. Comparison of the eigenvalue and computation time for full core problems

Configuration	Method	COMET	MCNP
FC-ABO	Eigenvalue	1.06538	1.06575
	Uncertainty (pcm)	9	3
	Run Time* (hour)	4.6	40.4
FC-ABI	Eigenvalue	0.80987	0.81075
	Uncertainty (pcm)	9	3
	Run Time* (hour)	4.3	39.8
FC-CRT	Eigenvalue	1.00006	1.00023
	Uncertainty (pcm)	9	3
	Run Time* (hour)	4.5	40.2

*MCNP calculation was performed on an 84-CPU computer cluster without stripe-wise fission density tallied. Note: Even with a 44-day run time the estimated uncertain on stripe-wise FDD would range from 1% to 6%. The COMET calculations were performed on a single processor with both assembly and stripe-wise FDs computed.

The comparison of the radially-integrated axial FD distributions computed by COMET and MCNP for the three full core benchmark problems are plotted in *Figure 9-13* - *Figure 9-15*

and tabulated in the Appendix (see Tables A.1-A.3). It is found that the axial FDs computed by COMET are in excellent agreement with those computed by MCNP.

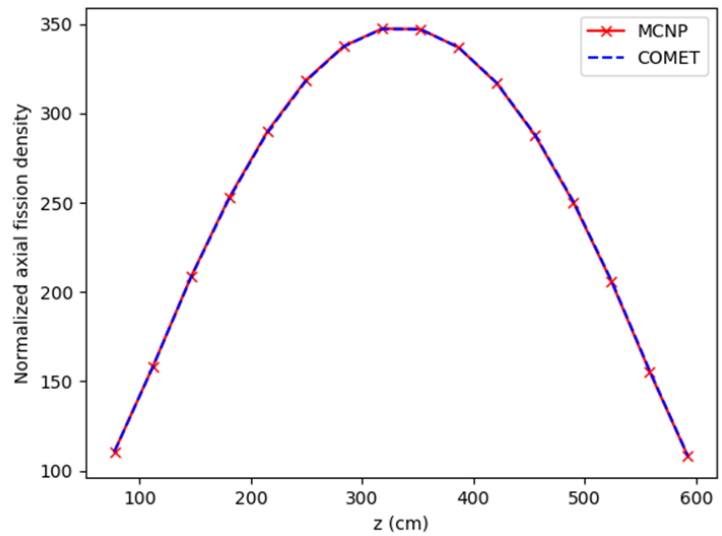

Figure 9-13. The radially-integrated fission density distributions computed by COMET and MCNP for the FC-ABO benchmark problem

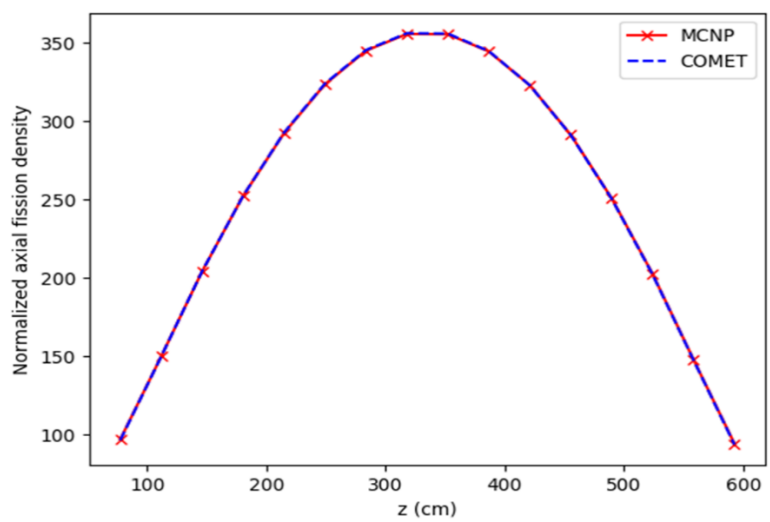

Figure 9-14. The radially-integrated fission density distributions computed by COMET and MCNP for the FC-ABI benchmark problem

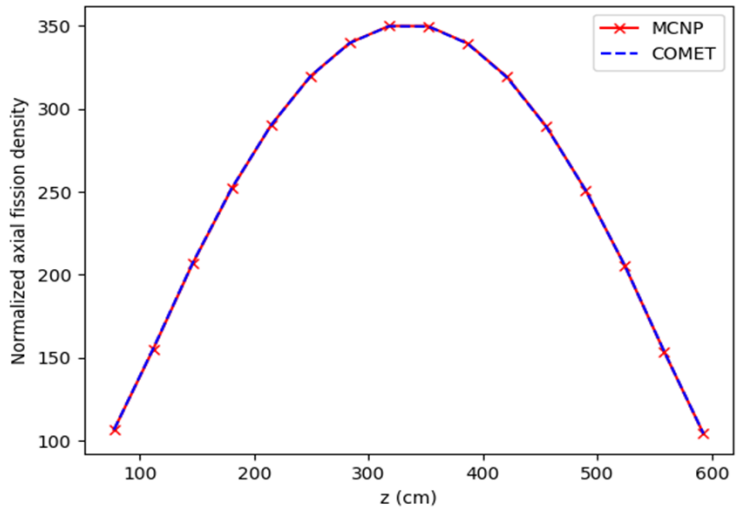

Figure 9-15. The radially-integrated fission density distributions computed by COMET and MCNP for the FC-CRT benchmark problem

Since the three full core benchmark problems have 120º rotational symmetry, the MCNP assembly FDs averaged over the three azimuthal sections were used as the reference solutions. The relative difference between the COMET and the reference assembly FDs and the deviation of the MCNP FDs from the symmetric average as well as the MCNP FD uncertainties are summarized in Table 9-12. The stripe-wise FDs computed by COMET for the three full core benchmark problems in axial slice 10 are shown in *Figure 9-16* - *Figure 9-18*. Assembly-averaged and stripe-wise FDDs is a set of selected assemblies are provided in the Appendix (see Table A.4-A7).

Table 9-12. Comparison of the assembly-averaged fission density distribution computed by *COMET and MCNP*

		MCNP FD uncertainty	Deviation of MCNP FD from the symmetry	Relative difference between COMET and reference assembly FD
FC-ABO	AVG	0.32%	0.62%	0.35%
	MRE	0.27%	0.56%	0.31%
	RMS	0.40%	0.76%	0.47%
	MAX	0.67%	2.79%	1.90%
FC-ABI	AVG	0.34%	0.52%	0.34%
	MRE	0.28%	0.47%	0.30%
	RMS	0.42%	0.67%	0.43%
	MAX	0.70%	2.95%	1.55%
FC-CRT	AVG	0.35%	0.87%	0.56%
	MRE	0.30%	0.82%	0.48%
	RMS	0.44%	0.99%	0.65%
	MAX	0.75%	3.69%	2.82%

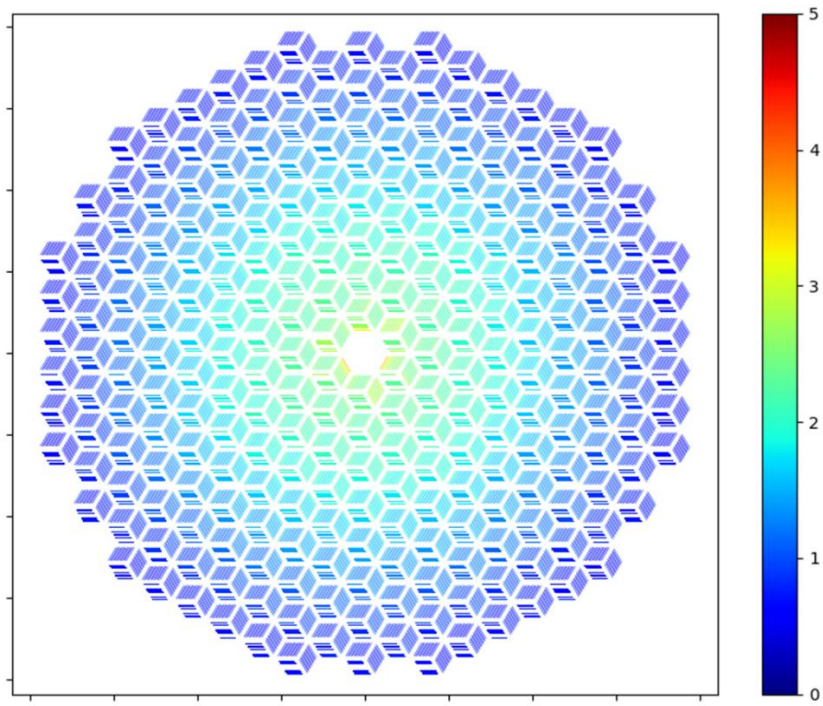

Figure 9-16. Stripe-wise fission density distributions computed by COMET for the FC-ABO benchmark problem in axial level 10

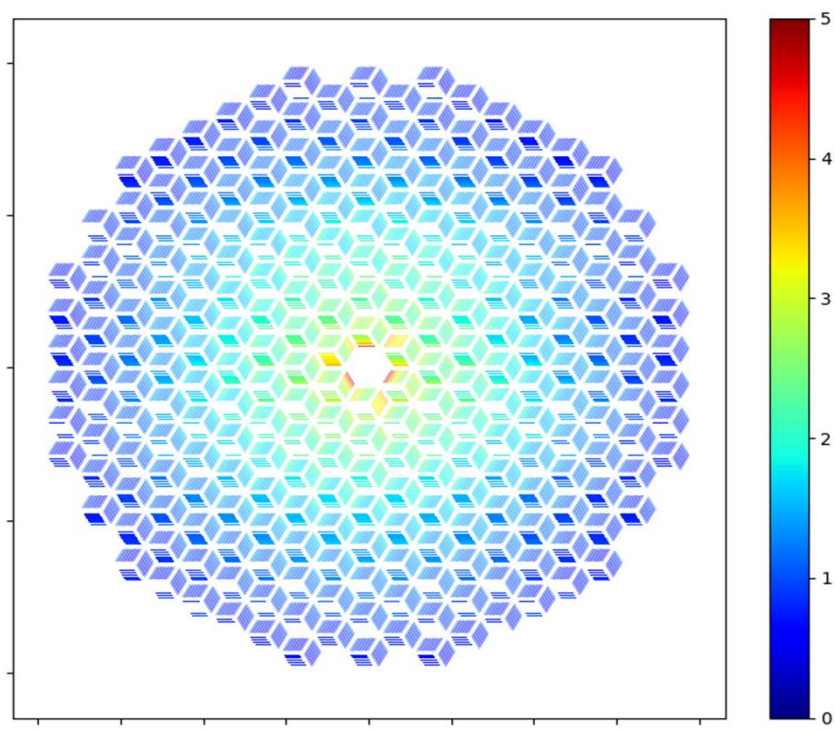

Figure 9-17. Stripe-wise FDs computed by COMET for the FC-ABI benchmark problem in axial level 10

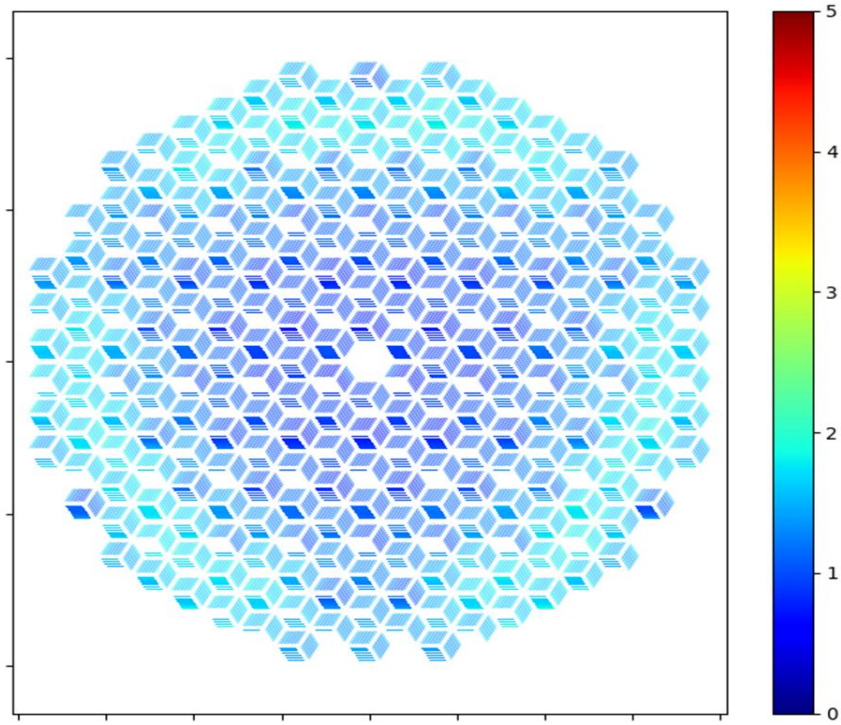

Figure 9-18. Stripe-wise fission density distributions computed by COMET for the FC-CTR benchmark problem in axial level 10

It can be seen from Table 9-12 that the assembly FDs calculated by COMET agree very well with the reference solutions for the three full core configurations. The average and mean relative differences vary from 0.32% - 0.56% and 0.30% - 0.40%, respectively, less than two standard deviations of the corresponding MCNP uncertainties. It is also found that the average, mean, and maximum deviations of the MCNP assembly FD from its corresponding symmetric average are in the range of 0.52% - 0.87%, 0.47% - 0.82%, and 2.79% - 3.69%, respectively. This indicates that the assembly FDs predicted by COMET agree better with the reference solutions than the corresponding MCNP results without using the symmetry. It should be noted that the deviation of the MCNP FDs from its corresponding symmetric average cannot be explained by the Monte Carlo uncertainties. It can be seen from *Figure 9-19* that MCNP overestimates the assembly FD in the lower-left corner. This clearly indicates that the fission source is not well converged. To resolve this issue, many (at least >50) independent MCNP runs are necessary (Zhang and Rahnema, 2017) to obtain a converged solution.

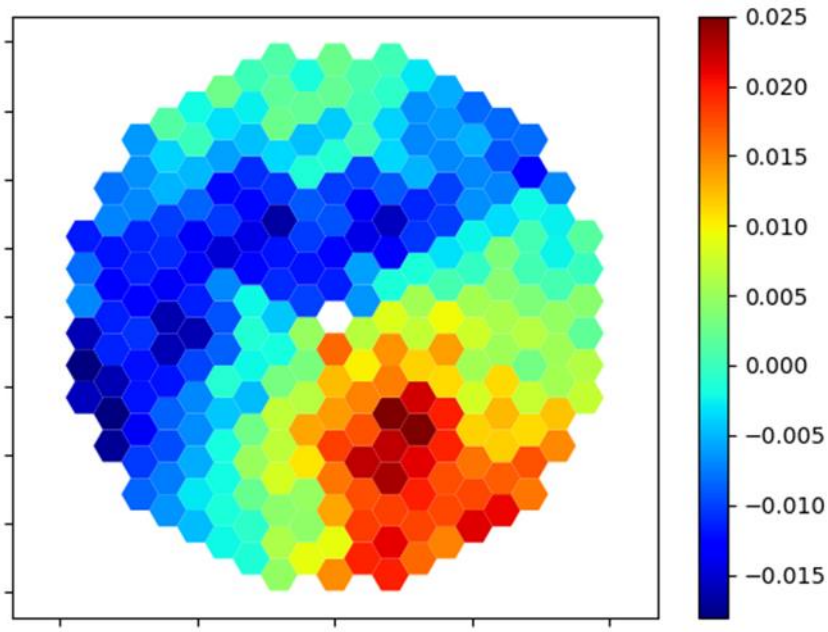

Figure 9-19. The deviation of MCNP assembly fission density distribution from the symmetry in axial level 9 (z=337.41 – 372.09 cm) in the FC-CRT benchmark problem

As seen from *Table 9-11* each COMET core calculation took 4.3 – 4.6 hours on a single CPU with the eigenvalue, assembly and stripe-wise FDs calculated, while each MCNP core calculation took about 40 hours on an 84-CPU cluster without tallying the stripe-wise FDs. It is estimated that it would take about 44 days on the same cluster for MCNP to tally the FD in all fuel stripes with an uncertainty of up to 6%. As a result, 2,200 days of computation time would be required to complete the suggested 50 independent MCNP runs to achieve a reasonably well-converged fission source.

9.4.3. Summary

A 3D full core benchmark problem typical of fluoride-salt-cooled high-temperature reactor cores in prismatic configuration has been developed. The problem was derived from the AHTR concept by simplifying the geometry and material specification of the original conceptual design while retaining the multiple heterogeneities and major physical characteristics of the core that are important from the neutronics point of view. The fuel assembly and core descriptions can be used to define benchmark problems with the desired complexity in "2D" and 3D configurations including single or multi-assembly to whole core problems. These problems with benchmark solutions such as that obtained via continuous energy stochastic transport methods can be used for various applications such as evaluating the performance of deterministic transport lattice and core analysis methods as well as diffusion methods for core analysis, performing cross section sensitivity analysis, and testing various methods approximations (e.g., multigroup, low order transport, etc.).

The continuous energy COMET method/code was used to solve two single-assembly and three AHTR full core configurations. In the single assembly benchmark problems, it was found that

COMET with the expansion order {2,2,2,2} is sufficient for the eigenvalue and assembly FD calculations. The eigenvalue computed by COMET is in good agreement with those calculated by MCNP, with a discrepancy of about 80 pcm. The COMET assembly FDs agree very well with the Monte Carlo reference solutions. However, the expansion order {4,4,2,2} is needed for COMET to achieve a similar accuracy in stripe-wise FDs. The average and mean relative differences between the COMET {4,4,2,2} and MCNP stripe-wise FDs vary from 0.39% to 0.46% and from 0.38% to 0.39%, which are within three standard deviations of MCNP uncertainties. Similarly, the COMET results are in very good agreement with the reference solutions for the three full core configurations. The discrepancy in the eigenvalues predicted by COMET and MCNP is in the range of 17 – 88 pcm. The assembly FDs computed by COMET are found to agree better with the reference solutions than those calculated by MCNP without using the core symmetry. It is also found that the direct use of the Monte Carlo method for AHTR full core calculations when the FD is tallied in all fuel stripes is impractical because of the prohibitive computation resource requirement, while each COMET full core calculation took about 4.5 hours on a single CPU.

The benchmark calculations against Monte Carlo have indicated that the continuous energy COMET can serve as an excellent method for obtaining high fidelity solutions (e.g., the stripe-wise FDD) to AHTR full core problems because of COMET's high fidelity and high computational efficiency. As a result, the stripe-wise FDD generated by the continuous energy COMET can be taken as a reference solution to the stylized AHTR benchmark problems.

References

Holcomb et al., 2011. "Core and Refueling Design Studies for the Advanced High Temperature Reactor", Report# ORNL/TM-2011/365.

Leppänen, J., Pusa, M., Viitanen, T., Valtavirta, V., Kaltiaisenaho, T., 2015. The SERPENT Monte Carlo Code: Status, Development, and Applications in 2013. Ann. of Nucl. Energy 82 (2015) pp.142-150.

Mosher, S., Rahnema, F., 2006. The Incident Flux Response Expansion Method for Heterogeneous Coarse Mesh Transport Problems. Transport Theory and Statistical Physics, 34, 1-26.

Philips, J. A., Barnes, C. M., and Hunn, J. D. 2010. Fabrication and Comparison of Fuels for Advanced Gas Reactor Irradiation Tests. Proceedings of HTR 2010, Prague, Czech Republic, Oct. 18–20.

Rahnema, F. and Zhang, D., 2018. Continuous energy coarse mesh transport (COMET) method. Annals of Nuclear Energy, 115, 601-610.

Varma V. K., et. al., 2012. "AHTR Mechanical, Structural, and Neutronic Preconceptual Design", report # ORNL/TM-2012/320.

X-5 Monte Carlo Team, 2005. MCNP—A General Monte Carlo N-Particle Transport Code, Version 5. Los Alamos National Laboratory.

Zhang, D. and Rahnema, F., 2012. An Efficient Hybrid Stochastic/Deterministic Coarse Mesh Neutron Transport Method. Annals of Nuclear Energy, 41, pp. 1-11.

Zhang, D. and Rahnema, F., 2017. Monte Carlo solution convergence analysis via COMET in a stylized integral inherently safe LWR benchmark problem. Annals of Nuclear Energy, 100, pp. 3-11.

Zhu, Y., Hawari, A.I., 2017. Thermal Neutron Scattering Cross Section of Liquid FliBe. In: Progress in Nuclear Energy 101 (2017) 468-475.

Ilas, D., Holcomb, D.E., Varma, V.K., 2012. dvanced High-Temperature Reactor Neutronic Core Design. *International Topical Meeting on Advances in Reactor Physics (PHYSOR) 2012*, Knoxville, TN, USA, April 15-20, 2012, ANS.

Huang, M.L., Petrovic, B., 2014. Use of MCDancoff Correction Factor for Multi-Group Fuel Depletion Analyses of Liquid Salt Cooled Reactors. *PHYSOR 2014*, Kyoto, Japan, September 28 – October 3, 2014.

Gentry, C., Maldonado, G.I., Chvala, O., Petrovic, B., 2017. Neutronic Evaluation of a Liquid Salt-Cooled Reactor Assembly. *Nucl. Sci. and Eng.*, **187**, 166-184.

Huang, L. M., Petrovic, B., 2018. Development of Methodology for Efficient Fuel Design Evaluation of the Advanced High Temperature Reactor (AHTR). Submitted to Annals of Nuclear Energy.

Ramey, K., Petrovic, B., 2018. Monte Carlo Modeling and Simulations of AHTR Fuel Assembly to Support V&V of FHR Core Physics Methods. *Annals of Nuclear Energy*, **118**, 272-282.

Rahnema, F., Petrovic, B., Singh, P., Burke, P., Noorani, H., Sun, X., Yoder, G., Tsvetkov, P., Zhang, J., Zhang, D., Ilas, D., 2017. The Challenges in Modeling and Simulation of Fluoride-Salt-Cooled High-Temperature Reactors. *White Paper CRMP-2017-9-001*, Georgia Institute of Technology.

Rahnema, F., Zhang, D., Petrovic, B., Diamond, D., Serghiuta, D., Edgar, C., Fratoni, M., Gougar, H.S., Hawari, A., Hu, J., Hudson, N., Ilas, D., Maldonado, I., Neutronics Phenomena Identification and Ranking Table (PIRT) for Fluoride High-Temperature Reactor (FHR). *Trans. Am. Nucl. Soc.*, **115**, 1078-1080.

Rearden, B. T., Jessee, M. A., 2016 "SCALE 6.2.1: A Comprehensive Modeling and Simulation Suite for Nuclear Safety Analysis and Design; Includes ORIGEN and AMPX," *ORNL/TM-2005*/39, Version 6.2.1, Oak Ridge National Laboratory, Oak Ridge, Tennessee.

9.5. Sensitivity Analyses Using Pseudo-2D Fuel Assembly Model

SERPENT was selected for sensitivity studies because it has proven to be efficient for conducting reactor physics analyses in a variety of reactor types and for running depletion simulations. In particular, its Woodcock delta-tracking is effective for FHR fuel containing many TRISO particles. A detailed SERPENT pseudo-2D fuel element (a reflected slice of a single fuel element) model has been developed to perform simulations to improve

understanding of core physics and quantify impact of variation in fuel design and modeling assumptions.

Core physics parameters of interest include neutron flux, fission rate, power density, fuel temperature, and burnup. Specifically, modeling aspects investigated include: group-wise flux distributions, boundary condition (BC) treatment, particle-wise power distribution, material-wise spectra, and assembly depletion. Sensitivity studies were also conducted quantifying the significance of certain parameters, including: thermal scattering library usage and graphite density perturbation.

9.5.1. Base Model

The SERPENT 2D assembly model uses 9 w% (in ^{235}U) enriched fuel in TRISO particles with all layers (buffer, inner pyrolytic carbon, silicon carbide, and outer pyrolytic carbon) explicitly modeled. The TRISO particles are placed in a cubic lattice with a packing fraction of 40%. Within each fuel stripe of a fuel plank, fuel kernels are placed in three rows of 233 kernels and one row of 110 kernels on the central interior of the plank (Petrovic, Ramey, and Flaspoehler, 2017). Assembly visualization with emphasis on this TRISO placement can be found in Figure 9-20. There is no burnable poison (Europium) in this model.

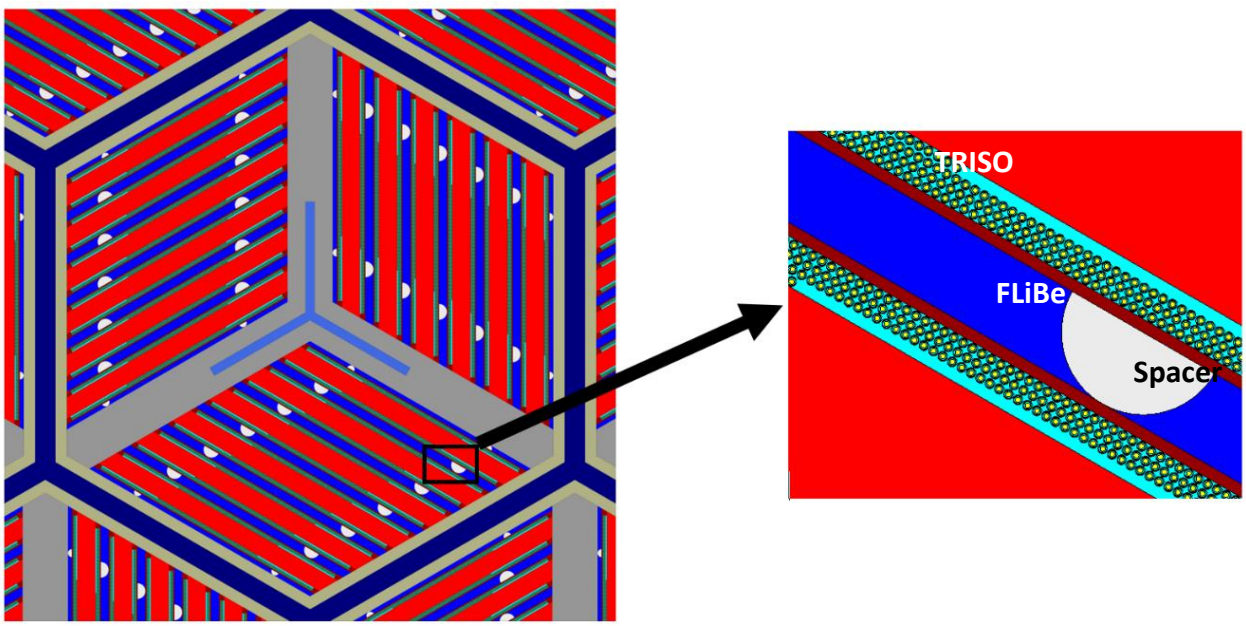

Figure 9-20. SERPENT 2D assembly model.

The dimensions of the SERPENT 2D assembly model are taken from the design reference (Varma et al., 2012) and are shown in Table 9-13.

Table 9-13. 2D SERPENT assembly dimensions.

Parameter	Length [cm]	Parameter	Length [cm]
Fuel Kernel Radius	0.02135	Fuel Plank Length	22.51666
Fuel Buffer Radius	0.03135	Large Spacer Radius	0.69999
IPyC Radius	0.03485	Small Spacer Radius	0.34999
SiC Radius	0.03835	Control Blade Arm Width	0.8
OPyC Radius	0.04235	Control Blade Arm Length	10
Kernel Lattice Pitch	0.09266	Inner Wrapper Hex Apothem	21.5
Model Height (100 Kernels)	9.266	Outer Wrapper Hex Apothem	22.5
Fuel Stripe Length	21.5898	Assembly Pitch Hex Apothem	23.4

The fuel used in the TRISO kernels is a non-stoichiometric UCO mixture corresponding to the AGR-2 fuel type (Phillips, Barnes, and Hunn 2010). The non-normalized relative atomic densities used for the simulations are: 2.2505E-03 for ^{235}U, 2.2468E-02 for ^{238}U, for 3.5594E-02 ^{16}O, and 9.7636E-03 for C. The material properties of *Table 3-1* were also obtained from the design reference, but some adjustments needed to be made for the thermal scattering treatment of the graphite in the model. They are listed in the "Modeled As" column. The "Structural" material in *Table 3-1* is used for the Y-structure and assembly wrapper regions. While these are intended to be manufactured as C-C composite materials, they are modeled as graphite.

Table 9-14. 2D SERPENT assembly material properties.

Material	Density [g/cc]	Temperature [K]	Modeled As
Fuel	10.9	1110	9 w% UCO
Buffer	1	1110	Carbon
IPyC	1.9	1110	Graphite using 1200 K S(α,β)
SiC	3.2	1110	
OPyC	1.87	1110	Graphite using 1200 K S(α,β)
Matrix	1.75	1110	Graphite using 1200 K S(α,β)
Meat	1.75	1110	Graphite using 1200 K S(α,β)
Sleeve	1.95	948	Graphite using 1000 K S(α,β)
Spacer	1.75	1029	Graphite using 1000 K S(α,β)
Structural	1.75	948	Graphite using 1000 K S(α,β)
FLiBe	1.957888	948	

9.5.2. Flux Distributions

The neutron flux distribution in the SERPENT 2D assembly model was obtained for three groups: 1x10^{-5} – 3 eV (thermal), 3 eV – 1 MeV (intermediate), and 1 – 20 MeV (fast). The normalized flux distribution for each group is seen in
Figure 9-21. As expected, the fast flux is largest near the fuel stripes of the fuel planks and the thermal flux is largest where there is a significant amount of carbonaceous moderator

(in the corners of the Y-shape structure between the fuel plank regions). The intermediate flux is very flat though: slightly favoring the fast flux distribution due to the high energy ceiling on the intermediate group, but varying by less than 5% from the average anywhere in the assembly. Runtime parameters of
Figure 9-21 were: 1.8 million particles per cycle, 50 inactive cycles, 1000 active cycles, and a runtime of 19.3 hours on 24 processors. Statistical uncertainty on eigenvalue was 2 pcm with individual flux mesh tally uncertainties around 30 pcm. The flux distribution studies of subsection 3.2 and 3.3 use a 100x100 mesh on the assembly geometry.

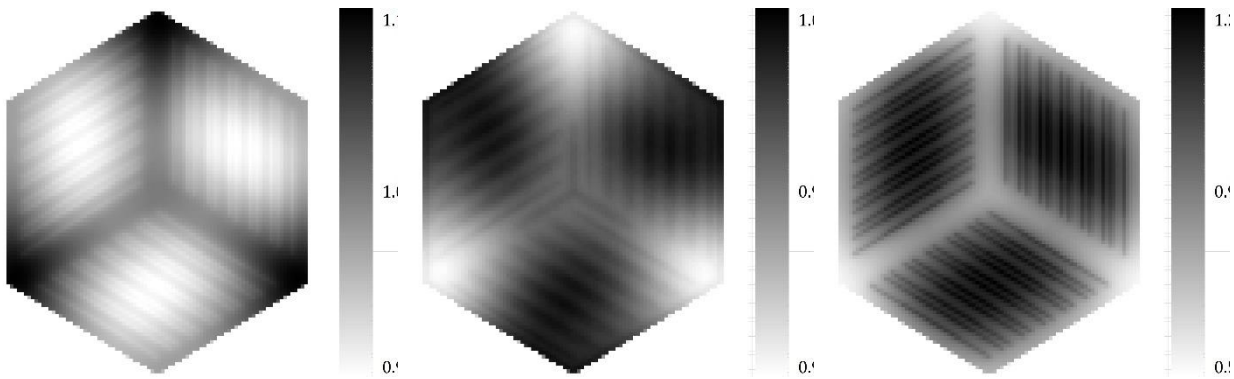

Thermal ($1x10^{-5}$–3 eV) Intermediate (3 eV–1 MeV) Fast (1–20 MeV)

Figure 9-21. Normalized 3-group flux distributions.

9.5.3. Problem Symmetry and Boundary Conditions Treatment

One of the concerns of conducting 2D assembly analyses in some other Monte Carlo codes is the inability to accurately model the periodic BC for the hexagonal shape of the FHR assembly. The correct treatment is to use a periodic BC because of the orientation of fuel planks such that a side with a long plank dimension is next to a side with short plank dimensions in an adjacent assembly and vice versa (Figure 9-20). However, some codes can only use a mirror BC, which places long plank dimension next to long plank dimension and short plank dimension next to short plank dimension. The two BC treatments have been modeled in otherwise replica simulations, and the results show that the eigenvalue difference is negligible (7 ± 3 pcm). However, if the group-wise flux distributions are examined for the mirror reflection model and compared with the correct periodic treatment, a larger difference of up to 4% (for the fast group) is revealed (
Figure 9-22).

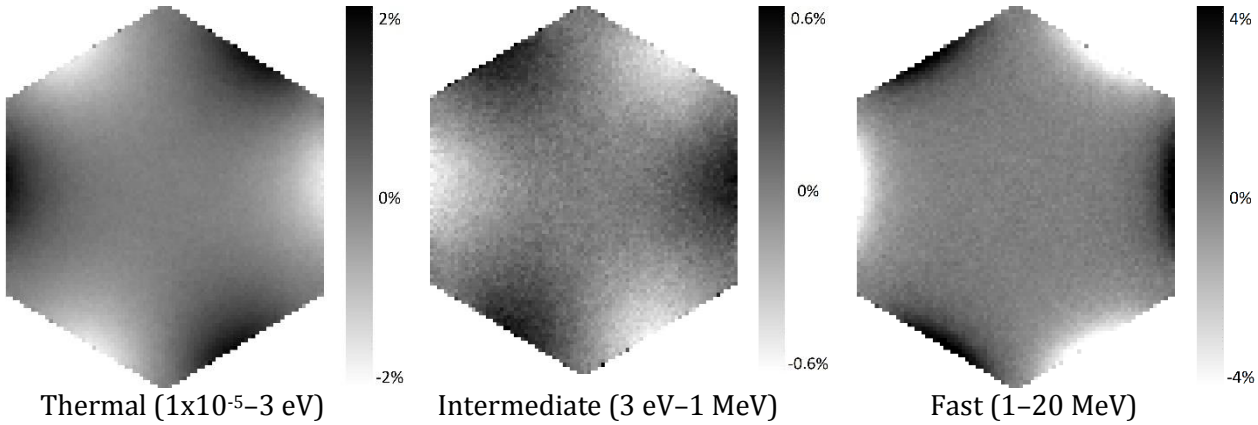

Figure 9-22. Difference in normalized 3-group flux distribution due to reflective BC. (Periodic BC taken as reference.)

Differences in
Figure 9-22 are taken with respect to the reference periodic BC results. In the thermal group, mirror reflection overpredicts the flux near the boundaries with short fuel plank dimensions and similarly underpredicts the flux near the boundaries with the long fuel plank dimension. The fast and intermediate groups see the opposite trend, with overprediction favoring the long dimension. In this analysis, the difference between mirror and periodic BCs is nontrivial. A follow-up study on the impact on fission energy deposition shows very similar results to the thermal distribution in
Figure 9-22: overprediction on the boundaries with the short plank dimension. With the source distribution near the boundary consequently also varying by ±2%, some caution needs to be applied to other detailed 2D studies of AHTR-like assemblies using mirror reflection. If quick estimates are desired and some spatial error in the source distribution is tolerable, then using mirror reflection and potentially modeling only one third of fuel assembly may still be acceptable.

9.5.4. Particle-Wise Power Distribution

The previous subsections used a 100x100 mesh on the assembly geometry to obtain their results. When trying to obtain a power distribution from that same mesh, the results exhibit high variability, significantly more that the power density varies in different TRISO particles, since that arbitrary mesh captures different fractions of TRISO particles in each mesh element. Since the SERPENT 2D model uses TRISO particles placed in a cubic lattice, a separate mesh was placed for each fuel stripe to include a single TRISO particle in each mesh element. This allows for particle-wise tracking of tallies, which can produce a particle-wise power distribution (Figure 9-23). Note that in the results of Figure 9-23, the fuel stripe alignment is shifted from that in the actual assembly and they are grouped closer as well. The mesh for each fuel stripe is 110 or 233 particles long, 3 or 4 particles wide, and individual TRISO mesh elements are square.

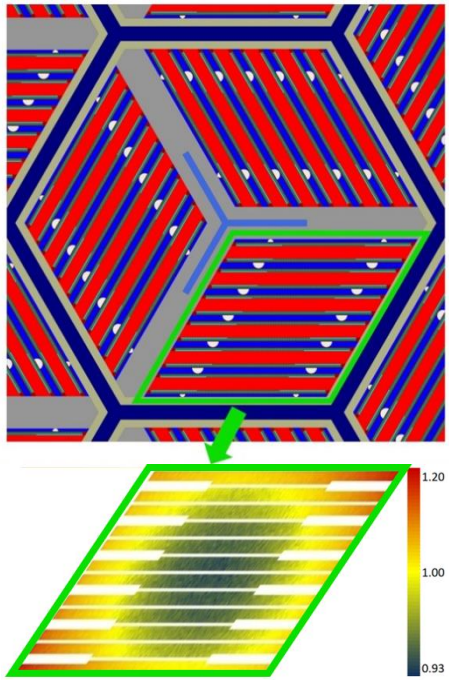

Figure 9-23. Individual TRISO particle normalized power distribution.

Runtime parameters of the simulation corresponding to Figure 9-23 were: 1.6 million particles per cycle, 50 inactive cycles, 1000 active cycles, and a runtime of 18.9 hours on 24 processors. The model statistical uncertainty was 2 pcm on eigenvalue and the peak statistical uncertainty for all TRISO particles was 573 pcm. When compared with Figure 9-21, this power distribution reflects neutron physics because the power peaks where the thermal flux is the highest (the peripheral corners of the Y-shape structure). While some statistical noise is observable in Figure 9-23, the results are within a reasonable tolerance (less than 0.6% everywhere). These results may serve to optimize the placement of burnable poisons to reduce intra-assembly peaking factors, and support determining the number of depletion regions within each fuel plank. Extending particle-wise tallying to full core models is likely not feasible, certainly not practical, and may not provide new information beyond that obtained by assembly-level simulations.

9.5.5. Material-Wise Spectra

In addition to understanding the spatial flux distribution, it is also important to know the energy distribution of the neutron flux. Figure 9-24 presents the average flux spectrum for the entire assembly as well as spectra for all individual constituent materials. In Figure 9-24, “Matrix” denotes the graphite in the fuel stripe surrounding the TRISO particles, “Meat” denotes the graphite inside the fuel plank beyond the fuel stripes, “Sleeve” is the 0.1 cm graphite region between the fuel stripes and the coolant, “Structural” refers to the Y-shaped C-C composite region in the middle of the assembly separating the fuel plank regions, “Wrapper” denotes the C-C composite perimeter around the assembly, “iflibe” is coolant in the channels between the fuel planks, “yflibe” refers to coolant in the Y-shaped control blade slot (model assumes control blade is fully withdrawn), and “oflibe” refers to

the inter-assembly coolant outside of the Wrapper region. For both lethargy scales in Figure 9-24 and Figure 9-25, u=0 is taken at E=20 MeV. Runtime parameters of simulation used to generate Figure 9-24 and Figure 9-25 were: 2 million particles per cycle, 100 inactive cycles, 2000 active cycles, and a runtime of 45.1 hours on 24 processors.

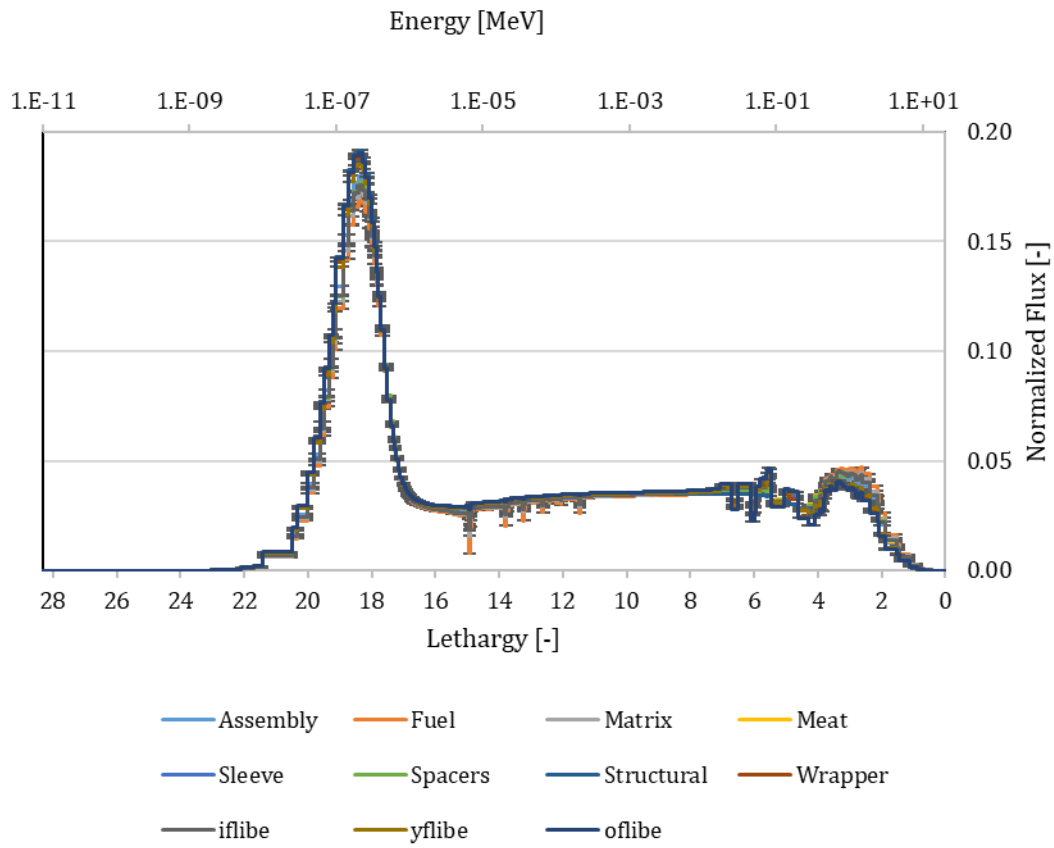

Figure 9-24. Material-wise flux spectra.

As can be observed from Figure 9-24, the spectrum seen by each material in the FHR assembly does not differ that much from the assembly-averaged spectrum. If the spectral difference is calculated for each material from the assembly average, then the results shown in Figure 9-25 are obtained.

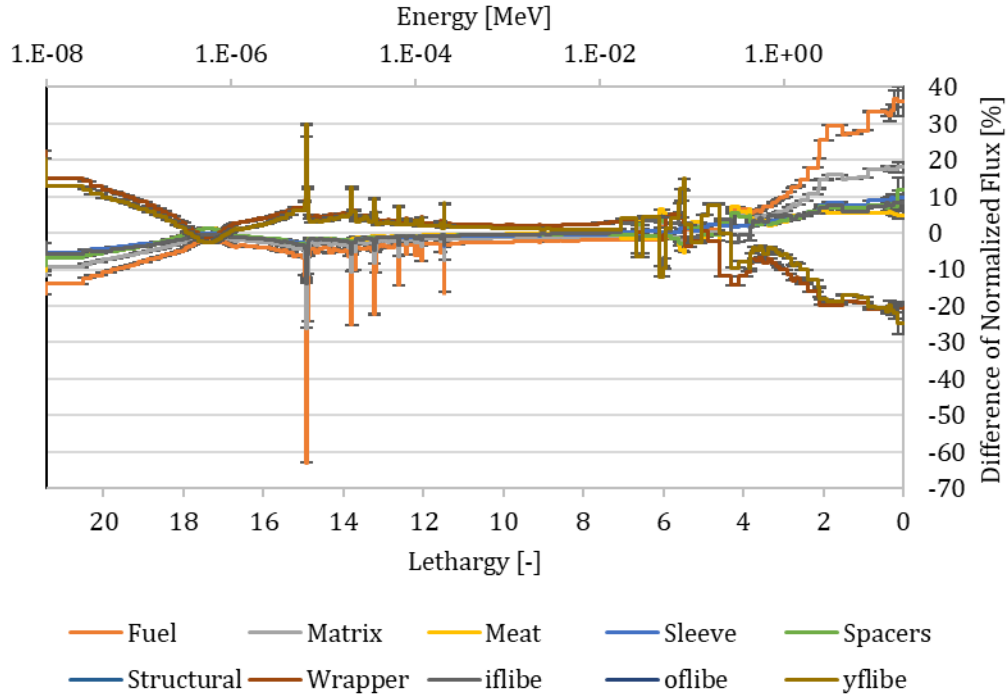

Figure 9-25. Material-wise flux spectra differences.

The largest differences in Figure 9-25 appear in the fuel, but this is expected. The absorption resonances in the fuel are apparent in the approximately 5-300 eV range. Since fast fission neutrons are born in fuel, the fuel exhibits the fast neutron flux above the average. The opposite case is seen in materials far away from fuel such as structural, wrapper, oflibe, and yflibe. These materials see systematically lower flux in the fast range, but also higher in the thermal range. Above 0.01 eV, all materials have spectra within +/- 20% of the assembly average, except for fuel in the high energy range and at lowest fuel resonance.

9.5.6. Error Propagation in Assembly Depletion Simulations

For future fuel cycle studies, it is important to know how precise statistics (converged results) are necessary when running depletion simulations to obtain sufficiently accurate isotopics. In Table 9-15, three depletion cases are considered to a burnup of 100 MWd/kgHM. The cases have the number of active particles per step differ progressively by an order of magnitude. The reference case (best statistics) is the basis for evaluating the acceptability of the faster simulations with worse statistics: standard (middle case) and preliminary (fewest particles). All depletion simulations detailed below assumed a power of 224.3 kW over the 9.266 cm height, used 33 burnup steps, and each step used 100 active and 10 inactive cycles.

Table 9-15. Runtime statistics of various depletion simulations.

	Particles/Generation	CPUs	Runtime	Average k Error
Preliminary	10,000	24	1.06 h	60 pcm
Standard	100,000	24	9.37 h	21 pcm
Reference	1,000,000	24	94.2 h	6 pcm

The result of the reference depletion simulation can be seen in Figure 9-26, which presents the change in eigenvalue due to burnup. While almost all currently considered refueling schemes have a maximum batch discharge burnup of 80 MWd/kgHM, this analysis goes to 100 MWd/kgHM to cover the variability between and within assemblies and potential variations in the refueling scheme.

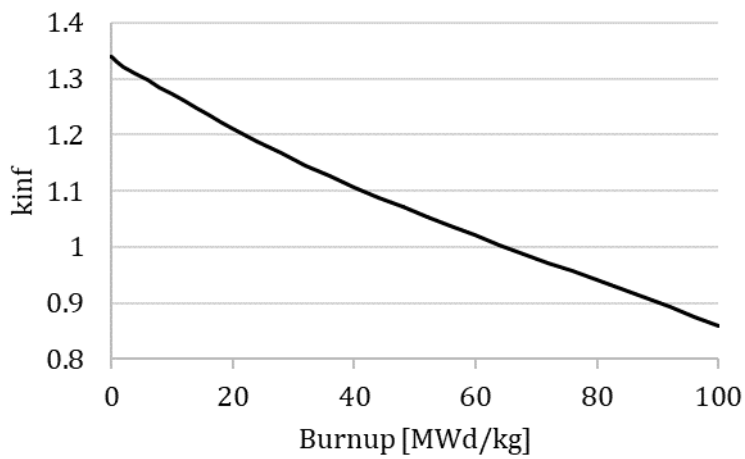

Figure 9-26. Eigenvalue change of fresh assembly with burnup.

For the "Standard" and "Preliminary" cases, differences in isotopics were determined for each burnup step with respect to the reference simulation for 91 isotopes. In some cases, it was necessary to remove comparison for the initial appearance of some isotopes with extremely low and completely negligible concentrations which exhibited large relative difference due to numerics, but stabilized later as soon as the concentration reached a meaningful value. Maximum relative positive and maximum relative negative differences, denoted as "extreme relative differences", are presented in Figure 9-27. As can be observed, the preliminary results have isotopic differences up to about 0.5-1% in the middle of cycle, with initial differences close to 2% near the beginning of cycle. The standard depletion case performed better than the preliminary case (as expected). While it also sees larger differences toward the beginning of cycle, it stabilizes to have 0.2-0.3% extreme differences at the middle and end of cycle. Figure 9-27 may be used to estimate and justify the number of particles needed to achieve a desired level of isotopic precision for future depletion simulations.

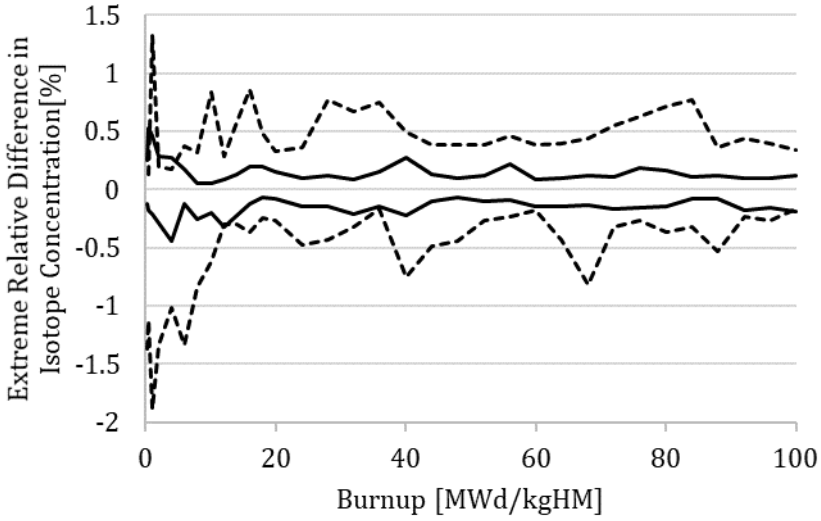

Figure 9-27. Extrema of relative isotope concentration differences. Solid lines are the min/max differences for the standard (10^7 histories) vs reference (10^8 histories) simulation, and the dashed lines are the min/max differences for the preliminary (10^6 histories) vs reference (10^8 histories) simulation.

9.5.7. Thermal Scattering Library Usage for Carbonaceous Materials

S(α,β) thermal scattering matrices are important for moderating materials. The free gas assumption becomes invalid for low energy neutrons and accounting for bound atoms becomes necessary. Table 9-16 shows the results for several simulations testing the impact of using different S(α,β) matrices. The assumed temperature used in the seven cases differ from those listed in *Table 3-1*, but densities remain unchanged. The fuel temperature (1110 K), SiC temperature (1000 K), and FLiBe temperature (948 K) remain constant for all cases, and the only difference is the material temperature of graphite (as well as C-C composite) media and their associated usage of S(α,β) matrices. Case B uses S(α,β) for TRISO graphite layers, fuel plank graphite, and plank spacers, but not for the Y-shaped C-C composite structure in the middle nor C-C composite wrapper around the assembly. Runtime parameters of cases considered in Table 9-16 were: 1 million particles per cycle, 50 inactive cycles, 1000 active cycles, and runtimes of about 45 hours on 8 processors each.

Table 9-16. Results of simulations with different S(α,β) treatments.

Case	Graphite Temperature [K]	Use of S(α,β)	Eigenvalue*
A	1000	None	1.39672
B	1000	1000 K on all but structural and wrapper	1.39596
C	1000	1000 K on all	1.39597
D	1000	1200 K on all	1.39343
E	1200	1200 K on all	1.39271
F	1200	1000 K on all	1.39529
G	1200	None	1.39319

**All simulations had a reported statistical uncertainty of 2 pcm.*

If the results of cases B and C are compared, notice there is a negligible effect on the eigenvalue. Because the C-C composite regions are far from fuel, the impact on eigenvalue is essentially trivial. However, recalling from
Figure 9-21, the thermal flux for the assembly is highest in the Y-shaped C-C composite material, so this result is somewhat surprising. For ease of comparison of cases C-F, Table 9-17 was generated. The change in S(α,β) matrix reference temperature was far more significant than material temperature change from 1000 to 1200 K (-254 pcm versus -68 pcm). Moreover, the change from (1000 K, 1000 K) to (1200 K, 1200 K) can almost be considered as a linearization of the individual effects (-326 pcm versus -322 pcm). Overall, while the impact of using different temperatures or different S(α,β) matrices is not trivial, it is limited to a few hundred pcm.

Table 9-17. Relative eigenvalue differences (in pcm) for cases C-F (with respect to case C).*

		Temperature [K]	
		1000	**1200**
S(α,β) Reference Temperature [K]	**1000**	0 (reference)	-68
	1200	-254	-326

**All differences have a statistical uncertainty of 3 pcm.*

9.5.8. Graphite Density

Material properties of the carbonaceous materials assumed in the current reference design are based on the typical historical properties of such materials. However, manufacturing capabilities may differ from those assumed in analyses. This includes the nominal density of graphite (and carbonaceous materials), as well as the manufacturing tolerance, which are both very important to the FHR design since there is a large amount of graphite in an assembly, and it acts as the main moderator. Table 9-18 quantifies the impact of varying the density of graphite in all relevant regions within an assembly, from their reference values in *Table 3-1*. For the last two rows, "All (sum Δ)" is the sum of all six individual contributions, while "All (simulated)" is the result from simultaneously modeling all six changes in SERPENT. The comparison between the two shows what would be guessed as the impact from all individual perturbations versus the actual impact. One can conclude

from Table 9-18 that accurately knowing the specifications of graphite density is important to core physics and will impact core reactivity and reaching the desired cycle length. The combined impact is 1751 pcm for 10% density change in all carbonaceous materials. The 10% density variation is consistent with the order of magnitude of historical density variation of various carbonaceous materials; the manufacturing tolerance will of course be much smaller. Runtime parameters of cases considered in Table 9-18 were: 160,000 particles per cycle, 50 inactive cycles, 1000 active cycles, and runtimes of about 17.5 hours on 8 processors each.

Table 9-18. Material-wise graphite density sensitivity.

Modified Material	k(-10%)*	Normal*	k(+10%)*	Δk(-10%) [pcm]	Δk(+10%) [pcm]
Matrix	1.39174	1.39327	1.39494	-153 ± 7	167 ± 7
Meat	1.38448	1.39327	1.4018	-879 ± 7	853 ± 7
Sleeve	1.39213	1.39327	1.39457	-114 ± 7	130 ± 7
Spacer	1.39301	1.39327	1.39367	-26 ± 7	40 ± 7
Structural	1.38875	1.39327	1.39776	-452 ± 7	449 ± 7
Wrapper	1.39084	1.39327	1.39577	-243 ± 7	250 ± 7
All (sum Δ)				-1867 ± 7	1889 ± 7
All (simulated)	1.3727	1.39286	1.41037	-2016 ± 7	1751 ± 7

**Each simulation had a reported statistical uncertainty of 5 pcm.*

9.5.9. Initial Assessment of SERPENT Parallel Efficiency

Monte Carlo simulations require long simulation times and may potentially become practical only on a parallel computer cluster. To assess SERPENT performance in a parallel computational environment, parallel simulations were performed on several clusters. Initially, parallel performance was tested on a single multi-CPU cluster node: B2-BP (8 CPUs), B2-CD (16 CPUs), PACE (24 CPUs) and B3 (32 CPUs). The obtained parallel speedup and parallel efficiency is shown in Figure 9-28.

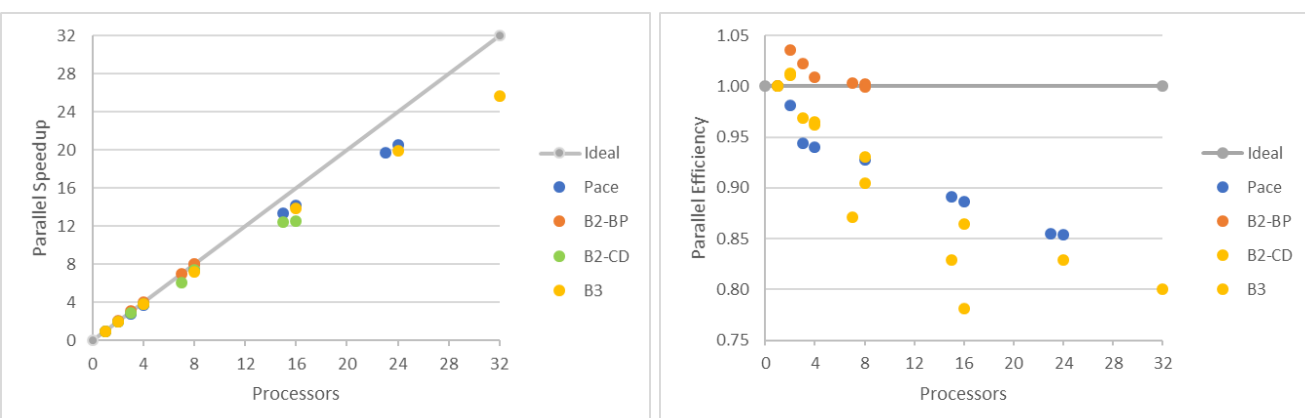

Figure 9-28. Parallel speedup (left) and parallel efficiency (right) for SERPENT fuel assembly simulations on several configurations with up to 32 CPUs.

At 16 CPUs, parallel efficiency is reduced to 85-90% for most cases. For 32 CPUs, it is further reduced to 80%. This moderate reduction in efficiency is acceptable for this limited number of CPUs (up to 32), but it may suggests further degradation for a larger clusters. The reduction in efficiency was higher than expected, i.e., a better parallel performance was anticipated. One possible explanation is that the overall cluster load at the time of testing contributed to some performance degradation. Additionally, the strong scaling used in testing (with the same number of histories irrespective of the number of CPUs) may have contributed to the parallel efficiency degradation. Therefore, the testing was extended to a larger cluster, as described in the next section.

9.5.10. Assessment of SERPENT Parallel Efficiency on a Larger Parallel Cluster

Additional tests were performed for a more prototypic, large parallel cluster configuration, with up to 192 CPUs available on multiple cluster nodes. Both weak and strong scaling simulations were performed:

- Weak scaling simulations, which use the same number of particles per core (CPU). All cases used $4x10^5$ neutrons/cycle/ core with 20 inactive and 100 active cycles.
- Strong scaling simulations, which use the same number of particles per simulation. All cases used 10^6 neutrons/cycle with 20 inactive and 100 active cycles.

Results are shown in Figure 9-29

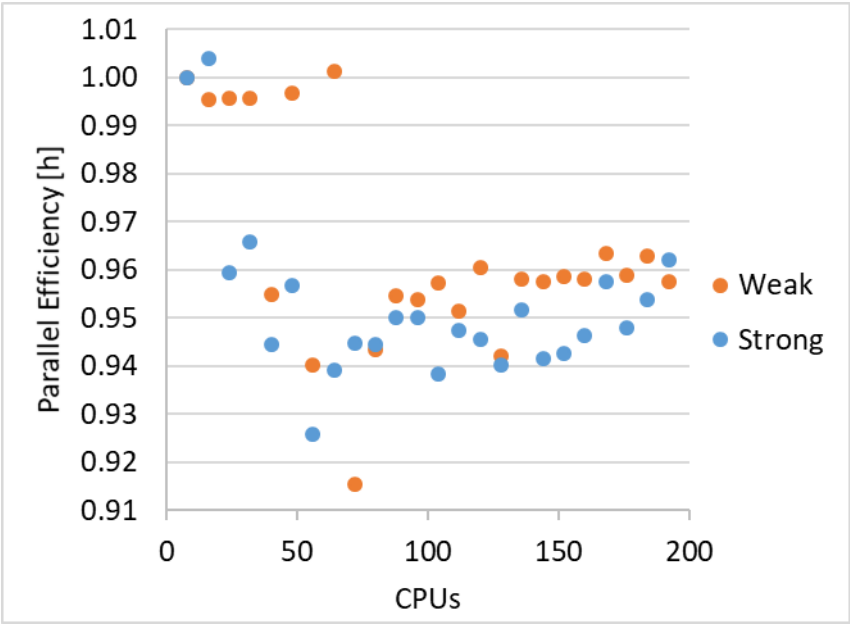

Figure 9-29. Parallel speedup (left) and parallel efficiency (right) for SERPENT fuel assembly simulations on several configurations with up to 192 CPUs.

Both the weak and strong scaling results show good parallel efficiencies, with both performing at 94% or better for most cases. Neither shows signs of efficiency degrading below 94% up to 192 cores, which represents most of typical users. Further testing on a larger machine to investigate efficiency at higher parallelism would be interesting to assess the practical limits of parallel simulations for the SERPENT code.

We note that a parallel version of SCALE was not available/established at the time when these tests were performed, but became available in the meantime. Future SCALE release is expected to incorporate the SHIFT Monte Carlo code, which is expected to exhibit good parallel efficiency.

9.5.11. Summary of Observations Related to Modeling Assumptions

The AHTR design is attractive from a safety and high thermal efficiency standpoint, but due to its complex geometry and double heterogeneity it presents significant modeling and simulation challenges. This study presents results of sensitivity studies. Due to its capability to explicitly represent arbitrary geometry, Monte Carlo is the method of choice for obtaining accurate results. SERPENT was used with continuous energy cross sections to model an FHR fuel assembly with enrichment of 9% and overall CHM around 400 assuming a regular cubic lattice for distribution of TRISO particles, with packing fraction of 40%. A slice of the assembly is considered with reflective top/bottom BCs, results being integrated axially to obtain 2D radial results. Calculations were performed on a parallel cluster, typically utilizing 8 to 32 CPUs, with simulations requiring about a day to achieve desired statistics. Main results may be summarized as follows:

- Detailed flux distribution was examined for three coarse energy groups: thermal – up to 3 eV; intermediate – 3 eV to 1 MeV; fast – above 1 MeV. Peaking factors were 1.133, 1.025, and 1.223 for the three groups, respectively. As expected, fast flux peak is observed in fuel stripes, while the thermal flux peak is observed in the region promoting thermalization, i.e., where the Y-shape meets the assembly wrapper.
- AHTR fuel assembly consists of three identical regions, rotated relative to each other by 120°; this corresponds to periodic BCs in infinite lattice simulations. If instead a reflective BC was applied (e.g., aiming to reduce the size of the problem to one third of assembly), the introduced error in the eigenvalue difference is negligible, i.e., 7 ± 3 pcm. However, impact on the flux distribution—while also limited—is more pronounced, with deviations from the correct solution with periodic BC being ±2.0%, ±0.6 and ±4.0%, for the thermal, intermediate and fast group, respectively.
- Fuel performance will be impacted by the individual (local) power i.e., fission density, of each TRISO particle (each kernel). Therefore, non-uniformity in the fission density of individual kernels was examined; normalized values range from 0.920 to 1.195 with 1σ of 0.006. That is, within-assembly peaking factor is about 1.2, not accounting for lattice non-uniformity.
- Variation in neutron spectra in different materials and regions was examined and compared against the assembly-averaged spectrum. Ten different regions were considered including fuel, plank "meat", graphite matrix, assembly wrapper, internal and

external FLiBe, and so on. Over most of the energy range the difference in spectrum is just a few percent, remaining within ±10% between approximately 0.1 eV and 1 MeV. For thermal neutrons below 0.1 eV, the difference increases toward ±20% for lower energies down to 0.005 eV. Above 1 MeV, the difference is more pronounce in fuel itself, where the fissions are occurring, reaching +30% around 5 MeV, while in other regions it remains within ±20%.

- Impact of the number of histories on the precision and error propagation of depletion calculations was examined. The simulations used 33 burnup steps to deplete fuel to a burnup of 100 MWd/kgHM. Reference calculation used 10^8 active histories per burnup step, requiring around 1000 hours on 24 CPUs, with the corresponding standard deviation in eigenvalue of 6 pcm. Cases denoted as "standard" and "preliminary" used 10 times and 100 times fewer histories, respectively, with the corresponding standard deviation of eigenvalue of 21 and 60 pcm. Maximum differences over many isotopes were in the 0.2-0.3% range for the former, and in the 0.5-1.0% range for the latter, with typical differences being notably smaller.
- The AHTR assembly contains multiple carbonaceous materials of different forms, compositions, and temperatures. Impact of this variability was examined by assigning a specific temperature and specific thermal scattering data (S(α,β) matrices) to each carbonaceous region. Variation in the eigenvalue was in all cases within a few hundred pcm, so not large but not negligible either.
- Thermalization of neutrons is largely due to carbonaceous materials, and significantly less to FLiBe. Moreover, while the FLiBe density is determined by the temperature, and does not change much, density of carbonaceous materials can vary significantly (from several percent to up to about ten percent) depending on the exact form and production process. Changing the density of all carbonaceous materials by 10% result in a significant change of eigenvalue, around 1750 pcm, with fractional contributions of each component consistent with its mass and volume fraction.
- SERPENT was found to scale well for parallel simulations up to the considered maximum number of 192 CPUs, with parallel efficiency remaining above 94% in most cases.

9.5.12. References

Leppänen, J., Pusa, M., Viitanen, T., Valtavirta, V., Kaltiaisenaho, T., 2015. The SERPENT Monte Carlo Code: Status, Development, and Applications in 2013. Ann. of Nucl. Energy 82 (2015) pp.142-150.

Phillips, J.A., Barnes, C.M., Hunn, J.D., 2010. Fabrication and Comparison of Fuels for Advanced Gas Reactor Irradiation Tests. Proceedings of HTR 2010 Prague, Czech Republic, October 18-20, 2010.

Varma, V.K., Holcomb, D.E., Peretz, F.J., Bradley, E.C., Ilas, D., Qualls, A.L., Zaharia, N.M., 2012. AHTR Mechanical, Structural, and Neutronic Preconceptual Design. National laboratory report ORNL/TM-2012/320.

Zhu, Y., Hawari, A.I., 2017. Thermal Neutron Scattering Cross Section of Liquid FLiBe. In: Progress in Nuclear Energy 101 (2017) 468-475.

9.6. Cross-Verification of SCALE, SERPENT and MCNP

A number of studies have identified difficulties and examined possible approaches to accurate modelling of FHR designs (see, for example, [2]-[8]). Therefore, it is desirable to develop core physics benchmarks, generate reference solutions with Monte Carlo methods using continuous energy nuclear data, and enable V&V of deterministic methods that by necessity involve discretization of the space-energy phase space. The spherical shape of fuel particles implies that there is no directly equivalent 2D geometry. The study presents a pseudo-2D model (a finite slice of a 3D model with reflective top and bottom boundary conditions) of FHR fuel element and defines benchmark calculations to be performed in support of cross-comparison and V&V of reactor physics codes.
Subtask 3.7.1 (V&V of Neutronics Codes in Support of Licensing) identifies the SCALE code package as the "preferred computational toolbox" by the DOE. Therefore, part of this study is to demonstrate both the accuracy and usefulness in modelling the FHR with SCALE as compared with other frequently used codes such as MCNP and SERPENT.

9.6.1. Consistent Assembly-level Models

Specifically, highly consistent MCNP [9], SCALE [10] and SERPENT [11] models have been developed. The KENO-VI model in SCALE6.2 and SERPENT model aim to very closely match all geometric and isotopic details of the MCNP models previously developed within the project. Comparisons of the multiplication factor, neutron flux and fission rate distribution, and peaking factors are presented and good agreement has been observed.

To enable assessing accuracy of reactor physics analyses through cross-comparison of results of several codes, their respective simulations would ideally represent identical models. While exactly identical models may not be possible, due to subtle differences in fine details of each code, with Monte Carlo codes it is typically possible to exactly reproduce the given geometry, and to use cross sections based on the same continuous energy nuclear data (possibly with some small differences in the detailed treatment). To reduce the number of variables and allow systematically examining potential differences in results and understanding their causes, the cross-verification (cross-comparison) presented here is limited to FHR single fuel element pseudo-2D modeling.

The pseudo-2D model consists of a finite slice of the active portion of fuel element, containing an integer number of TRISO particles, i.e., divisible with the assumed fuel lattice axial pitch value, with reflective top and bottom boundary conditions. It should be noted that, in contrast to extruded geometries such as the PWR fuel, the spherical shape of TRISO particles implies that the geometry is not uniform in the axial direction, hence there is no true 2D equivalent, and instead this "pseudo-2D" model is used.

Main parameters characterizing the FHR fuel element geometry are given in [1], [6] and [7]. However, some additional detail are specified here to ensure that all geometrical details are unambiguously defined. Moreover, the geometry of the fuel stripes (fuel-stripe dimensions,

packing fraction of fuel stripes, etc.) within the planks is such that it matches the design's reference full-core heavy-metal loading and carbon-to-heavy-metal ratio.

Figure 9-30 shows the fuel element layout. The fuel-planks are made of graphite and have a width of 23.1 cm. The fuel-stripes in the models are designed to have a parallelepiped lattice that is 202 particles wide in the x-direction, 4 TRISO particles thick in the y-direction, and 5936 particles tall in the z-direction. The pitch of the lattice in the x-direction was chosen to be 0.09406cm to make fuel planks that have an active width of 19cm. In the z-direction, a pitch of 0.09266cm was chosen so that the lattice matches the active-core height of 550cm. Lastly, the y-direction pitch of 0.09128cm and the stripe-thickness were chosen to achieve a 40% packing fraction and a full-core heavy-metal loading of 17.48MT. Dimensions for the layout of graphite within a fuel element are given in Table 9-19 and shown in Figure 9-30. Additionally, spheres of europium poisons are centered within fuel planks to help control reactivity. The models use europium spheres in a parallelepiped lattice that is 5 cells wide with an x-direction pitch of 4cm, 1 cell thick in the y-direction, and a z-direction pitch of 0.09936cm. In other words, there are 5 poison particles distributed along each fuel plank. Dimension of structural fuel elements (Y-shape in the middle, wrapper around) are shown in Figure 9-30, while the positions of semi-cylindrical fuel spacers are listed in Table 9-20.

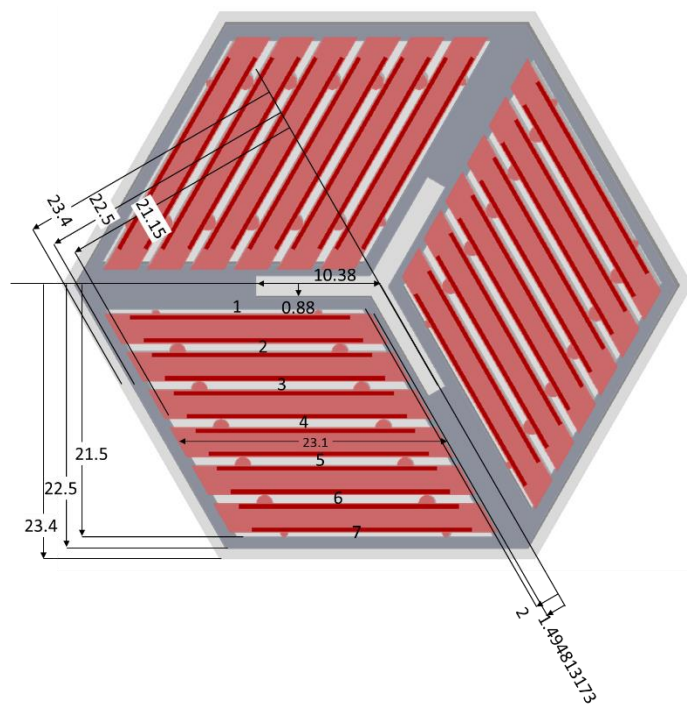

Figure 9-30. FHR fuel element geometry.

Table 9-19. Bottom-left spacer-grid placements.

channel	x	y	radius
1	-18.91929	-2.35	0.35
1	-4.91929	-2.35	0.35
2	-17.0429	-5.6	0.7
2	-3.0429	-5.6	0.7
3	-15.16651	-8.85	0.7
3	-1.16651	-8.85	0.7
4	-13.29012	-12.1	0.7
4	0.70988	-12.1	0.7
5	-11.41373	-15.35	0.7
5	2.58627	-15.35	0.7
6	-9.53735	-18.6	0.7
6	4.46265	-18.6	0.7
7	-8.0651	-21.15	0.35
7	5.9349	-21.15	0.35

The position of the fuel stripes in the bottom-left diamond-shaped third, with respect to coordinate axes with origin at the center of the fuel element, are given in Table 9-20. The other two diamond-shaped thirds are obtained by rotation by 120°.

Table 9-20. Bottom-left fuel-stripe placements.

	x_{min}	x_{max}	y_{min}	y_{max}
1	-21.2562	-2.25609	-2.81512	-2.45
2	-20.1102	-1.11012	-4.8	-4.43488
3	-19.3798	-0.3797	-6.06512	-5.7
4	-18.2339	0.76627	-8.05	-7.68488
5	-17.5034	1.49668	-9.31512	-8.95
6	-16.3575	2.64266	-11.3	-10.9349
7	-15.6271	3.37307	-12.5651	-12.2
8	-14.4811	4.51904	-14.55	-14.1849
9	-13.7507	5.24946	-15.8151	-15.45
10	-12.6047	6.39543	-17.8	-17.4349
11	-11.8743	7.12585	-19.0651	-18.7
12	-10.7283	8.27182	-21.05	-20.6849

Geometrically identical models have been developed for MCNP [9], SCALE [10] (for KENO-VI) and SERPENT [11]. Visual comparison of all three models is presented in Figure 9-32 and Figure 9-33. Due to the complex nature of the proposed fuel element's geometry, different modelling approaches have to be taken that are unique to each software package. Some of these details can be seen in Figure 9-32 and Figure 9-33 in the fuel planks and coolant channel regions where artificial lines representing planes are shown that result from modelling decisions.

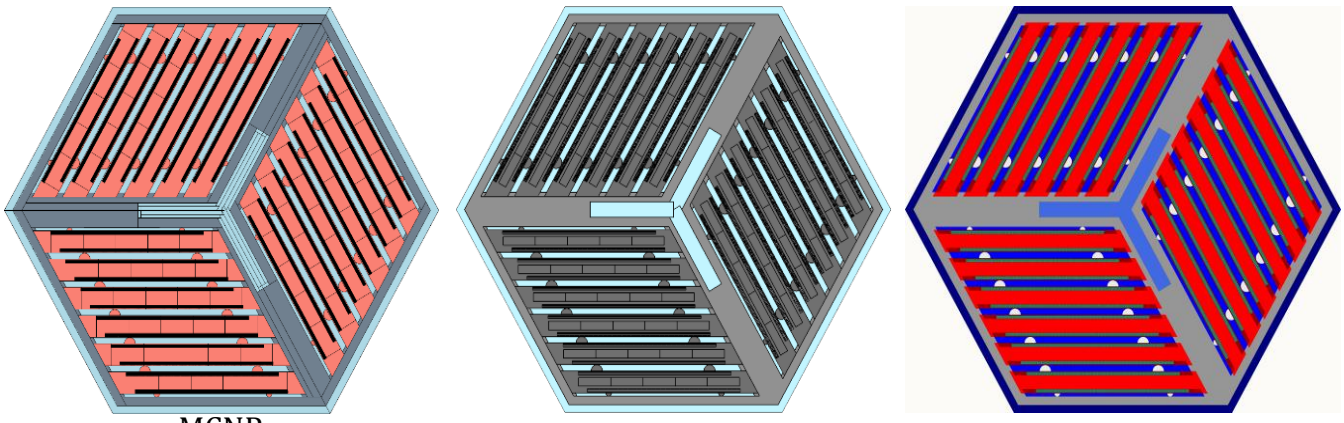

MCNP SCALE SERPENT

Figure 9-31. Comparison of fuel element geometries.

Figure 9-32. Comparison of fuel element geometries in Monte Carlo codes.

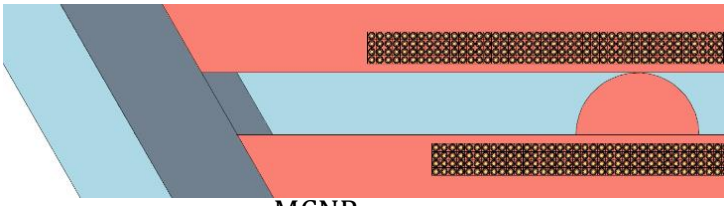

MCNP

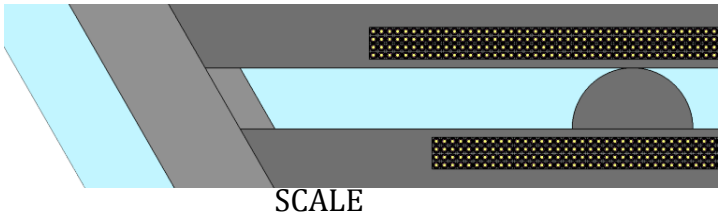

SCALE

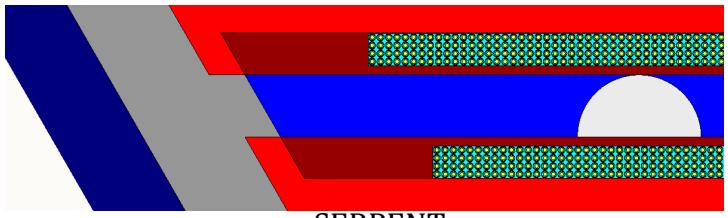

SERPENT

Figure 9-33. Fuel-stripe, spacer-grid, and C-C-box placement within geometry.

9.6.2. Cross-Comparison results

With each model, pseudo-2D fuel element calculations with radially periodic boundary were performed for a reactivity uncontrolled (unpoisoned) case containing no burnable poisons (BPs) and a poisoned case with BP in form of europium spheres. The following set of tallies were implemented within each model to provide a basis to verify models:

1. effective multiplication factor (k-eff)
2. fission-rate distributions (full plank, full stripe, fifth-stripe)
3. fuel element peaking factors
4. 100x100 mesh tally for fast flux (E>0.1MeV), epithermal flux (0.1MeV>E>3eV), and thermal flux (E<3eV)
5. flux spectra using default SCALE 252-group structure.

Each software has different tallying capabilities which can make it difficult to obtain comparable quantities for cross-verification. Again, this issue arises from the complex geometry of the fuel element. For example, the KENO-VI sequence in SCALE can only tally fluxes or fission distributions on a single mesh, but a single mesh cannot capture the fission distribution without partially cutting through the TRISO particles. This makes it difficult to get a smooth tally for the fission distribution over each individual fuel stripe compared with MCNP or SERPENT where putting a simple 5x1 mesh tally over each stripe for fission densities is easily implemented. In order to obtain fifth-stripe fission densities from KENO-VI, the fuel stripes have to be divided into 5 separate material regions for each stripe. Dividing the problem in this way results in an input file containing 180 material descriptions for the fuel instead of 1, 180 geometry units describing 180 TRISO particles instead of 1, 36 lattices describing the individual fuel stripes instead of 1, and 36 units containing the 36 fuel stripes instead of 1. This makes an already complicated input file roughly 180x larger.

Monte Carlo (MC) parameters and run times for each simulation are given in Table 9-21. It should be noted that adding tallies for cross-verification slowed down MCNP by a large factor of about 3X. This could be due to the low number of particles per cycle adding too much message passing between processes. Also, when Europium BPs are introduced to the geometry, the SERPENT runtime went up by a factor of roughly 5. This issue was further investigated and associated with the deterioration in efficiency of Woodcock delta tracking

in SERPENT. In contrast, Woodcock delta tracking performs well in the uncontrolled case and should be credited for the faster execution of SERPENT as compared to SCALE.

Table 9-21. MC parameters and run times for each case.

Case	Skipped Cycles	Active Cycles	Particles per Cycle	Wall-clock Time [h]	Total CPU Time [h]	CPUs
Uncontrolled (No Burnable Absorber)						
MCNP 6.1.1	50	200	25(10^3)	6.9	220.3	32
SCALE 6.2.2	50	200	50(10^3)	2.1	68.3	32
SERPENT 2.1.29	50	200	50(10^3)	0.5	16.2	32
Poisoned (Eu Burnable Absorber)						
MCNP 6.1.1	50	200	25(10^3)	6.3	200.0	32
SCALE 6.2.2	50	200	50(10^3)	2.4	76.3	32
SERPENT 2.1.29	50	200	50(10^3)	2.5	81.0	32

9.6.2.1. Multiplication and Fission Distribution

Multiplication factors (k_{eff}) and peaking factors for all cases are provided in Table 9-22. The results for k_{eff} are generally in good agreement with limited discrepancies most likely coming from slight differences in the treatment of cross-sections. MC tallies for fifth-stripe fission densities for all cases were converged to under 0.14% standard deviation. The peaking factors calculated from these values (as shown in Table 9-22) are in good agreement. The plank peaking factors and stripe peaking factors are nearly identical in all cases, and within the statistical uncertainty, while the maximum difference in fifth-stripe peaking factors is under 1%. Figure 9-34 and Figure 9-35 show full-stripe and fifth-stripe fission density distributions which demonstrates close agreement and consistent results among codes in each case.

Table 9-22. Multiplication and peaking factors calculated by MCNP, SCALE and SERPENT.

Case	k_∞	Plank Peaking Factor	Stripe Peaking Factor	Fifth-Stripe Peaking Factor
Uncontrolled (No Burnable Absorber)				
MCNP 6.1.1	1.39466 ± 0.00022	1.042	1.064	1.148
SCALE 6.2.2	1.39605 ± 0.00016	1.041	1.063	1.146
SERPENT 2.1.29	1.39944 ± 0.00021	1.042	1.067	1.155
Poisoned (Eu Burnable Absorber)				
MCNP 6.1.1	1.08658 ± 0.00022	1.050	1.075	1.172
SCALE 6.2.2	1.09551 ± 0.00020	1.048	1.074	1.174
SERPENT 2.1.29	1.09386 ± 0.00027	1.050	1.079	1.183

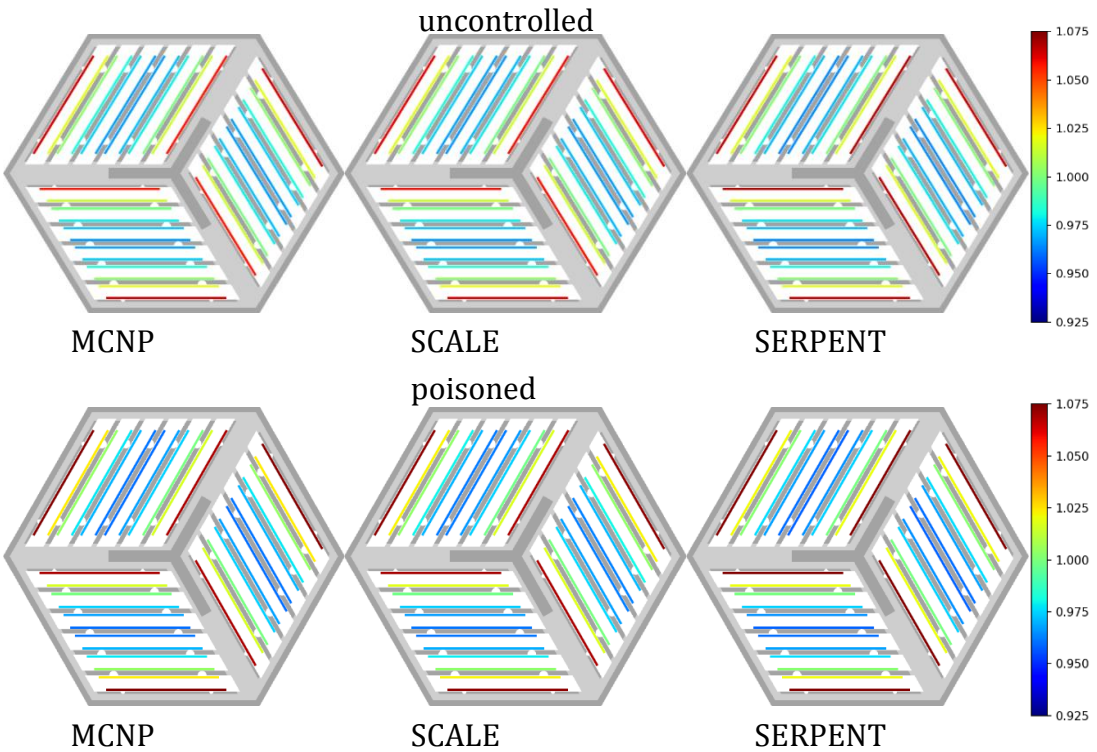

Figure 9-34. Full-stripe fission density distribution for each simulation.

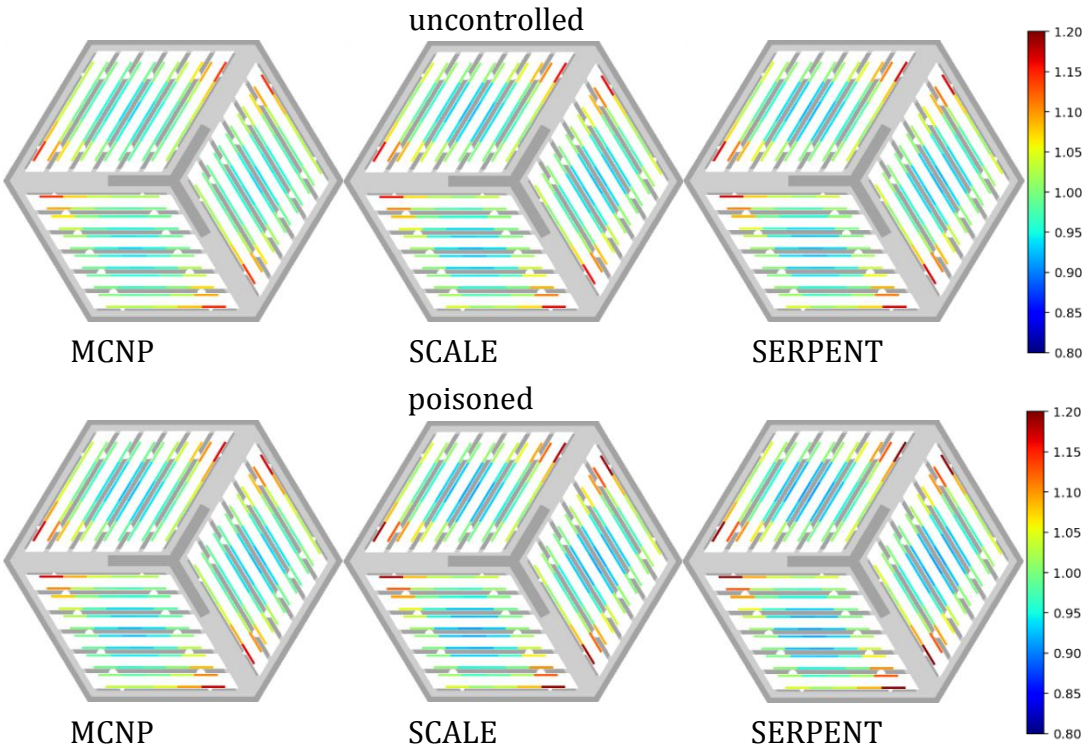

Figure 9-35. Fifth-stripe fission density distributions for each simulation.

9.6.2.2. Neutron Spectrum

A comparison of problem-integrated neutron spectra (tallied on SCALE's 252-group library structure) for the uncontrolled cases with no BPs is shown in Figure 9-36. Figure 9-37 shows the spectra for the poisoned cases. The results are in close agreement for both cases. However, SCALE does have a slightly harder spectrum than SERPENT and MCNP. For preliminary results, these differences are considered to be insignificant and may be partly due to the statistical noise. Figure 9-38 shows the spectra for both cases using MCNP in order to demonstrate the overall spectrum hardening effect of BPs.

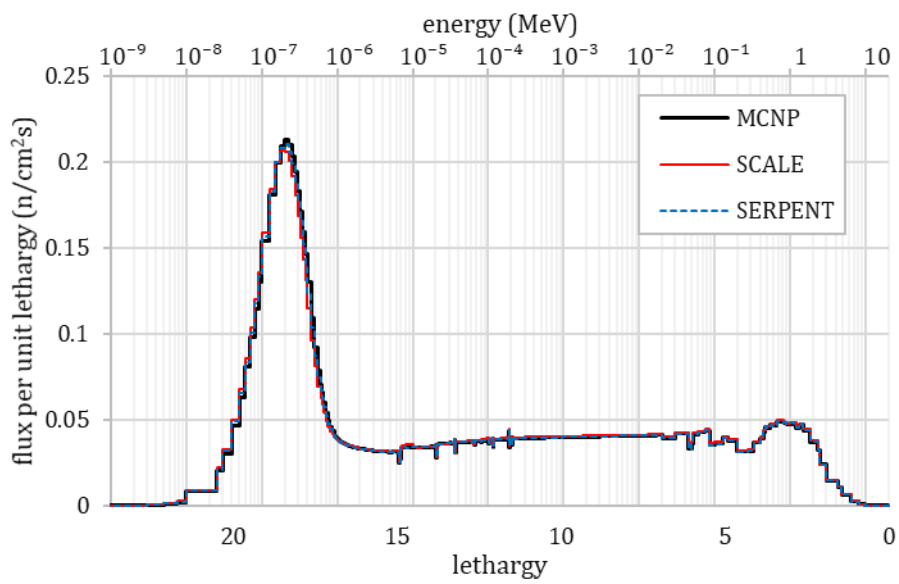

Figure 9-36. Total flux per lethargy for each model using an uncontrolled 2D assembly model.

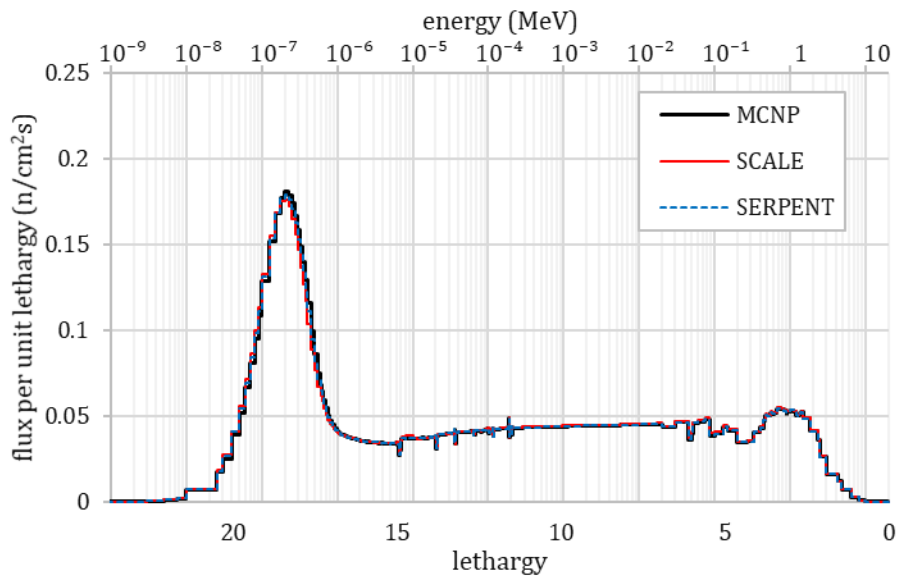

Figure 9-37. Total flux per lethargy for each model using a poisoned 2D assembly model.

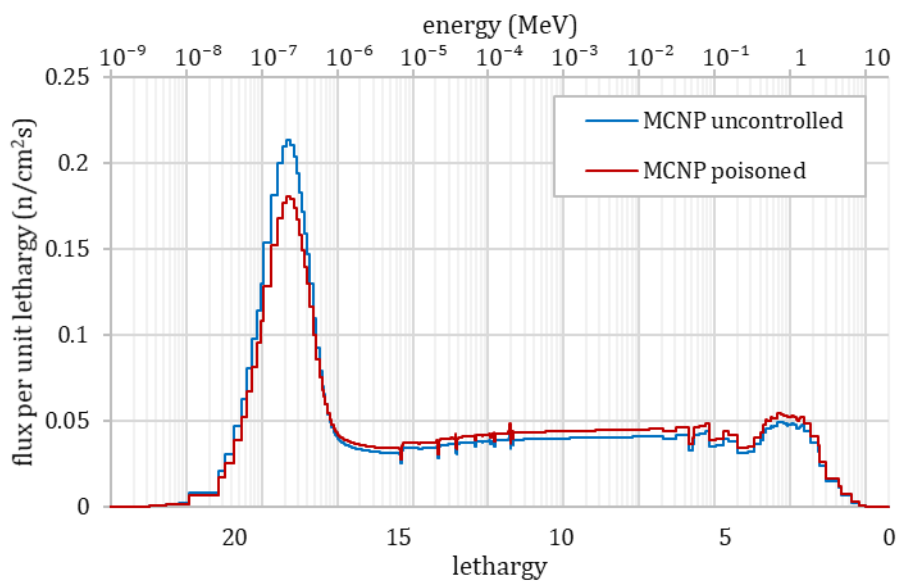

Figure 9-38. Normalized total flux per unit lethargy for MCNP cases showing the effect of using burnable poisons vs. an uncontrolled model.

9.6.2.3. Neutron Flux and Distribution

Lastly, 3 broad-group mesh tallies are compared for each case in Figure 9-39, Figure 9-40, and Figure 9-41 showing fast (E>0.1MeV), epithermal (0.1MeV>E>3eV), and thermal (E<3eV) flux distribution, respectively. For each simulation, regardless of the use of BPs, the fast distributions in Figure 9-39 are all in very close agreement which is expected since the poisons are nearly transparent to fast neutrons.

The epithermal distribution shown in Figure 9-40 shows the most discrepancy between codes, but it should be noted that the scale has a more narrow range. The differences in the low-flux blue region that are visually noticeable are less than 1% and are most likely at least partly a consequence of using a limited number of particles in SCALE and MCNP.

The thermal-flux distributions in Figure 9-41 highlight the impact of the europium poisons on absorbing thermal neutrons as can be seen in the poisoned cases having a "polka-dotted" pattern across each fuel plank; again, each software produces mesh-tally results that are mutually in good agreement.

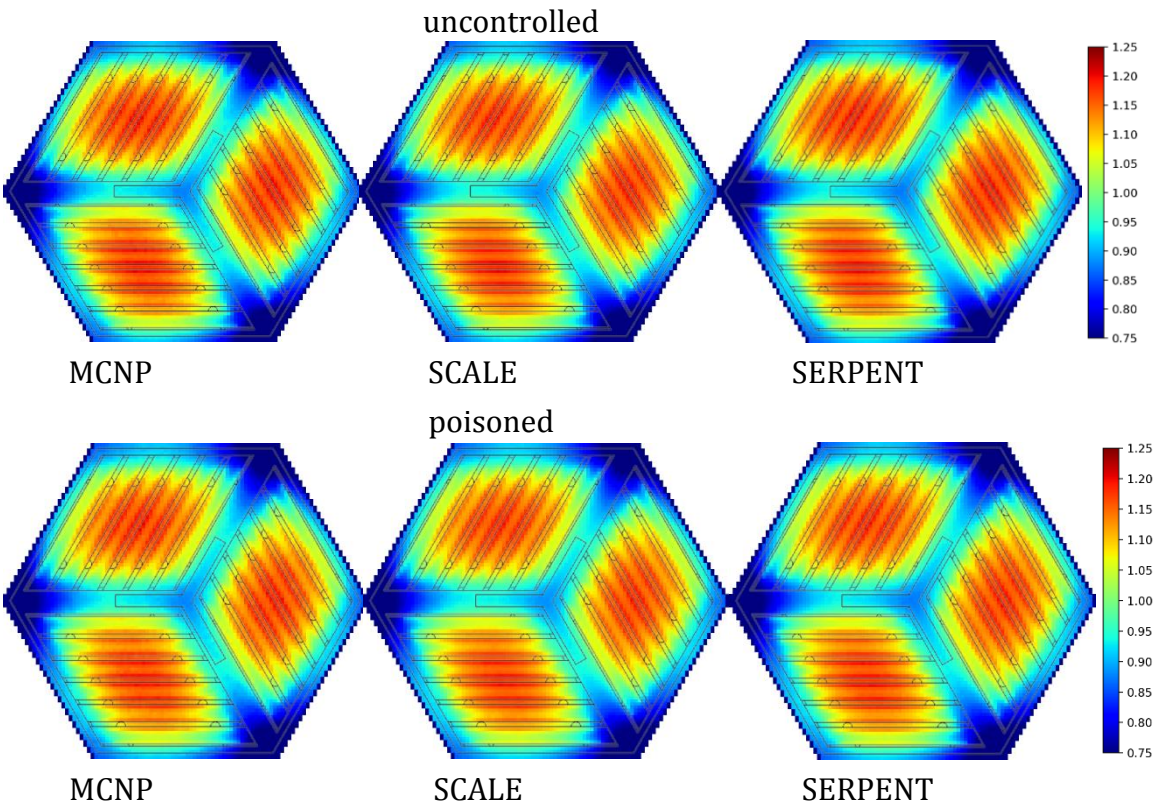

Figure 9-39. Normalized fast (E>0.1MeV) neutron flux distribution.

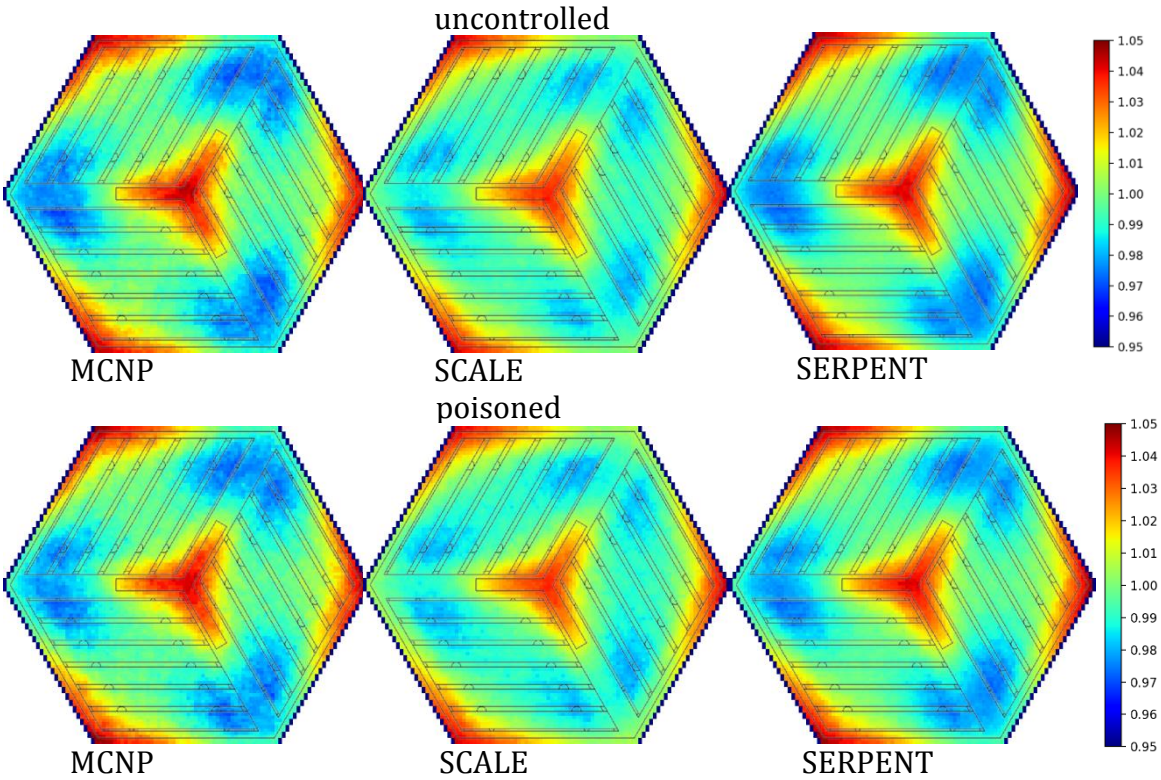

Figure 9-40. Normalized epithermal (0.1MeV>E>3eV) neutron flux distribution.

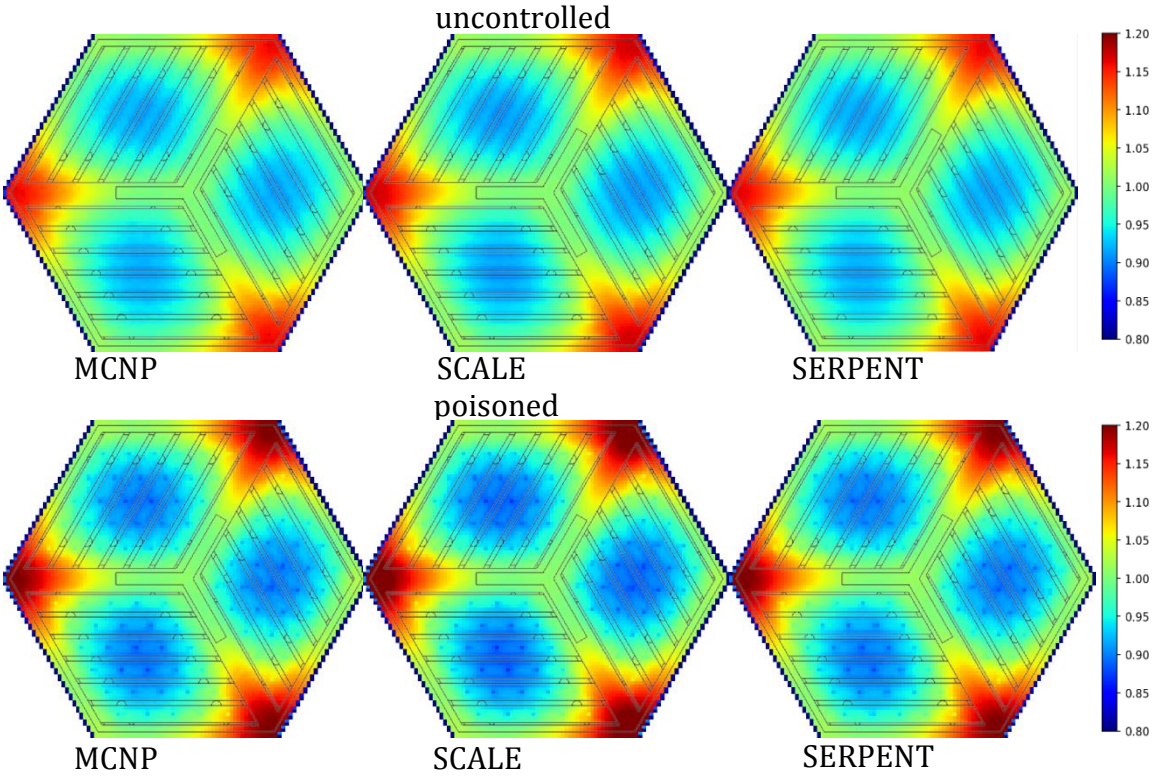

Figure 9-41. Normalized thermal (E<3eV) neutron flux distribution.

9.6.3. Summary of Codes Cross-Verification

In support of the V&V of the reactor physics analyses of FHR, focusing on Monte Carlo code packages, identical pseudo-2D fuel element models were generated for MCNP, SCALE and SERPENT code packages. In SCALE, the KENO-VI sequence was used for all simulations. Due to the complex geometry of this design, typical comparisons for fission rate distribution (e.g., pin-wise distributions in LWRs) are not applicable to FHR design. Instead, a set of relevant tallies was established, and results show very good agreement among all codes in terms of multiplication factors, peaking factors, fission density distribution, flux spectra, and flux distribution. In summary, the considered Monte Carlo codes, using continuous energy cross sections, when applied to consistent models, generated very consistent results. Lacking experimental data, this cross-verification improves our confidence into validity and applicability of these codes to analyze FHR reactors.

9.6.4. References

[1] V.K. Varma, D.E. Holcomb, F.J. Peretz, E.C. Bradley, D. Ilas, A.L. Qualls, N.M. Zaharia, "AHTR Mechanical, Structural, and Neutronic Preconceptual Design," *ORNL/TM-2012/320*, Oak Ridge National Laboratory (2011).

[2] D. Ilas, D.E. Holcomb, V.K. Varma, "Advanced High-Temperature Reactor Neutronic Core Design," *International Topical Meeting on Advances in Reactor Physics (PHYSOR) 2012*, Knoxville, TN, USA, April 15-20, 2012, ANS (2012).

[3] M.L. Huang, B. Petrovic, "Use of MCDancoff Correction Factor for Multi-Group Fuel Depletion Analyses of Liquid Salt Cooled Reactors," *PHYSOR 2014*, Kyoto, Japan, September 28 – October 3, 2014, ANS (2014).

[4] C. Gentry, G.I. Maldonado, O. Chvala, B. Petrovic, "Neutronic Evaluation of a Liquid Salt-Cooled Reactor Assembly," *Nucl. Sci. and Eng.*, **187**, 166-184 (2017).

[5] L. M. Huang, B. Petrovic, "Development of Methodology for Efficient Fuel Design Evaluation of the Advanced High Temperature Reactor (AHTR)," submitted to Annals of Nuclear Energy (2018).

[6] K. Ramey, B. Petrovic, "Monte Carlo Modeling and Simulations of AHTR Fuel Assembly to Support V&V of FHR Core Physics Methods," *Annals of Nuclear Energy*, **118**, 272-282 (2018).

[7] F. Rahnema, B. Petrovic, P. Singh, P. Burke, H. Noorani, X. Sun, G. Yoder, P. Tsvetkov, J. Zhang, D. Zhang, D. Ilas, "The Challenges in Modeling and Simulation of Fluoride-Salt-Cooled High-Temperature Reactors," *White Paper CRMP-2017-9-001*, Georgia Institute of Technology (2017).

[8] F. Rahnema, D. Zhang, B. Petrovic, D. Diamond, D. Serghiuta, C. Edgar, M. Fratoni, H.S. Gougar, A. Hawari, J. Hu, N. Hudson, D. Ilas, I. Maldonado, "Neutronics Phenomena

Identification and Ranking Table (PIRT) for Fluoride High-Temperature Reactor (FHR)," *Trans. Am. Nucl. Soc.*, **115**, 1078-1080 (2016).

[9] "MCNP—A General Monte Carlo N-Particle Transport Code," Version 6.1, LA-UR-03-1987, Los Alamos National Laboratory, Los Alamos, N.M., 2013.

[10] "SCALE 6.2.1: A Comprehensive Modeling and Simulation Suite for Nuclear Safety Analysis and Design; Includes ORIGEN and AMPX," *ORNL/TM-2005*/39, Version 6.2.1, Oak Ridge National Laboratory, Oak Ridge, Tennessee (2016).

[11] J. Leppänen, M. Pusa, T. Viitanen, V. Valtavirta, T. Kaltiaisenaho, "The SERPENT Monte Carlo Code: Status, Development, and Applications," *Ann. of Nucl. Energy*, **82,** 142-150 (2015).

9.7. Assessing Feasibility and Practicality of FHR Monte Carlo Full Core Simulations

Ultimately, reactor physics analysis needs to be performed for the full 3D core model, with adequate spatial tallies (for flux and fission power distribution), with adequate number of depletion regions, coupled with thermal-hydraulic feedback, and allowing simulation of reactivity control (control rods movements). Moreover, such simulations need to be performed over each reactor cycle (represented by a certain number of burnup steps), and each simulation needs to be adequately converged (skip sufficient number of generations), and adequately converged (simulate and tally sufficient number of active histories). Considering that even a single static (no depletion or feedback) simulation of a single fuel assembly could take several CPU days, it is clear that full calculation will require colossal computational resources.

In this section, we aim to estimate the order of magnitude of efforts needed to accomplish such prototypic analysis, on a prototypic industry-used parallel cluster. This estimate is obtained by extrapolating and synthesizing results of smaller simulations and relies on many ad hoc assumptions. As such, it is subject to large uncertainty due to over- or underestimate. It would not be surprising that the uncertainty reaches an order of magnitude, or even more; nevertheless, this estimate is expected to provide a qualitative indication of the level of difficulty in making such analyses practical.

9.7.1. Impact of Tallies on Simulation Runtime

We start by investigating one weak point of most Monte Carlo codes, reduction in execution speed due to tallying, which may be very significant. Of course, in order to produce useful results, any simulations has to use tallies to obtain information on local power, spectra, fluxes, fuel isotopic changes, and so on. Most codes incorporate multiple options and multiple approaches, offering multiple tally types. The so called mesh tallies are usually very efficient and introduce only a small overhead, while some other tallies may drastically

increase the simulation time. Beside the mesh tallying capability, SERPENT offers tallies by material, cell, or universe. Runtimes needed for each type of tallies in otherwise identical SERPENT runs, for a full 3D core model, are presented in Table 9-23.

While all simulations were run in parallel on multiple cores, the results of the third column are the expected runtimes on a single core. The two spatial meshes (Cartesian and hexagonal) had virtually no impact on runtime when compared to the reference transport-only simulation. The material, cell, and universe tallies each slowed-down the simulation by a factor of about 20. This is very significant and would likely limit their use in future simulations, unless improved.

Table 9-23. SERPENT runtime for different tally types.

Tally Type	Number of Tally Elements	CPU Time to Simulate 10^6 Neutrons [h]	Slowdown Factor
None	0	2.54	1 (reference)
Cartesian Mesh	7500 (50x50x3)	2.57	1.01
Hexagonal Mesh	5776 (19x19x16)	2.56	1.01
Material	4032 (252x16)	47.1	18.9
Cell	4032 (252x16)	55.4	21.8
Universe	4032 (252x16)	51.9	20.4

9.7.2. Estimate of Runtime for a Prototypic Analysis

In a standard cycle analysis, additional factors will impact the simulation time: depletion, use of predictor/corrector methodology, thermal hydraulic feedback, criticality iterations, etc. All of them combined will increase the required runtime by more than hundred-fold from that of a single statepoint.

We consider the following prototypic analysis

- **Problem considered:** AHTR core with 252 fuel assemblies, one cycle depletion, with simplified feedback and criticality search.
- **Modeling assumptions:** 4,032 depletion regions, 5 burnup steps with predictor-corrector methodology. Thermal-hydraulic feedback and criticality assumed both resolved with 3 iterations.
- **Monte Carlo simulation parameters:** 10^6 neutrons per cycle, 150 inactive and 850 active generations.
- **Tallying:** 4,032 depletion regions, using either the materials tally currently available in SERPENT (20x slowdown) or a significantly more efficient mesh tally (currently in development, assumed practically no slowdown).

- **Computational resources:** parallel cluster with ~200 cores (Xeon E5 2.4 GHz or similar).

Table 9-24 summarizes the CPU time and wall-clock time obtained using these assumptions. A single analysis, over a single cycle, on a 200-CPU cluster, with current tallying approach would thus take ~10 month!! Accounting for uncertainties, this may be "as short" as one month, or as long as several years. In either case, it cannot be considered feasible.

Table 9-24. Estimated full core single cycle simulation runtime using SERPENT.

	Current material tallies	**Efficient mesh tally**
Static simulation (no depletion) on a single core, 10^6 histories, no tallies	2.4 h	2.4 h
Static simulation on a single core, 10^6 hist per generation, 1,000 generations, no tallies	2,400 h	2,400 h
Same, with tallies	48,000 h	2,400 h
Each burnup step with predictor/corrector (2x), with thermal hydraulic feedback and criticality search (3 iterations)	288,000 h	14,400 h
Same, on a 200-CPU cluster, assuming perfect parallel effiiency	1,440 h	72 h
Cycle depletion (5 steps) with T/H feedback and criticality iterations	**7,200 h (~10 months)**	**360 h (~2 weeks)**

With more efficient tallying, the wait time is reduced to ~2 weeks. This is definitely feasible, and acceptable for performing a single benchmark analysis, or perhaps even a small, limited number of analyses, but clearly not practical for repetitive design or safety/licensing analyses.

In summary, assuming that more efficient tallying is developed and implemented, full Mont Carlo simulation is feasible for single benchmark cases, or very few confirmatory analyses, but far from practical for design or licensing multiple analyses.

9.8. Conclusions

To support the verification and validation of neutronics simulation tools, codes, and methodologies, a set of benchmark problems typical of FHRs has been developed. The

problem was derived from the AHTR concept by simplifying the geometry and material specification of the original conceptual design while retaining the multiple heterogeneities and major physical characteristics of the core that are important from the neutronics point of view. The fuel assembly and core benchmark problems can be used with the desired complexity in "2D" and 3D configurations including single or multi-assembly to whole core problems. The continuous energy COMET method/code was used to solve these benchmark problems. The eigenvalue and fission density distributions predicted by COMET agree very well with those computed by MCNP. The benchmark calculations against Monte Carlo have also indicated that the continuous energy COMET can serve as an excellent method for obtaining high fidelity solutions (e.g., the stripe-wise fission density distribution) to FHR full core problems because of COMET's high fidelity and high computational efficiency. As a result, the stripe-wise fission density distributions generated by the continuous energy COMET can be taken as a reference solution to the stylized FHR benchmark problems.

In addition, main Monte Carlo codes SCALE, SERPENT and MCNP were employed and evaluated in this study. A reduced-size core model consisting of a finite-height slice of a single fuel element was developed and employed with appropriate boundary conditions.

Sensitivity studies to quantify impact of modeling approaches and nuclear data produced the following results and findings:

- Detailed flux distribution was examined for three coarse energy groups: thermal – up to 3 eV; intermediate – 3 eV to 1 MeV; fast – above 1 MeV. Peaking factors were 1.133, 1.025, and 1.223 for the three groups, respectively. Fast flux peaks in fuel stripes, while the thermal flux peaks where the Y-shape meets the assembly wrapper.
- AHTR fuel assembly consists of three identical regions, rotated relative to each other by 120°; this corresponds to periodic BCs in infinite lattice simulations. If instead a reflective BC was applied (e.g., aiming to reduce the size of the problem to one third of assembly), the introduced error in the eigenvalue difference is negligible, i.e., 7 ± 3 pcm. However, impact on the flux distribution—while also limited—is more pronounced, with deviations from the correct solution being ±2.0%, ±0.6 and ±4.0%, for the three groups.
- Fuel performance will be impacted by the individual (local) power i.e., fission density, of each TRISO particle (each kernel). Therefore, non-uniformity in the fission density of individual kernels was examined; normalized values range from 0.920 to 1.195 with 1σ of 0.006. That is, within-assembly local peaking factor is about 1.2.
- Variation in neutron spectra in different materials and regions was examined and compared against the assembly-averaged spectrum. Ten different regions were considered including fuel, plank "meat", graphite matrix, assembly wrapper, internal and external FLiBe, and so on. Over most of the energy range the difference in spectrum is just a few percent, remaining within ±10% between approximately 0.1 eV and 1 MeV, and increasing toward ±20% below 0.1eV and reaching +30% around 5 MeV.
- Impact of the number of histories on the precision and error propagation of depletion calculations was examined. The simulations used 33 burnup steps to deplete fuel to a burnup of 100 MWd/kgHM. Reference calculation used 10^8 active histories per burnup step, requiring around 1000 hours on 24 CPUs, with the corresponding standard deviation in eigenvalue of 6 pcm. Cases denoted as "standard" and "preliminary" used 10

times and 100 times fewer histories, respectively, with the corresponding standard deviation of eigenvalue of 21 and 60 pcm. Maximum differences over many isotopes were in the 0.2-0.3% range for the former, and in the 0.5-1.0% range for the latter, with typical differences being notably smaller.

- The AHTR assembly contains multiple carbonaceous materials of different forms, compositions, and temperatures. Impact of this variability was examined by assigning a specific temperature and specific thermal scattering data (S(α,β) matrices) to each carbonaceous region. Variation in the eigenvalue was in all cases within a few hundred pcm, so not large but not negligible either.
- Thermalization of neutrons is largely due to carbonaceous materials, and significantly less to FLiBe. Moreover, while the FLiBe density is determined by the temperature, and does not change much, density of carbonaceous materials can vary significantly (from several percent to up to about ten percent) depending on the exact form and production process. Changing the density of all carbonaceous materials by 10% result in a significant change of eigenvalue, around 1750 pcm, with fractional contributions of each component consistent with its mass and volume fraction.
- SERPENT was found to scale well for parallel simulations up to the considered maximum number of 32 CPUs. Some degradation of parallel efficiency (to 80%) was observed, but it may be due to the weak scaling performed in this assessment. Future studies may consider a larger cluster (more CPUs) and perform both weak and strong scaling assessment.

This chapter also presents results of cross-verification through cross-comparison of the results of the three Monte Carlo codes, SCALE, SERPENT and MCNP. Detailed comparisons have demonstrated that the codes produce consistent results when applied to carefully developed consistent models. Results show very good agreement among all codes in terms of the multiplication factor, peaking factors, fission density distribution, flux spectra, and flux distribution.

Finally, regarding the computational resources required, extrapolating requirements to full core simulations shows that a single or a very limited number of benchmark simulations—while taking long time (days/weeks on a parallel cluster) and high memory—is feasible, but it is still far from being practical, and development of improved and novel methodologies is needed.

Appendix A. Fission density distributions

The radially integrated axial fission density distribution in the core for the all control blades out, all control blades in and the critical core configurations are presented in Tables A.1-A.3. The normalized assembly-averaged FD and the normalized stripe-wise FDDs in selected fuel assembly coarse meshes at two axial slices/levels are provided in Tables A.4-A7. The assembly-averaged FDs are normalized to the total number of fuel assembly coarse meshes in the core (4,032). The stripe-wise FDD is normalized to the total number of fuel stripes in all the coarse meshes in the core (145,152). The following indexing is used to identify the locations for which fission density distributions are provided.

- The axial levels are denoted by the indices 1 – 16 from the bottom to the top.
- The selected assemblies are denoted by the index "iz-X", where "iz" represents the axial level index, and "X" stands for the radial locations ("A"-"E") as shown in Figure A.1.
- The fuel stripes are denoted by the indices 1 – 32 as shown in Figure A.2.

The one-sigma statistical uncertainty for the FDs are as follows.

- The axial FD uncertainty is less than 0.0002%
- The assemble averaged FD uncertainty is less than 0.003%
- The stripe-wise FD uncertainty is less than 0.02%

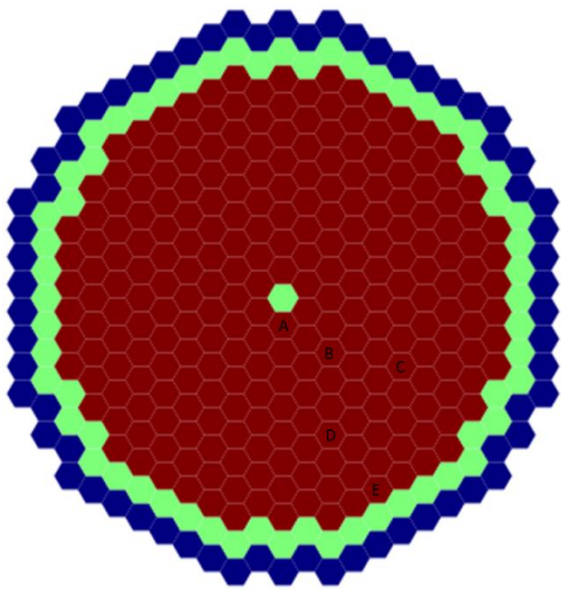

Figure A.1. Location for the locations selected fuel assemblies are identified by letters A-E

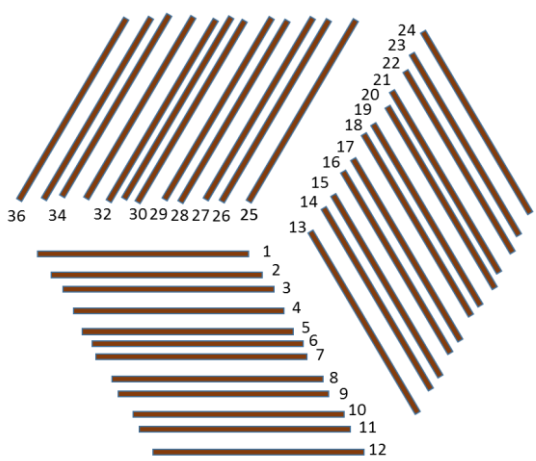

Figure A.2. Fuel stripe indices

Table A.1. Normalized radially-integrated axial FDs computed by COMET for FC-ABO

Axial Level	1	2	3	4	5	6	7	8
Axial FD	0.4378	0.6254	0.8249	1.0007	1.1477	1.2617	1.3395	1.3787
Axial Level	9	10	11	12	13	14	15	16
Axial FD	1.3782	1.338	1.2593	1.1442	0.9962	0.8195	0.619	0.4293

Table A.2. Normalized radially-integrated axial FDs computed by COMET for FC-ABI

Axial Level	1	2	3	4	5	6	7	8
Axial FD	0.3832	0.5951	0.811	1.0019	1.162	1.2863	1.3711	1.4137
Axial Level	9	10	11	12	13	14	15	16
Axial FD	1.4128	1.3685	1.2821	1.1562	0.9948	0.8029	0.5861	0.3721

Table A.3. Normalized radially-integrated axial FDs computed by COMET for FC-CRT

Axial Level	1	2	3	4	5	6	7	8
Axial FD	0.4235	0.6178	0.8215	1.0011	1.1513	1.2679	1.3474	1.3875
Axial Level	9	10	11	12	13	14	15	16
Axial FD	1.3869	1.3457	1.2651	1.1474	0.9961	0.8155	0.6109	0.4145

A.4. Normalized assembly averaged fission densities computed by COMET for the selected assemblies

Assembly / Core	1-A	1-B	1-C	1-D	1-E	9-A	9-B	9-C	9-D	9-E
FC-ABO	0.8278	0.686	0.4989	0.4724	0.2404	2.63	2.1585	1.5684	1.4848	0.7592
FC-ABI	0.812	0.5966	0.4178	0.3957	0.2282	3.0122	2.204	1.5425	1.4604	0.8349
FC-CRT	0.2562	0.3073	0.3198	0.4405	0.5366	0.8522	1.0105	1.0522	1.4438	1.7521

A.5. Normalized stripe-wise fission densities computed by COMET for the selected assemblies in the FC-ABO benchmark problem

Stripe / Assembly	1	2	3	4	5	6	7	8	9	10	11	12
1-A	0.9041	0.8513	0.8304	0.8028	0.7913	0.7765	0.7712	0.7675	0.7686	0.7787	0.7895	0.8239
1-B	0.7434	0.7133	0.7023	0.6888	0.6835	0.678	0.6766	0.6782	0.6812	0.6929	0.7034	0.7351
1-C	0.5502	0.5289	0.5211	0.5121	0.5086	0.5055	0.5049	0.5072	0.5098	0.5195	0.5278	0.5525
1-D	0.5225	0.4991	0.4901	0.4784	0.4734	0.4672	0.4648	0.4634	0.464	0.4695	0.4752	0.4942
1-E	0.2665	0.2536	0.2484	0.2417	0.2387	0.2348	0.2333	0.2321	0.2322	0.2347	0.2375	0.247
9-A	2.8853	2.7076	2.6367	2.5421	2.5025	2.452	2.4337	2.4212	2.4251	2.4592	2.4955	2.6088
9-B	2.3424	2.2453	2.2091	2.1647	2.1474	2.1294	2.125	2.1313	2.1418	2.1814	2.2166	2.3209
9-C	1.7319	1.663	1.6375	1.6077	1.5962	1.5861	1.5842	1.5921	1.6014	1.634	1.6616	1.7425

9-D	1.6446	1.5694	1.54	1.5018	1.4855	1.4656	1.4581	1.4546	1.4572	1.4763	1.4956	1.5582
9-E	0.8381	0.7969	0.78	0.7582	0.7484	0.7364	0.7315	0.7286	0.7293	0.7386	0.7483	0.7804
Stripe / Assembly	13	14	15	16	17	18	19	20	21	22	23	24
1-A	0.8559	0.8298	0.8231	0.8221	0.8259	0.8431	0.8572	0.8946	0.9209	0.9846	1.0278	1.1347
1-B	0.7165	0.6893	0.6802	0.6704	0.6676	0.6676	0.6699	0.6788	0.6862	0.7054	0.7197	0.7572
1-C	0.5089	0.4912	0.4857	0.4803	0.4792	0.4808	0.4834	0.4913	0.4976	0.5131	0.5245	0.5533
1-D	0.496	0.4795	0.4744	0.47	0.4693	0.4717	0.4746	0.4833	0.4899	0.506	0.5175	0.5468
1-E	0.2432	0.2346	0.2323	0.2309	0.2314	0.2343	0.2369	0.2436	0.2483	0.2592	0.2666	0.2845
9-A	2.7115	2.63	2.61	2.61	2.6248	2.687	2.7371	2.8696	2.9622	3.1862	3.3374	3.7081
9-B	2.2552	2.1678	2.1382	2.1059	2.0968	2.0966	2.104	2.1334	2.1581	2.222	2.2695	2.3927
9-C	1.6001	1.5431	1.5251	1.507	1.5035	1.5083	1.5166	1.5427	1.5635	1.6147	1.6521	1.7465
9-D	1.5597	1.5066	1.4899	1.4749	1.4724	1.4798	1.4891	1.5175	1.539	1.5921	1.6299	1.7255
9-E	0.767	0.7381	0.7299	0.7247	0.7256	0.7345	0.7427	0.7641	0.7793	0.8146	0.8389	0.8971
Stripe / Assembly	25	26	27	28	29	30	31	32	33	34	35	36
1-A	0.8222	0.7875	0.7756	0.761	0.7564	0.7524	0.7527	0.7577	0.7633	0.7785	0.7911	0.8261
1-B	0.7168	0.684	0.6723	0.6573	0.652	0.6465	0.6456	0.6481	0.6518	0.6631	0.6729	0.701
1-C	0.5234	0.4971	0.4873	0.4741	0.469	0.4627	0.4608	0.4601	0.4614	0.4668	0.4723	0.4894
1-D	0.4797	0.4578	0.4501	0.4402	0.4368	0.4331	0.4326	0.4342	0.4368	0.4442	0.4508	0.4694
1-E	0.2416	0.2319	0.2285	0.2249	0.2238	0.2238	0.2244	0.228	0.231	0.2395	0.2459	0.2636
9-A	2.5965	2.4855	2.4471	2.4002	2.3852	2.3727	2.3738	2.3908	2.4093	2.4596	2.5011	2.6156
9-B	2.2569	2.1522	2.1144	2.0663	2.0493	2.0319	2.0293	2.0381	2.0507	2.0883	2.1206	2.2125
9-C	1.6467	1.5631	1.5316	1.4894	1.4731	1.4532	1.4471	1.4456	1.4503	1.4688	1.4871	1.5435
9-D	1.5086	1.439	1.4143	1.3824	1.3715	1.36	1.3586	1.3643	1.373	1.3978	1.4196	1.4807
9-E	0.7659	0.7356	0.725	0.7144	0.7111	0.7121	0.7149	0.7282	0.7387	0.7689	0.7912	0.8524

A.6. Normalized stripe-wise fission densities computed by COMET for the selected assemblies in the FC-ABI benchmark problem

Stripe / Assembly	1	2	3	4	5	6	7	8	9	10	11	12
1-A	0.8474	0.7975	0.7771	0.7562	0.7479	0.7443	0.7446	0.7533	0.7604	0.7812	0.796	0.8362
1-B	0.6073	0.5897	0.5834	0.5819	0.5825	0.5907	0.596	0.6109	0.6201	0.642	0.6561	0.6919
1-C	0.4284	0.4171	0.4134	0.4135	0.4145	0.4216	0.426	0.4379	0.445	0.4619	0.4726	0.4994
1-D	0.4065	0.3931	0.388	0.3853	0.3848	0.3885	0.3911	0.3992	0.4043	0.4171	0.4254	0.4472
1-E	0.227	0.2191	0.2161	0.2143	0.2138	0.2158	0.2172	0.222	0.225	0.2327	0.2379	0.2511
9-A	3.1525	2.9592	2.8796	2.7964	2.7635	2.7474	2.7478	2.7798	2.8067	2.8862	2.9432	3.0965
9-B	2.2469	2.1793	2.155	2.1478	2.149	2.1787	2.1986	2.2544	2.2891	2.3723	2.426	2.5617

9-C	1.584	1.5407	1.5259	1.5252	1.5285	1.5541	1.5706	1.6148	1.6419	1.7057	1.7464	1.8479
9-D	1.503	1.4516	1.4321	1.421	1.4184	1.4317	1.4413	1.4718	1.4911	1.5395	1.5713	1.6539
9-E	0.8327	0.8025	0.7907	0.7832	0.781	0.7878	0.7929	0.8102	0.8216	0.8504	0.8696	0.919
Stripe / Assembly	13	14	15	16	17	18	19	20	21	22	23	24
1-A	0.7706	0.7629	0.7653	0.7867	0.8037	0.8512	0.8824	0.9551	0.9999	1.1002	1.1626	1.3078
1-B	0.5703	0.5563	0.5527	0.5562	0.5608	0.5771	0.588	0.6132	0.6281	0.6595	0.6786	0.7215
1-C	0.3914	0.3823	0.3802	0.3831	0.3866	0.3984	0.4063	0.4242	0.4349	0.4571	0.4705	0.5006
1-D	0.3832	0.375	0.3731	0.3766	0.3802	0.3922	0.4001	0.4181	0.4286	0.4509	0.4642	0.4943
1-E	0.214	0.207	0.2051	0.2063	0.2082	0.2151	0.2198	0.2306	0.2371	0.2507	0.2589	0.2772
9-A	2.8526	2.8238	2.8326	2.9136	2.9779	3.159	3.2788	3.5593	3.7335	4.1246	4.3696	4.9385
9-B	2.1083	2.0549	2.0408	2.0526	2.0688	2.1284	2.1687	2.2623	2.3182	2.437	2.5094	2.6725
9-C	1.4457	1.4111	1.4027	1.4129	1.4253	1.4685	1.4976	1.5642	1.604	1.6879	1.7391	1.8534
9-D	1.4155	1.384	1.3766	1.3886	1.4014	1.4454	1.4744	1.5413	1.5808	1.6648	1.7155	1.8296
9-E	0.7816	0.7552	0.7483	0.7524	0.7593	0.7848	0.8022	0.8427	0.8669	0.9183	0.9495	1.0188
Stripe / Assembly	25	26	27	28	29	30	31	32	33	34	35	36
1-A	0.7113	0.6904	0.6841	0.6833	0.6855	0.6987	0.708	0.7304	0.7444	0.7747	0.794	0.8379
1-B	0.5716	0.5513	0.5444	0.5405	0.5405	0.5482	0.554	0.5693	0.5791	0.6011	0.6151	0.6477
1-C	0.4049	0.389	0.3832	0.3789	0.378	0.3818	0.385	0.3941	0.4	0.4137	0.4226	0.4435
1-D	0.3699	0.3574	0.3532	0.3514	0.3518	0.3574	0.3617	0.3723	0.3791	0.3941	0.4037	0.4256
1-E	0.2176	0.2124	0.2108	0.2119	0.2131	0.2191	0.2229	0.2332	0.2396	0.2553	0.2654	0.2903
9-A	2.6295	2.5506	2.5268	2.5233	2.5315	2.5804	2.6153	2.6988	2.7514	2.8655	2.9382	3.104
9-B	2.1135	2.0371	2.0107	1.9959	1.9958	2.0242	2.0461	2.1034	2.1401	2.2227	2.2756	2.399
9-C	1.4961	1.4362	1.4143	1.398	1.3946	1.4086	1.4206	1.4547	1.4769	1.5285	1.5618	1.6411
9-D	1.3661	1.3187	1.3031	1.2959	1.2974	1.3183	1.3342	1.374	1.3995	1.4557	1.4918	1.5748
9-E	0.7959	0.7765	0.7707	0.7749	0.7792	0.8016	0.8159	0.8547	0.8789	0.9384	0.9767	1.0713

A.7. Normalized stripe-wise fission densities computed by COMET for the selected assemblies in the FC-CRT benchmark problem

Stripe / Assembly	1	2	3	4	5	6	7	8	9	10	11	12
1-A	0.2373	0.2302	0.2279	0.228	0.2288	0.2336	0.2368	0.2452	0.2505	0.2628	0.2707	0.2901
1-B	0.3218	0.3102	0.3064	0.3021	0.3008	0.3002	0.3008	0.3036	0.3063	0.3139	0.32	0.3369
1-C	0.3011	0.2943	0.2925	0.2947	0.2969	0.305	0.3102	0.3229	0.3308	0.3487	0.3601	0.3872
1-D	0.4638	0.449	0.4444	0.4401	0.4394	0.4405	0.4425	0.4487	0.4538	0.467	0.4773	0.5044
1-E	0.5561	0.5317	0.5228	0.5124	0.509	0.5071	0.5083	0.5159	0.5229	0.5439	0.5604	0.6049
9-A	0.7866	0.7617	0.7535	0.7529	0.7552	0.7706	0.7812	0.809	0.8267	0.868	0.8948	0.9599

9-B	1.059	1.0199	1.0067	0.9917	0.9874	0.9852	0.9872	0.997	1.0064	1.0326	1.0538	1.1113
9-C	0.9923	0.9688	0.9624	0.9687	0.9755	1.0018	1.019	1.0611	1.0875	1.1471	1.1854	1.2761
9-D	1.5216	1.4714	1.4556	1.4403	1.4374	1.4408	1.4472	1.4684	1.4857	1.531	1.5659	1.6574
9-E	1.8096	1.7291	1.6998	1.6662	1.6557	1.6522	1.6582	1.6886	1.7157	1.7934	1.8531	2.0121
Stripe / Assembly	13	14	15	16	17	18	19	20	21	22	23	24
1-A	0.2682	0.2609	0.2581	0.2583	0.2587	0.2637	0.2664	0.2746	0.2788	0.2895	0.2957	0.3117
1-B	0.3221	0.3075	0.3022	0.2955	0.2931	0.2907	0.2906	0.2921	0.2941	0.3001	0.305	0.3187
1-C	0.3088	0.2962	0.2917	0.2893	0.2895	0.2946	0.2984	0.3089	0.3153	0.33	0.3391	0.3607
1-D	0.4505	0.4303	0.4231	0.4138	0.4106	0.4074	0.4073	0.4095	0.4124	0.4208	0.4278	0.4469
1-E	0.5641	0.5417	0.5339	0.5255	0.5228	0.5222	0.5235	0.5299	0.5352	0.5496	0.5603	0.5888
9-A	0.9023	0.8776	0.8678	0.868	0.8687	0.8847	0.8932	0.9197	0.9333	0.9687	0.9891	1.0428
9-B	1.0595	1.0107	0.9928	0.9701	0.962	0.9542	0.9538	0.9596	0.9668	0.988	1.0052	1.0524
9-C	1.0177	0.9756	0.9603	0.9519	0.9521	0.9683	0.9809	1.0154	1.0369	1.0862	1.1171	1.1903
9-D	1.4774	1.41	1.3858	1.3546	1.3438	1.3333	1.3331	1.3413	1.3517	1.3813	1.4057	1.4718
9-E	1.8337	1.7594	1.7331	1.7048	1.6956	1.6936	1.6981	1.7201	1.7384	1.7881	1.8247	1.9216
Stripe / Assembly	25	26	27	28	29	30	31	32	33	34	35	36
1-A	0.2389	0.2312	0.2288	0.2288	0.2298	0.2356	0.2398	0.2501	0.2568	0.2717	0.2813	0.303
1-B	0.3316	0.3166	0.3113	0.3047	0.3025	0.3004	0.3003	0.3022	0.3043	0.3103	0.3153	0.3293
1-C	0.3206	0.3097	0.306	0.305	0.3057	0.312	0.3164	0.3282	0.3356	0.3528	0.3637	0.3891
1-D	0.4835	0.4596	0.4506	0.439	0.4346	0.4297	0.4283	0.4289	0.4307	0.4372	0.4429	0.4605
1-E	0.5614	0.5386	0.5308	0.5227	0.52	0.519	0.5195	0.5242	0.5281	0.5392	0.5477	0.5719
9-A	0.7908	0.7651	0.7571	0.7572	0.7609	0.7807	0.795	0.8304	0.8533	0.9042	0.9372	1.0116
9-B	1.0912	1.0412	1.0232	1.0011	0.9936	0.9869	0.9867	0.9932	1.0005	1.0214	1.0384	1.0862
9-C	1.0558	1.0192	1.0067	1.0032	1.0051	1.0259	1.0406	1.0798	1.1044	1.1615	1.1977	1.2826
9-D	1.586	1.5065	1.4767	1.4381	1.4234	1.4071	1.4029	1.4054	1.4119	1.4346	1.4547	1.5147
9-E	1.8434	1.7664	1.7394	1.7114	1.7015	1.6977	1.6988	1.7142	1.7268	1.764	1.7923	1.8733

10. Verification and Validation of Thermal Hydraulics Codes, Tools, and Methodologies in Support of Licensing

Verification and validation (V&V) of analysis tool is one of the challenges for Fluoride salt-cooled High-temperature Reactor (FHR) can be commercially deployed. To support reactor licensing, the applicability of existing analysis tools to FHR modeling, simulation, and safety analysis need to be carefully evaluated with appropriate experimental data. Characterization of challenges of model and code V&V is an important first step to enhance our understanding of the reactor response under different transient and accident scenarios, and to further improve the reactor design. Therefore, V&V of thermal hydraulics modeling and simulation tools in support of FHR licensing becomes the main objective of this task. Advanced High Temperature Reactor (AHTR), one of the FHR design concepts, is adopted as the FHR reference design in this report.

A thermal hydraulics phenomena identification and ranking table (TH-PIRT) study was performed in parallel with a neutronics and structural material PIRT studies for the AHTR. In the TH-PIRT study, the key thermal hydraulics phenomena that warrant further study and research for AHTR analysis are identified to support the validation of thermal hydraulics system-level analysis codes and computational fluid dynamics simulation (CFD) tools. Four major limitations on current system-level analysis codes of obtaining high accuracy simulation results are also identified in this task. A review of system analysis codes that are commonly used in nuclear thermal hydraulics analysis and CFD simulation codes are carried out. In addition, a literature review of the analysis performed earlier in the literature for AHTR is also included in this report.

The primary objective of this study is to perform a code validation with existing data to evaluate the fidelity and accuracy of the simulation results. Two system-level codes, namely RELAP5 SCDAPSIM/MOD 4.0 and System Analysis Module (SAM), are selected for benchmark study due to their potential thermal hydraulics modeling and capabilities for AHTR. Experimental data from a single-phase natural circulation loop is used as one of the code validation studies. In addition, experimental data from a low-temperature DRACS test facility (LTDF) is also utilized for RELAP5 and SAM code validation. An extensive test matrix was developed for the LTDF tests including DRACS startup and pump trip scenario. The code simulation results of RELAP5 and SAM show good agreement with the experimental data. A high-temperature fluoride salt test facility (HT-FSTF) has been designed and constructed for testing heat exchangers and performing transient natural circulation tests. The experimental data of these experiments will be used for the further code validation once they become available.

Once good agreement between RELAP5/SCDAPSIM/MOD 4 simulation results and molten salt experimental data is obtained, the code is also used for AHTR thermal hydraulics transient analysis to demonstrate the safety of the AHTR design. An AHTR reactor model has been developed in RELAP5 with the fluted tube DRACS heat exchanger (DHX) and

natural draft DRACS heat exchanger (NDHX) designs proposed in a parallel study of this integrated research project (IRP). Reactor steady-state normal operation and two transient scenarios, namely, loss of forced circulation (LOFC) and loss of multiple DRACS loops are analyzed using the RELAP5 AHTR model. During the transients, the decay heat is removed by the ambient air, fully relying on passive natural circulation/convection. The simulated results of both transient scenarios show a sufficient decay heat removal capability by the proposed DRACS design in the AHTR. Our study indicates that RELAP5 and SAM are potentially applicable to FHR thermal hydraulic system analysis. Further code validation will be performed once the experimental data from HT-FSTF become available in the future.

10.1. Address phenomena identified by a PIRT panel for a reference FHR design

The purpose of thermal hydraulics phenomena identification and ranking table (TH-PIRT) is to support FHR modeling, safety analysis, and ultimately licensing by identifying key phenomena that potentially impose significant challenges on thermal hydraulics modeling and simulation of an FHR reference design, i.e., AHTR. A TH-PIRT panel was assembled to perform the PIRT study focused on the thermal hydraulics of the AHTR. Two accident scenarios, namely, the SBO and simultaneous withdrawal of all control rods, were discussed in detail by the panel during a 2.5-day PIRT study. For the event of SBO, four FOMs were identified, namely the peak vessel temperature, DRACS coolant temperature in the NDHX, peak temperature of the DHX, and average temperature increase of the carbonaceous materials in the core. For the event of simultaneous withdrawal of all control rods, the hot-leg salt temperature and maximum kernel temperature were defined as the FOMs. During the TH-PIRT study, phenomena identification, importance rankings, and knowledge level rankings were performed. In addition, the phenomena that were recommended by the panel for further consideration are discussed and for some of those phenomena, corresponding path forward is also proposed. It is suggested that further research be carried out to increase our knowledge levels, improve the current AHTR design, and perform design evaluation and safety analysis for the AHTR. Furthermore, the panel strongly suggested multidimensional CFD simulations and system-level analyses coupled with neutronics analysis be performed for AHTR safety margin quantification during reactor normal operation as well as transient and accident conditions.

For the event of SBO, the following phenomena require further investigation:

- Geometry of the fuel plates, i.e., those deviations from their original geometry
- Thermal conductivity of FLiBe
- Viscosity of FLiBe
- Wall friction in the core
- Core flow asymmetry
- Upper plenum mixing
- Fluidic diodicity
- Lower plenum mixing
- DHX performance
- NDHX performance

- DRACS piping heat loss
- Chimney natural circulation and performance
- KF-ZrF_4 thermo-physical properties

For the event of simultaneous withdrawal of all control rods, the following phenomena are categorized further investigation are needed:

- Thermal conductivity of the carbonaceous materials
- Thermal conductivity of fuel stripe
- Thermal conductivity of FLiBe
- Viscosity of FLiBe
- Core heat transfer coefficient
- Primary coolant flow bypass fraction
- Upper plenum mixing
- Heat transfer to fusible links for the control rods
- Primary pump performance
- P-IHX performance
- Intermediate pump performance
- I-PHX performance
- Power cycle performance

It should be noted that while the AHTR was used as the reference design for the current TH-PIRT study, the identified TH-PIRTs are expected to be generally cross-cutting to other FHR designs [10.1-2].

10.2. Identify requirements on codes/methodologies to support licensing

Thermal hydraulics modeling is critical for reactor safety analysis and licensing review to ensure that the reactor design is able to stay in the safe condition during reactor normal operation, transient and accident conditions. Thermal hydraulics modeling should obtain the ability of evaluating the decay heat removal and thermal hydraulics impacts on overall system integrity. In addition to the safety analysis, optimization of plant economics performance via thermal hydraulics analysis is essential for designing a reactor system, including pumping power, heat exchanger size and salt inventory. Computational analyses need to be verified and validated (V&V) to evaluate the code reliability by comparing simulation results with analytical solutions and scaled experimental data. Furthermore, it is vital to understand the gaps and limitations of the codes in analyzing FHRs since most of the current system analysis codes were mainly developed for light water reactors (LWRs) and need to be modified for their applications to FHRs.

The following issues identified in this section include some limitation and gaps in the system-level analysis codes such as RELAP5 and TRACE, some of the issues also exist in the CFD code.

- Large uncertainties in liquid salt thermophysical properties
- Lack of heat transfer and friction factor models/correlations for advanced/novel heat exchanger designs
- Lack of capability in modeling phase change between liquid and solid phases
- Coupling thermal hydraulics and neutronics analysis

Large uncertainties in liquid salt thermophysical properties

Thermophysical properties of liquid salts vary considerably from one experiment to the other. For example, the measured thermal conductivity of FLiNaK ranges from 0.6 to 4.5 W/m-K from the literature [10.3]. For code analysis, the molten salt thermophysical properties in each system code should be consistent. In addition, it is noted that the uncertainties of the thermophysical properties can be significant. For example, the uncertainty of the reported viscosity is estimated to about 10% [10.3]. The salt thermophysical property uncertainty will lead to considerable deviations in code simulations such as the temperature and heat transfer coefficient. Therefore, it is strongly suggested that the used molten salt properties should be clearly reported in any code analysis. Furthermore, the code simulation results could also provide an analysis of the effect of salt thermophysical property uncertainties on the code simulation results.

Lack of heat transfer and friction factor models/correlations for advanced/novel heat exchanger designs

There are various designs of heat exchangers proposed for the advanced reactors due to their improved heat transfer performance, such as coiled tube and fluted tube heat exchangers. Heat transfer correlations for some of these advanced heat exchanger designs have not been fully developed for molten salt. Also, to better simulate the heat transfer and fluid flow in an integral system, system-level codes should be flexible in implementing heat transfer and pressure drop models/correlations for specific heat exchanger designs. In our study, some transient tests, including DRACS startup and pump trip scenarios, were performed in our Low-Temperature DRACS test facility (LTDF) to investigate the thermal performance of the scaled-down DRACS facility. In our benchmark study of the LTDF RELAP5/SCDAPSIM/MOD4.0, the code results initially showed under-predicted temperatures in the primary loop when using the default built-in heat transfer correlations. The heat transfer correlations for the bundle and finned tubes were later implemented into the code and improved benchmark results were obtained with the experimental data [10.4]. For the friction coefficient, Zweibaum et al. pointed out, based on the benchmark results of the CIET test facility that RELAP5-3D over-predicted the natural circulation mass flow in the transition regime. The CIET test facility was designed primarily for testing natural circulation performance using Dowtherm A oil as the working fluid. It was suggested that the friction factor correlations should be further investigated in the RELAP5-3D code [10.5].

Lack of capability in modeling of phase change between liquid and solid phases

In FHRs, molten salt works in the liquid state as coolant. However, molten salt solidification may occur during an overcooling accident such as overcooling by air in the cold leg of a DRACS loop. The partial flow blockage by the solid salt will result in higher flow resistance and higher pressure drop in the loop. This issue of molten salt solidification and re-melting need to be further investigated both in experiments and thermal hydraulics modeling and analysis. System-level analysis codes, such as RELAP5 and TRACE, currently have limited

capabilities in modeling the phase change phenomena between the liquid and solid phases since these are not issues in the light water reactors.

Coupling thermal hydraulics and neutronics analysis

In reactor safety analysis, the most critical component is non-arguably the reactor core. To ensure the safety of the reactor operation, it is critical to investigate the coupling of the thermal-hydraulics and neutronic analysis to take into account important multiphysics phenomena such as the thermal feedback effects to reactor physics analysis. In AHTR, the control rods (control blades) are independently driven and connected to their own leader rods and control rod blades drive. During a thermal hydraulics PIRT panel exercise, the panelists pointed out that the event of simultaneous withdrawal of all control rods is worth investigating since this event inserts a large reactivity in a very short period time. Coupling the thermal-hydraulics and neutronic analysis is one of the key requirements to model this scenario [10.1-2].

10.3. Review the Issues with Existing Codes and Methodologies

10.3.1. Review of System Analysis Codes

RELAP5-3D

RELAP5-3D is a system analysis code developed by Idaho National Laboratory (INL) mainly for the analysis of transients and accidents in light water reactor and advanced reactors. RELAP5-3D is capable of performing multi-dimensional thermal-hydraulic and kinetic modeling. In addition, the properties of four molten salts are implemented into RELAP5-3D code, including FLiBe, FLiNaK, $NaBF_4$-NaF and NaF-ZrF_4 [10.6].

University of California, Berkeley developed a RELAP5-3D model for the pebble-bed AHTR analysis. For the verification and validation of the RELAP5-3D, the code is benchmarked against the experimental data from the CIET Test Bay, which is utilized for testing natural circulation performance [10.7]. The working fluid for the CIET Test Bay is Dowtherm A oil for representing fluoride salt in low temperature test. In the RELAP5-3D model, the heat loss model is added with 5-cm thick fiberglass insulation on the piping. The mass flow rate of simulation results is compared with the analytical results and experimental data, and both comparisons show that RELAP5-3D over-predict natural circulation mass flow rate in the transition regime (see Figure 10-1). The reason for the differences between the simulation results and experimental data may be due to the fact that the friction factor correlations are not well predicted in the code. In this research, it is suggested that the friction correlations should be further investigated in the RELAP5-3D code.

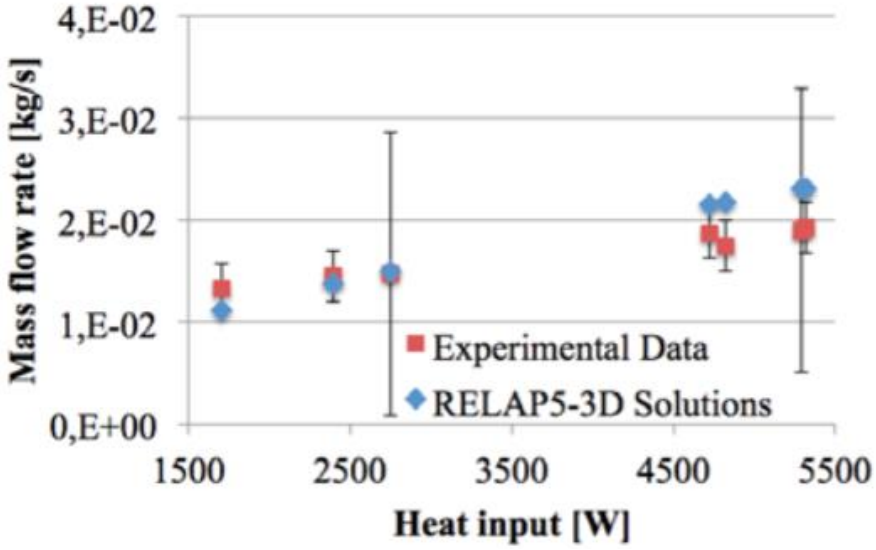

Figure 10-1 Comparison of experimental and RELAP5-3D natural circulation mass flow rates with different heat inputs [10.7].

The scaled PB-AHTR model has also been developed in the RELAP5-3D code for analyzing the steady-state conditions and transient problems [10.8]. In the PB-AHTR model, it includes the components of the core, P-IHX, intermediate loop, DHX and NDHX, as shown in Figure 10-2. The results of transient analysis show that DRACS is capable of maintaining the peak coolant temperature below the safety limits during accidents. The study also points out that the problem of overcooling can be prevented by controlling the air flow rate.

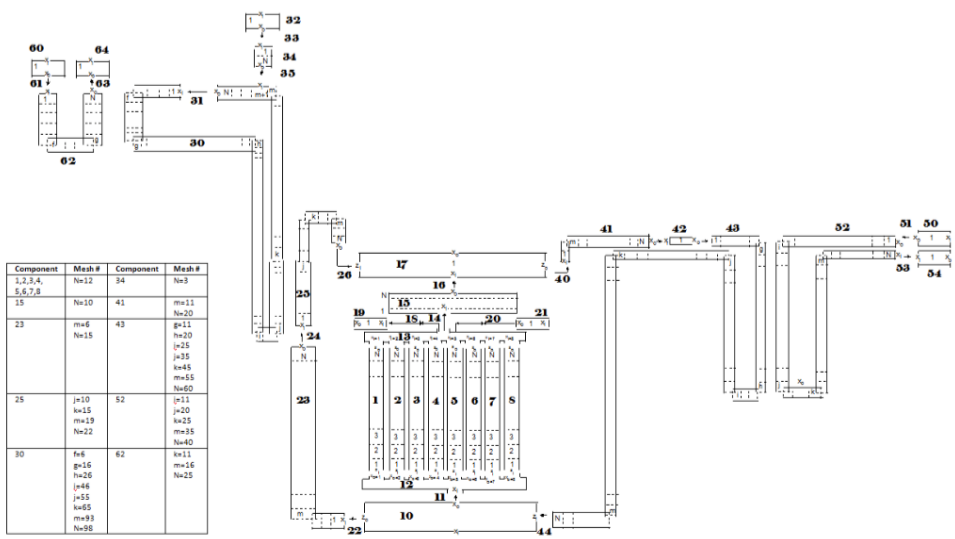

Component	Mesh #	Component	Mesh #
1,2,3,4, 5,6,7,8	N=12	34	N=3
15	N=10	41	m=11 N=20
23	m=6 N=15	43	g=11 h=20 j=25 j=35 k=45 m=55 N=60
25	j=10 k=15 m=19 N=22	52	j=11 j=20 k=25 m=35 N=40
30	f=6 g=16 h=26 j=46 j=55 k=65 m=93 N=98	62	k=11 m=16 N=25

Figure 10-2 Plant model in RELAP5-3D [10.8].

TRACE

The TRAC/RELAP advanced computational engine (TRACE) is developed by U.S. Nuclear Regulatory Commission (NRC) for analyzing transient and steady-state neutronic-thermal-hydraulic behaviors in light water reactors. The capabilities of four NRC's system codes were combined into the TRACE code including the TRAC-P, TRAC-B, RELAP5 and RAMONA. In the previous work by Richard et al., the properties of four molten salts, FLiBe, FLiNaK, $NaBF_4$-NaF and NaF-ZrF_4, are implemented into the TRACE code that can be applied to advanced reactor analysis [10.9].

The AHTR model simulated by TRACE code is utilized for developing the design for AHTR and performing transient analysis [10.10]. The TRACE model of AHTR is shown in Figure 10-3. The full-scale TRACE model includes primary loops and three DRACS loops. Molten salts, FLiBe and KF-ZrF_4, are used as the working fluid in the primary loop and DRACS loop, respectively. For the primary loop, it consists of multiple components including the core, downcomer, hot leg, cold leg, pumps and P-IHXs. For the DRACS loop in the AHTR TRACE model, DHX and DRACS air cooler (DAC) are included. In addition, the heat transfer correlations for the DHX and DAC are implemented into the TRACE code. Steady-state of normal operation and transient of loss of forced flow (LOFF) are simulated with the TRACE code, and the steady-state results are close to the design values. However, the author suggested that the implemented correlations for heat exchangers were mainly for low Prandtl numbers and experiments would be needed to validate the correlations for molten salts with relatively large Prandtl numbers.

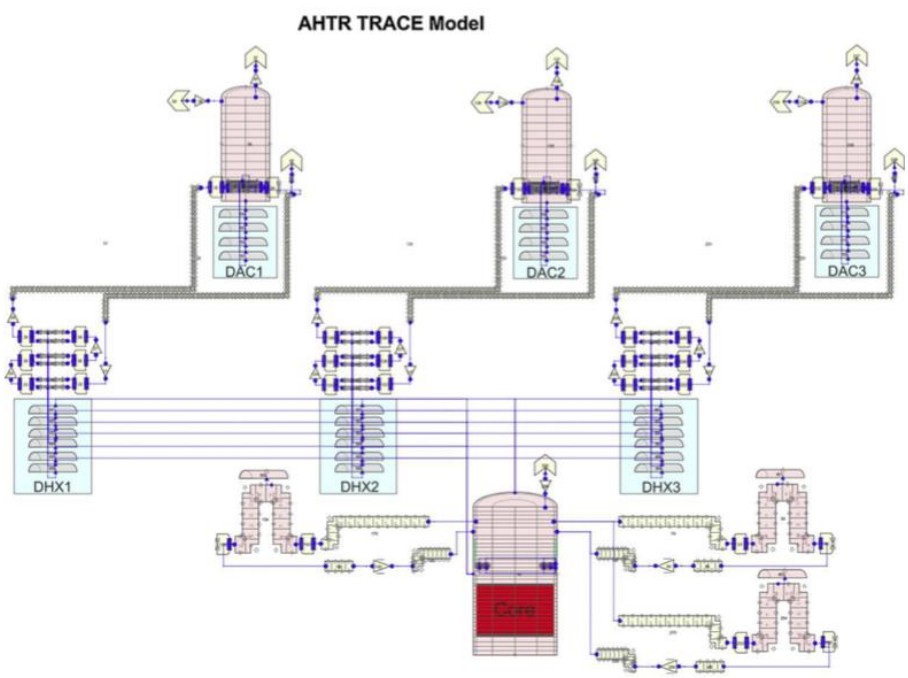

Figure 10-3 TARCE model of AHTR [10.10].

RELAP5/SCDAPSIM/MOD 4.0

RELAP5/SCDAPSIM/MOD 4.0 is a one-dimensional system code developed by Innovative System Software, LLC, and the code development is based on RELAP5 MOD 3.3 and RELAP5 MOD 3.2 models [10.11]. This code contains increased capability, improved modeling accuracy and integrated graphic display. For the code validation, the simulation results of a DRACS startup scenario have been benchmarked with the experimental results of a low temperature DRACS test facility (LTDF), as shown in Figure 10-4 [10.12]. The LTDF constructed at the Ohio State University (OSU) uses water as the surrogate coolants. Another test facility at the OSU is called high temperature DRACS test facility (HTDF), which utilizes FLiNaK and KF-ZrF_4 as the primary and secondary coolant, respectively. Both the LTDF and HTDF models built in RELAP5/SCDAPSIM/MOD 4.0 are shown in Figure 10-5. The objectives of the LTDF and HTDF are to test the thermal performance of DRACS in removing the decay heat. The properties of two molten salts, FLiNaK and KF-ZrF_4, are added into the code. The simulation results of the HTDF will also be benchmarked with the experimental data for code validation. In addition, the code can be further used to perform the FHR related analysis.

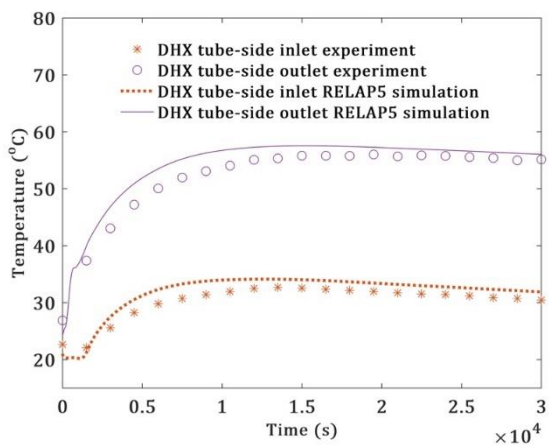

(a)

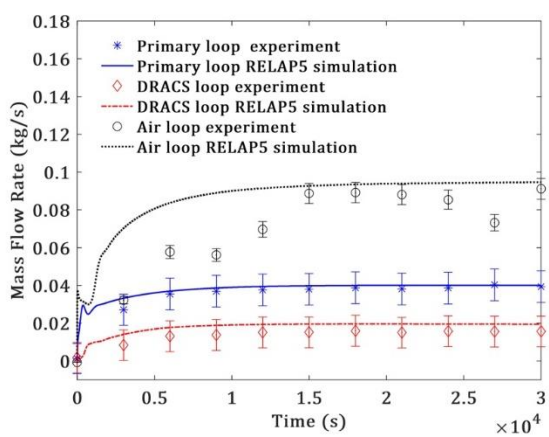

(b)

Figure 10-4 Experiment data compared with RELAP5 simulation results: (a) Temperature comparison; (b) Mass flow rate comparison [10.12].

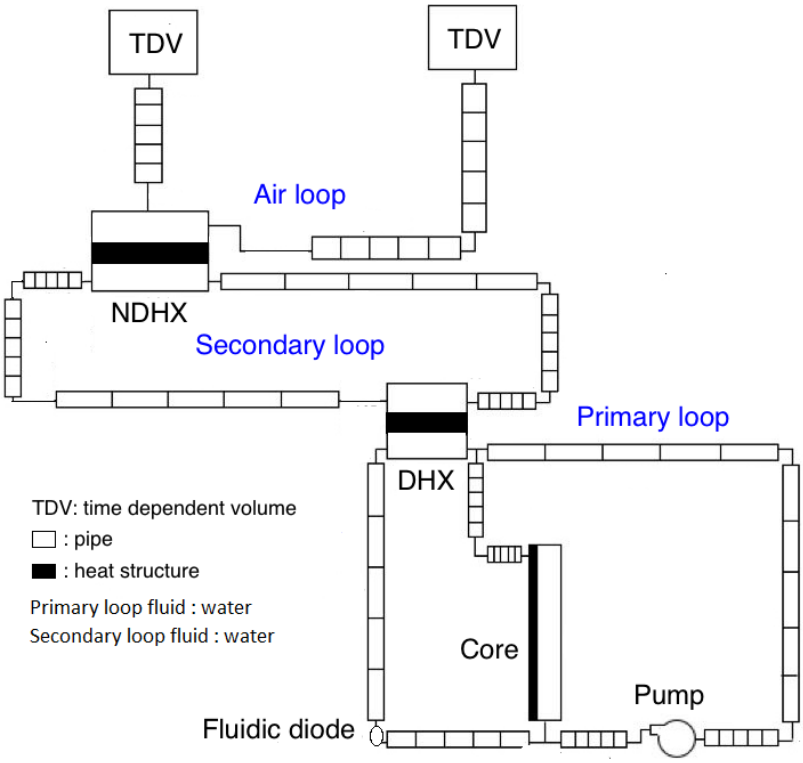

(a)

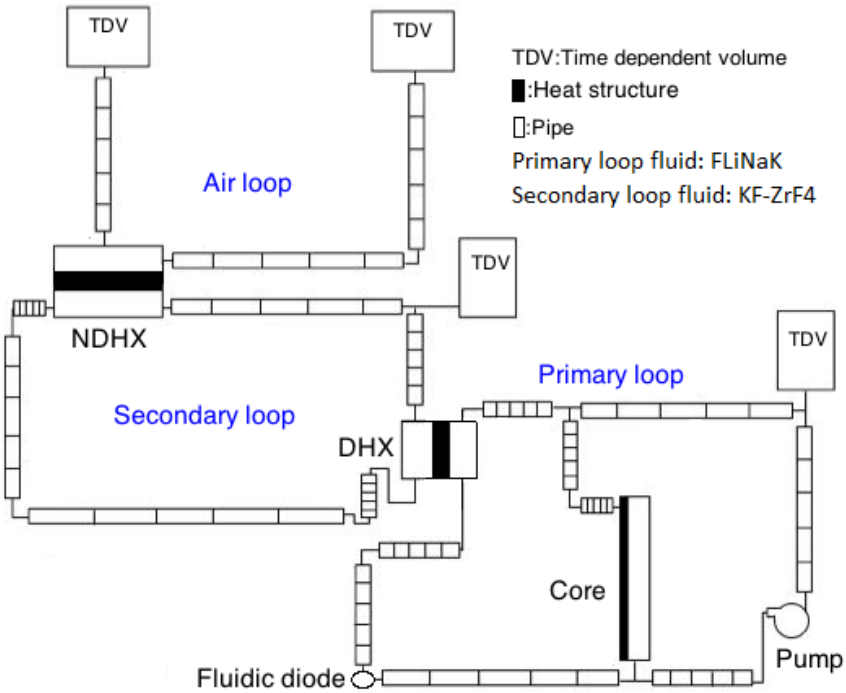

(b)

Figure 10-5 (a) LTDF model and (b) HTDF model in RELAP5 [10.12].

The System Analysis Module (SAM)

The System Analysis Module (SAM) is an advanced and system-level analysis tool that is being developed at Argonne National Laboratory under the U.S. DOE Office of Nuclear Energy's Nuclear Energy Advanced Modeling and Simulation (NEAMS) program [10.13]. Based on the MOOSE framework [10.14], SAM takes advantage of advances in modern software environments, numerical methods, and physical models to build a flexible multi-physics framework for integration with other computational tools. Modeling on advanced reactors is one of the major targets for the code development of SAM including SFRs (sodium fast reactors), LFRs (lead-cooled fast reactors), and FHRs (fluoride-salt-cooled high temperature reactors) or MSRs (molten salt reactors) [10.15]. SAM has been coupled with other system-level codes such as SAS4A/SASSYS-1and computational fluid dynamic (CFD) for SFR analysis. The benchmark study on EBR-II test using SAM has been carried out for an unprotected loss of forced cooling flow test and an unprotected loss of heat rejection test. The simulation results in both benchmark studies showed good agreement with experimental data especially on the transient response of the primary loop flow in natural circulation regime and thermal stratification in the reactor pool for heat rejection test [10.16]. In addition, an SFR 3-D full-core (hexagon lattice) model for conjugate heat transfer has been developed in SAM and verified by a test problem with 7 fuel assemblies. In the 3D core model, the subassembly flow was represented by 1-D parallel channels and duct walls and inter-assembly gaps in 2-D. The simulation results showed very good agreement compared with a CFD simulation [10.17]. With its successful validation with experimental results of SFRs, the code validation and verification (V&V) in for molten salt-cooled reactors is expected to carry out.

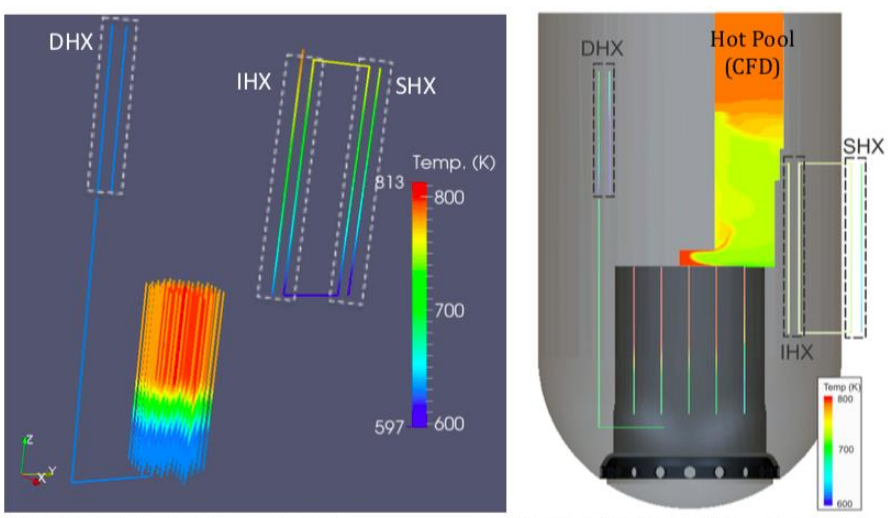

(a) SAM model with 61 core channels (b) Coupled SAM and CFD code simulation

Figure 10-6 SAM simulation results of of an SFR [10.13].

However, these current version of system codes still lack code validation due to available experimental data are limited. Also, the following listed issue are required to be improved in these system codes for obtaining accurate simulation results.

- Large uncertainties in liquid salt thermophysical properties
- Lack of heat transfer and friction factor models/correlations for advanced/novel heat exchanger designs
- Lack of capability in modeling phase change between liquid and solid phases
- Coupling thermal hydraulics and neutronics analysis

10.3.2. Review of CFD Codes

A review of CFD codes for modeling and analysis of fluid flow and thermal mixing in the AHTR upper plenum is performed. There is a distinct lack of literature regarding the thermal-hydraulic analysis of FHRs in general, especially when the focus is narrowed down to just the upper plenum area. Avigni [10.18] has included a preliminary and simplified analysis of the AHTR upper plenum area as part of his dissertation. There are some publications available for transient analyses and for system-wide analyses, but neither of those areas is particularly applicable for the data needed for the upper plenum-focused analysis. The whitepaper for FHR modeling and simulation [10.19] lists eight different resources available and viable for thermal-hydraulic analysis. As the focus of this CFD focused research is on the upper plenum and flow and core flow only, the codes and programs focused on overall system analysis are not considered. The remaining options are: ANSYS Fluent, STAR-CCM+, COMSOL, OpenFOAM, and Nek5000.

ANSYS Fluent (Finite Volume CFD Software)

Fluent is a commercial CFD software that is capable of simulating multi-physics applications. The advantages of using this software are: Well-validated modeling capabilities (especially important due to lack of other V&V methods); it has previously been used for simulation and design of liquid-salt-cooled reactor components. The disadvantages of using this software are: large computational requirements, even with access to a high-computing cluster simulation take a long time; integration with other multiphysics tools potentially lacking (needs to be investigated); proprietary access, so only recreation of or direct access to data is readily available to others with access to a license. Despite the limitations, ANSYS Fluent is currently considered the most viable choice for AHTR upper plenum modeling. Yoder et al. performed parametric studies for the design of vortex diodes in DRACS using Fluent (See Figure 10-7) [10.20]. Three fluids (FLiBe, FLiNaK and water) were used in simulations. Initial experimental results of diodicity using water as fluid showed similar trends as the result obtained by Fluent. In addition, Lippy et al. used Fluent to design a P-IHX with similar boundary conditions to MSBR's shell-and-tube heat exchanger [10.21].

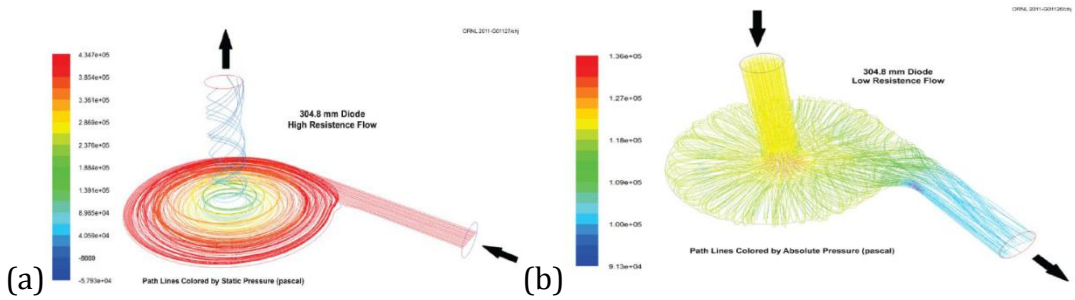

(a) (b)

Figure 10-7 Path lines colored by static pressure for FLiBe salt for a static pressure drop of 426 kPa: (a) Reverse flow direction; (b) Forward flow direction [10.20].

STAR-CCM+ (CFD Software)

STAR-CCM+ is a three-dimensional CFD code and conjugates heat transfer analysis using Reynolds-average Navier-Stokes (RANS) methods. STAR-CCM+ can be used to solve problems involving multi-physics and complex geometries. Yoder et al. investigated fluid the velocity and temperature profile in a 1/3 fuel assembly of the AHTR and also made some simplifications for the calculation, including neglecting the thin graphite fuel plate skin [10.22]. Figure 10-8 and Figure 10-9 show the structures for the calculation and the simulation results, respectively. Flow in the larger gap channel is turbulent, while flow in the smaller gap is not. The maximum temperature occurs in the innermost plate because of the peaked power profile and reduced flow profile. Hence, the size of the smaller channel needs to be increased. Figure 10-10 shows the fluid velocity profile in the upper plenum. These simulation results are beneficial to the design optimizations of the AHTR fuel assembly and upper plenum. Similar to ANSYS Fluent, the disadvantage of STAR-CCM+ is: expensive computation is required for modeling upper plenum mixing and AHTR core flow.

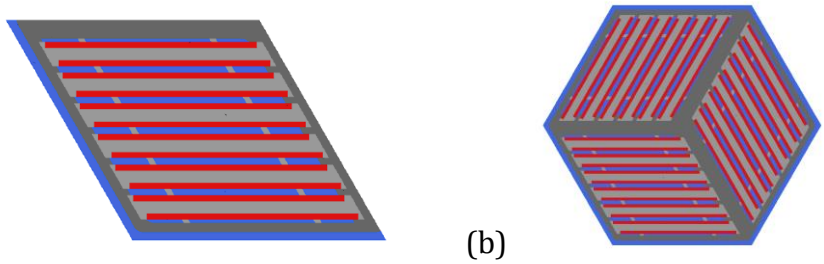

(a) (b)

Figure 10-8 Fuel assembly geometry: (a) 1/3 of an fuel assembly; (b) An full fuel assembly [10.22]

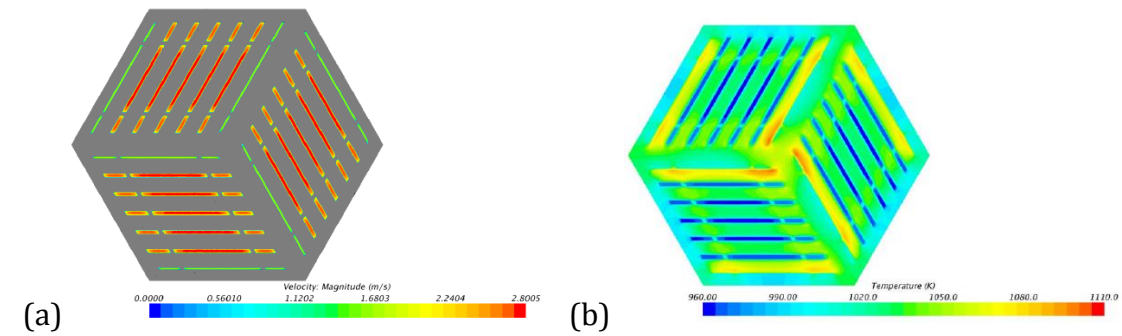

(a) (b)

Figure 10-9 Simulation results: (a) Velocity profile in coolant channels at top of fueled region; (b) Temperature profile in coolant channels at top of fuled region [10.22]

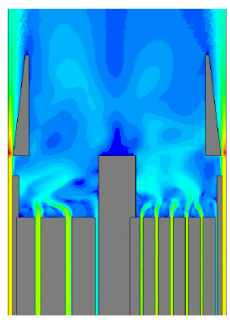

Figure 10-10 Upper regions of the AHTR fuel assembly [10.22].

COMSOL (Finite Element Multiphysics Software)

COMSOL is a simulation software based on finite element analysis (FEM) while ANSYS fluent is based on finite volume (FVM). COMSOL can be used to perform multi-physics and multi-scale analyses of various phenomena. FEM is overall with higher accuracy and more versatile compare to FVM. The finer meshes helps in obtaining more accurate results with lower numerical diffusion. Qualls et al. studied the fuel compact and graphite temperature profile in an assembly in FHR demonstration reactor (DR). Several assumptions were made as follows: (1) neglect of heat generation in the graphite; (2) same heat generation rate in the fuel compacts; (3) adiabatic boundary on graphite block sides; and (4) neglect of bypass flow [10.23]. Figure 10-11 shows the compact-averaged fuel temperature profiles. Temperature of the fuel compact at the edge is 936°C, while the temperature of the fuel compact center is 973°C. The maximum fuel temperature is conservatively calculated (slightly below 1200°C) using radial/axial peaking factors, maximum coolant temperature, and a low heat transfer coefficient.

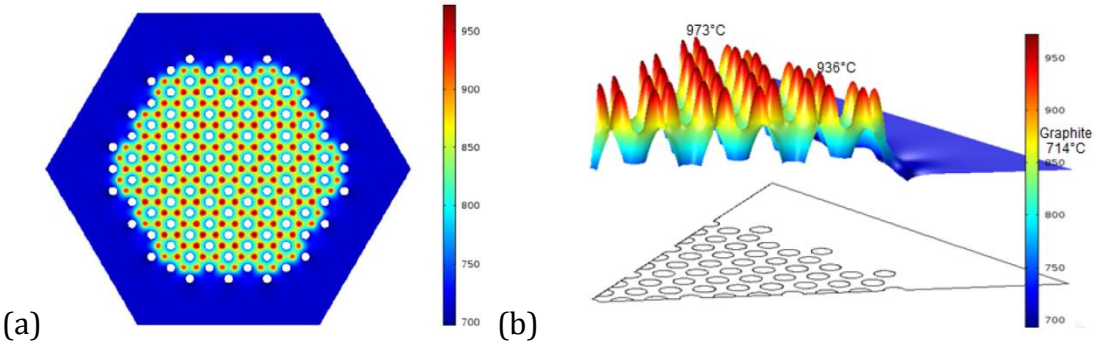

Figure 10-11 COMSOL results: (a) Cross-sectional temperature in an average fuel block; (b) Temperature profile in the fuel and graphite [10.23].

A group of researchers in University of California, Berkeley studied the coolant and fuel temperature profile in the 2009 PB-AHTR core under normal operating conditions [10.24]. Figure 10-12 shows the geometric structure and simulation results. The average outlet coolant temperature is 700°C, while the maximum coolant temperature is about 70°C higher in some regions. The outlet plenum should be properly designed to make coolant sufficiently mixed. The maximum fuel temperature is 1,110°C, which is contributive to the analysis of fuel degradation.

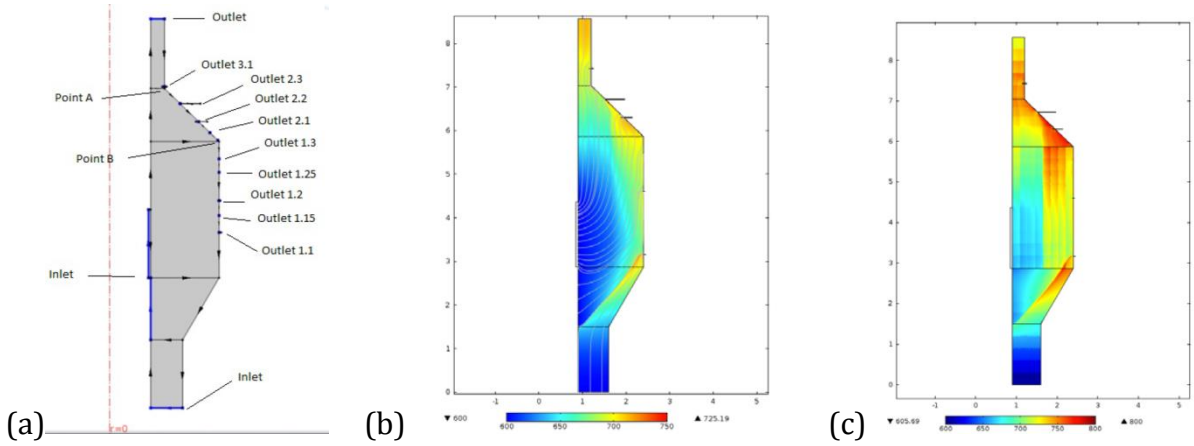

Figure 10-12 Simulation of the annular PB-AHTR core: (a) Geometric configuration; (b) Bulk coolant temperature profile; (c) Fuel temperature profile (average kernel temperature in fuel pebble) [10.23].

OpenFOAM (Finite Volume Code)

The advantages of this software are: It is an open-source program, thus readily available to anybody; C++ toolbox therefore very customizable; has been coupled with neutronics codes before; computation time quicker than some other options. The disadvantages are: dependent on existing libraries; creation of new libraries tedious; time spent debugging

and writing code could potentially outweigh runtime saved; low order solver; typical problems are set up by modifying existing files, but unknown if files exist for this situation. Ultimately, it was eliminated as direct comparisons between Nek5000 makes it an unfavorable choice both in respects to fidelity and computation time [10.25].

Nek5000 (Spectral Finite Element Code)

The advantages of this program are: It is an open-source program from the NEAMS program, thus readily available to anybody; high-order solver; typically, quicker and more accurate than lower-order solvers such as OpenFOAM; While Nek5000 is for thermal-hydraulics, it can be coupled with Diablo (another NEAMS software) for the structural interactions and Proteus for neutronics analysis. The disadvantages are: It runs best in a Linux environment, which not everybody has access to; time spent debugging and writing code could potentially outweigh runtime saved; typical problems are set up by modifying existing files, but unknown if files exist for this situation. Ultimately it was decided that this is a semi-viable choice; will be working on in exploring this option further, but it will be on the side (with the main focus being on the Fluent model) due to the steep learning curve and potential problems in setup.

10.4. Code Validation and Identification of Issues for Code Improvement

To support FHR licensing, thermal hydraulics code verification and validation is one of the important and necessary tasks to ensure the fidelity of simulation codes and therefore the applicability of the simulation results for FHR applications. This section presents our code validation study with a main focus on natural circulation flow regime. AHTR relies on natural circulation/convection flows in DRACS to passively remove decay heat when the reactor is shut down during accidents. It is important to ensure the code capability of modeling such natural circulation flows in the validation study. In our study, an existing analysis code RELAP5 is initially selected for code validation and in particular RELAP5/SCDAPSIM/MOD 4.0 is selected due to its flexibility of implementing thermodynamic properties of molten salts and heat transfer correlations. In addition, due to the move of the research team from The Ohio State University to the University of Michigan, the team lost its access to a molten salt test facility that was originally proposed in the proposal to be used to generate experimental data for code validation. In view of that, the research team with consultation to the project principal investigator, technical monitor, and DOE project manager, decided to use SAM for code-to-code benchmark with RELAP5 based on its advanced numerical feature and potential capability of modeling FHRs.

In this section, the code validation and benchmark study include:

- RELAP5 code validation on LTDF startup and pump trip scenario
- SAM code validation on a single-phase natural circulation loop (startup scenario) at Purdue University
- SAM code validation on LTDF pump trip scenario

10.4.1. RELAP5/SCDAPSIM/MOD 4.0 code benchmark of startup and pump trip scenarios

In this project, REALP5 MOD 4.0 has been selected as one of system analysis code to perform analysis for both the Low-temperature DRACS test facility (LTDF) and High-temperature DRACS test facility (HTDF) constructed at the OSU. The LTDF was built, following a detailed scaling study, to investigate the decay heat removal performance by natural circulation [10.26-27]. Pressurized (10 bar) distilled water is used as a surrogate to molten salt in the primary loop and distilled water near the atmospheric pressure is used as the working fluid in the DRACS loop (i.e., the "secondary" loop in the LTDF). Three electric cartridge heaters, each rated at 2 kW, are used to simulate the core heating in the primary loop. These 1.0-m long heater rods with stainless steel 304 (SS304) sheath are vertically oriented and arranged in a triangular pattern. The water in the primary loop is pressurized to eliminate any potential of water boiling on the heater rod sheath surface. A primary pump is installed in the primary loop to drive the flow prior to a transient that would lead to the shutdown of the reactor and the initiation of the natural circulation flow in the primary loop. In addition, a fluid diode simulator is used in the LTDF, in which two ball valves provide two distinctively different flow resistances in the two opposite flow directions (i.e., very large flow resistance in the upward flow direction but significantly smaller flow resistance in the downward direction). Two heat exchangers in the LTDF, namely, the DHX and NDHX, transfer heat from the primary coolant, i.e., pressurized water to the ambient air. The overall structure of the HTDF is similar to the LTDF, but the coolants in the primary and DRACS loops are FLiNaK and KF-ZrF4, respectively (see Figure 2). Seven electric cartridge heaters are used in the simulated core, with a total nominal power of 10 kW (The total actual heating capacity of the seven heaters is 70 kW). A disc-shape vortex diode is employed as a passive flow controller in the primary loop. The shell-and-tube type DHX is vertically oriented and consists of a total of 80 5/8'' BWG-18 tubes, each with a length of 0.325 m. For the NDHX in the HTDF, 36 plain tubes (1/2'' BWG-16) are arranged in a staggered fashion in two rows. The entire HTDF facility is made of stainless steel 316H. Figure 10-13 (a) and (b) show the schematic of the LTDF and HTDF, respectively. To validate the RELAP5/SCDAPSIM/MOD 4.0 code, the simulation results are compared with experimental data on selected scenarios including startup and pump trip scenarios of the LTDF. In addition, the startup and pump trip transients have also been calculated and discussed as follows.

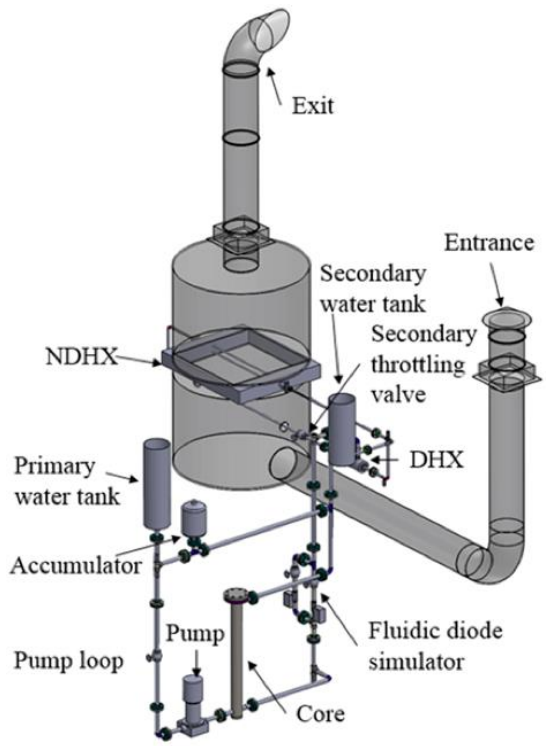

(a)

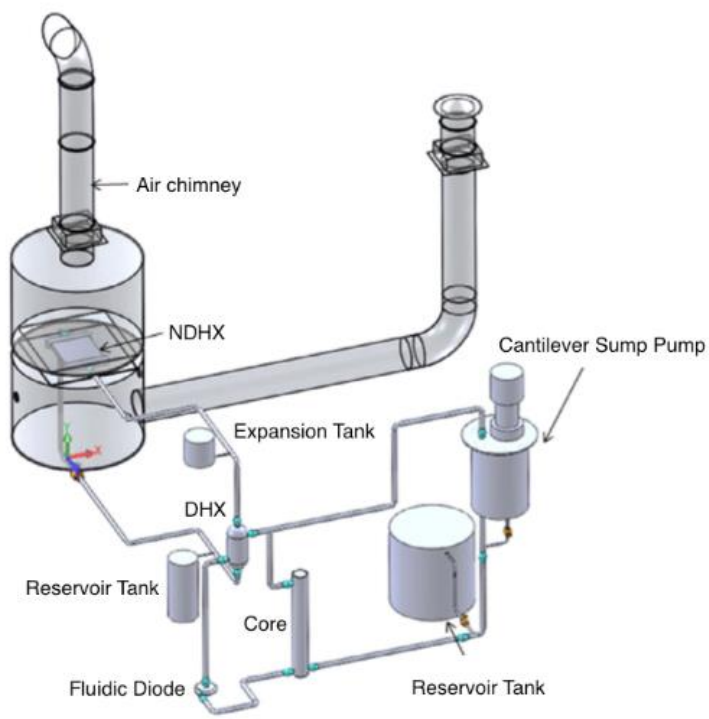

(b)

Figure 10-13 Schematic of (a) LTDF (b) HTDF

10.4.1.1. Startup Scenarios in LTDF

Startup is one of the scenarios performed by the test facility to investigate how natural convection is established and when the steady state is reached by providing power from the core. The startup scenario in the LTDF demonstrates the establishment of natural circulation/convection after the heat up of the primary water while the coolants in the three loops are all stagnant initially. One of the branches in the primary loop where the primary pump is located. The pump side of primary loop is closed by a valve, so the primary water only can flow through the DHX branch. When the DRACS startup scenario is initiated, a constant heating power of 2 kW is provided to the system by the electric heaters, based on 1% of the core decay power (200 kW) in the prototypic reactor design. The benchmark of the RELAP5 simulation results with the LTDF experimental data for the DRACS startup baseline case is discussed first.

*Figure 10-14*to *Figure 10-16*show the benchmark results of the fluid temperatures and mass flow rates in the three loops, with a time scale of 0 to 30,000 s. The temperature transient responses from both the experiment and simulation indicate that the system reaches a quasi-steady state at approximately 16,000 s from the event initiation when the temperature difference between inlet and outlet of DHX and NDHX are close to a constant. *Figure 10-14*shows the water inlet and outlet temperatures on the DHX shell side in the primary loop (i.e., the primary water in DHX in on the shell side and DRACS water in DHX and NDHX is on the tube side.). At 30,000 s, the water inlet and outlet temperatures on the DHX shell side obtained from the RELAP5 simulation are approximately 2 °C lower than those in the experimental data, which represents an error of approximately 2.5%. The water inlet and outlet temperatures on the DHX tube side (i.e., the DRACS loop) are shown in*Figure 10-15*. Compared to the experimental results, the RELAP5 simulation over-predicts the DHX tube-side temperatures during water heat up with maximum temperature 3 °C at 9,000s. However, the temperature differences of DHX tube side are less than 1 °C (less than 3% difference) at 30,000 s . *Figure 10-16*shows the NDHX air-side inlet and outlet temperatures from both the experiment and RELAP5 simulation. The air-side inlet temperature is given by the actual values measured in the experiment (Note the relatively large air temperature variation, over 6 ^{o}C, during the 30,000 s of the experiment time). After quasi-steady state, the water temperatures in the primary loop from simulation results decrease with time due to air inlet temperature decreasing. However, the temperatures in the primary loop are kept stable in the experiment data, due to the heat losses and the discrepancy of thermal inertia and storage heat in the structures between the LTDF modeling and experiment. From the startup transient, the overall fluid temperature responses in the three loops from the RELAP5 simulation results exhibit reasonably good agreement with the experimental data during the DRACS startup transient. From*Figure 10-17*, it is clear that natural circulation flows are gradually established during the transient. As shown in the experimental data, the air mass flow rate remains oscillatory throughout the experiment duration. This is primarily because the air inlet chimney points to a fix direction and thus is heavily affected by the natural wind (direction and wind speed).

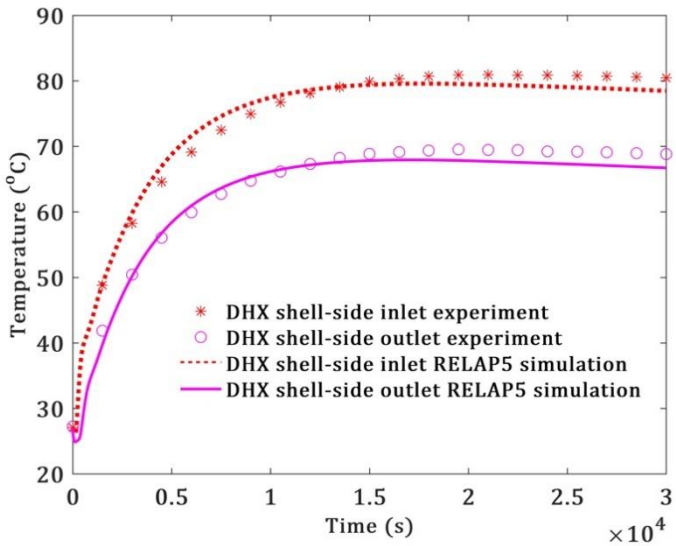

Figure 10-14. LTDF benchmark results of the DHX shell-side (primary loop) water inlet and outlet temperatures during DRACS startup transient.

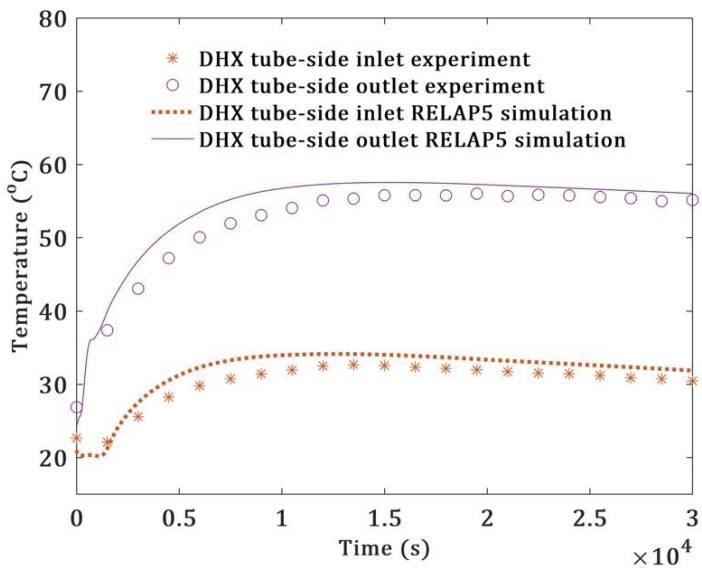

Figure 10-15. LTDF benchmark results of the DHX tube-side (DRACS loop) water inlet and outlet temperatures during DRACS startup transient.

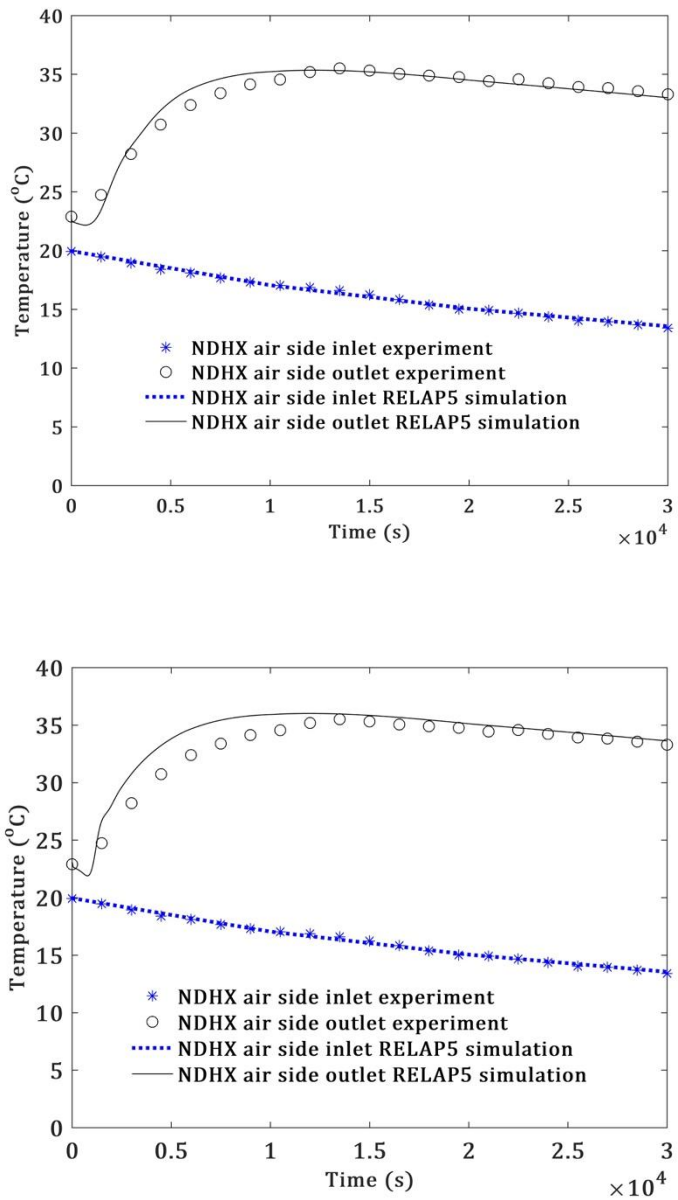

Figure 10-16. LTDF benchmark results of the air inlet and outlet temperatures during DRACS startup transient.

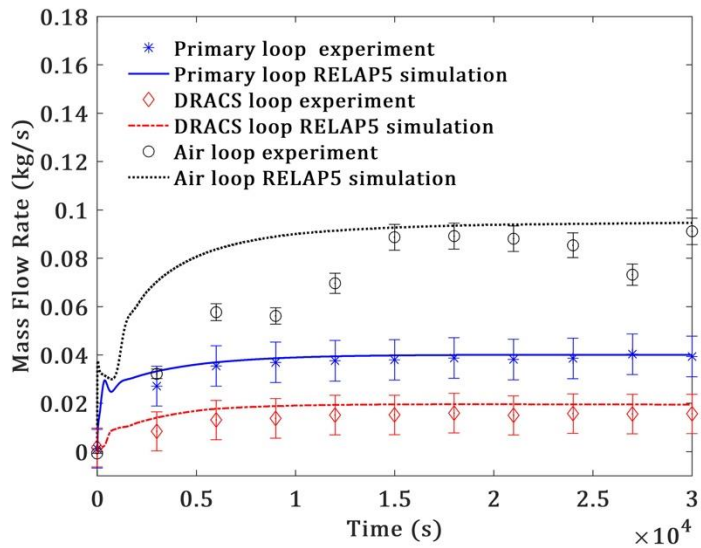

Figure 10-17. LTDF benchmark results of the fluid mass flow rates in the three loops during DRACS startup transient.

10.4.1.2. Pump Trip Scenarios in LTDF

The primary pump trip scenario represents the event of loss of forced flow (LOFF) in FHRs. The DRACS thermal performance under natural circulation condition is studied in this scenario. For the initial condition, the primary pump provides a constant water mass flow rate of 1.75 kg/s in the primary loop to both DHX-side branch (upward flow) and the simulated core branch (upward flow) with 0.04 and 1.71 kg/s, respectively. A constant heating power of 2 kW is given in the simulated core before and after pump trip. At time 0 s, the primary pump coast down and reach fully stop at 20 s. Figure 10-18shows that when the primary pump trip is initiated, the primary loop loses its driving force and that the flow in the primary loop (in the DHX-side branch) reverses due to the buoyancy and a much smaller flow resistance in the fluidic diode's forward (downward) direction. After the flow reversal, a natural circulation flow in the primary loop is established (upward flow in core branch and downward flow in DHX-side branch).

Figures 11-13 provide the benchmark results of the temperature transient responses in the three loops. Similar to the DRACS startup scenario, the NDHX air-side inlet temperature is obtained from the experimental data and is used as a boundary condition in the RELAP5 calculation. The air inlet temperature decreases with time, which causes the fluid temperatures in the three loops to decrease as well. InFigure 10-19, the DHX shell-side inlet temperature peak is resulted from the sudden flow decrease in the primary loop after the loss of driving force from the primary pump. In addition, the RELAP5 simulation results show faster temperature decreases in both the DHX shell-side inlet and outlet temperatures as compared to the experiments. This is primarily the discrepancy of thermal inertia in the structures between the LTDF model and experiment. From the benchmark results for the primary pump trip scenario, we can conclude that reasonably good

agreement between the experimental data and RELAP5 simulation results are obtained and that the DRACS system provides a sufficient heat removal capability.

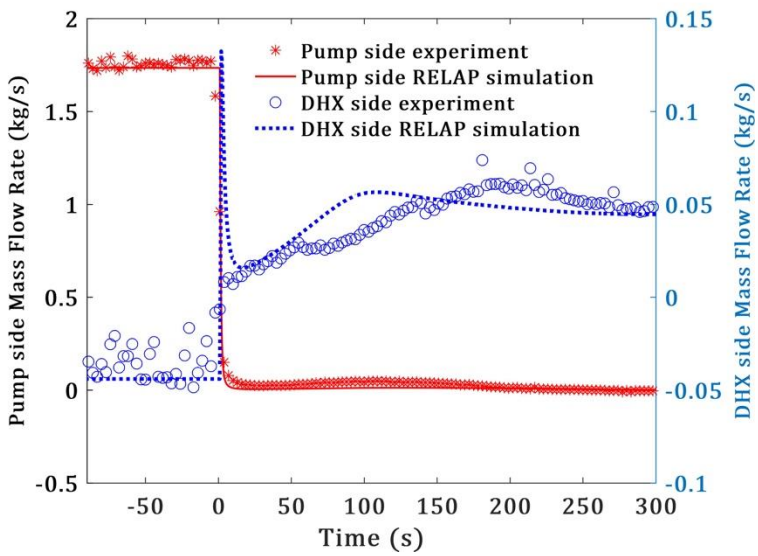

(a)

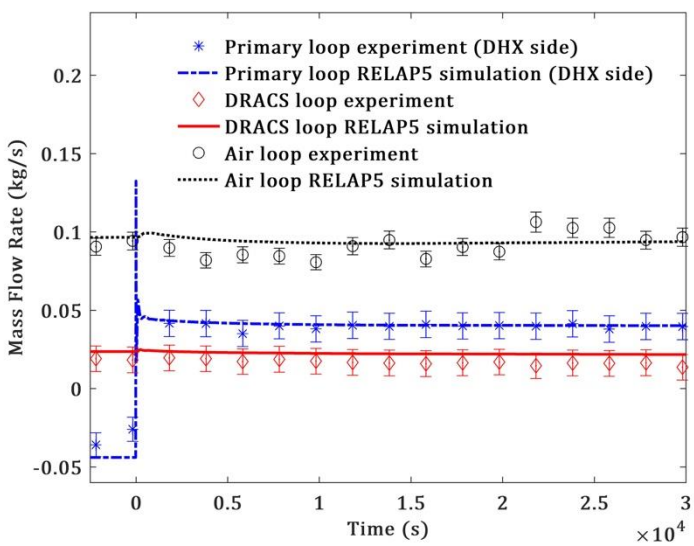

(b)

Figure 10-18. LTDF benchmark results of the mass flow rates of (a) pump side branch and DHX side branch of the primary loop (b) the three loops during the primary pump trip scenario.

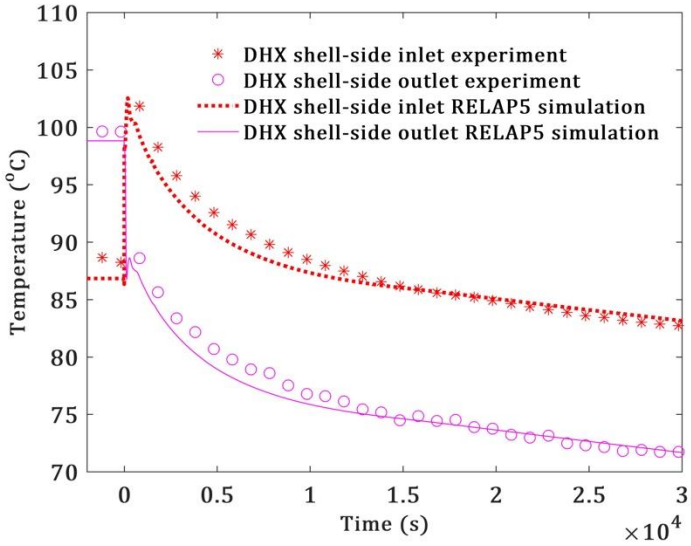

Figure 10-19. LTDF benchmark results of the DHX shell-side (primary loop) water inlet and outlet temperatures during the primary pump trip scenario.

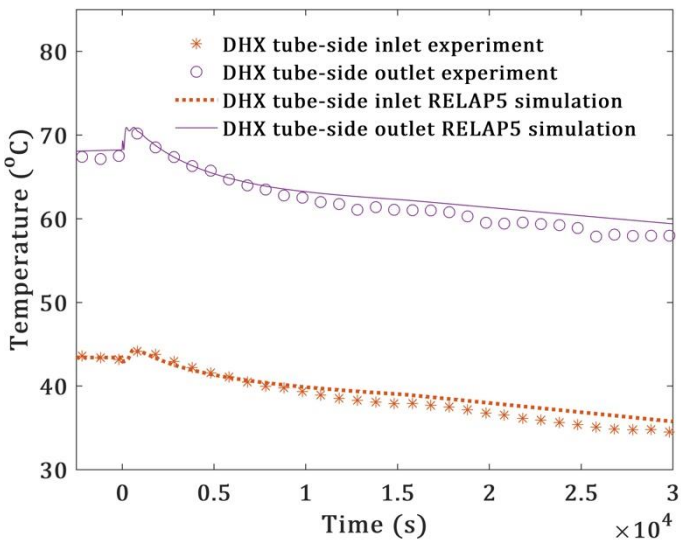

Figure 10-20. LTDF benchmark results of the DHX tube-side (DRACS loop) water inlet and outlet temperatures during the primary pump trip scenario.

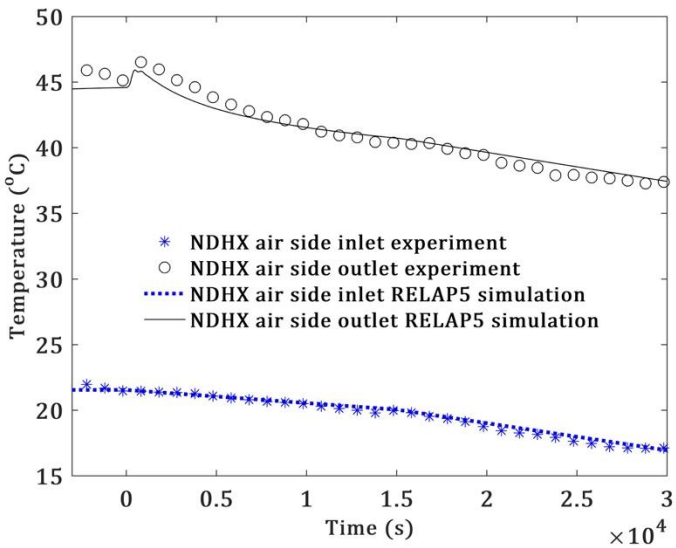

Figure 10-21. LTDF benchmark results of the air inlet and outlet temperatures during the primary pump trip scenario.

10.4.2. Benchmark study on a natural circulation loop using SAM

Experiments from a single-phase natural circulation loop are selected for benchmark study of SAM. The experiments used water as the working fluid, shown in Figure 10-22 [10.28]. Two tube bundles were placed in two different vertical legs of the natural circulation loop to serve as the heat source and heat sink to the natural circulation loop, respectively. Higher-temperature water that was controlled by mixing steam and hot water was fed into the source tube bundle (on the tube side) to provide heat to the natural circulation loop. On the other hand, the relatively cold water that flowed into the sink tube bundle provided cooling to the natural circulation loop. The inlet and outlet to each of the tube bundles could be interchanged, allowing for both counter-flow and parallel-flow arrangements in each of the tube bundles. The natural circulation loop was working at the atmospheric pressure. The source bundle was constructed by twenty-one copper tubes arranged in a rectangular array and the sink bundle was made of seven copper tubes arranged in a triangular array. The shell tube in the natural circulation loop was made of Kimax glass with a 76.2 mm inner diameter. The detail geometry information is listed in Table 10-1.

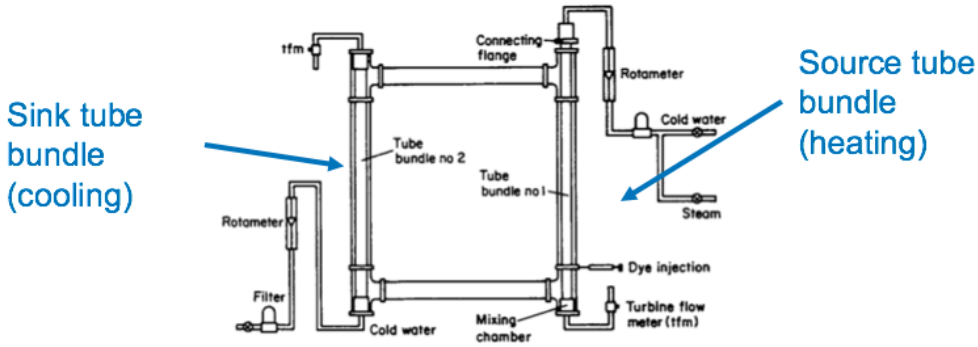

Figure 10-22 Schematic of the experimental natural circulation loop [10.28]

Table 10-1 Dimensions of tube bundles and the natural circulation loop [10.28]

Specification	Source tube bundle	Sink tube bundle
Tube number	21	7
Tube outer diameter (mm)	9.55	19.05
Tube thickness (mm)	1.587	1.02
Pitch to diameter ratio	1.33	1.25
Length of horizontal leg (m)	1.5	1.5
Shell side cross-sectional area (m^2)	0.003064	0.002565
Shell side hydraulic diameter (mm)	19.5	24.5
Length of vertical leg (m)	1.5	1.5

The flow rate of the circulating fluid in the loop was not measured due to the low velocities of natural circulation that would result in large measurement uncertainties. The flow rates of both the open tube bundle loops (source and sink) were measured with the Brooks flowmeter with an uncertainty of ±2%. T-type thermocouples with a measurement uncertainty of ±0.5°C were utilized to measure the temperatures in the natural circulation loop. Differential thermocouples were used in the heating and cooling tube bundles with an uncertainty of ±0.25°C. The maximum experimental error of the heat addition from the hot water to the natural circulation loop was about ±5%.

The nodalization of the natural circulation test loop model is built in SAM (Figure 10-23). The time-dependent junction1 (PBTDJ1) and junction2 (PBTDJ2) are inlet boundaries in which the flow velocities and temperatures are assigned to simulate the source of the hot water and cold water, respectively. The PB time-dependent volume1 (PBTDV1) and volume2 (PBTDV2) are the boundaries to simulate the sink of each open loop.

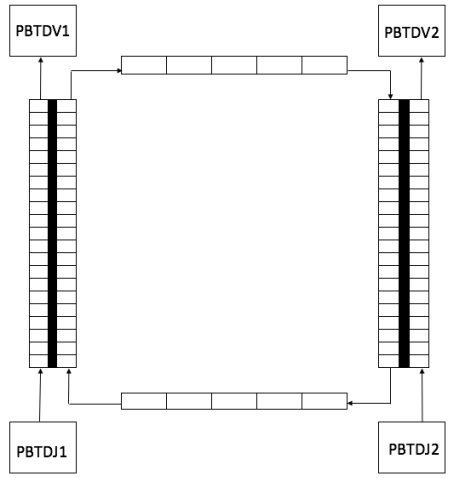

Figure 10-23 Nodalization of the natural circulation loop in SAM

The different time and spatial integration schemes are compared to investigate the differences in the different numerical schemes for modeling the natural circulation loop. Parallel flow in the source tube of startup case is also used as the base test case. SAM supports several time integration schemes, such as the explicit Euler, implicit Euler (or backward Euler), backward differentiation formula-second order (BDF2), Crank Nicolson, and Runge-Kutta methods [10.29]. Two time integration schemes are chosen, including the backward Euler and BDF2 as shown in Eqs. 11.6 and 11.7. In Figure 10-24, due to the first order accuracy of the backward Euler time integration, the result of the mass flow rate shows over-damped peaks compared to the result from the second-order accurate time integration scheme of BDF2. Though the quasi-steady state mass flow rates in both time integration schemes are identical, the higher-order accuracy time integration scheme is recommended to capture the phenomena more accurately during the transient. Trapezoidal rule and Gaussian quadrature rule are compared for different spatial integration schemes as shown in Figure 10-25. Trapezoidal rule is recommended for the numerical integration for first-order elements while Gaussian quadrature rule is recommended for second-order elements in SAM. The two numerical schemes are described in Eqs. 11.8 and 11.9, respectively. Trapezoidal rule is in second-order accuracy. For Gaussian quadrature rule, the error is hard to estimate when it depends on the $2n$ order derivative but can exactly integrate polynomials of order $2n - 1$ with n quadrature points, with exponential convergence rates. Therefore, SAM provides at least second-order accuracy for space integration.

$$f(u^{n+1}, t^{n+1}) = \frac{u^{n+1} - u^n}{\Delta t} \tag{10.6}$$

$$f(u^{n+1}, t^{n+1}) = \frac{\frac{3}{2}u^{n+1} - 2u^n + \frac{1}{2}u^{n-1}}{\Delta t} \tag{10.7}$$

$$\int_a^b f(x)dx = (b-a)\frac{[f(a)+f(b)]}{2} \tag{10.8}$$

$$\int_a^b f(x)dx = \sum_i f(x_i)w_i \tag{10.9}$$

where x_i is the quadrature point and w_i is the weighting factor.

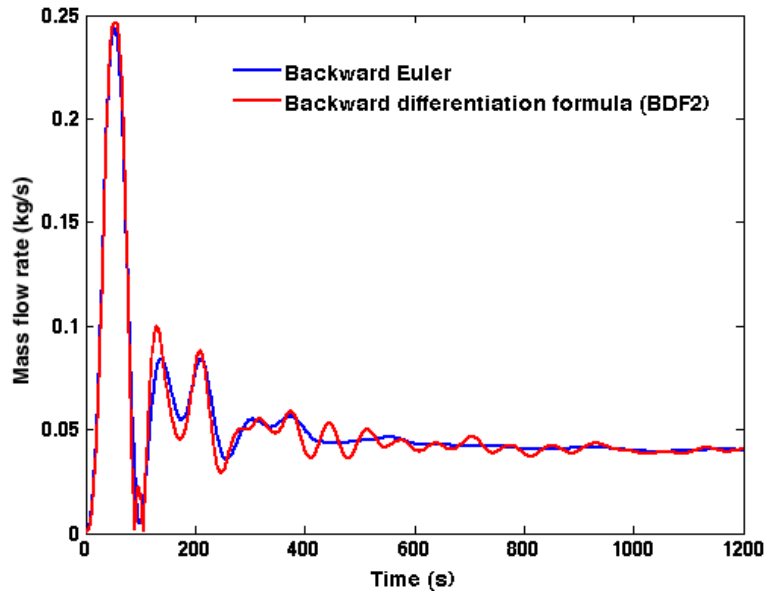

Figure 10-24 Time integration scheme comparison of backward Euler and BDF2

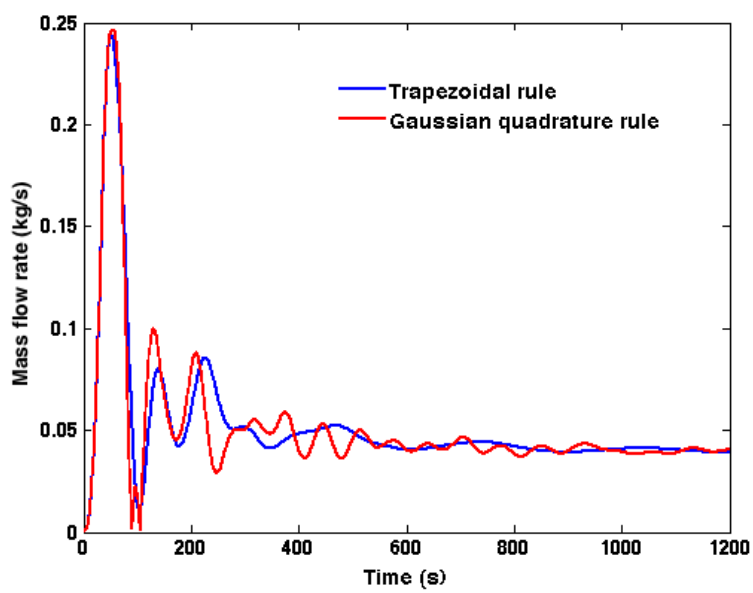

Figure 10-25 Spatial integration schemes comparison of trapezoidal rule and Gaussian quadrature rule

To summarize, BDF2 and Gaussian quadrature rules are selected as the numerical schemes for the benchmark study of the natural circulation loop. In addition, the Streamline-Upwind/Petrov-Galerkin (SUPG) method [10.30] is also applied in the model. The SUPG is a stabilization method by introducing an artificial diffusion in the streamline direction to all terms to prevent oscillations in convection-dominated problems in the FEM. The method of Jacobian-Free Newton Krylov (JFNK) is utilized to solve non-linear equations in SAM. All the unknowns are solved simultaneously by JNFK and preconditioning is required to solve the equations efficiently. The Jacobian matrix is used for the preconditioning. The calculation time of SAM depends on the numbers of the nonlinear equations solved in Newton method and linear equations by the Krylov solver [10.31].

In the referenced paper [10.28], three tests were performed, including start up, step change of heat input (increased) and step change of heat input (decreased). However, the operation conditions and its initial heat input for step changes are not provided in the paper. As a consequence, only start up transients can be utilized for the benchmark study. The initial condition of the water is assumed at a constant temperature of 293 K. A small initial velocity of (10^{-4} m/s) is given for water in every loop. At the initiation of the start up, the hot water starts to flow in the source tube bundle whereas the cold water flows through the sink tube bundle. The flow arrangements in the sink tube for both test cases are counter flow. The boundary conditions of both start up transients are listed in Table 10-2.

Table 10-2 Boundary conditions of parallel flow and counter flow in source tube [10.28]

Case	Parallel flow in source tube
Heating water mass flow rate (kg/s)	0.168
Cooling water mass flow rate (kg/s)	0.055
Heating water inlet temperature (°C)	49.1
Cooling water inlet temperature (°C)	14.0

Figure *10-26* shows the benchmark results for the water temperatures at the source tube inlet and outlet for the counter flow case. From the simulation results, the overall trend of the source tube inlet and outlet temperatures agree well with the experimental data. The differences for the quasi-steady state values are within 1 °C. Though the mass flow rate of the natural circulation loop is not measured in the experiment, the simulation result for the parallel flow case is provided in Figure 10-27. The initial peak of the mass flow rate is resulted from the imbalance of the heating and cooling rates to the natural circulation loop. As a consequence, a larger buoyancy force is required to initiate the natural circulation.

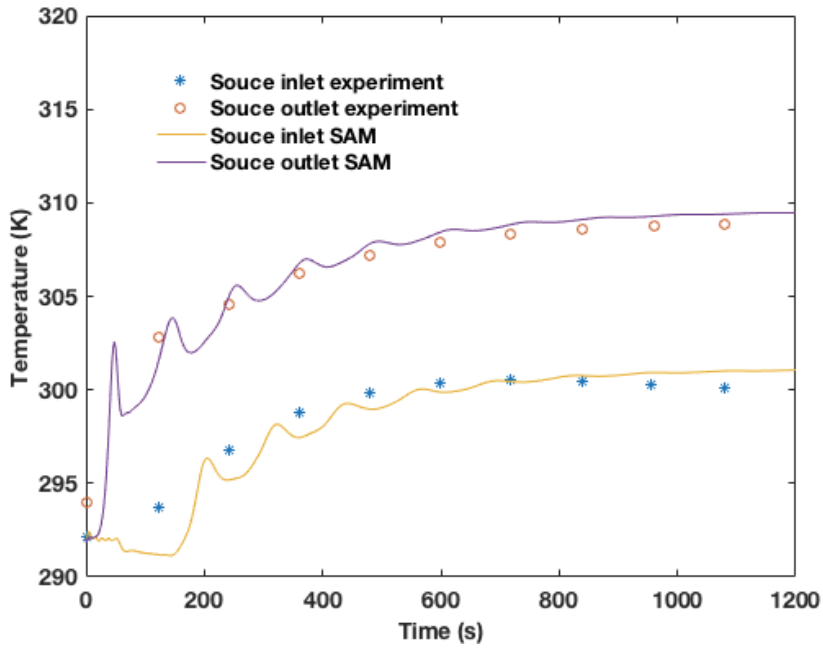

Figure 10-26 Benchmark results of the source tube inlet and outlet temperature of counter flow case (startup scenario)

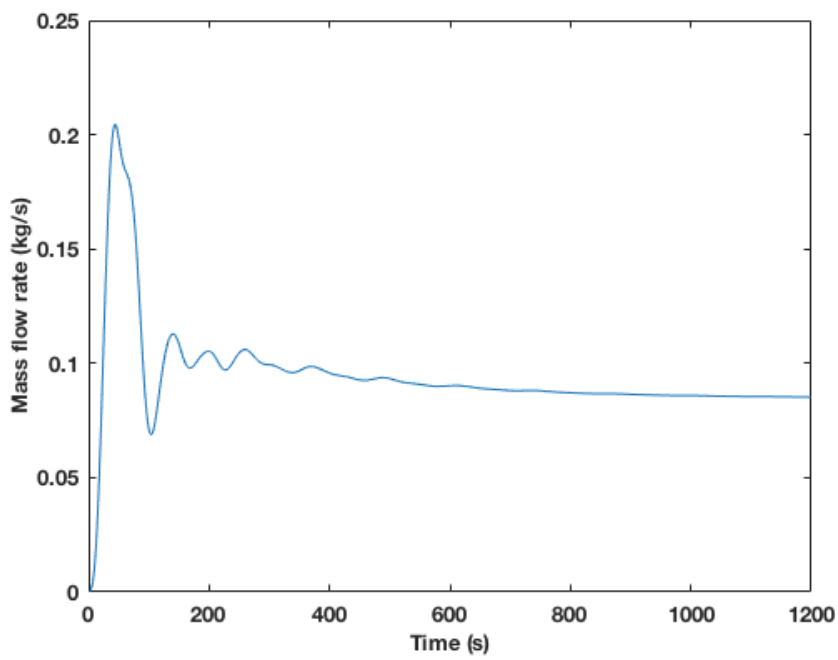

Figure 10-27 Simulation results of the mass flow rate in the natural circulation loop of counter flow case (startup scenario)

10.4.3. Code-to-code Comparison between RELAP5 and SAM

For system-level code validation, RELAP5 and SAM are selected for AHTR modeling of steady-state and transients. Prior to code validation, a code-to-code comparison is carried out first to investigate the differences of the code structures and implemented correlations in both RELAP5 and SAM. The comparison of the friction factors as functions of the Reynolds number implemented in RELAP5 and SAM is shown in Figure 10-28. When the Reynolds number is lower than 64, the two codes have different approaches dealing with the friction factors. In RELAP5, the friction factor ($f = 64/Re$) is used while in SAM, the friction factor is simplified as $f = 1$. However, this region ($Re < 64$) corresponds to very small velocities and is not applicable for most cases. The overall comparison shows that the single-phase friction factors are similar in both codes.

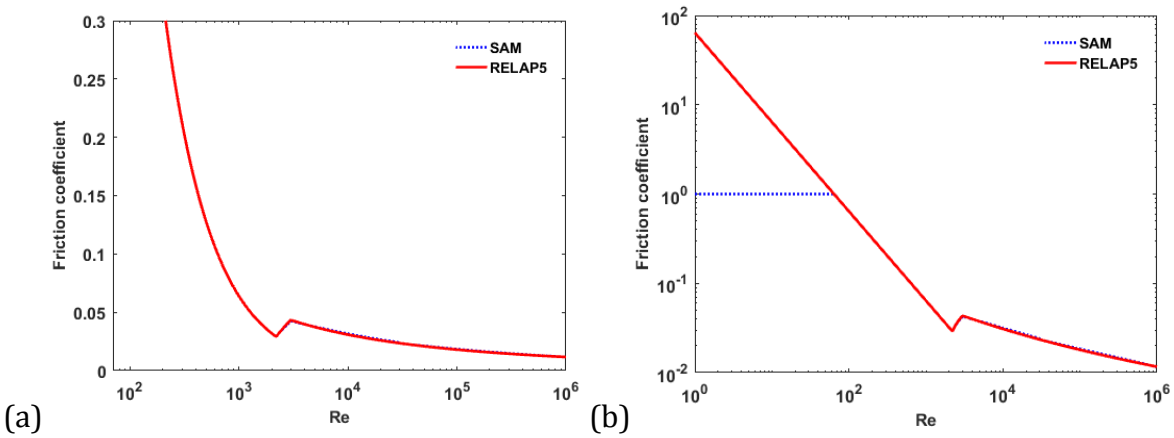

Figure 10-28 Comparisons of the friction factors in SAM and RELAP5 in (a) linear scale (b) logarithm scale

A simple loop model is built to carry out a code-to-code comparison of SAM and RELAP5 as shown in Figure 10-29. The model consists of a closed primary loop and an open secondary loop. Water is the working fluid for both loops. The first time-dependent volume (TDV1) is utilized to stabilize the pressure in the primary loop. The time-dependent junction (TDJ) and time-dependent volume (TDV2) in the secondary loop are used to simulate the water source and the water sink. The DHX is the heat exchanger that couples the heat transfer of the two loops. The start up transient of the natural circulation loop is chosen for the code-to-code comparison. The initial temperature of all the fluid is 293 K. A non-zero initial velocity (10^{-4} m/s) is given to stabilize the calculation when the flow establishes natural circulation. At the initiation of the loop start up, 2 kW of heating power is provided by the heater in the primary loop as the heat source. The inlet boundary condition of the secondary loop including the water temperature and mass flow rate are 290 K and 0.5 kg/s, respectively. The comparison of the primary mass flow rates is shown in Figure 10-30. Natural circulation is established in the primary loop as the primary loop reaches a stable mass flow rate of 0.1 kg/s. The overall trends during the start up are similar in both codes. However, there are more fluctuations in the calculation results from SAM, which is believed due to the difference of the code structure between SAM and RELAP5. In this calculation, BDF2 with a second-order accuracy time scheme is used in SAM. On the other hand,

RELAP5 uses semi-implicit methods with a first-order accuracy, which causes fluctuations to be over-damped.

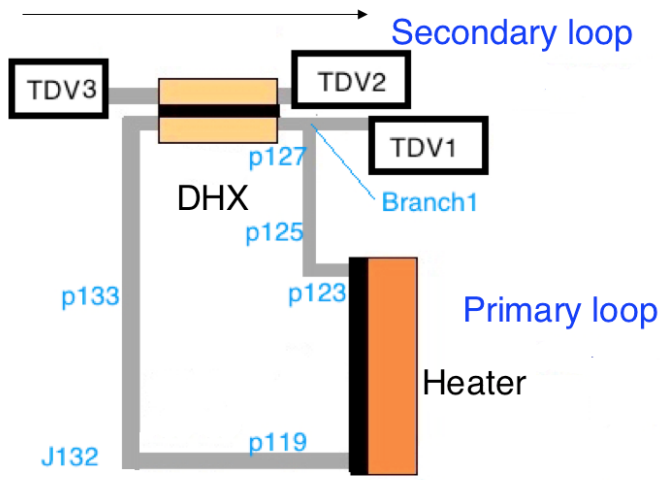

Figure 10-29 Simple loop model in SAM

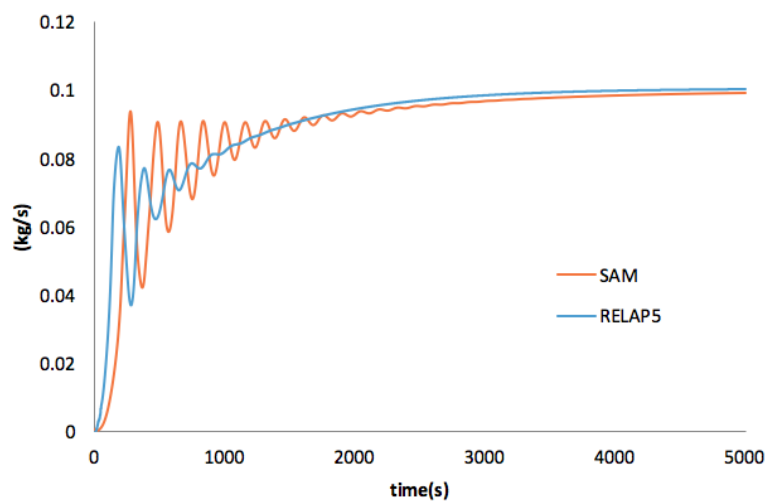

Figure 10-30 Comparison of the primary mass flow rates calculated from SAM and RELAP5

10.4.4. LTDF SAM model

In this section, a benchmark study using SAM for a LTDF is carried out. A schematic of the input model built for LTDF is shown in Figure 10-31. This model consists of the primary loop, the DRACS loop, and the air loop. The primary pump in the LTDF model provides the driving force for the primary loop to simulate reactor normal operation. DHX and NDHX are the two heat exchangers that provide the loop coupling and transfer heat in the LTDF system. Figure 10-32 shows a schematic of the LTDF SAM model from Paraview. ParaView

is an open-source tool that is able to provide visualization application and data analysis. Parameters including the temperature, velocity, pressure, fluid density and heat transfer coefficient can be chosen to investigate the results in the loaded model. In addition, the transient simulation results from SAM can be visualized through Paraview to show animation for each time step.

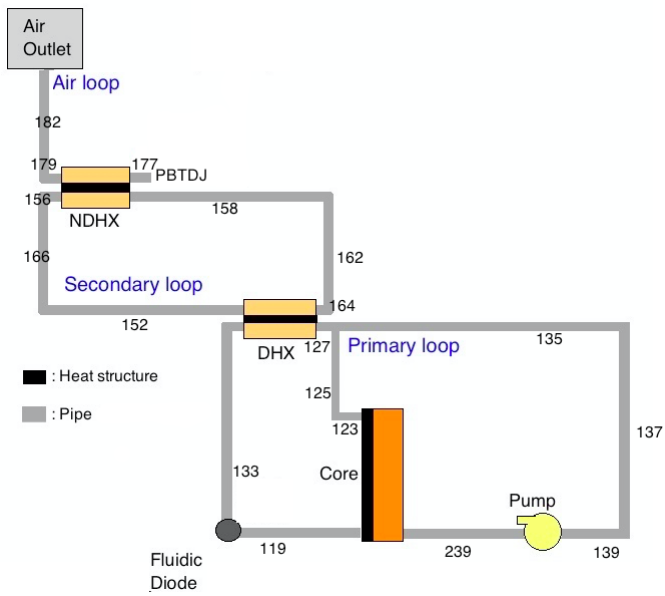

Figure 10-31 Schematic of LTDF SAM model

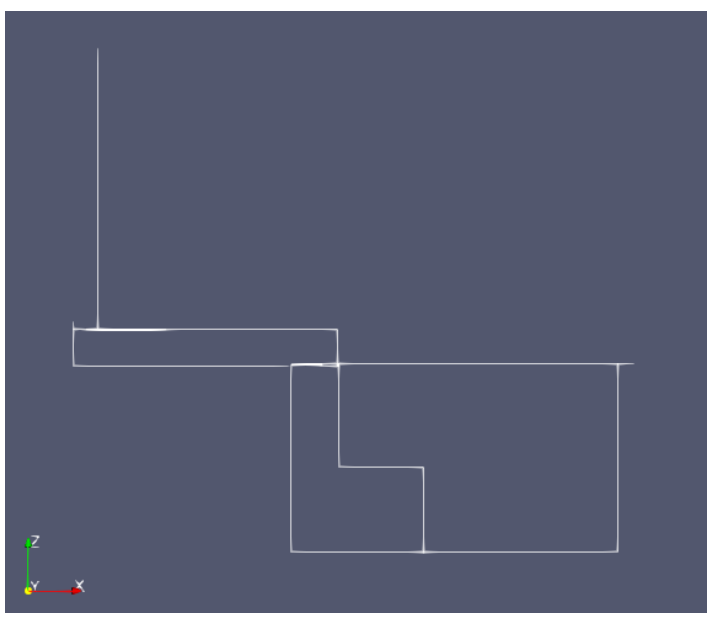

Figure 10-32 LTDF model in Paraview

In the LTDF model built in SAM, the inputs for the DHX and NDHX models are listed in Table 10-3 and Table 10-4. Equations 11.10 and 11.11 are the heat transfer correlations used for modeling the DHX and NDHX, respectively [10.31-32]. In addition, a pump trip curve is applied to the SAM input based on the experimental data, shown in Table 10-3. For the SAM LTDF model, the Gaussian quadrature integration method is selected as the numerical scheme for the benchmark study of the LTDF. The JFNK method is utilized to solve the nonlinear equations in SAM. All the unknowns are solved simultaneously by JNFK and preconditioning is required to solve the equations efficiently.

Table 10-3 DHX inputs in SAM

DHX	Shell side	Tube side
Area (m^2)	0.0094	0.0034
Hydraulic diameter (m)	0.02043	0.00739
Tube length (m)	0.36	
Heat transfer surface area density (flow area/wetted perimeter) (m)	185.96	514.12
Tube wall thickness (m^2)	0.0012	
Working fluid	water	water

Table 10-4 NDHX inputs in SAM

NDHX	Tube side	Air side
Area (m^2)	0.0103	0.4385
Hydraulic diameter (m)	0.0159	0.6767
Tube length (m)	0.9	
Heat transfer surface area density (flow area/wetted perimeter) (m)	251.968	5.911
Tube wall thickness (m^2)	0.0009	
Working fluid	water	air

$$Nu = 0.35Re^{0.6}Pr^{0.36}\left(\frac{X_t^*}{X_l^*}\right)^{0.2}(Pr/Pr_w)^{0.25} \tag{10.10}$$

$$Nu = 0.134\left(\frac{\rho v_{max} d_o}{\mu}\right)^{0.68} Pr^{0.33}\left(\frac{e_f}{S}\right)^{0.18}\left(\frac{Y}{S}\right)^{-0.14} \tag{10.11}$$

Table 10-5 Measurement uncertainties of LTDF instruments

Instrument	Model	Instrument uncertainty
Ultrasonic flow meter	ADM 7407/Flexim	1% of reading + 9 mm/s
Thermal mass flow meter	9840MPNH/Eldridge	1% of reading + (0.5% + 0.05%/°C) of full scale (ref: 21°C)
Thermocouple	TMQSS-125G-6 / Omega	0.5°C or 0.4% of full scale
Watt transducer	PC5-117EY25/Ohio Semitronics	0.5% of full scale

The main objective of this task is to perform a code validation using the system-level analysis codes with surrogate fluids and also molten salt experimental data when they become available. The benchmark study of the Low-Temperature DRACS test Facility (LTDF) pump trip scenario has been carried out using SAM (System Analysis Module). The heat transfer correlations used for modeling the DHX and NDHX are also listed in it. A schematic of a SAM input model built for Low-Temperature DRACS test Facility (LTDF) with three coupled loops included is shown in Figure 10-31.

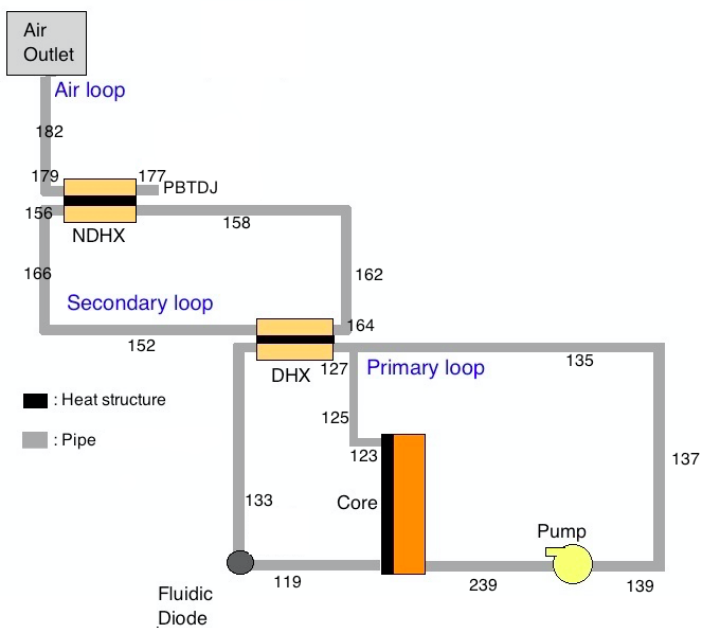

Figure 10-33 Schematic of LTDF

In the previous quarterly report, a heat loss model was not included in the LTDF SAM model since the LTDF system model was under development. For benchmark analysis, heat losses from the test facility to the environment can affect the accuracy of simulation results.

Therefore, during the current reporting period a heat loss model is built into the LTDF SAM model to more accurately simulate the LDTF in SAM. The heat loss model includes the piping structures and two-inch thick insulation on the piping. A constant temperature 300 K (17 °C) is used for the environment air temperature. A constant natural convection heat transfer coefficient of W/m^2-K is also utilized to model the heat transfer from insulation surface to the environment for each structure. The heat transfer coefficient from the insulation outer surface to the ambient air is calculated based on Eq. 11.1, which is usually used for natural convection in vertical plates [10.33].

$$Nu = \left\{0.825 + \frac{0.387Ra^{1/6}}{[1 + (0.492/Pr)^{9/16}]^{8/27}}\right\}^2 \tag{10.1}$$

Pr: Prandtl number
Ra: Rayleigh number

In modeling the LTDF pump trip scenario in SAM, the Gaussian quadrature integration and implicit-Euler methods are selected repectively as the spatial and temporal integration schemes for the benchmark study. The method of Jacobian-Free Newton Krylov (JFNK) is utilized to solve the non-linear equations in SAM. All the unknowns are solved simultaneously by JFNK and preconditioning is required to solve the equations efficiently. The calculation time of SAM depends on the numbers of the nonlinear equations solved using the Newton method and the linear equations by the Krylov solver.

The LTDF is heated up with a 2-kW power provided by the heaters in the simulated core to the system. The heating process reaches a steady state to simulate the conditions of DRACS under reactor normal operation, which also serves as the initial condition for the pump trip scenario. From the experimental data, 294.46 K is used for the air inlet temperature to the NDHX as the boundary condition for the system. An updated comparison of the SAM simulation results and the corresponding experimental data at steady state with heat losses considered is listedTable 10-6, including the coolant temperatures and mass flow rates in each loop. The temperatures and mass flow rates between the SAM simulations and experimental data are less than 2.6% and 5%, respectively. It is noted that measurement uncertainties of the coolant temperature of thermal couples are ± 0.5°C at 95% confidence level. The uncertainties of ultrasonic flow meters for water flow rate measurements in the primary and DRACS loops are about ±0.0089 kg/s and ± 0.0033 kg/s, respectively, at 95% confidence level. The uncertainty of thermal mass flow meter for air flow measurement is about ± 0.01 kg/s at 95% confidence level. The mass flow rates from SAM simulation are within the measurement uncertainties at 95% confidence level.

Table 10-6 Comparison of SAM simulation results and experimental data at steady state before pump trip

	DHX shell-side outlet temp. (K)	DHX shell-side inlet temp. (K)	DHX Tube-side inlet temp. (K)	DHX Tube-side outlet temp. (K)	Air inlet temp. (K)	Air outlet temp. (K)	DHX mass flow rate (kg/s)	Pump mass flow rate (kg/s)	DRACS mass flow rate (kg/s)	Air mass flow rate (kg/s)
Experimental data	361.17	373.57	316.15	340.57	294.46	318.36	0.044	1.729	0.020	0.093
SAM simulation	359.57	370.98	317.67	341.47	294.46	317.69	0.046	1.733	0.021	0.09
Relative difference between simulation and experimental data	1.6 K	2.59 K	1.52 K	0.9 K	0 K (boundary condition)	0.67 K	4.5 %	0.17 %	5 %	3.2 %

*Note: temp.= temperature

Figure 10-34 to Figure 10-37 show the SAM simulation results compared with experimental data during primary pump trip scenario including the water and the air temperatures and mass flow rates in the three loops. During the transient, the uncertainties of the heat transfer correlations used in the DHX and NDHX and heat loss modeling from the LTDF to the environment can contribute to the discrepancies between the simulation results and experimental data. From Figure 10-37, the air mass flow rate in the simulation decreases with time after the pump trip while the mass flow rates in the other two loops are stable during the transient. Based on heat balance, if mass flow rate decreases, the temperature difference between the inlet and outlet of the NDHX will increase if the heat transfer rate remains similar. After 20,000 s, the air mass flow rate becomes lower than the experimental data and the temperature difference between the air inlet and outlet of NDHX becomes larger than the experimental data. The air temperatures in the NDHX also affect the water temperatures in the other two loops, which leads to the discrepancies between the simulation results and experimental data. From Figure 10-34 at 28,000 s, the DHX shell-side outlet temperature in the SAM simulation is 2 ^{o}C higher than the experimental data. The DHX tube-side inlet temperature in the SAM simulation is 3 ^{o}C higher than the experimental data, as shown in Figure 10-35. However, the overall simulation results from SAM are in good very agreement with the experimental data for the pump trip scenario.

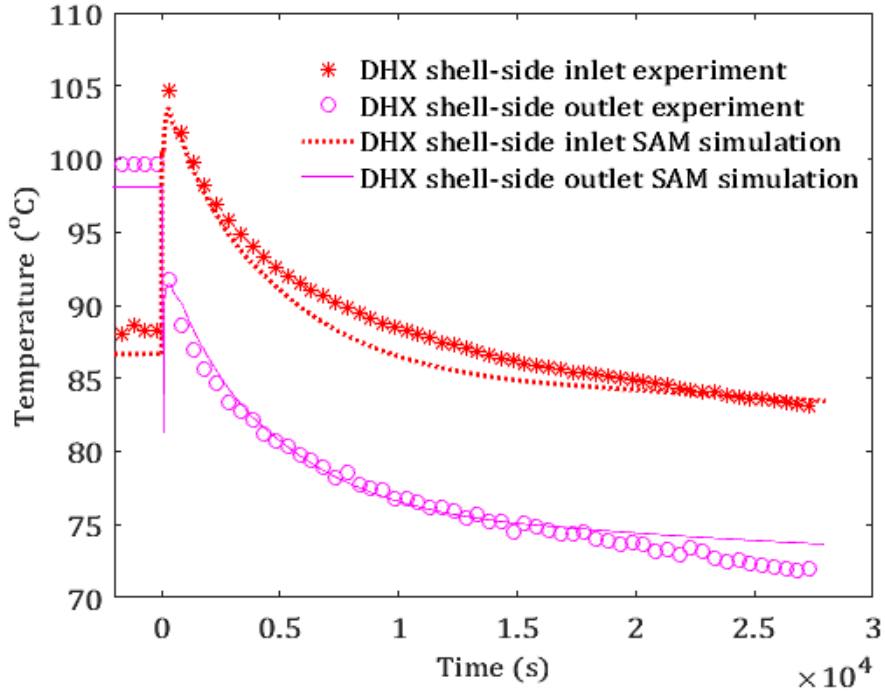

Figure 10-34 Comaparison of the SAM simulation results and experimental data for the DHX shell-side inlet and outlet temperatures

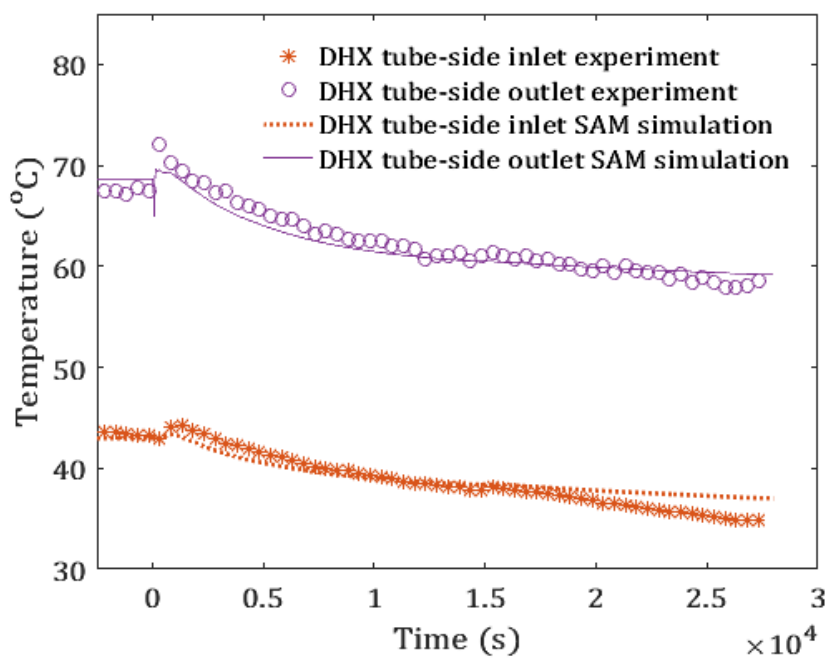

Figure 10-35 Comaparison the SAM simulation results and experimental data for the DHX tube-side inlet and outlet temperatures

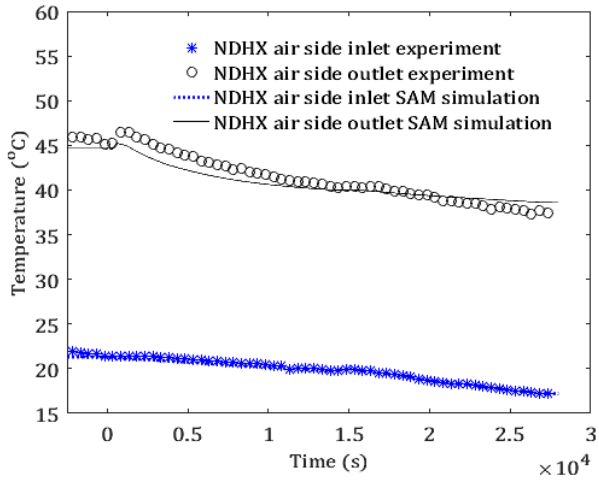

Figure 10-36 Comaparison of the SAM simulation results and experimental data for the NDHX air-side inlet and outlet temperature

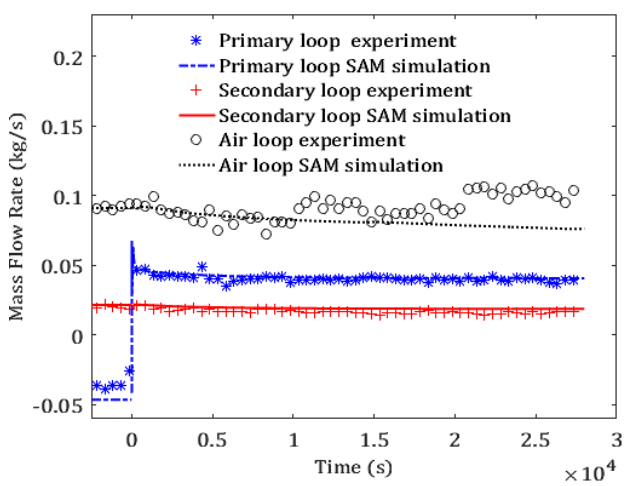

Figure 10-37 Comaparison of the SAM simulation results and experimental data for mass flow rates in the three loops

Figure 10-38 shows the water and air temperatures at the LTDF in three different times during the pump trip scenario from theParaView outputs. After the pump trip is initiated, the distribution of water and air temperature along the thee coupled loops can be observed. The velocity distributions of the primary loop before and after the pump trip initiation in the LTDF are also shown in Figure 10-39 from Paraview. After the primary pump trip, the water velocity in the DHX branch change from a negative value to a positive value, which represents the flow reversal phenomenon. The primary flow is mainly driven by natural circulation where the simulated core and DHX are the heat source and heat sink, respectively. From Figure 10-39 (b), the velocity on the pump side is nearly 0 m/s due to no presence of heat sink on the pump side to provide buoyance force in the pump branch.

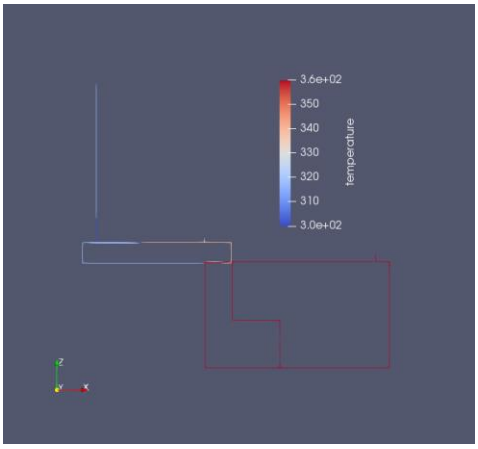

(a)

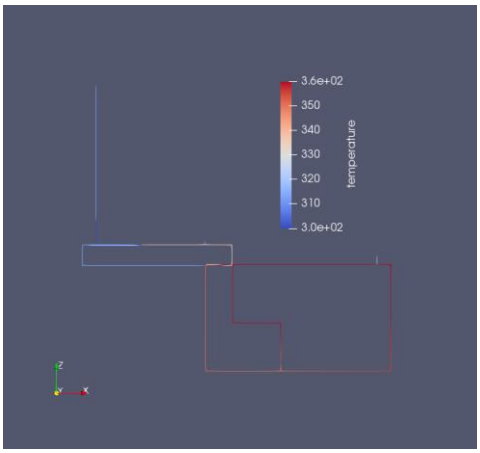

(b)

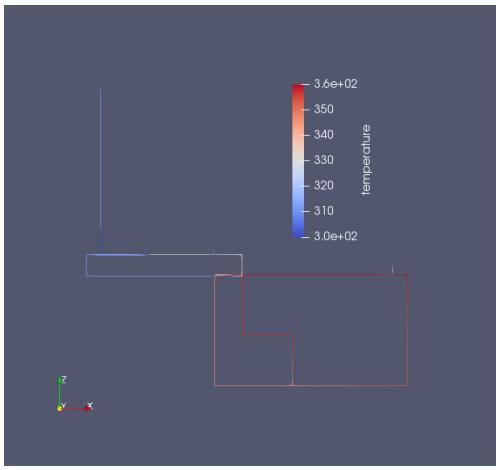

(c)

Figure 10-38 Water and air temperature distributions in LTDF at (a) 0 s, (b) 10,000 s and (c) 20,000 s after pump trip initiation

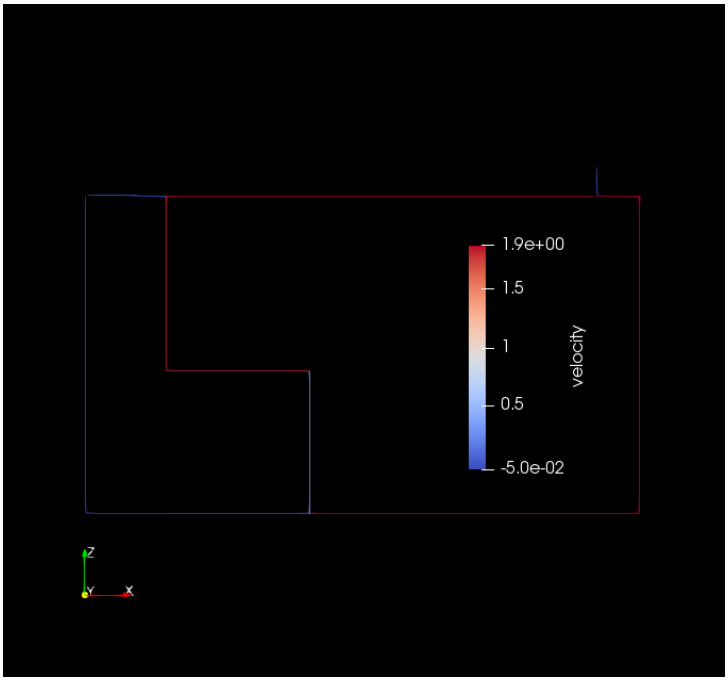

(a)

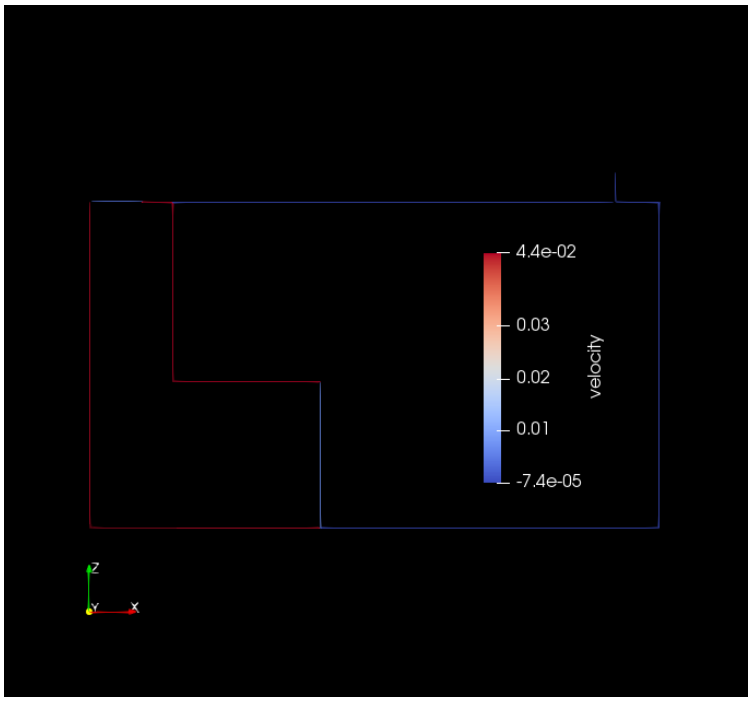

(b)

Figure 10-39 Velocity of primary loop at (a) 0s and (b) 10,000 s after pump trip initiation

This report sumarrizes the benchmark study of the LTDF pump trip scenario using SAM for code/model validation. The molten salt experimental data of HT-FSTF will be used for code validation as the future work under this task when the experimental data are available. Furthermore, the AHTR SAM model is also under development. The AHTR SAM model will be used for steady-state and transient analysis for two scenarios,including Loss of Forced Circulation (LOFC)and loss of multiple DRACS loops.

10.5. AHTR System Analysis using RELAP5

The code validation study discussed in 10.4 shows good agreement between the RELAP5 code predictions and experimental data. The RELAP5 code is therefore selected to perform AHTR thermal hydraulics transient analyses. Molten salt thermodynamic properties and heat transfer correlations for fluted tube are implemented into the RELAP5 code. An AHTR RELAP5 model is developed to perform system analysis for two transient scenarios, namely LOFC and loss of multiple DRACS loops, and to investigate and demonstrate the passive heat removal capability of the proposed fluted-tube DHX and NDHX designs for AHTR.

10.5.1. Implementation molten salt properties into RELAP5/SCDAPSIM/MOD 4.0

RELAP5 code was mainly developed for light water reactor transient analyses. Understandably, molten salts were not available in our current RELAP5 code for FHR transient analysis. Willams et al. [10.34] have investigated molten salts thermodynamic and transport properties at different temperatures. Davis et al. [10.35] implemented properties of molten salts into the RELAP5-3D/ATHENA code, including FLiBe, FLiNaK, $NaBF_4$-NaF and NaF-ZrF_4. Anderson and Sabharwall [10.36] reviewed thermophysical properties of molten salts for the secondary loop to be implemented into RELAP5-3D. Based on the research done by Davis et al. and Anderson and Sabharwall, the correlations of molten salts implemented in RELAP5-3D were adopted in our current research. Fluid properties of two molten salts, FLiNaK and KF-ZrF_4 have been implemented into RELAP5/SCDAPSIM/MOD 4.0 code for future FHR analysis.

It is assumed that the specific heats of the two molten salts are constant because the changes with temperature are small. The densities of the two molten salts are functions of the temperature and pressure. The relavant properties of FLiNaK and KF-ZrF_4 are listed as follow.

The density ρ (kg/m^3) and isothermal compressibility κ (1/Pa) are shown in Eqs. (10.1) and (10.2). $\rho(T)$ in Eqs. (10.3) and (10.4) are the density function depending on the temperature of FLiNaK and KF-ZrF_4.

$$\rho = \rho_T[1 + \kappa(P - P_0)] \tag{10.1}$$

$$\kappa = 2.3 \times 10^{-11} e^{0.001T} \tag{10.2}$$

$$\rho(T)_{FLiNaK} = -0.73(T - 273.15) + 2530 \tag{10.3}$$

$$\rho(T)_{KFZrF_4} = -0.887(T - 273.15) + 3416 \tag{10.4}$$

where P_0 is the reference pressure, which is set as the pressure at the triple point. T is temperature in Kelvin.

The coefficient of thermal expansion β (1/K) is defined as:

$$\beta = \frac{1}{\nu}\left(\frac{d\nu}{dT}\right)_p = -\frac{1}{\rho}\left(\frac{d\rho}{dT}\right)_p \tag{10.5}$$

The thermal expansion coefficient of the two salts FLiNaK and $KFZrF_4$ are given as:

$$\beta(T)_{FLiNaK} = \frac{0.73}{-0.73(T - 273.15) + 2530} \tag{10.6}$$

$$\beta(T)_{KFZrF_4} = \frac{0.887}{-0.887(T - 273.15) + 3416} \tag{10.7}$$

The specific heat c_p (J/kg-K) of the two salts are assumed as constants, shown in Table 10-7.

Table 10-7 Specific heat of FLiNaK and KF-ZrF_4

Salt	Specific heat (J/kg-k)
FLiNaK	1,884
KF-ZrF_4	1,046

The liquid dynamic viscosity μ (kg/m-s) with temperature of the two salts are given as:

$$\mu\,(T)_{FLiNaK} = 4 \times 10^{-5} e^{(4170/T)} \tag{10.8}$$

$$\mu\,(T)_{KFZrF_4} = 1.59 \times 10^{-5} e^{(3179/T)} \tag{10.9}$$

Eqs. (10.10) and (10.11) are for the surface tension σ (N/m) of FLiNaK and $KFZrF_4$

$$\sigma(T)_{FLiNaK} = -1.2 \times 10^{-4}(T - 273.15) + 0.26 \tag{10.10}$$

$$\sigma(T)_{KFZrF_4} = -7.134 \times 10^{-5}(T - 273.15) + 0.182 \tag{10.11}$$

The thermal conductivity k (W/m^2-K) are expressed in Eqs. (10.12) and (10.13):

$$k(T)_{FLiNaK} = 5 \times 10^{-4}T + \frac{32}{41.3} - 0.34 \tag{10.12}$$

$$k(T)_{KFZrF_4} = 5 \times 10^{-4}T + \frac{32}{103.9} - 0.34 \tag{10.13}$$

The following correlation is for the saturation line of FLiNaK and KF-ZrF_4. Because of the lack of experimental data for these two salts, this correlation obtained from the saturation line of FLiBe is utilized for the two salts [10.34].

$$P_{sat} = 133.32 \times 10^{(9.04-10500/T)}, \tag{10.14}$$

where T_{sat} and P_{sat} are the saturation temperature and saturation pressure, respectively.

The melting point is set as the triple point temperature T_0 . The triple point pressure P_0 can be calculated from the saturation line. Both the critical temperature T_{crit} and critical pressure P_{crit} are obtained from the saturation line. These properties of FLiNaK and KF-ZrF_4 are list in Table 10-3 [10.34-36].

Table 10-8 Triple point temperature T_0 , triple point pressure P_0, critical temperature T_{crit} and critical pressure P_{crit} of FLiNaK and KF-ZrF_4

Salt	T_0 (K)	P_0(Pa)	T_{crit} (K)	P_{crit} (Pa)
FLiNaK	727.15	5.3×10^{-4}	2138.9	1.8023×10^{6}
KF-ZrF_4	663.15	2.145×10^{-5}	2138.9	1.8023×10^{6}

10.5.2. RELAP5 AHTR Model

One of the objective in this study is to perform steady state and transient simulation of AHTR for evaluating the reactor design and investigate the capability of passive heat removal system. An AHTR model has been built in RELAP5/SCADAPSIM/MOD 4.0 [10.11]. In our current study, thermodynamic and transport properties of FLiBe, FLiNaK, and KF-ZrF_4 have been implemented into the RELAP5 code. The model includes three primary loops, three intermediate loops, three DRACS loops, and three air loops. For the reactor vessel, there are four rings of fuel assemblies, an upper plenum, and a lower plenum. In the AHTR design, FLiBe is utilized as the coolant in the primary loops and KF-ZrF_4 is the coolant in the three intermediate loops and three DRACS loops. Figure 10-40 shows a schematic of the AHTR RELAP5 model.

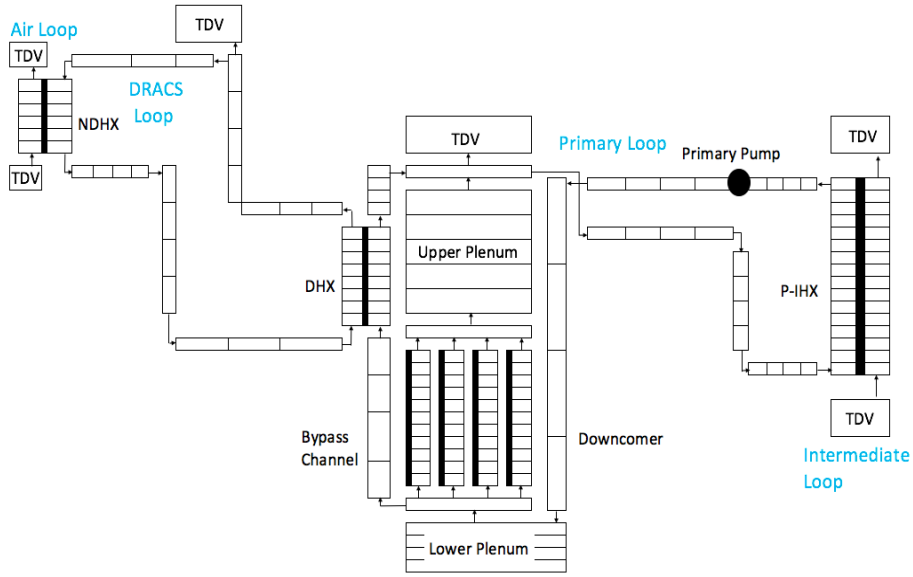

Figure 10-40. Schematic of the AHTR RELAP5 model

For the downcomer in AHTR design, it is divided vertically into eight angular regions, three for primary loops, three for DRACS (bypass flow), one for maintenance cooling system, and another for the refueling lobe in the AHTR design. In the current AHTR RELAP5 model, only six regions of the downcomer are considered, three for the primary loops and three for the bypass flow.

During reactor normal operation, the core flow and three by pass flows merge at top of upper plenum, then the merged flow separates into three primary loops. The flow separation point corresponds to the branch in the AHTR RELAP5 model. Primary salt flow through P-IHXs and transfer heat to intermediate loops, then flow back to the downcomers. Each primary loop has a primary pump to provide driving force. Three primary flows merged in the branch that connect to the lower plenum. Above the upper plenum, there is a time-dependent volume (TDV) to setup the system pressure by assigning a constant pressure boundary of 101.3 kPa. In the AHTR design, the cover gas (argon) in the reactor vessel is utilized to prevent chemical reactions in the primary salt with the surrounding air. In addition, the cover gas can be treated as the pressure boundary inside the reactor vessel.

In this AHTR RELAP5 model, there are also three intermediate loops connecting to P-IHXs and utilizing KF-ZrF_4 as working fluid. The intermediate loops are simplified as open loops by using two TDVs to simulate the source and sink of the intermediate fluid. A time-dependent junction (TDJ) is used to control the mass flow rate in each intermediate flow coming from the source TDV.

Other than the primary flow, the other flow paths to the top of upper plenum are bypass flow. The three bypass channels connect to the lower plenum and merge at the upper plenum. DRACS heat exchanger (DHX) locates at each bypass channel to transfer heat to the

DRACS loops. In addition, fluidic diode, a passive flow controller, locates upstream the DHX in each bypass channel. During reactor normal operation, the bypass flow directions are upward since they are driven by the primary pumps. After pump tripped, the bypass flows will start to reverse since the natural circulations are established. The fluidic diodes provide larger flow resistance for upward bypass flows to decrease heat loss to DRACS loops during reactor normal operation. The small amount of heat can keep the DRACS salt in liquid state. However, there is no design value of parasitic heat loss and diodicity of fluidic diode in AHTR. In other words, the simulation results can be utilized as references to determine the the final design. The disc-shaped vortex fluidic diode with a diameter of 304.8 mm is employed in the design. Based on CFD analysis, the form loss coefficient for upward and downward flow are 24.25 and 4.5, respectively.

As shown in Figure 10-40, there are DHX and NDHX in each DRACS loop and the ultimate heat sink is air environment for the passive heat removal system. In the AHTR design, the coolant in DRACS loops is KF-ZrF_4. There is no pump in the DRACS since it mainly depends on natural circulation/convection to remove the decay heat from core. For the air loops, two TDVs are utilized to simulate the source and sink of ambient air of the air chimney.

In the RELAP5 code, heat structures represent solid materials in the model, which are usually used as heat transfer components with calculation of heat conduction and heat convection. There are four types of heat structures in the current AHTR RELAP5 model, including the four core rings, three P-IHXs, three DHXs, and three NDHXs. The design values and RELAP5 input data of the heat structures are provided as follows.

Core

In the AHTR design, there are 252 fuel assemblies in the reactor core and the total core thermal power is 3400 MWth. In our AHTR RELAP5 model, 252 assemblies are separated into four concentric rings. At this stage, a uniform power distribution is assigned to the fuel assemblies in each ring. The right boundary coordinate and left boundary coordinate are 0 and 0.01275 m, respectively. The number is chosen from half of the fuel plate thickness. The heat transfer area is calculated based on the contact surface between the fuel plates and primary coolant. The flow area, power, and heat transfer area of the four rings are summarized in Table 10-9.

Table 10-9. Coolant flow areas and the power of four core rings

	Ring 1	**Ring 2**	**Ring 3**	**Ring 4**
Assembly number	18	42	88	104
Flow area (m^2)	0.87	2.02	4.25	5.01
Power (MW)	243	567	1187	1403
Heat transfer area (m^2)	1193.6	2785.1	5835.5	6896.5

P-IHX

There are three design options for the P-IHX in their research since the tube side and shell side can be either on the primary loop or intermediate loops. The alternative salt coolant in the intermediate loops, FLiNaK, is also considered in their study. It is mentioned that the P-IHX designs are still in the preliminary stage, further study and investigation of the heat exchangers are required. The option of the primary coolant salt as the shell side and the intermediate coolant salt on the tube side in the P-IHX is chosen for our AHTR RELP5 model. Table 10-10 shows the RELAP5 input data for the P-IHX. The material of the tubes is not mentioned in the reference, so Hastelloy N is assumed as the heat structure material, which is the same as the tubes in DHX and NDHX. The left boundary and right boundary are the radius of tube inner wall and tube outer wall, respectively. The tube wall in this P-IHX model is divided into five meshes. Based on a node independence analysis, 10 meshes are chosen for the P-IHX in our current AHTR RELAP5 model.

Table 10-10. P-IHX input data of AHTR RELAP5 model

Left boundary coordinate (m)	0.00987
Right boundary coordinate (m)	0.01111
Heat structure mesh number	5
Total Heat transfer area (m^2)	8000.0
Mesh number	10

DHX

The single-wall fluted tube design for DHX and NDHX are utilized in this AHTR RELAP5 model with increased heat transfer capabilities. The Non-Dominated Sorting in Genetic Algorithms (NSGA) [10.38] is utilized to optimize the DRACS design based on evaluating the constructing cost and heat transfer capabilities. The geometric information is listed in *Table 10-11*and *Table 10-12*Horizontal design for the fluted tubes is adopted since less tube length is needed as compared to the vertical orientation arrangement.

NDHX

The single-wall design of the fluted tubes in NDHX is adopted since it can effectively reduce the total tube length compared to the double-wall tube design. However, if the single-wall tube design is adopted, the passive air chimney actuation mechanism should also be adopted to prevent tritium release to the ambient air during reactor normal operations. The optimum single-wall NDHX design is listed in the Table 10-12.

Table 10-11. Specification of single-wall fluted tube DHX

DHX	
Tube arrangement/ tube type	Horizontal triangular/ Fluted tube
Tube material	Hastelloy N
Tube size (mm)	D_{bi} = 10.67, D_{eo} = 16.64, t_w = 0.508, p = 8.23, N_s = 4, L = 3000
Tube number	2100
Number of rows/columns	140/15
Pitch to diameter ratio	1.5
Tube-side fluid and shell-side fluid	KF-ZrF_4/ FLiBe
Heat removal capacity (MW)	8.5
DHX-NDHX vertical height difference (m)	8.15
DRACS loop piping diameter/ length(m)	0.3/56.3
Core-DHX vertical height difference (m)	10

Table 10-12. Specification of single-wall fluted tube NDHX

NDHX	
Tube arrangement/ tube type	Inline horizontal / Fluted tube
Tube material	SS 316H
Tube size (mm)	D_{bi} = 10.67, D_{eo} = 16.64, t_w = 0.508, p = 8.23, N_s = 4, L = 2500
Tube number	2625
Number of rows/columns	25/105
Pitch to diameter ratio	1.5
Tube-side fluid and shell-side fluid	KF-ZrF_4 / Air
Heat removal capacity (MW)	8.5
NDHX-chimney vertical height difference (m)	18.3
Chimney inner/outer shell diameter (m)	3.7/4.7

Because the fluted tubes are adopted in the DHX and NDHX designs, heat transfer correlations in fluted tubes were implemented into the RELAP5/SCDAPSIM/MOD4.0 code. In these correlations, the Nusselt number is a function of the Reynolds number, Prandtl number and fluted tube geometry. Equations 11.1 and 11.2 are heat transfer correlations for fluted tube with a certain range of the Reynolds number [10.39]. In the RELAP5/SCDAPSIM/MOD4.0, the correlation basically divides the Reynolds number into two regions. If the Reynolds number is lower than 5,000, Eq. (10.1) will be used as the heat transfer correlation. Similarly, heat transfer correlation shown in Eq. (10.2) will be utilized when the Reynolds number is larger than or equal to 5,000. In the current design, the fluted tube geometry of DHX and NDHX are the same. The geometry parameters of the current tube design are listed in Table 10-13.

$$Nu = 0.014 Re^{0.842} Pr^{0.4} e^{*-0.067} p^{*-0.293} \theta^{*-0.705} \quad \text{for } 500 \leq Re \leq 5{,}000 \tag{10.1}$$

$$Nu = 0.064 Re^{0.773} Pr^{0.4} e^{*-0.242} p^{*-0.108} \theta^{*0.599} \quad \text{for } 5{,}000 \leq Re \leq 82{,}000 \tag{10.2}$$

where the three dimensionless parameters, p^*, e^* and θ^*, in the fluted tube heat transfer correlations represent:
p^* = nondimensional flute pitch (p/D_v)
p = flute pitch (mm)
D_v = volume-based fluted tube diameter (mm)
e^* = nondimensional flute depth (e/D_v)
e = flute depth (mm)
θ^* = nondimensional flute helix angle ($\theta/90$)
θ = flute helix angle ($tan^{-1}(\pi D_v/N_s)$) (deg)
N_s = number of flute starts

Table 10-13. The geometry parameters of fluted tubes in DHX and NDHX

Flute pitch (mm)	0.0082
Nondimensional flute pitch	0.7083
Flute depth (mm)	0.0025
Nondimensional flute depth	0.2132
Flute helix angle (deg)	50.33
Nondimensional flute helix angle	0.5592
Volume-based fluted tube diameter (mm)	0.012

10.5.3. Steady-State of Reactor Normal Operation Results with Air Chimneys Closed

Since the single-wall design of fluted tubes is adopted in the current NDHX design, the air chimney is considered to be closed during reactor normal operation to eliminate the tritium release into the ambient. The steady-state situations are calculated for reactor normal operation in the AHTR RELAP5 model with air chimneys closed. In addition, trip valves located in the air chimneys are utilized to control the chimney opening.

In the AHTR RELAP5 model, a 3400-MW thermal power is provided from the core, the same as the AHTR design value. For the boundary conditions of the model, the inlet temperature and total mass flow rates of the three intermediate loops are set as 600°C and 43,200 kg/s, respectively, and the inlet temperatures of the air loops are set as a constant value of 30°C.

FromTable 10-14, the simulation results of AHTR RELAP5 model is set to match the design values, including the core inlet temperature, core outlet temperature, and core mass flow rate. In addition, even though the air chimneys are closed, there is still natural circulation in the DRACS loops, indicated by the small total DRACS mass flow rate.

Table 10-14. AHTR design value and RELAP5 simulation results in a steady state of reactor normal operation [10.37]

	AHTR design value	AHTR RELAP5 model
Thermal power (MWth)	3400	3400
Core mass flow rate (kg/s)	28,500	28,500
Core inlet/outlet temperature (°C)	650/700	650/700
One bypass mass flow rate (kg/s)	N/A	2700
Parasitic heat loss/thermal power (%)	N/A	0.076
Intermediate loop hot/cold leg temperature (°C)	675/600	675/600
Total intermediate loop mass flow rate (kg/s)	43,200	43,200
One DRACS mass flow rate (kg/s)	N/A	53.5
DRACS hot leg/cold leg temperature (°C)	N/A	642/650
One air mass flow rate (kg/s)	N/A	0.5

10.5.4. Loss of Forced Circulation (LOFC)

The performance of decay heat removal in three DRACS loops during LOFC is investigated first using the AHTR RELAP5 model. Before transient, AHTR is in normal operation, and the air chimneys are closed to reduce the heat loss and decrease the tritium release to the environment. The comparison of AHTR design value and RELAP5 simulation results of steady-state conditions in reactor normal operation are listed inTable 10-14. The AHTR

RELAP5 model matches the available design value of AHTR including temperatures and mass flow rates.

When LOFC is initiated (0 s), all pumps including the three primary pumps and three intermediate pumps are tripped and fully stop at 100 seconds. The three air chimneys are passively opened and the reactor scrams at 0 s. The decay power curve referenced from the typical pressurized water reactor (PWR) decay power curve is applied to simulate reactor scram in LOFC.

The comparison of the decay power, heat removal rate of the three primary loops, and heat removal rate of the three DRACS are shown inFigure 10-41. The heat removal rate of the three primary loops decreases rapidly after LOFC is initiated due to loss of forced flow. Though the primary loops lose forced flow, natural circulation is established in the primary loops and are demonstrated to be able to remove a small amount of heat after the start of LOFC. The decay heat removal rate of three DRACS loops surpasses the reactor decay power at 5 hours after LOFC is initiated. Within the 5-hour time span, the reactor temperature increases over time and should be investigated to prevent molten salt and structure temperature from exceeding their material limits. It can be observed that the decay heat is mainly removed by the three DRACS loops and the heat removal rate shows fairly stable values during the transient.

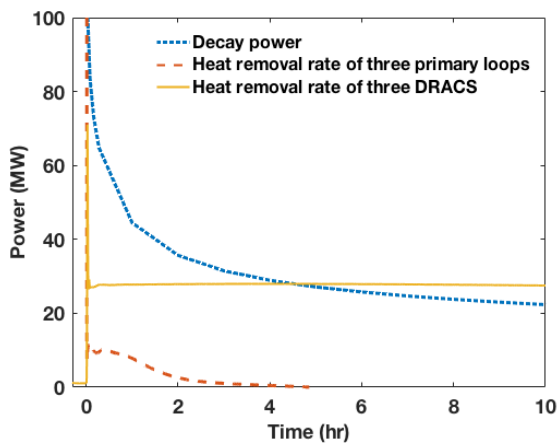

Figure 10-41. Comparison of the decay power, heat removal rate by three primary loops, DRACS heat removal rate of three DRACS loops during LOFC.

The core inlet and outlet temperatures are 650°C and 700°C before the transient, respectively. In LOFC simulation as shown in, the peak core outlet temperature and maximum fuel temperature during the transient are less than 750 °C, which are hundreds degree lower than the salt boiling (1400°C) or fuel damage (1600°C) temperature [10.37]. After around 5 hours, the decay power is lower than the DRACS heat removal rates, which also results in the core inlet and outlet temperatures decrease.

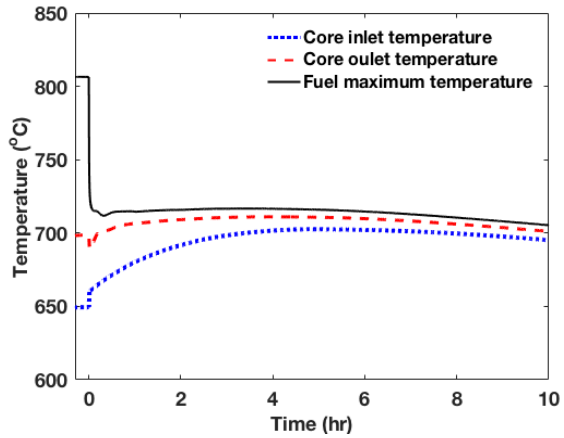

Figure 10-42. Core inlet and core outlet temperature during LOFC

The inlet and outlet temperatures of the DHX bypass side and the mass flow rate of one bypass channel are shown in Figure 10-43 and Figure 10-44, respectively. Before LOFC, the bypass flow is driven by the primary pumps from the lower plenum through the DHX to the upper plenum. During, normal operation, the temperature difference of the DHX inlet and outlet in the bypass side is minimal since the heat sink of DRACS is closed, as shown inFigure 10-43. Due to smaller flow resistance in fluidic diodes in the downward flow direction and natural circulation flow in the reactor vessel, the bypass flows start to reverse after pump trip, indicated by the negative value of the mass flow rate. Figure 10-44illustrates that the natural circulation in bypass channels reach an equilibrium state, the mass flow rate in one bypass channel is calculated as 400 kg/s at about 1,000 s. The flow reversal also results in the temperature increase in the bypass channel where the flow comes from the upper plenum corresponding to core outlet temperature.

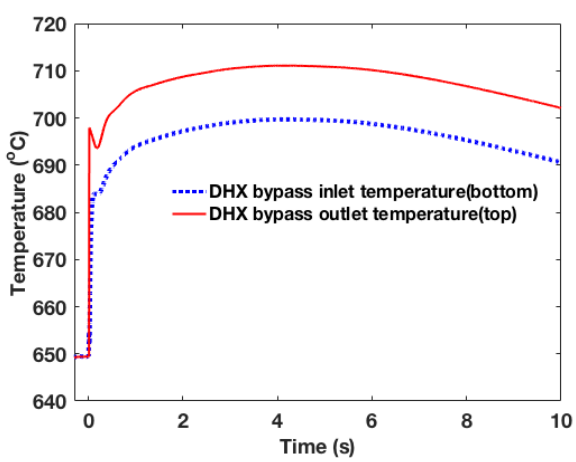

Figure 10-43. DHX inlet and outlet temperatures in bypass channel side during LOFC

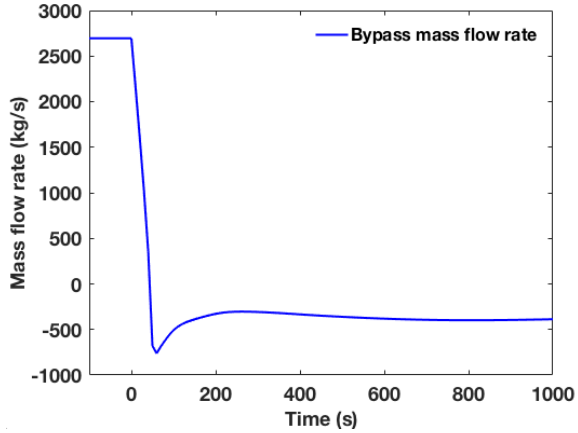

Figure 10-44. Mass flow rates in each bypass channel during LOFC

Figure 10-45 demonstrate the DRACS cold leg and hot leg temperatures. Similar to Figure 10-47, only small amount of heat transfer through the DRACS loop since air chimneys are closed before the transient. The salt hot leg temperature in the DRACS loop increases during the transient due to the molten salt temperature increase in the DHX bypass side after LOFC is initiated. In addition, the rapid temperature drop in the DRACS cold leg is caused by the large temperature difference between DRACS salt and inlet air (30°C). After air chimney is opened, the rapid cooling in NDHX may result in salt freezing at the cold leg of the DRACS loops.

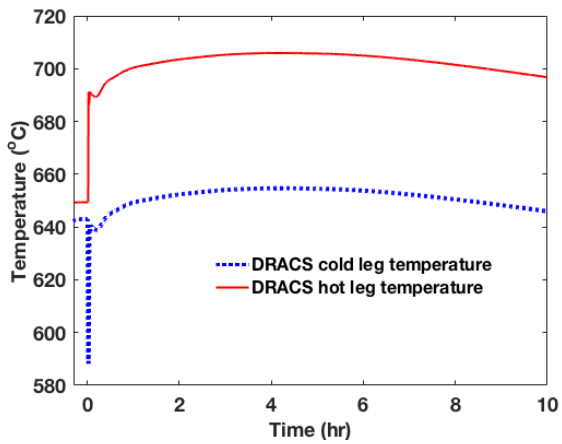

Figure 10-45. DRACS hot-leg and cold-leg temperatures during LOFC

The transient responses of DRACS mass flow rates and air mass flow rates can be observed in Figure 10-46. After air chimneys are passively opened at 0 s, a natural circulation is established in each air loop, and the air flow reaches a stable value. The established natural circulation in each DRACS loop is then followed. At 110 s, the DRACS mass flow rate peak of 232 kg/s is caused by a sudden increase in the primary salt temperature in bypass channel and increased cooling from air chimney. The RELAP5 simulations results of LOFC scenario

in AHTR show that the three DRACS loops with proposed single-wall fluted tube DHX and NDHX are capable of removing the decay heat by natural convection.

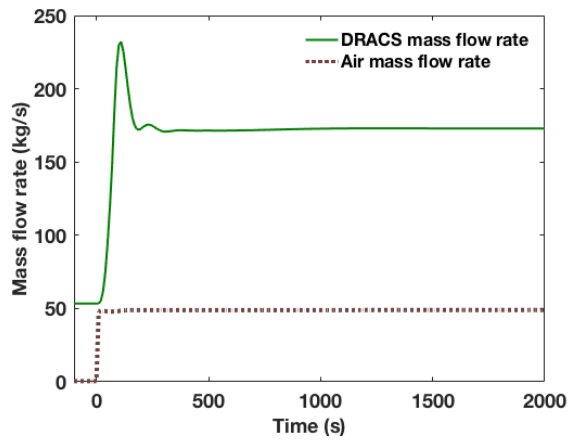

Figure 10-46. Mass flow rates of each DRACS and air loop during LOFC

10.5.5. Simulation of Loss of Two DRACS Loops

In this study, loss of two DRACS loops is considered as one of the most severe scenarios. During the reactor normal operation, the air chimneys of the three DRACS loops remain closed to minimize the heat losses and any tritium release to the environment. When the event of loss of two DRACS loops occurs, only one DRACS loop is capable of removing the decay heat as designed. The other two air chimneys in DRACS failed to open, which results in the ambient air being blocked from the DRACS and the DRACS loops losing their designed cooling capabilities. When this scenario is initiated, the reactor is scrammed at 0 s and the primary salt mass flow rates driven by the three primary pumps decrease to 0 kg/s linearly during the first 100 s. Figure 10-47 shows a comparison of the decay power and heat removal rate from DRACS and primary loops. From the simulation results of loss of two DRACS loops, the open/available DRACS loop is capable of removing about 10 MW decay heat during the transient. The DRACS total heat removal rate shows about 2 MW larger than that provided by the open DRACS loop since the other two closed DRACS loops are also able to remove 1-MW decay heat each by natural convection and heat conduction. In our calculation, the DRACS heat removal rate exceeds the decay power after 50 hours from the reactor scram. *Figure 10-48* demonstrates the DRACS heat removal in a smaller time scale, and the results show the DRACS heat removal rate increases linearly within the first 2,000 s after the scenario is initiated.

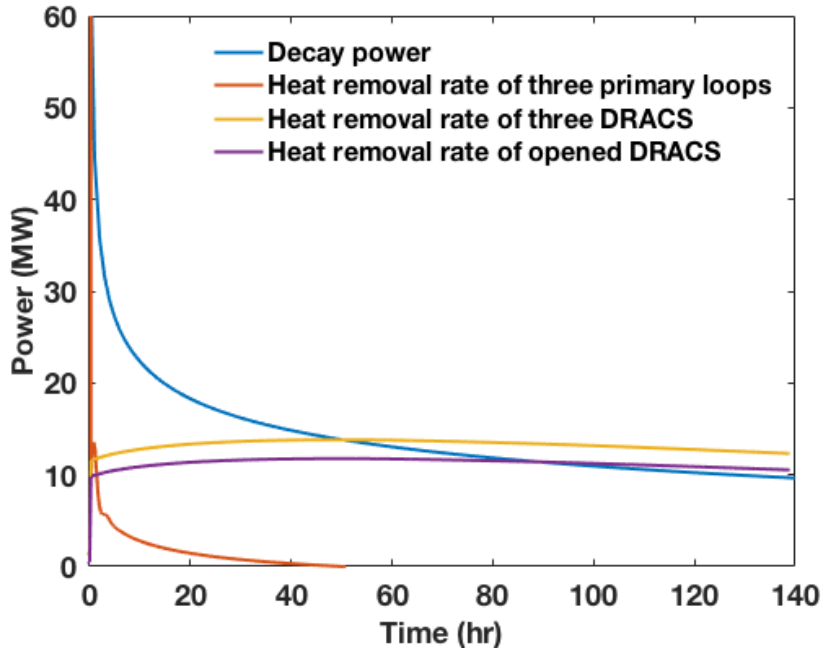

Figure 10-47. Comparison of heat removal rates by DRACS and primary loops, and decay power during loss of two DRACS loops

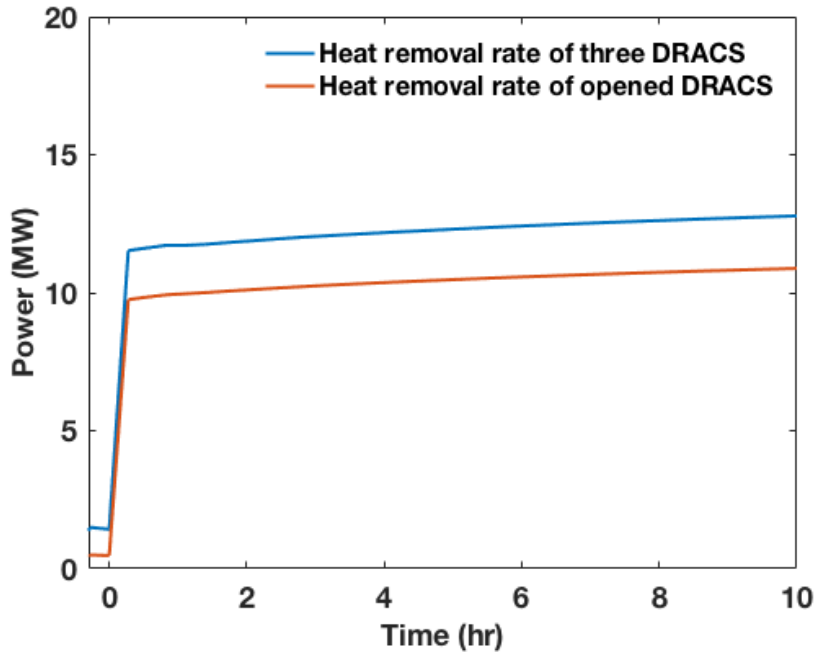

Figure 10-48 Heat removal rates by three DRACS loops and open DRACS loop during loss of two DRACS loops

Figure 10-49 shows the core outlet peak temperature and fuel peak temperature reach 830 and 832 °C at about 50 hours into the scenario. Similar to LOFC, the maximum fuel temperature is close to the molten salt core outlet temperature since the fuel stripe is fairly thin (25.5 mm) and the fuel can be effectively cooled by the primary molten salt. The core outlet peak temperature is about 130 °C higher than that during the reactor normal operation, but it is still 550 °C lower than the molten salt boiling temperature and 350 °C from structure material failure temperature limit.

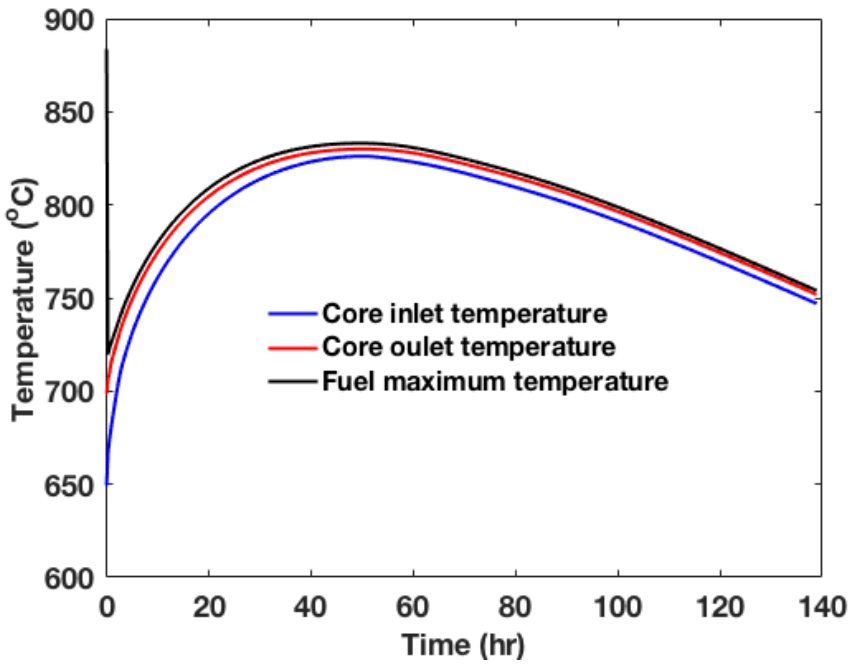

Figure 10-49 Core inlet and core outlet temperature during loss of two DRACS loop during loss of two DRACS loops

The inlet and outlet temperatures on the DHX bypass side are shown in *Figure 10-50*. The mass flow rates of two are shown Figure 10-51. Before the pump trip, the bypass flow comes from the lower plenum and flows through the DHX; and the flow rate is positive. The bypass flows start to reverse when negative values of the mass flow rates are indicated in the figure. The higher mass flow rate corresponds to the working DRACS loop. The results also show that the salt mass flow rate is about 125 kg/s in the other two closed DRACS loops, which indicates the establishment of natural circulation in the two bypass channels even the heat removal rate is small. After the flow reversal, the bypass flow comes from the upper plenum in the vessel, which corresponds to the core outlet temperature. For the inlet and outlet temperatures of the DHX bypass flow, the temperature difference is about 10 and 55 °C for the closed and opened DRACS loops, respectively.

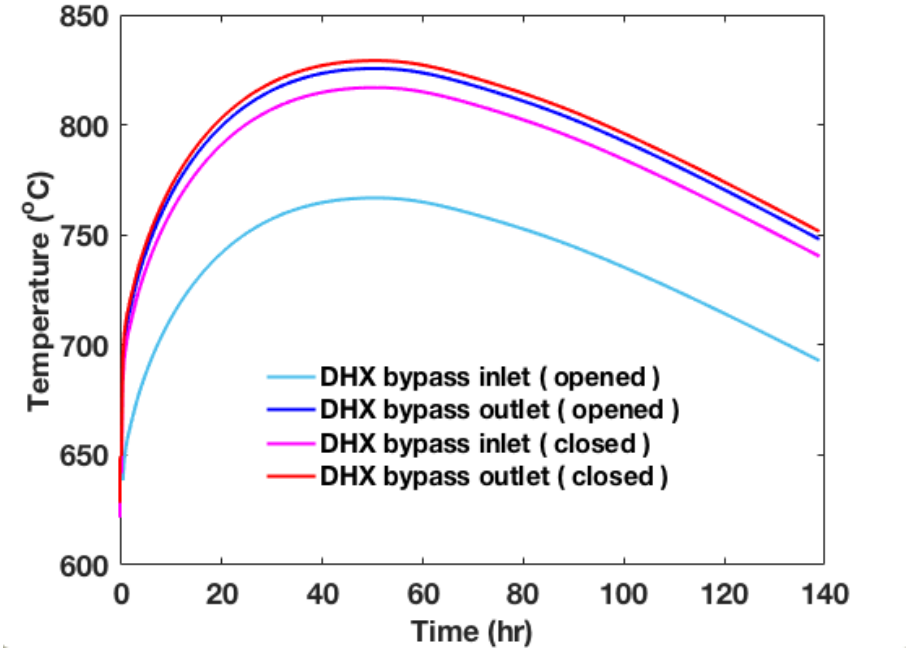

Figure 10-50 DHX inlet and outlet temperatures in bypass channel side during loss of two DRACS loop

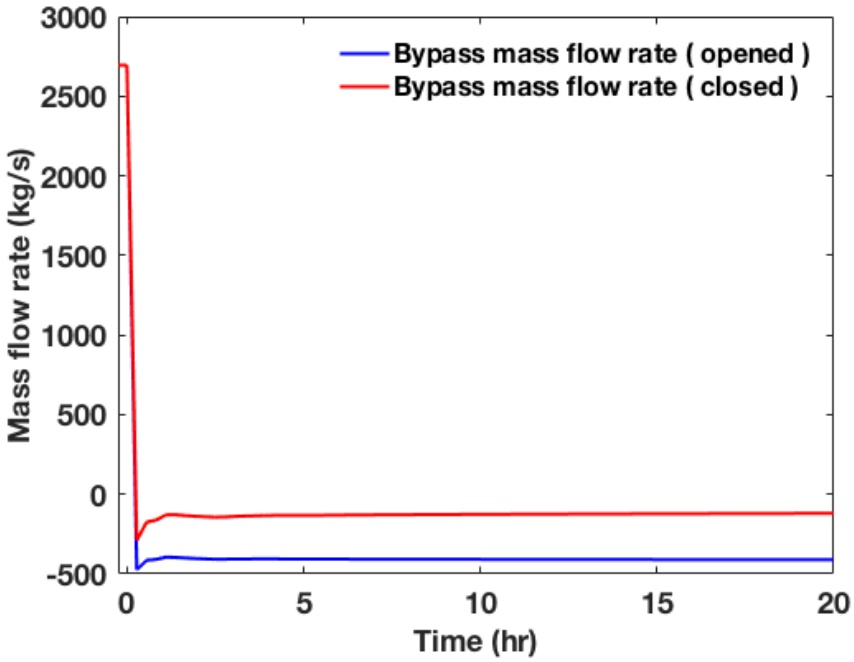

Figure 10-51 Mass flow rates in each bypass during loss of two DRACS loops

The DRACS cold leg and hot leg temperatures are shown in Figure 10-52 and Figure 10-53 in different time scales. After the pump trip and reactor scram, the decay heat removal relies on the cooling of the open DRACS loop. From Figure 10-52, the DRACS temperatures

of the closed and open loop hot legs increase almost linearly to above 680 °C in 0.3 hours after the scenario is initiated. In Figure 10-53, the DRACS temperatures slowly decrease with time after about 50 hours. Similar to DHX bypass flow temperatures, the closed DRACS loops have relatively higher temperatures compared with the open DRACS. Due to cooling from the opened air chimney, the DRACS cold leg temperature is about 70 °C lower than its hot leg temperature. The mass flow rate in each of the DRACS loops is shown in Figure 10-54. The results show there is natural circulation flow established in the closed DRACS loops with lower mass flow rates due to the temperature difference between DHX shell-side and NDHX air side.

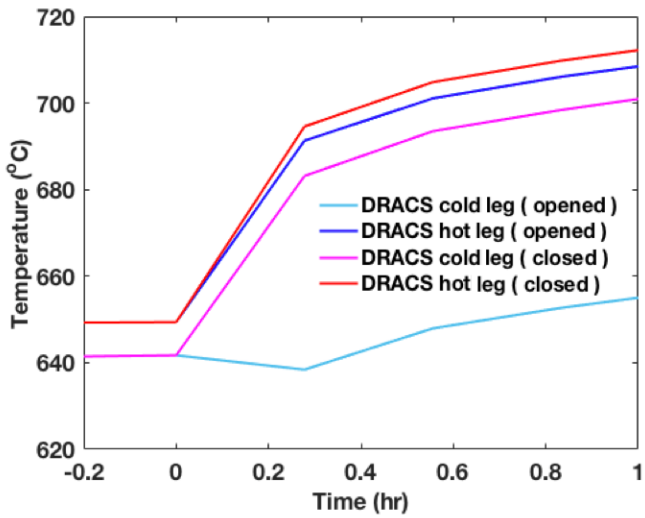

Figure 10-52 DRACS hot-leg and cold-leg temperatures during the first hour of the loss of two DRACS loop scenario

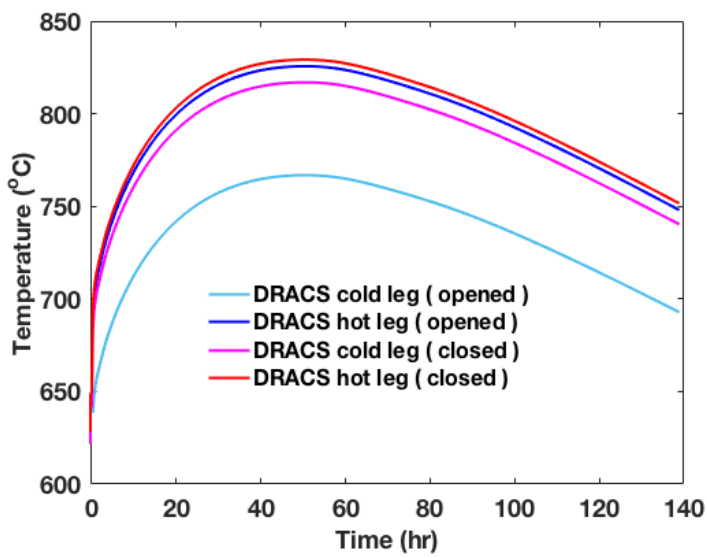

Figure 10-53 DRACS hot-leg and cold-leg temperatures during loss of two DRACS loops

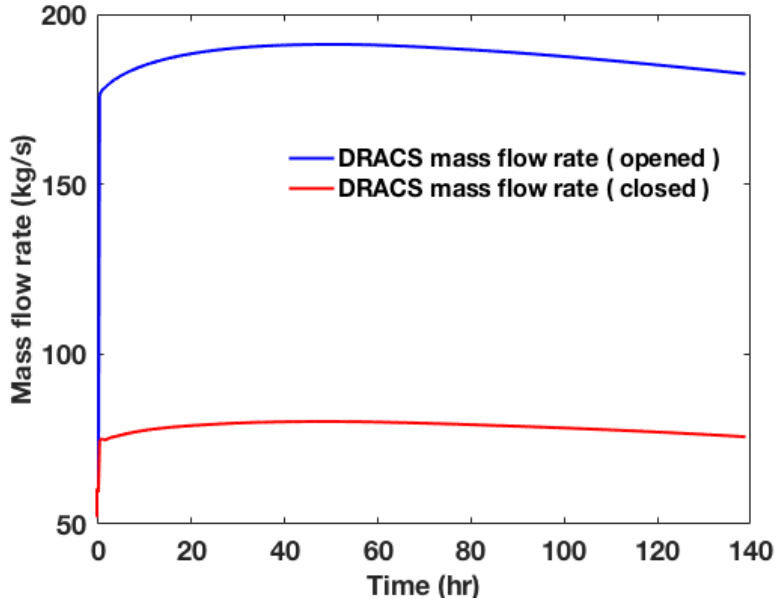

Figure 10-54 Mass flow rates of the DRACS loops during loss of two DRACS loops

Figure 10-55 and Figure 10-56 show the air inlet and outlet temperatures and air mass flow rates. The air inlet temperature is set at a constant temperature of 30 °C as one of the boundary conditions of the system. For the open air chimney, the air outlet temperature increases from 80 to 200 °C. In addition, the quick increase of the air mass flow rate after the air chimney opens indicates that the natural circulation flow is established to remove the decay heat from the core to the ambient air.

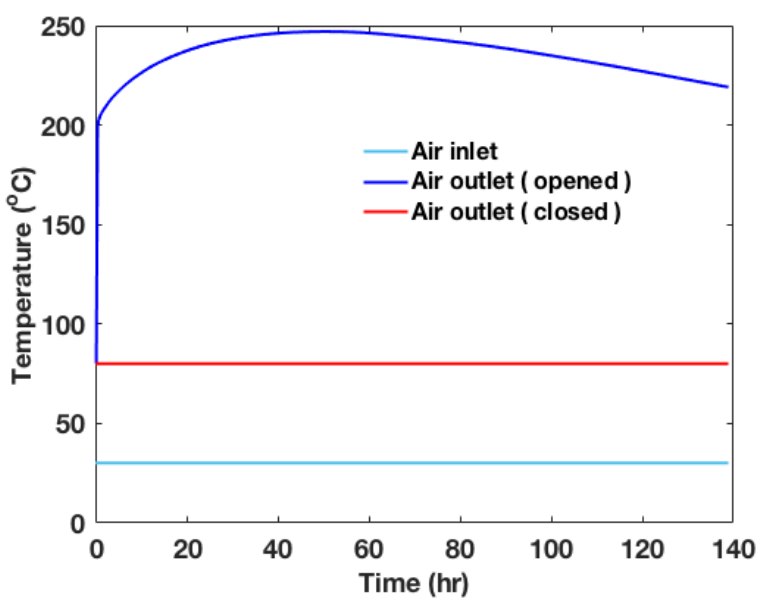

Figure 10-55 Air inlet and outlet temperatures during loss of two DRACS loops

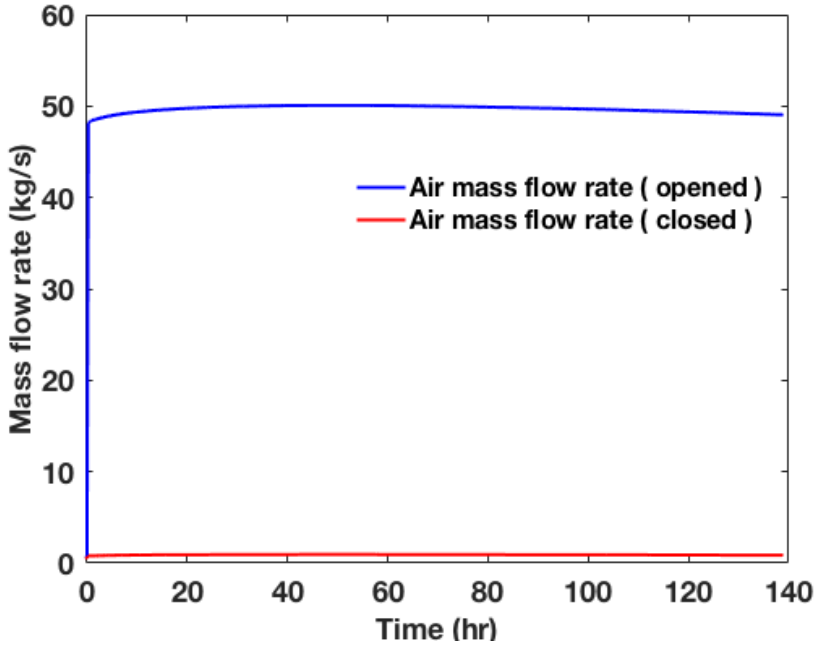

Figure 10-56 Mass flow rates of the air loops during loss of two DRACS loops

10.5.6. Heat Transfer from Reactor vessel to Silo Wall

AHTR mainly relies on DRACS as a passive means of removing decay heat during reactor shutdown. The decay heat can also transfer in solid structures by heat conduction, between argon gas gaps by thermal radiation and eventually to the underground surrounding. The thermal response of heat structures from the reactor vessel to the silo wall should be investigated under various transients to ensure the integrity of the reactor vessel, guard vessel and silo wall by staying within temperature limits. A literature review is carried out on reactor cavity cooling system (RCCS) designs for FHRs. In addition, a heat transfer analysis for AHTR is provided based on a parametric study of the thickness of thermal insulation to be applied on the reactor vessel.

Review of RCCS design: Liquid-Salt-Cooled Very High-Temperature Reactor (LS-VHTR)

LS-VHTR is a liquid-salt-cooled reactor design with passive safety systems [10.40]. It combines various technologies, including coated-particle graphite-matrix fuels, a liquid-fluoride-salt coolant, and high-temperature Brayton power cycles. Figure 10-57 shows a schematic of LS-VHTR [10.40]. A Reactor Vessel Auxiliary Cooling System (RVACS) is proposed for LS-VHTR, with its design adopted from the decay heat removal system for the sodium-cooled Super Power Reactor Inherently Safe Module(S-PRISM) [10.41]. The core baseline design was optimized for LS-VHTR to ensure the top-level safety with RVACS as its passive heat removal system.

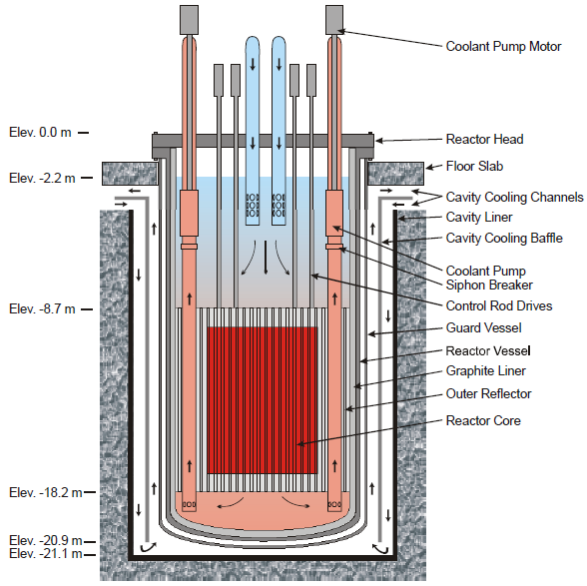

Figure 10-57 Schematic of LS-VHTR [10.40]

Ingersoll et al. [10.40] built a one-dimensional model for the LS-VHTR using RELAP5-3D and benchmarked it against a multidimensional ABAQUS model for the fuel block. The RELAP5-3D model consists of a RVACS as shown in Figure 10-58. The core barrel and an annulus inside the reactor vessel filled with cold salt act as a thermal blanket for the reactor. The dimension information of the RVACS is provided in Table 10-15.

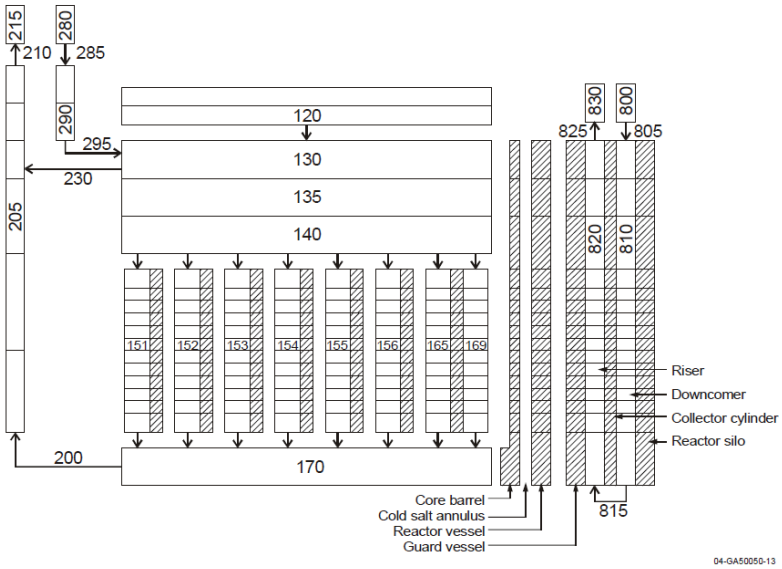

Figure 10-58 RELAP5-3D model of LS-VHTR [10.40]

Table 10-15 Geometry information of RVACS in LS-VHTR [10.40]

RVACS of LS-VHTR	
Reactor vessel inner diameter (m)	8.02
Reactor vessel wall thickness (m)	0.1
Gap between reactor vessel and guard vessel (m)	0.2
Guard vessel wall thickness (m)	0.025
Riser gap thickness (m)	0.178
Collector cylinder wall thickness (m)	0.0254
Collector cylinder insulation thickness (m)	0.0508
Active heat transfer length (m)	18.4

Some of the design parameters of LS-VHTR are listed in Table 10-16. A simulation of the LOFC accident is performed using the RELAP5-3D LS-VHTR model. When an LOFC is initiated, component 285 (flow source) linearly decreases to 0 in 10 s. The reactor receives the scram signal at 1 s after the accident is initiated and the control rods fully insert into the fuel at 3 s. The main heat transfer processes involved after reactor shutdown include natural circulation of the primary liquid salt in the reactor vessel; heat conduction in the core barrel, reactor vessel and guard vessel; and thermal radiation between the vessel wall and guard vessel. During LOFC, RVACS is the only decay heat removal system for the reactor in which air removes the decay heat to the environment by natural circulation.

Table 10-16 LS-VHTR nominal design parameters [10.40]

Core power (MW)	2,400
Mass flow rate (kg/s)	10,264
Core inlet temperature (°C)	900
Core outlet temperature (°C)	1000
Average fuel temperature (°C)	1093
RCCS/RVACS heat removal rate (MW)	6.2

In Figure 10-59, the predicted RVACS heat removal rate enhances overtime due to the primary heat up in the reactor that increases the temperature difference between the reactor vessel and the heat sink. After about 60 hours, the heat removal capability of RVACS exceeds the decay heat generation rate. The thermal performance of LS-VHTR is further illustrated in Figure 10-60. Right after the initiation of LOFC, a flow reversal phenomenon occurs in the reactor core and the primary salt flow changes from forced circulation to natural circulation. The temperatures shown in Figure 10-60 increase due to the imbalance between the decay heat generation rate and the heat removal rate by RVACS. The predicted maximum fuel temperature is about 200 °C lower than the FLiBe boiling temperature (1430°C), which provides in a considerably safe range.

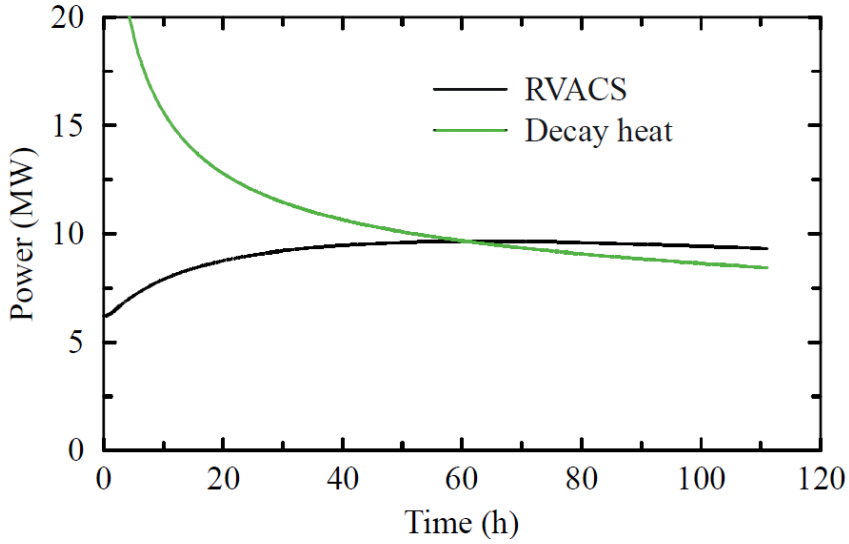

Figure 10-59 Comparison of RVACS heat removal rate and core decay heat generation rate during LOFC for LS-VHTR [10.40]

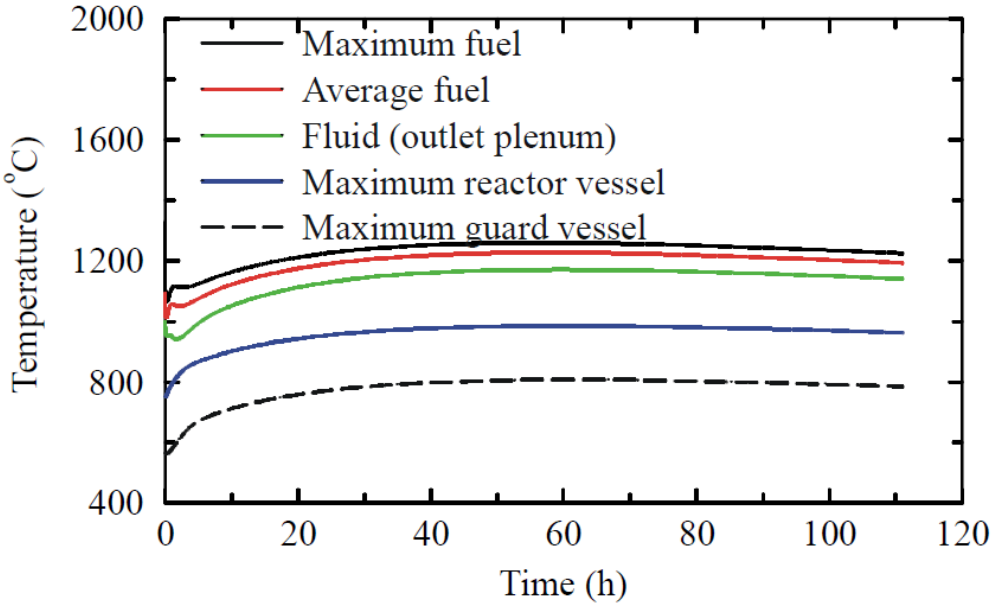

Figure 10-60 Thermal performance following a LOFC [10.40]

<u>Review of RCCS design: AHTR Vessel and Thermal Shields</u>

The heat losses and structure temperatures during various transients in AHTR have been investigated by Verma et al. [10.29]. Two thermal shields are utilized for the reactor silo cooling system to reduce the heat losses to the silo wall from 15 to 5 MW. The response of AHTR to an accident has been analyzed with passive decay heat removal by DRACS and

through two thermal shields. In this model, the reactor silo is assumed to be actively cooled to 27 °C. The inner shield is heated to temperatures above the freezing point of the primary salt to prevent salt freezing during reactor startup. After reactor startup, the heaters for the inner shield are turned off. The temperatures of the reactor vessel, and inner and outer shields are analyzed for two different surface emissivity values of the thermal shields, shown in Figure 10-61. The comparison of the two plots indicates the emissivity of the surfaces of those shields affects significantly the heat loss rate. In Figure 10-61 (a), the outer shield with a higher emissivity value has a higher heat loss rate and higher temperature differences between the vessel and the shields. Radiation heat transfer is the dominant mechanism to transfer heat from the reactor vessel to the silo wall. It is desirable to keep the silo concrete at a sufficiently low temperature range (below 100 °C). If the Reactor Silo Cooling System loses its cooling capacity, the temperature of the concrete may exceed 100 °C and then an active RVACS could be cooperated to remove the heat.

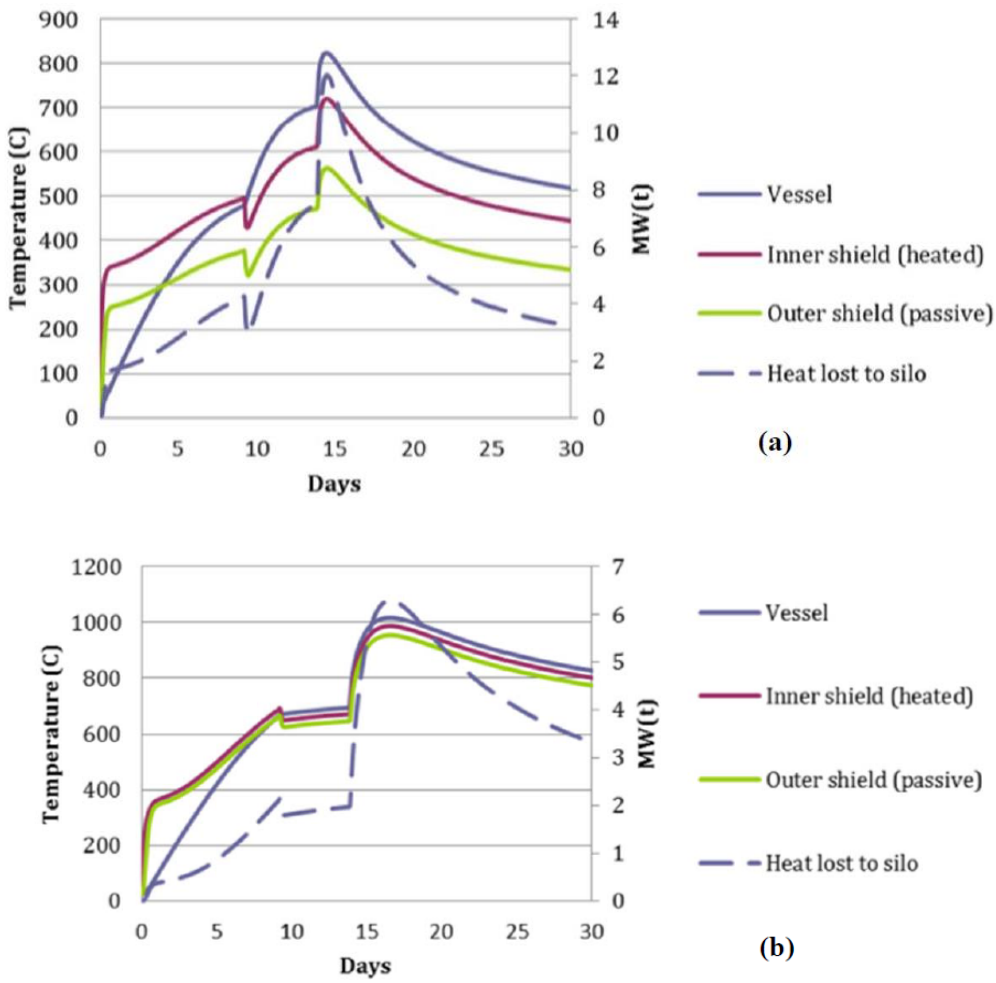

Figure 10-61. Response of AHTR to LOFC accident with: (a) high emissivity and (b) low emissivity of thermal shields [10.37]

Heat transfer from reactor vessel to silo wall model for AHTR

In the AHTR vessel heat loss model by Verma et al. [10.37], the silo wall is actively cooled during transients. This active cooling condition is not adequate when the reactor silo cooling system loses its electric power. Therefore, a design is proposed in this project based on entirely passive heat removal from the reactor vessel to the silo wall. A simulation of an LOFC accident is also performed using the AHTR RELAP5 model with the vessel model added. A constant temperature of 30 °C in the surrounding soil at 5 m away from the silo wall is assumed as one of the boundary conditions in this simulation. The design concept uses the environment as one of the heat sinks after reactor scram to remove the decay heat from the reactor core. However, it is challenging to justify the boundary condition of the environment. Therefore, the relatively large distance (5 m) is chosen as the cooling boundary. In this case, the effect of the thickness of the thermal insulation to the reactor vessel is also investigated to ensure the silo temperature is kept in a safe range. Figure 10-62 shows a schematic of the heat transfer path from the primary salt via the reactor vessel to the environment (soil). The thickness of various heat structures is mentioned in the report [10.37] as a design basis, including a 10-mm thick Hastelloy N liner, 50-mm thick Alloy 800H vessel wall, 200-mm thick argon gap No. 1, and a 25-mm thick guard vessel, etc. However, the thickness value of the argon gap No. 2 and silo wall are not listed in the design reference report. Therefore, a thickness of 200 mm is assumed for both the argon gap No. 2 and silo wall in this RELAP5 AHTR model. Heat structure properties used in the model are listed in Table 10-17. The thermal radiation model is activated between the thermal insulation wall and the guard vessel, and the guard vessel and the silo wall. The emissivity value of each surface is assumed to be 0.75 [10.37].

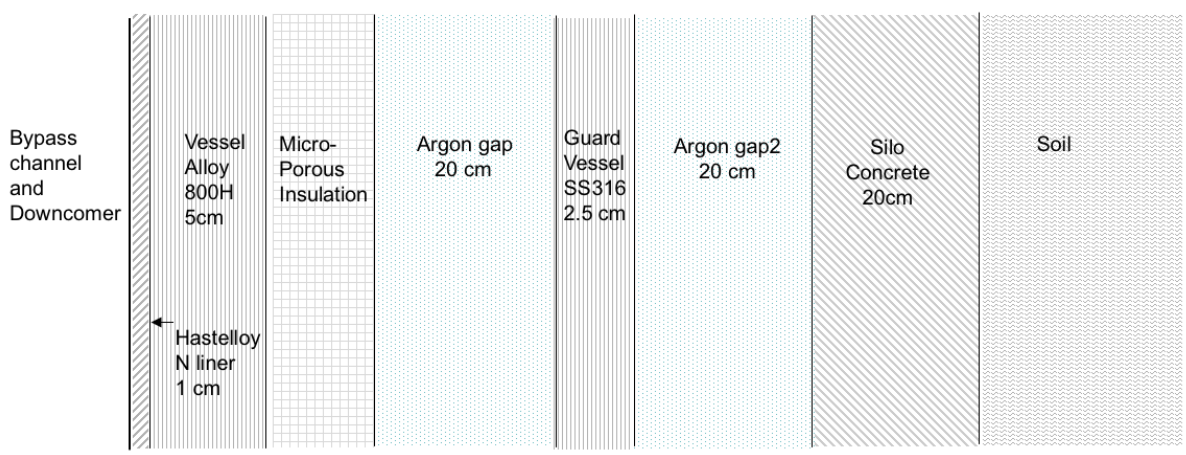

Figure 10-62. Schematic of the heat transfer path from the primary salt to the surrounding soil

Table 10-17. Thermal properties of heat structures

Material (T=700 °C)	Thermal conductivity (W/m-K)	Density (kg/m³)	Specific heat (kJ/kg-K)
C-C- composite	129	2200	1.903
Hastelloy N	23.6	8860	0.578
Alloy 800 H	24.7	7940	0.460
SS-316	16.3	8000	0.5
Micro-porous insulation	0.06	300	0.8
Concrete	0.8	2400	0.9
Soil	0.3	1600	1.480

Micro-porous insulation is chosen as the thermal insulation material to the reactor vessel wall due to its capability of high temperature conditions. The thickness of the insulation will affect the silo temperature. To keep the silo temperature below 80 °C during reactor normal operation, several thickness values are tested. Table 10-18 shows the silo wall temperature and the heat losses through the vessel wall during reactor normal operation with different thermal insulation thickness values. The heat losses are insignificant compared to the total reactor thermal power. In addition, compared to the analysis by Verma et al. [10.37], the constant soil temperature boundary at 5-m distance away from the silo wall reduces the heat loss significantly. The temperature distribution from the vessel wall to the soil surrounding for a 150-mm thick thermal insulation to the reactor vessel wall is shown in Figure 10-63. The thermal insulation provides the largest thermal resistance for the heat transfer process, which limits the temperature rises in the guard vessel and silo wall.

Table 10-18. Steady-state simulation results with different thermal insulation thickness values

Insulation thickness (mm)	Silo wall temperature (°C)	Heat loss through vessel wall (MW)
0	585	1.84
50	104.46	0.24
100	81.78	0.16
150	74.16	0.12

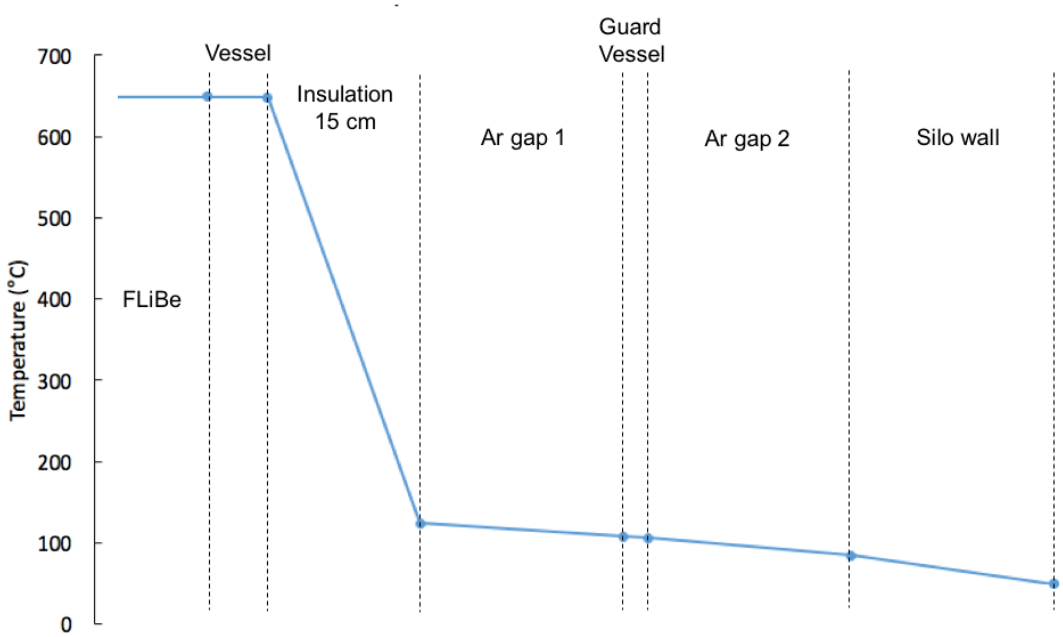

Figure 10-63. The temperature distribution from the vessel wall to the soil surrounding during reactor normal operation with a 150-mm thermal insulation to the reactor vessel

References

[10.1] X. Sun, G.L Yoder, R.N. Christensen, S. Shi, H.C. Lin, S. Zhang and X. Wu, "Thermal Hydraulics Phenomena Identification and Ranking Table (PIRT) for Advanced High Temperature Reactor (AHTR)," University of Michigan, Ann Arbor, MI (2017).

[10.2] H.C. Lin, S. Zhang, D. Diamond, S. Bajorek, R. Christensen, Y. Guo, G. Yoder, S. Shi, Q. Lv and X. Sun, "Phenomena identification and ranking table study for thermal hydraulics for Advanced High Temperature Reactor," *Annals of Nuclear Energy*, **124,** pp. 257-269 (2019).

[10.3] R. Romatoski and L. W. Hu, "Fluoride Salt Coolant Properties for Nuclear Reactor Applications: A Review," *Annals of Nuclear Energy*, **109**, pp. 635-647 (2017).

[10.4] H.C. Lin, Q. Lv, S. Shi, X. Sun, R. Christensen and G. Yoder, "Code validation of a scaled-down DRACS model in RELAP5/SCDAPSIM/MOD 4.0," *Annals of Nuclear Energy*, **124**, pp. 257-269 (2019).

[10.5] N. Zweibaum, R.O. Scarlat and P. F. Peterson, "Verification and Validation of a Single-Phase Natural Circulation Loop Model in RELAP5-3D," International Users Group Seminar (2013).

[10.6] C. Davis, "Implementation of Molten Salt Properties into RELAP5-3D/ATHENA," INLEEL\EXT-05-02658, Idaho National Laboratory (2005).

[10.7] N. Zweibaum, R. O. Scarlat and P. F. Peterson, "Verification and Validation of a Single-Phase Natural Circulation Loop Model in RELAP5-3D," International Users Group Seminar (2013).

[10.8] C. Galvez, "Design and Transient Analysis of Passive Safety Cooling Systems for Advanced Nuclear Reactors," Ph.D. dissertation, University of California, Berkeley

(2011).
[10.21] J. Richard, D. Wang, G. Yoder, J. Carbajo, D. Williams, B. Forget, and C. Forsberg. "Implementation of Liquid Salt Working Fluids into TRACE," Proc. the International Congress on Advances in Nuclear Power Plants (2014).
[10.22] D. Wang, G. L. Yoder, D. W. Pointer, and D. E. Holcomb, "Thermal Hydraulics Analysis of the Advanced High Temperature Reactor," *Nuclear Engineering and Design*, **294**, pp. 73-85 (2015).
[10.11] A. Tiwari, B. Allison, J. K. Hohorst, R. J. Wagner, and C. Allison, "Insertion of lead lithium eutectic mixture in RELAP/SCDAPSIM Mod 4.0 for Fusion Reactor Systems," *Fusion Engineering and Design*, **87**, pp. 156-160 (2012).
[10.12] H-C Lin, Q. Lv, S. Shi, X. Sun, R. Christensen and G. Yoder, "Code Validation of a Scaled-down DRACS Model in RELAP5/SCDAPSIM/MOD 4.0," *Annals of Nuclear Energy*, **124**, pp. 257-269 (2019).
[10.13] R. Hu, "SAM User's Guide for Beta Testing," Nuclear Engineering Division, Argonne National Laboratory, Lemont, IL (2016).
[10.14] D. Gaston, C. Newman, G. Hansen and D. Lebrun-Grandie, "MOOSE: A Parallel Computational Framework for Coupled Systems of Nonlinear Equations," *Nuclear Engineering and Design*, **239**, pp. 1768-1778 (2009).
[10.15] R. Hu, "SAM User's Guide for Beta Testing," Nuclear Engineering Division, Argonne National Laboratory, Lemont, IL (2016).
[10.16] R. Hu and T. Sumner, "Benchmark Simulations of the Thermal-Hydraulic Responses During EBR-II Inherent Safety Tests Using SAM," Proceeding of ICAPP'16, San Francisco, US, April 17-20 (2016).
[10.17] R. Hu and Y. Yu, "Pseudo 3-D Full-Core Conjugate Heat Transfer Modeling of Sodium Fast Reactors," Proceeding of NURETH-16, Chicago, US, August 30-September 4 (2016).
[10.18] P. Avigni, "On-line Refueling for the Advanced High Temperature Reactor," Doctoral dissertation, Georgia Institute of Technology (2017).
[10.19] F. Rahnema, B. Petrovic, P. Singh, P. Burke, D. Zhang, H. Noorani, X. Sun, G. Yoder, P. Tsvetkov, J. Zhang, and D. Ilas, "The Challenges in Modeling and Simulation of Fluoride-Salt-Cooled High-Temperature Reactors," Georgia Institute of Technology (2017).
[10.20] G.L. Yoder, Y. Elkassabgi, G. Leon, C. Fetterly, J. Ramos and R. Cunningham, "Vortex Diode Analysis and Testing for Fluoride Salt-Cooled High-Temperature Reactors," ORNL/TM-2011/425, Oak Ridge National Laboratory (2011).
[10.21] M.S. Lippy, "Development of a Minichannel Compact Primary Heat Exchanger for a Molten Salt Reactor," 15821, Master Thesis, Virginia Polytechnic Institute and State University (2011).
[10.22] G.L. Yoder, A.T. Bopp, D.E. Holcomb, W.D. Pointer, and D. Wang, "Advanced High Temperature Reactor Thermal Hydraulics Analysis and Salt Clean-up System Description," ORNL/TM-2014/499, Oak Ridge National Laboratory (2014).
[10.23] A. Qualls, B. Betzler, N. Brown, J. Carbajo, M. Greenwood, R. Hale, T. Harrison, J. Powers, K. Robb, and J. Terrell, "Preliminary Demonstration Reactor Point Design for the Fluoride Salt-Cooled High-Temperature Reactor," ORNL/TM-2015/700, Oak Ridge National Laboratory (2015).

[10.24] L. Li, C. Galvez, and P.F. Peterson, "Coupled RELAP5-3D and MCNP5 Baseline Core Model of the Annular Pebble Bed Advanced High Temperature Reactor (PB-AHTR)," Proc. the 19th International Conference on Nuclear Engineering (2011).
[10.25] M.A. Sprague, "A Comparison of NEK5000 and OpenFOAM for the DNS of Turbulent Channel Flow, "In Presentation at NEK5000 Users Meeting (2010).
[10.26] Q. Lv, H.C. Lin, X. Sun, R.N. Christensen, T.E. Blue, G.L. Yoder, D.F., Wilson, and P. Sabharwall, "Experimental Study of DRACS Thermal Performance in a Low-Temperature Test Facility," *Nucl. Tech*., **196**(2), pp. 319-337 (2016).
[10.27] Q. Lv, X. Wang, I.H. Kim, X. Sun, R.N. Christensen, T.E. Blue, G.L. Yoder, D.F., Wilson, and P. Sabharwall, "Scaling Analysis for the Direct Reactor Auxiliary Cooling System for FHRs," *Nucl. Eng. and Des.*, **285**, pp. 197-206 (2015).
[10.28] K. Hallinan and R. Viskanta, "Dynamics of a Natural Circulation Loop: Analysis and Experiments," Heat *Transfer Engineering*, **7**, pp. 43-52 (1986).
[10.29] R. Hu, "SAM Theory Manual," ANL/NE-17/4, Argonne National Laboratory (2017).
[10.30] A. Brooks and T. Hughes, "Streamline Upwind/Petrov-Galerkin Formulations for Convection Dominated Flows with Particular Emphasis on the Incompressible Navier-Stokes Equations," *Computer Methods in Applied Mechanics and Engineering*, **32**, pp. 199-259 (1982).
[10.31] D. Knoll and D. Keyes "Jacobian-free Newton-Krylov Methods: A Survey of Approaches and Applications," *Journal of Computational Physics*, **193**, pp. 357–397 (2004).
[10.32] A. Zukauskas and R. Ulinskas, "Heat Transfer in Tube Banks in Cross Flow," Taylor & Francis (1988).
[10.33] D. Briggs and E. Young, "Convection Heat Transfer and Pressure Drop of Air Flowing across Triangular Pitch Banks of Finned Tubes," *Chem. Eng. Prog. Symp. Ser,* **59**(41), pp. 1-10 (1963).
[10.33] S. Churchill and H. Chu, "Correlating Equations for Laminar and Turbulent Free Convection from a Vertical Plate," *International Journal of Heat and Mass Transfer*, **18**(11), pp.1323-1329 (1975).

[10.34] D. Williams, "Assessment of Candidate Molten Salt Coolants for the NGNP/NHI Heat Transfer Loop," ORNL/TM-2006/69, Oak Ridge National Laboratory, Oak Ridge, TN (2006).
[10.35] C. Davis, "Implementation of Molten Salt Properties into RELAP5-3D/ATHENA," INLEEL/EXT-05-02658, Idaho National Laboratory (2005).
[10.36] N. Anderson and P. Sabharwall, "Molten Salt Mixture Properties ($KF-ZrF_4$ and $KCl-MgCl_2$) for Use in RELAP5-3D for High-Temperature Reactor Application," *Nuclear technology*, **178**, pp. 335-340 (2012).
[10.37] V.K. Varma, D.E. Holcomb, F.J. Peretz, E.C. Bradley, D. Llas, A.L. Qualls, and N.M. Zaharia, "AHTR Mechanical, Structural, and Neutronic Preconceptual Design," ORNL/TM-2012/320, Oak Ridge National Laboratory, Oak Ridge, TN (2012).
[10.38] F. Rahnema et al., "Integrated Approach to Fluoride High Temperature Reactor and Licensing Challenges (FHR-IRP)," *FY 2016 Q4 Quarterly Report,* IRP-14-7829 (2016).
[10.39] V. Srinivasan, "Experimental and Numerical Investigation of Heat Transfer and

Pressure Drop in Flow through Spirally Fluted Tubes," Ph.D. Dissertation, The Ohio State University (1993).

[10.40] D.T. Ingersoll, K. T. Clarno, C. W. Forsberg, J. C. Gehin, R. W. Christensen, C. B. Davis, G. L. Hawkes, J. W. Sterbentz, T. K. Kim, T. A. Taiwo, and W. S. Yang, "Status of Physics and Safety Analyses for the Liquid-Salt-Cooled Very High-Temperature Reactor (LS-VHTR)," ORNL/TM-2005/218, ORNL, (2005).

[10.41] A. Hunsbedt and P. M. Magee, "Design and Performance of the PRISM Natural Convection Decay Heat Removal System," Proceedings of the International Topical Meeting on Safety of Next Generation Power Reactors, Seattle Washington, May 1–5, pp. 844–51, (1988).

11. Highlighting Contributions from National Laboratory Partner

Oak Ridge National Laboratory (ORNL) contributed to three main tasks during this project.

1. **Static corrosion testing in FLiBe**
   - Salt preparation
   - Capsule testing
   - Post-test evaluation
2. **Dynamic testing with FLiNaK using ORNL's Liquid Salt Test Loop (LSTL) facility**
   - Prepared test assembly for insertion in FLiNaK loop
   - Modeling of molten salt loop using TRACE
3. **Consulting**
   - PIRT -Neutronics, thermal hydraulics, materials/corrosion

Static corrosion testing in FLiBe

A new laboratory for beryllium handling was reconditioned and furbished with new equipment to provide the necessary means for FLiBe production and testing at ORNL (Figure 11-1). The new laboratory is located inside Building 4505, Room 26 under the Advanced Reactor Engineering group . The laboratory completed the refurbishment of the working space, installed recently acquired equipment and received the designed vessel, crucible and scrub systems for FLiBe purification.

A first batch of FLiBe salt was purified using a hydrofluorination process. The LiF and BeF_2 salts were weighed and placed in the processing crucible, and the crucible flange was installed, all in an inert glove box. The crucible was installed in the processing furnace and gas line connections were made to the HF, H_2 and Ar supply systems. The off-gas water bubbler system was prepared for operation by filling the tanks with water and installing bubbler lines. This system is designed to remove residual HF from the process exhaust gas stream before releasing the remaining H_2 and Ar to the hood exhaust. The furnace was heated to ~600 ^{o}C over a four day period while maintaining argon flow through the sweep region of the crucible and through the crucible dip tube in order to assure complete drying of the salt and prevent plugging of the dip tube during the melt process. The HF and H_2 gas flows were started at the end of CY 2017. When starting the HF flow, it was discovered that the HF bottle was operating at higher pressure than was expected. This can occur over time due to the anhydrous HF reacting with the bottle, forming hydrogen and increasing bottle pressure. The HF bottle was vented through a molecular sieve in order to remove the H_2. Once this was done, the HF and H_2 flows were reinitiated. The hydrofluorination process was operated for approximately 35 days and was completed on 11/27/2017.

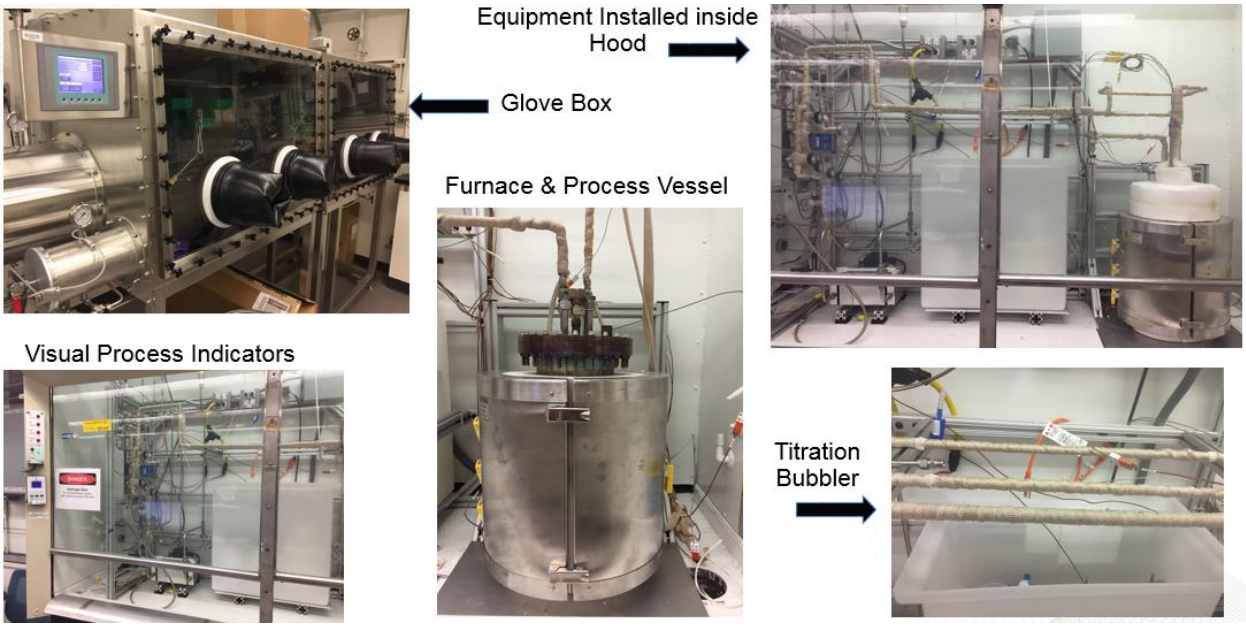

Figure 11-1 Finished new laboratory work space for FLiBe purification and testing inside building 4505-R26 at ORNL.

The process was stopped during this period on several occasions to weigh the HF bottle (to determine how much HF was being used) and because of issues with the HF flowmeter. During processing, water samples were taken from the bubbler clean-up system on 18 different occasions in order to assess the progress of the process. These samples were titrated to determine the amount of HF being used by the process vs that being passed through to the exhaust gas stream. A total of over 400 g of HF were used during hydrofluorination. As the amount of HF used in the salt hydrofluorination process itself becomes less, the process is nearing completion. After the hydrofluorination was complete, H_2 flow was maintained an additional one and a half days in order to ensure that all HF was removed from system. An Ar purge was then continued for an additional two days to remove all residual H_2. The furnace was then shut off, allowing the purified salt to freeze. The processing vessel was moved back into the glove box, and the purified salt was freed from the crucible vessel. Figure 11-2 shows the block of purified salt in the glove box. The crystalline structure within the salt as seen in this picture, is a good indication that the salt has been purified. However, ICP evaluation of the purified salt will give quantitative information about the salt purity.

Figure 11-2 First FLiBe purification batch completed (1.6 L).

During the second and third quarters, ORNL personnel designed and evaluated cleaning procedures for purified salt post-fragmentation and capsule loading processes inside the glove box. It should be noted that ORNL furnished and reconditioned a new laboratory for beryllium processing. Therefore, new research safety procedures were developed and evaluated to accommodate beryllium management at this new location. ORNL safety guidelines and procedures require the testing of beryllium levels before and after a salt cleaning process were initiated. Therefore, continuous swipe samples were taken around the laboratory and inside the glove box where the purified FLiBe salt resided. The swipes were evaluated internally (ORNL's Be detection lab) and produced acceptable Be levels. However, work inside the glove box was suspended until all samples results were known. Typical turn-around time for Be testing is around three weeks, but it may change depending on work load. Inner capsules were weighed and inserted into oxidation resistant capsules as planned. In addition, the ORNL team worked on the maintenance and instrumentat calibration of the FLiNaK loop in preparation for the dynamic corrosion testing planned as part of this IRP collaborative effort.

Afterwards the purified salt was broken up into small pieces, it was weighed and inserted into capsules along with test coupons in preparation for static corrosion testing. The Mo capsules were hydrogen fired using an Argon-Hydrogen mixture at 900 ^{o}C along with the graphite spacers. The specimens were located inside the Mo inner capsules with inner graphite spacers between them. The capsules were inserted into a furnace to perform isothermal tests on them with two main test durations of 500 hours and 2000 hours. ORNL performed additional testing using the produced FLiBe salt on other materials that are not part of this collaborative effort, as shown in Figure 11-3.

Sample Material	Capsule Material	Test Temperature		Test Duration	
		704 C	750 C	500 h	2000 h
316L SS	Mo	X		X	
Hastelloy N	Mo	X		X	
Hastelloy N	Mo		X	X	
Haynes 244	Mo	X		X	
Haynes 244	Mo		X	X	
Alloy #48	Mo	X		X	
Alloy #48	Mo		X	X	
Alloy #48	Mo		X		X
Alloy #49	Mo	X		X	
Alloy #49	Mo		X	X	
Alloy #49	Mo		X		X
Alloy #50	Mo	X		X	
Alloy #50	Mo		X		X
Alloy #51	Mo	X		X	
Alloy #51	Mo		X		X
Alloy #52	Mo	X		X	
Alloy #52	Mo		X		X
Graphite Sample	Mo		X	X	
Graphite Sample	Mo		X		X
SiC Sample	Mo		X	X	

Figure 11-3 Various materials tested using the produced FLiBe salt a) Summary of samples tested during first stage of program b) Capsules after 500 hrs test.

Dynamic testing in FLiNaK

Dynamic corrosion tests of the selected samples will be carried out using the Liquid Salt Test Loop (LSTL) at ORNL. Various technical meetings have been organized in order to discuss the action plan for this subtask. Corrosion tests included the design and implementation of a sample-holder insertion system capable of exposing the desired samples to salt flow. The selected design consisted of plates and cylindrical washers stacked together using the cylindrical washers as spacers for the different plate samples as shown in Figure 11-4. The sample-holder was designed considering the potential influence on corrosion tests from velocity gradients in the axial direction (perpendicular to main flow direction inside the sump tank) due to its proximity to the pump. The location of the sample-holder insertion port has been selected to be port number two of the sump tank. This port has flanged type connectors and maximizes the sample diameter to 1.8" OD. In addition, a retractable insertion system was designed to locate the sample-holder at the bottom of the sump tank while avoiding structural obstacles surrounding the port. The dynamic test is planned to be performed in the first quarter of FY19, but it is subject to the LSTL full operation schedule and availability.

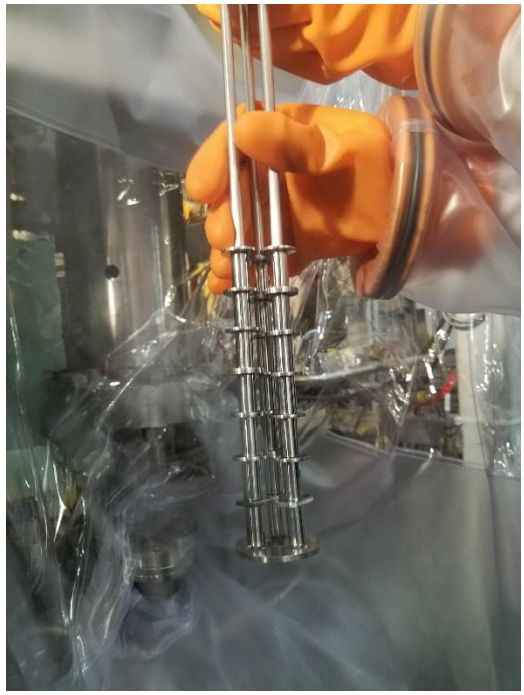

Figure 11-4 Sample holder for dynamic testing being inserted into ORNL's FLiNaK loop

A pictorial of the LSTL used for dynamic testing is shown in Figure 11-5. The loop was developed to provide infrastructure and operational knowledge to test high temperature salt systems. A non-intrusive inductive heating system technique was developed to provide thermal-fluid experimentation. The current test section provides pebble heating prototypic of nuclear fuel (volumetric). It demonstrated the use of SiC as a structural material for use in molten salt systems and is instrumented with various instrumentation.
The LSTL loop was modeled using the TRACE code. This code was modified during this project to support FHR analysis. Some of the main modification and highlight of the code includes the addition of several salt properties such as LiF-BeF2, KF-ZrF4,NaF-ZrF4 andLiF-NaF-KF. The correlations used in the code for calculation of pressure drop were modified and new ones were implemented, such as Ergun and Eisfeld. In addition, the following correlations were added to provide estimates of heat transfer parameters Wakao and Van Saden.

The code predicted various test scenarios of interest with satisfactory results. Figure 11-6 shows a pump coast down example ran during the test matrix selection.

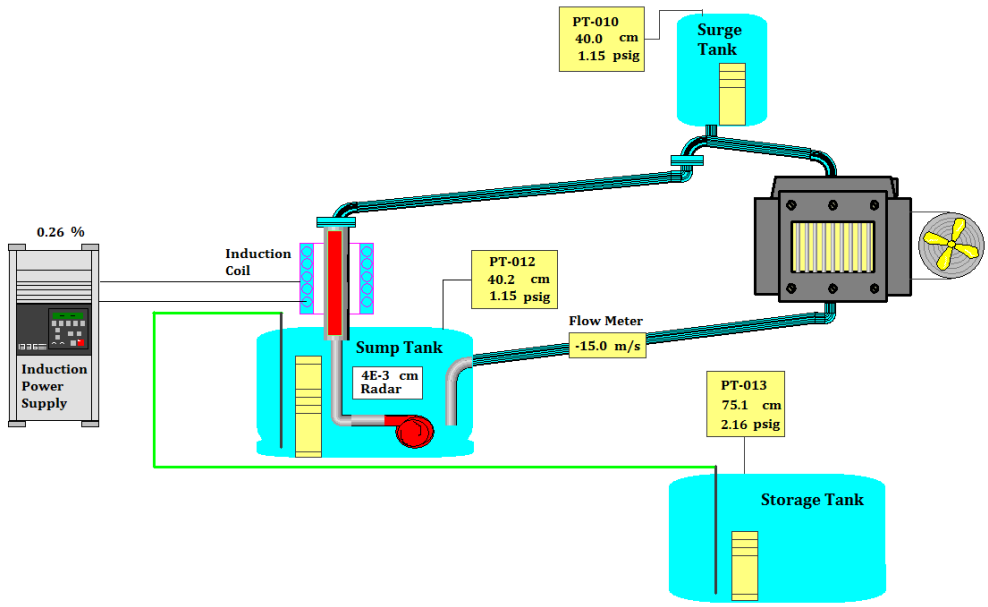

Figure 11-5 ORNL Liquid Salt Test Loop (LSTL) used for molten salt/corrosion dynamic testing

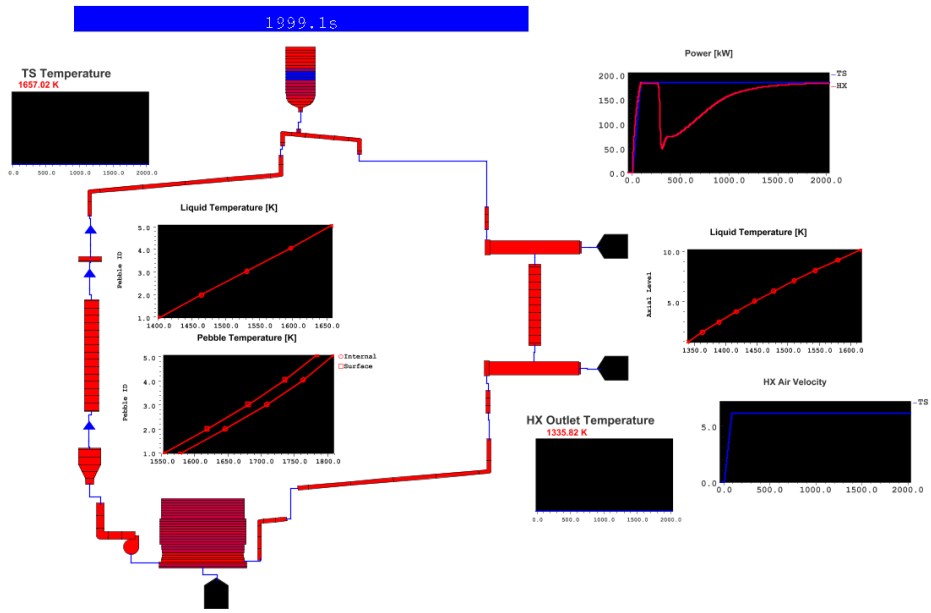

Figure 11-6 TRACE code simulation of a pump coast down in the LSTL facility

Consulting

Continuous consulting was provided during the duration of the collaborative effort. The ORNL team participated at the problem identification ranking table (PIRT) as panelist experts in the areas of thermal-hydraulics, materials/corrosion and neutronics.
Various experts in the mentioned areas provided comments and expertise advice at the specific PIRT events. Specifically, Dr. Dan Ilas attended PIRT celebrated in December 8-10, 2015 as a neutronics expert, Dr. Kevin Robb and Dr. Elvis Dominguez-Ontiveros provided expertise advise during the thermal-hydraulics PIRT event celebrated on May 24-26, 2016, Dr. Jim Keiser, Dr. Weiju Ran and Dr. Grady Yoder provided expert advise during the materials PIRT event celebrated in November of 2016. Dr. Domiguez-Ontiveros, Dr. Robb, Dr. Ilas and Dr. Yoder participated in the combined PIRT event in November 2016.
The consulting for corrosion testing/process/test specimens with Georgia Tech was provided by Dr. Dominguez-Ontiveros, Dr. Keiser , Dr. Muralidharan and Dr. Yoder.
All involved personnel from ORNL provided expertise advice and comments during the whole duration of the project.

12. Conclusion

This report constitutes efforts made on various IRP tasks during the whole performance period. As a starting point to determine the phenomena that potentially need to be addressed in support of licensing of the FHR M&S tools, this project convened four Phenomena Identification and Ranking Table (PIRT) panels in the areas of neutronics, thermal hydraulics, materials, and multiphysics. All the PIRT reports have been published. The relevant PIRT phenomena are summarized in this report. These results represent the broader, global issues related to M&S of FHRs specifically, and are expected to facilitate more accurate modeling as they are addressed.

FHR designs inherently produce orders of magnitude more tritium due to the use of FLiBe coolant. A methodology for calculating tritium production rates over the lifetime of a reference AHTR design was developed and implemented. For the reference case, 21.5 MCi of accumulated tritium remain at the end of the 100-year lifetime. Initial production rates are the highest due to 6Li in FLiBe at a rate of 13,700 Ci/day. Equilibrium production rates for all cases converge to roughly 3,700 Ci/day. Higher fuel enrichment (19.75% vs 9%) leads to a lower initial production rate but eventually converges to a similar rate at equilibrium.

In the area of liquid salt impurity removal, redox and corrosion control, the available purification methods were first discussed, including the liquid/liquid extraction using liquid Bi-Li which has been applied in MSBR and electrochemical purification which is developed based on Pyroprocessing. A method to analyze soluble/soluble redox reaction in a molten salt system and designed an electrochemical sensor for redox potential control was developed. Then, the methods to analyze electrochemical measurement data to obtain

the fundamental properties including the redox potential, diffusion coefficient and exchange current density were developed. All these fundamental information is important for salt purification system development. In measurements of corrosion products in the salts, a new analysis method for Cr fluorides in the salt was developed. In addition, the solubility of La_2O_3 in the salt as function of temperature was measured. In demonstration of the separation iodine ions from the molten salt, two kinds of working electrode materials (metal W and graphite) were investigated. Thermodynamic assessments for the Bi-Pr, Bi-Ce, and Bi-Er have been carried out through CALPHAD method using sub-regular model and two-sublattice model. The solubility of fission products (Pr, Ce, and Er) and the correlations between solubility and temperature were obtained. Furthermore, the activity coefficients of fission products in liquid bismuth at different concentrations and temperatures were also evaluated based on the assessed thermodynamic parameters. The activity and activity coefficient of K in liquid Bi at different concentrations for the temperature of 973 K was investigated. It is found activity continuously increases with concentration while activity coefficient decreases initially and then increases with the increasing concentration.

In the area of advanced visual instrumentation, the effort was focused on development, evaluations, and demonstrations of the FHR instrumentation options together with visual/optical reactor performance characterization methods using the TRIGA reactor a prototypic optically (visually) accessible reactor environment. The actual reactor operation data have been compiled and used to support sensitivity studies as well as model validation efforts. Performed simulations indicate significant noise levels that potentially may complicate reconstructions of localized values of in-core parameters in FHRs. The project accomplishments include developing two 3D reconstruction methods, assessment of emulation options for scaling experimental results from TRIGA to FHR conditions, and design of the multiphysics sensor probe concept realizing optical and mixed-field sensing capabilities within a single integrated probe configuration. One of the developed 3D reconstruction methods assumes exclusive fiberoptics-based technology options. The 2nd method is based on the integration of multi-field distributed sensing approaches using fiberoptics-based and optical (image-based) technology options. The obtained results demonstrate efforts towards developing methods allowing taking advantage of optical transparency while recovering in-core 3D information with high feature resolution. Results obtained for fiberoptics sensors suggest future use of this sensor type to supplement optical sensing. However, extensive R&D efforts are required. Similarity achievability has been investigated to assess usefulness of research reactor environments such as TRIGA in FHR-related R&D. The obtained results support developing methods allowing conversion and correlation of TRIGA data to FHRs.

For the heat exchanger task, a coupled heat and mass transfer model was developed and benchmarked against the experimental data in the literature to assist a DWHX design. The analysis indicated that the DWHX design with helium as the annular fluid can efficiently reduce the tritium leakage. Molten salt experiments in the future are necessary to further validate the coupled heat and mass transfer model.

In the area of V&V of neutronics codes/methods, a set of benchmark problems typical of FHRs has been developed. The problem was derived from the AHTR concept by simplifying the geometry and material specification of the original conceptual design while retaining the multiple heterogeneities and major physical characteristics of the core that are important from the neutronics point of view. The fuel assembly and core benchmark problems can be used with the desired complexity in "2D" and 3D configurations including single or multi-assembly to whole core problems. The continuous energy COMET method/code was used to solve these benchmark problems. The eigenvalue and fission density distributions predicted by COMET agree very well with those computed by MCNP. The benchmark calculations against Monte Carlo have also indicated that the continuous energy COMET can serve as an excellent method for obtaining high fidelity solutions (e.g., the stripe-wise fission density distribution) to FHR full core problems because of COMET's high fidelity and high computational efficiency. As a result, the stripe-wise fission density distributions generated by the continuous energy COMET can be taken as a reference solution to the stylized FHR benchmark problems.

Accurate neutronics analysis of Fluoride-salt High-temperature Reactors (FHRs) is challenged by the complex reactor core geometry combined with the double heterogeneity of TRISO fuel. Validation is not possible or at best is very limited due to the lack of prototypic experimental data, and therefore extended verification and cross-comparison of results obtained by several Monte Carlo codes was performed. Investigations and analyses were performed to address: (a) Impact of modeling approaches and sensitivity to nuclear data; (b) Verification of code performance through cross-verification of results; and, (c) Feasibility of detailed Monte Carlo simulations.

Three Monte Carlo codes were employed including SCALE, SERPENT and MCNP. A reduced-size core model consisting of a finite-height slice of a single fuel element was used. Sensitivity to modelling assumptions, as well as the impact of perturbation in dimensions, temperatures and cross sections were examined. Verification through cross-comparison of the results of the three Monte Carlo codes demonstrated that the codes produce consistent results when applied to carefully developed consistent models. Extrapolating requirements to full core simulations shows that a single or a very limited number of benchmark simulations is feasible, but it is still far from being practical, and development of improved and novel methodologies is needed.

In the area of thermal hydraulics V&V, codes/methods System-level code benchmark and validation using existing experimental data in the literature is carried out in our study. Compared to other RELAP5 versions, RELAP5/SCDAPSIM/MOD 4.0 is chosen for this study due to the flexibility of implementing the thermodynamic properties of molten salts and heat transfer correlations. On the other hand, SAM provides advanced numerical options and has demonstrated, to a certain degree, successful validation against experimental data related to SFRs. Both codes are chosen for thermal hydraulics code validation. The experimental data from the single-phase natural circulation test loop at Purdue University and LTDF at OSU are adopted for the study. Overall, the simulation results are in good agreement with the experimental data for both natural circulation and forced circulation flow regimes. Future benchmark and validation studies using molten salt experimental

data will be performed once experimental data from HT-HSTF become available. In addition, an AHTR model has been developed using RELAP5/SCDAPSIM/MOD 4.0 for evaluating the proposed DRACS design and reactor response of AHTR under various transient scenarios. System analyses for two transient scenarios, namely, LOFC and loss of two DRACS loops out of the three loops are performed. The simulation results of both scenarios demonstrate the single-wall fluted tube designs of DHX and NDHX for AHTR can effectively remove the decay heat from the reactor core in the two transient scenarios.

In the area of qualification of alloys for structural applications, results from the corrosion tests showed that the chromium content of alloys had an indirect correlation with the alloys' performance. Results have also shown that the impurities in molten salts have a significant effect on the corrosion behavior of alloys. It is indicated that an addition of moisture in tested range had a relatively smaller effect on the corrosion behavior of alloys. However, an addition of metal fluorides, like NiF_2, had a significant effect on the intergranular degradation of Hastelloy N and other alloys. As there is a finite amount of impurities in the limited amount of salts used for static corrosion tests, the effect of salt volume on the corrosion rate was evaluated. The overall corrosion increased with an increase in the salt volume, which indicates that the impurities are consumed in the corrosion reaction over time, and the salt volumes used in a test can have an effect on the measured degradation rate. Results also indicated that the corrosion rate decreases over time due to the consumption of a limited amount of impurities in the salt. In most FHR designs a significant amount of graphite will be used, which will come in touch with the molten salt and may even come in touch with other structural alloys. To see the effect of the presence of graphite on structural alloys, initial set of tests were carried out with pure elements in graphite crucible. It was found that chromium and tungsten readily formed carbides at the surface during these tests. The surface carbide layer was found to significantly increase the corrosion resistance of chromium in a molten FLiNaK environment. Furthermore, results from this work have indicated that the carbonates in the molten salt could be a probable mechanism for the carbon transportation in molten fluoride salts. This provides a mechanism to slow down corrosion of alloys in molten fluoride salts.